

AD-A205 188

4

CHEMICAL
RESEARCH,
DEVELOPMENT &
ENGINEERING
CENTER

CRDEC-SP-88031

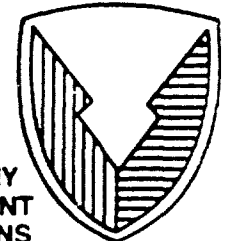
PROCEEDINGS OF THE 1987 SCIENTIFIC
CONFERENCE ON OBSCURATION AND
AEROSOL RESEARCH

Elmer H. Engquist
Karen A. Sistek

BATTELLE - EDGEWOOD OPERATIONS
Edgewood, Maryland 21040

October 1988

DTIC
ELECTE
S 6 MAR 1989 D
E



U.S. ARMY
ARMAMENT
MUNITIONS
CHEMICAL COMMAND

This document has been approved
for public release and may be
distributed in unlimited.

Aberdeen Proving Ground, Maryland 21010-5423

REPRODUCED FROM
BEST AVAILABLE COPY

89 3 06 137

Disclaimer

The findings in this report are not to be construed as an official Department of the Army position unless so designated by other authorizing documents.

Distribution Statement

Approved for public release; distribution is unlimited.

REPORT DOCUMENTATION PAGE				Form Approved OMB No. 0704-0188	
1a. REPORT SECURITY CLASSIFICATION UNCLASSIFIED			1b. RESTRICTIVE MARKINGS		
2a. SECURITY CLASSIFICATION AUTHORITY			3. DISTRIBUTION / AVAILABILITY OF REPORT Approved for public release; distribution is unlimited.		
2b. DECLASSIFICATION / DOWNGRADING SCHEDULE			4. PERFORMING ORGANIZATION REPORT NUMBER(S) CRDEC-SP-88031		
4. PERFORMING ORGANIZATION REPORT NUMBER(S)			5. MONITORING ORGANIZATION REPORT NUMBER(S)		
6a. NAME OF PERFORMING ORGANIZATION Battelle-Edgewood Operations		6b. OFFICE SYMBOL (if applicable)	7a. NAME OF MONITORING ORGANIZATION		
6c. ADDRESS (City, State, and ZIP Code) 2113 Emmorton Pk. Road - Suite 200 Edgewood, Maryland 21040			7b. ADDRESS (City, State, and ZIP Code)		
8a. NAME OF FUNDING / SPONSORING ORGANIZATION CRDEC		8b. OFFICE SYMBOL (if applicable) SMCCR-RSP-B	9. PROCUREMENT INSTRUMENT IDENTIFICATION NUMBER		
8c. ADDRESS (City, State, and ZIP Code) Aberdeen Proving Ground, Maryland 21010-5423			10. SOURCE OF FUNDING NUMBERS		
		PROGRAM ELEMENT NO	PROJECT NO.	TASK NO.	WORK UNIT ACCESSION NO.
			1C161102	A71A	
11. TITLE (Include Security Classification) Proceedings of the 1987 Scientific Conference on Obscuration and Aerosol Research					
12. PERSONAL AUTHOR(S) Engquist, Elmer H.; and Sistek, Karen A.					
13a. TYPE OF REPORT Special Publication		13b. TIME COVERED FROM 87 Jun to 87 Jun	14. DATE OF REPORT (Year, Month, Day) 1988 October		15. PAGE COUNT 735
16. SUPPLEMENTARY NOTATION COR: Edward W. Stuebing, Ph.D., SMCCR-RSP-B, (301) 671-3089					
17. COSATI CODES			18. SUBJECT TERMS (Continue on reverse if necessary and identify by block number)		
FIELD	GROUP	SUB-GROUP	Obscurants, Aerosols, Absorption, Infrared, Plumes (A)		
15	06	02	Obscuration, Sizing, Transmission, Light Scattering, Extinction, Smoke (continued on reverse)		
19. ABSTRACT (Continue on reverse if necessary and identify by block number) In this report, 54 papers presented at the 1987 Scientific Conference on Obscuration and Aerosol Research are included under the headings of Physical and Chemical Properties of Aerosols, Aerosol Characterization Methods, and Optical Properties of Aerosols.					
20. DISTRIBUTION / AVAILABILITY OF ABSTRACT <input checked="" type="checkbox"/> UNCLASSIFIED/UNLIMITED <input type="checkbox"/> SAME AS RPT <input type="checkbox"/> OTIC USERS			21. ABSTRACT SECURITY CLASSIFICATION UNCLASSIFIED		
22a. NAME OF RESPONSIBLE INDIVIDUAL SANDRA J. JOHNSON			22b. TELEPHONE (Include Area Code) (301) 671-2914		22c. OFFICE SYMBOL SMCCR-SPS-T

UNCLASSIFIED

18. SUBJECT TERMS (continued)

Aerosol properties

Electromagnetic scattering
Millimeter wave radiation
Submillimeter wave radiation
Visible radiation
Electromagnetic waves
Spherical particles
Mie scattering
Rayleigh scattering
Raman scattering
Concentration sampling
Particle dynamics
Diffusive mixing
Aerosol growth
Nucleation
Smoke generation
Aerosol generation
Photoionization
Conductivity
Chemical characterization
Phosphorus smoke
Fluorescence
Aerosol clusters
Spheres
Cylinders
Rough particles
Irregular particles
Nonspherical particles
Particle aggregates
Particle chains
Infrared emission
Cooperative scattering
Dependent scattering
Multiple scattering
Radiative transfer
Coagulation
Condensation
Liquid drop
Drop growth
Fog oil smoke
Diesel oil smoke
Particle mechanics
Atmospheric optics
Atmospheric dispersion
Cloud dynamics
Scavenging
Aerosol collectors
Aerosol elimination
Aerosol characterization
Particle sizing
Hygroscopic smokes
Particle size distribution
Particle orientation distribution

Optical constants
Optical properties
Anomalous diffraction
Attenuated total reflection
Reflection spectroscopy
ATR
Far-infrared
Refractive index
Index of refraction
Inversion
Inversion techniques
Gypsum
Natural minerals
Minerals
Metal
Metallic particles
Powdered minerals
Complex refractive index
Effective media
High energy laser
Particles
Aerosol particles
SERS
Surface Enhanced Raman Scattering
Dielectric particles
Conducting particles
Cylindrical particles
Fibers
Conducting fibers
Gas-aerosol reactions
Transport phenomena
Aerosol measurement
Spheroids
Laser pulses
Optical pulses
Pulse propagation
Clouds
Laser
Radiation transport
Fourier analysis
Plume mechanics

UNCLASSIFIED

PREFACE

The 1987 Chemical Research, Development and Engineering Center Scientific Conference on Obscuration and Aerosol Research was held 26-30 June 1987 at the Edgewood Area Conference Center of Aberdeen Proving Ground, Maryland. The Conference is held annually, the last full week in June, under the direction of Dr. Edward Stuebing, Research Area Coordinator, Aerosol Science, from whom it receives its unique and productive character.

The Conference is an informal forum for scientific exchange and stimulation amongst investigators in the wide variety of disciplines required for Aerosol research and a description of an obscuring aerosol and its effects. The participants develop some familiarity with the Army aerosol and obscuration-science research programs and also become personally acquainted with the other investigators and their research interests and capabilities. Each attendee is invited to present any aspect of a topic of interest and may make last minute changes or alterations in his presentation as the flow of ideas in the Conference develops.

While all participants in the Conference are invited to submit papers for the Proceedings of the Conference, each investigator, who is funded by the Army Research Program, is requested to provide one or more written papers that document specifically the progress made in his funded effort in the previous year and which indicate future directions. Also, the papers for the Proceedings are collected in the Fall to allow time for the fresh ideas that arise at the Conference to be incorporated. Therefore, while the papers in these proceedings tend to closely correspond to what was presented at the Conference, there is not an exact correspondence.

The reader will find the items relating to the conference itself, photographs, the list of attendees, and the agenda, in the appendixes following the papers and the indexes pertaining to them.

The use of trade names or manufacturers' names in this report does not constitute an official endorsement of any commercial products. This report may not be cited for purposes of advertisement.

Distribution of this document is limited to conference attendees to reduce the risk of its unauthorized disclosure while providing a valuable exchange of unclassified information. The proceedings are not to be used as reference material for other persons or organizations. It is incumbent on the recipient to safeguard the contents, control the dissemination, and destroy properly in accordance with DoD Industrial Security Directive 5220.22-M or Information Security Directive 5220.1-R.

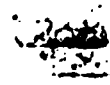
Reproduction of this document in whole or in part is prohibited except with permission of the Commander, U.S. Army Chemical Research, Development and Engineering Center, ATTN: SMCCR-SPS-T, Aberdeen Proving Ground, Maryland 21010-5423. However, the Defense Technical Information Center and the National Technical Information Service are authorized to reproduce the document for U.S. Government purposes.

This report has been approved for release to the public.

Blank

CONTENTS

	Page
I. AEROSOL DYNAMICS	11
DETERMINATION OF LIQUID VAPOR PRESSURES FROM SINGLE PARTICLE GEOMETRICAL RESONANCES G. O. Rubel	13
LIQUID DROP EVAPORATION DYNAMICS BY ACOUSTIC LEVITATION IN A HORIZONTAL WIND TUNNEL M. Seaver and T.J. Manuccia	17
A THEORY OF VERTICAL PNEUMATIC TRANSPORT IN A DRAFT TUBE (TRANSPORT LINE) AT CHOKING H. Littman and M. H. Morgan III	23
MEASUREMENT OF THE CONDENSATION COEFFICIENT OF WATER IN THE UMR CLOUD SIMULATION CHAMBER D. R. White, J. L. Kassner, J. C. Carstens, D. E. Hagen, J. L. Schmitt, D. J. Alofs, A. R. Hopkins, M. B. Trueblood; and M. W. Alcorn	29
PHOTO-OXIDATION OF SULFUR DIOXIDE WITH OH RADICAL IN THE PRESENCE OF WATER VAPOUR AND AMMONIA TO FORM CONDENSATION NUCLEI Patrick M. Nolan and James P. Friend	39
THE COAGULATION AND DISPERSION OF NONSPHERICAL AEROSOL PARTICLES WITH INERTIAL MEMORY IN A TURBULENT FIELD I. Gallily and M. Pekarevich	95
"LIFT-OFF" OF BUOYANT HORIZONTAL PLUMES M. Poreh and J. E. Cermak	103
STUDIES IN AEROSOL FORMATION AND GROWTH H. Kosuge and J. R. Brock	107
II. AEROSOL CHARACTERIZATION METHODS	115
OPTICAL PROPERTIES OF SELECTED MINERALS, METALS, OPTICAL MATERIALS, SOOT, AND LIQUIDS Marvin R. Querry and David M. Wieliczka	117

Accession For	
NTIS GRA&I	<input checked="" type="checkbox"/>
DTIC TAB	<input type="checkbox"/>
Unannounced	<input type="checkbox"/>
Justification	
By _____	
Distribution/	
Availability Codes	
Dist	Avail and/or Special
A-1	



AEROSOL PARTICLE ANALYZER MEASUREMENTS
Philip J. Wyatt, Christian Jackson, David L. Hicks, and Yu-Jain Chang 129

PARTICLE DISCRIMINATION USING THE AEROSOL PARTICLE ANALYZER
J. R. Bottiger 139

SUPERRESOLUTION TECHNIQUE FOR AEROSOL HOLOGRAPHY
Peter D. Scott and David T. Shaw 151

AN ANALYTICAL EXPRESSION FOR THE AXIAL PRESSURE PROFILE IN A SPOUT-FLUID BED EQUIPPED WITH DRAFT TUBE
M. H. Morgan III and H. Littman 157

COMPUTER MODELING OF DIESEL FUEL/FOG OIL SMOKE CLOUD
Kenneth L. Evans and Tate T. H. Tsang 163

X-RAY FLUORESCENCE DETECTION OF MEDIUM AND HIGH Z AEROSOLS
George M. Thomson, Richard A. Markland, and Sandra M. Thomson 179

CLUSTERS: STUDIES OF AEROSOL PRECURSORS
W. B. Tzeng, J. J. Breen, R. G. Keesee, P. D. Dao, S. Morgan, and A. W. Castleman, Jr. 187

GENERAL REMARKS ON EQUILIBRIUM CONFIGURATIONS OF N POINT CHARGES ON A SPHERE
Burt V. Bronk and Robert H. Frickel 191

OPTICAL CONSTANTS OF MINERALS, LIQUIDS, AND METALS FROM THE MILLIMETER TO THE ULTRAVIOLET
R. J. Bell, R. W. Alexander, Jr., L. A. Newquist, R. Van Diver, M. A. Ordal, L. L. Long, and M. R. Querry 201

A NOVEL INTERFEROMETER FOR MEASUREMENTS OF OPTICAL PROPERTIES AT MILLIMETER WAVELENGTHS
R. J. Bell, R. W. Alexander, Jr., R. Van Diver, S. Fry, M. A. Ordal, L. L. Long, and L. Newquist . . . 217

SENSITIVITY OF FRACTAL ANALYSIS FOR DESCRIBING PARTICLE SHAPES
P. A. Lawless, M-T. Hsieh, and P. C. Reist 225

III. NONLINEAR EFFECTS AT HIGH ENERGY	237
TIME RESOLVED SPECTRA OF PLASMAS INITIATED BY SINGLE AEROSOLS: AN UPDATE A. Biswas, H. Latifi, L. J. Radziemski, and R. L. Armstrong	239
EXPERIMENTAL AND THEORETICAL ANALYSIS OF THE INTERACTION OF LASER RADIATION WITH FLUID CYLINDERS AND SPHERES D. R. Alexander, J. P. Barton, S. A. Schaub, M. A. Emanuel, and J. Zhang	251
ENERGY BALANCE IN LASER-IRRADIATED VAPORIZING DROPLETS A. Zardecki and R. L. Armstrong	273
EXPLOSIVE VAPORIZATION OF A SINGLE WATER DROPLET BY PULSED LASER RADIATION J. C. Carls and J. R. Brock	279
INDUCED TURBULENCE IN AEROSOL-LOADED ATMOSPHERES Shirish M. Chitanvis	289
IV. WORKSHOP: HANDLING INDIVIDUAL PARTICLES	303
OPTICAL LEVITATION OF SINGLE PARTICLES Thomas R. Lettieri	305
AEROSOL JET ETCHING OF FINE PATTERNS Y. L. Chen, J. R. Brock, and I. Trachtenberg	315
V. OPTICAL PROPERTIES OF AEROSOLS	321
STATUS OF THE MICROWAVE SCATTERING FACILITY (MSF) UPGRADE R. T. Wang	323
ANGULAR SCATTERING FROM SINGLE SUSPENDED CYLINDERS J. D. Eversole, H.-B. Lin, and A. J. Campillo	341
EFFECTS OF SIMPLE SHADOWING ON VARIATIONAL CALCULATIONS B. J. Stoyanov and R. A. Farrell	347
THE SCATTERING OF LIGHT FROM A DIELECTRIC KNOT R. D. Haracz, L. D. Cohen, and A. Cohen	357

SCATTERING FROM A HELIX AND RANDOMLY ORIENTED LONG CYLINDERS AND THE INFINITE CYLINDER THEORY APPROACH A. Cohen, R. D. Haracz, and L. D. Cohen	365
THE SCATTERING OF FEMTOSECOND OPTICAL PULSES BY SMALL DIELECTRIC SPHERES G. T. Bennett, E. S. Fry, W. E. White, P. Herb, G. W. Kattawar, and W. Xu	387
RADIATIVE TRANSFER CALCULATIONS FOR DETECTING A TARGET BEHIND OBSCURING ATMOSPHERES T. Duracz and N. J. McCormick	395
AN EXACT FORMULA FOR THE ACCURACY OF A CLASS OF COMPUTER SOLUTIONS OF INTEGRAL EQUATION FORMULATIONS OF ELECTROMAGNETIC SCATTERING PROBLEMS D. K. Cohoon	401
SCATTERING OF LIGHT BY FINITE CYLINDERS D. K. Cohoon	413
DETERMINATION OF MOLECULAR ORIENTATION AT THE SURFACE OF AN AEROSOL PARTICLE BY MORPHOLOGY DEPENDENT PHOTOSELECTION L. M. Folan and S. Arnold	443
THEORY OF ENHANCED ENERGY TRANSFER BETWEEN MOLECULES EMBEDDED IN SPHERICAL DIELECTRIC PARTICLES S. D. Druger, S. Arnold, and L. Folan	453
RAPID ACQUISITION OF RAMAN SPECTRA FROM OPTICALLY LEVITATED PARTICLES G. Moncivais, J. C. Carls, and J. R. Brock	467
THEORETICAL CALCULATION ON SCATTERING BY SPHEROIDAL PARTICLES AND COMPARISON WITH MICROWAVE EXTINCTION MEASUREMENTS Wan-Xian Wang and R. T. Wang	473
THE SIMPLEST RADIAL WAVE FUNCTIONS IN THE CALCULATION OF LIGHT SCATTERING BY A SPHEROIDAL PARTICLE W-X. Wang	489
ABSORPTION BY AGGREGATED SPHERES Leland Pierce and Herschel Weil	495
VARIOUS GEOMETRICAL DESIGNS FOR ELECTRODYNAMIC PARTICLE TRAPS AND THEIR CHARACTERISTICS H.-B. Lin, J. D. Eversole, and B. Bronk	513

EXPERIMENTAL INVESTIGATION OF POST BREAKDOWN EFFECTS	
A. Biswas, P. Shah, R. L. Armstrong, and L. J. Radziemski	521
THE SCATTERING OF ELECTROMAGNETIC RADIATION BY MULTILAYER, ANISOTROPIC PARTICLES WITH SPHERICAL SYMMETRY	
D. K. Cohoon	533
LIGHT SCATTERING BY ORIENTED AND RANDOMLY DISPERSED CHIRAL PARTICLES	
Shermila B. Singham	571
EXPERIMENTAL TEST OF A TIME-DEPENDENT INVERSE SCATTERING ALGORITHM	
R. A. Elliott, T. Duracz, and N. J. McCormick	581
BACKSCATTERING ENHANCEMENT OF WAVES IN RANDOM MEDIA	
V. K. Varadan, V. V. Varadan, and Y. Ma	591
ELECTROMAGNETIC ABSORPTION IN A CHIRAL COMPOSITE LAYER	
Vijay K. Varadan, Vasundara V. Varadan, and Akhlesh Lakhtakia	597
SUMMARY OF RECENT WORK AT THE UNIVERSITY OF MICHIGAN RELEVANT TO ELECTROMAGNETIC WAVE SCATTERING AND ABSORPTION BY SMALL PARTICLES	
Herschel Weil and Thomas M. Willis III	603
AVERAGE INTENSITY SCATTERED BY DENSELY DISTRIBUTED NONSPHERICAL PARTICLES	
Y. Ma, V. K. Varadan, and V. V. Varadan	613
BACKSCATTER ENHANCEMENT OF INFRARED AND OPTICAL RADIATION FROM FINITELY CONDUCTING PARTICLES WITH SMOOTH AND VERY ROUGH SURFACES--FIRST ORDER AND MULTIPLE SCATTER	
Ezekiel Bahar and Mary Ann Fitzwater	619
LIGHT SCATTERING BY AN ARBITRARILY CONFIGURED CLUSTER OF SPHERES	
K. A. Fuller and G. W. Kattawar	631
THE POSSIBILITY OF USING SEVEN DIMENSIONAL ELECTROMAGNETIC THEORY TO SOLVE THREE DIMENSIONAL LIGHT SCATTERING PROBLEMS	
D. K. Cohoon	645

OBLIQUE INCIDENCE RADIATIVE HEATING OF ANISOTROPIC AEROSOL PARTICLES WHOSE REGIONS OF CONTINUITY OF TENSORIAL ELECTROMAGNETIC PROPERTIES ARE DELIMITED BY COAXIAL CYLINDERS COVERED BY IMPEDANCE SHEETS	
D. K. Cohoon	667

INDEXES FOR PAPERS IN THESE PROCEEDINGS

A. Index of Authors of Papers in These Proceedings	707
B. Index of Authors' Organizations and Countries (if not U.S.A.) for Papers in These Proceedings	709

APPENDIXES

A. Photographs of Conference Attendees	711
B. List of Conference Attendees.	717
C. Conference Agenda	727

1. AEROSOL DYNAMICS

Blank

DETERMINATION OF LIQUID VAPOR PRESSURES
FROM SINGLE PARTICLE GEOMETRICAL RESONANCES

G. O. Rubel
U.S. Army Chemical Research, Development and Engineering Center
Aberdeen Proving Ground, Maryland 21010-5423

ABSTRACT

This paper presents a methodology for determining the evaporation rate and vapor pressure of arbitrary liquids using geometrical light scattering resonances. The technique involves the measurement of the 90 degree elastic light scattering from single droplets, and the detection of periodic resonances in the light scattering pattern resulting from constructive interference between surface waves and the incident beam. Using well known relationships between the resonance periodicity and the change in droplet size, the vapor pressure of dimethylphthalate is determined within ten percent of previously reported values.

INTRODUCTION

In the past, classical ASTM methods have been used to measure the vapor pressure of volatile liquids. Recently, a new method was introduced that uses electrodynamic trapping of single particles to determine droplet evaporation rates and their concomitant vapor pressures [1]. The technique rests upon using a combination of static and oscillating electric fields to balance the droplet against its own weight. By monitoring the time dependent droplet balancing voltage, we are able to determine the droplet evaporation rate. The method is rapid and highly accurate. In this paper, a technique for measuring liquid vapor pressures using 90 degree light scattering is introduced that eliminates the need for monitoring the droplet balancing voltage. By measuring the 90 degree light scattering during droplet evaporation, we are able to detect the geometrical resonances that appear due to constructive interference between refracted surface waves and the incident radiation. From the periodicity in the resonances, the time dependent droplet size is determined. Using classical expressions for continuum evaporation, the liquid vapor pressure is determined from the droplet evaporation rate.

EXPERIMENT

Electrodynamic suspension of single droplets has proven to be a valuable tool in the investigation of a wide range of phenomena in aerosol physics. The principle for droplet suspension is based on developing a phase lag between the droplet motion and the oscillating electric field. For linear electric fields, the droplet experiences a net time--averaged force that opposes the weight of the droplet. In addition, if a static electric field that exactly balances the particle weight is impressed across the chamber, the droplet remains stationary at the null point of the oscillating field. Successive droplet masses are determined from the successive balancing voltages, assuming constant droplet charge.

Figure 1 shows a schematic of the electrodynamic droplet suspension chamber, approximately 60 cm³

in volume, and the associated electrooptical circuitry. The static electric field is impressed across the top and bottom electrodes that are electrically insulated from the central electrode using two 200 volt d.c. power supplies in series. An oscillating voltage of 500 to 1000 volts is applied across the central electrode that establishes a linear electric field inside the chamber and provides the appropriate restoring force for the charged droplet. As the droplet evaporates, the static voltage is reduced to maintain the droplet at the null point of the chamber.

A dimethylphthalate (DMP) droplet is generated by applying a high voltage to a capillary tube that contains the DMP (index of refraction of 1.5138.) At a critical voltage, a spray of charged droplets is generated, and they are guided into the chamber using focusing fields. All droplets except one are removed from the chamber. The droplet is accurately positioned at the electrical null point by monitoring the light scattered by the droplet at 90 degrees (Fig. 1 .) Light from a 2 mW helium-neon laser (6328-A wavelength) is targeted onto the droplet and the light scattered at 90 degrees is detected with a split photodiode. The split photodiode consists of two diode panels that independently respond to the light scattered by the droplet. The signal from the two diodes is passed through a difference/sum amplifier that outputs into a digital multimeter. If the droplet is positioned at the null point, then the difference output reads zero. If the droplet moves up or down, the difference output will be nonzero, and the static voltage is adjusted to bring the difference output back to zero. The balancing voltage is recorded on a y-t recorder.

The sum output of the amplifier represents the total light scattered at 90 degrees by the droplet and is recorded on a y-t plotter that is driven by a quartz drive. The light is projected onto the split photodiode using a 32mm objective that is focused onto the droplet. The acceptance angle of the microscope is approximately 4 degrees. The initial droplet size is determined using a telemicroscope that is fitted with a scanning graticule. Using back illumination of the droplet, we were able to measure the droplet diameter within one micrometer.

RESULTS AND DISCUSSION

Figure 2 shows the measured 90 degrees far-field light scattering for an evaporating DMP droplet, the initial diameter of which is 84 micrometers. Because the chamber is unsaturated with DMP vapors, the droplet evaporates and resonances in the light scattering are observed. The signature of the resonance is that of a broad peak that is followed by two sharp peaks. The second sharp peak is superimposed onto a broad peak whose amplitude is smaller than the first broad peak. This distinctive pattern was also observed by Ashkin and Dziedzic [2] in the measurement of the radiation pressure on Cargille droplets the index of refraction of which is 1.51. Chylek et al. [3] showed that the sharp and broad peaks are associated with second and third order electric and magnetic resonances,

respectively. Interestingly, while the relative amplitudes of the peaks varies, their spacing remains invariant. In the present case, the spacing between successive resonances is 1.3 minutes. From Figure 2 we are able to establish an accurate measure of the time for the appearance of successive resonances as shown in the accompanying table.

As stated earlier, the appearance of a resonance is due to constructive interference between surface and incident waves, and this will only occur for specific droplet sizes. Chylek et al. [3] derived an expression for the separation between the resonances in terms of the liquid index of refraction that applied to droplets the size of which was very much greater than the incident wavelength. Using the Mie solution to single particle light scattering, they showed that the separation in the size parameter obeyed the relation

$$\Delta x = \frac{\tan^{-1}(m^2-1)^{1/2}}{(m^2-1)^{1/2}}$$

where m is the index of refraction and x is the droplet size parameter defined as the ratio of the droplet circumference to the radiation wavelength. For DMP, $\Delta x = 0.75$. At constant radiation wavelength, we then have a measure of the droplet size at successive resonance, namely $\Delta a = -0.75\lambda/2\pi$

One may use this relation to define the droplet radius at successive resonances, i.e.,

$$a_i = a_o - i(t) \frac{0.75\lambda}{2\pi}$$

Using continuum theory to model the transport of vapors away from the droplet, the liquid vapor pressure can be determined from the relation

$$P = -\frac{\rho RT}{2D_g M_w} \frac{\Delta a^2}{\Delta t}$$

where temperature, D_g is the gas phase diffusion coefficient, and M_w is the molecular weight of the vapor. Using the data in Fig. 2, along with the expression for the liquid vapor pressure, we obtain for DMP the vapor pressure 9.37×10^{-4} mmHg at 20C. This value is in good agreement with the literature value of 1.0×10^{-3} mmHg as reported by Frostling [4].

REFERENCES

1. G. Rubel, On the Evaporation Rate of Multicomponent Oil Droplets, *J. Colloid Interface Science*, Vol. 81, No. 1, 188, 1981.
2. A. Ashkin and J.M. Dziedzic, Observation of Optical Resonances of Dielectric Spheres by Light Scattering, *Applied Optics*, Vol. 20, No. 10, 1803, 1981.
3. P. Chylek, J.T. Kiehl, and M.K.W. Ko, Optical Levitation and Partial Wave Resonances, *Physical Review A*, Vol. 18, No. 5, 2229, 1978.
4. H. Frostling, Vapour Pressure Determinations of Phthalic Esters by Analysis of a Static Aerosol with the Aid of a Flame Ionization Instrument, *J. Aerosol Science*, Vol. 1, 341, 1970.

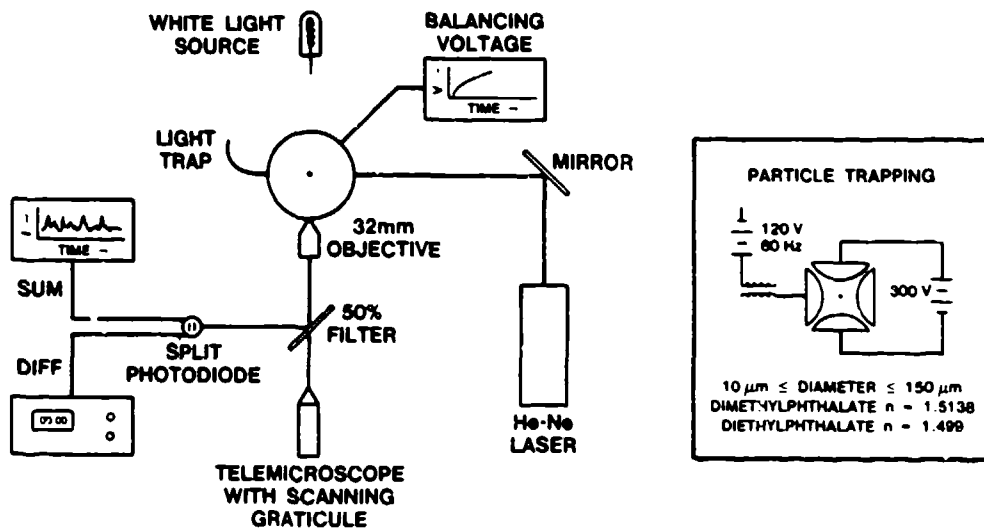


FIGURE 1. ELECTRODYNAMIC PARTICLE SUSPENSION CHAMBER AND ASSOCIATED ELECTROOPTICAL CIRCUITRY

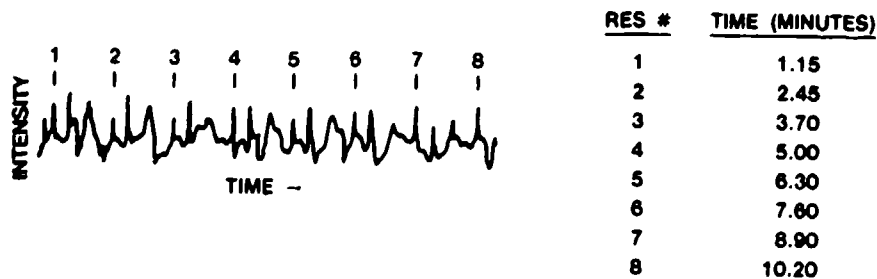


FIGURE 2. NINETY DEGREE LIGHT SCATTERING FROM AN EVAPORATING DMP DROPLET. Periodicity of resonances is shown.

LIQUID DROP EVAPORATION DYNAMICS BY ACOUSTIC LEVITATION IN A HORIZONTAL WIND TUNNEL

Mark Seaver and T. J. Manuccia
Optical Sciences Division
Code 6540
Naval Research Laboratory
Washington DC 20375

ABSTRACT

We have built the first combination acoustic levitator and horizontal wind tunnel. Comparison of our data for the evaporation of water with known water evaporation data indicates that while the precision is excellent the accuracy can be off by as much as 100%. Potential sources of this discrepancy are discussed. Qualitative experiments into the evaporation of 1-butanol/water mixtures demonstrate switching from one-phase to two-phase behavior and back in this partially miscible system. Future directions include solving the accuracy discrepancy, applying in-situ optical diagnostics to monitor gaseous species uptake by liquid drops, further improvements in apparatus design and additional studies of evaporating mixtures.

INTRODUCTION

Acoustic levitation offers two advantages over electrodynamic levitation when it comes to studies of single aerosol particles. First, one can easily set up a laminar flow of gas around the particle which effectively removes the chamber walls from consideration in the particle-gas system dynamics. The second advantage lies in the ability to levitate uncharged particles.

With these considerations in mind we have built the first combination wind tunnel and acoustic levitator. In this report we briefly describe the apparatus, evaluate instrument performance and discuss preliminary results from evaporation studies of the partially miscible mixture, 1-butanol/water.

APPARATUS

Acoustic levitation relies on a nonlinear acoustic effect¹. The levitation force in rectangular coordinates is given by

$$F_{\text{levitate}} = \left(\frac{5\pi p_1^2}{6\rho c^2} \right) kr^3 \sin(2kx)$$

Where p_1 is the acoustic intensity, ρ is the particle density, c is the speed of sound in the gas, k is the wave vector and r is the particle radius. Note that the r^3 term will cancel in the force balance expression making the levitation dependent only on particle density. In a cylindrical resonator such as ours the sin term is replaced by appropriate Bessel functions in the radial dimension. At frequencies which excite high order Bessel modes our system produces multiple trapping positions thus allowing future investigations into the effects of near neighbors on particle behavior.

We have built our cylindrical resonator around the working section of an open-jet horizontal wind tunnel. Using a modulated smoke wire for flow visualization we see laminar flow in the velocity range 50-300 cm/s. Drop sizes range from a maximum diameter of ~2mm down to ~100 μ m.

A minimum particle size arises because of an acoustic force node coaxial with the wind tunnel jet. Because of this node the horizontal restoring force depends on particle size. Thus, the node allow small drops to be pushed horizontally through a "mountain valley" by the drag force until the drops reach a point where the vertical force no longer exceeds the gravitational force. Operation of the resonator in a Bessel mode with no azimuthal nodes would enable particles of any size to be levitated.

Air conditioning equipment allows us to vary the relative humidity and gas composition. Constant temperature coils wrapped around the wind tunnel control the temperature to $\pm 0.2^\circ\text{C}$ over the range 10-35 $^\circ\text{C}$. Air temperature is measured with a thermocouple. Relative humidity is determined from wet bulb measurements. When liquids other than water are used the wet bulb wick is immersed in the appropriate liquid to give a temperature for the evaporating drop.

Drop size measurements are made from photographs taken with a microscope of known magnification. Because the acoustic field distorts the drops into oblate spheroids, both a horizontal and a vertical diameter

are measured. From these measurements the drop surface area and volume are calculated.

THEORY

The evaporation rate, in terms of surface area (S), for a volatile liquid in still air is given by

$$\left(\frac{dS}{dt}\right)_0 = \left(\frac{8\pi D_v M_d}{\rho_d R}\right) \left(\frac{p_\infty}{T_\infty} - \frac{p_d}{T_d}\right) \quad (1)$$

In this equation D_v is the diffusion coefficient of liquid vapor in the gas, M_d is the molecular mass of the liquid, ρ_d is the density of the liquid, R is the gas constant, p_∞ and p_d are the vapor pressures of the liquid in the gas stream and at the drop surface respectively and T_∞ and T_d are the gas and drop temperatures. For moving air this expression is multiplied by the so called ventilation coefficient, f_v . An empirical correlation for f_v has been given by Pruppacher and Beard².

$$f_v = 0.78 + 0.308 (NS_c)^{1/3} (NRe)^{1/2} \quad NRe > 4$$

In this equation NS_c (Schmidt number) = kinematic viscosity/liquid vapor diffusivity and NRe is the drop Reynolds number.

Our data can be compared with theory by plugging our measurements of NRe vs time into eq. 1 and integrating. The resulting calculated surface area vs time behavior is then compared with the surface area vs time data determined by the experiment.

EXPERIMENTAL

Figure 1 shows the results of five separate experiments measuring the evaporation of water under constant conditions. Each experiment started out with a drop of a different size. Therefore we have scaled the

time axis so that all drops of the same surface area coincide in time. Such scaling illustrates the precision of our measurements as well as definitively ruling out the possibility of contaminated water. Similar data precision has been obtained for all pure and mixed liquids evaluated to date. Such precision enables us to distinguish between the evaporation behavior of liquids at temperatures differing by as little as 1°C and wind speeds differing by 15%.

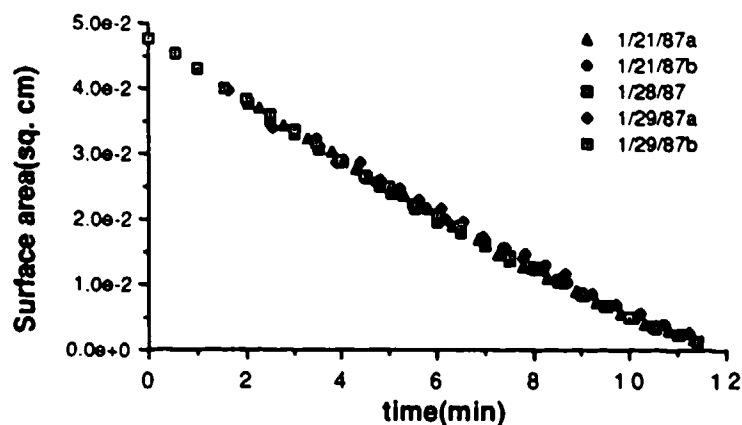


FIGURE 1. WATER EVAPORATION (135 cm/s; 12.6°C; 40% R.H.). Data is shifted in time so that drop surface areas coincide.

Slopes obtained for plots of S vs t for water at various wind velocities, relative humidities, and temperatures display differences with their calculated counterparts which range from 10% to 100%. Thus our accuracy is not reliable. One possible explanation for these discrepancies lies in our indirect determination of the drop temperature. If the actual drop is absorbing a small amount of energy from the acoustic field it will heat up. A 1.5°C temperature rise in the water drop would account for the largest discrepancy. An alternative explanation lies in the relative humidity measurement. However, much larger changes in relative humidity (>10%) are required to account for the observed disagreements. In the case of other pure liquids such as 1-butanol or undecane, the agreement between calculated evaporation slopes and measured slopes is

better than 15%. Further investigation into this aspect of the levitator is underway.

We have observed a puzzling behavior in the evaporation of 1-butanol/water mixtures. At relative humidities below 80% the S vs t curves for the mixture are smooth, reminiscent of fig. 1. When the relative humidity exceeds 80% one can visually observe two-phase behavior. That is one sees small drops of one liquid circulating on/in the larger drop. These small drops grow in size until the system coalesces back to a single phase. When we monitor the drop surface area as this behavior occurs we generate the S vs t plot seen in Fig. 2. It is interesting to note that the discontinuity in the curve coincides with the return to one phase behavior. We are also surprised by the fact that the evaporation rate of the butanol rich surface is not perturbed by the presence of increasing amounts of water rich material on or just below the drop surface until all the butanol rich liquid has evaporated.

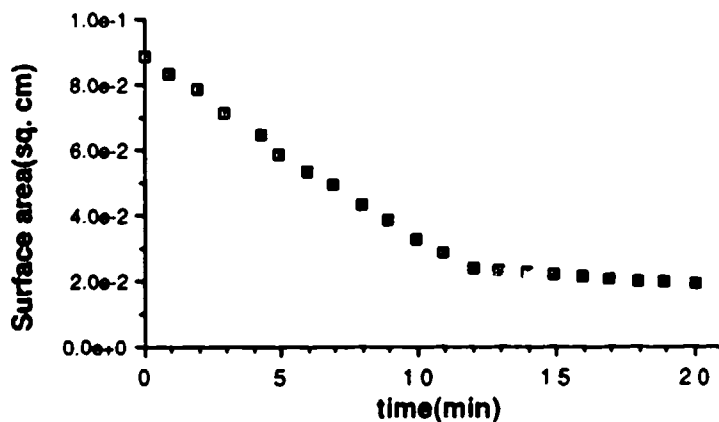


FIGURE 2. 1-BUTANOL/WATER EVAPORATION (9/1; 150 cm/s; 12.2°C; 92% R.H.). Two-phase behavior begins at about 5 min and ends at the discontinuity.

We have also seen discontinuous behavior in the evaporation of undecane/1-butanol mixtures and undecane/tridecane mixtures. Both of these latter mixtures are fully miscible systems whereas 1-butanol/

water is only partially miscible. The miscibility limits are ~8% 1-butanol in water and ~20% water in 1-butanol near room temperature.

SUMMARY

In summary, we have built and tested the first combination acoustic levitator and wind tunnel. Tests indicate that precise measurement of drop evaporation can be made under controlled conditions of wind speed, temperature and gas composition. The absolute accuracy of the method requires further testing to resolve the reason(s) behind discrepancies in the measured versus calculated evaporation of water. In the partially miscible system, 1-butanol/water, we observe evaporating drops switch from single-phase to two-phase systems and back. The two-phase behavior occurs only when the relative humidity exceeds 80%.

1 R. T. Beyer, Nonlinear Acoustics, (Naval Sea Systems Command, Dept. of the Navy, Washington DC, 1974) ch. 3.

2 K. V. Beard and H. R. Pruppacher, J. Atmos. Sci. **28**, 1455 (1971).

A THEORY OF VERTICAL PNEUMATIC TRANSPORT IN
A DRAFT TUBE (TRANSPORT LINE) AT CHOKING

H. Littman and M. H. Morgan III
Department of Chemical Engineering
Rensselaer Polytechnic Institute
Troy, New York 12180-3590

ABSTRACT

This paper presents a new theory for calculating the choking gas velocity in a draft tube. The only experimental information required is the axial pressure profile and the particle mass flowrate in the tube. Axial profiles for the voidage, gas and particle velocities, and slip velocity can then be calculated.

The choking gas velocity is important practically as it determines the minimum volumetric gas flowrate needed to move the particles through the line at a particular flowrate.

INTRODUCTION

In the design of equipment for spraying particulate aerosols, it is important to be able to predict the minimum gas velocity necessary to move the particles in dilute phase flow, and to determine the voidage of the particles exiting the draft tube (or transport line) and the mass flowrate of the particulates. There is no fundamental theory in the literature for predicting any of the aforementioned quantities. The partly theoretical approaches and data which exist are useful primarily in testing the general soundness of our approach.

In this paper, a new theory is presented for calculating the choking velocity, given only the axial pressure profile and the particle mass flowrate. Once the choking velocity is known the axial profiles for the voidage, gas and particle velocities, and slip can be calculated. Gas velocities close to choking are indeed practical because the air required to move a given amount of particles in a given time period is minimized.

THEORY

A. Field equations

The mass and momentum balance equations for the draft tube in Figure 1 are as follows:

$$\frac{d}{dz} (\epsilon_t u_t) = 0 \quad (1)$$

$$\frac{d}{dz} [(1-\epsilon_t)v_t] = 0 \quad (2)$$

$$\rho_f \frac{d}{dz} (\epsilon_t u_t^2) = -\epsilon_t \frac{dp_t}{dz} - B(u_t - v_t)^2 \quad (3)$$

$$\rho_p \frac{d}{dz} [(1-\epsilon_t)v_t^2] = -(1-\epsilon_t) \frac{dp_t}{dz} + B(u_t - v_t)^2 - (1-\epsilon_t)(\rho_p - \rho_f)g \quad (4)$$

Integrating equations 1 and 2, we obtain

$$\epsilon_t u_t = c_1 = W_{gt}/\rho_f A_t \quad (5)$$

$$(1-\epsilon_t)v_t = c_2 = W_{pt}/\rho_p A_t \quad (6)$$

Combining equations 3 and 4, we obtain the overall momentum balance for gas and particles

$$\rho_f \frac{d}{dz} (\epsilon_t u_t^2) + \rho_p \frac{d}{dz} [(1-\epsilon_t)v_t^2] = -\frac{dp_t}{dz} - (1-\epsilon_t)(\rho_p - \rho_f)g \quad (7)$$

Using equations 5 and 6, equation 7 can be placed in the following form

$$\gamma(\epsilon_t) \frac{d\epsilon_t}{dz} + (\rho_p - \rho_f)g (1-\epsilon_t) = -\frac{dp_t}{dz} \quad (8)$$

where

$$\gamma(\epsilon_t) = \frac{\rho_p c_2^2}{(1-\epsilon_t)^2} - \frac{\rho_f c_1^2}{\epsilon_t^2} \quad (9)$$

Equations 5, 6 and 8 can be solved for u_t , v_t and ϵ_t if the experimental pressure profile is available, and the boundary conditions specified.

B. Boundary conditions at choking and the choking gas velocity.

Although the boundary conditions at choking are unknown, reasonable assumptions can be made. Let us consider first the conditions at the top of the draft tube. Assume that

$$\frac{d\epsilon_t}{dz} = 0 \quad \text{at } z = H_t \quad (10)$$

Since equation 6 shows that $dv_t/dz = 0$ when $d\epsilon_t/dz = 0$, we are assuming that the particles are not accelerating at the top of the draft tube. In a long transport line, this is undoubtedly the case.

Using equation 10 in equation 8, the voidage at the top of the draft tube is

$$\epsilon_t = 1 - \frac{(-dp_t/dz)}{(\rho_p - \rho_f)g} \quad \text{at } z = H_t \quad (11)$$

At the inlet, we assume that

$$\gamma(\epsilon_t) = 0 \quad \text{at } z = 0 \quad (12)$$

so that by equation 8

$$\epsilon_t = 1 - \frac{(-dp_t/dz)}{(\rho_p - \rho_f)g} \quad \text{at } z = 0 \quad (13)$$

Equations 11 and 13 are the equations for calculating the voidage at the inlet and outlet to the draft tube. What is needed experimentally is the axial pressure profile which can then be differentiated numerically to determine the gradient. The inlet gradient is obviously more inaccurate because of the curvature there.

From equation 9

$$\frac{c_1}{c_2} = \left(\frac{\rho_p}{\rho_f}\right)^{1/2} \left(\frac{\epsilon_t}{1-\epsilon_t}\right) \quad \text{at } z = 0 \quad (14)$$

If the particle mass flowrate at choking is measured then c_1 can be calculated from equation 14. The volumetric flowrate of gas at choking is

$$Q_c = \frac{c_1}{\epsilon_t(H_t)} \frac{\pi}{4} d_t^2 \quad (15)$$

Q_c is the minimum gas needed to move the particles through the transport line and $\epsilon_t(H_t)$ is the minimum voidage. It is apparent that if our criteria for calculating $\epsilon_t(0)$ and $\epsilon_t(H_t)$ (equations 10 and 12) are correct then an axial pressure profile in the tube is all that is required to obtain the conditions at choking, solution of equation 8 gives the axial voidage profile in the draft tube and the average voidage in the draft tube is

$$\langle \epsilon_t \rangle = \int_0^1 \epsilon_t(z) d(z/H_t) \quad (16)$$

The gas and particle velocity and slip velocity profiles are calculated using equations 5 and 6.

C. The slip velocity at inlet.

For coarse particles the slip velocity is of the order of the terminal velocity (Capes and Nakamura, 1973, Day et al., 1987) so that for a particular system, we can write

$$\frac{u_t - v_t}{u_T} = k \quad \text{at } z = 0 \quad (17)$$

where the functional relationship is currently unknown.

Using equations 5, 6 and 17

$$k = \frac{\left\{ \left(\frac{\rho_p}{\rho_f}\right)^{1/2} - 1 \right\}}{u_T} \frac{c_2}{[1-\epsilon_t(0)]} \quad (18)$$

Grbavčić (1986) gives an axial pressure profile and the particle mass flowrate at choking for corn kernels ($\langle d_p \rangle = 8.08$ mm, $\rho_p = 1290$ kg/m³). With $u_T = 11.64$ m/s and $c_2 = 0.0661$ m/s, $k = 1.57$. This is a very reasonable number as Day et al. (1987) found $k = 1.8$ for 2.73 mm. glass spheres at the inlet to a spouted bed.

REFERENCES

- Capes, C.E. and K. Nakamura, Can. J. Chem. Eng. 51 31 (1973).
 Day, J.Y., M.H. Morgan III and H. Littman, Chem. Eng. Sci. 42 1461 (1987).
 Grbavčić, Z.B., 1986, private communication.

NOTATION

c_1, c_2	constants
d_t	tube diameter
g	gravitational acceleration
H_t	height of draft tube
p_t	fluid pressure (dynamic)
Q_c	volumetric flowrate of gas at choking
u_t	interstitial fluid velocity
v_t	interstitial particle velocity
W_{gt}	mass flow rate of gas
W_{pt}	mass flow rate of particles
z	vertical coordinate measured from tube inlet

Greek symbols

β	fluid-particle interphase drag coefficient
$\gamma(\epsilon_t)$	defined by eq. (9)
ϵ_t	voidage in draft tube
ρ_f	fluid density
ρ_p	particle density

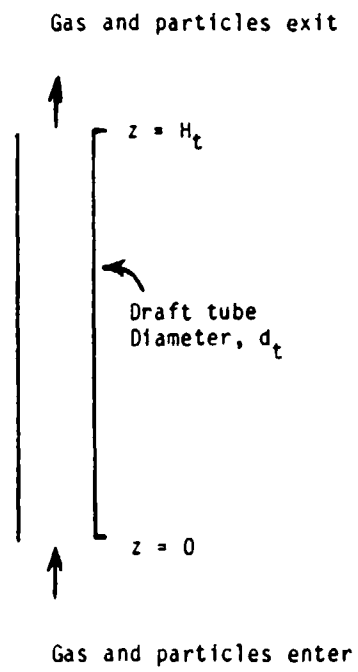


Figure 1. Schematic diagram of draft tube.

Blank

MEASUREMENT OF THE CONDENSATION COEFFICIENT OF WATER IN
THE UMR CLOUD SIMULATION CHAMBER

D.R. White, J.L. Kassner*, J.C. Carstens, D.E. Hagen, J.L. Schmitt,
D.J. Alofs, A.R. Hopkins, M.B. Trueblood, and M.W. Alcorn

RECENT PUBLICATIONS:

D.R. White, J.L. Kassner*, J.C. Carstens, D.E. Hagen, J.L. Schmitt, D.J. Alofs, A.R. Hopkins, M.B. Trueblood, W.L. Walker, and M.W. Alcorn, "University of Missouri-Rolla Cloud Simulation Facility: Proto II Chamber", Rev. Sci. Instrum., 58(5), May 1987.

ABSTRACT

Measurements of the condensation coefficient of water under conditions closely approximating those in natural atmospheric cloud have been made in the cooled-wall UMR cloud simulation chamber. Current measurements disclose a value of condensation coefficient near unity at the outset of the experiment, generally decreasing to lower values ($\sim .01$) as the experiment progresses. The significance of the magnitude of condensation coefficient in atmospheric cloud is briefly discussed.

*Current affiliation: D.D. Hulsart Co., Inc., Tuscaloosa, AL 35401

I. INTRODUCTION

The measurement of the condensation coefficient of water is important in a number of areas. We approach this problem from the cloud physics side, so our concern is with the dropwise condensation of water under normal atmospheric conditions. We begin by a few definitions and a brief discussion of why we regard the condensation coefficient to be significant in Cloud Physics.

The condensation coefficient, β , may be defined as the probability that a water molecule, upon striking a liquid water surface, sticks to that surface.

Condensation growth of a cloud drop is accompanied by heat conduction (due to the latent heat of condensation), and the thermal accommodation coefficient, α , is the thermal counterpart to β . It represents the extent to which "air molecules" accommodate to the temperature of the liquid surface (or the drop)

$$\alpha = \frac{E_i - E_r}{E_i - E_S}$$

where E_i = ave. energy/molecule of incoming stream
 E_r = ave. energy/molecule of reflected stream
 E_S^* = ave. energy/molecule of a stream corresponding
to surface temperature.

The most familiar form of drop growth theory is that adapted to the low supersaturations found in atmospheric clouds (e.g. Fitzgerald, 1970; Fukuta and

Walter, 1970; Carstens, 1979). Carstens' version may be written to reasonable approximation as follows:

$$(a + \lambda) \frac{da}{dt} = D_{\text{eff}} \frac{\rho_{\text{eq}}(T_{\infty})}{\rho_{\lambda}} [S(t) - S_{\text{sat}}(a)] \quad (1)$$

where

$$\lambda = D_{\text{eff}} \left(\frac{\ell_{\beta}}{D} + \frac{\ell_{\alpha} \tilde{\text{Ln}}_g}{pK} B \right), \quad (2)$$

$$\frac{1}{D_{\text{eff}}} = \frac{1}{D} + \frac{\tilde{\text{Ln}}_g}{pK} B, \quad (3)$$

$$\ell_{\beta} = \frac{4D}{\bar{v}} \frac{1}{\beta}, \quad (4)$$

$$\ell_{\alpha} = \frac{8K}{n_g R \bar{v}_g} \frac{\gamma-1}{\gamma+1} \frac{1}{\alpha}, \quad (5)$$

and where $S_{\text{sat}}(a)$ is normally written

$$S_{\text{sat}}(a) = 1 + \frac{r^*}{a} - \frac{Am_g}{a^3} \quad (6)$$

where r^* and A are constants, and m_g is the mass of dissolved salt (e.g. Rogers, 1976). Here $\rho_{\text{eq}}(T_{\infty})$ represents the ambient saturation vapor density; B is the slope of the vapor saturation curve at ambient temperature (i.e. $B = de_g/dT_{\infty}$); and the remaining terms are defined in Appendix A.

II. IMPORTANCE IN DROP GROWTH

A. Influence on growth rate

An important question is the following: "How rate influencing is the accommodation process, represented by the above parameters, in drop growth?" Under ordinary atmospheric conditions where water vapor is a dilute species with respect to air, one normally assumes that diffusion and conduction are the major rate controlling

steps in condensation growth. Plainly, however, if $\beta \rightarrow 0$ the condensation probability takes over as the rate controlling step. Condensation rates are rather different depending on which process predominates. The matter may be put briefly by looking at the "resistance" term in the transport of vapor molecules to the surface of a drop of radius a .

Suppose for the sake of argument we ignore latent heat in the formalism represented by equation(1). Then $D_{\text{eff}} = D$, and (1) can be rewritten

$$a \frac{da}{dt} = \frac{\rho_{\text{eq}}(T) [S(t) - S_{\text{sat}}(a)]}{\rho_l \frac{1+\lambda/a}{D}}$$

where $(1+\lambda/a)/D$ can be regarded as a resistance. For diffusion controlled growth this resistance is given simply by $\frac{1}{D}$; for growth controlled jointly by diffusion and surface accommodation this resistance may be written approximately by:

$$\frac{1 + \frac{\lambda}{a\beta}}{D} = \frac{1 + \frac{\text{Knudsen number}}{\beta}}{D}$$

where λ is the mean free path of diffusant (vapor) molecule. Thus if either $\beta \rightarrow 0$ or $a \rightarrow 0$ the process tends to be dominated by surface kinetics.

B. Significance in Cloud Physics

One of the nagging problems in cloud physics has been the repeated observation that cloud drop size distributions are broader than conventional (closed parcel) theory implies. The most popular explanation appeals to mixing, but inexplicably broad size distributions have also been observed (Jensen and Baker, 1986) for unmixed, i.e., adiabatic, parcels. In the unmixed case the value of β is of significance, for if it is sufficiently small it is capable of accounting for that portion of the distribution extending to the small-size end of the spectrum (Warner, 1969).

III. THE SEARCH FOR β

A. Existing measurements of β

The problem with which we are here concerned arises in establishing an experimental value for β . Past measurements disclose a scattershot of values ranging from 0.001 to 1.0, with cloud physicists often taking a value of around 0.036 as a sort of compromise (Pruppacher and Klett, 1978). It is in fact hard to justify a choice for β based on existing measurements. The general consensus among researchers is that the condensation coefficient for a "pure" surface ought to be unity (Mozurkewich, 1986); a common hypothesis involved to "explain" the variety of values

actually measured is that trace contaminants may strongly affect such measurements. Thus the existence of trace contaminants in the real atmosphere may mean that the condensation coefficient is significantly low under ordinary meteorological conditions.

B. The UMR program

There would seem to be little point in simply adding another value of β to the variety already in the literature. Yet this variety attests to the importance of the phenomenon and entreats a resolution to the problem. We have therefore started a systematic program aimed at measuring the condensation coefficient of water over a broad range of carefully controlled conditions. We have adopted the hypothesis that departures of β from unity ($\beta < 1$) are attributable to contamination. Hence an important part of our program will consist of precautions to ensure system purity, as well as subsequent deliberate introduction of selected "contaminants". In addition ambient supersaturations will be varied over a broad range, starting with magnitudes typical of atmospheric cloud, (~ 0.03) and extending to values approaching those associated with homogeneous nucleation ($S \sim 4.0$). High supersaturations are produced in the UMR fast expansion chamber. Low values are produced in the UMR cloud simulation chamber. The program has been started with the simulation chamber.

IV. MEASUREMENT OF β IN THE UMR SIMULATION CHAMBER

A. OVERVIEW OF THE FACILITY

The simulation facility consists of a dynamic cooled-wall expansion chamber which simulates in-cloud thermodynamics. The hallmark of this device is the close instantaneous tracking of its wall temperature with respect to that of the interior gas. This dynamic tracking suppresses the free convection that would otherwise occur at the walls, and permits prolonged experiments under well controlled conditions.

Sample preparation consists of (1) careful filtering of outside air, followed by (2) humidification, and (3) introduction of a prepared aerosol consisting of cloud condensation nuclei. This sample is introduced into the chamber where it is subjected to an isentropic expansion. The resulting cloud is analyzed by direct photography, laser scattering, or sample withdrawal.

B. Sample preparation

Preparation begins by drawing in outside air (1-2 l/sec) and passing it through a coarse surgical cotton filter. Water vapor is removed by passing the air through a

refrigerant dryer ($\sim 0^{\circ}\text{C}$), followed by a silica gel dessicant column and low temperature ($- 40^{\circ}\text{C}$) freeze dryer. Finally the air passes through a column of activated carbon granules (to remove residual organics), followed by an absolute filter rated at 99.97% efficient at $0.3 \mu\text{m}$.

The clean dry air is then humidified by passing it through a pair of humidification columns. (The dew point of the air at 17°C is consistently 0.355°C below the outlet temperature.)

Finally a prepared aerosol, monodisperse NaCl nuclei in these experiments, is introduced into the clean moist air sample at a mixing ratio of 1:100 or less. At this point the sample is ready to be introduced into the simulation chamber.

C. Sample introduction

The sample is introduced into the chamber from top to bottom. It first enters the inlet manifold chamber above the top and then is introduced uniformly into the chamber by means of 164 distinct ports located between the thermoelectric modules (so as not to interfere with their operation). This inlet system is duplicated as an outlet system at chamber bottom.

The chamber is flushed for a minimum of 15 minutes and continues until a measurement of the aerosol concentration shows an acceptably stable value for 5 min. When all systems are operating normally the chamber is sealed by closing the inlet and outlet valves. After a period of equilibration the chamber is ready for a cloud-generating expansion.

D. Aerosol preparation

Part of the clean dry air sample is used as a carrier gas for the four furnace NaCl aerosol generator (the procedure is described in some detail by Alofs et al., 1979). A boat containing granulated NaCl is placed in the first furnace region ($\sim 730^{\circ}\text{C}$). This gives off NaCl vapor which, when cooled ($\sim 300^{\circ}\text{C}$) in the region between furnaces # 1 and 2, forms an aerosol by homogeneous nucleation. Subsequent reevaporation and condensation narrows the size distribution (Kitani and Ouchi, 1967), producing mean sizes with diameters between 0.01 and 0.08 microns. (Geometric standard deviation $\sim .12$; CCN concentrations approach $10^5/\text{cm}^3$.)

The NaCl aerosol is further narrowed by passing it through a TSI classifier. Once a monodisperse CCN is produced, it is immediately introduced into the clean moist air system prior to entering the simulation chamber. Chamber concentrations currently

range from 25 to 150 CCN/cm³.

E. Isentropic cooling

The desired time-temperature-pressure control profile is loaded into the control computer. The computer uses this profile to generate a signal to the wall controllers and the expansion valve of the chamber.

Wallcooling

Wall temperature control is based on the use of thermoelectric modules to pump heat between the thin (0.96 cm) inner wall and thick (7.6 cm) fluid-thermostated outer wall. Wall temperature is controlled by separate analog controller circuits for each 15.25 x 30.5 cm control section of wall. Each controller receives two inputs, one from the output of a thermometer mounted on the wall section and the other from a control computer. Based on a comparison of these signals, the controller outputs a command signal to the programmable switching power supply which then causes the wall section to heat or cool so as to drive the difference signal to zero.

Expansion

The expansion consists of the controlled removal of air radially from the sensitive volume through a series of small ports (16 ports, 0.79 mm dia. per 61 cm height) located between side wall heat sink sections. These ports are collected into a channel which is connected to an expansion manifold. An eight bit digital valve controls flow into or out of the chamber. This valve is connected to a vacuum ballast tank (for expansion) which in turn is connected to a continuously running 45 l/min. mechanical vacuum pump.

Pressure is the measured variable during the isentropic expansion. It is measured by a differential strain gauge pressure transducer with its reference side connected to the sensing volume of a vacuum-referenced dead weight gauge.

The TEM's can cool the inner wall surface at rates up to 10°C/min for temperatures from + 40 to 10°C below the temperature of the heat sink. Below this range the maximum cooling rate decreases until the lowest temperature of 35°C below the heat sink temperature is reached. Maximum heating rate exceeds 10°C/min for all temperatures. At present the chamber at 20°C regularly shows an rms spread of 0.01°C or less in the temperature of the 40 measured control sections with a peak-to-peak spread of less than 0.050°C. For the interior walls 30°C below the heat sink temperature, the rms increases to 0.075°C and the peak-to-peak spread approaches 0.5°C.

Observation and sizing: Mie scattering

Because of this wall-tracking feature the walls are necessarily opaque. Access to the chamber is provided by three 2.3 cm diameter windows: two directly opposite each other and one at 72° from the forward direction. Each window is 1.6 mm thick Sapphire coplanar with the inner wall. About 4 mm behind the coplanar window another window (or other element) can be placed. Temperature control is achieved by passing CO₂ gas between plates. A transistor thermometer sensor is in contact with the edge of the window and its signal used for control.

The window at 72° provides a port either for photography or low light level TV camera. Photographic illumination is provided by a Xenon flash lamp. Its beam is shaped with lenses and a slit into a vertical sheet of light in the chamber. All drops in the light are in focus for the camera lens and these are registered on film. TV illumination is provided by the laser beam.

Actual measurements of drop sizes are made by Mie scattering. The 4° forward pattern is sufficiently structured so as to identify specific peaks with particular drop radii. Thus a series of peaks and valleys permit one to directly infer drop radius vs time for a monodispersed cloud.

Results

The condensation coefficient was inferred directly from drop growth rates using continuum theory. (We have avoided the temptation to lower pressure, so as to enhance the role of surface kinetics, because we preferred not to rely on theories in the transition regime of Knudsen number.) The theory is basically that presented by Carstens (1979); it is similar to the often-quoted theory of Fukuta and Walter (1972), except with convective mass flux (Stefan flow) and enthalpy flux included.

Preliminary data has now been taken. All the data show a rather large spread in the vicinity of $\beta = 1$ for the early stages of growth, out to about 6 micron radius. Thereafter the value of β drops monotonically reaching values as low as 0.005 near radii of 15 μ . These data were generated by subjecting a monodisperse aerosol to linear "ramped" cooling rates of 10°C/min. Figure 1 illustrates the trend of this data for several 10°C/min runs.

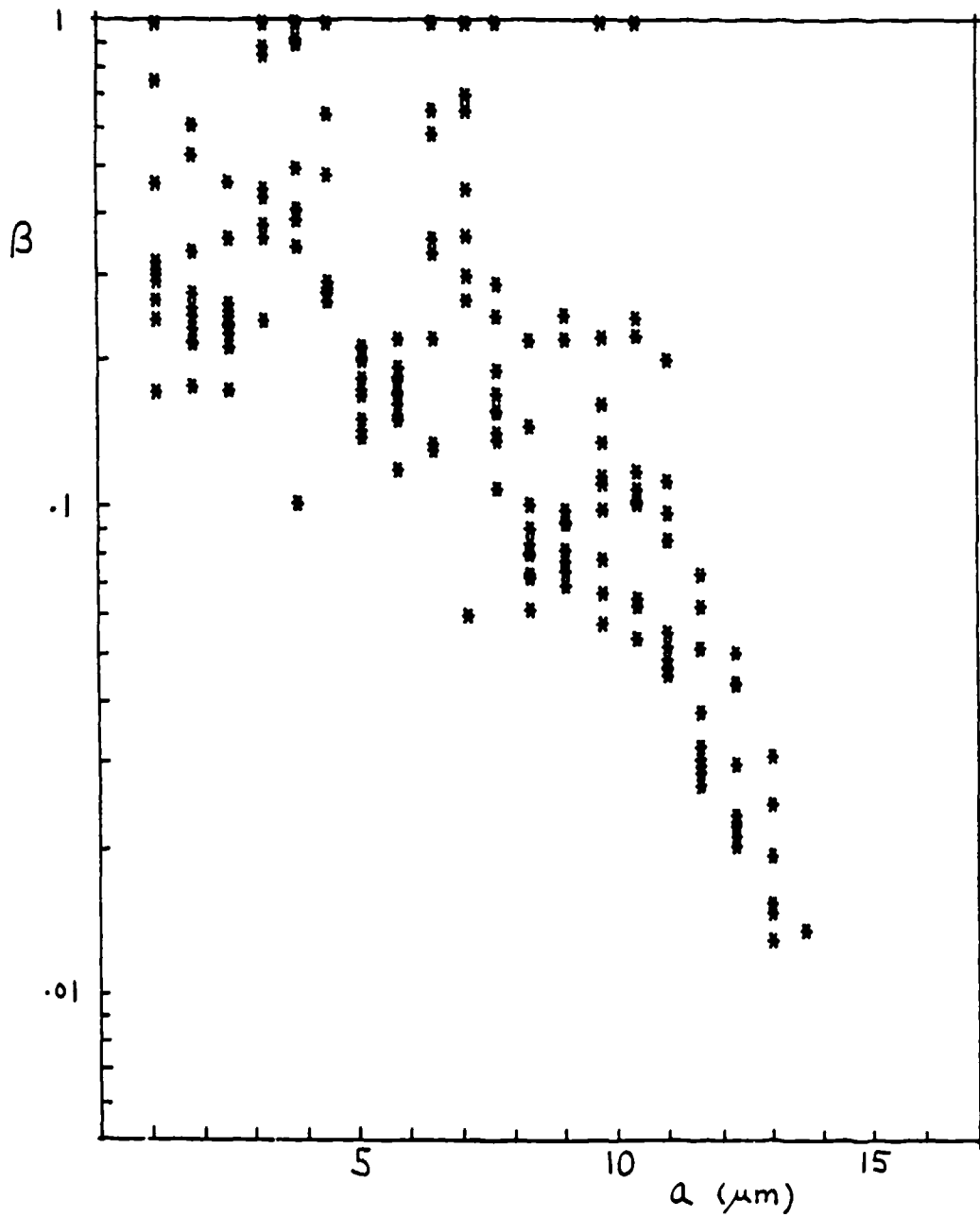


FIGURE 1

APPENDIX A: LIST OF SYMBOLS

In the following list the tilde over a variable designates it as a molar quantity, e.g., L denotes latent heat in cal/gm, and \tilde{L} cal/mole.

English symbols

a drop radius
 D diffusion coefficient, water vapor in air
 e_s vapor pressure
 K thermal conductivity, air
 L latent heat of condensation
 n_g molar concentration, air (moles/cm³)
 p pressure
 R universal gas constant
 S supersaturation ratio
 T temperature
 \bar{v}_g average speed, gas molecule

Greek symbols

α thermal accommodation coefficient
 γ ratio of specific heats (const. pressure: const. vol.)
 ρ_l density (gms/cm³), liquid water

REFERENCES

- Alofs, D.J., 1979: "Nucleation Experiments with Monodisperse NaCl Aerosols", J. Appl. Meteor. 18, 1106-1117.
- Carstens, J., 1979: "Drop Growth in the Atmosphere by Condensation: Application to Cloud Physics", Adv. in Coll. & Int. Sci., 10, 285-314.
- Fukuta, N., and L.A. Walter, 1970: "Kinetics of Hydrometeor Growth from a Vapor Spherical Model", J. Atmos. Sci., 26(8), 1160-1172.
- Jensen, J.B., and M.B. Baker, 1986: "An Observational Study of Cloud Droplet Spectra in Continental Study of Cloud Droplet Spectra in Continental Cumulus Clouds", Proc. AMS Conf. on Cloud Phys. Vol. 2 (preprints), Snowmass, CO.
- Kitani, S., and S. Ouchi, 1967: Preparation of Monodisperse Aerosols of Sodium Chloride", J. Coll. Int. Sci., 23, 200-202.
- Mozurkewich, M. 1986: "Aerosol Growth and the Condensation Coefficient for Water: A Review", Aerosol Sci. Techn., 5(2), 223-236.
- Pruppacher, H.R., and J.D. Klett, 1978: "Microphysics of Clouds and Precipitation", Dordrecht, Reidel.

Rogers, R.R., 1976: "A Short Course in Cloud Physics", Pergamon.

Warner, J., 1969: "The Microstructure of Cumulus Cloud. Part II. The Effect of Droplet Size Distribution of the Cloud Nucleus Spectrum and Updraft Velocity", J. Atmos. Sci., 26, 1272-1282.

**Photo-oxidation of Sulfur Dioxide with OH Radical in the
Presence of Water Vapour and Ammonia to Form Condensation
Nuclei**

Patrick M. Nolan and James P. Friend*

GEO-CENTERS, 10903 Indian Head Highway, Ft. Washington, MD 20744*
*Mailing address: c/o Cdr/CRDEC, U.S. Army Chem. Rsch, Dev. & Engr. Ctr.
ATTN: SMCCR-RSC-C/Nolan, Aberdeen Proving Ground, MD 21010-5423

*Department of Chemistry, Drexel University, Philadelphia, Pennsylvania
19104

ABSTRACT

The formation of condensation nuclei by photo-oxidation of sulfur dioxide by OH radical was studied. In one experiment a reaction mixture of sulfur dioxide, ozone, water vapour, and zero-air was photolyzed by employing a krypton-fluoride laser (248nm). In a similar experiment ammonia was added to the reaction mixture.

In each experiment the photolysis of ozone produced oxygen in the singlet D state (O¹D). The O¹D reacted with water vapour to form OH radicals which was the primary reactant for the oxidation of sulfur dioxide. A mechanism which describes the formation of condensation nuclei is presented. Rate constants for the isomerization of sulfur trioxide hydrate and for the mono-, di-, and tri-hydrates of sulfuric acid were estimated.

A separate experiment examines the production of particles. From ion chromatography data and examination of electron-micrographs the particles were determined to be (NH₄)₂SO₄. The particles were reacted in a maturation system and were collected with a point-to-plane electrostatic precipitator. The particles were analyzed on an electron scanning microscope and their sizes ranged between 0.3 and 0.8 microns.

Introduction.

Much work has been done on the gas-phase kinetics of the photo-oxidation of sulfur dioxide molecules. Presently, experimental evidence seems to support the mechanism recently proposed by Calvert and Stockwell¹. The mechanisms of stratospheric formation of sulfuric acid bearing aerosols at relatively low concentrations of water vapour are still a subject of debate. Few studies in which a complete chemical system containing SO₂, OH, O₂, and H₂O have been reported in terms of

condensation nuclei formation. The purpose of this investigation is to examine all possible reaction mechanisms which lead to the formation of condensation nuclei and to propose a theory that describes the rate of formation of condensation nuclei as a function of reactant concentrations and light intensity.

An experimental flow reactor has been employed to examine the reaction between SO_2 , OH, O_2 , and H_2O . In one set of experiments ammonia gas was also added to the reaction vessel. The formation of condensation nuclei was monitored as a function of varying amounts of SO_2 , O_3 , H_2O , and laser power. A krypton-fluoride excimer laser was used to photolyze ozone to produce atomic oxygen in the singlet-D state. The oxygen atoms subsequently reacted with water vapour to produce the OH radical. The OH radical concentration can be accurately calculated from the power output of the monochromatic light source, known concentrations of O_3 and H_2O , and the absorption cross section of O_3 . To minimize wall effects, the flow reactor was designed so the reaction takes place where the laser beam passes through in the center of the reaction vessel. The experimental results are interpreted to give a possible chemical kinetic pathway for condensation nuclei formation.

When the photolyzed reaction mixture was exposed to ammonia gas the production of large ammonium sulfate aerosol particles was observed and identified by electron-microscopy and by ion chromatography. By examining the particle morphology it was concluded that the particles were neutralized in the gas-phase. The presence of such large particles demonstrates the existence of condensation nuclei in the reactor and that the gas-phase photo-oxidation of SO_2 products are H_2SO_4 molecules.

Experimental.

The experimental apparatus was designed to measure the production of condensation nuclei as a function of sulfur dioxide, ozone, water vapour, and ammonia concentrations, and laser power (Figure 1). The apparatus is conveniently divided into six relatively independent blocks: reactants concentration (production and dilution) and flow control, reactant mixing, reaction vessel, laser, detection of products and laser power, and data acquisition. A separate set of experiments required the construction of a maturation chamber and particle collection device to study the aerosol particle formation when the photolyzed reactant mixture was reacted with ammonia. A brief outline of the experimental procedure is discussed below. However, a detailed description of each

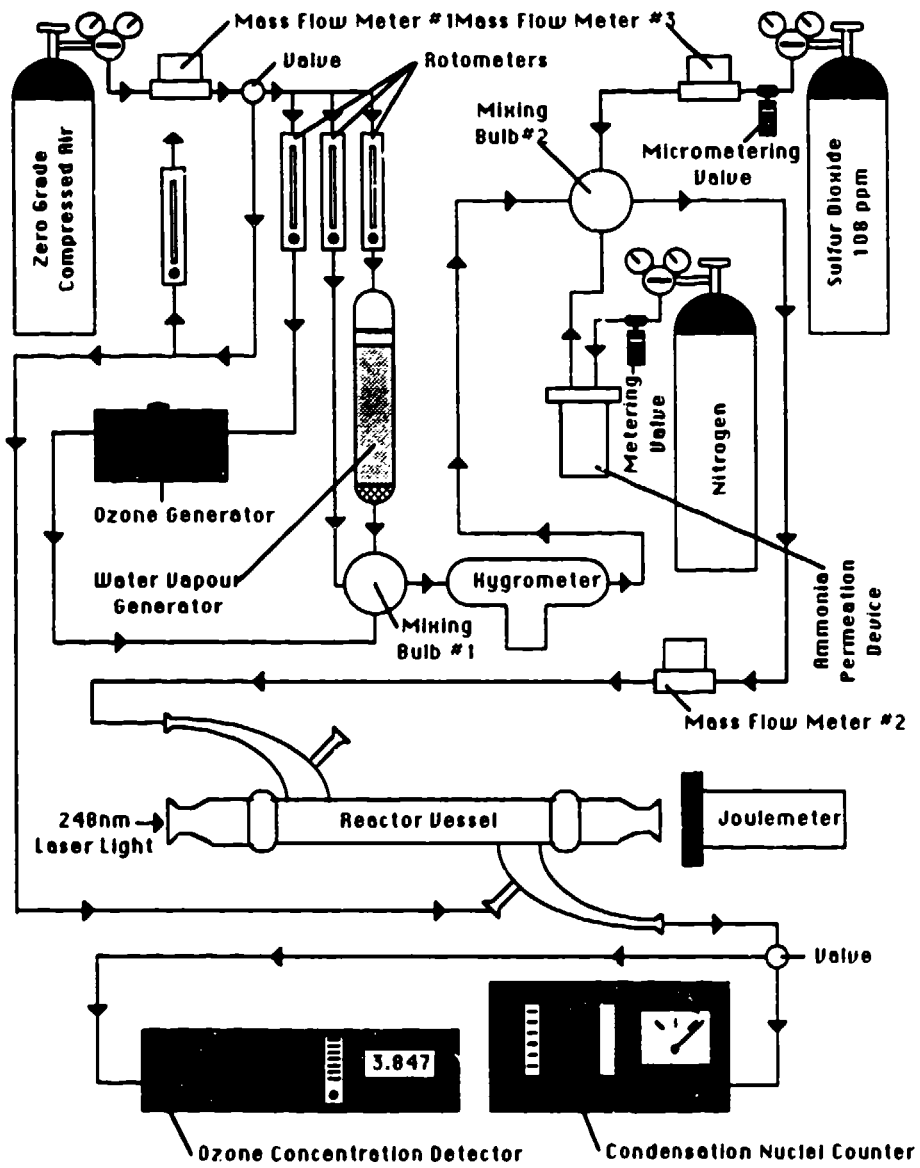


Figure 1. Schematic of Experimental Flow Apparatus.

component is given in Nolan's² work

The sulfur dioxide concentration is set by diluting a known concentration of sulfur dioxide/zero air mixture. The ozone concentration is controlled by varying the amount of O₂ exposed to the photolyzing radiation and the water vapour concentration is varied by changing the flow rate of zero air through a hydrated molecular sieve bed. Also, the ammonia concentration was controlled by changing the temperature of a permeation device.

The reactants were then mixed and conducted to the reaction vessel where the mixture was photolyzed with a krypton-fluoride excimer laser to produce OH radical. Subsequently, the OH radical attacks the sulfur dioxide, which further reacts to produce condensation nuclei. The condensation nuclei concentration is detected with a condensation nuclei counter. Also, the power of each laser pulse was monitored with a joulemeter. The peak laser power output was determined and stored on a peak/detect sample/hold integrated circuit. The analog data from the condensation nuclei counter and the peak/detect sample/hold integrated circuit were converted to digital form and then stored in memory for further data manipulation (Figure 2).

In a separate set of experiments the photolyzed mixture enters a maturation chamber containing ammonia. At various elapsed times the resultant aerosol particles were purged from the maturation chamber and collected on a carbon mount by utilizing a point-to-plane particle electrostatic precipitator. The samples were analyzed on an electron scanning microscope.

Results.

A typical experimental curve is displayed in Figure 3. The figure displays the condensation nuclei concentration, particles per microliter, as a function of time in seconds. The characteristic shape of the curve can be described as a composite of instrumental features and diffusion properties. Time zero corresponds to the laser trigger with an 8 or 9 second delay before any condensation nuclei are detected. This lack of response arises from the 3 seconds travel time from the reaction vessel to the condensation nuclei counter intake orifice and the 5 to 6 seconds response time of the condensation nuclei counter. Within 1 to 2 seconds, the condensation nuclei concentration is at its maximum. The pulsed-plateau feature, approximately 1 second in duration, is an instrumental artifact caused by the adiabatic expansion of the Wilson cloud chamber. The curve width is approximately 17 to 18 second long, which is the time needed to sweep out the reaction chamber of products.

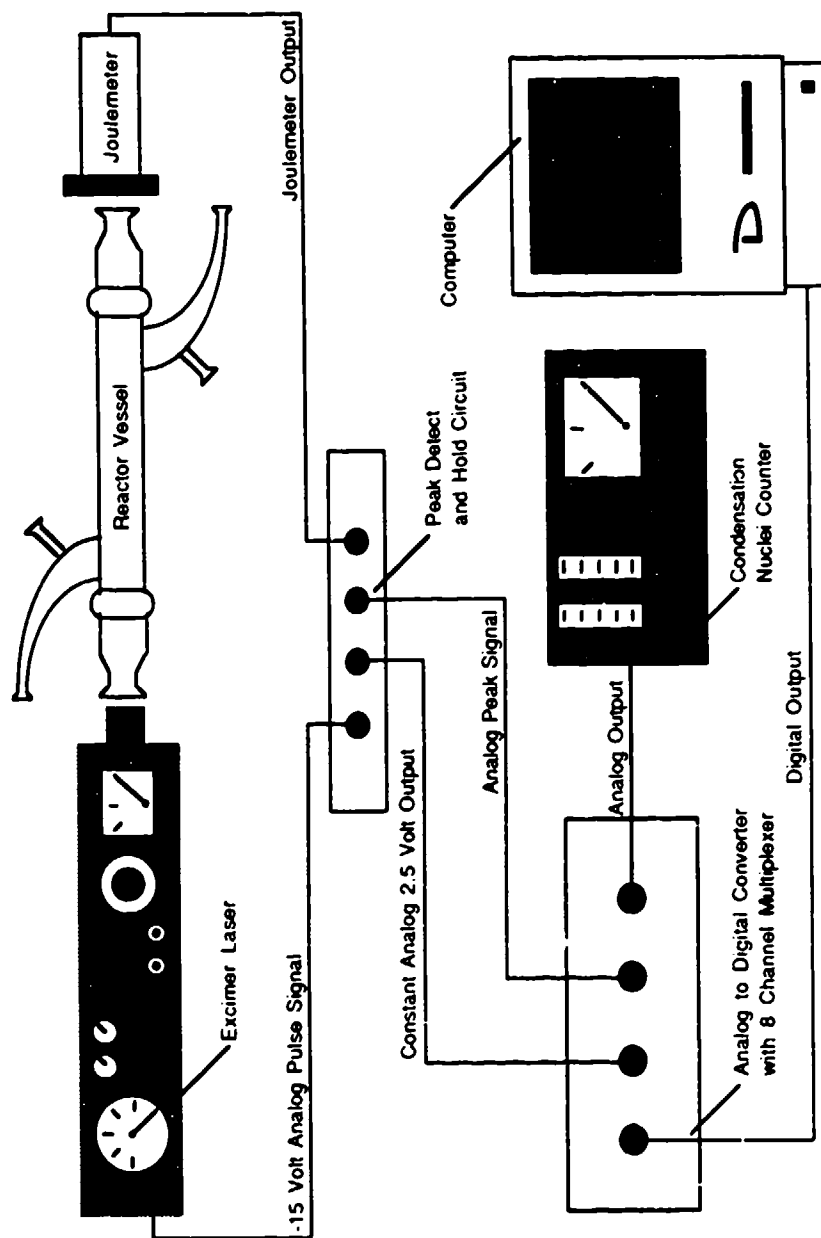


Figure 2. Schematic of Electronic Layout.

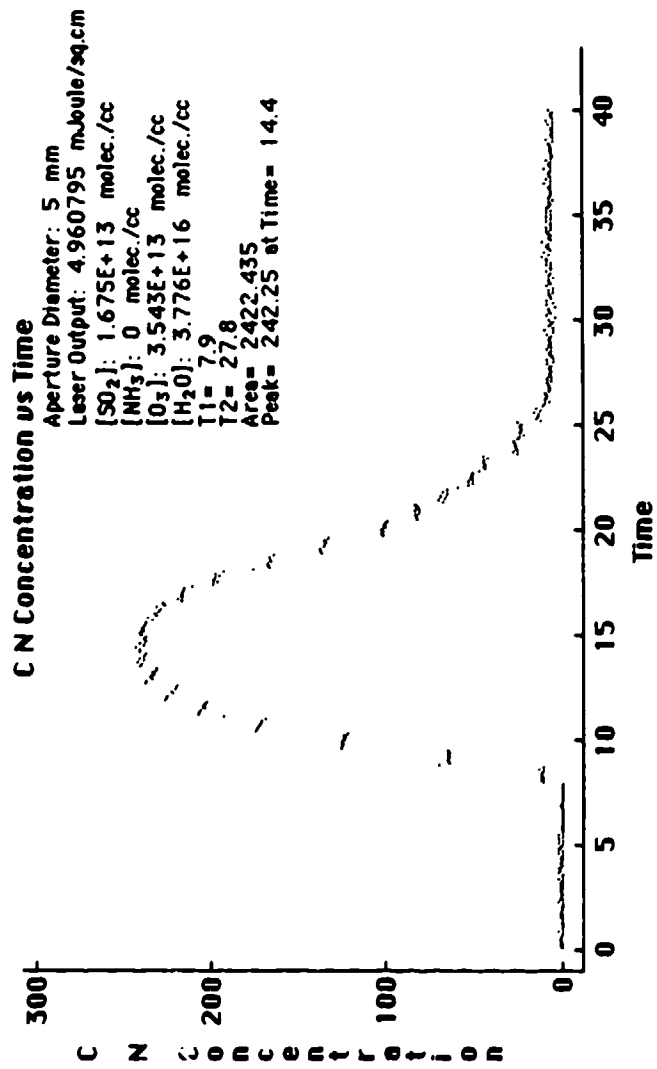


Figure 3. Raw Data Display of Condensation Nuclei Concentration as a Function of Time.

The decay side of the curve is a little more drawn out due to upstream longitudinal diffusion of the condensation nuclei.

3. Presentation of Integrated Data.

The curve is integrated over time, yielding the area under the curve (particle sec/cc). To obtain the total number of condensation nuclei (CN) produced in the reaction chamber, the area under the curve (A) is multiplied by the flow rate (ω), in the case, a constant with a value of $2.511 \times 10^4 \mu\text{L}/\text{sec}$.

$$\text{CN} = \omega A \quad (\text{Eq. 1})$$

To determine the dependency of condensation nuclei formation on the number of photons, a plot of the logarithm of the total number of condensation nuclei verses logarithm of the laser power is performed (see Graphs 1-4).

The data are re-organized to demonstrate the dependency of the total condensation nuclei production as a function of reactant concentrations at different laser powers (see Graphs 5-8). A laser power is selected on the $\text{Log}(\text{CN})$ vs. $\text{Log}(\text{Laser Power})$ plots to yield the condensation nuclei concentration at each reactant concentration. A laser power range from 5.00 to 12.6 mJoule/pulse is chosen.

All samples are collected on carbon mounts. The electron-micrographs are obtain on a Jeol JSM-35CF electron scanning microscopy. The electron scanning potential is operated between 15 KV to 20 KV to minimize sample degradation. Magnifications of samples ranged from X3000 to X20000. Most samples are scanned perpendicular to the surface of the carbon mount. One of the samples is scanned at an angle 50° to examine the three-dimensional morphology of the particles

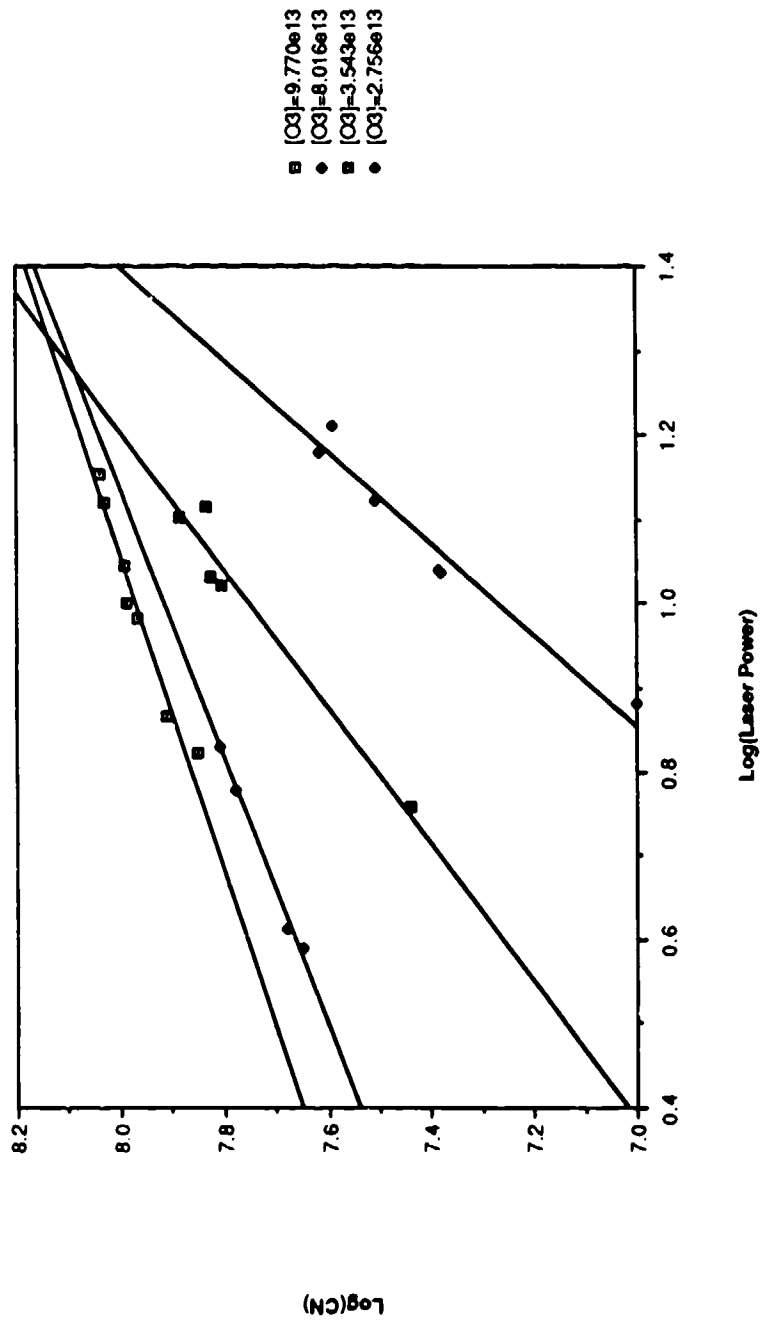
DISCUSSION

1. Introduction

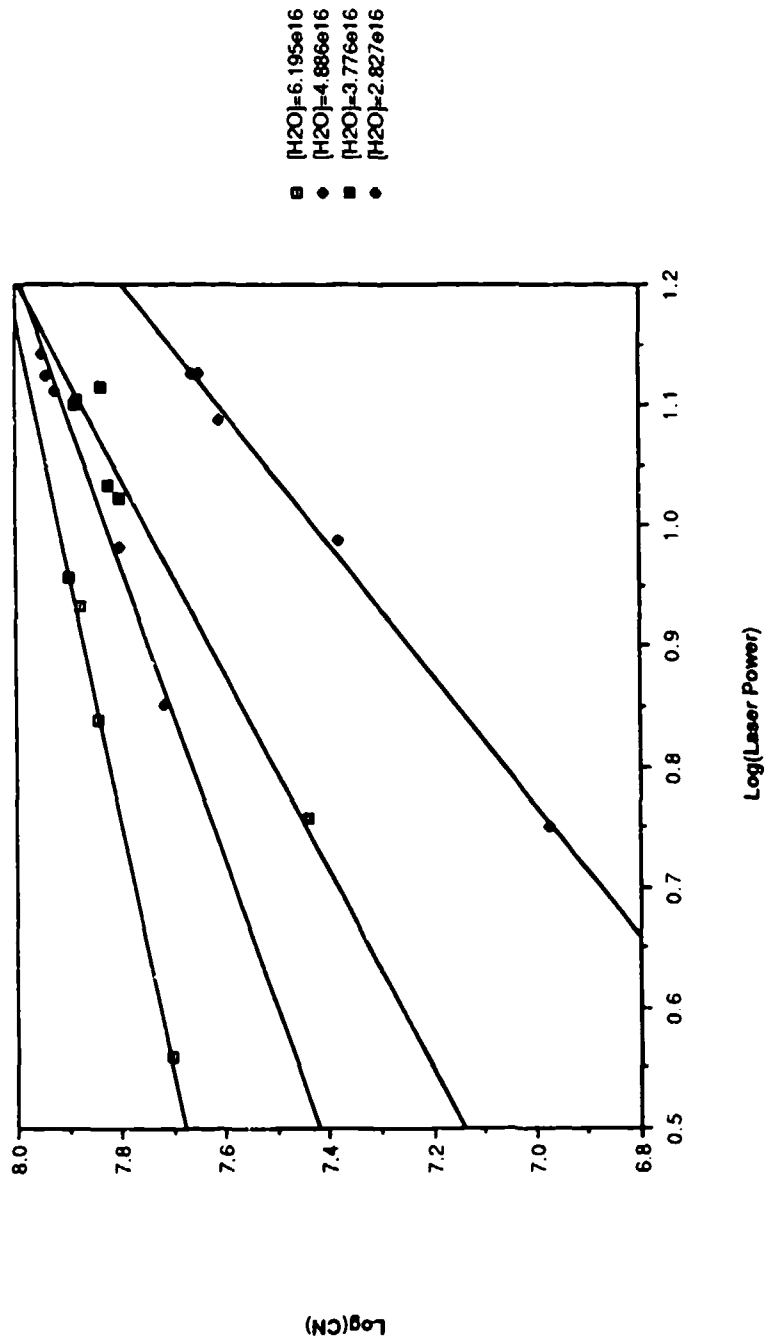
In view of recent publications, which demonstrate the importance of the OH radical as a reactant in the oxidation process of stratospheric SO_2 , the flow reactor has been designed to study the formation of condensation nuclei. The experiments are performed under atmospheric-like conditions, where the total air pressure is kept at 1 atmosphere, the relative humidity at 1 to 6 percent, and trace amounts (ppm range) of sulfur dioxide and ozone are present.

This discussion is primarily concerned with explaining the formation of condensation nuclei from a chemical kinetic point of view. A detailed investigation into all known relevant reactions to discern the chemical mechanism which leads to the production of condensation

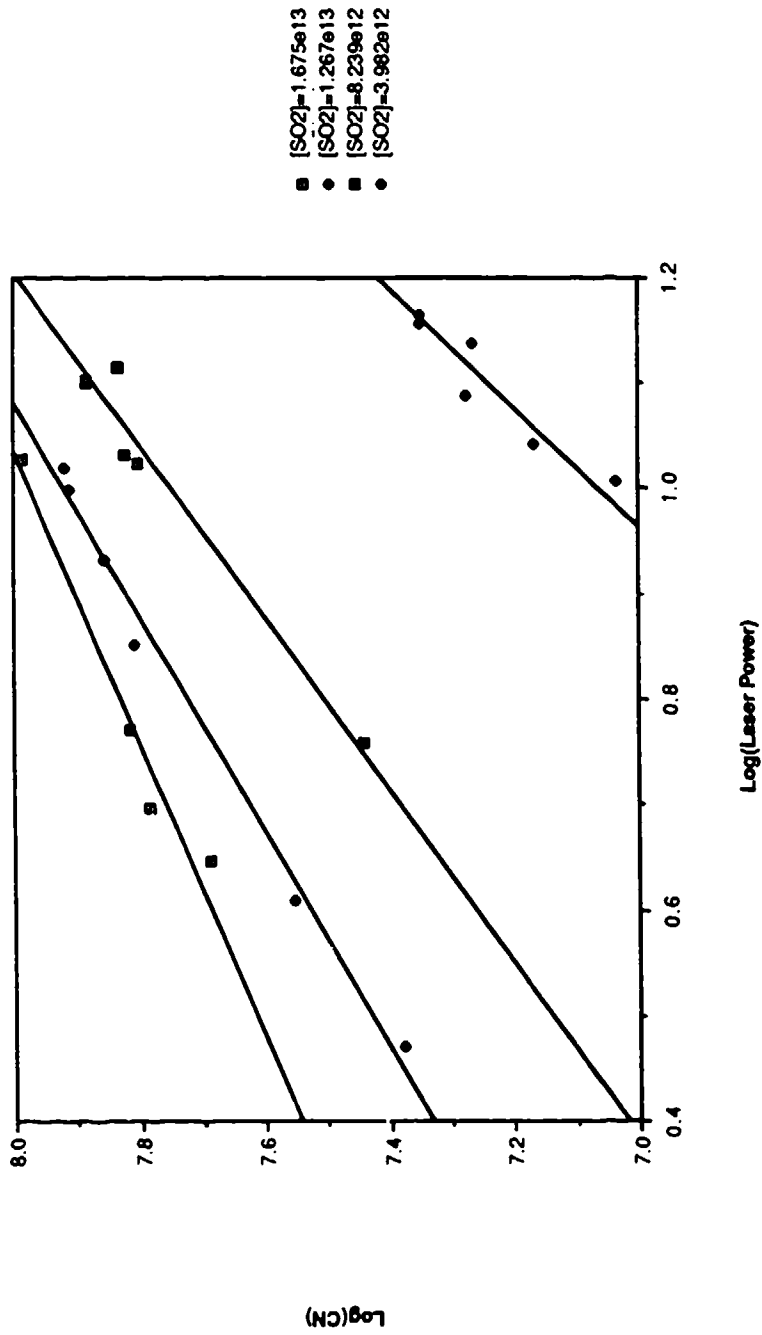
Graph 1. Log(CN) vs. Log(Laser Power) at Different O3 Concentrations



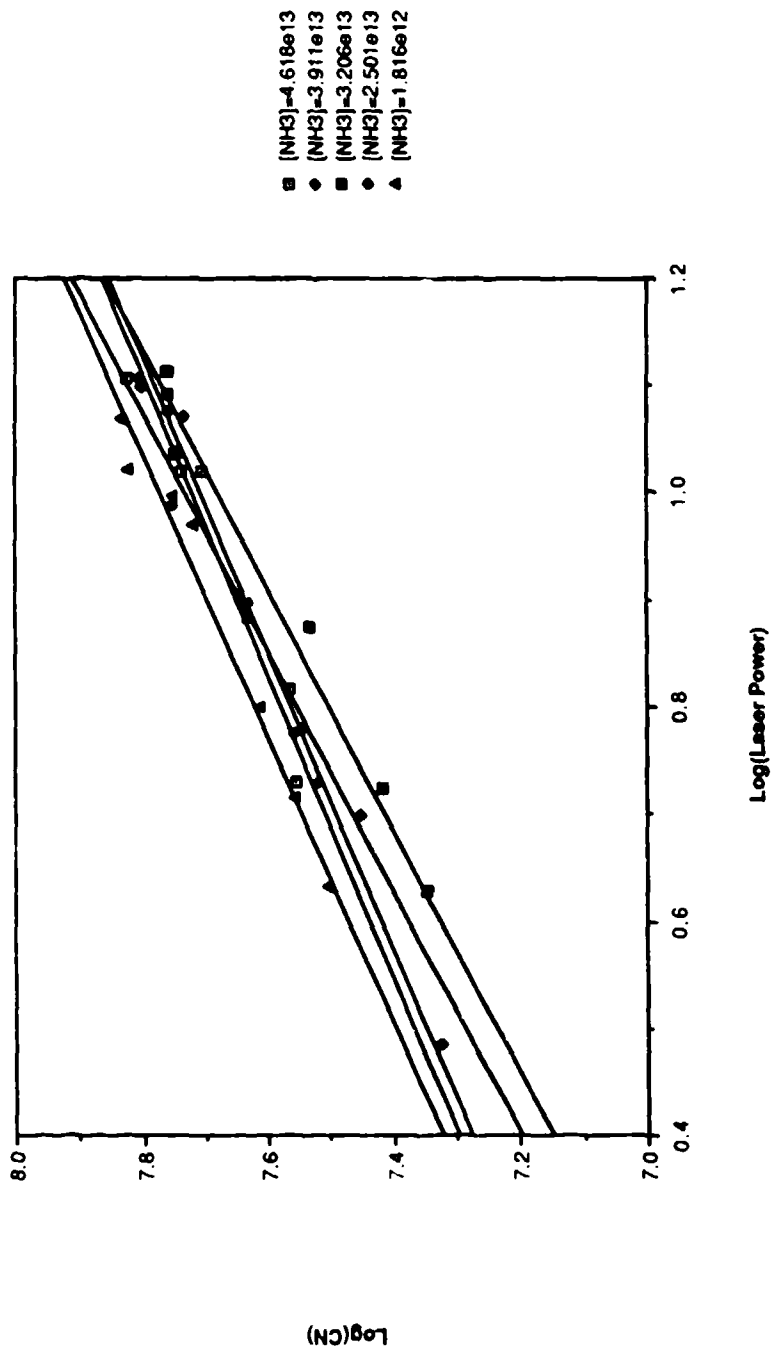
Graph 2. Log(CN) vs. Log(Laser Power) at Different H2O Concentrations



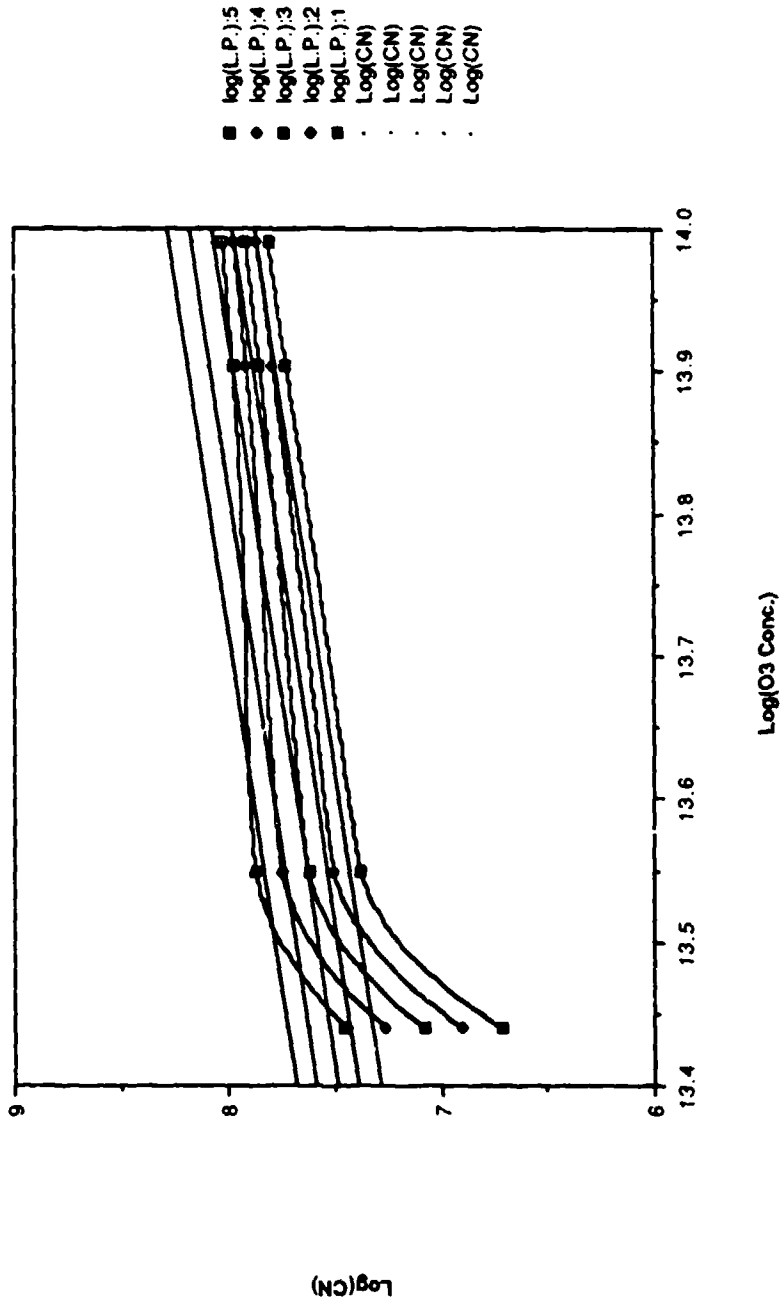
Graph 3. Log(CN) vs. Log(Laser Power) at SO2 Concentrations



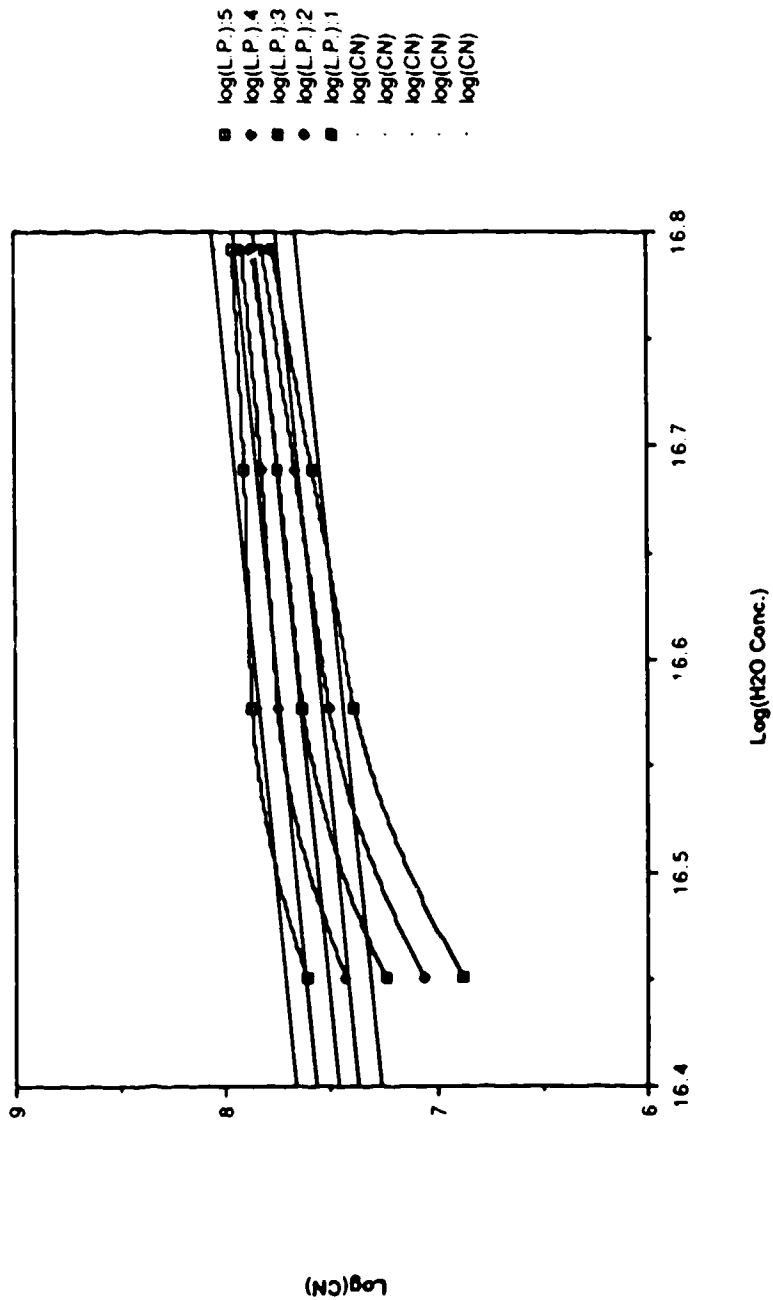
Graph 4. Log(CN) vs. Log(Laser Power) at Different NH3 Concentrations



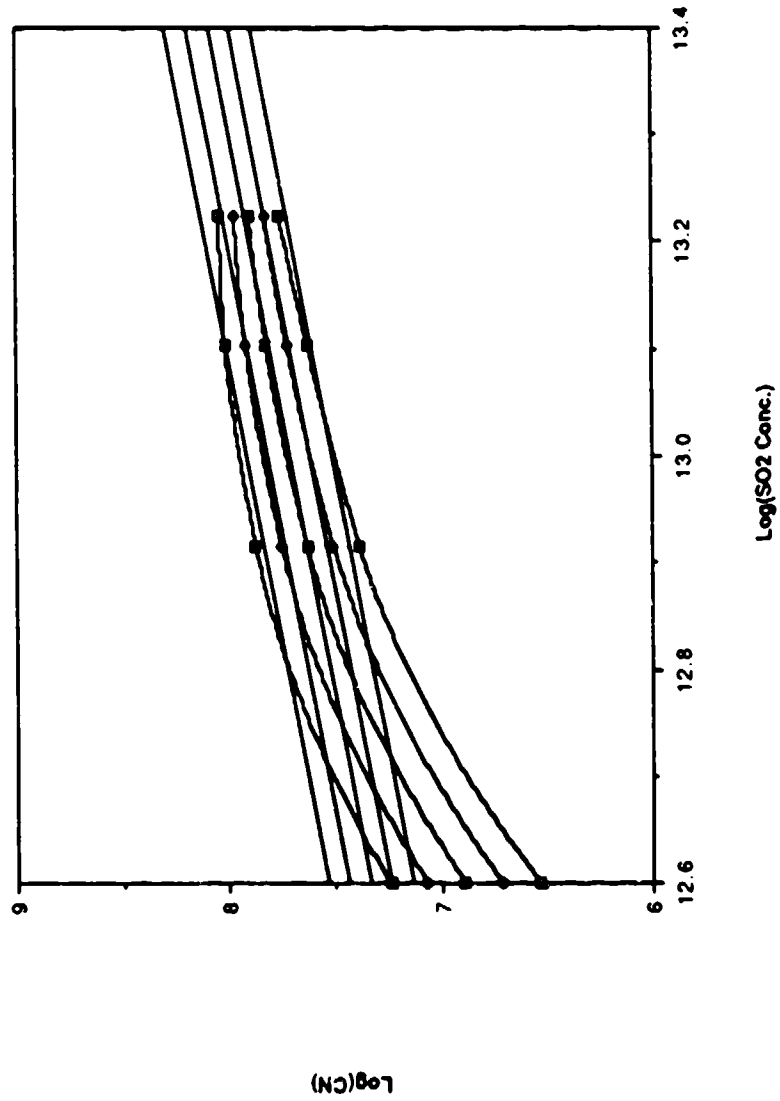
Graph 5. Comparison of Theoretical and Experimental Results (O3)



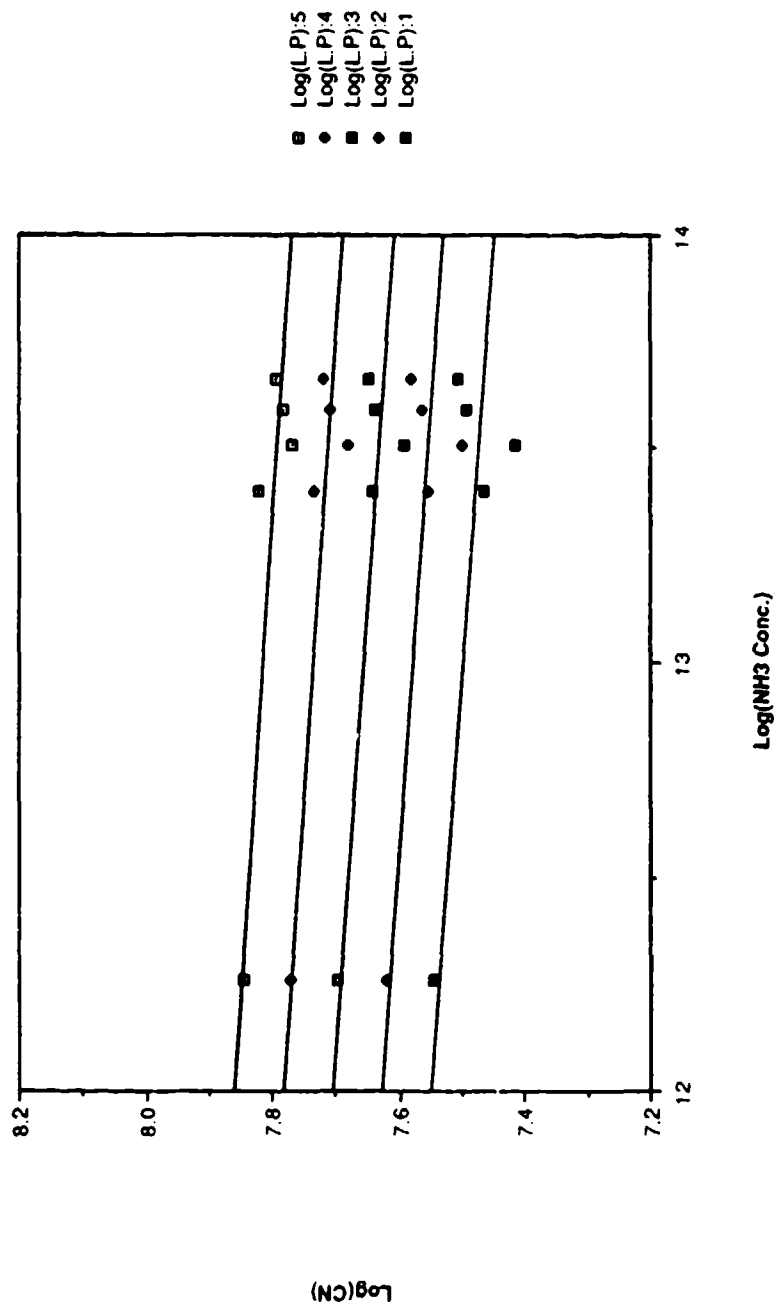
Graph 6. Comparison of Theoretical and Experimental Results (H2O)



Graph 7. Comparison of Theoretical and Experimental Results (SO2)



Graph 8. Log(CN) vs. Log(NH3 Conc.) at Different Laser Powers



nuclei is presented. The experimental data are compared to predictions of heteromolecular homogeneous nucleation theory. Also, evaluation of wall effects and scavenging of reactants and intermediates is given. An error analysis is performed to determine the degree of correlation of experimental data to theoretically predicted results. A brief interpretation of the experiments with the growth of ammonium sulfate aerosol is given.

2. Calculation of OH, SO₂, HSO₃, SO₃, and H₂SO₄ Diffusion Coefficients.

The flow reactor is designed primarily to minimize wall effects and to allow an accurate calculation of the initial concentration of OH radical present in the system. The removal of OH radical due to reaction with the reactor walls is negligibly small because the radicals are generated by the laser pulse in the center of the reactor vessel. The OH radical would have to traverse a minimum distance of 2.25 cm before coming in contact with the reactor wall.

The diffusion coefficient for the OH radical is calculated to be 0.371 cm²/sec by employing Fuller's³ method for predicting binary gas-phase diffusion coefficients. The diffusion coefficients for SO₂, HSO₃, SO₃, and H₂SO₄ are also calculated from the following equation:

$$D_{\text{Air}, X} = [(1.00 \times 10^{-3}) (T)^{1.75} (1/M_{\text{Air}} + 1/M_X)]^{1/2} / P [(\sum_{\text{Air}} v_i)^{1/3} + (\sum_X v_i)^{1/3}]^2 \quad (\text{Eq. 2})$$

where T is the temperature (298 K), P is the pressure (1 atm), M_{Air} and M_X are the molar masses of air (28.8 g/mole) and the particular component of interest, X, in grams per mole, respectively. The $\sum_{\text{Air}} v_i$ (11.10) and $\sum_X v_i$ (7.46) are the total special atomic diffusion volumes (unitless variable) of air and component X, respectively. The diffusion coefficients for the reactants, intermediates, and products are also calculated using Eq. 2 and are presented in Table 1. A time of 10.7 seconds is needed for an OH radical molecule to travel a mean perpendicular distance, $\langle x \rangle$, of 2.25 cm by employing the following relationship:⁴

$$\langle x \rangle = 2(Dt/\pi)^{1/2} \quad (\text{Eq. 3})$$

or

$$t = (\langle x \rangle / 2)^2 \pi / D \quad (\text{Eq. 4})$$

In Table 1 are given the translation times for OH, SO₂, HSO₃, SO₃, and H₂SO₄ to travel a mean distance of 2.25 cm.

Table 1. Calculated Diffusion Coefficients and Translation Times for OH, SO₂, HSO₃, SO₃, and H₂SO₄.

Species	Spec. At. Dif. Vol.	M.W. (g/mole)	D. C. (cm ² /sec)	Trans Time(sec.)
OH	7.49	17	0.371	10.7
SO ₂	27.96	64	0.172	23.1
HSO ₃	44.42	81	0.152	26.2
SO ₃	40.44	80	0.155	25.7
H ₂ SO ₄	42.88	98	0.137	29.0
Air	11.10	37.8	-----	-----

With the OH radical reaction characteristic time (τ), on the order of milliseconds ($\tau=10^{-3}$ sec.), it is obvious that essentially all of the OH radical will react before making contact with the wall.

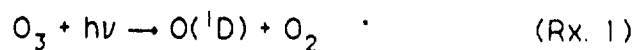
Using a molar mass of 98 g/mole for sulfuric acid and a total special atomic diffusion volume of 42.88, the diffusion coefficient is calculated to be 0.137 cm²/sec. Sulfuric acid has the smallest diffusion coefficient because of its large atomic diffusion volume. The OH radical and the reaction intermediates are rapidly removed by reactions and from the diffusion coefficient values (Table 1), one can conclude that the OH radical and the intermediate reactants will not reach the reactor wall within the reaction time frame. However, the OH radical could react with the teflon tube connecting the reactor vessel to the condensation nuclei counter and also react with the condensation nuclei counter's internal plumbing. The sulfur trioxide hydrate and sulfuric acid molecules diffuse very slowly (0.137 cm²/sec) and since all of the condensation nuclei are swept out of the reaction vessel within 20 seconds, virtually none of the sulfur trioxide hydrate and sulfuric acid molecules will react with the reactor wall.

The individual reactions which participate in the total reaction mechanism of condensation nuclei formation are analyzed in terms of the reactant concentrations and their rate constants in the following sections.

3. Reaction of OH Radical.

A. Production of OH Radical.

The OH radical is produced first by photolyzing ozone to form O(¹D) which subsequently reacts with water vapour to produce two OH radical molecules.





A krypton-fluoride excimer laser, which lases at 249nm, is used to photodissociate ozone in the Hartley bands (200 to 390nm) region.⁸ The krypton-fluoride excimer laser is an excellent photodissociation source since it lases near the peak absorption of ozone in the Hartley bands. The monochromaticity of the light source allows one to calculate the total number of quanta absorbed by the ozone molecules without summing over a wavelength range. The total number of quanta absorbed (I_a) is computed from the total energy incident on the system (E), the fraction of energy absorbed by the system (Q_m), and the volume (V) of the irradiated system:⁹

$$I_a = EQ_m \lambda / V h c_s \quad (Eq. 5)$$

where,

$$Q_m = 1 - 10^{-\epsilon c l} \quad (Eq. 6)$$

and where, λ is the wavelength of the incident light, h is Planck's constant, c_s is the speed of light, ϵ is the absorption cross section of ozone ($cm^2/molecule$), c is the concentration of ozone ($molecule/cm^3$), and l is the path length (cm). The absorption cross section of ozone at 248.5nm was recently reported to be $1.082 \times 10^{-17} cm^2/molecule$ by Molina and Molina.¹⁰ The cylindrical reaction volume of the system is simply the product of the area of the laser beam (πr^2) and the path length (l) of the laser beam:

$$V = \pi r^2 l \quad (Eq. 7)$$

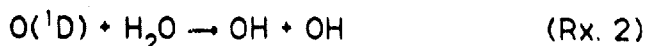
The radius (r) of the laser beam is 0.25cm and the path length from one quartz window to the other quartz window is 34.8cm, yielding a reaction volume of $6.83cm^3$

The concentration of $O(^1D)$ atoms, ($[O(^1D)]_0$), produced from the photodecomposition of ozone can be defined as:

$$[O(^1D)]_0 = I_a \phi(O^1D) \quad (Eq. 8)$$

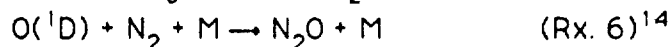
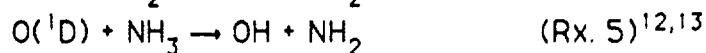
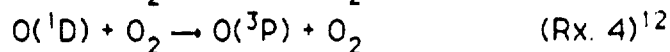
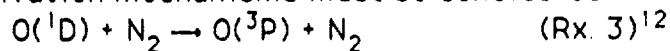
where, $\phi(O^1D)$ is the quantum yield of the ozone photodecomposition to produce $O(^1D)$ molecules. The subscript "0" denotes the instantaneous formation of $O(^1D)$ molecules at time zero. In fact, the photodecomposition mechanism is virtually instantaneous compared to any chemical reaction. Amimoto et al.¹¹ measured the quantum yield of ozone $\phi(O^1D)$ at 248nm and reported a value of 0.85.

The production of the OH radical molecule is described by the following chemical mechanism:



However, to compute quantitatively the concentration of the OH radical,

the following O(¹D) deactivation mechanisms must be considered:



The rate of removal of O(¹D) can be characterized predominantly by Rxs. 2, 3, and 4. When ammonia is present in the reaction system, Rx. 5 does not contribute significantly to the overall rate of removal of O(¹D) because of the small rate constant and the relatively small amounts of NH₃. Also, the termolecular reaction, Rx. 6, can also be neglected because of the small rate constant. So, the rate law for the disappearance of O(¹D) is as follows:

$$-d[\text{O}(\text{}^1\text{D})]/dt = k_2[\text{H}_2\text{O}][\text{O}(\text{}^1\text{D})] + k_3[\text{N}_2][\text{O}(\text{}^1\text{D})] + k_4[\text{O}_2][\text{O}(\text{}^1\text{D})] \quad (\text{Eq. 9})$$

Eq. 9 can be rewritten as:

$$-d[\text{O}(\text{}^1\text{D})]/dt = (k'_2 + k'_3 + k'_4)[\text{O}(\text{}^1\text{D})] \quad (\text{Eq. 10})$$

where $k'_2 = k_2[\text{H}_2\text{O}]$, $k'_3 = k_3[\text{N}_2]$, $k'_4 = k_4[\text{O}_2]$.

The integrated rate expression for Eq. 10 is,

$$\ln[\text{O}(\text{}^1\text{D})]/[\text{O}(\text{}^1\text{D})]_0 = -(k'_2 + k'_3 + k'_4)t \quad (\text{Eq. 11})$$

and if, $[\text{O}(\text{}^1\text{D})] \ll [\text{H}_2\text{O}]$, $[\text{O}(\text{}^1\text{D})] \ll [\text{N}_2]$, and $[\text{O}(\text{}^1\text{D})] \ll [\text{O}_2]$ then Eq. 11 can be integrated to yield:

$$\ln[\text{O}(\text{}^1\text{D})] = -(k'_2 + k'_3 + k'_4)t + C \quad (\text{Eq. 12})$$

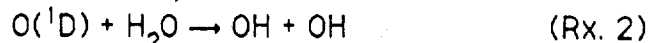
and when $t = 0$ then $C = \ln[\text{O}(\text{}^1\text{D})]_0$.

Finally, after evaluating the constant of integration Eq. 12 can be expressed as a product of pseudo-first-order reactions:

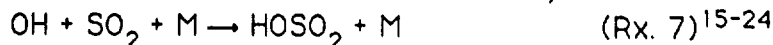
$$[\text{O}(\text{}^1\text{D})] = [\text{O}(\text{}^1\text{D})]_0 \exp-(k'_2 + k'_3 + k'_4)t \quad (\text{Eq. 13})$$

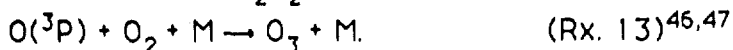
B. Removal of OH Radical.

If the rate of production of OH radical is much greater than the rate of removal of OH radical, then the rate law expression is separable. One can certify the validity of this assumption by considering the chemical reaction which forms the OH radical,



and the chemical reactions which consume the OH radical,





The $\text{O}(^3\text{P})$ species is consumed more rapidly by Rx. 10 than by Rx. 13; therefore Rx. 10 is unimportant with respect to OH radical depletion. At 1 atmosphere the pseudo-first-order rate constant for Rx. 13 is roughly, 10^5 sec^{-1}

The second order reactions, (Rx. 11 and Rx. 12), can also be neglected because of their relatively small rate constants compared to the faster pseudo-first-order reactions. For instance, setting $[\text{H}_2\text{O}] \approx 10^{16} \text{ molecule/cm}^3$, $[\text{SO}_2] \approx 10^{12} \text{ molecule/cm}^3$, $[\text{O}_3] \approx 10^{13} \text{ molecule/cm}^3$, $[\text{M}] \approx 10^{19} \text{ molecule/cm}^3$, $[\text{NH}_3] \approx 10^{12} \text{ molecule/cm}^3$, and using the rate constants in Table 2,⁴⁸ then the pseudo-first-order rate constants are as follows: $k_2 \approx 10^6 \text{ sec}^{-1}$, $k_7 \approx 1.0 \text{ sec}^{-1}$, $k_8 \approx 10^{-1} \text{ sec}^{-1}$, and $k_9 \approx 10^{-1} \text{ sec}^{-1}$. It is obvious that the production of OH radical is roughly a million times faster than the rate of depletion of OH radical, ($k_2 \gg (k_7 + k_8 + k_9)$). The production of OH radical can be considered to be instantaneous compared to the depletion of OH radical and so the rate of formation expression can be written as:

$$d[\text{OH}]/dt = k_2[\text{H}_2\text{O}][\text{O}(^1\text{D})] \quad (\text{Eq. 14})$$

And if $k'_2 = k_2[\text{H}_2\text{O}]$ and $[\text{O}(^1\text{D})] = [\text{O}(^1\text{D})]_0 \exp-(k'_2 + k'_3 + k'_4)t$, then Eq. 14 becomes:

$$d[\text{OH}]/dt = k'_2 [\text{O}(^1\text{D})]_0 \exp-(k'_2 + k'_3 + k'_4)t \quad (\text{Eq. 15})$$

or in integration form

$$\int d[\text{OH}] = k'_2 [\text{O}(^1\text{D})]_0 \int \exp-(k'_2 + k'_3 + k'_4)t dt. \quad (\text{Eq. 16})$$

After integration, Eq. 16 becomes:

$$[\text{OH}] = -k'_2 [\text{O}(^1\text{D})]_0 / (k'_2 + k'_3 + k'_4) \exp-(k'_2 + k'_3 + k'_4)t + C.$$

(Eq. 17)

At $t = 0$, $C = k'_2 [\text{O}(^1\text{D})]_0 / (k'_2 + k'_3 + k'_4)$ and so the concentration of OH radical as a function of time is:

$$[\text{OH}] = k'_2 [\text{O}(^1\text{D})]_0 / (k'_2 + k'_3 + k'_4) [1 - \exp-(k'_2 + k'_3 + k'_4)t] \quad (\text{Eq. 18})$$

As was demonstrated earlier, Rx. 2 ($\tau \approx \times 10^{-7}$) is ten thousand times faster in producing OH radical than for the reaction which depletes OH radical. Therefore, essentially all OH radical molecules are produced before they can react via the chemical mechanisms in Rxs. 7, 8, and 9.

Table 2. Reactions and Rate Constants.

Rx #	Reaction	Rate Constant	PFO-Rate Const. ^o	Ref. #
2	$O(1D) + H_2O \rightarrow OH + OH$	2.2×10^{-10}	2.2×10^6	48
3	$O(1D) + N_2 \rightarrow O + N_2$	2.6×10^{-11}	5.2×10^8	48
4	$O(1D) + O_2 \rightarrow O + O_2$	4.0×10^{-11}	2.0×10^8	48
5	$O(1D) + NH_3 \rightarrow OH + NH_2$	2.5×10^{-10}	-----	48
6	$O(1D) + N_2 + M \rightarrow N_2O + M$	3.5×10^{-37}	1.7×10^2	48
7	$OH + SO_2 + M \rightarrow HOSO_2 + M$	3.0×10^{-31}	7.4×10^6	48
8	$OH + O_3 \rightarrow HO_2 + O_2$	6.8×10^{-14}	6.8×10^{-1}	48
9	$OH + NH_3 \rightarrow H_2O + NH_2$	1.6×10^{-13}	1.6×10^6	48
10	$OH + O(^3P) \rightarrow O_2 + H$	3.3×10^{-11}	-----	48
11	$OH + OH \rightarrow H_2O + O$	1.9×10^{-12}	-----	48
12	$OH + OH + M \rightarrow H_2O_2 + M$	6.9×10^{-31}	-----	48
13	$O(^3P) + O_2 + M \rightarrow O_3 + M$	6.0×10^{-34}	7.3×10^4	48

cont. Table 2.

Rx. #	Reaction	Rate Constant	PFO-Rate Const. *	Ref. #
14	$O(^3P) + SO_2 + M \rightarrow SO_3 + M$	7.7×10^{-34}	1.9×10^{-2}	48
15	$HO_2 + SO_2 \rightarrow SO_3 + OH$	9.0×10^{-16}	9.0×10^{-4}	48
17	$O(^3P) + O_3 \rightarrow O_2 + O_2$	8.0×10^{-15}	8.0×10^{-2}	48
18	$HO_2 + OH \rightarrow H_2O + O_2$	7.0×10^{-11}	-----	48
19	$HO_2 + O_3 \rightarrow OH + 2O_2$	2.0×10^{-15}	2.0×10^{-2}	48
20	$HO_2 + HO_2 + M \rightarrow H_2O_2 + O_2 + M$	4.9×10^{-32}	-----	48
21	$HO_2 + O_2 \rightarrow SO_3 + HO_2$	4.0×10^{-13}	2.0×10^6	48
26	$SO_3 + H_2O + M \rightarrow SO_3 \cdot H_2O + M$	9.0×10^{-13}	9.0×10^3	48
28	$SO_3 \cdot H_2O \rightarrow H_2SO_4$	1.23×10^{-4}	-----	2
29	$H_2SO_4 + H_2O + M \rightarrow H_2SO_4 \cdot H_2O + M$	1.0×10^{-10}	1.0×10^6	2
30	$H_2SO_4 \cdot H_2O + H_2O + M \rightarrow H_2SO_4 \cdot (H_2O)_2 + M$	1.0×10^{-11}	1.0×10^5	2
31	$H_2SO_4 \cdot (H_2O)_2 + H_2O + M \rightarrow H_2SO_4 \cdot (H_2O)_3 + M$	1.0×10^{-12}	1.0×10^4	2

cont. Table 2.

Concentration of reactants for pseudo-first-order (PFO) are given below.

⁴⁸ Average value of the rate constants for model calculations recommended by NASA, Jet Propulsion Laboratory.

²Rate constants based on theoretical kinetic model given in this work.

Concentration of reactants used in this study.

$[M] = 2.46 \times 10^{19}$ molecule/cc; $[O_2] = 4.93 \times 10^{18}$ molecule/cc; $[N_2] = 1.97 \times 10^{19}$ molecule/cc

$[SO_2] = 10^{12}$ molecule/cc; $[O_3] = 10^{13}$ molecule/cc; $[H_2O] = 10^{16}$ molecule/cc

For reactants with variable concentrations only the order of magnitude is given.

The limit of Eq. 18 as time goes to infinity is:

$$(\lim t \rightarrow \infty) [\text{OH}]_{\infty} = k'_2 [\text{O}(\text{}^1\text{D})]_0 / (k'_2 + k'_3 + k'_4) \quad (\text{Eq. 19})$$

Since $[\text{OH}]_{\infty}$ can be considered to be formed instantaneously, OH radical consumption near $t=0$ is negligible and $[\text{OH}]_{\infty}$ will equal $[\text{OH}]_0$.

$$[\text{OH}]_0 = k'_2 [\text{O}(\text{}^1\text{D})]_0 / (k'_2 + k'_3 + k'_4) \quad (\text{Eq. 20})$$

Again, the subscript "o" denotes the initial concentration of OH radical at the beginning of Rxs. 7, 8, and 9.

By combining Eqs. 5, 6, and 8, one can see that the $[\text{O}(\text{}^1\text{D})]_0$ concentration is explicitly dependent on the laser power (E) and the concentration of ozone (c).

$$[\text{O}(\text{}^1\text{D})]_0 = \phi(\text{}^1\text{D})E\lambda(1 - 10^{-\epsilon c}) / Vhc_s \quad (\text{Eq. 21})$$

Since, $\epsilon c \ll 1$ one can expand $10^{-\epsilon c}$ in a Taylor series:

$$10^{-\epsilon c} = \exp^{-(\ln 10)\epsilon c} = \exp^{-2.303\epsilon c} \approx 1 - 2.303\epsilon c. \quad (\text{Eq. 22})$$

Eq. 21 can be rewritten as:

$$[\text{O}(\text{}^1\text{D})]_0 = 2.303\phi(\text{}^1\text{D})E\lambda\epsilon c / Vhc_s \quad (\text{Eq. 23})$$

By substituting Eq. 23 into Eq. 20 and recalling that $k'_2 = k_2[\text{H}_2\text{O}]$ and $c = [\text{O}_3]$, the $[\text{OH}]_0$ concentration is a linear function of laser power and ozone concentration.

$$[\text{OH}]_0 = k_2[\text{H}_2\text{O}]2.303\phi(\text{}^1\text{D})E\lambda\epsilon[\text{O}_3] / (Vhc_s(k_2[\text{H}_2\text{O}] + k'_3 + k'_4)) \quad (\text{Eq. 24})$$

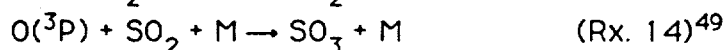
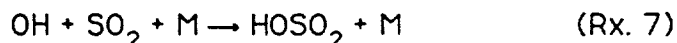
Furthermore, if $k_2[\text{H}_2\text{O}] \ll (k'_3 + k'_4)$ then $(k'_2 + k'_3 + k'_4)$ reduces to $(k'_3 + k'_4)$ and Eq. 24 can be rewritten as:

$$[\text{OH}]_0 = k_2[\text{H}_2\text{O}]2.303\phi(\text{}^1\text{D})E\lambda\epsilon[\text{O}_3] / (Vhc_s(k'_3 + k'_4)) \quad (\text{Eq. 25})$$

Under the experimental conditions, Eq. 25 reflects the linear dependence of OH radical concentration production as function of water vapour concentration. By employing Eq. 25 typical experimental values of OH radical concentrations in the center of the reactor vessel ranged from 9.3×10^{10} molecule/cm³ to 1.5×10^{12} molecule/cm³.

4. Reactions of Sulfur Dioxide.

To be complete, it is important to consider other possible photo-oxidation mechanisms of sulfur dioxide. In this experimental system, sulfur dioxide molecules can possibly react by these three chemical mechanisms:



However, under the experimental conditions, Rx. 14 is at least a hundred times slower than Rx. 7 even when the $O(^3P)$ concentration is at its maximum, i.e., the $O(^3P)$ concentration at the beginning of the reaction.

The photolysis of ozone also produces oxygen atoms in the ground state $O(^3P)$. Sparks et al. reported a quantum yield of, $\phi(O(^3P)) = 0.1$, for the formation of $O(^3P)$.⁵⁴

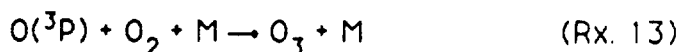


By analogy, Eq. 23 is rewritten and the $O(^3P)$ initial concentration is:

$$[O(^3P)]_0 = 2.303\phi(O(^3P))E\lambda\epsilon cI/Vhc_s \quad (\text{Eq. 26})$$

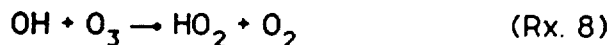
Using a laser power of 14 m joules and an ozone concentration of roughly 10^{13} molecule/cm³, an estimate of the upper limit of the $O(^3P)$ concentration is approximately 10^{11} molecule/cm³.

The relative importance of the photo-oxidation of sulfur dioxide by $O(^3P)$ is also analyzed in terms of $O(^3P)$ depletion. The following reactions account for all other possible $O(^3P)$ depletion mechanisms in the reaction system.

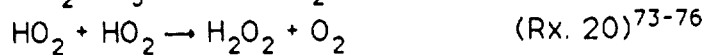
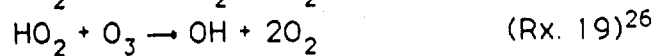


If $[M] > [O_2] \gg [O_3] > [SO_2] > [O(^3P)]$ then Rxs. 13, 14, and 17 can be evaluated as pseudo-first-order reactions. Rx. 10, for all practical purposes, is a second order reaction since $[O(^3P)] = [OH]$ and therefore is relatively unimportant. The pseudo-first-order rate constants are calculated using the rate constants in Table 2 and the following concentrations $[SO_2] = 10^{12}$ molecule/cm³; $[O_3] = 10^{13}$ molecule/cm³, $[O_2] = 4.93 \times 10^{18}$ molecule/cm³; $[M] = 2.46 \times 10^{19}$ molecule/cm³. The pseudo-first-order rate constants are: $k_{13} = 7.3 \times 10^4 \text{ sec}^{-1}$; $k_{14} = 1.9 \times 10^{-2} \text{ sec}^{-1}$; $k_{17} = 8.0 \times 10^{-2} \text{ sec}^{-1}$. Virtually all of $O(^3P)$ reacts with the diatomic oxygen (Rx. 13) because of the six orders of magnitude difference in the pseudo-first-order rate constants ($k_{13} \gg k_{17} > k_{14}$). Therefore, Rx. 14 is of no consequence in this experimental system.

The HO_2 radical is produced by the reaction of OH radical (Rx. 8) with ozone and also by the reaction of bisulfite with diatomic oxygen (Rx. 21, vide infra).¹⁵



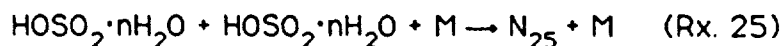
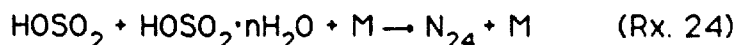
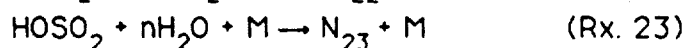
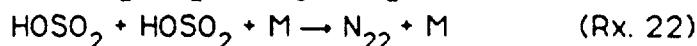
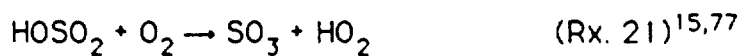
The HO_2 radical reacts at a much faster rate with the OH radical (Rx. 18) and the O_3 molecule (Rx. 19) than it reacts with the SO_2 molecule in Rx. 15.



At the start of the reaction the HO_2 radical is consumed predominantly by Rx. 18 because of the large rate constant and the significant initial OH radical concentration. After some time when the OH radical concentration drops about three orders of magnitude, Rx. 19 predominates as the primary mechanism for HO_2 radical consumption. Using the rate constants provided in Table 2 and assuming that $[\text{SO}_2] = 10^{12}$ molecule/cm³ and $[\text{O}_3] = 10^{13}$ molecule/cm³, the pseudo-first-order rate constants for Rx. 15 and Rx. 19 are calculated ($k'_{15} = 10^{-5}$ sec⁻¹; $k'_{19} = 10^{-1}$ sec⁻¹). The rate constant for the reaction of the HO_2 radical with O_3 (Rx. 19) is approximately four orders of magnitude greater than the rate of reaction of the HO_2 radical with SO_2 (Rx. 15). On the basis of the aforementioned rate analysis, Rx. 15 is not of any importance with respect to sulfur dioxide oxidation in this reaction system. One can conclude that the primary chemical mechanism for the photo-oxidation of sulfur dioxide occurs via the reaction with the OH radical molecule (Rx. 7).

5. Reaction of Bisulfite.

Next, the fate of the bisulfite radical is examined. Also, uncharacterized chemical mechanisms are proposed (Rx 22-25) to examine the possible contribution of other bisulfite radical reactions to the overall reaction scheme. In Rxs. 22 through 25 the N_{xx} denotes a condensation nucleus.

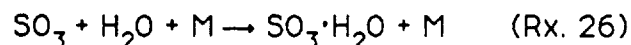


Rx. 21 is characterized with a reported rate constant of 4.37×10^{-13} cm³/molecule sec.⁷⁷ The $[\text{O}_2] = 4.93 \times 10^{18}$ molecule/cm³ yields a pseudo-first-order rate constant of 2.15×10^6 sec⁻¹. In view of the extremely large pseudo-first-order rate constant for Rx. 21 and the relatively low HOSO_2 concentration, it is safe to say that the second

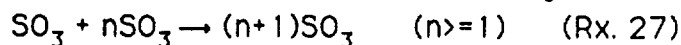
order reaction between bisulfite radical molecules (Rx. 22) is probably not a logical mechanism for the production of condensation nuclei. At low relative humidities, between 1% through 5%, $[H_2O] \approx 10^{16}$ molecule/cm³, Rx. 23 would have to have a rate constant of around 10^{-10} cm³/molecule sec just to be competitive. This rate constant is about two to three orders of magnitude larger than the large rate constant of adduct hydration in Castleman's²³ work. However, to dominate in rate of formation of condensation nuclei, a rate constant of approximately 10^{-8} cm³/molecule sec would have to exist. The former scenario (10^{-10} cm³/molecule sec) is highly unlikely and the latter scenario (10^{-8} cm³/molecule sec) is even more unlikely. The higher order Rx. (Rx. 24 and Rx. 25) which depend on the precursor reaction (Rx. 23) can also be discounted on the basis of the above explanation. The fate of the bisulfite radical clearly reacts by the hydrogen abstraction mechanism with dioxygen to form sulfur trioxide and HO₂ radical.

6. Reaction of Sulfur Trioxide.

The sulfur trioxide molecules subsequently react with water molecules to form the SO₃·H₂O adduct.²³



Castleman et al.²³ proposes that the direct production of H₂SO₄ is probably not the case since it would have to proceed via a four-centered mechanism and would have to have a much lower rate constant than their experimentally obtained value of 9.1×10^{-13} cm³/molecule sec. Also, Castleman et al.²³ did not observe any polymerization of SO₃.



Castleman et al.⁷⁸ also performed some Complete Neglect of Differential Overlap (CNDO/2) calculations yielding information on the thermodynamic stability of the SO₃·H₂O adduct and the H₂SO₄ molecule. Since CNDO/2 calculations are most appropriate for determining relative stabilities, the CNDO/2 energy values for the SO₃·H₂O adduct and the energy barrier to H₂SO₄ production has been rescaled to agree thermodynamic data. Castleman et al.⁷⁸, calculated a value of -23.1 kcal/mole from the JANAF tables at 0 K for the thermodynamic binding energy of the H₂SO₄ species.

The SO₃·H₂O adduct is found to have moderate thermodynamic stability

with an estimated re-scaled binding energy of -15.2 kcal/mole. The estimated re-scaled binding energy for the peak energy barrier which leads to the formation of H_2SO_4 is -11.9 kcal/mole. In other words, a 3.3 kcal/mole energy barrier has to be overcome to produce the more stable H_2SO_4 species. The negative binding energies implies that the reactions to form $\text{SO}_3 \cdot \text{H}_2\text{O}$ and H_2SO_4 are exothermic.

7. Isomerization of Sulfur Trioxide Hydrate.

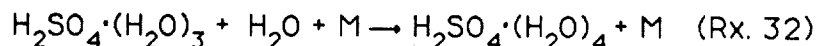
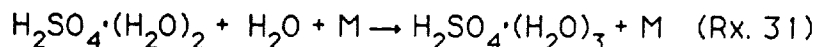
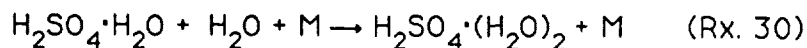
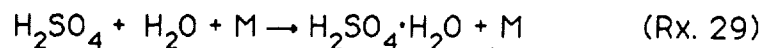
It is apparent that the energy released to form the $\text{SO}_3 \cdot \text{H}_2\text{O}$ adduct formation is more than enough to overcome the energy barrier of 3.3 kcal/mole for the hydrogen rearrangement mechanism. From the CNDO/2 calculations, the minimum energy pathway for the isomerization mechanism is proposed to occur via the hydrogen "hopping" from one of the oxygen atom to the other oxygen atom.



At this point, Rx. 28 is uncharacterized with respect to a rate constant. However, to get a general feel for the rate constant regime, the literature was reviewed to find other gas-phase isomerization reactions. The rate constant for the isomerization of methyl isocyanide at 503 K was found to be about 6×10^{-4} at higher pressures.⁷⁹

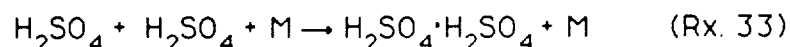
8. Reaction of Sulfuric Acid.

The thermodynamic properties of aqueous sulfuric acid solutions and hydrates is presented in the work by Giauque, Hornung, Kurzler, and Rubin.⁸⁰ They reported stable hydrates of sulfuric acid to be mono-, di-, tri-, tetra-, and hemihexa-hydrate. All free energy changes for the formation of hydration are found to be positive and thus the intermediate hydrates are stable with respect to lower and higher hydrates. On this basis, the reverse process for dehydration is not considered. Given below are the hydration reactions of sulfuric acid.

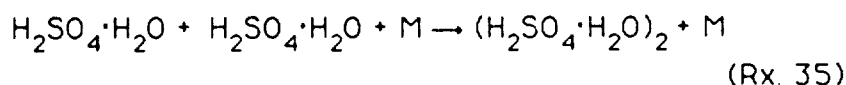
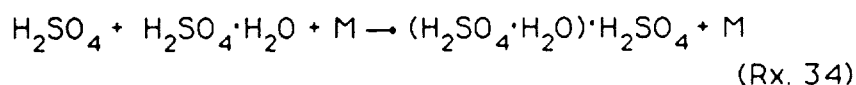


The dimerization of sulfuric acid has been considered and discounted because it is in direct competition with Rx. 29. A relatively

large pseudo-first-order rate constant of around 10^2 sec^{-1} is calculated for Rx. 29 using a conservative rate constant of $1 \times 10^{-14} \text{ cm}^3 \text{ molecule}^{-1} \text{ sec}^{-1}$ and a water vapour concentration of $10^{16} \text{ molecule/cm}^3$. In view of the large pseudo-first-order rate constant for Rx. 29 and since the dimerization of sulfuric acid is a second-order reaction and the H_2SO_4 concentration is small, Rx. 33 is highly unlikely to occur.



At best if Rx 29 is considered to be instantaneous, Rx. 34 and 35 are still second-order reactions with a maximum reactant concentration equal to that of H_2SO_4 .



Rxs. 34 and 35 are reduced to the same problem as the dimerization reaction and are also of little consequence in the total reaction scheme.

9. Scavenging Reactions.

Beside the gas-phase reactions, one must consider the removal of reactants or intermediates by adsorption onto particles generated by the gas-phase reactions. The gas-phase reactions would be affected if the reactants or the intermediates are removed to an appreciable extent by adsorption. For simplicity's sake the time evolution of particle development is not considered and the worst case scenario is presented. All scavenging rates are calculated on the assumption of an instantaneous particle population and on a typical experimental particle number density. Furthermore, the "collision adsorption efficiency" coefficient (γ) is assumed to be unity. The maximum scavenging rates are estimated by employing the collision frequency model which estimates the number of collisions that result in the removal of reactant or intermediate, per unit time on the surface of the particle. If the particles are more massive than the gas-phase molecules then the particles can be assumed to be stationary with respect to the gas-phase molecules. For a spherical particles the adsorption collision frequency or maximum rate of scavenging is defined as:²³

$$R_p = Z_{p-c} = \gamma \pi r_p^2 N_p C v_c \quad (\text{Eq. 26})$$

and,

$$v_c = (8kT/\pi m_c)^{1/2} \quad (\text{Eq. 27})^{81}$$

where, γ is the collision adsorption efficiency coefficient, r_p is the radius of the particle, N_p is number density of particle, C is the concentration of the reactant or the intermediate component, v_c is the average velocity of the reactant or the intermediate component, k is the Boltzmann's constant, T is the absolute temperature, and m_c is the molecular mass of the reactant or the intermediate component. Eq. 29 can be rearranged to yield:

$$R_p = k_p C \quad (\text{Eq. 28})$$

where scavenging rate constant k_p is defined as $\gamma \pi r_p^2 N_p v_c$. The gas-phase pseudo-first-order rate constant for the particular reaction under consideration is defined in general terms as k_g . The rate constants for scavenging of OH radical, bisulfite radical, sulfur trioxide, and sulfuric acid are compared with respective gas-phase pseudo-first-order rate constants (vide infra). If the ratio of gas-phase to scavenging rate constants is much greater than 1 then the scavenging process is negligible, i.e., the gas-phase reaction rate is much faster than the scavenging rate.

From the estimated rate constant ratios (k_g/k_p) in Table 3, the scavenging process does not significantly alter the gas-phase kinetics scheme by depleting the concentration of the OH radical, the bisulfite radical, or the sulfur trioxide molecule. For instance, even in the worse case scenario, the OH radical reacts at least 300 times faster in the gas-phase than by adsorption on the particles.

Table 3. Parameter List for Calculating Gas-Phase Reaction Rate to Particle Scavenging Rate Ratios.

Species	Mass (m_c)	Velocity (v_c)	k_g^*	k_p	k_g/k_p
OH	2.83×10^{-23}	6.09×10^4	7.4×10^0	2.39×10^{-2}	3.10×10^2
HOSO ₂	1.34×10^{-22}	2.79×10^4	2.2×10^6	1.10×10^{-2}	2.00×10^8
SO ₃	1.40×10^{-22}	2.81×10^4	9.1×10^3	1.10×10^{-2}	8.27×10^5
H ₂ SO ₄	1.63×10^{-22}	2.54×10^4	-----	9.96×10^{-3}	-----

m_c (g/molecule); v_c (cm/sec)

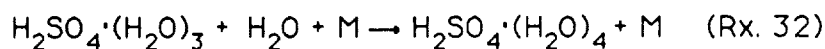
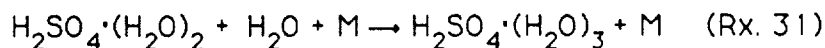
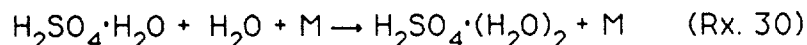
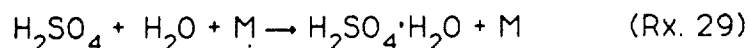
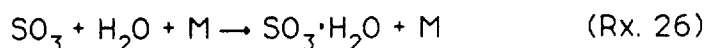
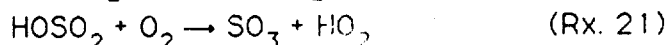
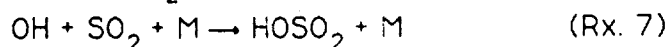
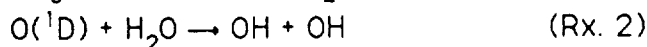
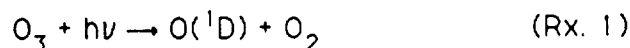
Temperature = 298 K; $N_p = 5 \times 10^5$ particle/cm³; $\gamma = 1$; $r_p = 5 \times 10^{-7}$ cm

*Calculated pseudo-first-order rate constants using the rate constants in Table 2 and the following concentrations: [SO₂] = 10^{12} molecule/cm³;

$[H_2O] = 10^{16}$ molecule/cm³; $[O_2] = 4.93 \times 10^{18}$ molecule/cm³; $[M] = 2.46 \times 10^{19}$ molecule/cm³

10. Summary of Reactions.

In summary, based upon the initial reaction conditions and the known relevant reactions and their relative rates, the inferred mechanism for the production of condensation nuclei is summarized in the following:



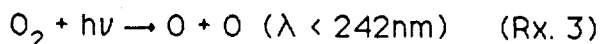
The above reaction scheme has been simplified and only considers the reactions which lead to the formation of condensation nuclei. The reader should note that other side reactions that compete for O(¹D) atoms and OH radical molecules are not included in the total reaction scheme to focus attention on the reactions which directly participate in the production of condensation nuclei.

In the binary homogenous nucleation theory, discussed later, nuclei formation occurs when a critical constellation of n-m-mers forms containing n molecules of H₂SO₄ and m molecules of H₂O. In this search for a chemical kinetic mechanism, the actual molecule or molecules that are nuclei are not known. However, in view of the preceding discussion on H₂SO₄ formation and the known ability of H₂SO₄ to form hydrates, it is reasonable to suppose that sulfuric acid and any of its hydrates can be considered to be a condensation nucleus. The production of condensation nuclei in this reaction system is a function of the O₃ concentration, the H₂O concentration, and the SO₂ concentration. The O₂ concentration and M concentration are in large excess and are held constant for all

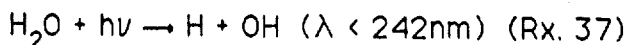
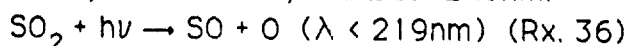
experiments described herein. The O₃ molecule is a reactant source for the production of O(¹D) atom in Rx. 1. The O(¹D) atom reacts with a H₂O molecule to produce the OH radical. The bisulfite radical is formed from the reaction of the OH radical with the SO₂ molecule. Moreover, Rx. 7 is in competition with two other reactions for the OH radical. The OH radical concentration is also depleted at comparable rates by Rx. 8 and Rx. 9.

The bisulfite radical is further oxidized by the diatomic oxygen to produce SO₃. In the presence of water vapour, the SO₃ molecule is rapidly hydrated to produce the moderately stable SO₃·H₂O adduct. The SO₃·H₂O adduct subsequently isomerizes to the more thermodynamically stable sulfuric acid species. The H₂SO₄ molecule is the basic starting component of the condensation nuclei. Finally, the hygroscopic H₂SO₄ species is hydrated. The H₂SO₄ and its hydrates are considered to be condensation nuclei.

The mechanistic route for the formation of condensation nuclei is partially experimentally substantiated by individually excluding one of the reactants. In the absence of the UV radiation source (249nm), i.e., the dark reaction, the formation of condensation nuclei is not observed. This observation would eliminate the notion that SO₂ hydration or SO₂ oxidation by ozone is a precursor mechanism for the formation of condensation nuclei. The formation of condensation nuclei was not observed when ozone is omitted from the reaction system. One can conclude that the production of condensation nuclei does not occur via the photolysis of O₂, SO₂, or H₂O. Diatomic oxygen absorbs below 242nm,⁸² sulfur dioxide absorbs in the 340-390nm, 260-340nm, 180-240nm, and 180-110nm region⁸³ and water vapour absorbs below 242nm.⁸⁴ At 249nm none of the reactants absorb to produce an excited state molecule or photodissociate.



Rx. 5 occurs between 340-390nm, 260-340nm, and 220-240nm.



In addition, when sulfur dioxide is also omitted from the reaction system and the laser is pulsed, no formation of condensation nuclei is observed. This observation is consistent with the idea of H₂SO₄ or some

oxidized SO_2 species acting as a nucleating agent.

The production of condensation nuclei is not observed when the laser is pulsed in the absence of added water vapour. This empirical result is interpreted as the lack of production of OH radical molecules by Rx. 2 in which water vapour is a reactant.

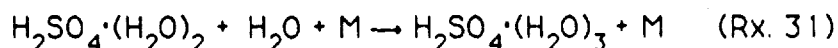
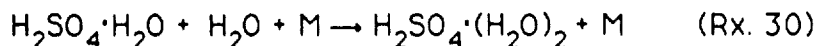
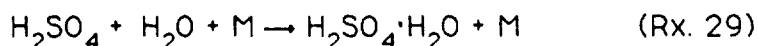
11. Theoretical Kinetic Model.

The reaction scheme and assumptions presented above are used to setup theoretical kinetic rate model. Each reaction step is arranged in a differential rate format in accordance with kinetic rate law. The particular reaction step is expressed in terms of a rate constant and the participating reactants. Also, each differential rate expression will consist of the appropriate terms which mathematically describe the appearance and disappearance of the reactant of interest. Most of the differential rate expressions are simplified by eliminating the time dependence of a particular reactant. The mathematical simplification is achieved by assuming an excess of one of the reactants, thereby, reducing a mixed second-order reaction to pseudo-first-order reaction. Most of the reaction steps are found to be in the form of non-homogeneous, first order, linear, differential equations. The final rate expression for the formation of sulfuric acid tri-hydrate is quite overwhelming at first glance. The final rate expression is nothing more than a series of exponential functions with a pre-exponential constant. The large number of exponential terms in the final integrated rate expression arise from the original exponential dependency on the disappearance of the OH radical. Upon the initial integration step the original exponential is regenerated along with an additional exponential integration factor. After each integration step an additional exponential integration term is generated for each existing exponential term. The development of the kinetic model, the assumptions invoked, and the rate expressions for OH radical formation, OH radical consumption, bisulfite formation, sulfur trioxide formation, sulfur trioxide hydrate formation, sulfuric acid formation, sulfuric acid mono-hydrate formation, sulfuric acid di-hydrate formation, and sulfuric acid tri-hydrate formation are presented elsewhere²

12. Determination of Rate Constants for Reactions 28, 38 and the Hydration Reactions of Sulfuric Acid.

The total reaction scheme proposed earlier (vide supra) has many well defined rate constants with the exceptions of Rxs. 28, 38, and the hydration reactions of sulfuric acid (Rxs. 29-31). The values of the rate

constants for the following reactions are generated from the computer model which best fits the experimental results as judged by a subjective process. The results given below are calculated on an Apple Macintosh computer using a rate calculation program written in Microsoft Basic, see appendix B for algorithm and code details. The computer program was designed with edit fields to facilitate changes in reactant concentrations and laser power. Each unknown rate constant is varied individually and the results are analyzed. To simulate experimental conditions, described by the particle/cm³ vs. time curves, the total number of condensation nuclei is calculated by integrating from typical integration limits, 8 to 28 seconds, (see Figure 3.) and then multiplying by the flow rate (2.511x10⁴ μL/sec).



It is found that, Rxs. 28, 38, 29, 30, and 31 are not interrelated with respect to rates of reaction. The lack of interdependency of the individual rate constants will become more apparent later in this discussion.

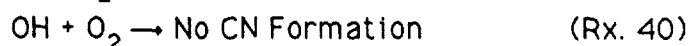
A. Determination of the Pseudo-First-Order Rate Constant for Reaction 38.

The reasoning behind the postulation of Rx. 38 is the necessity to express the dependence of condensation nuclei formation as a function of sulfur dioxide concentration. If Rx. 38 is not proposed, even at the fast rate of condensation nuclei formation using the kinetic nucleation model, all of the OH radicals will react with SO₂ within the experimental time regime (28 seconds). Increasing the sulfur dioxide concentration only serves to expedite the oxidation of sulfur dioxide. Without Rx. 38, the reaction of the OH radical with SO₂ will always go to stoichiometric completion which eliminates the SO₂ concentration dependency. Since, the oxidation of sulfur dioxide with the OH radical is the primary reaction for the formation of the SO₂ oxidized species, another mechanism is proposed to compete for the OH radical. Introducing Rx. 38 restores the dependency on the sulfur dioxide concentration. Increasing

the sulfur dioxide concentration will increase the rate of formation of the oxidized sulfur species, in essence making Rx. 7 compete for the OH radical. It is essential that Rx. 38 be in the total reaction scheme for any nucleation mechanism to work as function of sulfur dioxide concentration. Furthermore, Rx. 38 removes the concentration dependency on ammonia and also greatly reduces the concentration dependency on ozone. This type of behavior becomes apparent when one considers the that the OH radical is also consumed at a competitive rate by reacting with ammonia (Rx. 9) and ozone (Rx. 8). If the pseudo-first-order rate constant for Rx. 38 is much larger than the pseudo-first-order rate constants for Rx. 8 and Rx. 9 then the sum of the pseudo-first-order rate constants is simply k_{38} .

The pseudo-first-order rate constant is determined to be $1 \times 10^3 \text{ sec}^{-1}$ for Rx. 38. Rate constants for Rx. 28, 29, 30, 31, and 38 are generated by the computer model which best fit the experimental results. The formation of condensation nuclei remains insensitive if the pseudo-first-order rate constant is increased above $1 \times 10^3 \text{ sec}^{-1}$.

The possible identification of the X component is now examined. The pseudo-first-order rate constant for Rx. 38 is roughly two orders of magnitude larger than the pseudo-first-order rate constant for Rx. 8 and Rx. 9. The pseudo-first-order rate constant for Rx. 38 is a composition of the rate constant and the concentration of X. To generate a pseudo-first-order rate constant of $1 \times 10^3 \text{ sec}^{-1}$, either the rate constant or the reactant concentration must be large. There are two possibilities with respect to large reactant concentrations, one is the reaction of OH radical with H_2O and the other is the reaction with O_2 .



Under the reaction conditions where $[\text{H}_2\text{O}] = 10^{16} \text{ molecule/cm}^3$ the rate constant for Rx. 39 would have to be around $10^{-13} \text{ cm}^3/\text{molecule sec.}$, which is reasonable. The O_2 concentration in the reactor vessel is $4.93 \times 10^{18} \text{ molecule/cm}^3$ which yields a rate constant for Rx. 40 of $4.93 \times 10^{-15} \text{ sec}^{-1}$. The rate constant for Rx. 40 is not unreasonable and is a plausible reaction, along with Rx. 39, for the depletion of OH radical.

Another possible gas-phase reaction with OH radical is the reaction with hydrocarbon impurities (Rx. 41) in the zero air.⁸⁵ A specification for zero air is that the total hydrocarbon (THC) content must be less than 1 ppm.



A 1 ppm THC concentration would translate into a hydrocarbon impurities

concentration of 2.46×10^{13} molecule/cm³. Zero air is manufactured from a cryogenic mixture of liquid nitrogen and liquid oxygen which is obtained from ambient tropospheric air. The major hydrocarbon component of ambient air is methane, roughly a thousand time greater than other hydrocarbons⁸⁶, and so the THC content in zero air is assumed to be methane. Davis et al.⁸⁷ studied the reaction between OH radical and methane (CH₄) and obtained a rate constant of 7.7×10^{-15} cm³ molecule⁻¹ sec⁻¹ by measuring the resonance fluorescence of the OH radical in a discharge flow tube apparatus. A pseudo-first-order rate constant of 1.9×10^{-1} sec⁻¹ was obtained for the reaction of OH radical with methane. The reaction of OH radical with methane does not react quick enough to satisfactorily explain Rx. 38.

Carbon monoxide is also another possible contaminant in zero air because of CO concentration in ambient air⁸⁶ and the manufacturing process described above.



The rate constant for the reaction between OH radical and CO is 1.5×10^{-13} cm³ molecule⁻¹ sec⁻¹. In order for CO to play an important role in the consumption of OH radical, the CO concentration in the zero air would have to be around 100 ppm. However, Beno⁸⁸ observed an enhancement of the rate constant in the presence of water vapour. Beno's⁸⁸ observation near room temperature (338 K) would lower the CO concentration in the zero air by approximately a factor of two to obtain a pseudo-first-order rate constant large enough to account for Rx. 38.

B. Determination of the First-Order Rate Constant for Reaction 28.

The isomerization of SO₃·H₂O to H₂SO₄ is the rate determining step for formation of condensation nuclei. The isomerization step does not alter the reactants' concentration dependency. Since Rx. 28 is the rate determining step and does not depend on the concentration of reactants, it only regulates the amount of condensation nuclei produced at given time. Varying k_{28} does not change the dependency of reactants concentration on the formation of condensation nuclei and therefore is independent of other reaction steps and their associated rate constant. The rate constant for the isomerization mechanism is determined to be 1.23×10^{-4} sec⁻¹ by the method discussed at the beginning of section 12. A rate constant of 1.23×10^{-4} sec⁻¹ yields the appropriate condensation nuclei concentrations. This gas-phase isomerization rate constant seems reasonable compared to that of the isomerization of methyl

isocyanide (for rate constant, vide supra). The isomerization of methyl isocyanide is a good comparison because it is a unimolecular gas-phase reaction in which both the bonding structure and atom positioning is changed ($\text{CH}_3\text{NC} \rightarrow \text{CH}_3\text{CN}$).

C. Determination of the First-Order Rate Constants for the Mono-, Di-, and Tri-Hydrates of Sulfuric Acid.

The first-order rate constants for the mono-, di-, tri-hydrates of sulfuric acid are $1 \times 10^{-10} \text{ cm}^3 \text{ molecule}^{-1} \text{ sec}^{-1}$, $1 \times 10^{-11} \text{ cm}^3 \text{ molecule}^{-1} \text{ sec}^{-1}$, and $1 \times 10^{-12} \text{ cm}^3 \text{ molecule}^{-1} \text{ sec}^{-1}$. The third body concentration, $[\text{M}] = 2.46 \times 10^{19} \text{ molecule/cm}^3$, is included in the hydration rate constants. The rate of formation of condensation nuclei is insensitive to the variation of the values of the hydration rate constants. This is true if the rate of hydration is much faster than the rate of isomerization ($k_{28} \ll k_{29}, k_{30}, k_{31}$). The magnitudes of the hydration rate constants are chosen based on the rate constant obtained by Castleman²³ in the hydration of sulfur trioxide. The only reason for the different values of the rate constants is that when the hydration rate constants are equal the exponential part of rate expression vanishes.

14. Review of Theoretical Model and Error Analysis.

A sensitivity analysis is performed on final rate expression for the production of condensation nuclei by mathematically evaluating each term in the final integration rate expression independently at time equals 1 second and typical reactant concentrations. The ninth term, given below, is roughly a thousand times more sensitive, with respect to condensation nuclei formation, than the first term in the equation.

$$\frac{(k_{31} k_{30} k_{29} k_{26} k_{21} k_7 [\text{OH}]_0 / (k_{21} - (k_7 + k_8 + k_{38}))) (k_{26} - (k_7 + k_8 + k_{38})) (k_{28} - (k_7 + k_8 + k_{38})) (k_{29} - k_{28})}{(k_{30} - k_{28}) (k_{31} - k_{28}) (1 - \exp(-k_{28} t))}$$

The first term is far less sensitive than the other terms in the equation, with the exception of the forty-first term. The ninth term is the most sensitive because of the pre-exponential collection of constants or the pre-exponential term, $(k_{31} k_{30} k_{29} k_{26} k_{21} k_7 [\text{OH}]_0 / (k_{21} - (k_7 + k_8 + k_{38}))) (k_{26} - (k_7 + k_8 + k_{38})) (k_{28} - (k_7 + k_8 + k_{38})) (k_{29} - k_{28}) (k_{30} - k_{28}) (k_{31} - k_{28})$. The isomerization rate constant is eliminated from the numerator upon the final integration of the rate expression. With the isomerization rate constant gone, the pre-exponential term is roughly five orders of magnitude larger than the other pre-exponential terms.

The ninth term mathematically describes the rate limiting step for the isomerization of sulfur trioxide hydrate to sulfuric acid. The same conclusion can be reached if the sulfuric acid hydration mechanisms are assumed to be in steady-state. The final integrated rate expression can be simplified by comparing the relative magnitudes of the pseudo-first-order rate constants of the total reaction scheme. If one of the rate constants in a term which is the difference between rate constants in the denominator is much larger than the other then the difference reduces to just the larger rate constant and will cancel with the appropriate rate constant in the numerator. For example if $k_a \gg k_b$ then $k_a k_b / k_a - k_b$ reduces to just k_b . Using the pseudo-first-order rate constant from Table 2, one can conclude the following: $k_{21}' \gg (k_7' + k_8' + k_9' + k_{38}')$; $k_{26}' \gg (k_7' + k_8' + k_9' + k_{38}')$; $k_{28}' \gg (k_7' + k_8' + k_9' + k_{38}')$; $k_{29}' \gg k_{28}'$; $k_{30}' \gg k_{28}'$; $k_{31}' \gg k_{28}'$; $k_{38}' \gg (k_7' + k_8' + k_9')$. Since all the other terms in the final integrated rate expression are insignificant compared to the ninth term, it is reduced to:

$$N_{30} = (k_7'/k_{38}') [SO_2][OH]_0 (1 - \exp(-k_{28}'t)) \quad (\text{Eq. 30})$$

Eq. 30 could have been derived directly if the steady-state approximation was invoked for the appropriate reactions based upon the above inequalities. In the limit, Eq. 30 demonstrates that the final condensation nuclei concentration will equal only a fraction of the initial OH radical concentration because of the rate constant ratio. The numerator of the ratio of the pseudo-first-order rate constant is for the reaction of the OH radical that produces condensation nuclei. The denominator is for the reaction that consumes the OH radical without production of condensation nuclei. However, when the final integration rate expression was derived the relative differences in the rate constants or pseudo-first-order rate constants were not known. The closed analytical rate expression was derived without the steady-state approximation as not to prejudice the kinetic model or restrict its flexibility.

Substituting Eq. 25 into Eq. 30 yields: $N_{31} =$

$$(k_7' k_2 [O_3][H_2O][SO_2] E 2.303 \phi(O^1D) \lambda \epsilon I / (k_{38}' V h c_s (k_3' + k_4')))(1 - \exp(-k_{28}'t)). \quad (\text{Eq. 31})$$

Eq. 31 is a good approximation for calculating the condensation nuclei concentration as a function of time. One can see that the condensation nuclei formation rate has a first order dependency on the ozone concentration, water vapour concentration, sulfur dioxide concentration, and laser power. The first order dependency can be illustrated by a

log-log plot of the condensation nuclei concentration as a function of reactants concentration and laser power at given time interval. The slope of the log-log plots will be unity (see Graphs 5-8).

All relative percent errors are presented in terms of total condensation nuclei not the logarithm of the total condensation nuclei. The relative percent error is defined as:

$$|O - A|/A \times 100\%. \quad (\text{Eq. 32})$$

Where O is the experimentally observed value and A is the accepted or theoretical value. The relative percent error of the total condensation nuclei is presented to reflect the true error not the error of the compressed difference between the logarithmic values.

The values generated by the theoretical kinetic model are in very good agreement with the experimental data for the higher reactant concentrations. In the regions of higher concentrations of SO_2 , O_3 , and H_2O , the relative percent error varied from 0.6% to 43.0%, however, the average relative percent deviation is 11.6%. The low concentration points of SO_2 , O_3 , and H_2O have a much higher relative percent error, which vary from 21.1% to 76.0%. It should be noted that the relative percent error for lower concentration points decreases with increasing laser power, i.e., higher OH radical concentrations.

Given below are Graphs 18 through 20 which compare the kinetic theory to experimental data. At the higher reactant concentration, the kinetic model agrees well when compared to experimental data. The average slopes of the reactants concentration dependency and laser power dependency of the experimental data, in general, behave in the same manner as the kinetic model predicts. All of the slopes for the log-log plot of CN as a function of reactants concentration are approximately 1, with the exception of the ammonia concentration plots which have a slope of zero. The slopes of the ammonia concentration plots for the experimental data are slightly negative. The theoretically kinetic model also predicts a slightly negative dependency on condensation nuclei formation as a function of the ammonia concentration.

15. Homogeneous Heteromolecular Nucleation Model.

Using the homogeneous heteromolecular nucleation method described by Mirabel and Katz,⁸⁹ the upper limit of the nucleation rate is calculated. If all of the oxidized species of sulfur dioxide is converted instantly to sulfuric acid, (Rx. 7 is the rate determining step) the sulfuric acid concentration is 1.30×10^{11} molecule/cm³ at a laser power

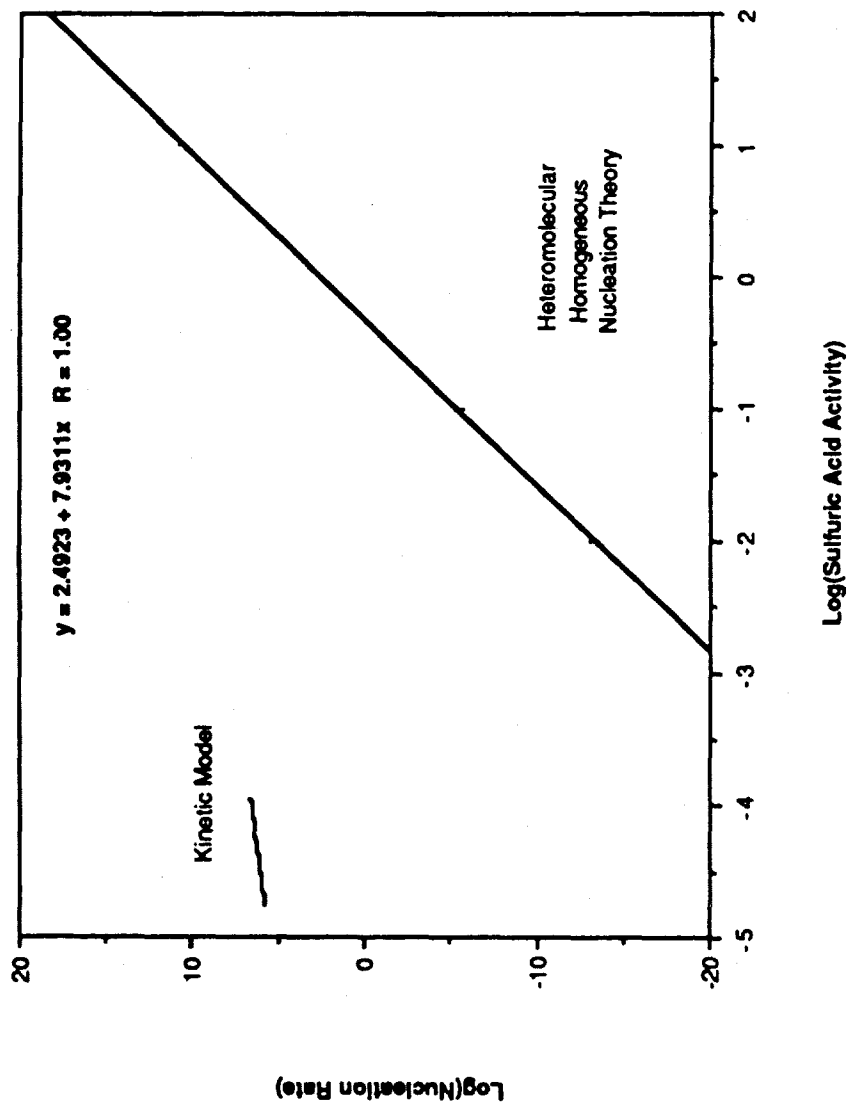
of 12.6 mjoule and an ozone concentration of 9.770×10^{13} molecule/cm³. However, the sulfuric acid concentration calculated above is based on the postulated reaction between X and OH radical (Rx. 38). At 293 K the pressure of sulfuric acid in the vapour-phase is calculated to be 3.94×10^{-6} torr by employing $p = (n/V)kT$, where $k = 1.0354 \times 10^{-19}$ cm³ torr K⁻¹ molecule⁻¹. Using a value of 3.1×10^{-5} torr⁹⁰ for the vapour pressure of pure sulfuric acid, yields an activity of 1.27×10^{-1} . At the highest experimental water vapour concentration, a relative humidity of about 6%, the theoretical rate of nuclei formation is approximately 2.4×10^{-5} particle/cm³ sec. An estimate of an experimental rate of nucleation is calculated from the total number of particles formed under the same reactant concentrations as above and dividing it by the reaction volume, i.e., volume of the laser beam, and average residence time in the reactor. The total number of particles formed in an experiment is calculated at an ozone concentration of 9.770×10^{13} molecule/cm³ and a laser power of 12.6 mjoule (Log(L.P.) = 1.1). The total number of particles formed is calculated to be 1.051×10^8 particle. The laser beam has a diameter of 0.25 cm and a length of 34.8 cm which yields a reaction volume of 6.83 cm³. If the reaction is assumed to proceed through the entire particle counting process (28 seconds) then a nucleation rate of 5.5×10^5 particle/cm³ sec is calculated.

To obtain the number of sulfuric acid molecules contained in a critical nucleus at a relative humidity of 6%, which is predicted by heteromolecular homogeneous nucleation theory, a log-log plot of the nucleation rate as a function of sulfuric acid activity is performed. The nucleation rates are graphically extrapolated to 6% R.H. from the work done by Mirabel and Katz.⁸⁹ Nucleation rate were adjusted for the vapour pressure of pure sulfuric acid ($p^0 = 3.1 \times 10^{-5}$ torr) obtained by Chu and Morrison.⁹⁰

The plot yields a slope of roughly 8 which corresponds to the number of sulfuric acid molecules in the critical nucleus (see Graph 9). The experimental data has an average slope of around 1 with respect to sulfur dioxide, i.e., one sulfur bearing species per nucleus (see Graph 9).

Homogeneous heteromolecular nucleation theory does not correlate well with the experimental data because of the low nucleation rate (2.4×10^{-5} particle/cm³ sec) and the larger number of sulfuric acid molecules per nucleus (8 H₂SO₄ molecule/nucleus). Graph 9 illustrates the difference in the dependency of nucleation rates and number of sulfuric acid molecules in each nucleus as a function of sulfuric acid activity for the experimental data and the homogeneous heteromolecular nucleation theory.

Graph 9. Heteromolecular Homogeneous Nucleation Theoretical



16. Estimation of Experimental Reproducibility.

Since there is no dependence of the nuclei formation on ammonia vapour concentration, the experimental ammonia data can serve as an experiment for reproducibility (see Graph 4). A maximum relative percent error of 28.6% is obtained from the low laser power ammonia data set. An overall average relative percent error of 9.0% is calculated from the ammonia data set. It can be inferred from the experimental reproducibility that the experimental results correlate well with the theoretical kinetic model, except for the low reactant concentration points.

17. Ratio of Oxidized Sulfur Dioxide to Condensation Nuclei Formation.

Not all of the oxidized sulfur dioxide is converted into condensation nuclei within the time frame of this experiment (8 to approximately 28 seconds). To determine quantitatively the amount of intermediate ($\text{SO}_3 \cdot \text{H}_2\text{O}$) to product conversion ($\text{H}_2\text{SO}_4 \cdot (\text{H}_2\text{O})_3$), a single plot of the condensation nuclei rate ($\text{molecule cm}^{-3} \text{sec}^{-1}$) and the oxidized sulfur dioxide concentration (molecule/cm^3) is performed.

The condensation nuclei rates are estimated from the raw data curves by dividing the peak condensation nuclei concentrations by the time of occurrence of the peak which is corrected to account for an estimated average CNC delay time of 6 seconds (see Figure 3 for typical raw data curve). The condensation nuclei concentrations are converted from nuclei/micro-liter into nuclei/ cm^3 and are also multiplied by 100 to account for the dilution factor upon exiting the reactor vessel to the condensation nuclei counter. The condensation nuclei concentration dilution is the ratio of the reaction volume (laser beam volume) of 6.83 cm^3 and the reactor vessel volume of 683 cm^3 .

The oxidized sulfur dioxide concentrations are calculated by taking the limit at infinite time of the integrated rate expression which leads to the formation of the sulfur trioxide hydrate species. The concentration of oxidized SO_2 species for each experiment was calculated from the integrated rate expression using the experimental concentrations of SO_2 , H_2O , O_3 , and NH_3 and laser power. The slope of the linear regression line of the condensation nuclei rate verses oxidized sulfur dioxide concentration yields an isomerization rate constant on $4.0 \times 10^{-5} \text{ sec}^{-1}$.

Out of roughly 25,000 oxidized sulfur dioxide molecules, one

condensation nucleus is produced. This result is consistent with the idea of an isomerization reaction. The experimentally determined isomerization rate constant is about 3 times slower than the value predicted by kinetic model.

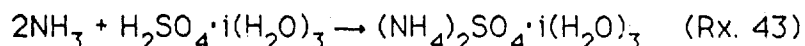
Because of cycling of the CNC sampling system and the phasing of the laser pulse with the CNC cycle, the times for the actual maximum may be in error by as much as 2 seconds. Further, phasing differences between the laser pulse and the CNC cycling are expected to cause uncertainty in the value of the peak concentrations in the raw data curves. Thus the slope of the line of Graph 10 is not expected to be as accurate an estimate of the rate coefficient (k_{28}) for nuclei formation as the more refined technique used in arriving at the kinetic model value. The kinetic model eliminates the time and phasing uncertainties by integrating the experimental raw data curves of nuclei concentration versus time. Another reason for the difference in the rate coefficient is that the kinetic model value was chosen preferentially to fit the data obtained at higher reactant concentrations, whereas the plot of Graph 10 includes all experiments.

18. Formation of Ammonium Sulfate Aerosol Particles.

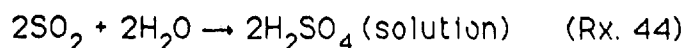
A. General Discussion of Ammonium Sulfate Particle Formation.

Originally the maturation chamber apparatus was designed to study the particle growth evolution as a function of time. However, even at the shortest times the aerosol particles reached a maximum size of around 0.3 to 0.5 microns (see Figures 4-7). The shortest time is about 120 seconds, which is the time required for the photolyzed mixture to pass through the maturation chamber containing ammonia gas followed by the deposition of the particles onto the ESM mount.

The gas-phase reaction between ammonia and condensation nuclei is as follows:



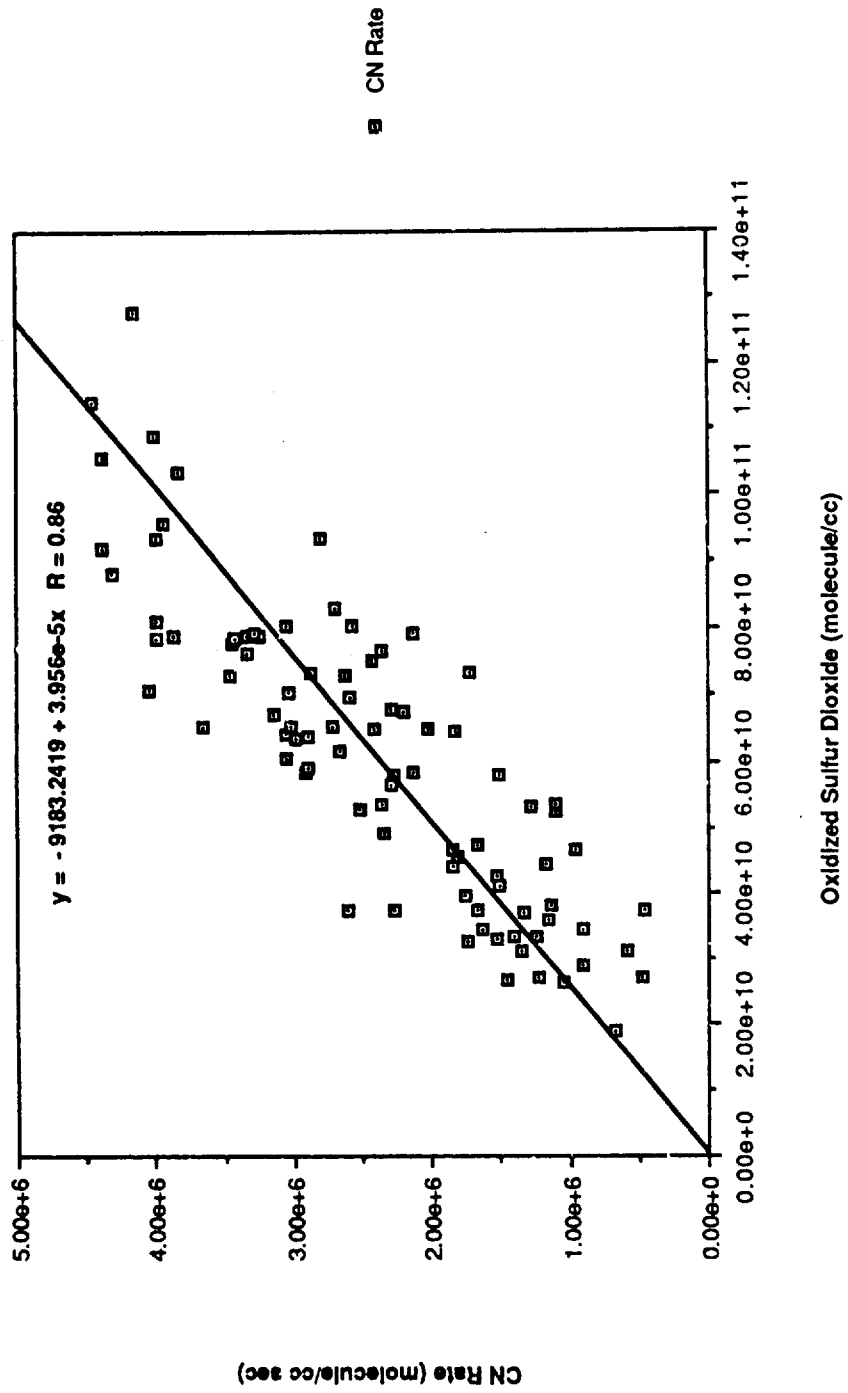
The subsequent rapid growth into aerosol particles was explained by Friend et al.⁹¹ to be the heteromolecular oxidation of SO_2 in the solution of the droplet. The ammonium ion acts as a catalyst to oxidize SO_2 to sulfuric acid.



(Rx. 16 is catalyzed by NH_4^+ and salt embryo.)

The ammonium sulfate particles in this experiment were formed at low

Graph 10. CN Rate vs. Oxidized Sulfur Dioxide



relative humidities (4%). This result offers a possible explanation why ammonium sulfate particles are found in dry air over deserts and also in remote clean tropospheric air.

B. Qualitative Determination of Particle Composition.

The aerosol composition is determined by employing two separate methods. The first method is accomplished by collecting small amounts of the aerosol on an ESM mount. Multiple samples are collected on the ESM mount to build up the particle concentration to a significant level to be analyzed on a ion chromatograph. However, after 100 samples were collected on a single ESM mount and diluted in only 5.0 ml of deionized water, the ammonium sulfate concentration was not large enough to yield a reliable ammonium to sulfate ion ratio. The retention times on the ion chromatograph did yield a positive qualitative identification of the ammonium and sulfate ions. The morphology of sulfuric acid and ammonium compounds was studied by Bigg.⁹² Electron-micrograph samples of ammonium sulfate, ammonium bisulfate, and ammonium persulfate were prepared to demonstrate the distinct and different appearance of each compound. By comparing the electron-micrographs obtained in this study to Bigg's⁹² micrographs, the products were clearly determined to be ammonia sulfate particles. The absence of a water halo indicates that the ammonium sulfate particles are created in the airborne phase, not on the ESM mount. The water halo is indicative of sulfuric acid particles because of its hygroscopic properties.

The particle growth rate could not be determined within the time regime of the experiment (2 minutes). However, the presence of larger ammonium sulfate particle would also substantiate the existence of condensation nuclei formed in the photolysis experiment. Also, the maturation experiment confirmed that the final oxidized product of SO_2 was the sulfate species.

19. Comparison of Nucleation Models: Advantages and Disadvantages.

The traditional homogeneous heteromolecular nucleation theory does not account for the large rate of particle formation observed under the experimental conditions in this work. Also, homogeneous heteromolecular nucleation theory fails to predict the number of condensation nuclei present in the Junge layer. At 218 K and a sulfuric acid partial pressure of 1.15×10^{-9} torr, Hamill et. al.⁹³ calculates an upper limit of 3.7×10^{-11} particle/cm³ sec for the nucleation rate via a homogeneous heteromolecular nucleation mechanism. This value

corresponds to one new particle formed per cubic centimeter every 850 years, whereas a rate of about 10^3 times greater is needed to explain the observed concentrations in the atmosphere.

There are some drawbacks with the conventional nucleation theory. Homogeneous heteromolecular nucleation theory does not have a lower limit boundary condition that preserves the identity of sulfuric acid. In the absence of this boundary condition it is possible to have fractional sulfuric acid molecules in the droplet. Homogeneous heteromolecular nucleation mechanism is derived from thermodynamics and depends upon macroscopic thermodynamic parameters. The free energy is treated as a macroscopic quantity and does not take into account the intermolecular and intramolecular interaction which could lead to the formation of small stable clusters.

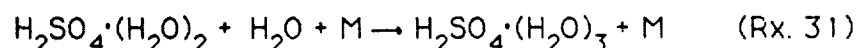
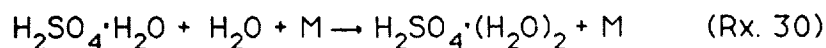
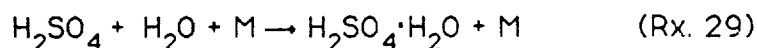
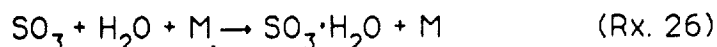
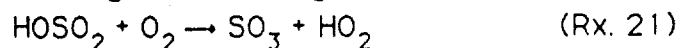
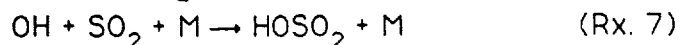
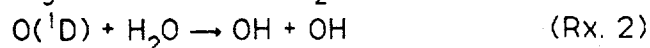
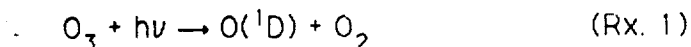
Moreover, terms like surface tension and contact angle are really meaningless on the microscopic level. How does one measure or calculate the contact angle or surface tension of clusters containing 10 to 20 molecules that are only a few molecules in depth? A statistical mechanics approach would greatly improve the homogeneous heteromolecular nucleation theory. Unfortunately, statistical mechanics often becomes intractable when dealing with the liquid phase. The advantage of the homogeneous heteromolecular nucleation model is its ability to calculate the Gibbs free energy with a few thermodynamic quantities, e.g., vapour pressure of the pure component and the surface tension at different mole fractions. The homogeneous heteromolecular nucleation model is well suited at upper limits where the nucleation parameters reach their thermodynamic bulk properties, e.g., surface tension, contact angle, and bulk liquid phase properties. However, homogeneous heteromolecular nucleation is based on the assumption that gas phase molecules are non-ideal, i.e., they condense. At high gas phase concentrations the molecules behave less ideally and should not be treated as an ideal gas, i.e., $p \neq (n/V)RT$.

The kinetic model has the advantage of calculating the rate of reaction directly from the integrated rate law and also affords a more detailed physical explanation of the individual steps. The total rate expression can be simplified by employing the steady-state approximation, if applicable to larger reaction schemes, to make the final analytical solution more manageable. However, the kinetic model requires the knowledge of the rate constants for each individual step. If the situation allows, the importance of the particular mechanism can be minimized by selecting relatively large rate constants which is equivalent to invoking the steady-state approximation.⁹⁴ In some cases

second-order reactions in a consecutive reaction scheme cannot be solved analytically but can be approximated by a series expansion and neglecting the higher order terms. Mixed second-order reactions can also be simplified if one of the components is in large excess, a thirty-fold excess or more. The kinetic model is best suited to schemes having a small number of elementary reaction steps where most of the rate constants are known.

20. Conclusion.

In conclusion a detailed investigation of known relevant reactions and their corresponding rate constants has led to a chemical mechanism which describes the formation of condensation nuclei.



However, to restore the dependency of condensation nuclei formation on the sulfur dioxide concentration a reaction between the OH radical and an unknown species was postulated (Rx. 38). Various reactions have been investigated under the experimental condition which could satisfy the postulated reaction. From the reaction scheme a kinetic model was developed. With a few verifiable assumptions a closed analytical solution was derived. Proposed rate constants for the isomerization of sulfur trioxide hydrate and for the mono-, di-, and tri-hydrates of sulfuric acid were calculated from the kinetic model. In the higher reactant concentration region the kinetic model correlates well with the experimental data (average relative error of 11.6%). At the lower reactant concentration region the kinetic model has a higher relative error range from 21% to 76%.

Applying heteromolecular homogeneous nucleation theory to our data yields a nucleation rate of 2.4×10^{-5} nuclei/cm³ sec. The heteromolecular homogeneous nucleation theory also predicts that each

critical nucleus contains 8 sulfuric acid molecules (see Graph 9). Nucleation theory does not explain the the high nucleation rates and the first-order dependency on sulfur dioxide concentration obtained in this study.

Also, wall effects and reactant or intermediate scavenging was found to be negligible. The time resolution of the maturation experiment (2 minutes) was found to be too low compared to the ammonium sulfate particle formation rate. However, from ion chromatography data and the particle morphology examined by electron scanning microscopy the particle composition is determined to be ammonium sulfate.

These results have determined that the final photo-oxidation products of sulfur dioxide is sulfuric acid. The formation of the large ammonium sulfate particles would suggest that condensation nuclei were formed from the photolysis of the reaction mixture.

Finally, a detailed investigation into the disappearance of the OH radical in the presence of SO_2 , O_3 , and H_2O is recommended. An experiment should be designed to investigate the proposed reaction (Rx. 38) in this work.

REFERENCE

1. Stockwell, W. R., and J. G. Calvert, *Atmos. Environ.*, 17, 2231, (1983).
2. Nolan, P. M., "Condensation Nuclei Formation by Photo-oxidation of Sulfur Dioxide with OH Radical in the Presence of Water Vapour and Ammonia", (Doctoral Dissertation, Drexel University, Philadelphia, PA, 1987).
3. Fuller, E. N., P. D. Schettler, and J. C. Giddings, *Ind. Eng. Chem.*, 58, 19, (1966).
4. Atkins, A. W., "Physical Chemistry", (W. H. Freeman and Company, San Francisco, 1985), p. 679.
5. Zellner, R., G. Wager, and B. Himme, *J. Phys. Chem.*, 3196, 84, (1980).
6. Wine, P. H. and A. R. Ravishankara, *Chem. Phys.* 69, 365, (1982).
7. Okabe, H., "Photo-Chemistry of Small Molecules, (John Wiley & Sons, New York, 1978), p. 244.
8. Okabe, H., "Photo-Chemistry of Small Molecules, (John Wiley & Sons, New York, 1978), p. 240.
9. Calvert, J. C. and J. N. Pitts, Jr., "Photochemistry", (John Wiley and Sons, New York, 1966) p. 588.
10. Molina, L. T. and M. J. Molina, *J. Geophys. Res.*, 91, 14501, (1986).
11. Amimoto, S. T., A. P. Force, J. R. Wiesenfeld, and R. H. Young, *J. Chem. Phys.*, 73, 1244, (1980).
12. Streit, G. E., C. J. Howard, A. L. Schmeltekopf, J. A. Davison, and H. I. Schiff, *J. Chem. Phys.*, 65, 4761, (1976).
13. Sander, N. D., J. E. Butler and J. R. McDonald, *J. Chem. Phys.*, 73, 5381, (1980).

14. Kajimoto, O. and R. J. Cvetanovic, *J. Chem. Phys.*, 64, 1005, (1976).
15. Marigitan, J. J., *J. Phys. Chem.*, 88, 3314, (1984).
16. Leu, M. T., *J. Phys. Chem.*, 86, 4558, (1982).
17. Wine, P. H., and R. J. Thompson, A. R. Ravishankara, D. H. Semmes, C. A. Gump, A. Torabi, and J. M. Nicovich, *J. Phys. Chem.*, 88, 2095, (1984).
18. Cox, R. A., *Inter. J. Chem. Kinet. Symp.*, 1, 379, (1975).
19. Davis, D. D., A. R. Ravishankara, and S. Fischer, *Geophys. Res. Letters*, 6, 113, (1979).
20. Atkinson, R., R. A. Perry, and J. N. Pitts, *J. Chem. Phys.*, 65, 306, (1976).
21. Castleman, A. W. and I. N. Tang, *J. Photochemistry*, 6, 349, (1977).
22. Harris, G. W., R. Atkinson, and J. N. Pitts, *Chem. Phys. Lett.*, 69, 378, (1980).
23. Castleman, A. W., R. E. Davis, H. R. Munkelwitz, I. N. Tang, and W. P. Wood, *Int. J. Chem. Kinet. Symp.*, 1, 629, (1975).
24. Cox, R. A., and D. Shepperd, *Nature (London)*, 284, 330, (1980).
25. Kurylo, M. J., *Chem. Phys. Lett.*, 23, 467, (1973).
26. Zahniser, M. S. and C. J. Howard, *J. Chem. Phys.*, 73, 1620, (1980).
27. Anderson, J. G. and F. Kaufman, *Chem. Phys. Lett.*, 19, 483, (1973).
28. Ravishankara, A. R., P. H. Wine, and A. O. Langford, *J. Chem. Phys.*, 70, 984, (1979).
29. Stuhl, F., *J. Chem. Phys.*, 59, 635, (1973).

30. Smith, I. W. M. and R. Zellner, *Int. J. Chem. Kinet.*, Symp. 1, 341, (1975).
31. Perry R. Atkinson, R. A., and J. N. Pitts, Jr., *J. Chem. Phys.*, 64, 3237, (1976).
32. Silver, J. A. and C. E. Kolb, *Chem. Phys. Lett.*, 75, 191, (1980).
33. Stephens, R. D., *J. Phys. Chem.*, 88, 3308, (1984).
34. Westenberg, A. A., N. de Haas and J. M. Roscoe, *J. Phys. Chem.*, 74, 3431, (1970).
35. Lewis, R. S. and R. T. Watson, *J. Phys. Chem.*, 84, 3495, (1980).
36. Howard, M. J. and I. W. M. Smith, *J. Chem. Soc., Faraday Trans. II*, 77, 997, (1981).
37. Brune, W. H., J. J. Schwab, and J. G. Anderson, *J. Phys. Chem.*, 87, 4503, (1983).
38. Keyser, L. F., *J. Phys. Chem.*, 87, 837, (1983).
39. Westenberg, A. A. and N. de Haas, *J. Chem. Phys.*, 58, 4066, (1973).
40. McKenzie, A. and M. F. R. Mulcahy, and J. R. Stener, *J. Chem. Phys.*, 59, 3244, (1973).
41. Clyne, M. A. A. and S. Down, *J. Chem. Soc., Faraday Trans. II*, 70, 253, (1974).
42. Trainor, D. W. and C. W. von Rosenberg, Jr., *J. Chem. Phys.*, 61, 1010 (1974).
43. Farquharson, G. K. and R. H. Smith, *Aust. J. Chem.*, 33, 1425, (1980).
44. Wagner, G. and R. Zellner, *Ber. Bunsenges. Phys. Chem.*, 85, 1122, (1981).
45. Kijewsky, H. and J. Troe, *Helv. Chim. Acta.*, 55, 205, (1972)

46. Klais, O., P. C. Anderson, and M. J. Kurylo, *Int. J. Chem. Kinet.*, 12, 469, (1980).
47. Lin, C. L. and M. T. Leu, *Int. J. Chem. Kinet.*, 14, 417, (1982).
48. "Chemical Kinetics and Photochemical Data for use in Stratospheric Modeling", (NASA, Jet Propulsion Laboratory, Pasadena California, 1985).
49. Hampson, R. F., Jr., and D. Garvin, Eds, "NBS Spec. Publ. (U. S.), No. 513, (1978).
50. Nielsen, O. J., P. Pagsberg, and A. Sillesen, "Investigation of SO₂, Oxidation Initiated by CH₃O₂, HO₂, and OH Using Pulse Radiolysis and Kinetic Spectroscopy, (Riso National Laboratory, Denmark, 1987).
51. Graham R. A., A. M. Winer, R. Atkinson, and J. N. Pitts, Jr., *J. Phys. Chem.* 83, 1563, (1979).
52. Burrows, J. P., D. I. Cliff, G. W. Harris, B. A. Thrush and J. P. T. Wilkinson, *Proc. Roy. Soc. (London)*, A368, 463, (1979).
53. Payne, W. A., L. J. Stief, and D. D. Davis, *J. Am. Chem. Soc.*, 95, 7614, (1973).
54. Sparks, R. K., L. R. Carlson, K. Shobatake, M. L. Kowalczyk, and Y. T. Lee, *J. Chem. Phys.*, 72, 1401, (1980).
55. Wine, P. H., J. M. Nicovich, R. J. Thompson, and A. R. Ravishankara, *J. Phys. Chem.*, 87, 3948, (1983).
56. Davis, D. D., W. Wong, and J. Lephardt, *Chem. Phys. Lett.*, 22, 273, (1973).
57. McCrumb, J. L. and F. Kaufman, *J. Chem. Phys.*, 57, 1270, (1972).
58. West, G. A., R. E. Weston, Jr., and G. W. Flynn, *Chem. Phys. Lett.*, 56, 429, (1978).

59. Arnold, I. and F. J. Comes, Chem. Phys., 42, 231, (1979).
60. Keyser, L. F., J. Phys. Chem., 85, 3667, (1981).
61. Thrush, B. A. and J. P. T. Wilkinson, Chem. Phys. Lett., 81, 1, (1981).
62. Sridharan, U. C., L. X. Qiu, and F. Kaufman, J. Phys. Chem., 85, 3361, (1981).
63. Temps, F. and H. Gg. Wagner, Ber. Bunsenges. Phys. Chem., 86, 119, (1982).
64. Chang, J. S. and F. Kaufman, J. Phys. Chem., 82, 1683, (1978).
65. Hack, W., A. W. Preuss, and H. Gg. Wagner, Ber. Bunsenges. Phys. Chem., 82, 1167, (1978).
66. Lii, R-R., R. A. Gorse, Jr., M. C. Sauer, Jr., and S. Gordon, J. Phys. Chem., 84, 819, (1980).
67. Hochanadel, C. J., T. J. Sworski, and P. J. Ogren, J. Phys. Chem., 84, 3274, (1980).
68. Demore, W. B., J. Phys. Chem., 86, 121, (1982).
69. Cox, R. A., J. P. Burrows, and T. J. Wallington, Chem. Phys. Lett., 84, 217, (1981).
70. Braun, M., A. Hofzumahaus, and F. Stuhl., Ber. Bunsenges. Phys. Chem., 86, 597, (1982).
71. Burrows, J. P., R. A. Cox, and R. G. Derwent, J. Photochem., 16, 147, (1981).
72. Kurylo, M. J., O. Klais, and A. H. Laufer, J. Phys. Chem., 85, 3674, (1981).
73. Cox, R. A. and J. P. Burrows, J. Phys. Chem., 83, 2560, (1979).

74. Thrush, B. A. and G. S. Tydall, *J. Chem. Soc. Faraday II*, 78, 1469, (1982).
75. Thrush, B. A. and G. S. Tydall, *Chem. Phys. Lett.*, 92, 232, (1982).
76. Kircher, C. C. and S. P. Sander, *J. Phys. Chem.*, 88, 2082, (1984).
77. Gleason, J. F., A. Sinha, and C. J. Howard, *J. Phys. Chem.*, 91, 719, (1987).
78. Holland, P. M. and A. W. Castleman, Jr., *Chem. Phys. Lett.*, 56, 511, (1978).
79. Johnston, H. S., "Gas Phase Reaction Rate Theory", (The Ronald Press Co., New York, 1966), p. 269.
80. Glauque, W. F., E. W. Horning, J. E. Kunzler, and T. R. Rubin, *J. Am. Chem. Soc.*, 82, 62, (1960).
81. Castellan, G. W., "Physical Chemistry, Second Edition, (Addison-Wesley Publishing Co., Massachusetts, 1971), p. 70.
82. Okabe, H., "Photo-Chemistry of Small Molecules", (John Wiley & Sons, New York, 1978), p. 177.
83. Okabe, H., "Photo-Chemistry of Small Molecules", (John Wiley & Sons, New York, 1978), p. 247.
84. Okabe, H., "Photo-Chemistry of Small Molecules", (John Wiley & Sons, New York, 1978), p. 201.
85. Private Communication with Dr. A. Bandy, July, 1987.
86. Rudolf, J., D. H. Ehhalt, U. Schimdt, A. Khedim, "2nd Symposium, Composition of the Nonurban Troposphere", (American Meteorological Society, Boston, Mass., 1982).
87. Davis, D. D., S. Fischer, and R. Schiff, *J. Chem. Phys.*, 61, 2213, (1974).

88. Beno, M. F., C. D. Jonah, and W. A. Mulac, *Int. J. Chem. Kinet.*, 17, 1091, (1985).
89. Mirabel, P., and J. L. Katz, *J. Phys. Chem.*, 60, 1138, (1974).
90. Chu, K. and R. A. Morrison, "Environmental and Climatic Impact of Coal Utilization", J. J. Singh and A. Deepak, Eds., (Academic Press, New York, 1980), p. 293.
91. Friend, J. P., R. Leifer, and M. Trichon, *J. Atmos. Sci.*, 30, 465, (1973).
92. Bigg, E. K., *Tellus*, 38B, 62, (1986).
93. Hamill, P., C. S. Kiang, and R. D. Cadle, *J. Atmos. Sci.*, 34, 150, (1977).
94. Laidler, K. J., "Chemical Kinetics, Third Edition" (Harper & Row, Publishers, New York, 1987), p. 282.

Blank

The Coagulation and Dispersion of Nonspherical Aerosol Particles with Inertial Memory in a Turbulent Field

Isaiah Gallily and Miriam Pekarevich
Department of Atmospheric Sciences
The Hebrew University of Jerusalem
Jerusalem, Israel

I. Introduction and aim of study

By coagulation of particles one defines any process in which two or more particles collide to form a liquid droplet (if the former originally were liquid) or a (loose) aggregate of rigid particles if the former were rigid.

The dispersion of particles is a process in which the mutual distance between them increases with time.

Both processes may be effected by various mechanisms. Thus, coagulation may occur due to Brownian motion, gravitational settling, and turbulent effects (Fig. 1), while dispersion can be produced by Brownian or turbulent diffusion.

In the atmosphere, when the aerosol particles are generated in a limited space such as a "point" or a "line", coagulation and dispersion are inter-connected since - after sufficient time - dispersion will arrest coagulation (Fig. 2),

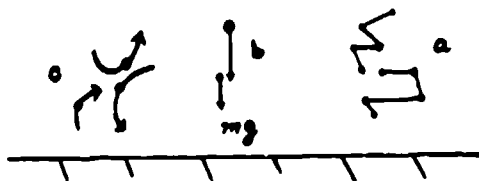


Fig. 1. Some possible mechanisms of coagulation (a- Brownian, b- gravitational, c - turbulent) (schematic).

Thus, contrary to the many studies on particles' coagulation (coupled with some other process) in a restricted environment, which were performed with the aid of a "simulating box", the situation in the free atmosphere is quite different (Fig. 2).

Most studies on coagulation, and dispersion, have been limited to the case of spherical particles though the majority of aerosol systems, for example, are composed of nonspherical particles.

Thus, we thought it worthwhile, from the practical as well as from the academic points of view, to study the problem of coagulation/dispersion of:

- i. nonspherical aerosol particles, and under
- ii. typical atmospheric turbulent conditions.

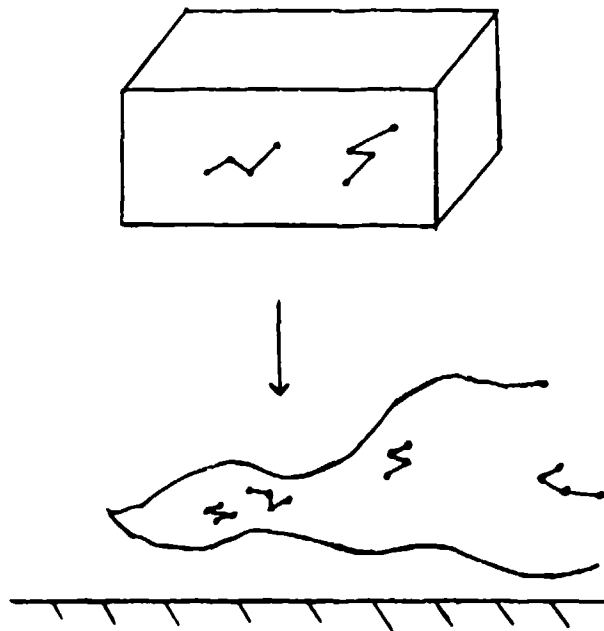


Fig. 2. The "Box Model" of restricted environment transferred to the "Coagulating Cloud" model in a free atmosphere (Schematic).

To adhere to situations which are usually met with in real life, we restricted ourselves to (typical) particle sizes below the Kolmogoroff's (typical) eddy size, η ,

$$\eta = (\nu^3/\epsilon)^{1/4} \quad (1)$$

(ν - kinematic viscosity, ϵ -dissipation rate);

Likewise we dealt with particles whose motion is influenced by their inertia, namely, with particles with inertial memory.

II. The studied system and method of investigation

The system we chose to deal with was composed of:

- i. Spheroidal prolate ellipsoids (of unit density) which were taken to simulate elongated particles,
- ii. A Kolmogoroff's regime of turbulence which is local isotropic.

Unlike the study of Saffman and Turner (1) that was concerned with the coagulation of spherical particles and that used an analytical method of treatment, with quite a gross approximation, we could not find any way of analytical solution to the problem.

The reason is assumed to be the factor of the rotation of our particles which introduced three new additional degrees of freedom to the motion of particles.

Hence, we resorted to a Monte Carlo numerical method in which each particle trajectory was calculated for consecutive time intervals, Δt_i , and the process repeated enough times till an asymptotic behaviour was reached.

Particle translation was solved according to the equation

$$m \, dv/dt = mg + F_f \quad , \quad (2)$$

and its rotation, according to the Euler expression

$$I_1 \dot{\omega}_1 - (I_2 - I_3) \omega_2 \omega_3 = L_1 \quad \text{etc.} \quad (3)$$

where m was the mass of the particle, v its velocity (in an inertial system of coordinates), F_f the fluiddynamic resistance to its translation, I_1 its moment of inertia for its (inner) axis 1, ω_1 its rotational velocity, and L_1 the fluiddynamic torque which acts on it, etc.

F_f was taken according to Brenner (2) to be

$$F_f = \mu K \cdot (v - u_0) \quad (4)$$

K being the Oberbeck transition tensor (3), and u_0 the undisturbed fluid velocity.

L_1 etc. was taken according to Jeffery (4). (It should be noted that both F_f and L_1 etc. could have been obtained from "Slender Body Theory" or the singularity-integral expressions).

III. The calculational way

In the Monte Carlo calculations, the initial position of particles' centers was body-centered cubic, and their initial orientation was (rectangularly) random.

The gradient of the fluids' velocity within each Kolmogoroff's eddy, which engulfed each particle, was taken to be:

- i. Constant for the time Δt_i ,
- ii. Normally random for consecutive time intervals.

The velocity u_0 of the fluid at each time interval was thus

$$u_{0,i} = u_{0,i} + (\partial u_{0,i} / \partial x_j) dx_j \quad (5)$$

(As Δt_i was smaller than the Kolmogoroff's typical time, the constancy of the velocity gradients seemed logical).

The Monte Carlo method appeared to us to be straightforward; however, it put quite a strain on our computer.

IV. Results

Up to now we have run numerical experiments in a 2-D and a 3-D space. We neglected in these experiments :

- i. The fluiddynamic interaction between two particles which near each other on their way to coagulation,
- ii. Collisions between particles containing more than one elementary spheroid.

The reason for the second neglect layed in the assumption that, till such collision would have become important, dispersion will dilute the aerosol cloud to such an extent that coagulation would essentially cease.

Another factor which was neglected concerns what we call the "Neighbours' Effect" (Fig. 3). This effect relates to the (physical) extent of the particle source:

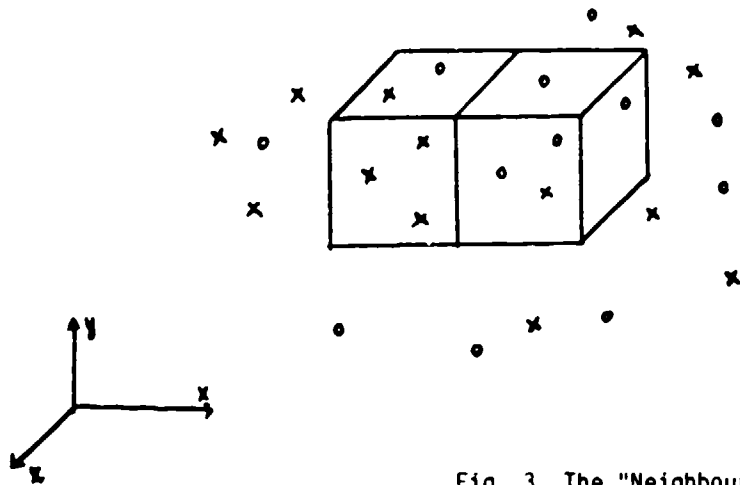


Fig. 3. The "Neighbours' Effect" (schematic)

namely, that particles originated from one part of an extended source (say the "circular particles") may also collide and coagulate with particles originated from a neighbouring part of the source (say, the "crosses" particles) (Fig. 3).

This "Neighbours' Effect" adds a non-linearity to the coagulation process.

The prolate particles had a log-normal size distribution with no correlation between their length and their width, and with a geometric mean of:

- i. 10^{-3} cm for the length and 10^{-4} cm for the equatorial axis in the 2-D case, and
- ii. 4×10^{-4} cm for the length and 1×10^{-4} cm for the equatorial axis in the 3-D case.

The geometric standard deviation in both cases was $1.2 \times$ the geometric mean.

In the experiments, the initial sizes of the particles were (randomly) selected from the above size distribution.

Concerning the initial concentration of the particles, these were $10^6 / \text{cm}^2$ for the 2-D space and $10^9 / \text{cm}^3$ for the 3-D space, which we thought to be close to reality.

Turbulence was characterized in our Kolmogoroff's range by: dissipation rate of $1000 \text{ cm}^2 / \text{sec}^3$ and kinematic viscosity of $0.15 \text{ cm}^2 / \text{sec}$.

With these values, the Kolmogoroff's typical eddy size was about 4×10^{-2} cm, its typical translational velocity (which was the initial velocity of our particles) was $(\epsilon \nu)^{1/3} \approx 1$ cm/sec, and its typical eddy existence-time $(\nu / \epsilon)^{1/2} \approx 10^{-2}$ sec.

Finally, we should add that, to obviate the unsolved problem of dealing with aggregate of more than one primary spheroid (see above), we adhered to the procedure that, after each (coagulative) collision in the Monte Carlo experiment, the involved particles were re-separated and replaced in a (normally) random fashion in space.

In the following we bring, as an example, a dispersion pattern of our particles in a 2-D space (Fig. 4) and a table showing their collision (Table I).

Typically, in this (2-D) case about 15-20% of the original number of particles underwent their first collision during a (typical) time of 3×10^{-2} sec.

The total initial number of the particles was 100, arranged in a 10×10 array.

For a 3-D case, the percentage of collision decreases to about 10% (of the original number) during a (typical) time of about 5×10^{-4} sec. This is expected as the addition of an extra dimension to space increases the chance that the particles will also move side-ways and miss each other.

V. References

1. Saffman, P.G. and Turner, J.S., J. Fluid Mech. 1, 16 (1956).
2. Happel, J. and Brenner, H., "Low Reynolds Number Hydrodynamics", p. 226, Prentice-Hall, 1965.
3. *ibid.*, p. 225-6.
4. *ibid.*, p. 227.

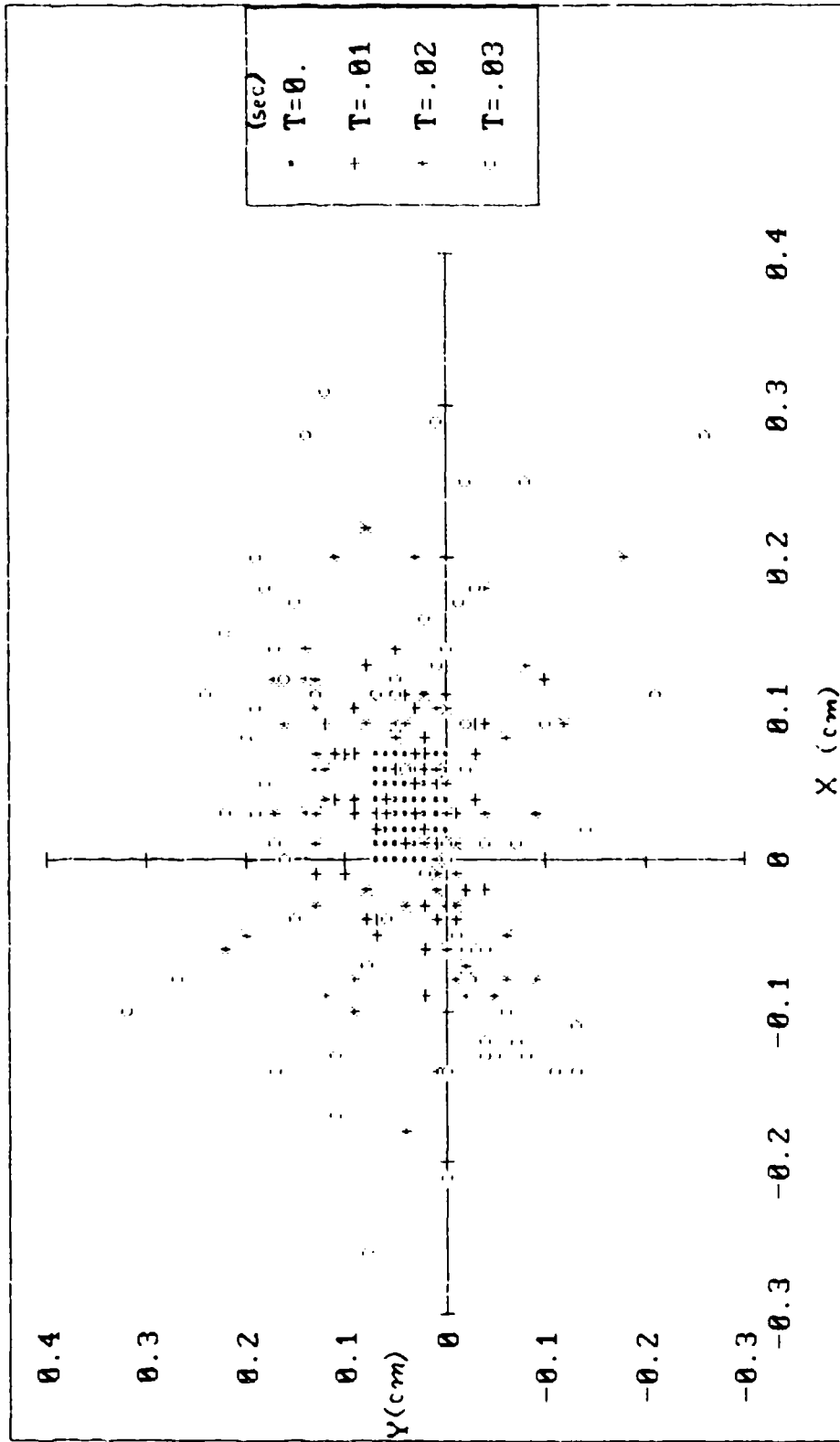


Fig. 4. Particle dispersion in a frame of reference which moves with the mean wind; 2-D motion; typical results

TIME (J x 10 ⁻³ sec)	PARTICLE K	PARTICLE L
1	21	31
1	39	40
1	73	84
3	64	76
5	2	12
5	11	33
6	54	98
7	63	100
8	7	85
8	87	100
10	44	58
11	44	100
12	5	85
15	5	26
16	— 62	65
28	56	92

Table I: Collisions between particle K and particle l (followed by re-separation); typical results

Blank

"LIFT-OFF" OF BUOYANT HORIZONTAL PLUMES

M. Poreh and J. E. Cermak
Colorado State University
Fort Collins, Colorado 80523

RECENT PUBLICATIONS:

A) M. Poreh and J. E. Cermak, "Experimental Study of Aerosol Plume Dynamics; Part I: Wind-tunnel Study of Diffusion and Deposition of Particles with Appreciable Settling Velocities," Annual Progress Report to CRDC, CER86-87MP-JEC1, September 1986.

B) M. Poreh and J. E. Cermak, "Experimental Study of Aerosol Plume Dynamics; Part II: Wind-tunnel Study of Buoyant Horizontal Emissions," Annual Progress Report to CRDC, CER86-87MP-JEC5, November 1986.

ABSTRACT

Wind-tunnel simulation of the concentration field and "lift-off" of buoyant plumes from point source with horizontal exit velocities show a previously unknown, coupled dependence of the plume on the buoyancy flux and the horizontal momentum flux at the source. Further study of buoyant emissions from line and area sources is suggested.

INTRODUCTION

The possible "lift-off" (see Figure 1) of a layer of buoyant gas of thickness H in a shear flow was initially analyzed by Briggs (1971), who proposed that "lift-off" occurs when $L_p = gH(\Delta\rho/\rho_a)/v^{*2} = 0(2)$, where v^* is the shear velocity and $\Delta\rho/\rho_a$ is the relative reduction in density. Flow visualizations by Meroney (1979) did not reveal, however, a lower limit to buoyancy which could induce "lift-off" in plumes. Plumes with less buoyancy will just travel a longer distance along the ground before lift-off.

In an unpublished note, Briggs suggested that the observation of Meroney might indicate that plumes need some vertical growth before they could lift-off, and proposed to increase the value of L_p by an order of magnitude (from Hall et al., 1980).

The vaguely defined concept of lift-off and lack of concentration measurements has stimulated this study, in which both the buoyancy flux and the horizontal momentum flux at the source were varied.

SUMMARY OF THE RESULTS

The experimental configurations and the results are fully described in reference B) cited above. A typical photograph of a buoyant plume is shown in Figure 1. Figures 2a and 2b show typical concentration profiles downstream from the source. Figure 2a depicts the effect of the dimensionless buoyancy flux $F^* = (\Delta\rho/\rho_a)g Q/(\pi U^3 \delta)$, where Q is the discharge, δ is the thickness of the boundary layer and U the mean velocity at $z = \delta$. Figure 2b depicts the effect of the dimensionless horizontal momentum flux $M^* = 4\rho Q^2/(\rho_a\pi^2 d^2 U^2 \delta^2)$.

One clearly sees that the height of the maximum of the various concentration profiles, $h_{max}(x)$, increases with F^* and decreases with M^* , as also documented in Figure 3. A possible measure of lift-off

is the reduction with distance of the ground-level dimensionless concentration $C^*(0) = C(0) U \delta^2 / (C_0 Q)$, where C_0 is the source concentration, versus that of the maximum dimensionless concentration C_{max}^* . Typical variations of these values are shown in Figure 4. The positions of the nine graphs in this figure were selected so that upper graphs show runs with larger values of the dimensionless buoyancy flux, whereas the graphs to the right show runs with higher dimensionless momentum flux. The graphs clearly suggest that by increasing the momentum flux, "lift-off" is delayed or completely eliminated. The ratio of $C(0)/C_{max}$ at $x/\delta = 1.67$, for example, turned out to be a function of $F^*/(M^*)^{1/2}$, as shown in Figure 5.

The study has also shown that at large distances the maximum dimensionless concentration varies approximately as $250 (M^*)^{1/2} (F^*)^{-2/3} (x/\delta)^{-2}$.

Planned Future Studies

The results of the investigation suggest that a similar systematic study of buoyant emissions from line and area sources will also yield new information on their behavior and dependence on the initial conditions.

REFERENCES

1. Briggs, L. A. (1973) Lift-off of Buoyant Gas Initially on the Ground. ADTL Contribution File No. 87 (Draft), Nov. 1973, Air Resources Atmospheric Turbulence and Diffusion Lab., NOAA, Oak Ridge, Tennessee.
2. Meroney, R. N. (1979) Lift-off of Buoyant Gas Initially on the Ground. J. Industrial Aerodynamics, October 1979, 5, Nos. 1 and 2.
3. Hall, D. J., Barrett, C. F. and Simmonds, A. C. (1980) Wind Tunnel Model Experiments on a Buoyant Emission from a Building, Warren Spring Laboratory, Department of Industry, Gunnels Wood Road, Stevenage, Hertfordshire SG1 2BX.

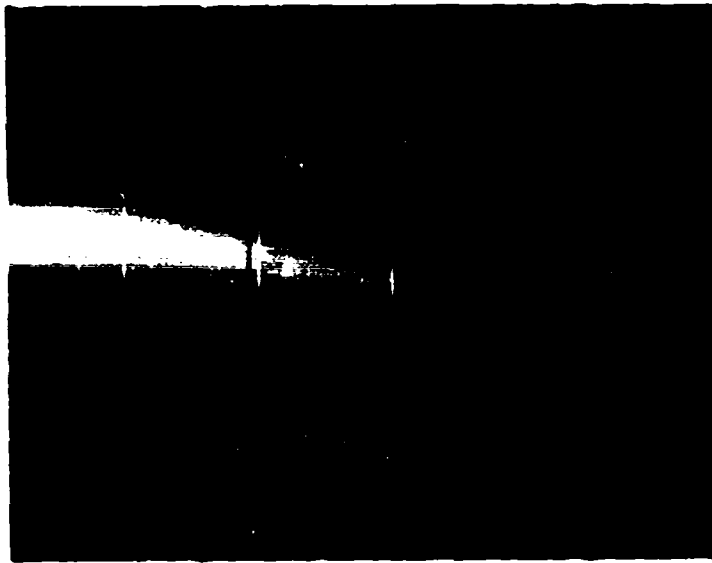


FIGURE 1. A PHOTOGRAPH SHOWING THE MEAN PLUME BOUNDARIES AND APPARENT "LIFT-OFF."

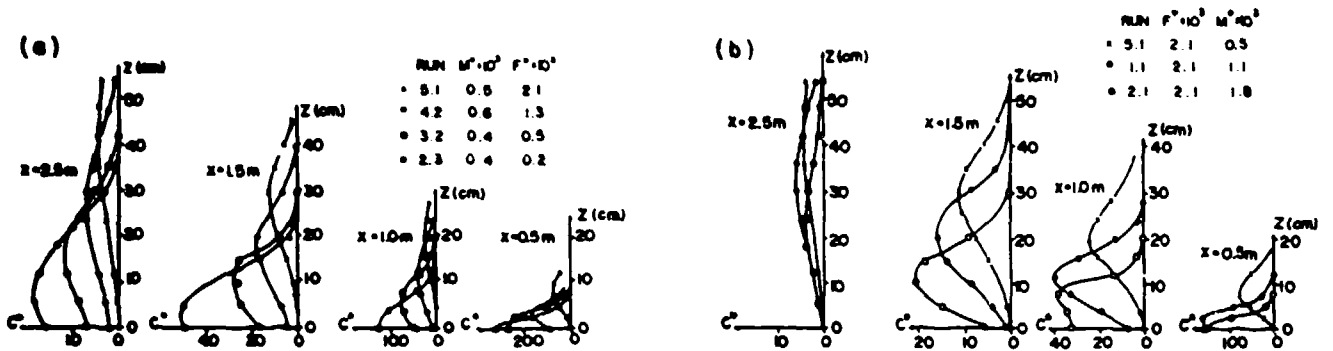


FIGURE 2. TYPICAL CONCENTRATION PROFILES DEMONSTRATING (a) THE EFFECT OF F^* , AND (b) THE EFFECT OF M^* .

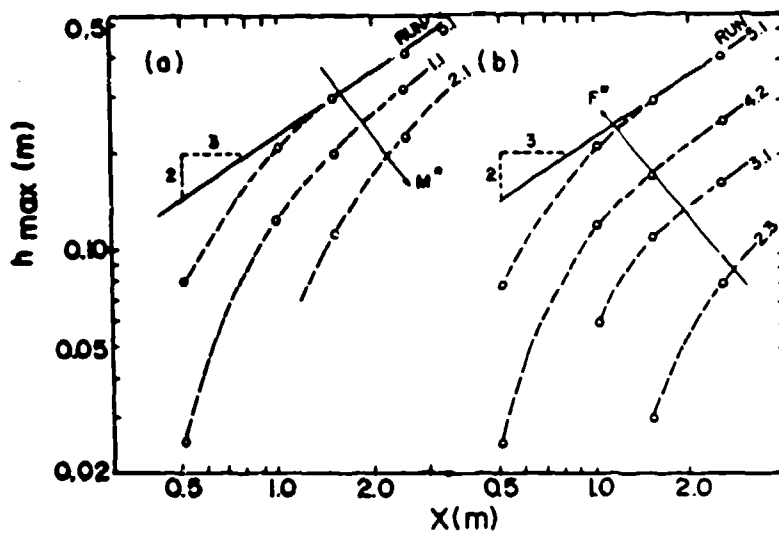


FIGURE 3. HEIGHT OF THE MAXIMUM IN THE CONCENTRATION PROFILES FOR (a) DIFFERENT VALUES OF M^* , F^* = CONSTANT, AND (b) DIFFERENT VALUES OF F^* , M^* = CONSTANT.

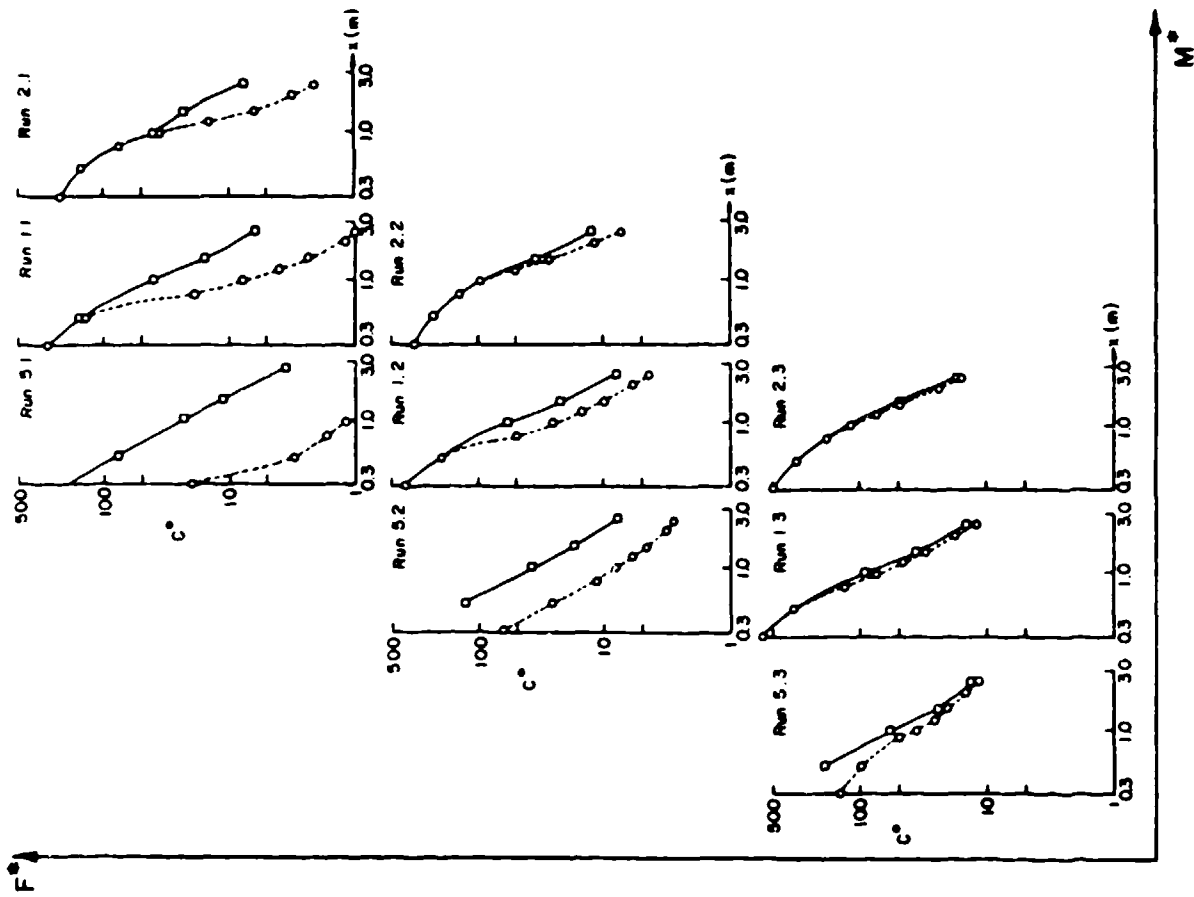


FIGURE 4. GROUND-LEVEL (---) AND MAXIMUM (—) DIMENSIONLESS CONCENTRATIONS. (The position of the different runs in the figure is according to the values of F^* and M^* in these runs.)

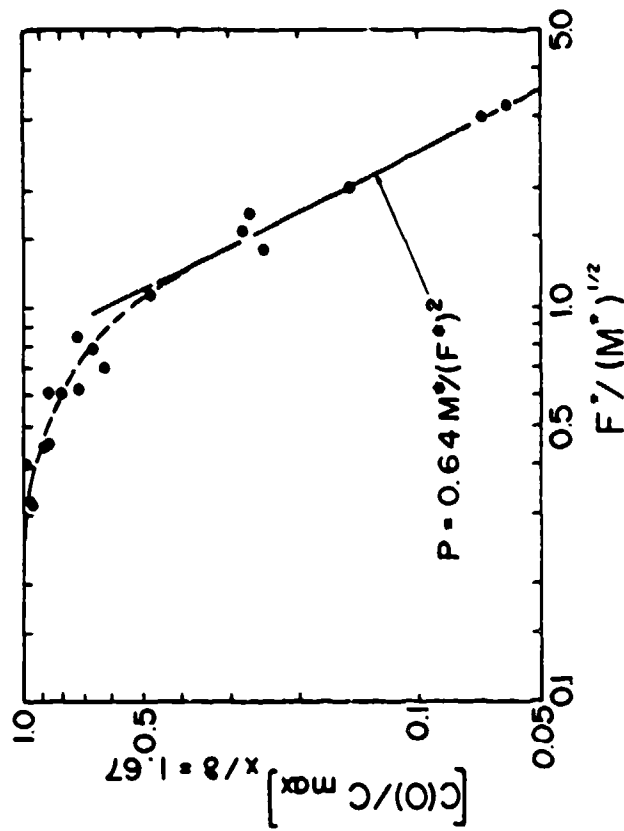


FIGURE 5. THE DEPENDENCE OF THE CONCENTRATION RATIO $C(0)/C_{max}$ AT $x/\delta = 1.67$ ON F^* AND M^* .

STUDIES IN AEROSOL FORMATION AND GROWTH

H. Kosuge and J. R. Brock

Department of Chemical Engineering

University of Texas, Austin, Texas 78712

RECENT PUBLICATIONS, SUBMITTALS FOR PUBLICATION AND PRESENTATIONS:

1. J. C. Carls and J. R. Brock, "Explosion of a water droplet by pulsed laser heating", *Aerosol Sci. Tech.* 7,79-91 (1987).
2. S. G. Kim and J. R. Brock, "Growth of ferromagnetic particles from cation reduction by borohydride ions" *J. Colloid Int. Sci.* 116,431-443 (1987).
3. J. R. Brock and J. Oates, "Moment simulation of aerosol evaporation", *J. Aerosol Sci.* 18,59-64 (1987).
4. J. R. Brock, D. Zehavi and P. J. Kuhn, "Formation and growth of binary aerosol in a laminar coaxial jet", *J. Aerosol Sci.*, In Press.
5. S. C. Davies and J. R. Brock, "Laser evaporation of droplets", *Appl. Opt.* 26,786-793 (1987).
6. S. C. Davies and J. R. Brock, "Laser propagation through an evaporating polydisperse aerosol", *Appl. Opt.* 26,1865-1876 (1987).
7. S. G. Kim and J. R. Brock, "Aerosol growth and dynamics" in R. Kohl, Ed., *Proceedings of the 1986 CRDEC Scientific Conference on Obscuration and Aerosol Research*, R. H. Kohl and Assoc., 1987.
8. J. C. Carls and J. R. Brock, "Laser induced explosion of particles", in R. Kohl, Ed., *Proceedings of the 1986 CRDEC Scientific Conference on Obscuration and Aerosol Research*, R. H. Kohl and Assoc., 1987.
9. S. C. Davies and J. R. Brock, "Laser evaporation of droplets", in R. Kohl, Ed., *Proceedings of the 1986 CRDEC Conference on Obscuration and Aerosol Research*, R. H. Kohl Assoc, 1987.
10. Y. L. Chen, J. R. Brock, and I. Trachtenberg, "Aerosol jet etching of fine patterns", *Appl. Phys. Lett.*, In Press.
11. A. Dove and J. R. Brock, "Sulfate aerosol modeling using the EPA Philadelphia Aerosol Field Study", U. S. Environmental Protection Agency Report, 200 pp. 1987.
12. J. C. Carls and J. R. Brock, "Explosive vaporization of a single water droplet by pulsed laser radiation", Abstract AAAR Annual Meeting, Seattle, September 1987.
13. H. Kosuge and J. R. Brock, "Aerosol evolution in jets expanding into low pressure regions", Abstract AAAR Annual Meeting, Seattle, September 1987.
14. J. C. Carls and J. R. Brock, "Laser induced explosion of water droplets by laser radiation", Workshop on Physics of Directed Energy Propagation in the Atmosphere, Las Cruces, N. M., January 1987.
15. J. R. Brock, "Formation and Growth of Ferromagnetic Particles", Department of Physics, University of Paris at Orsay, January 1987.
16. J. R. Brock, "Aerosol Formation and Growth", University of Paris VIII Val de Marne, January 1987.
17. J. R. Brock, "A Complex Terrain Model for Aerosol Dispersion", Chemical Modeling Conference, CRDEC, August 1987.

ABSTRACT

Current work on aerosol formation and growth is summarized. In work initiated this past year, a two dimensional Flux Corrected Transport (FCT) code has been developed to obtain a detailed description of nucleation and particle growth in a jet expanding into a low pressure region. The complex shock structures found on jet expansion have been studied. Very high nucleation rates are found to occur in the region behind the rear facing shock. The onset point of particle nucleation has been found to be strongly affected by the stagnation temperature but relatively insensitive to the stagnation pressure. In a separate study, an approximate theory has been developed for the composition distributions obtained from experiments on binary aerosol formation in laminar coaxial jets. The theory agrees qualitatively with the experimental finding that, at smaller concentrations of the less volatile component in the parent vapor mixture, the smaller particles in the resultant aerosol size distribution are enriched in the less volatile component.

INTRODUCTION

The optical, physico-chemical, biological and other properties of aerosols depend on such characteristics of the particles as size, shape, composition, concentration, etc. These are determined by the fundamental processes of aerosol formation, growth and dynamics. For this reason, an important part of our work has been directed toward understanding these fundamental processes and their interaction with atmospheric motion. We begin with a description of current work on particle nucleation and growth occurring in jets expanding into low pressure regions. This is followed by a brief presentation of comparisons between theory and experiment for the composition distributions of binary oil particles formed by nucleation and growth in a laminar coaxial jet.

AEROSOL NUCLEATION IN JETS EXPANDING INTO LOW PRESSURE REGIONS

An important mechanism for production of aerosol involves the sudden adiabatic cooling and subsequent particle nucleation which may occur in fast jets, explosions, laser detonations, etc.. As a means of studying this mechanism we have initiated analysis of the nucleation and growth of particles occurring in jets expanding into low pressure regions; this physical system is encountered in many applications such as in high altitude rocket plumes and molecular beam experiments. Although many studies have been carried out on free jet expansion, most of the numerical studies have been concerned with one dimensional systems. As a prelude to possible experimental studies, we have developed a model of nucleation and growth occurring in a two dimensional axisymmetric expanding jet.

The physical system modeled is shown schematically in Fig. 1. The assumptions in the analysis are that the flow is axisymmetric, inviscid and compressible. The ideal carrier gas with constant heat capacity ratio contains a single condensable vapor. It is also assumed that any particles formed are passive contaminants. Under these conditions, the governing equations are the Euler equations supplemented by the classical homogeneous nucleation equation and the particle growth equations. These equations are solved numerically using the flux corrected transport (FCT) method and a time splitting procedure. The calculation domains are both the nozzle and the expansion chamber (see Fig. 1). In implementing any numerical procedure, it is important to validate the code. We have carried out comparisons between our calculations and experiment (I. Dueker and Koppenwaller, in S. S. Fisher, Ed., *Rarefied Gas Dynamics*, Academic Press, vol. II, 1190, 1981; II. Dankert and Koppenwaller, in R. Compargue, Ed., *Rarefied Gas Dynamics*, Academic Press, vol II, 1107, 1979). Fig. 2 shows a comparison between our model predictions and experiment (I) for the Mach numbers at steady state along the jet axis for free expansion with the same stagnation conditions as used in the experiments ($P_0=2.9E3$ Pa, $T_0=160K$). Fig. 3 shows a comparison between model predictions and experiment (II) for the pressure distributions at steady state, again with the same stagnation conditions as in II ($P_0=7.6E4$ Pa, $T_0=280K$). In both figures, the abscissa is the dimensionless distance from the nozzle exit and the dashed lines represent the experimental results. From these figures, it can be seen that there is reasonably good agreement between our model predictions and experiment. This suggests that our model provides a reasonably accurate representation of the flow field in the free jet expansion.

Fig. 4 shows the pressure distribution at $t=4E-5$ s. following initiation of the free jet expansion for the

stagnation conditions, $P_0=2.9E5$ Pa, $T_0=160K$. At this small time, steady state conditions have not been reached so that the shock surfaces cannot be definitely identified with the barrel shock and Mach disk observed in steady state experiments using schlieren photography. There are two shocks, a forward facing shock and a rear facing shock. In the related temperature distribution, the temperatures fall rapidly downstream of the nozzle behind the rear facing shock because of the conversion of internal energy to kinetic energy that occurs in an isentropic expansion. This creates a region of high supersaturation behind the shock, leading to rapid nucleation and particle growth.

Fig. 5 shows the effect of stagnation temperature on nucleation rates for $P_0=2.9E5$ Pa and $t=6E-5$ s. As stagnation temperature increases the point for onset of nucleation shows substantial movement away from the nozzle. By contrast, as shown in Fig. 6, as stagnation pressure changes, for $T_0=160K$, $t=6E-5$ s, there is little change of the point of onset of nucleation with respect to the nozzle; this is found for other stagnation temperatures.

Currently, we plan to carry out studies of particle nucleation and growth in the free jet expansion. Inasmuch as cluster formation is at the moment a very popular topic in materials research, a very large amount of experimental data is available which can be used for comparison with our model calculations. Since small cluster formation in free jets shows "magic number" and other phenomena, the dynamics of cluster formation provided by our model may provide a vehicle for a test of nucleation and particle growth theories.

COMPOSITION DISTRIBUTIONS IN BINARY OIL AEROSOLS

The principal purpose of our work on formation and growth of liquid aerosols has been to investigate the dependence of the disperse properties of binary aerosols, formed by homogeneous nucleation, on the physicochemical properties of the parent vapor mixture. These studies have been carried out experimentally by following the condensation of oil vapors in a laminar coaxial jet. A full description of the experimental system has been published (Brock, Zehavi and Kuhn, *J. Aerosol Sci.* 17,11-23 (1986)) and will not be repeated here. An approximate moment formulation of the evolution of the spatially averaged single and binary component particle size distribution has been used to provide a theoretical comparison with the experimental results. This formulation involves use of classical binary nucleation theory for modeling the formation and growth of binary oil aerosol. This has been used to provide one of the first confirmations and details of the dynamics for the observed composition distributions obtained in our experiments.

An experimental investigation of the variation of composition with aerosol particle size was made for the system dibutyl phthalate (DBP) and diethylhexyl sebacate (DEHS). These experimental results are shown in Fig. 7 for an initial oil vapor composition of 80% DBP-20% DEHS and overall vapor concentration of $1.91E-5$ g/cc, nitrogen carrier gas flow rate of 178 cc/min, and a nozzle temperature of 270 °C. In this figure the four interior curves represent averages of samples taken on four impactor stages. The distributions indicated were calculated using the known impactor stage efficiencies by the method described by N. A. Fuchs. Of the four distributions, the one with the smallest modal value at around $0.5 \mu m$ has a composition of 39 % DEHS, the next at around $0.65 \mu m$ has a composition of 23.3 % DEHS, the next at around $0.8 \mu m$ has a composition of 21.2 % DEHS, and the last at

around $0.9 \mu\text{m}$ has a composition of 19.5 % DEHS. In considering these experimental results it should be noted that the use of an impactor introduces uncertainty owing to, among other factors, the relatively large range of particle sizes depositing on a given stage. Also, DPB has a sufficiently high vapor pressure that complete condensation of DBP was not achieved at the usual sampling point 20 cm from the nozzle exit. The moment theory results for DEHS-DBP at similar conditions are shown in Fig. 8 giving the normalized binary distribution, $f(D_p, y)$ where y is the mass percent of DEHS and D_p is the particle diameter. Only the general trends are significant in Fig. 8 since, as noted above, no dispersion mechanisms are accounted by the present theory. As is evident, the figure shows that the smaller particles in the distribution are enriched in DEHS, a finding in qualitative agreement with the experimental results presented in Fig. 7. Under similar conditions (20% initial squalane (SQ) mass fraction in the vapor), the distribution for the lower vapor pressure system dihexylphthalate - squalane (DHP-SQ) resembles that given in Fig. 8, except that for the DHP-SQ system the distribution is somewhat narrower. However, a similar qualitative result is obtained-- namely, that the smaller particles in the distribution are enriched in the less volatile component, SQ in this case.

This observed variation of composition with particle size is attributed to several processes. As confirmed by simulation results, the initial nuclei formed at high supersaturations are greatly enriched in the less volatile component. As growth proceeds, the lighter component tends to evaporate from the smaller particles as a result of the Kelvin effect and differential heating of the smaller particles. These factors contribute to a differential rate of condensation with particle size between the lighter and heavier components onto the aerosol particles and therefore to the observed variations noted in Figs. 7 and 8.

It may also be noted from Figs. 7 and 8 that for a particle of given diameter there is variation in composition. This prediction could not be confirmed by our experimental methods more accurately than that provided by Fig. 7 which must be regarded as only a qualitative guide to such variation. The variation in composition with particle size displayed in Fig. 7 is derived from our experimental impactor measurements and impactor efficiency curves with the assumption of lognormal distributions; this figure therefore contains the implied experimental and theoretical uncertainties associated with these methods. A practical method for measuring the composition of individual particles in a distribution would be desirable. It is sufficient here to examine the reasonableness of the variation in composition at a given particle size in the absence of coagulation, as in our experiments. It should be emphasized that the variations observed here in particle size and composition arise from the nucleation process. Without the nucleation process, if one begins with a monodisperse distribution in both size and composition, then this monodispersity will be preserved with increasing time, since there is no coagulation and condensation is occurring. With the nucleation process, any initial monodispersity is "forgotten" and the dispersion in size and composition is determined by the aerosol nucleation and growth processes. Nucleation will produce classes of nuclei whose growth trajectories may converge at a particular time at a given particle size but with different compositions. Similarly, other nuclei will have trajectories converging at a particular time at a given composition with different particle sizes. We reiterate that the distributions displayed in Figs. 7 and 8 are intended only to provide

a qualitative idea of the variations in aerosol particle size and composition.

It would be desirable to obtain experimental data of high quality for the composition distributions of binary aerosols. However, the moment theory developed by us (J. R. Brock, D. Zehavi, and P. J. Kuhn, *J. Aerosol Sci.*, In Press) appears to explain present experimental observations and provides a qualitative guide to the dynamics of the development of the composition distribution for binary aerosols.

ACKNOWLEDGMENT

This work was supported under contract DAAK11-83-K-0006 from CRDEC, U. S. Army.

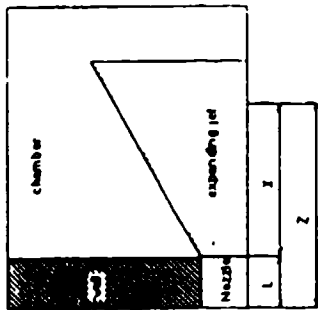


Figure 1. Schematic diagram of expanding jet

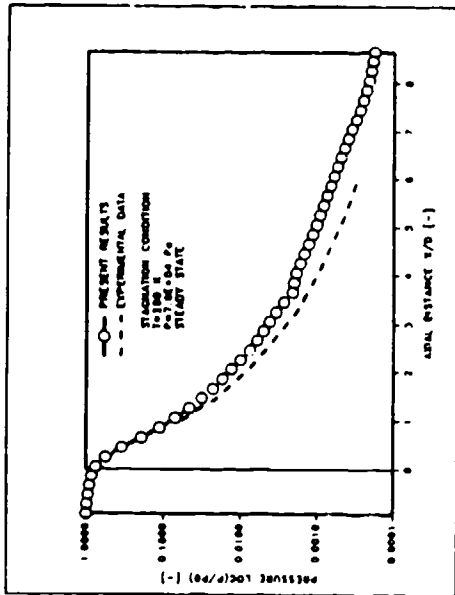


Figure 3. A comparison of the pressure distribution along the jet axis

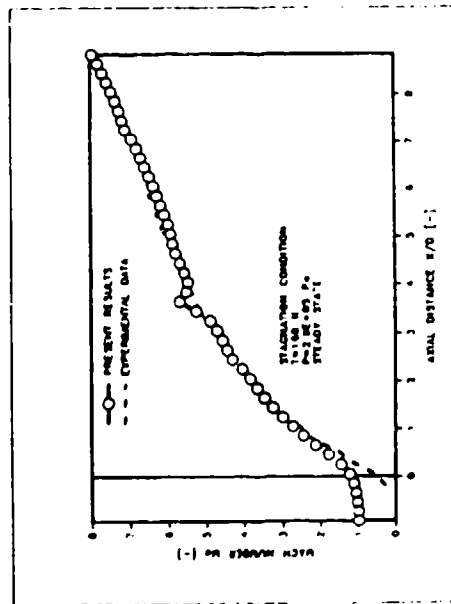


Figure 2. A comparison of Mach number along the jet axis

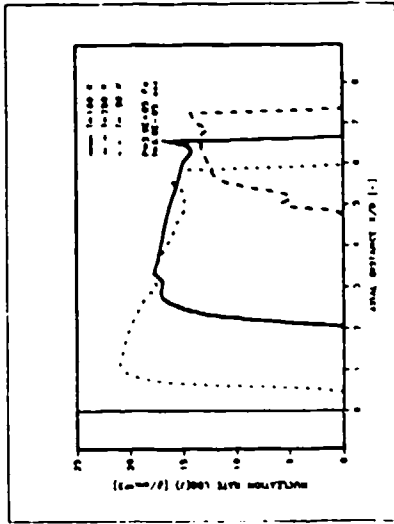


Figure 5. Effect of stagnation temperature on nucleation rate.

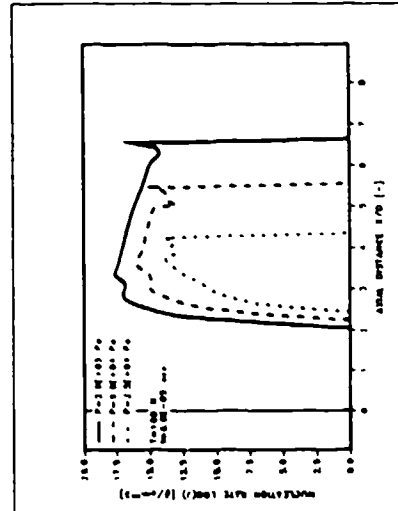


Figure 6. Effect of stagnation pressure on nucleation rate.

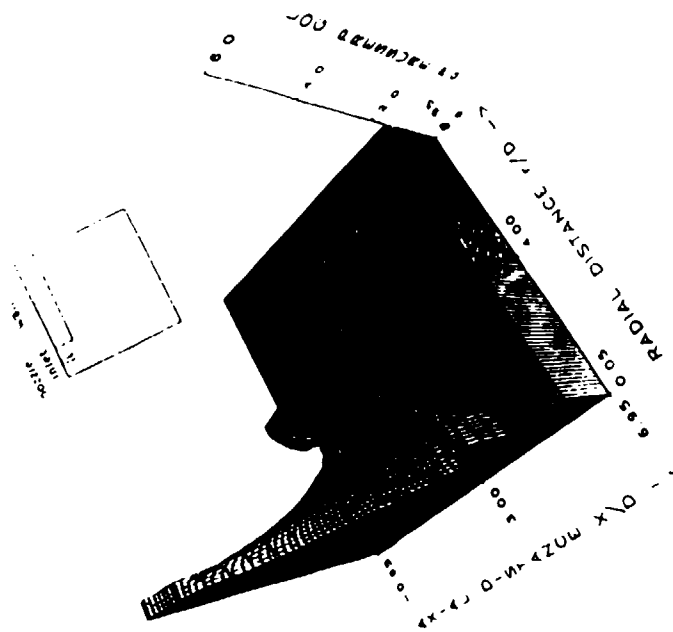


Figure 4. Pressure distribution at $t=4E-5$ sec.

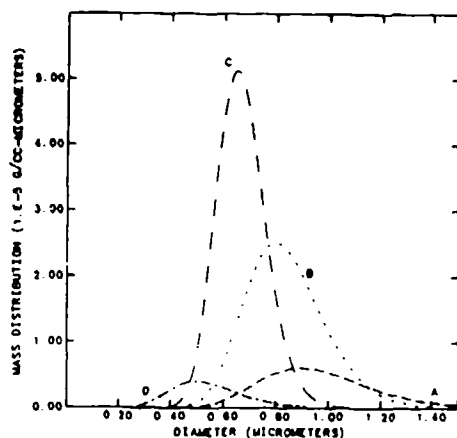


Figure 7. Experimental mass distributions of an aerosol formed by condensation of an initial vapor with 20 mass % DEHS in DBP. Separate distributions derived from stages 3, 4, 5 and 6 of six stage cascade impactor. Units of distributions are $1E-5$ g/cc- μ m. Average compositions for each stage are: Curve A = 19.5% DEHS; Curve B=21.2 % DEHS; Curve C=22.3% DEHS; Curve D=39% DEHS.

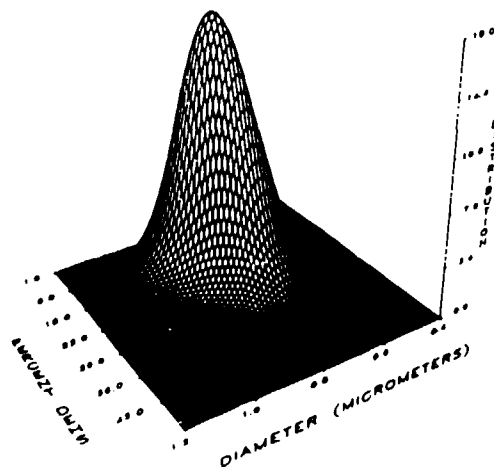


Figure 8. Calculated normalized binary frequency distribution for an initial oil vapor mixture containing 20 mass % DEHS in DBP corresponding to conditions of Fig. 7. D_p is particle diameter and y is mass % DEHS. Units of frequency are $0.2/\mu$ m

11. AEROSOL CHARACTERIZATION METHODS

Blank

OPTICAL PROPERTIES OF SELECTED MINERALS, METALS,
OPTICAL MATERIALS, SOOT, AND LIQUIDS

Marvin R. Querry and David M. Wieliczka
Department of Physics
University of Missouri-Kansas City, Missouri 64110

RECENT PUBLICATIONS, SUBMITTALS FOR PUBLICATION, AND PRESENTATIONS:

A) M.R. Querry, W.P. Roach, D.L. Striley, and C.T. Heese, "Optical Properties of Powders, Liquids, and Metals in the Infrared, Visible, and Ultraviolet Spectral Regions," p. , Proceedings of the 1986 CRDEC Scientific Conference on Obscuration and Aerosol Research, R.H. Kohl, Ed., submitted September 1986.

B) R.W. Alexander, Jr., R.J. Bell, L. Newquist, M.A. Ordal, L.L. Long, and M.R. Querry, "Optical Properties of Powders, Liquids, and Metals at Millimeter and Submillimeter Wavelengths," p. , Proceedings of the 1986 CRDEC Scientific Conference on Obscuration and Aerosol Research, R.H. Kohl, Ed., submitted September 1986.

C) R.J. Bell, R.W. Alexander, Jr., L. Newquist, M.A. Ordal, and M.R. Querry, "Methods for Measuring Surface Impedances in the Submillimeter and Far Infrared," p. Proceedings of the 1986 CRDEC Scientific Conference on Obscuration and Aerosol Research, R.H. Kohl, Ed., submitted September 1986.

D) M.R. Querry, "Optical Constants of Selected Liquids, Solids, and Powders," Presentation at the 1987 CRDEC Scientific Conference on Obscuration and Aerosol Research, June 23, 1987.

E) M.A. Ordal, R.J. Bell, R.W. Alexander, Jr., L.L. Long, and M.R. Querry, "Optical Properties of Au, Ni, and Pb at Submillimeter Wavelengths," Appl. Opt. 26, 744 (1987).

F) L.L. Long, R.J. Bell, R.W. Alexander, Jr., and M.R. Querry, "Preparation Dependent Properties of Pressed Pellets of Montmorillonite in the Far Infrared," Appl. Opt. 26, 1372 (1987).

G) M.R. Querry and W.P. Roach, "Optical Properties of Polycrystalline Molybdenum," J. Opt. Soc. Am. A3, No. 13, 82 (1986), Presented at the 1986 Annual Meeting of the Opt. Soc. Am., Seattle, WA, 19-24 October.

H) W.P. Roach and M.R. Querry, "Optical Properties of Polycrystalline Molybdenum," Appl. Phys. Commun. 7, 84 (1987), Presented at the Thirty-Fourth Annual Midwest Solid State Conference, St. Louis, MO, 24-25 October 1986.

I) D.L. Striley and M.R. Querry, "Optical Constants of NaCl, KCl, CsBr, and CsI," Appl. Phys. Commun. 7, 85 (1987), Presented at the Thirty-Fourth Annual Midwest Solid State Conference, St. Louis, MO, 24-25 October 1986.

J) D.L. Striley, "Optical Properties of Sodium Chloride, Potassium Chloride, Cesium Iodide, and Cesium Bromide," M.S. Thesis, University of Missouri-Kansas City, (1987).

K) M.R. Querry, "Optical Constants of Minerals and Other Materials from the Millimeter to the Ultraviolet," Final Technical Report for CRDEC Contract DAAA-15-85-K-0004, Approx. 315 pp., submitted August 1987.

CONTRIBUTIONS TO THE U.S. ARMY CRDEC COMPUTER DATABASE FOR OPTICAL CONSTANTS:

A) M.R. Querry and D.L. Striley, "Optical Constants of NaCl: 60-45,450 cm^{-1} ," (1987).

B) M.R. Querry and D.L. Striley, "Optical Constants of KCl: 60-45,450 cm^{-1} ," (1987).

- C) M.R. Querry and D.L. Striley, "Optical Constants of CsI: 60-45,450 cm^{-1} ," (1987).
- D) M.R. Querry and D.L. Striley, "Optical Constants of CsBr: 67-45,945 cm^{-1} ," (1987).
- E) M.R. Querry, "Optical Constants of BaF_2 : 60-45,450 cm^{-1} ," (1987).
- F) M.R. Querry, "Optical Constants of ZnS: 60-40,000 cm^{-1} ," (1987).
- G) M.R. Querry, "Optical Constants of ZnSe: 460-20,000 cm^{-1} ," (1987).
- H) M.R. Querry and B.P. Clayman, "Optical Constants of Colloidal Montmorillonite Pellets: 50-4,000 cm^{-1} ," (1987).
- I) M.R. Querry and B.P. Clayman, "Optical Constants of Colloidal Kaolin Pellets: 50-4,000 cm^{-1} ," (1987).
- J) M.R. Querry and B.P. Clayman, "Optical Constants of Colloidal Illite Pellets: 50-4,000 cm^{-1} ," (1987).
- K) M.R. Querry and B.P. Clayman, "Optical Constants of Colloidal Composite Clay Pellets: 50-4,000 cm^{-1} ," (1987).
- L) M.R. Querry, "Optical Constants of UMKC Diesel Soot Pellet: 180-4,000 cm^{-1} ," (1987).
- M) M.R. Querry, "Optical Constants of NMSU Diesel Soot Pellet: 180-45,450 cm^{-1} ," (1987).
- N) M.R. Querry, "Optical Constants of NMSU Heated Diesel Soot Pellet: 180-45,450 cm^{-1} ," (1987).
- O) M.R. Querry, "Optical Constants of Anhydrite, E Parallel to X: 180-4,000 cm^{-1} ," (1987).
- P) M.R. Querry, "Optical Constants of Anhydrite, E Parallel to Y: 180-4,000 cm^{-1} ," (1987).
- Q) M.R. Querry, "Optical Constants of Anhydrite, E Parallel to Z: 180-4,000 cm^{-1} ," (1987).
- R) M.R. Querry, "Optical Constants of Dolomite, E Parallel to c-axis: 200-4,000 cm^{-1} ," (1987).
- S) M.R. Querry, "Optical Constants of Dolomite, E Perpendicular to c-axis: 250-4,000 cm^{-1} ," (1987).
- T) M.R. Querry and W.P. Roach, "Optical Constants of Molybdenum: 180-48,465 cm^{-1} ," (1987).
- U) M.R. Querry "Optical Constants of Zirconium: 180-45,450 cm^{-1} ," (1987).
- V) M.R. Querry, "Optical Constants of Manganese: 180-45,450 cm^{-1} ," (1987).
- W) M.R. Querry, D. Wieliczka, and S. Weng, "Optical Constants of Polydimethylsiloxane (SF-96): 180-12,210 cm^{-1} ," (1987).
- X) D. Wieliczka, S. Weng, and M.R. Querry, "Optical Constants of Dimethylmethylphosphonate (DMMP): 180-12,430 cm^{-1} ," (1987).
- Y) S. Weng, M.R. Querry, and D. Wieliczka, "Optical Constants of Diisopropylmethylphosphonate (DIMP): 180-12,285 cm^{-1} ," (1987).
- Z) M.R. Querry, D. Wieliczka and S. Weng, "Optical Constants of Diethylphthalate (DEP): 180-12,350 cm^{-1} ," (1987).

ABSTRACT

This paper concerns the measurement of the optical properties of twenty-five materials and determination of the optical constants of twenty-three of those materials. Future work will be concerned with measurement of the optical properties as a function of temperature for several other materials and determination of the optical constants of those materials. The work reported here was supported by U.S. Army CRDEC contract DAAA-15-85-K-0004.

INTRODUCTION

The twenty-three materials for which optical properties were measured and optical constants were determined were:

Montmorillonite	Molybdenum	CsBr	DIMP
Kaolin	Zirconium	ZnS	DEP
Illite	Manganese	ZnSe	DES
Composite Clay	NaCl	BaF ₂	Diesel Soot
Anhydrite	KCl	SF-96	1) unheated
Dolomite	CsI	DMMP	2) heated.

In this paper we present examples of the results of those investigations. For a more detailed description of the investigations, readers are referred to the Final Technical Report for CRDEC contract DAAA-15-85-K-0004 which has been submitted and is currently being reviewed by CRDEC personnel. The report provides graphical and tabular presentations of the optical properties and optical constants. More detailed tabular listings of the optical constants can be obtained from the CRDEC Computer Database for Optical Constants by contacting M.E. Milham at CRDEC.

MINERALS

The minerals that we investigated were three clays: montmorillonite, kaolin, illite; and two crystalline materials: anhydrite, and dolomite. A composite mixture of equal proportions by mass of the three clays was also investigated. The clay samples were compressed into 13 mm diameter by approximately 1 mm thick pellets and

near-normal incidence reflectance spectra were acquired in the 50-50,000 cm^{-1} wave-number region.¹ The spectra in the 50-4,000 cm^{-1} wave-number region were used to obtain the optical constants using Kramers-Kronig methods. As an example of this work, in Figure 1 we present graphs of the reflectance spectrum and the real and imaginary parts of the complex refractive index $n+ik$ for kaolin.

Crystalline samples of anhydrite and dolomite were cleaved or cut and polished, respectively, to obtain samples for measurements of the reflectance spectra for the X,Y,Z directions of anhydrite and for the ordinary and extraordinary rays of dolomite. Kramers-Kronig analysis of the reflectance spectra provided spectral values of the optical constants. A graphical presentation of the resultant spectra for the X-direction of anhydrite appears in Figure 2.

METALS

The metals that we investigated were molybdenum, zirconium, manganese, and zinc. Polycrystalline bulk samples of each metal were obtained and mechanically polished¹ in preparation for acquisition of their near-normal incidence reflectance spectra which were measured for each of the four metals throughout the 180-45,454 cm^{-1} wave-number region. The spectra for Mo, Zn, and Mn were extended into the vacuum ultraviolet spectral region and Kramers-Kronig methods were used to determine the optical constants. Vacuum ultraviolet reflectance spectra for zinc were not found in the scientific literature, so for zinc we obtained some very tentative values of the optical constants by Kramers-Kronig analysis of the 180-45,454 cm^{-1} reflectance spectrum. The results for molybdenum are presented in Figure 3.

OPTICAL WINDOW MATERIALS

Optical window materials that we investigated were NaCl, KCl, CsI, CsBr, BaF₂, ZnS, and ZnSe. Polycrystalline samples of ZnS and ZnSe, and crystalline samples of the other five materials were used to acquire reflectance spectra for each of the seven materials. Transmittance spectra were also obtained for ZnSe. The optical constants were, in general, obtained using Kramers-Kronig methods. The results for ZnS are presented in Figure 4. The vacuum ultraviolet reflectance spectrum of ZnS previously measured by Hunter, Angel, and Hass² were used to extend the reflectance spectrum for

the Kramers-Kronig analysis.

DIESEL SOOT

The optical properties of three samples of Diesel soot were investigated. Two of the samples were provided by Prof. Thor Stromberg, Dept. of Physics, New Mexico State University. The two NMSU samples were collected from the open burning of Diesel fuel. One sample, referred to hereafter as NMSU heated soot, was heated to about 320°C for about one-half hour to drive off any unburned hydrocarbons; the other, NMSU unheated soot, was the Diesel soot as collected. The third sample, UMKC soot, was collected from open burning of Diesel fuel in a burner that was constructed at UMKC.

Pellets of each of the three Diesel soot samples were prepared using a procedure similar to that used for the clays.¹ It was very difficult to prepare pellets with seemingly specular surfaces. However, after numerous attempts a pellet was obtained for each of the three samples.

Near normal incidence (6.5 deg) reflectance spectra of the three pellets were acquired in the 180-4,000 cm^{-1} region of the infrared, and for the two NMSU samples reflectance spectra were also acquired in the 220-2,500 nm region of the uv-vis-nir. The UMKC soot pellet, which was very fragile, was damaged in the process of acquiring the uv-nir spectra.

Complex refractive indices were obtained for the three samples by application of Kramers-Kronig methods to the reflectance spectra. We could not find in the scientific literature any information about the optical properties of soots in the vacuum ultraviolet spectral region; thus the KK analysis was made without extrapolation of the reflectance spectra into the vacuum ultraviolet. The resultant values of n and k are probably in error in the uv-vis regions. The reflectance spectrum and resultant values of $n+ik$ for the unheated NMSU Diesel soot pellet are presented in Figure 5.

LIQUIDS

The optical properties of five liquids were investigated; the liquids were SF-96, DMMP, DIMP, DEP, and DES. The infrared near-normal incidence reflectance spectra of SF-96, DMMP, DIMP, and DEP were measured throughout the 180-4,000 cm^{-1} wave-number

region using an open sample dish in a closed/purged reflectance unit. The same procedure applied to DES was unsuccessful because the sample would evaporate before the spectrum could be measured.

In the near-infrared region ($4,000-12,500 \text{ cm}^{-1}$) a thin wedge-shaped cell³ was used to obtain four or more transmittance spectra of each of the five liquids. The spectrum for the imaginary part of the complex refractive index $n+ik$ was determined for each liquid from the transmittance spectra. The wedge-shaped cell was also used in the $500-4,000 \text{ cm}^{-1}$ region to determine the k spectrum for DES.

Separate Kramers-Kronig algorithms applied to the reflectance and k spectra of each liquid provided $n+ik$ spectra and n spectra, respectively. Results for DMMP are presented in Figures 6 and 7. In the infrared ($180-4,000 \text{ cm}^{-1}$) $n+ik$ for DMMP are from Kramers-Kronig analysis of the reflectance spectrum. In the near infrared ($4,000-12,500 \text{ cm}^{-1}$ or $800-2,500 \text{ nm}$) the n spectrum for DMMP is from Kramers-Kronig analysis of the k spectrum. The reflectance spectrum in the near infrared was computed for s polarization at 6.5 degree angle of incidence using the appropriate generalized Fresnel reflectance equation and spectral values of $n+ik$ for DMMP.

REFERENCES

1. M.R. Querry, W.P. Roach, D.L. Striley, and C.T. Heese, "Optical Properties of Powders, Liquids, and Metals in the Infrared, Visible, and Ultraviolet Spectral Regions," p , Proceedings of the 1986 CRDEC Scientific Conference on Obscuration and Aerosol Research, R.H. Kohl, Ed., In Preparation.
2. W.R. Hunter, D.W. Angel, and G. Hass, "Optical Properties of Evaporated Films of ZnS in the Vacuum Ultraviolet from 16 to 200 nm," J. Opt. Soc. Am. 68, 1319-1322 (1978).
3. I.L. Tyler, G. Taylor, and M.R. Querry, "Thin-Wedge-Shaped Cell for Highly Absorbant Liquids," Appl. Opt. 17, 960-963 (1978).

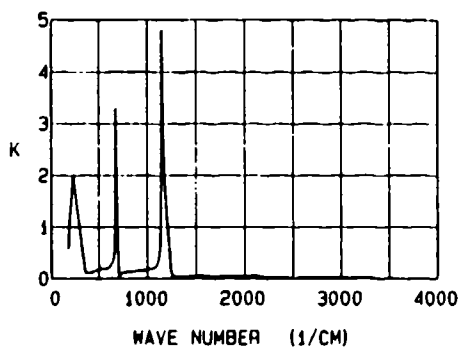
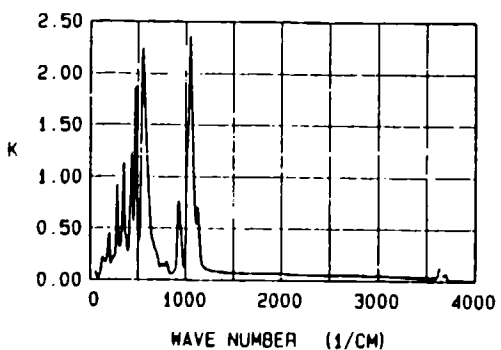
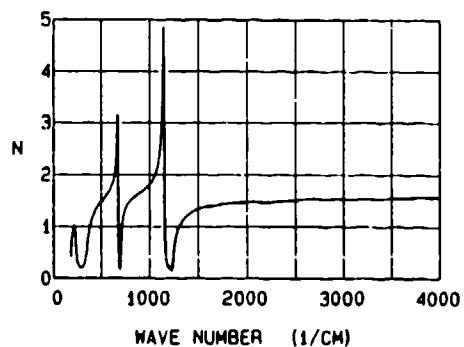
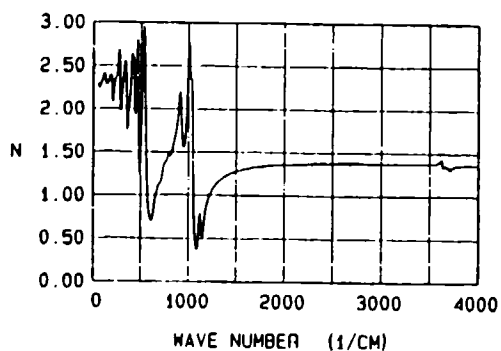
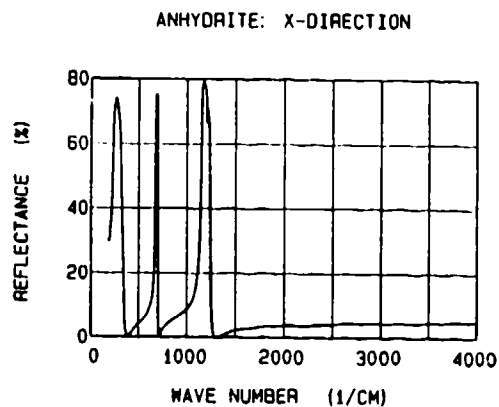
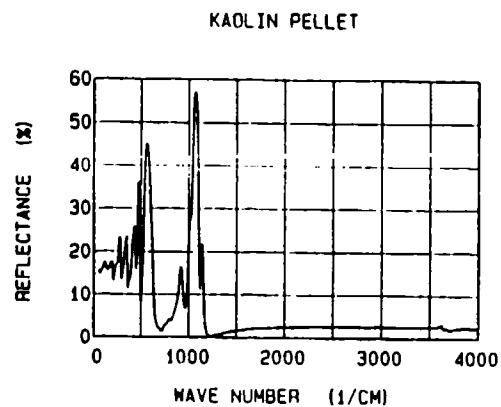


FIGURE 1. KAOLIN PELLET. The upper, center, and lower graphs are respectively the measured, near-normal incidence reflectance spectrum and the real and imaginary parts of the complex refractive index determined from KK analysis of the reflectance spectrum.

FIGURE 2. ANHYDRITE CRYSTAL: X-DIRECTION. The upper, center, and lower graphs are respectively the measured near-normal incidence reflectance spectrum and the real and imaginary parts of the complex refractive index determined from KK analysis of the reflectance spectrum.

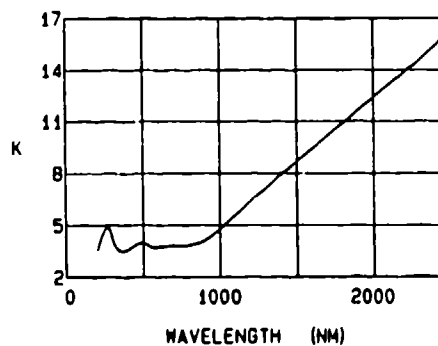
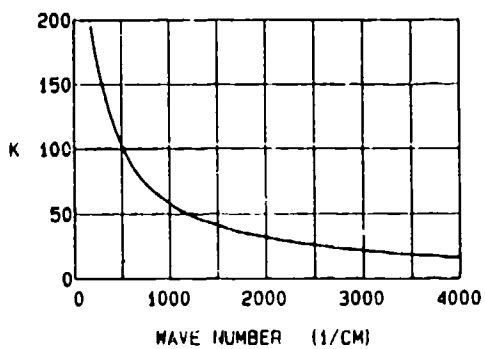
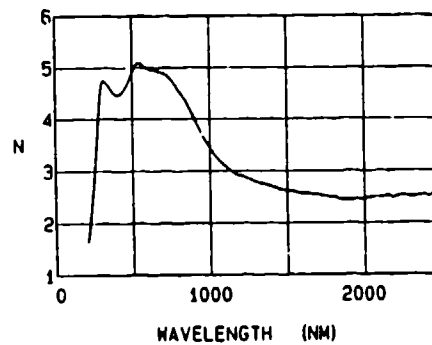
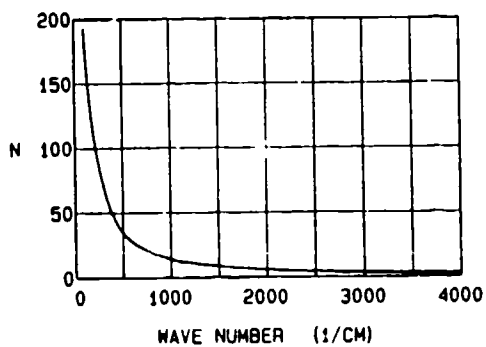
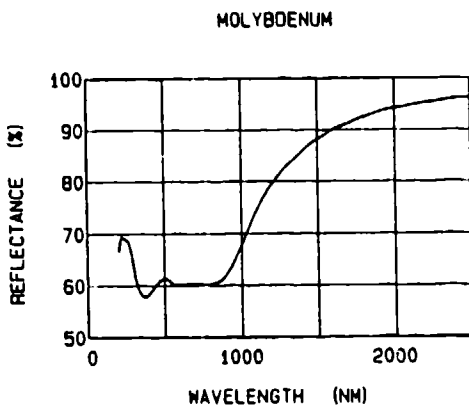
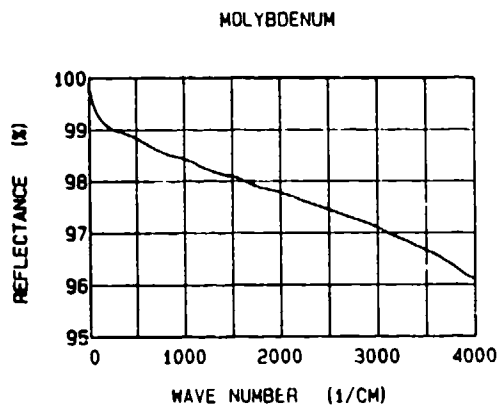


FIGURE 3. MOLYBDENUM. The upper, center, and lower graphs are respectively the reflectance spectrum and the real and imaginary parts of the complex refractive index determined from KK analysis of the reflectance spectrum. The infrared ($0-4,000 \text{ cm}^{-1}$) and the near infrared-visible-ultraviolet ($206-2,500 \text{ nm}$; $48,465-4,000 \text{ cm}^{-1}$) spectra are on the left and right, respectively.

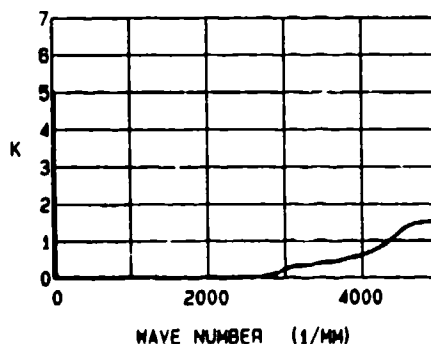
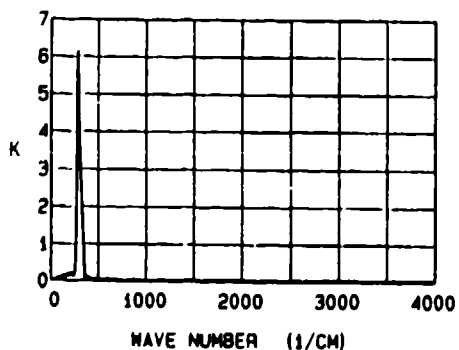
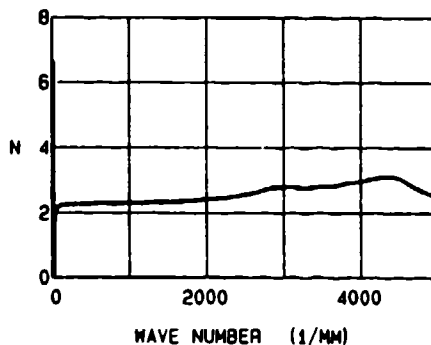
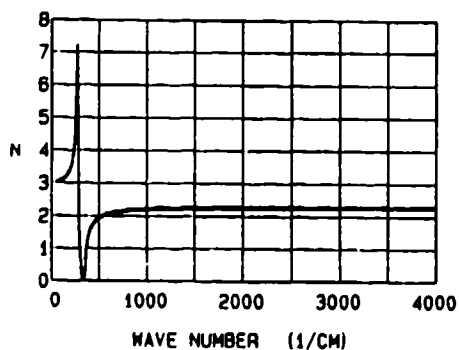
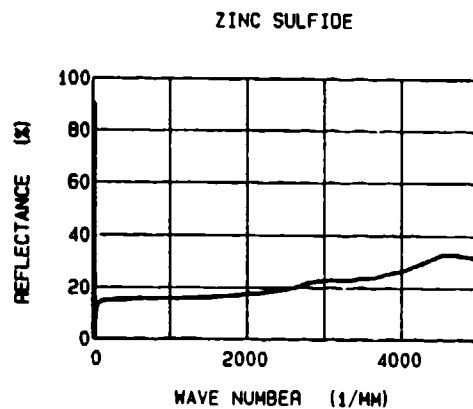
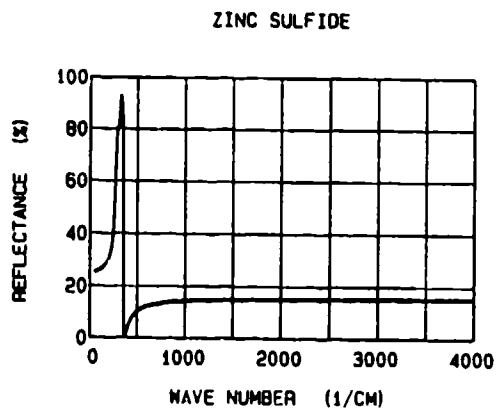
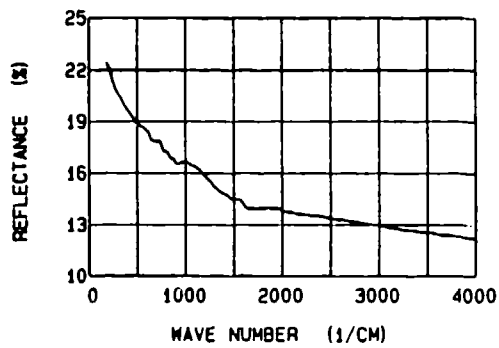


Figure 4. ZINC SULFIDE. The upper, center, and lower graphs are respectively the reflectance spectrum and the real and imaginary parts of the complex refractive index determined from KK analysis of the reflectance spectrum. The infrared ($60-4,000 \text{ cm}^{-1}$) and the infrared-near infrared-visible-ultraviolet ($60-5,000 \text{ mm}^{-1}$) spectra are on the left and right, respectively.

NMSU UNHEATED SOOT PELLET



NMSU UNHEATED SOOT PELLET

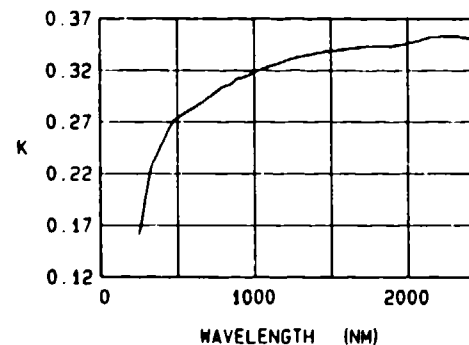
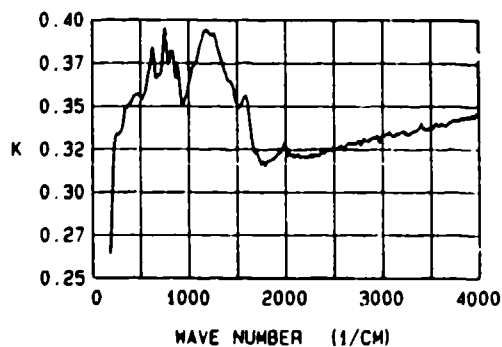
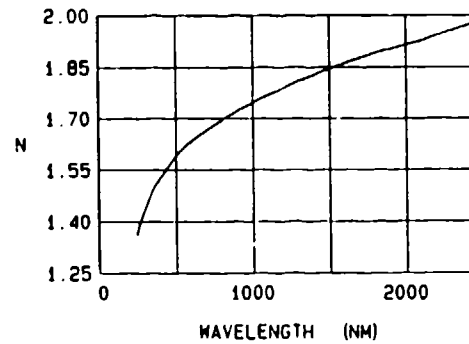
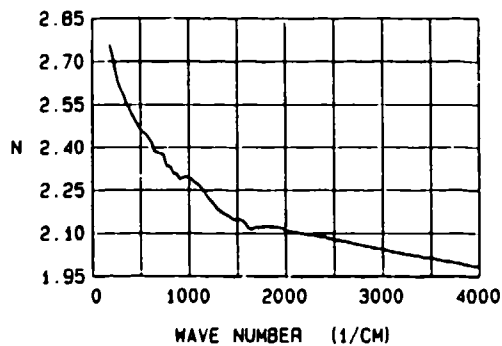
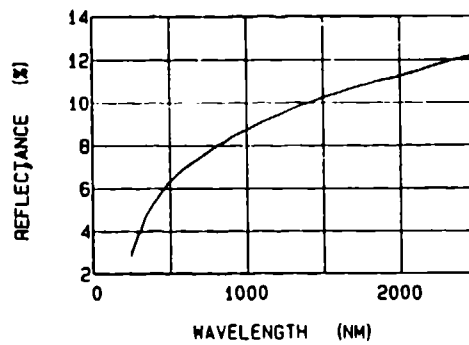


FIGURE 5. NMSU UNHEATED SOOT PELLET. The upper, center, and lower graphs are respectively the reflectance spectrum and the real and imaginary parts of the complex refractive index determined from KK analysis of the reflectance spectrum. The infrared ($180-4,000 \text{ cm}^{-1}$) and the near infrared-visible-ultraviolet ($220-2,500 \text{ nm}$; $45,450-4,000 \text{ cm}^{-1}$) spectra are on the left and right, respectively.

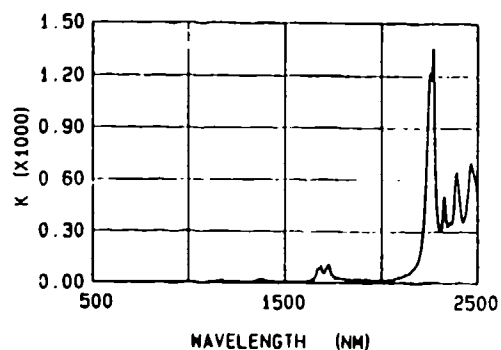
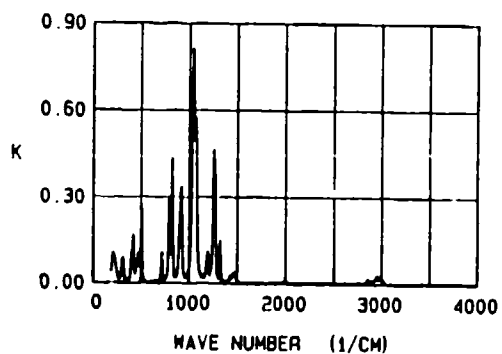
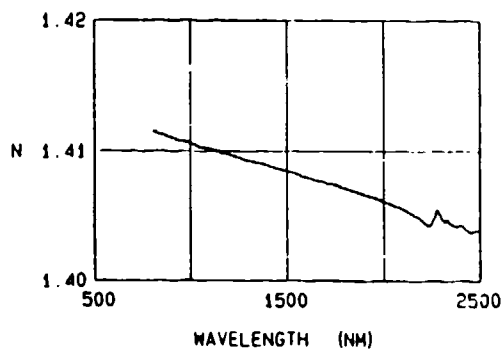
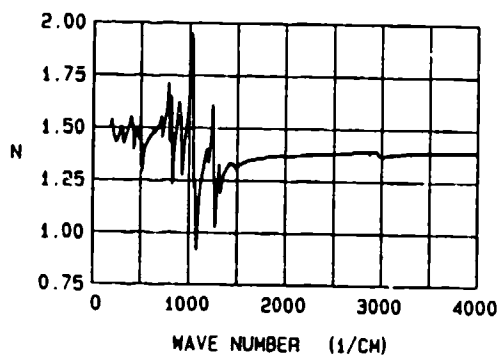
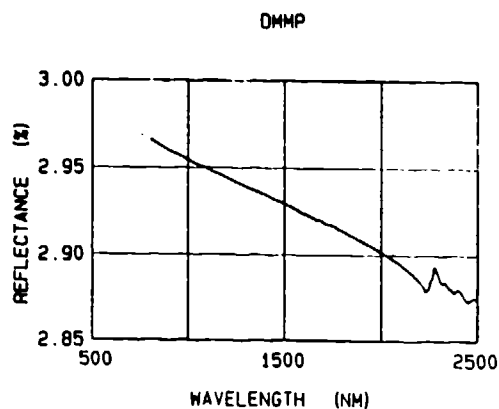
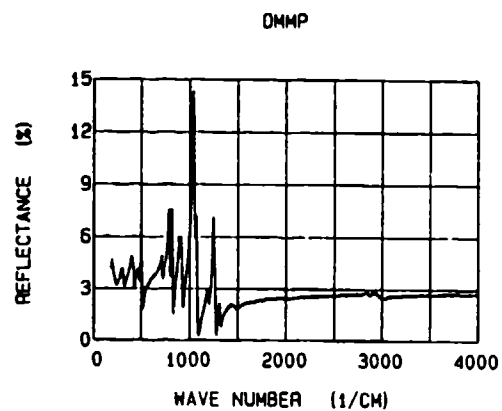


FIGURE 6. DMMP. The upper, center, and lower graphs are respectively the measured reflectance spectrum and the real and imaginary parts of the complex refractive index determined from KK analysis of the reflectance spectrum.

FIGURE 7. DMMP. The lower, center, and upper graphs are respectively the imaginary part of the complex refractive index K determined from transmittance measurement, the real part N determined from KK analysis of K , and the reflectance spectrum computed using N , K , and the Fresnel equation for normal incidence.

Blank

Aerosol Particle Analyzer Measurements

Philip J. Wyatt, Christian Jackson, David L. Hicks,
and Yu-Jain Chang
Wyatt Technology Corporation
Santa Barbara, CA 93130

RECENT PUBLICATIONS, SUBMITTALS FOR PUBLICATION AND PRESENTATIONS:

A) Philip J. Wyatt, Kevin L. Schehrer, Steven D. Phillips, Christian Jackson, Yu-Jain Chang, Randalh G. Parker, David T. Phillips, and Jerrold R. Bottiger, "Aerosol Particle Analyzer", accepted by Applied Optics for a cover feature in early 1988.

B) Philip J. Wyatt and Steven D. Phillips, US Patent #4693602, "Method and apparatus for measuring the light scattering properties of small particles" issued 15 September 1987.

ABSTRACT

A brief description of the DAWN aerosol particle analyzer is followed by a discussion of some of the data collected using the instrument.

THE INSTRUMENT

The DAWN-aerosol system allows the light scattered from individual particles to be measured at up to 72 angular positions in three dimensions (14 are currently operational) and at two large forward and rear scattering areas, at a rate of up to 200 particles per second. Some real-time analysis of the particles is possible (e.g. symmetry of scattering, approximate indication of particle size) and more detailed later analysis is easily accomplished by storing the data on the dedicated PC.

The system consists of six main components (see Fig. 1.)

1. **Laser.** The laser light source used is currently a 10 mW He-Cd laser emitting a 442 nm beam of nominal diameter 0.3 mm. This beam is aligned through the center of the scattering chamber.

2. Scattering Chamber. The scattering chamber is a sphere with an internal diameter of 40 mm, and outer diameter of 100 mm. There are entry and exit apertures for the laser beam and the particle stream (which are at right angles to each other). Then the detector positions consist of two large apertures for fiber bundles subtending an azimuthal angle of almost 2π and about $\pm 10^\circ$ of polar angle centered on 20° and 160° respectively, as well as 72 small apertures arranged in four great circles. These great circles have the laser beam as a common diameter, and are arranged at 45° intervals, the first being parallel to the plane of polarization of the laser beam. These ports are either plugged and sealed or contain a detector.

3. Scattered light detectors. For the 72 small ports the detector consists of an optical collimator with an acceptance angle of $\pm 1.25^\circ$ attached to an optical fiber, which is in turn attached to the photocathode of a photomultiplier tube. The optical bundles collect light directly and transmit it to two photomultiplier tubes.

4. Electronics. The photomultiplier outputs are amplified by six decade logarithmic amplifiers whose signals are then processed. Any one of the detector channels may be used as a trigger channel which is constantly monitored and when the output signal crosses a pre-selected threshold the outputs from all channels are sampled and then multiplexed, converted to a 12 bit digital representation, and stored in the memory of a personal computer.

5. The Data Processing Software corrects for dark current and background scattering as well as inherent sensitivity differences between the detector channels. When the instrument triggers on a particle the resultant corrected intensities can be displayed and/or stored on rotary memory means for further analysis of optical observables.

6. Aerosol Handling Hardware. A set of pumps, valves and regulators sample, dilute and introduce aerosol particles entrained in a fine laminar stream through the center of the chamber intersecting the laser beam one particle at a time.

SELECTED DATA

The following figures show the results of the analysis of scattering patterns from a variety of particles. Data was collected using the two fiber bundles and 14 angular detectors, (the fiber bundle data are not discussed in this paper). Some measurements were made with polaroid analyzers placed in front of the optical collimators in order to distinguish between polarized and depolarized scattering. For example Fig. 2. shows the ratio of polarized to depolarized scattering measured at 55° in the vertical plane for 210 latex spheres. It can readily be seen that there is, as expected, very little depolarized scattering, except for a few isolated particles which are most likely clumps. Fig. 3 shows the scattering from a single latex sphere of nominal diameter 730 nm . On one side of the scattering chamber the detectors had analyzers aligned in the direction of polarization of the beam, while on the other side they were aligned perpendicular to the beam polarization. Note the distinctive minimum at 40° and maximum at 55° of the polarized scattering, and the small amount of depolarized scattering at the lowest angles rapidly falling to zero as the scattering angle increases.

Figures 4 and 5 show data from individual bronze and aluminum particles respectively. Again the measurements are made in the vertical plane with detectors on either side of the chamber having analyzers arranged perpendicular to each other. The position of the detectors in the polar direction are somewhat different from Fig. 3. Of interest is the anticipated minimum for depolarized scattering at 90° , the large amount of backscatter, and

the similar intensities of both polarized and depolarized scattering in the forward and backwards directions.

Figures 6 and 7 show measurements made without any polaroid analyzers of a small iron filing and solder powder. Note the similar overall intensity of the measurements but the marked symmetry of the intensities from the solder powder particles compared to those from the filings suggesting that the former is a near spherical powder.

Figures 8,9,and 10 show scattered intensities measured from individual rod shaped *Bacillus subtilis* . The great differences in the scattering patterns indicates the differing alignment of the rods as they pass the beam, sometimes producing symmetrical scattering, and sometimes strikingly asymmetrical scattering.

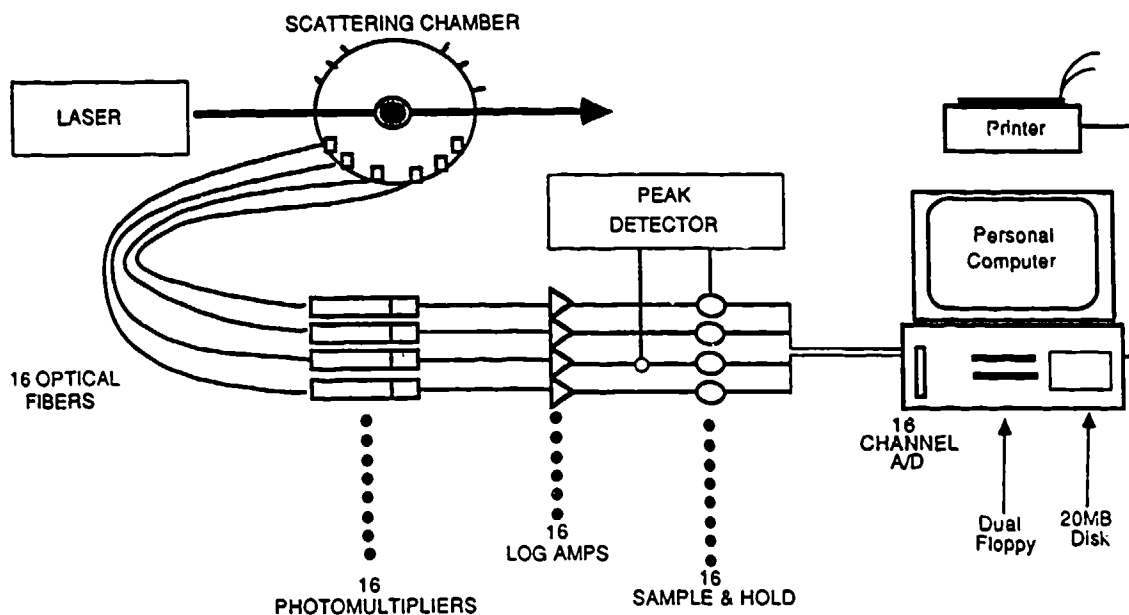


FIGURE 1. AEROSOL PARTICLE ANALYZER Main system components.

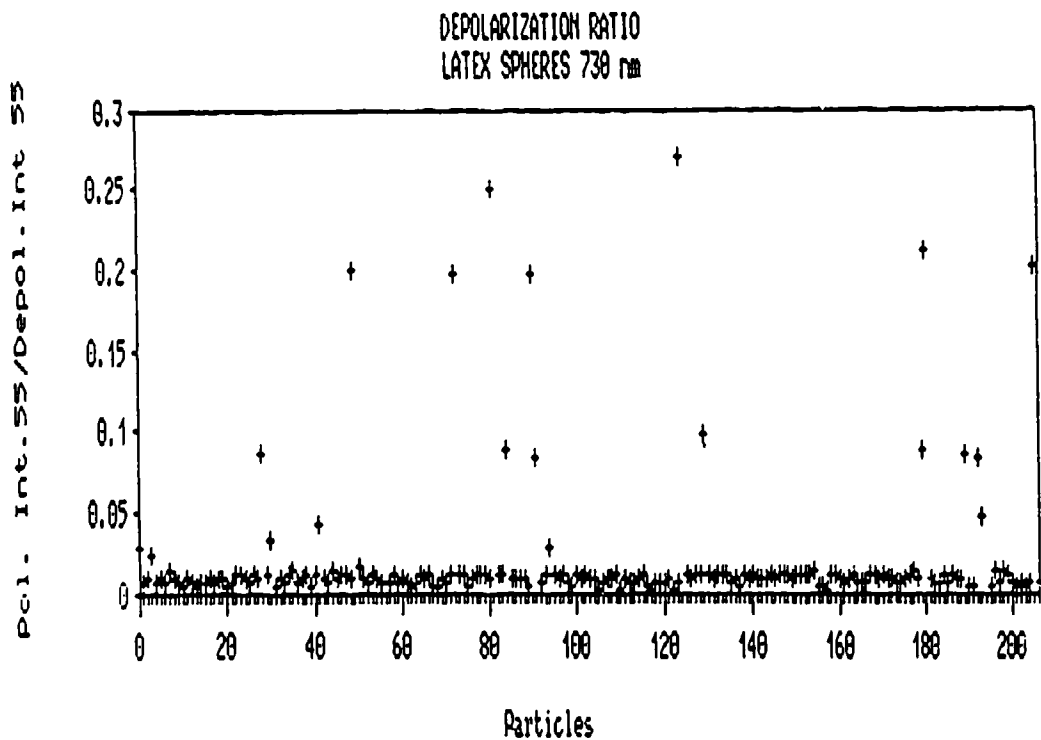


FIGURE 2. DEPOLARIZATION RATIO FOR LATEX SPHERES.

Latex Sphere 730 nm showing depolarization

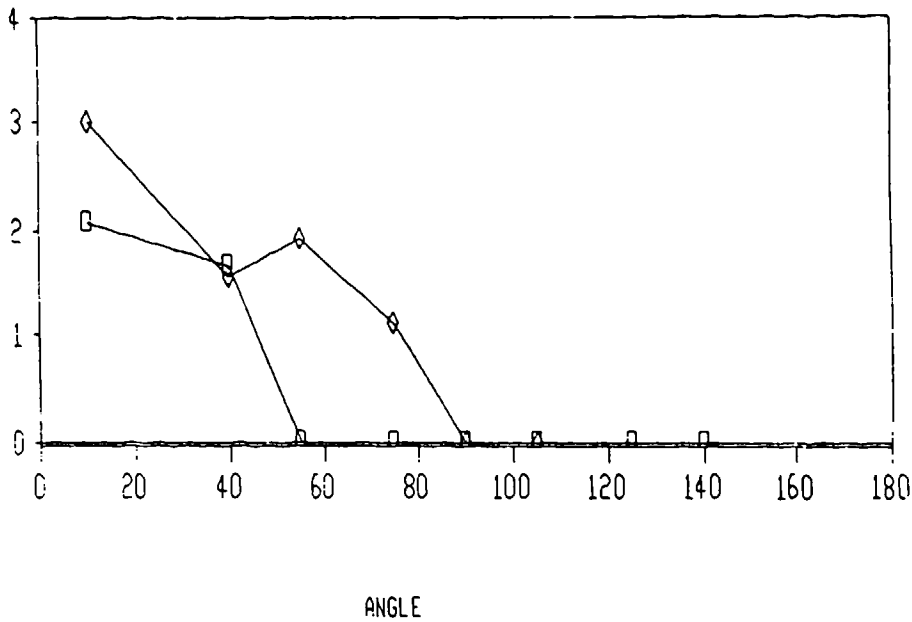


FIGURE 3. SCATTERING PATTERN FROM LATEX SPHERE.
Polarized and depolarized scattering in the vertical plane.

ALUMINUM

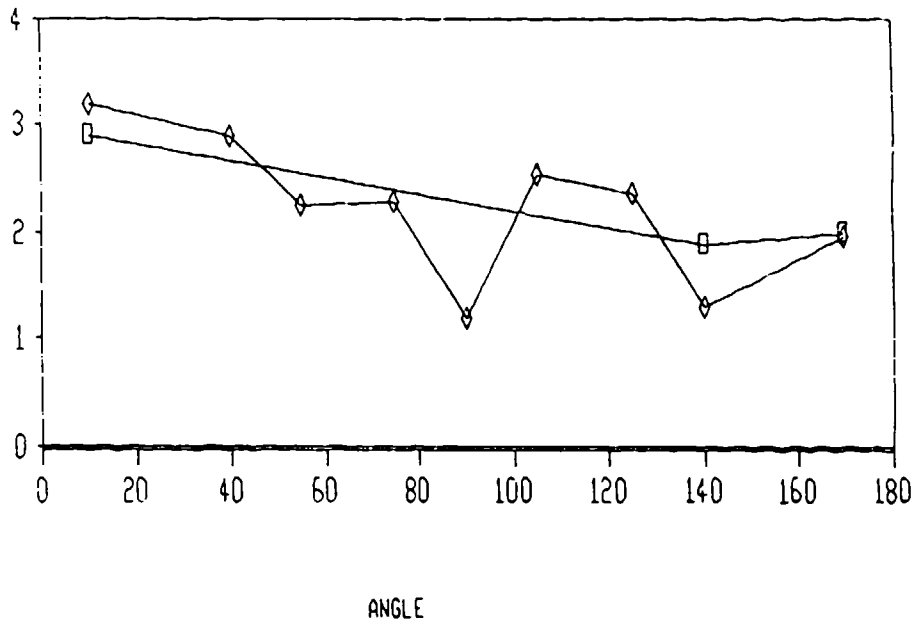


FIGURE 4. SCATTERING PATTERN FROM BRONZE DUST.
Polarized and depolarized scattering in the vertical plane.

BRONZE

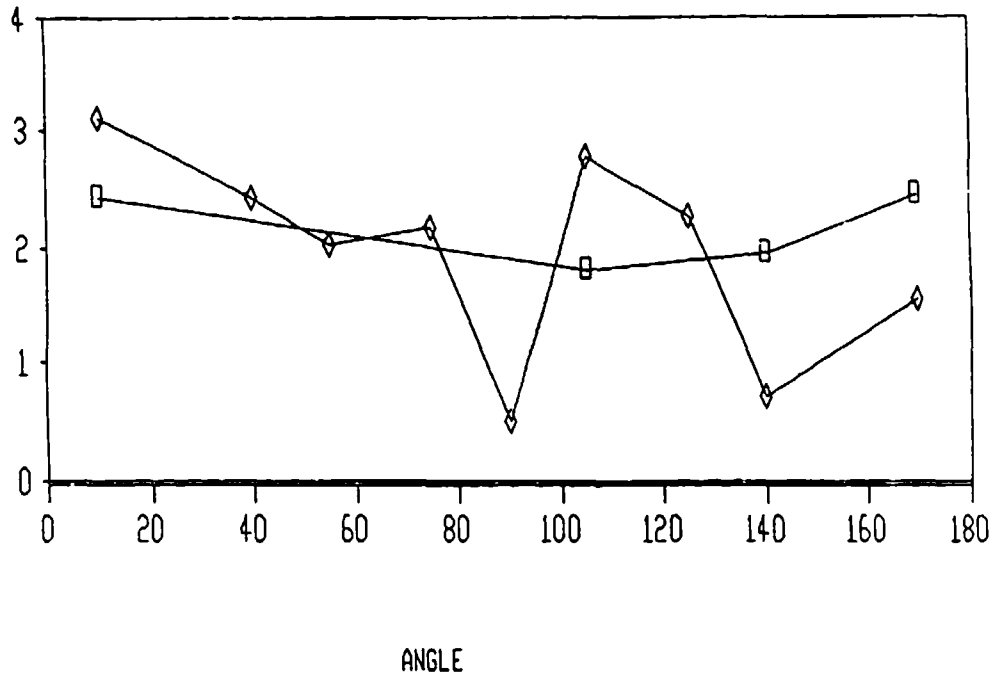


FIGURE 5. SCATTERING PATTERN FROM ALUMINUM PARTICLE.
Polarized and depolarized scattering in the vertical plane.

IRON FILING

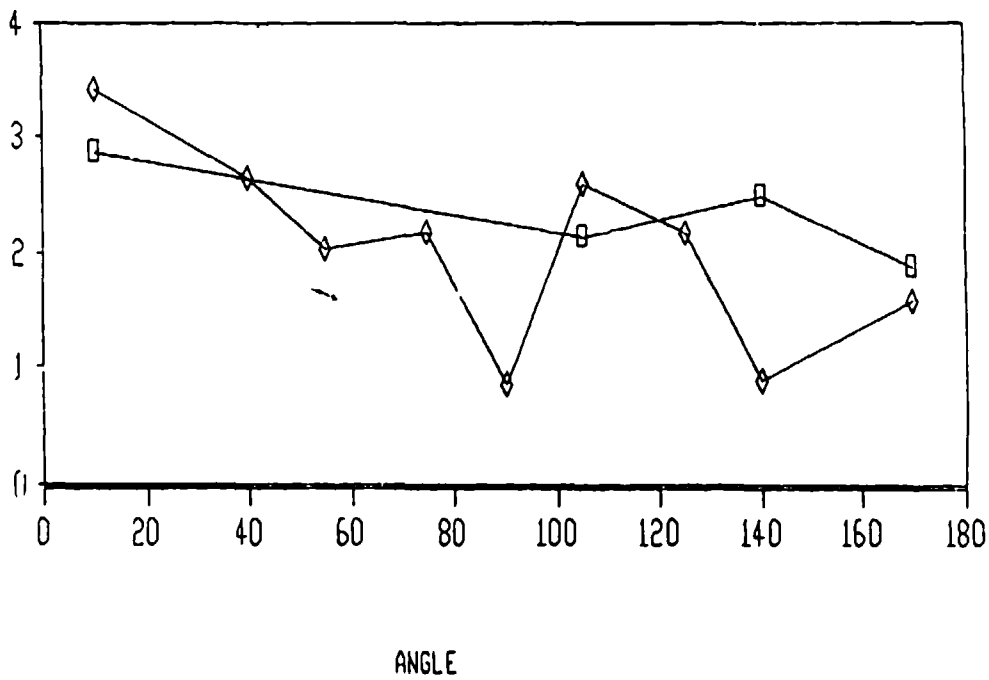


FIGURE 6. SCATTERING PATTERN FROM IRON FILING.
Measured in the vertical plane.

SOLDER POWDER

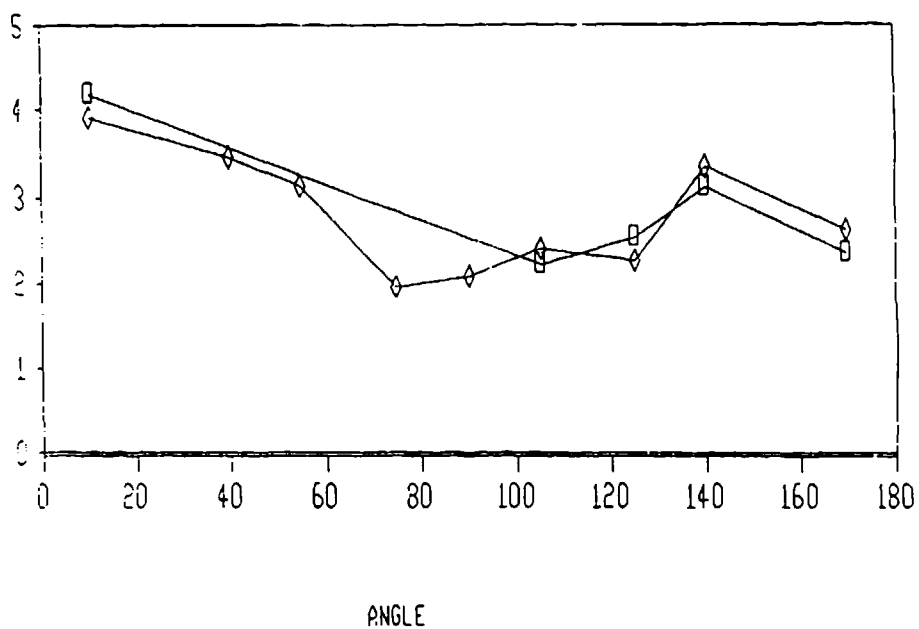


FIGURE 7. SCATTERING PATTERN FROM SOLDER POWDER.
Note the right-left symmetry.

Bacillus subtilis

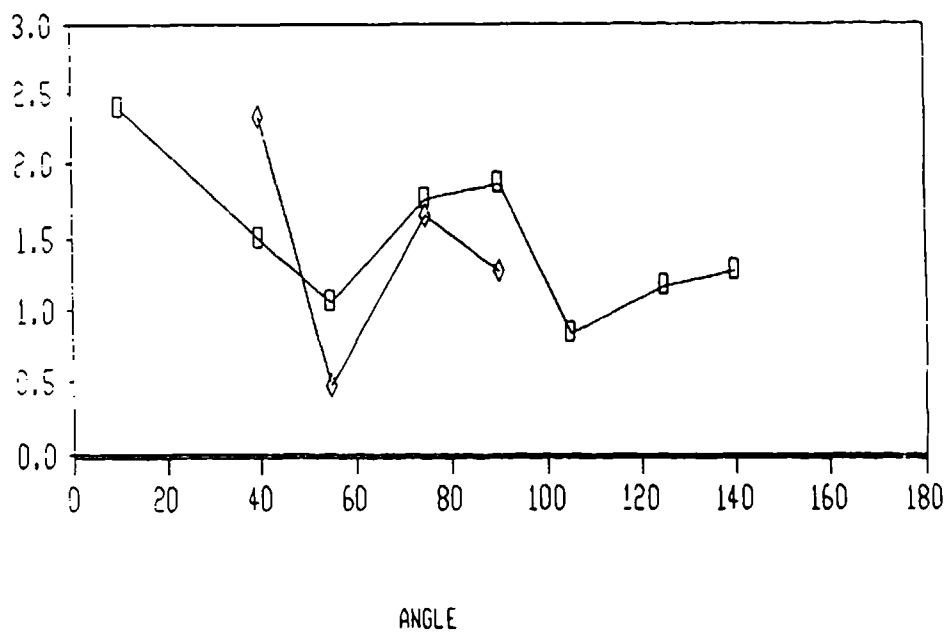


FIGURE 8. SCATTERING FROM *BACILLUS SUBTILIS*.

Bacillus subtilis

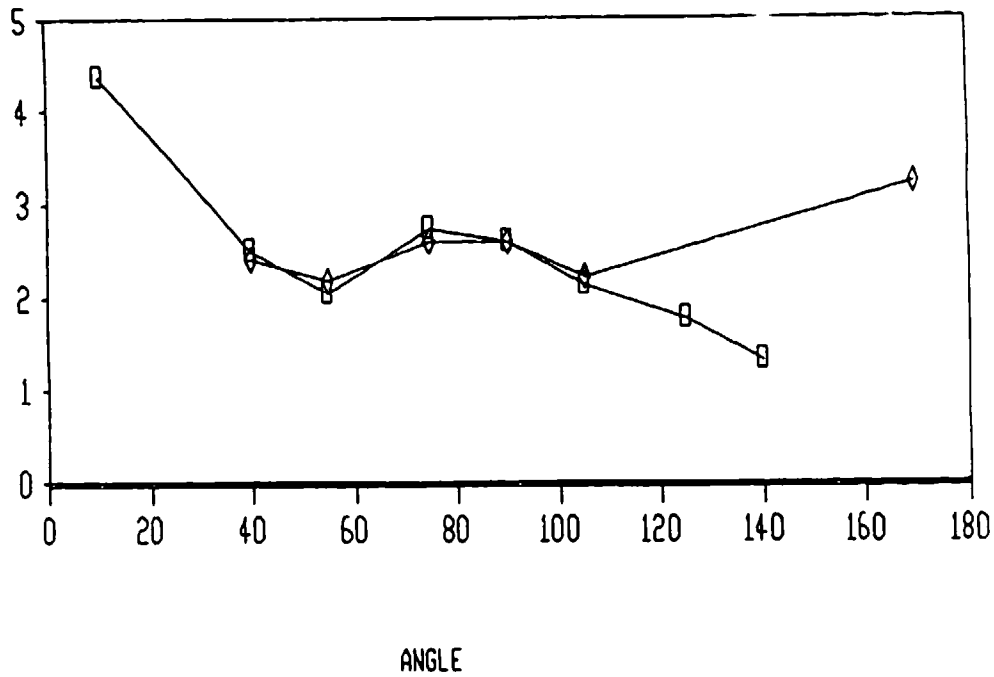


FIGURE 9. SCATTERING FROM *BACILLUS SUBTILIS*.

Bacillus subtilis

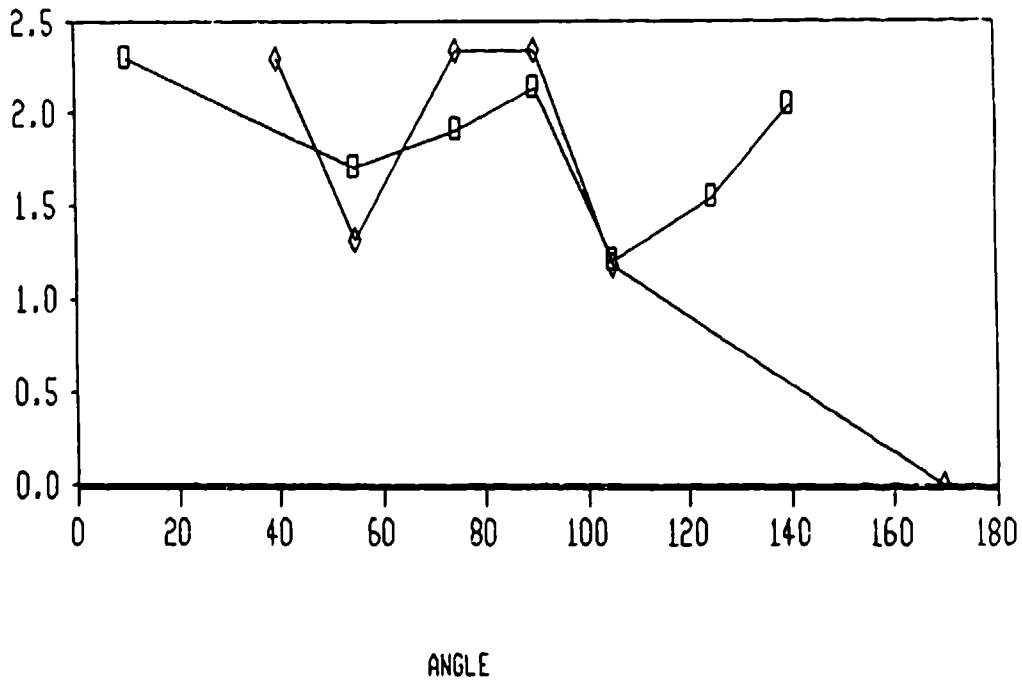


FIGURE 10. SCATTERING FROM *BACILLUS SUBTILIS*.

Blank

PARTICLE DISCRIMINATION USING
THE AEROSOL PARTICLE ANALYZER

J. R. Bottiger
Research Directorate, CRDEC
Aberdeen Proving Ground, MD 21010-5423

RECENT PUBLICATIONS, SUBMITTALS FOR PUBLICATION AND PRESENTATIONS:

The present paper is the author's first submission on this subject.

ABSTRACT

An instrument capable of rapidly sampling single particles from an aerosol and recording their light scattering patterns has been built by Wyatt Technology Corporation and delivered to CRDEC. This paper reports on its use in distinguishing spherical from nonspherical particles. Future work will include improving the instrument's signal-to-noise ratio and exploring the suitability of various measurement combinations as aerosol characterization parameters.

INTRODUCTION

The Wyatt Technology Corporation (WTC) has delivered to CRDEC a light scattering instrument termed an Aerosol Particle Analyzer. It is the first model produced by WTC in their SBIR supported program to develop a commercially viable instrument for the rapid characterization of very fine aerosol particles, and is of interest to the Army in particular for its potential to characterize airborne biological entities and, on a larger scale, obscurant aerosols. The instrument is similar in spirit to Boeing's Multichannel Nephelometer, also operated in our laboratory, but is considerably reduced in size and complexity as befitting a device intended ultimately for practical rather than research applications.

An aerosol handling system draws sample particles from a test aerosol and causes them to singly traverse a He-Cd laser beam at the center of a spherical

chamber. The chamber is drilled with 72 port holes laid along four great circles from which the scattered light may be observed. Fourteen separate photomultiplier tubes are attached to fourteen optical fibers terminated with SEL-FOC grin lenses which may be inserted into any of the viewing ports; the leftover 58 ports are plugged. A wide range of experimental configurations are available, depending on which ports are selected for viewing, the polarization state of the incoming laser beam, and the orientation of linear polarizers (if used) covering the SEL-FOC lenses. Detailed information on the aerosol particle analyzer may be found elsewhere. This paper concerns itself with a simple characterization of aerosol particles and the instrument's applicability to that analysis.

THE EXPERIMENT

Only eight of the fourteen detectors were used in this work; they filled eight available ports at the scattering angle of 40 degrees. That is, the detectors were along the circumference of a circle perpendicular to the laser beam, 45 degrees apart in azimuth, and at a 40 degree angle from the illuminated particle relative of the laser beam. The laser beam, which is emitted linearly polarized, was converted to circularly polarized light with a quarter-wave plate before entering the scattering chamber. The remaining six detectors were deployed along one of the great circles, but for present purposes we shall simply ignore the data that was collected from them.

Now it is clear from the symmetry of this configuration that if light is scattered from a spherical particle all eight detectors should receive the same flux, while an irregularly shaped particle should scatter varying amounts into the different directions. Actually, any particle exhibiting axial symmetry and oriented with its symmetry axis parallel to the incident beam will scatter circularly polarized light in an azimuthally independent fashion, but we think such an object is sufficiently rare among the particles measured in this work

that we may in practice associate uniformity among the detectors with the presence of either a very small (Rayleigh) scatterer or a spherical scatterer.

A convenient measure of the uniformity of the scattered light is provided by the ratio of the standard deviation among the detectors to the average of the detectors, SD/AVG. If v_i ($i=1$ to n) are the (calibrated) outputs of the detectors, then

$$SD/AVG = \sqrt{\frac{n \sum v_i^2}{(\sum v_i)^2} - 1}$$

The quantity SD/AVG of course vanishes when the detectors are equally illuminated. It can be shown that SD/AVG attains its maximum possible value, $\sqrt{n-1}$, when only one detector is illuminated and the remaining $v_i = 0$. One can imagine that occurring for example in the scattering from a high aspect ratio fiber oriented such that the sharp forward scattering cone happens to intersect only one detector.

We now define a quantity called the sphericity index (SPX) as

$$SPX = 1 - \frac{1}{\sqrt{n-1}} \frac{SD}{AVG}$$

It varies from zero, in the worst case of only one detector being illuminated, to unity when all detectors are equally illuminated. There is no rigorous correlation, but it seems reasonable to associate "how spherical a particle is" with its measured sphericity index, perfect spheres having $SPX = 1$, and objects very far from spherical, such as high aspect ratio flakes and fibers, having sphericity indices much lower, perhaps approaching zero.

Another simple quantity we shall examine is the "brightness" of a particle, which is defined to be the average output (in calibrated microamps) of the eight detectors. Ideally, for particles of a given material, brightness and particle

size should be positively related, at least over some usefully large range. In these experiments however there is no relationship between brightness and particle size except in a limiting sense, for several reasons. The most obvious one is that the particles are brought to the laser beam by a tube 1mm in diameter, while the beam, with a Gaussian intensity profile, is only about 0.1mm across. Thus a large range of impact parameters relative to the beam will occur; a few particles actually cross at the center of the beam, more cross at varying distances from it, and in fact most miss it altogether. A sample of identical particles then will exhibit a variety of brightnesses, ranging from zero up to a maximum corresponding to transit through the beam center.

The object of the following experiments was to use the aerosol particle analyzer to gather sphericity index and brightness measurements on some spherical and nonspherical aerosol samples.

Aerosol flows were adjusted to provide a few hundred particles per second crossing the laser beam, verified by monitoring one of the detectors with an oscilloscope. As the average transit time was only on the order of 10 microseconds the probability of more than one particle being illuminated at a time is negligible. Although much faster collection software is now available from WTC, I used the original software which takes about a half second to store all the data from one collection event and reset, and thus sampled about two particles per second from those available.

Collected data were automatically stored in a binary file on the instrument's PC-XT. After all measurements were completed the data were translated to an ASCII file and then imported onto Lotus 1-2-3 spreadsheets for analysis and preparation of plot files.

A holder for small copper screens was incorporated into the exhaust line leading particles out of the scattering chamber. Some fraction of those sample particles which actually traversed the laser beam then were collected on the

screens for viewing under the electron microscope.

RESULTS

Holding to light scattering custom, we began by looking at Dow polystyrene spheres. Spheres of diameter .945 micrometers (std. dev. = .0064) in water were aerosolized with a tsi model 3460 Tri-jet Aerosol Generator and introduced into the aerosol particle analyzer. Data from 500 particles were collected and analyzed. Figure 1a shows each particle's position on a bivariate brightness/SPX plot. Some observations and remarks about figure 1a follow:

1. As anticipated, most of the particles had a sphericity index close to unity. An error in any detector's measurement can only serve to lower the SPX of a sphere, so readings approach unity as a limit. The majority of particles fall into a horizontal patch with $SPX > 0.9$. The vertical spread of the patch and its distance from unity is a measure of the system signal-to-noise ratio, given that the scatterers within it are essentially perfect spheres. Note that the patch becomes tighter and closer to $SPX = 1$ as brightness increases.

2. A few, perhaps 10%, of the particles are distinctly nonspherical. Some may be "junk" particles of unknown origin contaminating the system, others are certainly clusters of two or more spheres stuck together. An electron microscope's view of a section of the copper screen which intercepted some of these spheres as they were exhausted out of the scattering chamber is shown in figure 2a. It is a typical view of the screen, and several clusters are evident.

3. One of the eight detectors is designated to be the trigger detector. Its output is continuously monitored by an analog discrimination circuit and data is collected only from particles whose signal at the trigger detector exceeds a threshold value set by the operator. The threshold set for these and all measurements below corresponded to a brightness value of about 0.7

microamps. This is the reason there are no particles in the upper left corner of the figure.

4. A nonspherical particle can happen to throw enough light into the trigger detector to set off a data collection cycle while scattering less light into the other detectors, resulting in a particle's brightness (average of the eight detectors) being less than the threshold equivalent brightness. This is observed along the left side of figure 1a where nonspherical particles with brightnesses well under the 0.7 microamp threshold may be found.

5. As described in the previous section, the Gaussian intensity profile across the narrow laser beam combined with the relatively broad column of particle trajectories leads to a distribution favoring lower brightness values, at least down to where the influence of the threshold level is felt.

Figures 1b and 1c show the one-dimensional frequency distributions of sphericity index and brightness for the same particles of figure 1a.

The above measurement was repeated for a sample of 0.330 micrometer diameter spheres also aerosolized with the tsi tri-jet. The results, shown in figures 3a-3c are very similar to those of the .945 micrometer spheres. The only clear difference is in the lower maximum brightness level (particles passing through center of laser beam) of the smaller spheres.

To see if these characterizations would look different for a system of nonspherical particles, an aerosol of MgO smoke was produced. A small piece of magnesium ribbon was burned in a sealed 5 gallon bell jar, then, after a wait of about 15 minutes to allow larger particles to settle out, a sample of the white cloud was drawn into the aerosol particle analyzer. A microphotograph of the copper sampling screen in figure 2b shows the MgO cloud to consist of cubes, the largest single ones being about a half micrometer in size. Much smaller cubes cluster together forming clumpy or chainlike structures with dimensions of 1-2

micrometers.

Data on 500 MgO particles are shown in figures 4a-4c. The brightness distribution, being primarily a function of beam geometry, is not distinguishable from those of the spherical aerosol samples, but the sphericity index distribution has changed markedly. While there are still particles with SPX near unity, the clustering of data points there has been replaced by a roughly uniform distribution from $SPX = 0.5$ to $SPX = 1$.

Measurements were attempted on aerosol samples containing large particles expected to be even less spherical than the MgO. One set of measurements was made on aluminum flakes 10-20 micrometers in diameter, and another on minus 11 fibers about 10 micrometers thick. However the resulting data plots looked essentially like those for MgO in figure 4. Later SEM examination of the copper sampling screens showed that the scatterers actually measured were indeed MgO cubes and clusters, sometimes combined with .945 polystyrene spheres, as in figure 2c. Apparently few or none of the larger specimens made it all the way through the pump and tubing of the instrument's aerosol sampling hardware; instead they impacted onto tubing surfaces already contaminated with particles from the earlier experiments releasing many small fragments which continued downstream to finally pass through the laser beam. Though not producing useful data, the incident illustrates the importance of maintaining cleanliness in the system, and of visually inspecting sample particles with the electron microscope to insure a positive identification.

CONCLUSIONS

The distribution of the sphericity index - a measure of the azimuthal uniformity with which an object scatters circularly polarized light - appears to be a viable descriptor for use in characterizing an aerosol. On the other hand, brightness as used here is of virtually no value, being more a characterization

of the apparatus rather than the aerosol particles. In that sense figures 1a, 3a, and 4a are not truly bivariate plots of the aerosol. A more useful coordinate might be a particle size index defined, for example, by brightness when all particles are equally illuminated, or in any case by the ratio of certain forward and backward detectors. In fact the WTC instrument provides two large acceptance angle detectors in the near forward and near backward directions for that purpose, but I was unable to use them because of extra stray light in the chamber caused by a beam focusing lens I added to increase signal levels for the individual detectors.

Steps should be taken to modify the instrument as necessary to obtain a serviceable particle size estimate, or index. A laser with increased beam power may be necessary, or at least desirable. In addition, much of the aerosol sampling system - which I had to alter from WTC's original design because of the scattering chamber's unfortunate tendency to leak - is clearly not satisfactory with respect to sampling bias and cleanliness. An inlet diaphragm pump currently used must be eliminated, and shorter straighter runs of easily replaceable tubing should be used.

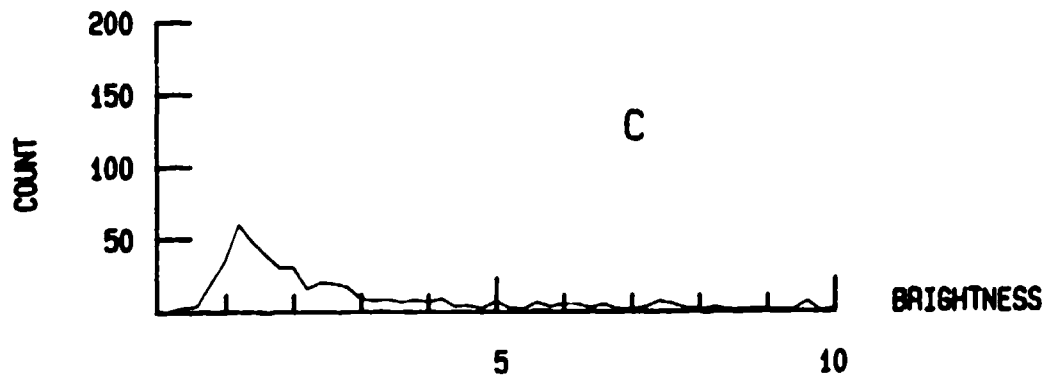
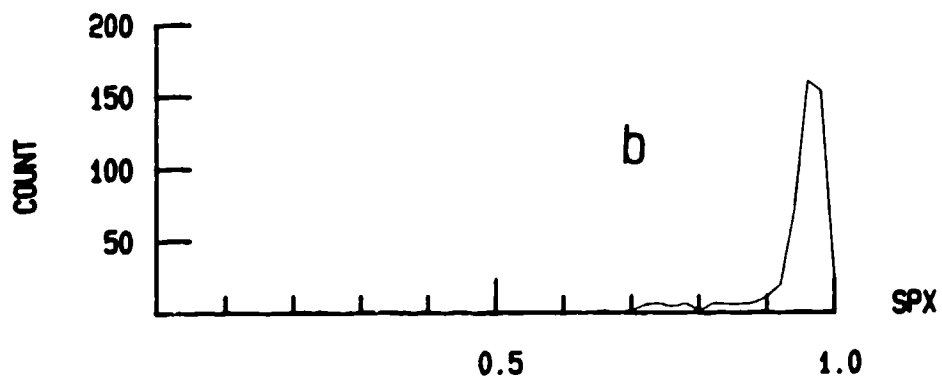
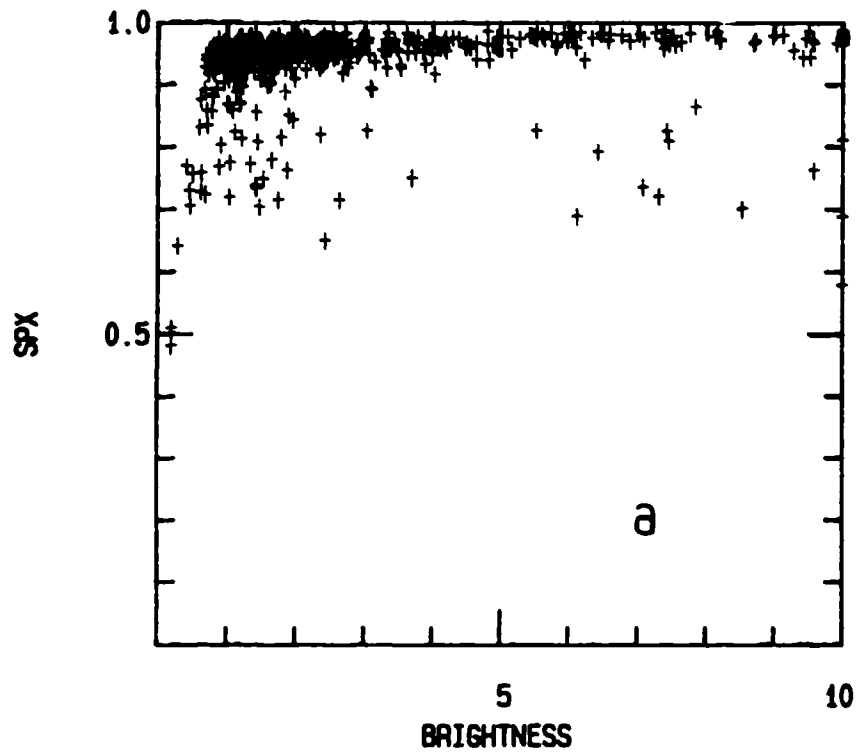
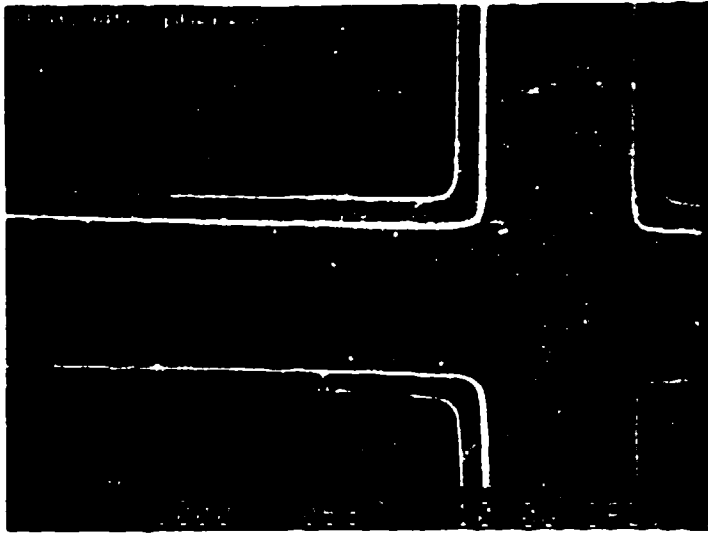


FIGURE 1: Sphericity index (SPX) and brightness for 500 polystyrene latex spheres with diameter = 0.945 micrometers.

a



b



c



FIGURE 2: SEM photographs of a) 0.945 micrometer polystyrene spheres, b) MgO smoke particles, c) contaminant freed from walls by Al flake.

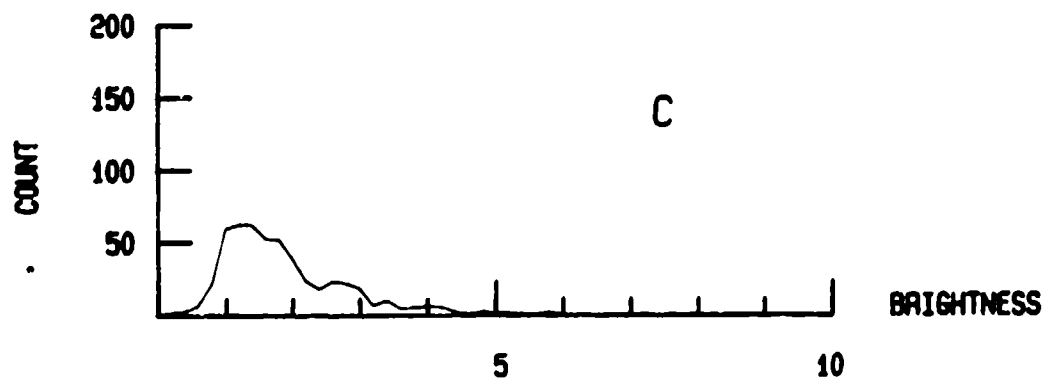
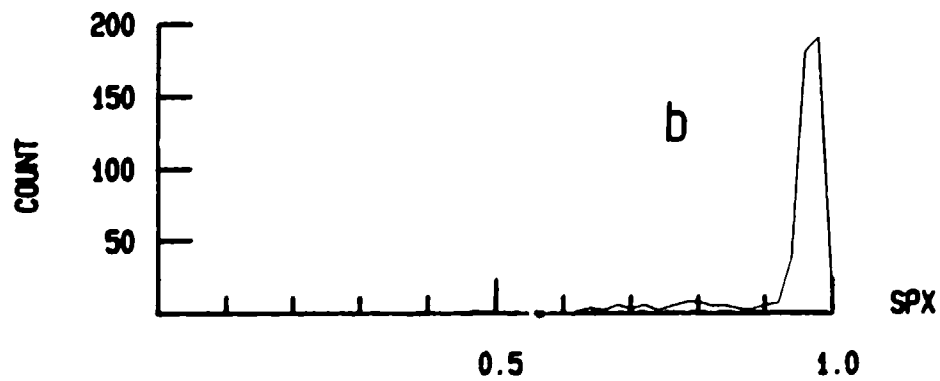
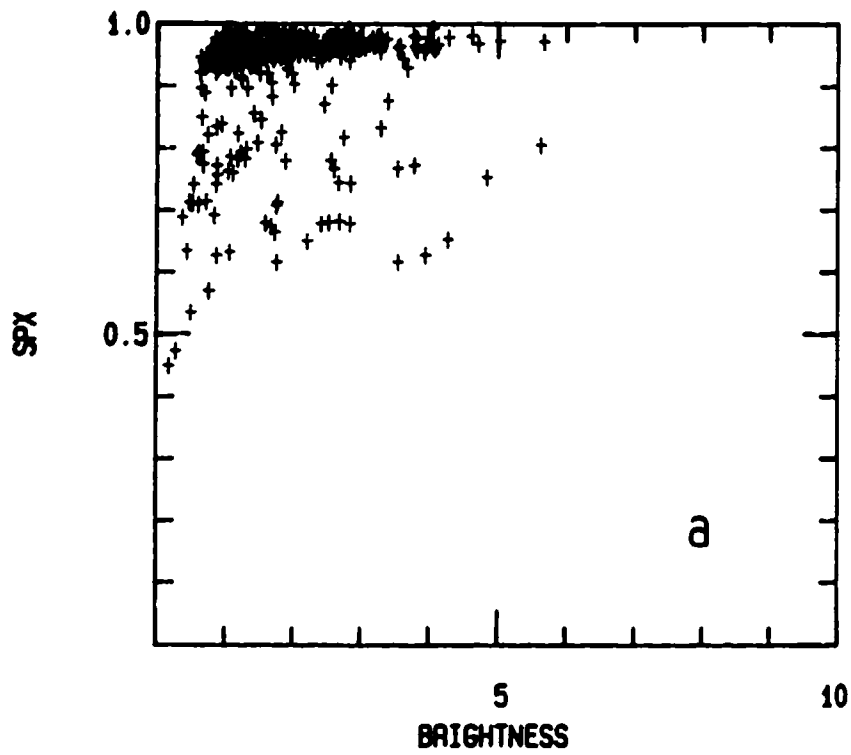


FIGURE 3: Sphericity index (SPX) and brightness for 500 polystyrene latex spheres with diameter = 0.330 micrometers.

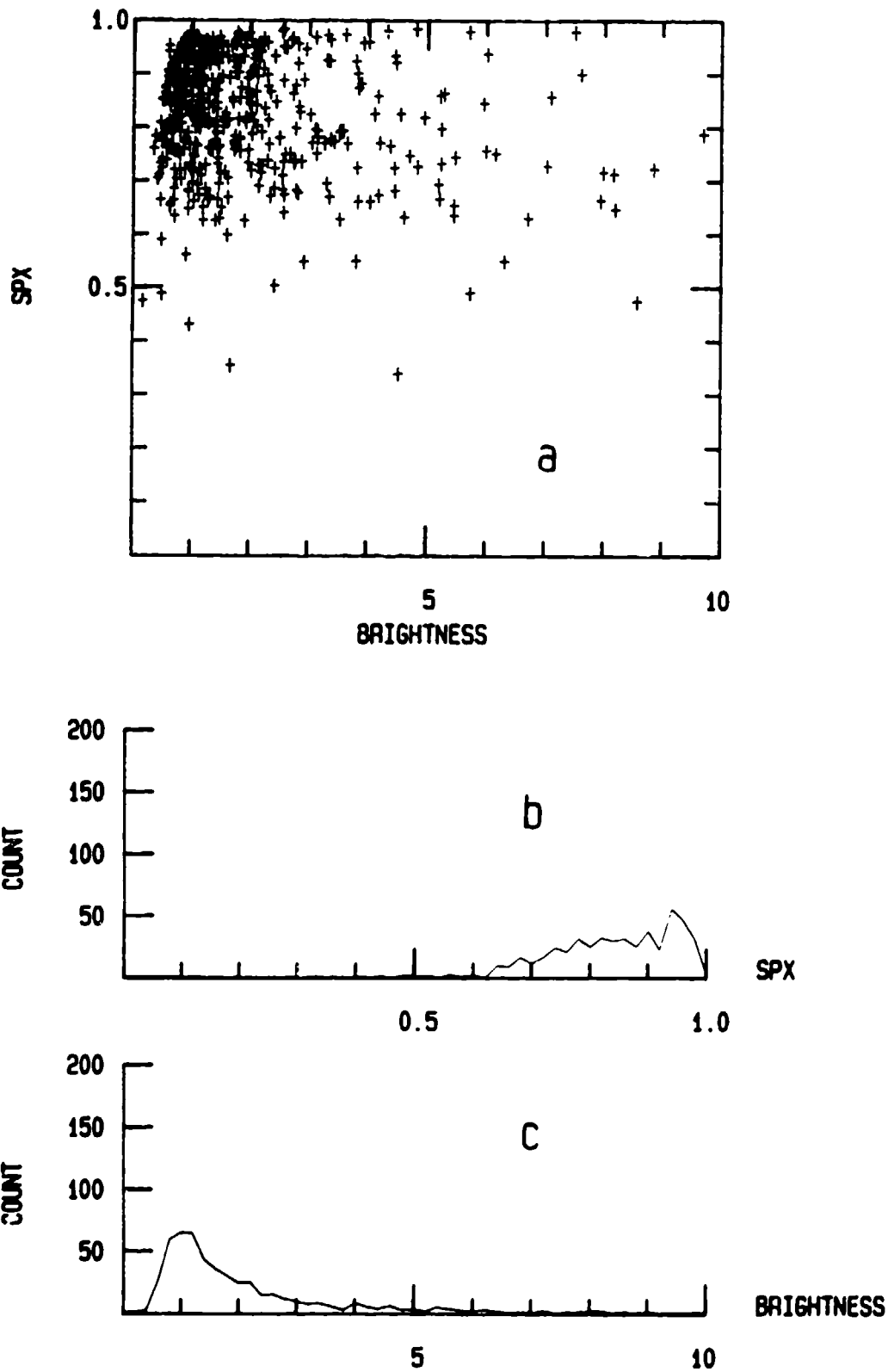


FIGURE 4: Sphericity index (SPX) and brightness for 500 particles of MgO smoke.

Superresolution Technique for Aerosol Holography

by

Peter D. Scott and David T. Shaw
State University of New York at Buffalo
Laboratory for Power and Environmental Studies
Amherst, NY 14260

Abstract

Digital decoding, rather than optical reconstruction, of in-line aerosol holograms permits algorithmic image enhancement and analysis to be conveniently implemented. Here a modified Gerchberg - Papoulis superresolution algorithm is reported and preliminary results demonstrating resolution enhancement shown

1. Introduction

Holography is a well-established technique for the characterization of aerosols and particle fields. Combining high resolution with a depth of field corresponding to hundreds to thousands of ordinary photographs, holography is frequently the only alternative where 3D images of aerosols are required. Of the many forms of holography which have been developed since its invention by Gabor in 1947, the original on-axis or in-line form has remained the choice for most particle field and aerosol applications. Simplicity and robust tolerance of noise, vibration and limited coherence particularly recommend in-line technique for adverse environments, for instance industrial flues (for particulate studies) and aircraft wing mounting (for fog and icing studies) [1]. This report considers resolution improvement only for in-line holograms, though similar procedures could be considered for off-axis and volume holograms as well.

In the idealized case of infinite hologram format, complete coherence, diffraction limited optics and linear fine-grained film the theoretical resolution limit for in-line holography agrees with that for ordinary photographic imaging using the same illumination. At visible wavelengths the Rayleigh criterion suggests an ultimate resolution for idealized systems in the range one half to one micrometer. In practice, the physical parameter most prominently limiting resolution is the finite size of the film on which the hologram is recorded. This in turn is frequently constrained by the limited low level contrast of the film.

The use of practical sized hologram formats dictates that the higher frequency components of the image, which are scat-

tered at larger angles to the optical axis, are not recorded. Thus these frequency components are not available for reconstruction. Reported resolution for in-line setups, as well as our own experience, suggest 10 - 20 micrometers as a best routinely attainable resolution using conventional techniques and formats.

2. Superresolution

Frequency components of an illuminated object corresponding to wavelengths shorter than the illuminating wavelength will not propagate. Any image formed at a distance from the object, regardless of method, will demonstrate a complete loss of spatial frequencies of $1/\lambda$ and greater. Additional high frequency bands may also be missing due, for instance, to finite film format.

Complete absence of a range of frequencies in the recorded image does not necessarily imply that it is futile to attempt to restore these frequencies. Missing frequency bands clearly cannot be restored using linear filters, but no such restriction obtains with nonlinear constrained procedures.

Consider the case in which the Fourier transform of a 2D object is known only within a bounded region in the spatial frequency plane. Since there are infinitely many ways to extrapolate the transform, each corresponding to a different object, the missing frequency data appears irreversibly lost. Suppose, however, it may be assumed that the object is spacelimited. A classic result in complex analysis is that spacelimited objects possess analytic Fourier transforms. Then since analytic functions are completely determined by their value over any finite neighborhood, the transform can be fully recovered from the given information.

Techniques which restore frequency components lying beyond the measured bandwidth are called superresolution techniques (in machine vision the designation subpixel resolution is common). Introduction of these methods is frequently greeted with some skepticism, since it is a fundamental principle of linear signal processing

Let $\psi_z(x,y)$ be the scalar optical field producing the hologram as in (1). The magnitude $|\psi_z(x,y)|$ is known for $|x| \leq X$, $|y| \leq Y$ since the hologram has been measured there, i.e. $|\psi(i,j)|$ is known for $|i| \leq N$, $|j| \leq M$. Select extrapolation factors α , $\delta > 1$. The hologram will be extrapolated to the discrete domain $|i| \leq [\alpha N]$, $|j| \leq [\delta M]$.

Take as initial guess in the spatial domain the conventional reconstruction (3a) setting $I(i,j)$ equal to its measured value in $|i| \leq N$, $|j| \leq M$ and zero for $N < |i| \leq [\alpha N]$, $M < |j| \leq [\delta M]$. Modify the initial guess reconstruction by enforcing all spatial constraints (including bounded spatial extent, and opacity real and bounded by zero and unity). As in the GP and the phase retrieval algorithms, proceed to the transform domain with the transform of the constraint-enforced object (convolve with $h_z(x,y)$). In this domain enforce the measured magnitude constraint in the inner region $|i| \leq N$, $|j| \leq M$ and return to the spatial domain (convolve with $h_z^*(x,y)$). Iterate until the summed RMS changes under constraint enforcement in both domains falls negligible.

This algorithm operates like the GP algorithm, except that the Fourier domain is replaced by the field domain $\psi_z(x,y)$ and the phase of the field is recovered along with the magnitude (hologram) extrapolation.

5. Results

An all-digital 1D simulation is shown in Figure 1. The original pulse is of unit amplitude and duration seven samples, centered at the origin. The conventional reconstruction (initial guess) demonstrates twin image and high frequency attenuation due to cropping of the hologram at 32 samples (equivalent resolution limit 3.0 pixels). The algorithm attempts to extrapolate the hologram by a factor 4 to 128 samples. The iterations were terminated (prior to convergence criterion) at 15 iterations. Note that by the 15th iteration, the 3.0 pixel resolution limit was clearly exceeded.

An all-digital 2D simulation of a pair of objects is shown in Figures 2 and 3. Note that the conventional reconstruction (Fig. 2c) barely resolves the pair. Profiles of grey levels along the vertical axis (white) and horizontal axis (black) are shown in Fig. 3a. Fig. 2d shows the reconstruction after a four-fold extrapolation (15 iterations), with profiles shown in Fig. 3b. Note the increased sharpness of the horizontal grey level change between the objects in Fig. 3b as compared with Fig. 3a.

6. Conclusions and further work

The above results demonstrate resolution enhancement for simulated in-line holography through the use of a GP-like superresolution technique. Limited resolution, especially along the optical axis, has frequently been mentioned as a factor limiting the usefulness of in-line holography for aerosol characterization and metrology. The phase retrieval / hologram extrapolation algorithm is one of a class of methods based on superresolution which may enhance available resolution. The present results are preliminary but encouraging. The algorithm must be systematically applied to real holograms, and this work is underway.

7. References

- [1] JD Trolinger, "Particle and flow field holography," Proc. SPIE 532, 1985, 40-62.
- [2] BR Frieden, "Image enhancement and restoration," in *Picture Processing and Digital Filtering*, TS Huang ed., Springer, New York, 1975.
- [3] G Liu and PD Scott, "Phase retrieval and twin-image elimination for in-line Fresnel holograms," J. Opt. Soc. Am. A 4, 1987, 159-65.
- [4] L Onural and PD Scott, "Digital decoding of in-line holograms," Optical Eng., to appear Nov 1987.
- [5] A Papoulis, "A new algorithm in spectral analysis and bandlimited extrapolation," IEEE Trans. Cir. Sys. 22, 1975, 218-29.

8. Figures

(see overleaf)

that resolution goes with measurement bandwidth, and that you can't amplify or enhance what isn't there. With constraints, however, the link between resolution and measurement bandwidth weakens, and frequency cutoffs can sometimes be exceeded.

A wide variety of superresolution techniques have been developed, based on analytic continuation, positivity constraints, statistical principles such as maximum entropy and maximum likelihood, and model-based techniques. These methods have been applied to an equally diverse group of applications: coherent and incoherent microscopy, adaptive sonar array processing, spectroscopy, astronomy and ultrasonic imaging are important examples [2].

Here we present preliminary results which suggest that superresolution may be productively applied to in-line holographic decoding as well. These methods may help expand the range of use of holographic imaging for scientific and engineering application by permitting resolution improvement toward, or even perhaps beyond, the diffraction limit.

3. Digital reconstruction from in-line holograms

The scalar field impressed on an image plane at a distance z along the optical axis from an object plane illuminated by a plane wave of wavelength λ is

$$\psi_z(x,y) = (1-a(x,y)) ** h_z(x,y) \quad (1)$$

where $h_z(x,y)$ is the usual quadratic phase kernel of the Fresnel Kirchoff approximation, $**$ is 2D convolution, and $a(x,y)$ is the real planar opacity function of the object distribution. 3D aerosol distributions would occupy a superposition of such planes. For convenience in the development a planar object is assumed. The hologram of $a(x,y)$ at z is then $|\psi_z|^2$ or

$$I_z(x,y) = 1-2a(x,y)**\text{Re}h_z(x,y) \quad (2)$$

where transmitted energy is assumed to dominate diffracted and $1**h_z = 1$ has been used. Reconstruction from the hologram $I_z(x,y)$ is conventionally accomplished by reilluminating the developed hologram with the same illumination, having the effect of replacing $a(x,y)$ by $-I_z(x,y)$ in (1). Upon recalculat-

ing the intensity, the image of the reconstructed object is [3]

$$R_z(x,y) = (1+I_z(x,y)) ** 2\text{Re}h_z(x,y) \quad (3a)$$

$$= 2(1-a(x,y)) + I_z(x,y) \quad (3b)$$

The first term in (3b) is the desired object, and the second the twin image (double-distance hologram).

If the hologram $I_z(x,y)$ is digitally sampled, the reconstruction convolution (3a) may be computed algorithmically rather than instantiated optically. If digital decoding is used, the twin image may be algorithmically suppressed, either by stabilized inverse filtering [4] or phase retrieval [3]. Digital reconstruction is most efficiently implemented using the Fast Fourier Transform algorithm as described in the two foregoing references.

In (3b) it is assumed that reconstruction derives from an infinite-format hologram. Restricting the input $I_z(x,y)$ to a finite pupil has two principal effects. A pupil artifact (hologram of the pupil function) is added to the reconstruction, and the high frequency content of the reconstruction is sharply reduced for objects located near the optical axis. This is seen most clearly in the case of an object sufficiently small to use the Fraunhofer approximation. The hologram then corresponds to the object's Fourier transform modulus (modulated by a zone lens factor), and cropping the hologram clearly eliminates all information relative to high frequency content.

4. Phase retrieval / hologram extrapolation algorithm

Algorithms which enforce constraints successively in the spatial domain and a spectral or image domain form an important class of superresolution methods. Here we combine the Gerchberg - Papoulis (GP) algorithm for spectral extrapolation [5] with hologram phase retrieval [3] to seek superresolution type enhancement for holographic images.

Begin with a hologram $I_z(x,y)$ of extent $|x| \leq X$, $|y| \leq Y$. Sample with x and y sampling period of Δ to produce $I(i,j)$ for $|i| \leq N$, $|j| \leq M$ ($M = [X/\Delta]$, $N = [Y/\Delta]$, $[]$ indicates integer part). Assume the object to be reconstructed is small and centered near the origin in the spatial plane. Superresolution in the reconstruction of this object is equivalent to recovering unmeasured regions of the hologram (hologram extrapolation).

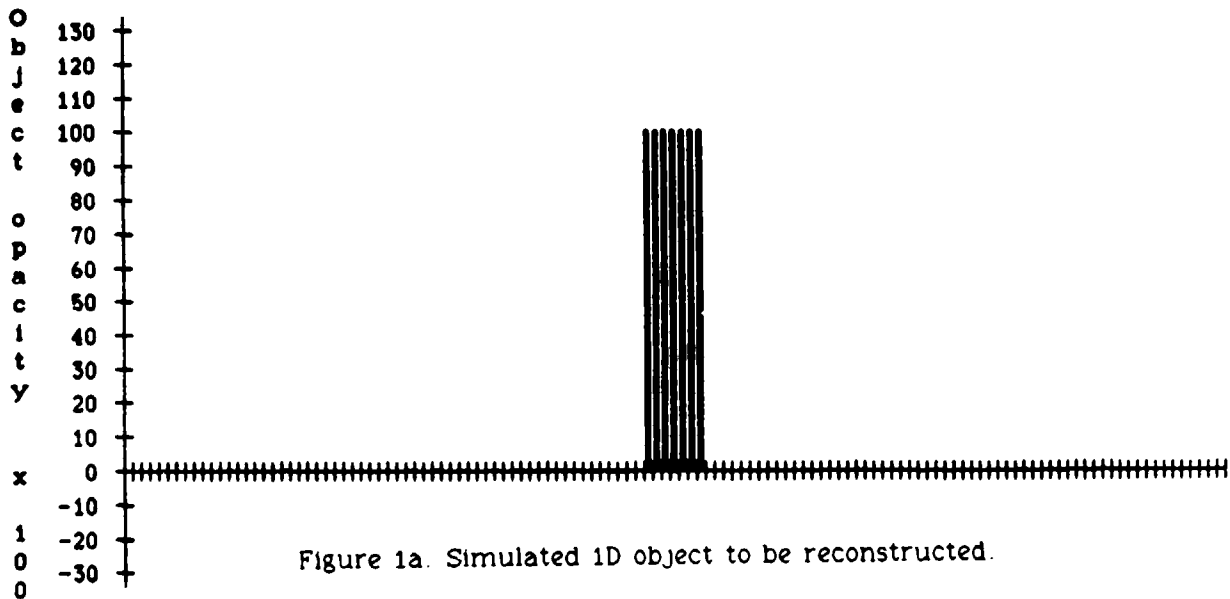


Figure 1a. Simulated 1D object to be reconstructed.

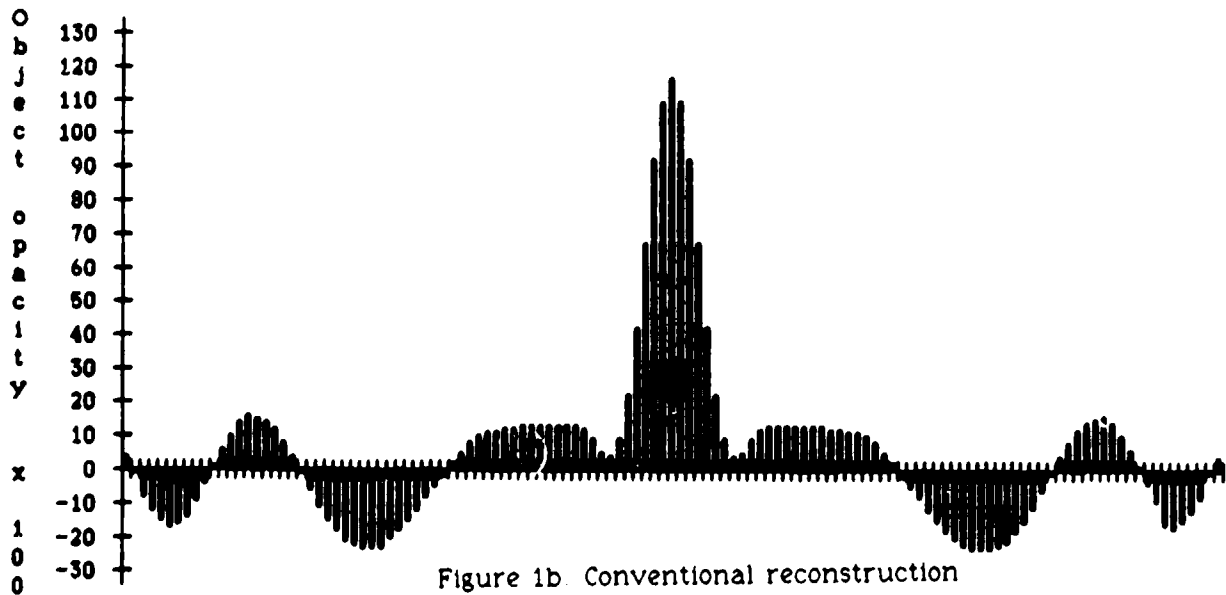


Figure 1b. Conventional reconstruction

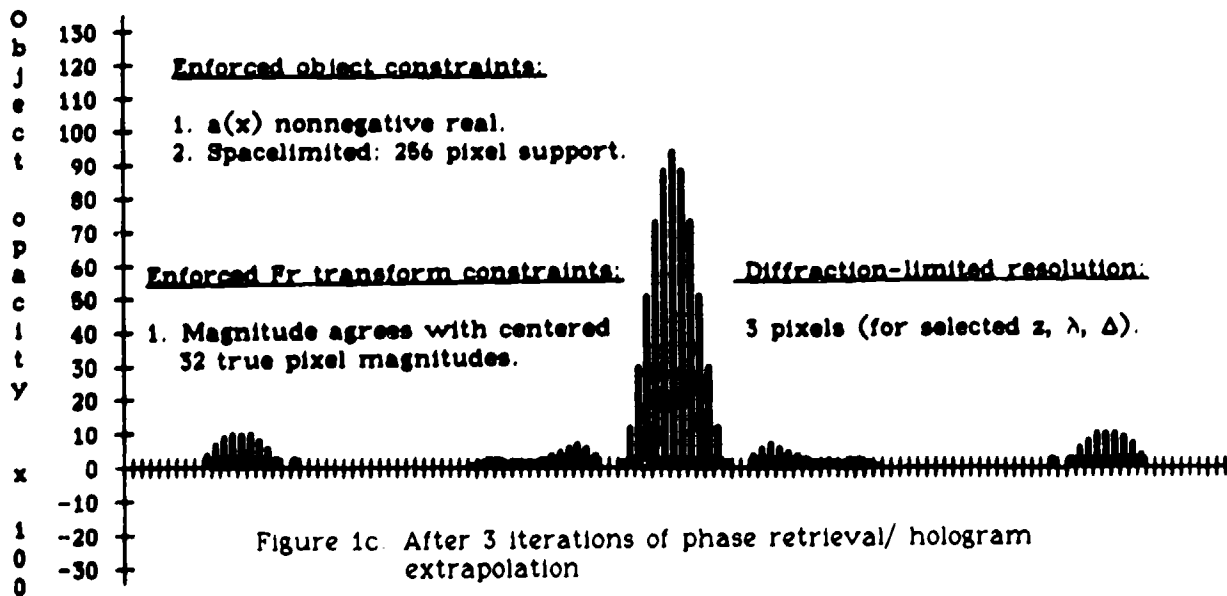


Figure 1c. After 3 iterations of phase retrieval/ hologram extrapolation

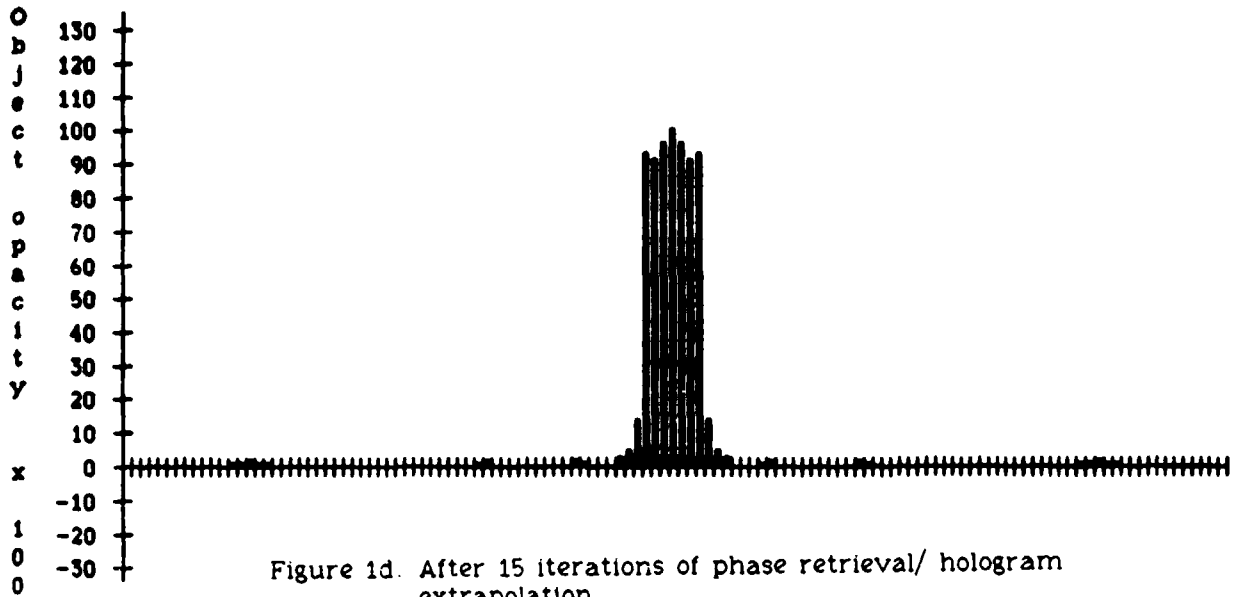


Figure 1d. After 15 iterations of phase retrieval/ hologram extrapolation.

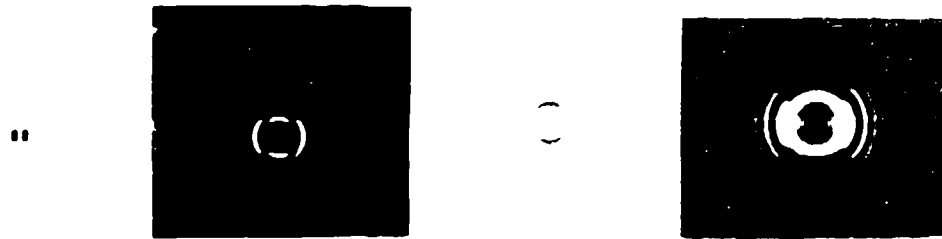


Fig. 2a. Pair of objects. 2b. Cropped hologram 2c. Conventional 2d. After 15 iterations. reconstruction.

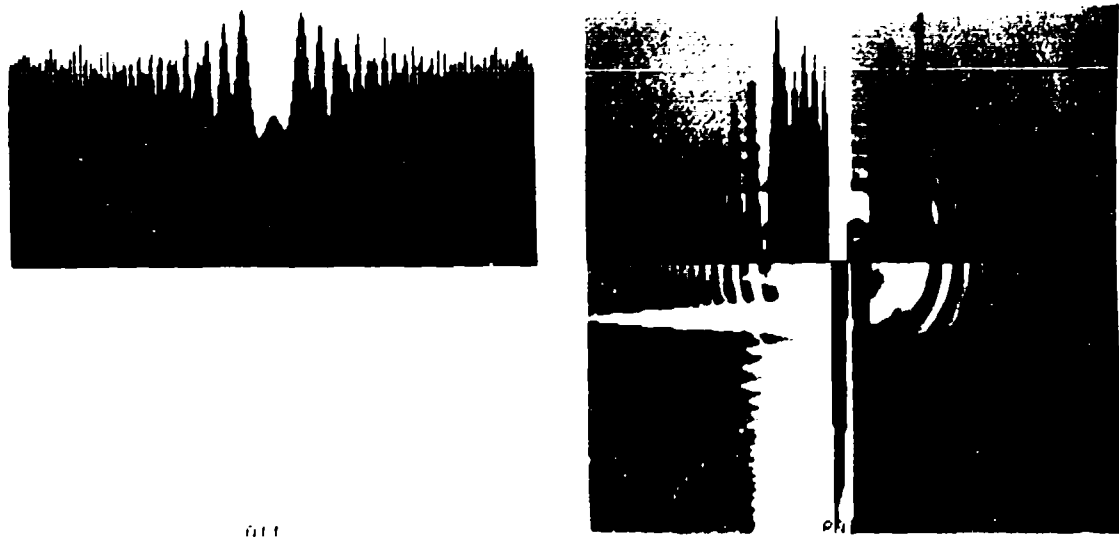


Fig. 3a. Horizontal and vertical profiles of Fig. 2c.

3b. Horizontal and vertical profiles of Fig. 2d. Note the resolution improvement over 3a.

Blank

AN ANALYTICAL EXPRESSION FOR THE AXIAL PRESSURE PROFILE
IN A SPOUT-FLUID BED EQUIPPED WITH DRAFT TUBE

M.H. Morgan III and H. Littman
Department of Chemical Engineering
Rensselaer Polytechnic Institute
Troy, New York 12180-3590

ABSTRACT

A new expression for the pressure profile in pneumatic transport systems is developed. The resulting model is found to fit coarse particle data in systems spouted with air extremely well (within $\pm 8\%$ on average). In addition a pressure identity relating the overall draft tube pressure drop to the inlet and outlet pressure gradients is also deduced. The validity of the latter is also established.

INTRODUCTION

A knowledge of the axial pressure profile within a draft tube fed by a spout-fluid bed feeder is critical to the design of such systems. Without this information, a first principles prediction of either the voidage distribution or the particle transport rate through the draft tube is not possible. Furthermore, in many practical systems, direct pressure profile measurements are not feasible or are difficult to obtain. Clearly, from both a computational and experimental vantage point, being able to predict this quantity simplifies design.

Limited experimental measurements of the axial pressure profile in these systems have been reported by Claflin and Fane(1983) and Grabvacic et al.(1986). To date, no theoretical models exist. In this paper, an analytical model for the profile is developed from variational considerations. Only a knowledge of the overall draft tube pressure drop and outlet pressure gradient is assumed. In addition, a pressure identity relating the overall system pressure drop to the inlet and outlet pressure gradients is also deduced.

THEORY

A variational formulation similar to that posed in Morgan (1986) for the axial pressure profile in a spouted bed of coarse particles is devised for a draft tube system. In our analysis, radial pressure gradients are neglected and it is assumed that $-d^2P^*/dz^2$ must decrease monotonically with axial distance, z . The genesis of this approach arises from the fact that all the experimental pressure profiles observed to date exhibit this characteristic. Even in those cases where a maximum is observed in the pressure profile one finds that $-d^2P^*/dz^2$ decreases monotonically with z . Hence the following isoperimetric variational problem was posed for the axial pressure profile in the

draft tube. In Morgan and Littman (1987), the general formulation of this particular problem is discussed in detail.

Consider the functional

$$J(P^*) = \int_{\zeta=0}^{\zeta=1} \sqrt{1 + \left(\frac{-d^2 P^*}{d\zeta^2}\right)^2} d\zeta \quad (1)$$

in terms of the dimensionless second derivative of pressure and distance to have an extremum where the admissible curves satisfy the boundary conditions

$$\left. \frac{-d^2 P^*}{d\zeta^2} \right|_{\zeta=0} = \infty \quad (2)$$

$$\left. \frac{-d^2 P^*}{d\zeta^2} \right|_{\zeta=1} = 0 \quad (3)$$

and the constraint functional

$$\int_0^1 \left(\frac{-dP^*}{d\zeta}\right) d\zeta = \frac{\Delta P_T}{\Delta P_{mF}} \quad (4)$$

Physical justification for the boundary and integral conditions are briefly discussed below. Firstly, equation 2 follows from the requirement that a precondition for particle transport into the draft is the existence of a large accelerating potential at the entrance to the draft tube. The magnitude of this potential is bounded by the specification given in equation 2. The second boundary condition (eqn. 3) follows from experimental observation which indicates that the pressure at the outlet to the draft tube varies linearly with distance. Differentiation of such a profile leads directly to equation 3. Intuitively, one can surmise that these two boundary conditions are natural limits for such systems. The integral constraint given in Equation 4 implies that the pressure in the system is always maximized at a given fluid flowrate. A similar argument was posed in Morgan and Littman (1987) for the axial particle flowrate profile in spouted beds. This particular operational feature of spouted beds is an intriguing one. The reason why this is the case remains an unanswered question.

General methods of solution for equations (1) through (4) are outlined in Weinstock (1952). The solution to this system of equations is

$$\frac{\left. \frac{-dP^*}{d\zeta}(\zeta) \right|_{\zeta=0} - \left. \frac{-dP^*}{d\zeta} \right|_{\zeta=0}}{\left. \frac{-dP^*}{d\zeta} \right|_{\zeta=1} - \left. \frac{-dP^*}{d\zeta} \right|_{\zeta=0}} = f(\zeta) = [1 - (1-\zeta)]^{2/3} \quad (5)$$

Integration of equation (5) gives an expression for the pressure profile within the draft tube.

That equation is

$$P^*(\zeta) - P^*(0) = G(\zeta) \left[\left(\frac{-dP^*}{d\zeta} \right)_{\zeta=1} - \left(\frac{-dP^*}{d\zeta} \right)_{\zeta=0} \right] + \left(\frac{-dP^*}{d\zeta} \right)_{\zeta=0} \zeta \quad (6)$$

where

$$G(\zeta) = 0.785 - 1/2 \left[(1-\zeta) \sqrt{1-(1-\zeta)^2} + \text{Arc sin}(1-\zeta) \right]$$

Evaluating the above result at $\zeta=1$ leads to the following pressure identity.

$$\frac{\Delta P_T}{\Delta P_{mF}} = 0.215 \left(\frac{-dP^*}{d\zeta} \right)_{\zeta=0} + 0.785 \left(\frac{-dP^*}{d\zeta} \right)_{\zeta=1} \quad (7)$$

Equation (7) implies that only a knowledge of two of the terms appearing in that equation are required for a complete specification of the pressure profile given in equation (6). Presently there are no correlations available for the quantities appearing in equation (6). A future paper will address this issue. In the next section the general validity of both equations 6 and 7 are established.

DISCUSSION OF RESULTS

In Table 1 the agreement between the predicted and experimental overall pressure drop values for several operating scenarios are summarized. The predicted pressure drops shown there were calculated from equation 6 using the experimental values of the inlet and outlet pressure gradients given in that table. The data shown there are for coarse particles of CaCO_3 spheres ($1.2 \text{ mm} < d_p < 3.0 \text{ mm}$) spouted with room temperature air. The effect of both draft tube separation distance and inlet pressure gradient on overall pressure drop are shown there. The average agreement between theoretical and experimental values is within $\pm 8\%$.

An evaluation of the general pressure drop relationship is provided in Table 2. These three different experimental profiles are compared in Figure 1 with predictions obtained from the general pressure drop relationship (Equation 6). This pressure relationship requires only a knowledge of two of the parameters appearing in equation 7. Given the respective experimental values of $\Delta P_T/\Delta P_{mF}$ and $-dP/d\zeta/\zeta=1$ provided in Table 1, complete pressure profiles were calculated for the first three cases. In general, we found excellent agreement between theoretical and experimental values with only an average percentage error of $\pm 3\%$. Of specific interest is case #3 where $(-dp^*/dz)_{z=0}$ is less than 0. In this particular case the experimental pressure curve exhibits a maximum. Physically such cases arise in high momentum systems when the separation distance, z is

small and the draft tube entrance resides in the inlet region of the jet. The size of this inlet region, z^* has recently been reported by Morgan and Littman (1987) for air spouted beds. That correlation shown below indicates that z^* is proportional to the momentum at z^* .

$$\frac{z^*}{H} = 1.46M(z^*/H) \quad (8)$$

In this region the fluid entry into the spout-fluid bed region is accompanied by a rise in the axial pressure between 0 and z^* (Rovero et al. (1983) and Day et al. (1987)) and a positive inlet pressure gradient results. Experimentally it has been shown that a substantial lowering of the draft tube separation distance, z below z^* will result in a shut off of particle flow. In the design of such delivery systems care must be taken to maintain this separation distance, $z > z^*$.

REFERENCES

- Claflin, J.K., and A.G. Fane, Can. J. Chem. Eng., 61, 356, 1983.
- Day, J.Y., H. Littman and M.H. Morgan III, Chem. Eng. Sci., 42, 1461, 1987.
- Grbavcić, Z.B., Private communication, 1987.
- Morgan, M.H., III, "Fluidization V", K. Ostergaard and A. Sorensen, Ed., Engineering Foundation 1986, p. 249.
- Morgan, M.H., III and H. Littman, Chem. Eng. Sci., 1987 (under review).
- Rovero, G., C.M.H. Brereton, N. Epstein, J.R. Grace, L. Casalegno and N. Picinini, Can. J. Chem. Eng. 61, 289, 1983.
- Weinstock, R., "Calculus of Variations", Chapter 4, 1952.

NOMENCLATURE

$G(\zeta)$	=	defined in equation
H	=	bed height
z	=	distance between inlet orifice and draft tube entrance
$M(\frac{z^*}{H})$	=	spout momentum at z^*
P	=	total pressure
p^*	=	ΔP_{mF}
ΔP_{mF}	=	overall fluidization pressure drop
ΔP_T	=	overall pressure drop across draft tube
ΔP_z	=	pressure drop for height, z
z	=	vertical coordinate measured from spout inlet
z^*	=	location of maximum axial pressure in the spout

Greek Symbols

ζ	=	z/H
---------	---	-------

TABLE 1. VERIFICATION OF THE PRESSURE IDENTITY

z	$(-dp/dz)_{z=0}$	$(-dp/dz)_{z=H}$	$\Delta P/H$ - Expt	$\Delta P/H$ - Predicted
mm	kPa/m	kPa/m	kPa/m	kPa/m
125	7.85	2.45	3.92	3.61
75	2.67	1.96	2.47	2.24
50	-0.20	1.96	1.66	1.50
80	3.20	1.00	1.28	1.47
80	2.29	0.75	1.12	1.08
80	1.71	0.65	0.81	0.88
80	0.60	0.50	0.52	0.52

TABLE 2. COMPARISON OF EXPERIMENTAL AND PREDICTION PRESSURE PROFILES IN THE DRAFT TUBE

<u>Case 1</u>		
z	ΔP_z (Predicted)	ΔP_z (Experimental)
0.1	45	50.0
0.3	112	115
0.5	163	170
0.7	205	210
0.9	242	245
1.0	260	260

<u>Case 2</u>		
z	ΔP_z (Predicted)	ΔP_z (Experimental)
0.2	37	42
0.4	71	74
0.6	103	104
0.8	133	139
1.0	164	164

<u>Case 3</u>		
z	ΔP_z (Predicted)	ΔP_z (Experimental)
0.1	3.2	1.0
0.2	10.3	8.0
0.3	19.5	22.0
0.5	42.1	48.0
0.7	68.5	72.0
0.9	97.1	96.0
1.0	112.0	112.0

Blank

COMPUTER MODELING OF DIESEL FUEL/FOG OIL SMOKE CLOUD

Kenneth L. Evans
U.S. Army Chemical Research, Development and Engineering Center
Aberdeen Proving Ground, Maryland 21010-5423, USA

Tate T. H. Tsang
University of Kentucky
Lexington, Kentucky 40506-0046, USA

ABSTRACT

The objective of this work is to study the effects of ambient temperature, atmospheric stability condition and particle size on the screening performance of diesel fuel and fog oil smoke. A first order closure model is used to describe the turbulent diffusion of the smoke in the atmospheric surface layer. Mean values of wind speed and diffusivity in the vertical direction are obtained by the use of the Monin-Obukhov similarity theory. The two-dimensional cross-wind line source model also includes the aerosol kinetic processes of evaporation, sedimentation and deposition. Fifty-six case studies were simulated on a supercomputer. Numerical results are in qualitative agreement with observations.

1. INTRODUCTION

Successful and reliable predictions of the effectiveness of aerosol obscurants require quantitative understanding on many physico-chemical processes. Although field tests on the dispersion of an aerosol plume can provide invaluable information, they are expensive. Furthermore, data acquisition and analysis on the extinction coefficient, wind velocities, vertical diffusivity, temperature profile, heat flux, turbulence structure, particle size distribution and particle number concentration are formidable tasks. Thus, it is not surprising to learn that it took four years of preparation for several teams of investigators to obtain reliable micrometeorological data on turbulence structure in a convective boundary layer study in northwestern Minnesota (Kaimal et al., 1976). In the light of this fact, computer modeling becomes a valuable and versatile tool to study the dispersions of a plume of volatile aerosol. Of course, the modeling work needs to be validated by reliable experimental data. In fact, modeling and field tests should complement each other and form an integral approach to provide reliable data base.

In this work, we are interested in the persistency of a volatile aerosol dispersed in the atmospheric surface layer. For modeling purposes, this problem involves the transport of aerosol and the aerosol kinetic processes. Transport of aerosol includes the processes of advection, diffusion, sedimentation and deposition. Aerosol kinetic processes include particle growth by coagulation and condensation. It also includes particle shrinkage by evaporation. Brook (1973) appeared to be the first investigator to combine the model for the transport of aerosol with the model of aerosol kinetics. Some qualitative conclusions were drawn for the particulate pollution problem in an urban city. First order turbulence closure model (K-theory) was used in his formulation. Recently, such progress has been made in computer modeling of atmospheric turbulence by second order closure models (Donaldson, 1973) and by Large Eddy Simulations (LES) (Wyngaard, 1984). In general, second order

closure models and LES can provide much more detailed information on turbulence structure than the K-theory model, which is a mean field theory model for turbulence. However, the computational costs for these advanced turbulence models are much higher than that for the K-theory model. Furthermore, aerosol kinetic processes have not been implemented in LES and second order closure models. If these processes are included in these advanced turbulence models, the computational costs would be prohibitive even on a supercomputer, since hundreds of partial differential equations have to be solved (the time averaged dependent variable is $n(x,y,z,t,m)$, where m is the mass of a given size class of an aerosol cloud). In this work, the K-theory model is used as a first attempt to study the effects of ambient temperature, atmospheric stability condition and the initial mean particle diameter on the dispersion of a volatile aerosol in the atmospheric surface layer.

Tsang and Brook (1982a) simulated the dispersion of a cross-wind line source problem including the coagulation of aerosol. Such work was extended to investigate the effect of disposition and coagulation on the extinction coefficient of a screening smoke (Tsang and Brook, 1982b). It was concluded that the aerosol kinetic processes of coagulation and deposition have a profound effect on the persistency of the screening smoke. Later, Tsang and Brook (1983a) studied the dispersion of a plume of volatile aerosol under neutral atmospheric stability condition. The line source size distribution was characterized by a log normal distribution with source strength of 0.3307 g/(m² sec), geometric mean diameter of 0.6 μm, and geometric standard deviation of 2.24. It was found that Galerkin Finite Element Method for evaporation and Orthogonal Collocation Method on Finite Elements for diffusion gave satisfactory results for a heavy oil with vapor pressure 9.6 x 10⁻⁶ mmHg and a light oil with vapor pressure of 1.5 x 10⁻³ mmHg. In this work, we simulate the dispersion of volatile aerosol from line sources of higher source strength, narrower size distribution, and more volatile compounds. Our objective is to study the effects of ambient temperature, atmospheric stability condition and mean particle diameter on the persistency of the screening smoke.

2. THEORY

The steady state K-theory model in a system, which is spatially homogeneous in y-direction (i.e., a cross-wind line source problem), can be written as,

$$u(z) \frac{\partial n}{\partial x} + \frac{\partial}{\partial m} [\psi n] = \frac{\partial}{\partial z} \left[K(z) \frac{\partial n}{\partial z} + G_z(m) \frac{\partial n}{\partial z} \right] \quad (1)$$

$$u(z) \frac{\partial n}{\partial x} = \frac{\partial}{\partial z} \left[K(z) \frac{\partial n}{\partial z} - \frac{1}{c_v} \int_0^{\infty} \psi n dm \right] \quad (2)$$

Equations (1) and (2) are subject to the following boundary conditions:

$$n = \frac{Q_0}{u(h)} \delta(Z-h) n_0(m) \quad \text{at } x=0 \quad (3)$$

$$s = 1.0 \quad \text{at } x=0 \text{ and } Z=h \quad (4)$$

$$\int \frac{n}{Z} = \int \frac{s}{Z} = 0 \quad \text{at } Z=H \quad (5)$$

$$nV_d = K_s \int \frac{n}{Z} \quad \text{at } Z=0 \quad (6)$$

$$\int \frac{s}{Z} = 0 \quad \text{at } Z=0 \quad (7)$$

In Equation (2.1), $n = n(m,x,Z)$ is the number density function. $n(m,x,Z)dm$ is the number of particles having masses in the range m and $m + dm$ at downwind position x at vertical height Z . $u(Z)$ is the wind profile. $K(Z)$ is the diffusivity profile. $G_Z(m)$ is the gravitational settling velocity for the particle with mass m , $G_Z(m) = \rho_p D_p^2 g / 18 \mu$, where ρ_p is the particle density, D_p the particle diameter, g the gravitational acceleration, and μ the viscosity of air. $\Psi(m,s)$ is the condensation/evaporation rate for a particle with mass m and saturation ratio s . $s = C/C_v$ where C and C_v are vapor concentration and equilibrium vapor concentration, respectively. In Equation (1), advection, evaporation, diffusion and sedimentation processes are described by these four terms accordingly. Equation (2) is the mass balance of the evaporating species. The last term is the contribution due to the evaporation of aerosol particles. Equation (3) describes the cross-wind line source. Q_0 is the source strength, h is the source height. δ is the delta function and $n_0(m)$ is the source size distribution. In this work, log-normal distributions are used. In Equation (5), H is the thickness of the atmospheric surface layer. In Equation (6), V_d is the deposition velocity for particle with mass m . Its numerical values can be obtained from Sehmel (1980). For the evaporation process, we use the following approximate expression, due to Fuchs and Sutugin (1971):

$$\Psi(m,s) = 4 (3/4 \rho_p)^{1/3} \times D_{gj}^{1/3} c_v (s - e^{Ke}) \times \left(1 + \frac{1.33Kn + 0.71}{1 + Kn^{-1}} \right)^{-1/2} \quad (8)$$

where the diffusion coefficient D_{gj} of vapor j in host gas is related to the mean molecular speed \bar{v}_j and the mean free path L_j by $D_{gj} = \frac{1}{3} \bar{v}_j L_j$. In Equation (8), ρ_p is the particle density; Kn the Knudsen number, $Kn = 2L_j/D_p$; and D_p is the particle diameter. Ke is the Kelvin number, $Ke = 4 \gamma / D_p kT$. γ is the surface tension, v the particle's molecular volume, and kT the thermal energy.

Some of the important observables of $n(m)$ are the total particle number concentration N ,

$$N = \int_0^{\infty} n(m) dm \quad (9)$$

the particle mass concentration M ,

$$M = \int_0^{\infty} mn(m) dm; \quad (10)$$

and the total extinction coefficient σ_{ext} , obtained from the normalized extinction efficiency $Q_{ext}(p, m, \lambda)$ (Bohren & Huffman, 1983):

$$\sigma_{ext}(p, m, \lambda) = \left(\frac{3}{4p}\right)^{2/3} \int Q_{ext}(p, m, \lambda) m^{2/3} n(m, t) dm \quad (11)$$

where p is the refractive index of the aerosol under the irradiation of an electromagnetic beam of wavelength λ .

The stability of the atmosphere can be classified into six different Pasquill stability classes (Pasquill, 1961; Gifford, 1976). Classes A through C represent unstable atmospheric conditions. Class D represents neutral condition, and classes E and F represent stable atmosphere. The wind profile-flux relationships depend strongly on the atmospheric stability.

For the numerical solution of Equations (1) and (2), data for the wind profile $u(z)$ and the vertical diffusivity profile $K(z)$ must be known. These data in the atmospheric surface layer can be provided by extensive measurements, by the advanced turbulence models such as LES or by the well-known Monin-Obukhov similarity. Lamb (1979) used the wind profile obtained from LES to calculate the dispersion of a contaminant in a convective boundary layer. Alternatively, if the friction velocity u_* , the Obukhov length L and the surface roughness z_0 are known, $u(z)$ and $K(z)$ can be obtained from a given interpolation formula, which can fit the micro-meteorological data.

For adiabatic surface layer (neutral atmospheric condition), the wind profile can be described by the well-known logarithmic wind profile, which has been verified experimentally. In this work, the wind profile and the diffusivity profile under neutral atmospheric stability condition were taken from Panosky (1974) and Smith (1975), respectively.

For diabatic surface layer, it is a common practice to analyze the wind profile in terms of the dimensionless wind shear, ϕ_m as,

$$\phi_m = \frac{kz}{u_*} \frac{\partial u}{\partial z} \quad (12)$$

In Monin-Obukhov similarity theory, ϕ_m is a function of the dimensionless height ξ , $\xi = z/L$. In this work, we use the interpolation formula proposed by Businger et al. (1971):

$$\phi_m = (1 - 15\xi)^{(-1/4)} \quad (13)$$

$$\phi_m = 0.74 (1 - 9\xi)^{(-1/2)} \quad \xi < 0$$

Unstable
Condition

and

$$\begin{aligned} \phi_m &= 1 + 4.7 \xi \\ \phi_h &= 0.74 + 4.7 \xi \end{aligned} \quad \begin{array}{l} \xi > 0 \\ \text{Stable} \\ \text{Condition} \end{array} \quad (14)$$

where ξ is the dimensionless temperature gradient defined as,

$$\xi = \frac{kz}{\theta_s} \frac{\bar{\theta}}{z} \quad (15)$$

$\bar{\theta}$ is the mean potential temperature and θ_s is the scaling temperature, $\theta_s = - \frac{\overline{w'T'}}{u_s}$.

At neutral atmospheric condition ($\xi = 0$), Equations (13) and (14) give $\phi_m = 1$, which corresponds to a logarithmic wind profile. The eddy diffusivity for heat transfer in a diabatic layer is given by,

$$K_h = \frac{k u_s z}{\phi_h} \quad (16)$$

In air pollution study, it is a common practice to use the eddy diffusivity for heat and mass transfer interchangeably.

Equation (12) with Equation (13) or (14) can be integrated to give the wind profiles for unstable and stable atmospheric conditions (Paulson, 1970).

$$\frac{u(z)}{u_s} = \frac{1}{k} \left[\ln \left(\frac{z}{z_0} \right) - \psi_1 \right] \quad \begin{array}{l} \xi < 0 \\ \text{Unstable} \\ \text{Condition} \end{array} \quad (17)$$

where $\psi_1 = 2 \ln \left[\frac{1 + \bar{x}}{2} \right] + \ln \left[\frac{1 + \bar{x}^2}{2} \right] - 2 \tan^{-1} \bar{x}$, $\bar{x} = \left(1 - 15 \xi \right)^{(1/4)} - 1 = \phi_m$.

Also,

$$\frac{u(z)}{u_s} = \frac{1}{k} \left[\ln \left(\frac{z}{z_0} \right) + 4.7 \xi \right] \quad \begin{array}{l} \xi > 0 \\ \text{Stable} \\ \text{Condition} \end{array} \quad (18)$$

Use of Equations (13), (14) and (16) provide the following diffusivity profiles in a diabatic surface layer,

$$K(z) = \frac{k u_s z}{0.74} \left[1 - 9 \frac{(z + z_0)}{L} \right]^{0.5} \quad \begin{array}{l} \xi < 0 \\ \text{Unstable} \\ \text{Condition} \end{array} \quad (19)$$

Also,

$$K(z) = \frac{k u_s z}{0.74 + 4.7 (z + z_0)/L} \quad \begin{array}{l} \xi > 0 \\ \text{Stable} \\ \text{Condition} \end{array} \quad (20)$$

In this work, Equations (17) and (19) are used to calculate the wind and diffusivity profiles for unstable atmospheric conditions, whereas Equations (18) and (20) are used for stable atmospheric conditions. The surface roughness, Z_0 , is chosen to be 6 cm, which corresponds to a field of uncut grass, unharvested crops and scrub (Deacon, 1949). For unstable stability condition of class B and stable condition of class F, we used Golder's plot (1972) which shows the relationship between Pasquill's turbulence types as a function of the Monin-Obukhov length L and surface roughness Z_0 . In summary, for stability class B, we chose the Monin-Obukhov length L to be -16.67 m and the friction velocity u_* to be 0.26 m/s. These are typical experimental values for a convective boundary layer subjected to unstable atmospheric conditions (Kaimal et al., 1976). For stability class F, we used the values of 16.67 m and 0.13 m/s for the Obukhov length and friction velocity, respectively. Again, these values are typical of a stable boundary layer (Caughey et al., 1979). The wind profiles and the diffusivity profiles for stability classes of B, D and F are in qualitative agreement with Smith's result (1975).

3. RESULTS AND DISCUSSION

Numerous case studies were carried out to investigate the effects of ambient temperature, atmospheric stability condition and the initial mean particle size on the dispersion of a plume of volatile aerosol. Simulated heavy oil (Fog Oil) and light oil (a diesel fuel) are used to study the effect of volatility of different chemical compounds on the total extinction coefficient. A line source of constant strength of $0.54 \text{ g/m}^2\text{sec}$ is used for all simulations. It is assumed that the aerosol generated by the near ground source can be characterized by a log-normal distribution. The geometric mean particle diameter of the source is either $0.5 \mu\text{m}$ or $2 \mu\text{m}$, and the geometric standard deviation is 1.4. Table 1 summarizes the physical properties of the fog oil and the diesel fuel used in this study.

The method of fractional steps is used for the numerical solution of Equations (1) and (2). Orthogonal collocation on finite elements (O.C.F.E.M.) is used for vertical diffusion. Three finite elements are used in the Z direction. Six interior collocation points are used within each element. Shifted Legendre polynomial is used in the collocation method. Tsang and Brook (1982a) tested the O.C.F.E.M. method for different cross-wind line source problems. They showed that O.C.F.E.M. provided more accurate results than the central finite difference method.

The numerical solution for the evaporation of an aerosol cloud is a formidable job. Most numerical methods for the evaporation process suffer either spurious oscillation or numerical diffusion. Spurious oscillation manifests itself as the dependent variable oscillates between

positive and negative values of almost the same order of magnitude over some region whereas numerical diffusion lowers the peak value of the distribution. Obviously, both spurious oscillation and numerical diffusion are undesirable in the evaporation/condensation of aerosols.

Using a Galerkin Finite Element Method (G.F.E.M.) with natural boundary condition, Tsang and Brook (1983b) were the first to provide accurate results for evaporation of aerosol of low volatility (The vapor pressure of a compound is a measure of its volatility.). For compounds of higher volatility, the G.F.E.M. fails because of severe spurious oscillation. The extinction coefficient and the number concentration calculated from Equations (11) and (9) will be erroneous. Tsang and Korgaonkar (1987) devised a novel numerical scheme which combined the positive definite method by Smolarkiewicz (1984) with the G.F.E.M. It is found that the novel numerical scheme can remove most the spurious oscillation, and the numerical results compare favorably with the cases for which analytical solutions are available. In this work, the G.F.E.M. method is used for the evaporation of the fog oil and Tsang and Korgaonkar's numerical scheme is used for the evaporation of the diesel fuel.

Simulations were carried out on a vector supercomputer, CYBER 205. An unvectorized version runs approximately 1.5 - 2 times faster than scalar mainframe computers, such as IBM 3081 and CYBER 175. In this work, vectorization is done by VAST, an automatic vectorizer by Pacific-Sierra Research Corporation. It was found that vectorization speeds up the computation, and a typical simulation on CYBER 205 is six to ten times faster than IBM 3081.

Figure 1 shows the isopleths of the total extinction coefficient for a plume of fog oil smoke at 60°F under neutral atmospheric conditions (stability class D). The initial mean particle diameter is 0.5 μm and the wavelength of irradiation is 0.5 μm . Also shown in the figure are the isopleths for the smoke plume at the same ambient temperature but under different atmospheric stability conditions. It is obvious that more smoke is dispersed upward for unstable atmospheric condition (stability class B), and the screening effect of the smoke for stable atmospheric condition (stability class F) is far more persistent than that for the neutral atmospheric condition. The extinction coefficient σ_{ext} is a measure of the persistence of the smoke plume. This can be explained by the fact that the vertical diffusivity $K(Z)$ for stability class B is several times higher than that for stability class D. The latter is also several times higher than the diffusivity for stability class F. Notice also that at higher temperature of 80°F, the smoke becomes less persistent because of the higher evaporation rate.

Figure 2 shows the isopleths for the same case studies in Figure 1 except that the wavelength of irradiation is 3 μm . Of particular importance is the fact that the $\sigma_{\text{ext}}(\lambda = 0.5 \mu\text{m})$ in Figure 1 is about 200 times higher than the $\sigma_{\text{ext}}(\lambda = 3 \mu\text{m})$ in Figure 2. This is due to the fact that for

particles smaller than $0.5\mu\text{m}$, the normalized extinction efficiency for irradiation with wavelength $0.5\mu\text{m}$ is one to two orders of magnitude higher than that for irradiation with wavelength $3\mu\text{m}$.

For $2\mu\text{m}$ particles, Figure 3 compares the persistency between the fog oil and the diesel fuel smoke. Obviously, the fog oil smoke is more persistent than the diesel fuel smoke, $\sigma_{\text{ext}}(\text{fog oil})/\sigma_{\text{ext}}(\text{diesel fuel}) \approx 10$. This can be explained by the fact that the diesel fuel is much more volatile than the fog oil. Evaporation broadens the particle size distribution and lowers the number concentration. Comparison of the extinction coefficient isopleths in Figures 3 and 4 shows that they are not much different from each other. It is because of the fact that the change of the particle size distribution due to the evaporation of $2\mu\text{m}$ particles is gradual and the normalized extinction efficiency approaches the geometric limit of two. It should be pointed out that the same source strength is used for all the case studies. Comparison of Figures 1 and 3 shows that for the same source strength of fog oil smoke, the extinction coefficient for $0.5\mu\text{m}$ particle is only 1.5 times higher than that for $2\mu\text{m}$ particles, even though the number concentration for $0.5\mu\text{m}$ particle at the source is about 64 times higher than that for $2\mu\text{m}$ particles. It is because smaller particles evaporate faster and thus disappear sooner than larger particles. For the near-infrared irradiation of $3\mu\text{m}$, comparison of Figures 2 and 4 shows that for the same source strength of fog oil smoke, $2\mu\text{m}$ particles are almost one hundred times more persistent than $0.5\mu\text{m}$ particles. Again, it is due to the effect of evaporation.

Figures 5 and 6 demonstrate the most adverse effect due to the atmospheric condition. For stability class B, the smoke is dispersed upward and the evaporation rate for $0.5\mu\text{m}$ particle at 80°F is very high. For this case study, even the fog oil aerosol cloud does not form a persistent screen.

4. CONCLUSIONS

The ambient temperature, the atmospheric stability condition and the initial particle size have profound effects on the behavior of a volatile aerosol plume dispersed in the atmospheric surface layer. In general, evaporation becomes increasingly important as the ambient temperature increases and the initial particle size decreases. The smoke forms a more persistent screen in the stable atmosphere. Its persistency decreases in the unstable atmosphere because much smoke is dispersed upward. Also, smoke particles generated by a less volatile compound are far more persistent than those generated by a more volatile compound.

REFERENCES

- Bohren, C. F., and Huffman, D. R. (1983): Absorption and Scattering of Light By Small Particles. John Wiley and Sons, New York.
- Brook, J. R. (1973): Paraday Symposium No. 7, "Fogs and Smokes", Chemical Society, London.
- Businger, J. A., Wyngaard, J. C., Izumi, Y., and Bradley, E. F., (1971): J. Atmos. Sci., 28, 181-189.
- Caughey, S. J., Wyngaard, J. C., and Kaimal, J. C., (1979): J. Atmos. Sci., 16, 1041-1052.
- Deacon, E. L., (1949): Q. J. R. Meteorol. Soc., 75, 89-103.
- Donaldson, C., (1973): In Workshop on Micrometeorology (D. A. Haugen, ed.). Amer. Meteorological Soc., Boston.
- Fuchs, N. A., and Sutugin, A. G., (1971): In Topics in Current Aerosol Research (G. M. Hidy and J. R. Brock, eds.). Pergamon, Oxford, Vol. 2, 1-60.
- Gifford, F. A. Jr., (1976): Nuclear Safety, 17, 68-86.
- Golder, D., (1973): Boundary Layer Meteorology, 3, 47-58.
- Kaimal, J. C., Wyngaard, J. C., Haugen, D. A., Cote, O. R., Izumi, Y., Caughey, D. J., and Readings, C. J., (1976): J. Atmos. Sci., 33, 2152-2169.
- Lamb, R. G., (1978): Atmospheric Environment, 12, 1297-1304.
- Panofsky, H. A., (1974): Ann. Review Fluid Mech., 6, 147-177.
- Pasquill, F., (1961): Meteorol. Mag., 90, 33-49.
- Paulson, C. A., (1970): J. Applied Meteorology, 9, 857-861.
- Sehmel, G. A., (1980): Atmospheric Environment, 14, 983-1011.
- Smith, F. B., (1975): Sci. Prog., 62, 121-151.
- Smolarkiewicz, P. K., (1984): J. Comp. Phys., 54, 325-362.
- Tsang, T. H., and Brook, J. R., (1982a): Atmospheric Environment, 16, 2229-2235.
- Tsang, T. H., and Brook, J. R., (1982b): Applied Optics, 21, 1588-1592.
- Tsang, T. H., and Brook, J. R., (1983a): Aerosol Science and Technology, 2, 429-436.
- Tsang, T. H., and Brook, J. R., (1983b): Aerosol Science and Technology, 2, 311-320.
- Tsang, T. H., and Korgaonkar, N., (1987): "Effect of Evaporation on the Extinction Coefficient of an Aerosol Cloud" (Aerosol Science & Technology, Accepted for Publication).
- Wyngaard, J. C., (ed.), (1984): DTIC, AD-A146381.

Table 1. Physical Properties of the Fog Oil and the Diesel Fuel

		<u>Fog Oil</u>	<u>Diesel Fuel</u>
Density (g/cm ³)	40°F	0.9050	0.8664
	60°F	0.8894	0.8500
	80°F	0.8679	0.8285
Vapor Pressure (mm Hg)	40°F	7.32x10 ⁻⁷	3.41x10 ⁻³
	60°F	4.16x10 ⁻⁶	1.048x10 ⁻²
	80°F	2.0x10 ⁻⁵	2.90x10 ⁻²
Surface Tension (dynes/cm)	40°F	23.56	27.21
	60°F	22.97	26.42
	80°F	22.38	25.63
Refractive Index	= 0.5 μm	1.513	1.467
	= 3.0 μm	1.489-0.0021	1.411-0.0051
Molecular Weight (g/mole)		330	220

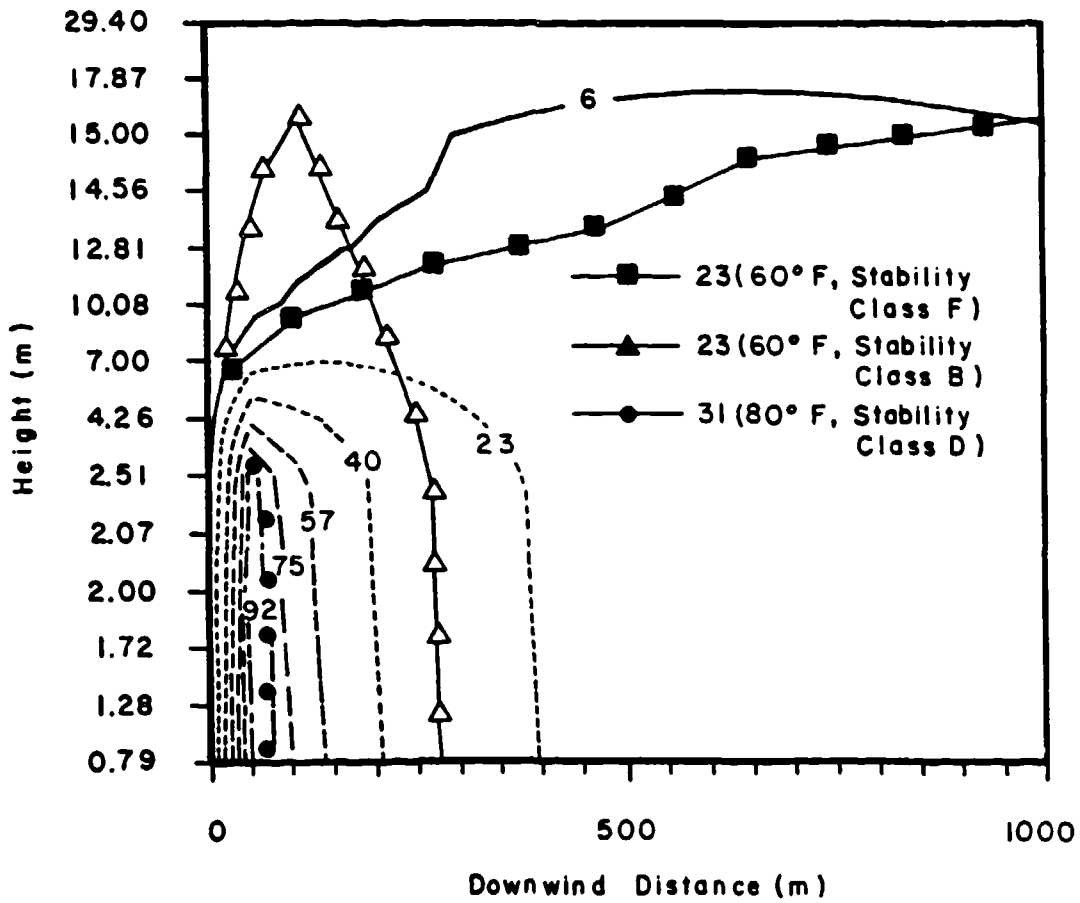


Figure 1. Isopleths of Total Extinction Coefficient σ_{ext} in a Plume of Fog Oil Aerosol at 60°F and Stability Class D. The Initial Mean Particle Diameter is $0.5\mu\text{m}$. The Wavelength of Irradiation is $0.5\mu\text{m}$. σ_{ext} in cm^{-1} are Equal to the Values Given on Isopleths Times 5×10^{-5} .

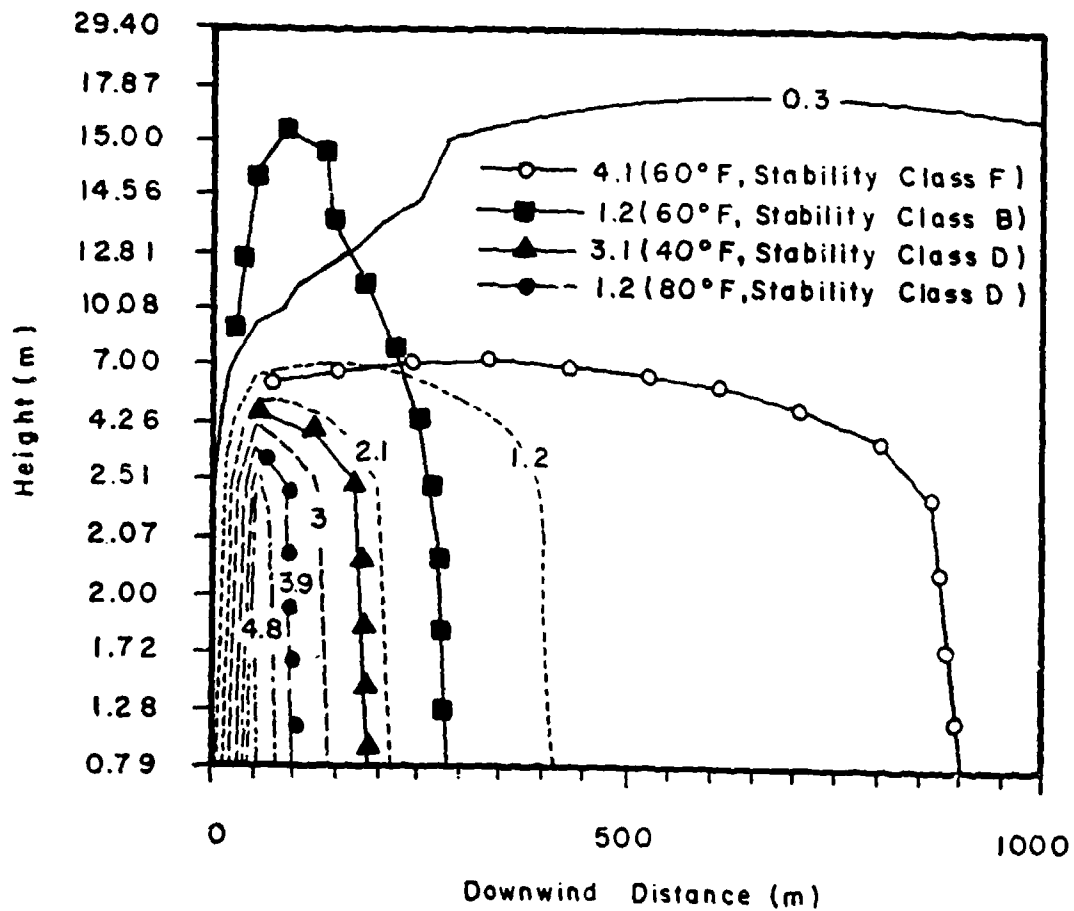


Figure 2. Isopleths of Total Extinction Coefficient σ_{ext} in a Plume of Fog Oil Aerosol at 60°F and Stability Class D. The Initial Mean Particle Diameter is $0.5 \mu\text{m}$. The Wavelength of Irradiation is $3.0 \mu\text{m}$. σ_{ext} in cm^{-1} are Equal to the Values Given on Isopleths Times 5×10^{-6} .

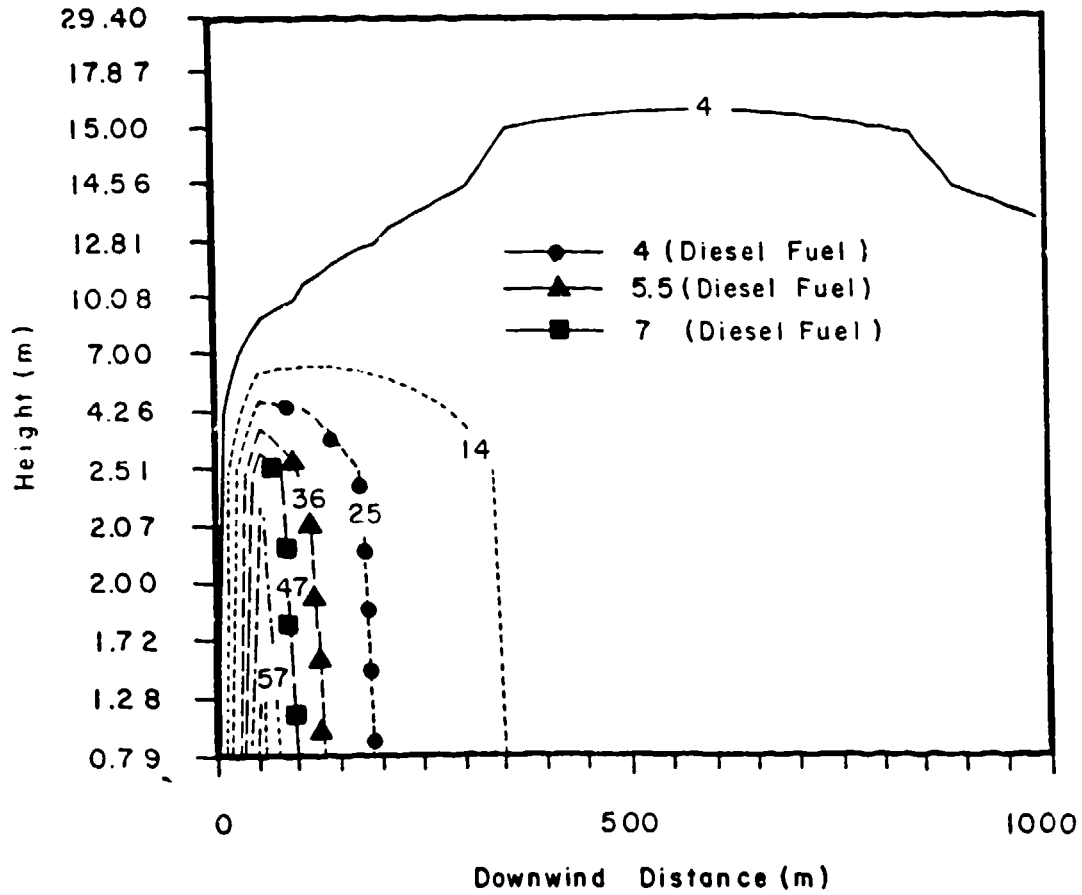


Figure 3. Isopleths of Total Extinction Coefficient σ_{ext} in a Plume of Fog Oil Aerosol at 60°F and Stability Class D. The Initial Mean Particle Diameter is $2.0\mu\text{m}$. The Wavelength of Irradiation is $0.5\mu\text{m}$. σ_{ext} in cm^{-1} are Equal to the Values Given on Isopleths Times 5×10^{-5} .

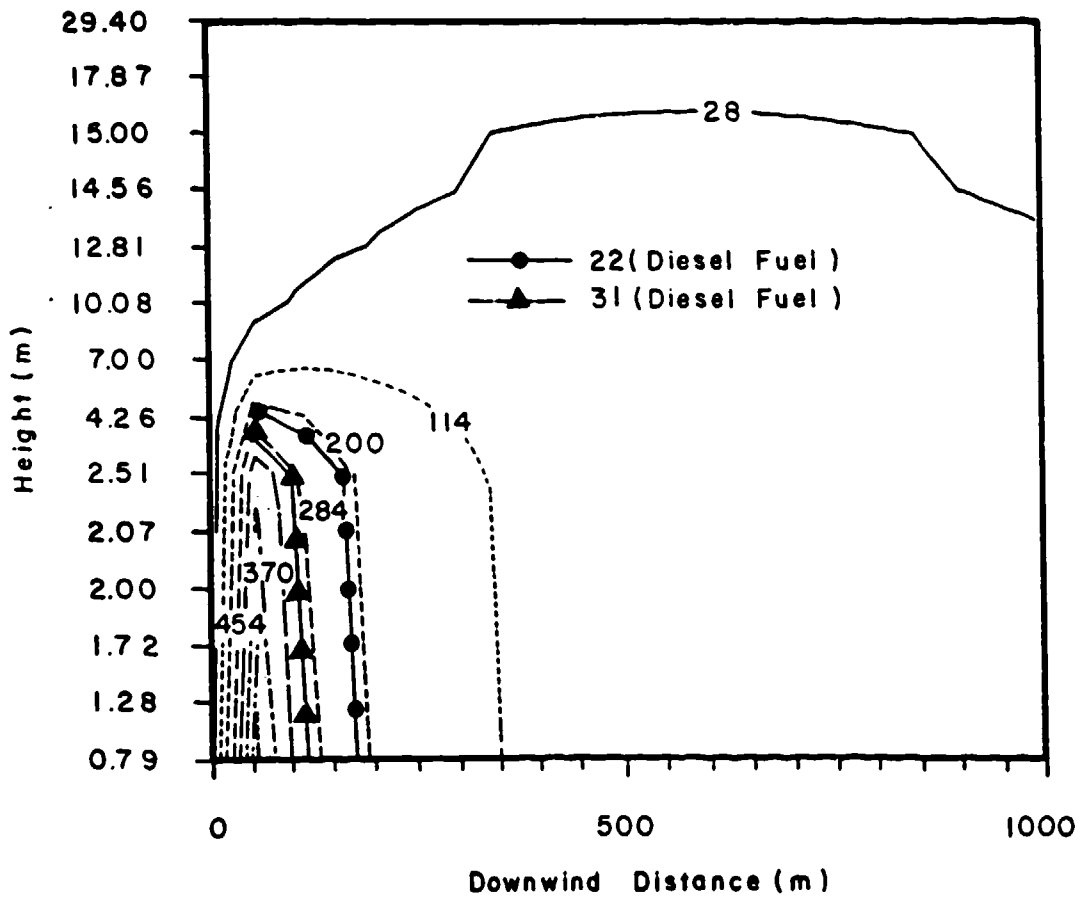


Figure 4. Isopleths of Total Extinction Coefficient σ_{ext} in a Plume of Fog Oil Aerosol at 60°F and Stability Class D. The Initial Mean Particle Diameter is $2.0\mu\text{m}$. The Wavelength of Irradiation is $3.0\mu\text{m}$. σ_{ext} in cm^{-1} are Equal to the Values Given on Isopleths Times 5×10^{-6} .

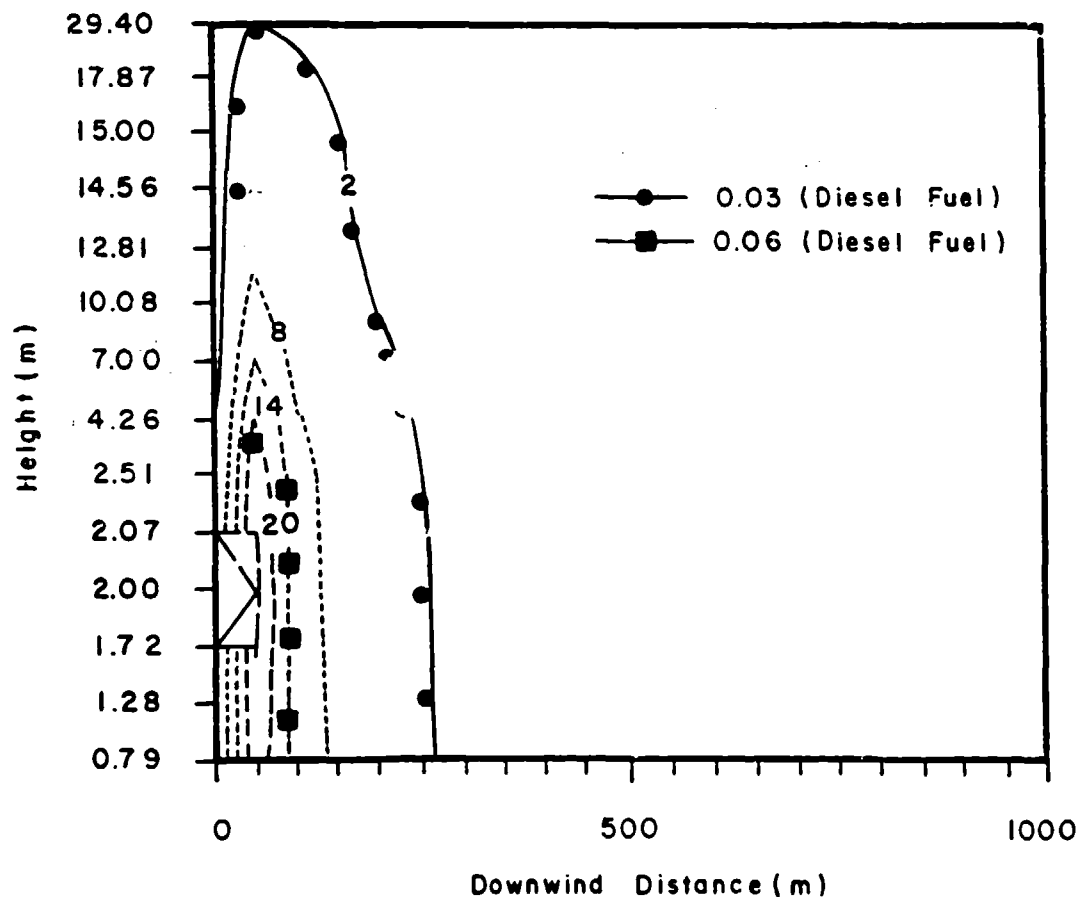


Figure 5. Isopleths of Total Extinction Coefficient σ_{ext} in a Plume of Fog Oil Aerosol at 80°F and Stability Class B. The Initial Mean Particle Diameter is $0.5 \mu\text{m}$. The Wavelength of Irradiation is $0.5 \mu\text{m}$. σ_{ext} in cm^{-1} are Equal to the Values Given on Isopleths Times 5×10^{-5} .

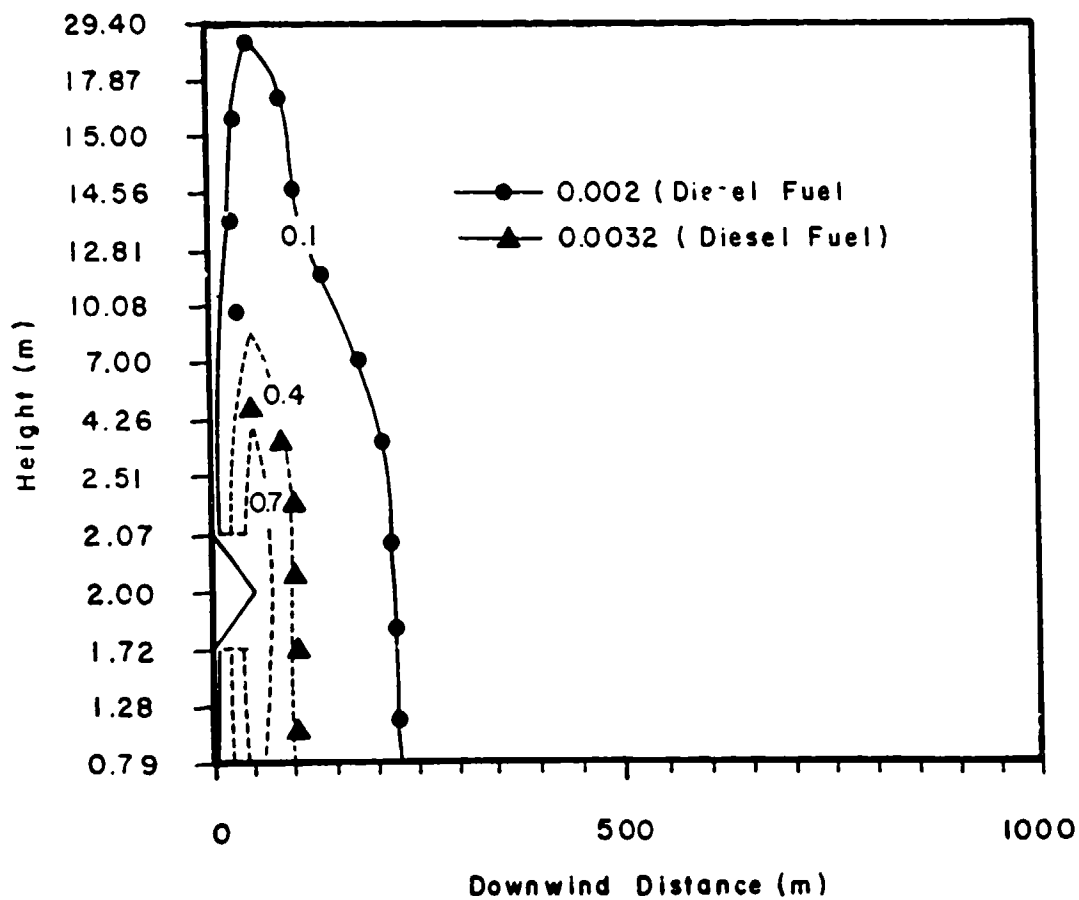


Figure 6. Isopleths of Total Extinction Coefficient σ_{ext} in a Plume of Fog Oil Aerosol at 80°F and Stability Class B. The Initial Mean Particle Diameter is 0.5 μm . The Wavelength of Irradiation is 3.0 μm . σ_{ext} in cm^{-1} are Equal to the Values Given on Isopleths Times 5×10^{-6} .

X-RAY FLUORESCENCE DETECTION OF MEDIUM AND HIGH Z AEROSOLS

George M. Thomson and Richard A. Markland
U.S. Army LABCOM Ballistic Research Laboratory
Aberdeen Proving Ground, Maryland 21005

Sandra M. Thomson
U.S. Army AMCCUM Chemical Research, Development and Engineering Center
Aberdeen Proving Ground, Maryland 21010

RECENT PUBLICATIONS, SUBMITTALS, FOR PUBLICATION AND PRESENTATIONS:

G. M. Thomson and S. M. Thomson, Proc. of IX Smoke Symposium, Tech Report AMCPM-SMK-T-001-85; Vol 1, page 123; Adelphi, MD (1985).

ABSTRACT

Continued development of a device that measures the concentration of individual elements with atomic number $Z > 20$ contained within aerosol dust or smoke particles/droplets is reported. The device separates out the aerosol's non-gaseous components by pumping it through a section of a tape made of filter paper. After gathering particles for a fixed period of time the tape advances, forcing a new section to intercept the airstream while bringing the exposed section in front of a 25 mCi Cd-109 radioactive source. The source bombards the tape's contents with 22 keV x-rays. These, in turn, induce fluorescence in the trapped atoms, that is, they cause the atoms to emit x-rays of their own at lower, but still easily measurable (if $Z > 20$), characteristic energies. A spectral analysis of the fluorescent x-rays provides raw data that reveals the abundance of each individual element in the aerosol simultaneously. Note that the x-ray method is independent of the state of chemical combination of the species in question. A prototype device has been tested on aerosols containing elements such as uranium, iron, tungsten, copper, lead and zinc. For all these materials it readily detected concentrations of 20 micrograms per cubic meter or less in periods of three minutes. At concentrations in the few milligram/cubic meter range measurement times of a minute or less were easily achieved. A second generation system is now in the final stages of construction which consists of three parallel-operating sampler/analyzers controlled by a single processing unit. The completed system will be used to monitor levels of potentially hazardous dusts at BRL indoor firing ranges.

1. INTRODUCTION

In this presentation we report continued progress in development of a monitor to assess the concentration of medium to high atomic number elements appearing as aerosolized particles. The device couples a state-of-the-art microanalytical technique, x-ray fluorescence, to automatic sampling in order to obtain high sensitivity, reliability, and species selectivity; all in a format that may be adapted to a wide variety of problems. At the limits of its sensitivity it can measure concentrations as low as several micrograms per cubic meter in three minutes or less. For the higher concentrations typical of obscuration, large reductions in response time are realized and different, simpler, forms of the basic method may be possible. The x-ray fluorescence dust detector has potential uses wherever airborne dusts containing copper, lead, cadmium, mercury, iron, or a host of other elements may be encountered. In the following few pages the detector's overall features, capabilities, as well some of its potentials for future use in obscuration are discussed. The basic principles of this device were introduced in a paper which described our

first prototype device (Thomson and Thomson 1985). This report both updates efforts to install a detection system to protect BRL workers from hazardous depleted uranium dusts aerosolized during munitions testing and reviews some of the most important features of fluorescence detection.

2. THE APPARATUS

To understand how the detector works examine Figure 1, a layout drawing of its component parts. The first stage of operation starts when a mechanical pump draws air from the test region through a connecting pipe at a flow rate that may be adjusted from between 0.0 and 0.1 cu. meters/sec. In the pipe the air is intercepted by a tape of filter paper (Schleicher and Schuell type 604) which traps and holds any significant particles with a minimum of flow resistance. Sample accumulation continues until a given volume of air has passed. At this time the exposed tape advances into the radiation field of an annular x-ray-emitting 25 millicurie Cadmium-109 radioactive source and a new section of tape moves into the airstream. The x-rays produced by the radioactive source have a well-defined energy near 22 keV. When they impinge on the atoms in the collected sample material, the sample atoms fluoresce, that is, they produce x-rays of their own. The fluorescent x-rays also possess well-defined energies which are characteristic of the producing species.

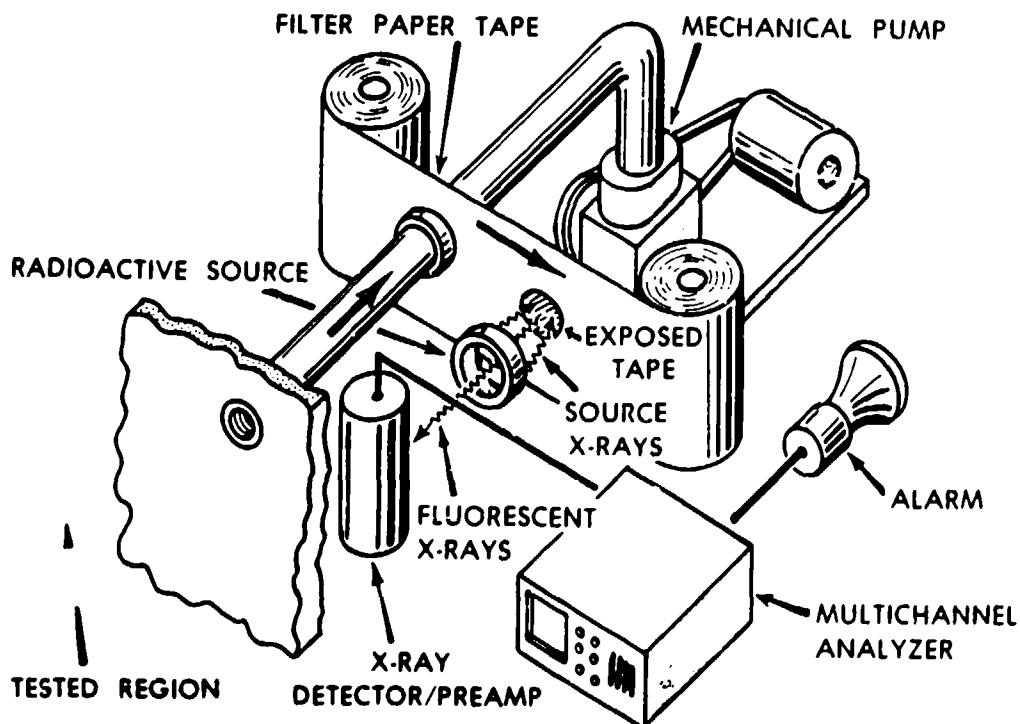


Figure 1. A component layout of the x-ray fluorescence dust detector.

It is this quality that is used to identify the elemental species in the aerosol. As examples, if the source x-rays impact on iron, fluorescent x-rays are produced with energies of 6.4 keV and 7.1 keV, while, if the target is uranium, fluorescent x-rays are emitted at 13.6 keV, 17.2 keV, and 20.1 keV. Regardless of what elements gave rise to them, any fluorescent x-rays passing through the annular source's center strike a proportional counter (Reuter Stokes P3-0803-294). This device generates a fast electrical pulse whose height is proportional to energy of the x-ray. Pulses from the proportional counter in turn are directed into a multichannel analyzer where they are sorted out by pulse height/x-ray energy. The counts under each peak stored in analyzer memory are indicative of the abundance of the corresponding element in the sample. It is this quantity that forms the essential output of the detector. If its numerical value exceeds some preselected value, one can have the analyzer trigger an alarm or exert some other control. An example of a multichannel analyzer pulse height spectrum for an iron sample is shown in figure 2 along with a similar spectrum acquired from the tape alone. The large low energy peak corresponds to iron K characteristic x-rays.

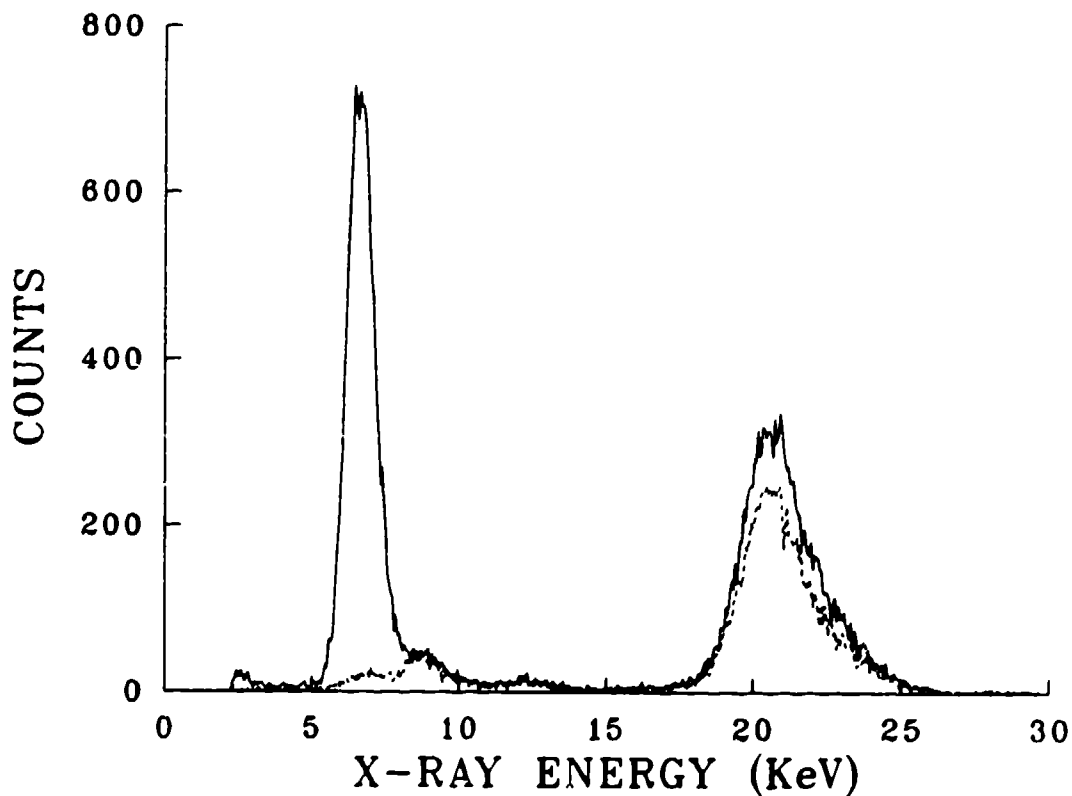


FIGURE 2. The output of the multichannel analyzer when 1 μ g of iron is accumulated on the tape (upper curve) is shown along with like data from a tape without iron (lower curve). The low energy peak is from iron K x-rays, while the high energy peak is due to source x-rays that have backscattered from the tape.

Recently we have constructed a system for sampling aerosols containing depleted uranium dusts created within BRL's indoor firing ranges. It consists of three parallel-operating samplers controlled by a single digital control unit. The control is capable of sequencing the samplers after a user selectable amount of time or number of counts. The output of each sampler is stored in one segment of the memory of a multichannel analyzer. From the memory the counts corresponding to any elements in any chosen sampler can be singled out and sent to a computer. Provision is also made for immediate display of any one element from each sampler directly on the control panel. Figure 3 shows a photo of the control unit and one sampler. In normal operation they would be separated by up to 150 feet with the sampler located close to the potentially hazardous aerosol, and the controller in the operating area.

2. ANALYSIS

In order to use the data it is essential to relate the observed counts corresponding to one line of a given element N to that element's concentration in the target aerosol C . First, one must subtract from the raw data those spurious counts produced by source x-rays backscattering, inelastically from the paper tape and sample. The tape's contribution is found by counting an unexposed section of tape for an equal length of time, while the sample's must be interpolated from the non-peak portions of the spectrum. Having obtained a value for N , we can use the expression:

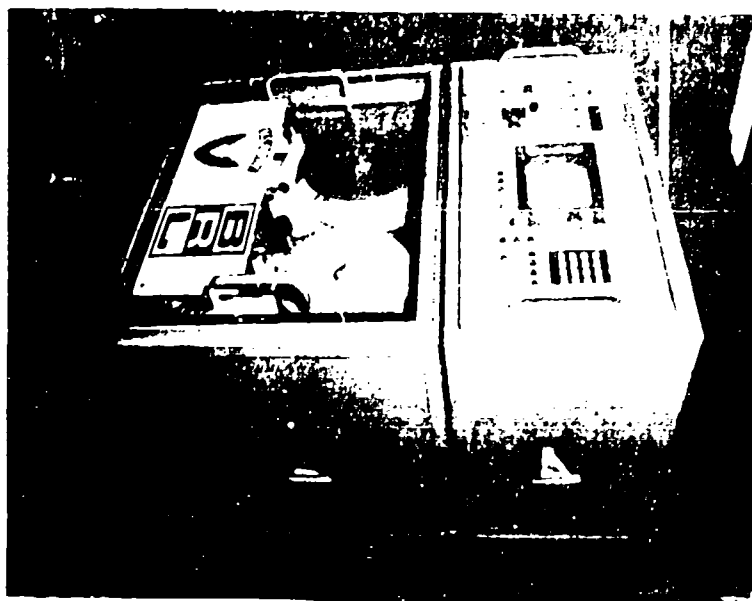


Figure 3. A photograph of the aerosol monitor apparatus.

$$C = KN/VEat$$

(1)

where V is the volume of air passed through the sampler during the user chosen sampling/counting interval, t ; E is the system trapping efficiency, the fraction of the particles entering the inlet at end up adhering to the tape; a is the source activity; and k is the sensitivity. The latter quantity relates the mass of the sought-for element deposited on the filter tape to the counts found in the selected spectral region during a unit time as normalized to a standard source activity. The sensitivity takes into account the source-target-detector geometry, the detection efficiency, and the overall x-ray fluorescence physics.

Determination of V is usually a straightforward problem. E and k , on the other hand, are considerably more involved. Assessment of E has to be performed for each individual situation. One must be careful to insure that the sample is representative, that particles are not deposited in the flow path components, and that the filter paper is fine enough to trap all particle without undue restriction of flow volume. Turning now to the second quantity K , we have measured it by carefully preparing filter tape sections with a known amount of the elemental species in question deposited in a geometry which is as close as possible to that laid down by the sampler. This calibration sample is then counted by fluorescence for a given period of time. Results of this kind are shown in figure 4 for uranium. Similar determinations have been successfully carried out for iron.

3. RESULTS

In range tests at the Ballistic Research Laboratory a prototype has detected and reported uranium levels of about 6 micrograms per cubic meter in sampling times of about 3 minutes with a 2:1 signal to noise ratio (S/N). For the case of iron, a similar test series was carried out in a chamber at Chemical Research and Development Center. The limit of detectability was found to be about 20 micrograms at a 2:1 S/N. At higher concentrations, in the milligram per cubic meter range, the sampling time could be reduced to less than a minute. Other tests reveal sensitivities similar to iron for copper, chromium, zinc and nickel. The apparatus exhibited other features that can be useful in obscurant situations. For example, in tests at a welding shop, the detector was able to pick hundred microgram per cubic meter iron fumes out of smokes having much higher concentrations of lower Z materials formed from solvents and fluxes. This result implies that tagging of oil-based or other low Z obscurants with higher Z materials may be useful. Indeed the multi-element capability of the fluorescence method may lend itself to multiple tagging schemes in which the output of different generators could be individually identified in near-real time.

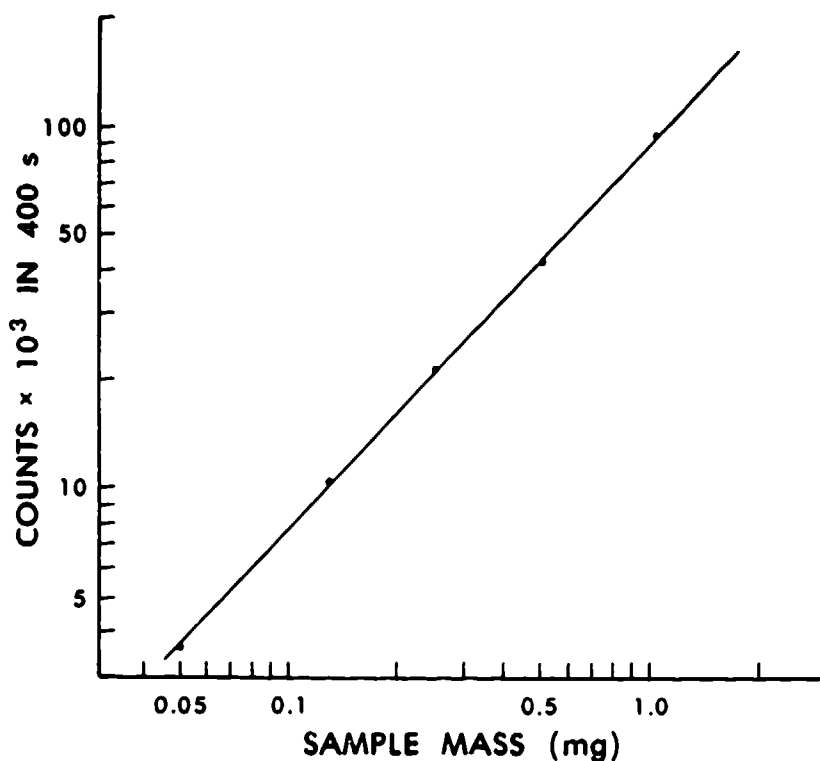


FIGURE 4. A plot of the fluorescent x-ray counts observed in 400 seconds while various amounts of uranium are bombarded with x-rays from a Cd - 109 source. The line shows a least squares fit to the measured points.

Recently we have been carrying out experiments to ascertain whether or not one could dispense with the pumps and filter paper needed to concentrate particulates in thin aerosols when working with dense obscurants. Such a device would irradiate the aerosol cloud in-situ and consequently be far simpler to build, operate and control. It appears that this concept is feasible if one substitutes an electron-impact type x-ray source for the radioactive source. A forthcoming paper will discuss direct fluorescence in detail.

4. CONCLUSIONS

The apparatus has several qualities which may be important advantages over other means of aerosol assessment.

(a). Assessment is virtually real-time. Fluorescence gives results within minutes after sampling begins when concentrations are near its sensitivity limit. The delay reduces to several seconds when higher doses are encountered such as in obscuration.

(b). The unit is completely self-contained. All functions are carried out in one unit, on site, with a minimum of operator intervention.

(c). The detector can be used on many elemental species. It signals the presence of any element with $Z > 20$ existing as a solid or as a droplet. For obscurants that do not contain elements in this range, the extreme sensitivity permits use of small quantities of heavier tagging elements.

(d). Response is virtually independent of the state of chemical combination of the element scrutinized. It provides a reliable measure of how much of a given material has gotten airborne. Combined with absorption measurements, it can reveal an obscurant's efficiency.

(e). The method has multiple species capability. The BRL apparatus can simultaneously monitor one, two, or several different elemental species either individually or collectively. It permits the tagging of individual obscurant generator output and the evaluation of their separate contributions to clouds produced by multi-generator arrays.

(f). X-ray fluorescence is flexible. It can be adapted to a wide range of aerosol characterization tasks involving concentration levels from more than grams down to micrograms per cubic meter and it lends itself to rugged designs suitable for field use.

(g). Results can be easily put on a quantitative footing through a simple calibration procedure that requires only a few minutes.

(h). The equipment required is not particularly hazardous. Of course, some care must be exercised in dealing with the radioactive sources, but in all cases the x-rays involved are not very penetrating and can be shielded easily.

Blank

CLUSTERS: STUDIES OF AEROSOL PRECURSORS

W. B. Tzeng, J. J. Steen, R. G. Keesee, P. D. Dao, S. Morgan and A. W. Castleman, Jr.

Department of Chemistry
The Pennsylvania State University
University Park, PA 16802

RECENT PUBLICATIONS, SUBMITTALS FOR PUBLICATION AND PRESENTATIONS:

A) A. W. Castleman, Jr., S. Morgan, P. D. Dao, O. Echt, and R. G. Keesee, "The Relation of Cluster Dissociation, Magic Numbers, and Thermodynamic Stabilities: Consideration of Ammonia Clusters Studied Via Multiphoton Ionization," J. Chem. Phys., submitted.

B) S. Morgan, R. G. Keesee, and A. W. Castleman, Jr., "Studies of Clusters Using Laser Techniques: Dissociation Processes of Methanol Clusters Following Multiphoton Ionization," Proceedings of the 1986 CRDC Conference on Obscuration and Aerosol Research, June, 1986.

ABSTRACT

The distributions and dissociation of ammonia cluster ions formed via multiphoton ionization of neutral clusters were studied using a time-of-flight mass spectrometer equipped with a reflectron. Findings concerning the trends of rates and the magic number are shown to be consistent with simple considerations based on theories of unimolecular decomposition in conjunction with thermochemical data available for the ammonia system.

INTRODUCTION

Studies of the dynamics of formation, energetics, and structure of microclusters enable an investigation of the basic mechanisms of aerosol formation at the molecular level. The advent of several new experimental techniques provides methods for ascertaining the factors controlling the formation of prenucleation embryos, their stability, and the influence of their properties on nucleation. Associated work on the reactivity of neutral and ionic clusters provides data useful in elucidating the nature of reactions that might occur in the droplet phase surrounding an aerosol particle.

A subject of considerable interest in the field of cluster research concerns the origin of magic numbers, a term which has been used to describe the anomalous abundance of certain sizes of clusters in an otherwise smoothly varying cluster distribution. A systematic study of the dissociation of ammonia clusters following their ionization by multiphoton laser techniques provides direct proof of the importance of the metastability of the cluster ions and of the extensive dissociation processes which affect the resulting cluster distributions.

It is evident that the ionization process itself has influence on the observed magic numbers. Considerations presented herein account for the appearance of magic numbers, their correspondence with the thermodynamical stability of clusters, and the trends of metastable dissociation rates with cluster size.

EXPERIMENTAL

The apparatus used in these studies has been described in detail elsewhere.^{1,2} Hence, only a brief description of the features relevant to the present study are given. Neutral ammonia clusters are formed in the supersonic expansion of gaseous ammonia from a pulsed nozzle source. The molecular beam is crossed by a laser beam from a Nd:YAG pumped dye laser, equipped with a wavelength extension system which provides frequency doubling and mixing capabilities.

In the present study, neutral clusters of NH₃ are ionized via non-resonant multiphoton absorption at the focus of a pulsed 266 nm wavelength laser beam. Ions formed are then accelerated in an electrostatic field to approximately 2 KeV, deflected by a few degrees in a transverse field in order to separate the ion and neutral beams, and subsequently detected by a particle multiplier. The reflectron is employed to separate daughter and parent ions in order to measure rates of dissociation. The time-of-flight spectrum of the ions is digitized and signal averaged in a transient recorder.

RESULTS AND DISCUSSION

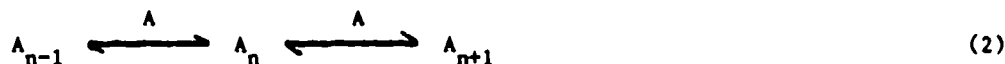
An extensive investigation of the unimolecular (evaporative) dissociation of ammonia cluster ions has been conducted. A trend of increasing evaporative rate coefficient with cluster size is found for the loss of one monomer unit from clusters ranging in size from the 1- to 25-mer as shown in Figure 1.

Based on a simple RRK treatment of unimolecular rates³ the dissociation rate constant would decrease with the number of oscillators if the energy content of the system was a fixed value. The limiting rate constant may be expressed in the form of Arrhenius equation

$$k = A e^{-E_0/kT} \quad (1)$$

Hence, in the case of a thermal distribution, clusters with low bond energies should display larger rates of dissociation.

Another essentially equivalent way of viewing the origin of the magic numbers follows from consideration of a clustering sequence:



In the case of a thermal distribution of clusters the equilibrium constant for each step is given by the ratio of the forward and reverse rate constants. Since the rates of the forward reactions and entropy values of adjacent clusters do not vary greatly with cluster size for moderate and large cluster ions,^{4,5} they may be taken to be approximately constant. Therefore,

$$\frac{k_{r,n+1}}{k_{r,n}} = e^{-\frac{(\Delta H_{n-1,n} - \Delta H_{n,n+1})}{RT}} = e^{-\frac{\Delta(\Delta H_n)}{RT}} \quad (3)$$

This leads to a simple prediction, namely, for a thermal population, the relative dissociation rates of clusters of adjacent size should increase with cluster size. Work is in progress to assess whether these relationships pertain to the description of dissociation dynamics following cluster ionization.

Studies of ammonia clusters by electron impact⁶ and multiphoton¹ ionization methods show that there is a smooth distribution of cluster sizes except for the anomalously large abundance for the protonated pentamer, written in terms of the central core ion as $\text{NH}_4^+ \cdot (\text{NH}_3)_4$. In Figure 2, the enthalpy changes of successive clusterings of ammonia onto NH_4^+ are plotted versus number of ligands n . The magnitude of the enthalpy change with cluster size is seen to be smoothly decreasing from the monomer to the tetramer at which point there is a dramatic drop for five and beyond. These observations concerning magic numbers in cluster systems are in accord with the above consideration. This follows from the fact that, from Equations (1) and (3), the dissociation rate of a cluster would be expected to undergo an abrupt change in the region of a discontinuous break in an otherwise smooth trend of bond energy (or ΔH°) with cluster size.

In conclusion, the present results provide direct evidence that cluster ion stabilities and dissociation processes govern the magic numbers in hydrogen bonded systems. Further studies are in progress in our laboratory to determine the extent to which this conclusion can be extended to other systems.

ACKNOWLEDGMENTS

We would like to acknowledge the contributions of Olof Echt and the support of the U. S. Army Research Office, Grant No. DAAG29-85-K-0215, and the Department of Energy, Grant No. DE-AC02-82-ER60055.

REFERENCES

1. O. Echt, P. D. Dao, S. Morgan, and A. W. Castleman, Jr., *J. Chem. Phys.* **82**, 4076 (1985).
2. S. Morgan and A. W. Castleman, Jr., "Unimolecular Dissociation of Protonated Methanol Clusters," *J. Chem. Phys.*, to be submitted.
3. P. J. Robinson and K. A. Holbrook, *Unimolecular Reactions*, Wiley Interscience (1972).
4. W. Krame, B. Kamke, H. U. Kiefl, and I. V. Hertel, *J. Chem. Phys.* **84**, 1325 (1986).
5. W. Begemann, S. Dreihöfer, K. H. Meiwes-Broer, and H. O. Lutz, *Z. Phys. D.* **3**, 183 (1986).
6. J. J. Breen, K. Kilgore, K. Stephan, R. Sievert, B. D. Kay, R. G. Keesee, T. D. Mark, J. Van Doren, and A. W. Castleman, Jr., *Chem. Phys.* **91**, 305 (1984).
7. I. N. Tang and A. W. Castleman, Jr., *J. Chem. Phys.* **62**, 4576 (1975).
8. M. R. Arshadi and J. H. Futrell, *J. Chem. Phys.* **78**, 1482 (1974).
9. D. D. Nelson, G. T. Fraser, and W. Klemperer, *J. Chem. Phys.* **83**, 6201 (1985).
10. N. Lee, R. G. Keesee and A. W. Castleman, Jr., *J. Colloid and Interface Science* **75**, 555 (1980).

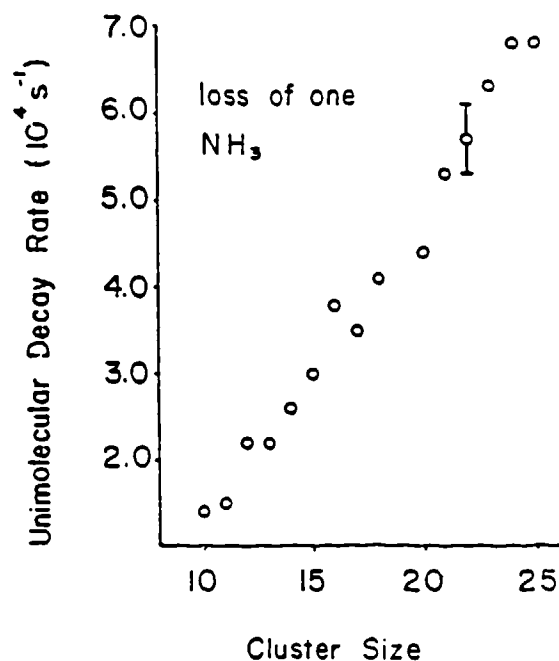


FIGURE 1. Rate of evaporative unimolecular dissociation of ammonia cluster ions versus size of the cluster, N .

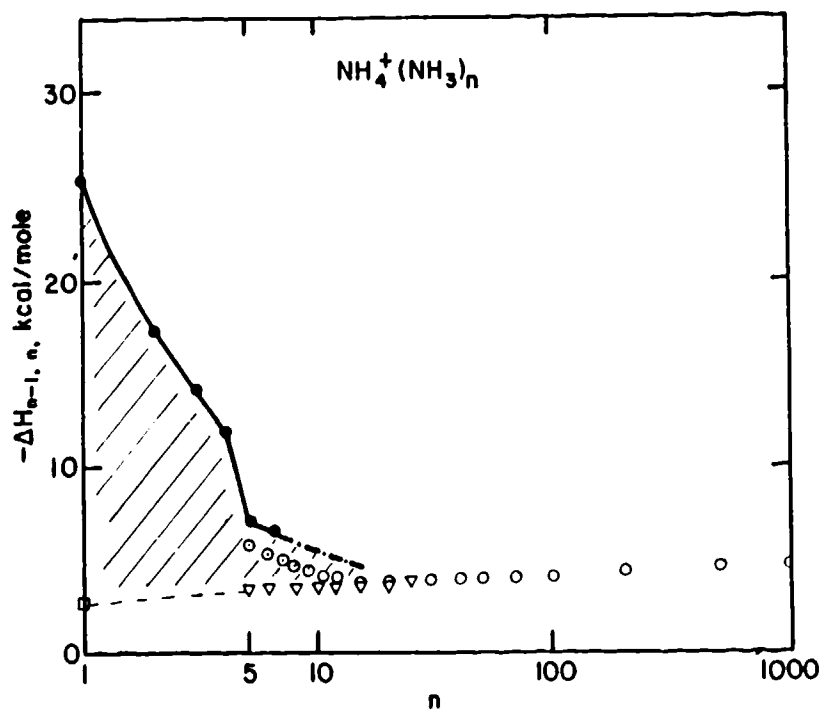


FIGURE 2. $-\Delta H_{n-1, n}^{\circ}$, enthalpies for successive additions of NH_3 onto NH_4^+ are plotted versus number of ligands n . Data for $n=1-4$ are taken from Ref. 7 while data for $n=5,6$ are from Ref. 8. The expected trend for a neutral system is also shown as a dashed curve. The bond energy for the neutral dimer shown by a square is taken from Ref. 9. The open circles represent trends expected for a charged classical liquid drop model, while the open triangles are the corresponding predictions for a neutral droplet (10). The cross-hatched area between the ion and neutral curves represents the excess energy in a cluster due to the re-orientation of the ammonia molecules to accommodate a charge.

GENERAL REMARKS ON EQUILIBRIUM CONFIGURATIONS
OF N POINT CHARGES ON A SPHERE

Burt V. Bronk and Robert H. Frickel
Research Directorate
U.S. Army Chemical Research, Development and Engineering Center
Aberdeen Proving Ground, Maryland 21010-5423

RECENT PUBLICATIONS, SUBMITTALS FOR PUBLICATION AND PRESENTATIONS:

A) Robert H. Frickel and Burt V. Bronk, "Configurations of Charges on a Sphere", Report CRDEC-TR-87040 from CRDEC, Aberdeen Proving Ground, MD 21010-5423, April 1987.

B) Robert H. Frickel and Burt V. Bronk, "Symmetries of Configurations of Charges on a Sphere," submitted to Canadian Journal of Chemistry, 1987.

ABSTRACT

The configurations of lowest interaction energy were obtained for sets of N point charges confined to the surface of a sphere and interacting via a mutual Coulomb repulsion. As N varied between 4 and 107, many interesting patterns were observed and the symmetries of these patterns were determined. Since the number of symmetries occurring is limited, some general observations on the patterns can be made. It is expected that some of these observations made for the present limited idealized case will also apply to physically realizable crystallizations occurring on the surface of microscopic spheres.

INTRODUCTION

The ancient problem of projecting the map of the world onto a plane is a reminder that the organization of structures on a spherical surface is not compatible with the well known structures of crystals in two or three dimensions. Since we are interested in observable properties of aerosols under all weather conditions, phase changes on the surface of liquid droplets are to be expected and we would like to have some insight into the possibilities and limitations of geometries for crystals formed on the surface of a sphere. Empirical knowledge of such structures is limited or absent, therefore, we have chosen to start with the idealized but well defined problem of determining the equilibrium arrangement for N charged particles that interact with each other via Coulomb

forces, and are constrained to remain on the surface of a sphere. This problem is closely related to the more general problem of finding the minimum energy arrangement for N particles on a sphere interacting with energy

$$E = \frac{1}{2} \sum_{i=1}^N \sum_{j=2}^N |r_i - r_j|^{-m}$$

where m is a real number greater than zero. The Coulomb case (m=1) has been previously considered for $N \leq 16$ and many of the cases found are similar to those found for higher values of m (i.e. short range repulsion)^{1,2}. We have extended the calculation to many higher values of N up to N=107. The large number of cases tabulated in the present paper allows us to make some new general observations on the patterns of occurrence of the symmetries obtained. Further, in one case we found an equilibrium configuration which was lower in energy than the previously published configuration.

The actual calculations were done by a kind of molecular relaxation. The tangential component of the Coulomb force on each charge due to all the other charges on the sphere was calculated at a given time. Each charge was then allowed to move a distance equal to the tangential force multiplied by a time increment, delta, as though moving in a highly viscous fluid. When the tangential forces were negligible (to about nine significant figures) the calculation stopped. In all but one or two cases, the charges assumed a configuration with the global symmetry of a non-trivial point group. Repeat calculations usually (but not always) led to identical configurations. These configurations were empirically stable against small random perturbations. Therefore we conclude that all or at least most of the stationary points found in our computer experiments were real minima. To verify this would be straightforward, but very laborious and expensive in the case of a large number of particles, since it requires that all eigenvalues of a high dimensional quadratic form be positive. Further, there is no known procedure for establishing that a given minimum is the lowest or global minimum, although the converse is established whenever a new lower minimum is found, as we did in several cases.

RESULTS

The actual configurations obtained were visualized by projecting the positions of the charged particles onto the interiors of two circles representing the hemispheres in an equal area projection (cf. Figures 1 thru 8). The hemispheres are each seen as though looking down thru a transparent sphere so that identical figures on the two circles imply a reflection plane thru the equator. The lines shown join nearest neighbors, with different tracings indicating slightly different distances. The numbers on

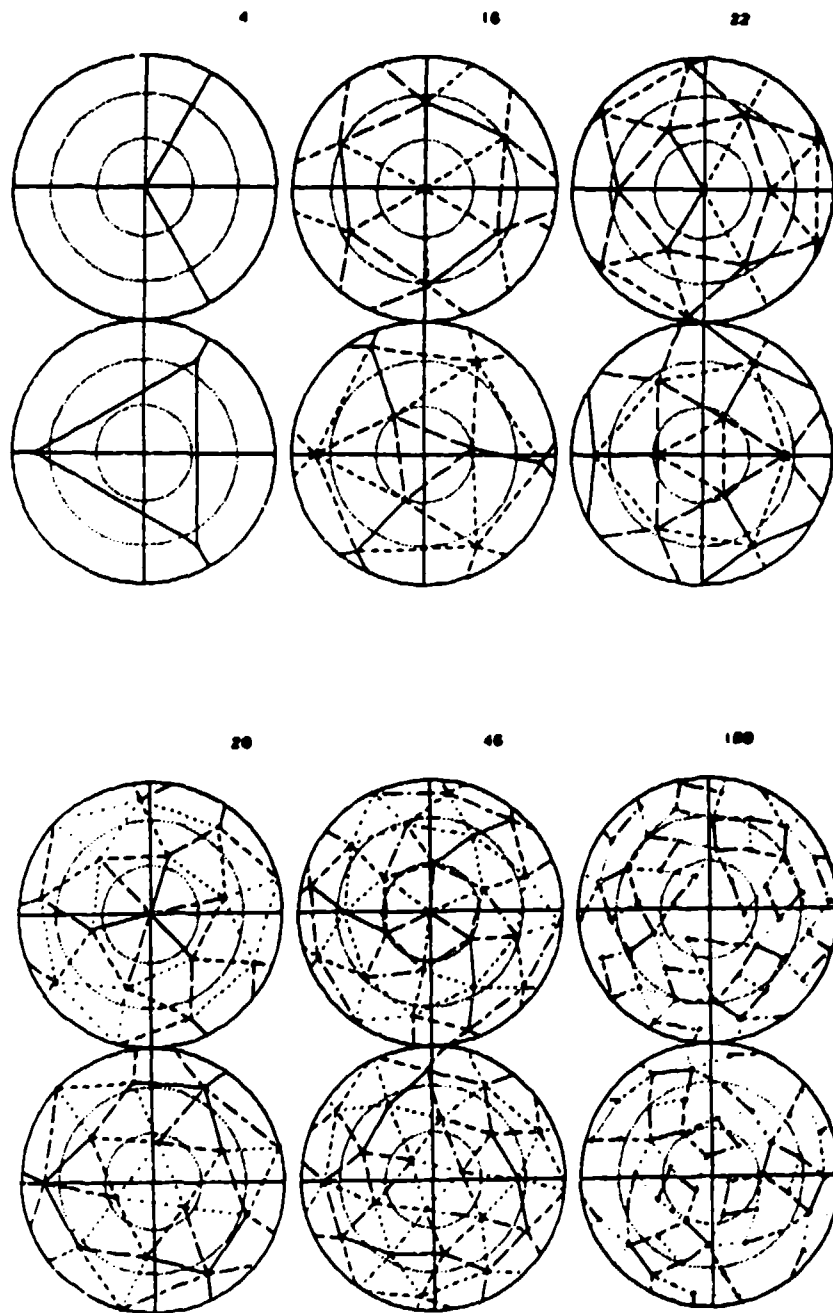


Figure 1. Tetrahedral symmetry. Note that the 4- and 22-charge configurations have reflection planes. Some of the edges have been omitted from the 100-charge configuration to make the symmetry more apparent.

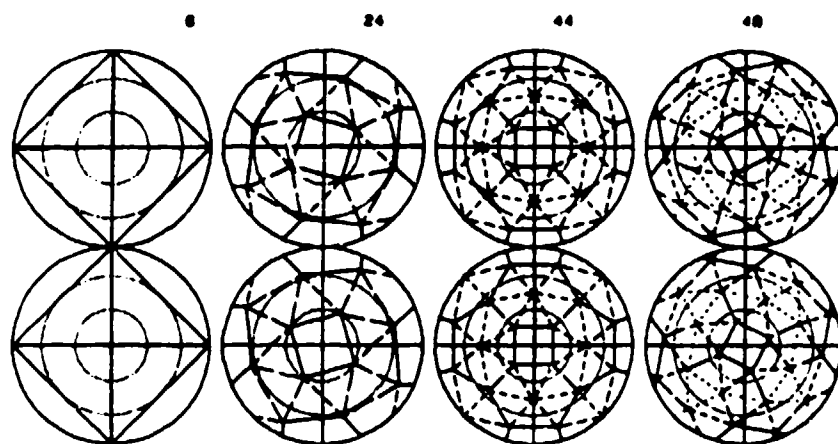


Figure 2. Octahedral symmetry. Only the 6- and 44- charge configurations have reflection planes.

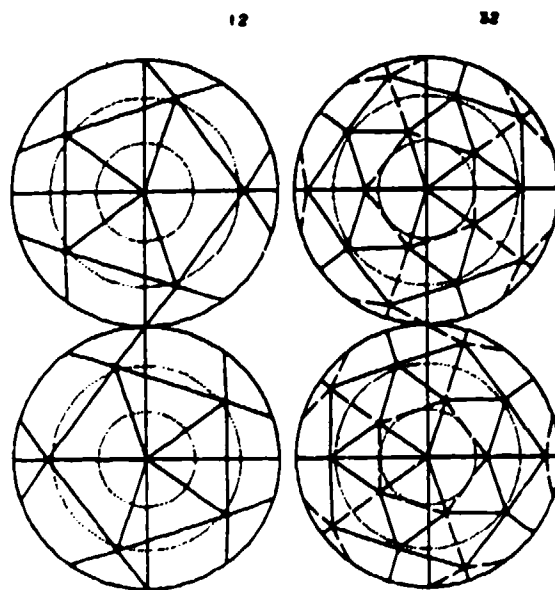


Figure 3. Icosahedral symmetry.

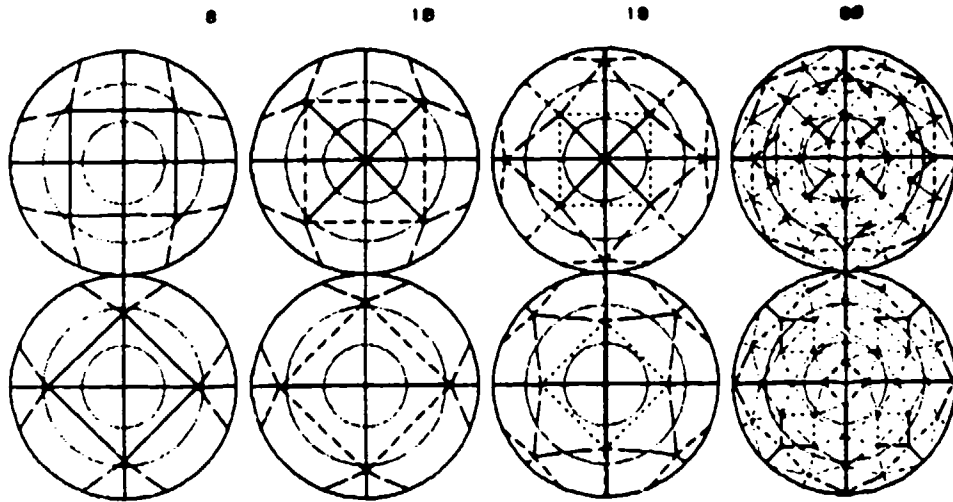


Figure 4. D_{4d} symmetry.

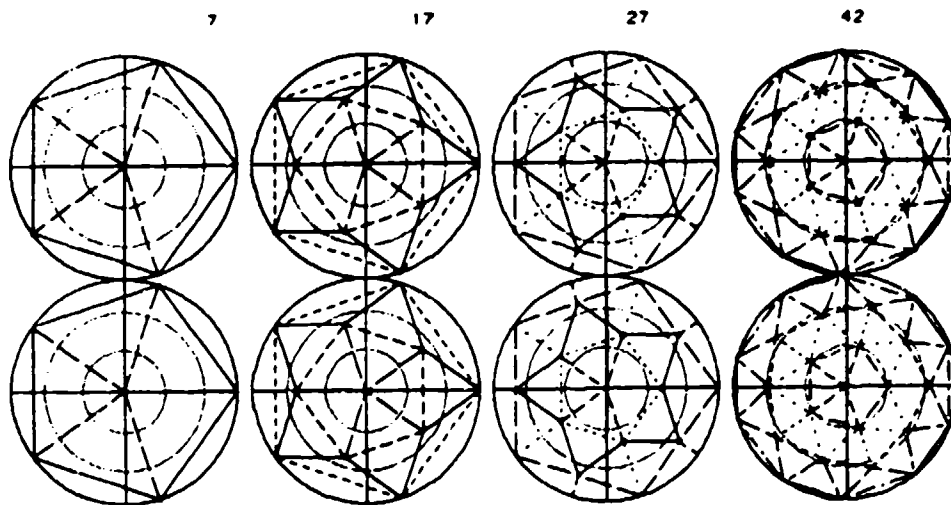


Figure 5. D_{5h} symmetry.

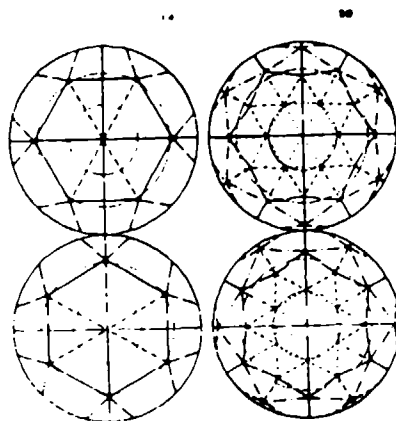


Figure 6. D_{6d} symmetry.

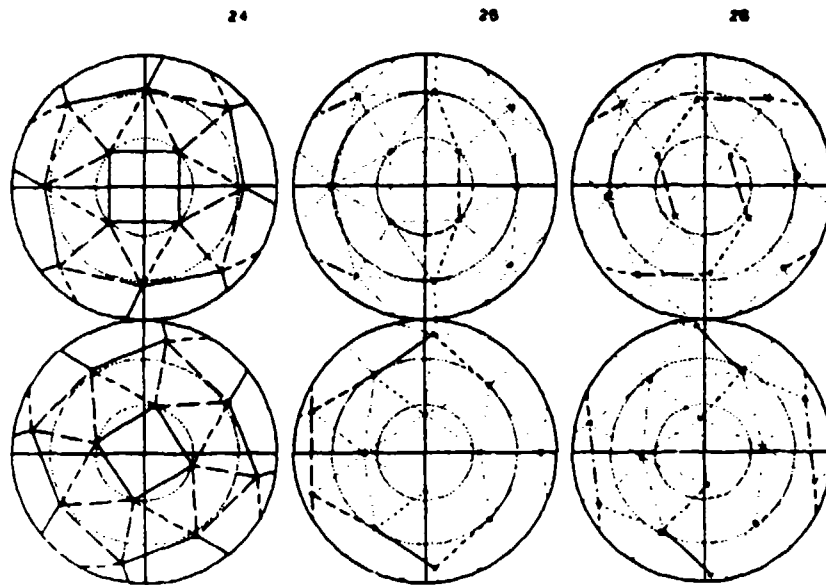


Figure 7. Continuity over change in number of charges. One can see the distortion of the figure in the upper hemisphere as additional charges find their way into the lower hemisphere.

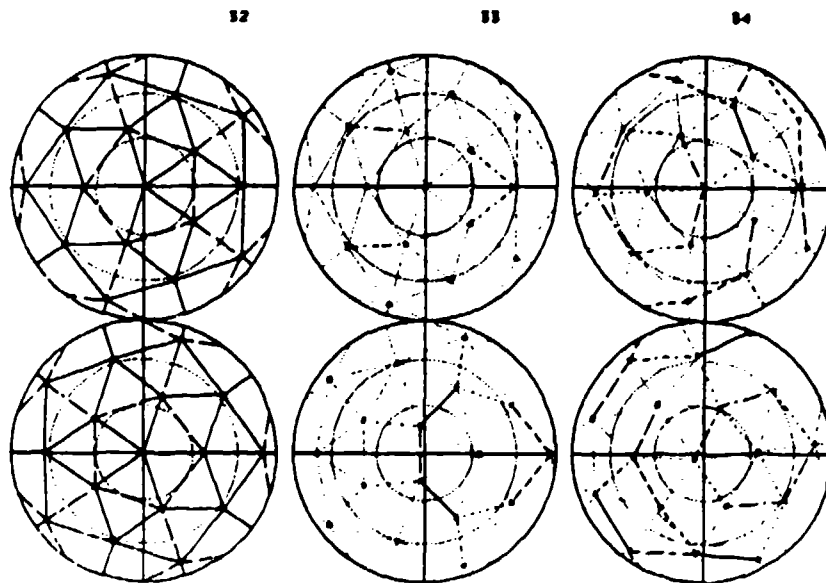


Figure 8. Continuity over change in charge number, starting with the highly symmetric 32-charge configuration. Retention of the five-pointed star in the upper hemisphere of the 33- and 34-charge configurations can be seen.

TABLE I.
POINT GROUP CLASSIFICATION OF EQUILIBRIUM CONFIGURATIONS

<u>Symmetry</u>	<u>Number of charges</u>
D _∞	2
Icosahedral	12*, 32*, 72, 20**+, 30**+
Octahedral	6*, 24, 44*, 48, 8**+, 14**+
Tetrahedral	4*, 16, 22*, 28, 46, 100
D _{6d} (S _{12v})	14, 50
D _{4d} (S _{8v})	8, 10, 18, 80, 16+, 32+
D _{5vh}	7, 17, 27, 42
D ₅	67, 77
C _{5v}	11+
D _{3vh}	3, 5, 9, 20, 39, 41
C _{3v}	31, 7+
D ₃	15, 23, 29, 45, 51, 57, 60, 63, 69, 75, 78, 101, 102
C ₃	49, 52, 61+, 94+
D ₂	30, 34, 36, 40, 58, 64, 68, 74+, 90, 94, 104, 106
C _{2v}	11, 13, 19, 21, 38, 43, 53
C ₂	26, 35, 37, 54, 55, 56, 59, 62, 63, 65, 66, 70, 71, 73, 76, 81, 82, 83, 84, 85, 86, 87, 88, 89, 91, 92, 93, 95, 96, 97, 98, 99, 103, 105+, 107
C _s (reflection only)	25, 33, 47, 79, 94+
C ₁ (no symmetry)	61, 74, 105

*with all reflection planes

+additional configuration with higher energy

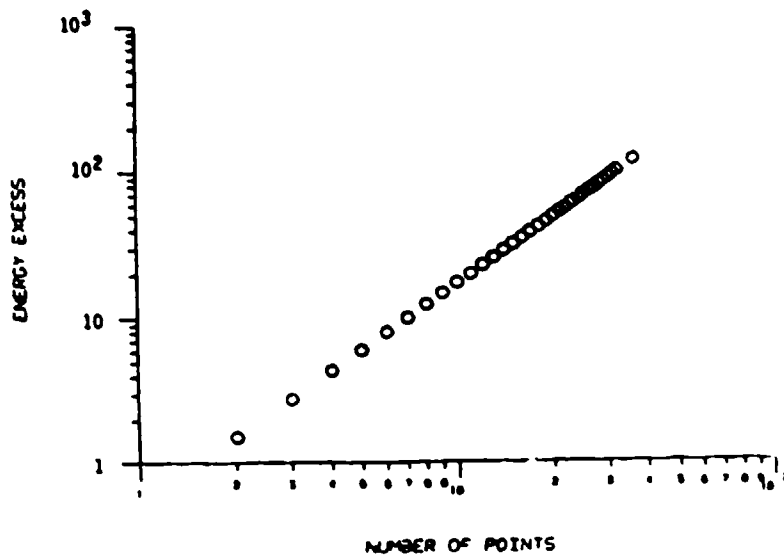


Figure 9. Energy deficit $E_0 = n^2/2 - E_n$ vs n .

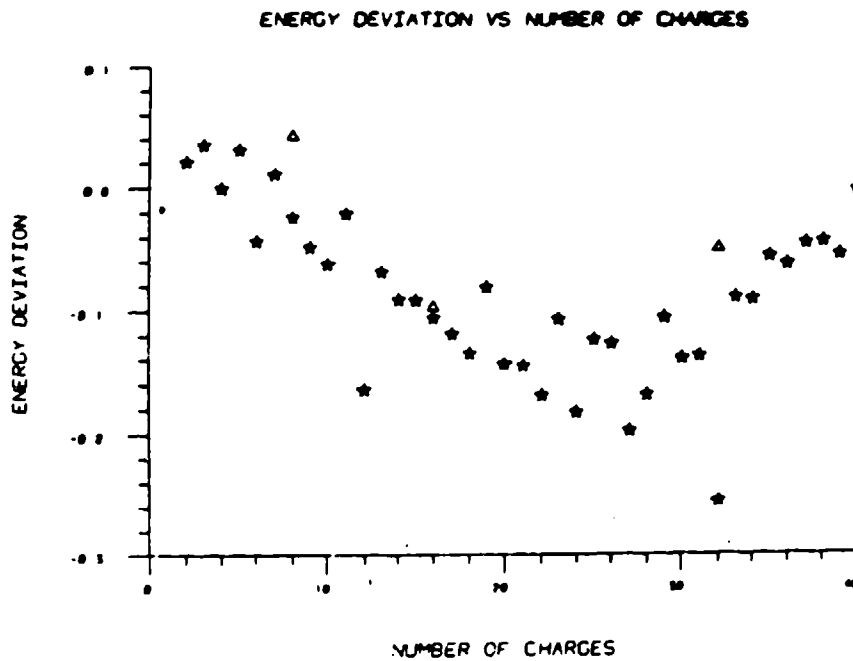


Figure 10. Deviation of E_0 from a straight line on log-log plot of E_0 vs n . Deviation for non-minimal configurations (cube and D_{4d} configurations for 16 and 32 points) are shown as triangles. The deviation for the dodecahedron is off scale above.

the figures give the number of charged particles considered. The point group classifications for equilibrium configurations are presented in Table I.

The configurations with the symmetry groups of the regular polyhedra are shown in Figures 1 thru 3. The octahedrally symmetric configurations shown in Figure 2 bear a close resemblance to the other four-fold rotationally symmetric figures in Figure 4. In both cases all charges come in sets of four equivalent points resting at the corners of squares. Note however the lack of reflection or reflection-rotation planes for $N=24$ or $N=48$.

The icosahedral figures shown in Figure 3 have a resemblance to the other five-fold rotationally symmetric figures shown in Figure 5. All the five-fold figures have $N=2+5n$ with n an integer. No five-fold figure was found for n larger than eight, and the n equals seven case is missing. In the later case, however, the figure (not shown) may be rotated to show a five pointed "Betsy Ross star" with an almost equilateral pentagon inside on one hemispherical face. Only two cases with six-fold symmetry were found. These are shown in Figure 6.

While identical symmetries are often not retained when N increases by one, there are cases where part of the figure shows a quasicontinuous change. This may be seen in Figures 7 and 8.

The total Coulomb energy of a charge configuration may be fit to $N^2/2$ with the deviation from this value giving a straight line on a log-log plot as shown in Figure 9 for N less than 40. In Figure 10 we show the deviation of the actual graph from a straight line on the log-log plot. (A more precise approximation for the total configuration energy is given below.) The highly symmetric cases (eg. $N=12$ and 32) generally have energies falling below that of their neighbors as indicated on this plot. Nevertheless, some highly symmetric cases fall well above the straight line of the log-log plot. This is illustrated by the cube, (a triangle in Figure 10) and the dodecahedron, whose point falls far above the graph of Figure 10. Neither of these polyhedra represents a global energy minimum.

In addition to the cases just mentioned, several additional local energy minima were found which were not global minima. For $N=94$, for example, there were three different configurations giving local minima (see Table I). Since the energy minima are very shallow, the different configurations only differ in the fifth or sixth significant figure of the energy.

GENERAL OBSERVATIONS

We have now examined a sufficient number of cases to warrant some general observations. Since most of these probably arise from the general character of spherical geometry, we expect that some of them will hold for other types of interactions on a sphere. The

observations follow:

1. No seven-fold or higher symmetries occur as minimal equilibrium configurations. (Only two cases with six-fold symmetry were observed.)
2. The total configuration is well approximated by the continuous charge energy, $N^2/2$. By considering the discrete nature of the charges we arrived at an even more accurate approximation given by

$$E = N(N-1)(1 - 1/\sqrt{N})/2$$

3. Nearest neighbor numbers approach six as N increases. For N=106 it averages to 5.887.
4. Rotational symmetry is more common than reflectional symmetry. Inversion symmetry which requires both C_2 and i is uncommon.
5. Different local minima for the same particle number occur.
6. Relative variation in individual particle energies decreases with N.

We expect to present data supporting observations 3., 6. and 2. elsewhere. Observation 1. is interesting to compare with three dimensional crystals where seven-fold symmetry is not possible. (According to standard theory, five-fold symmetry was "not possible" until recently.) It is easy to construct a seven-fold symmetric figure for N=9 on the sphere, but that is only a stationary point. The observation on nearest neighbor number suggests that six-fold symmetry will be the highest observed when N becomes large. The nearest neighbor number is expected to approach closer to six, the well-known exact close packing nearest number for the plane. It is not expected to reach six for finite N however as one must deform the sphere to map it onto the plane.

We point out that the coordinates and further details for configurations up to N=32 are available in our CRDEC report listed on the first page of this article.

REFERENCES

1. T.W. Melnyk, O. Knop, and W.R. Smith, Can. J. Chem. 53, 1745-1761 (1977).
2. B.W. Clare and D.L. Kepert, Proc Roy. Soc. Lond., A405, 329-344 (1986).

Optical Constants of Minerals, Liquids, and Metals from the
Millimeter to the Ultraviolet

R. J. Bell, R. W. Alexander, Jr., L. A. Newquist, R. Van Diver
M. A. Ordal, and L. L. Long

Physics Department, University of Missouri-Rolla
Rolla, MO 65401

and

Marvin R. Querry
Physics Department, University of Missouri-Kansas City
Kansas City, MO 64110

RECENT PUBLICATIONS, SUBMITTALS FOR PUBLICATION AND PRESTATIONS:

A) M. A. Ordal, R. J. Bell, R. W. Alexander, L. L. Long, and M. R. Querry,
"Optical Properties of Au, Ni, and Pb at Submillimeter Wavelengths", Appl. Opt.
26, 744 (1987).

B) L. L. Long, R. J. Bell, R. W. Alexander, Jr., and M. R. Querry,
"Preparation Dependent Properties of Pressed Pellets of Montmorillonite in the
Far Infrared," Appl. Opt. 26, 1372 (1987).

C) R. W. Alexander, Jr., R. W. Bell, L. L. Long, M. A. Ordal, L. Newquist,
and M. R. Querry, "Optical Properties of Powders, Liquids, and Metals at
Millimeter and Submillimeter Wavelengths," Proceedings of the 1986 CRDEC
Scientific Conference on Obscuration and Aerosol Research, R. W. Kohl, editor.

D) R. J. Bell, R. W. Alexander, Jr., Larry Newquist, and Mark A. Ordal,
"Methods for measuring surface impedances in the submillimeter and far
infrared," Proceedings of the 1986 CRDEC Scientific Conference on Obscuration
and Aerosol Research.

E) R. J. Bell, R. W. Alexander, Jr. and R. Van Diver, "A Novel
Interferometer for measurement of optical properties at millimeter wavelengths,"
Proceedings of the 1987 CRDEC Scientific Conference on Obscuration and Aerosol
Research [following paper.]

F) R. J. Bell, R. W. Alexander, Jr., L. A. Newquist, R. Van Diver, M. A.
Ordal, L.L. Long, and M. R. Querry, "Optical constants of minerals, liquids, and
metals from the millimeter to the ultraviolet," Proceedings of the 1987 CRDEC
Scientific Conference on Obscuration and Aerosol Research [this paper.]

G) M. A. Ordal, R. J. Bell, R. W. Alexander, Jr., and L. A. Newquist "The
optical properties of Al, Fe, Ti, Ta, W and Mo at submillimeter wavelengths,"
submitted to Applied Optics.

H) R. J. Bell, R. W. Alexander and M. R. Querry. "Optical constants of
Minerals and other materials from the millimeter to the ultraviolet," submitted
as a Chemical Research, Development and Engineering Center Contractor's Final
Report, DAAA 15-85-K-0004, June 1987.

ABSTRACT

This paper reports the continuation of previous work to measure the optical constants of natural minerals, liquids and metals from the millimeter to the ultraviolet. Included in this paper are data for gypsum, crystalline quartz, ZnO, DMMP, aluminum, titanium, tungsten, tantalum, molybdenum, vanadium, and stainless steel. Work was performed at two campuses of the University of Missouri--the Rolla Campus and the Kansas City Campus. The millimeter and submillimeter (far infrared) measurements were made on the Rolla Campus and the infrared, visible and ultraviolet measurements were made on the Kansas City Campus. This wide spectral range means that Kramers-Kronig analyses can be made with better precision than when reflectance data is available only over a limited spectral range.

The motive for the measurement of refractive indices of gypsum, both as a single crystal and as a powder, in the far and near infrared was to establish a material for use as a standard. This goal had originally been proposed in the Friday morning discussion section of this annual June CRDEC Conference at Aberdeen. In the same session, quartz was proposed as a standard for a hard material.

The work reported was performed under the U. S. Army CRDEC contract DAAA-15-85-K-0004 (M. Milham and J. Embury).

I. INTRODUCTION

The materials studied may be grouped into three classes defined by the techniques used to measure the refractive indices. These three classes are discussed below. Tables of optical constants for the materials measured have been entered into the CRDEC computer data bank.

NATURAL MINERALS: Measurements of the refractive indices of natural minerals were made by measuring the reflectance of either single crystals (where available) or of pressed powder pellets. The powders were pressed with no binder. A discussion of this method of sample preparation appears in our recent paper "Preparation dependent properties of pressed pellets of montmorillonite in the far infrared" in Applied Optics.¹ Of particular note is gypsum. At one of the Friday morning "Discussion Sessions" at the annual CRDEC Aberdeen Conference on Obscuration and Aerosol Science, it was decided that gypsum would make an excellent standard for the pressed powder technique for soft materials because it is available in single crystalline form and presses into high quality surface pellets. This project has been completed as a joint effort of the UMR and UMKC groups and a paper is being prepared for publication.² Oscillator model fits were made to the reflectance to provide a convenient parameterization of the optical constants. Quartz was discussed as a standard for hard materials.

METALS: The measurement of the optical constants of metals at long wavelenths at long wavelenths -- greater than 100 micrometers -- is very difficult because metals are so highly reflecting. Two techniques are available, stacked plane parallel waveguides³ and non-resonant cavities.^{4,5} Both techniques were tried in our laboratory and the non-resonant cavity method proved superior and required smaller amounts of sample. As part of our feasibility study of plane parallel waveguides, we measured the absorption coefficient of Teflon in the submillimeter.⁶ The results were published in Applied Optics. For the nonresonant cavity, we improved the analysis used to obtain the optical constants from the measurements.⁵ In order to obtain optical constants over a wide frequency range, our UMR data was combined with infrared, visible and UV measurements made at UMKC or with data from the literature. The resulting data sets covered a very wide frequency range allowing a good Kramers-Kronig analysis of the measured reflectances to give optical constants. The Drude model for metals was found to fit the data for many metals in the submillimeter frequency region.⁵

LIQUIDS: The UMKC laboratory is well-known for its measurements of the optical properties of liquids in the infrared and visible. These were made by measuring the reflectance of a horizontal pool of the sample liquid and the performing a Karmers-Kronig analysis to obtain refractive indices. This technique is difficult to extend to the far infrared and instead, we measure transmittances of liquids in cells with either TPX or silicon windows. Very few measuements of liquids have been made in the far infrared. DMMP proved to be very strongly absorbing in the submillimeter and a special cell was constructed to allow very thin samples to be measured.

II. NATURAL MINERALS:

GYP SUM: Gypsum was studied, at least in part, because it was decided at one of the Friday morning informal discussions at the annual CRDEC Aberdeen Conference on Obscuration and Aerosol Research that it would make a good standard for studies of natural minerals using the pressed powder technique. The pressed powder technique had originally been shown to be useful for natural

minerals by the UMKC laboratory. The conferees chose gypsum because it was soft, anisotropic, available as a single crystal and pressed to form pellets with very smooth surfaces. Gypsum has a Mohs' hardness of 2. We have just published a paper discussing the pressed pellet technique in the far infrared.¹ An important observation we made was that the pressed pellet has a surface skin that is denser than the average pellet density. This means that the optical constants measured from the pressed pellet are nearer the bulk values than the average density of the pellet would indicate. For gypsum, we also measured the optical constants for all three crystalline axes. A comparison of the pressed pellet optical constants with those of the single crystal allowed us to conclude that the pellet had an effective density 0.91 that of the single crystal and that all three crystalline orientations were represented equally on the sample surface. That is, the pressing operation resulted in little preferential orientation of the crystallites on the pellet surface. Gypsum was discussed in our paper in last year's proceedings of this conference.⁷ See that paper for spectra of the three orientations of a single crystal and for a powder sample. Here we give improved oscillator fit parameters for the three crystalline axes.

The reflectance was measured from 10 to 400 cm^{-1} at UMR and from 400 to 4,000 cm^{-1} at UMKC. The dispersion analysis was done on the combined data set. Table 1 gives the oscillator fit parameters for the three crystalline axes. The form of the dielectric constant used to fit the reflectance data was

$$\epsilon(\omega) = \epsilon_{\infty} + \sum_j \frac{A_j \omega_{0j}^2}{\omega_{0j}^2 - \omega^2 - i\gamma_j \omega} \quad (1)$$

In general, our experience was that the oscillator fit gave better results than a Kramers-Kronig analysis, especially in regions where k was small. However, a good oscillator fit required the reflectance to be measured over a wide frequency range, necessitating measurements at both the UMR and UMKC laboratories. An oscillator fit is often called a dispersive analysis.

ZINC OXIDE: Zinc oxide, or zincite is a very soft material (Moh hardness 4) that pressed into pellets under moderate pressure. These pellets had a smooth, mirror-like surface. Zinc oxide also crystallizes in the hexagonal system. The lengths of the a and c axes are 3.25 and 5.21 Å, respectively. It

is positive uniaxial with $n_o = 2.013$ and $n_e = 2.029$ at the sodium D line. Its specific gravity ranges from 5.64 to 6.68.

The measured reflectance in the 10 to 350 cm^{-1} range is shown in Fig. 1. Bear in mind that this material was not measured at shorter wavelengths. Such measurements will be needed if a Kramers-Kronig analysis to obtain optical constants is wanted.

QUARTZ: Quartz has a Mohs' hardness of 7. The Friday morning Aberdeen conference session decided it would be a good standard for hard materials. Reflectance data for quartz was available in the literature. Kramers-Kronig analysis was used to find n and k . For the spectral range from 20 to 370 cm^{-1} , the data of Russell and Bell was used.⁸ Spitzer and Kleinman's⁹ measurements were used from 370 to 1,600 cm^{-1} . Figure 2 shows n and k for the ordinary ray, while Fig. 3 shows the same for the extraordinary ray. The oscillator fit parameters are shown in Table 2 for the two crystalline axes.

III. METALS

The optical constants of metals are particularly difficult to measure in the far infrared and millimeter spectral regions because they are so highly reflecting. Two techniques have been employed which in effect make use of a large number of reflections. These are the plane parallel waveguide method (described in ref. 3) and the non-resonant cavity method (described in our recent paper, ref. 5). After considerable experimentation, we decided that the non-resonant cavity method is better in the 10 to 350 cm^{-1} spectral range. We developed an improved theory to analyze the non-resonant cavity measurements. This is described in our paper entitled "Optical properties of Au, Ni, and Pb at submillimeter wavelengths", published in Applied Optics.⁵

ALUMINUM: A polished polycrystalline aluminum sample was measured using the nonresonant cavity. The measured normalized surface impedance is shown in Fig. 4 as points with error bars. Literature values (from ref. 10) are shown at shorter wavelengths. The values of ϵ_1 and ϵ_2 obtained from combining our long wavelength measurements with data from ref. 10 and performing a Kramers-Kronig analysis are shown in Fig. 5. This data is being prepared for publication.¹¹

TITANIUM: A polished polycrystalline titanium sheet was measured using the nonresonant cavity. Our measured real part of the normalized surface impedance is shown in Fig. 6. Data at shorter wavelengths from ref. 10 are shown as the dot dash line. Figure 7 shows ϵ_1 and ϵ_2 derived from the Kramers-Kronig analysis of our data combined with the short wavelength data from ref. 10. This data is being prepared for publication.¹¹

TUNGSTEN: Polished polycrystalline tungsten sheet was measured with the nonresonant cavity. Figure 8 plots the measured normalized surface resistance with error bars and data from ref. 10 for shorter wavelengths (dash dot and dotted line). Once again the dielectric constant was obtained from a Kramers-Kronig analysis of our data and the ref. 10 data. The results are shown as the solid lines in Fig. 9. The dash dot and dotted lines show the ref. 10 only results. This data is being prepared for publication.¹¹

TANTULUM: A polished polycrystalline tantulum sheet was studied in the nonresonant cavity. Figure 10 shows the normalized surface impedance. Our nonresonant cavity data are plotted as the points with error bars and the data from ref. 10 is plotted as the dash dot line. Once again, our data was combined with the literature data and Kramers-Kronig analyzed to obtain ϵ_1 and ϵ_2 . The results are plotted in Fig. 11 as the solid lines. The dash dot line (almost on top of the solid line) is the literature values alone. This data is being prepared for publication.¹¹

MOLYBDENUM: A polished polycrystalline molybdenum sheet was studied in the nonresonant cavity. In Fig. 12 is plotted our measured points for the normalized surface resistance. The dash dot line shows the datum from ref. 10. Again, Kramers-Kronig analysis yielded ϵ_1 and ϵ_2 . They are plotted in Fig. 13.

STAINLESS STEEL: A sheet of polished stainless steel was measured in the nonresonant cavity. The measured real part of the surface resistance is plotted versus wavenumber in Fig. 14. We have not attempted a Kramers-Kronig analysis because of the lack of reflectance measurements at shorter wavelengths.

VANADIUM: A polished vanadium sheet was measured with the nonresonant cavity. The measured real part of the surface resistance is plotted versus wavenumber in Fig. 15. No Kramers-Kronig analysis was made because no data was

available at shorter wavelengths.

IV. LIQUIDS

The UMR group has measured the transmission spectra of two liquids, diesel fuel and dimethyl methyl phosphonate (DMMP). Measuring just the transmission spectrum allows a determination of only the absorption coefficient (or equivalently, the imaginary part of the refractive index, k). Difficulties with absorption in the vapor phase in our instrument have prevented reflection measurements such as have been made at shorter wavelengths by the UMKC laboratory. The spectra were measured for a empty cell and diesel fuel filled cells of varying thickness. The log of the ratio of the transmission of the filled cell to the empty cell is plotted as a function of the cell thickness. The slope of this line is the absorption coefficient, $\alpha(\omega)$. The imaginary part of the refractive index, k can be obtained from α by the relation $k = 2\pi\alpha/\lambda$.

DMMP: DMMP is a much more strongly absorbing material than is diesel fuel. As a result a cell that allowed much shorter path lengths was purchased. Experimentation showed that path lengths in the 25 to 100 micrometers range were required. This caused some difficulties in assuring proper cell loading. Silicon windows were used because DMMP was found to interact slowly with the TPX windows. The measured absorption coefficient versus wavenumber is shown in Fig. 16. Figure 17 presents our measured values of k versus wavenumber.

V. SUMMARY AND FUTURE WORK

Optical constants have been measured over a wide wavelength range and for a wide variety of materials. We plan to extend this work to the measurement of the temperature dependence of optical constants. Optical constants as a function of temperature are needed for calculations of radiation transport of laser beams through aerosols.

TABLE 1: OSCILLATOR FIT PARAMETERS FOR GYPSUM

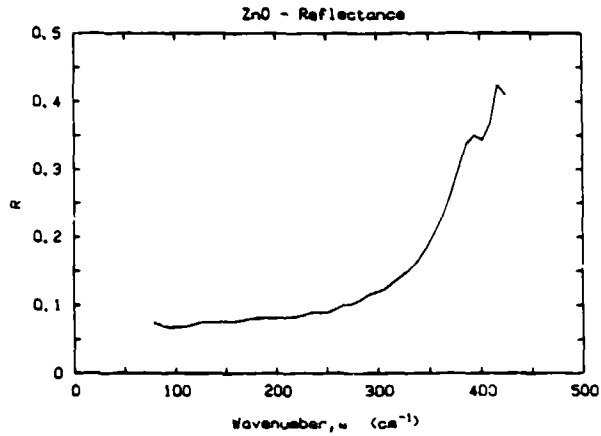
j	A _j	γ _j (cm ⁻¹)	ω _{0j} (cm ⁻¹)
X-axis			
1	0.2421	18.170	1135.1
2	0.0956	8.844	666.5
3	0.4265	91.616	447.6
4	1.0642	128.976	333.7
5	2.6027	97.859	210.4
6	1.1337	17.840	207.9
7	2.9672	8.064	117.6
ε _m = 2.625			
Y-axis			
1	0.0432	53.718	3530.1
2	0.0108	23.198	1684.3
3	0.0943	16.953	1131.2
4	0.1422	8.832	1121.0
5	0.1740	37.910	594.8
6	1.9611	103.472	545.6
7	0.1033	81.043	412.2
8	0.3038	30.126	302.0
9	0.5991	26.178	217.3
10	0.5799	7.367	191.3
11	1.2839	27.657	165.3
ε _m = 2.147			
Z-axis			
1	0.0379	55.059	3403.0
2	0.0166	10.335	1622.6
3	2.5834	13.904	1108.0
4	0.1623	23.915	592.8
5	0.1434	85.412	542.2
6	0.6468	42.698	295.8
7	1.1131	40.671	220.2
8	1.0278	19.926	175.1
ε _m = 2.162			

TABLE 2: OSCILLATOR FIT PARAMETERS FOR QUARTZ

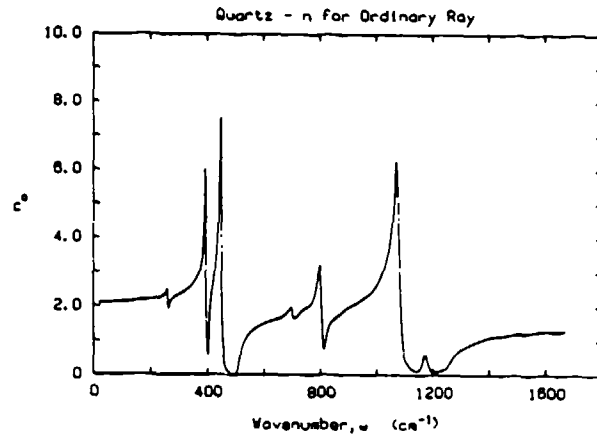
j	A _j	γ _j (cm ⁻¹)	ω _{0j} (cm ⁻¹)
Ordinary Ray			
1	0.009	134.	1227
2	0.010	6.98	1163
3	0.67	7.61	1072
4	0.11	7.17	797
5	0.018	8.36	697
6	0.852	4.05	450
7	0.36	2.76	394
8	0.050	7.36	263
9	0.0006	4.49	128.4
ε _∞ = 2.356			
Extraordinary Ray			
1	0.011	183.	1220
2	0.67	7.45	1080
3	0.10	7.78	778
4	0.006	21.56	539
5	0.05	7.13	509
6	0.699	4.56	495
7	0.72	5.10	364
ε _∞ = 2.383			

Sources of Quartz data were refs. 8 and 9.

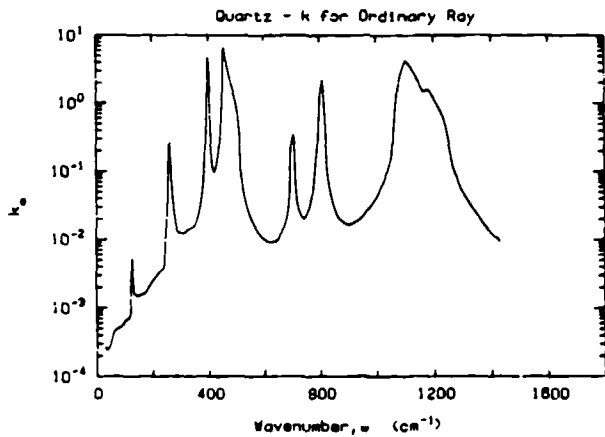
FIGURES



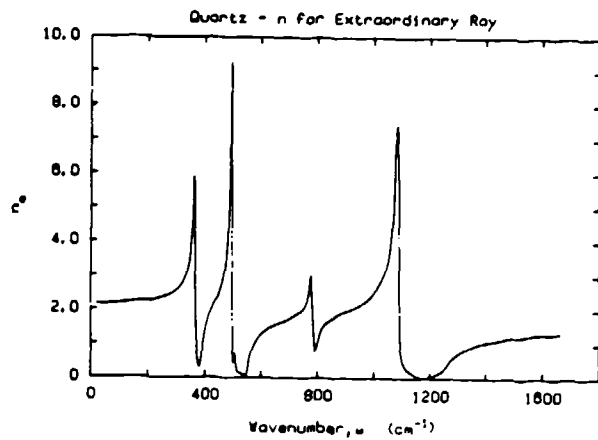
1. Reflectance of a Pressed Pellet of Zinc Oxide.



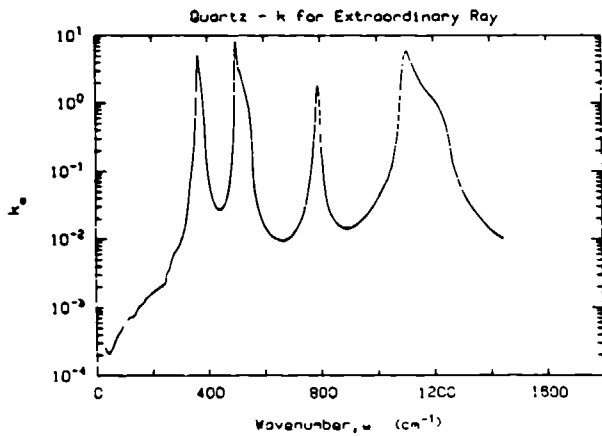
2a. Real Part of the Refractive Index, n' , for the Ordinary Ray of Quartz.



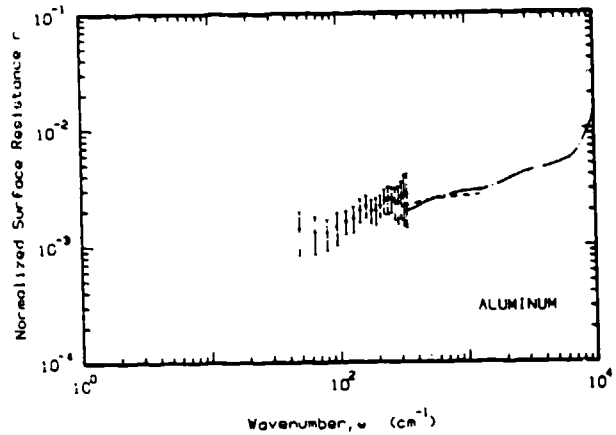
2b. Imaginary Part of the Refractive Index, k' , for the Ordinary Ray of Quartz.



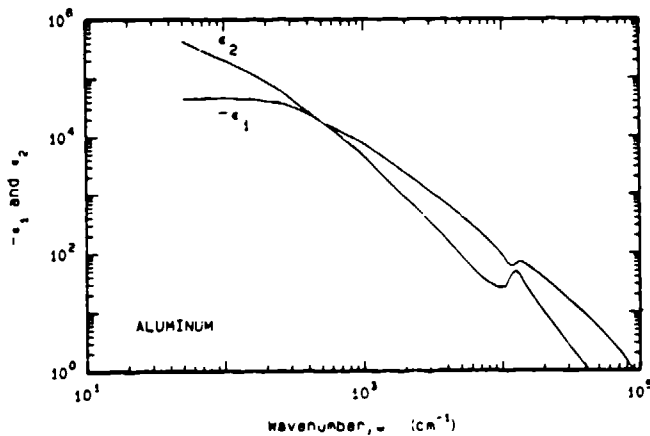
3a. Imaginary Part of the Refractive Index, n'' , for the Extraordinary Ray of Quartz.



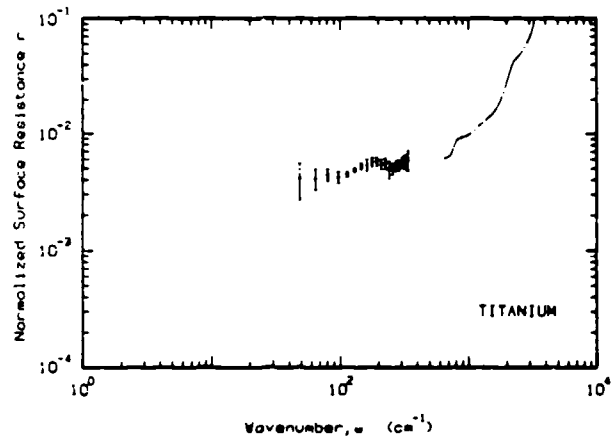
3b. Imaginary Part of the Refractive Index, k , for the Extraordinary Ray of Quartz.



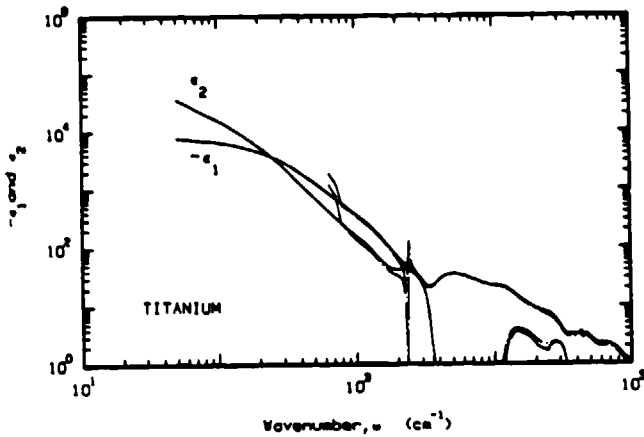
4. Real part of the Normalized Surface Resistance for Aluminum. Points with error bars are our nonresonant cavity measurements, while the dashed and dash dot curves for shorter wavelengths are from ref. 10.



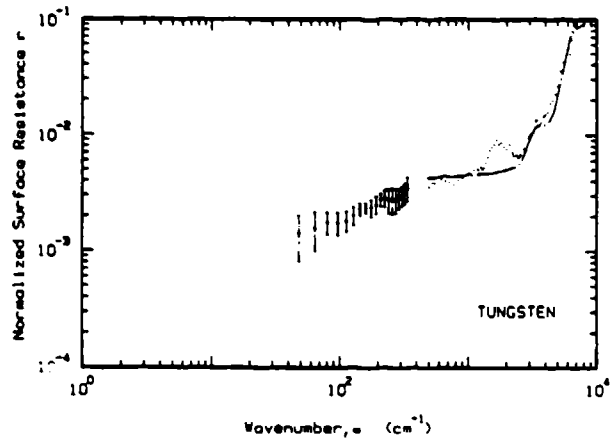
5. ϵ_1 and ϵ_2 for Aluminum. The solid curve was obtained from the Kramers-Kronig analysis of our resonant cavity data plus the short wavelength data of ref. 10.



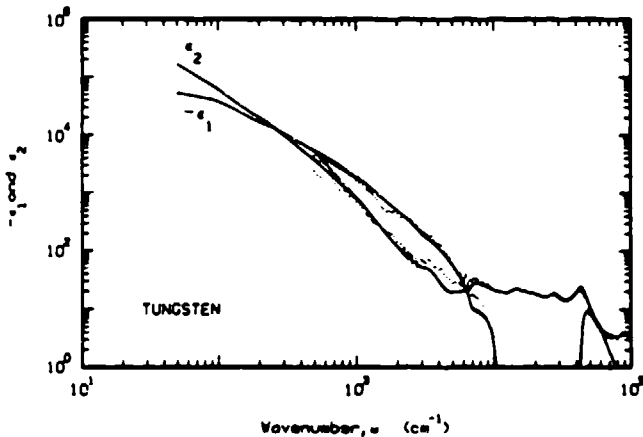
6. Real Part of the Normalized Surface Resistance of Titanium. Our nonresonant cavity measurements are shown as data points with error bars. Data from ref. 10 are shown as the dash dot line.



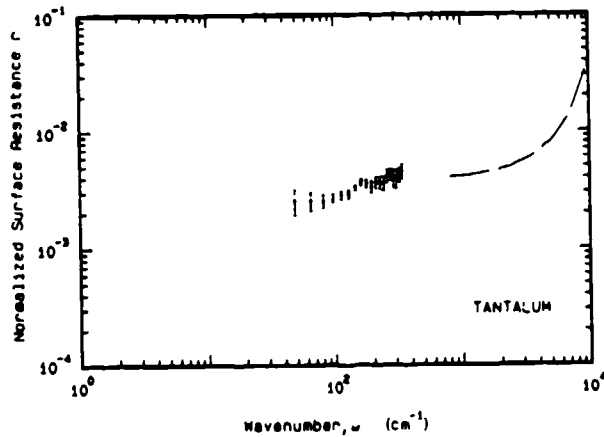
7. ϵ_1 and ϵ_2 for Titanium. The solid curves show the Kramers-Kronig results for a data set consisting of our long wavelength nonresonant cavity data and literature data (ref. 10). The dash dot curve is the ref. 10 data alone.



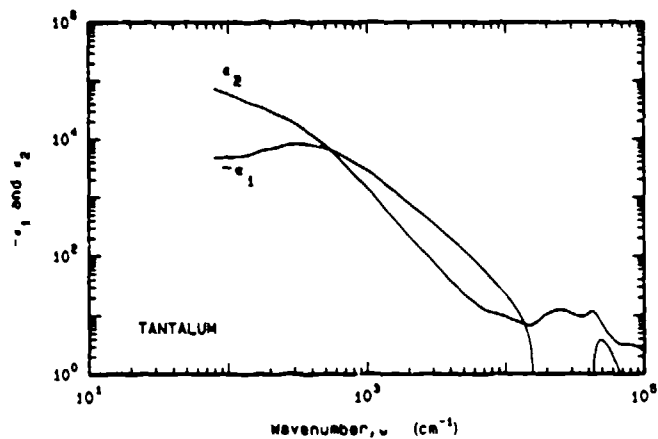
8. Real Part of the Normalized Surface Resistance for Tungsten. Our nonresonant cavity measurements are shown by the points with error bars. The shorter wavelength data shown by the dash dot and dotted lines are from ref. 10.



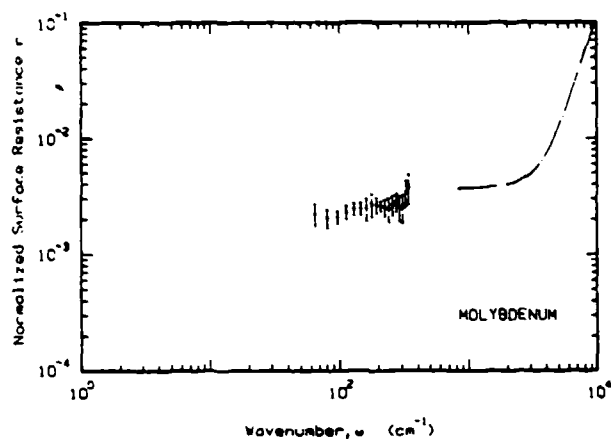
9. ϵ_1 and ϵ_2 for Tungsten. The solid curves are for our data plus the short wavelength data from ref. 10. The dotted and dash dot curves are the ref. 10 data alone.



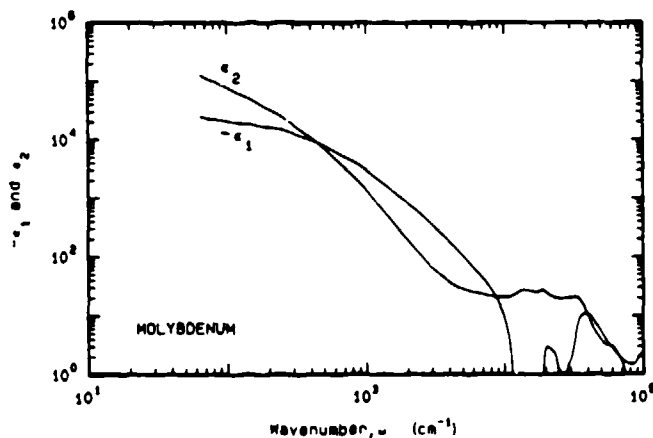
10. Real Part of the Normalized Surface Resistance for Tantalum. Our nonresonant cavity measurements are shown by the points with error bars. The shorter wavelength data shown by the dash dot line are from ref. 10.



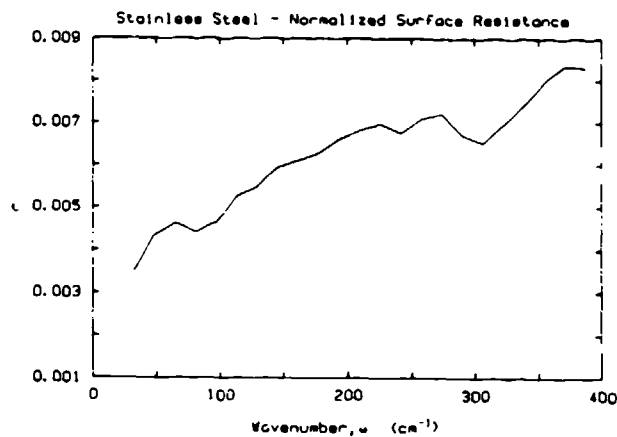
11. ϵ_1 and ϵ_2 for Tantalum. The solid curves are for our data plus the short wavelength data. The dash dot curves are the ref. 10 data alone.



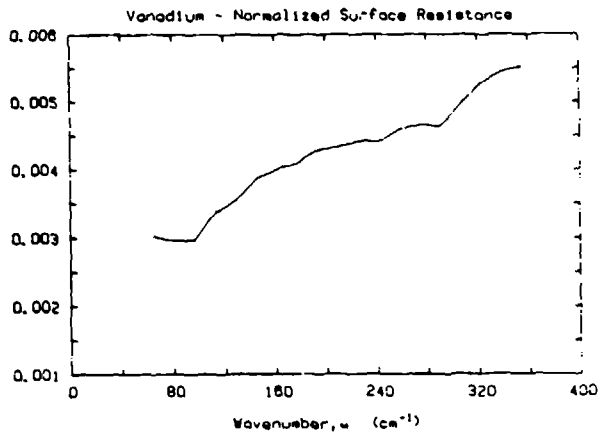
12. Real Part of the Normalized Surface Resistance for Molybdenum. Our nonresonant cavity measurements are shown by the points with error bars. The shorter wavelength data shown by the dash dot line are from ref. 10.



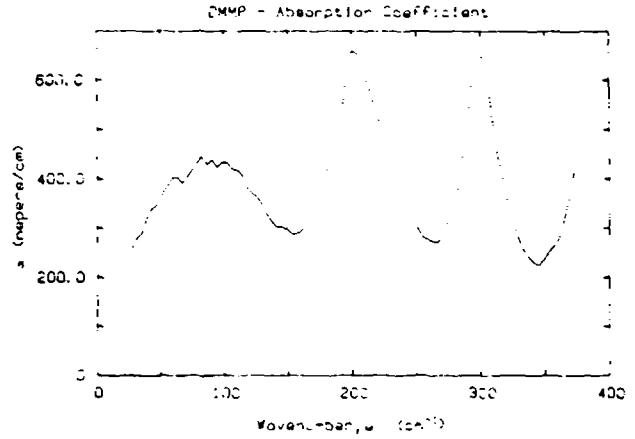
13. ϵ_1 and ϵ_2 for Molybdenum. The solid curves are for our data plus the short wavelength data. The dash dot curves are the ref. 10 data alone.



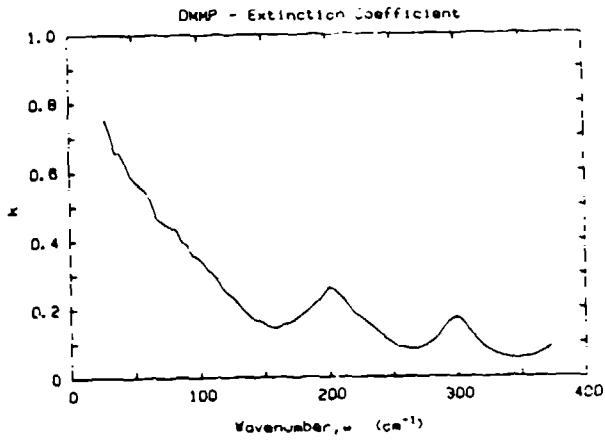
14. Real Part of the Normalized Surface Resistance, r , versus wavenumber for Stainless Steel.



15. Real Part of the Normalized Surface Resistance, r , versus wavenumber for Vanadium.



16. Absorption Coefficient, α , versus wavenumber for DMMP.



17. Imaginary Part of the Refractive Index versus wavenumber for DMMP.

VI. REFERENCES

1. Larry L. Long, R. J. Bell, R. W. Alexander, Jr., and Marvin R. Querry, "Preparation dependent properties of pressed pellets of montmorillonite in the far infrared", Appl. Opt. 26, 1372 (1987).
2. L. L. Long, R. J. Bell, R. W. Alexander, Jr., and M. R. Querry, "Optical Constants of Gypsum and Calcite Single Crystals and Powders", to be published.
3. G. Brandli and A. J. Sievers, "Absolute Measurement of the Far-Infrared Surface Resistance of Pb," Phys. Rev. B5, 3550 (1972).
4. M. A. Ordal, Robert J. Bell, R. W. Alexander, Jr., L. L. Long, and M. R. Querry, "Optical Properties of fourteen metals in the infrared and far infrared: Al, Co, Cu, Fe, Pb, Mo, Ni, Pd, Pt, Ag, Ti, V, and W", Appl. Opt. 24, 4493 (1985).
5. Mark A. Ordal, Robert J. Bell, Ralph W. Alexander, Jr., Larry L. Long, and Marvin R. Querry, "Optical Properties of Au, Ni, and Pb at submillimeter wavelengths", Appl. Opt., 26, 744 (1987).
6. Mark A. Ordal, Robert J. Bell, Ralph W. Alexander, Jr., and Raymond E. Paul, "Absorption Coefficient of Dupont Teflon FEP in the 20 - 130 wave-number range, Appl. Opt. 24, 2746 (1985).
7. R. W. Alexander, Jr., R. W. Bell, L. L. Long, M. A. Ordal, L. Newquist, and M. R. Querry, "Optical Properties of Powders, Liquids, and Metals at Millimeter and Submillimeter Wavelengths," Proceedings of the 1986 CRDEC Scientific Conference on Obscuration and Aerosol Research, R. W. Kohl, editor.
8. E. E. Russell and E. E. Bell, J. Opt. Soc. Am. 57, 341 (1967).
9. W. G. Spitzer and D. A. Kleinman, Phys. Rev. 121, 1324 (1961).
10. J. H. Weaver, C. Krafka, D. W. Lynch, and D. D. Koch, Physics Data, Optical Properties of Metals, Part I: The Transition Metals and Part II: The Noble Metals, Aluminum, Scandium, Yttrium, The Lanthanides, and the Actinides, (Fachinformationszentrum, Karlsruhe, Federal Republic of Germany, 1981).
11. M. A. Ordal, R. J. Bell, R. W. Alexander, Jr., and L. A. Newquist "The optical properties of Al, Fe, Ti, Ta, W and Mo at submillimeter wavelengths," submitted to Appl. Opt.

Blank

A Novel Interferometer for Measurements of
Optical Properties at Millimeter Wavelengths

R. J. Bell, R. W. Alexander, Jr., R. Van Diver,
S. Fry, M. A. Ordal, L. L. Long, and L. Newquist

Physics Department, University of Missouri-Rolla
Rolla, MO 65401

RECENT PUBLICATIONS, SUBMITTALS FOR PUBLICATION AND PRESENTATIONS:

A) M. A. Ordal, R. J. Bell, R. W. Alexander, L. L. Long, and M. R. Querry, "Optical Properties of Au, Ni, and Pb at Submillimeter Wavelengths", Appl. Opt. 26, 744 (1987).

B) L. L. Long, R. J. Bell, R. W. Alexander, Jr., and M. R. Querry, "Preparation Dependent Properties of Pressed Pellets of Montmorillonite in the Far Infrared," Appl. Opt. 26, 1372 (1987).

C) R. W. Alexander, Jr., R. W. Bell, L. L. Long, M. A. Ordal, L. Newquist, and M. R. Querry, "Optical Properties of Powders, Liquids, and Metals at Millimeter and Submillimeter Wavelengths," Proceedings of the 1986 CRDEC Scientific Conference on Obscuration and Aerosol Research, R. W. Kohl, editor.

D) R. J. Bell, R. W. Alexander, Jr., Larry Newquist, and Mark A. Ordal, "Methods for measuring surface impedances in the submillimeter and far infrared," Proceedings of the 1986 CRDEC Scientific Conference on Obscuration and Aerosol Research.

E) R. J. Bell, R. W. Alexander, Jr., S. Fry, R. Van Diver, M. A. Ordal, L. L. Long, and L. Newquist, "A Novel Interferometer for measurement of optical properties at millimeter wavelengths," Proceedings of the 1987 CRDEC Scientific Conference on Obscuration and Aerosol Research (this paper).

F) R. J. Bell, R. W. Alexander, Jr., L. A. Newquist, R. Van Diver, M. A. Ordal, L. L. Long, and M. R. Querry, "Optical constants of minerals, liquids, and metals from the millimeter to the ultraviolet," Proceedings of the 1987 CRDEC Scientific Conference on Obscuration and Aerosol Research (preceding paper).

G) M. A. Ordal, R. J. Bell, R. W. Alexander, Jr., and L. A. Newquist "The optical properties of Al, Fe, Ti, Ta, W and Mo at submillimeter wavelengths," submitted to Applied Optics.

H) R. J. Bell, R. W. Alexander and M. R. Querry, "Optical constants of Minerals and other materials from the millimeter to the ultraviolet," submitted as a Chemical Research, Development and Engineering Center Contractor's Final Report, DAAA 15-85-K-0004, June 1987.

ABSTRACT

We have developed a new type of interferometer to measure the complex reflectivity of graphite samples at millimeter wavelengths. Since graphite at these frequencies has reflectances of the order of 90-97 percent usual techniques do not work. Also, to obtain reasonable complex dielectric functions one has to control reflectances to accuracies of the order of ± 0.3 percent or better. This is achieved with wave front division in this novel asymmetric

interferometer. We obtain reflectances $\approx 0.939 \pm 0.3$ and phase angles $\approx (-180^\circ + 0.2^\circ)$ for pressed pellets of Dixon 200-10 graphite at $\omega = 1.1 \text{ cm}^{-1}$ (33 GHz). The instrument is still under development.

I. INTRODUCTION

Graphite's high reflectances makes it necessary to perform very careful measurements in order to obtain the complex reflectivity, r . Slight errors (± 1 percent) in the measurements can cause the real part of the dielectric constant, ϵ_1 , to shift by factors of two while the imaginary part of the dielectric function, ϵ_2 , can shift an order of magnitude. Until recently we could only obtain the complex dielectric function found by Kramers-Kronig analysis of reflectance measurements from the UV continuously to $\omega = 1.1 \text{ cm}^{-1}$. With this new instrument, we obtain ϵ_1 , and ϵ_2 without the extremely broad band (5 decades in frequency) reflectance measurements. In our interferometer we use computer fits of the entire data scan to obtain r . This requires a theoretical analysis of the instrument in its entirety. With the sample (reference material) in one arm of the interferometer we are able to obtain the complex r . Homodyning is achieved at the detector by mixing the radiation from the sample with that straight from the source. That is, mix the weak radiation from the sample with the strong radiation at the detector directly from the source producing increased sensitivity to the sample reflectivity.

II. THE OPTICAL DESIGN

In Fig. 1 one has an optical diagram of the asymmetric instrument.¹ Beam 0 from the source to the detector, beam 2 goes from the source to the sample, beam 3 is a diffracted beam from the sample to the pick-up spherical mirror and beam 4 is a continuation of the diffracted beam to the detector for homodyning. The process can be described for the fields as

$$E = E_1 + E_2 \quad (1)$$

and

$$EE^* = (E_1 + E_2)(E_1^* + E_2^*) = E_1E_1^* + E_2E_2^* + 2\text{Re}(E_1^*E_2) \quad (2)$$

where E_1 goes directly to the detector and E_2 is via the sample. With a chopper one can modulate E_2 in front of the sample and not E_1 resulting in discrimination against the strong $E_1E_1^*$ term leaving

$$EE^* = E_2E_2^* + 2\text{Re}(E_1^*E_2) \quad (3)$$

where $E_2 E_2^*$ is very weak while $2\text{Re}(E_1^* E_2)$ dominates.

For Fraunhofer diffraction the optical components are separated by about 50λ and the distances are about 40 sample diameters. For these studies $d_1=35$ cm, $d_2=49$ cm, $d_3=62$ cm, $d_4=50$ cm, $\alpha=6.05^\circ$ and $\bar{\alpha} \approx 8.8^\circ$. The background radiation is controlled by first moving the sample in a continuous drive resulting in a cosine oscillation with respect to sample position and second by eliminating back reflection (including those involving SEW, surface electromagnetic waves) with a special cone (the "stealth" cone) behind the sample. For the SEW on the cone, we currently have students deriving the expected SEW responses of the cone to incident radiation.

III. THE OPERATION AND SELF-CALIBRATION

Though we have derived the detailed equations of the instrument, one has only to look at the simple theoretical conclusions to see how it works. The intensities after mixing of the two coherent fields are given by

$$I = A \left[1 - B \frac{x}{2} \right] + C \left[1 - D \frac{x}{2} \right] \cos \left[\frac{E x}{2} + F \right] \quad (4)$$

where $(x/2)$ is the distance the sample is moved from the beginning position in a scan. The first and weak term is from $E_2 E_2^*$ and, of course, the second term is from the sample with C being the amplitude proportional to the sample reflectivity amplitude, r_0 . The reflection phase angle is in F . We use the Aystant (McMillian and Company) program to obtain A , B , D , E , & F for a given scan. By scanning with a reference material (Ag or brass) we are able to obtain the sample reflectivity amplitude from

$$r_{OS} = \left[\frac{C_{\text{sample}}}{C_{\text{reference}}} \right] r_{OR} \quad (5)$$

Also, we obtain the phase angle for the sample by subtracting F 's while correcting for sample-reference thicknesses. Finally, we correct for small angular effects and non-normal incidence to obtain the sample's phase angles and complex dielectric functions:

$$Q_s + \pi = J_{OS} = \tan^{-1} \left\{ \frac{\tan (F_s - F_r) + J_r + J_t - 4\pi\omega[\Delta d(o)] \cos \bar{\beta}}{\cos \bar{\beta}} \right\} \quad (6)$$

$$\epsilon_{1s} \approx \frac{16 \left[A_{Os}^2 - 4R_{Os} \sin^2 J_s \right]}{A_{Os}^4 \left[1 + \frac{A_{Os}}{2} + 4 \frac{J_{Os}^2}{A_{Os}^2} \right]^2}, \quad (7)$$

and

$$\epsilon_{2s} \approx \frac{64 \sqrt{R_{Os}} \sin J_{Os}}{A_{Os}^3 \left[1 + \frac{A_{Os}}{2} + \frac{4 J_{Os}^2}{A_{Os}^2} \right]^2}. \quad (8)$$

where J_r is for the reference material, J_t is for the side of the head, $[\Delta d(0)]$ is for the difference between the sample and reference thicknesses, $\bar{\alpha}$ is the effective angle of incidence of the sample (integrated over sample and detector horns), and $A_{Os} = 1 - R_{Os}$ for $R_{Os} = r_{Os}^2 =$ reflectance. With our values and $\bar{\alpha} \approx 8.8^\circ$, currently we have $\epsilon_1 \approx 3 \times 10^3$ and $\epsilon_2 \approx 1 \times 10^3$ for $R \approx 0.939$ and $J_s \approx 2^\circ$ for Dixon 200-10 pressed (10 tons) graphite pellets which were about 1.260 cm in diameter. See Fig. 3 for ϵ_1 and ϵ_2 .

To see how well the system performs note Fig. 4 in which C of Eq. (4) is plotted vs. $\frac{x}{2}$ the distance the sample is moved. The "asystant" fit was with Eq. (4) and had an overall correlation coefficient of 4 nines or an F test of 2×10^5 .

The measured decrease of intensity vs. distance from the source horn (measured using a Goly cell detector of small window design $\frac{3}{16}$ inch) was I/R^2 , the angular distribution of radiation was Gaussian, the diameter correction was for that of a circular aperture in diffraction theory and the head thickness correction behaved as $(1 + \text{const } L)$ where L is 1/2 the thickness of the sample.² All of this will be reported in more detail at a later date; at which time the diffraction theory will be used as a test of the measuring accuracies of the instrument.

Finally, the sensitivity of ϵ_1 and ϵ_2 to the reflection phase angle of the sample (R_{Os} fixed at 0.9479) is shown in Fig. 5. It illustrates the care one has to exercise in the measurement of $J_s(0) \approx 0.2^\circ$.

IV. SUMMARY AND FUTURE WORK

We consider this a preliminary report on the instrument and its ability to measure the complex reflectivity of highly reflecting graphite samples. At $\omega = 1.1 \text{ cm}^{-1}$ we have that $R_{0s} = 0.939$ and $J_s = 0.2^\circ$ with $\epsilon_1 \approx 3 \times 10^3$ and $\epsilon_2 \approx 1 \times 10^3$. We're currently improving the calibration accuracies and changing modulator techniques.

V. REFERENCES

1. R. J. Bell (with R. W. Alexander, Jr.), Introductory Fourier Transform Spectroscopy (Academic Press, NY, 1972).
2. C. F. Bohren and D. R. Huffman, Absorption and Scattering of Light by Small Particles (J. Wiley & Sons, NY, 1983).

FIGURES

HOMODYNING SPECTROMETER

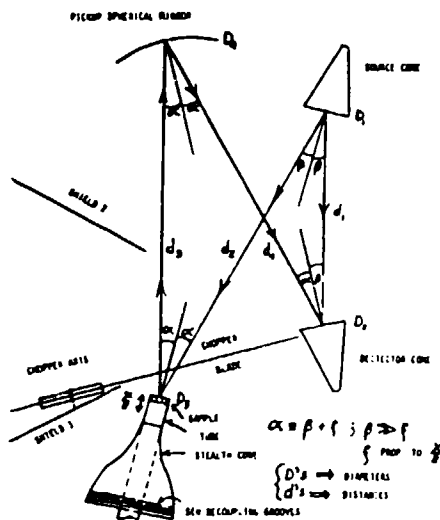


Figure 1: Optical Diagram of the UMR homodyning, asymmetric interferometer using division of the wave front.

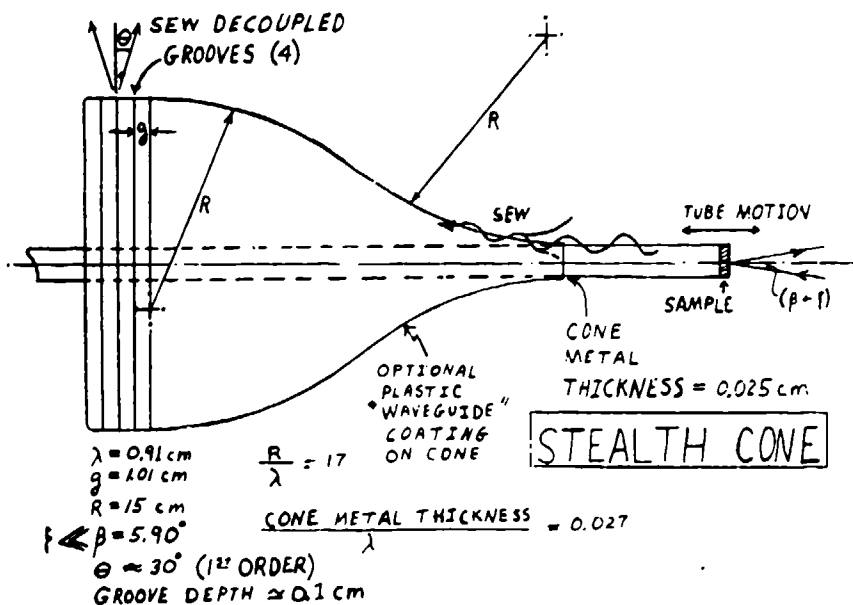


Figure 2: Diagram of the antireflecting background cone.

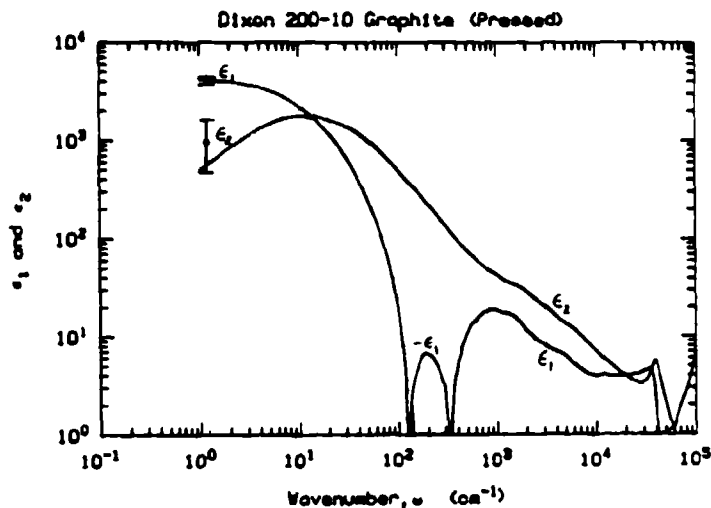


Figure 3: Real and imaginary parts of the dielectric function of a pressed pellet of Dixon 200-10 graphite. The solid lines are from Kramers-Kronig analysis and the data points are from the homodyning interferometer.

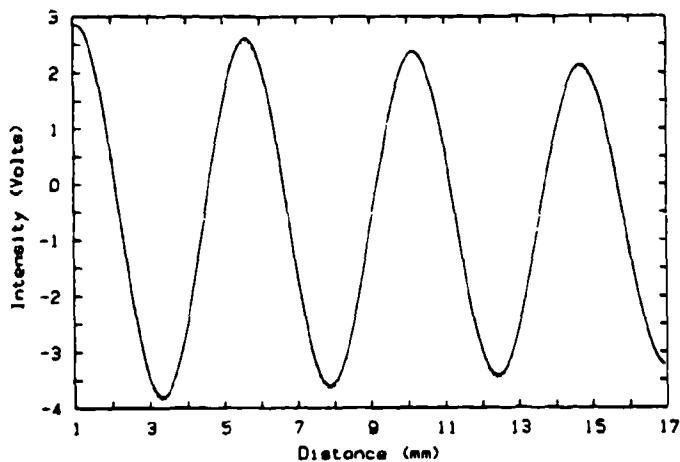


Figure 4: Intensity $RE(E_1^* E_2)$ vs. $x/2$ for the interferometer. The dots are the data and the solid line is the "asystant" program's fit of the data using Eq. (4). The correlation coefficient was 0.9999.

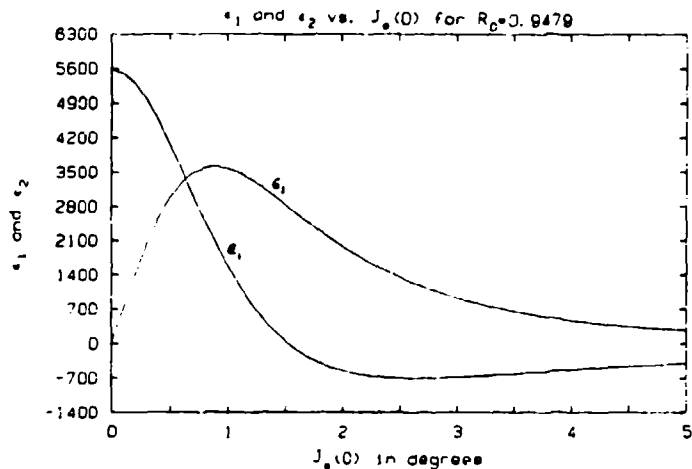


Figure 5. Theoretical plot of ϵ_1 and ϵ_2 vs. J_B for a fixed reflectance of 0.9479 for the pressed Dixon 200-10 graphite samples.

Blank

SENSITIVITY OF FRACTAL ANALYSIS FOR DESCRIBING PARTICLE SHAPES

P. A. Lawless
Research Triangle Institute
Research Triangle Park, North Carolina 27709

M-T. Hsieh and P. C. Reist
University of North Carolina
Chapel Hill, North Carolina 27514

RECENT PUBLICATIONS, SUBMITTALS FOR PUBLICATION AND PRESENTATIONS:

- A) P. C. Reist, M-T. Hsieh, and P. A. Lawless, "Fractal Analysis of Irregularly Shaped Aerosol Particles Grown at Reduced Pressures," submitted to J. Aerosol Science, 1987.
- B) P. A. Lawless, P. C. Reist, and M-T. Hsieh, "Aerosol Formation with Exploding-Wire Generators," presented at the 1986 CRDEC Scientific Conference on Obscuration and Aerosol Research.
- C) Ming-Ta Hsieh, P. C. Reist, and P. A. Lawless, "Analysis of Particle Agglomeration Mechanisms with Fractal Geometry," presented at the 1986 CRDEC Scientific Conference on Obscuration and Aerosol Research.
- D) P. A. Lawless, A. S. Damle, and P. C. Reist, "An Experimental Study of Gas Pressure Effects on the Coagulation Growth of Metallic Aerosols," presented at the 1985 CRDEC Scientific Conference on Obscuration and Aerosol Research.

ABSTRACT

This paper was presented at the poster session of the 1987 CRDEC conference for the purpose of showing the application of fractal analysis to images of real aerosol particles and determining the ability of the analysis to pick out characteristic details of the aerosol growth processes.

INTRODUCTION

Irregularly shaped aerosol particles (such as flocs, fumes, and some mineral compounds) have random or pseudo-random structures which defy analytical description, much less systematic analysis. In a study of the growth of metallic aerosol particles at reduced pressures, we found such irregular particles in abundance. Even though the primary aerosol formed as near-monodisperse spheres of approximately the same diameter at all pressures, subsequent coagulation produced structures with different morphologies, having significant differences in the shapes of the particles formed at different pressures. Although the differences were subtle, they were distinctive. In an attempt to find adequate descriptors for these differences, we turned to the field of fractal geometry.

Theoretical models of particle conglomerates produced by various artificial growth laws delineated three basic types of growth, and each has a characteristic fractal dimension associated with it. To describe these growth laws, a cluster is assumed to be a large agglomerate made up of many individual subunits, called particles. Often a particle is nothing more than a single spherical aerosol, but it could be a cluster of aerosols so much smaller than other clusters that it exhibits a more particle-like behavior.

If growth occurs from particles approaching clusters on linear or ballistic trajectories, the resulting cluster forms in a very dense fashion, and the fractal dimension for ballistic growth is 1.95 (in two dimensions). The same structure would occur for a large scavenging cluster dropping through a cloud of smaller particles.

If growth occurs from particles approaching a cluster with a Brownian or random walk, penetration of the particle all the way to the interior of the cluster is unlikely, leading to a less dense particle with a fractal dimension of $5/3$ (theoretical result) or 1.73 (statistical model result).

If growth occurs from clusters approaching clusters, the agglomerate shows very little interpenetration of the two clusters, whether a Brownian or a ballistic trajectory is used. The resulting structure is even less dense, and fractal dimensions characteristic of it are 1.44 for the Brownian trajectory or 1.50 for the ballistic trajectory. These are summarized in Table I.

TABLE I. FRACTAL DIMENSIONS OBTAINED FROM TWO-DIMENSIONAL AGGREGATION MODELS

Model	D
Linear trajectory, particle-cluster	1.95 ± 0.002 [1]
Brownian trajectory, particle-cluster	$5/3$ [4]
Brownian trajectory, particle-cluster	1.73 ± 0.06 [1,2]
Linear trajectory, cluster-cluster	1.50 ± 0.05 [3]
Brownian trajectory, cluster-cluster	1.44 ± 0.02 [3]

It is to be hoped that particles grown under Brownian cluster-cluster aggregation conditions would all have fractal dimensions close to 1.44, or at least be easily distinguishable from particles grown in the Brownian particle-cluster mode. Furthermore, since our fractal analysis has to be performed on photomicrographs, it is to be hoped that the technique is insensitive to orientation effects of the three-dimensional particle on the microscope substrate. The work reported here addresses these questions.

FRACTAL ANALYSIS OF IMAGES

In the course of the investigation, we have settled upon two methods for the fractal analysis: the circular dilation method and the correlation method. The original dilation method was developed by Forrest and Witten [5], using square boxes. In this method a digitized electron micrograph is represented by values corresponding to the presence or absence of one point of a particle. A smallest box is picked with its geometric center near the center of mass of particle; then, a series of nested squares of increasing sizes is placed around it, and the number of "on" pixels in each square is

counted. For a fractal particle, this analysis yields a power-law relationship between the length of the side of the square, B, and the number of pixels, N, within it (i.e., $N(B) \sim B^D$, where D is the fractal dimension). Forrest and Witten also found that results were most reproducible when squares were chosen so that the center of mass of the particle coincided with their geometric centers.

One problem with this implementation is that it mixes information in the picture over a range of scales. The use of the square dilation blends information from pixels located at distance B/2 from the center with that from pixels located at 1.414 B/2 and the whole range in between. This makes comparison with other methods of calculating fractal dimension difficult and obscures some of the information in the picture. This difficulty is overcome using the "circular dilation" method.

In the circular dilation method, circles are used instead of boxes, and the pixels are counted as a function of the circle radius, R. The fractal dimension is computed in terms of the power-law dependence of pixels with radius: $N(R) \sim R^D$. The circular dilation is more difficult to implement as a computer program, but the results are superior.

An important limitation of both dilation methods is that the small scale structure is examined only in the vicinity of the center of dilation. It may be important to perform limited range dilations around other centers to obtain a truly representative picture of the structure. The use of a single expansion center also tends to introduce irregularities in the N(R) curve as various structures in the image are encompassed by the boxes or circles. These appear to be artifacts of the dilation and can be eliminated by averaging several different N(R) curves obtained from small displacements of the expansion center.

An analysis technique that overcomes these problems with the dilation methods is the use of the point-point density correlation function. [7] This function is the normalized summation of the product of pixel densities over all points as a function of a fixed distance between points:

$$C(l) = N^{-1} \sum_{\vec{r}} d(\vec{r}) d(\vec{r} - \vec{R}), \quad (1)$$

where: C = the correlation function,

\vec{R} = the separation distance,

\vec{r} = a position vector, and

d = the density of pixels at any position (0 or 1 for black/white images).

The correlation function determines the fractal dimension D through the relation:

$$C(R) = R^{D-d}, \quad (2)$$

where d is the space dimension ($d = 2$ for plane figures). The advantage of the correlation method is that it examines all points of the image at all scales of interest, automatically providing an average that can be achieved only with great effort using the dilation methods. The correlation function can be computed directly for the relatively small number of pixels involved in the images on an IBM PC computer. For larger numbers of pixels, fast Fourier transform (FFT) methods are more efficient.

Since the correlation function usually has a dependence on R of 0 to -1 , corresponding to fractal dimensions between 2 and 1, it is a more slowly varying function than the dilation mass fractal function, which would vary as R^2 to R over the same range of fractal dimension. It is convenient to compute a pseudo-correlation function from the mass fractal by dividing the mass fractal by R^2 for the box dilation or by πR^2 for the circular dilation. The resulting correlation function and pseudo-correlation functions can then be compared over a large range of R on a common basis.

SENSITIVITY ANALYSIS PROCEDURES

The comparisons of analysis methods and the sensitivity of the methods were approached in a threefold way. First, the fractal dimensions of a set of aerosol particles grown under the same conditions and sampled at the same time were individually measured. Second, tests of the ability of fractal analysis to recover a predetermined mass distribution function were made. And third, the dependence of the recovered fractal dimension on particle orientation was determined. In all situations, the circular dilation and correlation analyses were performed for intercomparison of their respective results; earlier analyses had shown that these two methods were in best agreement of all methods tested.

The reasons for this program follow. The method for measurement of fractal dimension in the primary study uses electron micrographs of the particles generated. However, the real particles are three dimensional, from evidence of low angle micrographs or stereo-pairs. Weitz and Huang [6] have demonstrated that as long as the particles are sparse enough, the two-dimensional projection of a three-dimensional particle will have the same fractal characteristics as the particle itself. This also means that the tilt angle of the SEM stage need not be corrected for, since all projections of a particle should be equivalent in the fractal sense. These conclusions are difficult to test without access to three-dimensional particles that can be rotated and projected in various ways, and we have chosen to use computer-generated particles for the tests.

RESULTS OF MEASUREMENTS COLLECTIONS OF REAL PARTICLES

Measurements of fractal dimension of individual particles were conducted on low magnification electron micrographs of filter samples taken from particles grown at 1-atmosphere and 0.1-atmosphere pressures. Prior analyses of individual particles grown under the same conditions had strongly

suggested that cluster-cluster agglomeration of the particles was the dominant growth mechanism, with fractal dimensions of about 1.45. The low magnification pictures (2000X to 4000X) sacrificed some small-scale detail but, on the whole, gave results similar to the ones taken at higher magnifications (20000X). The pixel sizes were appropriately scaled to give real physical sizes to the images.

Table II compares the fractal dimensions of the particle images on the two filter samples. The standard deviation of the average is given after the average; the high and low measured fractal dimensions are also given. The smallest particle measured at 0.1 atmosphere had a Feret's diameter of 1.7 micrometers and the largest had a Feret's diameter of 5.4 micrometers. The corresponding values at 1.0 atmosphere were 2.3 and 10.1 micrometers.

TABLE II. FRACTAL DIMENSIONS FOR PARTICLE ENSEMBLES

Pressure (atm)	Number of particles	D_c	Range (low, high)	D_d	Range (low, high)
0.1	10	1.35 \pm 0.06	1.25, 1.44	1.37 \pm 0.09	0.99, 1.37
1.0	15	1.40 \pm 0.15	1.10, 1.69	1.36 \pm 0.15	1.07, 1.70

From this table and the individually calculated values of fractal dimension, we can conclude that the circular dilation and the correlation methods are in good agreement with one another, both in mean and in individual values. The mean values of both ensembles are very consistent with a cluster-cluster growth hypothesis, but both ensembles show particles whose fractal dimensions are significantly less than the 1.44 value for that process. The 1.0-atmosphere group also shows one particle whose fractal dimension is characteristic of the particle-cluster growth mechanism.

The sampling of particles is admittedly limited; because of this, it is difficult to choose between the explanations that these numerical differences are based on real differences in the growth mechanisms or that they merely represent statistical "noise" in the analysis. It would be expected that a growing system of agglomerates would pass through a particle-cluster stage until all small particles are removed and then be in the cluster-cluster stage. It is not surprising to see evidence of this in the micrograph, but it is not conclusive.

RESULTS FOR RECOVERY OF MASS DISTRIBUTIONS

The second part of the testing procedure was to generate artificial mass distributions of point particles according to a power law and determine whether or not the fractal analysis could recover the original power law. Initially, this was to be a test of the accuracy of the hypothesis that the conclusion of Weitz and Huang [6] would apply to particles of this type.

The mass distributions were generated in a series of concentric shells. The smallest shell consisted of a single particle at the origin of the x, y, and z axes. In each successively larger cell, a number of point particles was distributed in a uniform random fashion over the surface of the shell, with the number determined to correspond to a given power law:

$$N(r) \sim r^g, \quad (3)$$

where g is the generating exponent. The total number of particles in any one distribution ranged from 250 to 350. The random distributions on the surface of the sphere were achieved by using polar coordinates for the placement process: the azimuthal angle was uniformly distributed over an angular range of 0 to 2π , while the polar angle was distributed as a sine function over the angular range of 0 to π . The corresponding x, y, and z coordinates were stored for each of the point particles. Although this method of generation did not guarantee that the center of mass remained at the origin of the coordinate system, in practice it was always within about half-a-shell thickness of the origin in the cases where it was computed.

The analysis program contained a module to rotate three-dimensional point coordinates through any observing angle and project the resulting distribution onto a plane. The size of particles associated with each coordinate could be predetermined. For this part of the testing, the sizes were kept deliberately small, with a radius of 2 pixels, to reduce overlap effects during the projection. The clusters are shown in Figure 1.

The generating exponents were varied from 0.1 to 20 for the tests. These exponents gave mass distributions highly concentrated near the coordinate origin (for $g \ll 1$), nearly uniformly concentrated throughout the volume ($g = 3$) and highly concentrated in the outermost shell ($g \gg 3$). The effects of the different generating exponents can be seen to some extent in Figure 1 under careful examination. The dilation (pseudo-correlation) and correlation functions are also shown next to each distribution. The correlation functions (open diamonds) show no discernable differences over the full range of generating exponents. The differences that do exist are mainly because of the changing number of points in the distributions, which had to be adjusted to keep some of the analysis arrays within bounds. The pseudo-correlation functions do show some distinct differences as the generating exponent increases, but there is no easily defined slope to the function that can be related to the generating exponent.

The only conclusion we can draw from this test is that too much information has been lost in projecting the three-dimensional distribution onto the plane for the fractal analysis to recover the generating function. It is possible that there is additional information in the correlation and

pseudo-correlation functions, in terms of second or third derivatives, which can be used to recover the generating function. However, those derivatives have not been considered an important part of the fractal analysis before now.

RESULTS OF ORIENTATION EFFECTS

To test for orientation effects, a simple theoretical particle was constructed. This particle was generated in a manner similar to the mass distributions but with several constraints. The radial mass distribution was determined in the same way as before. The azimuthal distribution of mass was confined to five planes spaced equally around the pole of the particle. This was done to help define the center of mass near the origin of the axes. The polar angle was the only coordinate allowed to vary in a random fashion. Beginning at a polar angle of $\pi/2$ near the origin, the polar angle was allowed to change in random amounts of up to a maximum of $\pi/15$ for each set of coordinates. This kept successive sets of coordinates close to each other, as would be the case in a real particle composed of contacting spheres. The number of particles at each radius was determined by the radial power law.

The final particle, composed of 116 individual particles, had the shape of a five-legged starfish when viewed along the polar axis but resembled some of the natural particles we have seen when viewed along other axes. This particle was projected onto the analysis plane with four different orientations and with different sizes assigned to the primary particle locations. The resulting images are shown in Figure 2.

The fractal dimensions computed from the images show distinct differences with the different sizes used for the primary particles. For each size of primary particles however, the changes of fractal dimension with orientation are much smaller. In neither set of fractal dimensions is the generating power law exponent (1.6) recovered. The behavior of the correlation and pseudo-correlation curves is quite similar for a given particle projection. The images composed of the smallest primary particles show more scatter in the curves, indicative of the gaps between the particles on the image.

These results indicate that orientation effects for a real particle will not seriously distort the measured fractal dimension. The fractal dimension that is measured would not change much if the particle could be oriented in other directions. However, the magnitude of the fractal dimension will be influenced strongly by the character of the projected particle. In particular, particles whose images covers the plane densely will have a larger fractal dimension than particles whose images are sparse, even though the mass distribution may follow the same power-law dependence, as with this artificial particle.

A visual comparison of this artificial particle with some of the images of real particles shows that similar images give similar fractal dimensions, which supports the use of artificial particles in this kind of study. In particular, it shows the relative importance of the size of the primary particle in determining the characteristics of the image. One factor that has not been stressed in the analysis of images is that all the primary particles in a real particle are in contact with their neighbors. If they are not, the disjoint parts are counted as separate particles. What this implies for the artificial particles is that the primary particles should be large enough to project a continuous image in order to simulate a realistic particle.

It would seem that there is additional information in the connectedness of real particles which is not being utilized by the fractal analysis. This connectedness reduces the variations seen in the correlation curves for the artificial particles. In fact, in Figure 2, the upper right orientation was deliberately connected using small diameter intermediate particles along the five rays of the image to produce the pseudo-correlation curve in the dilation analysis. Without that connection, the pseudo-correlation curve showed a pronounced dip and hump in the region from 4 to 10 pixels. The smoothness and straightness of the correlation curves is to a large extent due to the connectedness property.

CONCLUSIONS

In addressing the problems of interpreting the fractal dimensions of images of particles, we have come to the following conclusions:

- The circular dilation and the correlation methods give quite comparable results for the fractal dimensions of images. The correlation method averages its information over the whole particle and may, therefore, be more useful at small scales. The dilation method is more efficient at calculating fractal dimensions at large scales.
- The fractal dimensions of images of natural particles are reasonably consistent with one another for particles grown under similar circumstances. However, the deviations of the measured fractal dimensions may be too large to identify one growth mechanism over another.
- The fractal analysis using the correlation and dilation methods is not sensitive enough to recover a power-law-generating relationship for random distributions of mass. Additional information in the images may make such recovery more practical and should be investigated.
- The fractal analysis methods do seem to be robust in determining the fractal dimension at different orientations of particles. This is extremely important for the analysis of electron micrographs of particles, which are inherently two dimensional.

The connectedness property of real particles is an important factor in their fractal behavior. An artificial particle shows more variation of its fractal dimension with the apparent size of its primary particles than with radial mass distribution or particle orientation.

Fractal analysis of particles and their images shows some real promise in distinguishing growth mechanisms, but present analysis methods have some important shortcomings.

REFERENCES

- [1] Paul Meakin, "Diffusion-Controlled Cluster Formation in Two, Three and Four Dimensions," *Physical Review A*, Volume 27, pp. 604-607, 1983.
- [2] Paul Meakin, "Diffusion-Controlled Cluster Formation in 2 - 6 Dimensional Space," *Physical Review A*, Volume 27, pp. 1495-1507, 1983.
- [3] Paul Meakin, "Effects of Cluster Trajectories on Cluster-Cluster Aggregation: A Comparison of Linear and Brownian Trajectories in Two- and Three-Dimensional Simulations," *Physical Review A*, Volume 29, Number 2, pp. 997- 999, 1984.
- [4] T. A. Witten and L. M. Sander, "Diffusion-Limited Aggregation, A Kinetic Critical Phenomenon", *Physical Review Letters*, Volume 47, pp. 1400- 1403, 1981.
- [5] S. R. Forrest and T. A. Witten, "Long-Range Correlations in Smoke-Particle Aggregates", *J. of Physics A: Math. Gen.*, Volume 12, Number 5, pp. L109- L117, 1979.
- [6] D. A. Weitz and J. S. Huang, "Self-Similar Structures and the Kinetics of Aggregation of Golds Colloids," *Kinetics of Aggregation and Gelation*, F. Family and D. P. Landau, Editors, Proceedings of the International Topical Conference on Kinetics of Aggregation and Gelation, Athens, Georgia, 1984.
- [7] R. Richter, L. M. Sander, and Z. Cheng, "Computer Simulations of Soot Aggregation," *J. Coll. Interface Sci.*, Volume 100, pp. 203-209, 1984.

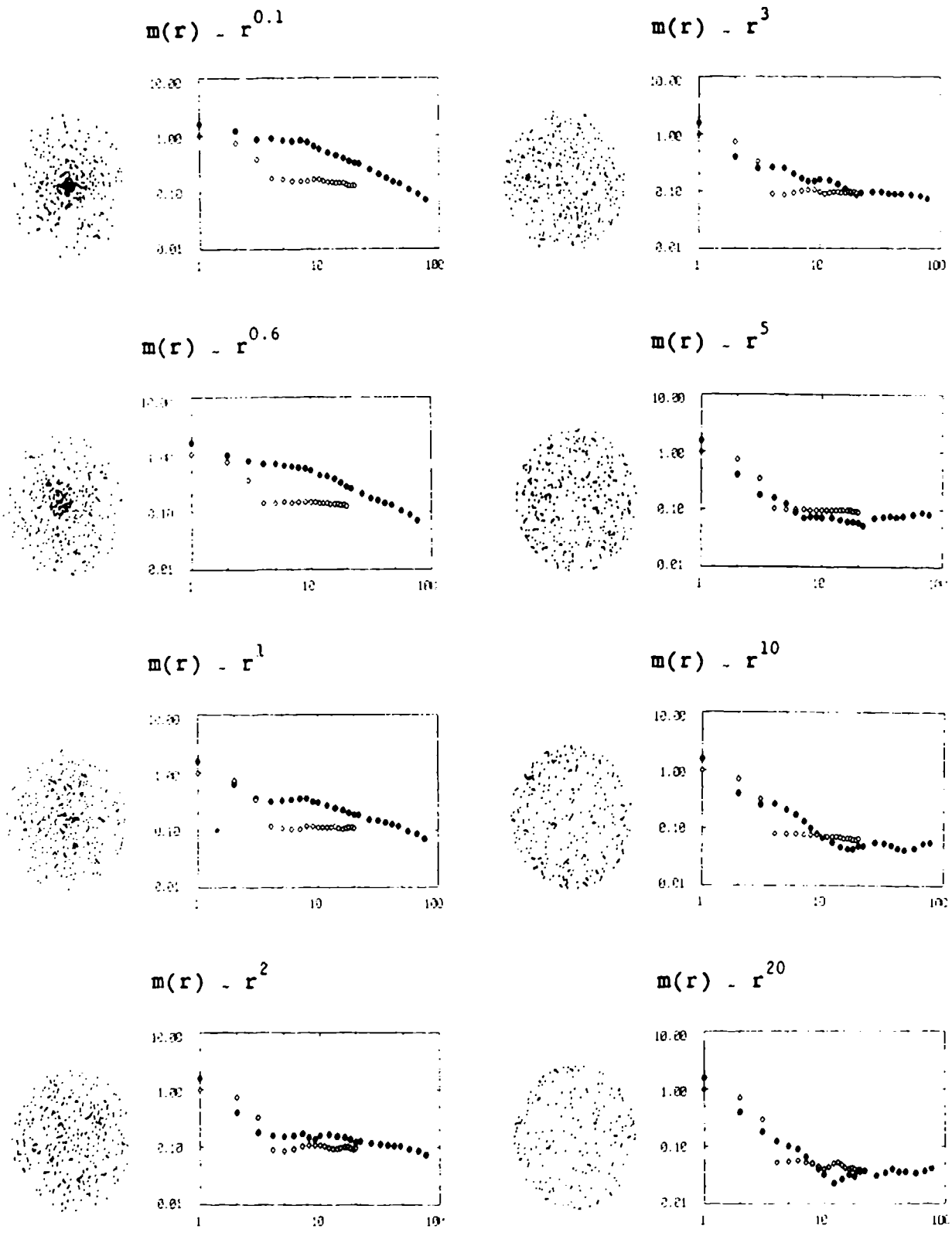
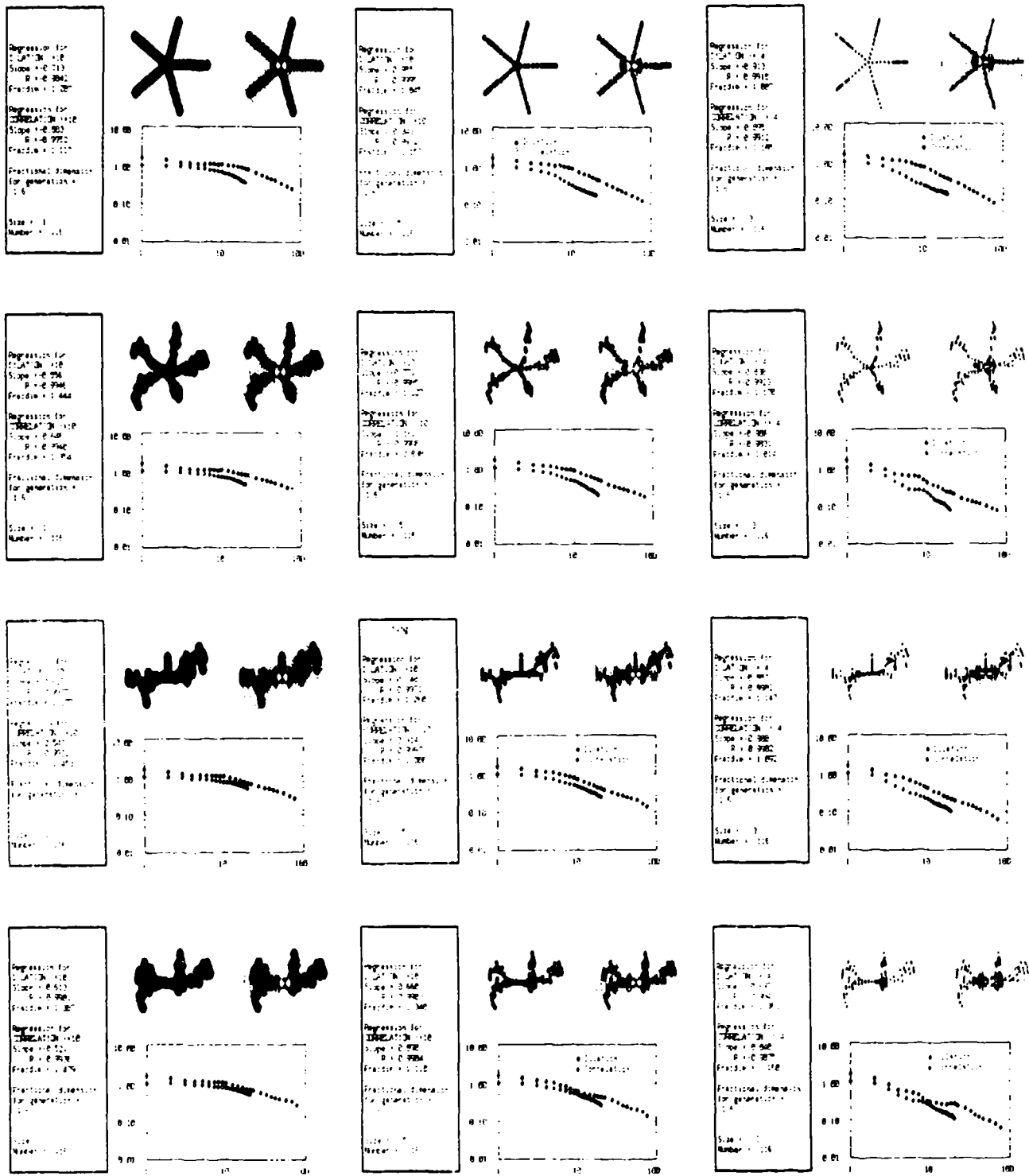


FIGURE 1. POWER-LAW MASS DISTRIBUTIONS for a range of generating exponents and correlation plots. Solid circles are dilation pseudo-correlation results; open diamonds are direct correlation results.



$$F_d = 1.37 \pm 0.07$$

$$F_c = 1.35 \pm 0.17$$

$$F_d = 1.22 \pm 0.13$$

$$F_c = 1.05 \pm 0.14$$

$$F_d = 1.18 \pm 0.09$$

$$F_c = 1.09 \pm 0.06$$

FIGURE 2. ORIENTATION AND PARTICLE SIZE RESULTS FOR ONE ARTIFICIAL PARTICLE. F_d is the fractal dimension by dilation (closed circles on correlation plots). F_c is the fractal dimension by correlation (open diamonds).

Blank

III. NONLINEAR EFFECTS AT HIGH ENERGY

Blank

TIME RESOLVED SPECTRA OF PLASMAS INITIATED
BY SINGLE AEROSOLS: AN UPDATE

A. Biswas
H. Latifi
L. J. Radziemski
R. L. Armstrong

Applied Laser/Optics
Physics Department
New Mexico State University
Las Cruces, NM 88003-0001

RECENT PUBLICATIONS, SUBMITTALS

A) A. Biswas et al, "Time-resolved spectroscopy of plasmas initiated on single, levitated aerosol droplets" Opt. Lett. 12, 313 (1987).

B) A. Biswas et al, "Irradiance and laser wavelength dependence of plasma spectra from single levitated aerosol droplets" submitted to Applied Optics, August (1987).

ABSTRACT

Spectra of plasmas initiated by a Nd:YAG laser on single, optically levitated, micron-sized droplets of a glycerine-saturated brine solution were investigated. Irradiance values on the order of 10^{11} W/cm² were used. There were chosen to be just above and just below the air breakdown threshold level for each of the three wavelengths investigated. Temporal development of the droplet plasma was monitored by observing neutral and once-ionized carbon and neutral sodium emission. The associated air plasma was monitored with once-ionized nitrogen emission. The dependence of the plasma on laser and sample parameters is discussed. This report brings this phase of our work on the study of aerosol-induced plasma emission to a close.

I. Introduction

When a laser beam propagates through the atmosphere, a variety of interactions occur between the beam and atmospheric constituents present along the propagation path. Both the aerosol and the molecular components of the atmosphere interact with the propagating beam. However, for many cases of practical importance, the aerosol interactions predominate. In this paper, we limit our discussion to aerosol-beam interactions.

Aerosol-beam interactions may be conveniently discussed as a function of the beam irradiance. At low irradiance, linear aerosol scattering and absorption are the dominant interactions removing energy from the beam.¹ With increasing irradiance, aerosol heating and vaporization become significant,²⁻⁴ and a variety of nonlinear optical phenomena may be observed in transparent droplets.⁵⁻⁷ High irradiance beams, in addition to the interactions already mentioned, may produce explosive vaporization with accompanying hydrodynamic effects,⁸⁻¹¹ and plasma formation.¹²⁻¹⁷ The present paper focuses on a study of laser-induced plasma formation in micron-sized, liquid aerosol droplets.

It has been known for some time that the presence of aerosols reduces the breakdown threshold of air below its clean-air value by several orders of magnitude.¹²⁻¹⁴ The initial experiments on aerosol-enhanced air breakdown were performed on small carbon particles irradiated by 10.6 μm light from a CO_2 laser.^{13,14} In this case, the experimental data were consistent with a model¹² in which the plasma was initiated by cascade ionization in the hot, dense vapor halo surrounding the intensely heated carbon particles.

More recently, aerosol-initiated plasmas have been observed for quasi-transparent liquid aerosol droplets irradiated by laser light near the visible region of the spectrum.¹⁵⁻¹⁷ No theoretical model exists for the mechanism of plasma initiation in this case although the importance of multi-photon absorption and hydrodynamic effects have been stressed in recent published work.¹⁵⁻¹⁷

Both spatial^{16,17} and temporal¹⁵ investigations have been performed for aerosol droplet-initiated plasmas. The results of these experimental studies have elucidated many features of the developing plasma fireball in the post-initiation phase, such as the existence and spatial structure of vapor plumes emanating from the irradiated

droplet,^{16,17} and the time development of line spectra and electron density within the plasma.¹⁵

In this paper, we present results which show the dependence of the aerosol-initiated plasma characteristics on the wavelength and intensity of the irradiating laser beam. Liquid droplets of a mixture of pure glycerine and saturated brine (NaCl) solution are optically levitated and subsequently irradiated with single pulses from an Nd:YAG laser. The fundamental, doubled, and tripled frequency lines of the Nd:YAG laser are used. Neutral (CI) and once-ionized (CII) lines of carbon, as well as the neutral (NaI) line of sodium serve as spectral probes of the droplet-initiated plasma, while the presence of once-ionized nitrogen (NII) lines monitor the production of an accompanying air plasma.

II. Experimental Considerations

Figure 1 is a schematic diagram of the experimental arrangement. Single droplet (50:50 glycerine + saturated brine solution) are optically levitated at the focus of an argon-ion laser. Droplets used in our experiments have diameters of $18 \pm 4 \mu\text{m}$ as measured by an imaging microscope. The levitated droplet is then aligned along the axis of a $0.5 \mu\text{m}$ scanning monochromator with a 1200 lines/mm grating as the dispersive element. The orientation of the spectrometer slit ($120 \mu\text{m}$ wide) is such that its length is parallel to the direction of the irradiating Nd:YAG laser beam. This enables the collection of a spatially averaged light signal from the entire region of the droplet-generated plasma. Details of the apparatus are listed in Table 1.

Light from the Nd:YAG laser, incident along a direction normal to the spectrometer axis, is brought to focus on the droplet (coincidence of the droplet and Nd:YAG beam may be directly observed using the microscope). A nominally 8 nsec Q-switched pulse from the Nd:YAG laser causes breakdown and plasma formation. The measured energies of the Nd:YAG pulse, at different wavelengths, and an estimate of the respective irradiances are shown in Table 2. For each wavelength, pulse energies just above and just below that required to cause air breakdown are selected. At laser energies below air breakdown threshold, plasma formation occurs only in the presence of a levitated droplet, suggesting that it is droplet-induced. At energies above air breakdown threshold, plasma formation occurs with and without the levitated droplet present. However, the plasma formed in the presence of the droplet is visually

brighter and larger; it also yields a higher overall signal (continuum and spectral line intensity).

For the 0.532 μm laser line, in addition to energies just above and below air breakdown threshold, other laser energies are used in order to investigate the effect of laser energy on the developing plasma.

A photomultiplier tube (PMT), mounted at the exit slit of the spectrometer measures the intensity of CI, CII, NaI and NII emission lines of the plasma. The photomultiplier output is processed by a transient waveform digitizer (5 nsec resolution) and subsequently fed to an on-line computer for storage and analysis.

Light collected by the spectrometer corresponding to a given spectral feature, consists of the spectral line intensity superimposed upon the plasma continuum. In order to determine the line intensity, two series of experimental runs are made, first with the spectrometer set "on-line" and second with the spectrometer set "off-line". The appropriate spectrometer setting was chosen by using a photodiode array detector. Time averaged single-shot plasma spectra generated by irradiating a single levitated droplet are shown in Figure 2. The Figure also indicates the on-line and off-line wavelengths used during this experiment.

III. Results and Discussion

Figure 3 is a typical data set showing the signal obtained with the photomultiplier-transient waveform digitized assembly. The spectral line intensity obtained after subtracting the off-line signal from the on-line is shown, a typical temporal profile of the laser pulse is also included in this figure. To obtain adequate signal-to-noise, as well as test the reproducibility of our method, five pairs of on-line, off-line differences are arithmetically averaged. The shot-to-shot reproducibility is good, showing time variations in the spectral intensity profiles of ± 7 ns. The observed jitter in the time response of the spectral intensities is attributed to a variety of inevitable experimental uncertainties such as: variations in the energy and pulse length of the irradiating laser beam; slight displacements in alignment of the levitated droplet with the focus of the irradiating laser beam.

The temporal development of the plasma may be described by a variety of diagnostic quantities. In this paper, we select the time after the arrival of the

laser pulse at which the line under study reaches its peak value, the so-called peak-time, T_p (see Fig. 3). This time is characteristic of dynamical processes occurring in the plasma, and is easily measurable using our transient waveform instrumentation.

Figure 4 shows the dependence of the T_p 's for the various probed species on the irradiating wavelength. Two comparisons are possible here, firstly, the effect of laser energy above and below air breakdown threshold at a given wavelength and, secondly, the effect of the laser wavelength. Each of these effects is addressed separately.

At $0.355 \mu\text{m}$ below air breakdown threshold, Figure 4(a), the probed spectral lines reach their peaks in the sequence CII, NII, NaI, CI while above air breakdown threshold, Figure 4(b), the sequence is NII, CII, NaI and CI. The T_p 's above air breakdown threshold are systematically larger than their counter-parts below air breakdown threshold. Moreover, the separation of the T_p 's between CII and CI are larger above air breakdown threshold. The fact that the T_p 's occur later for higher irradiance values may be explained by the fact that the deposition of more energy results in a higher initial electron density, with associated Stark-Broadening, so that the spectral lines emerge above the continuum at a later time. Concerning the T_p 's for NII and CII above and below air breakdown threshold, the reversal of the sequence may not be as significant, since above air breakdown threshold the peak times are seen to occur within one error bar. This suggests that above air breakdown threshold the air ionization occurs almost simultaneously with the droplet, while at lower laser energies the droplet ionizes first and subsequently the plasma from the droplet grows into the air ionizing it.^{16,17}

At $0.532 \mu\text{m}$ the sequence of the T_p 's is CII, NII, NaI, CI, both at higher (above air breakdown threshold) and lower (below air breakdown threshold) laser energies. The T_p 's are systematically greater at the higher laser energies, as are their relative separations. In particular, we note that the separations of CI and CII are larger at the higher energy. As in the case at $0.355 \mu\text{m}$, CII and NII T_p 's are closer above breakdown threshold. Thus, at $0.532 \mu\text{m}$ the observations are consistent with those at $0.355 \mu\text{m}$.

At $1.06 \mu\text{m}$, the sequence of CII, NII, and CI T_p 's is similar above and below air breakdown threshold, but the clustering of the NII and CII T_p 's above air breakdown

threshold, noted at lower wavelengths, is not observed. The behavior of NaI at 1.06 μ m is puzzling, and the following discussion attempts only a provisional interpretation. Since we average over the spatial coordinates in our measurements, a possible interpretation of the behavior of the NaI Tp below air breakdown threshold is that the Na emission occurs in a cooler region of the plasma and, hence, may be observed at earlier times. This is consistent with studies of the spatial structure of aerosol-initiated plasmas below air breakdown threshold which show that aerosol constituents are ejected from the bulk aerosol material where the plasma is initiated.^{16,17} Above air breakdown threshold, the plasma temperature is higher, the droplet is consumed by the developing plasma fireball, and the neutral species (both NaI and Cl) peak much later.

As we have noted above, the effects of increasing laser wavelength is to increase both the magnitude of the Tp's and their separation, with this effect most pronounced when going from 0.355 μ m to 0.532 μ m. Since the laser energy required for breakdown increases with wavelength (see Table 2) this effect might be due to energy rather than wavelength. In other words, the plasma generated by the longer wavelength laser radiation is simply hotter. We note, however, that the focal diameters also increase with wavelength. We estimate the focal diameters to be 27 μ m, 40 μ m, and 80 μ m for the 0.355 μ m, 0.532 μ m, and 1.06 μ m wavelengths, respectively, which would suggest the presence of a wavelength dependence. An additional factor which must be considered is that increased photon energies at lower wavelength will produce more photo-ionization^{18,19} thereby explaining earlier plasma initiation times. However, the Tp's shown in Figure 4 occur long after plasma initiation and there is no compelling evidence to suggest the Tp's will behave similarly, although the possibility cannot be ruled out. Further study is needed to resolve these difficult questions.

The dashed line in Fig. 4(a) shows the Tp for NII from air breakdown in the absence of the particle. Comparing these Tp's to the NII from droplet spectra suggests that the presence of the droplet delays the NII formation.

Figure 5 shows the dependence of Tp on laser energy at 0.532 μ m. The vertical dashed line marks the laser energy required to obtain air breakdown. An increase in laser energy from just below to just above air breakdown threshold shows that the separation between Tp's, as well as their magnitude, increases. The sequence (except

for the lowest energy) is CII, NII, NaI, CI. The same explanation cited in discussing Figure 4, namely that of larger energy deposition with higher initial electron densities and broadening, seems consistent here. However, at still higher energies the sequence changes to NaI, NII, CII, CI. The air ionization could be preceding the droplet ionization, but then NaI would not appear first. It may be suggested, as discussed earlier, that due to droplet explosion by the air initiated plasma, the NaI appears at a colder spatial region of the plasma. Thus, at laser energies significantly higher than air breakdown threshold the air plasma may be initiating the droplet ionization. The air plasma (in the absence of the droplet) is shown by the dashed curve, and again suggests that the presence of the droplet delays NII formation.

The ratio of once ionized to neutral carbon lines (CII/CI) has been measured as a function of the time after irradiation. This ratio is a semi-quantitative indication of the plasma temperature.²⁰ An exact calculation is not possible due to the lack of knowledge of the relative concentrations of air and droplet species contributing to the plasma.

IV. Conclusions and Recommendations

In this paper, plasma spectra were obtained for single, optically levitated, micron-sized droplets composed of a glycerine-brine solution mixture. Spectra of neutral and once-ionized species were obtained, both below and above air breakdown threshold, as a function of laser wavelength and energy.

For laser irradiance just below and just above breakdown threshold, the peak times, T_p , become larger and spread out in time with increasing laser wavelength. The peak times for the CII and NII emission lines are further seen to become noticeably clustered above air breakdown threshold when passing from laser wavelengths of $0.355\mu\text{m}$ to $0.532\mu\text{m}$. Ambiguities remain in the interpretation of the wavelength and energy dependence of the observed plasma emission.

Further work on this problem should attempt to resolve the ambiguities discussed earlier, and provide quantitative data on plasma properties. Problem areas that should receive attention include an extension of the plasma data to lower wavelengths, such as the $0.266\mu\text{m}$ third harmonic of the Nd:YAG laser, the determination of plasma temperature, and measurements of plasma properties during the initiation phase. In

Particular, at early times during the initiation phases, spatio-temporal data will be needed to interpret the dynamical properties of aerosol-initiated plasmas.

ACKNOWLEDGEMENTS

We acknowledge the assistance of Martin Dorsey and Hal Cottrell during the course of this work. This research was supported by U.S. Army Research Office grant DAAG-29-84-K-0180. We also acknowledge the support received from two U.S. Department of Defense instrumentation grants, DAAG-29-85-G-D012 and DAAL03-86-G-0119.

REFERENCES

1. H.C. Van de Hulst, Light Scattering by Small Particles, Dover, New York, 1981.
2. R.L. Armstrong, Appl. Opt. 23, 148 (1984).
3. G. Sageev, and J.H. Seinfeld, Appl. Opt. 23, 4368 (1984).
4. F.A. Williams, Int. J. Heat Mass Transfer 8, 575 (1965).
5. J.B. Snow, S.-X. Qian, and R.K. Chang, Opt. Lett. 10, 37 (1985).
6. H.-M. Tzeng, et al., Opt. Lett. 9, 499 (1984).
7. R.K. Chang, S.-X. Qian, and J. Eickmans, Proceedings of the Methods of Laser Spectroscopy Symposium, Rehovot, Israel, December 16-20, 1985.
8. R.L. Armstrong, J. Appl. Phys. 56, 2142 (1984).
9. R.L. Armstrong, P.J. O'Rourke, and A. Zardecki, Phys. Fluids 29, 3573 (1986).
10. S.M. Chitanvis, Appl. Opt. 25, 1837 (1986).
11. R.L. Armstrong, and A. Zardecki, Journal of Applied Physics (in press).
12. D.C. Smith, J. Appl. Phys. 48, 2217 (1977).
13. D.E. Lencioni, Appl. Phys. Lett. 23, 12 (1973).
14. D.E. Lencioni, Appl. Phys. Lett. 25, 15 (1974).
15. A. Biswas, et al, Opt. Lett. 12, 313 (1987).
16. J.H. Eickmans, W.-F. Hsieh, and R.K. Chang, Opt. Lett. 12, 22 (1987).
17. W.-F. Hsieh, J.H. Eickmans, and R.K. Chang, Opt. Lett. (in press).
18. H.T. Buscher, R.G. Tomlinson, and E.K. Damon, Phys. Rev. Lett., 15, 847 (1965).
19. A.J. Alcock, C. DeMichelis, and M.C. Richardson, Appl. Phys. Lett, 15, 72 (1969).
20. G. Bekefi (editor), Principles of Laser Plasmas, John Wiley and Sons, NY, 593 (1976).
21. L.J. Radziemski, T.R. Loree, D.A. Cremers, and N.M. Hoffman, Anal. Chem, 55, 1246 (1983).

Table 1

Experimental Apparatus and Settings

A. Lasers

1. Nd:YAG irradiating laser	Quanta-Ray DCR II A
Average Pulse width (FWHM)	8.5 ns
2. Argon Ion Laser	Lexel Model 85
Energy (CW)	400 mW

B. Laser-timing Components

1. Optical Trigger	EG&G Model 1301
2. Delay Generator	SRS Model-DG535

C. Detection System

1. Spectrometer	0.5m Jarrell-Ash
Grating	1200 1/mm, 550 nm blaze
Slit-width	120 μ m
2. Photomultiplier tube	Hamamatsu 1P28A
	-680 to -850V.
3. Photomultiplier Signal Processing	
Transient Waveform Digitizer	LeCroy Module TR8828
	2 ns resolution
4. Photodiode Array	Tracor Northern
	TN 6500
5. Disc Calorimeter	Sciencetech Model-365

Table 2

Laser Energies and Wavelengths Used

Wavelength (μm)	Average Pulse Width (ns)	Energy (mJ)	Irradiance (W/cm^2)
1.06	9.6	63	1.31×10^{11}
		87	1.80×10^{11}
0.532	8.5	20	1.87×10^{11}
		33	3.10×10^{11}
		40	$3 \times 10 \times 10^{11}$
		70	6.5×10^{11}
		110	1.03×10^{12}
0.355	7.5	12	2.79×10^{11}
		22	5.11×10^{11}

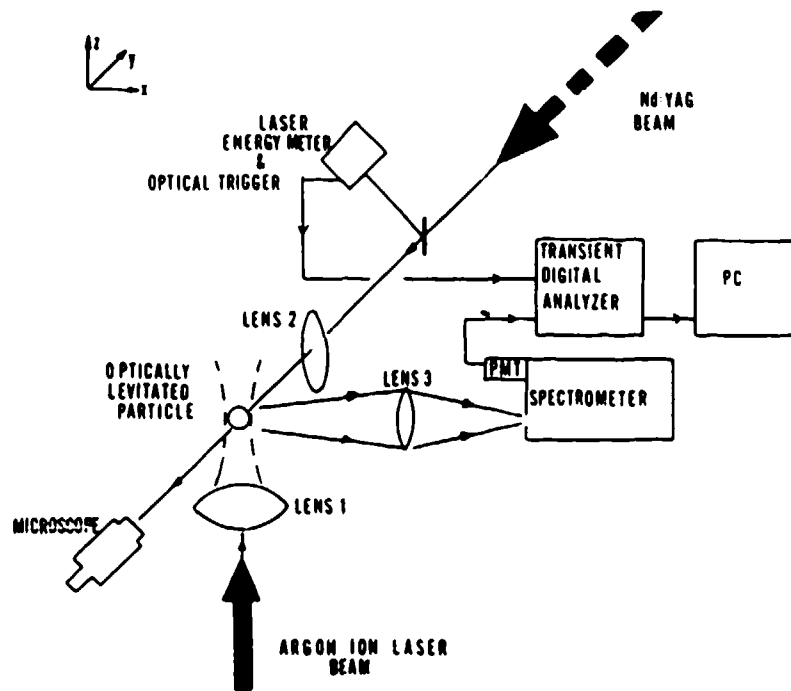


FIGURE 1. Schematic diagram showing experimental arrangement used to obtain time resolved spectra.

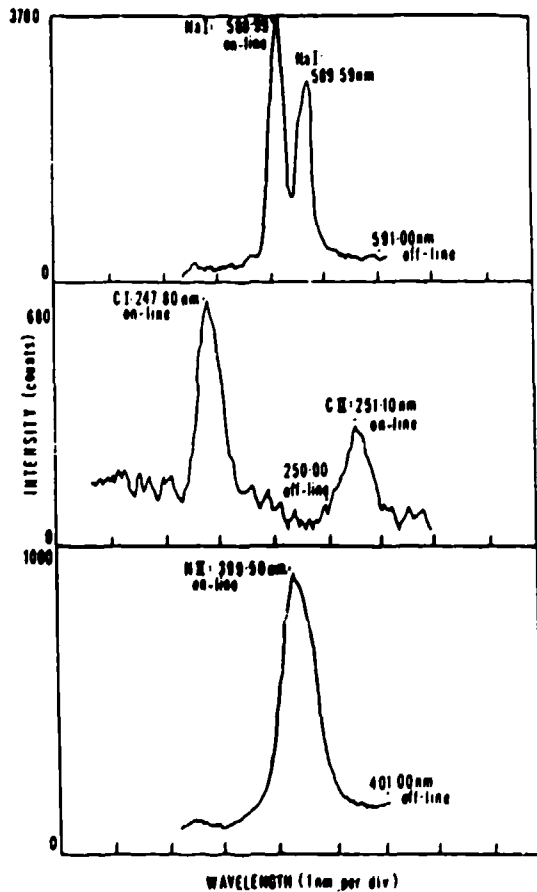


FIGURE 2. Time averaged single shot plasma spectra generated by irradiating a single levitated droplet.

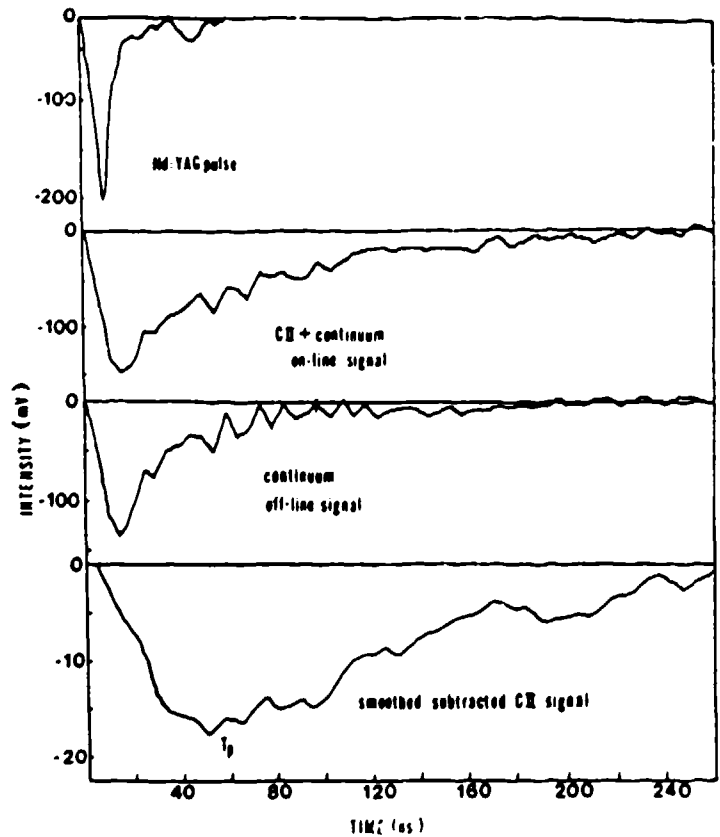


FIGURE 3. A typical data set showing the Nd:YAG pulse, on-line and off-line CII signals, and the CII line intensity as a function of time.

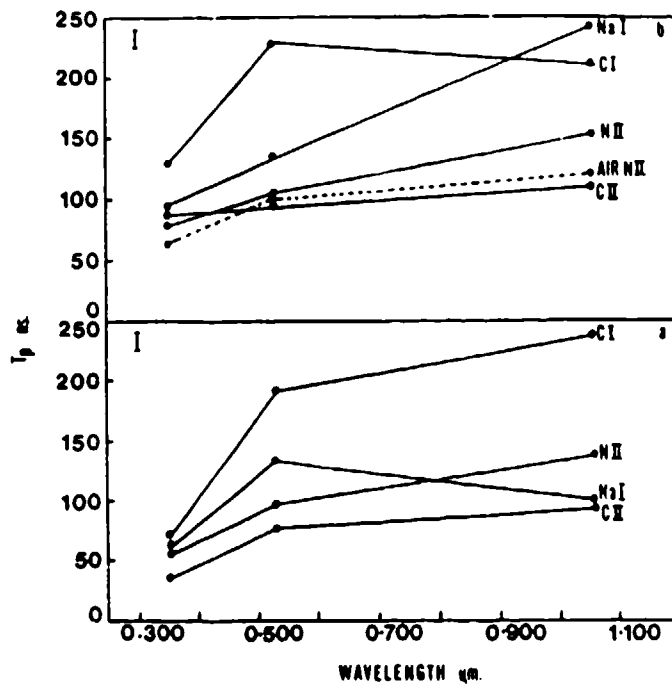


FIGURE 4. T_p 's for the different spectral species probed - plotted as a function of the irradiating wavelength (a) below air breakdown threshold (b) above air breakdown threshold.

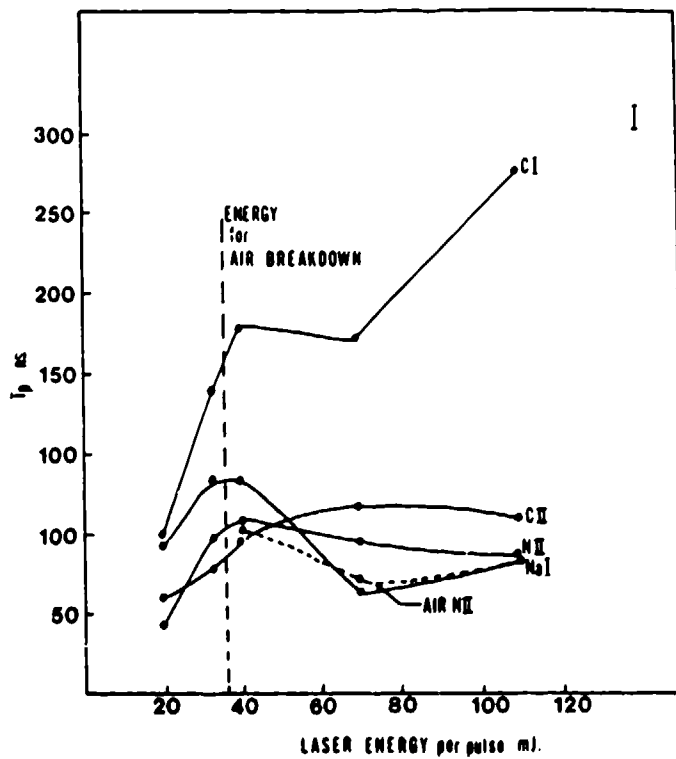


FIGURE 5. Dependence of T_p on laser energy at $0.532 \mu\text{m}$.

**EXPERIMENTAL AND THEORETICAL ANALYSIS OF THE INTERACTION
OF LASER RADIATION WITH FLUID CYLINDERS AND SPHERES**

D. R. Alexander, J. P. Barton, S. A. Schaub, M. A. Emanuel, J. Zhang
Laboratory for Electro-Optical Measurements
Department of Mechanical Engineering
University of Nebraska-Lincoln
Lincoln, NE 68588-0525

RECENT PUBLICATIONS, SUBMITTALS FOR PUBLICATION AND PRESENTATIONS:

- A). D. Alexander, "Experimental System for Real-Time Observation of Particle Dynamics at High Energy," Presentation at the 1985 CRDEC Conference on Obscuration and Aerosol Research, June 1985.
- B). D. Alexander, K. Wiles, S. Schaub, M. Seeman, "Effects of Non-Spherical Drops on a Phase Doppler Spray Analyzer," SPIE Vol. 573, p. 67, 1985.
- C). D. Alexander, "Nonlinear Effects of High Energy CO₂ Laser Illumination of Aerosol Drops," presentation at the 1986 CRDEC Conference on Obscuration and Aerosol Research, June 1986.
- D). J. Armstrong, "Experimental Study of the Explosive Vaporization of Aerosol Drops Under Irradiation by a CO₂ Laser," Masters Thesis, Mechanical Engineering Department, University of Nebraska-Lincoln, Lincoln, Nebraska, 68588, May 1986.
- E). D. Alexander and J. G. Armstrong, "Explosive Vaporization of Aerosol Drops Under Irradiation by a CO₂ Laser Beam," Appl. Opt. **26**, 533-538, 1987.
- F). D. Alexander, J. Barton, S. Schaub, and M. Fitzwater, "Beam Propagation Effects Resulting From The Electric Field Strengths For Spheres and Cylinders: Internal and Near Field," presentation at Workshop on the Physics of Directed Energy Propagation in the Atmosphere," U.S. Army Atmospheric Sciences Laboratory (ASL) at New Mexico State University, Las Cruces, New Mexico, January 27-28, 1987.
- G). D. Alexander, J. Barton, S. Schaub, and M. Emanuel, "Experimental And Theoretical Analysis of the Interaction of CO₂ Laser Radiation With Fluid Cylinders and Adjacent Spheres," presentation at the 1987 CRDEC Conference on Obscuration and Aerosol Research, June 1987.
- H). J. P. Barton, D. R. Alexander, and S. A. Schaub, "Surface Charges on Spherical Particles Induced by Polarized Irradiation," Manuscript submitted to Journal of Optical Society of America, September 1987.
- I). J. P. Barton, D. R. Alexander, and S. A. Schaub, "Internal and External Electromagnetic Fields for A Homogeneous Sphere With an Arbitrary Incident Beam," Manuscript submitted to Journal of Optical Society of America, September 1987.
- J). Mark Emanuel, "Explosive Vaporization of Spherical and Cylindrical Aerosols: Comparison Between Experimental Results Using A CO₂ Laser and Internal and Scattered Optical Fields," Master's Thesis, Mechanical Engineering Department, Laboratory for Electro-Optical Measurements, University of Nebraska-Lincoln, Lincoln, Nebraska, 68588, October 1987.

Abstract

Work performed under contract DAAA15-85-K-0001 for the past year is outlined. Both experimental and theoretical results have been obtained for the interaction of polarized electromagnetic laser radiation at $\lambda = 10.6 \mu\text{m}$ with spheres and cylindrical fluid columns. Theoretical research presented in H discusses the surface charges on spherical particles induced by polarized electromagnetic radiation. Research presented in I reviews the progress made in calculating the internal and external magnetic fields for a homogeneous sphere with an arbitrary incident beam intensity distribution. Experimental work on the characteristics of the explosive vaporization of spherical and cylindrical aerosols is presented in J. The work presented in this paper presents an overview of published work and other work undertaken during the past year. Future plans are to use excimer lasers to extend the research to short wavelengths and to irradiance values where nonlinear effects become important and to initiate solid particle interaction studies.

Introduction

The phenomena associated with the linear and nonlinear laser heating of spherical aerosol and cylindrical fluid columns is currently being investigated. In previous work,¹ we present a theoretical development for the calculation of electric surface charge density for a polarized plane electromagnetic wave incident upon a homogeneous particle. Electric field distribution calculations indicate a discontinuity in the normal component of the electric field across the surface of the sphere. This discontinuity in the normal component of the electric field is a result of accumulated electric charges on the surface of the sphere. Figure 1 gives the geometric arrangement and Figs. 2-6 illustrate that the free surface charge density has a complicated surface position dependence. In addition, if the spherical particle is polarizable, a polarization surface charge density is created which is in phase with the local internal surface normal electric field component but lags the free surface charge density by 90° . Besides providing physical insight, evaluation of surface charge densities may be important with regard to the understanding and determination of electromagnetic induced surface stresses. The external surface electric field will interact with the surface charges to create surface forces. These forces may contribute to the breakup of small particles subjected to intense laser illumination.

In a second paper,² we present a theoretical development and computer calculations for an arbitrary electromagnetic beam incident upon a homogeneous spherical particle (See Fig. 1). As a test of the arbitrary incident beam theory and the computer program, a Mie theory type incident plane wave was assumed. Consistent with the Mie theory development as presented in Born and Wolf³, the incident linearly polarized plane electromagnetic wave is assumed to propagate in the $+z$ axis direction with an electric field polarization in the x axis direction. Thus, after removing the $\exp(-i\omega t)$ time dependence

$$\vec{E}^{(i)} = E_o e^{ik_{oz}z} \hat{x} \quad (1)$$

and

$$\vec{H}^{(i)} = \sqrt{\epsilon_{ozt}} E_o e^{ik_{oz}z} \hat{y} \quad (2)$$

where E_o is the incident electromagnetic wave electric field amplitude. Substituting the incident electromagnetic field described by Eqs. (1) and (2) into the computer program produced results, as expected, identical to those of plane wave Mie theory. For illustration, Fig. 7 shows a computer program generated equatorial plane (x-z plane) plot of the normalized source function,

$$\hat{S} = \frac{|\vec{E}|^2}{|E_o|^2}, \quad (3)$$

for a 20.2 μm diameter water droplet in air with 10.6 μm wavelength (CO_2 laser wavelength) plane wave irradiation. (Size parameter $\alpha = 2\pi a/\lambda_o = 6$, complex relative index of refraction $\bar{n} = 1.18 + 0.07i$.)

An additional test of the validity of the arbitrary incident beam theory and the computer program was to use an incident linearly polarized plane electromagnetic wave but with arbitrary propagation direction and arbitrary electric field direction. As expected, the results were identical to that of plane wave Mie theory after taking into consideration a proper rotation of axis. For illustration, Fig. 8 shows, for otherwise the same conditions as Fig. 7, the normalized source function for an incident plane electromagnetic wave with the electric field in the x direction but propagating in the +y axis direction. The plot of Fig. 8 is identical in form and rotated 90° relative to that of Fig. 7 as expected.

The response of a spherical particle to an incident Gaussian beam is of current research interest. Recently, Simon *et al.*⁴ have reported an improved fundamental (TEM_{00} mode) Gaussian beam description that includes longitudinal, as well as transverse, components of electric and magnetic fields. Even though this fundamental Gaussian beam description does not exactly satisfy Maxwell's equations (as can be verified by direct substitution) it is an improvement over earlier paraxial descriptions and is a good approximation as long as the beam waist diameter is not small relative to the wavelength. The fundamental Gaussian beam description of Simon *et al.*⁴ was used with the arbitrary incident beam computer program. The propagation direction is along the +z axis, the

predominate electric field polarization is along the x axis, and the nominal electric field amplitude is E_0 .

For illustration, Figs. 9 and 10 are normalized source function plots for a fundamental Gaussian beam of $10.6 \mu\text{m}$ wavelength and $50.6 \mu\text{m}$ beam waist diameter incident upon a $20.2 \mu\text{m}$ diameter water droplet in air as was considered in Figs. 7 and 8. In Fig. 9 the center of the droplet is at the focal point of the focused beam and comparison with Fig. 7 indicates that, for these conditions, the features of the electric field distribution are essentially the same as for an incident plane wave. (As expected, in the limit of large beam waist diameter to sphere diameter ratio, the electromagnetic field distribution converges exactly to that of an incident plane wave). In Fig. 10 the center of the droplet is translated one droplet diameter along the y axis from the focal point of the beam and though the general form of the electric field distribution is similar to that of the sphere at the focal point, the normalized source function magnitude is larger near the focal point and smaller away from the focal point, as would be expected.

Temperature Measurements within a Cylindrical Water Column

In this section, experimental results are presented in which the temperature distribution across a cylindrical water column of approximately $100 \mu\text{m}$ in diameter has been measured. A small type K thermocouple probe with a junction diameter of $35\text{-}40 \mu\text{m}$ was used in the temperature measurements. To accurately position the thermocouple relative to the fluid column, the thermocouple was mounted on micrometer translators which allowed movement in three mutually perpendicular directions. A pulsed N_2 laser imaging system⁵ coupled to digital image processing system⁵ was used to visually locate and position the thermocouple at the desired location. The cylindrical column of fluid was generated using a Thermal Systems, Inc. (TSI) vibrating orifice generator. To obtain stable fluid columns, it was necessary to run the TSI generator without any frequency input and at a higher flow rate than normally recommended. The fluid columns were irradiated using an Advanced Kinetics 100 W CO_2 laser operating at $\lambda=10.6 \mu\text{m}$ in the continuous, multiline mode focused to a spot size of approximately $120 \mu\text{m}$.

The initial objective of the experiment was to measure the temperature distribution across the fluid column when the particle was on the threshold of explosive vaporization. To make this measurement, however, would require a non-intrusive measurement technique since the introduction of the thermocouple acts as a nucleation site to initiate the breakup process. From the laser

imaging system, it was readily observed that, prior to placement of the thermocouple within the fluid column, the laser was slightly below threshold irradiance for explosive vaporization since no explosive characteristics were observed. However, after placing the thermocouple within the fluid stream, considerable explosive behavior was observed as the drops impacted the thermocouple junction. Therefore, it was necessary to decrease the laser power level such that the laser was operating slightly below threshold irradiance when the thermocouple was within the fluid stream. With this restriction, the maximum temperature measured by the use of the thermocouple may be considerably lower than the temperature that exists within the stream in which no external intrusions are present. However, our attempts to measure the temperature distributions demonstrates that metastable conditions can be measured within the fluid column. A non-intrusive method of temperature measurement would be required if the actual temperature at which explosive vaporization occurs is to be accurately measured.

To measure the highest temperature possible, it was necessary to position the thermocouple probe as close to the heating area as possible without the thermocouple being heated by the laser. The temperature of the thermocouple probe without the presence of the fluid column was found to be approximately 38 °C compared to the ambient temperature of 22 °C. Since the temperature of the preheated water entering the focal point of the laser was 58 °C, the initial temperature of the thermocouple probe was not a significant heating effect in comparison.

Measurements were first taken on the illuminated area on the fluid column having maximum temperature. The thermocouple probe was then translated across the column in increments of approximately 10 μm . At each spatial location, 1000 data points were recorded using an A/D board in a PDP/73 computer data acquisition system in a 1 second interval and the average value used. Since the junction of the thermocouple was approximately 1/3 of the column diameter, the measurements at each position represent an average temperature of the fluid column over a diameter equivalent to the junction diameter.

Figure 11 shows the experimental results consisting of 5 passes through the fluid column. The micrometer readings made as the thermocouple traversed the column were normalized to the interval from -1 to 1. Note that the laser is propagating in the positive direction as shown on the abscissa. A maximum temperature of approximately 126 °C occurred on the illuminated side of the fluid column and was observed to decrease rapidly as the center of the column was approached.

On the shadow side of the fluid column, the temperature was found to be approximately 60 °C which was only 2 °C above the temperature of the water entering the laser focal point. The nature of this curve can be explained in a qualitative sense by examining Fig. 12 which shows the source function for a 100 μm infinite cylinder illuminated by a plane wave. The two curves are similar in shape with maximum values occurring on the illuminated side and decaying substantially as the center of the column was approached. As expected the major part of the energy was deposited on the illuminated side of the column which was confirmed by the measurements. Note that although the intensity of the incident beam is less than the threshold intensity for explosive vaporization if there were no thermocouple present, the measurements document that temperatures well in excess of the boiling point exist within the column.

Further investigations are underway to perform temperature measurements on other materials and to investigate the effects of irradiance on the measured temperatures.

CO₂ Laser Interactions with Cylinders of SFG-2 Fogoil and Methanol

Experimental work has been performed on cylinder-like fluid columns with a CO₂ laser operating in the multi-line mode at 10.6 μm with a maximum power density of 4×10^6 watts/cm². Figures 13 and 14 show the transition from shadow side initiated explosions in 80 μm methanol columns to front surface explosions in 90 μm methanol columns. Figure 15 shows the CO₂ laser beam interaction with a 90 μm column of SFG-2 fogoil. The fogoil explosions take place along the shadow side surface without much evidence of break through on the illuminated side. Also apparent in the original video tapes and original photographs was the appearance of large flares of a different index of refraction material thought to be dense smoke clouds or gaseous material. The fogoil was observed to produce a considerable amount of smoke during irradiation which was exhausted by using a hose connected to the laboratory exhaust system. A deposit of white powder like material was deposited on the exhaust tubing. The powder will be analyzed by CRDEC for composition.

The experimental results showed shadow side explosive behavior for 90 μm SFG-2 fogoil columns. The Mie scattering codes using an index of refraction provided by Dr. John White of CRDEC of $1.511 + 0.034i$ for 90 μm columns of fogoil had the maximum source function on the illuminated side. Two samples of the fogoil being used in our experiments were sent to Dr. Marvin Querry at the University of Missouri at Kansas City for an analysis of the index of refraction.

Results obtained by his laboratory indicate an index of refraction of $1.48 + 0.0055i$ for the real and imaginary part of the index of refraction at $\lambda = 10.6 \mu\text{m}$. Using this new value for the index of refraction, good agreement was obtained between experiments and the theoretical calculations showing the maximum source function on the shadow side of the column of fogoil.

Near Field Source Strengths and Dual Particle Interactions

Although the source function internal to the particle appears to be a primary driving force for the explosive behavior of aerosol particles subjected to laser radiation, also of interest is the strength of the source function which is external to the particle but still in the near field. Such information is important for modelling the propagation of laser beams through a cloud of aerosol particles in which secondary interactions between nearby particles could initiate the breakdown process. In particular, the source function in the direction of beam propagation has been investigated.

The geometry under consideration is shown in Fig. 1 in which the beam propagation is assumed to be in the positive Z direction with linear polarization in the X direction. The distance along the Z axis is normalized by the particle radius. Reference to the shadow side of the particle, would therefore, indicate consideration of Z (or r) values greater than unity.

To examine the effect of size parameter on the location and magnitude of the maximum external source function, a code implementing the Lorenz-Mie scattering solution was used to determine the location and magnitude of the maximum source function for various size parameters, $\alpha = \frac{2\pi a}{\lambda}$. The material under consideration was water with a refractive index of $n = 1.18 + 0.07i$. Figure 16 shows the results of the calculations. Here, the normalized radial position represents the location of the maximum external source function along the Z axis measured with respect to the particle center. As shown in Fig. 16, the maximum external source function always occurs within one particle radii from the shadow surface. It is apparent that the particle size has a significant effect on both the location and magnitude of the maximum external source function. Note that the maximum external source function for the water particle with $\alpha = 10$ shows more than a three-fold increase over the incident source function and is approximately 4 times the magnitude of the maximum source function observed internal to the particle ($S_{max,int} = 0.85$). It should be pointed out that the incident field is assumed to be a plane wave with uniform source function of unity magnitude.

In addition to the location and magnitude of the maximum external source function, the rate at which the maximum source function decays with increasing Z for a given particle size is of

interest. Figure 17 gives an indication of the rate at which this maximum source function decays with increasing distance from the particle. The number of radii plotted on the ordinate is found by determining the Z location corresponding to the point at which the source function decreases to 1.5. The value of 1.5 was chosen arbitrarily but represents a value, above which, will likely produce an effect that may be observed experimentally. Based on Fig. 17, a size parameter of approximately 8 appears to produce the greatest effect on the external field. For this size parameter, the source function has a maximum value of approximately 3.1 occurring at a radial location of 1.74. The source function continues to exceed 1.5 for an additional 5.8 drop radii.

Also of interest is the way the source function varies across the plane perpendicular to the propagation axis. In particular, the distribution of the source function at the location of the maximum external source function has been examined. The plane under consideration is the X-Y plane labeled P_3 as shown in Fig. 1. The results shown in Fig. 18 represent the source function distribution for a water droplet with a size parameter of 8 and where the X-Y plane is located at $Z_0 = 1.74$. Figure 18 shows a considerable amplification in the source function near the propagation axis which decays substantially within one-half particle radius.

To observe this phenomenon experimentally it was necessary to align two particles along the axis of the laser beam while maintaining a particle separation of approximately one drop diameter. In order to obtain a dual drop stream, a slight modification was made in the existing system used to generate single drop streams. The TSI vibrating orifice generator presently uses a thin steel orifice consisting of a single hole ranging in size from 10-100 μm . To generate the dual droplet stream, a focused argon laser beam was utilized to construct a new orifice with two holes with diameters of approximately 20 μm spaced approximately 40 μm from center to center. Figure 19. shows a digitized photograph of the dual droplet stream and laser interaction. Note that the beam is propagating from left to right on the image. Denoting particle 1 as the leftmost particle and particle 2 the rightmost particle, one readily observes that particle 2 is showing evidence of explosive behavior while in the shadow region of particle 1. Since both particles are nearly identical in size, the threshold for explosive behavior should be the same provided each is travelling at the same velocity through the stationary laser beam. As illustrated theoretically in Fig. 16-18 and experimentally in Fig. 19, it appears that particle 2 experiences a higher incident source function than particle 1 due to the amplification effect as discussed earlier in this report. The particles shown

in Fig. 19 are approximately $45 \mu\text{m}$ in diameter and the separation at the time of laser interaction was $35 \mu\text{m}$. Using these values, the source function which would exist at the surface of the second particle was calculated. The results shown in Fig. 20 show a source function of approximately 2.6 at a location $Z_0 = 2.5$. These theoretical results are consistent with the experimental observations since one might expect the second particle to explode first based upon these calculations. It should be pointed out the theoretical discussion neglects several factors. In reality, a situation such as the one described in the above sections would involve dual interactions between the electric fields of the adjacent particles. However, if one assumes that the backward scattered light from the second particle is small, the theoretical solution may provide a reasonable model of the physical situation. A second factor to be considered is the fact that the field incident on the first particle is actually a Gaussian beam rather than a uniform field as assumed by the Lorenz-Mie theory.

Conclusions

The current work reports the existence of a discontinuity in the normal component of the electric field. Based on the calculations the discontinuity in the normal component of the electric field is a result of accumulated electric charges on the surface of the sphere. The surface charge was shown to have a complicated surface position dependence. A more complete theoretical development as well as computer calculations have been presented for the first time on the interaction of a particle with an arbitrary incident intensity profile. Measurements of the temperature distribution through a laser heated fluid column showed that average temperatures as high as 126°C could be obtained. Differences in the location of where explosive vaporization occurred experimentally and what theoretical calculations predicted, resulted in a correction for the index of refraction for fogoil from $1.511 + 0.034i$ to $1.48 + 0.0055i$ at $\lambda = 10.6 \mu\text{m}$. The current work also illustrates that the electric fields can be quite high in the shadow region of a particle. Experimental work with dual drop streams clearly demonstrated the possibility that the focusing effect of one particle on a second particle can significantly lower the breakdown irradiance values for propagation through obscurant materials.

Acknowledgements

This work was supported by the Army Chemical Research and Development Engineering Center under Contract DAAA15-85-K-0001. The advice and assistance of Dr. O. Sindoni, Dr. E.

Stuebing, and Dr. J. White of the Chemical Research and Development Engineering Center are gratefully acknowledged.

References

1. J. P. Barton, D. R. Alexander, and S. A. Schaub, "Surface Charges on Spherical Particles Induced by Polarized Irradiation," Manuscript submitted to Journal of Optical Society of America, September 1987.
2. J. P. Barton, D. R. Alexander, and S. A. Schaub, "Internal and External Electromagnetic Fields for A Homogeneous Sphere With an Arbitrary Incident Beam," Manuscript submitted to Journal of Optical Society of America, September 1987.
3. M. Born and E. Wolf, *Principles of Optics*, (Pergamon Press, Oxford, 1970).
4. R. Simon, E.C.G. Sudarshan, and N. Mukunda, "Gaussian-Maxwell beams," J. Opt. Soc. Am. **3**, 536-540 (1986).
5. D. Alexander and J. G. Armstrong, "Explosive Vaporization of Aerosol Drops Under Irradiation by a CO₂ Laser Beam," Appl. Opt. **26**, 533-538, 1987.

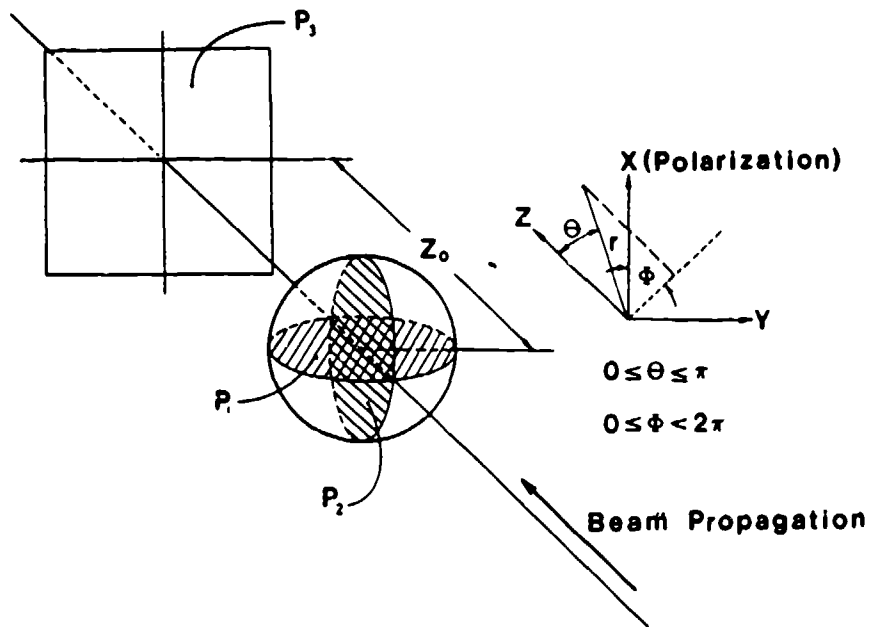


Fig. 1. Schematic of the geometry for the theoretical calculations.

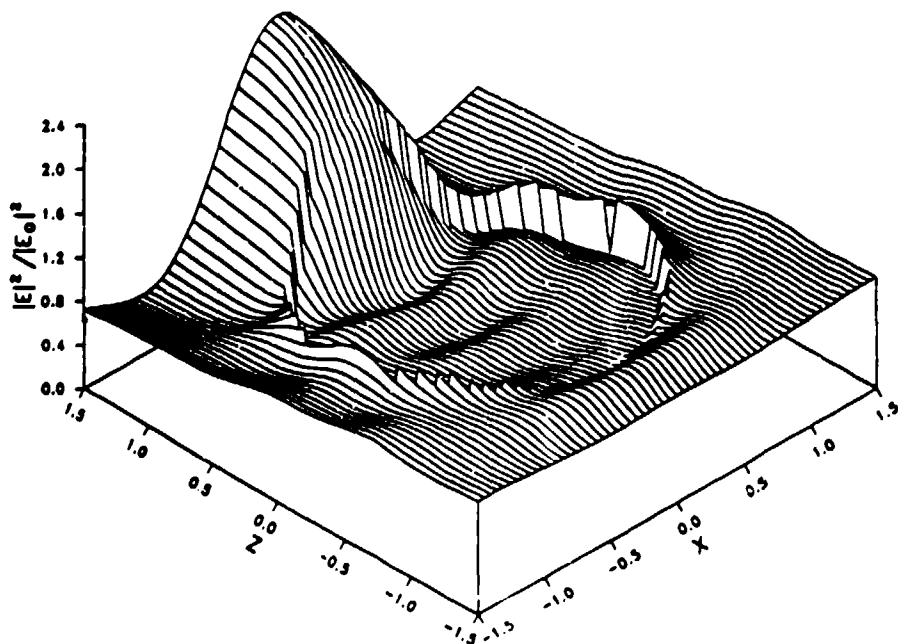


Fig. 2. Normalized source function in the plane of polarization (x-y plane) for a spherical particle with $\alpha = 5$ and $\tilde{n} = 1.18 + 0.07i$.

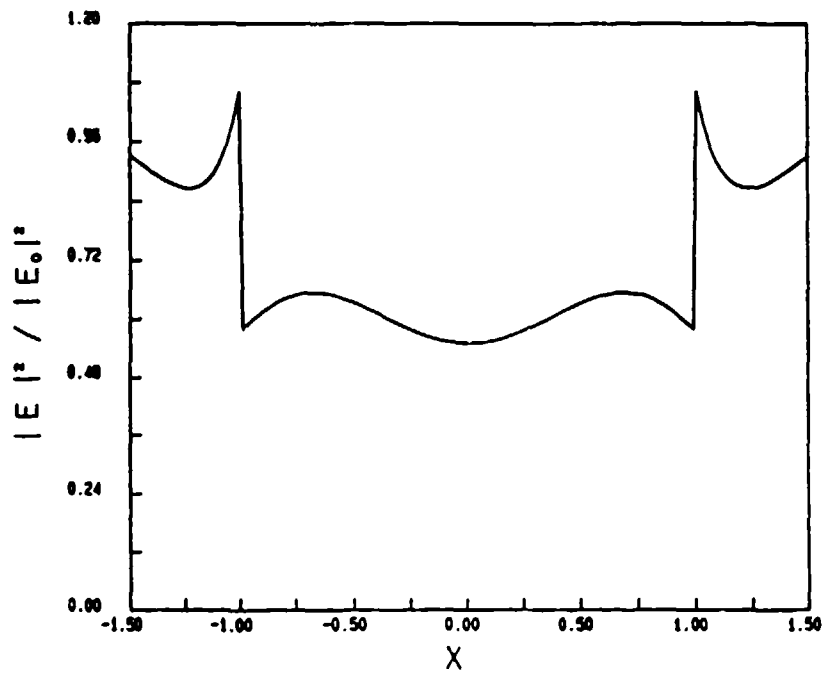


Fig. 3. Normalized source function along the transverse centerline (x axis) for a spherical particle with $\alpha = 5$ and $\bar{n} = 1.18 + 0.07i$.

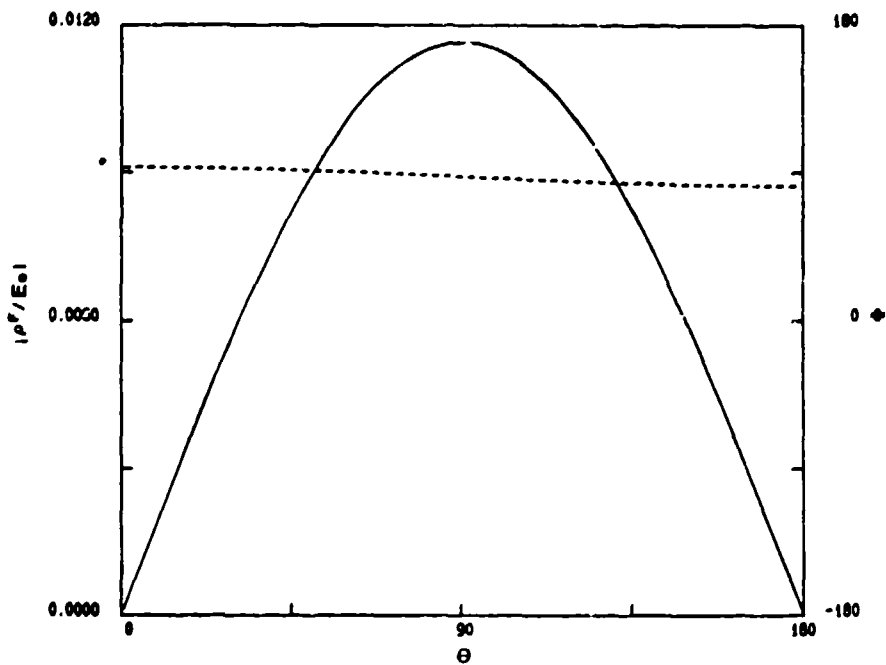


Fig. 4. Free surface charge density magnitude (— left y axis) and phase (--- right y axis) along the top of sphere surface ($\phi = 0$) for $\alpha = 0.1$ and $\bar{n} = 1.18 + 0.07i$.

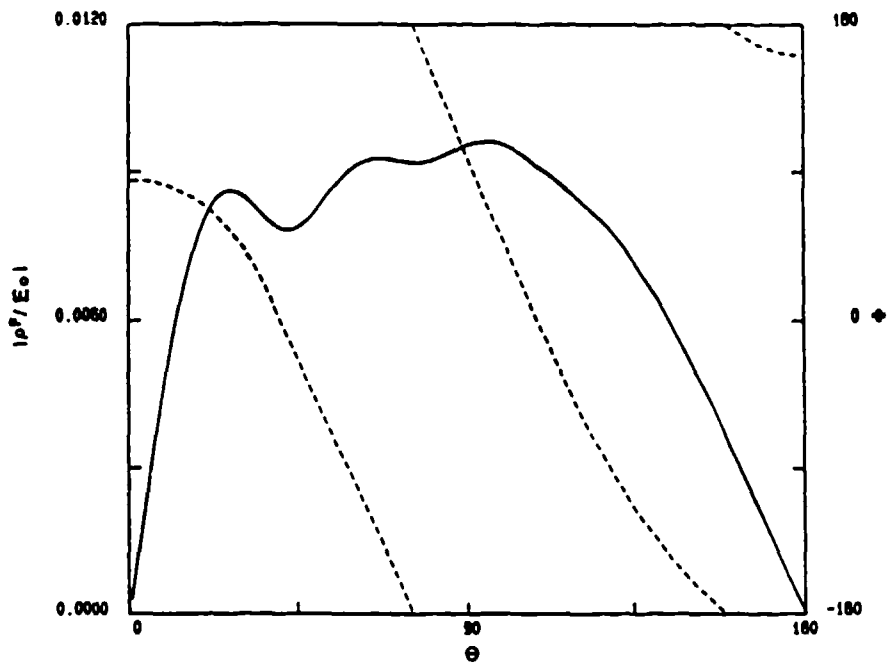


Fig. 5. Free surface charge density magnitude (— left y axis) and phase (--- right y axis) along the top of sphere surface ($\phi = 0$) for $\alpha = 5$ and $\bar{n} = 1.18 + 0.07i$.

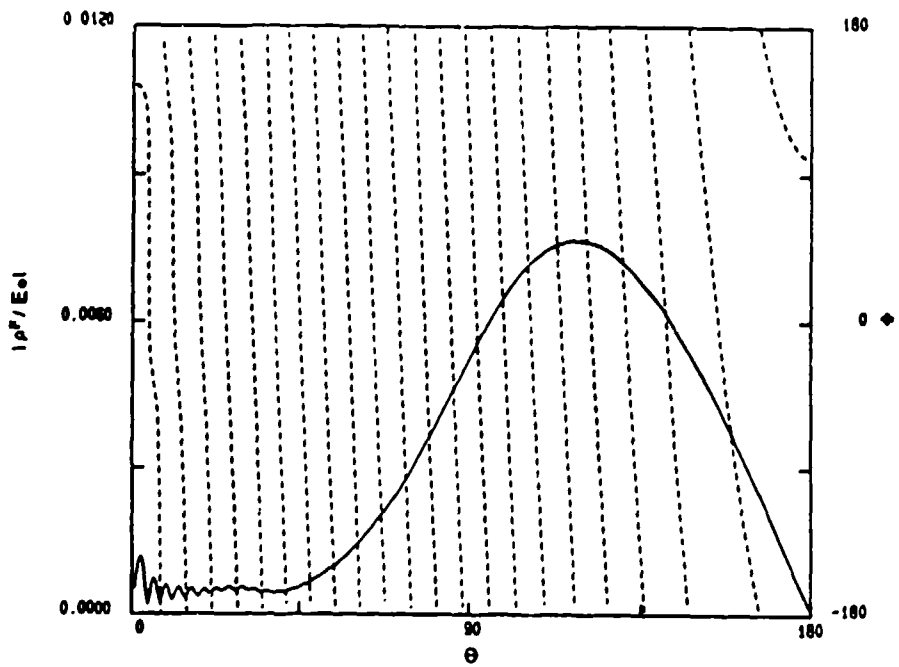


Fig. 6. Free surface charge density magnitude (— left y axis) and phase (--- right y axis) along the top of sphere surface ($\phi = 0$) for $\alpha = 50$ and $\bar{n} = 1.18 + 0.07i$.

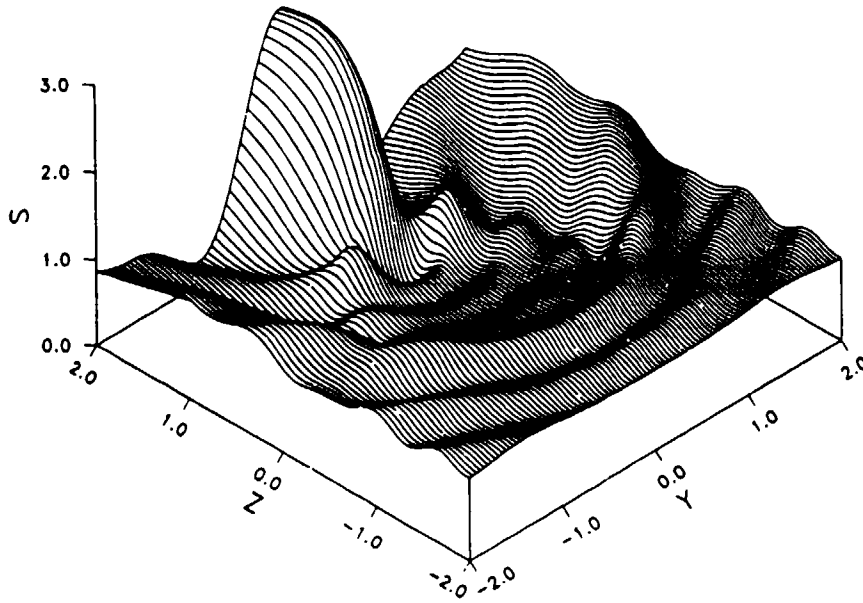


Fig. 7. Plane wave propagating in the $+z$ direction incident on a spherical particle with $\alpha = 6$ and $\bar{n} = 1.18 + 0.07i$. Spatial coordinates are normalized relative to sphere radius, a .

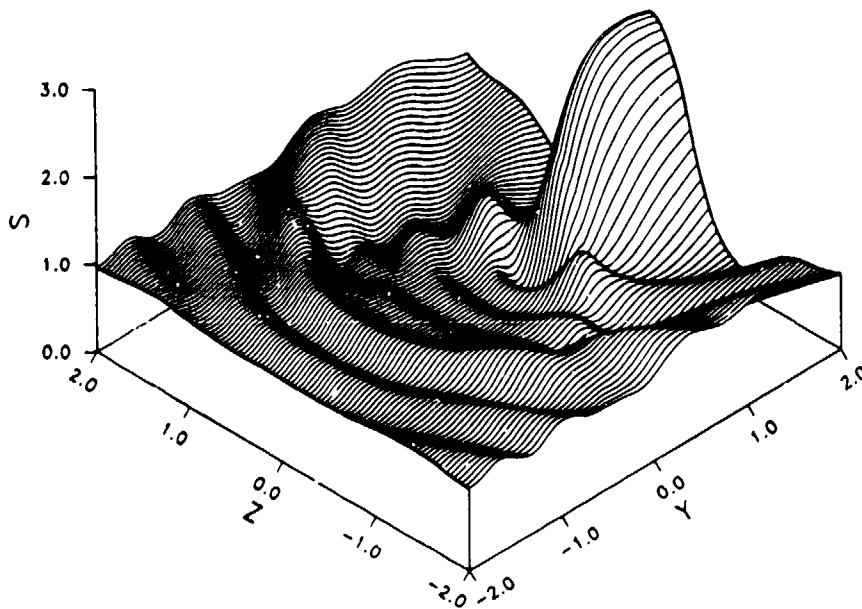


Fig. 8. Plane wave propagating in the $+y$ direction incident on a spherical particle with $\alpha = 6$ and $\bar{n} = 1.18 + 0.07i$. Spatial coordinates are normalized relative to sphere radius, a .

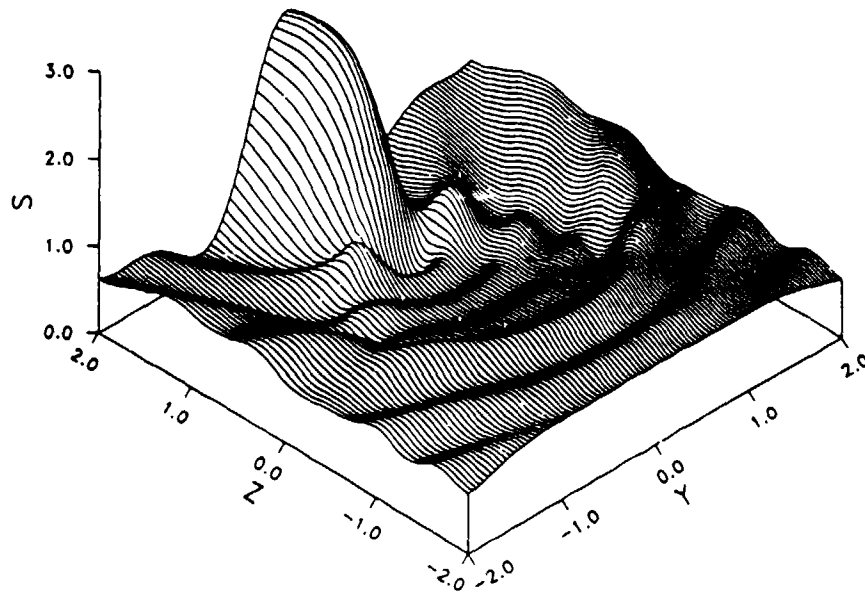


Fig. 9. Gaussian beam with a $5a$ beam waist diameter propagating in the $+z$ direction incident on a spherical particle located at the focal point with $\alpha = 6$ and $\bar{n} = 1.18 + 0.07i$. Spatial coordinates are normalized relative to sphere radius, a .

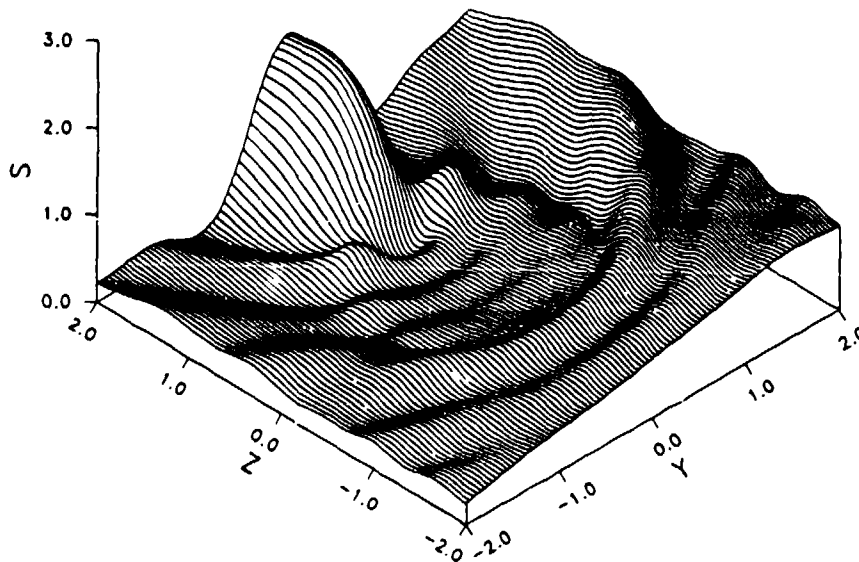


Fig. 10. Gaussian beam with a $5a$ beam waist diameter propagating in the $+z$ direction incident on a spherical particle located one sphere diameter along the y axis from the focal point with $\alpha = 6$ and $\bar{n} = 1.18 + 0.07i$. Spatial coordinates are normalized relative to sphere radius, a .

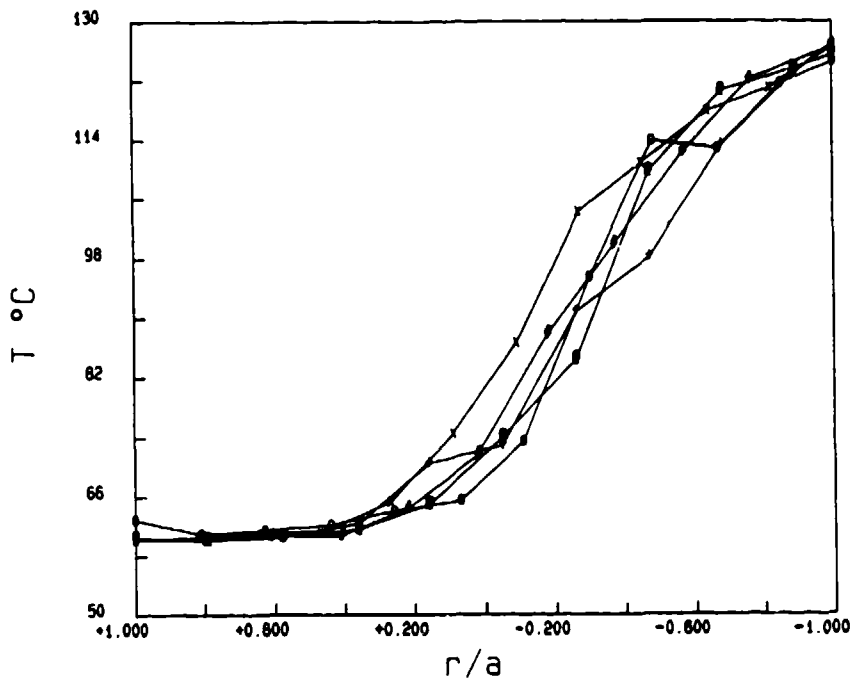


Fig. 11. Temperature distribution within a 100 μm cylindrical water column as a function of normalized radial position.

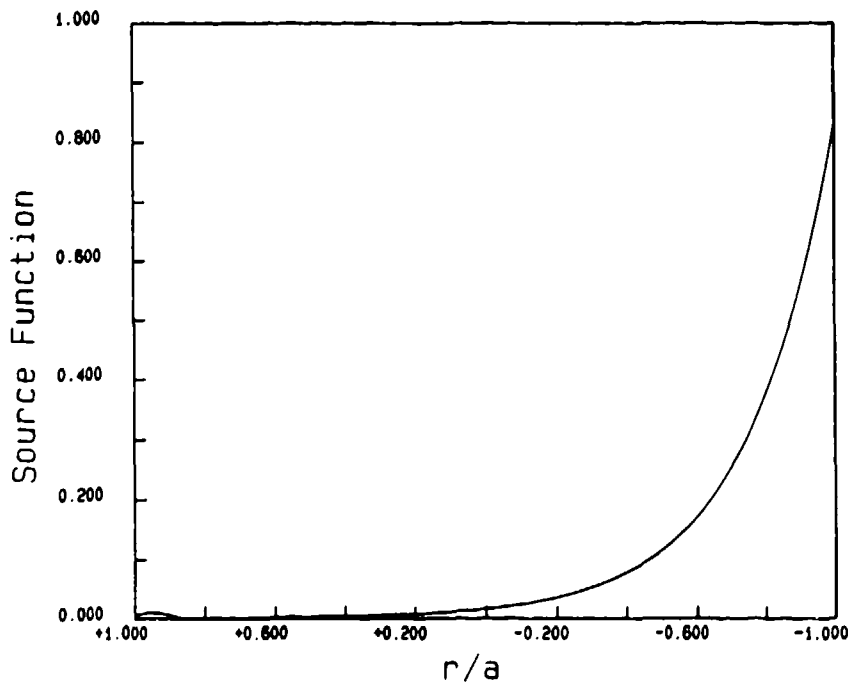


Fig. 12. Source function distribution along the centerline for a 100 μm cylindrical water column as a function of normalized radial position. Beam polarization is along the axis of the fluid column.

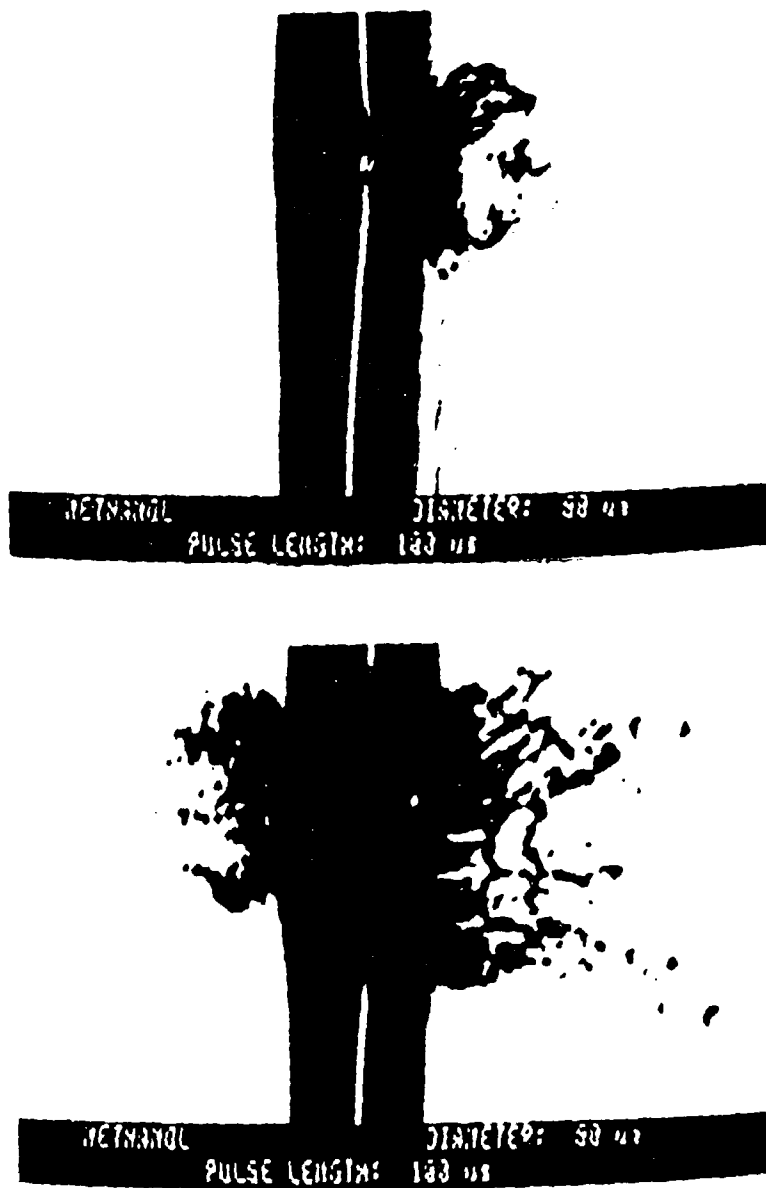


Fig. 13. Typical interaction of a 80 μm methanol fluid column with a 100 μsec laser pulse from a CO_2 laser operating at 10.6 μm . The laser beam is incident from left to right. Maximum irradiance was 0.62 MW/cm^2 .

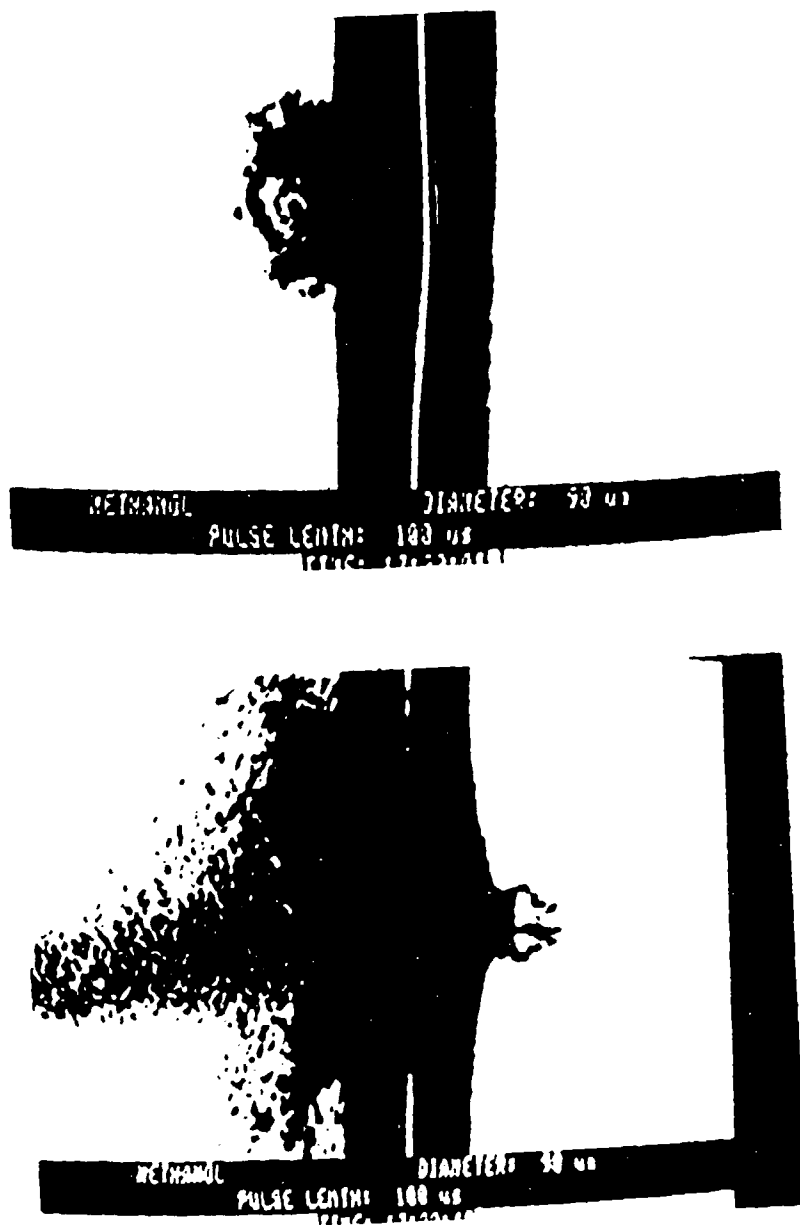


Fig. 14. Typical interaction of a 90 μm methanol fluid column with a 100 μsec laser pulse from a CO_2 laser operating at 10.6 μm . The laser is incident from left to right. Maximum irradiance was 0.62 MW/cm^2 .

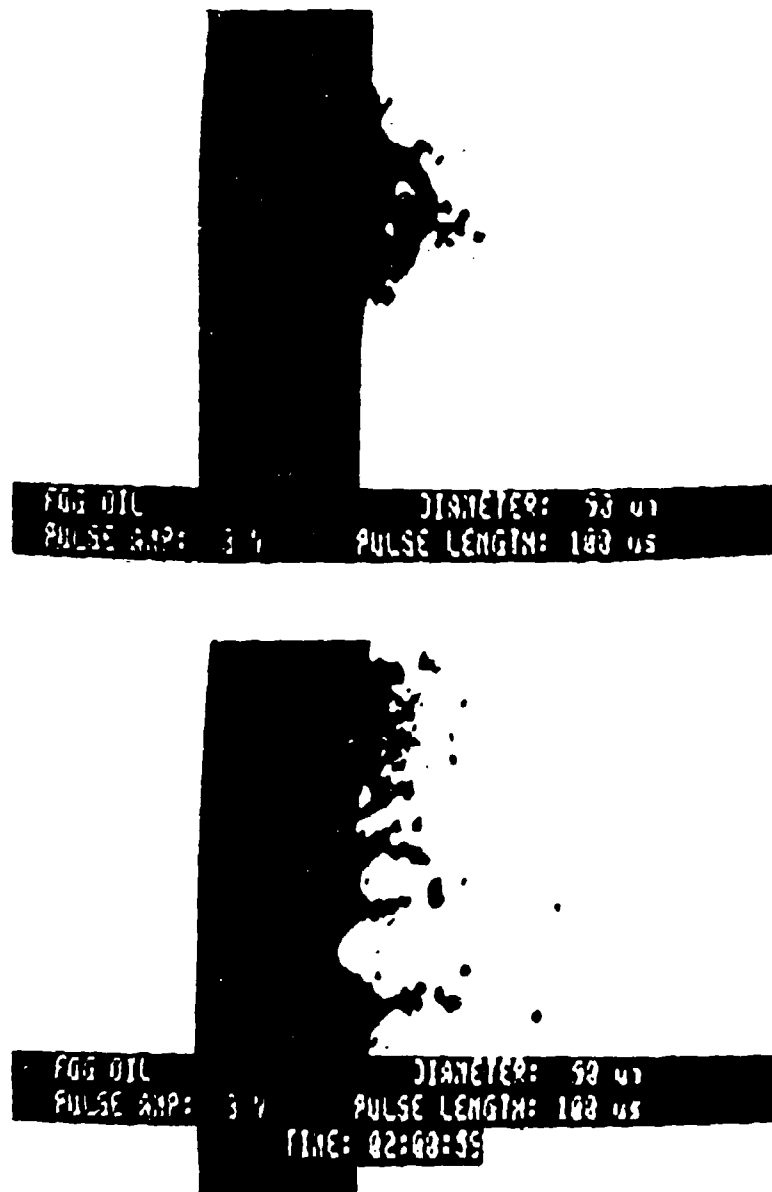


Fig. 15. Typical interaction of a 90 μ m foil fluid column with a 100 μ sec pulse from a CO₂ laser operating at 10.6 μ m. The laser beam is incident from left to right. Maximum irradiance was 0.62 MW/cm².

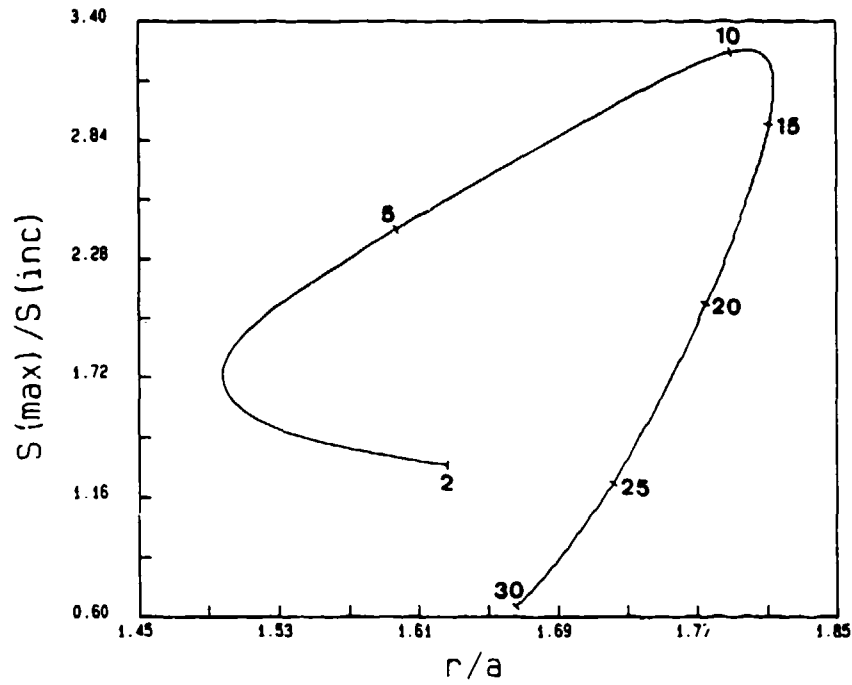


Fig. 16. Location and magnitude of the maximum external source function along the Z axis as a function of the size parameter, $\alpha = \frac{2\pi a}{\lambda}$.

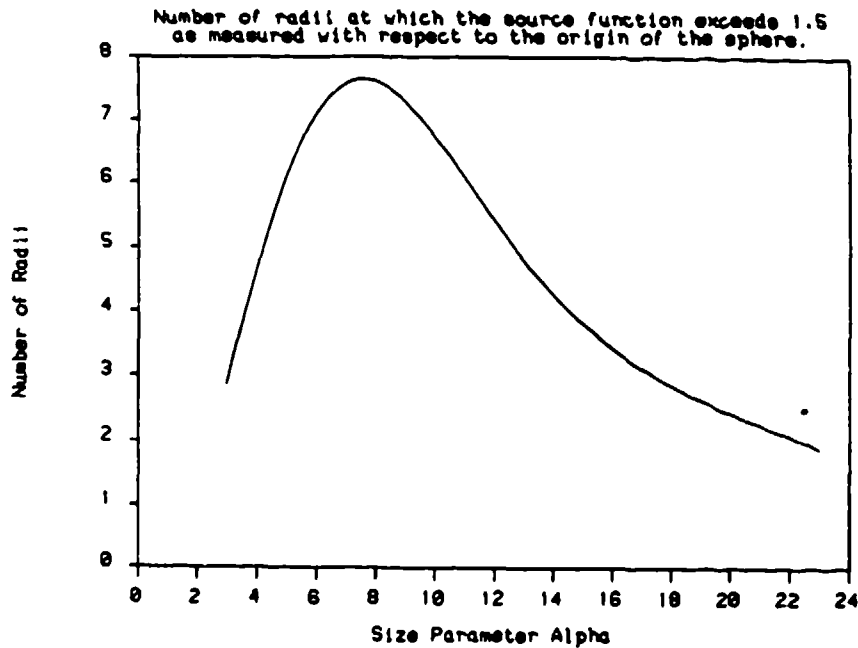


Fig. 17. Number of radii for which the external source function exceeds 1.5 as a function of size parameter for spherical water drops.

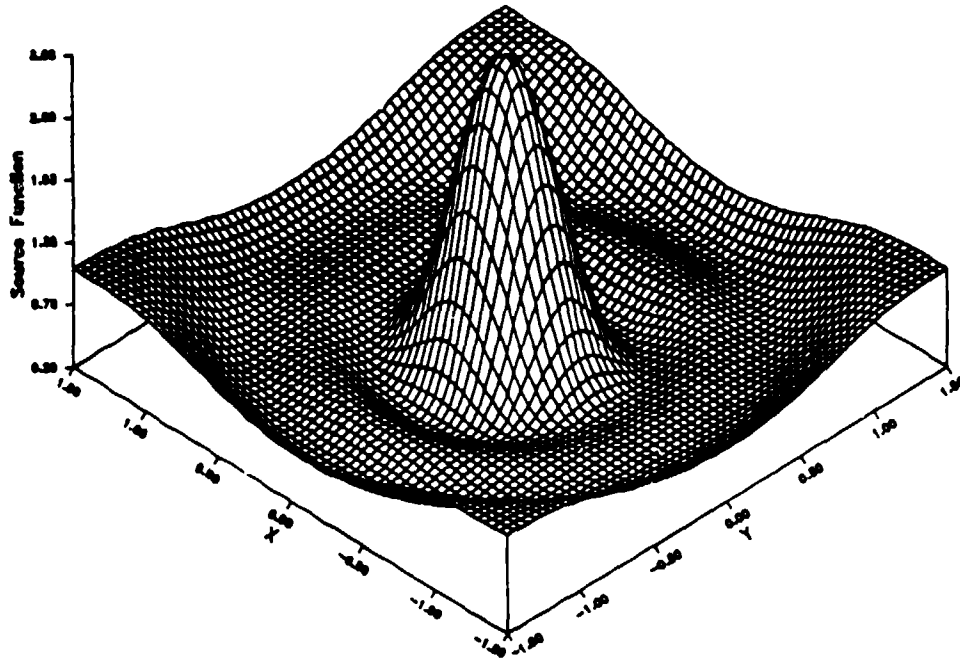


Fig. 18. External source function in the X-Y plane at $Z_0 = 1.74$ for water drops with size parameter, $\alpha = 8$.

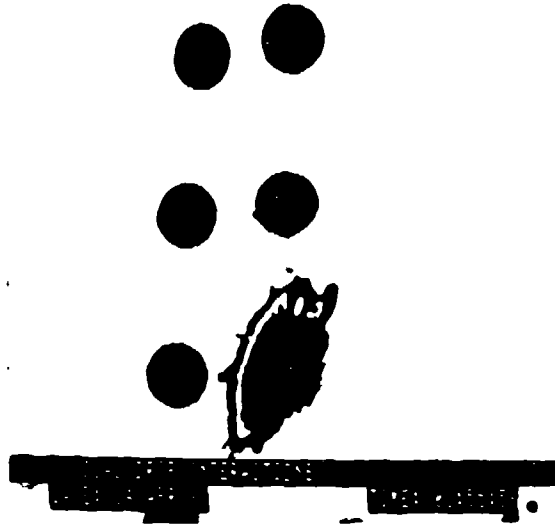


Fig. 19. Example of a second particle being in the high electric field behind the front particle. Demonstrates that the front particle does not explode but the second particle effectively sees a very large electric field and thus explodes. The beam is incident from the left to right. The particles are $45 \mu\text{m}$ in diameter with a separation of $35 \mu\text{m}$. The particles are illuminated with a CO_2 laser at $10.6 \mu\text{m}$ with an irradiance of $0.13 \text{ MW}/\text{cm}^2$.

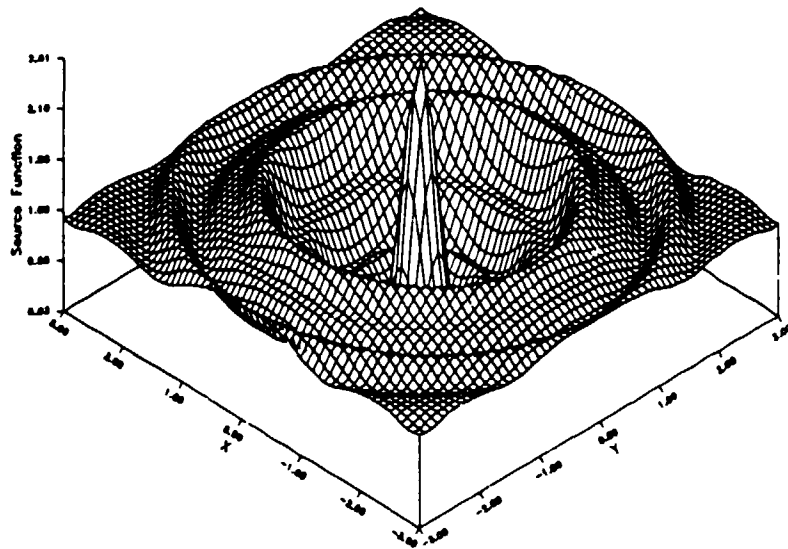
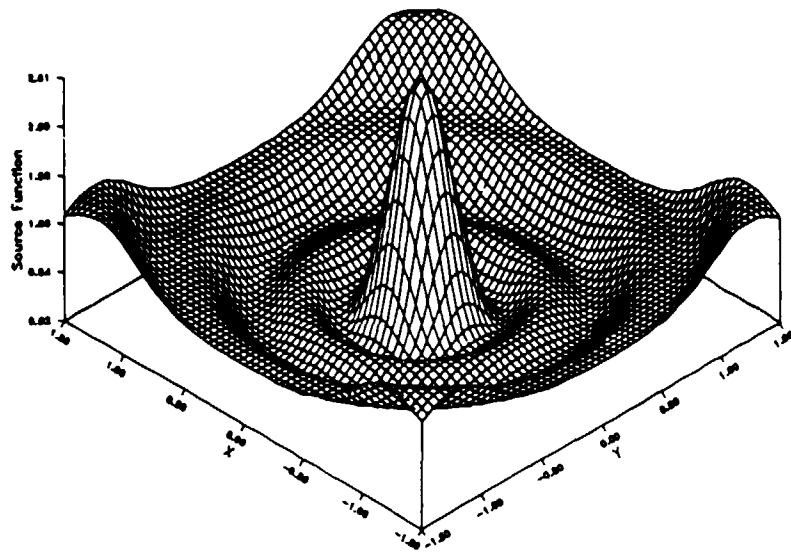


Fig. 20. External source function in the X-Y plane at $Z_0 = 2.5$ (See Fig. 1.) for $45 \mu\text{m}$ water drops.

ENERGY BALANCE IN LASER-IRRADIATED VAPORIZING DROPLETS

A. Zardecki
Theoretical Division, MS K723
Los Alamos National Laboratory
Los Alamos, NM 87545

R. L. Armstrong
Physics Department, Applied Laser Optics Group
New Mexico State University
Las Cruces, NM 88003

RECENT PUBLICATIONS, SUBMITTALS FOR PUBLICATION AND PRESENTATIONS:

A) A. Zardecki and S. A. W. Gerstl, "Off-Axis Scattering of Laser Beams Using Single and Multi-Gaussian Phase Function Approximation," Proceedings of the 1986 CRDEC Scientific Conference on Obscuration and Aerosol Research, R. H. Kohl, Ed., In Preparation.

B) R. L. Armstrong, P. J. O'Rourke, and A. Zardecki, "Vaporization of Irradiated Droplets," *Phys. Fluids*, **29**, 3573-3581 (1986).

C) A. Zardecki and S. A. W. Gerstl, "Multi-Gaussian Function Model for Off-Axis Laser Beam Scattering," Optical Society of America Annual Meeting, Seattle, October 19-24, 1986.

D) R. L. Armstrong and A. Zardecki, "Diffusive and Convective Vaporization of Irradiated Droplets," International Laser Science Conference, Seattle, October 20-24, 1986.

E) S. A. W. Gerstl, A. Zardecki, W. P. Unruh, D. M. Stupin, G. H. Stokes, and N. E. Elliot, "Off-Axis Multiple Scattering of a Laser Beam in Turbid Media: Comparison of Theory with Experiment," *Appl. Opt.* **26**, 779-785 (1987).

F) A. Biawas, H. Latif, P. Shah, L. J. Radziemski, and R. L. Armstrong, "Time-Resolved Spectroscopy of Plasmas Initiated on Single, Levitated Aerosol Droplets," *Opt. Lett.* **12**, 313-315 (1987).

G) A. Zardecki and S. A. W. Gerstl, "Multi-Gaussian Phase Function Model for Off-Axis Laser Beam Scattering," *Appl. Opt.* **26**, 3000-3004 (1987).

ABSTRACT

We analyse the interactions of atmospheric aerosols with a high-energy laser beam. The energy balance equation allows us to compute the conversion of the pulse energy into temperature increase, vaporization, conduction, and convection. We also include the shrinkage term whose significance has recently been discussed by Davies and Brock.

INTRODUCTION

The propagation of a high-flux beam of electromagnetic radiation through the atmosphere results in a variety of interactions between the beam and atmospheric aerosols present along the propagation path. At low irradiances,¹ linear absorption and scattering processes comprise the dominant aerosol-beam interactions. Aerosol heating and vaporization become important as the irradiance increases,²⁻⁶ for even higher irradiances hydrodynamic, plasma, and nonlinear optical phenomena may occur.⁷ The evaporation of micron-size water droplets irradiated by 10.6 μm light, for example, and vaporization by a laser with an irradiance $\sim 10^3$

W/cm², whereas for irradiance levels $\geq 10^6$ W/cm² hydrodynamic, plasma, and nonlinear optical effects become significant.

In this paper, we emphasize the intermediate irradiance regime, where aerosol heating and vaporization are important. In this case, the diffusive mass transport and conductive energy transport dominate the aerosol-beam interactions. A numerical analysis of the coupled aerosol-beam equations allows us to compute the energy conversion of the incident laser pulse. This will be given in the form of plots showing the fractional energy conversion. We include the droplet radius shrinking with time similar in form to that recently analyzed by Davies and Breck.⁵

AEROSOL HEATING AND VAPORIZATION

For an incompressible droplet of density ρ and constant specific heat C , the general energy conservation equation has the form

$$\rho \frac{\partial}{\partial t} (CT_L + \frac{1}{2}v^2) + \rho \nabla \cdot [(CT_L + \frac{P}{\rho} + \frac{1}{2}v^2)\mathbf{v}] + \nabla \cdot (-\kappa \nabla T_L) = W, \quad (1)$$

where T_L and \mathbf{v} are the droplet temperature and velocity at any point of the droplet, κ is the thermal conductivity, and W is the rate at which the energy is absorbed from the beam. For moderate fluxes considered here the kinetic energy term in the first term of Eq. (1) can be neglected as compared to the internal energy of the drop. If a denotes the instantaneous droplet radius, we obtain after integrating over the sphere with the radius $a + \epsilon$, where ϵ is an infinitesimally small number:

$$\frac{4\pi a^3}{3} \rho C \frac{dT}{dt} + 4\pi a^2 m [L + C(T - T_0)] - 4\pi a^2 K \left(\frac{\partial T}{\partial r} \right)_{r=a} + 4\pi a^2 \frac{m^3}{2\rho^2} = \pi a^2 Q_a F. \quad (2)$$

Here we have defined the mass flux $m = \rho v$; L is the heat of vaporisation, and T_0 and T_g refer to the ambient temperature and the temperature of the gas. The other symbols in Eq. (2), K , ρ' , Q_a , and F denote the thermal conductivity and density of the surrounding medium, Mie absorption efficiency factor, and the incident flux, respectively. Finally, the volume-averaged droplet temperature,⁶ is identified with the temperature T at the drop's surface. We note that the term $4\pi a^2 C(T - T_0)$ accounts for the droplet radius shrinking with time. If T_{boil} denotes the boiling temperature, the relative significance of this term can be expressed by the ratio $C(T_{\text{boil}} - T_0)/L$. For water droplets this does not exceed 15%; we retain, however, the shrinkage term for completeness.

Energy and mass conservation in the surrounding medium allow us to compute the mass and heat fluxes. If the explicit time dependence in the conservation equations is ignored, the desired relations are

$$m = \frac{D}{a} \ln \left[\frac{1 - Y_0}{1 - Y_0 \exp\left(\frac{LM}{R^2 T_0} - \frac{LM}{R^2 T}\right)} \right], \quad (3)$$

$$K \left(\frac{\partial T}{\partial r} \right)_{r=a} = - \frac{m C_p (T - T_0)}{\exp(m C_p a / K) - 1}, \quad (4)$$

where D , M , and C_p are the vapor-diffusion coefficient, molecular weight, and specific heat, respectively; R is the ideal gas constant, and Y_0 is the ambient-vapor mass fraction in the surrounding medium.

Inserting Eq. (4) into Eq. (2), and using the relation $m = -\rho \partial a / \partial t$, results in two coupled equations for the droplet temperature and radius. These equations have the form

$$\frac{\partial T}{\partial t} = \frac{3Q_a F}{4a\rho C} - \frac{3m}{4a\rho C} \left\{ L + \frac{C(T - T_0)}{m} + \frac{C_p(T - T_0)}{\exp(m C_p a / K) - 1} + \frac{m^2}{2\rho^2} \right\}, \quad (5)$$

$$\frac{\partial a}{\partial t} = - \frac{m}{\rho}. \quad (6)$$

The beam irradiance F is given by the solution to the transport equation, which—due to the dependence of the scattering and absorption coefficients on F —defines a nonlinear transport problem.

ENERGY DEPOSITION IN IRRADIATED DROPLETS

Equation (2) may be integrated term-by-term over the duration of the pulse and the volume of a single droplet to determine the distribution of incident beam energy into different dissipative modes. This yields:

$$E_H^{(0)} + E_V^{(0)} + E_C^{(0)} + E_S^{(0)} = E_P^{(0)}, \quad (7)$$

where $E_i^{(0)}$ ($i = H, V, C, S$) gives the energy deposited in heating, vaporisation, conduction, and drop shrinking, respectively, and where $E_P^{(0)}$ is the energy of the pulse deposited in a single drop. In Eq. (7), we have neglected the small contribution arising from the convection term. Integrating Eq. (7) over the volume swept by the beam, when the beam traverses a distance s , we get the energy balance equation for the laser beam. In fractional form, it reads

$$Q_H + Q_V + Q_C + Q_S = 1. \quad (8)$$

Here $Q_i = E_i / E_T$ ($i = H, V, C, S$) gives the fraction of the deposited beam energy. At a distance s from the input plane, E_T can be computed from the equation

$$E_T = E_0 - \int F(\mathbf{r}, t) dt d^2r, \quad (9)$$

where E_0 is the initial energy of the pulse.

In Fig. 1, we show the contributions of the energy terms in Eq. (8) for the low flux case in which the maximum value of the irradiance of a Gaussian pulse is 10^3 W/cm². For the sake of completeness, we also show in Fig. 2 the pulse irradiance as a function of the propagation distance x and the time t . In Figs. 3 and 4, we present similar results for a higher flux case corresponding to $F_{MAX} = 10^5$ W/cm².

CONCLUSIONS

In this paper, we have obtained solutions to the coupled system of droplet-beam equations, which are valid for beams of moderate irradiance. The results of these calculations illustrate features of interest such as punch-through and the significance of droplet vaporization. For the low flux case, as shown in Fig. 1, the beam energy is depleted primarily by the droplet vaporisation process. For the high flux case, Fig. 3, the beam energy essentially remains constant although droplet vaporization continues to be the dominant process.

In future work, we will extend these results into the regime where convective vaporization and hydrodynamic effects must be included.

REFERENCES

1. A. Ishimaru, *Wave Propagation and Scattering in Random Media*, (Academic Press, New York, 1978).
2. R. L. Armstrong, "Aerosol Heating and Vaporization by Pulsed Light Beams," *Appl. Opt.* **23**, 148-155 (1984).
3. R. L. Armstrong, "Propagation Effects on Pulsed Light Beams in Absorbing Media," *Appl. Opt.* **23**, 156-160 (1984).
4. R. L. Armstrong, S. A. W. Gerstl, and A. Zardecki, "Nonlinear Pulse Propagation in the Presence of Evaporating Aerosols," *J. Opt. Soc. Am.* **A2**, 1739-1746 (1985).
5. R. L. Armstrong, A. Zardecki, and S. A. W. Gerstl, "Hydrodynamics of Evaporating Aerosols Irradiated by Intense Laser Beams," in *Proceedings of the International Conference on Lasers '85*, edited by C. P. Wang (STS Press, McLean, VA, 1986), pp. 504-509.
6. R. L. Armstrong, P. J. O'Rourke, and A. Zardecki, "Vaporisation of Irradiated Droplets," *Phys. Fluids*, **29**, 3573-3581 (1986).
7. J. P. Reilly, "High Flux Propagation through the Atmosphere," in *Proceedings of SPIE*, Vol 410, edited by J. C. Leader (SPIE, Bellingham, WA, 1983), pp. 2-12.
8. S. C. Davies and J. R. Brock, "Laser Evaporation of Droplets," *Appl. Opt.* **26**, 786-793 (1987).

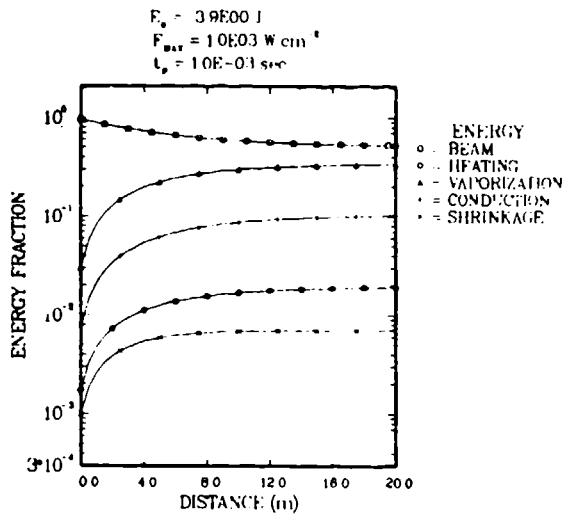


FIGURE 1. Energy balance for $5\mu\text{m}$ water droplets irradiated by $10.6\mu\text{m}$ laser radiation; $F_{MAX} = 1 \times 10^3 \text{ W/cm}^2$.

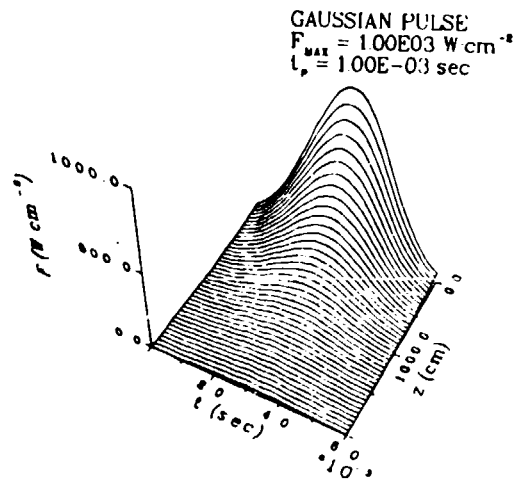


FIGURE 2. Spatio-temporal behavior of laser beam irradiance; $F_{MAX} = 1 \times 10^3 \text{ W/cm}^2$.

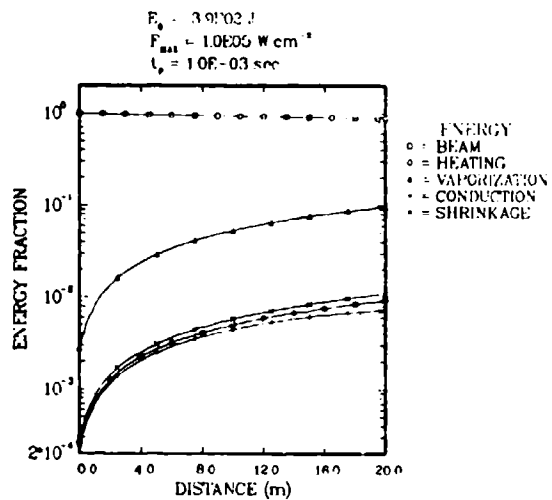


FIGURE 3. Same as Fig. 1, but $F_{\text{MAX}} = 1 \times 10^6 \text{ W/cm}^2$.

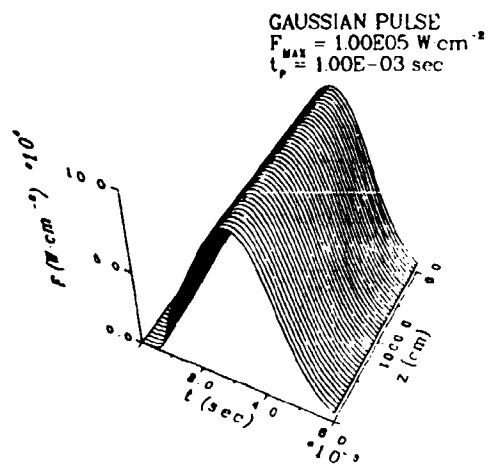


FIGURE 4. Same as Fig. 2, but $F_{\text{MAX}} = 1 \times 10^6 \text{ W/cm}^2$.

EXPLOSIVE VAPORIZATION OF A SINGLE WATER DROPLET BY PULSED LASER RADIATION.

J. C. Carls and J. R. Brock

Department of Chemical Engineering

The University of Texas at Austin, Austin, Texas 78712.

RECENT PUBLICATIONS, SUBMITTALS FOR PUBLICATION AND PRESENTATIONS:

1. J. C. Carls and J. R. Brock, "Explosion of a water droplet by pulsed laser heating", *Aerosol Sci. Tech.* 7,79-91 (1987).
2. S. G. Kim and J. R. Brock, "Growth of ferromagnetic particles from cation reduction by borohydride ions" *J. Colloid Int. Sci.* 116,431-443 (1987).
3. J. R. Brock and J. Oates, "Moment simulation of aerosol evaporation", *J. Aerosol Sci.* 18,59-64 (1987).
4. J. R. Brock, D. Zehavi and P. J. Kuhn, "Formation and growth of binary aerosol in a laminar coaxial jet", *J. Aerosol Sci.*, In Press.
5. S. C. Davies and J. R. Brock, "Laser evaporation of droplets", *Appl. Opt.* 26,786-793 (1987).
6. S. C. Davies and J. R. Brock, "Laser propagation through an evaporating polydisperse aerosol", *Appl. Opt.* 26,1865-1876 (1987).
7. S. G. Kim and J. R. Brock, "Aerosol growth and dynamics" in R. Kohl, Ed., *Proceedings of the 1986 CRDEC Scientific Conference on Obscuration and Aerosol Research*, R. H. Kohl and Assoc., 1987.
8. J. C. Carls and J. R. Brock, "Laser induced explosion of particles", in R. Kohl, Ed., *Proceedings of the 1986 CRDEC Scientific Conference on Obscuration and Aerosol Research*, R. H. Kohl and Assoc., 1987.
9. S. C. Davies and J. R. Brock, "Laser evaporation of droplets", in R. Kohl, Ed., *Proceedings of the 1986 CRDEC Conference on Obscuration and Aerosol Research*, R. H. Kohl Assoc, 1987.
10. Y. L. Chen, J. R. Brock, and I. Trachtenberg, "Aerosol jet etching of fine patterns", *Appl. Phys. Lett.*, In Press.
11. A. Dove and J. R. Brock, "Sulfate aerosol modeling using the EPA Philadelphia Aerosol Field Study", U. S. Environmental Protection Agency Report, 200 pp. 1987.
12. J. C. Carls and J. R. Brock, "Explosive vaporization of a single water droplet by pulsed laser radiation", Abstract AAAR Annual Meeting, Seattle, September 1987.
13. H. Kosuge and J. R. Brock, "Aerosol evolution in jets expanding into low pressure regions", Abstract AAAR Annual Meeting, Seattle, September 1987.
14. J. C. Carls and J. R. Brock, "Laser induced explosion of water droplets by laser radiation", Workshop on Physics of Directed Energy Propagation in the Atmosphere, Las Cruces, N. M., January 1987.
15. J. R. Brock, "Formation and Growth of Ferromagnetic Particles", Department of Physics, University of Paris at Orsay, January 1987.
16. J. R. Brock, "Aerosol Formation and Growth", University of Paris VIII Val de Marne, January 1987.
17. J. R. Brock, "A Complex Terrain Model for Aerosol Dispersion", Chemical Modeling Conference, CRDEC, August 1987.

ABSTRACT

The explosive vaporization of a single aerosol droplet by pulsed laser radiation is investigated. The conservation equations for mass, momentum, and energy have been solved for the asymptotic case of instantaneous heating and for the more general case of finite laser pulse length. The solution diverges from the asymptotic case as the pulse length

becomes comparable to and greater than the acoustic transit time. Extreme cooling in some regions of the flow allows the condensation of small clusters. The differential difference equations have been solved in conjunction with the transport model to show the effect of condensation on the flow.

INTRODUCTION

We are investigating the explosion of single water droplets by pulsed laser radiation. This process is important in studying laser propagation through the atmosphere and laser processing of materials. In addition, a single droplet interacting with intense radiation provides a good opportunity to study droplet compositions, extreme thermodynamic states, and states far from equilibrium. A survey of the current literature shows that there is great interest, both experimental and theoretical, in this problem. Recent papers which include a current literature review are (Chang et al, 1988) for experimental aspects, and (Carls and Brock, 1987) for modeling aspects.

First, we examine the asymptotic case of instantaneous heating. Then we relax the assumption of instantaneous heating and show how the fluid motion changes as the droplet is subjected to pulses of various lengths and intensities. Finally, we show how the motion is affected by condensation of the water into small clusters as the expansion proceeds.

The conservation equations for mass, momentum, and energy govern the hydrodynamic response of the system. The conservation equations are given in Figure 1, along with the heating source term used in subsequent calculations. These have been solved using a Flux Corrected Transport numerical method (Book et al (1982).) The droplet was assumed to be much smaller than the laser wavelength, implying that the electromagnetic field is constant over the droplet.

ASYMPTOTIC CASE

An asymptotic (numerical) solution has been obtained by using the limit of zero laser pulse length. This corresponds

to the case in which the pulse is so short that no fluid motion occurs during the pulse. The pulse length required can be determined by examining the time required for a sound wave to traverse the droplet, the "acoustic transit time". This characteristic time is defined as the droplet diameter divided by the droplet soundspeed. The asymptotic solution is rich in detail because of nonlinearity and coupling in the conservation equations. Some regions of the flow manifest shock waves, with associated shock heating. Other regions of the flow undergo rapid expansion and cooling. Strong cooling allows the possibility of condensation.

The details of the asymptotic solution are described and discussed fully in (Carls and Brock, 1987). Briefly, and referencing Figure 2, the fluid contains three discontinuities, two shock discontinuities and the contact discontinuity. The contact discontinuity is the interface between the water region and the surrounding ideal gas. It moves radially outward as the explosion proceeds. One shock wave is located in the ideal gas region and faces outward. The second shock is in the water region and faces inward, a "rear facing shock." The motion of both shocks as viewed from a stationary reference frame is radially outward. Radially inward of the water shock is a region of isentropic expansion and strong cooling. Condensation occurs first in this region.

FINITE PULSE LENGTH

To investigate departures from the asymptotic case, the model was modified to accept finite laser pulse lengths. The absorption coefficient was allowed to vary quadratically (see Figure 1) with density, following Zuev and Zemlyanov, (1983). Simulations over a wide range of pulse lengths and intensities have been conducted. The conditions for this series of calculations are given in Figure 3. Notice that the intensity varies inversely with the pulse length so that the total energy of the pulse is constant in each case.

Figure 4 shows how varying pulse length affects the amount of energy absorbed by the droplet. The figure shows that for pulse lengths less than about one tenth the acoustic transit time ($ATT = 250$ ps), the energy absorbed is approximately constant. The energy absorbed under these conditions and the fluid flow that results are virtually identical to the asymptotic case discussed earlier. As the pulse length becomes comparable to and greater than the

acoustic transit time, the energy absorbed by the droplet decreases. Thus, the hydrodynamics change and the flow characteristics diverge from the asymptotic solution.

Figure 5 shows the location of the contact discontinuity, the interface between the water (vapor) and the surrounding atmosphere, as a function of time for each of the different heating cases. This figure amplifies the conclusions from the previous figure. For the shortest pulse lengths, the fluid flow is indistinguishable from the asymptotic case, and the trajectory is identical in each case. As the pulse length becomes longer, the position of the contact discontinuity versus time diverges from the asymptotic case. Thus, we see the very important role the acoustic transit time plays in determining the nature of the solution.

The presence of small particles lowers the breakdown threshold of air under laser irradiation. One explanation for this phenomenon has been that absorbing particles explode and shock heat the surrounding air sufficiently to cause ionization (Steverding, 1974). The asymptotic solution shows that the air surrounding the droplet is heated to very high temperatures as it is shock heated by the exploding droplet. Thus, the results for the asymptotic case bear this theory out. However, as the pulse length becomes longer but with the total energy of the pulse constant, the amount of energy absorbed by the droplet becomes much less, and the maximum temperature to which the shock wave heats the surrounding atmosphere is much lower. The results for the more realistic case of finite pulse length show that the maximum air temperature is not high enough to cause much ionization, at least for the small droplets considered. Therefore, enhanced breakdown most likely originates through nonlinear absorption processes in the particle phase.

CONDENSATION

Condensation in the flowfield can significantly change the hydrodynamics through latent heat release and through depletion of monomer to the condensed phase. The possibility of condensation has been included in the simulation by solving the discrete growth/transport equations describing aerosol dynamics and convective transport of the aerosol (Hidy and Brock, 1970). The conservation equation for the number density of clusters containing "i" monomers is given in Figure 6. The terms on the right hand side of the equation are: addition due to nucleation, addition and loss

respectively due to condensation, addition and loss respectively due to evaporation, gain due to coagulation, and loss due to coagulation. Figure 7 shows the new equations of continuity and energy which contain source terms accounting for monomer loss, and latent heat addition.

Figures 8 - 11 show the results of the condensation calculation. Figure 8 shows the location of the contact discontinuity as a function of time for the condensing and the non-condensing cases. As can be seen from the figure, condensation causes the overall motion to slow, and the contact discontinuity does not travel as far in the same amount of time for the condensing case.

Figure 9 shows the variation in temperature for the condensing versus the non-condensing cases. Except in the high temperature shocked region on the right, the greatest temperature difference occurs in the region of lowest temperature (and highest supersaturation.) The condensation occurs most strongly in this region. In this region the temperature difference between the condensing and non-condensing cases increases as the temperature decreases. The rise in temperature is due to release of latent heat as the condensation proceeds. The shocked region on the right shows seemingly anomalous behaviour. This region shows both high levels of condensation and lower temperature compared to the non-condensing case. The high levels of condensation are due to the fact that the density in the shocked region is high, and so the collision frequency is much higher in this region. The increased collision frequency causes a condensation rate which is much higher than in the adjacent colder region, even though the supersaturation in the colder region is higher.

A possible explanation for the lower temperature in the shocked region is that because the overall effect of the condensation appears to be a deceleration of the fluid, the water vapor in the shocked region is not compressed and heated to such a high degree. The velocity of the vapor colliding with the shocked region is lower, leading to lower shock heating, and consequently to lower temperatures in the shocked region.

Figure 10 shows the logarithm of the number density versus radius at a particular time. As can be seen, the number densities are very high, increasing with decreasing temperature as is expected, except in the shocked region where the

number density is highest. Again, the higher number densities in the shocked region are due to higher collision rates and therefore higher condensation rates in this region. Notice how the relatively small scale oscillations in the temperature give rise to much larger perturbations in the number density.

Figure 11 shows the average cluster size in molecules versus radius at the same time level at Figure 10. The clusters formed in the condensations are very small, with the size decreasing with decreasing temperature (and increasing supersaturation.) The increase in the average size in the shocked region is because the supersaturation is lower in this region, leading to a larger critical cluster size, and therefore to a larger average size.

ACKNOWLEDGEMENTS

This work was supported under contract DAAK11-83-K-0006 from CRDEC, U. S. Army. Helpful discussions with Mel Lax, Shirish Chitanvis, Dave Pendleton, Ed Stuebing, and Richard Chang are gratefully acknowledged.

REFERENCES

- Book, D. L., Boris, J. P., Fry, M. A., Guirguis, R. H., and Kuhl, A. L. (1982). In *Lecture Notes in Physics. Eighth International Conference on Numerical Methods in Fluid Dynamics*, (E. Krause, ed.). Springer-Verlag, Berlin, v. 170, p. 143.
- Carls, J. C., and Brock, J. R. (1987). Explosion of a water droplet by pulsed laser heating, *Aer. Sci. Tech.* 7:79.
- Chang, R. K., Eickmans, J. H., Hsieh, W.-F., Wood, C. F., Zhang, J.-Z., and Zheng, J.-B. (1988). Laser induced breakdown in large transparent water droplets, *Appl. Opt.* in press.
- Hidy, G. M. and Brock J. R., *The Dynamics of Aerocolloidal Systems*, Pergamon Press, Oxford, 1970.
- Steverding, B. (1974). Ignition of laser detonation waves, *J. Appl. Phys.* 45:3507.
- Zuev, V. E. and Zemlyanov, A. A. (1983). Explosion of a drop under the action of intense laser radiation, *Sov. Phys. J.* 26:149.

**CONSERVATION EQUATIONS
& HEATING SOURCE TERM:**

$$\frac{\partial \rho}{\partial t} + (\nabla \cdot \rho \mathbf{V}) = 0$$

$$\frac{\partial \rho \mathbf{V}}{\partial t} + (\nabla \cdot \rho \mathbf{V} \mathbf{V}) = -\nabla p$$

$$\frac{\partial \rho E}{\partial t} + (\nabla \cdot \rho E \mathbf{V}) = -\nabla \cdot P \mathbf{V} - \nabla \cdot \mathbf{q}_r$$

where:

$$\nabla \cdot \mathbf{q}_r = \alpha(\rho) I$$

and:

$$\alpha(\rho) = \alpha_0 (\rho/\rho_0)^2$$

FIGURE 1. CONSERVATION EQUATIONS AND HEATING SOURCE TERM.

Schematic of Typical Solution:

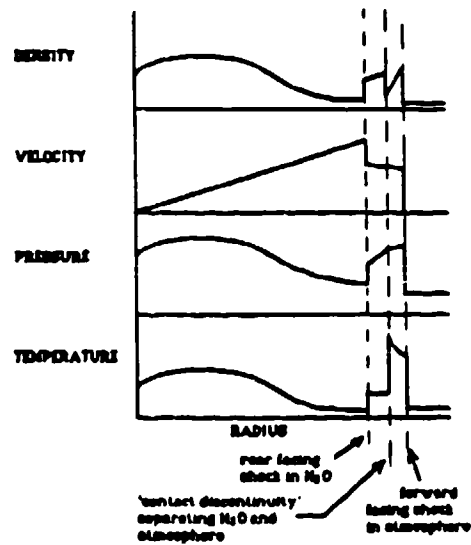


FIGURE 2. TYPICAL DENSITY, VELOCITY, PRESSURE, AND TEMPERATURE PROFILES FOR INSTANTANEOUS HEATING.

DATA ON HEATING SIMULATIONS:

* droplet radius (r_d): 1 micron

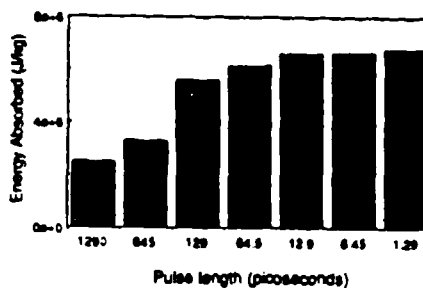
* Initial droplet temperature: 373 K

#	INTENSITY (W/cm ²)	PULSELENGTH (seconds)
1.	5×10^{12}	1.29×10^{-12}
2.	1×10^{12}	6.45×10^{-12}
3.	5×10^{11}	1.29×10^{-11}
4.	1×10^{11}	6.45×10^{-11}
5.	5×10^{10}	1.29×10^{-10}
6.	1×10^{10}	6.45×10^{-10}
7.	5×10^9	1.29×10^{-9}

NOTE: the total energy of the laser pulse is constant in each case.

FIGURE 3. INITIAL CONDITIONS AND LASER PULSE CHARACTERISTICS FOR HEATING SIMULATIONS.

ENERGY ABSORBED BY DROPLET FOR PULSES OF CONSTANT FLUENCE, BUT VARIOUS PULSE LENGTHS



TRAJECTORY OF CONTACT DISCONTINUITY FOR VARIOUS PULSE LENGTH, CONSTANT ENERGY

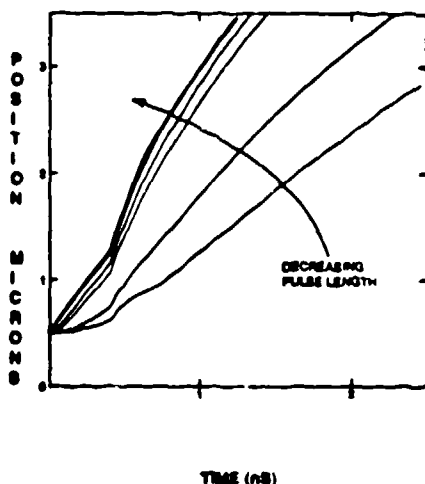


FIGURE 5. POSITION OF CONTACT DISCONTINUITY VERSUS TIME FOR VARIOUS LASER PULSES.

ACOUSTIC TRANSIT TIME:

$$\tau = r_d / C_0 = 250 \text{ pS}$$

FIGURE 4. ENERGY ABSORBED BY DROPLET FOR VARIOUS LASER PULSES.

CONDENSATION:

Conservation equation for the number density of clusters containing "i" monomers:

$$\begin{aligned} \frac{\partial n_i}{\partial t} + \nabla \cdot n_i \mathbf{V} = & J(\rho, \hat{U}) \delta_{i,i^*}(r) \\ & + c_{i-1} n_1 n_{i-1} - c_i n_1 n_i \\ & - d_i n_i + d_{i+1} n_{i+1} \\ & + \frac{1}{2} \sum_{j=1}^{i-1} \beta_{j,i-j} n_j n_{i-j} - n_i \sum_{j=1}^i \beta_{i,j} n_j \end{aligned}$$

FIGURE 6. CONSERVATION EQUATION FOR "i" SIZED CLUSTER.

POSITION OF CONTACT DISCONTINUITY VS. TIME: CONDENSING AND NON-CONDENSING VAPOR

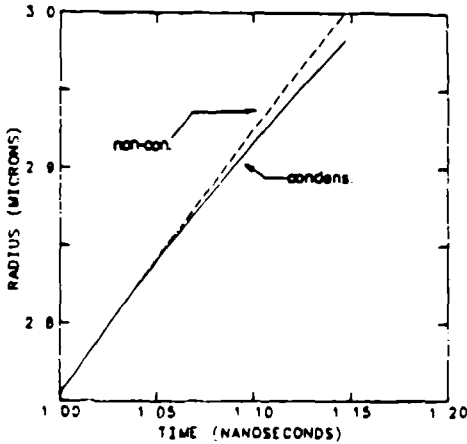


FIGURE 8. POSITION OF CONTACT DISCONTINUITY VERSUS RADIUS FOR CONDENSING AND NON-CONDENSING CASES.

CONDENSATION:

Fluid Conservation Equations:

Monomer Conservation Equation:

$$\frac{\partial n_1}{\partial t} + \nabla \cdot n_1 \mathbf{V} = \frac{dM}{dt}$$

Equation of Energy:

$$\frac{\partial \rho \hat{E}}{\partial t} + \nabla \cdot \rho \hat{E} \mathbf{V} = - \nabla \cdot P \mathbf{V} - \Delta H^{cond} m_1 \frac{dM}{dt}$$

FIGURE 7. EQUATION OF CONTINUITY FOR MONOMER AND OVERALL EQUATION OF ENERGY INCLUDING CONDENSATION SOURCE TERMS.

TEMPERATURE VS. RADIUS AT A
SELECTED TIME: CONDENSING AND
NON-CONDENSING VAPOR

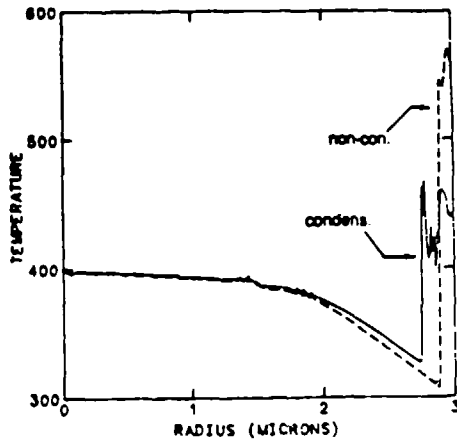


FIGURE 9. TEMPERATURE VERSUS RADIUS AT A
CHOSEN TIME FOR THE CONDENSING AND
NON-CONDENSING CASES.

LOG₁₀ OF NUMBER DENSITY VS. RADIUS
AT A SELECTED TIME

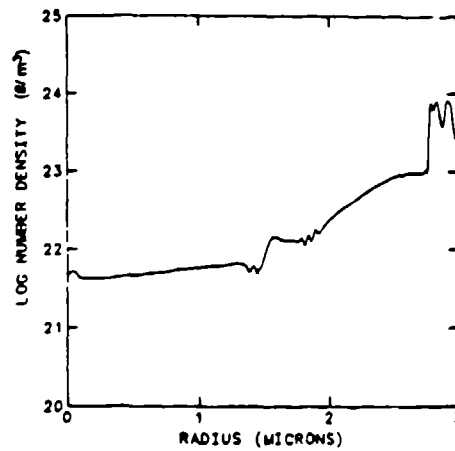


FIGURE 10. LOGARITHM OF NUMBER DENSITY
VERSUS RADIUS AT SAME TIME AS PREVIOUS
FIGURE.

AVERAGE CLUSTER SIZE OF
DISTRIBUTION VS. RADIUS AT A
SELECTED TIME

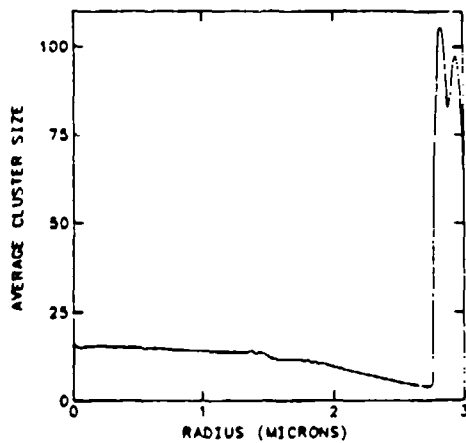


FIGURE 11. AVERAGE CLUSTER SIZE VERSUS
RADIUS AT SAME TIME AS PREVIOUS FIGURES.

Induced turbulence in aerosol-loaded atmospheres.

Shirish M. Chitanvis

Los Alamos National Laboratory, Theoretical Division, MS P-371,

Los Alamos, New Mexico, 87545.

A) S.M. Chitanvis, *Laser Induced turbulence in the atmosphere*, submitted to Phys. Fluids.

ABSTRACT.

We consider the effects of a pulse of radiation from a high energy laser beam on the ambient turbulence that exists in the atmosphere. The atmosphere is considered as a compressible, perfect gas being heated by the high energy laser pulse. We compute correlation functions of the temperature in the isobaric regime, which is deemed the most important for beam propagation. In this regime, the two-point correlation function is changed by a multiplicative factor that grows exponentially in time while the pulse is on. Empirical formulas permit us to connect temperature fluctuations which we can compute to the refractive index fluctuations of the atmosphere. These self-induced refractive index fluctuations will be useful in studying the propagation characteristics of high energy laser beams through the atmosphere.

1. Introduction.

In calculating the effects of a high energy laser beam propagating through the atmosphere, phenomena such as thermal blooming are considered.¹ However, it is customary to assume that the atmospheric turbulence remains unaffected by the high energy laser beam. We shall show in this paper that high energy lasers with a sufficiently high flux F can modify the existing turbulence in the atmosphere.

The problem of turbulence even without an external heat source is of course well known to be quite complicated.² In order to make simplifying assumptions that permit us to solve the problem within restricted regimes, we have identified three time scales of interest.^{A)} In the first case, the pulse length is shorter than the typical hydrodynamic time for the disturbance to propagate across the beam diameter. Thus, only local heating prevails, and the problem becomes quite simple. This is the " t^3 " regime referred to in thermal blooming literature.⁴ In this regime, the two-point temperature correlation function is changed by a small additive term which is quadratic in time. In the second regime, the pulse length is longer than the hydrodynamic time (but shorter than thermal conductivity effects to set in), so that pressure equilibration is achieved, and the process is considered to be isobaric.³ In this regime, the temperature correlations are changed by a multiplicative factor that grows exponentially in time. In the third regime the pulse length is longer than the characteristic thermal conductivity time, so that thermal diffusion sets in and modifies the correlation function.

In section II we have developed the hydrodynamics to be used in the second time regime, since it turns out that it is in this regime that the effects of the laser on the ambient turbulence are the largest.^{A)}

Besides purely atmospheric absorption, it is possible that randomly distributed natural and artificial aerosols can act as absorption centers, giving up part of their absorbed energy to the air. This extra energy, added in a random fashion through the propagation path can further enhance atmospheric turbulence. It is also possible that the addition of absorptive gases to the atmosphere will perform the same task. In fact, it is conceivable that such measures may induce turbulence to a greater degree than will "normal" atmospheric absorption.

Our results on induced turbulence suggest that the use of adaptive optics to correct the distorting effects of atmospheric turbulence on a high energy laser beam is more complicated than thought of before.

It is possible that in addition to general high energy laser propagation problems, our results might also have relevance in lidar remote sensing applications, where high energy lasers are utilized to maximize the return.⁵

II. The hydrodynamic model.

One generally computes correlation functions for the different hydrodynamic variables in turbulence theory. In the present case, we present the following physical reason for the existence of correlations between hydrodynamic variables. The atmosphere absorbs energy from the laser beam in a spatially random fashion at the molecular level, or there may be randomness in the structure of the beam. As time progresses, acoustic waves spread out from these random centers. Interference between these waves will give rise to correlations. We shall now compute ensemble averaged correlation functions.

We shall begin with the usual hydrodynamic equations for the atmosphere considered as single component fluid, and then point out the justifiable simplifying assumptions made:

$$\partial \rho / \partial \tau = - \nabla \cdot (\rho \mathbf{v}) \quad (2.1)$$

$$\rho (\partial \mathbf{v} / \partial \tau + \mathbf{v} \cdot \nabla \mathbf{v}) = - \nabla P + \eta \nabla^2 \mathbf{v} \quad (2.2)$$

$$\rho C (\partial T / \partial \tau + \mathbf{v} \cdot \nabla T) = - P \nabla \cdot \mathbf{v} + \kappa \nabla^2 T + \mathfrak{R}(r, \tau) \quad (2.3)$$

$$\mathfrak{R}(r, \tau) = \alpha(\lambda) I(r, \tau) \quad (2.4)$$

where ρ is the density, τ is the time, \mathbf{v} is the velocity, P is the pressure, η is the viscosity, C is the specific heat at constant volume, κ is the thermal conductivity, \mathfrak{R} is the external heat source due to the incident laser, $\alpha(\lambda)$ is the average absorption in the

atmosphere per unit length (including the effect of absorptive aerosols or gases), dependent on the wavelength λ of the laser beam, and I is the incident flux (W/cm^2).

In order to make the problem of laser induced turbulence tractable, we shall first assume that the incident pulse of electromagnetic radiation has a length $t_T > t_p > t_{hydro}$. Here, $t_{hydro} = d/c$, with d being the width of the laser beam (10cm to 100cm), c being the speed of sound (3.3×10^4 cm/sec), so that $t_{hydro} \sim 0.003$ sec to 0.03 sec, and t_T is the thermal conductivity time. Starting with Eqn.(2.3), we define t_T to be characteristic time for conductivity effects to be established as:

$$t_T = \rho_0 C d^2 / \kappa \quad (2.5)$$

Setting $\rho_0 \sim 10^{-3} gm/cm^3$ (density of air), $d \sim 10-100cm$, $\kappa \sim 2 \times 10^3$ erg/cm-sec- K ,⁵ we get $t_T \sim 20$ to 2000sec. Hence, the conductivity term is ignored in Eqn. (2.3).

The pulse length is long enough for pressure equilibration to have occurred. For this reason, in keeping with the conventional assumptions made in thermal blooming calculations,¹ we shall choose the pressure $P = P_0$ the constant ambient pressure. For computational purposes, we shall take t_p to 10 -100 msec. The equations to be used in this case are:

$$\partial p / \partial t = - \nabla \cdot (\rho v) \quad (2.6)$$

$$\rho (\partial v / \partial t + v \cdot \nabla v) = 0 \quad (2.7)$$

$$\rho C (\partial T / \partial t + v \cdot \nabla T) = -P_0 \nabla \cdot v + \mathcal{Q}(r,t) \quad (2.8)$$

It may be seen from Eqn(2.2) that it is reasonable to define t_{visc} , the characteristic time for viscosity effects to be established in air across the width d of the beam to be $t_{visc} = \rho_0 d^2 / \eta$. Setting $\rho_0 \sim 10^{-3} gm/cm^3$ (density of air), $d \sim 10-100cm$, $\eta \sim 2.0 \times 10^{-4}$ gm/cm-sec,⁶ we find that $t_{visc} \sim 10^3$ sec. Since pulse lengths of high energy

lasers are much shorter than this time, we shall ignore the viscosity term in Eqn. (2.2) in this paper.

It is implicitly assumed that the laser beam does not deposit sufficient energy to generate shock waves in the atmosphere.

In this paper, we explicitly ignore terms such as $-\nabla \cdot (\Pi \cdot E)$ [Π is polarization of the fluid, and E is the electric field] which might appear in Eqn.(2.2). This is because we have assumed that it is the absorption of heat that is the dominant mechanism for inducing turbulence in the atmosphere.

Another feature of Eqns.(2.6)-(2.8) is that unlike conventional treatments of turbulence,³ viscosity does not appear in them. This is because we are studying the "transient" effects of the laser beam on atmospheric turbulence on the time scale of the pulse length $t_p \sim 10 \text{ msec} - 0.1 \text{ sec}$.

IIa. The Isobaric Regime ($t_T > t_p > t_{\text{hydro}}$).

This is the isobaric regime in which dissipative effects may be safely ignored.

IIa.1. Temperature fluctuations.

We shall calculate temperature correlations in this subsection.

Starting from Eqn. (2.8), it is easy to show that $\mathcal{S}(r, r', \tau) = \langle T(r, \tau) T(r', \tau) \rangle$ satisfies the following equation:

$$\begin{aligned} \partial \mathcal{S}(r, r', \tau) / \partial \tau - [(\gamma - 1) / P_0] \langle [\mathcal{R}(r, \tau) + \mathcal{R}(r', \tau)] T(r, \tau) T(r', \tau) \rangle = \\ (2-\gamma) [\langle (\nabla \cdot u) T \rangle + \langle (\nabla' \cdot u') T T' \rangle] + \\ -\nabla \cdot \langle u T T' \rangle - \nabla' \cdot \langle u' T T' \rangle \end{aligned} \quad (2.9)$$

where we have used the perfect gas law $P_0 = (R/\mu)\rho T$ and $(R/\mu)/C_v = (\gamma-1)$. Here, μ is the molecular weight.

Since the laser beam (represented by \mathfrak{R}) induces changes in the temperature correlations and vice versa, we cannot decouple the third correlations that occur in the $\langle(\mathfrak{R} + \mathfrak{R}')TT'\rangle$ term in Eqn.(2.9). There exists a formal solution to the problem, based on techniques used in multiple scattering theory, where averages of products of random variables have to be taken. This solution is sketched in reference A and is given by:

$$\begin{aligned} \partial \mathfrak{S}(r, r', \tau) / \partial \tau - [(\gamma - 1) / P_0] \Sigma(r, r', \tau) \mathfrak{S}(r, r', \tau) = \\ (2-\gamma) [\langle (\nabla \cdot \mathbf{v}) T T' \rangle + \langle (\nabla' \cdot \mathbf{v}') T T' \rangle] + \\ -\nabla \cdot \langle \mathbf{v} T T' \rangle - \nabla' \cdot \langle \mathbf{v}' T T' \rangle \end{aligned} \quad (2.10)$$

where all the complications of decoupling the averages have been lumped into the "self-energy" Σ . Note that we have not imposed translational invariance on the averages in Eqn.(2.10), since it is obvious that the laser beam breaks this symmetry, at least in the direction of propagation. As shown in reference A,

$$\begin{aligned} \Sigma(r, r', \tau) = \langle [\mathfrak{R}(r, \tau) + \mathfrak{R}(r', \tau)] \rangle + \langle \mathfrak{R}(r, \tau) \int_0^\tau \delta \tau' \mathfrak{R}(r', \tau') \rangle \\ - \langle \mathfrak{R}(r, \tau) \rangle \int_0^\tau \delta \tau' \langle \mathfrak{R}(r', \tau') \rangle + O(\mathfrak{R}^3) \end{aligned} \quad (2.10a)$$

We see that the self-energy is expressed as the sum of an average, a mean-squared deviation, etc. Since \mathfrak{R} can be expressed as the square of the electric field, it follows that the self-energy is a function of second, fourth and higher order moments of the electric field. For practical purposes, one may be restricted to looking at the lower order moments alone. On an intuitive basis, one expects the higher order moments, such as the mean squared deviation (the second and third terms on the right hand side of

Eqn.(2.10)) to become important for longer paths of propagation, when the distorting effects of turbulence on the beam profile become stronger.

As is usual in the theory of turbulence, we see that the second order correlations are connected to the third order correlations. In Eqn.(2.9), a prime indicates the value of a function at the point (r',t) . In an effort to estimate the importance of third and higher order correlations, we derived the dynamical equations for the third order correlations $\langle vTT' \rangle$ and $\langle (\nabla \cdot v)TT' \rangle$, neglecting fourth and higher order correlations. These equations were derived using Eqn.(2.7) and Eqn.(2.8).

$$\partial \langle vTT' \rangle / \partial t = [(\gamma-1)/P_0] \Sigma \langle vTT' \rangle \quad (2.11)$$

$$\partial \langle (\nabla \cdot v)TT' \rangle / \partial t = [(\gamma-1)/P_0] \Sigma \langle (\nabla \cdot v)TT' \rangle \quad (2.11a)$$

The solutions to Eqns.(2.11) and (2.11a) are simple:

$$\langle vTT' \rangle = \langle vTT' \rangle_{eq} \cdot \exp [\{ (\gamma-1)/P_0 \} \int_0^t \delta\tau' \Sigma(r,r',\tau')] \quad (2.12)$$

$$\langle (\nabla \cdot v)TT' \rangle = \langle (\nabla \cdot v)TT' \rangle_{eq} \cdot \exp [\{ (\gamma-1)/P_0 \} \int_0^t \delta\tau' \Sigma(r,r',\tau')] \quad (2.12a)$$

where the subscript eq denotes the equilibrium value of the correlation functions in the atmosphere before the laser was turned on. The exponential dependence of the correlation function in the presence of the laser is worth noting.

We may now substitute Eqns. (2.12) and (2.12a) in Eqn. (2.10) and solve the resulting equation to get:

$$\zeta(r, r', \tau) = \zeta(r, r', 0) \exp \left[\left\{ \frac{\gamma - 1}{P_0} \right\} \int_0^\tau \delta \tau' \Sigma(r, r', \tau') \right] + \int_0^\tau \delta \tau' \left[\zeta(r, r', \tau') - \zeta'(r, r', \tau') \right] \quad (2.13)$$

where

$$\zeta(r, r', 0) = \langle T T' \rangle_{eq} \quad (2.14)$$

$$\zeta(r, r', \tau) = 2(2 - \gamma) \langle (\nabla \cdot v) T T' \rangle_{eq} \exp \left[\left\{ \frac{\gamma - 1}{P_0} \right\} \int_0^\tau \delta \tau' \Sigma(r, r', \tau') \right] \quad (2.15)$$

and

$$\zeta'(r, r', \tau) = 2 \nabla \cdot \{ \langle v T T' \rangle_{eq} \exp \left[\left\{ \frac{\gamma - 1}{P_0} \right\} \int_0^\tau \delta \tau' \Sigma(r, r', \tau') \right] \} \quad (2.16)$$

Equation (2.13), supplemented by the definitions in Eqns.(2.14)-(2.16) represents our approximate solution to the problem of laser induced turbulence in the atmosphere.

The main feature of Eqn.(2.13) is the exponential dependence on the heating source term. This dependence indicates that as time progresses, the fluctuations grow exponentially in time. It is as if a "wave" of intense electromagnetic radiation came along and swept up the the temperature fluctuations already existing in the atmosphere, amplifying them. Of course, it should be remembered that for times longer than t_{visc} and t_T our model is no longer valid.

The density and velocity correlation functions have been derived in reference A. And we shall not discuss them here, as the effect of the laser is most pronounced on the temperature, as compared to the other hydrodynamical variables.^{A)}

III. Laser Beam Propagation Characteristics.

We shall now concentrate on the isobaric regime which is accessible to high energy lasers in terms of pulse lengths. We shall also show that the effect on the turbulence in this regime can be significant, depending on the laser beam parameters. The wavelength λ of high energy lasers ranges from $0.25\mu\text{m}$ to $10.6\mu\text{m}$. And correlations at those spatial points separated by a distance of a few wavelengths will be important to the beam propagation. The reason for this is that the phase of the incident laser beam (which is given initially by $\exp(ik \cdot r)$) will change in a distance the order of a wavelength, and it is of interest to know if the refractive index of the medium changes on that length scale as well (see the next section for the connection between temperature fluctuations and refractive index fluctuations). This argument is analogous to the one used in linear propagation of laser beams through turbulence,⁷ where it is assumed that in the limit of geometric optics, only eddies with dimensions less than or equal to the inner length scale l_0 are important for optical propagation.

Let us note the following identity:

$$\langle (v-v')(T-T')^2 \rangle_{\text{eq}} = 2 \langle v'TT' \rangle_{\text{eq}} - 2 \langle v'TT' \rangle_{\text{eq}} \quad (3.1)$$

$$= 4 \langle v'TT' \rangle_{\text{eq}} \quad (3.1a)$$

Now, when $l_0 \gg |r-r'| \sim \lambda$, where l_0 is the inner length scale of the ambient turbulence³ $\langle (v-v')(T-T')^2 \rangle_{\text{eq}} \sim \langle v'TT' \rangle_{\text{eq}} \sim |r-r'|^3$. Similarly, $\langle \nabla' \cdot v'TT' \rangle_{\text{eq}} \sim |r-r'|^3$, $\nabla' \cdot \langle v'TT' \rangle_{\text{eq}} \sim |r-r'|^2$, while $\langle TT' \rangle_{\text{eq}} \sim \langle T \rangle^2$.

For this reason, using Eqn.(3.1a), the third order correlations may be ignored in Eqn. (2.19) when considering propagation of lasers operating in the micron wavelength region. A reasonable amount of simplification is then introduced into the expression for \mathcal{S} :

$$\mathcal{S}(r, r', \tau) = \langle TT' \rangle_{\text{eq}} \exp \left[i_0 \int^{\tau} \delta \tau' f(r, r', \tau) \right] \quad (3.2)$$

where

$$f(r, r', \tau) = \{(\gamma-1)/P_0\} \Sigma(r, r', \tau) \quad (3.2a)$$

In Eqn.(3.2), if we set $\tau = 0$ or $l = 0$ (l appears in f), we see that $\mathcal{S} = \langle TT' \rangle_{eq}$.

Since $\langle TT' \rangle_{eq} = \langle \delta T + \langle T(\gamma) \rangle (\delta T' + \langle T(\gamma') \rangle) \rangle_{eq} = \langle \delta T \delta T' \rangle_{eq} + \langle T(\gamma) \rangle \langle T(\gamma') \rangle_{eq}$, it is reasonable to define the fluctuation function in the presence of the laser source as

$$\langle \delta T \delta T' \rangle = \langle \delta T \delta T' \rangle_{eq} \exp\left\{ \int_0^\tau \delta \tau' f(r, r', \tau') \right\} \quad (3.3)$$

For the sake of definiteness, we note that $\langle \delta T \delta T' \rangle_{eq}$ is given in the inertial subrange ($l_0 < |r-r'| < L_0$) by:³

$$\langle \delta T \delta T' \rangle_{eq} = C_T^2 |r-r'|^2 / 3 \quad (3.4)$$

in the dissipative range, for $|r-r'| \ll l_0$ we have:³

$$\langle \delta T \delta T' \rangle_{eq} = [C_T^2 / l_0^{(4/3)}] |r-r'|^2 \quad (3.5)$$

Following the arguments given at the beginning of the section, Eqn.(3.5) is to be used in Eqn.(3.3). Note that Eqns.(3.4) and (3.5) give approximately equal numerical values for the fluctuations for $|r-r'| \approx l_0$.

In Eqn.(3.3), if we set $\tau = 0$ or $l = 0$ (l appears in f), we see that $\langle \delta T \delta T' \rangle = 0$. Also, when $\gamma = \gamma'$, $\langle \delta T \delta T' \rangle = 0$.

The right hand side of Eqn.(3.3) indicates the exponential way in which the ambient turbulence is amplified when the laser beam is turned on. The amplification factor defined as

$$A = \exp\left\{ \int_0^\tau \delta \tau' f(r, r', \tau') \right\} \quad (3.6)$$

The factor A performs two tasks. First of all, it magnifies the turbulence to an extent defined by the laser and medium parameters. Secondly, it defines the spatial profile (i.e. length scales) of

the modified turbulence as well. As defined by Eqn.(3.3), the exponent in Eqn.(3.6) is basically the sum of the powers of the flux absorbed at the two points r, r' . Now, as the beam propagates, the refractive index fluctuations will create incoherence within the extent of the beam. This incoherence is expressed for example by the mean-squared squared deviation in the intensity that occurs in Eqn.(2.2b). This incoherent pattern will be impressed on the temperature (or equivalently refractive index) fluctuations through Eqn.(3.3). Therefore, the typical length scales of these patterns will also be reflected in these fluctuations. If these length scales are smaller than l_0 , the inner scale of the Kolmogorov spectrum, they could dominate the behavior of the beam. As a zeroth order approximation (ambient turbulence), the coherence length is⁸ $\rho_{coh} \sim [C_n^2 (2\pi z/\lambda)^2]^{3/5}$, where C_n^2 is the structure constant of the refractive index fluctuations, z is the propagation distance, and λ is the wavelength. For $C_n^2 \sim 10^{-15} \text{ m}^{-2/3}$, $\lambda = 10.6\mu\text{m}$, $z = 1\text{km}$, $\rho_{coh} \sim 100\mu\text{m} \ll l_0 \sim 1\text{mm}$. The implication then is that such small scale fluctuations may appear in a full-fledged calculation of the propagation of the laser beam. The change in the beam profile due to thermal blooming will be superposed on the scintillations.

We will now estimate the order of magnitude of A for two different cases. For simplicity, we shall consider a beam that is uniform in both space and time and assume that Σ is given by the incident flux itself. As an example, we find that at $\lambda = 10.6\mu\text{m}$, with $t_p = 10\text{msec}$, $\alpha = 0.0003 \text{ m}^{-1}$, $P_0 = 10^5 \text{ N/m}^2$, $I = 10^8 \text{ W/cm}^2$, we get $A \sim e$.

Similarly, at $\lambda = 3.8\mu\text{m}$, $t_p = 10\mu\text{sec}$, $\alpha = 0.045 \text{ km}^{-1}$, with $P_0 = 10^5 \text{ N/m}^2$, $I = 10^8 \text{ W/cm}^2$, $A \sim 1.001$. On the other hand, we could artificially increase α by adding an absorptive substance which might increase the absorption in air by a few orders of magnitude. In this case $A \gg 1$.

IV. Connection with the refractive index fluctuations.

There is a simple empirical relation between refractive index fluctuations and temperature fluctuations which holds under ambient atmospheric conditions:⁹

$$\langle \delta n \delta n' \rangle = B \langle \delta T \delta T' \rangle \quad (4.1)$$

where B is a constant.⁹ We shall now assume that the same relationship holds when the laser is turned on.

It then follows from Eqn.(4.1) that

$$\langle \delta n \delta n' \rangle = \langle \delta n \delta n' \rangle_{\text{eq}} [\langle \delta T \delta T' \rangle / \langle \delta T \delta T' \rangle_{\text{eq}}] \quad (4.2)$$

$$= \langle \delta n \delta n' \rangle_{\text{eq}} A(r, r', t) \quad (4.2a)$$

where A is given by Eqn.(3.6).

Equation (4.2a) can be used in studying the propagation of laser beams, as it is this quantity that appears in most formulations of laser beam propagation through turbulence.

Our main concern with the use of Eqn.(4.1) is that we do not know its validity when an external heat source is turned on. But in the absence of better experimental data, we shall persist in using Eqn.(4.1).

V. Conclusions.

We have investigated the effect of high energy-lasers on ambient turbulence. Two-point correlation functions for the temperature were calculated in the isobaric regime. The effect of the laser, treated as a heat source, is most pronounced on temperature correlations. The correlations, such as the density and velocity correlations have been derived in reference A. We have argued that the isobaric regime is the most important as far as the beam propagation is considered.^{A)}

It is possible that the predictions of our theory may be checked experimentally.

Efforts are under way to calculate in a self-consistent fashion the effects of induced turbulence on a high energy laser beam propagating through the atmosphere. In this way we shall quantify further the discussion in section III.

VI. Acknowledgments.

I wish to acknowledge helpful discussions with J. Wallace and A. Zardecki on various aspects of the problem.

¹ P.B. Walsh and J.L. Ulrich, *Thermal blooming in the atmosphere*, Laser Beam propagation in the Atmosphere, "Topics in Applied Physics", Vol. 25, Ed. J.W. Strohben, Springer-Verlag (1978).

² V.I. Tatarskii, *The effects of the turbulent atmosphere on wave propagation*, NTIS document no. TT-68-50464, translated by the Israel Program for Scientific Translations, (1971).

^{A)}S.M. Chitanvis, *Laser Induced Turbulence in the atmosphere*, submitted to *Phys. Fluids*.

⁴ J. Wallace and M. Camac, *J. Opt. Soc. Am.* **60**,1587 (1970)

⁵ D.K. Killinger and N. Menyuk, *Laser remote sensing of the atmosphere*, *Science*,**235**,37 (1987)

⁶C.D. Hodgman, R.C. Weast, S.M. Selby, *Handbook of Chemistry and Physics*, Chemical Rubber Publishing Co., (1958)

⁷ S.F. Clifford, *The Classical theory of wave propagation in a turbulent medium*, Laser Beam propagation in the Atmosphere,

"Topics in Applied Physics", Vol. 25, Ed. J.W. Strohben, Springer-Verlag (1978).

⁸ V.E. Zuev, *Laser beams in the Atmosphere*, Consultants Bureau, 1982.

⁹ A. Ishimaru, *Wave Propagation in Random Media*, Vol II, Academic Press 1978.

IV. WORKSHOP: HANDLING INDIVIDUAL PARTICLES

Blank

OPTICAL LEVITATION OF SINGLE PARTICLES

Thomas R. Lettieri
National Bureau of Standards
Gaithersburg, MD 20899

ABSTRACT

Experimental techniques are presented for optically levitating single particles using laser radiation pressure.

INTRODUCTION

The acceleration and trapping of single microparticles by laser radiation pressure was first demonstrated by Ashkin in 1970 [1]. By focussing a CW laser beam onto single microspheres in liquid suspension, he was able to move dielectric particles along the beam axis and trap them between two counterpropagating laser beams. Since then, he and other researchers have been able to optically levitate many types of particles including liquid droplets [2], solid microspheres [3], bubbles and microballoons [4], multiplets [5] and, more recently, live viruses and bacteria [6]. Various geometries have been used in these experiments.

Optical levitation of single microparticles has several advantages over other levitation techniques such as electrostatic, electrodynamic, or radiometric suspension: (i) optical levitation is simple and uses little equipment; (ii) uncharged particles can be levitated; (iii) a wide range of diameters can be suspended; (iv) multiplets, assembled from single particles, can be levitated; (v) several individual particles can be stably levitated simultaneously; and (vi) particles can be stably trapped for many hours or even days. Optical levitation also has its limitations: (i) in general, only transparent or weakly absorbing particles can be stably suspended (metallic particles, for example, are not easily levitated); (ii) the upper size limit is about 50 μm in diameter; (iii) the particles usually sit in an intense electric field, which can cause problems with data interpretation; (iv) an optical trap is not strong enough to hold a particle in even a moderate gas-flow field; and (v) optical levitation requires the use of a relatively expensive laser (such as an argon-ion laser).

The present paper is intended to give some helpful, practical tips for optically levitating microparticles of different types. Topics considered include the use of vertical and horizontal laser beams, techniques for getting the particles into the laser beam, levitation of multiplets, and stabilization of particle motion by opto-electronic feedback circuitry.

OPTICAL-LEVITATION GEOMETRIES

Many types of optical-levitation geometries have been developed, each

having certain advantages and disadvantages. In general, an optical trap can be classified as: single or double beam; vertical or horizontal beam; and weak or strong focussing. There are also some specialized traps such as the gradient-force and the fiber-optic traps.

Single Vertical Beam

The simplest optical-levitation trap uses one focussed laser beam directed vertically upward (Figures 1 and 2). Here, the upward radiation-pressure force is balanced by gravity so that the particle sits in stable equilibrium either above or below the focal point [7].

Ashkin, Dziedzic, and others [8] have shown that a microsphere with refractive index greater than the surrounding medium will be trapped laterally by a force gradient across a laser beam having a TEM₀₀ (Gaussian) intensity profile (Figure 2). These forces bring the particle into the center of the beam where the net lateral force is zero. Thus, the microsphere sits in a potential well which, for a transparent particle in the proper size range, is stronger than the Brownian-motion and thermal forces on the particle. For a microsphere with refractive index less than the medium, say a microballoon or a bubble, the lateral forces of a TEM₀₀ profile will kick it out of the beam; in this case, a TEM₀₁* ("donut") laser mode can be employed [8].

A particle in a single-beam vertical trap can be stably suspended for many hours and can be easily manipulated by moving the focussing lens up, down, or side-to-side.

Double Horizontal Beams

In a double-beam optical trap, two laser beams are horizontal and counterpropagating; the particle will seek a stable equilibrium point at which the horizontal radiation-pressure forces cancel [9]. The particle is balanced upward against gravity by the gradient force across the Gaussian intensity cross-section of the TEM₀₀ beams [9]. A typical double-beam trap is shown in Figure 3. Here, the particle can be moved side-to-side by varying the intensities of the two beams; this is done using the variable beamsplitter. In this manner, the particle can be positioned for subsequent observation and analysis at the focus of a collection lens [10].

Gradient-Force Trap

A new type of optical trap, the gradient-force trap, uses a very strongly focussed laser beam which propagates downward [11]; the upward force of the strong intensity gradient balances the downward force of gravity (Figure 4). The advantage of this optical-levitation scheme is that absorbing particles can be trapped; however, the particles must be very small, on the order of a few nanometers. Ashkin and Dziedzic have used the gradient-force trap to catch and hold live viruses and bacteria for many hours of observation [11].

Fiber-Optic Trap

Pocholle et al. demonstrated that microparticles can be stably levitated above the end of an optical fiber by the radiation pressure of laser light transmitted through the fiber [12]. One advantage of this type of trap is that the optical path can be very complicated since the fiber is flexible. Thus, a microparticle can be levitated in normally inaccessible places [12].

EXPERIMENTAL CONSIDERATIONS

In this section, various experimental parameters and conditions for stable optical levitation are considered.

Particle Characteristics

Material In general, the particle must be made of a transparent or very weakly absorbing dielectric material, otherwise the particle will rapidly heat up and become unstable in the intense electric field of the laser beam. Examples of suitable materials are: optical-quality glass and quartz, polystyrene, silicone oil, glycerol, DOP, DBP, and DBS. The particle should be free of inclusions and surface contamination and should be as homogeneous as possible. Exceptions to this are the gradient-force trap, which has been used to stably levitate absorbing particles that are very small, and the "donut mode" trap, which has been used to levitate metal spheres.

Size For most optical traps, the size range for stable optical levitation is about 5 to 50 μm in diameter. At the lower size limit, Brownian motion tends to push the particle out of the beam, while at the upper size limit the particles are too massive for stable levitation. With the gradient-force trap, very small particles of a few nm can be levitated [11].

Laser Characteristics

Type The most common laser for optical-levitation purposes is the argon-ion laser, used either at the green or the blue wavelengths. Typical laser powers are on the order of 50 mW to 1 W. At low power, the particle will come to equilibrium close to the beam focus, so that the incident laser intensity varies greatly across the particle. [The extreme case is a "speared" particle which sits right at, and is much larger than, the beam focus]. At high laser power, the particle sits far from the focus, and the incident field is more uniform across the particle. The latter situation is better when comparing experimental data with theoretical calculations since the incident light more closely approximates a plane wave.

Other types of lasers have been used for optical levitation; the main requirement is that the power be sufficient to levitate the desired type of particle. For example, a copper vapor laser would be a good substitute for an argon laser, while a helium-neon laser would not. Both YAG and nitrogen lasers have also been used to stably levitate particles.

Transverse Mode As noted earlier, the TEM₀₀ (Gaussian) mode is used with solid particles, and the TEM₀₁* ("donut") mode is used with hollow particles.

Focussing The laser beam can be focussed with any positive lens having focal length from a few mm to a few cm. All else being equal, the stronger the focussing the stronger the trap; an f/number too large may result in a trap which is too weak to stably levitate the particle. Good choices for lenses are 5X and 10X microscope objectives.

Optical Cell

Stable optical levitation requires an optical cell to minimize air currents. A simple six-sided glass cell is sufficient; it could be made from glass microscope slides, or it could be a cuvette or other off-the-shelf optical cell. Absorbing materials should be avoided especially at the laser-beam input and output faces, since they can heat up and cause problems with thermal convection. A typical optical cell is shown in Figure 5.

LEVITATION OF DROPLETS, SOLID PARTICLES, AND MULTIPLETS

The experimental techniques for handling droplets, solid particles, and multiplets are somewhat different from each other.

Droplets

The easiest type of microparticle to optically levitate is a droplet. It can be generated by an atomizer, a Berglund-Liu aerosol generator, or other devices which can generate polydisperse or monodisperse droplets. After the droplets are produced, there must be some way to get them into the optical cell: a 1/2 to 1 mm hole in the top of the cell works fine. A funnel can be used to guide the particles through the hole and into the laser beam. In general, many droplets will fall through the hole; with some luck and skill, only one can be trapped. [If several are caught, all but one can usually be removed by momentarily interrupting the beam]. To minimize air currents, the hole should be moved out of the beam after the particle has been trapped; a sliding top works well for this purpose (Figure 5). Also, with atomizers there is little control over the size of the particle that will be trapped. Thus, some means for sizing the levitated droplet must be available, for example a microscope with a calibrated eyepiece reticle. The spacing of the Mie fringes at 90 degrees can also be used for this purpose [Lettieri, et al., Ref. 2].

A final consideration for droplets is that they must be slowly evaporating; that is, they must have a high vapor pressure. Rapidly evaporating droplets change size too quickly to come to stable equilibrium. Therefore, liquids such as water and most alcohols should be avoided unless some provision has been made to control the atmosphere, for example by supersaturation. Usable liquids include silicone oil, glycerol, index-matching liquids, DOP, DBP, DBS, and other clear, heavy oils.

Solid Particles

Solid particles can be launched into the laser beam by several techniques. The simplest method, shown in Figure 6, is to sprinkle the particles through a hole in the top of the optical cell using a "salt shaker" [10]. One drawback of this approach is that, since many particles fall through the hole, more than one particle will usually trap in the focussed beam. If this occurs, the extra particles can be removed by momentarily interrupting the beam until only one particle remains, as noted earlier. The other drawback of this approach is that there is no control over which particle levitates with regard to its size, sphericity, or surface quality.

To eliminate these drawbacks, a more sophisticated particle-launching procedure uses a piezo-electric or acoustic vibrator to shake the particles off the bottom of the cell [13]. Figure 7 shows the piezo-electric version of the vibration scheme. The procedure for trapping a particle with this arrangement is as follows. First, the optical cell is scanned horizontally until the desired particle is located (proper size, shape, cleanliness, etc.). Then, this particle is moved into the laser beam, and the focus brought down until it is just above the particle. The piezo-electric transducer is then "chirped" quickly through a range of frequencies (typically a few tens of kHz) in order to pop up the chosen particle. It should then trap at its equilibrium point, and the beam focus can be moved upward to its original position.

The above experimental considerations hold for solid particles, although they are still valid for hollow microballoons if a TEM₀₁* laser mode is used.

Multiplets and Aspheres

Ashkin and Dziedzic have assembled and levitated various types of multiplets and aspheres including doublets, triplets, spheroids, and spheres-within-spheres [14]; some of these are shown in Figure 8. The reader is referred to Reference 14 for details on how these particles are made by combining single microspheres and droplets.

FEEDBACK STABILIZATION OF LEVITATED PARTICLES

A microparticle in an optical trap undergoes Brownian motion which, if strong enough, can kick the particle out of the beam. Even if these forces are not strong enough, the particle may still bounce around too much for close observation and/or analysis. Thus, it is often desirable to stabilize a levitated particle by some means. For this reason, Ashkin and Dziedzic [15] designed an electro-optical feedback system which controls the laser intensity such that a levitated particle is locked in a fixed position (Figure 9). Briefly, the particle is imaged onto a split-field detector; the differential signal from the detector is amplified and fed to an electro-optical modulator which controls the laser intensity. If the particle drops, the intensity increases to raise it. Conversely, if the particle rises, the laser intensity decreases. There

is also a time-derivative term in the amplifier to dampen the particle motion. Note that this system appears to only lock the longitudinal position of the particle (along the laser-beam axis). However, the transverse position (across the beam) is also locked since transverse motion of a particle in a Gaussian beam is always accompanied by longitudinal motion (see Figure 2). With a feedback stabilization system, particle position can be fixed to better than 1 μm [15].

APPLICATIONS

The main application of optical levitation has been in high-resolution particle sizing using various light scattering techniques, primarily resonance light scattering (RLS). The RLS technique makes use of the sharp morphological resonances which occur in Mie scattering as a function of wavelength [16]. Single microspheres can be sized to better than 100 ppm using RLS, while size changes can be detected at the 10 ppm level [16]. In particular, the evaporation rate of levitated droplets has been accurately measured using RLS [17, 18]. Resonance light scattering has also been applied in measuring an accurate mean diameter for an ensemble of microspheres, although these were in liquid suspension rather than optically levitated [19].

High-resolution measurements of refractive index can also be made using RLS from optically levitated droplets. By matching experimental and calculated resonances, Chylek, et al. have simultaneously determined the refractive index and diameter of silicone oil droplets to better than 50 ppm [20].

Finally, Raman spectroscopy has been done on optically levitated particles, both solid microspheres [10] and liquid droplets [21]. One reason for levitating particles in spectroscopic applications is to keep them away from the substrate in order to avoid spurious effects such as particle deformation, Raman scattering and fluorescence from the substrate, and coupling of scattered light between the particle and the substrate [21]. Although other levitation schemes can be as effective for spectroscopic purposes, optical levitation has at least one major advantage, namely that the same laser beam which suspends the microparticle can also be used to excite the Raman spectra. Because of the high sphericity of optically levitated droplets, inelastic light scattering spectra show the same morphological resonances as do elastic Mie scattering spectra [10, 21]. However, Raman spectra of nonspherical microcrystals do not contain morphological resonances; these spectra are identical to that of the bulk material [10].

CONCLUSION

Optical levitation can be used to suspend single particles of many different types using relatively simple equipment. It has certain advantages over other single-particle suspension techniques, although its limitations preclude its use in some cases, especially where the particle is highly absorbing or is in a strong gas-flow field. Despite these shortcomings, optical levitation should find increasing application in experiments where a single, motionless particle is required.

REFERENCES

- [1] A. Ashkin, Phys. Rev. Lett. 24, 156 (1970).
- [2] A. Ashkin and J. Dziedzic, Science 187, 1073 (1975);
T. Lettieri, W. Jenkins, and D. Swyt, Appl. Opt. 20, 2799 (1981).
- [3] A. Ashkin and J. Dziedzic, Appl. Phys. Lett. 19, 283 (1971);
A. Ashkin and J. Dziedzic, Appl. Phys. Lett. 28, 333 (1976);
G. Roosen, Can. J. Phys. 57, 1260 (1979).
- [4] A. Ashkin and J. Dziedzic, Appl. Phys. Lett. 24, 586
(1974).
- [5] A. Ashkin and J. Dziedzic, Appl. Opt. 19, 660 (1980);
A. Ashkin and J. Dziedzic in "Light Scattering by
Irregularly Shaped Particles", D. Schuerman, ed. (Plenum Press,
New York, 1980).
- [6] A. Ashkin and J. Dziedzic, Science 235, 1517 (1987).
- [7] A. Ashkin and J. Dziedzic, Appl. Phys. Lett. 24, 586 (1974);
G. Roosen, Can. J. Phys. 57, 1260 (1979).
- [8] A. Ashkin, Phys. Rev. Lett. 24, 156 (1970); A. Ashkin,
Sci. Amer. 226, 63 (Feb. 1972); G. Roosen and C. Imbert,
Opt. Comm. 26, 432 (1978).
- [9] G. Roosen, Opt. Comm. 21, 189 (1977).
- [10] R. Thurn and W. Kiefer, Appl. Spec. 38, 78 (1984).
- [11] A. Ashkin, J. Dziedzic, J. Bjorkholm, and S. Chu, Opt.
Lett. 11, 288 (1986); A. Ashkin and J. Dziedzic, Science
235, 1517 (1987).
- [12] J. Pocholle, et al., Appl. Phys. Lett. 45, 350 (1984).
- [13] R. Thurn and W. Kiefer, Appl. Spec. 38, 78 (1984); A.
Ashkin and J. Dziedzic, Appl. Phys. Lett. 19, 283 (1971).
- [14] A. Ashkin and J. Dziedzic, Appl. Opt. 19, 660 (1980).
- [15] A. Ashkin and J. Dziedzic, Appl. Phys. Lett. 30, 202
(1977).
- [16] See for example: A. Ashkin and J. Dziedzic, Phys. Rev.
Lett. 38, 1351 (1977); P. Chylek, J. Kiehl, and M. Ko,
Phys. Rev. A 18, 2229 (1978); R. Benner, P. Barber, J.
Owen, and R. Chang, Phys. Rev. Lett. 44, 475 (1980); A.
Ashkin and J. Dziedzic, Appl. Opt. 20, 1803 (1981).
- [17] K. Fung, I. Tang, and H. Munkelwitz, Appl. Opt. 26, 1282
(1987).
- [18] T. Lettieri, W. Jenkins, and D. Swyt, Appl. Opt. 20, 2799
(1981).
- [19] T. Lettieri and E. Marx, Appl. Opt. 25, 4325 (1986).
- [20] P. Chylek, et al. Appl. Opt. 22, 2302 (1983).
- [21] T. Lettieri and R. Preston, Opt. Comm. 54, 349 (1985);
R. Preston, T. Lettieri, and H. Semerjian, Langmuir 1, 365
(1985).

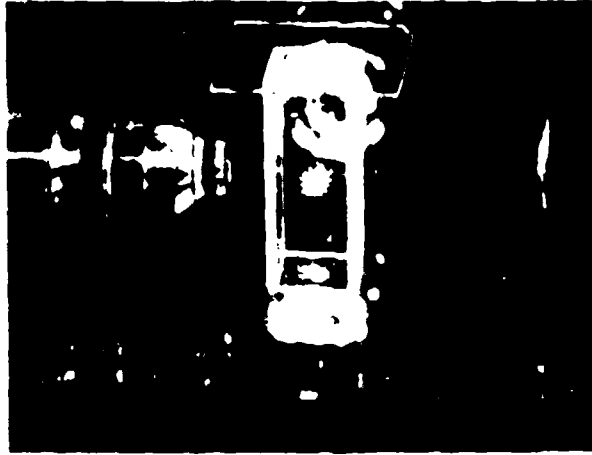


FIGURE 1. LEVITATED DROPLET. Photograph of a liquid droplet levitated on a vertical laser beam.

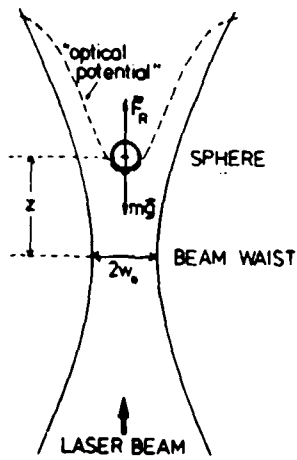


FIGURE 2. VERTICAL TRAP. Optical trap using one vertical, TEM₀₀-mode laser beam. From Ref. [10].

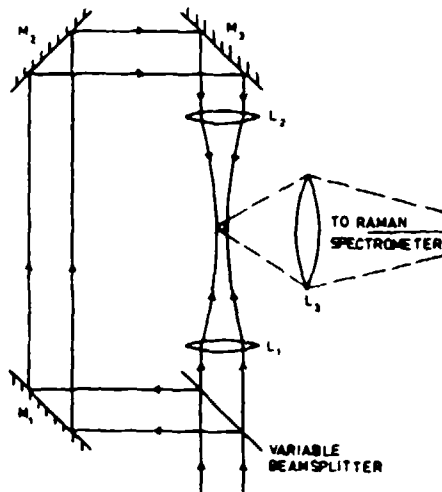


FIGURE 3. HORIZONTAL TRAP. Optical trap using two horizontal laser beams. From Ref. [10].

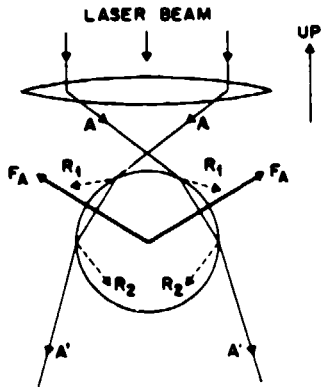


FIGURE 4. GRADIENT TRAP. Single-beam, gradient-force optical trap. From Ref. [11].

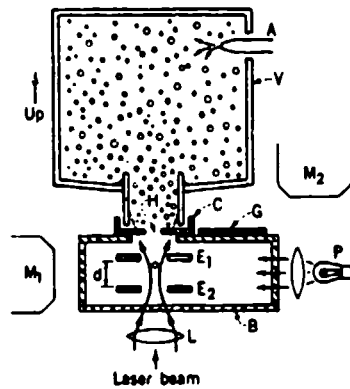


FIGURE 5. LEVITATION APPARATUS. From Ashkin and Dzidezic [2].

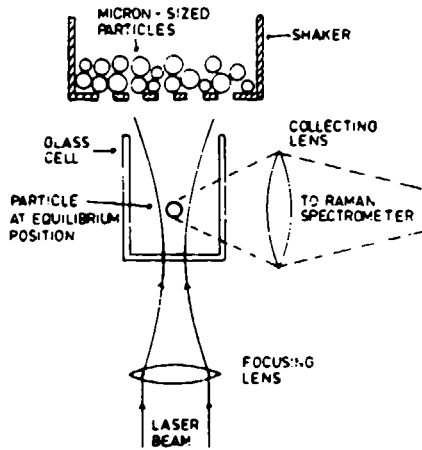


FIGURE 6. "SHAKER" METHOD. "Salt shaker" method for getting solid particles into laser beam. From Ref. [10].

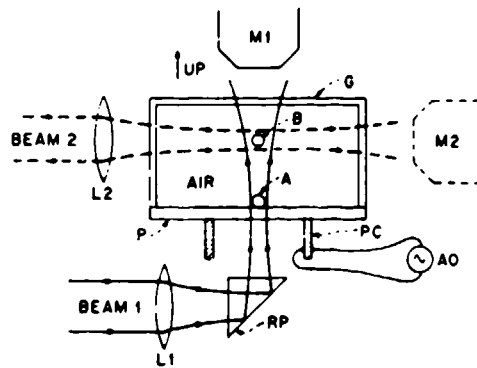


FIGURE 7. PZT METHOD. Piezo-electric "popper" for getting particles into laser beam. From Ashkin and Dziedzic, Ref. [3].

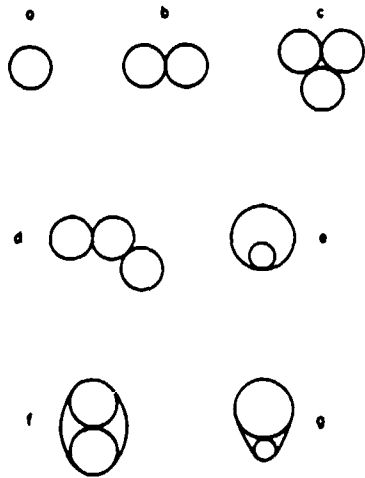


FIGURE 8. MULTIPLETS AND ASPHERES. Examples of multiplets and aspheres which have been made and optically levitated. From Ref. [14].

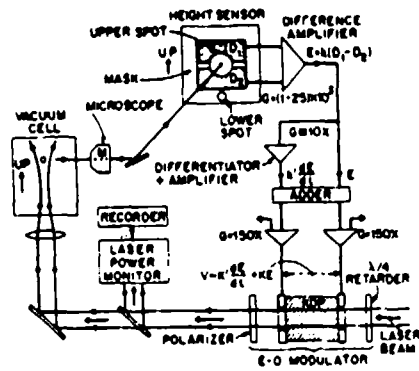


FIGURE 9. FEEDBACK APPARATUS. EO apparatus for feedback stabilization. From Ref. [15].

AEROSOL JET ETCHING OF FINE PATTERNS

Y. L. Chen, J. R. Brock and I. Trachtenberg
Department of Chemical Engineering
University of Texas, Austin, Texas 78712

ABSTRACT

Successful demonstration of a new etching technique, aerosol jet etching (AJE), is reported. AJE has been used to pattern fine lines with good anisotropy in silicon dioxide surfaces on silicon substrates using an hydrofluoric acid ultrafine aerosol jet.

INTRODUCTION

In aerosol science there has long been an interest in the interactions between aerosol particles and surfaces, as evidenced by numerous studies in filtration, impaction, lung deposition, atmospheric dry deposition, etc. However, in most cases, the particles considered in these applications have been chemically inert with respect to the surface material. There appear to be no references in the literature to investigations of interactions between highly reactive particles with surfaces. We have recently initiated studies of the interaction of highly reactive particles with surfaces with the application in view of producing fine patterns on the surfaces. Such patterning is commonly referred to as "etching".

Etching is an important process that is repeated several times during the fabrication of integrated circuits. Present etching technology includes "wet chemical etching" and "dry etching". Conventional wet etching is carried out by dipping devices to be etched in a bath of an etchant liquid, such as, for example, aqueous hydrogen fluoride solutions for etching silicon dioxide. Dry etching methods include plasma etching, reactive ion etching, ion beam milling, etc. These technologies each have their particular limitations^{1,2}. We have demonstrated a new etching technique, "aerosol jet etching" (AJE), which has been used to pattern fine lines in silicon dioxide surfaces on silicon substrates using an hydrofluoric acid aerosol jet. This new technique overcomes some of the limitations found in present etching technologies.

DESCRIPTION

Aerosol jet etching (AJE) was conceived as a technique which might have the potential for combining in one method the high selectivity of wet etching processes with the high degree of directionality (anisotropy) found with plasma etching or ion beam milling methods, but without some of the disadvantages of these methods^{1,2}. The basic ideas in AJE are illustrated in Fig. 1. An aerosol is generated by mixing an etchant vapor with an inert gas so as to bring about homogeneous nucleation of fine etchant particles. After nucleation and particle growth, the gas-particle mixture is then expanded into a partial vacuum (1 - 50 torr) through a nozzle. Because of their relatively

small mass, the gas molecules are scattered by collisions with the background gas molecules in the etching chamber and removed by pumping. The aerosol particles (typically 0.05 - 0.2 μm in diameter) are much more massive than the gas molecules and hence are largely unaffected by collisions with the background gas molecules over a substantial distance (several centimeters, depending on pressure). In this manner, a beam of energetic ultrafine particles can be directed onto a substrate to be etched. The etching reaction proceeds immediately after a particle hits the substrate. Etching rate can be controlled by adjusting the many process variables, such as particle size and concentration, substrate temperature, etc. While simple in outline, AJE involves many complex phenomena, including nucleation and particle growth processes, particle transport in compressible flow, and the impact, evaporation, and reaction processes of the ultrafine particles at the substrate surface. These last have hardly been explored in the literature.

RESULTS

In our first application of the AJE concept, we have investigated etching of silicon dioxide films (thermal oxide and phosphosilicate glass) on silicon with ultrafine aerosol consisting of the 38.2 weight % azeotrope of hydrofluoric acid. Both polymer photoresist and aluminum masks were used. In the course of this exploratory work, a number of process variables were studied, including chamber pressure, substrate temperature, carrier gas flow rate, and nozzle size and configuration. We discuss here only two important variables -- etching chamber pressure and substrate temperature.

As a first step, it was determined from a number of trials that a jet of a vapor mixture of water and HF impinging on SiO_2 surfaces in our system produced completely negligible etching rates. Therefore, all etching phenomena produced in our experiments can only be due to contact of liquid particles with SiO_2 . In order for this contact to occur, a necessary but not sufficient condition is that particles have sufficient inertia to impact on the surface and not be deflected substantially by the motion of the host gas. This impaction process has been extensively studied in the context of particle collection and classification by instruments termed inertial impactors^{2,3,4}. The efficiency with which particles of diameter D and mass density ρ in a directed jet impact on a surface is dependent on a number of parameters including Re the Reynolds number and Ma the Mach number of the jet leaving the nozzle, η the ratio of the downstream stagnation pressure to the upstream pressure, v ratio of the nozzle diameter to the distance of the impaction surface from the nozzle exit, and the so-called Stokes number, Stk : $Stk = \rho U D^2 C / 18 \mu d_n$, where U is the jet velocity, d_n the nozzle diameter, μ the viscosity of the gas in the jet, and C the Cunningham slip correction factor. Under our operating conditions, the ratio η of downstream stagnation pressures to upstream pressure is small, generally less than 0.1. We determined experimentally also that the flow through the nozzle is choked and therefore, $Ma = 1.0$. With decreasing particle size, represented nondimensionally by $Stk^{1/2}$, the pressure ratio η must decrease in order for impaction to occur. This is well illustrated from our experiments by Fig. 2 showing etch depth in μm for 1 minute etching time of thermal silicon dioxide as a function of etching chamber

pressure. The aerosol chamber pressure was constant at 700 torr. As can be seen, at an etching chamber pressure of 200 torr for a 1 minute etch the etch depth is small and is evidently decreasing to zero. Therefore at etching chamber pressures somewhat above 200 torr no etching would occur because the particles are unable to impact on the SiO₂ surface. From the data of Fig. 2, and other similar data, it is possible to estimate the upper bound diameter of the particles in our etching experiments. For the experimental conditions of Fig. 2, the diameter of the largest particle that impacts on the substrate surface is around 0.2 μm . This maximum diameter is also confirmed from estimates based on the theory of homogeneous nucleation and particle growth.

A necessary condition for etching to occur in the AJE process is particle impaction. However, impaction of a particle does not necessarily imply that the particle adheres to and wets the surface; it is, of course, the liquid-solid reaction that is responsible for etching. Therefore, it is first necessary that an impinging particle not "bounce off" (reflect from) the surface; it is common experience in impactor operation^{6,8,5} that bounce off is not an important factor in deposition for liquid particles. An additional condition is that the temperature of the impaction surface be below the so-called "Leidenfrost point"^{6,8,6}. Above this point, evolution of vapor from a particle is sufficiently rapid that a vapor barrier is created preventing the drop from wetting the surface. The Leidenfrost point is dependent on the temperature of the surface, the properties of the drop, and the properties of the surface, among other factors. However, the available information in the literature does not deal with the behavior on a heated surface of such small, energetic particles as used in this study. In any event, our experimental observations show that surface temperature is a critical variable in determining etch rate. In our experiments we were only able to control the substrate temperature; we have not measured surface temperatures at the point of impact of the particles. Fig.3 shows etch depth in μm in thermal silicon dioxide as a function of etch time in minutes at a chamber pressure of 35 torr with substrate temperature as parameter. It is clear that etching rate is critically dependent on the substrate temperature.

Immediately before the azeotrope particles, travelling at a substantial fraction of sonic velocity, hit the surface, their temperature is in the range 243 - 263K. If the particles wet the surface, *isolated* particles of diameter in the range 0.05 - 0.2 μm have thermal relaxation times of the order of a nanosecond or less, and evaporative lifetimes of the order of microseconds to milliseconds, depending on their temperature. With the assumption of adherence and surface wetting, from estimates of ranges of particle number concentration in the jet, the jet velocity, the evaporative lifetime, and particle size, it is possible to estimate the fraction of the impaction surface covered by particles at any instant. For our experiments, this fraction is estimated to be in the range 0.01 - 1.0, with the lower figure being typical for the smallest particles at the higher surface temperatures. Surface coverage above 1.0 is possible; this can occur at surface temperatures sufficiently low to permit particle coalescence on the surface and formation of liquid films. If liquid films form in AJE, one has almost a conventional wet etching process with consequent loss of anisotropy in etching. This leads to our experimental observation that higher degrees of anisotropic etching in AJE are achieved when the surface coverage is less than or equal to 1.0. The nearer to 1.0, the faster the etch rate. Therefore, control of etching chamber pressure, surface temperature, particle size and mass flux is important in

implementation of a rapid, anisotropic AJE process.

Fig. 4 shows a sequence of micrographs of etching of 0.9 μm PSG (10 mol% P_2O_5) on silicon substrate using an aluminum mask pattern for various etching times. The first micrograph shows the typical cratered surface found with AJE; such patterns are also found in etching thermal silicon dioxide. These craters are not produced by a single particle, since the particle diameters are at least an order of magnitude smaller than the typical crater diameter. We believe that craters are formed by a process involving initial rapid etching of certain preferred sites on the surface. These sites become the centers for preferential accumulation of impacting particles, leading to rapid crater growth. Finally, as shown in the last two micrographs in the sequence, the craters begin to coalesce and finally disappear exposing the underlying smooth silicon surface. In the final micrograph, the anisotropy is estimated to be around 0.7 (maximum anisotropy possible is 1.0). Fig. 5 shows an example of a fine line etch pattern produced by AJE on PSG on silicon.

Aerosol jet etching (AJE) is a novel technique which may combine the high selectivity of wet etching with the fine line anisotropic etching capability of some of the dry etching processes, but without some of their disadvantages. AJE significantly reduces the volume of environmentally hazardous waste products and results in no radiation damage. Already we have demonstrated that AJE is successful in fine line etching of silicon dioxide with reasonably good anisotropy, which, based on our present understanding of the process, we believe may improve with etch depth. AJE may therefore become of interest in the developing trench device technology. We are now investigating the application of AJE to other etchants and surfaces. In addition to the applications noted here, the phenomena observed in AJE are of fundamental interest and may have applications outside of fine line patterning, such as in machining, surface decontamination, etc.

ACKNOWLEDGMENT

We thank M. Schmerling for his generous assistance with SEM. This work was supported by the Texas Advanced Technology Research Program. We (I.T.) acknowledge the support of Texas Instruments Incorporated.

REFERENCES

1. *Thin Film Processes*, W. Kern and J. L. Vossen, eds. (Academic, New York, 1978).
2. C. M. Melliar-Smith, *J. Vac. Sci. Technol.* 13, 1008 (1976).
3. V. A. Marple and C. M. Chien, *Environ. Sci. Technol.* 14, 976 (1980).
4. P. Biswas and R. C. Flagan, *Environ. Sci. Technol.* 18, 611 (1984).
5. Y.-S. Cheng and H.-C. Yeh, *Environ. Sci. Technol.* 13, 1392 (1979).
6. A. A. Mills and N. F. Sharrock, *Eng. J. Phys.* 7, 52 (1986).

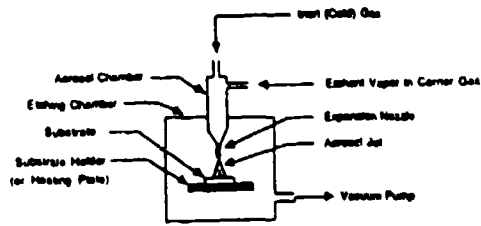


Fig. 1. Schematic diagram of aerosol jet etching (AJE) system.

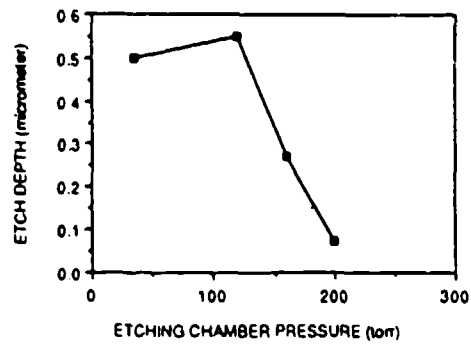


Fig. 2. Etch depth in thermal silicon dioxide versus etching chamber pressure for 1 minute etch time. Etching conditions: Silicon substrate, temperature, 30°C; Carrier gas flow rate, 790 cc/min.

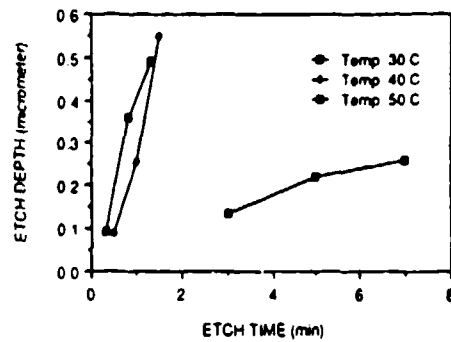


Fig. 3. Etch depth in thermal silicon dioxide versus etch time with substrate temperature as parameter. Etching conditions: Etching chamber pressure, 35 torr; Carrier gas flow rate, 790 cc/min.

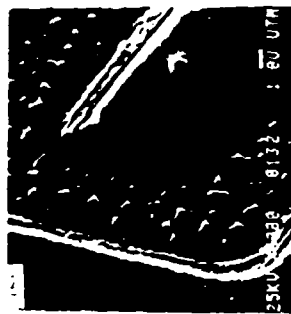
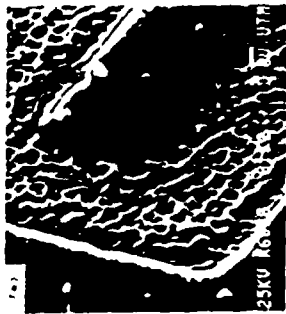


Fig 4 SEM micrographs from aerosol jet etching (AJE) of 0.9 μm PSG on silicon for various etch times: (a) 0.5 min.; (b) 0.8 min.; (c) 1.0 min. Anisotropy approximately 0.7. Substrate temperature is 150 $^{\circ}\text{C}$. Contaminants appearing in figures occurred because samples were not handled in a clean room.

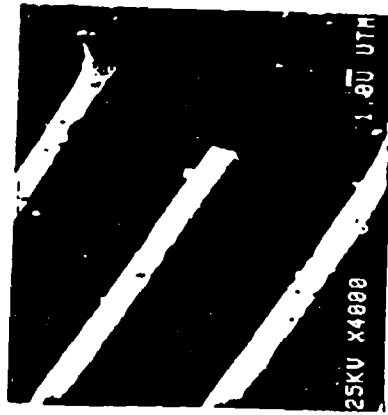


Fig 5 SEM micrograph from aerosol jet etching of 0.9 μm PSG on silicon. Substrate temperature is 30 $^{\circ}\text{C}$. Contaminants appearing in figure occurred because samples were not handled in a clean room.

V. OPTICAL PROPERTIES OF AEROSOLS

Blank

STATUS OF THE MICROWAVE SCATTERING FACILITY (MSF) UPGRADE

R. T. Wang

Space Astronomy Laboratory, University of Florida
1810 NW 6th Street, Gainesville, FL 32609

RECENT PUBLICATIONS, SUBMITTALS FOR PUBLICATION AND PRESENTATIONS:

- A) R. T. Wang, "The Microwave Scattering Facility (MSF)," in Proceedings of the 1986 CRDEC Conference, R. Kohl, ed. (in press).
- B) R. T. Wang, "Findings Through MSF Upgrade," Presented at the 1987 CRDEC Conference (June 1987).

ABSTRACT

This paper summarizes the status of the Microwave Scattering Facility (MSF) upgrade in terms of improved efficiency, accuracy and versatility of measurement operations. Emphasis was on identifying all factors which affect measurement, precision and accuracy. For example, the scattering chamber's temperature fluctuation was confirmed to be a major drift error source due to the uneven expansion/contraction of two wave paths - via waveguide and via free space - and hence the work done on the judicious readjustment of waveguide path lengths, circulation of water over extended lengths of pipes which are in thermal contact with the waveguides, minimizing microwave leaks and insulation of waveguides, use of new programmable microwave sources for monitoring the outcome, etc. The upgrade is not yet fully completed, but the major results to date are presented and discussed as they affect the measurements.

UPGRADING THE MSF AND THE FINDINGS

As reported previously [Ref.7], the remarkable advantages of the microwave technique over other optical methods lie in the precise controls/uses of the following critical factors in studying a single-scattering process:

1. Particle size (or the size parameter $x=2\pi a/\lambda$, a -radius, λ -wavelength).
2. Target shape (single particle or agglomerates).
3. Orientation/position of particle in the beam.
4. Polarization states of incident/scattered radiation.
5. Complex refractive index $m=m'-im''$ of target medium.
6. Discrimination of the true scattering against the unwanted, coherent background via the use of the microwave-unique compensation (or null) technique.
7. Absolute magnitude calibration of the scattered radiation.

Of these, #3, #5, #6 and #7 have been paid special attention during the MSF upgrade. This emphasis derived primarily from our experience in operating the MSF and partly from discussions with other Army-supported researchers who kindly voiced their criticisms and needs during the Army Research Office scattering workshop at Gainesville, FL, April 24-25, 1986. Fig. 1 depicts the present MSF schematic wherein the rerouted waveguide paths, temperature sensor positions, new equipment locations, etc., are shown to facilitate the discussion. Rather extensive figures and tables are also incorporated here for the same reason.

A. Target Orientation/Positioning Device

A device capable of quickly and precisely orienting/positioning a scatterer of desired shape in the beam, and which contributes little to the total scattering, is indispensable to the MSF. We have previously developed a PDP11/03 computer-controllable device [Ref. 4; sketched in Fig. 1] that employed a nylon-strings-only target mounting/suspension net (in the beam region) driven by an assembly of stepping motors, turntable, gears and rods in the out-of-beam region. This device performed the desired functions except that it required frequent maintenance - potentiometer wear, malfunctioning during wintertime, mechanical alignment, etc. A new VME-MIZAR controller system tied to the new PDP11/23 computer (Fig. 1) has therefore replaced the above motor control system. Instead of recording/monitoring target orientations through potentiometers, the new system works by direct counting of pulses transmitted to stepping motors of the drive mechanism, thereby eliminating the use of potentiometers and also alleviating the effort in target-orientation calibration. The installment of this new VME-PDP control system was also mandated by the need to control multiple equipment - microwave source, phase-lock counter, temperature sensors, line-voltage monitoring device, lock-in amplifier, etc. (see also Sec. C). Almost all interface computer programs driving these gears were written in C-language and are linked to the operator's Fortran programs for a variety of measurement runs.

B. Complex Refractive Index $m=m'-im''$ of Target Medium

The reliability of our complex refractive index measurement data using the well-established waveguide-slotted-line technique [2,3] was re-examined. Guided by the Factorial Experiment Technique [1], 3 acrylic and 3 expanded polystyrene waveguide samples, all about 20 years of age and of nearly the same size, density and fabrication process among each material group, were chosen from our inventory to repeat refractive-index measurements under 3 controlled environments: (a) placed in a vacuum chamber, (b) left in normal room conditions, and (c) enclosed in a water-vapor-saturated chamber. The new data sets were compared against each other, and, in particular, the sets by procedure (b) were compared against the old measurement results. Table I shows the comparisons, from which we deduce the following: (1) $m=m'-im''$ of acrylic material depends appreciably on humidity and on aging (perhaps by atmospheric oxidization), even though the physical dimension of a sample is rather stable. A typical result in Table I showed a shift from $m=1.61-iz0.006$ (1968) to $m=1.66-iz0.01$ (1986). (2) On the other hand, the expanded polystyrene samples absorbed little moisture (by weight-monitoring under the above environmental conditions (a), (b) and (c)) and registered little changes both

in $m-m'-im''$ and in density, even though both the sample volume and weight decreased by about the same 0.6% during these 20 years, most probably by sublimation of the ingredient volatile chemical.

Being a crucial parameter in a scattering process, $m-m'-im''$ of a target should be precisely known and should be stable, especially when the target is used as an absolute scattering-magnitude calibration standard. Based on the above findings, we have also conducted a search for other stable plastic materials and have recently prepared several new standard spheres/spheroids made of teflon/delrin. Both materials are distinctly different from plexiglass or expanded polystyrene in the measured refractive index ($m_{\text{teflon}} = 1.4319 - i0.0016$, $m_{\text{delrin}} = 1.7006 - i0.022$) and in specific gravity ($\rho_{\text{teflon}} = 2.1600$ grams/cc, $\rho_{\text{delrin}} = 1.4087$ grams/cc). Careful measurements on angular scattering (see also Sec. D) and on extinction are being made so that these new targets will be included as calibration standards. Studies of effective refractive indexes of mixtures (such as polystyrene and carbon) have also started and will be reported in the near future.

C. Microwave Compensation (or Null) Technique

Perhaps one of the most striking features of the MSF is the extensive use of this microwave-unique technique which enables us to discriminate the true scattering against the unwanted coherent background, even in the beam direction where the background intensity may be ~ 1000 times larger than the intensity scattered from a typical 5 cm diameter target. For the purpose of this discrimination, we split the radiation from the microwave source into two paths: one goes entirely through a waveguide (reference wave, with an optical path length denoted by L_R) and the other through the scatterer in free space via antennas and waveguides (direct wave, with a total optical path length denoted by L_D). These two waves recombine at a mixer hybrid junction (magic tee). For easier understanding of the null technique both a simplified hardware schematic and an appropriate vector diagram are depicted in Fig. 2. In the absence of a target in the beam, the unwanted direct wave is compensated (or nulled) by adjusting the amplitude (ψ) and phase (ϕ) of the reference wave so that the reference wave is equal in amplitude but 180° out-of-phase with respect to the unwanted direct wave. The output port of the magic tee will then register a minimum. The lower the signal level of this minimum, the better is the degree of nulling. As a target is hoisted into the beam, the unbalanced wave appearing in the same magic tee output port is exactly proportional to the scattered wave from the target. If the initial deep nulling condition can be maintained sufficiently long enough

for a typical measurement run, the compensation is said to be stable, and the target in the beam is allowed to go through a preselected sequence of orientations in space, thereby recording the orientation-dependent scattering. The absolute scattering magnitudes are calibrated by measuring, in quick succession, the scattering from standard targets of known magnitudes.

Accuracy of our MSF measurement is thus seen to depend critically on the stability of compensation; thus compensation drift would be a major source of error. Priority was therefore given to the isolation and remedy of the major sources of instability in upgrading the MSF. The following logical steps were taken:

(a) Step 1: Error Source Analysis

The null technique is essentially an interference technique employing two coherent waves from the same source. As mentioned earlier, one wave travels through an optical path length L_D and the other wave through L_R (cf. also Fig.2). An optical path length L is the algebraic sum of (effective refractive index \times physical length) along the wave path. For example, with a second suffix A or G to indicate whether the path is through air (whose refractive index can be assumed equal to 1) or through waveguide, respectively, we can explicitly write [6]:

$$\begin{aligned} L_D &= L_{DA} + L_{DG} \sqrt{1 - (\lambda/2a)^2} \\ L_R &= L_{RG} \sqrt{1 - (\lambda/2a)^2} \end{aligned} \quad (1)$$

where a is the wider dimension of a rectangular waveguide opening ($a=2.286$ cm for our X-band waveguides). Both L_D and L_R depend not only on the physical dimensions L_{DG} , L_{RG} and a , but also on the wavelength λ (or equivalently, on the frequency $f = c/\lambda$, c = speed of light in free space) of the microwave source. A stable compensation (or nulling) is possible if, and only if, the phase difference $P=2\pi(L_D-L_R)/\lambda$ between these two waves can be maintained constant ($=\pi$); i.e., uneven changes in L_D and L_R with respect to time cause the unwanted drift or noise using this technique. Furthermore, it has been noticed for a long time [6] that the environmental temperature T and the frequency stability of the microwave oscillator were the two dominant factors affecting the compensation stability of P . Hence, the error source analysis here is focused only on the effects of variations of T and f , neglecting other less dominant disturbances such as power-line fluctuations, building/ground vibrations, etc. Discussion is also confined to $\theta=0^\circ$ scattering where the effects of (T,f) show up most markedly due to the presence of large beam background, although the same argument holds for the other scattering

angles θ . Detailed algebraic derivations are omitted, and only those important formulae are listed.

$$\text{Time rate of null drift} = \frac{\Delta P(f, T)}{\Delta t} = \frac{\partial P}{\partial f} \frac{\Delta f}{\Delta t} + \frac{\partial P}{\partial T} \frac{\Delta T}{\Delta t} \quad (2)$$

Straightforward differentiations of Eqs. (1) yield the rate of drift due to frequency change and to temperature variation:

$$\frac{\partial P}{\partial f} = \frac{2\pi}{\lambda f} [L_{DA} + (L_{DG} - L_{RG})/\sqrt{1-(\lambda/2a)^2}] \quad (3)$$

$$\frac{\partial P}{\partial T} = \frac{2\pi}{\lambda} \left[\frac{\partial}{\partial T} L_{DA} + \frac{\partial}{\partial T} \{ (L_{DG} - L_{RG})/\sqrt{1-(\lambda/2a)^2} \} \right] \quad (4)$$

Eq. (3) shows that $\partial P/\partial f$ is minimized by a judicious adjustment of waveguide lengths so that

$$L_{DA} + (L_{DG} - L_{RG})/\sqrt{1-(\lambda/2a)^2} = 0. \quad (5)$$

Furthermore, it was found that this waveguide-length adjustment, Eq. (5), could also lead to minimizing the drift due to temperature change to

$$\frac{\partial P}{\partial T} = \frac{2\pi}{\lambda} \times 1.1 \times 10^{-5} (L_{DG} - L_{RG}) = 1.9^\circ/\text{C}, \quad (6)$$

if we take the coefficients of linear thermal expansion of concrete (on which the reference waveguide is laid) and brass (the waveguide material) respectively as [8]

$$\beta_{\text{concrete}} = 10^{-5}/^\circ\text{C} \quad \text{and} \quad \gamma_{\text{brass}} = 1.8 \times 10^{-5}/^\circ\text{C}. \quad (7)$$

Even with this judicious adjustment of waveguide lengths, Eq. (5), and with a well-stabilized oscillator frequency Eq. (6), shows that the system is virtually useless unless the target-scattered signal is much larger than (beam signal $\times \sin(\frac{\partial P}{\partial T} \frac{\Delta T}{\Delta t})$), where ΔT is the temperature drift over the run time Δt . Some measure of temperature control is obviously needed.

(b) Step 2: Stability Monitoring

In parallel to the preceding Step 1 analysis, quantitative monitoring of the scattering chamber temperature and powerline fluctuation versus time were deemed necessary in order to find the necessary fixes. Fourteen solid-state temperature sensors were therefore placed along the critical paths of compensation, 11 of which were directly attached to waveguides by thermally conducting glue, while the remaining 3 were supported at the tops of beam-height plastic pipes and could be moved around a large space of the chamber. The actual locations of these 14 sensors are shown in Fig. 1 via their ID numbers. The new VME and PDP11/23 computers recorded each sensor's temperature over an extended time period with/without circulating water along pipes in thermal contact with waveguides (water pipes during Step 2 covered only about 3/5 of the total waveguide length); and with/without microwave radiation. Figs. 3A-3D and Figs. 4A-4D depict some typical monitoring records without water circulation but with microwave radiation. Temperature reading of each sensor with ID is along ordinate while the recording time (at a 15-minute interval) is along abscissa. Midnight and 8:00 A.M. are marked by vertical dotted lines. In particular, Figs. 3B-3D demonstrate the degree of compensation drifts in 2 output channels (S_x and S_y in Fig. 1) which were nulled initially, to compare in absolute magnitude the recorded scattered signals S_x and S_y from a standard calibration sphere, the largest sphere then available. Figs. 5A-5D duplicate Figs. 4A-4D except that water is now running near the sensors #3 and #4. Much more flattened temperature profiles in Figs. 5C-5D than in the corresponding Figs. 4C-4D are clearly seen. Even more striking is the similarity between the compensation drift profiles (Fig. 3C & 3D) and the very common temperature variation trends versus time (Figs. 3A & 3B, Figs. 4A-4D, Figs. 5A-5D); i.e., both showing conspicuous changes until midnight hours, tapering until sunrise, and resuming rapid variation thereafter. These monitoring records also provided a quantitative explanation of why our $\theta=0^\circ$ measurements could only be performed successfully in early morning hours and confirmed our belief that constancy of chamber temperature was critical for the compensation technique.

To monitor the second source of disturbances to compensation, a new Superior Electric's Stabiline AC voltage monitor was installed to record power-line surges, sags and impulses under preset threshold potentials. Over a period of several weeks this device monitored perturbations both on the unstabilized and the Sorensen-stabilizer-controlled AC power sources. Both registered a number of such events which could contribute to experimental errors - knocking the new microwave source out of its frequency-lock, for example. The perturbations usually came in the form of short pulses, lasting about 0.5 - 1.5 cycles of line frequency especially when

equipment is turned on (or off). The unstabilized AC voltage was observed to vary as much as ± 10 volts in a particularly busy-loaded day.

(c) Step 3: Work on Improving Stability

Improvement was made on the aforementioned critical factors, especially those related to temperature controls. Along with the findings, the work is explained in roughly chronological sequence. (1) Although two new ventilation fans installed in the chamber ceiling did not minimize temperature fluctuations as much as hoped, they helped lower the near-ceiling temperature to more acceptable levels in summer. (2) In spite of a lot of design work, it is too expensive and time-consuming to stabilize the temperature of the whole chamber space. Instead, efforts were made to minimize the temperature variation of the waveguides, whose physical dimensions and hence optical path lengths were the most susceptible to such variations. (3) Having found that circulating water was the most effective agent for this purpose, a longer length of pipes in thermal contact with waveguides is clearly needed. (4) The reference waveguide RG_1 in Fig. 1 was found to be about 6 meters longer than the optimum length given by Eq. (5). It was decided that RG_1 should be rerouted (shortened) accordingly, and this in turn created a vibration-free, efficient water circulation. (5) A small, but not negligible amount of microwave radiation was found to be leaking from many waveguide joints over RG_1 and RG_2 , due to the improper use of flanges/bolts in 1982. These joints were repaired before all guides were tied to the pipes and sealed together by good-quality insulation tape. (6) Utmost care was taken not to transmit even the smallest perceptible mechanical vibration to antennas and other critical wave paths by pumping water. (7) The improvement made on the compensation stability, by a factor 3 in drift rate reduction, was far better than previously expected as noted in recent extinction/angular scattering measurement runs. (8) Since the null drift is caused only where the microwave radiation is split into 2 paths L_D and L_R in Fig. 2, the new programmable microwave oscillator (EIP 924) and frequency-locking counter (EIP 575) were relocated to the PDP-VME-housing control room without affecting stable performance. A 17 meter, 50-ohm microwave coaxial cable now connects the frequency-locked microwave signal to a new GaAs solid-state microwave power amplifier which then delivers one-watt power to L_D and L_R (see Figs. 1 and 2). This not only greatly improved the operation/monitoring efficiency, but also helped eliminate some earlier technical difficulties caused by using long GPIB interface cables. (9) Increases in the MSF capability by employment of the above new programmable microwave source cannot be assessed at this moment, but a few examples are shown in Fig. 6 where the compensation

stability versus frequency were measured before and after rerouting of reference waveguide paths. Note that these frequency sweeps were made without any temperature controls - no water circulation, no insulation of waveguides.

D. Absolute Magnitude Calibration of Scattering

Results of a light scattering study are much more detailed if all scattering quantities therein are calibrated in dimensionless absolute magnitudes [5] rather than just in relative magnitudes or in those units likely to cause confusion/inconvenience. This is especially true when attempts are made by other workers to compare their results with this study. The absolute magnitude calibration is carried out in our MSF by substitution: i.e., immediately before/after a measurement run for the target under study, substitute a standard target of known absolute magnitude, repeat the measurement (now called the calibration run) and obtain the desired calibration factor. For reliable calibration such standard targets must therefore have: (a) stable target parameters so that the scattering properties are little affected by environmental factors, (b) the scattering profiles in agreement with reliable exact theories (such as Mie theory), and (c) the scattering magnitudes covering a sufficiently large dynamic range.

For angular scattering studies, in particular, few of our standard targets were found to simultaneously satisfy the above rather stringent requirements (a), (b) and (c). For this reason we have conducted a search and have prepared several more new standards made of stable materials such as teflon or delrin. The measured scattering patterns of a new delrin standard sphere, for example, are compared to the Mie theory prediction using the measured target parameters. Figs. 7A-B shows the very close agreement between experiment and theory for this delrin ball (except at a few large scattering angles: $130^\circ \leq \theta \leq 160^\circ$). Notice that the agreement also includes the deep troughs occurring in the angular profiles. Compared to an old plexiglass standard sphere whose experimental and theoretical profiles are shown in Figs. 8A-8B, this new delrin standard sphere has a much larger dynamic range and can be used as a reliable standard more frequently.

SUMMARY

The Work performed during 1986-1987 in order to improve the speed, accuracy, reliability and versatility of our MSF is reported, including an analysis of systematic experimental error sources and remedial measures. The emphasized topics cover those related to refractive indexes of target media, target-orientation device, judicious use of the microwave-unique compensation technique, switching from old to new computer systems in controlling microwave equipment, and reliable absolute magnitude calibration of scattered radiation. The upgrade work will be continued so as not to interfere with our regular measurement program.

ACKNOWLEDGEMENTS

The author thanks J.L. Weinberg for administrative guidance and discussions. He also owes his gratitude to G. Eichhorn and J. McKisson for work in computer interface problems and electronics, to D. Ely, A. Weisenberger and Y. L. Xu for assistance in miscellaneous laboratory routines, and to T. Barnello and E. Klein for help in temperature-control related work. This work was supported by the Army Research Office and in part by the University of Florida's Division of Sponsored Research.

REFERENCES

1. Li, J.C.R., "Statistical Inference I," Edward Brothers, Inc., Ann-Arbor, Mich. (1964).
2. Roberts, S. and von Hippel, A., A New Method of Measuring Dielectric Constant and Loss in the Range of Centimeter Waves, J. Appl. Phys. 17. 610 (1946).
3. Schuerman, D.W. and Wang, R. T., Experimental Results of Multiple Scattering, Final Rept., DAAG 29-79-C-0055, Army Chemical Systems Laboratory, ARCSL-CR-81003, Aberdeen, MD (1981).
4. Schuerman, D.W., Wang, R.T., Gustafson, B.A.S. and Schaefer, R.W., Systematic Studies of Light Scattering. 1: Particle shape, Appl. Opt. 20 4039-4050 (1981).
5. van de Hulst, H. C., "Light Scattering by Small Particles," Wiley, N.Y. (1957).
6. Wang, R.T., "Electromagnetic Scattering by Spheres of Anisotropic Refractive Indices," Ph.D. Thesis, Rensselaer Polytechnic Institute, Troy, N.Y. (1968).
7. Wang, R.T., The Microwave Scattering Facility, in "Proc. of the 1986 CRDEC Scientific Conference in Obscuration and Aerosol Research," R. Kohl, ed., Army CRDEC, Aberdeen, MD (in Press).
8. Zemansky, M.W., ed., Sec. 4 of "American Institute of Physics Handbook," McGraw Hill, N.Y. (1957).

TABLE I. DIELECTRIC MEASUREMENT RESULTS

Repeated complex refractive index measurement results are tabulated here to show the effects of aging/environment for 2 dielectric materials. All the selected 6 dielectric waveguide samples are about 20 years old, and the data for each sample is bounded by dotted lines.

DATA ID	SAMPLE MATERIAL	DATE MEASURED/ ROOM TEMP. (T) & RELATIVE HUMIDITY (RH)	SAMPLE WAS PLACED IN:	SAMPLE DENSITY GRAMS/cc	MEASURED COMPLEX REFRACTIVE INDEX
DEP121.DT0	PLEXIGLASS	6-12-68, T=22°C	ROOM CONDITION	1.1830	m=1.614-i0.006
DEP121.DT1	"	12-23-86, T=20.8°C, RH=67%	"	1.1865	m=1.642-i0.010
DEP121.DT2	"	12-26-86, T=17.1°C, RH=62%	VACUUM CHAMBER FOR 3 DAYS	1.1851	m=1.638-i0.009
DEP122.DT0	PLEXIGLASS	6-12-68, T=22°C	ROOM CONDITION	1.1842	m=1.613-i0.006
DEP122.DT1	"	12-23-86, T=20.8°C, RH=67%	"	1.2035	m=1.659-i0.012
DEP123.DT0	PLEXIGLASS	6-12-68, T=22°C	ROOM CONDITION	1.1835	m=1.613-i0.005
DEP123.DT1	"	12-23-86, T=20.8°C, RH=67%	"	1.1874	m=1.642-i0.011
DEP123.DT2	"	12-26-86, T=17.1°C, RH=62%	WATER-VAPOR- SATURATED CHAMBER, 3 DAYS	1.1891	m=1.644-i0.012
DEP125.DT0	EXPANDED POLYSTYRENE	8-5-69	ROOM CONDITION	0.6348	m=1.360-i0.005
DEP125.DT1	"	12-23-86, T=20.8°C, RH=66%	"	0.6362	m=1.359-i0.004
DEP125.DT3	"	12-26-86, T=17.1°C, RH=62%	VACUUM CHAMBER FOR 3 DAYS	0.6359	m=1.358-i0.004
DEP126.DT0	EXPANDED POLYSTYRENE	8-5-69	ROOM CONDITION	0.6305	m=1.355-i0.008
DEP126.DT1	"	12-26-86, T=17.1°C, RH=62%	"	0.6331	m=1.356-i0.004
DEP127.DT0	EXPANDED POLYSTYRENE	8-5-69	ROOM CONDITION	0.6397	m=1.362-i0.004
DEP127.DT2	"	12-23-86, T=20.8°C, RH=67%	"	0.6420	m=1.362-i0.003
DEP127.DT3	"	12-26-86, T=17.1°C, RH=62%	WATER-VAPOR- SATURATED CHAMBER, 3 DAYS	0.6423	m=1.364-i0.003

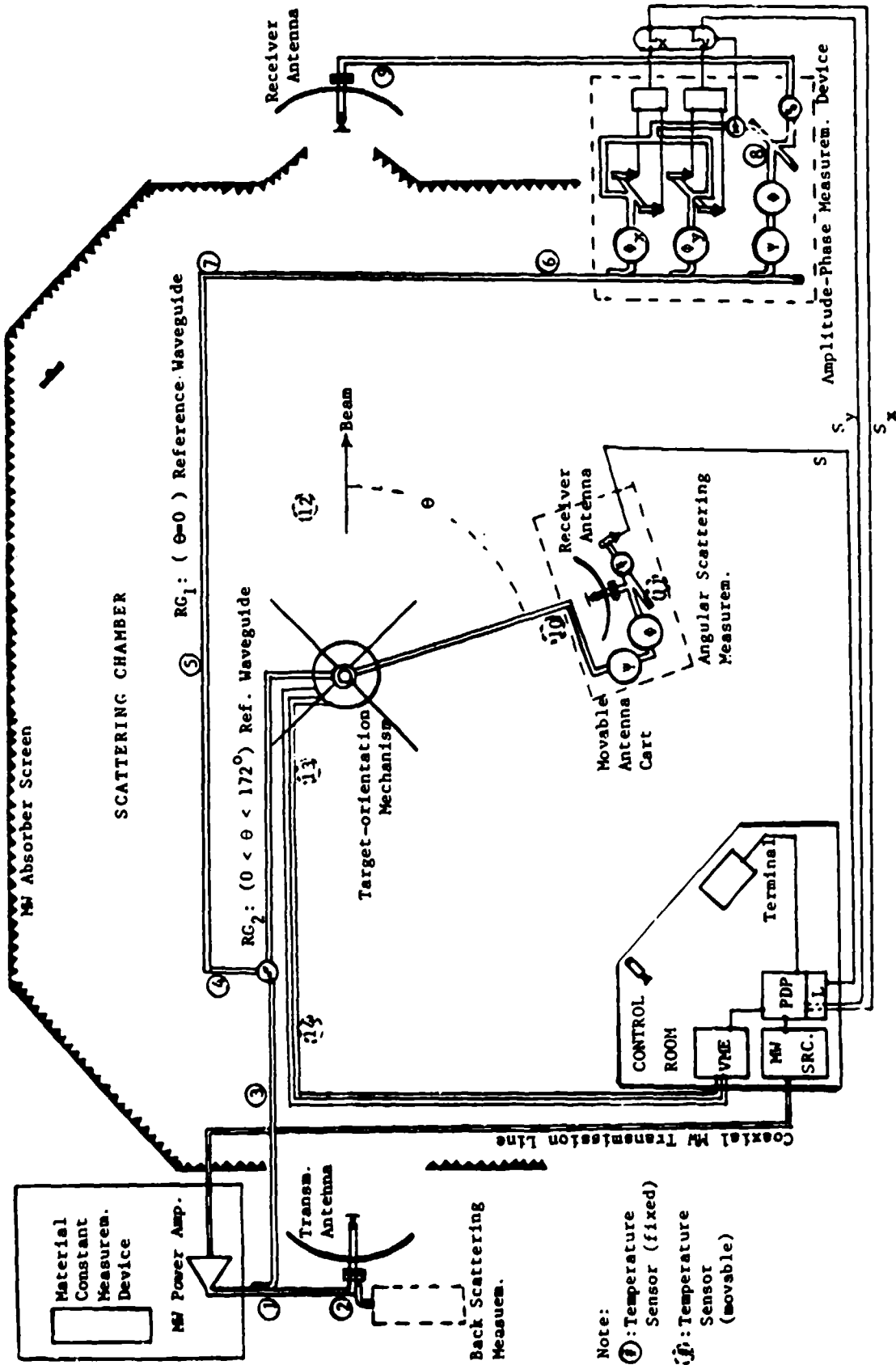


FIGURE 1. UPDATED MICROWAVE SCATTERING FACILITY (MSF) SCHEMATIC Space Astronomy Laboratory, University of Florida.

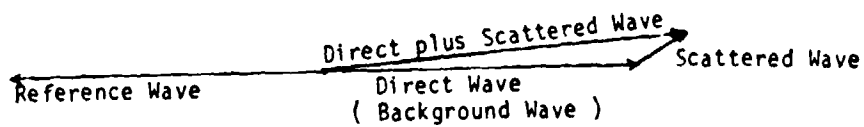
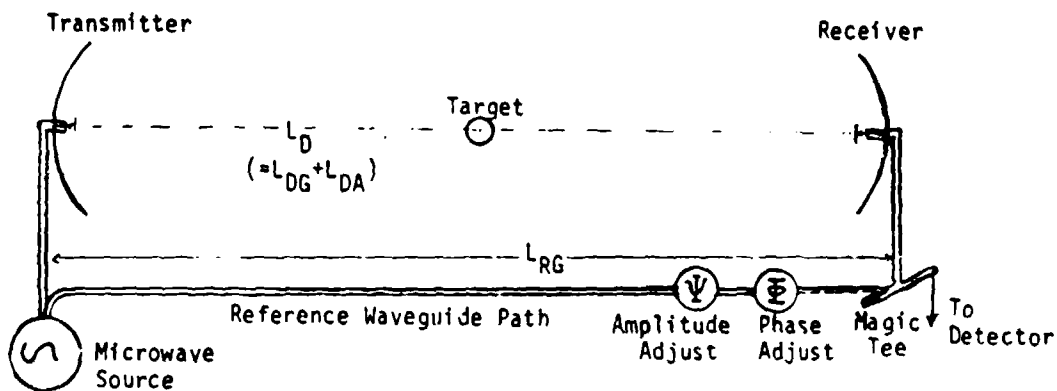
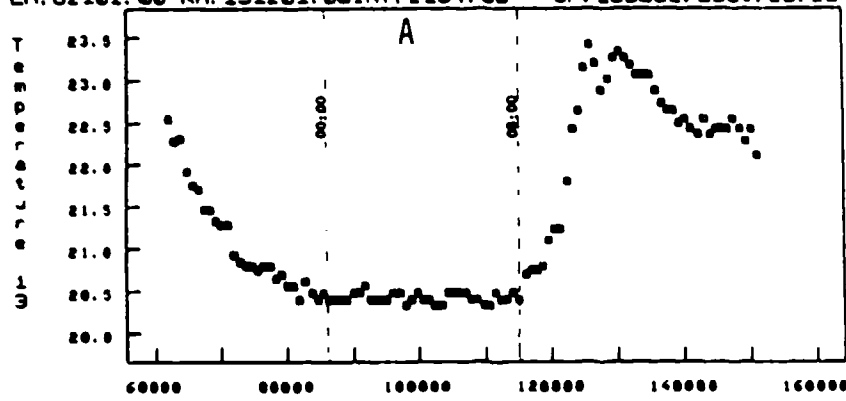


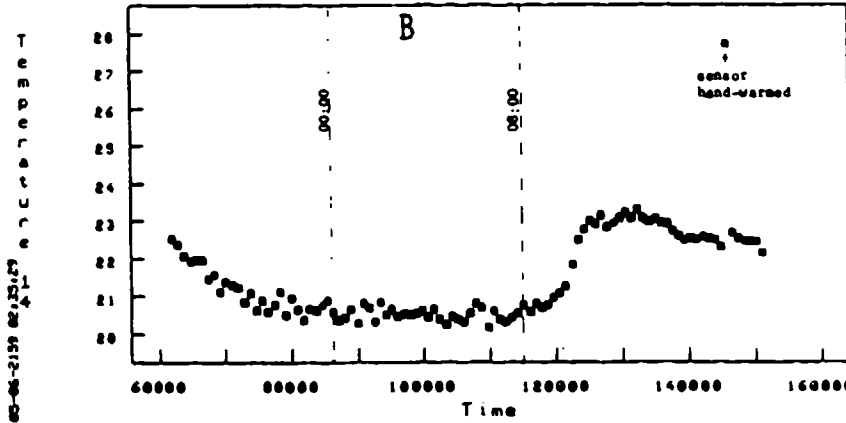
FIGURE 2. ON THE COMPENSATION (OR NULL) TECHNIQUE

Upper figure depicts the simplified hard-ware schematic of Fig. 1, while the lower figure shows the vector diagram of compensation.

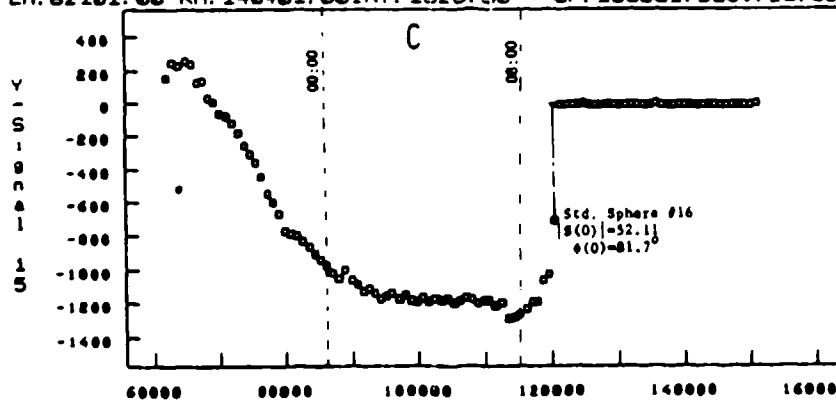


Nov. 17-18, 1986
MSF Temperature-Sensor's Readings vs Time

Sensor in the Free Space, Near Target Site

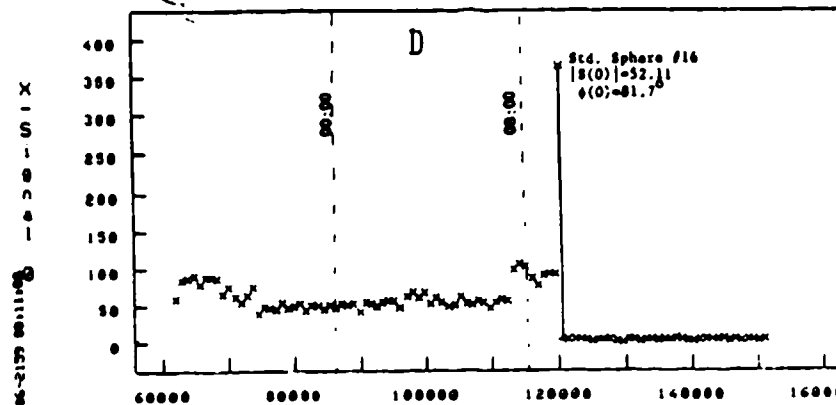


Sensor in the Free Space, Near Beam at Trans. Antenna



Nov. 17-18, 1986
Drift of X,Y Channel Signals vs Time

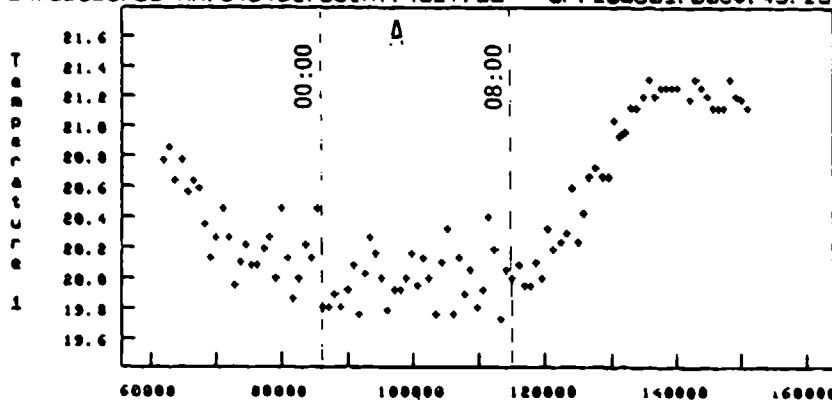
Phase-Sensitive Channel (Y)



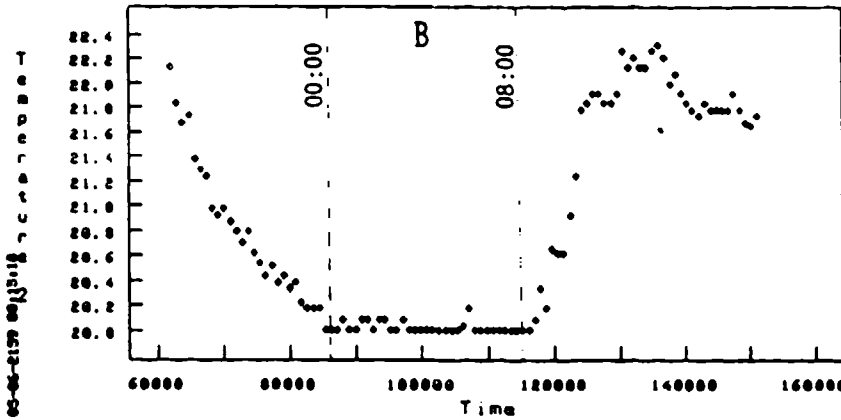
Amplitude-Sensitive Channel (X)

FIGURES 3A-3D. TEMPERATURE READINGS/COMPENSATION DRIFTS VERSUS TIME Figs. 3A & 3B are for temperature readings; while Figs. 3C & 3D record the drifts, where the scattering magnitudes X,Y recorded for a sphere are also shown at about 09:00 hour when the MW beam was turned off.

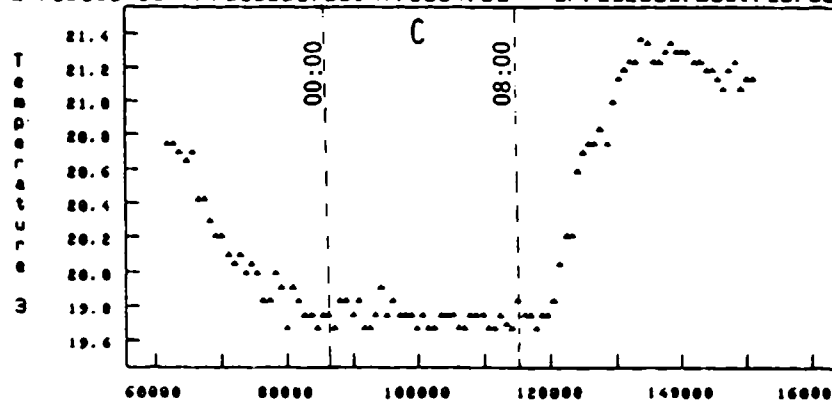
Nov. 17-18, 1986
MSF Temperature-Sensors' Readings vs Time



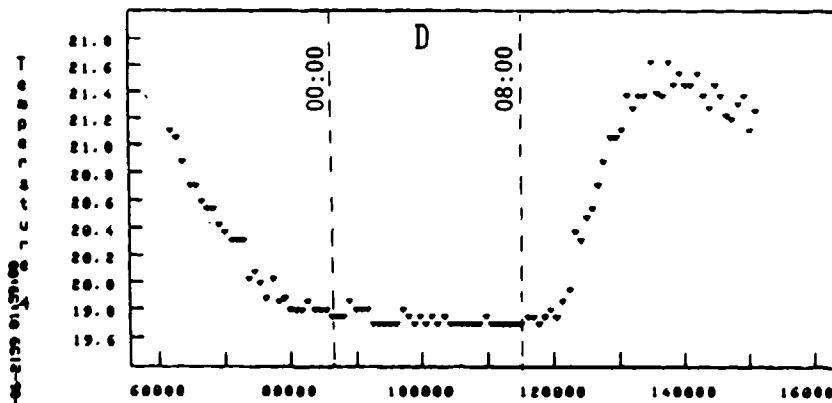
Sensor Near RG₁ Input



Sensor Near Transm. Antenna



Sensor Near RG₁ @ Absorber-Screen Opening

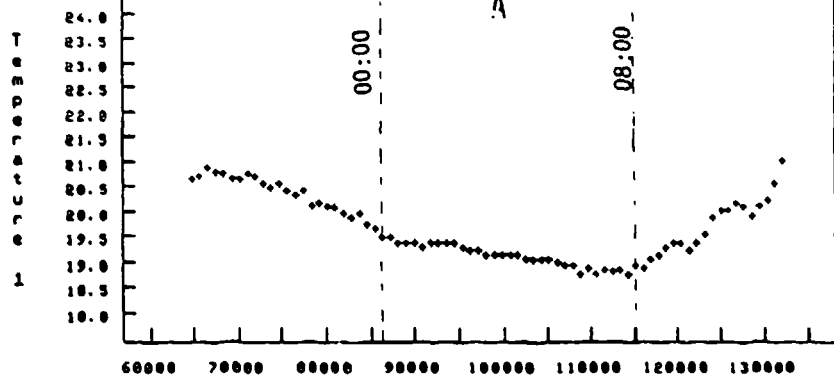


Sensor Near the RG₁-RG₂ Junction.
(without water circulation in the nearby pipe)

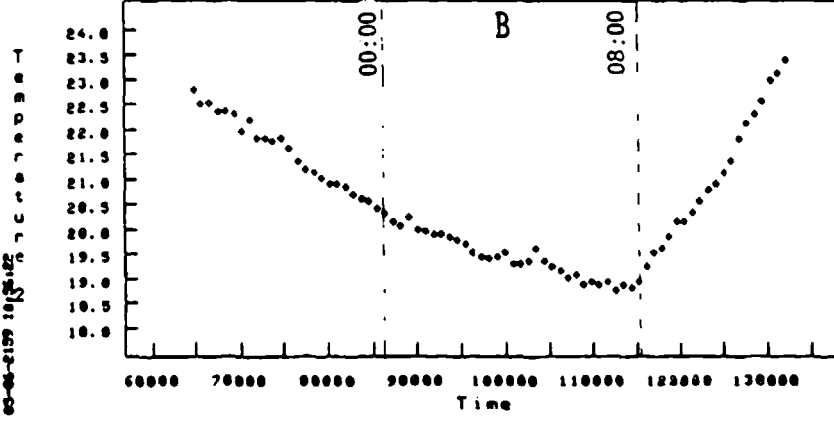
FIGURES 4A-4D. TEMPERATURE READINGS VERSUS TIME ACROSS MONITORING SENSORS Vertical dotted lines the hour marks: 00:00=midnight, 08:00=8 o'clock in the morning. Ordinate(with sensor ID#) in °C.

LM: 64801.00 RM: 64801.00 INT: 22.61 CP: 64801.00 CU: 22.61

Nov. 24-25, 1986
MSF Temperature-Sensor's Readings vs Time

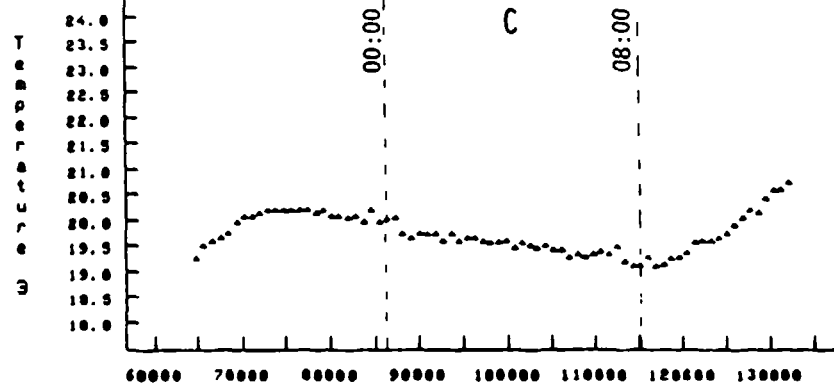


Sensor Near RG₁ Input

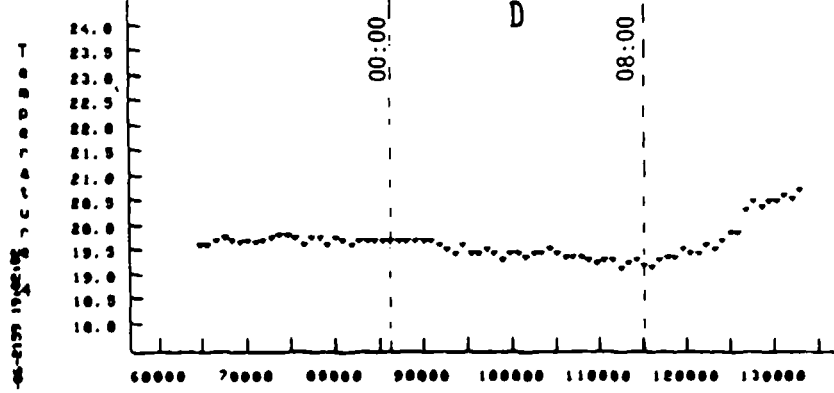


Sensor Near Transm. Antenna

LM: 64801.00 RM: 64801.00 INT: 19.61 CP: 64801.00 CU: 19.61



Sensor Near RG₁ @ Absorber-Screen Opening



Sensor near the RG₁-RG₂ Junction. (water circulating in the nearby pipe)

FIGURES 5A-5D. TEMPERATURE READINGS VERSUS TIME ACROSS MONITORING SENSORS 4D except that water was here circulating near the sensors #3 & #4.

Same as in Figs. 4A-4D

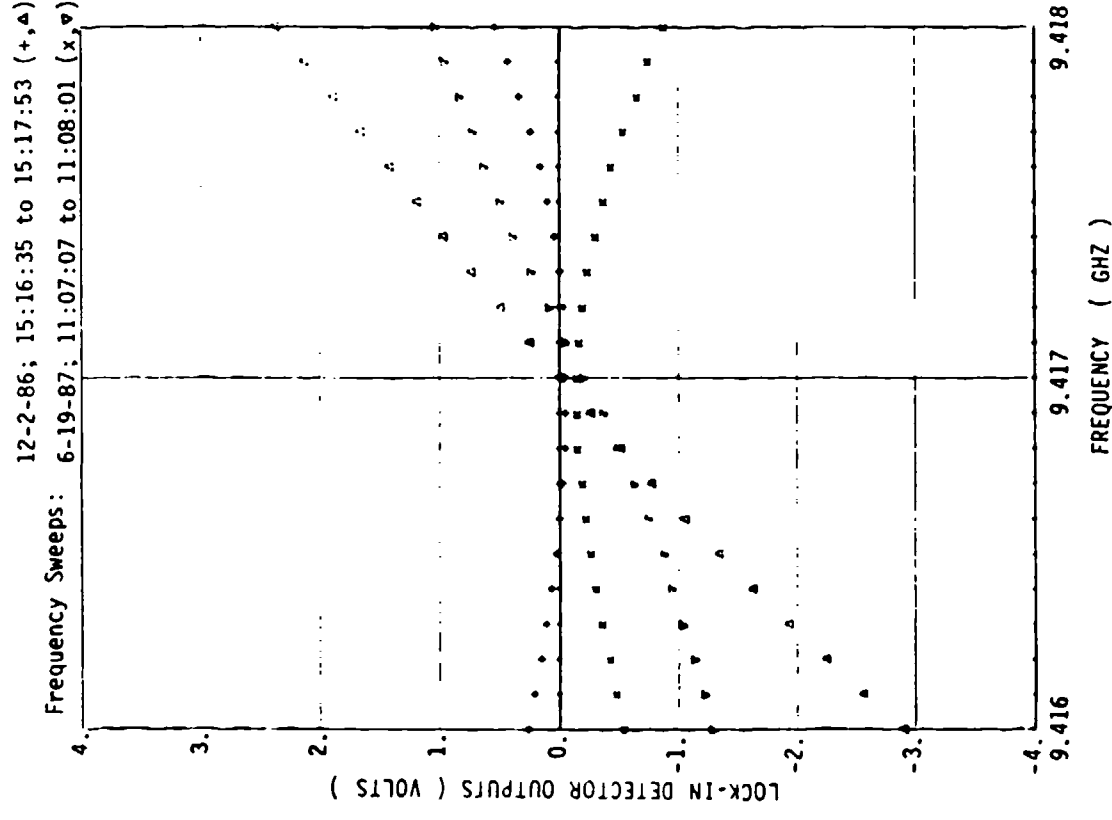
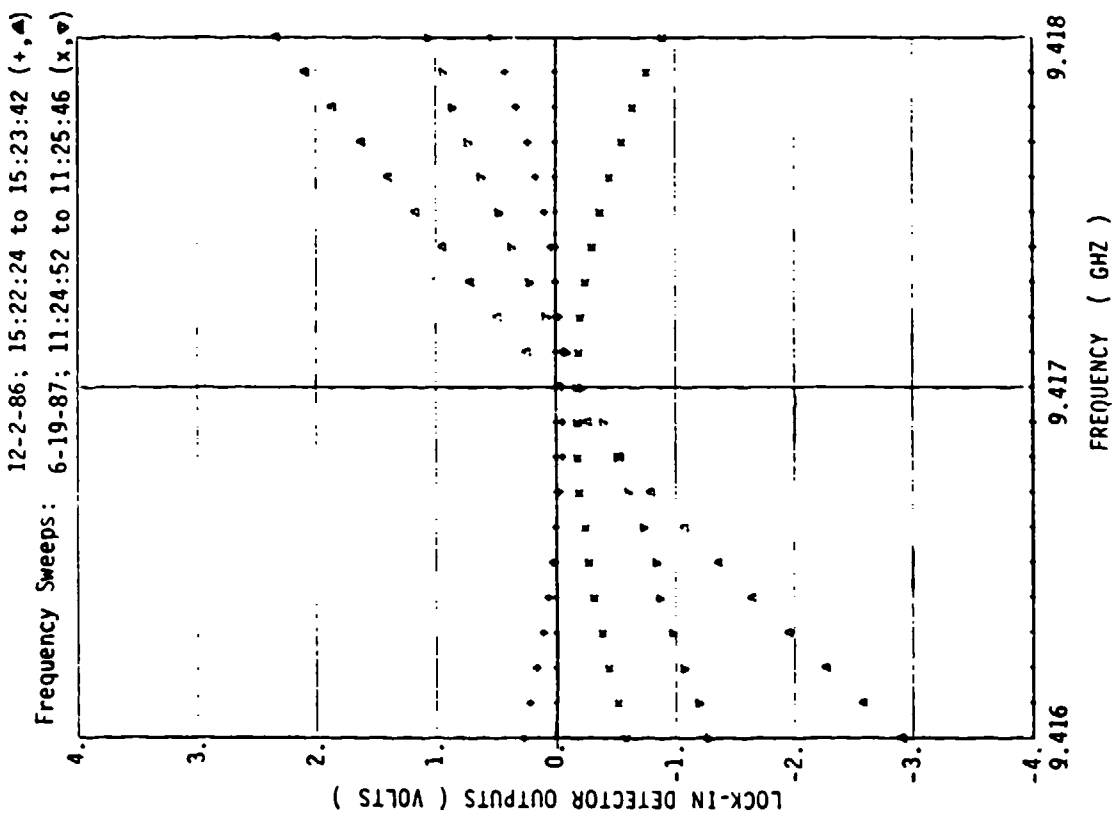


FIGURE 6. EFFECTS OF MICROWAVE OSCILLATOR FREQUENCY CHANGE ON THE STABILITY OF CANCELLATION

The beam direction (● = 0) background radiation was initially cancelled at the center frequency, 9.417 GHz, and the oscillator was programmed to sweep in frequency from 9.416 to 9.418 GHz in 20 equal intervals, recording thereby the perturbed cancellations on the phase-sensitive channel (marked ▲ or ▼) and the amplitude-sensitive channel (marked + or x) of the lock-in amplifier-detector outputs (amplification=1,000). Notice the improved phase-stability of the 6-19-87 compared to the 12-2-86 sweeps due to the judicious modification on the compensation-waveguide-lengths.

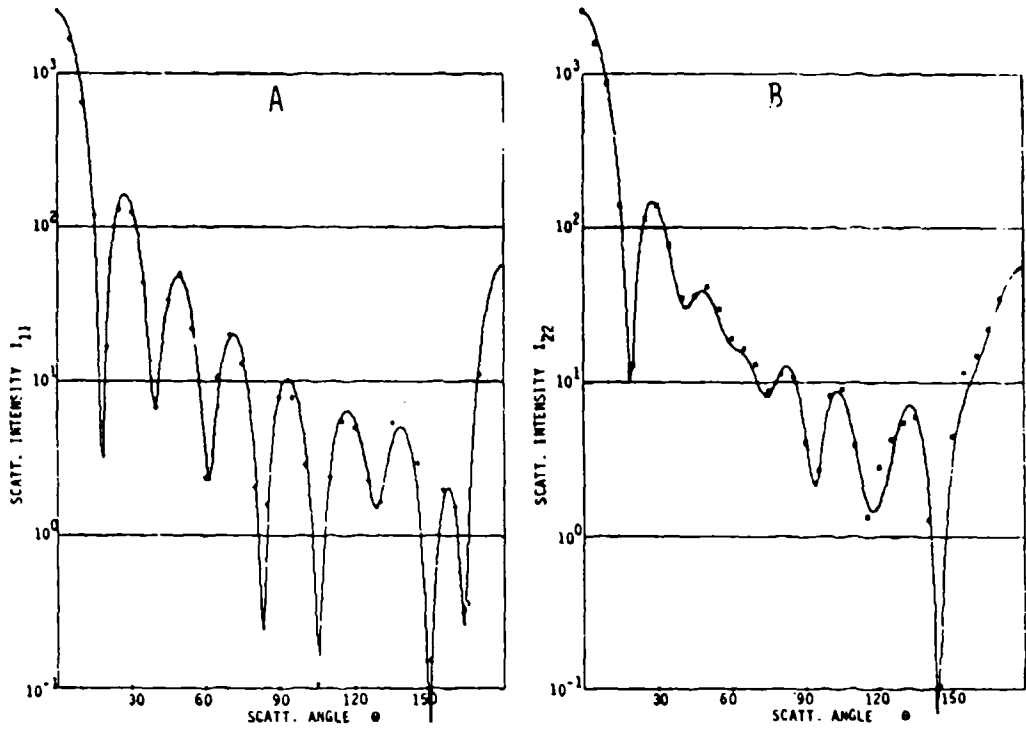


FIGURE 7. MICROWAVE ANGULAR SCATTERING BY A DELRIN BALL AND COMPARISON WITH MIE THEORY
 The sphere parameters: $x=9.375$, $m=1.7006-i0.0224$. Both the experimental (dots) and Mie theory results (continuous curves) are plotted in absolute magnitudes.

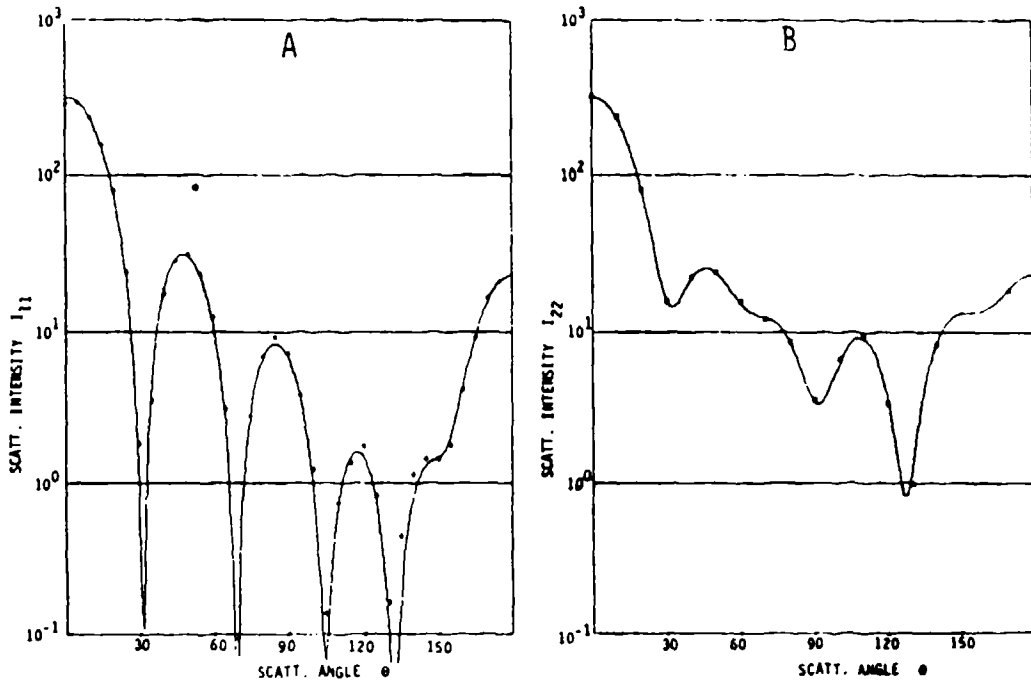


FIGURE 8. MICROWAVE ANGULAR SCATTERING BY A PLEXIGLASS BALL AND COMPARISON WITH MIE THEORY
 The sphere parameters: $x=5.001$, $m=1.629-i0.0125$. Both the experimental (dots) and Mie theory results (continuous curves) are plotted in absolute magnitudes.

Blank

Angular Scattering from Single Suspended Cylinders

J. D. Eversole
Potomac Photonics Inc.
College Park, Maryland 20742

H.-B. Lin and A. J. Campillo
Naval Research Laboratory
Washington, D. C. 20375

Recent Presentation

J. D. Eversole, H.-B. Lin, and A. J. Campillo, "Elastic Angular Scattering From Oriented Non-Spherical Particles", Proceedings of the 1987 International Symposium on Optical Particle Sizing: Theory and Practice, Rouen, France, May, 1987.

ABSTRACT

Elastic scattering measurements and observations have been made on single cylindrical particles suspended in an electrodynamic trap. Under certain circumstances the particles could be maintained in a stationary position and orientation, and scattered light intensities from a He-Ne laser were obtained as a function of angle. The particles were made by cutting and breaking quartz wool fibers which were then sorted by filtering. Suspended particles were cylinders approximately 7 micrometers in diameter with aspect ratios from 2 to 20. Photomicrographs were taken to determine the particle size, quality of the cylinder ends, and the extent of small dust or debris attached to the particle surface. Angular scattering patterns of the longer cylinders resembled the "infinite" cylinder case obtained by scattering from a macroscopic fiber. Differences observed in the shortest cylinders included a "broadening" of the cone of scattered radiation which increases with decreasing scattering angle, and a higher rate of intensity fall-off as a function of scattering angle. Current work has centered on reducing the cylinder diameter by etching the quartz fibers in hydrofluoric acid. An effort will be made to observe cylinders in the one micrometer diameter range to facilitate comparison with possible computational models.

Introduction

The work described here is part of an on-going program at the Naval Research Laboratory to determine optical properties of characterizable, nonspherical particles. While a substantial amount of prior information has been obtained for spherical particles over wide ranges of size and composition, relatively little work has been done with nonspherical particles. Furthermore, much of the available nonspherical particle data consists of an average over either size, shape, and/or orientation. Rigorous comparison of detailed theoretical and computational models requires experimental data for which composition, size, shape, and orientation are

known. Our approach has been to examine single particles, and obtain light scattering data at fixed orientations. This was achieved by suspending charged particles in an electrodynamic trap which has been modified to permit access to a wide range of scattering angles. Our main interest has been in rod-shaped or cylindrical particles with aspect ratios greater than 2, which may have applications as obscurants. Several candidate sources of such particles exist. However, in this study we have chosen to examine particles produced from $\sim 7 \mu\text{m}$ diameter quartz fibers which have a well-characterized scattering pattern as described below. Particles in this size range are easily imaged, so that size and shape information was taken directly by microscope observation and microphotography.

Experimental Arrangement and Procedure

Figure 1 is a schematic diagram of the basic experimental configuration showing the trap electrodes in relation to the incident laser beam and the photomultiplier tube (PMT) for detecting scattered light. In practice, the maximum range of the scattering angle, θ , was physically constrained to $\sim 120^\circ$ due to the electrode support and trap enclosure. An enclosure was required to prevent laboratory air currents from disturbing the suspended particle, and collection of scattered light was obtained through a wide window. An unfocused 3 mW polarized He-Ne laser was used as a light source. The PMT (Hamamatsu R-985) was mounted on a metal beam projecting from a machinist's rotary table which was driven by an ac synchronous motor. The resulting scan speed was $\sim 22^\circ/\text{min}$. Output of the PMT was amplified and plotted on a chart recorder. A narrow band laser filter (at 632.8) blocked extraneous room light, and for all but the smallest particles, collection optics other than apertures to block stray light were not required. Angular resolution was determined simply by the solid angle of the PMT photocathode, and was $\sim 0.3^\circ$.

The design of the electrodynamic trap was similar to that of previous investigators¹⁻⁵, but was distinguished from the classical bihyperboloidal trap by having the middle electrode split to permit optical access for angular scattering, and by the fact that the electrode surfaces were spherical rather than hyperboloidal. A detailed description of this arrangement and a comparison of its performance to other electrode geometries is available elsewhere.⁶ Particles were delivered to the trap by dragging a small polyethylene tube through a sample of the glass cylinders, by which some of them electrostatically attached to the tube. The tube was then lowered through a small hole in the upper end cap electrode and lightly tapped to allow some of the particles to fall through the trap. Application of the ac voltage at that point usually resulted in suspension of one or more of the particles. Multiple particles were eliminated from the trap by a process of momentarily reducing the ac

voltage. With one particle suspended, the dc voltage was applied and increased until the null point was reached as determined by observation through a microscope.

As the particles were initially captured, they usually were oriented in the vertical direction. This natural tendency may be due, at least in part, to an uneven distribution of surface charge since the longer particles were observed more stably oriented than the shortest. It is interesting to note that such natural orientations were not dependent on the presence of the dc (balancing) field. In the absence of this field, the trapped particle's motion was oscillatory at the ac voltage frequency, and usually described an arc or curve. Nevertheless, in many cases it could be observed that a particular orientation was maintained throughout the oscillation period despite aerodynamic drag forces which would orient a rod-shaped particle in the direction of its motion.

Results and Discussion

Nearly all of the scattering data was obtained with the laser beam horizontal and the cylindrical particles in the vertical orientation. Under this circumstance, as discussed previously, the scattered light is expected to be predominantly radiated in the horizontal (X-Y) plane. Indeed, an intense line of light, modulated along its length, could be directly observed by holding a piece of thin white paper to the chamber window. Since the chamber window was normal to the horizontal plane, the projected line of scattered radiation was straight. For the infinite cylinder case, represented by a taut fiber, the width of this line was primarily determined by the diameter of the incident beam (~1 mm). For the longer particles (aspect ratios greater than ~ 8) there were no differences discernable by eye in the appearance of their scattered light pattern compared to the macroscopic fiber. For a finite cylinder, some light scattering will occur in all directions due to the cylinder ends. With normal incidence geometry this type of scattering was much less intense than the characteristic scattering pattern just described.

In two cases with the shortest particles (aspect ratios ~3 or less), a distinct broadening of the scattered radiation line was observed. While the line remained narrow and sharp in the back scattered direction, it gradually became wider (~3X), and more fuzzy at the near-forward part of the window. Curving the screen to keep the projected radiation equi-distant from the particle did not significantly alter this pattern. While we have been unable to find any prediction or model for this observation, we believe it may be a characteristic of scattering from short aspect ratio cylinders.

Angular scattering in the horizontal plane was recorded from $\sim 35^\circ$ to 150° . Suspended cylinders oriented in the vertical direction provided well-defined and reproducible oscillatory patterns (scattergrams) over this range, with a rms signal to noise ratio for the longer particles was typically between 5 and 10%. Scattered light intensities from shorter particles were correspondingly weaker. In Figure 2 typical relative scattered light intensities are plotted versus angle for several different cases. Both vertical (TE) and horizontal (TM) incident beam polarizations were obtained as shown in the left and right columns respectively. The different cases are arranged by row from top to bottom: (a) $\sim 8\mu\text{m}$ diameter sphere, (b) "infinite" fiber, (c) long cylindrical particle, (d) intermediate length cylinder, and (e) short cylinder. Since the different particles were not precisely the same diameter, detail in the scattering patterns can not be compared. In general terms, however, the scattergram of the longest finite cylinder (c) resembles the patterns of the fiber (b) and the sphere (a) more closely than that of the shorter finite cylinders (d) and (e). From our observations, there is a general trend by which smaller aspect ratio cylinders were consistently distinguished that shows up best in scattering with a horizontally polarized beam; namely, that the rate of decrease of the relative scattered light intensity as a function of angle is significantly higher for shorter cylinders than for either the longer cylinders, fiber, or sphere. As yet, no predictive calculations are available to compare with these observations, partly because of computational difficulty due to the large diameters of the cylinders compared to the incident light wavelength. We are currently attempting to extend our experimental technique to cylinders with diameters of $\sim 1\mu\text{m}$, and are optimistic that we will soon be able to compare experimental data with a finite cylinder scattering model.

References

1. E.J. Davis, "Electrodynamic Balance Stability Characteristics and Application to the Study of Aerocolloidal Particles", Langmuir, **1**, 379 (1985).
2. S. Ataman and D.N. Hanson, "Measurement of Charged Drops", Ind. Eng. Chem. Fundam., **8**, 833, (1969), and J.W. Schweizer and D.N. Hanson, Stability Limit of Charged Drops, J. Colloid and Interface Sci., **35**, 417 (1971).
3. T.G.O. Berg and T.A. Gaukler, "Apparatus for the Study of Charged Particles and Droplets", AM. J. Phys., **37**, 1013, (1969).
4. C.B. Richardson and J.F. Spann, "Measurement of the Water Cycle in a Levitated Ammonium Sulfate Particle", J. Aerosol Sci., **15**, 563, (1984).
5. R.F. Wuerker, H.M. Goldenberg, and R.V. Langmuir, "Electrodynamic Containment of Charged Particles", J. Appl. Phys., **30**, 441, (1959).
6. J. D. Eversole and H.-B. Lin, "Effects of Design on Null Point Motion of Spheres Suspended in the Electrodynamic Balance", Rev. Sci. Inst. **58**, 1190, (1987).

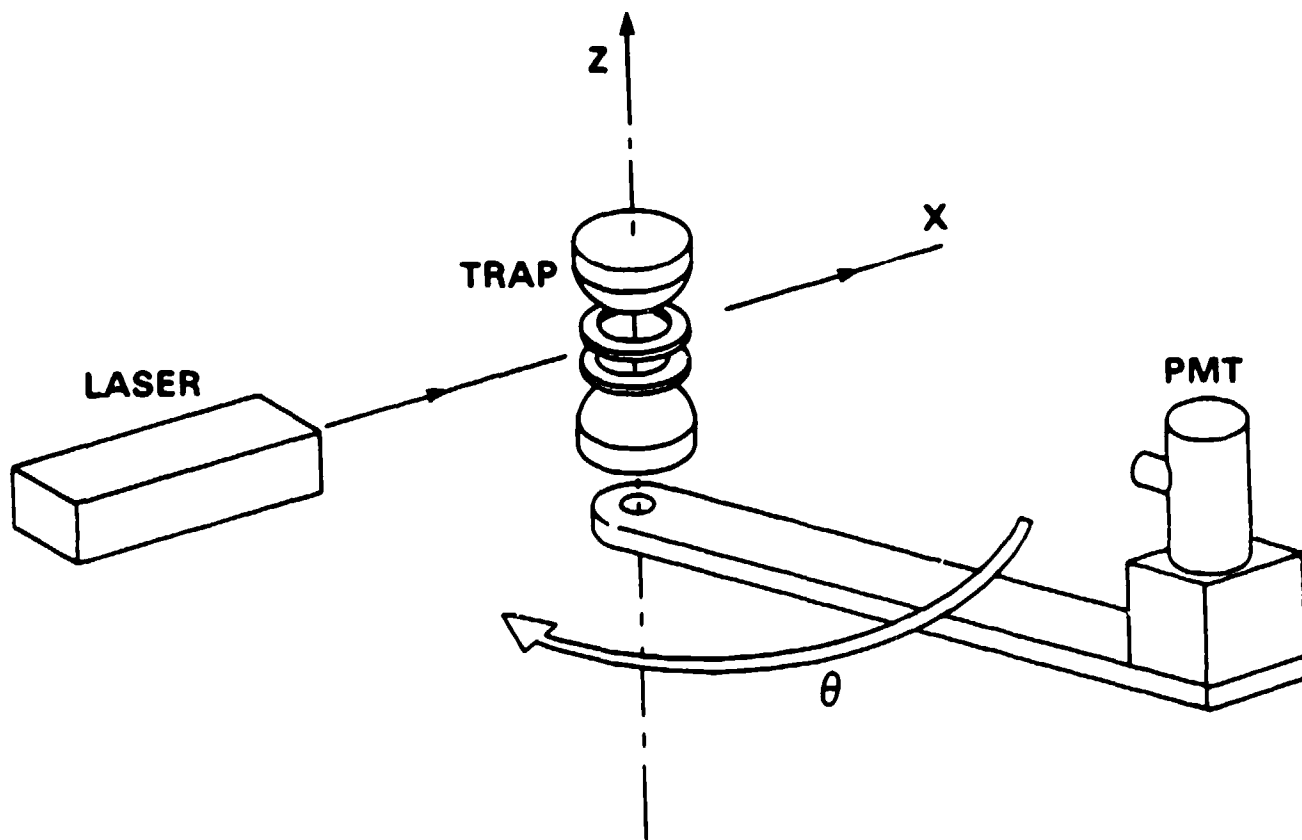


Figure 1. A schematic illustration of the basic experiment, showing the arrangement of the electrodynamic trap and light scattering apparatus.

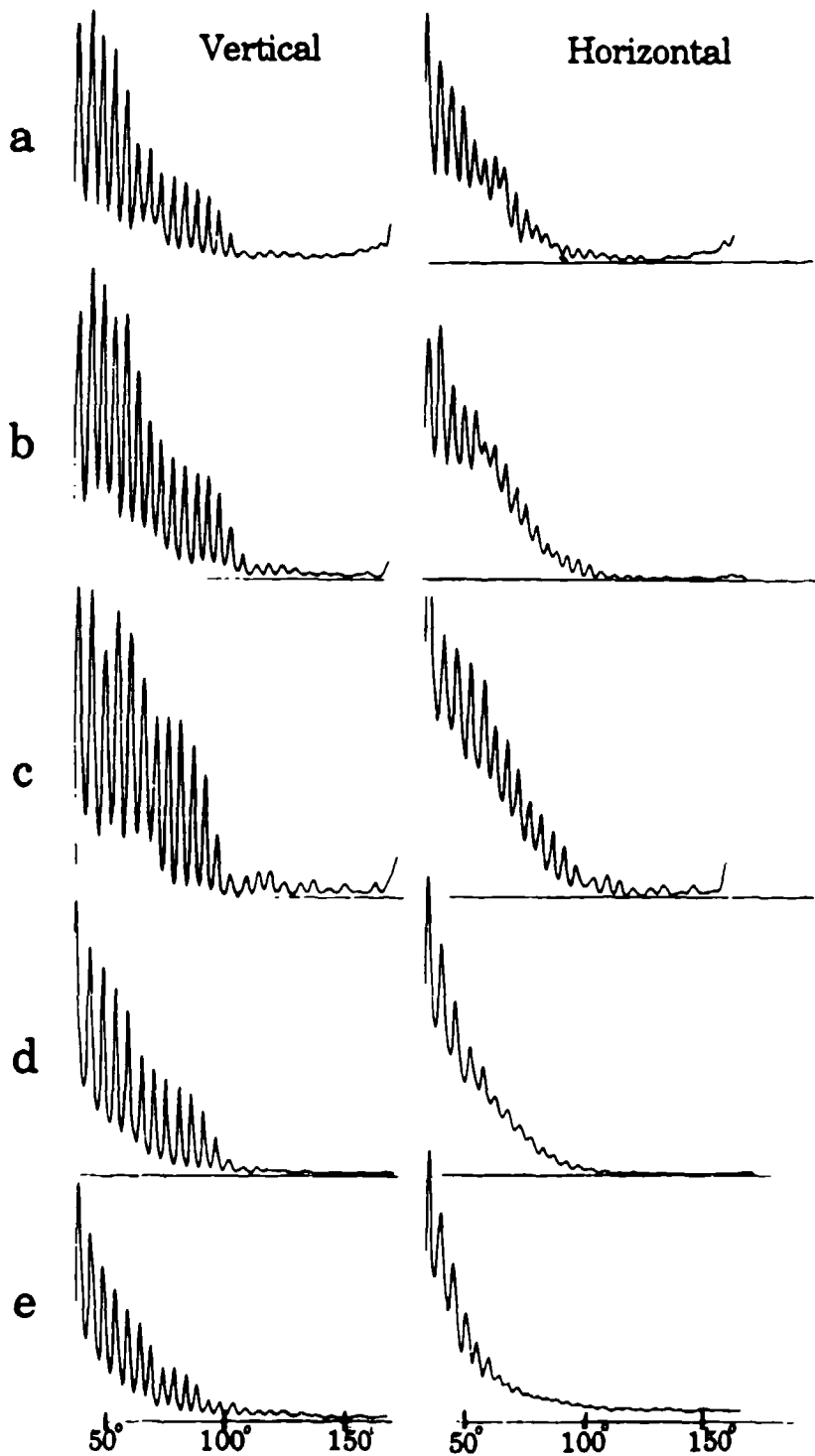


Figure 2. Scattergrams from various particles as described in the text. The left and right columns show vertical and horizontal incident polarizations respectively.

EFFECTS OF SIMPLE SHADOWING ON VARIATIONAL CALCULATIONS

B. J. Stoyanov and R. A. Farrell
The Milton S. Eisenhower Research Center
The Johns Hopkins University Applied Physics Laboratory
Laurel, MD 20707

RECENT PUBLICATIONS, SUBMITTALS FOR PUBLICATION AND PRESENTATIONS:

- A) J. A. Krill, J. F. Bird, and R. A. Farrell, "Trial Functions in Variational Calculations," in Proceedings of the 1982 CSL Scientific Conference on Obscuration and Aerosol Research (ed. by R. H. Kohl and Assoc., Tullahoma, TN, 1983), pp. 201-209.
- B) J. A. Krill and R. A. Farrell, "The Development and Testing of a Stochastic Variational Principle for Electromagnetic Scattering," in Wave Propagation and Remote Sensing, Proceedings of URSI Commission F 1983 Symposium (European Space Agency, Noordwijk, The Netherlands, 1983), pp. 299-307.
- C) B. J. Stoyanov and R. A. Farrell, "On the Asymptotic Evaluation of $\int_0^{\pi/2} J_0^2(\lambda \sin x) dx$," Math. Comp. **49**, 275-279 (1987).
- D) B. J. Stoyanov, J. A. Krill, J. F. Bird, and R. A. Farrell, "Broadband Trial Functions for Surface Scattering with Detailed Analysis for a Simple Model," in Proceedings of the 1986 CRDEC Scientific Conference on Obscuration and Aerosol Research (ed. by Kohl and Assoc., Tullahoma, TN, 1987), to appear.
- E) J. F. Bird, R. A. Farrell, E. P. Gray, and B. J. Stoyanov, "Trial Functions for Scattering from Surfaces of Arbitrary Roughness and Variational Test Calculations," in Proceedings of the 1986 CRDEC Scientific Conference on Obscuration and Aerosol Research (ed. by Kohl and Assoc., Tullahoma, TN, 1987), to appear.
- F) B. J. Stoyanov and R. A. Farrell, Effects of Simple Shadowing on Variational Calculations," presentation at the 1987 CRDEC Conference on Obscuration and Aerosol Research, June 1987.

ABSTRACT

Shadow-induced effects, expected to become important at high frequencies, can be adequately accounted for in the variational calculations by premultiplying the previously-introduced boundary-Born trial fields with a simple shadow-imitating factor. The amended trial fields, with the shadow-regulating parameter properly adjusted, yield variational scattering amplitudes and cross sections that are accurate at all frequencies and for all scattering directions. This is explicitly demonstrated for a simple test problem of a plane-wave scattering from an infinitely-long perfectly-conducting cylinder, for the TM polarization.

INTRODUCTION

The previously formulated [1,2] stochastic variational principle has significantly facilitated evaluation of the ensemble averages which inevitably arise in theoretical investigations of electromagnetic wave scattering in random media and from randomly-rough surfaces. This paved the way for more extensive applications of variational techniques to such problems [3-6].

Even with this simplification by virtue of the stochastic variational principle, however, the calculation of the required statistical averages, which was hardly feasible before, remains a formidable numerical task unless relatively simple trial fields are utilized. Therefore, it has been imperative to develop a practical procedure for generating efficient, yet simple, trial fields which would yield accurate variational results over the whole range of size-parameter ka (wavenumber times characteristic scatterer size).

A significant step in this direction was made several years ago [7] when it was found that, for perfect conductors, the desired accuracy can be achieved by modifying the classic Born trial fields so

that they become capable of satisfying the appropriate boundary conditions. The resultant "boundary-Born" trial fields were tested on simple model problems (whose exact solutions are known) such as a plane-wave scattering from an infinitely-long circular cylinder [7], a hemicylindrically-embossed plane [8,9] (originally introduced by Rayleigh [10] as a rough-surface scattering model), and from a sinusoidally-roughened surface [11]. For the first two problems, accurate scattering cross sections were obtained over remarkably broad ranges of ka , with exceptional accuracy for $ka \leq 1$. However, two notable discrepancies were found: the presence of narrow-band spurious spikes contaminated the variational results at a set of discrete frequencies, and the incorrect asymptotic ($ka \gg 1$) behavior held for forward scattering from the cylinder or for specular scattering from the hemicylindrically-embossed plane, especially so for the TM polarization.

Recently, while further developing the trial-field-generating procedure, we discovered that incorporating a factor to approximate shadowing (which is expected, on physical grounds, to become important at large ka values [12]) into the previously devised boundary-Born trial fields can lead to remarkable improvements in the variational results. In fact, the aforementioned discrepancies can be removed. This is illustrated for plane-wave scattering from a perfectly-conducting cylinder for TM polarization--which corresponds to sound-soft scattering in acoustics.

RESULTS AND DISCUSSION

Scattering of a plane wave by an infinitely-long conducting cylinder of radius a , whose axis is along the z direction, is depicted in Fig. 1, where \vec{k}_i, \vec{k}_s are the incident and scattered propagation vectors, respectively, and ϕ_s is the scattering angle. The usual polar coordinates ρ, ϕ are used to specify an arbitrary point in a plane normal to the cylinder axis. (Only the case of normal-incidence is considered because, for a perfect conductor, oblique-incidence can readily be deduced from this simpler problem [13].)

The Schwinger-type variational principle [12] for the scattering amplitude has the form

$$T^V = N\tilde{N}/D \quad (1a)$$

For TM polarization, the electric field is parallel to the cylinder axis, i.e., in the z direction, vanishes on the cylinder surface, and depends on \vec{k}_i . For this case, defining $\psi \equiv \psi(\vec{k}_i) = E_z$, one finds

$$N = -\frac{1a}{4} \int_0^{2\pi} d\phi e^{-ik a \cos(\phi - \phi_s)} \left. \frac{\partial \psi}{\partial \rho} \right|_{\rho=a} \quad (1b)$$

$$\tilde{N} = -\frac{1a}{4} \int_0^{2\pi} d\phi' e^{ik a \cos \phi'} \left. \frac{\partial \tilde{\psi}}{\partial \rho'} \right|_{\rho'=a} \quad (1c)$$

$$D = \frac{a^2}{16} \int_0^{2\pi} d\phi \int_0^{2\pi} d\phi' \left[\left. \frac{\partial \tilde{\psi}}{\partial \rho'} \cdot H_0^{(1)}(k|\vec{\rho} - \vec{\rho}'|) \frac{\partial \psi}{\partial \rho} \right] \right|_{\substack{\rho'=a \\ \rho=a}} \quad (1d)$$

These are line integrals along the cylinder circumference, and $H_0^{(1)}$, the Hankel function of first kind and zeroth order, represents (up to a constant factor) a two-dimensional free-space Green's function appropriate for this problem. Utilizing Graf's addition theorem [14], the double integral in Eq. (1d) can be reduced to a product of single integrals. Also, $\tilde{\Psi} = \Psi(-\vec{k}_S)$ represents the adjoint field, i.e., the solution of the reciprocal problem in which the source and observer are interchanged, so that the reciprocity relation [12] is satisfied due to the form of Eq. (1a). Thus, the adjoint field follows directly from the original one, by substitution $\phi \rightarrow \phi - \phi_S - \pi$. With the correct field Ψ (and, hence, $\tilde{\Psi}$), each of the integrals N , \tilde{N} , and D , as well as their ratio (1a), will yield the correct scattering amplitude $T(\phi_S)$. Knowing T , the differential cross section follows

$$\sigma = \begin{cases} (1/k^2 a^2) |T|^2, & \text{forward} \\ (4/\pi k a) |T|^2, & \text{otherwise,} \end{cases} \quad (2)$$

being conveniently normalized for forward- and back-scattering. On the other hand, when an approximate trial field is used for Ψ , the variationally-approximate $T^V(\phi_S)$ is obtained by Eqs. (1).

The previously devised boundary-Born trial field [7,9]

$$\Psi(\rho, \phi) = e^{ik\rho \cos\phi} - f(\rho) e^{ik a \cos\phi} \quad (3)$$

satisfies the applicable boundary condition, i.e., $\Psi|_{\rho=a} = 0$, provided the arbitrary function $f(\rho)$ is such that $f(a) = 1$. Note that when $f(\rho) \equiv 0$, the variationally-improved Born approximation for T^V obtains, which is, however, not accurate even for $ka \ll 1$. This is not surprising in view of the important role played by boundary conditions at low and moderate frequencies and the fact that the Born trial function, being just the incident plane wave, is unable to satisfy the boundary condition. When the boundary-Born trial field (3) is substituted into Eqs. (1), the as-yet arbitrary parameter

$$A \equiv -(1/k) \partial f(\rho) / \partial \rho \Big|_{\rho=a} \equiv -f'(a)/k \quad (4)$$

can be adjusted variationally so that its "stationary" value follows from the stationary condition

$$\partial T^V / \partial A = 0. \quad (5)$$

Also, it turns out by virtue of reciprocity that $\tilde{A} = A$ and $\tilde{N} = N$.

The variational cross section for forward scattering ($\phi_S = 0$), obtained with such a stationary value of parameter A , is compared with the exact result in Fig. 2a. For $ka < 1$, where the agreement is extremely good, the two curves would be indistinguishable on this scale and are not plotted. For $ka > 1$ broad, though small, anomalous wiggles appear, which eventually turn into the ripple for $ka \gg 1$. The variational cross section becomes appreciably smaller than the correct one for very large size-

parameters. This suggests that the variational result may have wrong asymptotic ($ka \gg 1$) behavior for forward scattering. Indeed, an asymptotic analysis of the integrals in Eqs. (1), using the results of [15], reveals that the stationary value of the parameter $A \rightarrow 2/\pi$ when $ka \rightarrow \infty$ and, up to the leading term,

$$T^V(\phi_S=0) \xrightarrow{ka \rightarrow \infty} -ka\pi^2/\ln(ka) \quad (6)$$

Thus, T^V/ka and, hence, σ^V , vanish logarithmically as $ka \rightarrow \infty$, whereas the correct $T \rightarrow -ka$ and $\sigma \rightarrow 1$ in this limit, when $\phi_S = 0$ [12].

It is well known [12] that the correct asymptotic ($ka \gg 1$) value of the scattering amplitude for forward scattering is due primarily to the shadow-forming wave which produces shadowing effects through interference with the incident plane wave. To approximate these effects in our trial field, we premultiply the boundary-Born trial field of Eq. (3) by a simple shadow-imitating factor, to get

$$\psi(\rho, \phi) = (1 - \beta \cos \phi) [e^{ik\rho \cos \phi} - f(\rho) e^{ik a \cos \phi}] \quad (7)$$

where β is an arbitrary (positive) parameter independent of ρ and ϕ . For this trial field, with the parameter A of Eq. (4) determined variationally by the stationary condition (5), it turns out, to the leading term in ka , that

$$A(\phi_S = 0) \xrightarrow{ka \rightarrow \infty} -(\pi\beta^3 - 8\beta^2 - 2\pi\beta + 8)/(4\beta \ln ka) \quad (8)$$

and

$$T^V(\phi_S = 0) \xrightarrow{ka \rightarrow \infty} -ka(\pi^2\beta^2/2)/(4\beta^2 + \pi\beta - 2) \quad (9)$$

The as-yet arbitrary parameter β is now adjusted so that the correct large ka -limit is obtained for T^V , i.e., $T^V(\phi_S = 0) \rightarrow -ka$ as $ka \rightarrow \infty$. This requires that

$$\beta = (\pi - \sqrt{32 - 3\pi^2})/(\pi^2 - 8) = 0.853\dots, \quad (10)$$

the other root being discarded as physically inappropriate. It might seem that choosing β in this way limits the applicability of this procedure to problems where the exact solution is known; however, all that is actually needed is the large ka -limit of the exact solution which can be obtained from the Kirchhoff (physical optics) approximation.

The surface current distribution obtained from Eqs. (7) and (10) has certain qualitative features that one expects from physical optics. In particular, the physical-optics picture is that the surface-current distribution, \vec{R} , can be expressed in terms of the incident-wave surface current, as

$$\vec{R} = \begin{cases} 2\vec{R}^{inc}, & \text{illuminated side} \\ 0, & \text{shadowed side,} \end{cases} \quad (11a)$$

which is, strictly speaking, valid only when $ka \gg 1$. While, using the definition

$$\tilde{R}(\phi) = -(2/i\omega\mu)\partial\psi/\partial\rho\Big|_{\rho=a} \quad (11b)$$

with Eq. (7) and the fact that the parameter A vanishes as $ka \rightarrow \infty$, we find that the surface-current density at very large size-parameters is

$$\tilde{R}^V(\phi_s = 0) \xrightarrow{ka \rightarrow \infty} (1 - \beta \cos\phi) \tilde{R}^{inc} \quad (11c)$$

The factor $(1 - \beta \cos\phi)$ varies from about 0.15 for $\phi = 0$ to 1.85 for $\phi = \pi$. Thus, the simple shadowing introduced in Eq. (7) is in approximate agreement with distribution (11a) for $ka \gg 1$, but is physically more plausible (especially for small and moderate ka 's) than the standard Kirchhoff approximation used in the earlier variational work [16-18], which sometimes leads to variational divergencies [19]. As noted above, all that was needed to properly fix β was the generic, readily obtainable, physical-optics result for forward scattering.

At small size-parameters ($ka \ll 1$), it can be shown that the shadowed-boundary-Born trial field (7) (with parameter A determined variationally via eq. (5)) provides the correct leading term for T^V , independently of β and ϕ_s , i.e.,

$$T^V \xrightarrow{ka \rightarrow 0} 1\pi/(2\ln ka) \quad (12)$$

Therefore, the boundary-Born trial field with the properly adjusted shadowing ensures the correct small and large ka -limits of the forward scattering amplitude. The corresponding cross section is displayed in Fig. 2b. For all size-parameters in the range $10^{-2} \leq ka \leq 10^2$ the error is less than 2%, and this slight error will eventually disappear at smaller and larger ka 's since the correct leading terms are guaranteed for these limits. [In view of this, there seems to be little point in removing the shadowing factor at small ka by using a ramp function to set $\beta = 0$ for, say, $ka < 1$. We note, however, that with a ramp function the shadowed trial field would go over to the original boundary-Born field which is exceptionally good in this ka -region. An approach similar to this was used in [9] to derive the semi-empirical formula for A for TE polarization.]

It is especially gratifying to have such accurate variational results (over the whole frequency band) for the forward direction in view of the so-called optical theorem [12,13,16,17] which allows one to find the total scattering cross section directly from the forward scattering amplitude, without carrying out the (sometimes tedious) integration over all scattering angles.

The beneficial effects of the simple shadowing introduced into the boundary-Born trial field are not confined to the forward direction only, but extend to other directions as well. Thus, with the original boundary-Born trial field of Eq. (3), the resultant backscatter ($\phi_s = 180^\circ$) cross section is very accurate for $ka \leq 0.8$ and has correct average behavior for moderate and large size parameters, but

is heavily contaminated by narrow-band spurious spikes beginning with some $ka > 1$, as Fig. 3a illustrates. In the earlier work [7], a preliminary cure to deal with these anomalous spikes was to use a kind of smoothing technique, by which they were significantly reduced, with the resulting accuracy better than 10% at all wavelengths. The recent variational result for backscatter, obtained with the shadowed-boundary-Born field (7) is shown in Fig. (3b). For these calculations the parameter A was determined by the stationary condition and the parameter β was selected to give the correct forward scattering in the large size parameter limit, i.e., by Eq. (10). All the anomalous spikes disappeared and the error is less than 2.5 percent, being largest in the resonance region. As noted above, the small size-parameter limit is given by Eq. (12) independent of ϕ_s , and is correct so that the error vanishes in this limit.

As an example of scattering at an arbitrary-angle, the cross sections at $\phi_s = 15^\circ$ obtained by employing the original and shadowed (with the same β -value of Eq. (10)) boundary-Born trial fields are shown, together with the exact result, in Figs. 4a and 4b, respectively. Only one anomalous spike still persists, while the error of about 2% at small ka will again disappear in the limit $ka \rightarrow 0$. This represents the worst case found at present; usually the variational results (with shadowing) are much better.

CONCLUDING REMARKS

Introducing simple shadowing into the original boundary-Born trial field for the TM scattering from an infinite cylinder results in remarkable improvements in the variational scattering amplitude and cross section, which become very accurate at all frequencies and for all scattering directions. Accounting for shadow-induced effects produces similar improvements in the variational results for the TM scattering from the hemicylindrically-embossed plane and, as was recently shown by D. E. Freund, for scattering from an acoustically-soft sphere. Presently, our efforts are directed at designing universally-efficient (yet simple) trial fields for the TE polarization, which would provide accurate results for all frequencies and scattering angles for this polarization as well.

ACKNOWLEDGMENTS

We would like to thank S. Favin for writing the computer programs to incorporate the shadowing effects. This work was supported in part by the Department of the Navy, Space and Naval Warfare Systems Command.

REFERENCES

1. R. W. Hart and R. A. Farrell, "A Variational Principle for Scattering from Rough Surfaces," IEEE Trans. Antennas Propag. AP-25, 708-710 (1977).
2. R. H. Andro and J. A. Krill, "Vector Stochastic Variational Expressions for Scatterers with Dielectric, Conductive, and Magnetic Properties," J. Opt. Soc. Am. 71, 978-982 (1981).

3. E. P. Gray, R. W. Hart, and R. A. Farrell, "An Application of a Variational Principle for Scattering by Random Rough Surfaces," *Radio Sci.* 13, 333-343 (1978).
4. J. A. Krill and R. A. Farrell, "Comparison Between Variational, Perturbational, and Exact Solutions for Scattering from a Random Rough-Surface Model," *J. Opt. Soc. Am.* 68, 768-774 (1978).
5. R. L. Weaver, "A Variational Principle for Waves in Discrete Random Media," *Wave Motion* 7, 105-121 (1985).
6. J. A. Ogilvy, "An Estimate of the Accuracy of the Kirchhoff Approximation in Acoustic Wave Scattering from Rough Surfaces," *J. Phys. D: Appl. Phys.* 19, 2085-2113 (1986).
7. J. A. Krill, J. F. Bird, and R. A. Farrell, "Trial Functions in Variational Calculations," in Proceedings of the 1982 CSL Scientific Conference on Obscuration and Aerosol Research (ed. by R. H. Kohl and Assoc., Tullahoma, TN, 1983) pp. 201-209.
8. J. A. Krill and R. A. Farrell, "The Development and Testing of a Stochastic Variational Principle for Electromagnetic Scattering," in Wave Propagation and Remote Sensing, Proceedings of URSI Commission F 1983 Symposium (European Space Agency, Noordwijk, The Netherlands, 1983), pp. 299-307.
9. B. J. Stoyanov, J. A. Krill, J. F. Bird, and R. A. Farrell, "Broadband Trial Functions for Surface Scattering with Detailed Analysis for a Simple Model," in Proceedings of the 1986 CRDEC Scientific Conference on Obscuration and Aerosol Research (ed. by R. H. Kohl and Assoc., Tullahoma, TN, 1987), to appear.
10. Lord Rayleigh, "On the light dispersed from fine lines ruled upon reflecting surfaces or transmitted by very narrow slits," *Phil. Mag.* 14, 350-359 (1907).
11. J. F. Bird, R. A. Farrell, E. P. Gray, and B. J. Stoyanov, "Trial Functions for Scattering from Surfaces of Arbitrary Roughness and Variational Test Calculations," in Proceedings of the 1986 CRDEC Scientific Conference on Obscuration and Aerosol Research (ed. by Kohl and Assoc., Tullahoma, TN, 1987), to appear.
12. P. M. Morse and H. Feshbach, Methods of Theoretical Physics, Part II, McGraw-Hill, New York (1953).
13. J. J. Bowman, T. B. A. Senior, and P. L. E. Uslenghi, Electromagnetic and Acoustic Scattering by Simple Shapes, Revised Printing, Hemisphere, New York (1987).
14. M. Abramowitz and I. A. Stegun (eds.), Handbook of Mathematical Functions, U.S. Government Printing Office, Washington, D.C. (1964).
15. B. J. Stoyanov and R. A. Farrell, "On the Asymptotic Evaluation of $\int_0^{\pi/2} J_0^2(\lambda \sin x) dx$," *Math. Comp.* 49, 275-279 (1987).
16. C. H. Papas, "Diffraction by Cylindrical Obstacle," *J. Appl. Phys.* 21, 318-325 (1950).
17. R. D. Kodis, "Variational Principles in High-Frequency Scattering," *Proc. Camb. Phil. Soc.* 54, 512-529 (1958).
18. J. F. Bird, "Analysis of All-Frequency Variational Behavior of the Kirchhoff Approximation for a Classic Surface-Scattering Model," *J. Opt. Soc. Am. A* 2, 945-953 (1985).
19. J. F. Bird, "Variational Divergence in Wave Scattering Theory with Kirchhoffian Trial Functions," *J. Opt. Soc. Am. A* 3, 2047-2054 (1986).

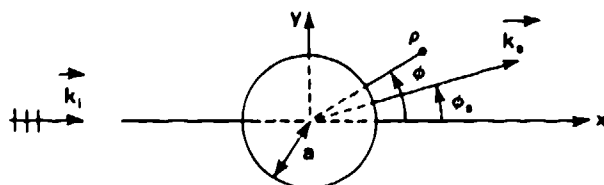


FIGURE 1. SCATTERING CONFIGURATION. Plane-wave scattering by an infinite circular cylinder at normal incidence.

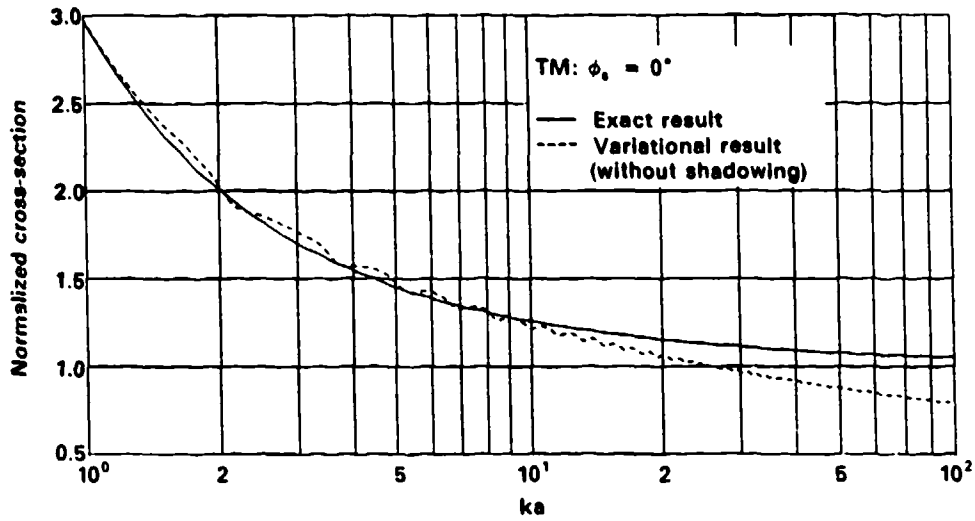


FIGURE 2a. TM FORWARD SCATTERING. The normalized variational cross section obtained with the boundary-Born trial field without shadowing (dashed curve) is compared with the exact result (solid curve) for forward scattering from cylinder. The error at $ka = 100$ is about 26 percent and is increasing with ka .

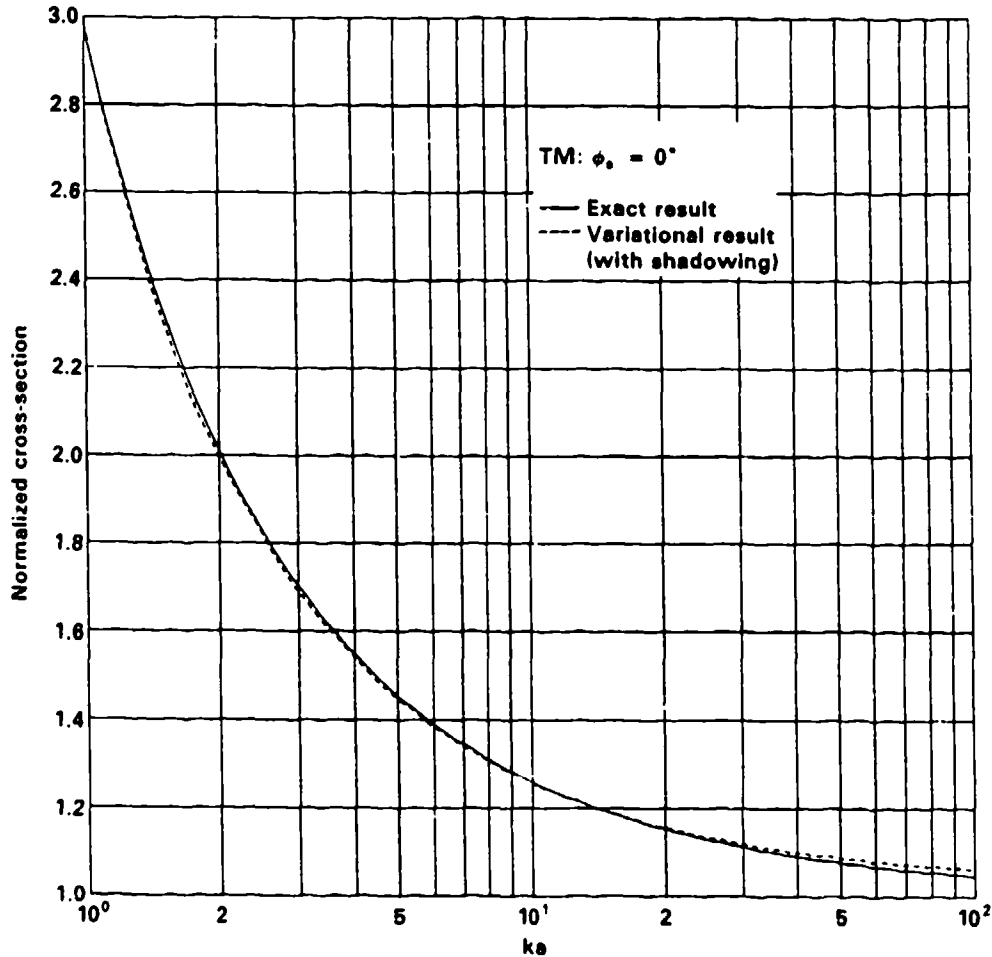


FIGURE 2b. SAME AS IN FIG. 2a, except that the normalized variational cross section (dashed curve) is now obtained with the shadowed-boundary-Born trial field. The error at $ka = 100$ is now less than 1.4 percent and will eventually disappear as $ka \rightarrow \infty$.

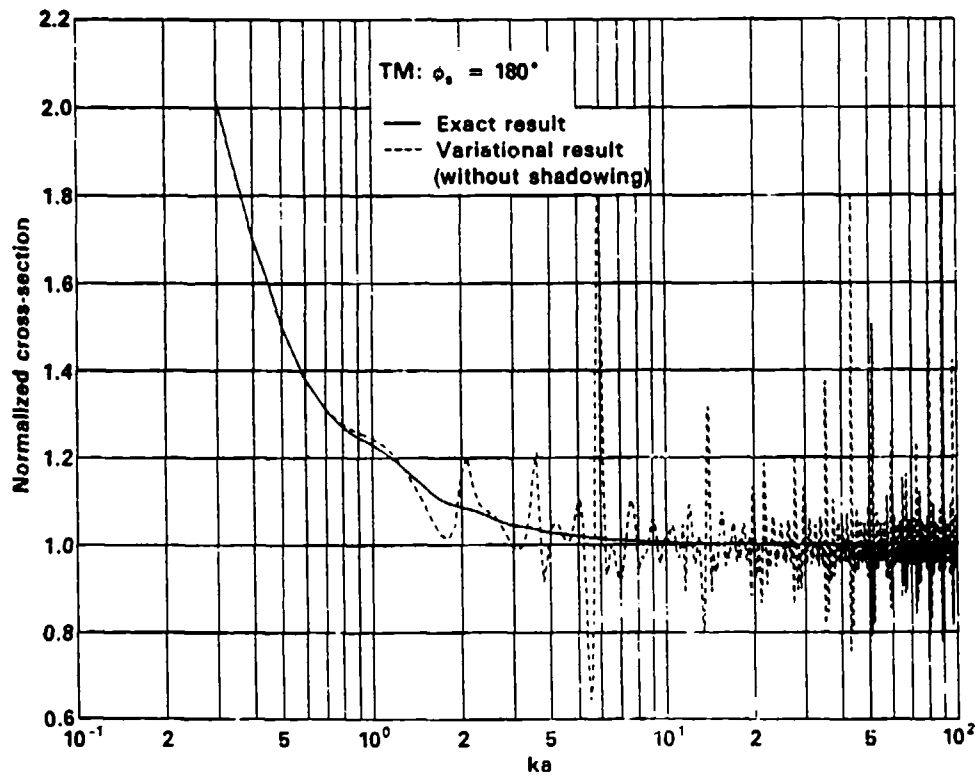


FIGURE 3a. TM BACKSCATTERING. The normalized variational cross section calculated by using the original boundary-Born trial function (dashed curve) is compared with the exact solution (solid curve) for backscattering.

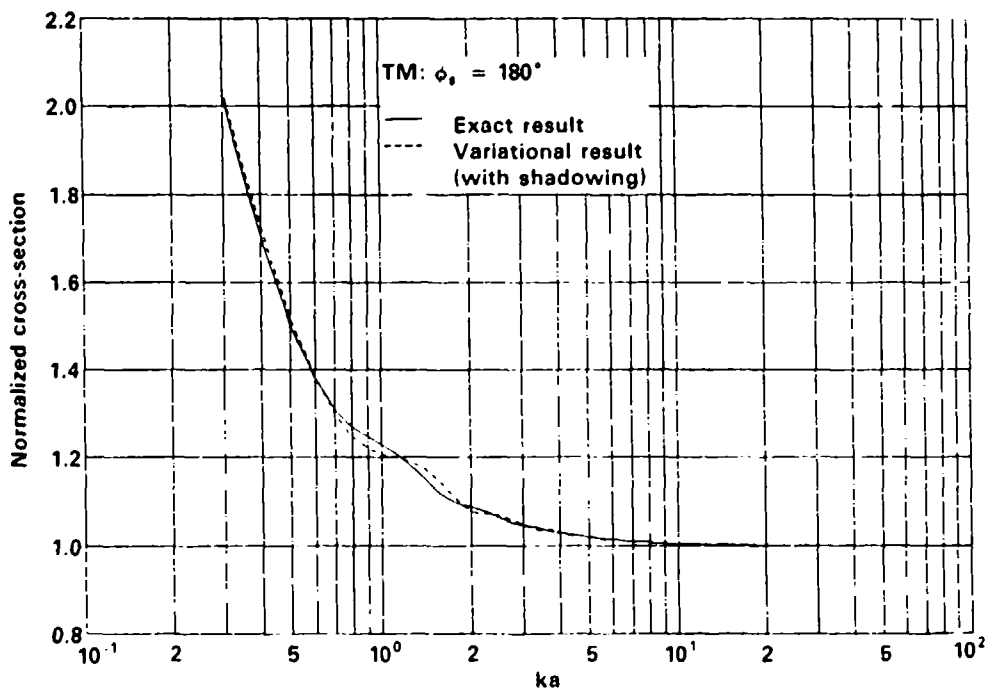


FIGURE 3b. SAME AS IN FIG 3a, except that the normalized variational cross section (dashed curve) is now calculated by using the shadowed-boundary-Born trial function. The maximum error of less than 2.5 percent occurs at $ka \sim 1.5$.

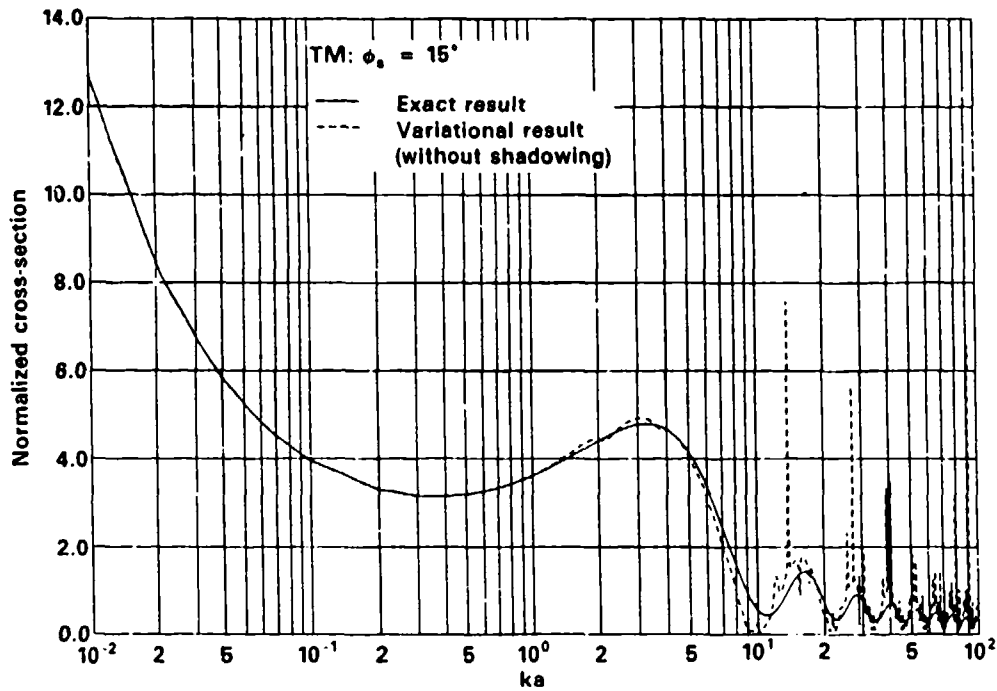


FIGURE 4a. TM ARBITRARY-ANGLE SCATTERING. The normalized variational cross section calculated by using the original (i.e., without shadowing) boundary-Born trial field (dashed curve) is compared with the exact solution (solid curve) for $\phi_s = 15^\circ$.

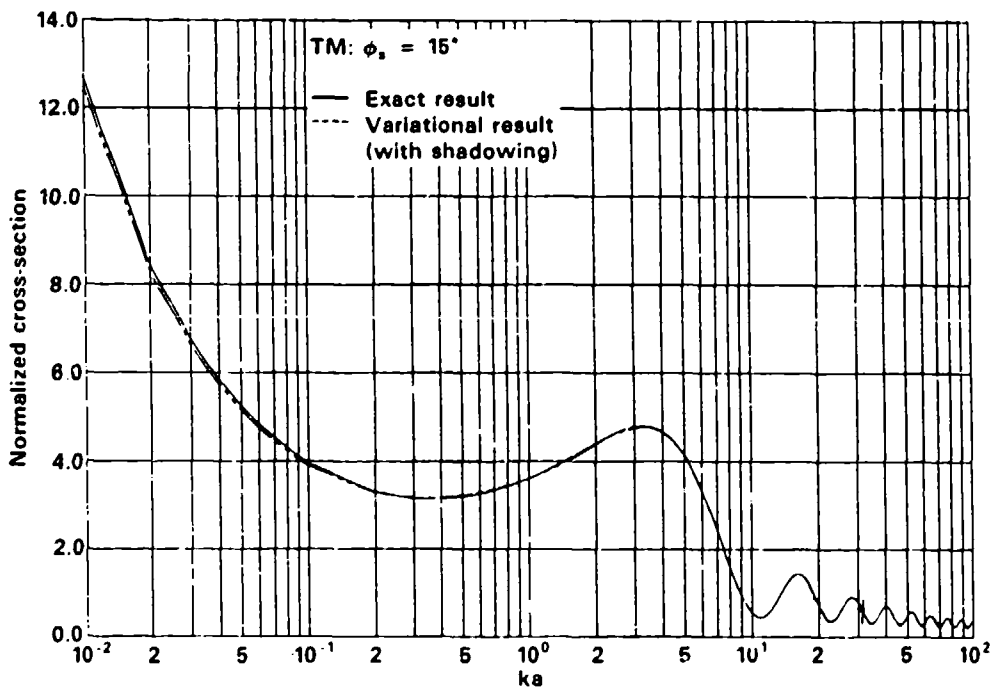


FIGURE 4b. SAME AS IN FIG. 4a, but now the variational result is obtained with the shadowed-boundary-Born trial field. Notice that all spurious spikes (except one at $ka \sim 31.3$) have disappeared and the error of less than 2 percent at small ka will fade away as $ka \rightarrow 0$.

THE SCATTERING OF LIGHT FROM A DIELECTRIC KNOT

Recent relevant publications:

1. R.D.Haracz, L.D.Cohen, A.Cohen, C. Acquista, "Light Scattering from Dielectric Targets Composed of a Continuous Assembly of Circular Disks", *Appl. Opt.* **25**, 4386 (1986)
2. R.D.Haracz, L.D.Cohen, A.Cohen, and Ru T. Wang, "Scattering of Linearly Polarized Microwave Radiation from a Dielectric Helix", *Appl. Opt.* Dec. 1987.

ABSTRACT

The scattering of light from a dielectric wire twisted into a knot is described and a comparison to a single -turn helix of the same volume is made. The first order Shifrin technique fully accounts for the geometry of the target, and we show how it is to be applied to complex shapes. It is found that the intensity patterns for the knot and the helix significantly differ in the first order.

INTRODUCTION

As an example of our recent modification to the Shifrin - Acquista method, which computes the scattering from objects which can be constructed from an assembly of circular disks, we report here on a calculation of the scattering of an E and M wave by a dielectric knot. The advantage of using the Shifrin approach here is that the first order calculation accounts for the target shape, thus permitting the technique to be applied to a wide variety of shapes. The clear disadvantage of the Shifrin approach is that it is limited to targets whose size parameter is less than 2, i.e. $2\pi am/\lambda < 2$, where "a" is the target dimension, λ is the wavelength, and "m" is the index of refraction of the target.

OUTLINE OF THEORY

The basic integral equation of the Shifrin-Acquista approach is

$$E_i(\vec{r}) = E_{inc,i}(\vec{r}) + \alpha D_{ij} \int_{\text{target}} dV' G(\vec{r}, \vec{r}') E_j(\vec{r}')$$

where

$$\vec{E}_{inc}(\vec{r}) = \vec{E}_0 e^{ik_0 \vec{r}}, \quad k_0 = 2\pi/\lambda$$

$$D_{ij} = \partial/\partial x_i \partial/\partial x_j + k_0^2 \delta_{ij}$$

$$G(r, r') = \exp \left[\frac{i k_0 |\vec{r} - \vec{r}'|}{|\vec{r} - \vec{r}'|} \right],$$

$$\text{and } \alpha = (m^2 - 1) / 4\pi$$

The Shifrin - Acquista solution for the above equation (1) is well documented for spheres, finite cylinders, and spheroids, and the present work uses this basic type of solution to obtain scattering solutions for more complex shapes. This approach has been applied to targets which can be formed from a long dielectric cylinder. In the present application the cylinder is considered to be bent into a knot. The target is then subdivided into N segments (which we consider to be disks). The appropriate equation then becomes

$$E_i(\mathbf{r}) = E_{inc,i}(\mathbf{r}) + \alpha \sum_{l=1}^N D_{ij} \int_{l^{th} \text{ disk}} dv' G(\mathbf{r}, \mathbf{r}') E_j(\mathbf{r}')$$

In essence we obtain the Shifrin solution for each disk and then form a coherent sum of the fields from the disks to form the solution for the entire target. To get a rapidly converging solution for each disk segment we need to introduce the effective field:

$$\vec{E}(\mathbf{r}) = [U^l(\mathbf{r}) A + (1 - U^l(\mathbf{r}))] \vec{E}_{eff}(\mathbf{r})$$

where $U^l(\mathbf{r}) =$ 1, if \mathbf{r} is within the l^{th} disk
 0, if \mathbf{r} is outside
 $A =$ polarization matrix

Next, the effective field is expanded in a power series in terms of α :

$$\vec{E}_{eff}(\mathbf{r}) = \vec{E}_{inc}(\mathbf{r}) + \sum_{n=1}^{\infty} \alpha^n \vec{E}_{eff}^{(n)}(\mathbf{r})$$

Substitution of the expression for $E(\mathbf{r})$ in terms of U and E_{eff} yields the integral equation for E_{eff}

$$E_{eff,i}(\mathbf{r}) = E_{inc,i}(\mathbf{r}) + \alpha \sum_{l=1}^N D_{ij} \int_{\text{all space}} dv' G(\mathbf{r}, \mathbf{r}') [U^l(\mathbf{r}') A_{ij}] E_{eff,k}(\mathbf{r}') + \alpha \frac{(\delta_{ij} - A_{ij})}{\alpha} E_{eff,j}(\mathbf{r}) U^l(\mathbf{r})$$

where l' marks one of the segments. Inserting the power series expansion of E_{eff} in terms of α , and collecting terms containing $\alpha^{(1)}$ yields the first order integral equation for E_{eff} (r outside the target).

$$E_{eff,i}^{(1)}(\mathbf{r}) = \sum_{l=1}^N \int dv' D_{ij} G(\mathbf{r}, \mathbf{r}') U^l(\mathbf{r}') A_{jk} E_{inc,k}(\mathbf{r}')$$

By equating all terms containing powers of α^2 we obtain the second order Shifrin approximation

$$E_{eff,i}^{(2)}(\mathbf{r}) = \sum_{l=1}^N D_{ij} \int dv' G(\mathbf{r}, \mathbf{r}') U^l(\mathbf{r}') A_{jk} E_{eff,k}^{(1)}(\mathbf{r}')$$

where

$$E_{\text{eff},k}^{(1)}(\mathbf{r}) = \sum_{l=1}^N D_{km} \int dv'' G(\mathbf{r}', \mathbf{r}'') U^l(\mathbf{r}'') A_{mn} E_{\text{inc},n}(\mathbf{r}'') \\ + \frac{[\delta_{km} - A_{km}]}{\alpha} E_{\text{inc},m}(\mathbf{r}') U^l(\mathbf{r}')$$

THE KNOT

A two view drawing of our model knot is shown in figure 1, along with the target frame of reference x_1, y_1, z_1 . This figure was placed over a coordinate grid and a series of 75 points were read from the grid which yielded a parametric representation of the knot, i.e., $x_1(l), y_1(l), z_1(l)$, where $l = 1, \dots, 75$. The knot was then broken into seven segments and a polynomial fit was made to each segment:

$$x_1(l) = c_3 l^3 + c_2 l^2 + c_1 l + c_0$$

$$y_1(l) = D_3 l^3 + D_2 l^2 + D_1 l + D_0$$

$$z_1(l) = F_3 l^3 + F_2 l^2 + F_1 l + F_0$$

Before the polynomial fit was applied, some adjustment was made to the coordinates to insure that no parts of the knot touched.

The vector which describes the location of each disk is given by

$$\hat{h}_1 = x_1(l) \hat{i}_1 + y_1(l) \hat{j}_1 + z_1(l) \hat{k}_1$$

in the target frame x_1, y_1, z_1 . The unit vectors in the disk frame are:

$$\hat{k}_1 = \frac{d\hat{h}_1}{|d\hat{h}_1|}, \quad \hat{j}_1 = \frac{\hat{k}_0 \times \hat{h}_1}{|\hat{k}_0 \times \hat{h}_1|}, \quad \hat{i}_1 = \frac{\hat{j}_1 \times \hat{k}_1}{|\hat{j}_1 \times \hat{k}_1|}$$

THE FIRST ORDER CONTRIBUTION TO E_{eff} FOR THE KNOT

The first order contribution to E_{eff} is composed of the coherent sum of the scattering from each of the disks comprising the knot.

$$E_{\text{eff},i}^{(1)}(\mathbf{r}) = \frac{e^{ik_0 r}}{k_0^2 r} \sum_{l=1}^N \frac{J_1(q_{\perp}^l a)}{(q_{\perp}^l a)} e^{iq_{\parallel}^l \hat{h}_1} [T_{\text{disk} \rightarrow \text{reference}}]_{ij} \\ \times (A_{jm} - \hat{r}_j \hat{r}_k A_{km}) E_{o,m}]_{\text{disk}}$$

where

$$(A)_{\text{disk}} = \begin{pmatrix} a_{TE} & 0 & 0 \\ 0 & a_{TE} & 0 \\ 0 & 0 & a_{TM} \end{pmatrix}$$

$$a_{TE} = 2 / (m^2 + 1) , \quad a_{TM} = 1 , \quad a = \text{radius of the wire}$$

$$\hat{q}_\perp^k = k_0 (\hat{r} - \hat{k}_0) , \quad q_\perp^1 = \text{component of } \vec{q} \text{ perpendicular to the disk}$$

RESULTS

We have computed the intensity for the knot

$$L_{22} = \left(\frac{k_0 r}{E_0} \right)^2 |E_{sc}|_{\theta_{pol}=0}^2$$

where the radius of the wire = 0.2 , $V = \pi a^2 L = 10.0$, $\lambda = 2\pi$, $m = 1.5$

Scattering from the knot is compared to the scattering from a single turn helix with the following parameters:

radius of wire = 0.2 , pitch = 0.5 , median radius of helix = 1.266
index of refraction = 1.5.

The volume is the same as for the knot : $v = 10$. Relative units are used, with the wavelength of the radiation being $\lambda = 2\pi$.

Figure 2 shows the orientation of the target frame with respect to the reference frame x_0, y_0, z_0 . In this frame z_0 is in the direction of incidence, x_0, y_0, z_0 is the scattering plane and $2\phi_0$ is the scattering angle. The intensities for the knot and the helix are shown in figures 3 and 4 , for the target orientations $(\theta_\tau = 0^\circ, \phi_\tau = 0^\circ)$ and $(\theta_\tau = 90^\circ, \phi_\tau = 90^\circ)$ respectively (see fig. 2) . We see that, in both cases, the patterns differ markedly, with the helix showing more extreme minima due to its higher degree of symmetry. Thus, the first order patterns clearly distinguish the two shapes.

Naturally, a first order calculation for something as complicated as a knot cannot be regarded as conclusive, even though our calculation takes account of this special geometry. Self interactive effects are not included in the first order.

Our work on the inclusion of self-interactions by solving the exact integral equation for the polarization matrix is nearing completion, and these effects will be reported at the next meeting of the Obscuration and Aerosol Research Conference.

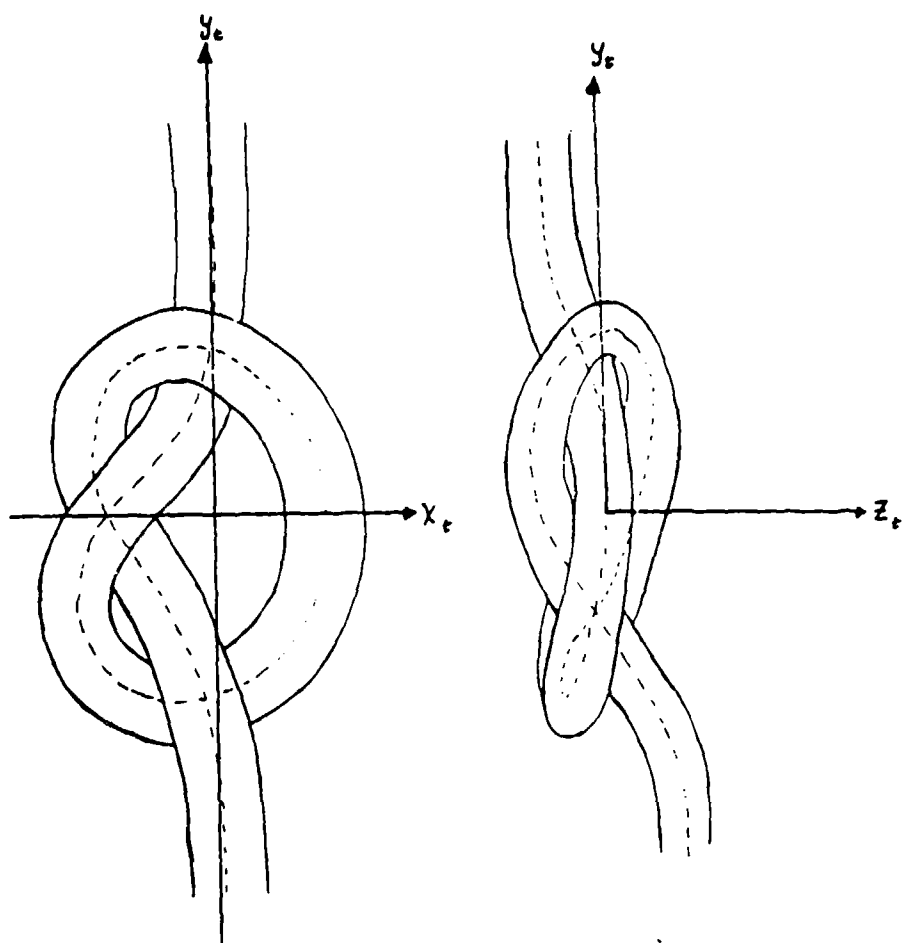


FIGURE 1. Two views of the dielectric knot that is used in this calculation in the target frame.

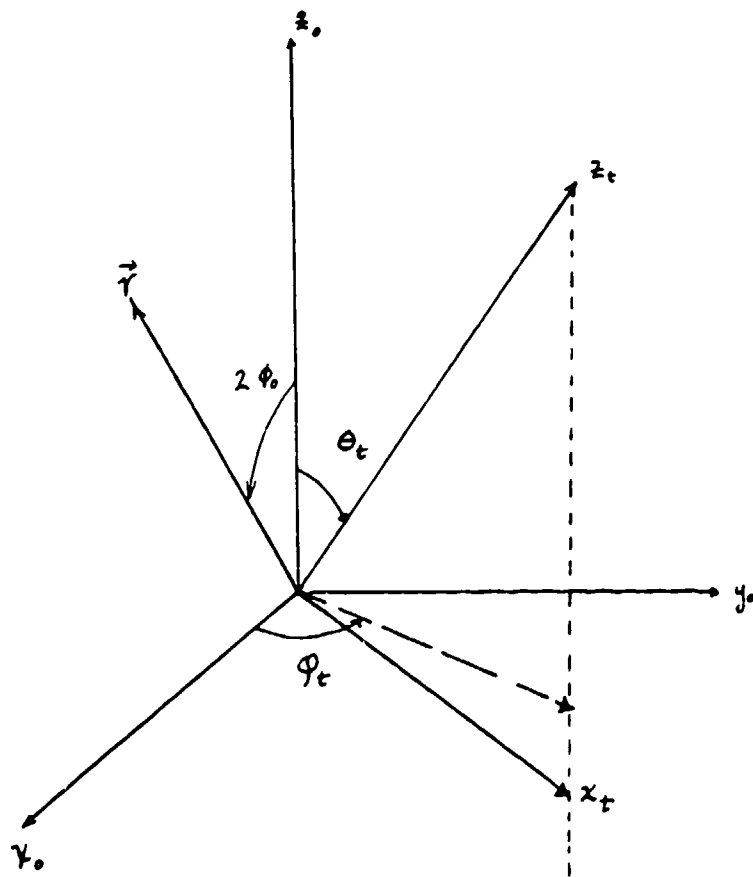


FIGURE 2. The target x_t, y_t, z_t and reference x_0, y_0, z_0 frames. The direction of incidence is along z_0 , the direction of scattering is in the x_0 - z_0 plane, and the target frame is oriented by the spherical angles θ_t, ϕ_t .

Data from "Intensity I-22"

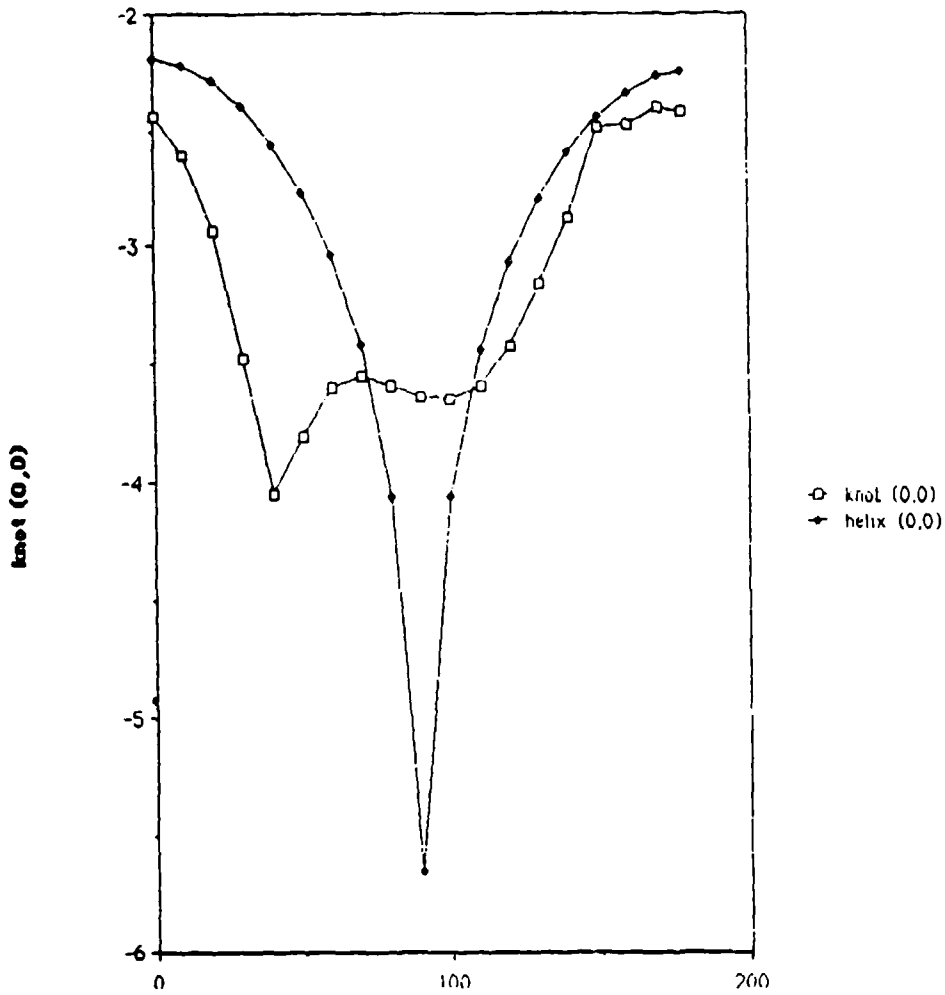


FIGURE 3. Comparison of the intensity patterns for the dielectric knot and single-turn helix. The intensities for the knot and helix are shown for the direction of incident radiation $\theta_i = 0^\circ$, $\phi_i = 0^\circ$.

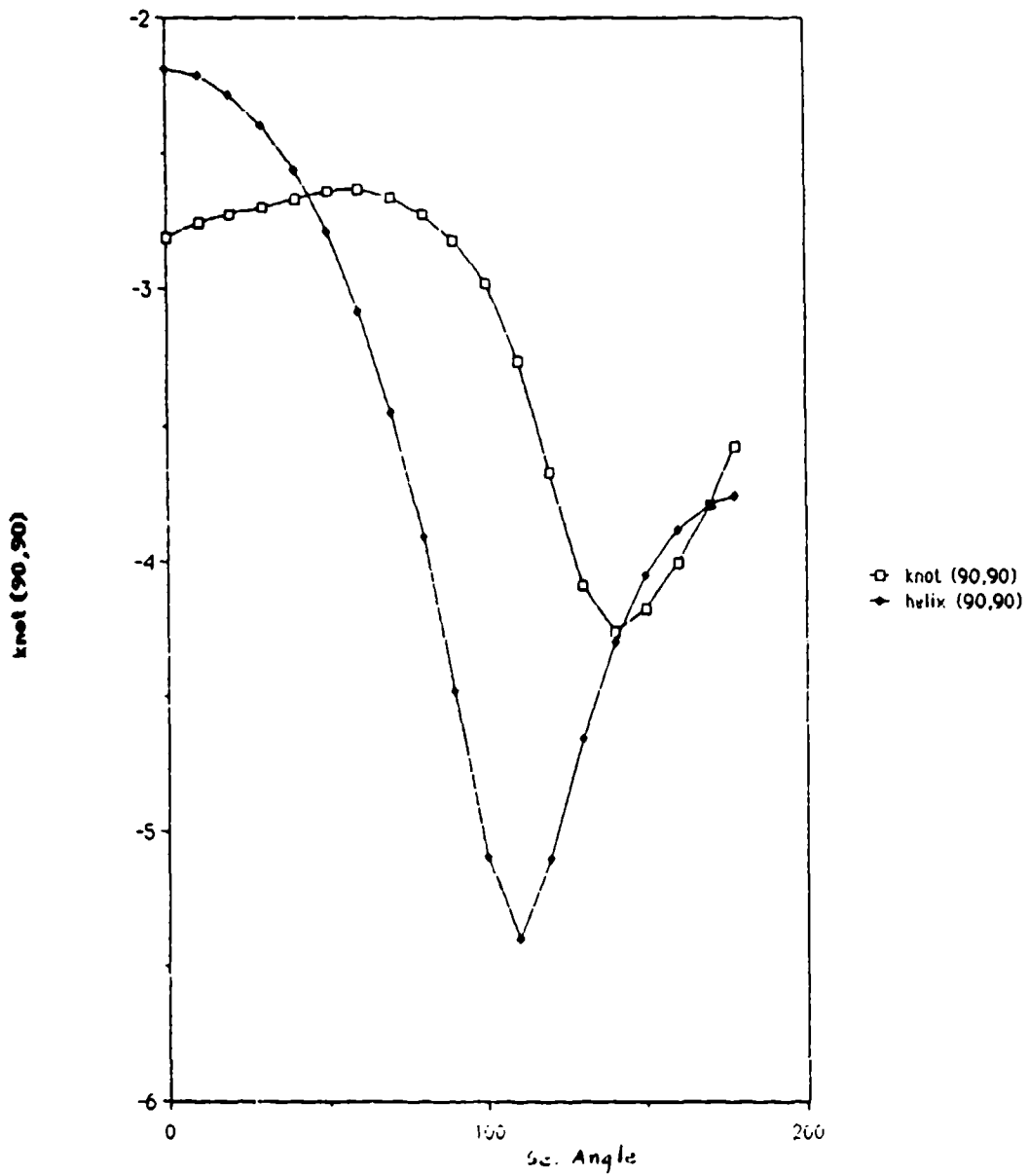


FIGURE 4. Comparison of the intensity patterns for the dielectric knot and single-tum helix. The intensities for the knot and helix are shown for the direction of incident radiation $\theta_i = 90^\circ$, $\phi_i = 90^\circ$.

SCATTERING FROM A HELIX AND RANDOMLY ORIENTED LONG CYLINDERS
AND THE INFINITE CYLINDER THEORY APPROACH

by

ARIEL COHEN^a), RICHARD D. HARACZ, and LEONARD D. COHEN

ABSTRACT

A two dimensional method for calculating the scattered intensities from a helical dielectric target is compared with experimental results. The wavelength of the incidence was 3.12cm and a wire made out of a plastic material, the refractive index of which was $1.625-0.012i$ and of a radius of 0.24cm, was curved to form a 7 loop helix of radius 1.83cm and having a pitch of 0.553cm. The theoretical calculations presented below coherently combined the scattered fields from all segments of the helix, each being regarded as a unit length of an infinite cylinder with a corresponding tilt angle relative to the incident radiation. The polarization of the incident radiation varies relative to the orientation of each segment of the target.

The comparison between the results of the calculations and the experiment shows good agreement.

The infinite theory is also used to compare experimental results on randomly oriented long ice crystals with the theoretical prediction.

INTRODUCTION

The scattering of light by long cylinders whose aspect ratios are larger than about 20 is characterized by sharp maxima appearing all within the envelope of a two dimensional cone¹⁻³. This cone has an apex angle which is equal to the angle between the incident light and the main axis of the long cylinder. As the aspect ratio increases, a larger portion of the scattered light from the cylinder is restricted to the above mentioned two-dimensional surface of a cone. Experimental results of 10.6 μ m radiation scattered by long metallic wires, were compared with theory⁴ and showed that:

A.- The angular dependence can be accurately predicted for long cylinders using the infinite cylinder theory.

B.- When the scattering plane (the plane in which the scattered light is measured) is not accurately maintained perpendicular to the wire for normal incidence, the scattered intensity measured in the scattering plane drops rapidly with increasing values of the scattering angle θ (between 0° and 90°).

When the aspect ratio is smaller than 20, the angular scattering within the cone described above will still follow in general the prediction of the infinite theory; but the incident light will also be scattered in other directions. This is supported by theory⁵ (for small size parameters) for finite cylinders or disks and by laboratory measurements on finite cylinders⁶. Recent laboratory measurements⁷ performed only within the cone (or within the plane, for normal incidence), also suggested that the general angular behaviour is weakly dependent on the aspect ratio as long as it exceeds the value of 20.

As a consequence the infinite theory was used to calculate the scattering by a helix.

It will be shown below that such wires in the shape of a helix can indeed be treated as long cylinders since it can be assumed that the edge effect of finite cylinders, with small aspect ratios giving rise to the off cone scattering is reduced to a negligible value by the adjacent segments of the long curved wire.

Finally, another example of the use of the infinite theory for the prediction of the scattering properties of long cylinders will be given considering the experimental results for randomly oriented long ice crystals.

THEORY

The far field scattering of a unit length of a tilted infinite cylinder is given by the following two components⁸:

$$S_1 = \left[b_{0I} + 2 \sum_{n=1}^{\infty} b_{nI} \cos(n\theta) \right] \cos \alpha + \left[2 \sum_{n=1}^{\infty} b_{nII} \sin(n\theta) \right] \sin \alpha \quad 1$$

and

$$S_2 = \left[a_{0II} + 2 \sum_{n=1}^{\infty} a_{nII} \cos(n\theta) \right] \sin \alpha + \left[2 \sum_{n=1}^{\infty} a_{nI} \sin(n\theta) \right] \cos \alpha \quad 2$$

where α is the polarization angle between the polarization plane of the linearly polarized incidence and the plane containing the cylinder axis and the incident light

(θ = the incident plane). For the definitions of the scattering coefficients b_{nI} , $b_{nII} = -a_{nI}$,

and a_{nII} , -see Ref. 2. These coefficients are dependent on the tilt angle ϕ .

The angle θ here is not measured relative to the incidence, but on a plane normal to the axis of the cylinder. $\theta = 0$ is along the incident direction.

Let ϕ be the tilt angle of the cylinder measured between the incident direction and the normal to the cylinder, and let β be the scattering angle relative to the incidence direction, then (see Fig. 1)

$$\sin \frac{\beta}{2} = \cos \phi \sin \frac{\theta}{2} \quad 3$$

The two dimensional scattering is characterized by the fact that for each scattering angle $\beta = 2 \phi_0$ relative to the incidence, only one absolute value of a rotation angle γ about the incidence corresponds to $2 \phi_0$ ($2 \phi_0$ and γ are the corresponding spherical angles, namely, the colatitude and the longitude angles).

Assuming that the incident light is along the z axis and the scattering plane is the x,z plane; then cylinders whose axes are aligned in the x,z plane will always give rise to scattered intensities in only two directions which are determined by the cylinder axis orientation and the scattering angle.

Only a cylinder whose axis is in the y direction, will scatter light in the full x,z plane.

For a general cylinder orientation, with spherical orientation angles ϕ and γ (see Fig.1), only those orientations for which $(\pi/2 - \phi) > |\gamma|$, will give rise to a scattering intensity in the x,z plane (other than the forward direction). Any other cylinder orientation will not produce scattering in the x,z plane.

The constraint equations are also discussed elsewhere⁹, and in addition to the equation 3 (where $\phi_0 = \beta/2$),

$$\cos \phi \sin \left(\frac{\theta}{2} \right) = \sin \phi_0 \quad 3a$$

there is the equation of constraint

$$\tan \phi = \cot \phi_0 \cos \gamma \quad 4$$

Thus, there are two equations relating γ , ϕ_0 and θ .

A CURVED WIRES

Because of the equation of constraint relating the orientation of the cylinder axis to the scattering angle β , light which is scattered in a given direction in space by a curved wire which is cut into several short and approximately straight segments, will thus be composed of coherent contributions from a small number of these segments (most of the segments violate the constraints mentioned above and do not contribute).

In the case of a helix, only two segments per loop contribute coherently for a given direction of scattering. We shall first discuss the case of a helix with a zero pitch (a toroid). Three different situations were considered:

- A.- The toroid is in the z,x plane;
- B.- The toroid is in the z,y plane; and
- C.- The toroid is in the x,y plane.

In all cases the center of the toroid is placed at (0,0,0).

In case A (where the toroid is in the scattering plane) -See Fig. 2a-, the light scattered in the direction of $2\phi_c$ will emerge from merely the two segments which have a tilt angle (relative to the normal to the scattering plane) $\phi = \pi/2 - \phi_c$.

The coherent sum is achieved by adding the scattered fields with a phase shift corresponding to

$$\Delta_A = 4 R \cos \phi = 4R \sin \phi_0 \quad 5$$

In case B - See Fig. 2_B-, the light scattered in any direction of $2 \phi_c$ originates from the same two segments of the toroid which are parallel to the y axis (top and bottom parts of the toroid). The scattered light is the coherent combination from two parallel cylinders being normal to the direction of incidence and separated by a distance of 2R.

The phase difference for this case is :

$$\begin{aligned} \Delta_B &= 2R (1 - \cos 2\phi_0) = 4R \sin^2 \phi_0 \\ \Rightarrow \Delta_B &= \Delta_A \sin \phi_0 \end{aligned} \quad 6$$

In case C - See Fig. 2_C-, only two segments separated by a distance of 2 R , and both parallel to the y axis, contribute to the coherent scattered light in any given scattering angle ϕ_0 .

The phase difference is thus :

$$\begin{aligned} \Delta_C &= 2R \sin 2\phi_0 \\ \Rightarrow \Delta_C &= \Delta_A \cos \phi_0 \end{aligned} \quad 7$$

When the pitch is greater than 0, the incident light is scattered to each given direction by two segments which slightly (depending on the pitch value) differ from the parallel segments mentioned above. Thus, for case C, when the main axis of the helix is normal to the incidence and normal to the scattering plane (the helix axis is normal to the y axis), the following treatment should be used:

Let β be the scattering angle in the x,z plane, then all segments are tilted relative to

the incident direction with the same tilt angle α .

That angle satisfies the equation:

$$\tan \alpha = \frac{\text{Pitch}}{2\pi R_{sp}} \quad 8$$

Since all segments should scatter light in the scattering plane x,z , the scattering angle β corresponds to $2\phi_0$ in equation 3. Hence, the cylindrical scattering angle θ which contributes to the scattering into β , is given by:

$$\Theta = 2 \arcsin \left[\frac{\sin\left(\frac{\beta}{2}\right)}{\cos \alpha} \right] \quad 9$$

However, it is useful to note that unless the helical pitch value is considerably smaller than its radius R_s , θ is not much different than β :

For example, according to equation 8, α in the experiment to be discussed in the next section is equal to

$$\alpha = \tan^{-1} \left(\frac{0.553}{2\pi \times 1.83} \right) = 2.75^\circ$$

$\Rightarrow \cos \alpha = 0.9988$; and by substitution of this last value in equation 9, it

follows that $\theta_{\text{experiment}} \rightarrow \beta_{\text{experiment}}$

Finally, for an arbitrary direction of incidence along,

$$\mathbf{L}_0 = a_i + b_j + c_k \quad 10$$

each segment has a corresponding tilt angle ϕ^* ($\phi^* = \pi/2 - \phi$) which is determined as follows:

The helical axis is taken in the z direction. The helix is characterized by its radius R_s and the pitch P . The unit vector of the line connecting the center of the coordinate system and the center of a segment of the helix is¹⁰:

$$h = (R \cos \alpha i + R \sin \alpha j + \frac{P \alpha k}{2\pi})/s \quad 11$$

where

$$s = \left[R^2 + \left(\frac{P}{2\pi} \right)^2 \right]^{\frac{1}{2}}$$

It follows that the unit vector along the axis of each segment is:

$$k_\alpha = -R \sin \alpha i + R \cos \alpha j + \frac{P}{2\pi} k \quad 12$$

where i,j,k in equations 10,11,and 12, are all defined in the original x,y,z frame of reference.

The tilt angle is thus given by:

$$\cos \phi^* = L_0 \cdot k_\alpha \quad 13$$

Similarly, the polarization angle is determined by the dot product of the vector normal to the incident plane (the plane containing the incident direction and the axis of the corresponding segment), and the direction of the linear polarization.

These two angles, along with the constraint equations discussed above, are used in equations 1 and 2 for the calculation of the scattering field added coherently from all pairs of segments in each given loop.

COMPARISON WITH EXPERIMENTAL RESULTS.

a) DIELECTRIC HELIX.

The experimental studies were performed using the microwave analog technique (Wang et al.¹¹) for a dielectric helix. A right handed, 7-turn helix of 3.66 cm outer diameter and of 4.35 cm axial length was formed from a 0.48 cm diameter plexiglass cylinder. The complex dielectric constant of this plastic material was $m = 1.626 - 0.012 i$ at the operating microwave wavelength $\lambda = 3.18$ cm. The microwave-unique compensation (or null) technique was employed in both extinction ($2\phi_0 = 0^\circ$) and in angular scattering ($10^\circ < 2\phi_0 < 170^\circ$) intensity measurements, and from the former one can also deduce the scattering intensity in the beam direction ($2\phi_0 = 0^\circ$). A brief explanation of measurement procedures using this technique is also described in Ref. 12. The measured scattering intensities (in absolute magnitude) are denoted I_{11} , and I_{22} . The intensity I_{11} is the case when both the receiving and transmitting antennas are polarized vertically, I_{22} is for both antennas polarized horizontally. The horizontal scattering plane corresponds to the x,z plane. Inspection of the experimental profiles I_{11} and I_{22} (Figs. 3-6) versus the scattering angle $2\phi_0$ shows that the scattering by the helical structure is dependent on the orientation of the helix in the beam; and also that the intensity may vary as much as four orders of magnitude as the scattering angle changes. On the possible measurement errors, see ref. 12.

Roughly estimated, the cumulative maximum errors are 5% if the absolute magnitudes of I_{11} and I_{22} are larger than 10^1 , up to approximately 20 % for those

between 10^0 and 10^1 , and may amount to as much as 100 % for those magnitudes having less than 10^{-1} .

The intensities calculated are I_{11} , where the directions of initial and final linear polarization are perpendicular to the scattering plane, and I_{22} , where the directions of linear polarization are in the scattering plane (the scattering plane is formed by the directions of incidence and scattering). The experimental results for $I_{11}(0,0)$, $I_{22}(0,0)$ are shown in Figs 3,4, and the results for $I_{11}(90,90)$ and $I_{22}(90,90)$ are shown in Figs. 5,6. Here, for example $I_{11}(90,90)$ corresponds to the helix orientation $\phi_t = 90^\circ$ and $\gamma_t = 90^\circ$. We note that the theoretical values drop to below 10^{-2} , even though the experiment predicts no such minima. This is due to the fact that the real target is not perfectly shaped, and hence the very sharp minima produced by an ideal helix would not be expected. However, the positions of the minima are of greatest importance as these are produced by the helix geometry, and we summarized these minima for one of the experiments from

Figures 3,4 as

Figures 5,6 as

$I_{22}(0,0) : 50^\circ, 75^\circ, 100^\circ, 140^\circ;$

$I_{22}(90,90) : 55^\circ, 90^\circ, 125^\circ$

$I_{11}(0,0) : 40^\circ, 70^\circ, 135^\circ,$

$I_{11}(90,90) : 45^\circ, 115^\circ$

Figures 7 through 10 contain the theoretical intensities $I_{11}(0,0)$, $I_{22}(0,0)$, $I_{11}(90,90)$, and $I_{22}(90,90)$ and the comparison of the theory and experiment. From the Figures we found that:

- (1) Good agreement between theory and experiment exists for forward versus back

scattering.

(2) Good agreement between theoretical and experimental values for the I_{11} intensities. The structure of the intensity patterns for $I_{11}(0,0)$ and $I_{11}(90,90)$ is particularly striking.

(3) The positions of most of the experimental minima generally agree well with the theory.

The conclusion is that the infinite theory can explain the general features of the spiral experiment. Since the infinite theory can be applied to an unlimited range of particle size parameters and refractive indices, this comparison provides a method by which one can predict the scattering of helical particles of any size, consistent with the limitation that double or higher order scattering within the particle itself can be ignored.

b) RANDOMLY ORIENTED INFINITE CYLINDERS-COMPARISON WITH EXPERIMENTAL RESULTS ON LONG ICE CRYSTALS^{13,14,15}.

We next calculate the intensities for light of wavelength 11 microns incident on cylinders with the complex index of refraction $m=1.29-0.0954 i$ and size parameter $x = 2\pi(30)/11 = 17.136$. These values are used in Ref. 13 in order to estimate the effect of the scattering of thermal radiation from randomly oriented ice crystals (which are long hexagonal prisms).

We note that in Fig. 11a, which are the results of Ref. 13, the use of an inaccurate averaging procedure leads to an average intensity that drops sharply to zero starting at about $2\phi_0 = 150^\circ$. We also note that the pattern becomes constant at scattering angles larger than about 80° . Our result, shown in Fig. 11b, reveals marked

differences. First, the pattern actually rises slightly at the larger scattering angles (very much like the pattern for spherical targets of the same refractive index and size parameter), and the pattern continues to show fluctuations over the full angular range. Finally, we make a comparison of our averaging procedure (which makes use of all of the constraint equations discussed above and elsewhere¹⁴) with the experimental results of Huffman et al.¹⁵ In this experiment, visible light of wavelength 0.55 microns is incident on ice crystals whose size parameter is $x = 2\pi(4)/0.55 = 45.7$ and the index of refraction is $m = 1.31$. Our results along with the experimental points are shown in Fig.12. Here, the experimental points are shown by black diamonds and the theory by open squares. We see that there is general agreement that extends over the whole range of the experiment (from 10° to 150°). In particular, we note that agreement is achieved at the largest scattering angle $2\phi_0 = 150^\circ$. It should be pointed out that the previous attempt to fit these data, reported in Ref. 15, did not follow the experimental pattern at 150° . The general large-angle pattern of the experiment is a slightly rising curve, a result only consistent with our calculations.

Footnote.

a) On leave for Hebrew University, Department of Atmospheric Sciences,
Jerusalem, Israel.

Acknowledgement.

This research was partially supported by the Army Chemical Research and Development Center.

References.

1. J. Wait, *Can. J. Phys.* **32**, 571 (1954).
2. M. Kerker, *The Scattering of Light and Other Electromagnetic Radiation*, Academic Press, New York, 1969.
3. C.F. Bohren, and D.R. Huffman, *Absorption and Scattering of Light by Small Particles* Wiley, New York, 1983.
4. A. Cohen, L.D. Cohen, R.D. Haracz, V. Tomaselli, J. Colosi, and K.D. Moeller, *J. Appl. Phys.* **56**, 1329 (1984).
5. L.D. Cohen, R.D. Haracz, A. Cohen, and C. Acquista, "Scattering of Light from Arbitrarily-Oriented Finite Cylinders," *Appl. Opt.* **22**, 742 (1983).
6. R. T. Wang , "Extinction by Bumbbells and Chains of Spheres" Proc. 1983 CRDC Conference, J. Farmer and R.H. Kohl, eds., Army CRDC-Sp-84009, pages 223-235;
R. T. Wang and B.A.S. Gustafson, "Angular Scattering and polarization by Randomly Oriented Dumbbells and Chains of Sphere," Proc. 1983 CRDC Conference, J. Farmer and R.H. Kohl, eds., Army CRDC-Sp-84009, pages 2237-247.
7. J. Eversole, " Angular Scattering From Single,Suspended Cylinders",1987 CRDEC Conference on Obscuration and Aerosol Research.
8. A. Cohen, *Opt. Letters* **5**, 150 (1980).
9. A. Cohen, L.D. Cohen, R.D. Haracz, and S. Egert, "Double Scattering by Randomly Oriented Long Cylinders",*J. Appl.Phys.*(1984)
10. R.D. Haracz, L.D. Cohen, A. Cohen, and C. Acquista, "Light Scattering from Dielectric Targets Composed of a Continuous Assembply of Circular Disks,"*Appl. Opt* (Dec., 1986).
11. R. T. Wang, "Electromagnetic Scattering from a Helix," Final Report,TCN-85-597 CRDC/Battelle (1986).

12. L.D. Haracz, L.D. Cohen, A. Cohen, and R.T. Wang, "Scattering of Linearly Polarized Microwave Radiation from a Dielectric Helix", *Appl. Opt.* (Dec 1987).
13. J.J. Stephens, *J. Atmos. Sci.* **37**, 435 (1980).
14. A. Cohen, R.D. Haracz, and L.D. Cohen, "Comparison Between Angular Scattering by Randomly Oriented Finite Cylinders and the Theory of Infinite Cylinders", *Proc. 1986 CRDC Conference*, R.H. Kohl and D. Stroud, eds., Army CRDC-Sp.
15. P. Huffman and W. G. Thursby, *J. Atmos. Sci.* **26**, 1073 (1969).

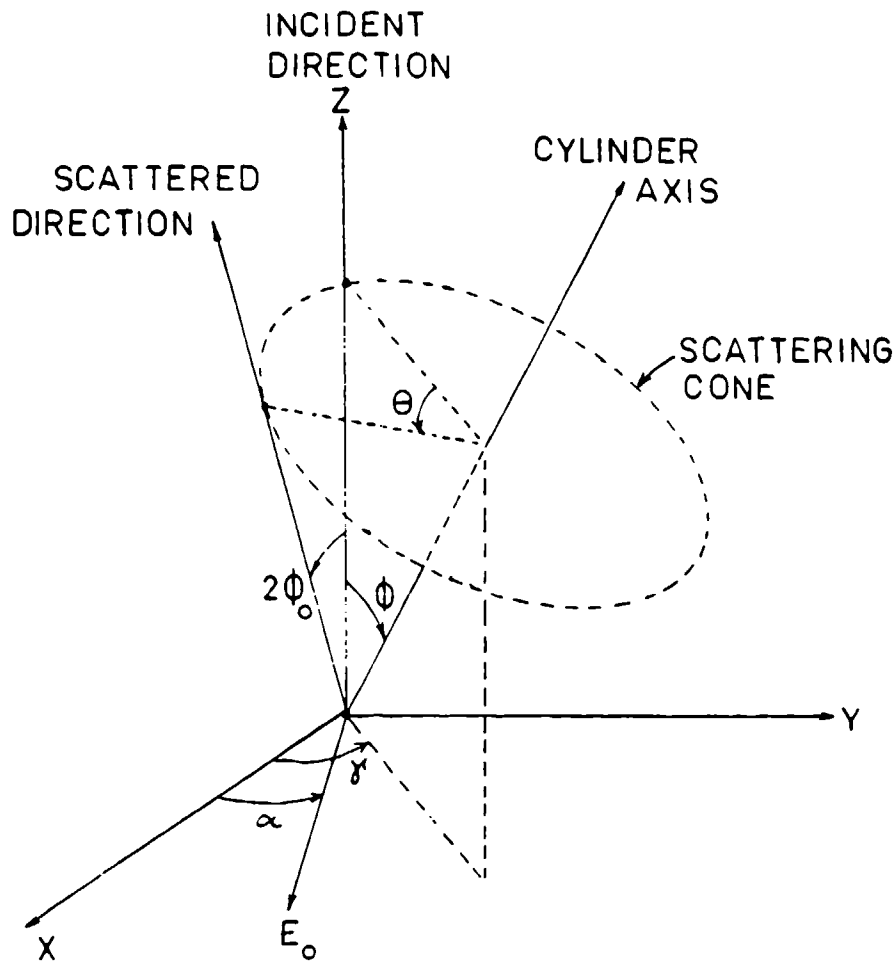


Fig. 1. The scattering geometry shown in the reference frame x,y,z , where the x,z plane is the scattering plane. The orientation angles of the cylinder axis are ϕ and γ , and the polarization angle of the linearly polarized wave is α . The scattering angle between the directions of the incidence and scattering is denoted $2\phi_0$. The scattering angle used in the theory for the infinite cylinder is measured in a plane perpendicular to the cylinder axis, and it is denoted θ .

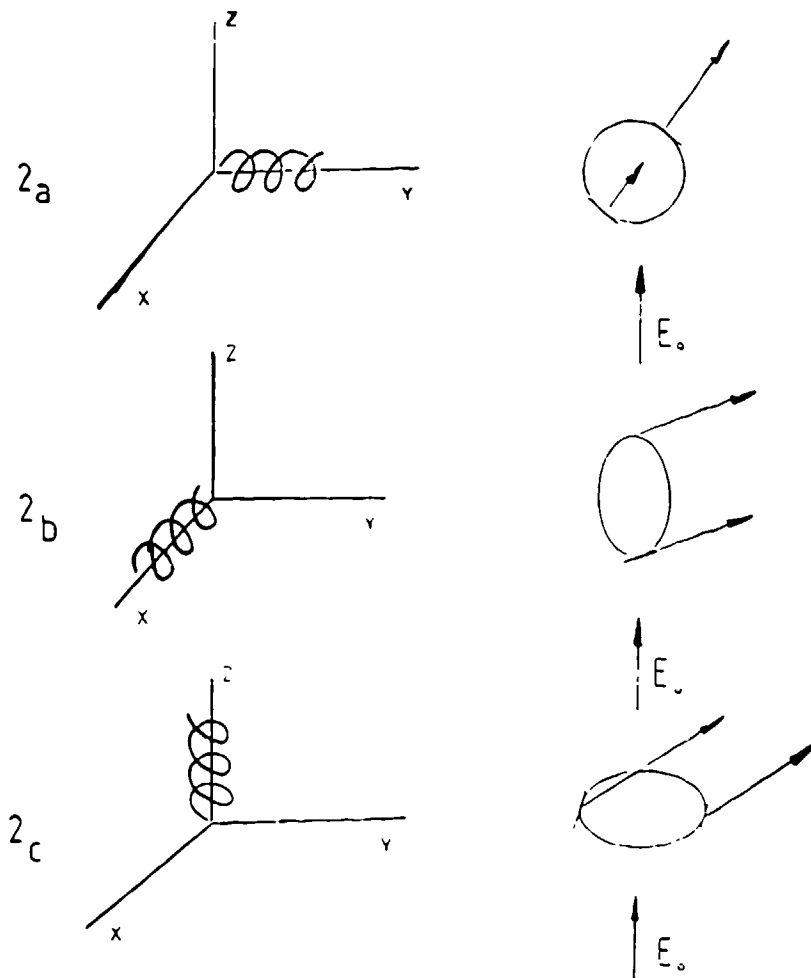


Fig. 2. The spirals and the rings shown in the reference frame. The main axis of the spiral and the corresponding ring is

- a.- parallel to the y axis.**
- b.-parallel to the x axis, and**
- c.-parallel to the z axis.**

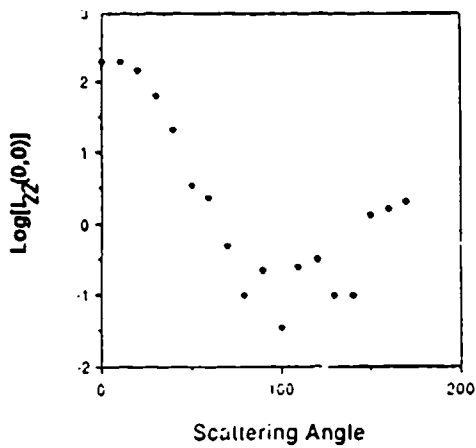


Figure 3

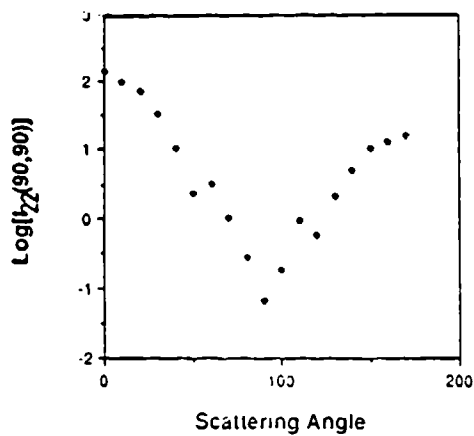


Figure 5

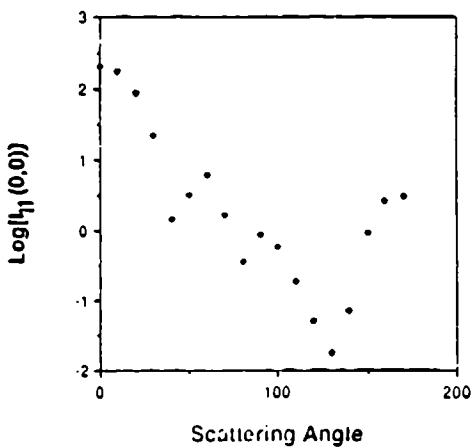


Figure 4

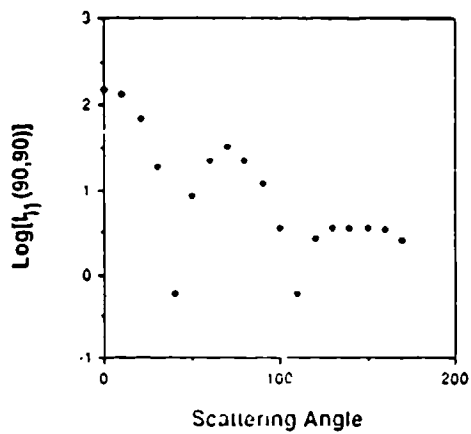


Figure 6

Figs. 3-4. The logarithm of experimental intensities I_{11} and I_{22} plotted against the scattering angle $2\phi_0$ for the spiral orientation $\phi_t = 0^\circ$ and $\gamma_t = 0^\circ$.

Fig. 5-6. Same as Fig. 5 for the spiral orientation $\phi_t = 90^\circ$ and $\gamma_t = 90^\circ$.

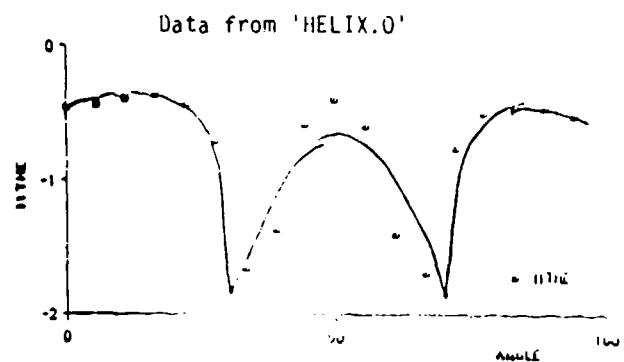
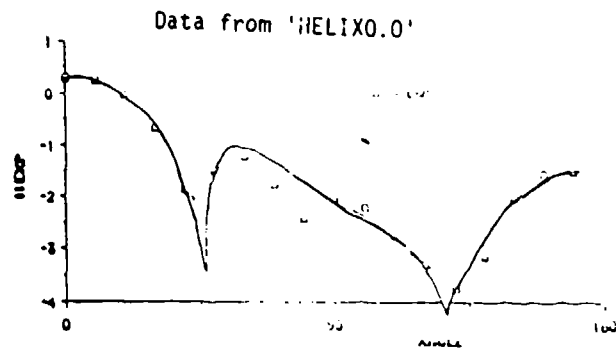


Fig. 7 A comparison between theory and experiment for the theoretical $\log(I_{11})$ plotted against the scattering angle θ_y for the orientation $\phi_1 = 0^\circ$ and $\gamma_1 = 0^\circ$

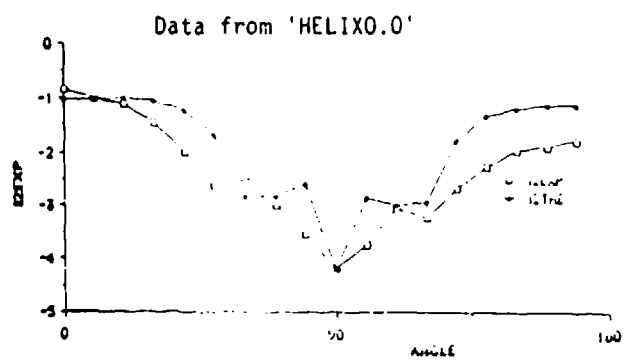


Fig. 8. A comparison between theory and experiment for the theoretical $\log(I_{22})$ plotted against the scattering angle θ_y for the orientation $\phi_1 = 0^\circ$ and $\gamma_1 = 0^\circ$

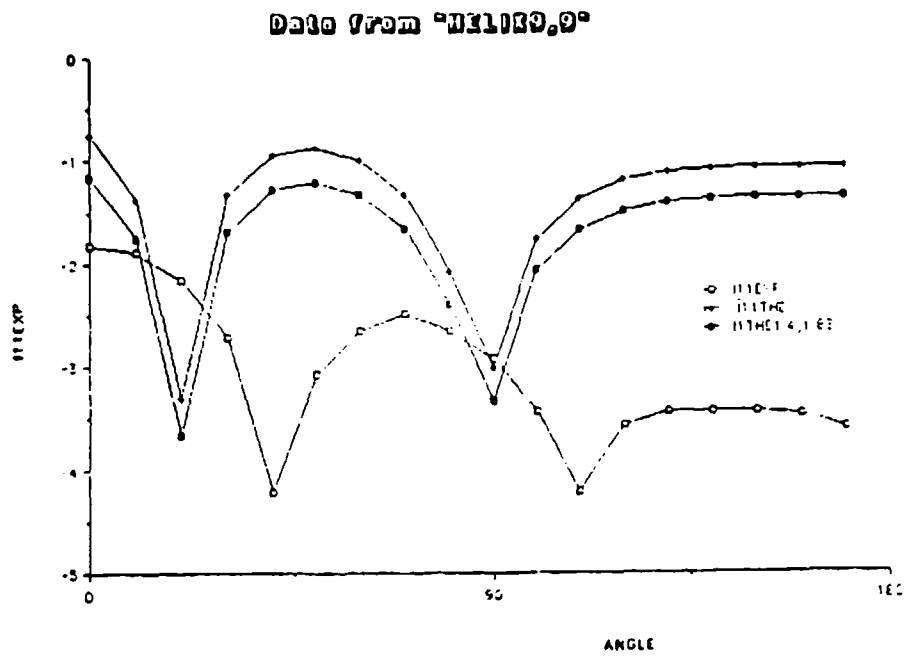


Fig. 9. A comparison between theory and experiment for the the $\log (I_{11})$ plotted against the scattering angle $2\psi_0$ for the orientation $\phi_1 = 90^\circ$ and $\gamma_1 = 90^\circ$.

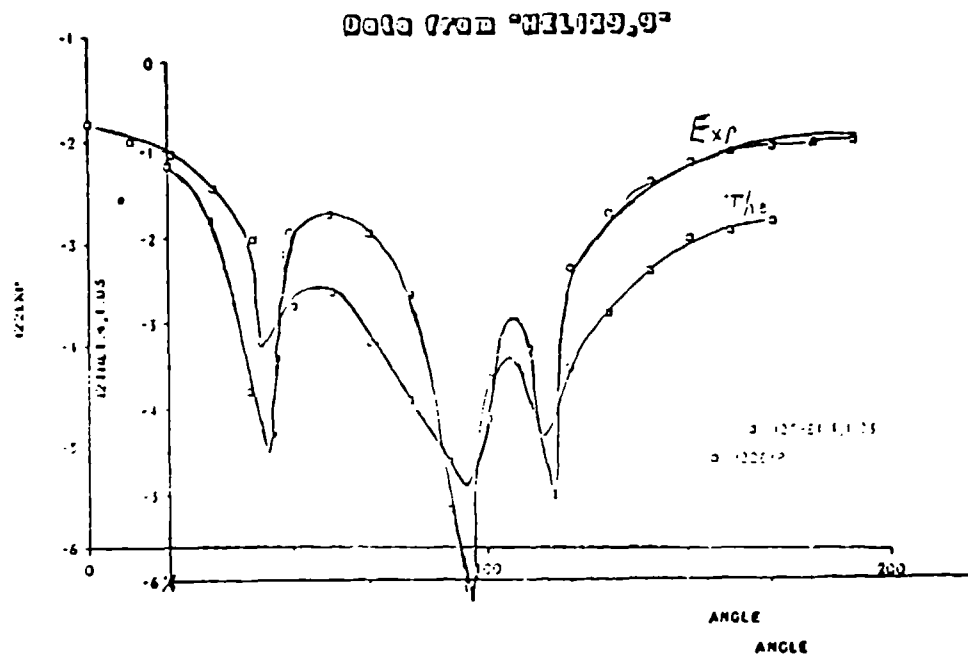


Fig. 10. A comparison between theory and experiment for the the $\log (I_{22})$ plotted against the scattering angle $2\psi_0$ for the orientation $\phi_1 = 90^\circ$ and $\gamma_1 = 90^\circ$.

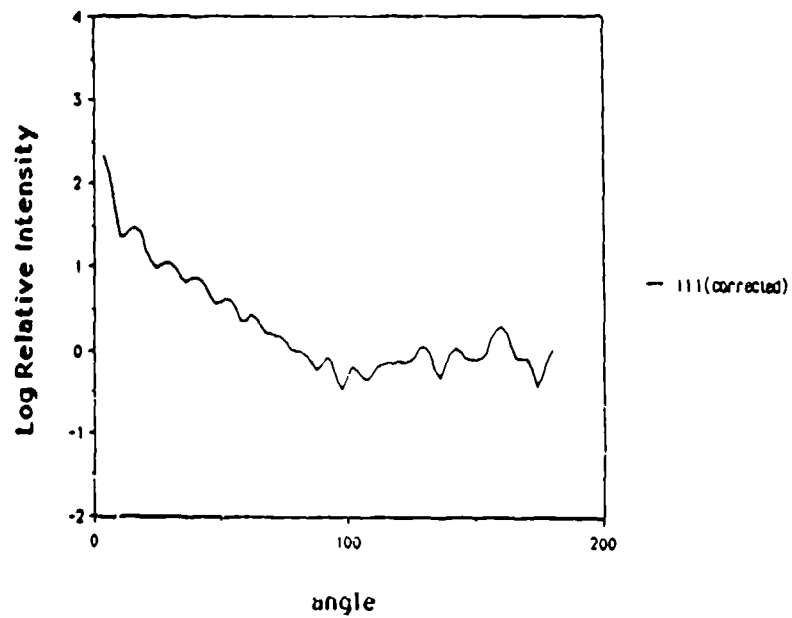
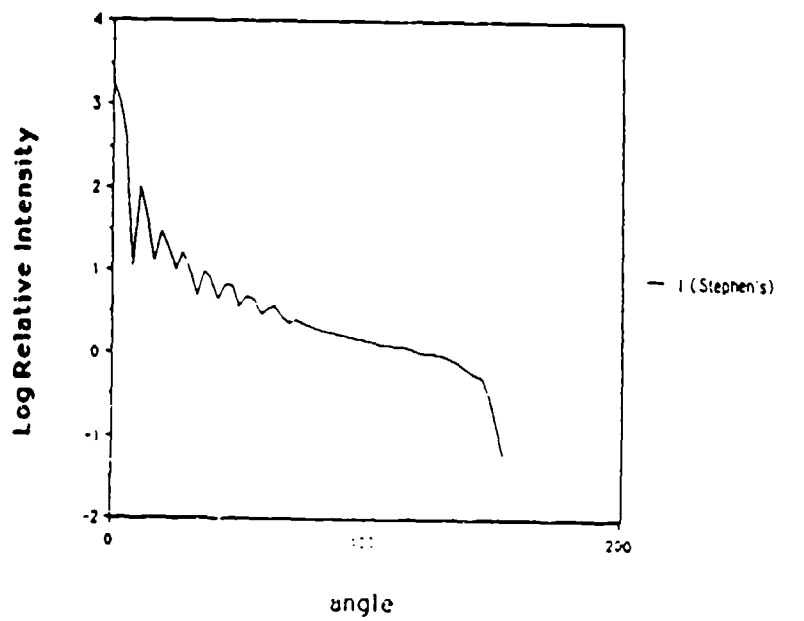


Fig. 11. The relative intensities for randomly oriented long cylinders versus the scattering angle $2\phi_0$ for $x = 17.173$ and $m = 1.29 - 0.0954 i$. a) The results of Ref. 13. b) Our corrected results.

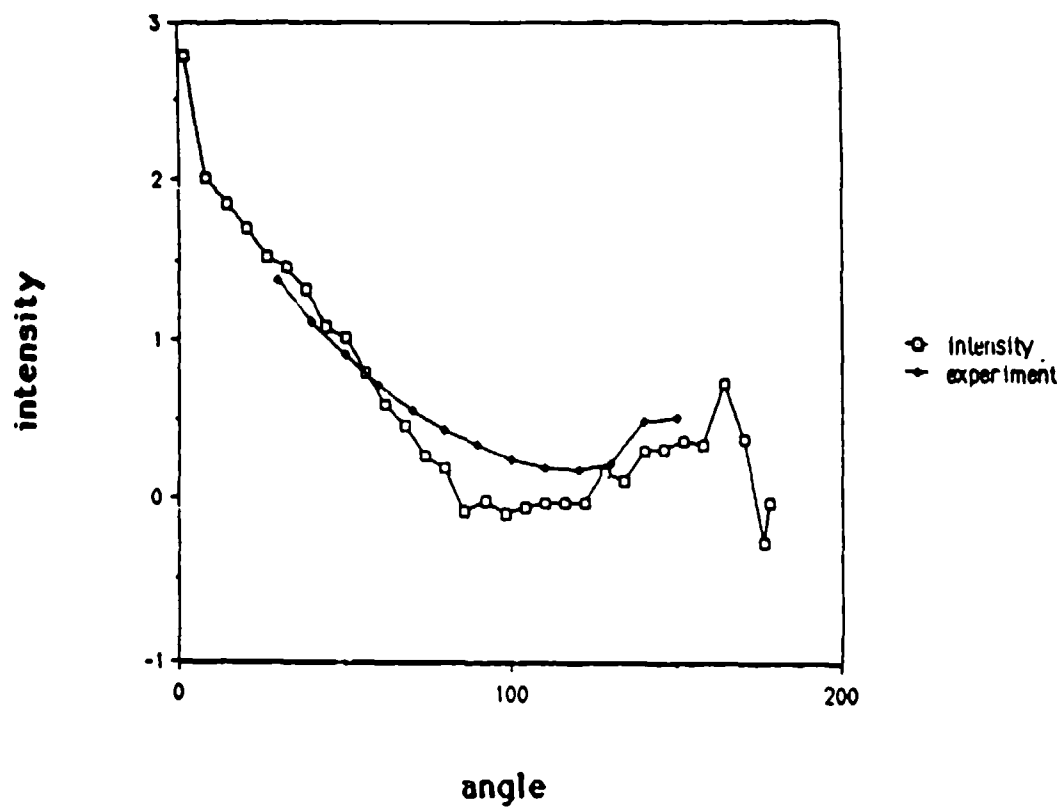


Fig. 12. The relative intensities for randomly oriented long cylinders versus the scattering angle $2\phi_0$ for $x = 45.7$ and $m = 1.31$. The experimental results are shown by black diamonds (Ref. 15) and our theoretical results are shown by open squares.

Blank

The Scattering of Femtosecond Optical Pulses by Small Dielectric Spheres

G. T. Bennett, E. S. Fry, W. E. White, P. Herb, G. W. Kattawar, and W. Xu
Texas A&M University, Physics Department
College Station, TX. 77843

Recent Publications, Submittals for Publication and Presentations:

A) E. S. Fry and X.-M. Gong, "Radiation Torque on a Cube: Geometric Optics Limit." Proceedings of the 1986 CRDEC Scientific Conference on Obscuration and Aerosol Research, R. H. Kohl, Ed., In press.

B) G. T. Bennett, E. S. Fry, W. E. White, P. Herb, G. W. Kattawar, and W. Xu, "Scattering of Femtosecond Laser Pulses by a Single levitated Sphere, " presented at the 1987 Annual Meeting of the American Association for Aerosol Research, Seattle, Washington, September, 1987.

C) G. T. Bennett, E. S. Fry, P. Herb, G. W. Kattawar and W. E. White, "Scattering of Femtosecond Laser Pulses by a Single Levitated Sphere," Journal of the Optical Society of America, in preparation.

Abstract

Studies of the scattering of ultrashort laser pulses by a single microsphere are underway. Emphasis is on the regime in which the physical length of the laser pulse is less than the diameter of the sphere which in turn is less than about 30 wavelengths of the laser radiation. Time averaged data are presented and it is shown that, in this case, bandwidth rather than pulse duration is the determining factor in the scattering results. Work is now underway to observe the scattering effects in the time domain where the pulse duration is indeed a decisive factor.

Introduction

The scattering of electromagnetic radiation by a microscopic sphere has already been studied extensively for the cases of incident plane waves¹ and Gaussian beams.²⁻³ However, there is an additional, very interesting case which occurs when the incident radiation is a pulse whose duration is so short that the physical length of the pulse is less than the diameter of the sphere. Although some work in this regime has been done in the radar region with relatively large spheres,⁴⁻⁵ there has been no work in the visible region of the spectrum where the corresponding sphere radius is much smaller.

Femtosecond pulses of ≈ 630 nm laser radiation are being used to study the scattering of such pulses by single microspheres with 10-20 μm diameters. Time averaged data for pulse widths down to 30 femtoseconds have been obtained. Future work includes studies of femtosecond pulse scattering in the time domain and studies of nonlinear laser-aerosol interactions.

Theory

For an infinite plane wave $E_0 e^{i\omega t}$, with frequency ω , one can use Mie theory¹ to predict the electromagnetic scattering $E_s(\omega, R)$, by a sphere of radius R . Furthermore, a short pulse, $E_p(t)$ can be described as a superposition of such infinite plane waves via the Fourier transform,

$$E_p(t) = \frac{E_0}{\sqrt{2\pi}} \int_{-\infty}^{\infty} A(\omega) e^{i\omega t} d\omega. \quad (1)$$

Thus, the scattered field of the pulse, $E_{sp}(t)$, is the appropriately weighted Fourier superposition of the plane wave scattered amplitudes $E_s(\omega, R)$,

$$E_{sp}(t) = \frac{1}{\sqrt{2\pi}} \int_{-\infty}^{\infty} A(\omega) E_s(\omega, R) e^{i\omega t} d\omega. \quad (2)$$

Now $E_{sp}(t)$ gives the time dependence of the scattered field and will be studied in future experiments, but in the present case we have observed only the time averaged scattered intensity. The corresponding scattered signal S is specifically given by,

$$S \propto \int_{-\infty}^{\infty} |E_{sp}(t)|^2 dt. \quad (3)$$

By Parseval's theorem we can write this as,

$$S \propto \int_{-\infty}^{\infty} |A(\omega)|^2 |E_s(\omega, r)|^2 d\omega. \quad (4)$$

Thus to calculate the time averaged scattering for short pulses one has to determine the spectral distribution of the incident pulse, apply Mie theory to calculate the scattering field for each frequency component, and then use Eq. 4.

Experiment

A schematic of the experimental arrangement is shown in Fig. 1. The femtosecond laser follows the design of Valdmanis, et.al.⁶ It produces ≈ 0.2 nJ pulses at a 100 MHz repetition rate

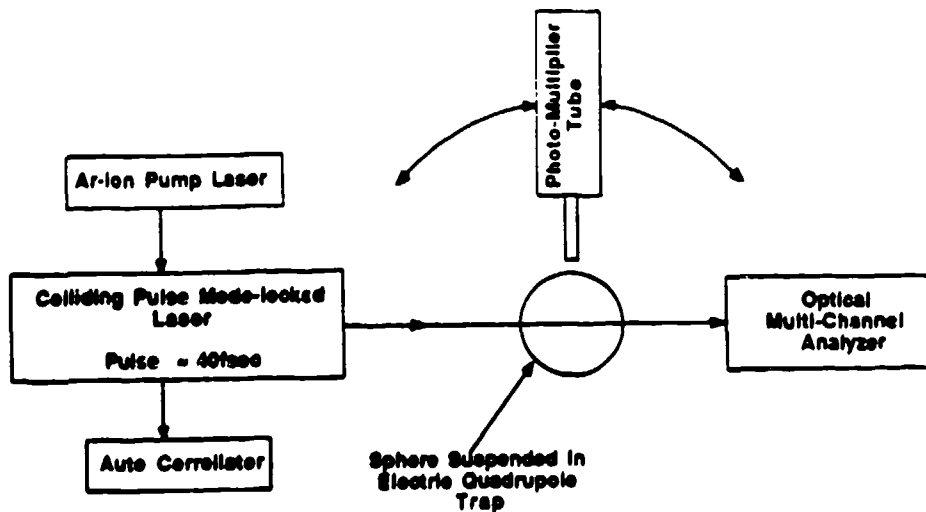


Figure 1. Block diagram of experimental setup

with pulse widths down to 28 fsec. In Fig. 1 the autocorrelator is used to monitor pulse width and the optical multichannel analyzer is used to monitor the spectral distribution of the pulse. The particle to be observed is suspended in an electric quadrupole trap⁷ which has a slit in the center ring electrode so that the angular distribution of the scattered intensity can be observed by a photomultiplier. The latter is mounted at the end of an arm that swings in a semicircle centered on the trap.

For the present data a glass microsphere was suspended in the trap. It was sized in the usual manner by measuring the angular distribution of the scattered intensity with a cw He-Ne laser and fitting the data with Mie results for different sphere radii. The index of refraction of the glass microsphere was 1.5097 at 630 nm and a best fit to the cw data gave a diameter of 15.0 μm .

At each pulse length for which scattering data is to be obtained, the spectral distribution is measured with the optical multichannel analyzer. The result for a 125 femtosecond pulse is shown in Fig. 2. This data is used to obtain $A(\omega)$, which is required for the theoretical predictions of short pulse scattering effects via Eq(4).

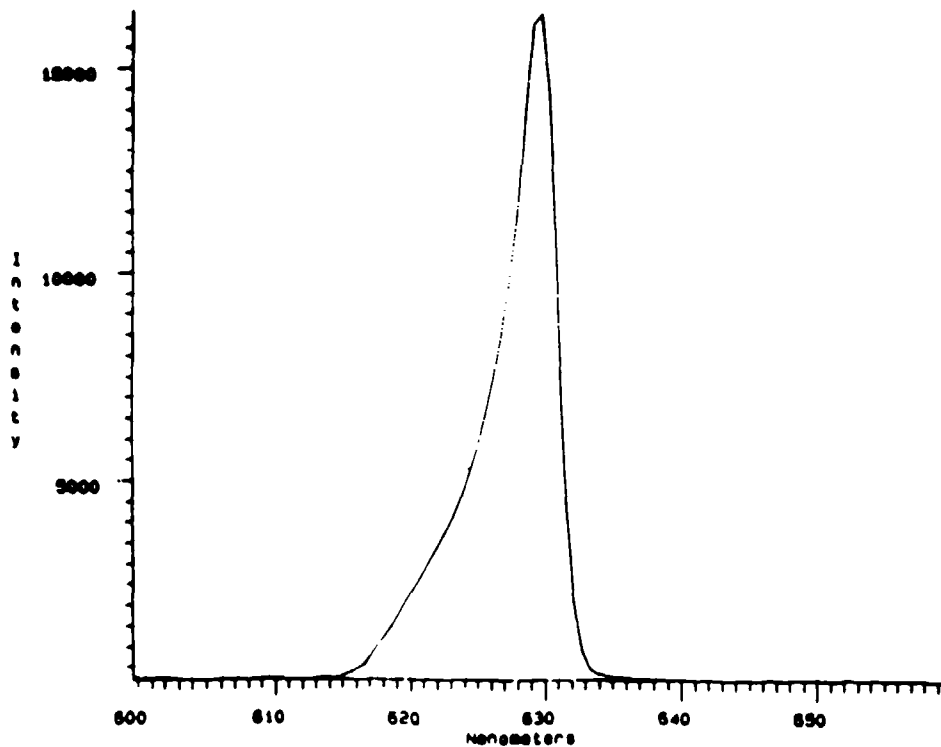


Figure 2. Spectral distribution of a 125 fsec. pulse.

Figs 3a and 3b show experimental results for 125 fsec and 54 fsec pulses, respectively. Also shown as a smooth curve superimposed on the data is the theoretical prediction using the spectral distribution measured for each pulse length. Clearly the effect of decreasing pulse length is to wash out the resonances. This is to be expected since the angular positions of the resonances depend on wavelength and as pulse length decreases, the wavelength spread increases, thereby averaging any given resonance over a wider angular range. It should also be noted that the resonances are shifted in angle for these two sets of data. This is a consequence of the fact that the peak wavelength of the laser shifts to the red as the pulse length decreases, in fact, in this example, the peak of the spectral distribution for the 54 fsec pulse was shifted 4 nm to the red from the peak of the 125 fsec pulse.

Conclusions

Our theoretical and experimental investigations show that the time averaged results for short pulse scattering are determined by pulse bandwidth, not pulse length. For example, both a pulse of a few femtoseconds and a cw laser with the same bandwidth as the pulse will give the same time averaged scattering results. On the other hand, measurements in the time domain will show significantly different effects and will provide a plethora of exiting new studies.

Future Directions

Time resolved scattering studies of microspheres are being initiated. These will eventually be extended to microscopic cubes in fixed orientations. Such studies will provide a new, direct probe of particle morphologies and could provide a definitive remote sensing tool for the size of raindrops, and for particle shapes in clouds and smokes. Time resolution on the femtosecond scale will provide a superb probe of the effects occurring in the weak localization of photons and such studies are being planned. Finally, studies of non-linear laser-aerosol interactions are being initiated. Such studies are especially suited to the femtosecond laser work for three important reasons: (1) Higher peak powers can presently be obtained with pulses in the femtosecond regime than by any other means. We expect to be able to achieve peak intensities up to 10^{19} watts/cm² at the focus after amplification. (2) This high peak power is achieved with a relatively low pulse energy, consequently the effects of the large electric fields associated with the pulse can be better isolated from the purely thermal effects. (3) The different ionization processes occurring can be distinguished in the time domain.

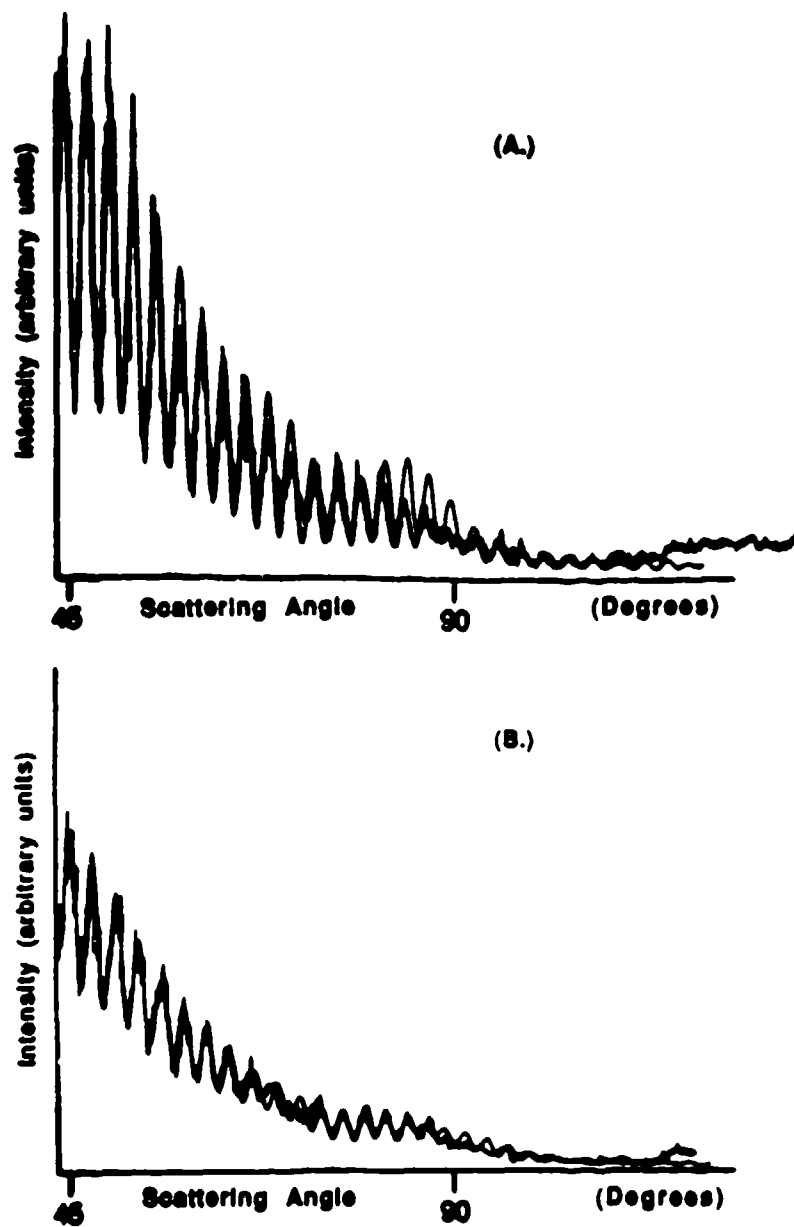


Figure 3. Comparison of experimental and theoretical (smooth curve) data for (A.) 125 fsec. and (B.) 54 fsec. pulses.

References

1. M. Kerker, *The Scattering of Light and Other Electromagnetic Radiation*, (Academic, New York, 1969).
2. L. W. Casperson, C. Yeh, and W. F. Yeung, *Appl. Opt.* **16**, 1104 (1977).
3. W. G. Tam and R. Coriveau, *J. Opt. Soc. Am.* **68**, 763 (1978).
4. J. Rheinstein, *IEEE Trans. Ant. Prop.* **AP-16**, 89 (1968).
5. S. K. Chaudhuri, F. B. Sleator, W.-M. Boerner, *Radio Sci.* **19**, 987 (1984).
6. J. Valdmanis, R. L. Fork, and J. P. Gordan, *Opt. Lett.* **10**, 131 (1985).
7. R. F. Wuerker, H. Shelton, and R. V. Langmuir, *J. Appl. Phys.* **30**, 342 (1959).

Blank

RADIATIVE TRANSFER CALCULATIONS FOR DETECTING A TARGET BEHIND OBSCURING ATMOSPHERES

T. DURACZ AND N. J. MCCORMICK
DEPARTMENT OF NUCLEAR ENGINEERING
UNIVERSITY OF WASHINGTON
SEATTLE, WASHINGTON 98195

ABSTRACT

Numerical radiative transfer calculations are presented for an idealized plane geometry atmosphere that is externally illuminated by a very short pulse of radiation. The results identify optical depths and/or surface albedos for which an external detector measuring the emerging irradiance could not detect the presence of an object obscured by the atmosphere.

I. INTRODUCTION

Light detection and ranging (lidar) devices are used to detect the location of objects in optically thin atmospheres for which the effects of scattering are small enough that they can be ignored or treated by an approximate correction. For atmospheres of interest here that are optically thick at the wavelength of the measurements, scattering effects must be incorporated by means of a multiple-collision analysis or use of the radiative transfer equation.

The linear Boltzmann equation is used here to analyze the propagation of radiation through a homogeneous atmosphere, and the scattering of radiation at the surface of the object behind the atmosphere is assumed to be isotropic (i.e., Lambertian reflection). Thus, the ability to detect the presence of the obscured object depends upon the direction and time characteristics of the incident radiation pulse, the single scattering albedo and phase function of the atmosphere, the albedo of the object and its distance from the surface of the atmosphere, the characteristics of the detector located external to the atmosphere, and the magnitude of the difference in signals when the object is present or absent.

For simplicity the incident illumination is assumed to be normally directed at the atmosphere and of an infinitesimal duration, while the atmosphere is described by the Rayleigh phase function and a variable single scattering albedo; the albedo of the surface of the object is also variable. For the detector, it is assumed that the backscattered irradiance (i.e., the angle-integrated flux crossing a detector surface that is parallel to the surface of the atmosphere) can be measured for a time interval after the pulse. The detection of the object is to be made from the time-integrated backscattered irradiance.

The limitations of these assumptions are worth noting. First, the slab geometry chosen for the calculation is certainly idealized since we expect neither a uniformly broad incident laser pulse nor a slab atmosphere nor a reflecting slab object behind it; if we can show, however, that it is not possible to detect such an object under such circumstances,

then there is no reason to expect a non-slab object could be detected behind a multiply-scattering atmosphere of a more complicated geometry. Second, for a normally-incident illumination the radiation is initially in the direction of the shortest distance to the object, so the time required for the object to perturb the backscattered irradiance is minimum and the magnitude of the decaying pulse is maximum; this illumination represents a worst case, however, in the sense that there is no azimuthal dependence of the backscattered radiance which might help in the detection of the object. Third, a Rayleigh scattering atmosphere represents a worst case when attempting to detect an object since a more forward scatterer would enhance the probability that radiation would move through the atmosphere, scatter off the object, and come back through the atmosphere to indicate the presence of the object. Finally, a Lambertian-reflecting object represents a worst case for detection since it backscatters the radiation uniformly in all directions.

II. THE METHOD OF ANALYSIS

To describe the transport of radiation within the obscuring atmosphere, the time-dependent radiative transfer equation is used,

$$(v^{-1}\partial_t + \mu\partial_x + 1) I(x, \mu, t) = \int_{-1}^1 p(\mu, \mu') I(x, \mu', t) d\mu', \quad (1)$$

where $I(x, \mu, t)$ is the radiant energy per unit area, μ , and time (i.e., the radiance integrated over the azimuthal angle). Also, μ is the cosine of the polar angle with respect to the x axis and t is the time in mean collision times (mct), as measured in terms of the scattering and absorption properties of the atmosphere and the speed of light; v is the speed of light in the atmosphere, as measured in units of inverse time, while $p(\mu, \mu')$ is the phase function. The distance x is measured into the atmosphere in units of mfp, the mean free path (i.e., the inverse of the extinction coefficient), from $x = 0$ at the surface of illumination to $x = X$ at the depth where the object is located if there is one present.

The ingoing radiance due to the pulse is given by

$$I(0, \mu, t) = \delta(\mu - 1) \delta(t), \quad 0 \leq \mu \leq 1, \quad (2)$$

and that reflected back into the atmosphere by the object at $x = X$ is

$$I(X, -\mu, t) = 2A \int_0^1 \mu I(X, \mu, t) d\mu. \quad (3)$$

The detector is to measure the backscattered irradiance

$$E(t) = \int_0^1 \mu I(0, -\mu, t) d\mu. \quad (4)$$

The backscattered irradiance can be integrated as a function of time to obtain a quantity Q , and for the calculations we selected the interval $2 \leq t \leq 20$ mct, i.e.,

$$Q = \int_2^{20} E(t) dt. \quad (5)$$

In principle this quantity could be used to infer either the surface albedo of an object when its depth of location is known, or the location when its albedo is known.

III. NUMERICAL RESULTS AND DISCUSSION

The calculations were done using the TIMEX program^{1,2} for a single scattering albedo of unity, for different surface albedos of the object ($A = 0, 0.2, 0.4, 0.6, 0.8,$ and 1.0), and for different optical depths of location of the object ($X = 1, 2, 3, 4, 5, 6,$ and ∞ mfp).

Fig. 1 shows the backscattered irradiance for a perfectly absorbing object ($A = 0$) behind a nonabsorbing obscuring atmosphere of depth X for $X = 1, 2, 4,$ and ∞ mfp. By way of comparison, results analogous to those in Fig. 1 are shown in Fig. 2 to illustrate the effect on the backscattered irradiance of a perfectly reflecting object ($A = 1$) at the same locations. Of course the figures represent the two extreme cases for the reflection from the object, so objects with $0 < A < 1$ would give results that lie between these.

The detection of the object depends upon the magnitude of the perturbation in the backscattered irradiance. Fig. 3 is a map of the time-integrated backscattered irradiance Q as a function of the object's surface albedo A and the location X . For any value of Q there is an isocline of possible values of $[X, A]$. The upper left-hand portion of the figure shows a region for objects with albedos $A > 0$; the lower left-hand portion shows a region for objects with $A \geq 0$. These two regions indicate the presence of an object. When there is no object, the value of $Q = 0.423$ and the line which corresponds to that value lies between the two regions and goes asymptotically to $X = \infty$. Thus the map provides a global picture of the detectability of an object behind a uniform obscuring atmosphere.

IV. COMMENTS

The results shown here represent a near-worst-case for attempting to detect an object through a thick obscuring atmosphere in the sense that if the atmosphere or the object scatters more anisotropically, detection would be somewhat easier.

It also should be emphasized that perhaps another way of detecting an object would be to use another observable instead of Q or in conjunction with Q to better resolve X and A for the object; further work to answer this question is presently underway.

ACKNOWLEDGMENTS

This work was supported by the U.S. Army Research Office DAAL03-86-K-0118 while computer time was provided by the San Diego Supercomputer Center.

REFERENCES

1. T.R. Hill and W.H. Reed, "TIMEX: A Time-Dependent Explicit Discrete Ordinates Program for the Solution of Multigroup Transport Equations with Delayed Neutrons", Radiation Shielding Information Center Computer Code CCC -274, Oak Ridge National Laboratory (1976).
2. For this calculation with TIMEX it is necessary to run the code twice to properly treat boundary conditions (2) and (3); in the first calculation, the uncollided source option is used, but this option does not properly allow for reflection at the object. In the second calculation, a very thin source is used to generate an isotropic angular distribution that is backscattered from the surface. The correct solution is obtained by adding the results of the first calculation plus the product of the fraction of photons reaching the object times the surface albedo times the results of the second calculation.

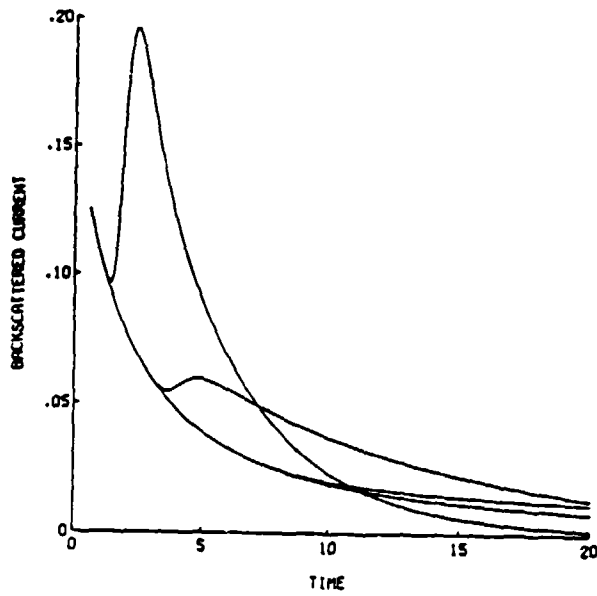


Fig. 1. Curves of the backscattered irradiance $E(t)$ versus time for a perfectly reflecting object behind a nonabsorbing obscuring atmosphere for (from top to bottom) depths of 1, 2, 4, and ∞ mfp.

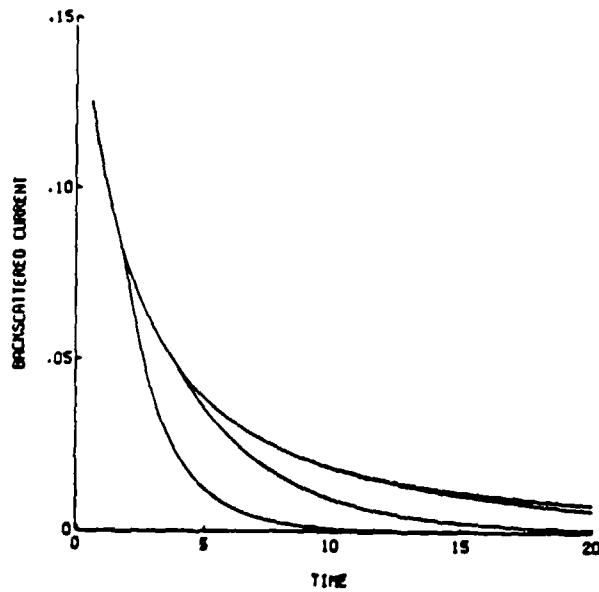


Fig. 2. Curves of the backscattered irradiance $E(t)$ versus time for a perfectly absorbing object behind a nonabsorbing obscuring atmosphere for (from top to bottom) depths of ∞ , 4, 2, and 1 mfp.

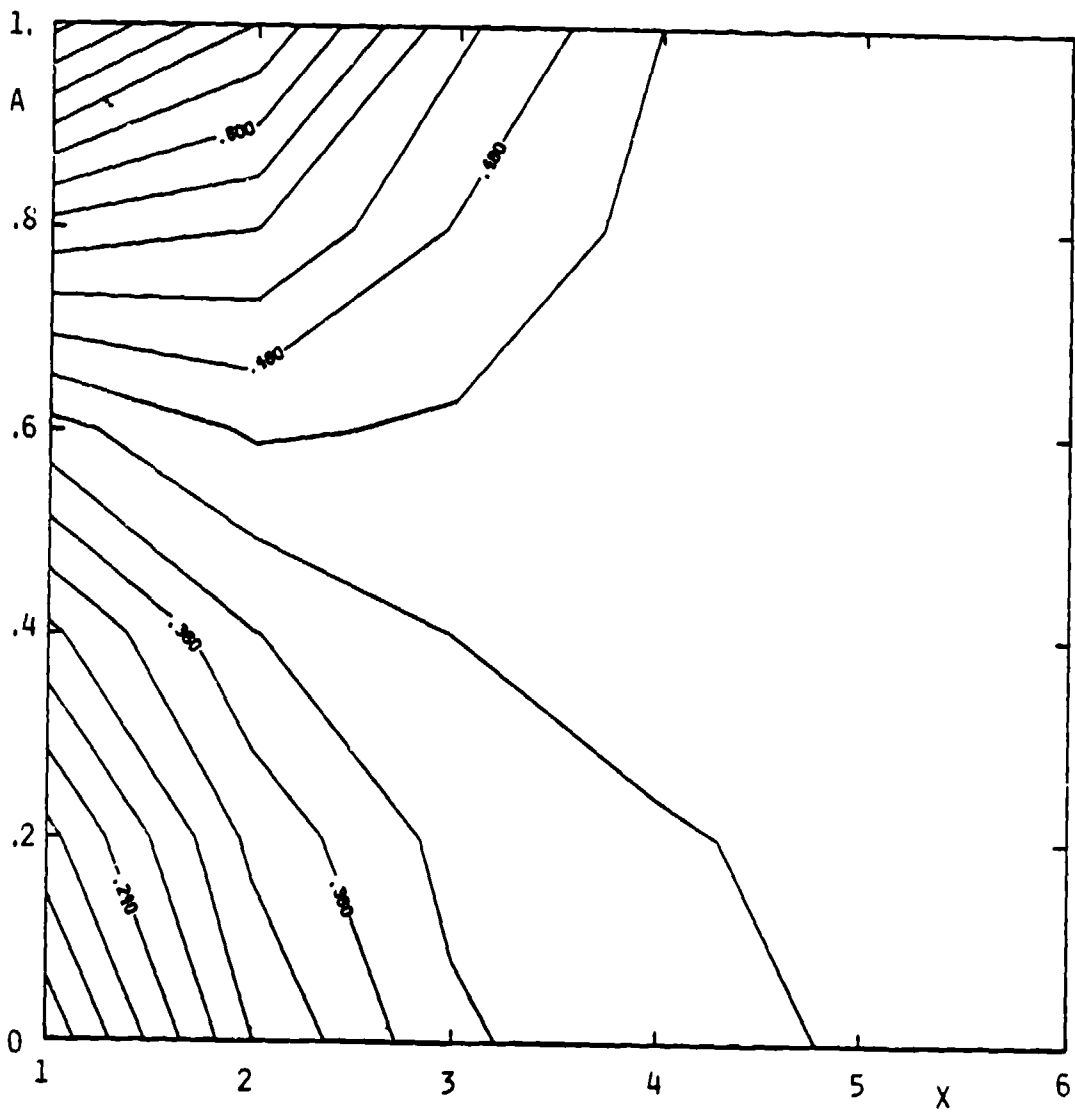


Fig. 3. Isoclines of Q , the time-integrated irradiance, in the parameter space [depth X , surface albedo A] for an obscured object.

Blank

AN EXACT FORMULA FOR THE ACCURACY OF A CLASS OF
COMPUTER SOLUTIONS OF INTEGRAL EQUATION
FORMULATIONS OF ELECTROMAGNETIC SCATTERING
PROBLEMS

D. K. Coohon
Department of Mathematics 038-16
Temple University
Philadelphia, Pennsylvania 19122

ABSTRACT

A method of improving the accuracy of traditional methods (Guru and Chen [6], Hagmann and Gandhi [7]-[8], Hagmann and Levin [9], and Livesay and Chen [13] of solving integral equations has been obtained. We now have exact formulas for the accuracy of projective approximation methods (Gohberg and Feldman [5], Neittaanmaki and Saranen [20]) for solving integral equations. For a class of approximation schemes for estimating the solution of integral equations of electromagnetic scattering, we can develop a systematic procedure for reducing the original infinite rank integral equation to an exact finite rank integral equation capable of being completely analyzed by digital computer. In this paper the method is illustrated for the popular pulse basis function method (Guru and Chen [6], Hagmann and Gandhi [7]-[8], Hagmann and Levin [9], and Livesay and Chen [13]).

1. INTRODUCTION TO PROJECTIVE APPROXIMATION METHODS

In this section we explain (i) linear interpolation, (ii) Fourier series approximations, and (iii) pulse basis functions as projective approximation methods.

A projection is a linear operator P on a vector space V with the property that $P^2 = P$. A projective approximation scheme is a linear mapping P from a vector space V into a subspace W of approximates of members of V with the property that P is the identity operator on W in the sense that $Pw = w$ for all w in W .

We now explain linear interpolation. A common example would be to approximate the space V of functions which are continuous on $[a, b]$ by members of a space W of functions which are linear on each of

$$S = ((x_0, x_1), (x_1, x_2), \dots, (x_{n-1}, x_n))$$

where $a = x_0 < x_1 < \dots < x_n = b$ and to define P by the linear interpolation rule,

$$Pf(x) = f(x_{i-1}) \left\{ \frac{(x_i - x)}{(x_i - x_{i-1})} \right\} + f(x_i) \left\{ \frac{(x - x_{i-1})}{(x_i - x_{i-1})} \right\} \quad (1.1)$$

if x belongs to an interval in the collection of subintervals, $[x_0, x_1], [x_1, x_2], \dots, [x_{n-1}, x_n]$ containing the open interval (x_{i-1}, x_i) . Note that if this is the case, then

$$P^2f(x) = Pf(x) \quad (1.2)$$

Next we interpret Fourier series or eigenfunction expansions and consider the space V to be the set of functions defined on an open set Ω of R^n which are square integrable with respect to Lebesgue measure ν and valued in a Hilbert space X with norm $|\cdot|_X$ with two functions f and g being equivalent on Ω if

$$\int_{\Omega} |f - g|_X^2 d\nu = 0 \quad (1.3)$$

where f and g are taken from the collection of Lebesgue measurable functions h from Ω into X which are square integrable over Ω in the sense that

$$\int_{\Omega} |f|_X^2 d\nu < \infty \quad (1.4)$$

We say that two functions f and g are orthogonal if

$$\int_{\Omega} (f, g)_X d\nu = 0, \quad (1.5)$$

where $(f, g)_X$ denotes the inner product in the Hilbert space X of the values of f and g so that

$$|f|_X^2 = (f, f)_X \quad (1.6)$$

If

$$F = \left\{ \phi_i : i \in I \right\}$$

is a finite set of pairwise orthogonal functions in V , then we let W be the smallest vector subspace of V containing F and note that a projection operator is defined by the rule,

$$Pf(x) = \sum_{i \in I} \left[\frac{\int_{\Omega} f(x) \phi_i(x) d\nu(x)}{\int_{\Omega} \phi_i(x)^2 d\nu(x)} \right] \phi_i(x) \quad (1.7)$$

The projection operator defined by equation (1.7) is the basis of Fourier series approximations and also eigenfunction expansions if we incorporate into $d\nu(x)$ weight functions associated with for Sturm-Liouville equations (for example).

The pulse basis function method has been used by Guru and Chen [6], Hagmann and Gandhi [7-8], Hagmann and Levin [9], and Livesay and Chen [13] to predict the results of electromagnetic interactions with complex structures by decomposing the scattering body into cells within each of which the induced electric vector is assumed to be a constant. The pulse basis function method makes use of the concept of the partition of an open set Ω of \mathbf{R}^n .

We have defined for each $x \in \mathbf{R}^n$ and each $r > 0$ the set

$$B(x,r) = \left\{ y \in \mathbf{R}^n : |x - y| < r \right\}$$

to be the ball of radius r centered at x . We let Ω be an open set in \mathbf{R}^n whose closure is bounded. A partition of Ω is a set $P(\Omega)$ of pairs (V_i, x_i) where $i \in I$ and the ball $B(x_i, r)$ is contained in V_i for some $r > 0$,

$$\bigcup_{i \in I} V_i = \Omega \quad (1.8)$$

and $\mu_n(V_j \cap V_k) = 0$ if (V_j, x_j) and (V_k, x_k) are distinct members of $P(\Omega)$

so that $x_i \neq x_j$ if and only if $i \neq j$ and $\mu_n(V_i \cap V_j) = 0$ where μ_n is the standard Lebesgue measure on \mathbf{R}^n where we let

$$P(\Omega)_1 = \left\{ V_i : (V_i, x_i) \in P(\Omega) \text{ for some } x_i \in V_i \right\} \quad (1.9)$$

and we define the functions

$$\chi_{V_i}(x) = \begin{cases} 1 & x \in V_i \\ 0 & x \text{ is not a member of } V_i \end{cases} \quad (1.10)$$

to be the characteristic functions or pulse functions associated with the sets V_i in $P(\Omega)_1$. The sets V_i are called cells in a cellular decomposition of Ω .

Definition 1.2. We define the projector P associated with the partition

$$P(\Omega) = \left\{ (V_i, x_i) : x_i \in V_i, i \in I, V_i \subset \Omega \right\} \quad (1.11)$$

which satisfies the conditions of definition (1.1) by the rule,

$$Pf(x) = \sum_{V_i \in P(\Omega)_1} \chi_{V_i}(z) f(z), \quad (1.12)$$

for all functions $f: \Omega \rightarrow \mathbf{C}^m$ where \mathbf{C}^m denotes complex m dimensional space for all positive integers m .

A direct calculation will show that the following is valid.

Proposition 1.1. If $(\mathbf{C}^m)^\Omega$ denotes the vector space of all mappings from Ω into \mathbf{C}^m (complex m dimensional space), then the mapping

$$P: (C^m)^n \rightarrow (C^m)^n \quad (1.13)$$

satisfies

$$PP = P \quad (1.14)$$

In practice we decompose the scattering body into cells and suppose that the electric vector is constant within each of these cells. Thus, there are three unknown components of a complex electric vector in each cell which means that our unknown functions are for three dimensional scattering problems valued in C^3 (complex 3 dimensional space). If there are N cells, the integral equation of electromagnetic scattering has the form,

$$(\mathbf{E} - \mathbf{E}^i)(p, \omega) = \frac{i\omega^2}{c^2} \int_{\Omega} \frac{(\epsilon - \epsilon_0) - i\sigma/\omega}{\epsilon_0} \mathbf{G}(p, q) \cdot \mathbf{E}(q) dv(q) \quad (1.15)$$

where

$$\mathbf{G}(p, q) = \left[\mathbf{I} + \left[\frac{1}{k_0^2} \right] \nabla(\nabla) \right] \left[\frac{\exp(ik_0|p-q|)}{4\pi|p-q|} \right] \quad (1.16)$$

may be approximated by the finite rank integral equation,

$$P_{\Omega}^x \mathbf{E} - P_{\Omega}^x \mathbf{E}^i = \frac{i\omega^2}{c^2} \int_{\Omega} \left[\frac{\epsilon - \epsilon_0 - i\sigma/\omega}{\epsilon_0} \right] (y) P_{\Omega}^x \mathbf{G}(x, y) \cdot P_{\Omega}^x \mathbf{E}(y) dv(y) \quad (1.17)$$

where \mathbf{G} is defined by equation (1.16). By equating coefficients of $\chi_{V_i}(x)$ on each side of (1.17) and evaluating integrals of known functions of y over the sets V_i we reduce the finite rank integral equation (1.17) to a system of $3N$ equations in $3N$ unknowns. However, we will show that the equation (1.17) is really the wrong finite rank integral equation to subject to computerization and furthermore that if we start with any valid projective approximation scheme and assume that the original infinite rank integral equation has a unique solution, then it can be reduced to a finite rank integral equation whose solution is exactly the projection of the exact solution of the original infinite rank integral equation.

In addition we remark that while the Neumann series, (Kleinman [12], Shifrin [22]) as it is usually applied in electromagnetic scattering, is only valid for scatterers which are nearly diaphanous in the sense that if

$$(\mathbf{I} - \mathbf{K})\mathbf{E} = \mathbf{E}^i$$

is the original integral equation describing the scattering of light from our aerosol particle, then the operator \mathbf{K} has to be contractive or have norm less than 1, the methods of this paper, although also using series of operators, are actually valid for scattering bodies with a wide range of electrical properties.

2. EXACT FORMULAS FOR THE ACCURACY OF APPROXIMATE SOLUTIONS OF INTEGRAL EQUATIONS

Let X be a Hilbert space and let $B(X)$ denote the Banach space of bounded linear transformations of X into itself. Let

$$K: \Omega \times \Omega \rightarrow B(X) \quad (2.1)$$

be such that if we let $h(x) = Tf(x)$, where

$$Tf(x) = \int_{\Omega} K(x,y)f(y)d\nu(y) \quad (2.2)$$

implies that $h = Tf$ is in $L^2(\Omega, X)$ whenever f is in $L^2(\Omega, X)$ where ν denotes Lebesgue measure on Ω and $L^2(\Omega, X)$ denotes the square integrable ν -measurable functions from Ω into X . Thus, let us assume that the original integral equation is

$$f(x) - g(x) = \lambda Tf(x) \quad (2.3)$$

where in practice in electromagnetic scattering, for example, $g(x)$ would denote the ambient source of light, Ω would denote the aerosol particle, and $f(x)$ would denote the total electromagnetic field that exists because of the presence of the aerosol particle Ω in the ambient electromagnetic field defined by $g(x)$. We define a projection operator,

$$P: L^2(\Omega, X) \rightarrow L^2(\Omega, X), \quad (2.4)$$

as a linear mapping from $L^2(\Omega, X)$ into a function in a finite dimensional subspace of this space which approximates the original function. We let Q^x be an operator on functions of x in Ω valued in the Banach space X such that

$$P \int_{\Omega} K(x,y)(Pf(y))d\nu(y) = \int_{\Omega} Q^x K(x,y)Pf(y)d\nu(y) \quad (2.5)$$

We introduce new operators L and N on $L^2(\Omega, X)$ by the rules,

$$Lf(x) = P \int_{\Omega} K(x,y)Pf(y)d\nu(y) = PTPf(x), \quad (2.6)$$

and

$$Nf(x) = \int_{\Omega} (K(x,y) - Q^x K(x,y)P)f(y)d\nu(y), \quad (2.7)$$

so that

$$T = L + N. \quad (2.8)$$

The usual approximate equation that we solve in practice is

$$Pf_n - Pg = \lambda PTPf_n(x) \quad (2.9)$$

We usually have to assume that the solution $u = Pf_n$ of the equation (2.9) is as close as we want to both the actual solution f of the original integral equation (2.3) and its approximation Pf . This might be true if Pg is close in norm to g and if λL is close in norm to g and if λL defined by (2.6) is close in operator norm to the exact integral transform λT . A consequence of these assumptions would be that the operator norm of the difference λN between λT , defined by (2.2) and (2.8), and $\lambda L = \lambda PTP$, where L is defined by (2.6) is a very small number. We will show in this paper that this widely used assumption ([6], [8], and [13]) while capable of yielding correct results with sufficient computing time is actually not needed. The only hypothesis that is needed is that the projector P be a good enough approximator that if N is defined by (2.1), (2.5), and (2.7), then

$$\max(|\lambda| \|N\|_\Omega, |\lambda| \|(P - I)N\|_\Omega) < 1 \quad (2.10)$$

where if S is any linear transformation of $L^2(\Omega, X)$ into itself, then

$$\|S\|_\Omega = \sup(\|Sf\|_\Omega : f \in L^2(\Omega, X) \text{ and } \|f\|_\Omega = 1) \quad (2.11)$$

with

$$\|f\|_\Omega^2 = \int_\Omega |f(x)|_X^2 d\nu(x) \quad (2.12)$$

for all functions f in $L^2(\Omega, X)$ where if w is in X and X happens to be a Hilbert space, then

$$\|w\|_X^2 = (w, w)_X. \quad (2.13)$$

where $(u, v)_X$ is the Hilbert space inner product of u and v with respect to the inner product of X and where otherwise more generally $\|w\|_X$ represents the Banach space norm of w . The inequality (2.10), which is our key assumption, is reasonable if the original equation actually has a solution and projection by the operator P actually provides us with a good approximation scheme. Ordinarily with projective approximation schemes we have a sequence of projectors whose images of a function g approach the function g being approximated. We use the assumption of inequality (2.10) to develop an exact finite rank integral equation whose solution is the projection under P of the exact solution of the

original infinite rank integral equation (2.3). The inequality (2.10) means that the operator G_λ can be defined by the rule,

$$G_\lambda = \sum_{k=1}^{\infty} \lambda^{k-1} N^k = N + \lambda N^2 + \lambda^2 N^3 + \dots \quad (2.14)$$

so that since

$$(I - \lambda N)(I + \lambda N + \lambda^2 N^2 + \dots)f = f \quad (2.15)$$

it will follow that

$$(I - \lambda N)(I + \lambda G_\lambda)f = f \quad (2.16)$$

for all f in $L^2(\Omega, X)$. Thus, we can in view of the relation,

$$\lambda T = \lambda N + \lambda L \quad (2.17)$$

which follows immediately from equation (2.8), express the original integral equation (2.3) in the form

$$f = g + \lambda Nf + \lambda Lf. \quad (2.18)$$

We see by rearrangement of terms in equation (2.18) that

$$(I - \lambda N)f = g + \lambda Lf \quad (2.19)$$

Applying the operator $I + \lambda G_\lambda$ to both sides of equation (2.19) and using the fact that if r is an operator of norm smaller than one,

$$(1 - r)(1 + r + r^2 + r^3 + \dots)f = f \quad (2.20)$$

it follows that

$$f = g + \lambda Lf + \lambda G_\lambda(g + \lambda Lf) \quad (2.21)$$

It is possible to represent the action of the operator N appearing in the decomposition, equation (2.17), of T in terms of G_λ , L , g , and f by realizing that equation (2.21) and (2.18) imply that

$$\lambda Nf = \lambda G_\lambda(g + \lambda Lf) \quad (2.22)$$

We now would like to apply the projection operator to both sides of equation (2.21). To help us we note that equation (2.6) and the

relation $P^2 = P$ implies that

$$PL = L. \quad (2.23)$$

Consequently, equations (2.21) and (2.23) imply that

$$Pf = Pg + \lambda Lf + \lambda P(G_\lambda(g + \lambda Lf)). \quad (2.24)$$

Substituting (2.22) into (2.24) we see that

$$Pf = Pg + \lambda Lf + \lambda PNf \quad (2.25)$$

We wish to reduce the integral equation (2.25) to an exact finite rank integral equation. We introduce an operator $L_{(K,P)}$ by the relation,

$$L_{(K,P)} = PT$$

so that in view of the fact that $L = PTP$, (equation (2.6)) it follows that

$$Lf = L_{(K,P)}Pf \quad (2.26)$$

We now see that (2.25) and (2.26) imply that equation (2.24) is equivalent to

$$Pf = Pg + \lambda PL_{(K,P)}Pf + \lambda PNf \quad (2.27)$$

While this is not a finite rank integral equation it suggests that an approximate finite rank integral equation,

$$Pf_\alpha = Pg + \lambda PLPf_\alpha + \lambda PNf_\alpha \quad (2.28)$$

might give a more accurate solution, a solution closer to f , than the solution Pf_α of the traditional approximate equation,

$$Pf_\alpha = Pg + \lambda PL_{(K,P)}Pf_\alpha \quad (2.29)$$

We will go much further than this, however, and reduce the equation (2.25) to a true finite rank integral equation whose solution will be the approximation Pf of the exact solution f of (2.3) and also give a precise and calculable formula for the difference $f - Pf$. We can do this by making use of the relation (2.16) whose validity follows from the basic assumption that P is a good enough approximator that inequality (2.10) is valid. This will permit us to achieve our goal of expression f in terms of our rough approximation Pf and the stimulating field g by an exact

formula. Going back to equation (2.19) we obtain the relationship,

$$f = \sum_{k=0}^{\infty} (\lambda N)^k (g + \lambda Lf) \quad (2.30)$$

Making use of the obvious relationship, $L = L_{(K,P)}P$, operating on both sides of (2.30) with N and substituting into equation (2.27) we see that

$$Pf = Pg + \lambda PL_{(K,P)}Pf + \lambda PN \sum_{k=0}^{\infty} (\lambda N)^k (g + \lambda L_{(K,P)}Pf) \quad (2.31)$$

Collecting the terms in equation (2.31) involving the unknown member Pf of a finite dimensional vector space, we have the relation,

$$Pf = Pg + \lambda PN \sum_{k=0}^{\infty} (\lambda N)^k g + \lambda P(L_{(K,P)} + N \sum_{k=0}^{\infty} (\lambda N)^k \lambda L_{(K,P)})Pf \quad (2.32)$$

Our first objective is achieved since equation (2.32) is a truly finite rank integral equation in the unknown member Pf of a finite dimensional vector space. The computer program giving a solution of this equation would provide us with the coefficients of the basis vectors of this finite dimensional vector space that appear in the representation of Pf ; in other words the linear combination of the basis vectors of the image of P with these coefficients is the exact value of Pf , the projection of the exact solution f of the original integral equation (2.3). Thus, from this point on we assume that Pf is known.

To finish this section we use our exactly determined value of Pf that was obtained by solving the finite rank integral equation under the assumption that $I - \lambda L$ is invertible on the image of the projection operator P , where $L = PTP$, and subtract the right sides of equations (2.18) and (2.25) obtaining the relation,

$$(f - Pf) = (g - Pg) + \lambda(I - P)Nf \quad (2.33)$$

which can be rewritten in the form

$$(I - \lambda(I - P)N)f = (g - Pg + Pf) \quad (2.34)$$

Again making use of the hypothesis (2.10) we conclude that the exact solution of the infinite rank integral equation is

$$f = \sum_{k=0}^{\infty} (\lambda(I - P)N)^k (g - Pg + Pf) \quad (2.35)$$

where Pf is the exact solution of the finite rank integral equation (2.32).

We have proven the following.

Theorem. If P is a projector from $L^2(\Omega, X)$ onto a finite dimensional vector space such that if L and N are defined by (2.6) and (2.7), respectively, and if inequality (2.10) is satisfied, then equation (2.32) is a finite rank integral equation whose solution is the projection Pf of the exact solution f of (2.3). Furthermore, if (2.32) has a unique solution, then the original infinite rank integral equation has a unique solution given by (2.35).

We note that we have reduced the question of uniqueness of the solution of an infinite rank integral equation to the uniqueness of the solution of a finite rank integral equation. We note also that we have an exact formula for the error associated with the discretization associated with the projection operator P .

3. REFERENCES

1. Barber, P.W., Om. P. Gandhi, M.J. Hagmann, Indira Chatterjee. Electromagnetic absorption in a multilayer model of man. IEEE Transactions on Biomedical Engineering. Volume BME-26 Number 7, pp 400-405(1979).
2. Calderon, A.P. and A. Zygmund. On the existence of certain singular integrals. Acta Mathematica Volume 88, pp 85-139 (1952)
3. Cohen, L.D., R. D. Haracz, A. Cohen, and C. Acquista. Scattering of light from arbitrarily oriented finite cylinders. Applied Optics Volume 21, pp 742-748(1983)
4. Colton, David and Rainer Kress. Integral equation methods in scattering theory. New York: John Wiley & Sons(1983).
5. Gohberg, I.C. and I. A. Feldman. Convolution equations and projection methods for their solutions. Providence, Rhode Island: American Mathematical Society(1974).
6. Guru, Bhag Singh and Kun-Mu Chen. Experimental and theoretical studies on electromagnetic fields induced inside finite biological bodies. IEEE Transactions on Microwave Theory and Techniques Volume MTT-24 No. 7(1976).
7. Hagmann, M. J. and O. P. Gandhi. Numerical calculation of electromagnetic energy deposition in man with grounding and reflector effects. Radio Science Volume 14 Number 6s pp 23-29(1979)
8. Hagmann, M. J. and O.P. Gandhi. Numerical calculation of electromagnetic energy deposition for a realistic model of man. IEEE Transactions on Microwave Theory and Techniques Volume MTT-27 Number 9 pp 804-809(1979)
9. Hagmann, M.J. and R. L. Levin. Nonlocal energy deposition--a problem in regional hyperthermia. IEEE Transactions on Biomedical Engineering Volume 33, pp 405-411(1986)
10. Haracz, Richard D., Leonard D. Cohen, and Ariel Cohen. Scattering of linearly polarized light from randomly oriented cylinders and spheroids. Journal of Applied Physics Volume 58 Number 9 , pp 3322-3327 (November, 1958)

11. Holt, A. R. and J. W. Shepherd. Electromagnetic scattering by dielectric spheroids in the forward and backward directions. *Journal of Physics A. Math. Gen.* Volume 12 Number 1, pp 159-166(1979)
12. Kleinman, R. E. Low frequency electromagnetic scattering In P. L. Uslenghi (Ed) *Electromagnetic Scattering* New York: Academic Press (1978)
13. Livesay, D. E. and Kun-Mu Chen. Electromagnetic fields induced inside arbitrarily shaped biological bodies. *IEEE Transactions on Microwave Theory and Techniques.* Volume MTT-22 Number 12, pp 1273 - 1280(1974)
14. Neittaanmaki, P. and Jukka Saranen. Finite element approximation of vector fields given by curl and divergence. *Mathematical Methods in the Applied Sciences* 3, pp 328-335(1981)
15. Neittaanmaki, Pekka and Jukka Saranen. Semi-discrete Galerkin approximation methods applied to initial boundary value problems for Maxwell's equations in anisotropic inhomogeneous media. *Proceedings of the Royal Society of Edinburgh* 89 A pp 125 - 133(1981)
16. Ramm, A. G. Numerical solution of integral equations in a space of distributions. *Journal of Mathematical Analysis and Applications* Volume 110 pp 384-390(1985)
17. Ramm, A.G. *Theory and applications of some new classes of integral equations.* New York: Springer Verlag (1980)
18. Saranen, Jukka On generalized harmonic fields in domains with anisotropic homogeneous media. *Journal of mathematical analysis and applications* Volume 88 Number 1, pp 104-115(1982)
19. Saranen, Jukka. Some remarks on the convergence of the horizontal line method for Maxwell's equations. *Jyvaskyla 10, Finland: University of Jyvaskyla Department of Mathematics Report 23* (1980)
20. Saranen, Jukka. Uber die Approximation der Losungen der Maxwellschen Randwertaufgabe mit der Methode der finite Elemente. *Applicable Analysis* Volume 10 pp 15-30(1980)
21. Shepherd, J. W. and A. R. Holt. The scattering of electromagnetic radiation from finite dielectric circular cylinders. *Journal of Physics A Math. Gen.* 16 pp 651-652(1983)
22. Shifrin, K. S. *Scattering of light in a turbid medium.* Moscow-Leningrad: Gosudarstvennoye Izdatel'stvo Tekniko-Tecreticheskoy Literatury Moscow Leningrad (1951)
23. Uzunoglu, N. K., N. G. Alexopoulos and J. G. Fikioris. Scattering from thin and finite dielectric cylinders. *Journal of the Optical Society of America* Volume 68 Number 2, pp 194-197(1978)
24. Uzunoglu, N. K. and A. R. Holt. The scattering of electromagnetic radiation from dielectric scatterers. *Journal of Physics A. Math. Gen.* Volume 10 Number 3, pp 413-424(1977)

Blank

SCATTERING OF LIGHT BY FINITE CYLINDERS

D. K. Coohon
Department of Mathematics 038-16
Temple University
Philadelphia, Pennsylvania 19122

ABSTRACT

The primary content of this report is the description of a computer program developed originally at Drexell University and modified for use at the Chemical Research, Development, and Engineering Center of Aberdeen Proving Ground. We describe (i) the mathematical basis of this program to predict the manner in which light is scattered by a simulated aerosol particle modeled by a finite length cylinder, (ii) the meaning of key FORTRAN variables used in various parts of the program, (iii) the input parameters and their units and meaning, and (iv) the output variables and their meaning. Our writing is deliberately expository on the level of the light scattering novice and may, therefore, be less elegant than the advanced reader might prefer.

We describe in this report an approximate method of solving the volume electric field integral equation describing the scattering of electromagnetic radiation by a penetrable nonmagnetic obstacle of arbitrary shape but possessing a permittivity and an electrical conductivity which can vary from point to point within the scatterer. The method uses Fourier analysis of distributions in the derivation of the approximations.

The integral equation considered in this paper has been widely studied, and physically motivated derivations of the equation have been provided. However, a mathematical proof seems to be absent from the literature. The author has under support by Southwest Research Institute numerically verified, that if the exact solution of the problem of describing scattering by a spheroid is substituted into the integral equation studied in this paper, then this integral equation is satisfied. The equivalence of this integral equation to the transmission problem of electromagnetism, where we assume that the Maxwell equations are satisfied in the interior and another set of Maxwell equations are satisfied in the exterior of the scattering cylinder, and where the difference between the solution of the exterior equations and the electric field E^i and the magnetic field H^i of the incoming radiation satisfy the Silver Muller radiation conditions, and where the usual regularity condition requiring continuity of tangential components of electric and magnetic fields across surface boundaries separating regions of regularity or smoothness of electrical properties is assumed to be valid, can be proven mathematically. While many numerical methods have been developed to attack the problem of solving this integral equation, none have been successful on existing computer systems when the scatterer shape is complex. The exact solution of this integral equation when the scatterer is a finite length cylinder is still not known, and no formula has been developed which is valid over a wide range of frequencies by any method. A method of improving the accuracy of traditional methods (Guru and Chen [6], Haggmann and Gandhi [7]-[8], Haggmann and Levin [9], and Livesay and Chen [13] of solving integral equations has been obtained, and this is discussed in this report.

The method of solution used by the program described in this report is an iterative scheme based on the Neumann Series. The method described in this report is particularly useful when considering the random orientation problem or the problem of scattering from a cloud whose particles have a given statistical distribution of orientations. The reason for this is that the iterative technique developed in this report that makes use of the Shiffirin method of calculating the action of multiple dimensional integral operators can be carried out very rapidly for particles with a sufficiently small index of refraction. The range of validity of this method and of the computer program are provided to the potential user of the program in this report.

1. INTEGRAL EQUATIONS AND LIGHT SCATTERING

The purpose of this section is to provide the user of the program with a description of both the equation that is solved by the computer program, and the method of solution that is used. The equation solved is the volume integral equation studied by Muller in his classical works and now widely used ([3]-[11]). This equation has the form

$$\mathbf{E} = \mathbf{E}^i + (\text{grad}(\text{div}) + k_0^2) \int (m^2 - 1) \left[\frac{\exp(ik_0|\mathbf{r} - \mathbf{r}_v|)}{4\pi|\mathbf{r} - \mathbf{r}_v|} \right] \mathbf{E}(\mathbf{r}_v) dV(\mathbf{r}_v) \quad (1.1)$$

where r is the observation point, E^i is the electric vector of the incoming field, E is the electric vector of the total electromagnetic field resulting from the interaction of the incoming radiation with the aerosol particle, and r_0 is the variable of integration which varies over the particle. The integral equation above has several advantages including the fact that it permits the analysis of light scattering by aerosol particles whose electrical properties are not the same at every internal point and that only the scatterer need be modeled. In using the finite element method a large area of air space surrounding the scatterer, namely the entire region where the ambient light is significantly altered by the presence of the particle, must be described in a computer model of light scattering. The disadvantage is that computer analysis can be very costly if the wrong approach is taken. In this report an approximate solution is obtained using the concept of Born series together with the use of Fourier analysis and complex variables to get an exact expression for higher dimensional iterates of the integral operator. This makes the problem of averaging over orientation quite tractable. In the above equation only E^i is known, the value of E both inside the integral and outside the integral must be determined. A typical procedure is to rewrite the integral equation (1.1) in the form

$$E = E^i + KE \quad (1.2)$$

where K represents the integral operator. If the norm, $|K|$ of the dyadic integral operator is smaller than one, then the integral equation (1.2) has a unique solution which is represented in the form

$$E = \sum_{n=0}^{\infty} (K)^n E^i \quad (1.3)$$

I remark that the reader can easily see the origin of the series solution (1.3) which is sometimes called the Neumann series by rewriting equation (1.2) in the form,

$$E - KE = E^i \quad (1.4)$$

and realizing that equation (1.3) is very similar to the geometric series

$$\frac{1}{1-R} = \sum_{n=0}^{\infty} R^n \quad (1.5)$$

relation that is valid if R is a complex number whose absolute value is smaller than one. The analogy is precisely the following relation,

$$(I - K)^{-1} = \sum_{n=0}^{\infty} K^n \quad (1.6)$$

where I is the identity operator which transforms every vector valued function E into itself, which is valid whenever the norm of the operator K is smaller than one. These are the conditions under which this equation has been solved in this report. The program developed in this report was adapted from the computer program written at Drexel University which is described in Acquista [1] and in the joint works of Ariel Cohen, Leonard Cohen, and Richard Haracz ([3]-[3]). Holt in [9] uses the volume integral equation (1.1) without using the assumption that the norm of K is smaller than one and has evidently obtained some results which agree very well with experiments. A surface impedance approach similar to that used by King [14] was used by Pedersen et al. [15] who also obtained numerical results which sometimes agreed very well with the results of light scattering experiments; Pedersen et al. however use a Pocklington type of theory and reduce the three dimensional integral operator to a surface integral by averaging over the cross section of the cylinder. The specific numerical values for which comparisons with theory and experiment are good are detailed in [9] and [15]. For example, a typical set of values for which Pederson got good results was for a tungsten wire with a wavelength to length ratio of .525 and a length to diameter ratio of 660. J. W. Shepherd and A. R. Holt [9] on the other hand appear to get excellent agreement with backscatter experiments for a finite cylinder with a length to radius ratio of 5 to 1, a circumference to wavelength ratio of 0.458, and a complex index of refraction given by

$$N - iK = 3.14 - i0.036 \quad (1.7)$$

The problem of developing a robust program for describing the interaction of light with a fat cylinder with a high complex index of refraction remains unsolved and would probably require a direct attack on the integral equation without using any assumptions about the size of the norm of the associated integral operator, and would probably use an extension of the methods of [9]. All of the above methods involve a discretization of the integral operator appearing in the integral equation (1.1), and they furthermore imply that there is some projective transformation onto a vector space of potential approximates of the solution of the integral equation. By the use of the word projective I am implying that the approximation of an acceptable approximate is equal to itself. We furthermore are considering at any time a finite dimensional vector space for a source of possible approximate solutions of our integral equation. An integral operator is said to be of finite

rank if its image is a finite dimensional space of functions. A best approximate of the real solution of the original integral equation (1.1) might be a function in a finite dimensional vector space which is as close as possible to the actual solution. We think of this best approximate as a projection of the actual solution onto the finite dimensional vector space in which we are looking for approximations to the actual solution of (1.1). If the space is chosen so that we can get reasonably close to the actual solution with a best approximate, we can show that there is an exact finite rank integral equation whose solution is the projection of the actual solution, and that furthermore there is a correction to this solution which can with enough systematic calculation give the exact solution to (1.1). Said differently, it is possible to get an approximation to the solution to (1.1) and to also have a mathematical value of the exact error associated with this approximation. It is also possible to develop a differential equation with solutions in a vector space of matrix valued functions of pairs of points in three dimensional space which yield a resolvent kernel R such that the solution \mathbf{E} of (1.1) is given by

$$\mathbf{E}^1 - R\mathbf{E}^1 = \mathbf{E} \quad (1.8)$$

so that the determination of the unknown \mathbf{E} is simply carried out by evaluating $R\mathbf{E}^1$ which involves evaluating an integral. To understand how we compute R we rewrite the equation (1.1) in the form

$$\mathbf{E} - \mathbf{E}^1 = \int_{\Omega} G(\mathbf{r}, \mathbf{r}_v) \mathbf{E}(\mathbf{r}_v) d\mathbf{v}(\mathbf{r}_v) \quad (1.9)$$

and then observe that the operator R described above is given by

$$R\mathbf{E}^1 = \int_{\Omega} R_{\lambda}(\mathbf{r}, \mathbf{r}_v) \mathbf{E}^1(\mathbf{r}_v) d\mathbf{v}(\mathbf{r}_v) \quad (1.10)$$

where

$$\frac{dR_{\lambda}}{d\lambda}(\mathbf{r}, \mathbf{r}_v) = \int_{\Omega} R_{\lambda}(\mathbf{r}, \mathbf{s}_v) R_{\lambda}(\mathbf{s}_v, \mathbf{r}_v) d\mathbf{v}(\mathbf{r}_v) \quad (1.11)$$

and where

$$R_0 = G \quad (1.12)$$

We discuss in this paragraph the validity of the integral equation whose solution was obtained by the computer program described in this report. In particular we want to know the connection between solutions of integral equations and the solution of the standard Maxwell equation boundary value problem. We seek solutions of the equations of Maxwell which are

$$\text{curl}(\mathbf{E}) = - \frac{\partial \mathbf{B}}{\partial t} \quad (1.13)$$

and

$$\text{curl}(\mathbf{H}) = \frac{\partial \mathbf{D}}{\partial t} + \mathbf{J} \quad (1.14)$$

where the constitutive relations for a general optical material (c. f. Reintjes [17], p 8) are defined through the introduction of a polarization vector \mathbf{P} by means of the relationship

$$\frac{\partial \mathbf{D}}{\partial t} + \mathbf{J} = \epsilon_0 \mathbf{E} + \frac{\partial \mathbf{P}}{\partial t} \quad (1.15)$$

and a magnetisation vector \mathbf{M} by the rule

$$\mathbf{B} = \mu_0(\mathbf{H} + \mathbf{M}) \quad (1.16)$$

In a nonmagnetic material we have $\mathbf{M} = 0$ and we find that \mathbf{P} is determined as the trace of the matrix product of the matrix whose number of rows is the number of states and whose (i, j) entry is the transition dipole matrix entry between states i and j and the density of states operator (Reintjes [17], p 22). For linearly responding materials which can be treated as a Lorents medium with a single type of oscillator, this relation is given more simply by

$$\mathbf{P} = N\mathbf{x} \quad (1.17)$$

where

$$m \frac{d^2 \mathbf{x}}{dt^2} + g \frac{d\mathbf{x}}{dt} + m\omega_0^2 \mathbf{x} = e\mathbf{E} \quad (1.18)$$

Substituting the solution of equation (1.18) coupled with (1.17) into the linear relationship,

$$\mathbf{P} = (\epsilon - \epsilon_0)\mathbf{E} - i(\sigma/\omega)\mathbf{E} \quad (1.19)$$

we obtain the standard dispersion relationships giving the complex index of refraction as a function of the frequency of the incident light for a simple one oscillator Lorents medium. We require that the Maxwell equations be satisfied inside and outside the scatterer, that the tangential components

of \mathbf{E} and \mathbf{H} be continuous across the boundary of the scatterer, and that the electric and magnetic vectors of the scattered radiation satisfy the Silver Muller radiation conditions. Thus, we require that

$$\mathbf{E}^s = \mathbf{E} - \mathbf{E}^i \quad (1.20)$$

which represents the difference between the total electric vector and the electric vector of the incident light beam, should satisfy the relationship,

$$\left(\lim_{R \rightarrow \infty} \int_{S_R} (|\text{curl}(\mathbf{E}^s) \times \mathbf{n} - ik_0 \mathbf{E}^s|^2) da \right) = 0, \quad (1.21)$$

where S_R is a sphere of radius R centered at a point in the bounded scatterer Ω . We multiply out the expression in the integrand appearing in the left side of equation (1.21) obtaining the relationship,

$$\begin{aligned} & (\text{curl}(\mathbf{E}^s) \times \mathbf{n} - ik_0 \mathbf{E}^s) \cdot (\text{curl}(\mathbf{E}^s)^* + ik_0 (\mathbf{E}^s)^*) = \\ & (|\text{curl}(\mathbf{E}^s) \cdot \mathbf{n}|^2 + k_0^2 (|\mathbf{E}^s|^2 - ik_0 (\mathbf{E}^s \times \text{curl}(\mathbf{E}^s)^*) \cdot \mathbf{n} + ik_0 ((\mathbf{E}^s)^* \times \text{curl}(\mathbf{E}^s)) \cdot \mathbf{n} \end{aligned} \quad (1.22)$$

In developing the above equation we have used the fact that

$$(\mathbf{A} \times \mathbf{n}) \cdot \mathbf{B} = (\mathbf{B} \times \mathbf{A}) \cdot \mathbf{n} \quad (1.23)$$

for all vectors \mathbf{A} , \mathbf{B} , and \mathbf{n} . This enables us to show that if \mathbf{E}^d denotes the difference between two representations of the electric field vector in the interior of the scatterer Ω which satisfies the Maxwell equations, (1.13) and (1.14), the radiation condition (1.21) and the condition that tangential components of the electric field \mathbf{E} and the magnetic field \mathbf{H} are continuous across the boundary of the scatterer that then

$$k_0 \omega \mu_0 \int_{\Omega} \sigma (|\mathbf{E}^d|^2) dv = 0. \quad (1.24)$$

This permits us to show that in a naturally arising collection of electromagnetic fields, there is only one solution of the Maxwell equations (1.13) and (1.14) inside and outside the scatterer Ω which satisfies the radiation condition (1.21) and the regularity conditions requiring continuity of tangential components of \mathbf{E} and \mathbf{H} across the boundary of Ω . Furthermore, by introducing the dual integral equation obtained by applying the curl operation to both sides of equation (1.1) and enforcing the first Maxwell equation (1.1), we can prove that the second Maxwell equation (1.14) is satisfied both inside and outside the scattering body. If we assume that the electrical properties are infinitely differentiable, we can prove that tangential components of \mathbf{E} and \mathbf{H} are continuous across the boundary of the scatterer. We note that by smoothing sharp edges, we can get as close as we please to describing an aerosol particle whose electrical properties change suddenly from those of free space by passing across the particle boundary by using infinitely smooth electrical properties. The particular form of the kernel function in the integral equation (1.1) ensures us that outside the scatterer

$$\mathbf{E} - \mathbf{E}^i = \mathbf{E}^s \quad (1.25)$$

satisfies the relation (1.21). This proves mathematically that the integral equation formulation (1.1) of the light scattering problem was completely equivalent to the standard Maxwell equation formulation. This is important, because we then know that if we can prove that we have developed a numerical scheme for correctly solving the integral equation (1.1), such as the iterative method described in this report, then we are confident that this is the exact solution of our light scattering problem under the milder assumption that the scattering process is correctly described by the solution of the standard transmission problem associated with linear Maxwell equations.

Since the term appearing in the integrand of equation (1.1) is infinite when the variable of integration \mathbf{r}' is exactly equal to the observation point \mathbf{r} , we have been concerned about the numerical interpretation of the action of the integral operator on an electromagnetic field, and we have carried out careful numerical experiments with a principle value interpretation which excises a sphere containing the observation point \mathbf{r} and breaks up the integration over Ω into a portion interior and exterior to this sphere which is contained in Ω . We have compared solutions which were obtained numerically with exact solutions for aerosol particles with special shapes. We have used the exact solution for scattering by a small spheroid in an electromagnetic field making use of the fact that the field inside an ellipsoid is nearly uniform (Stratton [18], page 213) if this ellipsoidal dielectric is small compared with the wavelength. Furthermore, exact formulas can be found for the components of the Polarisation vector inside an ellipsoidal dielectric in a uniform field, which is equivalent to the problem of a very small ellipsoidal dielectric in a plane wave light source. What I did was to assume that the scatterer was very small and take the observation point \mathbf{r} of equation (1.1) to be inside the ellipsoid. I then noted that the electric vector \mathbf{E} appearing in equation (1.1) was just a constant vector. I, therefore, substituted an arbitrary constant vector into (1.1). I

excised a small sphere about the observation point and evaluated the action of the integral operator on the constant vector inside this excised sphere using spherical coordinates by an exact formula; this just involved the evaluation of nine simple trigonometric integrals. I next cut a cylindrical hole in the ellipsoid whose axis passed through the center of the excised sphere and whose radius was exactly the radius of the excised sphere. I used a highly accurate Gauss quadrature scheme to evaluate the action of the integral operator outside the cylindrical shaft in my spheroid. I did the same kind of accurate integration over the region of the cylinder inside the spheroid and above and below my excised sphere. In carrying out the calculation, I made my excised sphere as large as possible to reduce the variation in the integrand in the portion of the spheroid that was outside the excised sphere. The following table shows the size and complex index of refraction of a spheroid subject to 60 cycle per second radiation.

SPHEROID DATA	
Minor Axis Length	$N - iK$
2 meters	$10^6 - i0.33/(60 \times 8.854 \times 10^{-12})$

The next table shows the comparison of two different methods of calculation. These are the exact calculation using spheroidal coordinates and the computations involving the development of a system of three equations in three unknowns based on the knowledge that (Stratton [18], page 213) the internal electric vector of a dielectric ellipsoid in a uniform field is a constant.

FIELDS INDUCED IN A SPHEROID				
axis ratio	$\text{Re}(E_x)_{\text{exact}}$	$\text{Im}(E_x)_{\text{exact}}$	$\text{Re}(E_x)_{\text{calculated}}$	$\text{Im}(E_x)_{\text{calculated}}$
3/2	$.2667743454 \times 10^{-10}$	$.2637426620 \times 10^{-7}$	$.266766 \times 10^{-10}$	$.263748 \times 10^{-7}$
4/2	$.2475938671 \times 10^{-10}$	$.2447806138 \times 10^{-7}$	$.244759 \times 10^{-10}$	$.244791 \times 10^{-7}$
5/2	$.2365922431 \times 10^{-10}$	$.2339072117 \times 10^{-7}$	$.236609 \times 10^{-10}$	$.233921 \times 10^{-7}$

This analysis of methods of comparing integral equation solutions of the problem of computing the fields induced in spheroids to the exact formulation using the Maxwell equations is not without relevance to the problem of describing scattering by spheroids. First of all the method of computation shows that when the observation point r is inside the scatterer, then the singular portion of the integral operator cannot be ignored, and that it is properly computed by excising a sphere containing the observation point and calculating the principle value integral over the sphere and over the common part of the interior of the scatterer and the exterior of the sphere containing the observation point. The integral equation used in producing the above table was the quasi static integral equation, but for particles whose size parameter is much smaller than a wavelength of light, the quasistatic analysis is very accurate. (Stratton [17], page 213) and Bohren and Huffman [2], pages 130-157) The integral equation used in the above analysis was the one obtained from equation (1.1) by setting

$$\exp(ik\sqrt{r-r_0}) = 1 \quad (1.26)$$

A second reason that a knowledge of this comparison is useful is due to the comparison (Haracs et al [8]) between exact spheroid calculations using spheroids that are similar in shape to a finite cylinder, and numerical solution of the integral equation when the scatterer is the finite cylinder circumscribing the spheroid or which has the same length and volume as the spheroid. The authors showed that good agreement was obtained when the index of refraction was 1.5 and the aspect ratio was 10 (Haracs et al. [8], page 3326).

The program at the present time produces as its output the intensities associated with the components of the electric vector of the scattered radiation that are parallel to the detector plane but perpendicular to the direction of propagation, and the component perpendicular to the direction of propagation, but this is inadequate since in recent years discussions at the CRDEC Aerosol Science Conference have confirmed that much more information is available from particles interrogated by electromagnetic radiation than is available from these two amplitudes which turn out to be related to the first two Stokes parameters of the scattered radiation. At the present time one of the preferred means of presenting this information is through the seven independent parameters of the four by four Mueller matrix (Bohren and Huffman [2]). To calculate the entries one could perform experiments on the object of interest by subjecting it to light with different polarizations and measuring with phase the electric vectors of the scattered radiation. The reason that this is correct is that the real and imaginary parts of the entries, $S_1, S_2, S_3,$ and S_4 , of the amplitude scattering matrix (Bohren and Huffman [2], pages 62-63) completely determine all sixteen entries of the four by four Mueller matrix (Bohren and Huffman [2], page 65). The formulas are listed explicitly in Bohren and Huffman [2], page 65. Thus, to show that everything can be obtained with the present program we simply have to show how to get the four complex entries of the amplitude scattering matrix.

In the next section we will explain how to get the unit vectors e_x and e_y in the direction of the

x and y axes, respectively, of the detector coordinate system. We assume that \mathbf{E}_0^0 is the electric vector of the scattered radiation when the electric vector of the incident radiation is parallel to the reference plane. We assume that \mathbf{E}_0^90 is the electric vector of the scattered radiation when the electric vector of the incident radiation makes an angle of 90 degrees with respect to the reference plane. Both of these quantities are computed by the program. Modulo the constant c therefore we see that the complex entries of the amplitude scattering matrix are given by

$$cS_1 = \frac{(\mathbf{E}_0^0 \cdot \mathbf{e}_{x_s})}{(\mathbf{E}_0^0 \cdot \mathbf{e}_{x_i})} \quad (1.27)$$

$$cS_2 = \frac{(\mathbf{E}_0^0 \cdot \mathbf{e}_{x_s})}{(\mathbf{E}_0^90 \cdot \mathbf{e}_{y_i})} \quad (1.28)$$

$$cS_3 = \frac{(\mathbf{E}_0^90 \cdot \mathbf{e}_{x_s})}{(\mathbf{E}_0^0 \cdot \mathbf{e}_{x_i})} \quad (1.29)$$

$$cS_4 = \frac{(\mathbf{E}_0^90 \cdot \mathbf{e}_{x_s})}{(\mathbf{E}_0^90 \cdot \mathbf{e}_{y_i})} \quad (1.30)$$

As we use the quantities calculated by equations, we see that the entries of the Mueller matrix are all proportional to $(|c|)^2$ which turns out to be given by

$$(|c|)^2 = \frac{1}{k_0^2 r^2} \quad (1.31)$$

where k_0 is the propagation constant of free space or $2\pi/\lambda$ where λ here denotes the wavelength of the light. This fact causes the entries of the Mueller matrix to be independent of the distance from the scatterer to the detector.

We now give a precise explanation of the computation of the entries of the Mueller matrix in terms of the entries of the amplitude scattering matrix. From Bohren and Huffman ([2], p 63) the amplitude scattering matrix is given by the relation,

$$\begin{pmatrix} \mathbf{E}^s \cdot \mathbf{e}_{x_s} \\ \mathbf{E}^s \cdot \mathbf{e}_{y_s} \end{pmatrix} = c \begin{pmatrix} S_2 & S_3 \\ S_4 & S_1 \end{pmatrix} \begin{pmatrix} \mathbf{E}^i \cdot \mathbf{e}_{x_i} \\ \mathbf{E}^i \cdot \mathbf{e}_{y_i} \end{pmatrix} \quad (1.32)$$

The Mueller matrix relates the Stokes parameters of the incident radiation to the Stokes parameters of the scattered radiation at each detector position. Since there are four Stokes parameters defined by the relations which are the action of quadratic forms on the incident radiation given by

$$\begin{pmatrix} I_s \\ Q_s \\ U_s \\ V_s \end{pmatrix} = \begin{pmatrix} |(\mathbf{E}^i \cdot \mathbf{e}_{x_i})|^2 + |(\mathbf{E}^i \cdot \mathbf{e}_{y_i})|^2 \\ |(\mathbf{E}^i \cdot \mathbf{e}_{x_i})|^2 - |(\mathbf{E}^i \cdot \mathbf{e}_{y_i})|^2 \\ (\mathbf{E}^i \cdot \mathbf{e}_{x_i})(\mathbf{E}^i \cdot \mathbf{e}_{y_i})^* + (\mathbf{E}^i \cdot \mathbf{e}_{y_i})(\mathbf{E}^i \cdot \mathbf{e}_{x_i})^* \\ i((\mathbf{E}^i \cdot \mathbf{e}_{x_i})(\mathbf{E}^i \cdot \mathbf{e}_{y_i})^* - (\mathbf{E}^i \cdot \mathbf{e}_{y_i})(\mathbf{E}^i \cdot \mathbf{e}_{x_i})^*) \end{pmatrix} \quad (1.33)$$

We now make some comments concerning the existence of the Mueller matrix. We note that combinations of I_s , Q_s , U_s , and V_s will give all possible combinations of products of the two quantities $\mathbf{E}^i \cdot \mathbf{e}_{x_i}$ and $\mathbf{E}^i \cdot \mathbf{e}_{y_i}$ and their conjugates. To see this we note that

$$(\mathbf{E}^i \cdot \mathbf{e}_{x_i})(\mathbf{E}^i \cdot \mathbf{e}_{x_i})^* = (1/2)(I_s + Q_s) \quad (1.34)$$

$$(\mathbf{E}^i \cdot \mathbf{e}_{y_i})(\mathbf{E}^i \cdot \mathbf{e}_{y_i})^* = (1/2)(I_s - Q_s) \quad (1.35)$$

$$(\mathbf{E}^i \cdot \mathbf{e}_{x_i})(\mathbf{E}^i \cdot \mathbf{e}_{y_i})^* = (1/2)(U_s - iV_s) \quad (1.36)$$

$$(\mathbf{E}^i \cdot \mathbf{e}_{y_i})(\mathbf{E}^i \cdot \mathbf{e}_{x_i})^* = (1/2)(U_s + iV_s) \quad (1.37)$$

We remark that equations (1.34) through (1.37) also hold with the superscript s which represents the scattered radiation replaced by the superscript i which is used to tell us for example that \mathbf{E}^i denotes the electric vector of the incident light beam. These equations have the form

$$(\mathbf{E}^i \cdot \mathbf{e}_x)(\mathbf{E}^i \cdot \mathbf{e}_x)^* = (1/2)(I_i + Q_i) \quad (1.38)$$

$$(\mathbf{E}^i \cdot \mathbf{e}_y)(\mathbf{E}^i \cdot \mathbf{e}_y)^* = (1/2)(I_i - Q_i) \quad (1.39)$$

$$(\mathbf{E}^i \cdot \mathbf{e}_x)(\mathbf{E}^i \cdot \mathbf{e}_y)^* = (1/2)(U_i - iV_i) \quad (1.40)$$

$$(\mathbf{E}^i \cdot \mathbf{e}_y)(\mathbf{E}^i \cdot \mathbf{e}_x)^* = (1/2)(U_i + iV_i) \quad (1.41)$$

Thus, it is clear from this and the expansion of the quadratic forms that there is a four by four matrix, which we will refer to as the Mueller matrix, which relates the Stokes parameters of the scattered radiation to the Stokes parameters of the incident radiation. Furthermore, this relationship is written in the form

$$\begin{pmatrix} I_s \\ Q_s \\ U_s \\ V_s \end{pmatrix} = |c|^2 \begin{pmatrix} S_{(1,1)} & S_{(1,2)} & S_{(1,3)} & S_{(1,4)} \\ S_{(2,1)} & S_{(2,2)} & S_{(2,3)} & S_{(2,4)} \\ S_{(3,1)} & S_{(3,2)} & S_{(3,3)} & S_{(3,4)} \\ S_{(4,1)} & S_{(4,2)} & S_{(4,3)} & S_{(4,4)} \end{pmatrix} \begin{pmatrix} I_i \\ Q_i \\ U_i \\ V_i \end{pmatrix} \quad (1.42)$$

We will now explain how we can in a systematic manner calculate the representation of all the Mueller matrix elements in terms of the entries of the amplitude scattering matrix by the use of the relations (1.38) through (1.41), their analogues for the incident radiation, and the matrix equation (1.32). We will illustrate our method with the following computation of the $(1,j)$ entries of the Mueller matrix for j running from 1 to 4. Substituting the matrix relation (1.32) into the right side of the expression for I_s given by equation (1.33) we see that

$$I_s = |c|^2 (|\mathbf{E}^i \cdot \mathbf{e}_x|^2 (S_2 S_2^* + S_4 S_4^*) + (\mathbf{E}^i \cdot \mathbf{e}_x)(\mathbf{E}^i \cdot \mathbf{e}_y)^* (S_2 S_3^* + S_4 S_1^*) + |\mathbf{E}^i \cdot \mathbf{e}_y|^2 (S_3 S_3^* + S_1 S_1^*) + (\mathbf{E}^i \cdot \mathbf{e}_y)(\mathbf{E}^i \cdot \mathbf{e}_x)^* (S_3 S_2^* + S_1 S_4^*)) \quad (1.43)$$

It will then follow after making the replacements suggested by equations (1.38) through (1.41) that

$$I_s = |c|^2 ((1/2)(I_i + Q_i)(|S_2|^2 + |S_4|^2) + (1/2)(U_i - iV_i)(S_3 S_2^* + S_1 S_4^*) + (1/2)(U_i + iV_i)(S_3 S_2^* + S_1 S_4^*) + (1/2)(I_i - Q_i)(|S_3|^2 + |S_1|^2)) \quad (1.44)$$

Thus, if we simply collect the coefficients of I_i in equation (1.44) we find that since

$$I_s = (|c|^2)(S_{(1,1)} I_i + S_{(1,2)} Q_i + S_{(1,3)} U_i + S_{(1,4)} V_i) \quad (1.45)$$

the Mueller matrix entry $S_{(1,1)}$ is given by

$$S_{(1,1)} = (1/2)(|S_1|^2 + |S_2|^2 + |S_3|^2 + |S_4|^2) \quad (1.46)$$

Collecting the coefficients of Q_i we find that

$$S_{(1,2)} = (1/2)(|S_2|^2 + |S_4|^2 - (|S_1|^2 + |S_3|^2)) \quad (1.47)$$

Since half of a number and its complex conjugate is the real part of the complex number, the factor (1/2) does not appear in the expression for $S_{(1,3)}$. We deduce that

$$S_{(1,3)} = \text{Re}(S_2 S_3^* + S_1 S_4^*) \quad (1.48)$$

where if

$$s = x + iy \quad (1.49)$$

denotes a complex number, then

$$\text{Re}(s) = x \quad (1.50)$$

and

$$\text{Im}(s) = y \quad (1.51)$$

The last term in the above expression is then determined to be

$$S_{(1,4)} = \text{Im}(S_2 S_3^* - S_1 S_4^*) \quad (1.52)$$

The remaining terms are given in Bohren and Huffman ([2], page 65) and are derived in the same way. The present computer program can therefore yield all the Mueller matrix entries as a function of detector angle.

3. LABORATORY, TARGET, AND DETECTOR COORDINATE SYSTEMS

In this section we treat three coordinate systems called the laboratory, the target, and the detector coordinate systems whose s axes respectively coincide with (i) the direction of propagation of the radiation, (ii) the axis of a scattering cylinder, and (iii) a line joining the center of this cylinder and a point detector of the light scattered by the cylinder. We will refer to these coordinate systems as respectively the $x_0-y_0-s_0$ coordinate system, the $x_a-y_a-s_a$ coordinate system, and the $x_d-y_d-s_d$ coordinate system. We let $e_{x_0}, e_{y_0}, e_{s_0}$ denote the unit vectors in the direction of the positive $x_0, y_0,$ and s_0 axes. We let $e_{x_a}, e_{y_a}, e_{s_a}$ denote the unit vectors in the direction of the positive $x_a, y_a,$ and s_a axes. We let $e_{x_d}, e_{y_d}, e_{s_d}$ denote the unit vectors in the direction of the positive $x_d, y_d,$ and s_d axes. The detector is in the plane containing the x_0 axis and the s_0 axis. In these coordinate systems the y_0 axis or the laboratory y axis and the detector y axis or the y_d axis coincide so that there is a simple two dimensional relationship between the coordinates of the laboratory axis and the detector axis given by

$$\begin{pmatrix} E_{x_d} \\ E_{y_d} \\ E_{s_d} \end{pmatrix} = \begin{pmatrix} \cos(2\phi_0) & 0 & \sin(2\phi_0) \\ 0 & 1 & 0 \\ -\sin(2\phi_0) & 0 & \cos(2\phi_0) \end{pmatrix} \begin{pmatrix} E_{x_0} \\ E_{y_0} \\ E_{s_0} \end{pmatrix} \quad (2.1)$$

where $2\phi_0$ is the angle between the line from the center of the cylinder to the detector and the s_0 axis. Coordinate transformations of the type given by equation (2.1) are members of the real orthogonal group and are inverted simply by interchanging rows and columns; consequently the inverse transformation is given by

$$\begin{pmatrix} E_{x_0} \\ E_{y_0} \\ E_{s_0} \end{pmatrix} = \begin{pmatrix} \cos(2\phi_0) & 0 & -\sin(2\phi_0) \\ 0 & 1 & 0 \\ \sin(2\phi_0) & 0 & \cos(2\phi_0) \end{pmatrix} \begin{pmatrix} E_{x_d} \\ E_{y_d} \\ E_{s_d} \end{pmatrix} \quad (2.2)$$

The s_d axis is obtained simply by rotating the s_0 axis toward the x_0 axis by an angle of $2\phi_0$. Since the y_d axis is the same as the y_0 axis, we see that the x_d axis is simply that line which passes through the origin of the original coordinate system and which is perpendicular to both the s_d axis and the y_d axis. The Fortran variable used in our program to denote the detector angle $2\phi_0$ is **TTO**.

We now discuss the relationship between the target coordinates and the the laboratory coordinates. The cylinder makes an angle of ϕ with respect to the s_0 axis and the axis of the scattering cylinder that is targeted so to speak by the incoming light beam, and the projection of this cylinder on the x_0-y_0 plane makes an angle of γ with respect to the x_0 axis. The FORTRAN names for these variables are given in the following table.

PHA	ϕ	angle of cylinder and s_0 axis
GA	γ	angle of cylinder shadow and x_0 axis

The two angles ϕ and γ can be used to express a point on the cylinder axis one unit away from the origin has spherical coordinates given $(1, \gamma, \phi)$ and consequently the unit vector in the direction of the positive s_a axis is with respect to the laboratory frame given by

$$e_{s_a} = \sin(\gamma)\cos(\phi)e_{x_0} + \sin(\gamma)\sin(\phi)e_{y_0} + \cos(\gamma)\cos(\phi)e_{s_0} \quad (2.3)$$

We get the unit vector in the direction of the positive y_a axis by the cross product formula,

$$e_{y_a} = \frac{e_{s_0} \times e_{s_a}}{|e_{s_0} \times e_{s_a}|} \quad (2.4)$$

The final unit vector the one in the direction of the positive x_a axis is given by

$$e_z = e_y \times e_x \quad (2.5)$$

To relate a vector expressed in the laboratory coordinate to one its representation in the target or cylinder axis coordinates we make the following transformation

$$\begin{pmatrix} E_{x_1} \\ E_{y_1} \\ E_{z_1} \end{pmatrix} = \begin{pmatrix} \cos(\gamma)\cos(\phi) & \sin(\gamma)\cos(\phi) & -\sin(\phi) \\ -\sin(\gamma) & \cos(\gamma) & 0 \\ \sin(\phi)\cos(\gamma) & \sin(\phi)\sin(\gamma) & \cos(\phi) \end{pmatrix} \begin{pmatrix} E_{x_0} \\ E_{y_0} \\ E_{z_0} \end{pmatrix} \quad (2.6)$$

We now define the polarisation angle α which represents the angle between the electric vector of the incoming radiation and the x_0 axis under the assumption that the electric vector of the incoming radiation lies in the x_0 - y_0 plane. The FORTRAN variable used in this program is defined in the following table.

ALFA	α	angle of E^i and the x_0 axis
------	----------	-----------------------------------

This definition of α means that the electric vector of the incident radiation is given by

$$E^i = E_0 \cos(\alpha) e_{x_0} + E_0 \sin(\alpha) e_{y_0} \quad (2.7)$$

To represent a vector given in axial or detector coordinates in laboratory coordinates you simply multiply by the inverse of the coefficient matrix in the above equation; this inverse matrix is obtained from the first coefficient matrix simply by interchanging rows and columns. One of the procedures carried out by the program is the execution of this matrix multiplication. In the original Drexel University ([3]-[8]) code this was written in the transparent form,

$\begin{aligned} \text{EOXA} &= \text{EO} * (\text{COS}(\text{PHA}) * \text{COS}(\text{GA}) * \text{COS}(\text{ALFA}) \\ &\quad + \text{COS}(\text{PHA}) * \text{SIN}(\text{GA}) * \text{SIN}(\text{ALFA})) \\ \text{EOYA} &= \text{EO} * (-\text{SIN}(\text{GA}) * \text{COS}(\text{ALFA}) \\ &\quad + \text{COS}(\text{GA}) * \text{SIN}(\text{ALFA})) \\ \text{EOZA} &= \text{EO} * (\text{SIN}(\text{PHA}) * \text{COS}(\text{GA}) * \text{COS}(\text{ALFA}) \\ &\quad + \text{SIN}(\text{PHA}) * \text{SIN}(\text{ALFA}) * \text{SIN}(\text{GA})) \end{aligned}$

where **ALFA** is the polarisation angle and **EO** is the length of the electric vector of the incoming radiation, and **GA** is the angle made by the cylinder shadow in the x_0 - y_0 plane, and **PHA** is the angle made by the cylinder axis and the direction of propagation of the radiation. To average over orientation we simply integrate the scattering intensity over the two angles γ and ϕ at each observation point. Gaussian quadrature is used to carry this out accurately and subroutine **GAUSS** is used to select the Gaussian quadrature points to carry out this surface integral.

3. THE PUPIL FUNCTION

The characteristic function of the cylinder scattering the light is the function on all of \mathbb{R}^3 , three dimensional space, which takes on the value 1 at points inside the cylinder and which takes on the value 0 at all other points. The **FUNCTION U** in the Drexel ([3]-[8]) code calculates the spatial Fourier transform of the characteristic function of the scattering cylinder at a specific point in three dimensional space depending on components of the vector **X** given by

$$\mathbf{X} = k_0 e_s - k_0 \quad (3.1)$$

where k_0 is the ratio of the angular frequency of the incoming light to the vacuum speed of light. The Fortran variables used are **IPAR** for the component parallel to the cylinder axis and **XPER** is the component perpendicular to the cylinder axis. Because of symmetry we naturally will change coordinates first and calculate this Fourier transform in the x_s - y_s - z_s coordinate system. Assuming that this has been done, we then change to cylindrical coordinates with respect to this coordinate system and write

$$u(x, y, s) = \int_0^R \int_{-\pi/2}^{\pi/2} \int_0^{2\pi} \left\{ \exp(i(r_s (\cos(\theta_s) \cos(\theta_s) + \sin(\theta_s) \sin(\theta_s)) + s s_s)) \right\} ds_s d\theta_s r_s dr_s \quad (3.2)$$

where (r_s, θ_s, s_s) is the representation in cylindrical coordinates of a point which varies over the cylinder. The integral with respect to s_s can be carried out exactly leaving us with

$$u(x, y, z) = \int_0^{R+\pi} \int_{-\pi}^{\pi} \exp(i(r r, \cos(\theta - \theta_0))) \left(\frac{\exp(i s h / 2) - \exp(-i s h / 2)}{i s} \right) d\theta, r, dr, \quad (3.3)$$

This further simplifies and in fact can be completely integrated if we make use of the following two facts which are established in Appendix B of the paper on scattering by infinite cylinders. The first one is the representation of the Bessel function of order 0 by the relationship,

$$J_0(w) = \left(\frac{1}{2\pi} \right) \int_{-\pi}^{\pi} \exp(-i w \cos(\theta)) d\theta \quad (3.4)$$

and the relation,

$$\int_0^R J_0(r) r dr = R J_1(R) \quad (3.5)$$

which can be proven by many methods including just using the series representation of the Bessel functions which is given by

$$J_m(r) = \sum_{n=0}^{\infty} \left(\frac{(-1)^n r^{2n+m}}{2^{2n+m} n! (n+m)!} \right) \quad (3.6)$$

Thus, we see that simply making use of these facts and the elementary relation

$$\frac{\sin(\psi/2)}{\psi/2} = \frac{\exp(i\psi/2) - \exp(-i\psi/2)}{i\psi}$$

we see that with ψ replaced by $sh/2$ that

$$u(x, y, z) = 2\pi R^2 h \left(\frac{J_1(Rr)}{Rr} \right) \left(\frac{\sin(sh/2)}{sh/2} \right) \quad (3.7)$$

The function u is defined in the Drexel ([3]-[8]) University code as follows

```

FUNCTION U(XPAR,XPER,A,H,XK)
P = SQRT(XPAR**2 + XPER**2)
X = XPAP*(H/2)*XK
Y = XPER*A*XK
C = ABS(X)
B = ABS(Y)
IF(C.LT.0.001) XA = 1-X**2/6+X**4/120
IF(C.GE.0.001) XA = SIN(X)/X
IF(B.LT.0.001) XB = (1-Y**2/8+Y**4/192)*0.5
IF(B.GE.0.001) XB = BESS1(Y)/Y
V = 3.14159265358979323*A**2*H
U = 2*V*XA*XB
RETURN
END

```

where the function BESS1 is the first order Bessel function J_1 , and the input variables XK , A , and H are defined in the following table

XK	the propagation constant of the wave
A	the radius of the cylinder
H	the length (or height) of the cylinder

4. THE INCOMING FIELD E VECTOR, XPAR, AND XPER

We discuss here the detector or target coordinate system and its use in providing a representation of the electric vector of the incoming radiation, in defining the polarization vector of the incoming radiation, and in defining another vector \mathbf{X} defined by

$$\mathbf{X} = k_0 \mathbf{e}_s - \mathbf{k}_0$$

and in defining \mathbf{XPAR} and \mathbf{XPER} by the rules,

$$\mathbf{XPAR} = \mathbf{e}_s \cdot \mathbf{X}$$

which means the component of \mathbf{X} parallel to the cylinder axis, and

$$\mathbf{XPER} = (\mathbf{X} \cdot \mathbf{e}_x) \mathbf{e}_x + (\mathbf{X} \cdot \mathbf{e}_y) \mathbf{e}_y,$$

which means the component of \mathbf{X} which is perpendicular to the cylinder axis. We note that by the definition of \mathbf{X} that it is independent of the polarization of the incoming radiation, but is related to the unit vector in direction of propagation and the unit vector pointing from the center of the scatterer to the detector. We develop components of this vector parallel and perpendicular to the unit vector, \mathbf{e}_s , pointing along the axis of the cylindrical scatterer so that while the vector itself is independent also of the orientation of the scattering cylinder, the manner in which it is decomposed is related to the scatterer orientation.

In this section we let $x_0, y_0,$ and s_0 denote the laboratory coordinates whose s axis is aligned with the direction of propagation of the radiation, and we let x_d, y_d, s_d denote the usual $x, y,$ and s coordinates in the system whose s axis coincides with a line from the detector to the origin of the laboratory frame where we assume that the detector is somewhere in the plane containing the x_0 axis and the s_0 axis. The origin of both coordinate systems is the center of the cylinder that is scattering the light. If we let \mathbf{e}_s denote the unit vector pointing from the origin to the detector and we let $2\phi_0$ denote the angle between the direction of propagation of the radiation and the line from the origin of the coordinate system to the detector. Then we clearly have

$$\mathbf{e}_s = \sin(2\phi_0) \mathbf{e}_x + \cos(2\phi_0) \mathbf{e}_z \quad (4.1)$$

If we further assume that the unit vector \mathbf{e}_y in the direction of the positive y axis of the detector coordinate system exactly coincides with the unit vector \mathbf{e}_y in the direction of the positive y axis of the laboratory coordinate system, then the unit vector \mathbf{e}_x in the direction of the positive x axis of the detector coordinate system can be obtained by taking the cross product of \mathbf{e}_y and the vector \mathbf{e}_s , obtaining

$$\mathbf{e}_x = -\sin(2\phi_0) \mathbf{e}_z + \cos(2\phi_0) \mathbf{e}_x \quad (4.2)$$

The above relationships between the basis elements defines an orthogonal transformation relating the representations in the two coordinate systems. The relation between detector and laboratory coordinates is given by

$$\begin{pmatrix} E_{x_d} \\ E_{y_d} \\ E_{s_d} \end{pmatrix} = \begin{pmatrix} \cos(2\phi_0) & 0 & \sin(2\phi_0) \\ 0 & 1 & 0 \\ -\sin(2\phi_0) & 0 & \cos(2\phi_0) \end{pmatrix} \begin{pmatrix} E_{x_0} \\ E_{y_0} \\ E_{s_0} \end{pmatrix} \quad (4.3)$$

and in the detector coordinates the relationship for the electric field vector components is a function of the coordinates of the field in the laboratory frame given by

$$\begin{pmatrix} E_{x_0} \\ E_{y_0} \\ E_{s_0} \end{pmatrix} = \begin{pmatrix} \cos(2\phi_0) & 0 & -\sin(2\phi_0) \\ 0 & 1 & 0 \\ \sin(2\phi_0) & 0 & \cos(2\phi_0) \end{pmatrix} \begin{pmatrix} E_{x_d} \\ E_{y_d} \\ E_{s_d} \end{pmatrix} \quad (4.4)$$

since the inverse of a member of the real orthogonal group is just its transpose. Since the electric vector of the incoming wave is perpendicular to its direction of propagation, we see that if at some time we freeze the vector which Acquista ([1], p 2933) assumed to have unit length is given by

$$\mathbf{E}_0 = \cos(\alpha)\mathbf{e}_x + \sin(\alpha)\mathbf{e}_y, \quad (4.5)$$

where α is the angle between the electric vector and the x_0 axis in the laboratory frame, then, we can use our matrix relationship to deduce that

$$\begin{aligned} \begin{pmatrix} E_{x_s} \\ E_{y_s} \\ E_{z_s} \end{pmatrix} &= \begin{pmatrix} \cos(2\phi_0) & 0 & -\sin(2\phi_0) \\ 0 & 1 & 0 \\ \sin(2\phi_0) & 0 & \cos(2\phi_0) \end{pmatrix} \begin{pmatrix} \cos(\alpha) \\ \sin(\alpha) \\ 0 \end{pmatrix} \\ &= \begin{pmatrix} \cos(2\phi_0)\cos(\alpha) \\ \cos(\alpha) \\ \sin(2\phi_0)\cos(\alpha) \end{pmatrix} \end{aligned} \quad (4.6)$$

Computation of the iterate of integral operators using Fourier analysis of distributions (in the Laurant Schwartz sense) where the Fourier transform of a function which would not normally have a Fourier transform is defined in terms of its action on a smooth function which vanishes outside of a closed interval. The normal action of a function f which might very well grow at infinity on a function g which is smooth and equal to zero identically outside of a closed interval is given by

$$(f, g) = \int_{-\infty}^{+\infty} f(x)g(x)dx$$

With this definition the action of the Fourier transform of f , which by the way completely defines f in the distribution sense, on a test function g is the action of f on the Fourier transform of g , which is defined in the classical sense. The function f can not grow too fast, however, since it has to be defined on all the Fourier transforms of functions g which are smooth and vanish outside a closed interval. These computations require the analysis of the vector

$$\mathbf{X} = k_0\mathbf{e}_s - \mathbf{k}_0 \quad (4.7)$$

which in the reference frame (laboratory frame) is given by

$$\mathbf{X} = k_0(\sin(2\phi_0)\mathbf{e}_x + \cos(2\phi_0)\mathbf{e}_z) - k_0\mathbf{e}_x. \quad (4.8)$$

Note that if γ is the angle between the s_0 axis and the axis of the scattering cylinder whose direction coincides with the unit vector \mathbf{e}_s , which is the unit vector in the direction of the positive s axis of the target coordinate system and if ϕ is the angle between the projection of the target axis on the plane containing the x_0 axis and the y_0 axis, then since $(1, \phi, \gamma)$ are the spherical coordinates of the tip of the vector \mathbf{e}_s in the x_0 - y_0 - s_0 coordinate system,

$$\mathbf{e}_s = \sin(\gamma)\cos(\phi)\mathbf{e}_x + \sin(\gamma)\sin(\phi)\mathbf{e}_y + \cos(\gamma)\mathbf{e}_z \quad (4.9)$$

If we take the dot product of our vector \mathbf{X} with the vector \mathbf{e}_s , then we get the component of the vector \mathbf{X} that is parallel to the target. This is the fortran variable \mathbf{XPAR} that is used in the Drexel University code described in Haracs, L. Cohen, and A. Cohen [8] and in the paper and technical report (Cohen, L., R. Haracs, and A. Cohen ([7](page 9, equation 6)) and appearing as an argument in the pupil function u as it is used to represent the electric vector of the scattered radiation in [6] (equation 18, page 745). Taking the dot product of \mathbf{X} with the vector \mathbf{e}_s , we see that

$$\mathbf{X} \cdot \mathbf{e}_s = k_0(\sin(2\phi_0)\sin(\phi)\cos(\gamma) + \cos(\phi)(\cos(2\phi_0) - 1)) \quad (4.10)$$

is the component of \mathbf{X} parallel to the axis of the cylinder. The coding in the original Drexel program

([3]-[8]) used to calculate **XPAR** is given in the following table.

$$\boxed{\text{XPAR} = \text{XK} * (\text{SIN}(\text{TTO}) * \text{COS}(\text{GA}) * \text{SIN}(\text{PHI}) + \text{COS}(\text{PHI}) * (\text{COS}(\text{TTO}) - 1))}$$

This is calculated in subroutine **FIRST** of the Drexel program

To find the other argument **XPER** used in [7](page 9, equation 6) we make use of the coordinate transformations in the real orthogonal group developed in the previous section. Remember that the target coordinate system is derived from a knowledge of the unit vectors in the direction of their positive coordinate axes which are given by equation (4.9) and the relation

$$e_\gamma = \frac{e_x \times e_z}{|e_x \times e_z|} \quad (4.11)$$

and

$$e_x = e_\gamma \times e_z \quad (4.12)$$

The matrix equation relating **X** in laboratory coordinates to **X** in target coordinates is given by

$$\begin{pmatrix} X_x \\ X_y \\ X_z \end{pmatrix} = \begin{pmatrix} \cos(\gamma)\cos(\phi) & \sin(\gamma)\cos(\phi) & -\sin(\phi) \\ -\sin(\gamma) & \cos(\gamma) & 0 \\ \sin(\phi)\cos(\gamma) & \sin(\phi)\sin(\gamma) & \cos(\phi) \end{pmatrix} \begin{pmatrix} k_0 \sin(2\phi_0) \\ 0 \\ k_0(\cos(2\phi_0) - 1) \end{pmatrix} \quad (4.13)$$

Carrying out the multiplication on the right side of (4.13) we see that the components of the representation of the vector **X** in the cylinder axis coordinate system are given by

$$X_x = k_0(\cos(\gamma)\cos(\phi)\sin(2\phi_0) - \sin(\phi)(\cos(2\phi_0) - 1)) \quad (4.14)$$

$$X_y = k_0(-\sin(\gamma)\sin(2\phi_0)) \quad (4.15)$$

$$X_z = k_0(\sin(2\phi_0)\sin(\phi)\cos(\gamma) + \cos(\phi)(\cos(2\phi_0) - 1)) \quad (4.16)$$

Thus, we see that we got the same answer that we had before for **XPAR** and that we can now from the equations (4.14) and (4.15) express the perpendicular component of **X** simply as the norm of the vector

$$\mathbf{V} = X_x e_x + X_y e_y \quad (4.17)$$

so that the perpendicular component of **X** is given by

$$\left(X_x^2 + X_y^2 \right)^{1/2} = k_0 \left[(\cos(\phi)\cos(\gamma)\sin(2\phi_0) - \sin(\phi)(\cos(2\phi_0) - 1))^2 + (-\sin(\gamma)\sin(2\phi_0))^2 \right]^{1/2} \quad (4.18)$$

This perpendicular component of **X** is called **XPER** and appears in equation (10) of reference [6] by L. Cohen, R. Haracs, A. Cohen, and C. Acquista. The FORTRAN statements in the Drexel ([3]-[8]) computer program producing the value of **XPER** is given in the following table.

$$\boxed{\text{XPER} = \text{XK} * \text{SQRT} \left((\text{COS}(\text{PHI}) * \text{COS}(\text{GA}) * \text{SIN}(\text{TTO}) + \text{SIN}(\text{PHI}) * (\text{COS}(\text{TTO}) - 1)) ** 2 + (\text{SIN}(\text{GA}) * \text{SIN}(\text{TTO})) ** 2 \right)}$$

5. THE SCATTERED RADIATION FIELD

Observe that if we express the induced electric vector as an infinite series of vector valued functions of the form

$$\mathbf{E} = \mathbf{E}^i + \sum_{n=1}^{\infty} (n-1)^n \mathbf{E}_n \quad (5.1)$$

and substitute this into equation (1.1) and truncate higher order terms, then the approximation to the effective scattered radiation is given by the component of the vector,

$$\mathbf{E} = \frac{\exp(ik_0 r)}{r} (k_0^2 u(T(k_0(\mathbf{e}_s - \mathbf{e}_s))) (E_x A_{TE} \mathbf{e}_x + E_y A_{TE} \mathbf{e}_y + E_z A_{TM} \mathbf{e}_z)) \quad (5.2)$$

that is perpendicular to the detector direction since this is the part of the vector is used in calculating Mueller matrix entries. In the above equation the transformation T simply changes the representation of a point in laboratory coordinates to the representation of a point in the target coordinate system where the z axis coincides with the axis of the cylinder so that the action of T is simply the matrix action in the following equation

$$\begin{pmatrix} X_{x_1} \\ X_{y_1} \\ X_{z_1} \end{pmatrix} = \begin{pmatrix} \cos(\gamma)\cos(\phi) & \sin(\gamma)\cos(\phi) & -\sin(\phi) \\ -\sin(\gamma) & \cos(\gamma) & 0 \\ \sin(\phi)\cos(\gamma) & \sin(\phi)\sin(\gamma) & \cos(\phi) \end{pmatrix} \begin{pmatrix} k_0 \sin(2\phi_0) \\ 0 \\ k_0 (\cos(2\phi_0) - 1) \end{pmatrix}$$

The angles used in the above equation are defined in the following table

THE INPUT ANGLE VARIABLES AND DEFINITIONS	
$2\phi_0$	angle between x_0 axis and s_d axis
α	angle between x_0 axis and \mathbf{E}_0
γ	angle between scatterer shadow and \mathbf{e}_x
ϕ	angle between \mathbf{e}_x and \mathbf{e}_s
\mathbf{E}_0	electric vector of incoming radiation
\mathbf{E}^s	the electric vector of the scattered wave
\mathbf{e}_x	unit vector of x axis of the detector frame
\mathbf{e}_y	unit vector of y axis of the detector frame

The electric vector of the scattered radiation is approximated by equation (5.2). This vector is produced by our computer program and is enough to calculate all the entries of the amplitude scattering matrix using formulas (1.27) through (1.30). To calculate the expression on the right side of equation (5.2) we need to know that for a finite cylinder,

$$A_{TE} = \frac{2}{m^2 + 1}$$

$$A_{TM} = 1$$

and that the components E_x , E_y , and E_z are given by the relations embodied in the matrix equation,

$$\begin{pmatrix} E_x \\ E_y \\ E_z \end{pmatrix} = \begin{pmatrix} \cos(\gamma)\cos(\phi) & \sin(\gamma)\cos(\phi) & -\sin(\phi) \\ -\sin(\gamma) & \cos(\gamma) & 0 \\ \sin(\phi)\cos(\gamma) & \sin(\phi)\sin(\gamma) & \cos(\phi) \end{pmatrix} \begin{pmatrix} E_{x_0} \\ E_{y_0} \\ E_{z_0} \end{pmatrix} \quad (5.3)$$

We apply equation (5.3) when the column vector in the laboratory frame represents the electric vector of the incoming radiation polarized an angle α away from the detector plane which contains the x and s axes of the laboratory frame which means that (5.3) is used with

$$E_x = E_0(\cos(\alpha)) \quad (5.4)$$

$$E_y = E_0(\sin(\alpha)) \quad (5.5)$$

and

$$E_z = 0. \quad (5.6)$$

The parameter k_0 is given by

$$k_0 = \frac{2\pi}{\lambda} \quad (5.7)$$

and the function u is defined by

$$u(X_x, X_y, X_z) = 2\pi A^2 H \left(\frac{J_1(A\rho)}{A\rho} \right) \left(\frac{\sin(s_z H/2)}{s_z H/2} \right) \quad (5.8)$$

where

$$\rho = XPER = ((X_x)^2 + (X_y)^2)^{1/2},$$

$$s_z = X_z,$$

and X_x is given by

$$X_x = XPAR = k_0(\sin(2\phi_0)\sin(\phi)\cos(\gamma)) + \cos(\phi)(\cos(2\phi_0)-1) \quad (5.9)$$

where X_x and Y_y are coordinates of a point represented in the coordinate system whose s axis coincides with the axis of the cylinder. and the variables A , H , and the function J_1 are defined in the following table

J_1	the Bessel function of order one
A	the radius of the cylinder
H	the length (or height) of the cylinder

We will now detail the calculation of the electric vectors of the scattered radiation in the detector coordinate system and in the laboratory coordinate system; we will also express the projections of the electric vector of the incoming radiation at the target in the detector coordinate system. Assuming zero phase of the incident radiation at the target location we see that

$$E_0 \sin(\alpha) \quad (5.10)$$

Equations (5.3) - (5.6) imply that in the target coordinate system the electric vectors of the scattered radiation are given by

$$E_x^i = E_0(\cos(\alpha)\cos(\gamma)\cos(\phi) + \sin(\alpha)\sin(\gamma)\cos(\phi)) \quad (5.11)$$

$$E_y^i = E_0(-\cos(\alpha)\sin(\gamma) + \sin(\alpha)\cos(\gamma)) \quad (5.12)$$

and

$$E_z^i = E_0(\cos(\alpha)\sin(\phi)\cos(\gamma) + \sin(\alpha)\sin(\phi)\sin(\gamma)) \quad (5.13)$$

However, in order to carry out the analysis in a systematic manner we need to go from the target to the detector coordinate system. The transform relating the representation in the target coordinate system to a representation in the detector coordinate system is given by

$$\begin{pmatrix} E_{x_s} \\ E_{y_s} \\ E_{z_s} \end{pmatrix} = T \begin{pmatrix} E_{x_n} \\ E_{y_n} \\ E_{z_n} \end{pmatrix}$$

where the matrix T is defined by the relation,

$$T = \begin{pmatrix} \cos(2\phi_0)\cos(\gamma)\cos(\phi) - \sin(2\phi_0)\sin(\phi) & -\cos(2\phi_0)\sin(\gamma) & \cos(2\phi_0)\sin(\phi)\cos(\gamma) - \sin(2\phi_0)\cos(\phi) \\ \sin(\gamma)\cos(\phi) & \cos(\gamma) & \sin(\phi)\sin(\gamma) \\ -\sin(2\phi_0)\cos(\gamma)\cos(\phi) - \cos(2\phi_0)\sin(\phi) & \sin(2\phi_0)\sin(\gamma) & -\sin(2\phi_0)\sin(\phi)\cos(\gamma) + \cos(2\phi_0)\cos(\phi) \end{pmatrix} \quad (5.14)$$

The transformation described by equation (5.14) can be used to transform the natural target coordinate system representation of the electric vectors of the scattered radiation, which in turn is naturally given in terms of the target coordinate system representation of the electric vectors of the incident radiation by the equations,

$$E_{x_s}^i = \frac{\exp(ik_0 r)}{r} u(\mathbf{X}) E_{x_n} \Lambda_{TE} \quad (5.15)$$

$$E_{y_s}^i = \frac{\exp(ik_0 r)}{r} u(\mathbf{X}) E_{y_n} \Lambda_{TE} \quad (5.16)$$

$$E_{z_s}^i = \frac{\exp(ik_0 r)}{r} u(\mathbf{X}) E_{z_n} \Lambda_{TM} \quad (5.17)$$

where

$$\mathbf{X} = X_x \mathbf{e}_x + X_y \mathbf{e}_y + X_z \mathbf{e}_z \quad (5.18)$$

with

$$X_x = k_0 \cos(\gamma) \cos(\phi) X_z = k_0 (\cos(\gamma) \cos(\phi) \sin(2\phi_0) - \sin(\phi) (\cos(2\phi_0) - 1)) \quad (5.19)$$

$$X_y = -k_0 \sin(2\phi_0) \sin(\gamma) \quad (5.20)$$

and

$$X_z = k_0 \sin(2\phi_0) \sin(\phi) \cos(\gamma) + k_0 (\cos(2\phi_0) - 1) \cos(\phi) \quad (5.21)$$

This will permit us to calculate explicitly the first iteration approximation to the scattering of light by a finite length cylinder. If we are considering short fibers then the polarisation matrix elements are slightly modified by the relations

$$\Lambda_{TE} = \frac{1}{(m^2 - 1)} g_{TE} - 1 \quad (5.22)$$

and

$$\Lambda_{TM} = \frac{1}{(m^2 - 1)} g_{TM} - 1 \quad (5.23)$$

where if

$$s = \left(1 - \frac{4A^2}{H^2}\right)^{-1/2} \quad (5.24)$$

then

$$g_{TE} = \frac{s(s^2 - 1)}{2} \left[\frac{s}{s^2 - 1} - (1/2) \ln \left(\frac{s + 1}{s - 1} \right) \right] \quad (5.25)$$

and

$$g_{TM} = (s^2 - 1) \left[(s/2) \ln \left(\frac{s + 1}{s - 1} \right) - 1 \right] \quad (5.26)$$

We note that if we let the aspect ratio of the cylinders go to infinity, then g_{TE} approaches .5 and g_{TM} approaches 1 and we get the polarisation matrix entries given by

$$\Lambda_{TE} = \frac{1}{m^2 + 1} \quad (5.27)$$

and

$$\Lambda_{TM} = 1 \quad (5.28)$$

The second order integration involves an integral over six dimensional space, but as each integral is a convolution, the integration can be simplified by the use of Fourier analysis. To do this simply recognise that the Fourier transform of a convolution is the product of the Fourier transforms. The basic idea is that if we are working with a range of parameters for which the Neumann series ultimately converges, then we can be assured of the accuracy of our computations if the first and second iterations agree.

6. THE USER GUIDE

This section of the code is the user guide to the Drexel ([3]-[8]) University computer program whose theory was described in this report. The first iterate version of the code described here is valid for H to A ratios between 20 and infinity and for indices of refraction ranging from 1. to 1.3 according to studies carried out by Drexel University ([3]-[8]). The formula for getting data in that will assure reasonable results is to require that

$$\Delta\Phi = 4\pi|m - 1|(a/\lambda) \leq 2 \quad (6.1)$$

where $\Delta\Phi$ denotes a phase shift within the cylinder, a is the cylinder radius, λ is the wavelength of the incoming light in microns, and m is the index of refraction of the material in the cylinder. If inequality (5.1) is violated Drexel ([3]-[8]) found that even with the iteration of the infinite cylinder solution, there was a discrepancy between the results of the first and second iterate calculations.

We now discuss the range of parameters, the accuracy, and the comparisons among methods of computation. We have adopted in requiring inequality (5.1) the stringent requirement that the second order iteration should provide a correction of less than one percent. Since we know that (5.1) will assure us that the mapping defined by

$$f(E) = E^i - KE \quad (6.2)$$

is a contraction mapping which will mean that if we start with any trial solution such as E^i that if we get successive approximations via the calculations

$$E_{n+1} = f(E_n) \quad (6.3)$$

that the sequence of approximations E_n will ultimately converge to the correct solution of the integral equation. Thus, if the first and second iterates agree to within one percent we can be reasonably sure that the first iterate actually gave the correct answer. If the first and the second iterates did not agree, it might still be true that the second iterate gave the correct answer, but we would then have to compute a third iterate to see if the two answers were the same. It has been shown through testing that if the aspect ratio is larger than 20 ([6], pages 746-748) and inequality (5.1) is satisfied, then the first iterate and the second iterate do agree to within one percent. This code should be used in conjunction with the double iteration code if one wishes to use it as predictive tool when the ratio of the length H to the cylinder radius A is smaller than 20. One could get a shape similar to that of a cylinder by inscribing a spheroid inside the cylinder of interest. Also, Cohen et al ([6], p 748) suggest using the extended boundary condition method when using this code for predictions of scattering from cylinders whose aspect ratio (fiber length to fiber diameter) is less than 20 to validate calculations. The solution of this integral equation is exactly the solution of the standard boundary value problem for the Maxwell equations by the equivalence proof outlined in section 1 of this report in which we explain the steps needed to show that the the formulation of the scattering problem using the integral equation (1.1) is equivalent to the standard transmission problem formulation using the Maxwell equations (1.13) and (1.14) and the radiation condition (1.21). This analysis shows that the integral equation we are using is the correct one. A systematic reduction of projective approximation schemes for approximating the solutions and incident field by members of finite dimensional vector spaces to finite rank integral equations can be developed. In Holt and Shepherd [9] such a scheme is developed to predict the scattering of light by low aspect ratio cylinders. With the aid of such methods coupled with a formula for the exact value of the error, one could conceivably solve the scattering problem for cylinders of any index of refraction and any aspect ratio and at the same time know the error associated with a computer algorithm which carries out the calculation. This is not true of the program described in this report, so we need to make calculations using more than one iterate and to compare with other reliable methods of calculation.

Another possible check on the accuracy of our computer code is comparison with the Pedersen, Pedersen and Waterman code. The program developed by Pedersen Pedersen and Waterman ([15]) has been acquired and incorporated into a UNIVAC file. For long thin tungsten wires, the theory developed in [15] has been compared with experimental results. The results of this

experiment which has been described by King and Wu [14] and by Pedersen et al ([15], pp 31 - 37) agrees well with the computer predictions by a visual inspection of graphs. The tungsten wire diameters ranged from 1 to 3 mils, the frequency of the radiation was 9.375 billion cycles per second (9.375 GHz), the conductivity is considered to be infinite, and in a graph of cross section versus angle of incidence where the theory and experiment agreed well, typical values include a length to wavelength ratio of .525 and a length to diameter ratio of 660. To carry out this comparison we would have to put in a conductivity or imaginary index of refraction into the Drexell code, and run a comparison for some nearly diaphanous but dissipative cylinders where the Pedersen code is known to be valid and where the inequality (5.1) is also valid. This would probably mean consideration of a very long thin and mildly dissipative structure with cylindrical symmetry. Although no attempt has been made in [15] to provide the user with any measure of the accuracy of the output of the computer program, this could be carried out theoretically and would then make the Pedersen approach a useful benchmark because of its rapid run time and because it is not restricted to diaphanous scatterers.

We now discuss the use of the infinite cylinder code in checking possible upper aspect ratio limits of the validity of this computer program. It has been shown (Ariel Cohen et al [4], page 698) that the theory of infinite cylinders can be applied to finite cylinders if the aspect ratio is larger than 100. A class of criteria is developed where under these circumstances the infinite cylinder scattering theory agrees with experimental measurement. Specific parameters are listed in the article by Cohen et al beginning on page 1331 of volume 56 of the Journal of Applied Physics (1984). Experiments were carried out for size parameters of 71.7 and a complex index of refraction of

$$m = (12 - 60i)$$

for the case where the electric vector of the incident light was parallel to the cylinder axis. In Cohen ([5], page 746) we find that the authors indicate that they found excellent agreement between the exact result for an infinite cylinder and the finite cylinder program described in this report when the reciprocal wavelength in microns is $k_0 = 0$, the radius is .1 microns, the index of refraction satisfies $m = 1.46$, the angle between the cylinder axis and the direction of propagation of the radiation is $\phi = \pi/6$ or ϕ equals 30 degrees, and the cylinder length is 100 microns giving an aspect ratio (length to diameter ratio) of 5000.

The random orientation program described next is interactive and requests information from the user. It delivers an averaged calculation for a variety of polarizations. At the present time the polarization angles considered are produced automatically by a DO LOOP inside the program. This could be modified by editing and could be made an interactive parameter. All physical units including the wavelength of the incoming radiation are given in microns. Typical data considered would be a cylinder with a .5 micron radius, and a 20 micron length giving a 20 to one ratio, and an index of refraction of 1.25, and a wavelength of one micron. The validity has been apparently checked when the length is 20 or greater, if the radius is .5 microns so results would have to be checked by using multiple iterations in case the above conditions were not satisfied. The fixed orientation program is simpler and can be derived from the random orientation by simply removing the integration over the orientation and reading values of γ and ϕ giving the orientation of the scattering cylinder.

We can prove using the method outlined in section 1 of this report that we are solving the correct integral equation. Analysis in this report proves that the integral equation that we are working with is correct. This program implements an improvement of a classical approximation of the solution of this equation developed by many authors including Ariel Cohen of Hebrew University in Jerusalem, Leonard Cohen of Drexel University in Philadelphia, and Richard Haracs of Drexel University in Philadelphia who were involved in the writing of this computer program ([1],[3] - [8], Bohren [2], and [19]). To finish this section we provide a table of the input variables and their meaning, and the output variables.

We now explain the input of data and the use of the program. The program is on the UNIVAC of MISD of Aberdeen Proving Ground. After signing onto the UNIVAC you have to copy the file COHOON*COHEN into your directory. Running programs ab initio on the UNIVAC is fairly complex and involves bringing in all needed subroutines and the FORTRAN library. The command for running the battery of programs is

ADD COHOON*COHEN.FINITECYLCOM

The details of using the FORTRAN compiler, mapping, linking the parts of the program, the main program, which is called COHOON*COHEN.FINITECYLINT, together with its subroutines, is taken care of automatically. The program asks the user interactively to supply data. He or she should enter the data requested separated by commas with no comma at the beginning or end and then depress the RETURN key on the keyboard.

We now discuss the input data. There are two requests for data that appear on the screen. The user is expected to simply respond to the questions. We will however list the variables and their meanings in the following table.

THE FIRST REQUEST TO THE USER	
NDAY	The number of the day of the month
MONTH	The number of the month of the year
YEAR	The number of the year

The next table gives information about the cylinder properties and size, the angular frequency divided by the speed or said differently the reciprocal of the wavelength when the wavelength is given in microns, and finally the magnitude of the electric vector.

THE SECOND REQUEST TO THE USER	
XM	The index of refraction of the scatterer
A	The radius of the cylinder in microns
H	The length of the cylinder in microns
XK	The reciprocal of the wavelength in reciprocal microns
EO	The incoming wave electric vector amplitude

To conclude we give a discussion of the output of the computer program. The key output variables are TOD and ALFAD, which describe the angle between the s -axis in the laboratory frame and the line from the origin to the detector and the angle between the electric vector of the incoming wave and the x_0 axis, respectively. The output intensity variables are XI22 and XI12. The variable, XI22, denotes the intensity calculated from the component of the electric vector of the scattered radiation parallel to the x -axis of the detector coordinate system. The variable, XI12, denotes the intensity calculated from the component of the electric vector of the scattered radiation that is perpendicular to the detector plane, which we have taken to be the plane containing the x_0 axis and the s_0 axis. The vector XI22 that we have defined can be thought of as being calculated from the component of the electric vector lying in the detector plane, the plane containing the x_0 axis and the s_0 axis that is perpendicular to the line joining the center of the cylinder to the point detector. The vector e_x is the cross product of e_y and the vector e_s . The angular variables and the intensity variables are all defined succinctly in the following table. In the table I have let E_s denote the electric vector of the scattered radiation.

THE OUTPUT AS A FUNCTION OF $2\phi_0$ AND α	
TTO	angle between x_0 axis and s_0 axis
ALFAD	angle of x_0 axis and E_0
XI22	$(E_s \cdot e_x)^2$
XI12	$(E_s \cdot e_y)^2$
E_0	electric vector of incoming radiation
E_s	the electric vector of the scattered wave
e_x	unit vector of x axis of the detector frame
e_y	unit vector of y axis of the detector frame

We consider here a problem of describing the scattering of light by a randomly oriented simulated aerosol particle represented by a finite length penetrable cylinder. Since we are integrating over the intensities computed from components of the electric vector of the scattered radiation that are parallel and perpendicular, respectively, to the detector plane containing the x_0 axis and the z_0 axis, we might expect that we would get different results when the electric vector to the detector plane which corresponds to $\alpha = 0$ and when the electric vector is perpendicular to the detector plane which corresponds to $\alpha = \pi/2$. This indeed turns out to be the case and it also turns out that for certain situations we might expect the XI22 for $\alpha = 0$ to be related to XI12 for $\alpha = \pi/2$. This indeed also turns out to be the case. A detailed study of this and related observations will be the subject of a future paper. Below we find the results for the case $\alpha = 0$

THE INPUT DATA XM, R, H, XK, E				
1.3	.5	10.0	1.	1.0

SCATTERING WHEN THE E VECTOR IS IN THE DETECTOR PLANE		
$2\phi_0$	XI22	XI12
0	.128897247934833662	.00815756566906
45	.0185914912777634318	.000184963828979569811
90	.000187548797106760846	.00015064385175556076
135	.00996771143664721220	.168084054364860006
180	.0161983903023829448	.000164821002167191503

We consider in this section a fixed orientation model and analyse the results of a single and double iteration calculation. We will give in the following table a calculation outside of the known range of validity of the program to show its limitations and the need for caution in using the program to describe the scattering of light by cylinders whose size and optical parameters do not satisfy the inequality (5.1)

THE INPUT DATA XM, R, H, XK, E				
1.3	.5	5.0	1.	1.0

FIRST ORDER RESULTS			
$2\phi_0$	α	XI22	XI12
0.00	0.00	.0361906	.2782563
45.00	0.00	.0128148	.000256797
90.00	0.00	.000449405	.00224702
135.00	0.00	.00302799	.0000368551
180.00	0.00	.000375925	.00000289035

RESULTS OF TWO ITERATIONS			
$2\phi_0$	α	XI22	XI12
90.00	0.00	.000416810	.0028389
135.00	0.00	.0039106	.0000371545

There are two estimations of the scattered field. We substitute the quasistatic solution for an infinite cylinder and act on that with the integral operator K to get $E^{(1)}$. We next act on $E^{(1)}$ to get $E^{(2)}$. This type of analysis is detailed in my report on exact finite rank integral equations. One can see that Drexel is assuming that they have a contraction mapping of the form

$$f(E) = E + KE$$

and that they are seeking a vector valued function E such that

$$f(E) = E$$

What are they doing when they start with their approximate value which they say is closer to the true value than is E? Is assuming that iterates of this value will bring them closer to the true value than will the iterate of the incident field.

The program can be modified so that it can take the appropriate form of the scattered electric vector and the two values, $E^s \cdot e_s$ and $E^s \cdot e_p$, can be used to calculate all four Stokes parameters. As the polarisation of the incoming wave varies these can be used to compute Mueller matrix entries. For example, the Stokes parameter I is given by

$$I = XPAR + XPER$$

and the Stokes parameter Q is given by

$$Q = XPAR - XPER.$$

According to Bohren ([2], page 53) the program could be used to evaluate all the entries of the Mueller matrix, a matrix which describes the relationship between the four Stokes parameters of the incident wave and those of the transmitted wave. The Mueller matrix entries can be computed by making computations of the Stokes vectors of the scattered radiation for incident radiation with different polarizations. However, we will give a discussion of how to do this in a way which is in harmony with the natural interpretation of the seven independent entries of the Mueller matrix (Bohren and Huffman [2], pages 63 through 68). The Mueller matrix is a 4 by 4 matrix which provides a relationship between the incident and scattered Stokes parameters. If you simply remember that a linear transformation is completely determined by its action on a set of basis vectors, you can see that one simply has to compute the action of the scattering operator on a linearly independent set of Stokes parameters for incoming radiation. It is very interesting, however, that the seven independent parameters used in defining the Mueller matrix can be related to the response of the scatterer to unpolarized light, the response of the scatterer to right circularly polarized light, the response of the scatterer to left circularly polarized light, and the response of the scatterer to light whose polarization angle with respect to the detector plane is 45 degrees. With the present program by getting IPAR and IPER one could easily get the 2 by 2 amplitude scattering matrix relating the two projections of the incoming radiation to the two projections of the electric vectors of the scattered radiation that are parallel and perpendicular to the detector plane. The precise formulas for the entries of the amplitude scattering matrix are given in equations (1.27) through (1.30) of this report. Once these are determined, the formulas in Bohren and Huffman ([2], page 65) give all the sixteen entries of the Mueller matrix relating the Stokes parameters of the incoming and scattered radiation. The traditional analysis for unpolarized light relates the Stokes parameters I , Q , U , V , ratio to I_0 to the matrix elements via the formulas

$$\begin{aligned} \frac{I_s}{I_i} &= S_{(1,1)} \\ \frac{Q_s}{I_i} &= S_{(2,1)} \\ \frac{U_s}{I_i} &= S_{(3,1)} \\ \frac{V_s}{I_i} &= S_{(4,1)} \end{aligned}$$

One of the Mueller matrix entries can be computed directly from calculations with polarizations parallel and perpendicular to the reference plane, which can be done quite easily with the output of the present program. We find that the (1,2) entry of the Mueller matrix is given by

$$S_{(1,2)} = \frac{I_0 - I_{90}}{2I_i}$$

where I_0 is the value of scattered intensity defined by

$$I = XPAR + XPER$$

when the polarization angle of the incoming radiation is zero, and where I_{90} is the value of the scattered intensity given by the above equation when the polarization angle of the incoming radiation is 90 degrees with respect to the detector plane. The $S_{(1,4)}$ entry of the Mueller matrix is given by

$$S_{(1,4)} = \frac{I_R - I_L}{2I_i}$$

where I_R is the scattered intensity associated with right circularly polarized light, I_L is the scattered intensity associated with left circularly polarized light, and I_i is the intensity of the incident light. These quantities would be difficult to get from the program directly, but by using two polarizations to calculate all the entries of the amplitude scattering matrix by equations (1.27) through (1.30) all the entries of the Mueller matrix can be calculated from the formulas in Bohren and Huffman ([2], page 65). This indirect calculation might help us infer the results of classical scattering experiments and might therefore serve as an experimental check on our calculations. Finally, if you consider the scattering amplitudes used to calculate XPAR and XPER, respectively for the 45 degree polarization, then from the phases of the projections of the electric vectors on the unit vectors e_x , and on the unit vector e_y , and a knowledge of the entries of the scattering amplitude matrix we see that

$$S_{(1,3)} = \text{Re}(S_2 S_3^* + S_1 S_4^*)$$

where the numbers S_2, S_3 represent the entries in the first row of the scattering amplitude matrix and the numbers S_4 and S_1 denote the entries in the second row of the scattering amplitude matrix which is defined by the two equations,

$$\mathbf{E}^i \cdot \mathbf{e}_x = c(S_2(\mathbf{E}^i \cdot \mathbf{e}_x) + S_3(\mathbf{E}^i \cdot \mathbf{e}_y))$$

and

$$\mathbf{E}^i \cdot \mathbf{e}_y = c(S_4(\mathbf{E}^i \cdot \mathbf{e}_x) + S_1(\mathbf{E}^i \cdot \mathbf{e}_y))$$

where

$$c = \frac{\exp(-ik(r-s))}{ikr}$$

is a factor in the definition of the entries of the amplitude scattering matrix which causes these entries to be in some sense independent of the distance of the scatterer to the observation point. The formulas for the entries of the amplitude scattering matrix are given in equations (1.27) through (1.30) of this report.

The program which gives the single and double iteration results is listed below.

```

C MAIN PROGRAM
  REAL EO
  OPEN(UNIT = 3, FILE = 'SCATOUT.TXT', FORM = 'FORMATTED',
  1 ACCESS = 'SEQUENTIAL', STATUS = 'NEW')
  PRINT *, 'THE DATE IS'
100 FORMAT(2X, 'THE DATE IS')
  READ *, NDAY, MONTH, NYEAR
  PRINT *, NDAY, '/', MONTH, '/', NYEAR
  WRITE(UNIT = 3, FMT = 101) NDAY, MONTH, NYEAR
101 FORMAT(2X, I2, '/', I2, '/', I2)
  PRINT *, 'SCATTERING FROM A SPIRAL'
  PI = 3.14159265358979323
  AA = PI/180
C IF SECOND ORDER CONTRIBUTION IS DESIRED PUT HIER=1, ELSE PUT
C HIER = 0
  PRINT *, 'ENTER THE VALUE OF HIER, 0 FOR FIRST ORDER,'
  PRINT *, 'ENTER HIER = 1 FOR FIRST AND SECOND ORDER'
C IF SINGLE ORIENTATION CALCULATIONS ARE DESIRED, THEN SET
C ORIENT = 1 AND OTHERWISE SET ORIENT = 0 IF AN AVERAGE OVER
C ORIENTATIONS IS DESIRED.
  READ *, ORIENT
  IF (HIER.EQ.1) WRITE(UNIT=3,FMT=1010)
1010 FORMAT(2X, 'THE FIRST TWO ORDERS ARE INCLUDED')
  PRINT *, 'ENTER THE INDEX, RADIUS, HEIGHT, KO, EO'
  READ *, XM, A, H, XK, EO
  PRINT *, 'INDEX -', XM, 'RADIUS -', A, 'HEIGHT -', H
  WRITE (UNIT = 3, FMT = 103) XM, A, H
103 FORMAT(2X, 'INDEX -', XM, 'RADIUS -', A, 'HEIGHT -', H
  ALPHA = (XM**2 - 1)/(4*PI)
C ISHP = 1 (CYLINDER), ISHP = 2 (PROLATE), ISHP = 3 (OBLATE)
C ISHP = 4 (SPHERE)
  READ *, ISHP
  IF(ISHP.EQ.1) GO TO 1000
  IF(ISHP.EQ.2) GO TO 2000
  IF(ISHP.EQ.3) GO TO 3000
  IF(ISHP.EQ.4) GO TO 3500
1000 ATE = 2/(XM**2 + 1)
  ATM = 1
  GO TO 4000
2000 AE = H/2
  BE = A
  EX = SQRT(1 - (BE/AE)**2)
  DEL = 1/EX
  DEL1 = 1 - DEL**2
  DEL2 = DEL1*ALOG(DEL + SQRT(DEL**2-1)) + DEL
  ATE = 2/(2 + DEL*(XM**2 - 1)*DEL1)
  ATM = 1/(XM**2 - DEL*(XM**2-1)*DEL2)

```



```

GO TO 4000
3000 AE = A
    BE = H/2
    EX = SQRT(1 - (BE/AE)**2)
    DEL = 1/EX
    DEL1 = 1 + DEL**2
    ACOT = PI/2 - ATAN(DEL)
    DEL2 = DEL1*ACOT - DEL
    ATE = 2/(2 + DEL*(XM**2 - 1))*DEL12
GO TO 4000
3500 ATE = 3/(XM**2 + 2)
    ATM = ATE
4000 CONTINUE
    IF(ORIENT.EQ.0) WRITE(UNIT=3,FMT=777)
    IF(HIER.EQ.0) THEN
        WRITE(UNIT = 3, FMT = 778)
    ELSE
        WRITE(UNIT = 3, FMT = 779)
    ENDIF

C    ITERATION OF THE POLARIZATION ANGLE
    DO 12 I = 1,1
        ALFA = (I-1)*PI/2
C    ALFA = THE ANGLE BETWEEN THE ELECTRIC VECTOR OF THE INCOMING
C    RADIATION AND THE DETECTOR PLANE OR THE POLARIZATION ANGLE
        ALFA = (I-1)*PI/2
        ALFAD = ALFA/AA
        PRINT *, 'ANGLE OF POLARIZATION =', ALFAD
        WRITE(UNIT = 3, FMT = 345) ALFAD
345    FORMAT(4X, 'THE POLARIZATION ANGLE =', F6.2)
        IF(ORIENT.EQ.1) THEN
            PRINT *, 'ENTER ORIENTATION OF POLAR AND AZIMUTHAL ANGLES IN DEGREES'
            READ *, PHAD, GAD
            WRITE(UNIT=3, FMT = 543) PHAD, GAD
543    FORMAT(4X, 'POLAR=', F6.2, 4X, 'AZIMUTH =', F6.2)
            PHA = PHAD*AA
            GA = GAD*AA
        ENDIF
C    ITERATION OF THE SCATTERING ANGLE
        PRINT *, 'ENTER SCATTERING ANGLES +1 IN DEGREES (START,END) AND INTERVAL'
        READ 8, IAS,IAE,INT
        ANGLE = (K-1)
        TOD = ANGLE
        TTO = TOD*AA
        TO = TTO/2
        PRINT *, 'SCATTERING ANGLE =', TOD
        IF(ORIENT.EQ.1) THEN
            EOXA = EO*(COS(PHA)*COS(GA)*COS(ALFA) + COS(PHA)*SIN(GA)*SIN(ALFA))
            EOYA = EO*(-SIN(GA)*COS(ALFA)+COS(GA)*SIN(ALFA))
            EOZA = EO*(SIN(PHA)*COS(GA)*COS(ALFA)+SIN(PHA)*SIN(ALFA)*SIN(GA))
C    GET THE FIRST AND SECOND ORDER CONTRIBUTIONS TO E IN THE REFERENCE
C    FRAME
            CALL FIRST(GA, PHA, EOXA, EOYA, EOZA, TO, ATE, ATM, EO, ESAXO, ESAYO, ESAZO,
1 A, H, XK, XM, ISHP)
            IF(HIER.EQ.1) THEN
                CALL SECND(GA, PHA, EOXA, EOYA, EOZA, TO, ATE, ATM, EO, ESAX2, ESAY2, ESAZ2,
1 A, H, XK, XM, ISHP)
            ELSE
                ESAX2 = 0
                ESAY2 = 0
                ESAZ2 = 0
            ENDIF
C    WE NOW COMBINE THE FIRST AND SECOND ORDER CONTRIBUTIONS
            ESAXO = ALPHA*ESAXO + ALPHA**2*ESAX2
            ESAYO = ALPHA*ESAYO + ALPHA**2*ESAY2
            ESAZO = ALPHA*ESAZO + ALPHA**2*ESAZ2
            XI22 = (ESAXO*COS(TTO) - ESAZO*SIN(TTO))**2
            XI12 = ESAYO**2
        ELSE
            CALL AVERAGE(TO,ALFA,ATE,ATM,EO,HIER,A,H,XK,XM,XI22,XI12)
        ENDIF
        PRINT *, 'I1R = ', XI22, 'I2R = ', XI12
        WRITE(UNIT=3, FMT = 700) TOD,ALFAD,XI22,XI12
    ENDIF

```

```

PRINT *, 'I1R -', XI22, 'I2R -', XI12
700 FORMAT(4X, 'TO -', F6.2, 2X, 'ALFA -', F6.2, 2X,
1 ' I22 -', E12.6, 2X, 'I12 -', E12.6)
12 CONTINUE
777 FORMAT(4X, ' THIS IS FOR AN AVERAGE OVER ORIENTATIONS')
778 FORMAT(RX, ' THIS RESULT INCLUDES ONLY THE FIRST ORDER')
779 FORMAT(4X, ' THIS RESULT INCLUDES THE FIRST TWO ORDERS')
END
SUBROUTINE AVERAG(TO, ALFA, ATE, ATM, EO, HIER, A, H, XK, XM, XI22, XI12)
DIMENSION PT(64), WT(64), X1(3), X2(3)
PI = 3.14159265358979323
AA = PI/180

X1(1) = 0
X1(2) = 0
X1(3) = 0
X2(1) = 0
X2(2) = 0
X2(3) = 0
N = 20
CALL GAUSS(PT, WT, N)
ALPHA = (XM**2 - 1)/(4*PI)
NN = 20
CALL GAUSS(PT, WT, N)
NN = 20
N1 = 1
N2 = 2
N3 = 1
DE = 0
IF(N1.EQ.3) DE = 0.01D0
C ITERATION OF RANGE
DO 11 IRANGE = N1, N2, N3
IF(IRANGE.EQ.3) NN = 1
C ITERATION OF AZIMUTHAL ANGLE
DO 11 I = 1, N
GA = PI*PT(I)
GAD = GA/AA
PB = ATAN(TAN(TO)/COS(GA))
C ITERATION ON THE POLAR ANGLE
DO 11 J = 1, N
GA = PI*PT(I)
GAD = GA/AA
PB = ATAN(TAN(TO)/COS(GA))
C ITERATION ON THE POLAR ANGLE
DO 11 J = 1, NN
IF(IRANGE.EQ.2) GO TO 77
IF(IRANGE.EQ.3) GO TO 79
PHA = (PB - DE)*PT(J)
GO TO 78
77 PHA = (PI - PB - DE)*PT(J) + (PB + DE)
GO TO 78
79 PHA = PB
78 CONTINUE
EOXA = EO*(COS(PHA)*COS(GA)*COS(ALFA) + COS(PHA)*SIN(GA)*SIN(ALFA))
EOYA = EO*(-SIN(GA)*COS(ALFA) + COS(GA)*SIN(ALFA))
EOZA = EO*(SIN(PHA)*COS(GA)*COS(ALFA) + SIN(PHA)*SIN(ALFA)*SIN(GA))
C THE FIRST AND SECOND ORDER CONTRIBUTIONS TO E IN THE REFERENCE FRAME
CALL FIRST(GA, PHA, EOXA, EOYA, EOZA, TO, ATE, ATM, EO, ESAXO, ESAYO, ESAZO,
1 A, H, XK, XM)
IF(HIER.EQ.1) THEN
CALL SECND(GA, PHA, EOXA, EOYA, EOZA, TO, ATE, ATM, EO, ESAX2, ESAY2, ESAZ2,
1 A, H, XK, XM)
ELSE
ESAX2 = 0
ESAY2 = 0
ESAZ2 = 0
ENDIF
C COMBINATION OF THE FIRST AND SECOND ORDER CONTRIBUTIONS
ESAXO = ALPHA*ESAXO + ALPHA**2*ESAX2
ESAYO = ALPHA*ESAYO + ALPHA**2*ESAY2
ESAZO = ALPHA*ESAZO + ALPHA**2*ESAZ2
XI = (XK/EO)**2
IF(IRANGE.EQ.1) FAC = SIN(PHA)*WT(J)*(PI*(PB-DE))
IF(IRANGE.EQ.2) FAC = SIN(PHA)*WT(J)*(PI - PB - DE)*PI
IF(IRANGE.EQ.3) FAC = (SIN(PHA)**2/SIN(TO))*WT(I)*PI*2.0*DE

```

```

X2(IRANGE) = XI*(ESAXO*COS(TTO) - ESAZO.SIN(TTO))**2*FAC
1 + X2(IRANGE)
X1(IRANGE) = XI*ESAYO**2*FAC + X1(IRANGE)
11 CONTINUE
X122 = (X2(1) + X2(2) + X2(3))/(2*PI)
X112 = X1(3)/(2*DE)
IF(N1.EQ.3) THEN
X122 = X2(3)/(2*DE)
X112 = X1(3)/(2*DE)
ENDIF
RETURN
END
SUBROUTINE GAUSS(PT,WT,N)
DIMENSION PT(64),WT(64),PTT(64),WTT(64)
WT(1) = 0.1527533871

WT(2) = 0.1491729864
WT(3) = 0.1420961093
WT(4) = 0.140961093
WT(5) = 0.1181945319
WT(6) = 0.1019301198
WT(7) = 0.0832767415
WT(8) = 0.0626720483
WT(9) = 0.0406014298
WT(10) = 0.0176140071
PT(1) = 0.0765265211
PT(2) = 0.2277858511
PT(3) = 0.3737060887
PT(4) = 0.5108670019
PT(5) = 0.6360536807
PT(6) = 0.7463319064
PT(7) = 0.8391169718
PT(8) = 0.9122344283
PT(9) = 0.9639719272
PT(10) = 0.9931285991
N2 = N/2
DO 7 I = 1,N2
PTT(I) = PT(I)
WTT(I) = WT(I)
7 CONTINUE
DO 5 I = 1,N
IF(I.GT.N/2) GO TO 13
PT(I) = (1 - PTT(N/2 + 1 - I))/2
WT(I) = WTT(N/2 + 1 - I)/2
5 CONTINUE
RETURN
END
FUNCTION BESS1(X)
SIGN = X/ABS(X)
X = ABS(X)
IF(X.GT.3) GO TO 10
Y = (X/3)**2
Z = X*(0.5-0.56249985*Y+.21093573*Y**2 - 0.3954289E-1*Y**3 +
1 0.443319E-2*Y**4 - 0.31761E-3*Y**5 + .1109E-4*Y**6)
GO TO 20
10 Y = 3/X
F1 = 0.79788456 +.156E-5*Y +.1659667E-1*Y**2 +.17105E-3*Y**3 -
1 0.249511E-2*Y**4 + 0.113653E-2*Y**5 - 0.20033E-3*Y**6
T1 = X-2.3561945+0.12499612*Y +0.565E-4*Y**2 -0.637879E-2*Y**3
1 0.74348E-3*Y**4 + 0.79824E-3*Y**5 - .29166E-3*Y**6
Z = F1*COS(T1)/SQRT(X)
20 X = SIGN*X
C23456789012345678901234567890123456789012345678901234567890123456789012
BESS1 = SIGN*Z
RETURN
END
FUNCTION U(XPAR,XPER,A,H,XK,ISHP)
P = SQRT(XPAR**2 + XPER**2)
IF(ISHP.EQ.1) GO TO 1000
IF(ISHP.EQ.2) GO TO 2000

```

```

IF(ISHP.EQ.3) GO TO 3000
IF(ISHP.EQ.4) GO TO 3500
1000 X = XPAR*A*XK
Y = XPER*A*XK
C = ABS(X)
B = ABS(Y)
IF(X.LT.0.001) XA = 1 - X**2/6 + X**4/120
IF(C.GE.0.001) XA = SIN(X)/X
IF(B.LT.0.001) XB = (1 - Y**2/8 + Y**4/192)*.5
IF(B.GE.0.001) XB = BESS1(Y)/Y
V = 3.14159265358979323*A**2*H
U = 2*V*XA*XB
GO TO 4000
2000 AE = H/2
BE = A
EX = SQRT(1.0 - (BE/AE)**2)
X = AE*SQRT(P**2 - (EX*XPER)**2)
U = 4.0*3.14159265358979323*BE*AE**2*(SIN(X) - X*COS(X))/X**3
C234567890123456789012345678901234567890123456789012345678901234567890
GO TO 4000
3000 AE = A
BE = H/2
EX = SQRT(P**2 - (EX*XPAR)**2)
U = 4.0*3.14159265358979323*BE*AE**2*(SIN(X) - X*COS(X))/X**3
GO TO 4000
3500 X = A*P
U = 4.0*3.13149265358979*A**3*(SIN(X) - X*COS(X))/X**3
4000 CONTINUE
RETURN
END
SUBROUTINE DETEC(TTO,XXO,YYO,ZZO,XOP,YOP,ZOP)
XCP = (XXO*SIN(TTO) + ZZO*COS(TTO))*SIN(TTO) - XXO
YOP = -YYO
ZOP = (XXO*SIN(TTO) + ZZO*COS(TTO))*COS(TTO) - ZZO
RETURN
END
SUBROUTINE FIRST(G,PHI,EX,EY,EZ,TO,ATE,ATM,EO,ESX,ESY,ESZ,
1 A,H,XKO,XM,ISHP)
XK = XKO
TTO = 2*TO
XPAR = (SIN(PHI)*COS(G)*SIN(TTO)+COS(PHI)*COS(TTO)-COS(PHI))
XPAR = XPAP*XKO
XPER = SQRT((COS(PHI)*COS(G)*SIN(TTO) - SIN(PHI)*COS(TTO) +
1 SIN(PHI))**2 + (SIN(G)*SIN(TTO))**2)*XKO
U1 = U(XPAR,XPER,A,H,XK,ISHP)
CONST = XK**2*U1
XX = EX*ATE
YY = EY*ATE
ZZ = EZ*ATM
EXX = COS(PHI)*COS(G)*XX-SIN(G)*YY+SIN(PHI)*COS(G)*ZZ
EYY = COS(PHI)*SIN(G)*XX+COS(G)*YY+SIN(PHI)*SIN(G)*ZZ
EZZ = -SIN(PHI)*XX + COS(PHI)*ZZ
C THE PORTION OF E PERPENDICULAR TO THE SCATTERED DIRECTION IS
C EXTRACTED.
CALL DETEC(TTO,EXX,EYY,EZZ,ESX,ESY,ESZ)
ESX = ESX*CONST
ESY = ESY*CONST
ESZ = ESZ*CONST
RETURN
END
SUBROUTINE SECND(G,PHI,EX,EY,EZ,TO,ATE,ATM,EO,ESX,ESY,ESZ
1 A,H,XKO,XM,ISHP)
DIMENSION FX(3),FY(3),FZ(3),PT(64),WT(64),PP(64),WW(64)
TTO = 2*TO
XK = XKO
DO 44 I = 1,3

```

```

FX(I) = 0.0
FY(I) = 0.0
FZ(I) = 0.0
N = 20
NN = 20
C2345678901234567890
XEP = .001
PI = 3.14159265358979323
CALL GAUSS(PT,WT,N)
CALL GAUSS(PP,WW,NN)
XKX = -XK*SIN(PHI)
XKY = 0.
XKZ = XK*COS(PHI)
RX = COS(PHI)*COS(G)*SIN(TTO) - SIN(PHI)*COS(TTO)
RY = -SIN(G)*SIN(TTO)
RZ = SIN(PHI)*COS(G)*SIN(TTO) + COS(PHI)*COS(TTO)
FTOTX = 0
FTOTY = 0
FTOTZ = 0
DO 100 I = 1,NN
PRINT *,I
DO 90 J = 1,N
THP = PT(J)*PI
DO 90 K = 1,N
PIP = 2*PI*PT(K)
DO 85 II = 1,3
IF(II.EQ.1) P = (PP(I)*(XK-XEP) + XEP)+XK
IF(II.EQ.2) P = XK - (PP(I)*(XK - XEP)+XEP)
IF(II.EQ.3) P = 2*XK/PP(I)
PX = P*SIN(THP)*COS(PIP)
PY = P*SIN(THP)*SIN(PIP)
PZ = P*COS(THP)
PDA2 = PX*EX + PY*EY
PDB2 = PZ*EZ
X1X = PX + RX*XK
X1Y = PY*RY*
X1Z = PZ*RZ*XK
X2X = -PX + SIN(PHI)*XK
X2Y = -PY
X2Z = -PZ - COS(PHI)*XK
X1PAR = X1Z
X1PER = SQRT(X2X**2 + X1Y**2)
X2PAR = X2Z
X2PER = SQRT(X2X**2 + X2Y**2)
U2 = U(X2FAR,X2PER,A,H,XK,IXHP)
FAC = 2.*PI**2
FAC1 = XK**2*ATE**2 + ATE*(1-ATE)/(XM**2 - 1)*(P**2 - XK**2)
FAC2 = XK**2*ATM**2 + ATM*(1 - ATM)/(XM**2 - 1)*(P**2-XK**2)
FAC3 = ATE**2*PDA2+ATM**2*PDB2
XF = 1.0
IF(II.EQ.3) XF = P**2
FX(II) = SIN(THP)*U1*U2*P**2/(P**2 - XK**2)*(FAC1*EX
1 - FAC3*PX)*WW(I)*WT(J)*WT(K)*FAC*XF
FY(II) = SIN(THP)*U1*U2*P**2/(P**2 - XK**2)*(FAC1*EY - FAC3*PY)*
1 WW(I)*WT(J)*WT(K)*FAC*XF
85 CONTINUE
IF(J.EQ.1.AND.K.DEQ.1) THEN
PRINT *, FX(1),FX(2),FX(3)
PRINT *, FY(1),FY(2),FY(3)
PRINT *, FZ(1),FZ(2),FZ(3)
ENDIF
FTOTX = (XK - XEP)*(FX(1) + FX(2))
1 + 1./(2.0*XK)*(FX(3) + FTOTX
FTOTY = (XK - XEP)*(FY(1)+FY(2))
1 + 1./(2.0*XK)*FY(3) + FTOTY
FTOTZ = (XK - XEP)*(FZ(1)+FZ(2))

```

```

1 + 1./(2.0*XK)*FZ(3) + FTOTZ
IF((J.EQ.1).AND.(K.EQ.1)) PRINT *, FTOTX, FTOTY, FTOTZ
90 CONTINUE
100 CONTINUE
C23456789012345678901234567890123456789012345678901234567890
PRINT *, FTOTX, FTOTY, FTOTZ
EXX = COS(PHI)*COS(G)*FTOTX - SIN(G)*FTOTY+
1 SIN(PHI)*COS(G)*FTOTZ
EYY = COS(PHI)*SIN(G)*FTOTX - COS(G)*FTOTY+
1 SIN(PHI)*SIN(G)*FTOTZ
EZZ = -SIN(PHI)*FTOTX + COS(PHI)*FTOTZ
PRINT *, EXX, EYY, EZZ
CALL DETEC(TTO, EXX, EYY, EZZ, ESX, ESY, ESZ)
ESZ = ESZ*XK**2/(2*PI**2)
ESY = ESY*XK**2/(2*PI**2)
ESX = ESX*XK**2/(2*PI**2)
PRINT *, ESZ, ESY, ESX
RETURN
END

```

8. REFERENCES

1. Acquista, Charles. Light scattering by Tenuous Particles: a generalisation of the Rayleigh-Gans-Rocard approach. *Applied Optics* Volume 15, Number 11 (November, 1976) pp 2932-2936
2. Bohren, Craig F. and Donald R. Huffman. *Absorption and Scattering of Light by Small Particles*. New York: John Wiley and Sons(1983)
3. Cohen, Ariel, Leonard D. Cohen and Richard D. Haracs. Angular scattering distributions by long copper and brass cylinders: experiment and theory. *Journal of Applied Physics* Volume 56 Number 5 (September 1, 1984) pp 1329-1332
4. Cohen, Ariel, Leonard D. Cohen, and Richard D. Haracs. Double Scattering by Randomly Oriented Long Cylinders. *Journal of Applied Physics* Volume 57. Number 3 (February 1, 1985) pp 698-703
5. Cohen, Ariel, Richard D. Haracs, and Leonard D. Cohen. Asymmetry factors for randomly oriented infinite cylinders. *Journal of Applied Physics* Volume 58. Number 3 (August 1, 1985) pp 1135-1140
6. Cohen, Leonard D., Richard D. Haracs, Ariel Cohen, and Charles Acquista. Scattering of Light from Arbitrarily Oriented Finite Cylinders. *Applied Optics*. Volume 22, Number 5 (March 1, 1983) pp 742-748
7. Cohen, Leonard D., Richard D. Haracs, and Ariel Cohen. *Electromagnetic Scattering Properties of Finite Cylinders and Spheroids* CRDC-CR-85041 Aberdeen Proving Ground, Maryland 21010-5423: U.S. Army Armament, Munitions and Chemical Command (November, 1985)
8. Haracs, Richard D., Leonard D. Cohen, and Ariel Cohen. Scattering of Linearly Polarized Light from Randomly Oriented Cylinders and Spheroids. *Journal of Applied Physics*. Volume 58 Number 9 (November 1, 1985) pp 3322-3327
9. Holt, A. R. and J. W. Shepherd. Electromagnetic Scattering by Dielectric Spheroids in the Forward and Backward Directions. *Journal of Applied Physics A. Math. Gen.* Volume 12 (1979) pp 159-165
10. Holt, A. R. Some Factors Affecting the Remote Sensing of Rain by Polarization Diversity Radar in the 3 to 35 Gigahertz Range *Radio Science* Volume 19, Number 5 (September-October 1984) pp 1399-1412
11. Holt, A. R. Acoustic, Electromagnetic and Elastic Wave Scattering: Focus on the T-matrix approach IN Varadan, V. V. and V. K. Varadan (eds) *Scattering Theory* (1980) pp 255-268
12. Ishimaru, A. *Wave Propagation and Scattering in Random Media*. Volume 1. New York: Academic Press(1978) p. 205
13. Kerker, Milton. *The Scattering of Light and Other Electromagnetic Radiation*. New York: Academic Press (1969)
14. King, R. W. and T. T. Wu. *The Scattering and Diffraction of Waves*. Cambridge, Massachusetts: Harvard University Press (1959)
15. Pedersen, Norman E., Jeanne C. Pedersen, and Peter C. Waterman. Final Report on Theoretical Study of Single and Multiple Scattering by Cylinders. CRDC-CR-86014 (a Chemical Research and Development Center Technical Report) Aberdeen Proving Ground, Maryland 21010-5423 U. S. Army Armament, Munitions, and Chemical Command (April, 1985)
16. Ras, S. and J. A. Lewinsohn. Scattering and Absorption by a Thin, Finite Dielectric Cylinder. *Applied Physics* 22 (1980) pp 61-69
17. Reintjes, John F. *Nonlinear optical parametric processes in liquids and gases*. New York: Academic Press (1984)

18. Stratton, Julius. *Electromagnetic Theory*. New York: McGraw Hill (1941)
19. Usunoglu, N. K., B. G. Evans, and A. R. Holt. Scattering of Electromagnetic Radiation by Precipitation Particles and Propagation Characteristics of Terrestrial and Space Communications Systems. *Proceedings Inst. Electr. Eng.* Volume 124 (1977) pp 417-424
20. Usunoglu and A. R. Holt. The Scattering of Electromagnetic Radiation from Dielectric Scatterers. *Journal of Physics A. Math. Gen.* Volume 10, Number 3 (1977) pp 413-424
21. van de Hulst, H. C. *Light Scattering by Small Particles*. New York: John Wiley and Sons, Inc. (1957)
22. Wait, J. R. Exact Surface Impedance for a Cylindrical Conductor. *Electr. Lett.* 15 (1979) pp 659-660
23. Wilton, Donald R. and Raj Mittra. A New Numerical Approach to the Calculation of Electromagnetic Scattering Properties of Two-Dimensional Bodies of Arbitrary Cross Section. *IEEE Transactions on Antennas and Propagation*, Volume AP-20, Number 3 (May, 1972) pp 310-317

Blank

Determination of Molecular Orientation at the Surface of an Aerosol Particle
by
Morphology Dependent Photoselection.

L.M. Folan and S. Arnold

Microparticle Photophysics Laboratory (MP³L)
Polytechnic University
333 Jay St., Brooklyn, N.Y. 11201

RECENT PUBLICATIONS, SUBMITTALS FOR PUBLICATION AND PRESENTATIONS:

- A. L.M. Folan, S. Arnold and S.D. Druger, Enhanced Energy Transfer within a Microparticle, Chem. Phys. Lett. 118, 322(1985).
- B. S. Arnold and L.M. Folan, A Fluorescence Spectrometer for a Single Electrodynamically Levitated Microparticle, Rev. Sci. Inst. 57, 2250(1986).
- C. L.M. Folan, Optical depth probing in a microparticle, Bull. Amer. Phys. Soc. 32, 605 (1987).
- D. S.D. Druger, S. Arnold, and L.M. Folan, Theory of Enhanced Energy Transfer between Molecules Embedded in Spherical Dielectric Microparticles, J. Chem. Phys. 87, 2649 (1987).
- E. S. Arnold, and L.M. Folan, A Spherical Void Electrodynamical Levitator, Rev. Sci. Inst. (to be published, Sept., 1987).
- F. L.M. Folan and S. Arnold, Determination of Molecular Orientation at the Surface of an Aerosol Particle by Morphology Dependent Photoselection, Opt. Lett. (Submitted August, 1987)

ABSTRACT

The orientation of fluorescent molecules on the surface of an aerosol particle has been determined for the first time by using a new technique, Morphology Dependent Photoselection. The excitation spectrum of the angularly averaged fluorescence from a single levitated particle is measured using an integrating sphere levitator. By utilizing the relative intensities of resonant peaks in this spectrum and knowledge of the polarization properties of different resonances we show that one may arrive at the orientation of molecules relative to the surface normal.

In this paper we report the first determination of the orientation of molecules on the surface of a spherical, micron sized particle. The method, referred to as Morphology Dependent Photoselection (MDPS), is based on photoselection¹ and the properties of the natural electromagnetic resonances of small dielectric particles.

Recently we reported the experimental observation of enhanced energy transfer between molecular species in liquid particles^{2,3}. To further investigate energy transfer a probe to the spatial distribution of active molecules was required. The probe was needed to ensure that segregation or aggregation do not occur in the particles and to allow investigation of systems where the molecules of interest are confined to the surface of the particle. The fluorescence excitation spectrum of a particle provides such a probe.

Fluorescence excitation spectra of fibers were reported by Owen et al⁴ and resonant features in emission spectra from spherical particles by Benner et al⁵, but no attempt has been made until the current work to derive specific information about the distribution and orientation of the fluorescent molecules from the spectra. In what follows we will show that through an understanding for the relative amplitude of various resonances one can gain information about the homogeneity of absorbers in the particle, and if the active molecules are at the particle surface, the orientation of the molecular absorption moment with respect to the surface normal can be inferred. The work described below involved applying an insoluble, surface active fluorescent dye to a glycerol sphere, measuring a fluorescence excitation spectrum of the composite particle and comparing the measurements with model calculations.

A schematic diagram of the experimental apparatus is shown in Fig. 1.

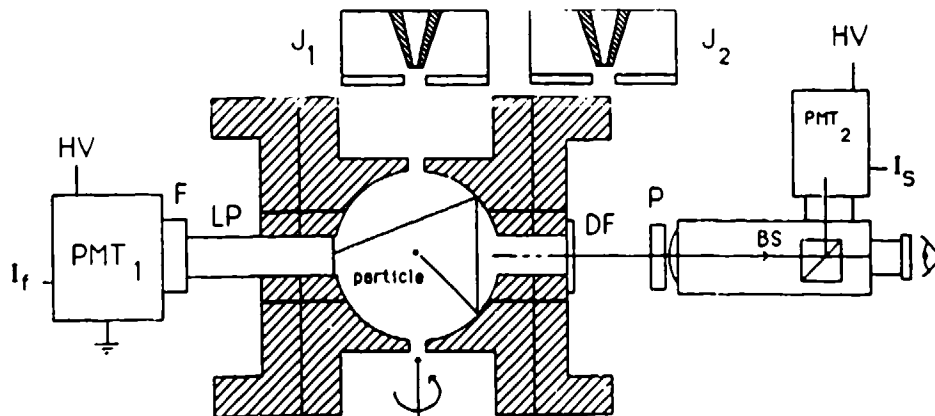


Fig. 1 A schematic diagram of the experimental apparatus.

The spherical void electrodynamic levitator (SVEL) uses a combination of dynamic and static forces to stably levitate single particles⁶. The electrode configuration was chosen so that once the interior surface is coated with a high diffuse reflector (Kodak product 6080) the SVEL becomes a nearly ideal integrating sphere. The integration significantly increases the signal level at the detector, and the signal magnitude obtained is proportional to the total cross-section for the scattering process (either elastic or inelastic). This is a key advantage in the present work. The total cross-section for fluorescence scattering is expected to be proportional to the particle's absorption cross-section, and (as we will show) it is the particle's absorption spectrum which enables us to determine the orientation of surface active molecules.

The excitation beam provided by a tunable cw dye laser was circularly polarized. Circular polarization was used to eliminate any possible azimuthal bias in the angular integration. The elastically scattered light was collected through a short pass dielectric filter ($\lambda_{\text{pass}} < 600 \text{ nm}$ (DF)) using a telescope (T) with F/6 optics. A polarizer (P) was used to select radiation polarized parallel to the scattering plane. For the small acceptance angle used in the experiments the elastic scattering spectrum near 90° is dominated by TM resonances. The integrated fluorescence signal was collected with a 1/8 inch glass light pipe (LP) and detected through a combination of dielectric and colored glass filters (F) with a photomultiplier tube (PMT). Fluorescence excitation and the elastic scattering spectra were recorded simultaneously in order to identify the type of mode (TM or TE) responsible for the resonances seen in the fluorescence excitation spectrum.

For a possible surface active species we chose DII(5). The molecule has a hydrophilic chromophore (dicarbocyanine head group) and hydrophobic aliphatic chains (two C_{18} tails). DII(5) and its homologue DII(3) (carbocyanine head group) have successfully been used to prepare Langmuir-Blodgett films on water⁷, and therefore DII(5) is expected to remain on the surface of a polar liquid like glycerol.

A glycerol particle was produced, charged and pushed in to the SVEL using the picopipette J_1 as described previously⁸. The pipette J_2 containing a 10^{-5} M DII(5) solution in chloroform was then positioned above the SVEL in place of J_1 . A chloroform particle was injected into the SVEL and made to collide with the levitated glycerol particle. The collision

was assisted by making the charge on the chloroform particle opposite to and smaller than the charge on the glycerol particle. When a collision occurred the particle was seen to recoil and DII(5) fluorescence was detected. The chloroform evaporated rapidly leaving a composite DII(5)-glycerol particle.

Fig.2 shows the integrated fluorescence excitation spectrum (upper spectrum) and 90° scattering for a composite particle 5.4μ in radius.

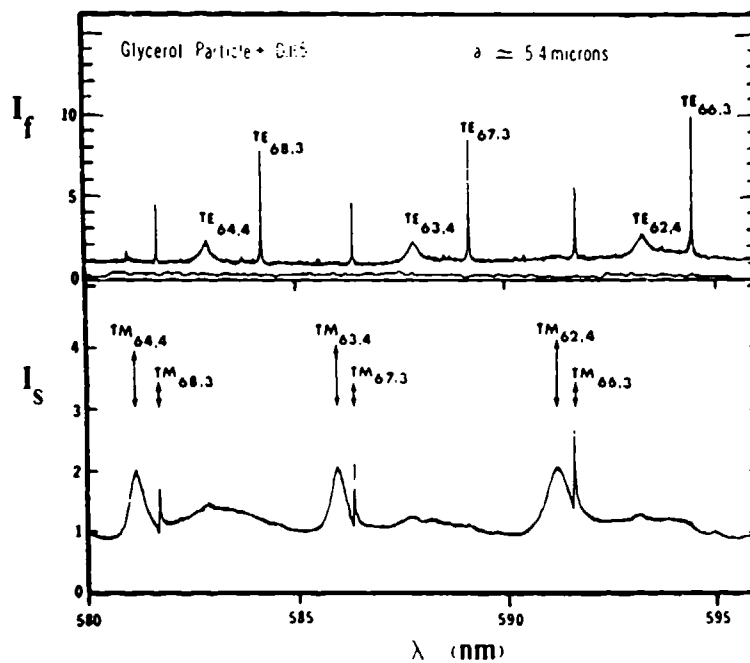


Fig.2 Fluorescence excitation (upper curve, labeled I_f) and 90° in plane polarized elastic scattering (lower curve, labeled I_s) of a 5.4μ micron radius glycerol particle with a submonolayer coating of the fluorescent dye DII(5).

The elastic scattering spectrum was used to size the particle through a procedure similar to that of Chylek et al⁹. Resonant modes found in the process are characterized by their generic class (TE or TM) and by mode numbers, n , and orders, s (e.g., $TE_{n,s}$). Allowances were made in the fit for a small amount of scattered light polarized perpendicular to the scattering plane

(due to imperfect alignment of the polarizer) and a small change in the particle radius due to evaporation. The primary thing to note in the excitation spectrum is that the TE resonances are systematically more intense than the TM resonances of the same number and order, and that both third (sharp) and fourth (broad) order resonances are present.

The excitation spectrum was modelled as follows. The angularly integrated fluorescence intensity was assumed to be proportional to the power absorbed by the particle. Since the power absorbed by a single molecule is in proportion to $|\mu \cdot E(\underline{r})|^2$, where μ is the absorptive transition moment, the power absorbed by the entire particle will be proportional to $\sum_{i=1}^N |\mu_i \cdot E(\underline{r}_i)|^2$, where N is the total number of absorbing molecules. The first step in

evaluating this sum is to consider the orientation of a molecule at a particular point \underline{r} within the particle. For a soluble material in a liquid there will be no preferred orientation and the angle between the transition moment and the field may be averaged over; in this bulk-random case the absorption spectrum will be in proportion to the volume average of $|E(\omega, \underline{r})|^2$, $\langle |E(\omega, \underline{r})|^2 \rangle_V$. In the case of absorbers confined spatially to the surface there are two major possibilities, the molecules may be randomly oriented with respect to the surface normal or they may take a specific orientation. In the surface-random case the molecular orientation at any particular position on the surface may once again be averaged out as in the bulk-random case and the absorption spectrum will be in proportion to the surface average of the square modulus of the field at the surface, $\langle |E(\omega, r=a)|^2 \rangle_S$. Finally, in the case of molecules which are orientated preferentially so that their absorptive moment is at an angle θ_m relative to the surface normal, one may only average over the orientation of the projection of the absorptive moment in the plane of the surface. In this circumstance the absorption spectrum will follow

$$\langle E_r^2(\omega, r=a) \rangle_S \cos^2 \theta_m + \langle E_t^2(\omega, r=a) \rangle_S \sin^2 \theta_m / 2, \quad (1)$$

where $E_t^2(\omega, r=a) = E_\theta^2(\omega, r=a) + E_\phi^2(\omega, r=a)$ and the factor of 1/2 in the second term expresses the fact that the in plane component of the absorption moment is equally likely to lie along a meridian or parallel of the sphere. In the surface-oriented(s-o),

surface-random(s-r) and bulk-random(b-r) cases the local fields were calculated from Mie theory.¹⁰ One gains an appreciation for the photoselection idea in examining Eqn.1 for a particular case. Since only TM modes have radial fields a molecule with a radial absorptive moment ($\theta_m=0$) cannot be excited by a TE mode, and thus all TE resonances would be absent in an absorption spectrum although the TM resonances would be strong

In analyzing the data in Fig.2 computations of the frequency dependences of $\langle |E(\omega, D)|^2 \rangle_V$, $\langle |E(\omega, r=0)|^2 \rangle_S$, and expression 1 were made using the particle radius (5.44 μ) and refractive index (1.470) obtained from the elastic scattering spectrum and incorporating the laser linewidth reported by the manufacturer (0.025nm). Calculations of the resonant peak height (peak height above the non resonant background) were performed for the resonances $TE_{68,3}$, $TM_{68,3}$, $TE_{64,4}$ and $TM_{64,4}$, using wavelength intervals of 0.0025 nm and averaging 10 points around the peak of interest. The loss due to the absorbers was included using an effective bulk imaginary part of the refractive index (κ). The κ value was determined by forcing the calculated peak height ratio $TE_{68,3}/TE_{64,4}$ to match the data. The ratios $TE_{68,3}/TM_{68,3}$ and $TE_{64,4}/TM_{64,4}$ were then used to decide whether the model calculations agreed with the experiment.

The bulk-random case gave values for the peak height ratios $TE_{68,3}/TM_{68,3}$ which were close to unity in sharp disagreement with the data. The $TE_{68,3}/TE_{64,4}$ ratio was found to be very sensitive to the κ value used in the calculations while the $TE_{68,3}/TM_{68,3}$ and $TE_{64,4}/TM_{64,4}$ ratios were found to be quite insensitive. Supplementary experiments using the highly soluble dye Sulforhodamine 101 yielded excitation spectra whose peak ratios were easily fit using the bulk random model. This led us to conclude that the Dil(S) molecules are not homogeneously distributed in the particle bulk.

In the surface random case the $TE_{68,3}/TM_{68,3}$ and $TE_{64,4}/TM_{64,4}$ ratios were again incompatible with the data and insensitive to choice of the effective κ value. Calculations were then performed for the surface oriented case. Expressions for the intensity ratios for a particular mode pair are easily obtained from Expression 1, for example

$$\frac{I(\text{TE}_{68,3})}{I(\text{TM}_{68,3})} = \frac{\langle E_t^2(\text{TE}_{68,3}, r=a) \rangle_S \sin^2 \theta_m / 2}{\langle E_r^2(\text{TM}_{68,3}, r=a) \rangle_S \cos^2 \theta_m + \langle E_t^2(\text{TM}_{68,3}, r=a) \rangle_S \sin^2 \theta_m / 2} \quad (2)$$

The sensitivity of the ratio to the molecular orientation θ_m in Eqn.2 is clearly seen. Had we taken a ratio of TE modes such as $\text{TE}_{68,3}/\text{TE}_{64,4}$ the dependence on θ_m would have dropped out since neither TE mode has any radial field component. This is especially useful since the $\text{TE}_{68,3}/\text{TE}_{64,4}$ ratio is very sensitive to κ and this sensitivity has been used in determining the effective κ value. On this basis we have computed both the $\text{TE}_{68,3}/\text{TM}_{64,3}$ and $\text{TE}_{68,4}/\text{TM}_{64,4}$ ratios as a function of molecular orientation, θ_m , and these computations are presented in Fig.3.

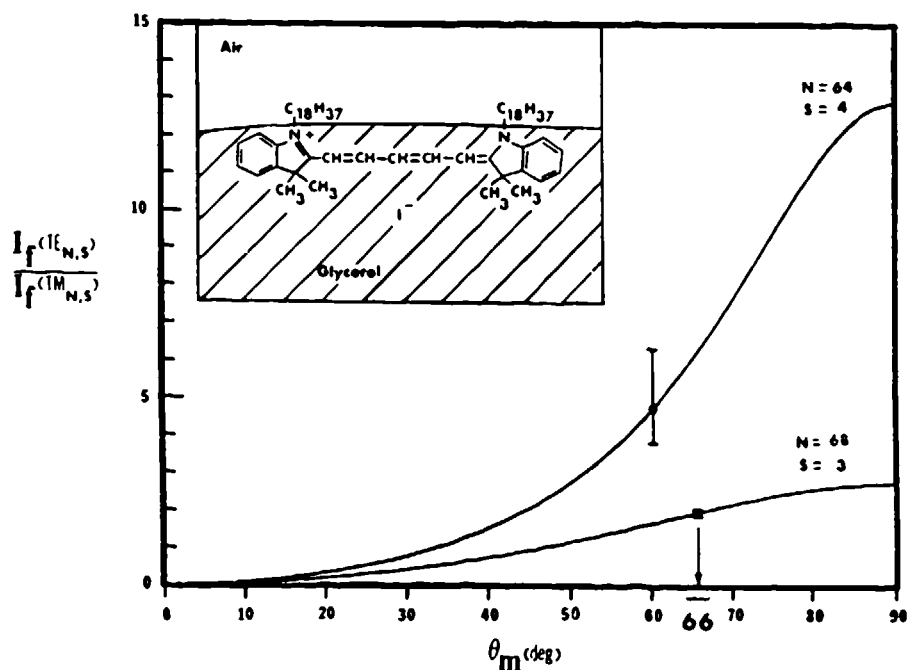


Fig.3 A plot of the theoretical fluorescence ratios $\text{TE}_{68,3}/\text{TM}_{68,3}$ and $\text{TE}_{64,4}/\text{TM}_{64,4}$ as a function of θ_m for $\kappa = 8 \times 10^{-6}$. The two points with error bars show the experimentally observed ratios for the data shown in Fig 2.

The two points with error bars indicate the measured ratios from Fig. 2. The $TE_{68,3}/TM_{64,3}$ data point yields an angle $\theta_m = 66^\circ \pm 2^\circ$. The $TE_{68,4}/TM_{64,4}$ point yields a less precise value for θ_m but the two determinations agree within experimental uncertainty.

The experimental results for the DII(5)-glycerol system are consistent with a model system in which the absorption moments make an angle of $66^\circ \pm 2^\circ$ with the surface normal ($24^\circ \pm 2^\circ$ from the surface).

Studies with the homolog DII(3) have shown that its emission moment is parallel to the conjugated bridge of the molecule and that the absorption moment makes an angle approx. 28° with the emission moment¹¹. Direct comparison of fluorescence depolarization by DII(3) and DII(5) at our laboratory indicates that the angle between the emission and absorption moments in the two homologues is the same to within a few degrees. Therefore the angle with the tangent determined from Morphologically Dependent Photoselection (MDPS) of $24^\circ \pm 2^\circ$ indicates that the conjugated bridge lies approximately in the surface plane consistent with our expectations. Thus it appears that MDPS is a realistic means for arriving at the orientation of molecules on the surface of a microparticle for those cases in which one knows the orientation of electronic transition moments relative to the molecule.

The spectral method described above is general in the sense that it can be extended to any other optical process whose rate is determined by the Fermi Golden Rule and for which a dipole approximation may be made. Photoemission is another such process for which sensitive experiments can be made and for which we are currently investigating the use of MDPS.

We are grateful for the cooperative support of the National Science Foundation and the Chemical Research Development and Engineering Center (CRDEC) of the Army through ATM-84-13574. One of us (L.M.F.) was supported in part by the US Joint Services Electronics Contract No. F49620-82-C-0084.

REFERENCES

1. A.C. Albrecht, J. Mol. Spec. 6, 84 (1961).
2. L.M. Folan, S. Arnold and S.D. Druger, Chem. Phys. Letters 118, 322 (1985).
3. S.D. Druger, S. Arnold and L.M. Folan, J. Chem Phys. 87, 2649 (1987).
4. J.F. Owen, P.W. Barber, P.B. Dorian and R.K. Chang, Phys. Rev. Letts. 47, 1075 (1981).

5. R.E. Benner, P.W. Barber, J.F. Owen and R.K. Chang, Phys. Rev. Lett. 44, 475 (1980).
6. S. Arnold and L.M. Folan, Rev. Sci. Instr. (in press).
7. A. Ruudol-Teixier and M. Vandevyver, Thin Solid Films 68, 129 (1980)
8. S. Arnold and L.M. Folan, Rev. Sci. Instrum. 57, 2250 (1986).
9. P. Chylek, V. Ramaswamy, A. Ashkin and J.M. Dziedzic, App! Opt. 22, 2302(1983).
10. "Absorption and Scattering of Light by Small Particles", C.F. Bohren and D.R. Huffman, John Wiley, New York 1983, Chapter 4.
11. D. Axelrod, Biophys. J. 26, 557 (1979).

Blank

Theory of Enhanced Energy Transfer Between
Molecules Embedded in Spherical Dielectric Particles

Stephen D. Druger
Materials Research Center and Department of Chemistry
Northwestern University, 2145 Sheridan Road, Evanston, IL 60201

Stephen Arnold, Lorcan M. Folan
Department of Physics and Institute for Imaging Science
Polytechnic University, 333 Jay Street, Brooklyn, NY 11201

RELEVANT PUBLICATIONS:

A) S. D. Druger and P. J. McNulty, Radiation Pattern of Fluorescence from Molecules Embedded in Small Particles: General Case, Appl. Opt. 22, 75 (1983).

B) S. D. Druger and P. J. McNulty, Radiation Pattern of Raman Scattering from Randomly-Oriented Molecules In or Near Small Particles, Phys. Rev. A29, 1545 (1984).

C) L. M. Folan, S. Arnold, and S. D. Druger, "Enhanced Energy Transfer Within a Microparticle", Chem. Phys. Lett. 118, 322 (1985).

D) S. D. Druger, S. Arnold, and L. M. Folan, "Theory of Enhanced Energy Transfer Between Molecules Embedded in Spherical Dielectric Particles", J. Chem. Phys., J. Chem. Phys. 87, 2649 (1987).

ABSTRACT

The effects of morphological resonances on intermolecular energy transfer and molecular fluorescence within an aerosol droplet are studied by developing and applying a theory based on electromagnetic solutions for a dielectric sphere, leading to results in terms of measurable spectral quantities for the donor and acceptor molecules separately in the bulk host medium. Mie resonances in droplets of about ten μm diameter are predicted to cause only moderate changes in the integrated radiative rate, while strongly enhancing the rate and quantum efficiency of energy transfer. Additional results obtained argue further for the role of Mie resonances in the recently-observed energy-transfer enhancement, and provide insight into the energy-transfer mechanism. Our results can now be applied in more-detailed calculations and in combined experimental/theoretical studies of enhanced energy transfer through Mie resonances. Parts of the theory describing fluorescence can be extended and employed in studies of interest with regard to fluorescent remote sensing.

This work results from a theoretical/experimental collaborative interaction between research efforts at Northwestern and at New York Polytechnic Universities; here we give an overview emphasizing new theoretical results.

I. INTRODUCTION

An improved understanding of molecular photophysical processes near the surface of an aerosol droplet is of intrinsic scientific interest as well as having practical value in obscuration science and in developing methods of remote sensing by fluorescent Lidar.

Experimental studies have shown that proximity to a *metallic* surface can strongly affect molecular photophysical processes¹⁻³ Proximity effects of this kind, while perhaps surprising at first glance, are implied^{4,5} by the way in which the presence of the interface modifies the appropriate boundary conditions and therefore the states of the electromagnetic field (including the vacuum states) thereby changing the electromagnetic interactions responsible for processes such as spontaneous emission and Raman scattering. Proximity to a dielectric (i.e., nonconducting) surface might be expected to have far smaller effects.

Experimental evidence has recently been found, however, for a very strong effect of surface proximity on energy transfer between molecules in a small dielectric droplet.⁶ The specific case in point⁶ is that of coumarin (C1) donors mixed with rhodamine 6G (R6G) acceptors in a glycerol host droplet (of about 10 μ m diameter). The coumarin is excited at wavelengths short enough for the R6G absorption to be small. Once excited, the C1 molecule relaxes internally and then either fluoresces or else transfers energy via dipole-dipole interaction to the R6G, which then relaxes and fluoresces.

For the bulk sample, the energy transfer is found essentially proportional to the acceptor concentration. But in an aerosol droplet of about 10 μ m diameter, the essential experimental results are:

- (1) The fluorescence (observed from a wavelength region where R6G fluorescence dominates) is essentially proportional to the C1 donor

concentration, but shows almost no dependence on the acceptor concentration.

- (2) At the lowest acceptor concentrations, the energy transfer is enhanced by a factor of $\sim 10^2$ relative to the bulk.
- (3) The lowest concentrations for which such effects are observed is about 10^{-7} molar.
- (4) Furthermore, the spectrum is in a regime where there are many sharp peaks attributable to the effect of Mie resonances in either the C1 or R6G [plus glycerol droplet] systems. In the combined C1+R6G [plus glycerol droplet] system, there is a noticeable weakening of the peaks in the region of maximum spectral overlap between C1 (donor) emission and R6G (acceptor) absorption, as would be expected if energy transfer is depleting the populations of excited donors in some regions of the droplet.

A goal of the theoretical work summarized here has been to explore the mechanisms apparently responsible for these effects. Although the small area under the narrow resonance emission peaks might make enhanced energy transfer via Mie resonances seem unlikely, we have already proposed that the experimental data are evidence for such a mechanism.⁶ Our arguments were based on the analogy between Mie resonances and cavity resonances.

Present theoretical efforts are now aimed at developing and applying a detailed analysis of the enhanced transfer effect based on electromagnetic solutions for an actual dielectric particle. The effects of the Mie resonances on energy transfer and on the competing process of fluorescence without transfer are both considered, and so the present research also contains inherent parts of our current theoretical work on fluorescence from molecules on and within an aerosol droplet.

II. NEW THEORETICAL RESULTS

We consider an initially-excited donor molecule embedded at location \vec{r}' within a continuous dielectric sphere containing a uniform distribution of acceptors. We seek to find the effect of Mie resonances of the dielectric sphere on:

- (1) energy transfer by the donor to all available acceptors, and
- (2) fluorescence by the donor into the far zone.

For energy transfer, we start from the Fermi golden rule for transition rates between each initial state consisting of the donor excited and the acceptor unexcited, coupled by dipole-dipole interactions to final states in which the donor is unexcited and the acceptor excited. More specifically, we use the rate (ultimately to be summed over all transitions)

$$w_{\text{tr}} = (2\pi/\hbar) |\vec{\mu}_d \cdot \vec{T} \cdot \vec{\mu}_a|^2 \delta(E_f - E_i)$$

where

$$\vec{\mu}_d = \langle \Phi_{df} | \sum_j e \vec{r}_j | \Phi_{di} \rangle$$

is the dipole moment for the transition from the donor in state $|\Phi_{di}\rangle$ to the donor in state $|\Phi_{df}\rangle$ (with a similar expression for the acceptor transition moment μ_a); also $E_f - E_i$ is the net change in total energy of the donor-acceptor pair, \vec{T} is the usual dipole-dipole interaction tensor in free space with (μ, ν) components given by

$$T_{\mu\nu} = (3X_\mu X_\nu - R^2 \delta_{\mu\nu}) / R^5,$$

where $\vec{R} = (X_1, X_2, X_3)$ is the distance vector between donor and acceptor.

Two issues involving important physical aspects of the problem are especially noteworthy. First, the presence of the interface modifies the dipole-dipole interaction H' , and the first issue is to determine the modified interaction. Second, important physical features enter into the specific way of summing over all transitions that contribute to the net transfer.

First, in free space, in the near zone, the matrix element of the dipole-dipole interaction has exactly the same form as the interaction energy between two classical oscillators, except that the dipole moments (i.e., $\vec{\mu}_D$ and $\vec{\mu}_A$) of the classical oscillators are replaced by quantum mechanical transition dipole matrix elements. The geometrical tensor \vec{T} is the same, however. Now, for the classical problem, the existence of the interface leads to an interaction still of the form $\vec{\mu}_D \cdot \vec{T} \cdot \vec{\mu}_A$, but with a modified geometrical tensor \vec{T} determined by solution of the electromagnetic boundary problem (i.e., with $\vec{T} \cdot \vec{\mu}_D$ giving the field at \vec{r} produced by the classical dipole at point \vec{r}'). Our ansatz for the quantum case is then to use the same classical \vec{T} that has been modified by the presence of the dielectric interface. This amounts to a semi-classical approximation in which the molecule is treated quantum mechanically, but the dielectric and the electromagnetic field are treated classically.

Second, the summation over transitions in the golden rule formula involves a physical constraint and a physical assumption. The constraint, overlooked in much of the previous fluorescence work, is that there is only one photon to be dissipated statistically through all final channels after a given initial excitation. We incorporate this constraint using a physical assumption of rapid relaxation to an equilibrium distribution of excited vibrational and electronic states between initial excitation and either fluorescence or energy transfer--the same equilibrium distribution⁷ as for the molecule in bulk. The constraint and assumption are combined (in the summation over all transitions for transfer) by expressing the combination of dipole matrix elements and initial occupation probabilities of donor states that occurs in terms of the experimentally observable spectral shape function for donor emission $f(ka)$, where $f(ka) d(ka)$ is the relative probability for

emission in wavenumber range $(k, k+dk)$ with a the radius of the droplet and with $\int f(ka) d(ka) = 1$. The quantum-mechanical dipole matrix elements for the acceptor are similarly expressed in terms of the experimentally observable extinction coefficient $\alpha(k)$ at the given wavenumber k . Thus, the resulting expressions are in terms of quantities found experimentally from the pure-donor emission spectrum in bulk and the pure-acceptor spectrum in bulk, rather than computed using the necessarily approximate methods of quantum chemistry.

The miscellaneous ingredients of the theory include averaging over all molecular orientations, and integrating formally over acceptor distributions (we hold the donor location \vec{r}' fixed, being interested in the averaged transition rates and branching ratios for a specific donor location). The result is an integral over wavenumbers that exhibits the usual sharp peaks at the Mie resonances. We sum the integrals over these peaks formally using a Lorentzian approximation (taking the peaks to be narrow).

All this leads to immense analytical simplification compared with the intermediate results. The Mie contributions to the transfer, measured relative to the free radiative rate, occur as sums over resonant wavenumbers k_0 for E-type and M-type resonances,

$$\frac{W'_{tr}}{W_{rad}} = N \pi \left[\frac{4\pi a^3}{3} \right] \left[\frac{3|n_1|^5}{8} \right] \\ \times \left\{ \sum_{k=k_0(E; l1)}^{\infty} k^2 f(ka) \alpha(k) \frac{|F_E^{(l)}|^2}{\gamma_0(E; l1)} \frac{A[|I_l(n_1 ka)|]}{(2l+1)} A[|j_l(n_1 kr')|^2] \right. \\ \left. + |n_1|^4 \sum_{k=k_0(M; l1)}^{\infty} (2l+1) k^2 f(ka) \alpha(k) \frac{|F_M^{(l)}|^2}{\gamma_0(M; l1)} |I_l(n_1 ka)| |j_l(n_1 kr')|^2 \right\}$$

Each E-type or M-type resonance at a corresponding wavenumber k_0 is labelled by indices (ℓ, i) which indicate the i^{th} resonance for mode number ℓ (where actually ℓ also labels the spherical harmonic $\bar{Y}_{\ell\ell m}$ of the multipole expansion term that gives rise to the resonance). The F, A, and I coefficients are combinations of spherical Bessel functions j_ℓ and Hankel functions $h_\ell^{(1)}$ whose specific form is not important in the overview being presented here, γ_0 denotes the width of the corresponding resonance, a is the radius of the droplet, and n_1 is its complex refractive index. The important features to note are (1) the spectral overlap between donor emission $f(ka)$ and acceptor extinction $\alpha(k)$ that tends to maximize transfer in the region of maximum spectral overlap, and (2) the occurrence of the inverse width γ_0 of the resonance, which tends to maximize transfer from the narrowest resonances, as we have previously argued⁶ was expected on the basis of the cavity analogy.

For fluorescence, we follow much the same procedure as in obtaining the rate for energy transfer, except that we use the photon emission rate from a classical oscillator divided by the energy $\hbar\omega$ of the photon rather than the Fermi golden rule, multiplying also by the well-known classical-to-quantum conversion factor for the dissipated power. The result

$$\frac{W'_{\text{rad}}}{W_{\text{rad}}} = \frac{\pi}{2} \left\{ \sum_{k=k_0(E; \ell i)}^{\infty} \frac{|n_1|^4}{(ka)^2} \frac{|G_E(\ell)|^2}{\gamma_0(E; \ell i)} f(ka) A[|j_\ell(n_1 kr')|^2] + \sum_{k=k_0(M; \ell i)}^{\infty} \frac{(2\ell+1)}{(ka)^2} \frac{|n_1|^2}{|n_2|^4} \frac{|G_M(\ell)|^2}{\gamma_0(M; \ell i)} f(ka) |j_\ell(n_1 kr')|^2 \right\}$$

has the same dependence on inverse width of the resonance. (Here the G coefficients are specific combinations of spherical Bessel functions and

spherical Hankel functions.) Also, each resonance has precisely the same radial dependence on donor location as for energy transfer.

III. COMPARISON WITH EXPERIMENT

To apply these results, we first estimate the imaginary part of the refractive index $\text{Im}(n_1)$ from experimental extinction data to be $\approx 10^{-6}$ at (fairly high) acceptor concentrations of 10^{-5} molar, and smaller at lower concentrations. Experimental data shows the maximum spectral overlap between donor emission and acceptor absorption to occur at $ka \approx 57$, corresponding to $l \approx 76$, so that resonances in this ka range produce the main contribution to the transfer. We have carried out fairly thorough studies of the resonances up to and somewhat beyond the relevant ka values and find, in particular, that the resonance widths are generally small and comparable in value for the first two orders but a factor of ten or more wider for higher orders. Under conditions where the imaginary part of the refractive index $\text{Im}(n_1)$ is smaller still, the first-order resonances for relevant ka values become even narrower (i.e., γ_0 becomes about a factor of 10^{-3} smaller than for second order resonances).

A. Cutoff concentration of the enhancement effect

To estimate the lowest acceptor concentration above which the transfer via Mie resonances leads to the enhanced energy-transfer effect, we consider a radial location r' of the donor that maximizes the effect of Mie resonances in both the energy transfer and fluorescence, and use representative experimental values of the parameters in our expressions for the fluorescence and energy-transfer rates. We find that the Mie contribution to the fluorescence rate $W'_{\text{rad}}/W_{\text{rad}}$ (i.e., relative to the rate in bulk) is given approximately by $3 \times 10^{-2} m$ where m is the number of resonance peaks that contribute (≈ 50). This is not negligible, but is still only of order 1 or

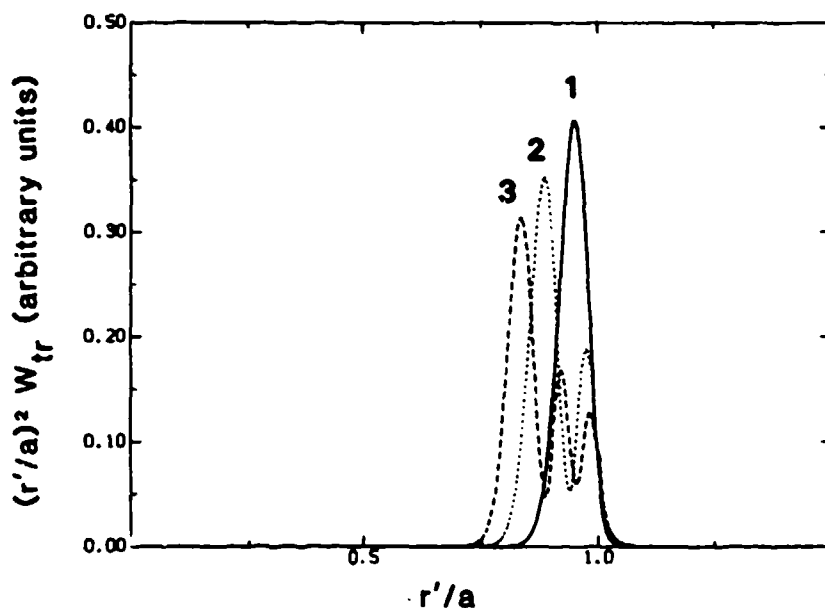


Fig. 1. Angular-averaged coupling of an electric dipole to an $l = 76$ E-type mode as a function of fractional radial position r'/a in and near an aerosol droplet of refractive index $1.47 + 10^{-7}i$, for resonances of orders 1, 2, and 3.

so. Although the particle environment affects the fluorescence rate also by means other than the Mie resonances, these effects are again not expected to be very profound. For energy transfer, however, we obtain a Mie resonance contribution that is proportional to the acceptor concentration and which is $\gg 1$ down to acceptor concentrations less than 10^{-7} molar [when $\text{Im}(n_1)$ is negligible, the contribution is $\gg 1$ down to 10^{-10} molar]. Then at radial donor locations near where the Mie resonance contribution is maximized, the branching ratio between energy transfer and fluorescence is predicted to be almost unity for all acceptor concentrations above this cutoff limit.

B. Dependence on donor location

The specific radial dependence on donor location (for a uniform acceptor distribution) is the same for the Mie resonance contributions to both fluorescence and energy transfer. It is plotted in Fig. 1 for a typical mode both inside and outside the droplet, and represents the coupling of a transition dipole to the Mie resonance of the particle. The enhanced-transfer effect is seen to be predicted for donors in a shell below the surface comprising about 15% of the volume. Actually, the same is true for acceptors, except that the dependence on acceptor radial location has been disguised by integrating over the uniform acceptor distribution.

Figure 1 also provides a physical explanation of why the enhanced-transfer effect occurs; namely, the coupling between two dipoles through the Mie resonance is enhanced for both dipoles in the active region, thereby enhancing the dipole-dipole transfer, but there is no comparable enhancement of the coupling between a dipole emitter anywhere inside the sphere to a dipole detector in the far zone, so that fluorescence is not similarly enhanced.

C. Estimate of the enhancement factor

We estimate the enhancement by estimating the branching ratios for transfer (with donor fluorescence as the competing process) both in the particle and in the bulk. The ratio of these two branching ratios gives the enhancement factor.

In the bulk, we assume that all excitation is transferred if an acceptor happens to fall within a critical distance ($R_0 \approx 50 \text{ \AA}$) but otherwise leads to donor emission. The probability of transfer is then the probability that an acceptor lies within a distance R_0 from the donor at the given acceptor

concentration. In the particle, all donors in the active region are assumed to transfer successfully, while all others deactivate by fluorescence.

The enhancement factor obtained as the ratio of the two branching ratios obtained under these assumptions is about 400 at 10^{-6} molar, in rough agreement with experiment.

D. Concentration dependence

An understanding of the concentration dependence then follows by a similar argument. If all donors in the active region transfer energy while all others fluoresce, there would be no dependence on acceptor concentration. Actually, the donors in the interior have a weak residual probability of ordinary Forster transfer, which depends linearly on acceptor concentration. The overall effect should be a weak dependence on acceptor concentration, which is what is actually observed.

E. Long-range character of the enhancement effect

Finally, Fig. 2 shows a typical dependence on relative location of the

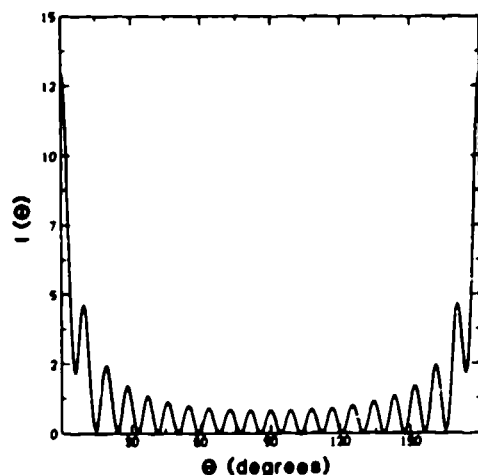


Fig. 2. Dependence of the Mie-resonance transfer rate on relative donor/acceptor position with both donor and acceptor on the same annular shell for $l = 20$, where θ is the angle between the donor/acceptor radius vectors. The plot for an $l = 75$ resonance is similar, except for the larger number of oscillations.

energy transfer rate through a single Mie resonance for donor and acceptor on the same annular shell, as computed from our theory for annular shells both inside and outside the sphere. Dipoles at diametrically opposite points of the shell are seen to produce the same Mie-resonance transfer-rate contribution as do nearby points. The long-range character of the Mie-enhanced transfer to distant points that are not diametrically opposite to the donor also becomes apparent.

IV. SUMMARY AND CONCLUSIONS

Our theoretical work on the enhanced energy-transfer effect now provides a quantitative treatment based on actual solutions for a dielectric sphere. While further and more quantitative work remains to be done in applying the present methodology and results to experiment, the present work leads already to a number of conclusions:

- (1) We obtain theoretical confirmation that enhanced transfer via Mie resonances should be the dominant contribution for a substantial region of the dielectric droplet.
- (2) Estimates are obtained in agreement with experiment for the enhancement factor and for the acceptor-concentration cutoff.
- (3) The Mie enhanced contribution is predicted to be long range in character.
- (4) A clearer picture than before emerges of how the transfer occurs, as well as a more general criterion possibly applicable to nonspherical geometries. Specifically, the enhancement is seen to result from enhanced coupling between the electromagnetic modes of the particle and a dipole at points within a localized active region, without comparably-enhanced coupling at dipole locations in the far zone.
- (5) The theory leads to quantitative expressions that can now be used and extended for further application and for use in more-detailed experimental studies.

The theoretical work reported here involves not only development of a theory of Mie-resonance effects on dipole-dipole energy transfer (which indirectly affect observed fluorescence), but also extension of previous work on

fluorescence by molecules near dielectric particles without dipole-dipole energy transfer. We expect our future theoretical efforts to build upon the present work in applications to fluorescence as well as in applications to energy transfer.

REFERENCES

1. A review is given, e.g., by R. R. Chance, A. Fock, and R. Silbey, *Advan. Chem. Phys.* **37**, 1 (1978).
2. D. Kleppner, *Phys. Rev. Lett.* **47**, 233 (1981).
3. M. Moskovits, *Rev. Mod. Phys.* **57**, 783 (1985).
4. G. Barton, *J. Phys.* **B7**, 2134 (1974).
5. E. Power and T. Thirunamachandran, *Phys. Rev.* **A25**, 2473 (1982).
6. L. M. Folan, S. Arnold, and S. D. Druger, *Chem. Phys. Lett.* **118**, 322 (1985).
7. See, e.g., J. B. Birks, *Organic Molecular Photophysics*, (Wiley, London, 1973), vol. I, p. 98 ff.

Blank

RAPID ACQUISITION OF RAMAN SPECTRA FROM OPTICALLY LEVITATED PARTICLES

G. Moncivais, J. C. Carls, and J. R. Brock
Chemical Engineering Department
University of Texas, Austin, Texas 78712

RECENT PUBLICATIONS, SUBMITTALS FOR PUBLICATION AND PRESENTATIONS:

1. J. C. Carls and J. R. Brock, "Explosion of a water droplet by pulsed laser heating", *Aerosol Sci. Tech.* 7,79-91 (1987).
2. S. G. Kim and J. R. Brock, "Growth of ferromagnetic particles from cation reduction by borohydride ions" *J. Colloid Int. Sci.* 116,431-443 (1987).
3. J. R. Brock and J. Oates, "Moment simulation of aerosol evaporation", *J. Aerosol Sci.* 18,59-64 (1987).
4. J. R. Brock, D. Zehavi and P. J. Kuhn, "Formation and growth of binary aerosol in a laminar coaxial jet", *J. Aerosol Sci.*, In Press.
5. S. C. Davies and J. R. Brock, "Laser evaporation of droplets", *Appl. Opt.* 26,786-793 (1987).
6. S. C. Davies and J. R. Brock, "Laser propagation through an evaporating polydisperse aerosol", *Appl. Opt.* 26,1865-1876 (1987).
7. S. G. Kim and J. R. Brock, "Aerosol growth and dynamics" in R. Kohl, Ed., *Proceedings of the 1986 CRDEC Scientific Conference on Obscuration and Aerosol Research*, R. H. Kohl and Assoc., 1987.
8. J. C. Carls and J. R. Brock, "Laser induced explosion of particles", in R. Kohl, Ed., *Proceedings of the 1986 CRDEC Scientific Conference on Obscuration and Aerosol Research*, R. H. Kohl and Assoc., 1987.
9. S. C. Davies and J. R. Brock, "Laser evaporation of droplets", in R. Kohl, Ed., *Proceedings of the 1986 CRDEC Conference on Obscuration and Aerosol Research*, R. H. Kohl Assoc., 1987.
10. Y. L. Chen, J. R. Brock, and I. Trachtenberg, "Aerosol jet etching of fine patterns", *Appl. Phys. Lett.*, In Press.
11. A. Dove and J. R. Brock, "Sulfate aerosol modeling using the EPA Philadelphia Aerosol Field Study", U. S. Environmental Protection Agency Report, 200 pp. 1987.
12. J. C. Carls and J. R. Brock, "Explosive vaporization of a single water droplet by pulsed laser radiation", Abstract AAAR Annual Meeting, Seattle, September 1987.
13. H. Kosuge and J. R. Brock, "Aerosol evolution in jets expanding into low pressure regions", Abstract AAAR Annual Meeting, Seattle, September 1987.
14. J. C. Carls and J. R. Brock, "Laser induced explosion of water droplets by laser radiation", Workshop on Physics of Directed Energy Propagation in the Atmosphere, Las Cruces, N. M., January 1987.
15. J. R. Brock, "Formation and Growth of Ferromagnetic Particles", Department of Physics, University of Paris at Orsay, January 1987.
16. J. R. Brock, "Aerosol Formation and Growth", University of Paris VIII Val de Marne, January 1987.
17. J. R. Brock, "A Complex Terrain Model for Aerosol Dispersion", Chemical Modeling Conference, CRDEC, August 1987.

ABSTRACT

An optical levitation and rapid scan spectrometer system has been developed which makes it possible to obtain accurate Raman spectra on single suspended particles in times of the order of 1 - 10 sec. and to track prominent Raman peaks in times in the range 0.1 - 1 sec. Experimental Raman spectra obtained with this system are presented for levitated glass microspheres and for bulk and suspended particles of dioctylphthalate and glycerol. In addition to the Raman bands, sharp peaks appear in the levitated particle spectra which are attributed to partial wave electromagnetic resonances.

INTRODUCTION

Recently there has been much interest in microprobe spectroscopy -- obtaining spectra from very small sample volumes. A number of investigators have reported Raman spectra obtained from single particles suspended by optical levitation^{1,2}. The ideal arrangement for Raman particle studies would be for the particle to be free of any supports and for it to be perfectly centered in the middle of a laser focus where the highest light intensity is found. These requirements are met by the technique of optical levitation, pioneered by Ashkin and coworkers at the Bell Laboratories. Here we report our first studies of Raman spectroscopy of optically levitated particles with an experimental arrangement that permits a considerable decrease in the time for acquisition of complete spectra over that previously reported^{1,2}; these previous times have been in the range of 10 -100 minutes while in our experiments useful acquisition times smaller than 1 second are possible. It should be pointed out, however, that our wavenumber resolution at these small times is much less than those achieved in these references^{1,2}.

PROCEDURE

The experimental arrangement for our studies is shown schematically in Fig. 1. The basic components of our system are a Spectra Physics 165 argon ion laser, 0.22 m SPEX monochromator, TN6500 Tracor Northern Rapid Scan Spectrometer, optical cell and collection and focussing optical elements. The light emitted from a particle captured in the optical focus in the suspension cell was collected at 90° using a 5X microscope objective. A Raman notch filter was placed between the microscope and the monochromator to eliminate the laser line and the signal was focussed into the spectrograph. In most of our experiments, an argon ion laser beam was used at around 250 mW operating at 488 nm in the TEM₀₀ mode. Droplets were also suspended using the 514.5 nm line and it was found that particle capture and suspension were facilitated at the longer wavelength.

With proper alignment of the optical system, it was relatively easy to capture particles. In experiments using 30 μm glass spheres, the spheres were introduced through a tube above the focal point of the laser beam. Liquid droplets were produced by aspiration into a chamber above an opening to the cell.

RESULTS

Raman spectra were obtained for bulk dioctylphthalate (DOP), bulk glycerol, and levitated particles of DOP, glycerol, and glass microspheres. Fig. 1 shows a comparison between the bulk DOP and a ~30μm suspended DOP particle. Fig. 2 is a similar comparison for bulk glycerol and a ~30μm glycerol particle. In both cases some of the Raman assignments³ are shown above the peaks for the bulk spectra. It can be seen that the agreement in the Raman peaks between bulk and particle phases is good. However, the suspended particles exhibit sharp peaks that are absent in the bulk spectra. These may be associated with the partial wave electromagnetic resonances reported in the literature^{1,2}. Fig. 3 shows the spectrum of a 30μm suspended glass microsphere; the peaks shown here correspond to those already reported for suspended glass microspheres².

The time necessary to acquire the spectra shown here varied from 1 - 10 seconds. This is in contrast to the previously reported times which varied from tens of minutes for glass microspheres² to hours for DOP particles¹. It should be pointed out, however, that the resolution in these experiments was far superior to ours; much, but not all, of the fine structure attributed to partial wave electromagnetic resonances is not observed in our spectra.

Here we have demonstrated the capability of obtaining accurate Raman spectra on a time scale significantly smaller than has been previously reported. This permits observation of transient chemical phenomena in suspended particles such as surface reactions, diffusion and reaction in particles, and chemical changes in particles induced by laser radiation. We plan to report work along these lines in the near future.

ACKNOWLEDGMENT

This work was supported under contract DAAK-83-K-0006 from CRDEC, U. S. Army.

REFERENCES

1. R. Lattieri and R. E. Preston, *Opt. Commun.* **54**, 349-352 (1985).
2. R. Thurn and W. Kiefer, *Appl. Spectrosc.* **38**, 78-83 (1984).
3. J. G. Grasselli and N. M. Richter, Eds. *Atlas of Spectral Data and Physical Constants of Organic Compounds*, CRC Press, Cleveland, 1975.

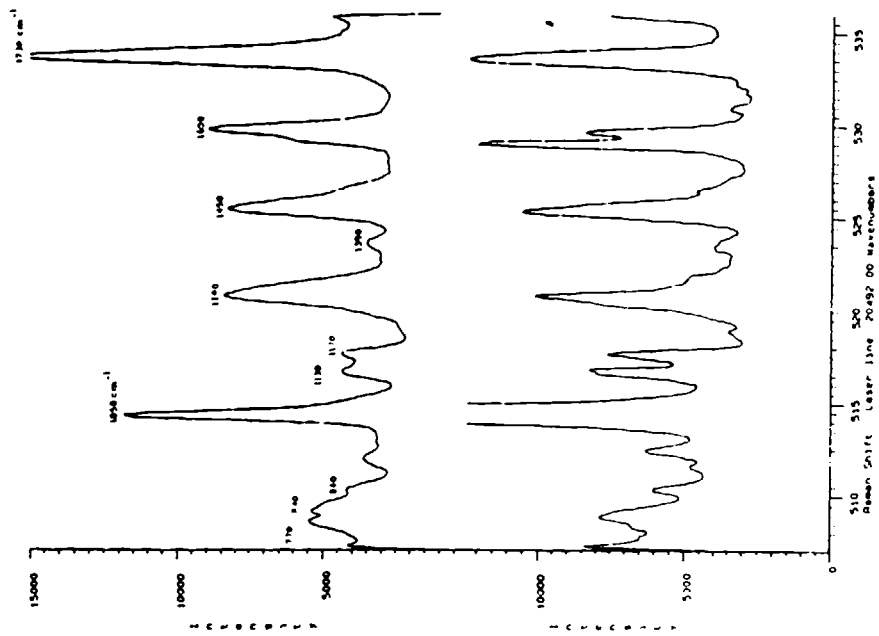
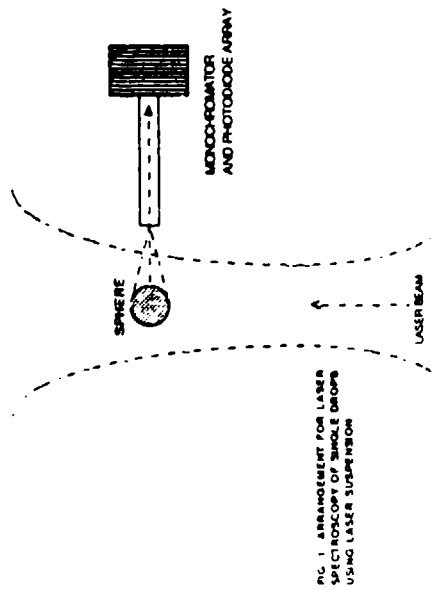


Figure 2. Raman spectra for bulk DOP (top) and optically levitated DOP particle (bottom)

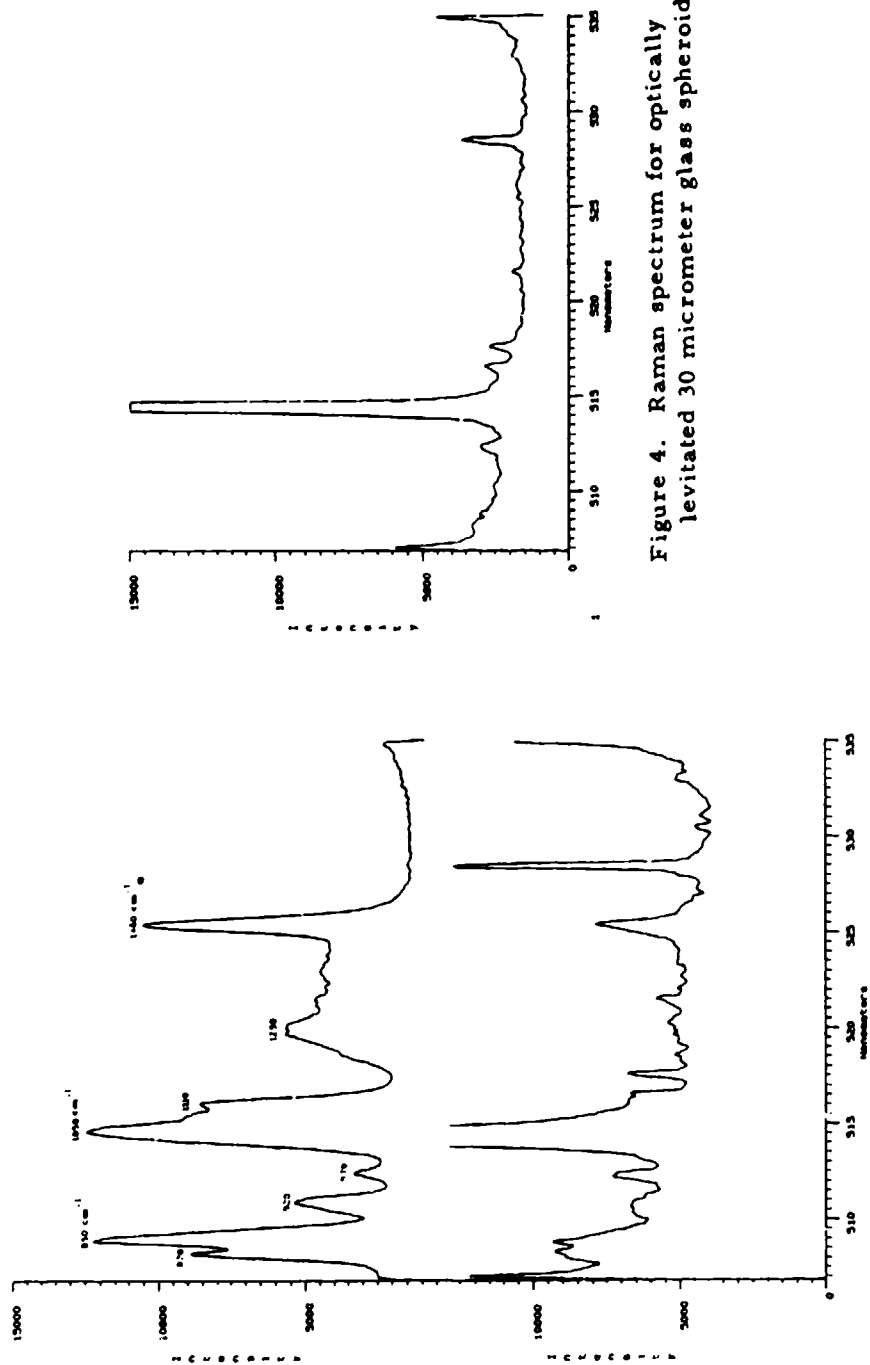


Figure 3. Raman spectra for bulk glycerol (top) and optically levitated glycerol particle (bottom).

Figure 4. Raman spectrum for optically levitated 30 micrometer glass spheroid.

Blank

THEORETICAL CALCULATION ON SCATTERING BY SPHEROIDAL PARTICLES
AND COMPARISON WITH MICROWAVE EXTINCTION MEASUREMENTS

Wan-Xian Wang and R.T. Wang
Space Astronomy Laboratory, University of Florida
Gainesville, FL 32609

RECENT PUBLICATIONS, SUBMITTALS FOR PUBLICATION AND PRESENTATIONS:

This paper is submitted to Journal of Electromagnetic Wave.

ABSTRACT

The new algorithms on calculations of the scattering coefficients have been applied to the prolate and oblate spheroids having very high aspect ratio and/or very large size and being either dielectric or metallic. The extinction P-Q plot comparisons, of prolate-prolate, prolate-cylinder, oblate-oblate, and oblate-disk with equal volume for different aspect ratios and size parameters, between theory and microwave measurements are provided, as reveals a good agreement to the extinction profiles for spheroids and a similarity of prolate to cylinder or oblate to disk in the extinction efficiency.

I. INTRODUCTION

The corrections and developments on the theory of scattering by prolate spheroidal particles as well as comparison with experiments had been studied by the authors.¹ In order to cover the specific gap in the case of moderate values of size parameter c ($=\kappa(a^2-b^2)^{1/2}$, where κ is wave number, a is semi-major axis, and b is semi-minor axis) and intermediate number n , the higher order terms of the ordinate expansions for spheroidal eigenvalues and those of asymptotic expressions for prolate and oblate eigenvalues must be added.^{2,3,4}

As the aspect ratio becomes higher, that is, the radial coordinate ξ for prolate ($=a/(a^2-b^2)^{1/2}$) goes to 1 or ξ for oblate ($=b/(a^2-b^2)^{1/2}$) is less than 1, we have to use the series expansions in powers of (ξ^2-1) for prolate or of (ξ^2+1) for oblate so as to calculate the spheroidal radial functions of the second kind, $R_{mn}^{(2)}(c, \xi)$ for prolate or $R_{mn}^{(2)}(-ic, i\xi)$ for oblate.

II. PROLATE AND OBLATE RADIAL FUNCTIONS $R_{mn}^{(2)}(c, \xi)$ AND $R_{mn}^{(2)}(-ic, i\xi)$

By employing the relation between the spheroidal radial and angular functions of the second kind, the prolate radial functions $R_{mn}^{(2)}(c, \xi)$ can be written in the form:

$$P_{mn}^{(2)}(c, \xi) = Q_{mn}(c) R_{mn}^{(1)}(c, \xi) \left[\frac{1}{2} \log \frac{\xi+1}{\xi-1} \right] + g_{mn}(c, \xi) \quad (1)$$

The implications of quantities contained in Eq.(1) refer to the paper.⁵

Just simply substituting $-ic$ to c and $i\xi$ to ξ in Eq.(1), and using the transformation of

$$\frac{1}{2} \log \frac{\xi+1}{\xi-1} \quad \text{for prolate} \quad \longrightarrow \quad i \left[\tan^{-1} \xi - \frac{\pi}{2} \right] \quad \text{for oblate} \quad (2)$$

we can obtain the oblate radial functions:⁶

$$R_{mn}^{(2)}(-ic, i\xi) = iQ_{mn}(-ic)R_{mn}^{(1)}(-ic, i\xi) \left[\tan^{-1} \xi - \frac{\pi}{2} \right] + g_{mn}^*(-ic, i\xi) \quad (3)$$

where

$$g_{mn}^*(-ic, i\xi) = (\xi^2+1)^{-\frac{m}{2}} \sum_{r=0}^m \beta_{2r} \xi^{2r} \quad \text{for } (n-m) \text{ odd} \quad (4-1)$$

$$g_{mn}^*(-ic, i\xi) = \xi(\xi^2+1)^{-\frac{m}{2}} \sum_{r=0}^m \beta_{2r} \xi^{2r} \quad \text{for } (n-m) \text{ even} \quad (4-2)$$

The coefficients β_{2r}^{mn} for $r \neq 0$ can be directly generated from the corresponding recursion system;⁶ the initial coefficients β_0^{mn} can be evaluated from:

$$\beta_0^{mn} = - \left[cR_{mn}^{(1)}(-ic, 10) \right]^{-1} \quad \text{for } (n-m) \text{ odd} \quad (5-1)$$

$$\beta_0^{mn} = \left[cR_{mn}^{(1)}(-ic, 10) \right]^{-1} - iQ_{mn}(-ic)R_{mn}^{(1)}(-ic, 10) \quad \text{for } (n-m) \text{ even} \quad (5-2)$$

where

$$R_{mn}^{(1)}(-ic, 10) = \frac{i^{n-m-1} 2^m m! c^{m+1} d_1^{mn}(-ic)}{(2m+3) \sum_{r=1}^m d_r^{mn}(-ic) \frac{(2m+r)!}{r!}} \quad \text{for } (n-m) \text{ odd} \quad (6-1)$$

$$R_{mn}^{(1)}(-ic, 10) = \frac{i^{n-m} 2^m m! c^m d_0^{mn}(-ic)}{(2m+1) \sum_{r=0}^m d_r^{mn}(-ic) \frac{(2m+r)!}{r!}} \quad \text{for } (n-m) \text{ even} \quad (6-2)$$

III. COMPARISONS WITH EXPERIMENTS

Since any mis-order of the spheroidal eigenvalues λ_{mn} will cause the infinite or incredible results on the diagram of P-Q plot (P and Q are the imaginary and real parts of the extinction efficiency, respectively), the eigenvalues must be in the increasing order with number n and m. Thus we have to carefully choose the Bouwkamp's or asymptotic method for the calculation of λ_{mn} near the gap mentioned in Section I. Tables 1,2, and 3 show the computational selection of these two methods for the spheroids with the aspect ratio 2:1,4:1,8:1, and 12:1.

Following are four groups of graphs for comparison of theoretical and experimental results

in the forms of P-Q plot: Group 1 is the comparison for prolate-prolate spheroids; Group 2 for prolate spheroid-cylinder; Group 3 for oblate-oblate spheroids; Group 4 for oblate spheroid-disk. In these groups, former particles are used in theoretical calculation, latter ones are measured with microwave equipments. In all figures, $x_v (=ka_v)$ is size parameter of spheroid, with a_v being the radius of equal-volume sphere, m is refractive index, subscripts th and ex denote whether theoretical or experimental, the running number in a pair of curves indicates the tilted angle of the particle axis from \vec{k} (propagational) direction as the axis is swept through 90° in the incident K-E and K-H planes.

The computational outcomes on the extinction profiles seem to fit well to the measurements if the instrumental drift due to the influence of temperature gradient, and a little variation of refractive index of particle over long period of time are taken into account. Actually, even a little fluctuation of this kind of drift and of refractive index will greatly deform the profiles on the P-Q plot.

The comparison between prolate spheroids and cylinders and that between oblate spheroids and disks under the equal-volume condition reveal that their extinction curves are very similar and the absolute magnitudes of extinction efficiency are close. The former results (for prolate spheroid-cylinder) are expected, but the latter ones come out beyond our original expectation. Apparently the edge effect in disk only exerts a little function to the extinction cross section compared with oblate spheroid.

IV. ACKNOWLEDGMENT

This research work is supported by the U.S. Army Research Office, Research Triangle Park, NC.

REFERENCES

1. Wan-xian Wang and R.T. Wang, "Corrections and Developments on the Theory of Scattering by Spheroid - Comparison with Experiments," presented at 1986 CRDEC Scientific Conference on Obscuration and Aerosol Research, Aberdeen, MD (June 1986).
2. Wan-xian Wang, "Power-Series Expansion of the Eigenvalues for Spheroidal Differential Equation," presented at 1986 CRDEC Scientific Conference on Obscuration and Aerosol Research, Aberdeen, MD (June 1986).
3. Wan-xian Wang, "Asymptotic Development of the Prolate Spheroidal Eigenvalues and eigenfunctions," presented at 1986 CRDEC Scientific Conference on Obscuration and Aerosol Research, Aberdeen, MD (June 1986).

4. Wan-Xian Wang, "Asymptotic Development of the Oblate Spheroidal Eigenvalues," presented at 1986 Scientific Conference on Obscuration and Aerosol Research, Aberdeen, MD (June 1986).
5. Wan-Xian Wang, "Coefficients a_r^{mn} in Spheroidal Radial Functions R_{mn} for High Aspect Ratio," presented at 1986 Scientific Conference on Obscuration and Aerosol Research, Aberdeen, MD (June 1986).
6. Wan-Xian Wang, "Coefficients b_r^{mn} in Spheroidal Radial Functions R_{mn} for High Aspect Ratio," presented at 1986 Scientific Conference on Obscuration and Aerosol Research, Aberdeen, MD (June 1986).

Table 1
 Computational Selection
 Method I: Bouwkamp's, Method II: Asymptotic
 2:1 and 4:1 Prolate Spheroids

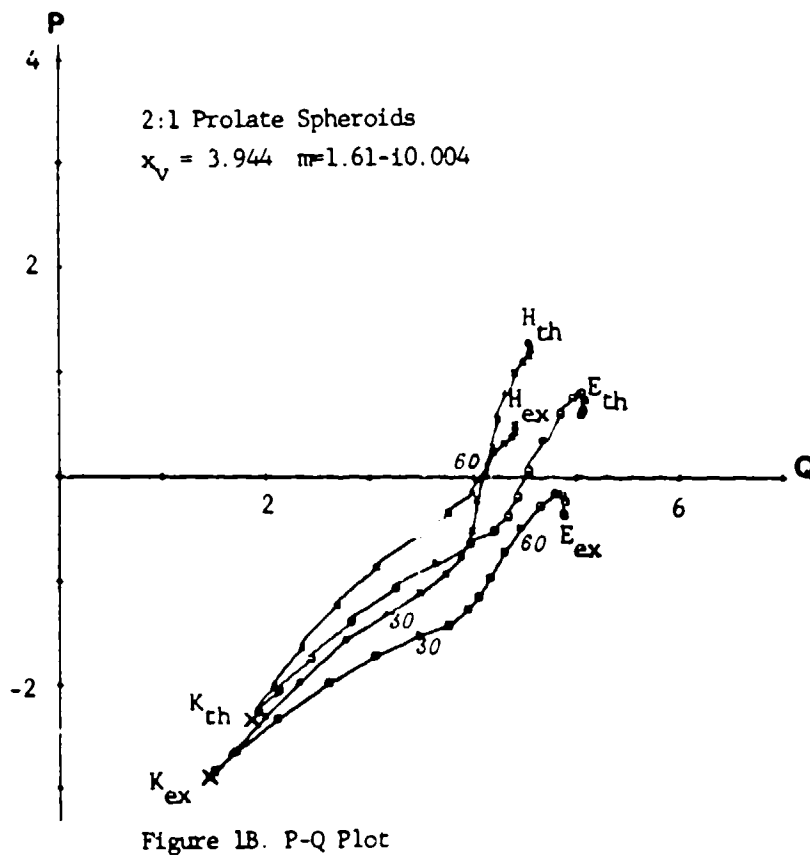
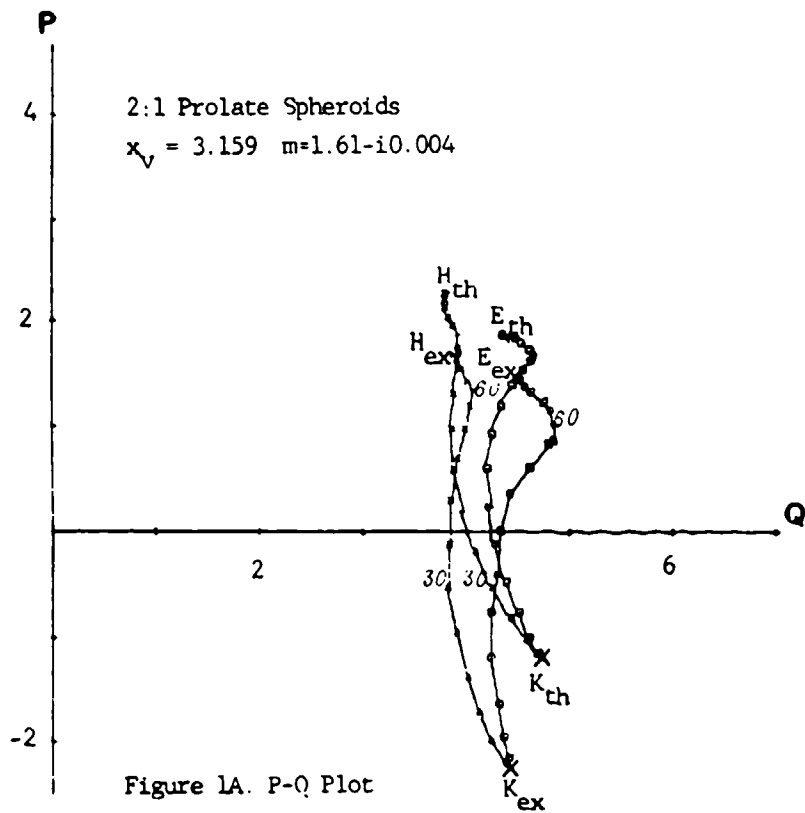
	$c \leq 7$		$7 < c \leq 10$		$10 < c \leq 12$		$12 < c$	
$m = 0$	$n \leq m+3$	II	$n \leq m+5$	II	$n \leq m+7$	II	$n \leq m+8$	II
	$n > m+3$	I	$n > m+5$	I	$n > m+7$	I	$n > m+8$	I
$2 \geq m \geq 1$	$n \leq m+2$	II	$n \leq m+4$	II		$n \leq m+6$	II	
	$n > m+2$	I	$n > m+4$	I		$n > m+6$	I	
$m \geq 3$	$n \leq m+1$	II	$n \leq m+3$	II		$n \leq m+5$	II	
	$n > m+1$	I	$n > m+3$	I		$n > m+5$	I	

Table 2
 Computational Selection
 12:1 Prolate Spheroids

	$c \leq 30$				$30 < c$	
$m = 0$	$n \leq m+15$	II			$n \leq m+22$	II
	$n > m+15$	I			$n > m+22$	I
$m = 1$	$n \leq m+14$	II			$n \leq m+19$	II
	$n > m+14$	I			$n > m+19$	I
$m = 2$	$n \leq m+13$	II				
	$n > m+13$	I				
$m = 3$	$n \leq m+12$	II				
	$n > m+12$	I				
$m = 4$	$n \leq m+11$	II				
	$n > m+11$	I				
$m = 5$	$n \leq m+10$	II			$n \leq m+16$	II
	$n > m+10$	I			$n > m+16$	I
	$c \leq 25$		$25 < c \leq 30$			
$m = 6$	$n \leq m+7$	II	$n \leq m+10$	II		
	$n > m+7$	I	$n > m+10$	I		

Table 3
 Computational Selection
 2:1, 4:1, and 8:1 Oblate Spheroids

	$c \leq 3$	$3 < c \leq 6$		$6 < c \leq 9$		$9 < c \leq 12$		$12 < c \leq 20$	
$m = 0$	I	$n \leq m+2$	II	$n \leq m+3$	II	$n \leq m+6$	II	$n \leq m+8$	II
		$n > m+2$	I	$n > m+3$	I	$n > m+6$	I	$n > m+8$	I
$2 \geq m \geq 1$	I	$n \leq m+1$	II	$n \leq m+2$	II	$n \leq m+5$	II	$n \leq m+7$	II
		$n > m+1$	I	$n > m+2$	I	$n > m+5$	I	$n > m+7$	I
$4 \geq m \geq 3$	I	I		$n \leq m+1$	II	$n \leq m+4$	II	$n \leq m+6$	II
				$n > m+1$	I	$n > m+4$	I	$n > m+6$	I
$m = 5$	I	I		I		$n \leq m+3$	II	$n \leq m+5$	II
						$n > m+3$	I	$n > m+5$	I
$m = 6$	I	I		I		$n \leq m+2$	II	$n \leq m+4$	II
						$n > m+2$	I	$n > m+4$	I
$8 \geq m \geq 7$		I		I		$n \leq m+1$	II	$n \leq m+3$	II
						$n > m+1$	I	$n > m+3$	I
$10 \geq m \geq 9$				I		I		$n \leq m+2$	II
								$n > m+2$	I



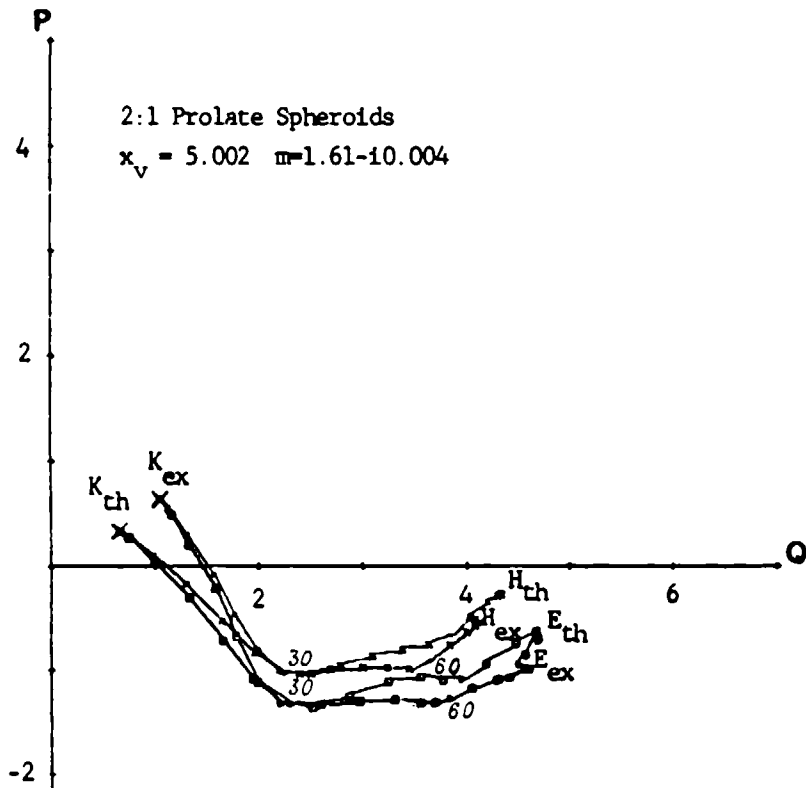


Figure 1C. P-Q Plot

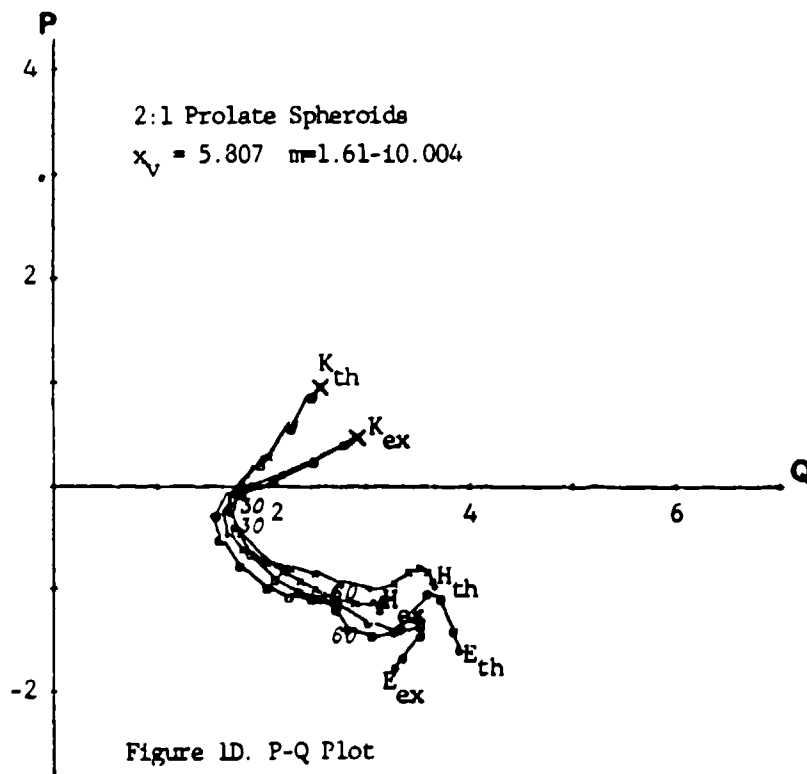


Figure 1D. P-Q Plot

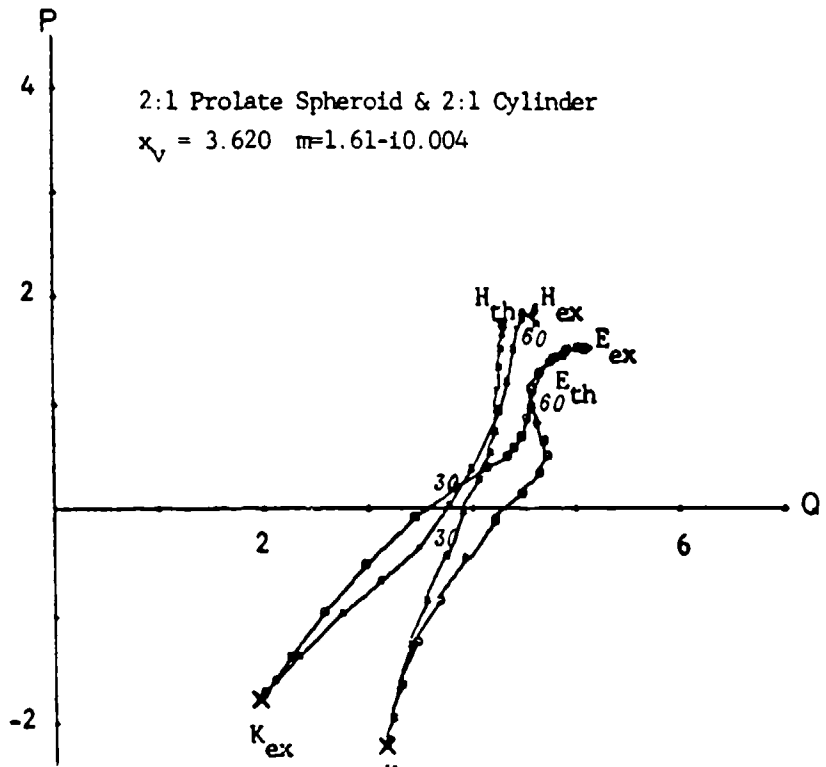


Figure 2A. P-Q Plot K_{th}

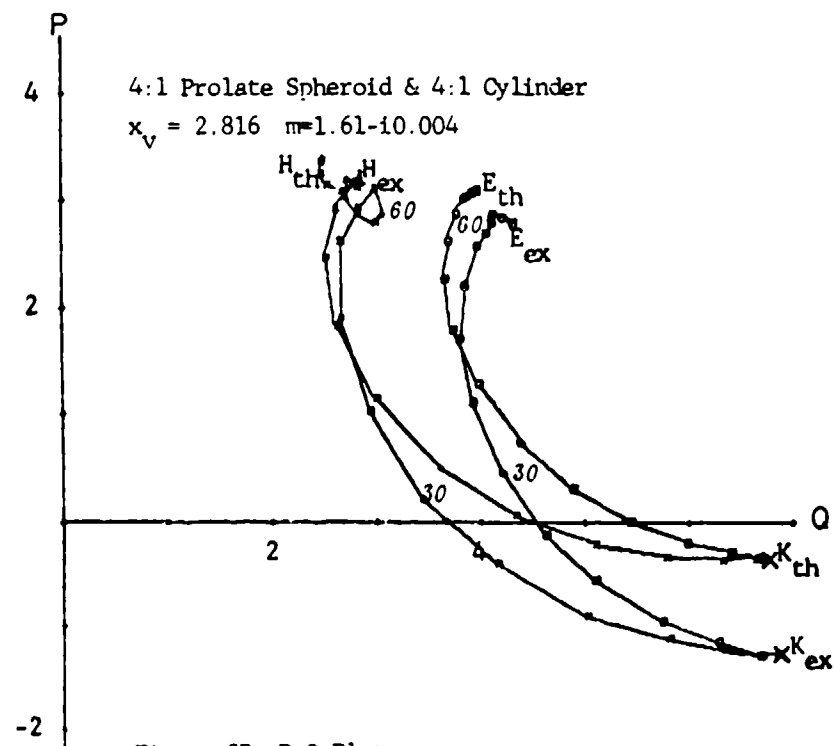
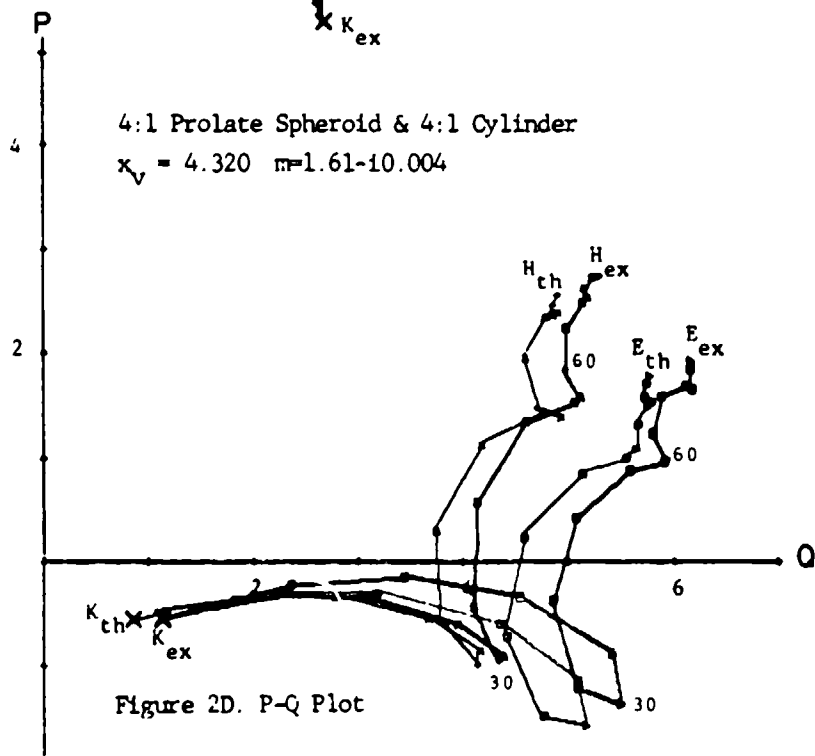
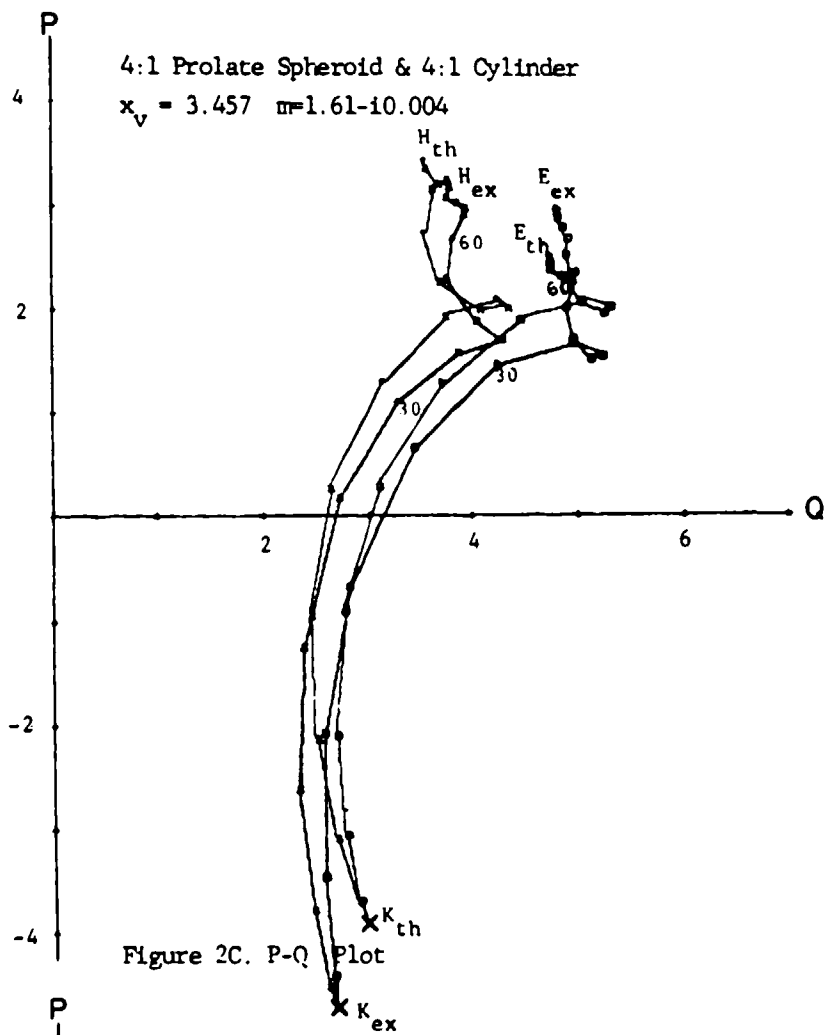
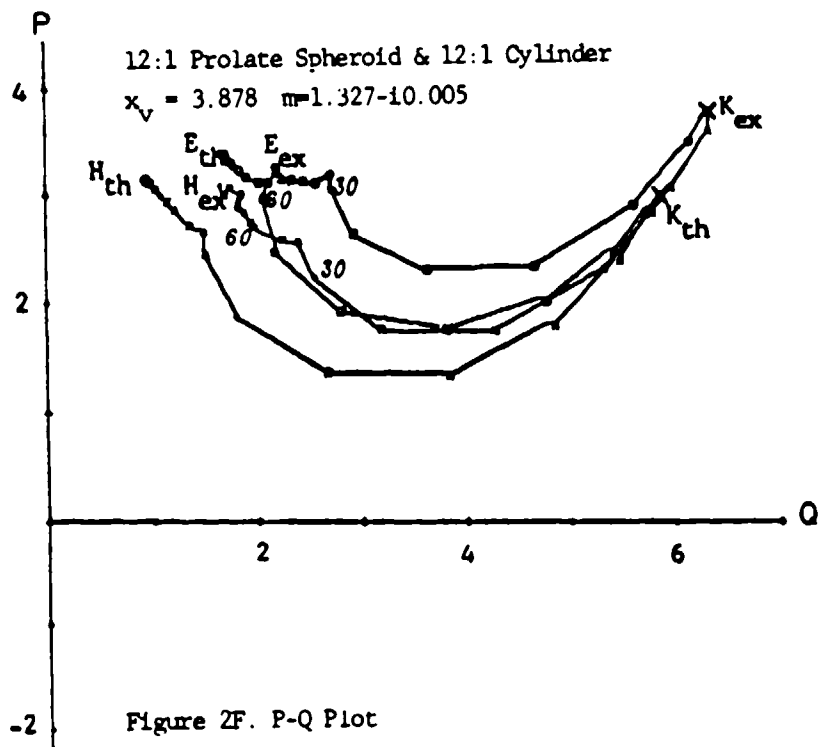
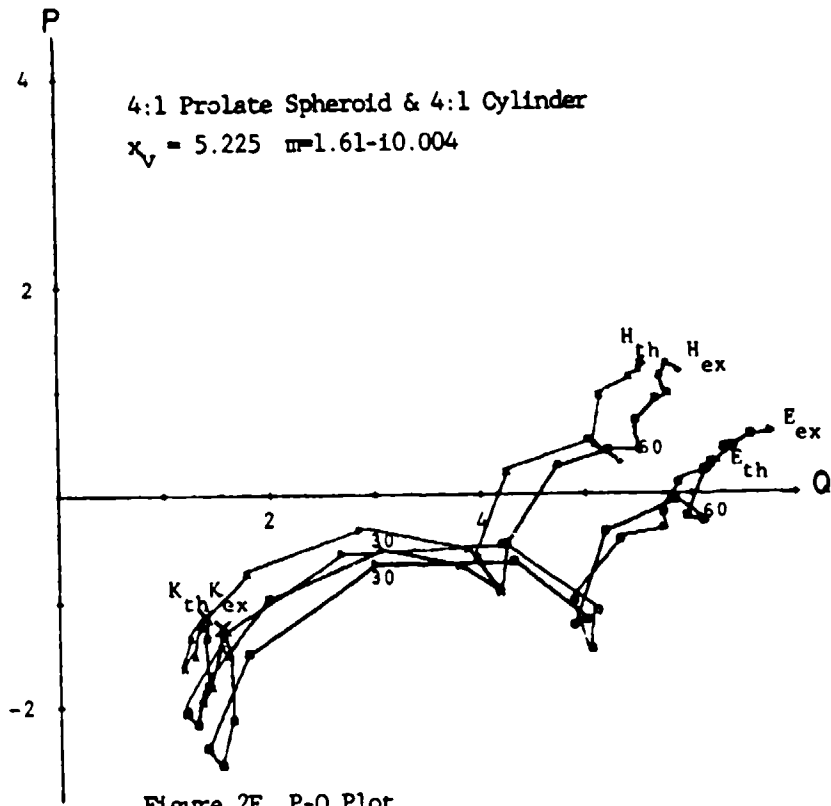
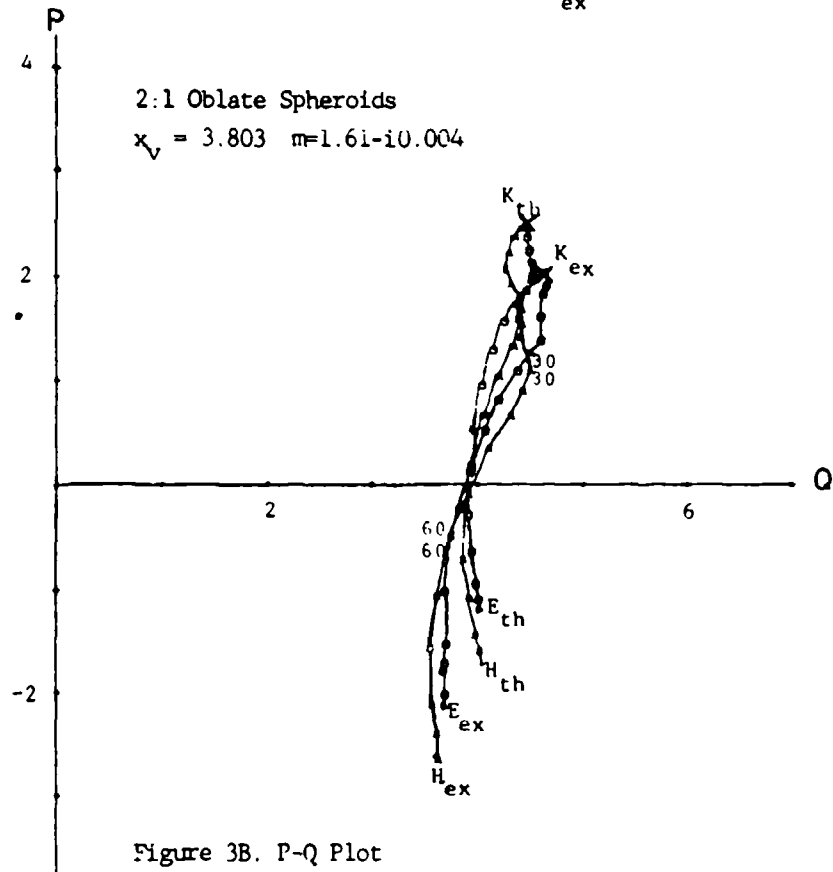
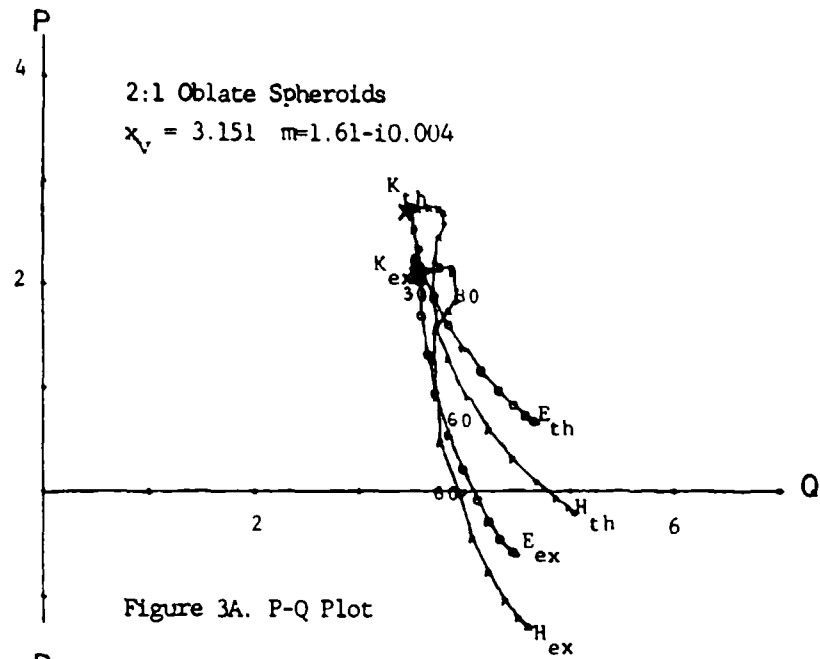
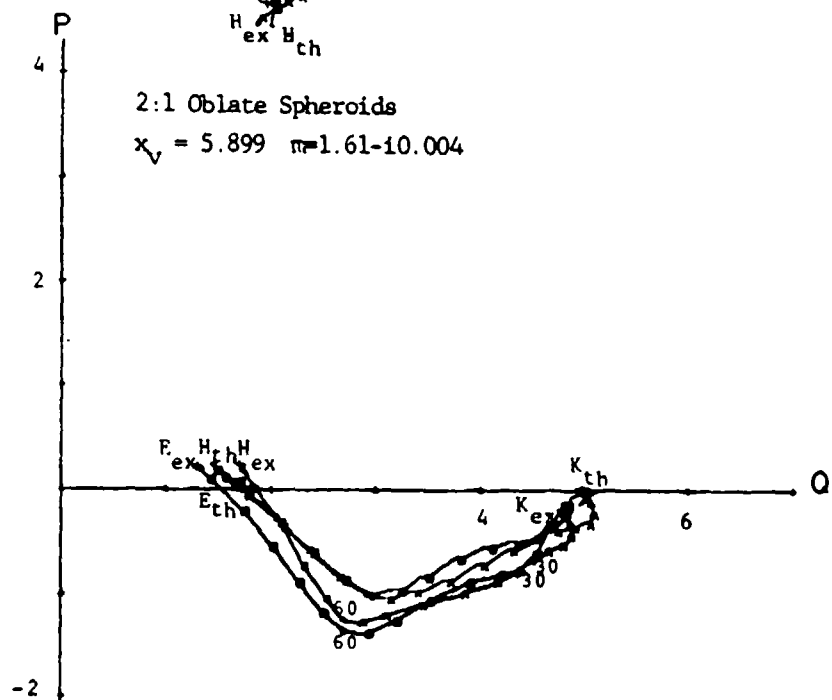
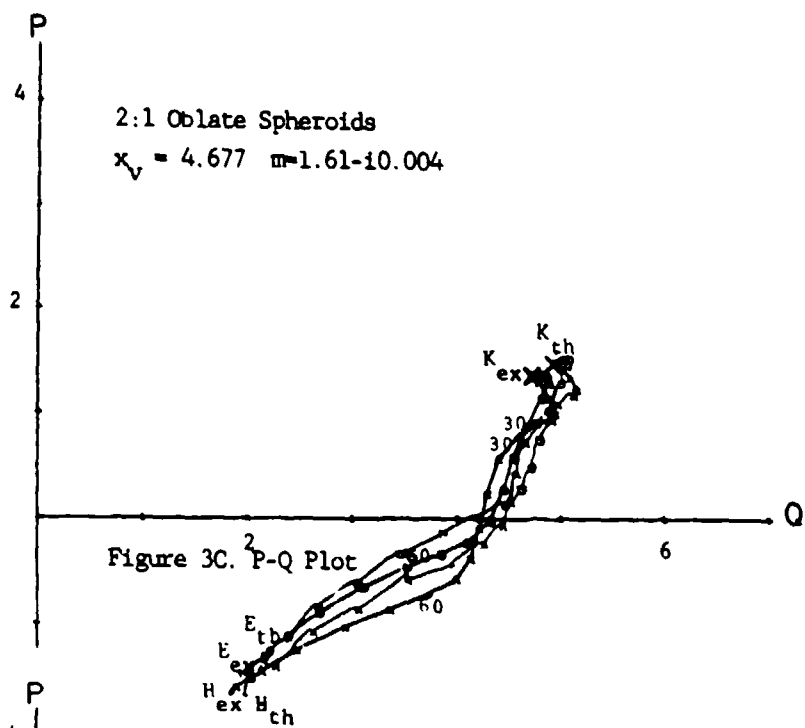


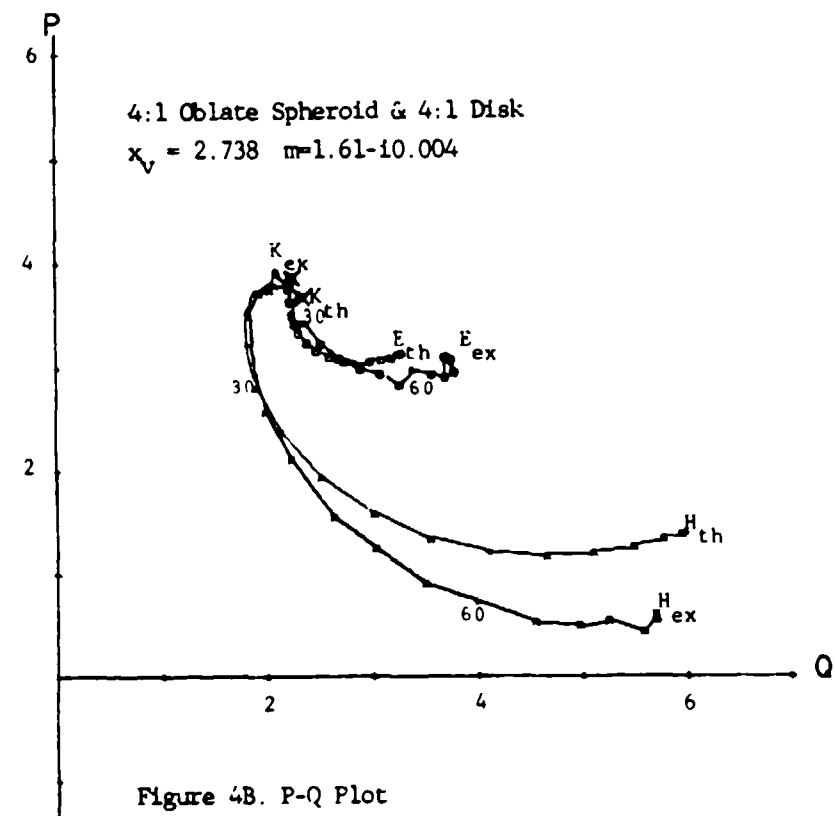
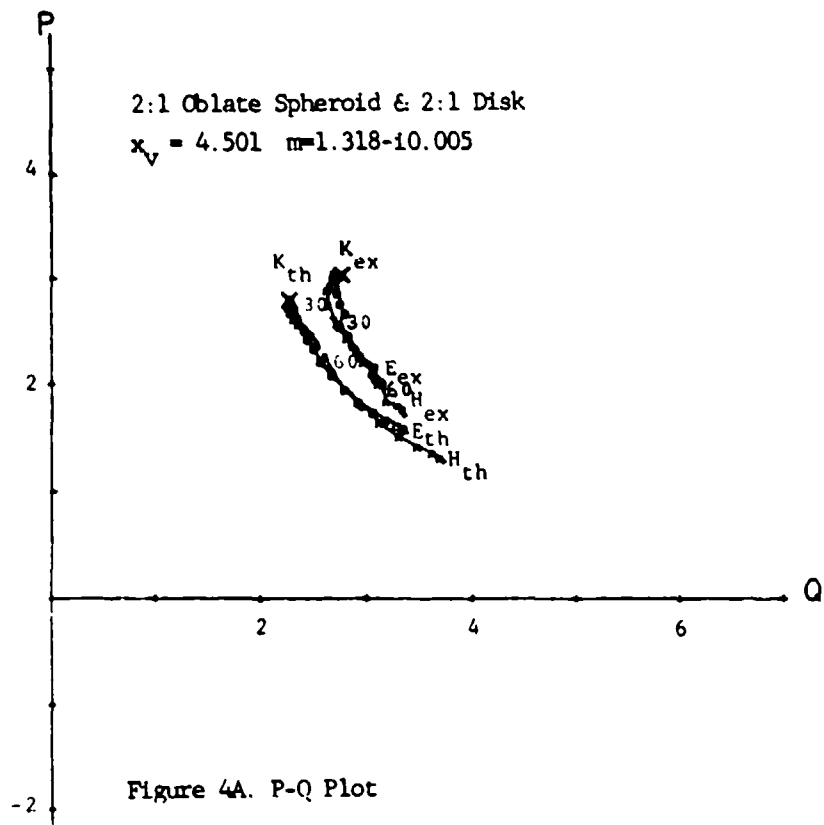
Figure 2B. P-Q Plot

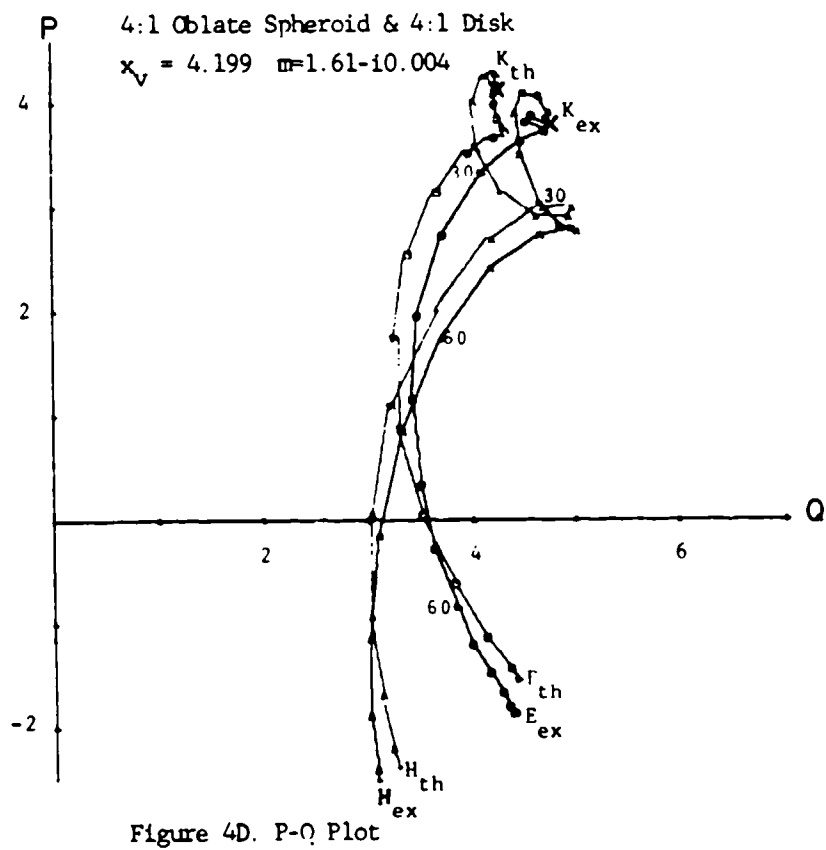
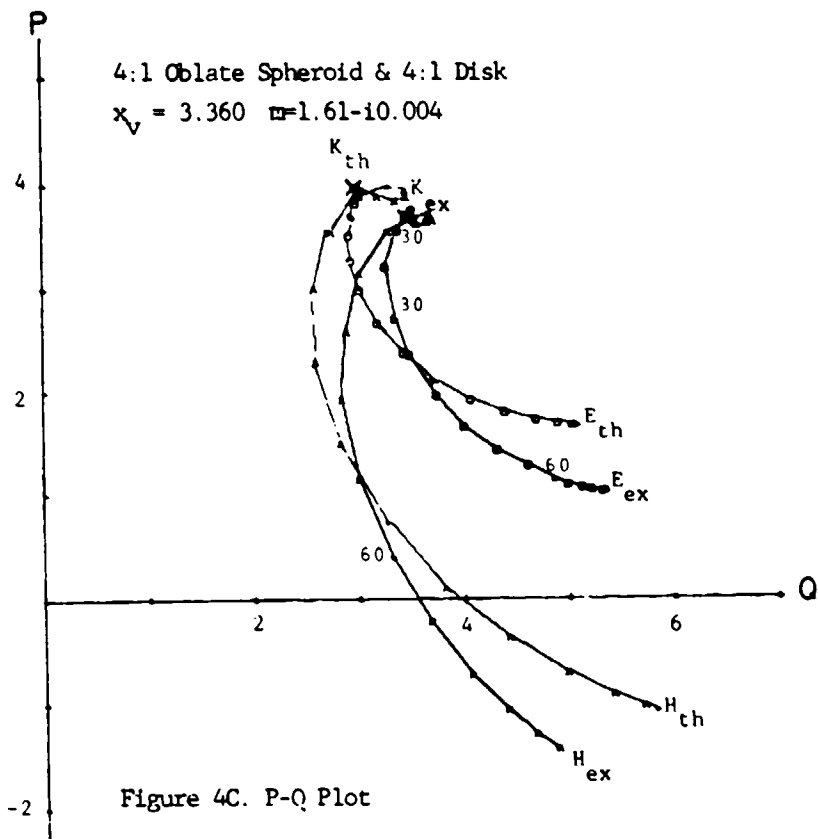












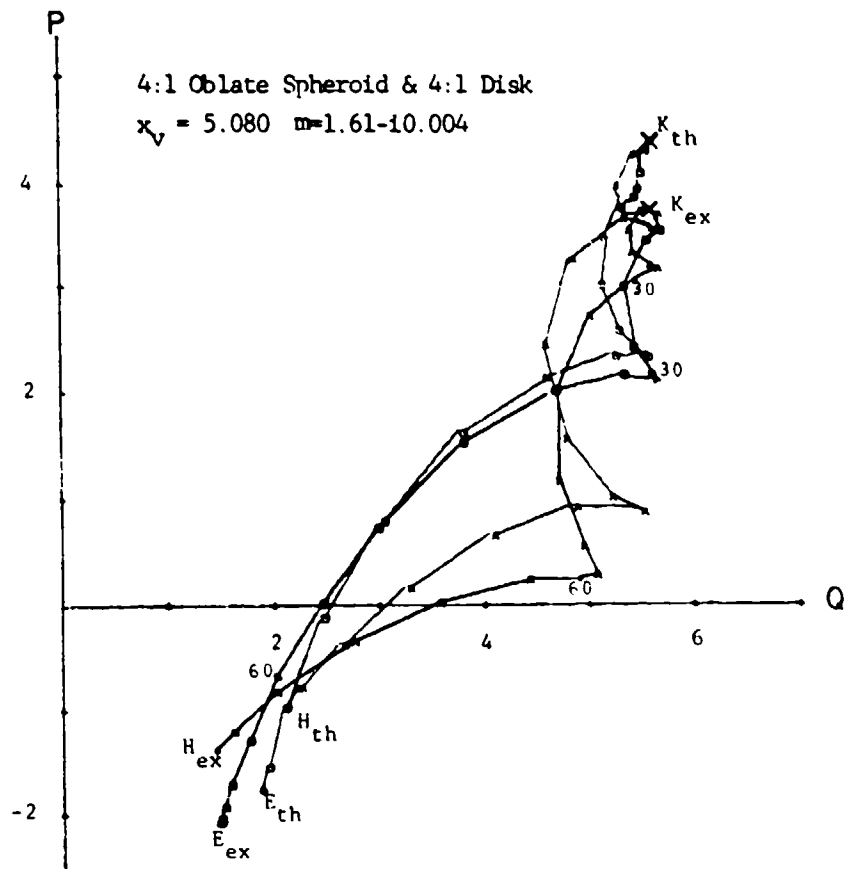


Figure 4E. P-Q Plot

Blank

THE SIMPLEST RADIAL WAVE FUNCTIONS IN THE CALCULATION OF
LIGHT SCATTERING BY A SPHEROIDAL PARTICLE

Wan-xian Wang
Space Astronomy Laboratory, University of Florida
Gainesville, FL 32609

RECENT PUBLICATIONS, SUBMITTALS FOR PUBLICATION AND PRESENTATIONS:

- A) Wan-xian Wang, "Power-Series Expansion of the Eigenvalues for Spheroidal Differential Equation", presentation at the 1986 CRDEC Conference on Obscuration and Aerosol Research, June 1986.
- B) Wan-xian Wang, "Asymptotic Development of the Prolate Spheroidal Eigenvalues and Eigenfunctions", presentation at the 1986 CRDEC Conference on Obscuration and Aerosol Research, June 1986.
- C) Wan-xian Wang, "Asymptotic Development of the Oblate Spheroidal Eigenvalues", presentation at the 1986 CRDEC Conference on Obscuration and Aerosol Research, June 1986.
- D) Wan-xian Wang, "Coefficients a_r^{mn} in Spheroidal Radial Functions R_{mn} for High Aspect Ratio", presentation at the 1986 CRDEC Conference on Obscuration and Aerosol Research, June 1986.
- E) Wan-xian Wang, "Coefficients b_r^{mn} in Spheroidal Radial Functions R_{mn} for High Aspect Ratio", presentation at the 1986 CRDEC Conference on Obscuration and Aerosol Research, June 1986.
- F) Wan-xian Wang and Ru T. Wang, "Corrections and Developments on the Theory of Scattering by Spheroid — Comparison with Experiments", presentation at the 1986 CRDEC Conference on Obscuration and Aerosol Research, June 1986.

ABSTRACT

The simplest forms of the spheroidal radial functions are obtained here by using new radial coordinate in the spheroidal differential equation.

INTRODUCTION

The spheroidal radial differential equation in prolate coordinate system can be expressed as

$$\frac{d}{d\xi} \left[(\xi^2 - 1) \frac{dR_{mn}}{d\xi} \right] - \left(\lambda_{mn} - c^2 \xi^2 + \frac{m^2}{\xi^2 - 1} \right) R_{mn} = 0 \quad (1)$$

where ξ is the radial coordinate, λ_{mn} and R_{mn} are the spheroidal eigenvalues and radial functions, of order m and degree n , respectively, with m and n being positive integers, and $n \geq m$. In oblate coordinate system, one just replaces c by $-ic$ and ξ by $i\xi$ in Eq.(1).

The expression of the spheroidal radial functions is usually written in the form:¹

$$R_{mn}^{(j)}(c, \xi) = \frac{1}{\sum_{r=0,1}^{\infty} d_r^{mn}(c) \frac{(2m+r)!}{r!}} \left(\frac{\xi^2 - 1}{\xi^2} \right)^{\frac{1}{2}m} \sum_{r=0,1}^{\infty} i^{r+m-n} d_r^{mn}(c) \frac{(2m+r)!}{r!} z_{m+r}^{(j)}(c\xi) \quad (2)$$

where $d_r^{mn}(c)$ are the expansion coefficients of the spheroidal angle functions S_{mn} with respect to the associated Legendre functions P_{m+r}^m , r is the summation index, and the prime over the summation symbol indicates that the summation is over only odd number of r when $(n-m)$ is odd, and over only even when $(n-m)$ is even. Superscript j for the radial functions $R_{mn}(c, \xi)$ and the spherical Bessel functions $z_{m+r}(c\xi)$ of order $(m+r)$ implies which of the four kinds of the spherical Bessel functions is referred to, that is, spherical Bessel, Neumann, and Hankel functions of the first and of the second, in order of $j=1,2,3, and 4, respectively.$

The expansion coefficients $d_r^{mn}(c)$ obey the recursion relation:

$$\frac{(2m+r+2)(2m+r+1)c^2}{(2m+2r+3)(2m+2r+5)} d_{r+2}^{mn}(c) + \left[(m+r)(m+r+1) - \lambda_{mn} + \frac{2(m+r)(m+r+1)-2m^2-1}{(2m+2r-1)(2m+2r+3)} c^2 \right] d_r^{mn}(c) + \frac{r(r-1)c^2}{(2m+2r-3)(2m+2r-1)} d_{r-2}^{mn}(c) = 0 \quad (r \geq 0) \quad (3)$$

Eq. (2) is the classical expression of the spheroidal radial functions.

THE SIMPLEST RADIAL FUNCTIONS

Now let us introduce another radial coordinate σ , and make the transformation

$$\sigma = (\xi^2 - 1)^{\frac{1}{2}} \quad (4)$$

then the relation of the first order derivatives between ξ and σ is

$$\frac{d}{d\xi} = (\sigma^2 + 1)^{\frac{1}{2}} \frac{1}{\sigma} \frac{d}{d\sigma} \quad (5)$$

With this new radial coordinate, Eq. (1) is converted to

$$(\sigma^2 + 1) \frac{d^2 R_{mn}}{d\sigma^2} + \frac{2\sigma^2 + 1}{\sigma} \frac{dR_{mn}}{d\sigma} - \left[\lambda_{mn} - c^2(\sigma^2 + 1) + \frac{m^2}{\sigma^2} \right] R_{mn} = 0 \quad (6)$$

Eq. (6) can be readily decomposed into three separate equations:

$$\sigma^2 \frac{d^2 R_{mn}}{d\sigma^2} + 2\sigma \frac{dR_{mn}}{d\sigma} + \left[c^2\sigma^2 - h(h+1) \right] R_{mn} = 0 \quad (7a)$$

$$\frac{d^2 R_{mn}}{d\sigma^2} + \frac{2}{\sigma} \frac{dR_{mn}}{d\sigma} + \left[c^2 - \frac{h(h+1)}{\sigma^2} \right] R_{mn} = 0 \quad (7b)$$

$$\frac{1}{\sigma} \frac{dR_{mn}}{d\sigma} + \left[\lambda_{mn} - h(h+1) + \frac{m^2 - h(h+1)}{\sigma^2} \right] R_{mn} = 0 \quad (7c)$$

where h is the order number of spherical Bessel function, being an arbitrary integer.

It is obvious that both Eqs. (7a) and (7b) have the same solution of spherical Bessel function of order h :

$$R_{lm} = z_h(c\sigma) \quad (8)$$

For simplicity, we denote $z_h(c\sigma)$ by z_h . Substituting the trial solution $R_{lm} = z_h$ into Eq. (7c), we have the following expressions:

$$\frac{1}{\sigma} \frac{dR_{lm}}{d\sigma} = \left[\frac{h}{(2h-1)(2h+1)} z_{h-2} + \frac{1}{(2h-1)(2h+3)} z_h - \frac{h+1}{(2h+1)(2h+3)} z_{h+2} \right] c^2 \quad (9a)$$

$$\frac{R_{lm}}{\sigma^2} = \left[\frac{1}{(2h-1)(2h+1)} z_{h-2} + \frac{2}{(2h-1)(2h+3)} z_h + \frac{1}{(2h+1)(2h+3)} z_{h+2} \right] c^2 \quad (9b)$$

Thus we can simply rewrite the radial functions in the form of the summation:

$$R_{lm} = \sum_h A_h z_h \quad (10)$$

With the substitution of Eq. (10) in Eq. (7c), which is a linear differential equation, the coefficients of spherical Bessel functions are found to be:

$$\text{term } z_{h-2}: \frac{(m^2 - h^2)c^2}{(2h-1)(2h+1)} A_h \quad (11a)$$

$$\text{term } z_h: \frac{(2m^2 + 1 - 2h(h+1))c^2}{(2h-1)(2h+3)} A_h + [\lambda_{lm} - h(h+1)] A_h \quad (11b)$$

$$\text{term } z_{h+2}: \frac{(m^2 - (h+1)^2)c^2}{(2h+1)(2h+3)} A_h \quad (11c)$$

Equating the term with the lowest order of spherical Bessel functions in Eq. (7c) gives

$$h = m \quad (12)$$

The other terms of the series in Eq. (10) can be obtained by taking

$$h = m + 2r \quad (13)$$

where r is an integer, with $r \geq 0$. Finally, we get the solution for the spheroidal radial functions, as follows:

$$R_{lm} = \sum_{r=0}^{\infty} A_{m+2r} z_{m+2r} \quad (14a)$$

For the sake of convenience, we use subscript $2r$ instead of $m+2r$ in the coefficient A , that is,

$$R_{lm} = \sum_{r=0}^{\infty} A_{2r} z_{m+2r} \quad (14b)$$

where the coefficients A_{2r} obey the recursion relation, the form of which is similar to Eq. (3):

$$\frac{4(m+r+1)(r+1)c^2}{(2m+4r+3)(2m+4r+5)} A_{2r+2} + \left[(m+2r)(m+2r+1) - \lambda_{mn} + \frac{2(m+2r)(m+2r+1)-2m^2-1}{(2m+4r-1)(2m+4r+3)} c^2 \right] A_{2r} + \frac{(2m+2r-1)(2r-1)c^2}{(2m+4r-3)(2m+4r-1)} A_{2r-2} = 0 \quad (15)$$

The ratio of the second coefficient to the first one, A_2/A_0 , can be specifically evaluated by deleting the last term in Eq.(15) and then setting $r=0$, that is,

$$\left[m(m+1) - \lambda_{mn} + \frac{c^2}{2m+3} \right] A_0 + \frac{4(m+1)c^2}{(2m+3)(2m+5)} A_2 = 0 \quad (16)$$

There are two non-trivial independent solutions for the second order differential Eq.(6). Examination of Eq.(15) reveals that as r approaches infinity, either A_{2r+2}/A_{2r} increases as $-16r^2/c^2$, or goes to zero as $-c^2/16r^2$. Of these two solutions, the former leads to a divergent series. Therefore we choose the latter, which can be generated from the upward recursion.

NORMALIZATION

The spheroidal radial functions $R_{mn}^{(j)}$, which satisfy the radial differential Eq.(6), are normalized so that, for $c\sigma \rightarrow \infty$, they have the asymptotic forms:

$$R_{mn}^{(1)} \rightarrow \frac{1}{c\sigma} \cos(c\sigma - \frac{m+1}{2}\pi) \quad (17a)$$

$$R_{mn}^{(2)} \rightarrow \frac{1}{c\sigma} \sin(c\sigma - \frac{m+1}{2}\pi) \quad (17b)$$

After normalization of the spheroidal radial functions, we find that

$$R_{mn}^{(1)}(c, \sigma) = \frac{\sum_{r=0}^{\infty} A_{2r} z_{m+2r}^{(1)}(c\sigma)}{\sum_{r=0}^{\infty} i^{m-n+2r} A_{2r}} \quad \text{for } (n-m) \text{ even} \quad (18a)$$

$$R_{mn}^{(2)}(c, \sigma) = \frac{\sum_{r=0}^{\infty} A_{2r} z_{m+2r}^{(2)}(c\sigma)}{\sum_{r=0}^{\infty} i^{m-n+2r+1} A_{2r}} \quad \text{for } (n-m) \text{ odd} \quad (18b)$$

$$R_{mn}^{(2)}(c, \sigma) = \frac{\sum_{r=0}^{\infty} A_{2r} z_{m+2r}^{(2)}(c\sigma)}{\sum_{r=0}^{\infty} i^{m-n+2r} A_{2r}} \quad \text{for } (n-m) \text{ even} \quad (18c)$$

$$R_{mn}^{(2)}(c, \sigma) = - \frac{\sum_{r=0}^{\infty} A_{2r} z_{m+2r}^{(1)}(c\sigma)}{\sum_{r=0}^{\infty} i^{m-r+2r+1} A_{2r}} \quad \text{for } (n-m) \text{ odd} \quad (18d)$$

ACKNOWLEDGMENT

This research work is supported by the U.S. Army Research Office, Research Triangle Park, NC.

REFERENCES

1. C. Flammer, Spheroidal Wave Functions, Stanford University Press (1957).

Blank

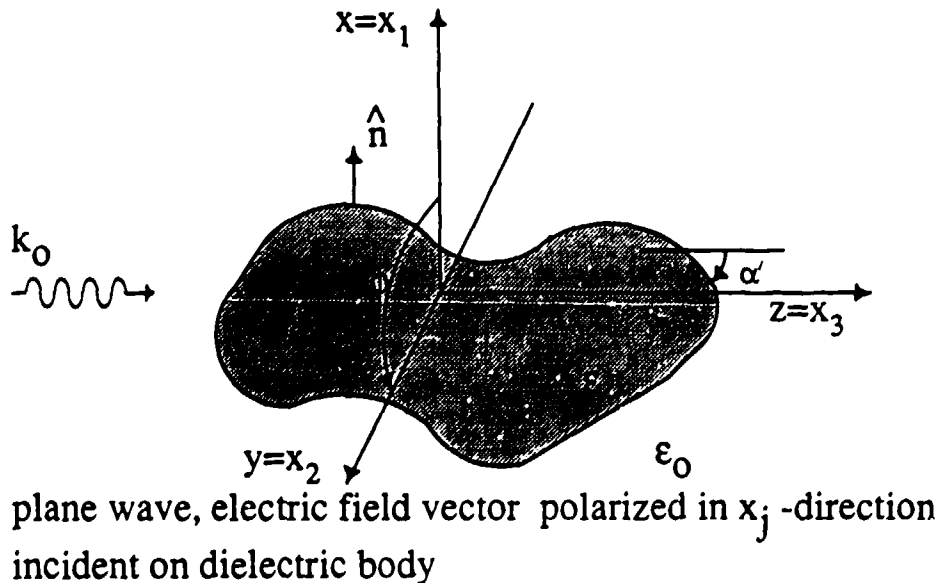
Absorption by Aggregated Spheres

Leland Pierce
Herschel Weil
The University of Michigan
Radiation Lab, EECS Dept.
Ann Arbor, MI 48109-2122

ABSTRACT

Work in progress on electromagnetic scattering and absorption from aggregated Rayleigh spheres is described. Absorption cross-sections are calculated at frequencies around that of visible light, and static internal and near-field equipotential lines are plotted. Future work will concentrate on plotting the electric field lines, improving our numerical procedure to allow more arbitrary shapes, particularly those with axial symmetry.

I. THEORY:



The work we present is an extension of the investigation described by Weil [1986]. It follows the formulation of Rayleigh theory given by Senior [1976]. The polarization tensor X_{ij} and the dipole moments P_i of the induced fields:

$$P_i = \epsilon_0 X_{ij} E_j$$

are found by considering the fields in the limit as $k_0 \rightarrow 0$. Hence one solves the statics problem.

Let Φ_j^s be the scattered, exterior potential and Φ_j be the total, interior potential. Then the conditions governing Φ_j^s and Φ_j for a unit electric field excitation of a scatterer of boundary B and unit outward normal \hat{n} are:

$$\begin{aligned} \nabla^2 \Phi_j^s &= 0 && \text{Outside } B \\ \Phi_j^s &= O(r^{-2}) \text{ as } r \rightarrow \infty \\ \nabla^2 \Phi_j &= 0 && \text{Inside } B \\ \Phi_j^s &= \Phi_j + x_j && \text{On } B \\ \frac{\partial}{\partial n} \Phi_j^s &= \epsilon \frac{\partial}{\partial n} \Phi_j + \hat{n} \cdot \hat{x}_j && \text{On } B \end{aligned}$$

By using Green's Theorem twice, once inside and once outside B , and combining the results, Senior obtained: *

$$\Gamma[\Phi_j^s + x_j] + (1 - \Gamma)[\epsilon \Phi_j + x_j] = \frac{(1 - \epsilon)}{4\pi} \int_B (\Phi_j^s - x_j') \frac{\partial}{\partial n'} \left(\frac{1}{R} \right) dS'$$

where $R = |\bar{r} - \bar{r}'|$, and

* This is the correct form of the corresponding equation which is given following eq. 19 in Senior (1976)

$$\Gamma = \begin{cases} 1, & \text{if } \bar{r} \text{ is external to B} \\ \frac{1}{2}, & \text{if } \bar{r} \text{ is on B} \\ 0, & \text{if } \bar{r} \text{ is interior to B} \end{cases}$$

Now specialize to a body of revolution in cylindrical coordinates ρ, ϕ, z :

$$dS' = \rho' d\phi' ds'$$

where s' is length along the body perimeter, S .

For an x -directed \bar{E} field the right hand side becomes:

$$= \frac{(1-\epsilon)}{4\pi} \int_0^{2\pi} \int_S (\Phi_1^* - x') \frac{\partial}{\partial n'} \left(\frac{1}{R} \right) \rho' d\phi' ds'$$

Since the total field will vary as $\cos\phi'$, along the body's perimeter it can be written in the form:

$$\Phi_1' = \Phi_1^* - x' = \frac{-1}{1-\epsilon} W_1(s') \cos\phi'$$

so the right hand side becomes

$$= -\frac{1}{4\pi} \int_S \left[\int_0^{2\pi} \cos\phi' \frac{\partial}{\partial n'} \left(\frac{1}{R} \right) d\phi' \right] W_1(s') \rho' ds'$$

Senior and Ahlgren [1972, eqn. 63, p. 20] put this expression into the form:

$$= -\frac{1}{4\pi} \int_S 2\cos\phi \{ \rho \cos\alpha' \Omega_2 + [(z' - z) \sin\alpha' - \rho' \cos\alpha'] \Omega_1 \} W_1(s') \rho' ds'$$

At $\phi = 0^\circ$ this gives:

$$\left. \begin{array}{l} \text{outside: } -\Phi_1^t(\bar{r}) \\ \text{bdry: } \frac{1}{2} \frac{(1+\epsilon)}{(1-\epsilon)} W_1(s) \\ \text{inside: } -\epsilon \Phi_1(\bar{r}) \end{array} \right\} = \rho + \frac{1}{2\pi} \int_S W_1(s') \{ \rho \cos \alpha' \Omega_2 + [(z' - z) \sin \alpha' - \rho' \cos \alpha'] \Omega_1 \} \rho' ds'$$

This is an integral equation for W_1 where \bar{r} is on the surface B. Similarly for the z-directed \bar{E} field excitation, the field along the body's perimeter can be written in the form:

$$\Phi_3^t = \frac{-1}{1-\epsilon} W_3(s')$$

$$\left. \begin{array}{l} \text{outside: } -\Phi_3^t(\bar{r}) \\ \text{bdry: } \frac{1}{2} \frac{(1+\epsilon)}{(1-\epsilon)} W_3(s) \\ \text{inside: } -\epsilon \Phi_3(\bar{r}) \end{array} \right\} = z + \frac{1}{2\pi} \int_S W_3(s') \{ \rho \cos \alpha' \Omega_1 + [(z' - z) \sin \alpha' - \rho' \cos \alpha'] \Omega_0 \} \rho' ds'$$

In these equations

$$\Omega_n = \int_0^\pi \frac{\cos^n(\Psi)}{R^3} d\Psi \quad n = 0, 1, 2$$

and

$$R = [(\rho + \rho')^2 + (z - z')^2] [1 - m \sin^2 \theta]$$

where

$$m = \frac{4\rho\rho'}{(\rho + \rho')^2 + (z - z')^2}$$

$$\theta = \frac{1}{2}(\pi - \Psi)$$

Senior and Ahlgren (p. 61) show that

$$\Omega_0 = \frac{1}{4} \left(\frac{m}{\rho\rho'} \right)^{3/2} \left[K(m) + 2m \frac{d}{dm} K(m) \right]$$

$$\Omega_1 = \left(\frac{m}{\rho\rho'} \right)^{3/2} \left[\left(1 - \frac{m}{2}\right) \frac{d}{dm} K(m) - \frac{1}{4} K(m) \right]$$

$$\Omega_2 = \frac{1}{m^2} \left(\frac{m}{\rho\rho'} \right)^{3/2} \left[2m \left(1 - \frac{m}{2}\right)^2 \frac{d}{dm} K(m) - \left(1 - \frac{m^2}{4}\right) K(m) + E(m) \right]$$

where K and E are Elliptic Integrals.

The Electric Polarizability Tensor is

$$X_{ij} = (1 - \epsilon_r) \int_B \hat{n} \cdot \hat{x}_i \Phi_j dS$$

For the case of rotational symmetry about the z-axis $X_{11} = X_{22} \neq 0$;

$X_{33} \neq 0$; $X_{ij} = 0, i \neq j$. Hence we need only find X_{11} and X_{33} .

The absorption cross-section can be expressed in terms of X_{ii} , and by averaging over all possible scatterer orientations (all assumed equally likely) one gets the average absorption cross-section:

$$\langle \sigma_A \rangle = \frac{k_0 V}{3} \text{Im.}(2X_{11} + X_{33})$$

where k_0 is the free-space wavenumber of the incident light, and V is the volume of one scatterer. The dimensionless quantity $\langle \sigma_A \rangle / k_0 V$ is used in the plots of absorption vs. frequency (in 10^{15} Hz) presented in the Results section.

II. PRACTICE:

The integral equations for W_1 and W_3 are solved using the moment method. We choose pulse basis functions and delta-function weighting functions to get a point-matching solution.

The body perimeter is broken up into equal-length arcs and the W 's are determined at the center of each arc. The integral becomes:

$$\int_{s'} W_i(s') K_i(\bar{r}, \bar{r}') \rho' ds' = \sum_{j=1}^N W_i(s_j) \int_{s_j - \Delta/2}^{s_j + \Delta/2} K_i(\bar{r}, \bar{r}') \rho' ds'$$

where j runs over every segment of the perimeter, and i is either 1 or 3.

A simple six-point integration scheme works well if \bar{r} is on the surface, and the surface has no cusps. However, to get the near fields, and accurate surface values for complicated shapes, a more sophisticated method must be used. This is because for \bar{r} near the surface $K(\bar{r}, \bar{r}')$ varies rapidly, hence a 6-point integration scheme will not capture it sufficiently.

Our method removes the rapidly-varying terms and integrates them analytically over the appropriate very small sub-segment (approximating it as straight, no longer curved). This can give us accurate field values near the surface and elsewhere. However, at the time of this conference the closest we have gotten to the surface for accurate off-surface values is about a tenth of the local radius of curvature of the body's surface. This is because we have yet to remove another singularity, as explained in the following section.

Singularity Extraction and Integration:

The troublesome terms are in the Ω_n 's . Specifically a $\frac{1}{m_1}$ term and a $\ln(\frac{1}{m_1})$ term. Both blow up as the field point approaches the surface (source point) in our integral equations. Since

$$K(m) \simeq (a_0 + a_1 m_1 + \dots + a_4 m_1^4) \\ + (b_0 + b_1 m_1 + \dots + b_4 m_1^4) \ln\left(\frac{1}{m_1}\right)$$

$$\frac{d}{dm} K(m) \simeq \left(\frac{b_0}{m_1} + (b_1 - a_1) + (b_2 - 2a_2)m_1 + \dots + (b_4 - 4a_4)m_1^3\right) \\ - (b_1 + 2b_2 m_1 + \dots + 4b_4 m_1^3) \ln\left(\frac{1}{m_1}\right)$$

$$E(m) \simeq 1 - \frac{1}{4} m_1 + \frac{1}{4} m_1 \ln\left(\frac{1}{m_1}\right)$$

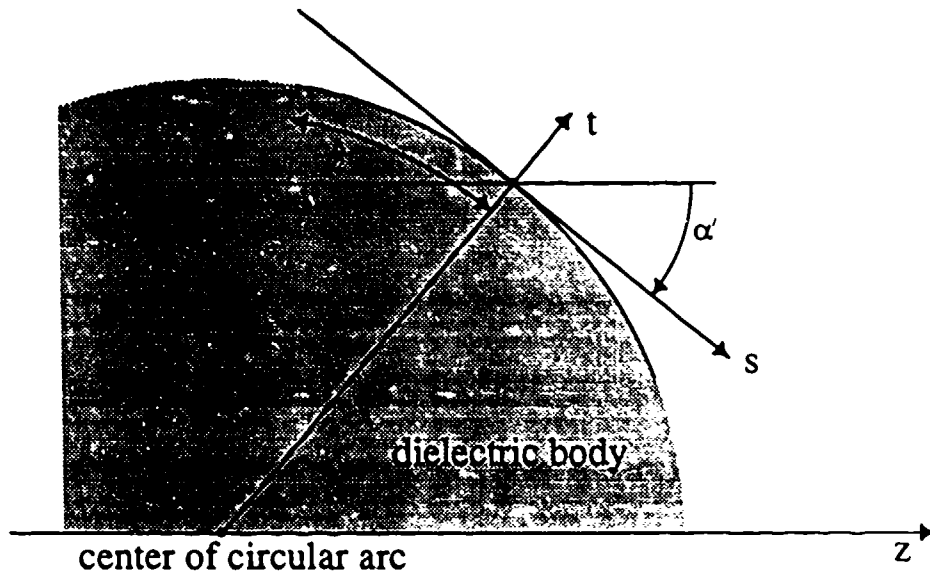
where $m_1 = 1 - m$. The troublesome terms are:

$$\begin{aligned} & \frac{b_0}{m_1} \quad \text{in the } \frac{d}{dm} K(m) \text{ term,} \\ & -b_1 \ln\left(\frac{1}{m_1}\right) \quad \text{in the } \frac{d}{dm} K(m) \text{ term,} \\ & \text{and } b_0 \ln\left(\frac{1}{m_1}\right) \quad \text{in the } K(m) \text{ term.} \end{aligned}$$

The constants a_i and b_i can be found in Abramowitz and Stegun [1964] . We pulled these terms out of the expressions for $K_i(\bar{r}, \bar{r}')$, integrated them analytically, then added them back in to the numerical integration which was done with the remaining terms.

The geometry to explain the following formulas for the analytic evaluations is

shown in the following figure.



We need to evaluate two integrals involving b_o/m_1 :

$$I_1 = \int_{-\frac{\Delta}{2}}^{\frac{\Delta}{2}} \frac{1}{m_1} ds' = 2 \sin \alpha' (s \sin \alpha' + t \cos \alpha') \ln \left[\frac{\Delta^2/4 - s\Delta + s^2 + (t' - t)^2}{\Delta^2/4 + s\Delta + s^2 + (t' - t)^2} \right] + \Delta$$

$$+ \frac{4(s \sin \alpha' + t \cos \alpha')(s \sin \alpha' + t' \cos \alpha')}{t' - t} \left[\tan^{-1} \left(\frac{\Delta - 2s}{2(t' - t)} \right) + \tan^{-1} \left(\frac{\Delta + 2s}{2(t' - t)} \right) \right]$$

$$I_2 = \int_{-\frac{\Delta}{2}}^{\frac{\Delta}{2}} \frac{s'}{m_1} ds' =$$

$$(s \sin \alpha' + t \cos \alpha') \left\{ (4s \sin \alpha' + 2t' \cos \alpha') \ln \left[\frac{\Delta^2/4 - s\Delta + s^2 + (t' - t)^2}{\Delta^2/4 + s\Delta + s^2 + (t' - t)^2} \right] + 4\Delta \sin \alpha' \right.$$

$$\left. + \frac{4[st' \cos \alpha' + s^2 \sin \alpha' - (t' - t)^2 \sin \alpha']}{t' - t} \left[\tan^{-1} \left(\frac{\Delta - 2s}{2(t' - t)} \right) + \tan^{-1} \left(\frac{\Delta + 2s}{2(t' - t)} \right) \right] \right\}$$

These integrals are combined with the other terms in the expressions for the Ω_n 's and then with others to make the K_i 's. The following expressions are for that part of each K_i that is singular:

$$K_{1\text{extra}} = \frac{2[s^2 + t^2 + t'^2 + 2t' \sin \alpha' (s \cos \alpha' - t \sin \alpha')]}{t' [s^2 + (t + t')^2 + 4t' \sin \alpha' (s \cos \alpha' - t \sin \alpha')]^{5/2}}$$

$$\cdot (s^2 + t^2 - t'^2) [t' \cos \alpha' I_1 + \sin \alpha' I_2]$$

$$K_{3\text{extra}} = \frac{4 \cos \alpha' [s \sin \alpha' + t \cos \alpha'] [s^2 + t^2 - t'^2]}{[s^2 + (t + t')^2 + 4t' \sin \alpha' (s \cos \alpha' - t \sin \alpha')]^{5/2}} [t' \cos \alpha' I_1 + \sin \alpha' I_2]$$

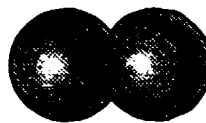
As of the date of this conference we are still in the process of doing the $\ln(m_1)$ term, but the analysis is similar.

III. RESULTS:

We simulated two spheres, both separate and overlapping. Two examples are the following:



separate



overlapping

The center-to-center separation of the two spheres is given in terms of the sphere diameter. For example, the separate spheres above have a center-to-center separation of about 2, whereas the two overlapping spheres have a center-to-center separation of about 0.8 .

The fields were plotted with a variety of separations and also at many different frequencies; each different frequency corresponds to a different ϵ for gold, tabulated in Physik Daten [1981] and plotted in fig. 1. The dimensionless average absorption cross-section, as described earlier, was plotted for each geometry as a function of frequency.

Our results agree qualitatively with gold colloid observations where the colloid looks deep red when the gold particles are distinct and changes to blue when the particles aggregate as described, for example, in Weitz, et. al. [1985]. This can be seen in the absorption spectra later in this paper. To convert the frequency

used there into wavelength one can use the formula:

$$\lambda(\text{in } \mu\text{m}) = \frac{0.3}{f \text{ (in } 10^{15} \text{ Hz)}}$$

Hence, the absorption spectrum plot for a single gold sphere can be seen to have its peak at about 0.58×10^{15} Hz, which corresponds to blue light, and then to tail off slowly after that. Therefore a single gold sphere, or a collection of widely separated gold spheres, will absorb blue light significantly more than the red and yellow and hence based on this analysis the un-aggregated colloid will appear reddish-yellow in white light. Similarly, for two aggregated spheres (separation = 1.0) the peak absorption is at 0.45×10^{15} Hz, corresponding to red light, while the absorption at the blue wavelengths is about five times less. Hence, in an aggregated colloid the red is absorbed more than the blue and it would look blue in white light.

Note that this analysis can also be easily applied to a variety of other materials including other metals, lossy materials, and smoke.

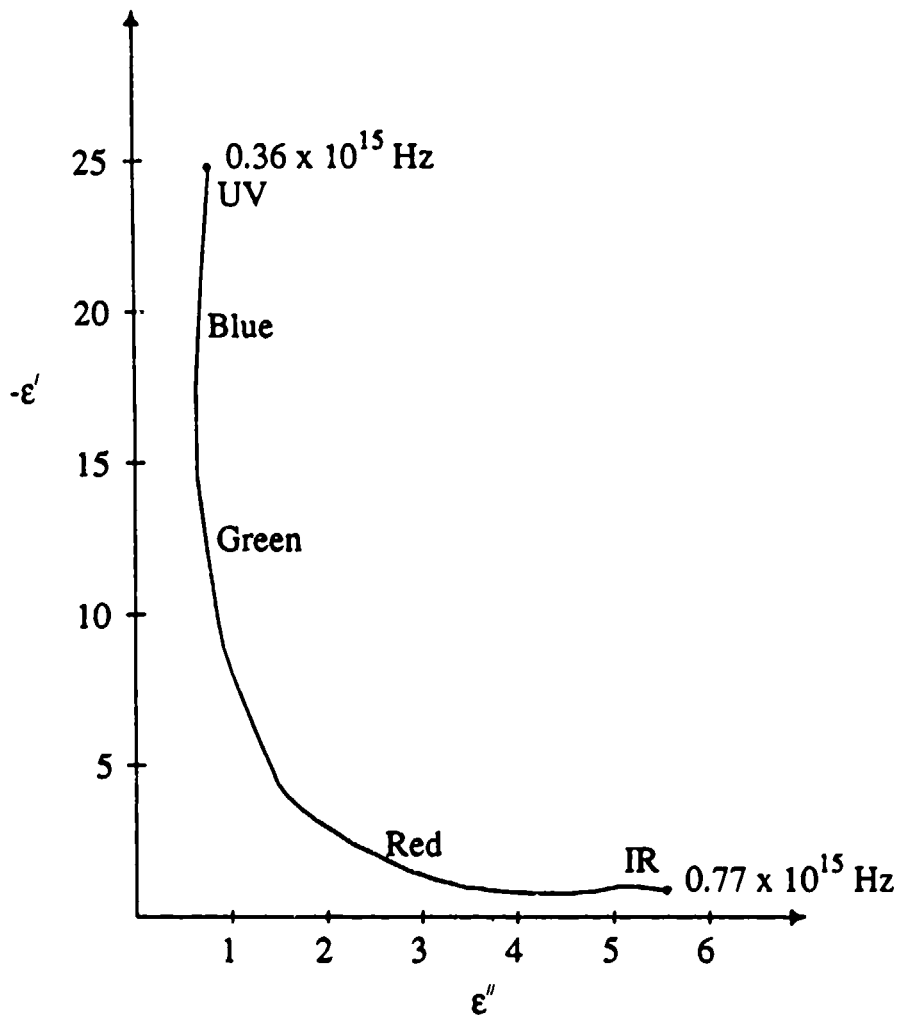
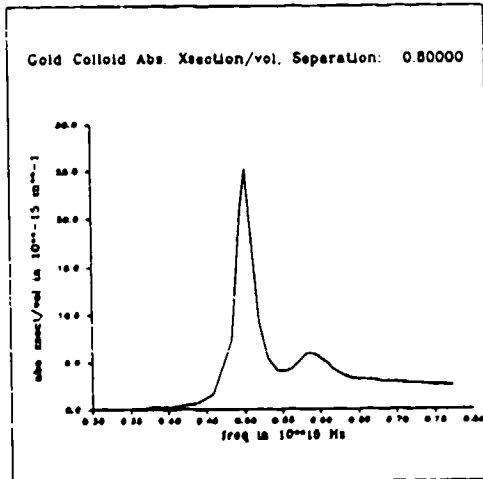
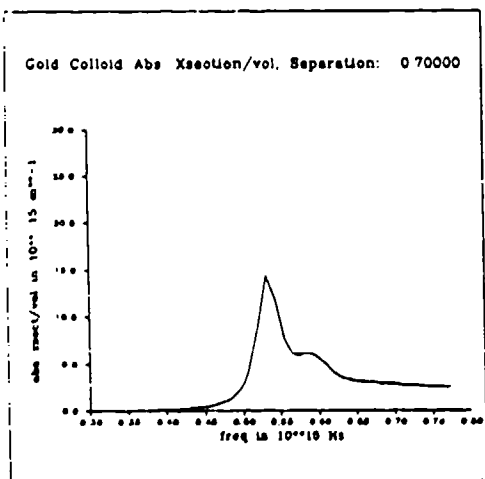
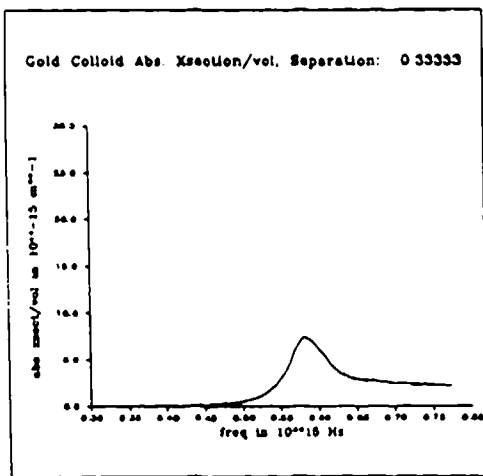
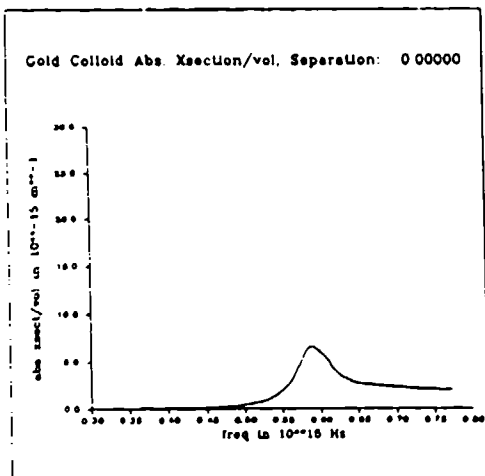
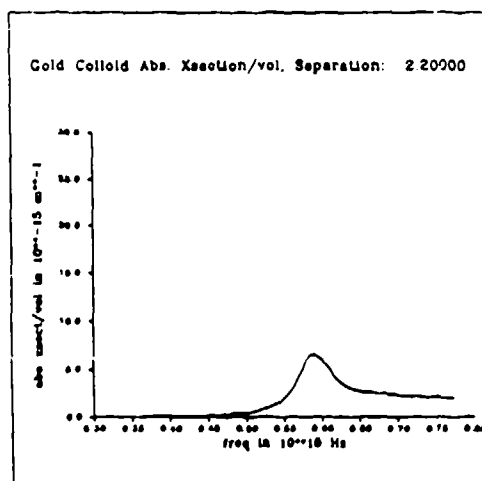
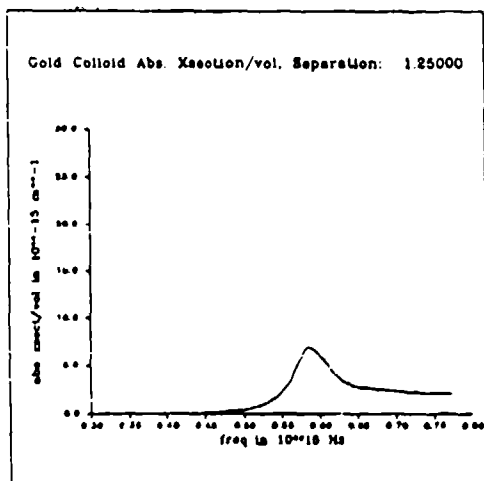
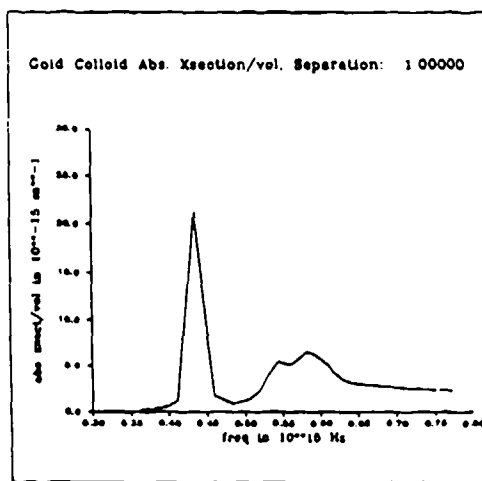
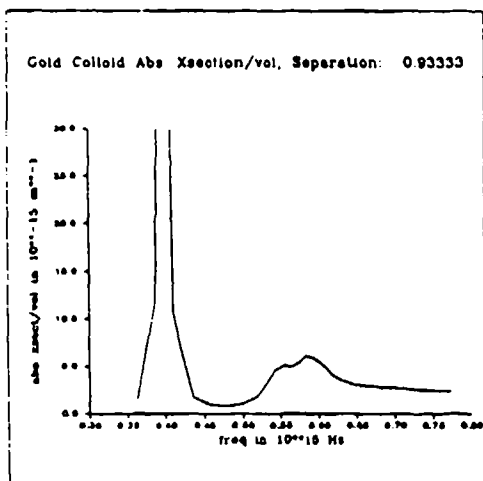


Figure 1: Permittivity in vicinity of visible and IR frequencies for gold. ($\epsilon_r = \epsilon' + j\epsilon''$)



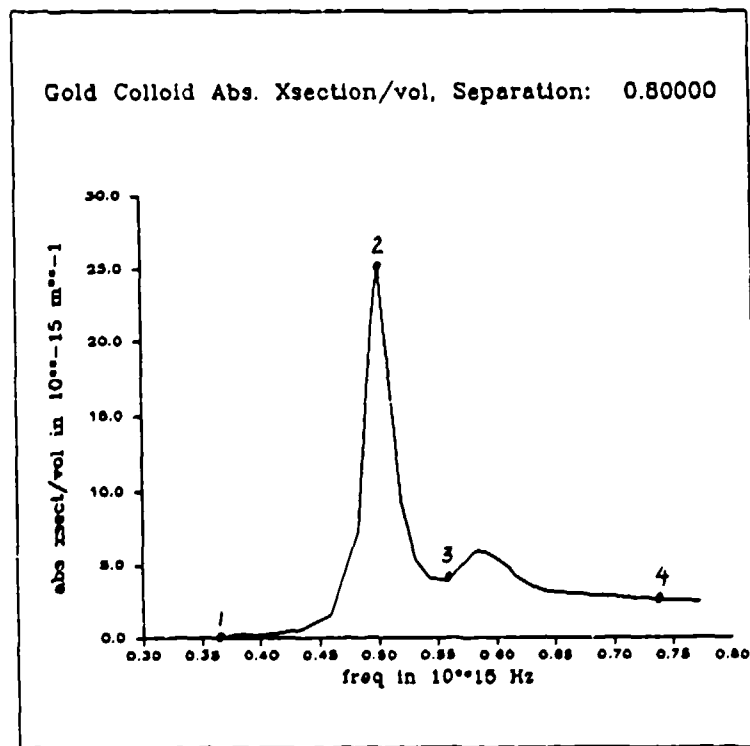
Absorption Cross-Section Spectra for Aggregated Spheres.



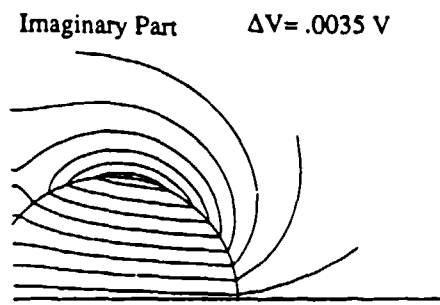
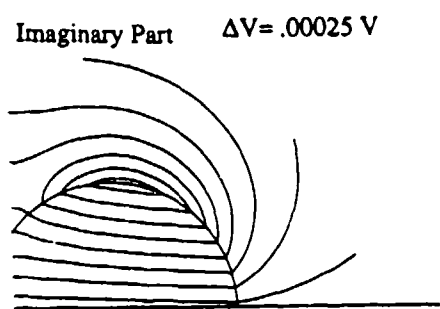
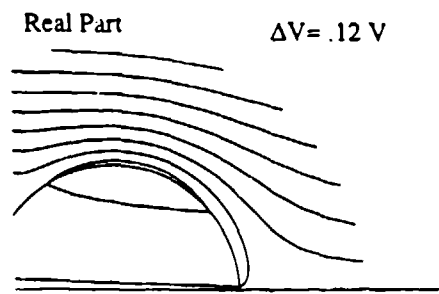
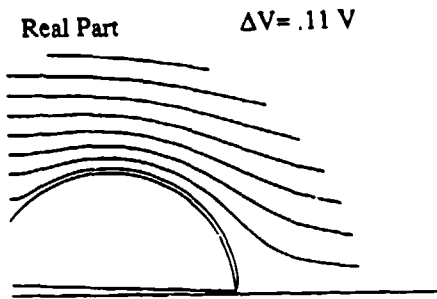
Absorption Cross-Section Spectra for Aggregated Spheres.

Equipotential Plots, selected frequencies

1. Each figure on the next two pages has the real part and imaginary part of the potential for a particular shape, frequency and 'incident' E-field direction.
x-directed means E is vertical at infinity.
z-directed means E is horizontal at infinity.
2. Each plot has 8 equipotential lines, but ΔV between them varies from plot-to-plot. Hence a large value for ΔV means that we have high local E-field concentrations.
3. ϵ_r in each plot is the value for the relative dielectric constant.
4. Each plot is associated with a point on the graph below. From that can be determined the 'frequency' in each field plot. They are static field plots with the only vestige of frequency being in the relationship of ϵ_r to f for gold.
5. All the plots are for a center-to-center separation of 0.8 between two solid spheres each with a radius of 0.5.
6. Only one quadrant in the x_1x_3 -plane is shown. The equipotential lines in the other quadrants may be obtained by symmetry.

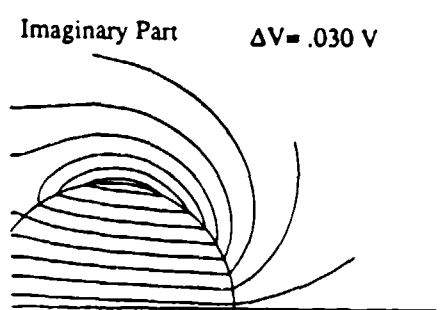
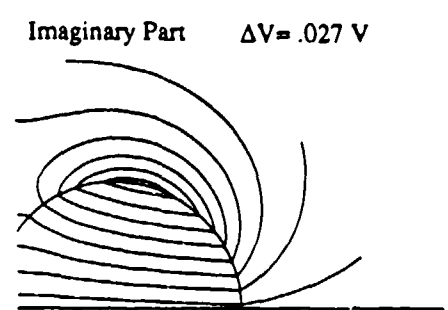
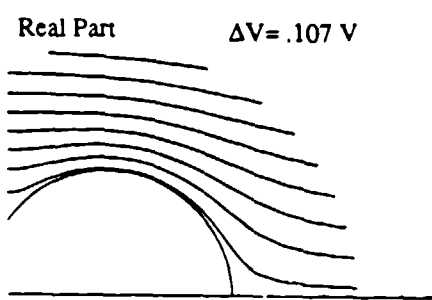
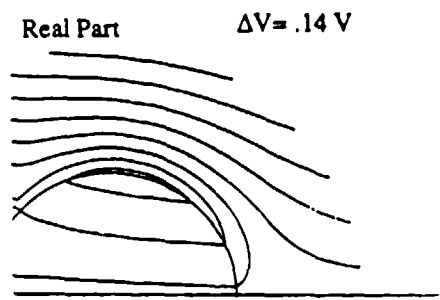


X-Directed Excitation



1: $\epsilon_r = -24.79 + j 0.79$

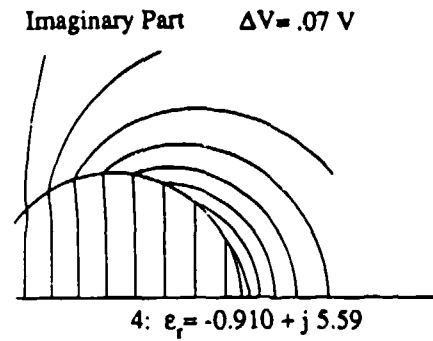
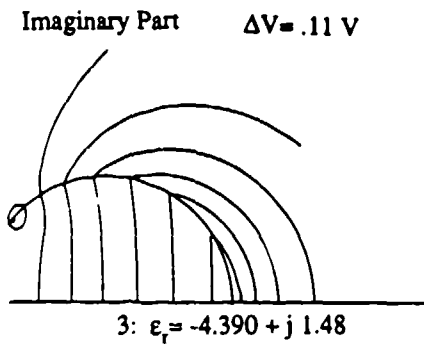
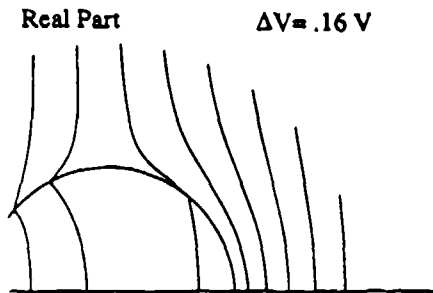
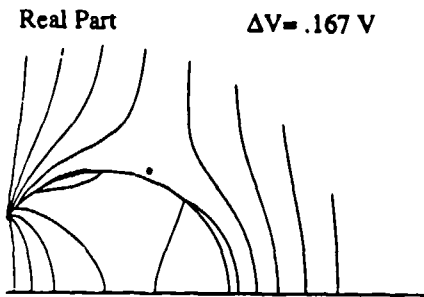
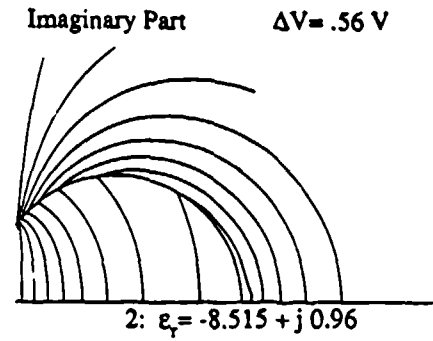
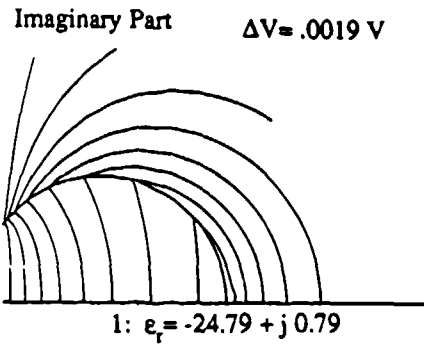
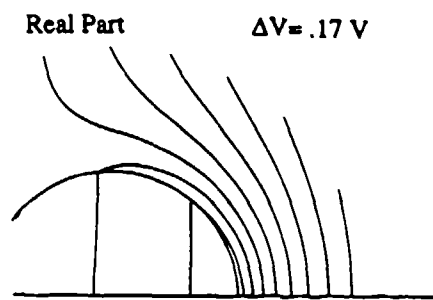
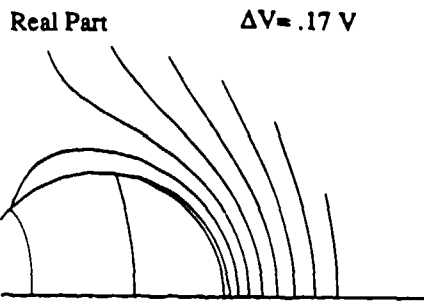
2: $\epsilon_r = -8.515 + j 0.96$



3: $\epsilon_r = -4.390 + j 1.48$

4: $\epsilon_r = -0.910 + j 5.59$

Z-Directed Excitation



References:

1. Abramowitz, M. and Stegun, I. A. , Handbook of Mathematical Functions. National Bureau of Standards, 1964.
2. Physik Daten; Part II, Fachinformationzentrum Energie, Physik, Mathematik, GMBH, Karlsruhe, 1981.
3. Senior, T.B.A. , Low-frequency scattering by a dielectric body. Radio Science, **11**, pp. 477-482, 1976.
4. Senior, T.B.A. and Ahlgren, T.J. , The numerical solution of low-frequency scattering problems. Univ. of Mich. Radiation Lab. Scientific report # 013630-9-T, Feb, 1972.
5. Weil, H. , Proceedings of the 1985 Scientific Conference on Obscuration and Aerosol Research. pp. 547-551. July 1986, Report # CRDEC-SP-86019.
6. Weitz, D. A., M. Y. Lin, C. J. Sandroff. Colloidal Aggregation Revisited: Surf Sci (Netherlands), Vol. 158, pp. 147-164, 1985. See especially p. 148 and p. 157.

Various Geometrical Designs for Electrodynamical Particle Traps and Their Characteristics

H.-B. Lin
*Naval Research Laboratory
Washington D.C.*

J. D. Eversole
*Potomac Photonics Inc
College Park, MD 20742*

B. Bronk
*U.S. ARMY CRDEC
Aberdeen Proving Ground, MD 21010*

Recent Publications

ABSTRACT

The bihyperboloidal electrodynamic particle trap has been used extensively for the study of individual particles, and has also received much theoretical consideration. While non-hyperboloidal levitation cells also have been employed previously, such designs are inherently less mathematically tractable, and consequently have received little theoretical attention. In order to gain confidence in the application of designs which deviate from the classic, bihyperboloid shape, we have adopted an empirical approach in which traps using a variety of electrode arrangements (including spherical surface electrodes, and "linear" quadrupoles such as are employed in mass spectrometers) have been quantitatively compared in their ability to suspend and stabilize similar particles. Of special interest is the condition of minimum particle motion occurring at the symmetry or null point of the cell. Comparison among some of the different cells was achieved by measuring the particles null point motion using scattered laser light. The scattered light is heterodyned with a frequency shifted reference beam, in effect forming an interferometer capable of resolving periodic motion with an amplitude of $0.02 \mu\text{m}$ (re 100 Hz). The trap designs studied in this way have demonstrated equivalent capability compared to the bihyperboloidal cell. The general characteristics of each design is discussed.

Introduction

Particle traps using alternating electric fields have been successfully employed as research tools for over two decades. Such traps are commonly referred to as quadrupole levitation cells or electrodynamic balances. The alternating electric field provides a pseudo-potential well to contain the charged particle, while a vertical static electric field is also usually provided to counter the force of gravity and maintain the particle at the potential well minimum. However, rigorous theoretical treatment of the electric field and particle equations of motion has only been achieved for the particular case of bihyperbolic electrode geometry. Although

a wide range of cell designs and electrode geometries have been used previously with apparent success,¹⁻⁹ observations under vacuum conditions show significant particle motion¹⁰. With the addition of damping forces from normal gas pressure, it is not clear to what extent residual particle motion remains.

We have attempted to quantify the difference between selected types of cells in comparison to the hyperboloid design in terms of the minimum or nullpoint motion of a trapped particle, and explore other specialized designs. The motivation behind this work has been two-fold: (a) to provide greater optical access to the particle for light scattering studies and (b) to determine the feasibility of particle storage and transfer. Our approach to this study was to make a quantitative determination of trapped particle motion using an interferometric optical technique. To our knowledge, previous observations and assessments of balanced particle motion have all been visual, and therefore somewhat subjective and difficult to compare. In this part of our study, three cells with different electrode surface shapes were fabricated and compared in terms of the amplitude of periodic motion of similar particles levitated in each. Measurement of particle motion was achieved by forming a Mach-Zehnder type of interferometer with scattered light from the particle. A heterodyne beat signal was generated by shifting the frequency of the reference beam a known amount and then recombining the scattered light with the shifted reference beam at a diode detector. By examining the resulting beat signal with a spectrum analyzer, this technique easily provided a resolution of the particle motion amplitude of about $0.02 \mu\text{m}$ (at frequencies greater than $\sim 100 \text{ Hz}$). Since several extensive descriptions of the theory of particle motion in the electrodynamic balance and its design have already been published,¹⁰⁻¹³ no attempt will be made to provide that background here. Greater detail of the experimental arrangement and measurement technique can also be obtained elsewhere.¹⁴

Results

Three different electrode designs were initially studied. These traps are cylindrical and Figure 1 shows the cross sectional schematic through the vertical (symmetry) axis for each: (a) the bihyperboloidal standard, (b) spherical surface approximation to (a), and (c) a variant of (b) with a horizontal mid-plane section of the center, or ring electrode removed. The conclusion from examining the null point motion of 30 and 11 mm diameter glass spheres suspended in the different traps at atmospheric pressure is that no difference can be determined down to the resolution of our measurement. Particle motion in response to an external force (such as gravity) was linear in each case as shown in Figure 2. Fig 2(a) shows the motion amplitude of a $30 \mu\text{m}$ glass sphere in the hyperbolic-surface trap (Fig. 1(a)), while in (b) the motion of an $11 \mu\text{m}$ glass sphere in the spherical-surface split-ring trap (Fig. 1(c)) is shown.

Linear types of traps which might be able to stably suspend multiple particle along a line of equilibrium rather than at a point were also considered. The initial

concept along these lines was to extend the cross sections shown in Fig. 1 along the dimension perpendicular to the page, thus transforming the center, or null point into a null line which is horizontal as shown in Figure 3(a). An alternative conception was to arrange four metal rods vertically with their ends joined to the corners of two plastic squares (top and bottom) as shown in Fig. 3(b). Diametrically opposite rods were electrically connected and the alternating potential was applied between the two pairs of rods forming an electrodynamic potential well along the center line vertical axis, entirely analogous to commercially available quadrupole mass spectrometers. To keep the particle from falling out the bottom of this trap, metal plates were placed on the inside surfaces of the square plastic end pieces, and a dc balancing voltage applied. The characteristics of these various designs have been listed in outline from below:

Spherical Surface - Split Ring Cell Characteristics

- Operation Identical to Classic Bihyperboloidal Cell - Particle Exhibits Normal Dynamics
- Ease of Particle Capture Similar to Bihyperboloidal Cell
- Stability at Null Point Indistinguishable from Bihyperboloidal Cell
- Offers Extended Viewing of Particle Between Split Rings and also Between Ring and Endcap Electrodes
- Provides continuous Scanning of Scattering Angle
- Simpler Geometry is Relatively Easy to Fabricate

Spherical Surface Cell - Linear Extension - Characteristics

- Operation Similar to Other Axis-symmetric Cells, Particle is Balanced Vertically by DC Voltage
- Particles Can Be Transported from One End of the Cell to the Other Along its Centerline by Either Electrostatics or Hydrodynamics
- Particles Can Be Delivered to the Trap either from the Ends, the Top, or the Sides
- Multiple Particles are Suspended in a Row Along the Centerline
- Particles are Subject to Greater Lateral Oscillations than in the Axis-Symmetric Cells

Vertical Linear Quadrupole Trap

- Particles are "Automatically" Balanced Vertically
- Vertical Position of the Particle is Determined by the DC Voltage
- Multiple particles are Suspended Vertically Along the Centerline
- Particles Can Be Delivered into the Trap Independently
- Lateral Oscillations Always Present

Obvious areas of future investigation would be to explore the pressure dependence of the null point stability measurement for the various trap designs since it is well-known that null point motion becomes visible under vacuum even for the bihyperboloidal design. Also it would be interesting to extend the range of particle size and/or mass to a lower limit than was possible with our current apparatus.

REFERENCES

1. H. Straubel, Dechema Monograph, **32**, 153, (1959).
2. S. Ataman and D.N. Hanson, Ind. Eng. Chem. Fundam., **8**, 833, (1969), and J.W. Schweizer and D.N. Hanson, J. Colloid and Interface Sci., **35**, 417 (1971).
3. T.G.O. Berg and T.A. Gaukler, AM. J. Phys., **37**, 1013, (1969).
4. C.B. Richardson and J.F. Spann, J. Aerosol Sci., **15**, 563, (1984).
5. R.F. Wuerker, H.M. Goldenberg, and R.V. Langmuir, J. Appl. Phys., **30**, 441, (1959).
6. H.H. Blau, D.J. McCleese, and D. Watson, Appl. Opt., **9**, 2522, (1970).
7. C.B. Richardson, H.-B. Lin, R. McGraw, and I.N. Tang, Aerosol Sci. and Tech., **5**, 103 (1986).
8. E.J. Davis and A.K. Ray, J. Colloid Interface Sci., **75**, 566, (1980).
9. A. Pluchino, Optics Lett., **11**, 276,(1986).
10. R.F. Wuerker, H. Sheldon, and R.V. Langmuir, J Appl. Phys. **30**, 347 (1959).
11. R.H. Frickel, R.E. Shaffer, and J.B. Stamatoff, Tech. Report ARCSL-TR77041, U.S. Army Armament Research and Development Command, Aberdeen, Maryland (1978).
12. A. Müller, Ann. Phys., **7**, 206, (1960).
13. E. James Davis, Langmuir, **1**, 379 (1985).
14. J. D. Eversole and H.-B. Lin, "Effects of Design on Null Point Motion of Spheres Suspended in the Electrodynamic Balance", Rev. Sci. Instr., **58**, 1190, (1987).

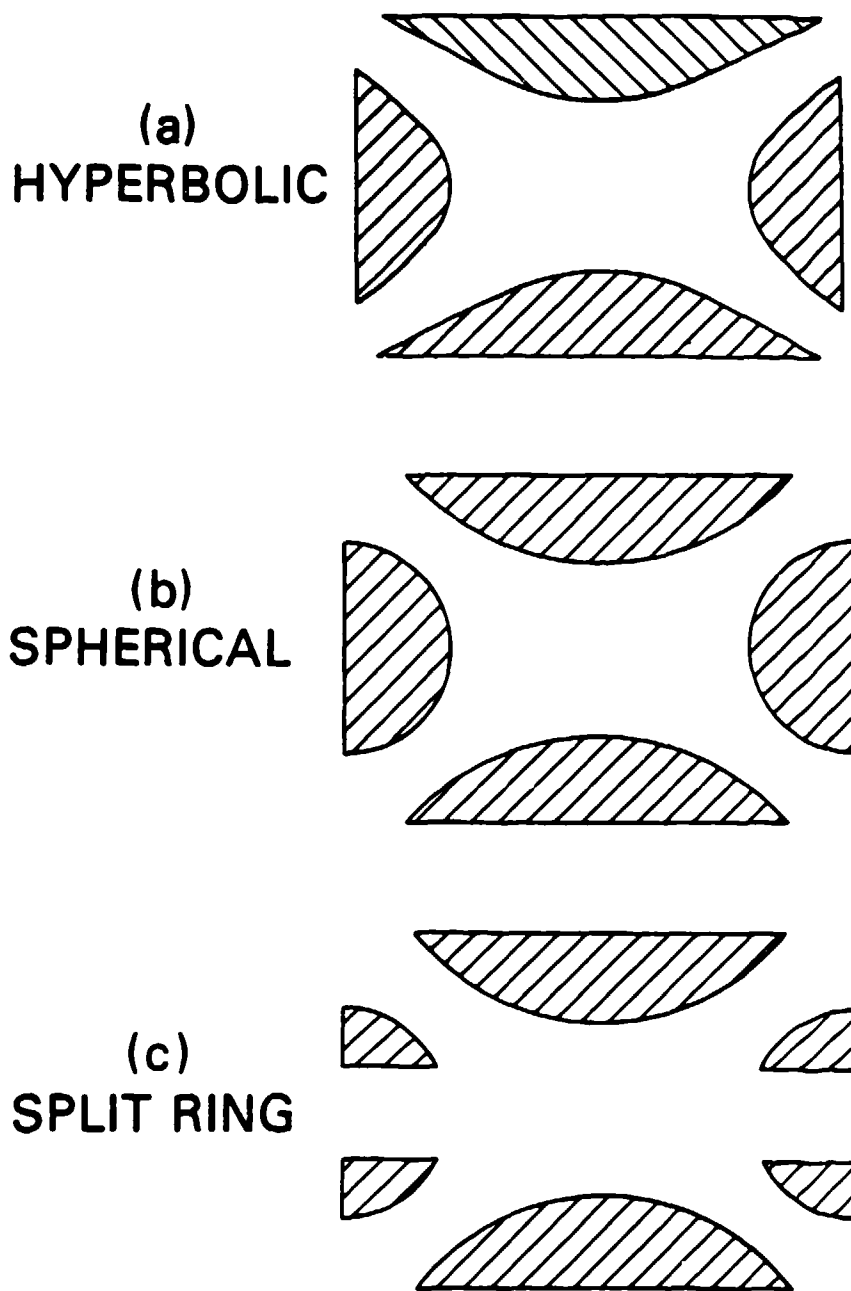


Figure 1. Schematic diagrams showing the cross sections of different electrode designs for the three quadrupole levitation cells studied: (a) hyperbolic, (b) spherical, and (c) is the same as (b) but with the mid-section of the ring electrode removed. The three cell designs are drawn to the same scale.

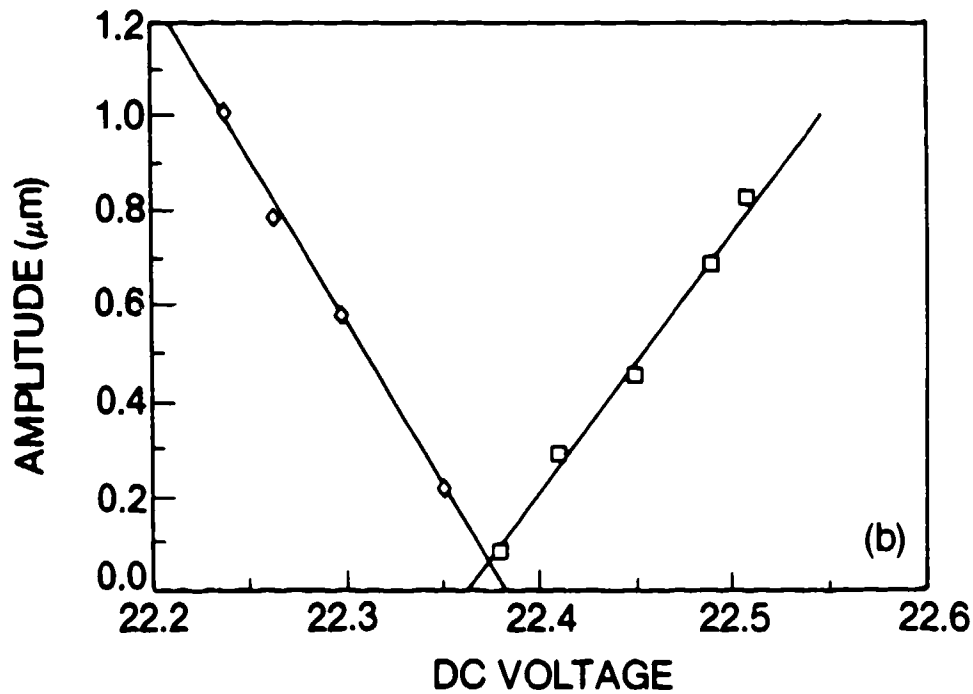
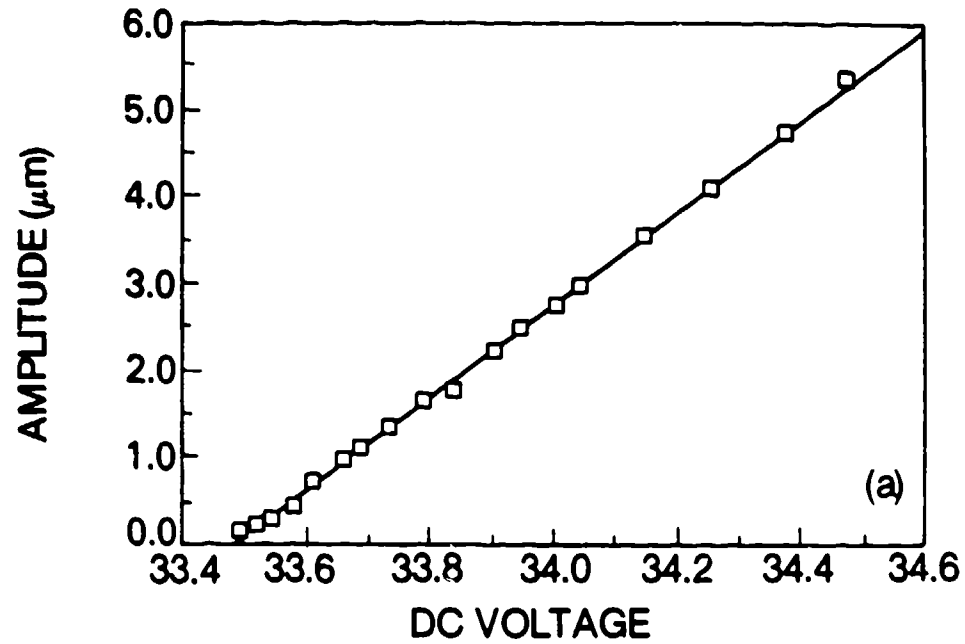


Figure 2. Graphs of particle displacement as a function of the d.c. balancing voltage showing good linearity in each case, and similar behavior among different cell designs and particle sizes: (a) from a 30 μm diameter sphere in the hyperbolic cell, and (b) from a 11 μm sphere in the split ring cell. In (b), two independent measurements are shown with increasing (squares), and decreasing (diamonds) d.c. voltage.

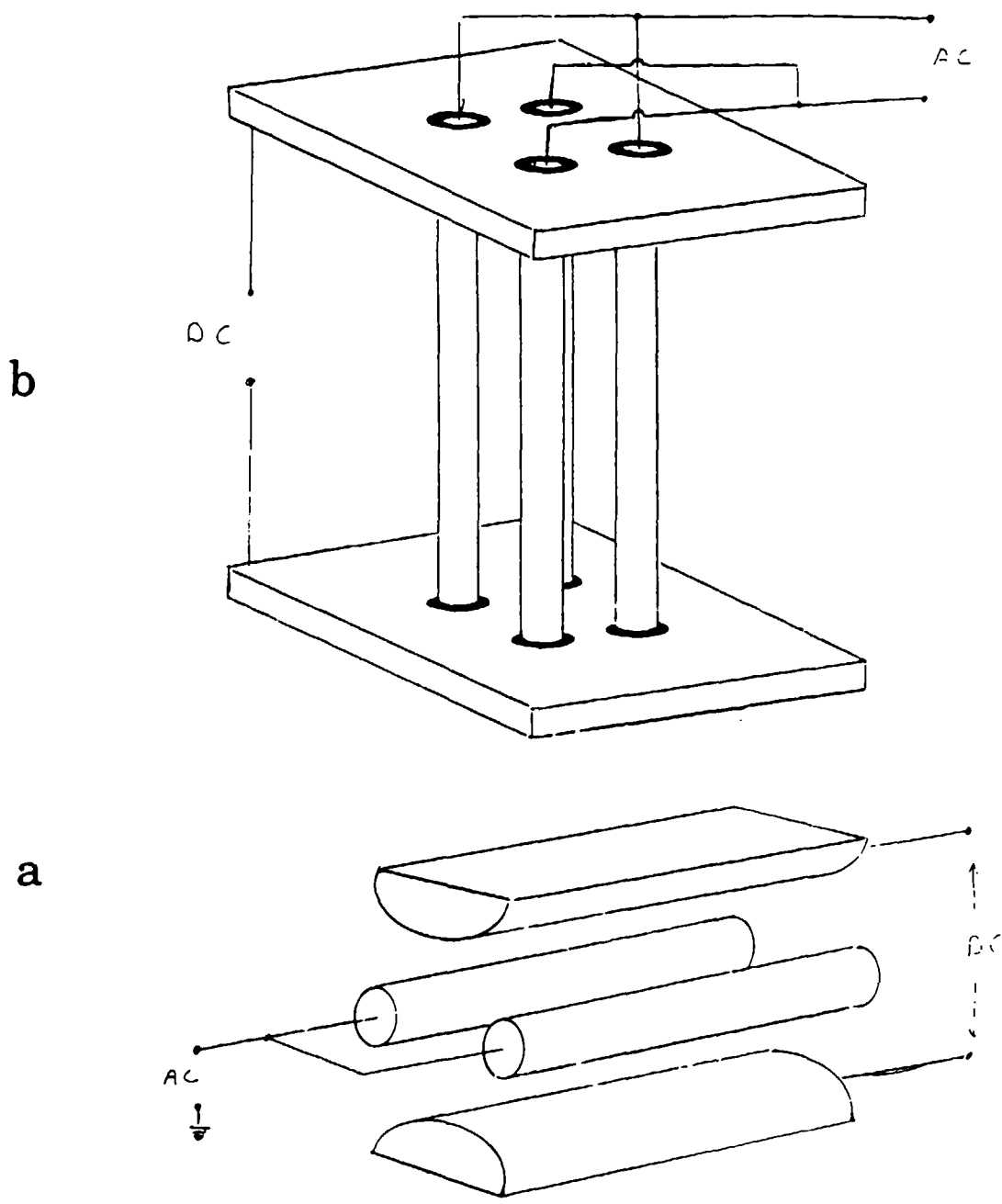


Figure 3. Schematic drawings of (a) the linear extension of the spherical surface trap, and (b) the verticle linear trap.

Blank

EXPERIMENTAL INVESTIGATION OF POST BREAKDOWN EFFECTS

A. Biswas
P. Shah
R. L. Armstrong
L. J. Radziemski

Applied Laser/Optics
Physics Department
New Mexico State University
Las Cruces, NM 88003-0001

ABSTRACT

Perturbations of the ambient medium by laser induced plasmas initiated in clean air, or on aerosols and solid surfaces, affect the passage of laser energy through the perturbed volume. The time and spatial extent of the perturbation is of interest in determining degradation of laser beam transmission. Photothermal spectroscopy and two-pulse breakdown threshold studies are being used to diagnose these effects. Significant probe perturbations were seen in the 0-5 μ s and 2 ms time scales. Preliminary explanations are offered and suggestions are made for further studies on these effects. We are planning to study the shocks formed by the plasmas. After that we will begin looking at the effects on irradiated (sub-plasma) aerosol droplets.

INTRODUCTION

There is continuing interest in the physics of laser-induced breakdown plasmas, the interaction of high irradiance laser beams with clean air and aerosols. Measurements have been made of explosive aerosol vaporization (1), shock-wave formation (2), spatially resolved spectra of exploding aerosol droplets (3), and time resolved spectra of plasmas formed on a single levitated aerosol droplets (4). Time dependent hydrodynamic effects have been subjects of theoretical analyses (5) and measurements (6). Afterglow measurements of a laser induced plasma in helium at a pressure of 10 atmospheres have been carried out using a He:Ne probe beam (7) where electron density, temperature and absorption coefficient of the plasma could be determined during the first 600 nanoseconds after the laser fired. In this work the shock wave was also studied.

In spite of all this work on the primary interaction causing laser induced breakdown, little attention has been given to the subsequent state of the medium. The resulting perturbations can be called post-pulse or second-pulse effects. One knows from much of the work above and other analyses (6) that a plasma causes a transient local high temperature and low density in the breakdown volume. The point of the present study is to determine for some conditions, the duration of the perturbation on the "second pulse". Two time resolved diagnostic techniques have been used. The first, photothermal spectroscopy (8), measures the ensuing wavefront perturbation. The point of departure of our study from the work reported (7) is to detect and study effects of the plasma long after the luminous afterglow. Furthermore our conditions are also different in that the plasma is formed at atmospheric pressure in the laboratory air. The photothermal signal we observe is due to either a lens effect or a deflection of the probe beam due to a transient perturbation altering the refractive index in a volume in and around the laser initiated plasma.

The second, the modification of the breakdown thresholds for the second pulse by the first pulse, is a direct measure of the ability of a second intense laser beam to pass through the plasma perturbed volume. At the beginning of this study little was known about the longevity of the perturbation of the medium. The measurements we have made have defined the temporal duration, at least for the set of conditions we have used. In general there might be two effects. First, the plasma formed by the first

pulse might leave enough free electrons so that, for a certain period of time, breakdown by a second pulse is more likely. This is equivalent to lowering the breakdown threshold. On the other hand the first plasma might disrupt the focusing properties of the medium so that the irradiance of the second pulse would be degraded, inhibiting plasma formation, and aiding second pulse transmission. This is equivalent to raising the breakdown threshold. As we shall see below, both effects have been observed.

EXPERIMENTAL SETUP

A plasma was initiated by focusing firstly, a Nd:YAG (0.532 μm) and secondly a pulsed CO_2 (10.6 μm) laser on to the surface of a nail (without the nail the CO_2 plasma could not form reproducibly). The He:Ne beam axis was aligned to be perpendicular to the initiated plasma axis. The focusing lens for initiating the plasma along with the nail on which the plasma is initiated is translated in 100 μm steps so that the He:Ne probes the plasma along the axis of the initiating beam. The total length scanned in this manner is about 7 mm of which the luminous region of the plasma extends up to 3-4 mm. The zero or start position for this scan is such that the He:Ne probe is almost flush with the surface of the nail on which the plasma initiates. Figure 1a shows the experimental arrangement schematically. The He:Ne beam is guided with the aid of the plane mirrors M1 and M2 (see figure 1a) to pass through a He:Ne line filter and brought to incidence on a 500 μm pinhole mounted in front of a photomultiplier tube. The photomultiplier (PMT) signal is then amplified and fed into a transient waveform digitizer with a 5 ns resolution. The details of the apparatus used are in Table 1.

In the absence of any plasma a steady dc signal of the He:Ne beam is observed. In the presence of the plasma the digitizer is triggered by the laser firing and post-pulse perturbations experienced by the He:Ne beam can be recorded as a function of the position of the probe and the time after the laser fired. The experimental arrangement also allows imaging the plasma on to the PMT by removing the He:Ne line filter so the time for which the luminous afterglow of the plasma lasts can be measured.

Some variations of the above described experimental setup have also been used. Sometimes the He:Ne beam was passed almost parallel to the plasma-initiating beam axis so that the plasma was now probed nearly along its axis. Furthermore plasmas were initiated on single optically levitated solid (glass microspheres) and liquid (glycerine droplets) and the He:Ne probed the resulting plasma (see Figure 1b).

For the two-pulse studies widely differing wavelengths required that separate optics be used to focus each beam. This dictated a counter-propagation arrangement, as illustrated in Figure 2. The relevant experimental parameters are contained in table I. It was critical that the beam be focused into the same volume in space. For alignment a 500 μm diameter pinhole was placed at the focus of the CO_2 beam. Each lens was manipulated until a plasma from each beam could be seen forming in the hole. The alignment was checked visually with the pinhole removed. With small time intervals between the two pulses, a muffled "pop" could be heard when the beams were correctly focused. Plasma formation was monitored by a fast photodiode which sensed the plasma light emitted, but was insensitive to either of the laser wavelengths. The signal from the photodiode went directly to a transient waveform digitizer. The temporal arrangement of the two laser pulses was controlled by a four-channel digital delay generator accurate to 2 ns. The two cases investigated were CO_2 first and Nd:YAG first. In the former the spacing between the two pulses was varied from 20 μs to 3.5 ms, in the latter from 50 μs to 1 s.

EXPERIMENTAL RESULTS

A. PHOTOTHERMAL PERTURBATIONS

In general we observe two types of signals, early and late, as shown in Figure 3a and 3b. Figure 3a shows a relatively sharp and well defined feature. As the plasma is translated across the He:Ne beam the time after the pump laser pulse that the peak of this signal appears changes and this perturbation is associated with the shock wave. This signal appears as a decrease in the dc level of the He:Ne due to blooming followed immediately by a focussing or enhanced peak. After the enhanced peak the dc level often shows a characteristic broader and shallower blooming effect. The amplitude of this perturbation and its temporal profile also varies with the position of the plasma being probed.

Figure 4 shows a position versus time plot of this perturbation for both the Nd:YAG and CO₂ plasma. The Nd:YAG pulse width is nominally 9 ns while the CO₂ pulse width is 85 ns. Correspondingly, the luminous afterglows of their plasmas last for 1 us and 9 us respectively. Thus the trace shown in Figure 4 for the Nd:YAG plasma, covers a spatial and temporal region starting during the lifetime of the luminous afterglow and lasting far beyond this region. For the CO₂ plasma the movement of the perturbation is observed essentially for times corresponding to the luminous lifetime of the plasma, and over a spatial region corresponding to a few millimeters beyond the boundary of the luminous afterglow.

The velocities of the travelling shock wave as estimated from the movement of these perturbations start at 3000-5000 m/s and slow down to 300-400 m/s for the regions studied. The decrease in velocity, however, is not uniform and exhibits large fluctuations. Another rather curious observation afforded by the traces of Figure 4 are positions in both the Nd:YAG and CO₂ laser initiated plasmas where rather sharp discontinuities in the position versus time curves appear. In fact corresponding to these discontinuities the shock wave velocity is zero or negative suggesting a momentary backward swing or halting of the shock wave. No definitive explanation for this behaviour is offered at this time, although we note that discussions of backward or reflected shocks have appeared in the literature (5). Other secondary effects were observed and are being analyzed. Some preliminary investigations of plasmas initiated on aerosols failed to show any difference in the early time perturbation associated with the shock wave, from the corresponding signal obtained in clean air.

The long term effect is irregular and not reproducible from shot to shot. It usually occurs 0.5 - 3 ms after the laser fires and a simple calculation of the thermal diffusion time t_h :

$$t_h = 4 w^2 / D$$

where w is the distance travelled by the thermal wave and D is the thermal diffusivity. Using the values of air at room temperature yields a value of t_h to be 1.2 ms which is of the order of the long term signals. These "thermal perturbations" are not observed in the absence of plasma formation. A comparison of plasmas initiated

in clean air and on a nail show that in the latter case the amplitude of these long term perturbations are severely attenuated. A tentative explanation offered for this observation is that the metallic nail may be acting as a heat sink conducting away most of the thermal energy thus causing a milder perturbation when the plasma volume is probed.

B. DUAL PULSE BREAKDOWN THRESHOLD

We used the Nd:YAG laser by itself at various repetition rates. We observed the frequency of breakdown as a function of YAG energy/irradiance and repetition rate. The repetition rates were varied from 0.1 to 23 Hz, corresponding to interpulse separations of 10 s to 43 ms. Only at the highest rate was there a discernable effect, an increase of about 10% in the energy/irradiance needed to produce breakdown. One possible source of the irradiance increase was heating of the YAG rod leading to increased beam divergence and a larger spot size. A higher energy per pulse would then be needed to obtain the same breakdown frequency. We checked this effect by keeping the flashlamps running at 23 Hz, but Q-switching at lower repetition rates. The increase in breakdown energy required appeared to be real and not associated with rod heating.

The second and most extensive set of experiments involved the counter propagating CO₂ and Nd:YAG beams focused into the same volume of space with the CO₂ pulse first. Typical signals observed for this arrangement are shown in Figure 5. In general we observed a significant decrease in the YAG-induced plasma signal after a CO₂ - initiated breakdown. We interpret this decrease in plasma light to mean a decreased coupling of YAG energy into the plasma. Indeed at the smaller time intervals (20 us to 250 us), the YAG plasma often did not initiate at all, evidence of an increase in the breakdown threshold. The effects were greatest at shortest interpulse separations, least for the longest. At a given separation, increasing the YAG energy in many cases increased the plasma signal and the frequency of breakdown. These results are summarized in Figure 6 which shows the decrease in peak YAG - induced plasma signal (called suppression) as a function of the interpulse time and YAG energy. The complex behaviour of the curves at later times remains to be explained.

Finally we conducted a set of experiments with the YAG pulse coming before the CO₂ pulse. Here the results were opposite to those observed above. The CO₂ was set so that the breakdown rate was about 5/10. Then the YAG was turned on with sufficient energy to form a plasma. The CO₂ breakdown rate rose to 10/10, evidence for a decrease in the breakdown threshold. It should be noted that the visual volume of the CO₂ plasma was 5 to 10 times larger than the YAG plasma.

With our conditions we have observed three effects:

- a. For the YAG only, a slight increase in breakdown threshold at about 40 ms interpulse separation;
- b. For the CO₂ first, an increase in the breakdown threshold out to about 3 ms interpulse separation;
- c. For the YAG first, a decrease in the breakdown threshold for the CO₂ out to beyond 500 ms.

It would appear that multiple effects are at work here. The results of (a) and (b) above would be consistent with a medium perturbation which caused defocusing leading to less energy deposition and thereby requiring higher irradiance to achieve breakdown. The medium perturbation theory is supported by the late signals seen in the photothermal experiments.

With regard to (c) above, the initial YAG plasma is so small compared to the CO₂ induced plasma that medium perturbation might not be significant. However, the first plasma does provide seed electrons for the subsequent CO₂ pulse, aiding rather than inhibiting breakdown, as observed with conventional pre-ionization (8).

Sometimes the breakdown threshold will vary depending on whether the electron diffusion in the laser focus is ambipolar or free-electron, the latter being much faster (8). We calculated the Debye length for both YAG and CO₂ plasmas and found it to be on the order of 2 to 10 μm . This is considerably smaller than the spot sizes listed in Table I, so ambipolar diffusion will dominate in all our experiments. Hence we expect no breakdown threshold variation due to this effect.

SUMMARY

A Nd:YAG Q-switched laser at 0.532 μm and a pulsed CO_2 laser at 10.6 μm were used to form plasmas which were probed with a He:Ne laser. Two types of perturbations were detected, the first one rather well defined and repetitive occurring within hundreds of nanoseconds to a few microseconds of the laser pulse was associated with a travelling shock wave. The second, more diffuse and irregular and occurring about 2-3 ms after the laser pulse was tentatively associated with thermal diffusion phenomena. The second diagnostic was carried out primarily with two lasers, a pulsed CO_2 (10.6 μm) and a pulsed Nd:YAG (1.06 μm). We observed both increases and decreases in the breakdown threshold for a second pulse passing through the same volume in which a laser induced plasma had been previously formed. The increase was observed when the initial plasma formed was by the CO_2 beam, the decrease when it was formed by the Nd:YAG beam.

ACKNOWLEDGEMENTS

We gratefully acknowledge the support of CRDEC provided through Contract No. DAAG29-81-D-0100 (Delivery Order 0026). We also acknowledge the support received from two U.S. Department of Defense instrumentation grants, DAAG-29-85-G-0012 and DAAL)3-86-G-0119, and a New Mexico State Arts and Sciences Minigrant, RC-86-25.

REFERENCES

1. P. Kafalas and A. P. Ferdinand, Appl. Opt. 12, 29 (1973).
2. P. Kafalas and J. Herrman, Appl. Opt. 12, 772 (1973).
3. J. H. Eichmans, W.-F. Hseih, and R. K. Chang, Opt. Lett. 12, 22 (1987).
4. A. Biswas, H. Latifi, P. Shah, L. J. Radziemski, and R. L. Armstrong, Opt. Lett. 12, 313 (1987).
5. R. L. Armstrong, P. J. O'Rourke, and A. Zardecki, Phys. Fluids 29, 3573 (1986); R. L. Armstrong and A. Zardecki, J. Appl. Phys. (in press).
6. L. J. Radziemski, T. R. Loree, D. A. Cremers, and N. M. Hoffman, Anal. Chem. 55, 1246 (1983).
7. G. Lampis and S. C. Brown, Phys. Fluids, 11, 1137 (1968).
8. R. T. Brown and D. C. Smith, Appl. Phys. Lett. 22, 245 (1973).

TABLE I
LASER AND DETECTION SYSTEM PARAMETERS

Laser:

(i) Nd:YAG laser	Quanta-Ray Nd:YAG Q-switched pulse width 9 ns energy per pulse 90-400mJ minimum spot size 40 um
(ii) CO ₂ laser	Tachisto TEA CO ₂ pulse width 85 ns energy per pulse 250-400 mJ minimum spot size 90 um
(iii) He:Ne laser	Spectra Physics 155

Detectors:

(i) photomultiplier tube	Hamamatsu R928 and P128A rise time 2 ns
(ii) photodiode	Scientech 301-020 rise time 1 ns

Data acquisition:

(i) Transient Digitizer	LeCroy TR 8828 (5 ns/pt.)
(ii) Digital delay generator	SRS DG535 , 4 channel 2 ns accuracy 20 us - 10 s delays
(iii) Amplifier	LeCroy 612A

Optics:

(i) focusing lens (Nd:YAG)	14 cm focal length glass
(ii) focusing lens (CO ₂)	5.0 cm Ge lens

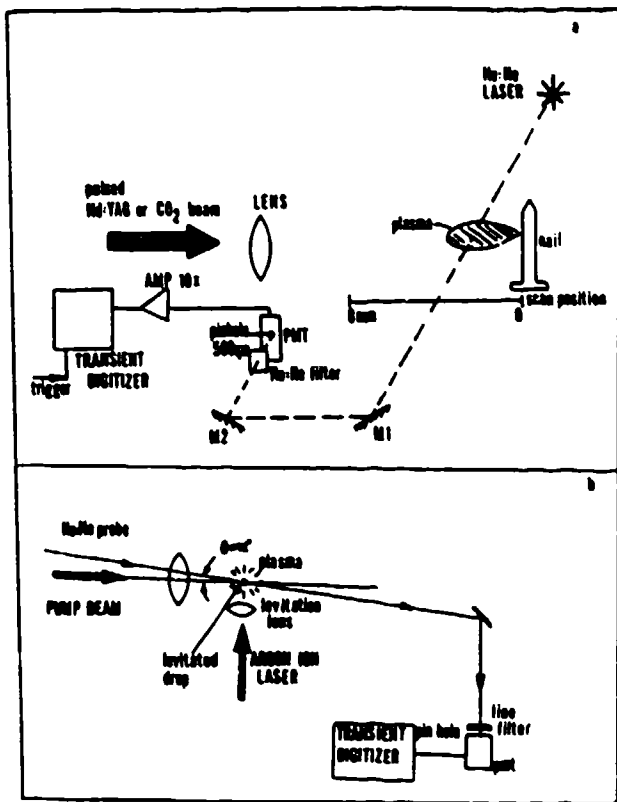


Figure 1. Experimental arrangement for observing photothermal signals (a) plasma scanning set-up (b) alternative set-up used to probe aerosol induced plasmas.

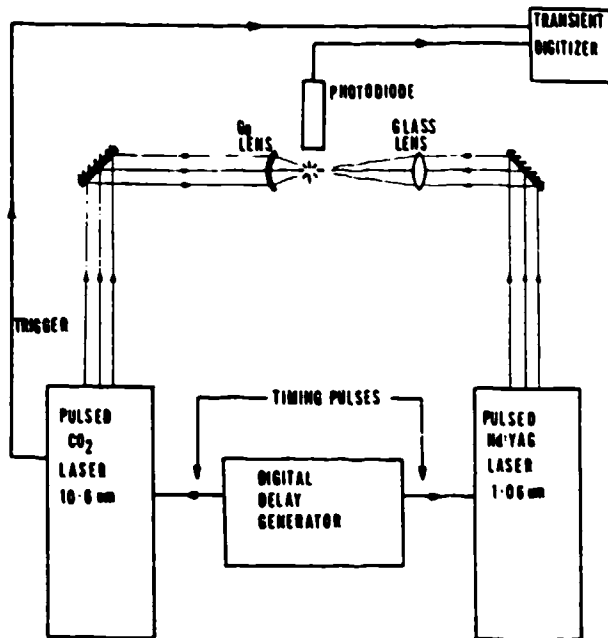


Figure 2. Schematic of experimental arrangement used to observe two-pulse breakdown-threshold effects.

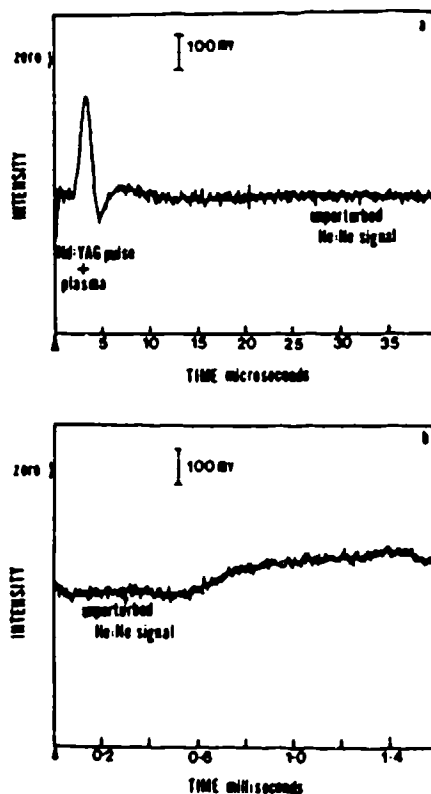


Figure 3. (a) Early photothermal signals. Note the signal is negative and the perturbation is positive going indicating probe beam attenuation (b) late photothermal signals; Shows the unperturbed He:Ne signal.

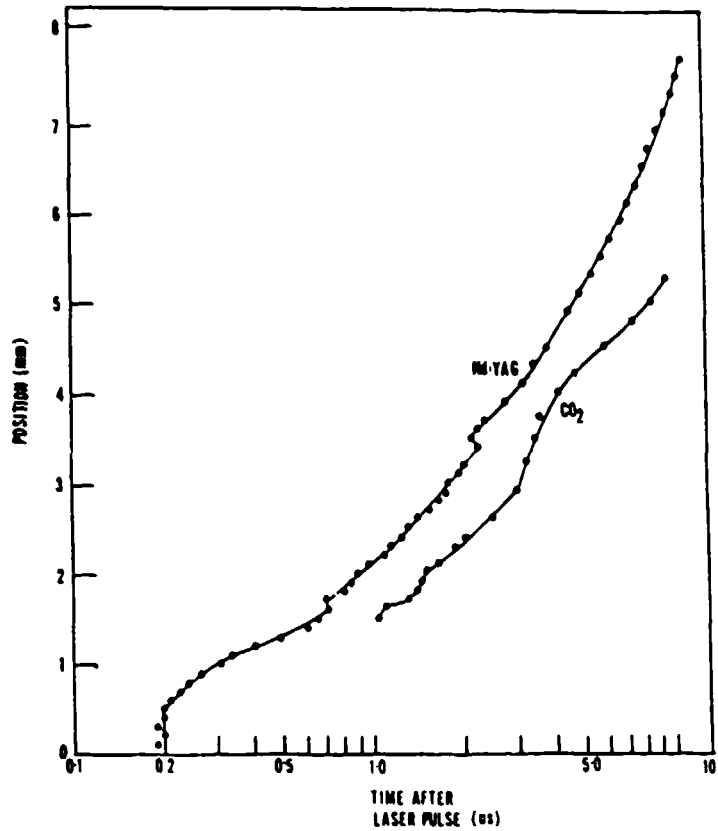


Figure 4. Plot showing the position vs. time after plasma-initiating laser pulse, for the early photothermal perturbation.

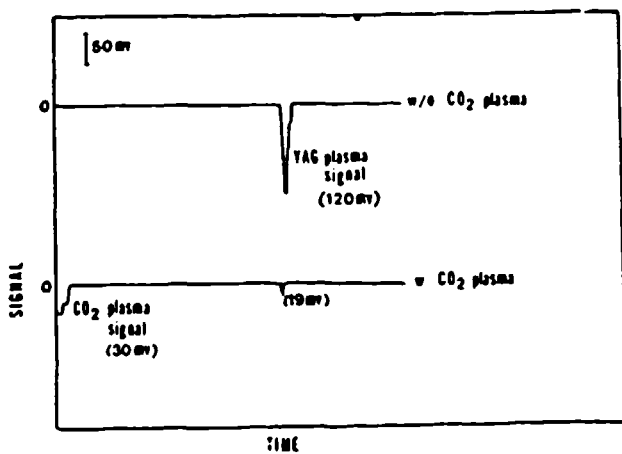


Figure 5. Typical two-pulse signals, in this case showing the lower YAG-induced plasma signal after a CO₂ induced plasma.

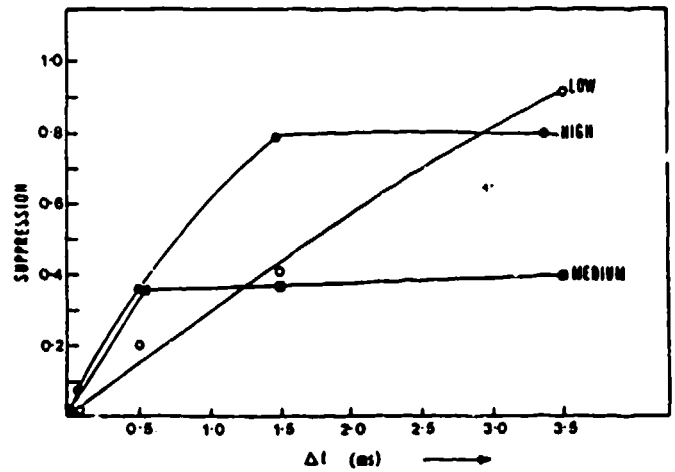


Figure 6. Ratio of YAG-induced plasma signal (preceded by CO₂-initiated plasma) to YAG-induced plasma signal (no previous plasma), called suppression. Low, medium, and high refer to YAG energies of 130, 250, and 400 mJ respectively.

THE SCATTERING OF ELECTROMAGNETIC RADIATION BY
MULTILAYER, ANISOTROPIC PARTICLES WITH SPHERICAL SYMMETRY

D. K. Cohoon
Department of Mathematics 038-16
Temple University
Philadelphia, Pennsylvania 19122

ABSTRACT

The purpose of this paper is to describe methods of resolving discrepancies between experimental observations of scattering by crystalline particles and attempts to explain these observations assuming that the electrical properties of these particles can be described by the use of scalar valued functions for the permittivity, conductivity, and permeability. We can develop coupled integral equations describing the interaction of electromagnetic radiation with a heterogeneous, penetrable, dispersive, anisotropic scatterer and can use several methods of solving these integral equations. The solution of the problem of describing scattering by an anisotropic sphere can be substituted into the integral equation to check the integral equation formulation of the problem. Conditions are given for the uniqueness of the solution of the associated transmission problem. Because of the multiple propagation constants in an anisotropic material, the trivial uniqueness arguments valid for isotropic scatterers do not have a guaranteed success in understanding the more complex interaction phenomena.

An exact analytical Mie-like solution has been obtained for fields induced in and scattered by an N layer sphere, where each layer has anisotropic constitutive relations. We show that as the tensor parameters change so that each layer becomes isotropic, then the distinct radial functions used in representing the electric and magnetic fields induced in the structure both converge to the same spherical Bessel and Hankel functions and all the propagation constants in each layer converge to the propagation constant k given by

$$k^2 = \omega^2 \mu \epsilon - i \omega \mu \sigma$$

and the solution approaches the ordinary Mie solution for an N layer sphere. The anisotropic sphere computer code, for the case of magnetic losses, dielectric losses, and dissipative impedance sheets, and perfectly conducting or penetrable inner cores has been validated by energy balance computations involving balancing the difference between the total energy entering the sphere minus the total energy scattered away with the sum of the surface integrals representing losses due to dissipative impedance sheets separating the layers plus the sum of the triple integrals over the layers whose values represent magnetic and dielectric losses within the anisotropic penetrable layers.

Two Bessel functions with two different complex indices depending on ratios of tangential and radial magnetic properties and ratios of tangential and radial electrical properties, respectively, participate in the solution in the case of scattering by the simplest anisotropic sphere. The scattering problem is solved for the case where the scatterer consists of (i) N anisotropic dielectric layers, (ii) N of these layers separated by sheets of charge or impedances, and (iii) a perfectly conducting core surrounded by $N - 1$ anisotropic layers.

1. INTRODUCTION

The atmosphere of the earth is filled with small anisotropic scatterers. It is important to understand the nature of the scattering of light for individual aerosol particles, to determine precisely how a cloud including these particles might impede the progress of the sunlight or a laser communication. These anisotropic scatterers have many sources including volcanic eruptions and human activity. The term anisotropic here refers to the constitutive relations between \mathbf{B} and \mathbf{H} and between \mathbf{D} and \mathbf{E} and \mathbf{J} and \mathbf{E} which are tensorial; in isotropic particles the Fourier transforms with respect to time of these quantities are related by scalars. We will use ϵ to denote the tensor permittivity of the anisotropic particle, and we let ϵ_0 denote the permittivity of free space. We let \mathbf{I} denote the 3 by 3 identity matrix. The tensor magnetic permeability is denoted by μ . We consider time harmonic radiation with frequency ω . By lumping together the frequency times the imaginary part of the permittivity tensor and the real part of the usual conductivity tensor we get a real tensor σ . The Maxwell equations for anisotropic materials, therefore, have the form

$$\text{curl}(\mathbf{H}) = i\omega\epsilon_0\mathbf{E} + (i\omega(\epsilon - \epsilon_0\mathbf{I}) + \sigma)\mathbf{E} \quad (1.1)$$

and

$$\text{curl}(\mathbf{E}) = -i\omega\mu_0\mathbf{H} - i\omega(\mu - \mu_0\mathbf{I})\mathbf{H} \quad (1.2)$$

Equations (1.1) and (1.2) together with the fact that the divergence of a curl is zero tell us that

$$\frac{\text{div}(\epsilon - \epsilon_0\mathbf{I} - i\sigma/\omega)\mathbf{E}}{\epsilon_0} = -\text{div}(\mathbf{E}) \quad (1.3)$$

Similarly, the fact that

$$\text{div}(\mu\mathbf{H}) = 0 \quad (1.4)$$

implies that

$$\text{div}(\mu\mathbf{H} - \mu_0\mathbf{H}) = -\mu_0\text{div}(\mathbf{H}) \quad (1.5)$$

Thus, thinking in terms of the traditional free space Maxwell equations with electric and magnetic currents \mathbf{J}_e and \mathbf{J}_m and electrical and magnetic charge densities ρ_e and ρ_m we see that equations (1.1) and (1.2) may be reexpressed in the form,

$$\text{curl}(\mathbf{H}) = i\omega\epsilon_0\mathbf{E} + \mathbf{J}_e \quad (1.6)$$

where \mathbf{J}_e is given by

$$\mathbf{J}_e = i\omega(\epsilon - \epsilon_0\mathbf{I})\mathbf{E} + \sigma\mathbf{E} \quad (1.7)$$

and the Maxwell equation driven by the magnetic current source term is given by

$$\text{curl}(\mathbf{E}) = -i\omega\mu_0\mathbf{H} + \mathbf{J}_m \quad (1.8)$$

where the magnetic current density \mathbf{J}_m is given by

$$\mathbf{J}_m = i\omega(\mu - \mu_0\mathbf{I})\mathbf{H} \quad (1.9)$$

The free space isotropic relations yield

$$\text{div}(\mathbf{E}) = \frac{\rho_e}{\epsilon_0} \quad (1.10)$$

and

$$\text{div}(\mathbf{H}) = \frac{\rho_m}{\mu_0} \quad (1.11)$$

which, respectively, provide us with an operational definition of stimulated electrical and magnetic charge density. Using a pill box concept and the fact that there is no current density in the exterior of the scatterer, we can in addition introduce the notion of surface electric and magnetic charge density which we denote by η_e and η_m , respectively. The surface electrical charge density is derived through the notion of picking a point on the bounding surface of the scatterer whose normal is \mathbf{n} and placing a thin volume around this point so that the exterior and interior portions of the boundary have area equal to A except for a portion of the bounding surface with a very small area whose normal is nearly perpendicular to the normal \mathbf{n} and so that if \mathbf{J}_+ is the current density at this point just outside the scatterer and \mathbf{J}_- denotes the current density at this point just inside the scatterer, then conservation of charge on the surface is defined approximately by the relation

$$A \left(\frac{\eta(t + \Delta t) - \eta(t)}{\Delta t} \right) + A ((\mathbf{J}_+ \cdot \mathbf{n}) - (\mathbf{J}_- \cdot \mathbf{n})) = 0 \quad (1.12)$$

which means since

$$\mathbf{J}_+ = 0 \quad (1.13)$$

that the surface charge density, electrical or magnetic, is given by

$$i\omega\eta = (\mathbf{J}_- \cdot \mathbf{n}) \quad (1.14)$$

Thus, the electrical surface charge density is given by equation

$$\eta_e = \left(\frac{-i}{\omega} \right) (\mathbf{J}_e \cdot \mathbf{n}) \quad (1.15)$$

and the magnetic surface charge density is given by

$$\eta_m = -i\omega((\mu - \mu_0\mathbf{I}) \cdot (\mathbf{H} \cdot \mathbf{n})) \quad (1.16)$$

To fully analyze these equations and relate them to the original transmission problem for an anisotropic heterogeneous penetrable scatterer, we need to construct equivalent sources. We will need to consider potentials due to volume and surface electric and magnetic charges and potentials due to volume electric and magnetic currents. From the continuity equation, the electrical charge density satisfies the relation,

$$\text{div}(\mathbf{J}_e) + \frac{\partial \rho_e}{\partial t} = 0 \quad (1.17)$$

where in our case \mathbf{J}_e is given by equation (1.7). A similar relationship for magnetic charge density is developed from a combination of equations (1.11) and (1.9) and the basic Maxwell equation (1.8). The continuity equation for magnetic charge density has exactly the right form in the sense that a valid equation is obtained by replacing e by m in equation (1.17). By defining electric and magnetic surface charges using the relationships,

$$i\omega\eta_e = ((i\omega(\epsilon - \epsilon_0\mathbf{I}) + \sigma) \cdot \mathbf{E}) \cdot \mathbf{n} \quad (1.18)$$

and

$$i\omega\eta_m = (-i\omega(\mu - \mu_0\mathbf{I}) \cdot \mathbf{H}) \cdot \mathbf{n} \quad (1.19)$$

we complete all we need to derive a coupled set of integral equations in the electric and magnetic field vectors involving both surface and volume integrals. With these definitions we represent the difference between the ambient and total electric vector in terms of gradients of the potentials of the electric volume and surface charge densities, the electric vector potential, and the curl of the magnetic vector potential. We similarly represent the difference between the total and ambient magnetic field intensity in terms of the gradients of the potentials of the volume and surface magnetic charge densities, the magnetic vector potential, and the curl of the electric vector potential. A coupled electric vector magnetic vector integral equation is immediately derived

from the relationships,

$$\mathbf{E} - \mathbf{E}^i = -\text{grad}(\Phi_e) - \text{grad}(\Psi_e) - i\omega\mathbf{A}_e - \left(\frac{1}{\epsilon_0}\right)\text{curl}(\mathbf{A}_m) \quad (1.20)$$

and

$$\mathbf{H} - \mathbf{H}^i = -\text{grad}(\Phi_m) - \text{grad}(\Psi_m) - i\omega\mathbf{A}_m + \left(\frac{1}{\mu_0}\right)\text{curl}(\mathbf{A}_e) \quad (1.21)$$

For scatterers with a general shape the set of equations implied by equations (1.20) and (1.21) are not solvable in closed form. We therefore assume that the scattering body has spherical symmetry and assume a special form of a tensor relationship between \mathbf{J}_e and \mathbf{E} and between the magnetic current density \mathbf{J}_m and the magnetic field \mathbf{H} in each layer of the structure. This will enable us to get an extension of the usual Mie solution. Specifically we assume that the scattering body Ω consists of N regions delimited by spheres defined by the equations $r = R_i$ for $i = 1, 2, \dots, N$, where the p th region is bounded by $r = R_p$ and $r = R_{p-1}$ if p is 2, 3, ..., or N and the core region is bounded by $r = R_1$. In the simplest solution discussed in this paper we assume that we have anisotropic constitutive relations defined in terms of the unit vectors \mathbf{e}_r , \mathbf{e}_θ , and \mathbf{e}_ϕ perpendicular to the radial, θ , and ϕ coordinate planes, respectively. For time harmonic radiation if \mathbf{D} is the dielectric displacement and \mathbf{J} is the ordinary electric field current density, then there are constants ϵ_r and σ_r in the radial direction and constants ϵ and σ for relations along the surface so that

$$\frac{\partial \mathbf{D}}{\partial t} + \mathbf{J} = (i\omega\epsilon_r + \sigma_r)\mathbf{E}_r\mathbf{e}_r + (i\omega\epsilon + \sigma)(\mathbf{E}_\theta\mathbf{e}_\theta + \mathbf{E}_\phi\mathbf{e}_\phi) \quad (1.22)$$

Furthermore, there exist constants related to the magnetic properties of the material denoted by μ_r and μ so that if \mathbf{B} is the magnetic flux

density, and the impinging radiation is time harmonic, then

$$\frac{\partial \mathbf{B}}{\partial t} = i\omega\mu_r\mathbf{H}_r\mathbf{e}_r + i\omega\mu(\mathbf{H}_\theta\mathbf{e}_\theta + \mathbf{H}_\phi\mathbf{e}_\phi) \quad (1.23)$$

If we simply require that tangential components of \mathbf{E} and \mathbf{H} are continuous across the boundaries $r = R_i$, then expansion coefficients can be related by 2 by 2 matrices as in (Bell, Cohoon, and Penn [1]). If we allow thin impedance sheets between the layers, then the expansion coefficients are also related by 2 by 2 matrices.

Normally when one thinks of scattering by a sphere, the spherical Bessel and Neumann functions come to mind. In our problem we will make use of two Bessel functions with a complex order and will require their evaluation at complex arguments. We assume that ν is complex and define a special function Ψ_ν by the rule

$$\Psi_\nu(z) = \frac{\pi^{1/2} J_{\nu+1/2}(z)}{2^{1/2} z^{1/2}} \quad (1.24)$$

where if we allow W to denote the Bessel function with index equal to $\nu + 1/2$ or specifically

$$W = J_{\nu+1/2}(z) \quad (1.25)$$

this means that the function W satisfies the Bessel differential equation,

$$z^2 \frac{d^2 W}{dz^2} + z \frac{dW}{dz} + (z^2 - (\nu + 1/2)^2)W = 0 \quad (1.26)$$

and then the function Ψ_ν defined by equations (1.24) through (1.26) satisfies the equation

$$\left(\frac{1}{z}\right) \left(\frac{\partial}{\partial z}\right)^2 (z\Psi) + \left[1 - \frac{\nu(\nu+1)}{z^2}\right]\Psi = 0 \quad (1.27)$$

We will need in order to implement our solution on the computer a knowledge of the Wronskian of the independent solutions of the Bessel

differential equation (1.26). It is known that

$$-Y_\nu(z) \frac{d}{dz} J_\nu(z) + J_\nu(z) \frac{d}{dz} Y_\nu(z) = \frac{2}{\pi z} \quad (1.28)$$

and this is enough to enable us to evaluate the expressions involving Wronskians of linearly independent solutions of differential equations satisfied by radial functions needed to represent the electric and magnetic fields in the anisotropic materials. We needed two types of differential equations, one with a term involving the ratio of tangential to radial magnetic permeabilities and the other involving a ratio of tangential to radial permittivities. The radial functions associated with a ratio of magnetic properties are denoted by $\Psi_{(n,p)}^{(a,j)}$. The Wronskian determinant, which we denote by Δ is for these functions given by the expression,

$$\Delta = \begin{aligned} & (\Psi_{(n,p)}^{(a,1)}(kR_p) \left(\frac{i}{\omega\mu^{(p)}kr} \right) \left(\frac{\partial}{\partial r} \right) (r\Psi_{(n,p)}^{(a,3)}(kr)) \Big|_{r=R_p} \\ & - \Psi_{(n,p)}^{(a,3)}(kR_p) \left(\frac{i}{\omega\mu^{(p)}kr} \right) \left(\frac{\partial}{\partial r} \right) (r\Psi_{(n,p)}^{(a,1)}(kr)) \Big|_{r=R_p} \end{aligned} \quad (1.29)$$

where the superscript 3 refers to a radial function which is singular at the origin and the superscript 1 refers to a radial function which is regular at $r=0$ in the integrability sense, and where the radial functions $\Psi_{(n,p)}^{(a,j)}$, are solutions of the differential equation,

$$\left(\frac{1}{r} \right) \left(\frac{\partial}{\partial r} \right)^2 (r\Psi_{(n,p)}^{(a,j)}) + \left[k^2 - \left(\frac{n(n+1)}{r^2} \right) \left(\frac{\omega\mu}{\omega\mu_r} \right) \right] \Psi_{(n,p)}^{(a,j)} = 0 \quad (1.30)$$

where the complex constant k is when r is in the p th layer given by

$$k^2 = \omega^2\mu^{(p)}\epsilon^{(p)} - i\omega\mu^{(p)}\sigma^{(p)} \quad (1.31)$$

The other radial functions $\Psi_{(n,p)}^{(b,j)}$ satisfy the differential equation,

$$\left(\frac{1}{r} \right) \left(\frac{\partial}{\partial r} \right)^2 (r\Psi_{(n,p)}^{(b,j)}) + \left[k^2 - \left(\frac{n(n+1)\zeta}{r^2} \right) \right] \Psi_{(n,p)}^{(b,j)} = 0 \quad (1.32)$$

where

$$\zeta = \left(\frac{i\omega\epsilon^{(p)} + \sigma^{(p)}}{i\omega\epsilon_r^{(p)} + \sigma_r^{(p)}} \right) \quad (1.33)$$

We remark that the entire theory could be made completely symmetric by introducing a magnetic charge conductivity so that the Maxwell equations would have the form,

$$\text{curl}(\mathbf{E}) = -i\omega\mu_0\mathbf{H} - (i\omega(\mu - \mu_0\mathbf{I}) + \sigma_m)\mathbf{H} \quad (1.34)$$

and

$$\text{curl}(\mathbf{H}) = i\omega\epsilon_0\mathbf{E} + (i\omega(\epsilon - \epsilon_0\mathbf{I}) + \sigma_e)\mathbf{E} \quad (1.35)$$

With these formulations of the Maxwell equations, we can use the potential representation of the electric and magnetic field vectors to write a surface volume integral equation system coupling the electric and magnetic vectors in the form, described by G. C. G. and Uslenghi ((8)) in their paper on electromagnetic scattering by anisotropic materials with a completely general shape.

As a part of this formulation we make use of the temperate rotationally invariant fundamental solution of the Helmholtz operator of free space derived in Treves [30] using the Haar measure on the

rotation group, given by

$$G(\mathbf{r}, \mathbf{s}) = \frac{\exp(-ik_0|\mathbf{r} - \mathbf{s}|)}{4\pi|\mathbf{r} - \mathbf{s}|} \quad (1.36)$$

The coupled electric vector magnetic vector integral equations describing the interaction of radiation with an anisotropic material are given by

$$\begin{aligned} \mathbf{E} - \mathbf{E}^i &= -\text{grad} \int_{\Omega} \frac{\text{idiv}(i\omega(\epsilon - \epsilon_0\mathbf{I}) + \sigma_e)\mathbf{E}}{\omega\epsilon_0}(\mathbf{s})G(\mathbf{r}, \mathbf{s})d\mathbf{v}(\mathbf{s}) \\ &+ \frac{i}{\omega\epsilon_0} \text{grad} \int_{\partial\Omega} ((i\omega(\epsilon - \epsilon_0\mathbf{I}) + \sigma_e) \cdot \mathbf{E}) \cdot \mathbf{n}(\mathbf{s})G(\mathbf{r}, \mathbf{s})d\mathbf{a}(\mathbf{s}) \\ &- i\omega\mu_0 \int_{\Omega} (i\omega(\epsilon - \epsilon_0\mathbf{I}) + \sigma_e) \cdot \mathbf{E}(\mathbf{s})G(\mathbf{r}, \mathbf{s})d\mathbf{v}(\mathbf{s}) \\ &- \text{curl} \int_{\Omega} (i\omega(\mu - \mu_0\mathbf{I}) + \sigma_m) \cdot \mathbf{H}(\mathbf{s})G(\mathbf{r}, \mathbf{s})d\mathbf{v}(\mathbf{s}) \end{aligned} \quad (1.37)$$

and

$$\begin{aligned} \mathbf{H} - \mathbf{H}^i &= -\text{grad} \int_{\Omega} \frac{\text{idiv}(i\omega(\mu - \mu_0\mathbf{I}) + \sigma_m)\mathbf{H}}{\omega\mu_0}(\mathbf{s})G(\mathbf{r}, \mathbf{s})d\mathbf{v}(\mathbf{s}) \\ &- \frac{i}{\omega\mu_0} \text{grad} \int_{\partial\Omega} ((i\omega(\mu - \mu_0\mathbf{I}) + \sigma_m) \cdot \mathbf{H}) \cdot \mathbf{n}(\mathbf{s})G(\mathbf{r}, \mathbf{s})d\mathbf{a}(\mathbf{s}) \\ &- i\omega\epsilon_0 \int_{\Omega} (i\omega(\mu - \mu_0\mathbf{I}) + \sigma_m) \cdot \mathbf{H}(\mathbf{s})G(\mathbf{r}, \mathbf{s})d\mathbf{v}(\mathbf{s}) + \\ &\text{curl} \int_{\Omega} (i\omega(\epsilon - \epsilon_0\mathbf{I}) + \sigma_e) \cdot \mathbf{E}(\mathbf{s})G(\mathbf{r}, \mathbf{s})d\mathbf{v}(\mathbf{s}) \end{aligned} \quad (1.38)$$

We can make use of the energy balance relationship described in [1] to express the total absorbed power in terms of coefficients used to express the radiation scattered away from the sphere and the expansion coefficients of the incident radiation. This gives us the extinction and scattering cross sections of our spherical structure. The same results are necessarily obtained by integration of the power density distribution over the interior of the sphere. This has been done for a variety of anisotropic structures as a check on our computer program. The triple integral and the formula in Bell et al [1] give answers agreeing to at least 7 decimal places when 12 point Gauss quadrature is used for integrating with respect to θ , ϕ , and r in each layer of the sphere. The agreement persists even when different ratios of real and imaginary parts of radial and tangential permittivity, and conductivity are used. The possibility of a purely anisotropic loss can be seen by observing the energy conservation relation (c.f. Jin Au Kong [18]) for a general anisotropic material. For isotropic materials the situation is different in that, for example, to have a magnetic loss in a linearly responding material one must have a magnetic permeability with a nontrivial imaginary part.

For an anisotropic material with a completely general shape the problem of computing the interaction at first glance may seem formidable. However, by the use of the method of Cohoon [3] and the

resolvent kernel methods presented by this author at the Midwest Conference on Differential Equations held at Vanderbilt University in Nashville, Tennessee on October 23-24, 1987 one can develop a robust method of solving the coupled system, given by equations (1.37) and (1.38), that does not require excessive computer memory.

THE INPUT DATA FREQUENCY, E LENGTH, NO OF REGIONS		
1. GHZ	1.00 V/M	2

INPUT DATA (SURFACE BOUNDARIES)	
2.50 CM	3.00 CM

ELECTRICAL AND MAGNETIC PROPERTIES REGION ONE		
PARAMETER	REAL PART	IMAGINARY PART
ϵ_r	50.	9.00
ϵ	60.	8.00
μ_r	1.00	0.80
μ	2.40	1.00
σ_r	0.50	0.80
σ	0.60	0.40

ELECTRICAL AND MAGNETIC PROPERTIES REGION TWO		
PARAMETER	REAL PART	IMAGINARY PART
ϵ_r	40.	1.00
ϵ	50.	2.00
μ_r	3.00	1.80
μ	5.40	2.00
σ_r	1.50	0.40
σ	1.80	0.60

AVG AND TOTAL ABSORBED POWER BY TRIPLE INTEGRATION	
6.62536D-02 W/M**3	7.49310489D-6 WATTS

AVG AND TOTAL ABSORBED POWER BY A POYNTING VECTOR ANALYSIS	
6.62536D-02 W/M**3	7.49310488D-6 WATTS

Table 1. The above table shows the results of an energy balance computation. Using only the expansion coefficients for the scattered radiation and the known expansion coefficients for the incoming radiation, the total absorbed power was computed. This was compared with a computation of the internal electric and magnetic losses using numerical triple integration over the layers.

3. REPRESENTATION OF THE FIELDS

We attempt to develop an electric vector representing a solution of the Maxwell equations in spherical coordinates in the interior of an anisotropic body. A priori we consider in the p th layer of the sphere three radial functions which we denote by $\Psi_{(n,p)}^{(a,j)}$, $\Psi_{(n,p)}^{(b,j)}$, and $\Psi_{(n,p)}^{(c,j)}$, and we assume furthermore that within this layer the electric vector \mathbf{E} of a solution of the Maxwell equations has the form,

$$\begin{aligned} \mathbf{E} = \sum_{(m,n) \in I} (a_{(m,n)} \Psi_{(n,p)}^{(a,j)}) & \left(im \frac{P_n^m(\cos(\theta))}{\sin(\theta)} \mathbf{e}_\theta - \frac{d}{d\theta} (P_n^m(\cos(\theta))) \mathbf{e}_\phi \right) e^{im\phi} + \\ & c_{(m,n)} \frac{\Psi_{(n,p)}^{(c,j)}(kr)}{kr} P_n^m(\cos(\theta)) e^{im\phi} \mathbf{e}_r + \\ b_{(m,n)} \left(\frac{-1}{kr} \right) & \left(\frac{\partial}{\partial r} \right) (r \Psi_{(n,p)}^{(b,j)}(kr)) \left\{ \left(\frac{d}{d\theta} \right) P_n^m(\cos(\theta)) \mathbf{e}_\theta + im \frac{P_n^m(\cos(\theta))}{\sin(\theta)} \mathbf{e}_\phi \right\} e^{im\phi} \end{aligned} \quad (2.1)$$

We will suppose that the material within the layers satisfies the constitutive relations described in the introduction. We define singular vector fields on the sphere by the rules,

$$\mathbf{A}_{(m,n)}(\theta, \phi) = \left(im \frac{P_n^m(\cos(\theta))}{\sin(\theta)} \mathbf{e}_\theta - \frac{d}{d\theta} P_n^m(\cos(\theta)) \mathbf{e}_\phi \right) e^{im\phi} \quad (2.2)$$

$$\mathbf{C}_{(m,n)}(\theta, \phi) = P_n^m(\cos(\theta)) e^{im\phi} \mathbf{e}_r, \quad (2.3)$$

and

$$\mathbf{B}_{(m,n)}(\theta, \phi) = \left(\frac{d}{d\theta} P_n^m(\cos(\theta)) \mathbf{e}_\theta + im \frac{P_n^m(\cos(\theta))}{\sin(\theta)} \mathbf{e}_\phi \right) e^{im\phi} \quad (2.4)$$

We now make use of the following Lemma to simplify the computation of the curl of vector fields and especially $\text{curl}(\mathbf{H})$.

Lemma 2.1. If $F(r)$ is a differentiable function of r , and if

$$\mathbf{A} = F(r) \mathbf{A}_{(m,n)}(\theta, \phi)$$

or, equivalently,

$$F(r) \mathbf{A}_{(m,n)}(\theta, \phi) = F(r) \left(im \frac{P_n^m(\cos(\theta))}{\sin(\theta)} \mathbf{e}_\theta - \frac{d}{d\theta} P_n^m(\cos(\theta)) \mathbf{e}_\phi \right) e^{im\phi} \quad (2.5)$$

$$\mathbf{C} = F(r) \mathbf{C}_{(m,n)}(\theta, \phi) = F(r) P_n^m(\cos(\theta)) e^{im\phi} \mathbf{e}_r \quad (2.6)$$

and

$$F(r) \left[\frac{d}{d\theta} P_n^m(\cos(\theta)) e_\theta + im \frac{P_n^m(\cos(\theta))}{\sin(\theta)} e_\phi \right] e^{im\phi} \quad (2.7)$$

then

$$\text{curl}(\mathbf{A}) = (n(n+1)) \frac{F(r)}{r} \mathbf{C}_{(m,n)}(\theta, \phi) + \left[\frac{1}{r} \frac{\partial}{\partial r} (rF(r)) \right] \mathbf{B}_{(m,n)}(\theta, \phi) \quad (2.8)$$

$$\text{curl}(\mathbf{C}) = \frac{F(r)}{r} \mathbf{A}_{(m,n)}(\theta, \phi) \quad (2.9)$$

and

$$\text{curl}(\mathbf{B}) = \left[-\frac{1}{r} \frac{\partial}{\partial r} (rF(r)) \right] \mathbf{A}_{(m,n)}(\theta, \phi) \quad (2.10)$$

Proof. This follows from the fact that in spherical coordinates if

$$\mathbf{v} = v_r e_r + v_\theta e_\theta + v_\phi e_\phi \quad (2.11)$$

$$\begin{aligned} \text{curl}(\mathbf{v}) &= \frac{1}{r(\sin(\theta))} \left[\frac{\partial}{\partial \theta} (\sin(\theta) v_\phi) - \frac{\partial v_\theta}{\partial \phi} \right] e_r + \\ &\frac{1}{r} \left[\frac{1}{\sin(\theta)} \frac{\partial v_r}{\partial \phi} - \frac{\partial}{\partial r} (r v_\phi) \right] e_\theta \\ &+ \frac{1}{r} \left[\frac{\partial}{\partial r} (r v_\theta) - \frac{\partial v_r}{\partial \theta} \right] e_\phi \end{aligned} \quad (2.12)$$

and the relation

$$\begin{aligned} -\frac{1}{\sin(\theta)} \left[\frac{d}{d\theta} \right] \left[\sin(\theta) \frac{d}{d\theta} P_n^m(\cos(\theta)) \right] + \left[\frac{m^2}{\sin^2(\theta)} \right] P_n^m(\cos(\theta)) \\ = n(n+1) P_n^m(\cos(\theta)) \end{aligned} \quad (2.13)$$

which is simply the differential equation of Legendre which is usually expressed in the form,

$$\frac{d}{dz} ((1-z^2) \frac{dW}{dz}) + (n(n+1) - \frac{m^2}{1-z^2}) W = 0 \quad (2.14)$$

where $z = \cos(\theta)$.

We now use the definition of \mathbf{E} , equation (2.1), the definition of the three sections, (2.2) - (2.4), in the tangent and the normal bundle of the sphere, and Lemma 2.1 to represent \mathbf{E} as

$$\begin{aligned} \mathbf{E} &= \sum_{(m,n) \in I} (a_{(m,n)} Z_n^{(a)}(r)) \mathbf{A}_{(m,n)}(\theta, \phi) + \\ &c_{(m,n)} \frac{Z_n^{(c)}(r)}{kr} \mathbf{C}_{(m,n)}(\theta, \phi) + b_{(m,n)} \left[\frac{-1}{kr} \frac{\partial}{\partial r} (r Z_n^{(b)}(r)) \right] \mathbf{B}_{(m,n)}(\theta, \phi) \end{aligned} \quad (2.15)$$

where

$$Z_n^{(a)}(r) = \Psi_{(n,p)}^{(a,j)}(kr) \quad (2.16)$$

$$Z_n^{(b)}(r) = \Psi_{(n,p)}^{(b,j)}(kr) \quad (2.17)$$

$$Z_n^{(c)}(r) = \Psi_{(n,p)}^{(c,j)}(kr) \quad (2.18)$$

where the functions on the right side of the equations (2.16) through (2.18) are defined by equations (1.30) through (1.33) but may actually be conceptualized at this stage of development as generalizations of these solutions. In developing the solution of the Maxwell equations we have to compute the curl of the vector field \mathbf{E} . We find that

$$\begin{aligned} \text{curl}(\mathbf{E}) = & \sum_{(m,n) \in I} \left(a_{(m,n)} \frac{Z_n^{(a)}(r)n(n+1)}{r} C_{(m,n)}(\theta, \phi) + \right. \\ & a_{(m,n)} \frac{1}{r} \frac{\partial}{\partial r} (rZ_n^{(a)}(r)) B_{(m,n)}(\theta, \phi) + c_{(m,n)} \frac{Z_n^{(c)}(r)}{kr^2} A_{(m,n)}(\theta, \phi) \\ & \left. + \frac{b_{(m,n)}}{kr} \left[\frac{\partial}{\partial r} \right]^2 (rZ_n^{(b)}(r)) A_{(m,n)}(\theta, \phi) \right) \quad (2.19) \end{aligned}$$

Equation (2.19) and the Maxwell equation (1.2) and equation (1.23) therefore imply that the magnetic field intensity is given by

$$\begin{aligned} \mathbf{H} = & \sum_{(m,n) \in I} \left(\left[\frac{i}{\omega\mu r} \right] a_{(m,n)} \frac{Z_n^{(a)}(r)n(n+1)}{r} C_{(m,n)}(\theta, \phi) + \right. \\ & a_{(m,n)} \left[\frac{i}{\omega\mu} \right] \frac{1}{r} \frac{\partial}{\partial r} (rZ_n^{(a)}(r)) B_{(m,n)}(\theta, \phi) + \\ & \left. \frac{i}{\omega\mu} \left[c_{(m,n)} \frac{Z_n^{(c)}(r)}{kr^2} + b_{(m,n)} \frac{1}{kr} \left[\frac{\partial}{\partial r} \right]^2 (rZ_n^{(b)}(r)) \right] A_{(m,n)}(\theta, \phi) \right) \quad (2.20) \end{aligned}$$

We now will get the final Maxwell equation relating the curl of the magnetic field intensity to the electric field vector through a tensor relationship. We find that equations (2.2) - (2.10) and (2.20) and the Maxwell equation (1.1) and the original representation, equation (2.1), of \mathbf{E} imply that

$$\text{curl}(\mathbf{H}) = \sum_{(m,n) \in I} ($$

$$a_{(m,n)} \left[\frac{i}{\omega\mu_r} \left(\frac{Z_n^{(a)}(r)n(n+1)}{r^2} \right) + \frac{i}{\omega\mu} \left(\frac{-1}{r} \left(\frac{\partial}{\partial r} \right)^2 (rZ_n^{(a)}(r)) \right) \right] A_{(m,n)}(\theta, \phi)$$

$$+ \frac{n(n+1)}{r} \left[\left(\frac{i}{\omega\mu} \right) \left[c_{(m,n)} \frac{Z_n^{(c)}(r)}{kr^2} + b_{(m,n)} \frac{1}{kr} \left(\frac{\partial}{\partial r} \right)^2 (rZ_n^{(b)}(r)) \right] C_{(m,n)}(\theta, \phi) \right]$$

$$+ \frac{1}{k_p r} \frac{\partial}{\partial r} \left[\frac{i}{\omega\mu} \left[c_{(m,n)} \frac{Z_n^{(c)}(kr)}{r} + b_{(m,n)} \left(\frac{\partial}{\partial r} \right)^2 (rZ_n^{(b)}(r)) \right] \right] B_{(m,n)}(\theta, \phi)$$

$$= \sum_{(m,n) \in I} ((i\omega\epsilon + \sigma)a_{(m,n)}Z_n^{(a)}(r)A_{(m,n)}(\theta, \phi) + (i\omega\epsilon_r + \sigma_r)c_{(m,n)} \frac{Z_n^{(c)}(r)}{kr} C_{(m,n)}(\theta, \phi) +$$

$$(i\omega\epsilon + \sigma)b_{(m,n)} \left[\frac{-1}{kr} \frac{\partial}{\partial r} (rZ_n^{(b)}(r)) \right] B_{(m,n)}(\theta, \phi) \quad (2.21)$$

The first differential equation that we derive is obtained by equating coefficients of the vector field $A_{(m,n)}$ on both sides of equation (2.21) and is given by,

$$\frac{iZ_n^{(a)}(r)n(n+1)}{r^2\omega\mu_r} + \left[\frac{-i}{\omega\mu} \right] \frac{1}{r} \left(\frac{\partial}{\partial r} \right)^2 (rZ_n^{(a)}(r)) = (i\omega\epsilon + \sigma)Z_n^{(a)}(r) \quad (2.22)$$

We can do this because of the orthogonality relationships,

$$\int_0^{2\pi} \int_0^\pi A_{(m,n)}(\theta, \phi) \cdot B_{(m,n)}(\theta, \phi) \sin(\theta) d\theta d\phi = 0 \quad (2.23)$$

and

$$A_{(m,n)} \cdot C_{(m,n)} = 0 = B_{(m,n)} \cdot C_{(m,n)} \quad (2.24)$$

Notice that the differential equation may be rewritten in the form,

$$\frac{-1}{r} \left(\frac{\partial}{\partial r} \right)^2 (rZ_n^{(a)}(r)) + Z_n^{(a)}(r) \left[\frac{n(n+1)\omega\mu}{r^2\omega\mu_r} \right] = k^2 Z_n^{(a)}(r) \quad (2.25)$$

where

$$k^2 = \omega^2 \mu \epsilon - i \omega \mu \sigma \quad (2.26)$$

We note that the ordinary spherical Bessel function satisfies the relationship,

$$\left(\frac{1}{r}\right) \left(\frac{\partial}{\partial r}\right)^2 (r j_n(kr)) + \left(k^2 - \frac{n(n+1)}{r^2}\right) j_n(kr) = 0 \quad (2.27)$$

which shows that when the two permeabilities approach one another, the radial function becomes simply a spherical Bessel function with an integer index.

The next radial differential equation can be obtained by equating coefficients of e_r on both sides of equation (2.21) and by making use of the properties of the traditional scalar spherical harmonics $P_n^m(\cos(\theta))$ (Bell, Cohoon, and Penn [2]). These considerations give us the relationship,

$$(i\omega\epsilon_r + \sigma_r)c_{(m,n)} \frac{Z_n^{(c)}(r)}{r} = \frac{i n(n+1)}{\omega\mu r} \left[c_{(m,n)} \frac{Z_n^{(c)}(r)}{r^2} + b_{(m,n)} \frac{1}{r} \left(\frac{\partial}{\partial r}\right)^2 (r Z_n^{(b)}(r)) \right] \quad (2.28)$$

The final radial differential equation is obtained by equating coefficients of the vector field, $B_{(m,n)}(\theta, \phi)$ defined by equation (2.4) on both sides of equation (2.21). This differential equation has the form

$$(i\omega\epsilon + \sigma)b_{(m,n)} \left(\frac{-1}{r}\right) \left(\frac{\partial}{\partial r}\right) (r Z_n^{(b)}(r)) = \frac{1}{r} \frac{\partial}{\partial r} \left[\frac{i}{\omega\mu} \left[c_{(m,n)} \frac{Z_n^{(c)}(r)}{r} + b_{(m,n)} \left(\frac{\partial}{\partial r}\right)^2 (r Z_n^{(b)}(r)) \right] \right] \quad (2.29)$$

We have consistency between the two differential equations, (2.28) and (2.29), if

$$\frac{(i\omega\epsilon_r + \sigma_r)c_{(m,n)}}{n(n+1)r} \left(\frac{\partial}{\partial r}\right) (r Z_n^{(c)}(r)) = -b_{(m,n)}(i\omega\epsilon + \sigma) \left(\frac{1}{r} \frac{\partial}{\partial r}\right) r Z_n^{(b)}(r) \quad (2.30)$$

We find that we get a very simple solution of these equations if we simply let

$$Z_n^{(b)} = Z_n^{(c)}(r) \quad (2.31)$$

and assume that

$$c_{(m,n)} = \frac{-n(n+1)(i\omega\epsilon + \sigma)}{(i\omega\epsilon_r + \sigma_r)} b_{(m,n)} \quad (2.32)$$

Under our simple hypothesis we derive two distinct radial differential equations. As in the traditional Mie solution (Bell, Cohoon, and Penn [1]) we have multipliers of the A vector fields which are of the same type that one gets by computing the curl of the product of a solution of the scalar Helmholtz equation by the unit vector e_r , and vector fields which have the same form as the curl of a vector field of this type. In the traditional solution ([1]) the coefficients multiplying the terms involving regular and singular radial functions times the first type of vector field are labeled with a and α , respectively, and the coefficients multiplying the terms involving the regular and singular functions times the second type of vector field are labeled with b and β , respectively.

Combining equations (2.28) and (2.29) and making use of the assumptions embodied in equations (2.30)–(2.32) give us the differential equation,

$$\frac{1}{r} \left(\frac{\partial}{\partial r} \right)^2 (rZ_n^{(b)}(r)) + \left[k^2 - \frac{n(n+1)}{r^2} \left(\frac{i\omega\epsilon + \sigma}{i\omega\epsilon_r + \sigma_r} \right) \right] Z_n^{(b)}(r) = 0 \quad (2.33)$$

Making use of this second radial differential equation, and making use of the relationships between the coefficients, equations (2.30) through (2.32), we will get a new representation of the magnetic field intensity \mathbf{H} that was originally given by equation (2.20). Specifically, we need to first look at the term involving the A vector in equation (2.20). The relevant observation, using equation (2.28), is that

$$\begin{aligned} & \left\{ c_{(m,n)} \frac{Z_n^{(b)}(r)}{r^2} + b_{(m,n)} \frac{1}{r} \left(\frac{\partial}{\partial r} \right)^2 (rZ_n^{(c)}(r)) \right\} = \\ & \left\{ \frac{-n(n+1)(i\omega\epsilon + \sigma)}{i\omega\epsilon_r + \sigma_r} \left(\frac{Z_n^{(c)}(r)}{r^2} \right) + \frac{1}{r} \left(\frac{\partial}{\partial r} \right)^2 (rZ_n^{(c)}(r)) \right\} b_{(m,n)} = \\ & = -i\omega\mu(i\omega\epsilon_r + \sigma_r) \left(\frac{Z_n^{(c)}(r)}{n(n+1)} \right) c_{(m,n)} = -k^2 Z_n^{(c)}(r) b_{(m,n)} \quad (2.34) \end{aligned}$$

Combining these equations we obtain a greatly simplified expression for \mathbf{H} of the form,

$$\mathbf{H} = \sum_{(m,n) \in I} \left(\frac{i}{\omega \mu_r} a_{(m,n)} Z_n^{(a)}(r) \frac{n(n+1)}{r} C_{(m,n)}(\theta, \phi) + \left[\frac{i}{\omega \mu} a_{(m,n)} \frac{1}{r} \frac{\partial}{\partial r} (r Z_n^{(a)}(r)) \right] B_{(m,n)}(\theta, \phi) + \frac{i}{\omega \mu} (-k) Z_n^{(b)}(r) b_{(m,n)} A_{(m,n)}(\theta, \phi) \right) \quad (2.35)$$

The simple relationships (2.15) and (2.35) give us easy matrix relationships between expansion coefficients used to represent the field in one layer to those used to represent the field in another layer. Details concerning these intralayer relationships are discussed in the next sections of the paper. We will discuss spherical structures with a metallic core, dielectric multilayers where the layers may have nontrivial magnetic properties, and structures where the layers are separated by charge sheets or very thin layers, referred to in the literature, as impedance sheets.

THE INPUT DATA FREQUENCY, E LENGTH, NO OF REGIONS		
1. GHZ	1.00 V/M	1

INPUT DATA (SURFACE BOUNDARIES)	
SPHERE RADIUS =	3.00 CM

ELECTRICAL AND MAGNETIC PROPERTIES CORE REGION INTERIOR TO THE IMPEDANCE SHEET		
PARAMETER	REAL PART	IMAGINARY PART
ϵ_r	10.	5.00
ϵ	15.	7.00
μ_r	21.00	2.00
μ	11.00	3.00
σ_r	3.00	1.00
σ	2.00	2.00

ELECTRICAL CONDUCTIVITY AND REACTIVITY OF THE IMPEDANCE SHEET		
PARAMETER	REAL PART	IMAGINARY PART
σ_s	1.00	3.20

AVG AND TOTAL ABSORBED POWER BY VOLUME INTEGRATION OVER THE INTERIOR AND SURFACE INTEGRATION OVER THE IMPEDANCE SHEET	
6.15132D-05 W/M**3	6.95697963D-9 WATTS

AVG AND TOTAL ABSORBED POWER BY A POYNTING VECTOR ANALYSIS	
6.15132D-05 W/M**3	6.95697963D-9 WATTS

Table 2.1 Energy balance computation for an anisotropic, spherically symmetric particle covered by a lossy, reactive impedance sheet. The typical Poynting vector calculation on the outer boundary covered by the impedance sheet yields the total absorbed power. This must match a computation involving a surface integral for the impedance sheet loss, plus the magnetic loss and the electric loss in the interior.

3. INTRALAYER RELATIONSHIPS

The purpose of this section is to develop matrix equations which relate the expansion coefficients in one layer to those in adjacent layers and ultimately to be able to express the expansion coefficients of the field in any layer to the expansion coefficients of the incident radiation. The program will treat both structures with metallic cores and dielectric multilayers with nontrivial magnetic properties. We will choose four expansion coefficients for each layer. These expansion coefficients will be $a_{(m,n)}^{(p)}$, $b_{(m,n)}^{(p)}$, $\alpha_{(m,n)}^{(p)}$, and $\beta_{(m,n)}^{(p)}$.

The electric vector in layer p is given by

$$\begin{aligned} \mathbf{E} = \sum_{(m,n) \in I} & \left(a_{(m,n)}^{(p)} Z_{(n,p)}^{(a,1)}(r) \mathbf{A}_{(m,n)}(\theta, \phi) + b_{(m,n)}^{(p)} \left[\frac{-1}{kr} \right] \frac{\partial}{\partial r} (r Z_{(n,p)}^{(b,1)}(r)) \mathbf{B}_{(m,n)}(\theta, \phi) + \right. \\ & \left. \left[\frac{-n(n+1)(i\omega\epsilon^{(p)} + \sigma^{(p)})}{i\omega\epsilon_r^{(p)} + \sigma_r^{(p)}} \right] b_{(m,n)}^{(p)} \frac{Z_{(n,p)}^{(b,1)}(r)}{kr} \mathbf{C}_{(m,n)}(\theta, \phi) + \right. \\ & \left. \alpha_{(m,n)}^{(p)} Z_{(n,p)}^{(a,3)}(r) \mathbf{A}_{(m,n)}(\theta, \phi) + \beta_{(m,n)}^{(p)} \left[\frac{-1}{kr} \right] \frac{\partial}{\partial r} (r Z_{(n,p)}^{(b,3)}(r)) \mathbf{B}_{(m,n)}(\theta, \phi) + \right. \\ & \left. \left[\frac{-n(n+1)(i\omega\epsilon^{(p)} + \sigma^{(p)})}{i\omega\epsilon_r^{(p)} + \sigma_r^{(p)}} \right] \beta_{(m,n)}^{(p)} \frac{Z_{(n,p)}^{(b,3)}(r)}{kr} \mathbf{C}_{(m,n)}(\theta, \phi) \right) \quad (3.1) \end{aligned}$$

It is now very easy in view of the relationships given in Lemma 1.1, where the vectors $\mathbf{A}_{(m,n)}$, $\mathbf{B}_{(m,q)}$, and $\mathbf{C}_{(m,n)}$ are given by equations (2.2), (2.3), and (2.4), respectively, to calculate the magnetic field intensity \mathbf{H} and show that in view of orthogonality relationships (2.23), (2.24), and the additional relationships, valid when the index q is different from n which state that

$$\int_0^{2\pi} \int_0^\pi \mathbf{A}_{(m,n)}(\theta, \phi) \cdot \mathbf{A}_{(m,q)}(\theta, \phi) \sin(\theta) d\theta d\phi = 0$$

and that

$$\int_0^{2\pi} \int_0^\pi \mathbf{B}_{(m,n)}(\theta, \phi) \cdot \mathbf{B}_{(m,q)}(\theta, \phi) \sin(\theta) d\theta d\phi = 0$$

that very simple relationships result when we equate tangential components of \mathbf{E} and \mathbf{H} across the boundaries.

The magnetic intensity vector \mathbf{H} is given by

$$\begin{aligned}
\mathbf{H} = \sum_{(m,n) \in I} & \left(\frac{i}{\omega \mu^{(p)}} \right) \left(-k_p b_{(m,n)}^{(p)} Z_{(n,p)}^{(b,1)}(r) \mathbf{A}_{(m,n)}(\theta, \phi) + a_{(m,n)}^{(p)} \frac{1}{r} \frac{\partial}{\partial r} (r Z_{(n,p)}^{(a,1)}(r)) \mathbf{B}_{(m,n)}(\theta, \phi) \right) \\
& \left(\frac{i}{\omega \mu_r^{(p)}} \right) a_{(m,n)}^{(p)} Z_{(n,p)}^{(a,1)}(r) \frac{n(n+1)}{r} \mathbf{C}_{(m,n)}(\theta, \phi) + \\
& \left(\frac{i}{\omega \mu^{(p)}} \right) \left(-k_p \beta_{(m,n)}^{(p)} Z_{(n,p)}^{(b,3)}(r) \mathbf{A}_{(m,n)}(\theta, \phi) + \alpha_{(m,n)}^{(p)} \frac{1}{r} \frac{\partial}{\partial r} (r Z_{(n,p)}^{(a,3)}(r)) \mathbf{B}_{(m,n)}(\theta, \phi) \right) \\
& + \left(\frac{i}{\omega \mu_r^{(p)}} \right) \alpha_{(m,n)}^{(p)} Z_{(n,p)}^{(a,3)}(r) \frac{n(n+1)}{r} \mathbf{C}_{(m,n)}(\theta, \phi) \quad (3.2)
\end{aligned}$$

The ordinary boundary value problem requires continuity of tangential components of \mathbf{E} and \mathbf{H} across the boundary layers

$$r = R_p \quad (3.3)$$

Making use of this and the orthogonality relationships we deduce that if we let

$$W_{(n,p)}^{(a,j)}(R_p) = \left(\frac{1}{k_p r} \right) \frac{\partial}{\partial r} (r Z_{(n,p)}^{(a,j)}(r)) \Big|_{r=R_p} \quad (3.4)$$

and

$$W_{(n,p+1)}^{(a,j)}(R_p) = \left(\frac{1}{k_{p+1} r} \right) \frac{\partial}{\partial r} (r Z_{(n,p+1)}^{(a,j)}(r)) \Big|_{r=R_p} \quad (3.5)$$

and if we let

$$\rho_p = \frac{\mu^{(p)} k_{p+1}}{\mu^{(p+1)} k_p}, \quad (3.6)$$

then the expansion coefficients are related by a matrix equation,

$$\begin{aligned}
& \begin{pmatrix} Z_{(n,p)}^{(a,1)}(R_p) & Z_{(n,p)}^{(a,3)}(R_p) \\ W_{(n,p)}^{(a,1)}(R_p) & W_{(n,p)}^{(a,3)}(R_p) \end{pmatrix} \begin{pmatrix} a_{(m,n)}^{(p)} \\ \alpha_{(m,n)}^{(p)} \end{pmatrix} = \\
& \begin{pmatrix} Z_{(n,p+1)}^{(a,1)}(R_p) & Z_{(n,p+1)}^{(a,3)}(R_p) \\ \rho_p W_{(n,p+1)}^{(a,1)}(R_p) & \rho_p W_{(n,p+1)}^{(a,3)}(R_p) \end{pmatrix} \begin{pmatrix} a_{(m,n)}^{(p+1)} \\ \alpha_{(m,n)}^{(p+1)} \end{pmatrix} \quad (3.7)
\end{aligned}$$

The matrix relationship (3.7) may be abbreviated as

$$S^{(p)}(R_p) \begin{pmatrix} a_{(m,n)}^{(p)} \\ \alpha_{(m,n)}^{(p)} \end{pmatrix} = S^{(p+1)}(R_p) \begin{pmatrix} a_{(m,n)}^{(p+1)} \\ \alpha_{(m,n)}^{(p+1)} \end{pmatrix} \quad (3.8)$$

We obtained the matrix relationship (3.7) by equating tangential components of \mathbf{E} and \mathbf{H} across the boundary of the spherical surface separating the layers, taking the inner product of both sides of this equation with respect to $\mathbf{A}_{(m,n)}$ and then integrating over the surface of this sphere.

A second matrix relationship is obtained by equating tangential components of \mathbf{E} and \mathbf{H} across the separating spherical boundary, taking the inner product of both sides of these equations with respect to the vector functions $\mathbf{B}_{(m,n)}$, and then integrating over the surface of the sphere; this second matrix equation relates the expansion coefficients $b_{(m,n)}^{(p)}$ and $\beta_{(m,n)}^{(p)}$ to those in layer $p + 1$, and is given by

$$\begin{pmatrix} Z_{(n,p)}^{(b,1)}(R_p) & Z_{(n,p)}^{(b,3)}(R_p) \\ W_{(n,p)}^{(b,1)}(R_p) & W_{(n,p)}^{(b,3)}(R_p) \end{pmatrix} \begin{pmatrix} b_{(m,n)}^{(p)} \\ \beta_{(m,n)}^{(p)} \end{pmatrix} = \begin{pmatrix} \rho_p Z_{(n,p+1)}^{(b,1)}(R_p) & \rho_p Z_{(n,p+1)}^{(b,3)}(R_p) \\ W_{(n,p+1)}^{(b,1)}(R_p) & W_{(n,p+1)}^{(b,3)}(R_p) \end{pmatrix} \begin{pmatrix} b_{(m,n)}^{(p+1)} \\ \beta_{(m,n)}^{(p+1)} \end{pmatrix} \quad (3.9)$$

The matrix relationship (3.9) may be rewritten in abridged form as

$$T^{(p)}(R_p) \begin{pmatrix} b_{(m,n)}^{(p)} \\ \beta_{(m,n)}^{(p)} \end{pmatrix} = T^{(p+1)}(R_p) \begin{pmatrix} b_{(m,n)}^{(p+1)} \\ \beta_{(m,n)}^{(p+1)} \end{pmatrix} \quad (3.10)$$

Define new matrices by the rules,

$$Q_{(m,n)}^{(p)} = S_{(m,n)}^{(p)}(R_p)^{-1} S_{(m,n)}^{(p+1)}(R_p) \quad (3.11)$$

and

$$R_{(m,n)}^{(p)} = T_{(m,n)}^{(p)}(R_p)^{-1} T_{(m,n)}^{(p+1)}(R_p) \quad (3.12)$$

Thus, if region $N+1$ is the region surrounding the sphere, we assume that $a_{(m,n)}^{(N+1)}$ and $b_{(m,n)}^{(N+1)}$ are all completely known. Thus, since

$$\alpha_{(m,n)}^{(1)} = \beta_{(m,n)}^{(1)} = 0 \quad (3.13)$$

for all nonnegative integers n and all integers m not smaller than $-n$ nor larger than $+n$. Thus, we see that as in the case of isotropic N layer spherical structures (Bell, Cohoon, and Penn [1]) we have the relationships,

$$\begin{pmatrix} a_{(m,n)}^{(1)} \\ 0 \end{pmatrix} = Q_{(m,n)} \begin{pmatrix} a_{(m,n)}^{(N+1)} \\ \alpha_{(m,n)}^{(N+1)} \end{pmatrix} \quad (3.14)$$

where the matrix $Q^{(m,n)}$ is given by

$$Q^{(m,n)} = Q_{(m,n)}^{(1)}(R_1)Q_{(m,n)}^{(2)}(R_2) \cdots Q_{(m,n)}^{(N)}(R_N) \quad (3.15)$$

The matrix relationship (3.14) yields two equations in two unknowns which in turn imply that

$$a_{(m,n)}^{(1)} = Q_{(1,1)}^{(m,n)} a_{(m,n)}^{(N+1)} + Q_{(1,2)}^{(m,n)} \alpha_{(m,n)}^{(N+1)} \quad (3.16)$$

and

$$0 = Q_{(2,1)}^{(m,n)} a_{(m,n)}^{(N+1)} + Q_{(2,2)}^{(m,n)} \alpha_{(m,n)}^{(N+1)} \quad (3.17)$$

Thus, we see that

$$\alpha_{(m,n)}^{(N+1)} = \frac{-Q_{(2,1)}^{(m,n)} a_{(m,n)}^{(N+1)}}{Q_{(2,2)}^{(m,n)}} \quad (3.18)$$

and

$$a_{(m,n)}^{(1)} = \left(Q_{(1,1)}^{(m,n)} + Q_{(1,2)}^{(m,n)} \left[\frac{-Q_{(2,1)}^{(m,n)}}{Q_{(2,2)}^{(m,n)}} \right] \right) a_{(m,n)}^{(N+1)} \quad (3.19)$$

Similarly, we see that

$$\beta_{(m,n)}^{(N+1)} = \frac{-R_{(2,1)}^{(m,n)} b_{(m,n)}^{(N+1)}}{R_{(2,2)}^{(m,n)}} \quad (3.20)$$

and

$$b_{(m,n)}^{(1)} = \left(R_{(1,1)}^{(m,n)} + R_{(1,2)}^{(m,n)} \left[\frac{-R_{(2,1)}^{(m,n)}}{R_{(2,2)}^{(m,n)}} \right] \right) b_{(m,n)}^{(N+1)} \quad (3.21)$$

where

$$R^{(m,n)} = R_{(m,n)}^{(1)}(R_1)R_{(m,n)}^{(2)}(R_2) \cdots R_{(m,n)}^{(N)}(R_N) \quad (3.22)$$

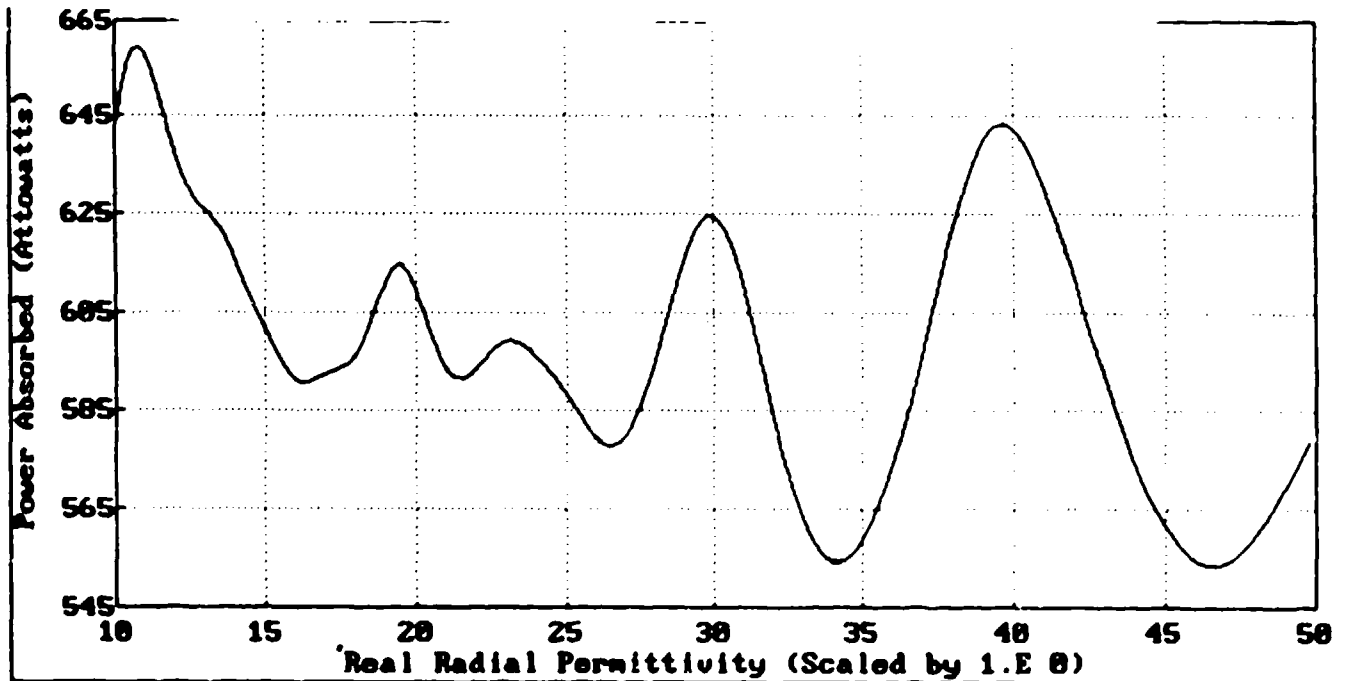
From these relationships the expansion coefficients in all layers can be determined from the expansion coefficients in the inner core of the multilayer structure. The basic relationships are

$$\begin{pmatrix} a_{(m,n)}^{(2)} \\ \alpha_{(m,n)}^{(2)} \end{pmatrix} = (Q_{(m,n)}^{(1)})^{-1} \begin{pmatrix} a_{(m,n)}^{(1)} \\ 0 \end{pmatrix} \quad (3.23)$$

and

$$\begin{pmatrix} b_{(m,n)}^{(2)} \\ \beta_{(m,n)}^{(2)} \end{pmatrix} = (R_{(m,n)}^{(1)})^{-1} \begin{pmatrix} b_{(m,n)}^{(1)} \\ 0 \end{pmatrix} \quad (3.24)$$

From equations (3.23) and (3.24) we see that all the coefficients in layer two are now completely known. By iterating these results we can get all the coefficients in layers three through N. Since we already know the expansion coefficients in layers one and two and in the region of free space surrounding the N layer structure we see that by making use of the formulas (3.1) and (3.2) we get the components of the electric and magnetic field vectors in each layer of the structure and in the region of free space surrounding the structure.



The above graph shows the effects of anisotropy on the total absorbed power for a .5 micron aerosol particle subjected to 600,000,000 Megahertz radiation. In the original droplet the radial and tangential relative permittivity were set equal to $50 + i$ and the real part of the radial permittivity was varied making the droplet anisotropic as soon as this real part differed from 50. The droplet was considered to be nonmagnetic, and the complex conductivity was set equal to zero. The field strength was 10 Volts per meter.

4. INTRALAYER RELATIONSHIPS WITH A PERFECTLY CONDUCTING CORE

Let us suppose that the inner core of an N layer structure is perfectly conducting which means that on this inner layer defined in spherical coordinates by

$$r = R_1 \quad (4.1)$$

the electric vector \mathbf{E} defined by equation (3.1) is identically zero which means that in view of the orthogonality relationships described in section 3 that

$$a_{(m,n)}^{(2)} Z_{(n,2)}^{(a,1)}(R_1) + \alpha_{(m,n)}^{(2)} Z_{(n,2)}^{(a,3)}(R_1) = 0 \quad (4.2)$$

and

$$b_{(m,n)}^{(2)} W_{(n,2)}^{(b,1)}(R_1) + \beta_{(m,n)}^{(2)} W_{(n,2)}^{(b,3)}(R_1) = 0 \quad (4.3)$$

where the Z function appearing in equation (4.2) is defined by equation (2.16) and equation (1.30), and the W function appearing in equation (4.3) is defined by equations (1.32), (1.33), (2.17), and (3.5). The Z and W functions associated with layer 2 are evaluated at the boundary separating the core from the first coating.

If as before we define $Q_{(m,n)}^{(p)}$ by the rule,

$$Q_{(m,n)}^{(p)}(R_p) = S_{(m,n)}^{(p)}(R_p)^{-1} S_{(m,n)}^{(p+1)}(R_p) \quad (4.4)$$

where

$$S^{(p)}(R_p) \begin{pmatrix} a_{(m,n)}^{(p)} \\ \alpha_{(m,n)}^{(p)} \end{pmatrix} = \begin{pmatrix} Z_{(n,p)}^{(a,1)}(R_p) & Z_{(n,p)}^{(a,3)}(R_p) \\ W_{(n,p)}^{(a,1)}(R_p) & W_{(n,p)}^{(a,3)}(R_p) \end{pmatrix} \begin{pmatrix} a_{(m,n)}^{(p)} \\ \alpha_{(m,n)}^{(p)} \end{pmatrix} \quad (4.5)$$

and

$$S^{(p+1)}(R_p) \begin{pmatrix} a_{(m,n)}^{(p+1)} \\ \alpha_{(m,n)}^{(p+1)} \end{pmatrix} = \begin{pmatrix} Z_{(n,p+1)}^{(a,1)}(R_p) & Z_{(n,p+1)}^{(a,3)}(R_p) \\ \rho_p W_{(n,p+1)}^{(a,1)}(R_p) & \rho_p W_{(n,p+1)}^{(a,3)}(R_p) \end{pmatrix} \begin{pmatrix} a_{(m,n)}^{(p+1)} \\ \alpha_{(m,n)}^{(p+1)} \end{pmatrix} \quad (4.6)$$

$$S^{(m,n)} = Q_{(m,n)}^{(2)}(R_2) Q_{(m,n)}^{(3)}(R_3) \cdots Q_{(m,n)}^{(N)}(R_N) \quad (4.7)$$

Thus, the coefficients in layer 2 are related to the expansion coefficients in the outer layer by means of the relation,

$$\begin{pmatrix} a_{(m,n)}^{(2)} \\ \alpha_{(m,n)}^{(2)} \end{pmatrix} = S^{(m,n)} \begin{pmatrix} a_{(m,n)}^{(N+1)} \\ \alpha_{(m,n)}^{(N+1)} \end{pmatrix} \quad (4.8)$$

Thus, using equation (4.2) and equation (4.8) we see that for each pair (m,n) of integers where n is nonnegative and the absolute value of m

does not exceed n we have three equations in the three a priori unknown coefficients, where only the expansion coefficients, $a_{(m,p)}^{(N+1)}$, are assumed to be known. Thus, if the determinant of the S matrix is defined by the rule,

$$\Delta(S^{(m,n)}) = S_{(2,2)}^{(m,n)} S_{(1,1)}^{(m,n)} - S_{(1,2)}^{(m,n)} S_{(2,1)}^{(m,n)} \quad (4.9)$$

then the solution of the system of equations is given by

$$a_{(m,n)}^{(2)} = \frac{\Delta(S^{(m,n)})Z_{(n,3)}^{(a,3)}(R_1)a_{(m,n)}^{(N+1)}}{S_{(1,2)}^{(m,n)}Z_{(n,2)}^{(a,1)}(R_1) + S_{(2,2)}^{(m,n)}Z_{(n,3)}^{(a,3)}(R_1)} \quad (4.10)$$

$$\alpha_{(m,n)}^{(2)} = \frac{\Delta(S^{(m,n)})Z_{(n,3)}^{(a,1)}(R_1)a_{(m,n)}^{(N+1)}}{S_{(1,2)}^{(m,n)}Z_{(n,2)}^{(a,1)}(R_1) + S_{(2,2)}^{(m,n)}Z_{(n,3)}^{(a,3)}(R_1)} \quad (4.11)$$

and the expansion coefficient of the scattered wave in the medium surrounding the sphere is given by

$$\alpha_{(m,n)}^{(N+1)} = - \left[\frac{S_{(1,1)}^{(m,n)}Z_{(n,2)}^{(a,1)}(R_1) + S_{(2,1)}^{(m,n)}Z_{(n,3)}^{(a,3)}(R_1)}{S_{(1,2)}^{(m,n)}Z_{(n,2)}^{(a,1)}(R_1) + S_{(2,2)}^{(m,n)}Z_{(n,3)}^{(a,3)}(R_1)} \right] a_{(m,n)}^{(N+1)} \quad (4.12)$$

The remaining expansion coefficients are derived in an analogous manner. By defining a matrix $T^{(m,n)}$ by the rule,

$$T^{(m,n)} = R_{(m,n)}^{(2)}(R_2)R_{(m,n)}^{(3)}(R_3) \cdots R_{(m,n)}^{(N)}(R_N) \quad (4.13)$$

where the R matrices appearing in equation (4.13) are defined by equations (3.9), (3.10), and (3.12), we see that we have the relationship between the expansion coefficients in the first penetrable layer surrounding the perfectly conducting core and the expansion coefficients in the region of free space surrounding the multilayer spherical structure given by

$$\begin{pmatrix} b_{(m,n)}^{(2)} \\ \beta_{(m,n)}^{(2)} \end{pmatrix} = T^{(m,n)} \begin{pmatrix} b_{(m,n)}^{(N+1)} \\ \beta_{(m,n)}^{(N+1)} \end{pmatrix} \quad (4.14)$$

For every pair (m,n) equation (4.14) and the relationship (4.3) demanded by the assertion that the tangential component of \mathbf{E} vanish on the boundary of the scatterer gives us again three equations in three unknowns. The solution of this system of equations is

$$b_{(m,n)}^{(2)} = \frac{\Delta(T^{(m,n)})W_{(n,2)}^{(b,3)}(R_1)b_{(m,n)}^{(N+1)}}{T_{(1,2)}^{(m,n)}W_{(n,2)}^{(b,1)}(R_1) + T_{(2,2)}^{(m,n)}W_{(n,2)}^{(b,3)}(R_1)} \quad (4.15)$$

$$\beta_{(m,n)}^{(2)} = \frac{\Delta(T^{(m,n)})W_{(n,2)}^{(b,1)}(R_1)b_{(m,n)}^{(N+1)}}{T_{(1,2)}^{(m,n)}W_{(n,2)}^{(b,1)}(R_1) + T_{(2,2)}^{(m,n)}W_{(n,2)}^{(b,3)}(R_1)} \quad (4.16)$$

and the expansion coefficient of the scattered wave in the medium surrounding the sphere is given by

$$\beta_{(m,n)}^{(N+1)} = - \left[\frac{T_{(1,1)}^{(m,n)}W_{(n,2)}^{(b,1)}(R_1) + T_{(2,1)}^{(m,n)}W_{(n,2)}^{(b,3)}(R_1)}{T_{(1,2)}^{(m,n)}W_{(n,2)}^{(b,1)}(R_1) + T_{(2,2)}^{(m,n)}W_{(n,2)}^{(b,3)}(R_1)} \right] b_{(m,n)}^{(N+1)} \quad (4.17)$$

where the determinant $\Delta(T^{(m,n)})$ is given by

$$\Delta(T^{(m,n)}) = T_{(2,2)}^{(m,n)} \cdot T_{(1,1)}^{(m,n)} - T_{(1,2)}^{(m,n)} \cdot T_{(2,1)}^{(m,n)} \quad (4.18)$$

This analysis enables us to assess the effectiveness of coatings on materials in impeding or transmitting radiation to a conducting core surrounded by penetrable but anisotropic materials with both nontrivial electrical and nontrivial magnetic properties. We can also calculate the absorbed and scattered radiation by using the expansion coefficients for the scattered radiation in the outer layer. The electric vector of the incident radiation is expressed in terms of known expansion coefficients by the relation,

$$\mathbf{E}^i = \sum_{(m,n) \in I} \left(a_{(m,n)}^{(N+1)} Z_{(n,N+1)}^{(0,1)}(r) \mathbf{A}_{(m,n)}(\theta, \phi) + b_{(m,n)}^{(N+1)} \left[\frac{-1}{k_0 r} \right] \frac{\partial}{\partial r} (r Z_{(n,N+1)}^{(0,1)}(r)) \mathbf{B}_{(m,n)}(\theta, \phi) + \right. \\ \left. -n(n+1) b_{(m,n)}^{(N+1)} \frac{Z_{(n,N+1)}^{(0,1)}(r)}{k_0 r} \mathbf{C}_{(m,n)}(\theta, \phi) \right) \quad (4.19)$$

where the superscript zero for the Z functions and their derivatives means that these functions are solutions of the ordinary Bessel equation (2.27) with $k = k_0$. All other expansion coefficients are expressed in terms of the expansion coefficients appearing in equation (4.19).

5. LAYERS SEPARATED BY IMPEDANCE SHEETS OR CHARGE LAYERS

The impedance sheet relationship states that at the surface

$$r = R_p \quad (5.1)$$

separating region p from region p + 1 we have

$$\mathbf{e}_r \times (\mathbf{H}_{p+1} - \mathbf{H}_p) = \sigma_s^{(p)} \mathbf{E}_p \quad (5.2)$$

The development of intralayer relationships through the use of equation (5.2) is enhanced if we simply use the definitions (2.5), (2.6), and (2.7) and observe that

$$\mathbf{e}_r \times \mathbf{C}_{(m,n)}(\theta, \phi) = 0, \quad (5.3)$$

$$\mathbf{e}_r \times \mathbf{B}_{(m,n)}(\theta, \phi) = -\mathbf{A}_{(m,n)}(\theta, \phi) \quad (5.4)$$

and

$$\mathbf{e}_r \times \mathbf{A}_{(m,n)}(\theta, \phi) = \mathbf{B}_{(m,n)}(\theta, \phi) \quad (5.5)$$

Making use of the above relationships, (5.3) through (5.5) and equation (3.2) which gives a representation

$$\begin{aligned}
\mathbf{e}_r \times (\mathbf{H}_{p+1} - \mathbf{H}_p) = \sum_{(m,n) \in I} & \left(\frac{ik_{p+1}}{\omega\mu^{(p+1)}} \mathbf{a}_{(m,n)}^{(p+1)} W_{(n,p+1)}^{(a,1)}(R_p) - \frac{ik_p}{\omega\mu^{(p)}} \mathbf{a}_{(m,n)}^{(p)} W_{(n,p)}^{(a,1)}(R_p) \right. \\
& + \frac{ik_{p+1}}{\omega\mu^{(p+1)}} \alpha_{(m,n)}^{(p+1)} W_{(n,p+1)}^{(a,3)}(R_p) - \frac{ik_p}{\omega\mu^{(p)}} \alpha_{(m,n)}^{(p)} W_{(n,p)}^{(a,3)}(R_p) \Big) \mathbf{B}_{(m,n)}(\theta, \phi) \\
& + \left(\frac{ik_{p+1}}{\omega\mu^{(p+1)}} \mathbf{b}_{(m,n)}^{(p+1)} Z_{(n,p+1)}^{(b,1)}(R_p) - \frac{ik_p}{\omega\mu^{(p)}} \mathbf{b}_{(m,n)}^{(p)} Z_{(n,p)}^{(b,1)}(R_p) \right. \\
& \left. \frac{ik_{p+1}}{\omega\mu^{(p+1)}} \beta_{(m,n)}^{(p+1)} Z_{(n,p+1)}^{(b,3)}(R_p) - \frac{ik_p}{\omega\mu^{(p)}} \beta_{(m,n)}^{(p)} Z_{(n,p)}^{(b,3)}(R_p) \right) \mathbf{A}_{(m,n)}(\theta, \phi) \quad (5.6)
\end{aligned}$$

If we assume a tensor relationship between the surface conductivity and the electric vector we obtain the relationship

$$\begin{aligned}
\mathbf{J}_e = \sum_{(m,n) \in I} & \left(\sigma_a \left(\mathbf{a}_{(m,n)}^{(p)} Z_{(n,p)}^{(a,1)} + \alpha_{(m,n)}^{(p)} Z_{(n,p)}^{(a,3)} \right) (R_p) \mathbf{A}_{(m,n)}(\theta, \phi) + \right. \\
& \left. - \sigma_b \left(\mathbf{b}_{(m,n)}^{(p)} W_{(n,p)}^{(b,1)} + \beta_{(m,n)}^{(p)} W_{(n,p)}^{(b,3)} \right) (R_p) \mathbf{A}_{(m,n)}(\theta, \phi) \right) \quad (5.7)
\end{aligned}$$

By making use of orthogonality we obtain the following relationships

$$\begin{aligned}
\rho_p \mathbf{a}_{(m,n)}^{(p+1)} W_{(n,p+1)}^{(a,1)}(R_p) + \rho_p \alpha_{(m,n)}^{(p+1)} W_{(n,p+1)}^{(a,3)}(R_p) = \\
\mathbf{a}_{(m,n)}^{(p)} W_{(n,p)}^{(a,1)}(R_p) + \alpha_{(m,n)}^{(p)} W_{(n,p)}^{(a,3)}(R_p) + \\
\frac{i\omega\mu^{(p)} \sigma_a}{k_p} \left(\mathbf{a}_{(m,n)}^{(p)} Z_{(n,p)}^{(a,1)}(R_p) + \alpha_{(m,n)}^{(p)} Z_{(n,p)}^{(a,3)}(R_p) \right) \quad (5.8)
\end{aligned}$$

and

$$\begin{aligned}
\rho_p \mathbf{b}_{(m,n)}^{(p+1)} Z_{(n,p+1)}^{(b,1)}(R_p) + \rho_p \beta_{(m,n)}^{(p+1)} Z_{(n,p+1)}^{(b,3)}(R_p) = \\
\mathbf{b}_{(m,n)}^{(p)} Z_{(n,p)}^{(b,1)}(R_p) + \beta_{(m,n)}^{(p)} Z_{(n,p)}^{(b,3)}(R_p) + \\
- \frac{i\omega\mu^{(p)} \sigma_b}{k_p} \left(\mathbf{b}_{(m,n)}^{(p)} W_{(n,p)}^{(b,1)}(R_p) + \beta_{(m,n)}^{(p)} W_{(n,p)}^{(b,3)}(R_p) \right) \quad (5.9)
\end{aligned}$$

In order to simplify the matrix relationships connecting expansion coefficients in layer p to those in layer $p + 1$ we introduce some new functions by the rules,

$$U_{(n,p)}^{(a,j)} = (W_{(n,p)}^{(a,j)} + \left\{ \frac{i\omega\mu^{(p)}\sigma_a}{k_p} \right\} Z_{(n,p)}^{(a,j)})(R_p) \quad (5.10)$$

and

$$V_{(n,p)}^{(b,j)} = (Z_{(n,p)}^{(b,j)} + \left\{ \frac{-i\omega\mu^{(p)}\sigma_a}{k_p} \right\} W_{(n,p)}^{(b,j)})(R_p) \quad (5.11)$$

Making use of the definitions in equations (5.10) and (5.11) we reproduce a setting similar to either that of section 3 or section 4 depending on whether or not the inner core is penetrable or perfectly conducting, respectively. The matrix relationships are

$$\begin{pmatrix} Z_{(n,p)}^{(a,1)}(R_p) & Z_{(n,p)}^{(a,3)}(R_p) \\ U_{(n,p)}^{(a,1)}(R_p) & U_{(n,p)}^{(a,3)}(R_p) \end{pmatrix} \begin{pmatrix} a_{(m,n)}^{(p)} \\ \alpha_{(m,n)}^{(p)} \end{pmatrix} = \begin{pmatrix} Z_{(n,p+1)}^{(a,1)}(R_p) & Z_{(n,p+1)}^{(a,3)}(R_p) \\ \rho_p W_{(n,p+1)}^{(a,1)}(R_p) & \rho_p W_{(n,p+1)}^{(a,3)}(R_p) \end{pmatrix} \begin{pmatrix} a_{(m,n)}^{(p+1)} \\ \alpha_{(m,n)}^{(p+1)} \end{pmatrix} \quad (5.12)$$

and

$$\begin{pmatrix} Z_{(n,p)}^{(b,1)}(R_p) & Z_{(n,p)}^{(b,3)}(R_p) \\ V_{(n,p)}^{(b,1)}(R_p) & V_{(n,p)}^{(b,3)}(R_p) \end{pmatrix} \begin{pmatrix} b_{(m,n)}^{(p)} \\ \beta_{(m,n)}^{(p)} \end{pmatrix} = \begin{pmatrix} \rho_p Z_{(n,p+1)}^{(b,1)}(R_p) & \rho_p Z_{(n,p+1)}^{(b,3)}(R_p) \\ W_{(n,p+1)}^{(b,1)}(R_p) & W_{(n,p+1)}^{(b,3)}(R_p) \end{pmatrix} \begin{pmatrix} b_{(m,n)}^{(p+1)} \\ \beta_{(m,n)}^{(p+1)} \end{pmatrix} \quad (5.13)$$

We note that in case

$$0 = \sigma_a = \sigma_b \quad (5.14)$$

the intralayer relationships (5.12) and (5.13) are exactly those given by equations (3.7) and (3.9), respectively.

The solution of the system of equations relating the expansion coefficients is therefore the same as the solutions given in section 3 and section 4 and that the Wronskian relationship shows that the determinant of the new coefficient matrices on the left sides of (5.12) and (5.13) are respectively equal to the determinant of the coefficient matrices of the left sides of equations (3.7) and (3.8). The inverses needed to define the analogue of the matrices defined by equations (3.11) and (3.12) have to exist.

6. ENERGY BALANCE RELATIONSHIP

In this section of our paper we demonstrate a powerful means of validating computer codes for describing the interaction of electromagnetic radiation with anisotropic structures whose regions of continuity of tensorial electromagnetic properties are delimited by spherical reactive and lossy impedance sheets with a common center. This was important since no previous workers have published any data regarding scattering by anisotropic spheres. We have found data concerning scattering by isotropic spheres with either a penetrable or a perfectly conducting core, but the standard references do not include calculations of bistatic cross sections of magnetically lossy spherical structures even when the layers are isotropic, and no energy balance computations for these magnetically lossy structures seems to have been published. This section provides data for magnetically lossy anisotropic structures. We keep track of the energy going into our structure and the radiation scattered away from our spherically symmetric multilayer structure. This can be carried out by a Poynting vector analysis over the outermost surface of the scatterer or by integrating the power density over the interior of the layers or the surfaces of lossy impedance sheets. We discuss here a simple calculation when impedance sheets are present. The sphere considered, also may have both magnetic and electrical losses. The constitutive relations are tensorial. In what follows if α is a tensor, then $\text{Re}(\alpha)$ is the tensor formed by computing the real part of each entry and $\text{Im}(\alpha)$ is the tensor formed by computing the imaginary part of each entry. When there are off diagonal elements it is possible to have losses, for example, from a permittivity tensor which has only real entries. If σ , ϵ , and μ are respectively the conductivity, permittivity, and permeability tensors, then losses arise, for diagonal tensors, from the real part of the conductivity tensor, the imaginary part of the permittivity tensor, and the imaginary part, $\text{Im}(\mu)$, of the permeability tensor.

The sum of the surface integrals of the energy per unit area per unit time deposited in the impedance sheets separating the regions of continuity of the tensorial electromagnetic properties of the material plus the triple integral of the power density over the interior of an anisotropic multilayer spherical structure is related to the expansion coefficients $\alpha_{(n,N+1)}$ and $\beta_{(n,N+1)}$ of the scattered radiation by the equation ((1)),

$$\begin{aligned}
& \sum_{k=1}^M \left[R_k^2 \int_0^{\pi} \int_0^{2\pi} \left(\text{Re}(\sigma_s^{(k)}) (|E_\theta|^2 + |E_\phi|^2) (R_k, \theta, \phi) \right) d\phi \right] \sin(\theta) d\theta + \\
& \int_0^R \int_0^{\pi} \int_0^{2\pi} (\omega \text{Im}(\mu) (|H_\theta|^2 + |H_\phi|^2) + \omega \text{Im}(\mu_r) |H_r|^2) r^2 \sin(\theta) d\phi d\theta dr + \\
& \int_0^R \int_0^{\pi} \int_0^{2\pi} (\omega \text{Im}(\epsilon) (|E_\theta|^2 + |E_\phi|^2) + \omega \text{Im}(\epsilon_r) |E_r|^2) r^2 \sin(\theta) d\phi d\theta dr + \\
& \int_0^R \int_0^{\pi} \int_0^{2\pi} (\text{Re}(\sigma) (|E_\theta|^2 + |E_\phi|^2) + \text{Re}(\sigma_r) |E_r|^2) r^2 \sin(\theta) d\phi d\theta dr = \\
& \frac{\pi |E_0^2|}{k_0^2} \left(\frac{\epsilon_0}{\mu_0} \right)^{1/2} \left| \text{Re} \sum_{n=1}^{\infty} (2n+1) (\alpha_{(n,N+1)} + \beta_{(n,N+1)}) \right| - \\
& \frac{\pi |E_0^2|}{k_0^2} \left(\frac{\epsilon_0}{\mu_0} \right)^{1/2} \sum_{n=1}^{\infty} (2n+1) (|\alpha_{(n,N+1)}|^2 + |\beta_{(n,N+1)}|^2) \quad (6.1)
\end{aligned}$$

The constitutive relations between $(\partial/\partial t)\mathbf{D} + \mathbf{J}$ and \mathbf{E} , for the case of time harmonic radiation, are given by the equation,

$$\begin{pmatrix} i\omega D_r + J_r \\ i\omega D_\theta + J_\theta \\ i\omega D_\phi + J_\phi \end{pmatrix} = \begin{pmatrix} i\omega\epsilon_r + \sigma_r & 0 & 0 \\ 0 & i\omega\epsilon + \sigma & 0 \\ 0 & 0 & i\omega\epsilon + \sigma \end{pmatrix} \begin{pmatrix} E_r \\ E_\theta \\ E_\phi \end{pmatrix} \quad (6.2)$$

The constitutive relations between $(\partial/\partial t)\mathbf{B}$ and the magnetic field \mathbf{H} are defined by the equation,

$$\begin{pmatrix} i\omega B_r \\ i\omega B_\theta \\ i\omega B_\phi \end{pmatrix} = \begin{pmatrix} i\omega\mu_r & 0 & 0 \\ 0 & i\omega\mu & 0 \\ 0 & 0 & i\omega\mu \end{pmatrix} \begin{pmatrix} H_r \\ H_\theta \\ H_\phi \end{pmatrix} \quad (6.3)$$

The above computations have enabled us to provide a reliable set of equations for the expansion coefficients of both the scattered and induced electromagnetic fields. If there were an error in the formulas that produced incorrect electromagnetic fields, one could be confident

that integrating an incorrect power density over one of the layers or over one of the delimiting impedance sheets would not have given a 7 to 10 digit agreement between the computations of the total absorbed power using an energy balance computation by numerically integrating the power density distribution over the layers and over the surfaces of the lossy impedance sheets and making a comparison between the Poynting vector calculation on the outer surface of the sphere of the total electromagnetic energy entering minus the total energy scattered away from the spherical structure. These computations should enable one to quickly identify any errors in algebra or transcription of the formulas to the computer algorithm.

One of the unique features of our anisotropic structure was the peculiar behavior of the fields near the center of the sphere. It turns out that if we have only an anisotropy in the real part of the permittivity and if the radial component exceeds the angular component, then there is an integrable singularity in the power density at the center and if the radial permittivity is smaller than the angular permittivity, then the electric field vector goes to zero at the origin. Furthermore, if the radial permittivity is larger than the angular permittivity, no combination of the two linearly independent solutions will yield a solution which is bounded at the origin.

In spite of the complexities of the interaction of radiation with anisotropic structures I found that I could achieve the 9 digit agreement in the two methods of computing the total absorbed power with a tensor product of Gaussian quadrature schemes and for the most part making use of only 1728 function evaluations per layer. I checked the Gaussian quadrature by using in addition a scheme which used 4096 function evaluations per layer and make sure that the two methods gave the same answer. I also checked the computations by artificially adding extra layers. In making the computations I also made certain that the exact formula for the incoming radiation and our series expansion in spherical harmonics gave numerically identical answers on the surface of the sphere, and had checking subroutines which calculated the tangential components of the electric and magnetic vectors on both sides of the delimiting surface. When the delimiting surface happened to be an impedance sheet I not only made sure that the impedance sheet boundary condition was satisfied, I also checked to make sure that the spherical harmonic expansion of the internal fields had converged.

THE INPUT DATA FREQUENCY, E LENGTH, NO OF REGIONS		
1. GHZ	1.00 V/M	2

INPUT DATA (SURFACE BOUNDARIES)	
2.50 CM	3.00 CM

ELECTRICAL AND MAGNETIC PROPERTIES REGION ONE		
PARAMETER	REAL PART	IMAGINARY PART
ϵ_r	50.	9.00
ϵ	60.	8.00
μ_r	1.00	0.80
μ	2.40	1.00
σ_r	0.50	0.80
σ	0.60	0.40

ELECTRICAL AND MAGNETIC PROPERTIES REGION TWO		
PARAMETER	REAL PART	IMAGINARY PART
ϵ_r	40.	1.00
ϵ	50.	2.00
μ_r	3.00	1.80
μ	5.40	2.00
σ_r	1.50	0.40
σ	1.80	0.60

AVG AND TOTAL ABSORBED POWER BY TRIPLE INTEGRATION	
6.62536D-02 W/M**3	7.49310489D-6 WATTS

AVG AND TOTAL ABSORBED POWER BY A POYNTING VECTOR ANALYSIS	
6.62536D-02 W/M**3	7.49310488D-6 WATTS

THE INPUT DATA FREQUENCY, E LENGTH, NO OF REGIONS		
1. GHZ	1.00 V/M	1

INPUT DATA (SURFACE BOUNDARIES)	
SPHERE RADIUS =	3.00 CM

ELECTRIC AND MAGNETIC PROPERTIES CORE REGION INTERIOR TO THE IMPEDANCE SHEET		
PARAMETER	REAL PART	IMAGINARY PART
ϵ_r	60.	10.00
ϵ_i	60.	10.00
μ_r	3.00	2.00
μ_i	3.00	2.00
σ_r	2.00	1.00
σ_i	2.00	1.00

ELECTRICAL CONDUCTIVITY AND REACTIVITY OF THE IMPEDANCE SHEET		
PARAMETER	REAL PART	IMAGINARY PART
σ_s	0.00	0.00

AVG AND TOTAL ABSORBED POWER BY VOLUME INTEGRATION OVER THE INTERIOR AND SURFACE INTEGRATION OVER THE IMPEDANCE SHEET	
5.11025D-02 W/M**3	5.77965703D-6 WATTS

AVG AND TOTAL ABSORBED POWER BY A POYNTING VECTOR ANALYSIS	
5.11025D-02 W/M**3	5.77965703D-6 WATTS

THE INPUT DATA FREQUENCY, E LENGTH, NO OF REGIONS

1. GHZ	1.00 V/M	1
--------	----------	---

INPUT DATA (SURFACE BOUNDARIES)

SPHERE RADIUS =	3.00 CM
-----------------	---------

**ELECTRICAL AND MAGNETIC PROPERTIES
CORE REGION INTERIOR TO THE IMPEDANCE SHEET**

PARAMETER	REAL PART	IMAGINARY PART
ϵ_r	10.	5.00
ϵ_i	15.	7.00
μ_r	21.00	2.00
μ_i	11.00	3.00
σ_r	3.00	1.00
σ_i	2.00	2.00

**ELECTRICAL CONDUCTIVITY AND
REACTIVITY OF THE IMPEDANCE SHEET**

PARAMETER	REAL PART	IMAGINARY PART
σ_s	1.00	3.20

**AVG AND TOTAL ABSORBED POWER
BY VOLUME INTEGRATION OVER THE INTERIOR AND
SURFACE INTEGRATION OVER THE IMPEDANCE SHEET**

6.15132D-06 W/M ³	6.96697963D-9 WATTS
------------------------------	---------------------

**AVG AND TOTAL ABSORBED POWER BY A
POYNTING VECTOR ANALYSIS**

6.15132D-06 W/M ³	6.96697963D-9 WATTS
------------------------------	---------------------

THE INPUT DATA FREQUENCY, E LENGTH, NO OF REGIONS		
1. GHZ	1.00 V/M	1

INPUT DATA (SURFACE BOUNDARIES)	
SPHERE RADIUS =	3.00 CM

ELECTRICAL AND MAGNETIC PROPERTIES CORE REGION INTERIOR TO THE IMPEDANCE SHEET		
PARAMETER	REAL PART	IMAGINARY PART
ϵ_1	60.	10.00
ϵ	60.	10.00
μ_1	3.00	2.00
μ	3.00	2.00
σ_1	2.00	1.00
σ	2.00	1.00

ELECTRICAL CONDUCTIVITY AND REACTIVITY OF THE IMPEDANCE SHEET		
PARAMETER	REAL PART	IMAGINARY PART
σ_0	5.00	3.00

AVG AND TOTAL ABSORBED POWER BY VOLUME INTEGRATION OVER THE INTERIOR AND SURFACE INTEGRATION OVER THE IMPEDANCE SHEET	
1.01541D-04 W/M**3	1.14840185D-8 WATTS

AVG AND TOTAL ABSORBED POWER BY A POYNTING VECTOR ANALYSIS	
1.01541D-04 W/M**3	1.14840185D-8 WATTS

7. CONCLUSIONS

Primary applications include the design of particles or structures with prescribed absorption and scattering cross sections, estimation of the internal energies and temperatures stimulated in the layers comprising our spherical structure or on the lossy impedance sheets separating these layers, and computation of bistatic radar cross sections of these structures. We could conceivably design a particle that would absorb most of the radiation of a given frequency and by embedding these spherical particles in a penetrable layer with a density that increased with depth design a selectively absorptive coating. One could through the use of power density distribution curves and the use of spectral distributions of energy density within these structures quickly design a coating that would offer the maximum protection against electromagnetic pulses or would solve other electromagnetic compatibility problems. The power density distribution curves may help one treat cancer with microwaves. By proving that one could adjust the sources that a hot spot could be focused at a tumor location anywhere within the spherical structure, one could prove within this simulated biological structure that one could raise the temperature of the tumor about 4 degrees centigrade and kill the tumor without harming the nearby normal tissue. This would provide encouragement for the general research problem in the more complex clinical problem of a real patient with a real tumor. Another possibility is the use of the sphere program which, because the solution is exact, and because the computing cost and time is so low that the program could be used effectively on a personal computer, one could design eye protective equipment to protect people from laser beams while permitting them to see with other parts of the visual spectrum. This could be done by designing a multilayer structure that is reflective or absorptive to the frequencies of laser which represents a potential threat to the eyes but which permits certain light frequencies to pass unhindered through the coating so that the individual wearing the protective device could still see.

Another use of the program would be to design coatings for metallic structures that would have prescribed absorption and scattering properties and to in general benchmark computer codes, such as integral equation solvers, by comparing the answers they get for complex spherical structures with those obtained by our exact solution. Figure 1 shows the power density distribution across the z-axis of a perfectly conducting sphere coated with an anisotropic layer, where the radiation is traveling from the negative z-axis toward the positive z-axis so that the illuminated side of the sphere is at $z = -3$. A typical calculation is the bistatic radar cross section computation which can be verified by measurement in an anechoic chamber. Figure 2 shows the bistatic radar cross section of the coated sphere related to Figure 1; this coating is magnetically lossy, and is itself covered by an impedance sheet.

Bistatic radar cross sections are defined in Ruck et al ([24], p 9) and in van de Hulst ([32], p 285) by the formula

$$\sigma = 4\pi^2 \frac{|\mathbf{E}^s|^2}{|\mathbf{E}^i|^2} \quad (7.1)$$

where r is the distance from the center of the sphere to the point where the calculation was carried out. In my bistatic cross section subroutine I simply made sure I was far enough away from the sphere that the expression σ was independent of r . While the program would have run faster if I used asymptotic expressions, this permitted me to track the cross section measurements as a function of r . What is usually plotted is 10 times the logarithm to the base 10 of σ divided by πa^2 as a function of the bistatic angle.

Comparisons were made with bistatic cross section data for spheres which can be found in van de Hulst ([32], pages 152 and 153) for penetrable non lossy spheres and in Ruck ([24], page 152). My calculations, not repeated here, were in agreement with these results although I made some improvement in the detail of these 1948 computations (van de Hulst [32], page 152, the figure legend).

Human tissue is anisotropic and may have absorption properties which would be of concern to bioelectromagneticists. Figure three shows the infinite spike in the power density distribution curve in the center of an anisotropic single layer structure whose radial permittivity exceeds the tangential permittivity. The structure is nonmagnetic, as is human tissue, and has a conductivity of .5 mhos per meter. There is no impedance sheet covering the structure. Note the high power density distribution near the center of the structure; if a cancerous tumor were located near this hot spot, we could probably destroy the cancer without harming the normal tissue excessively by raising it to a temperature of 4 degrees centigrade above the ambient temperature. The bistatic radar cross section, shown in Figure 4, while having an interesting structure does not appear at first glance to contain enough information by itself to enable an experimentalist to discern that he was working with an anisotropic structure. A more sensitive prober of the anisotropies of a penetrable structure than the bistatic cross section would probably have to be developed.

The program is also effective in treating very large anisotropic structures. In Figure 5 we see a power density distribution plot of a 1 meter diameter structure consisting of an isotropic .1 meter radius core with a radial and tangential permittivity of 50 surrounded by an anisotropic coating that is .4 meters thick and having a radial permittivity of 60 and a tangential permittivity of 40. Both structures had were nonmagnetic and had a conductivity of .5 mhos per meter. Figure 6 gives the bistatic radar cross section of this structure. The bistatic radar cross section appears to be very sensitive to the conductivity of the object. When I dropped the conductivity to .05 mhos per meter, the bistatic radar cross section developed much more structure. The latter is shown in Figure 7.

The code for computing both internal and external fields associated with the scattering of electromagnetic radiation by a multilayer anisotropic spherical structure with the inner core being either perfectly conducting or penetrable and with the possibility that the layers may be separated by impedance sheets appears to have many potential applications. The concept of charge sheets, for example, in view of the fact that my computations show that these structures have an extremely low absorption of energy may be useful in the design of a type of energy shield to protect structures from laser beams.

Another application would be particle design. The design structure proposed here could be used with cylinder or sphere scattering. The basic idea is to consider an objective function such as the absorption cross section or the scattering cross section and regard this objective function, which may itself be a prescribed function of the frequency of the incoming radiation and not just a single number, and consider it to be a function of layer thickness, tensor permittivity, tensor magnetic permeability, and tensor electric field conductivity. We would make the problem equivalent to minimizing a function of a real variable defined on a finite dimensional vector space by taking as the function to be minimized, the square of the difference between idealized values of the absorption or scattering cross section and the values calculated by the computer program at a finite number of frequencies.

We then would use the same operations research methods used to find submarines or lost transmitting objects such as a child lost in a foggy marsh by using gradient search to go in the direction of increasing sound or in this case a decreasing difference between calculated and desired properties of an objective function. We consider a .5 micron sphere subjected to 60,000,000 Megahertz radiation having an electric field strength of 1 Volt per meter, a relative electric permittivity with a real part equal to 50, a relative magnetic permeability of 1, zero conductivity and allow the imaginary part of the relative permittivity to move up from 0, then since when the imaginary part of permittivity is zero, there is zero absorption, and since as the imaginary part of the permittivity goes to infinity, there is also zero absorption as the energy would have zero penetration, there must then be some intermediate value at which the absorption would be a maximum. Figure 8 is a plot of absorbed energy as a function of the imaginary part of the permittivity and shows this feature. In our particle the maximum occurs when the imaginary part of the relative permittivity is slightly less than 1. Since there is scattering even when there is zero absorption, the scattering curve is more subtle. However, when the imaginary part of the permittivity goes to infinity, all radiation is scattered away so there must also be a minimum of the scattered radiation. This is shown in Figure 9.

The notion of minimization goes back to the basic mathematical concept of a lower semicontinuous function on a compact set, in this case the allowable or physically reasonable values of the design parameters, having a maximum. If the function on the compact set is continuous, then the function achieves both its maximum and minimum value. One way to think about this problem is to invert a highly nonlinear system of equations. By this I mean that if our objective were in fact realized by some choice of parameters, could we then from the objective function recover the parameters which produced it. Furthermore, given this could we get as close as we desire to a possibly nonrealizable objective function by being able to invert this transformation. If the functions being considered in a particle or coating design are smooth, we could use the concept of slack variables. For example if we wanted to describe the set

$$x^2 + y^2 < R^2$$

we could introduce the slack variable z and write it as

$$R^2 - (x^2 + y^2) = s^2$$

We note that the set of points P in the subset of n dimensional space defined by

$$g(Q) = 0$$

and at which a function f(Q) is locally a maximum or a minimum is among the critical points of the transformation T from n dimensional space into 2 dimensional space defined by

$$(u,v) = (f(Q),g(Q))$$

or precisely those points Q for which the 2 by n matrix whose first row consists of the first partial derivatives of f with respect to its n independent variables and whose second row consists of the first partial derivatives of g with respect to its independent variables has rank strictly less than 2. This means that if you pick any two columns out of this transformation differential matrix and form a two by two matrix, then this 2 by 2 matrix has a zero determinant. Finding these critical points and analyzing them will give a complete resolution of the smoke particle design problem. A computer program implementing this algorithm is available to the Chemical Research Development and Engineering Center of Aberdeen Proving Ground, Maryland(E. W. Stuebing, Private Communication). A more recent program to carry out unconstrained minimization of a function of several variables makes use of the Levenberg-Marquardt algorithm that was modified by Argonne National Laboratory and is available through the repository at the Naval Surface Weapons Center to government agencies. The conjugate gradient method or the method of steepest descent can be used to find the local minimums of a function of several variables, which in the case of a design problem with our sphere code or a code to describe scattering by a multilayer anisotropic cylinder which can be developed in a similar manner would be the impedance sheet properties, tensor electric and magnetic properties within a layer and layer thicknesses. The low central processing unit time required by the computer program described in this paper makes this type of design calculation practical.

8. REFERENCES

1. Bell, E. L., D. K. Cohoon, and J. W. Penn. Electromagnetic energy deposition in a concentric spherical model of the human or animal head. SAM-TR-79-6. Brooks AFB, Tx 78235: USAF School of Aerospace Medicine (December, 1979)
2. Cohoon, D. K., J. W. Penn, E. L. Bell, D. R. Lyons, and A. G. Cryer. A computer model predicting the thermal response to microwave radiation. SAM-TR-82-22. Brooks AFB, Tx 78235: USAF School of Aerospace Medicine (December, 1982)
3. Cohoon, D. K. An exact formula for the accuracy of a class of computer solutions of integral equation formulations of electromagnetic scattering problems (to appear in *Electromagnetics*)
4. Cosenza, M, L. Herrera, M. Esculpi, and L. Witten. Evolution of radiating anisotropic spheres in general relativity. *Physical Review D* Volume 25 Number 10 (May 15, 1982) pp 2527-2535.
5. Consenza, M., L. Herrera, M. Esculpi, and L. Witten. Some models of anisotropic spheres in general relativity. *Journal of Mathematical Physics* 22 (1) (January, 1981) pp 118-125.
6. Fymat, Alain L. Radiative properties of optically anisotropic spheres and their climatic implications. *Journal of the Optical Society of America*. Volume 72, Number 10 (October, 1982) pp 1307-1310.
7. Geim, A. K., V. T. Petrashov, and A. A. Svintsov. Helicon resonances in an anisotropic sphere. *Soviet Technical Physics Letters* 12 (7) (July, 1986) pp 361-362.
8. Graglia, R. D. and P. L. E. Uslenghi. Electromagnetic scattering from anisotropic materials, Part I General Theory. *IEEE Transactions on Antennas and Propagation* Volume AP-32 No. 8 (August, 1984) pp 867-869.
9. Greenberg, J. M., A. C. Lind, R. T. Wang, and L. F. Libelo IN Kerker, M. (Ed.) *Interdisciplinary Conference on Electromagnetic Scattering*. London: Pergamon Press (1963) p 123.
10. Herrera, L. and J. Ponce de Leon. Anisotropic spheres admitting a one parameter group of conformal motions. *Journal of Mathematical Physics* 26 (8) (August, 1985) pp 2018-2023.
11. Herrera, L., G. J. Ruggeri, and L. Witten. Adiabatic Contraction of Anisotropic Spheres in General Relativity. *The Astrophysical Journal* 234 (December 15, 1979) pp 1094-1099.
12. Holoubek, J. A Simple Representation of Small Angle Light Scattering from an Anisotropic Sphere. *Journal of Polymer Science Part A-2* Volume 10 (1972) pp 1461-1465.
13. Holoubek, J. Small Angle Scattering of Circularly Polarized Light from an Anisotropic Sphere. *Journal of Polymer Science* Volume 11 (1973) pp 683-691.
14. Hovhannessian, S. S. and V. A. Baregamian. The Diffraction of a Plane Electromagnetic Wave on an Anisotropic Sphere. *Izdatelstva Akad. Nauk of Armenia S. S. R. Physics* 16 (1981) pp 37-43
15. Ibanez, J. M. Collapse of Anisotropic Spheres in General Relativity: An Analytical Model. *The Astrophysical Journal*

- 284 (September 1, 1984) pp 381-383.
16. Kanoria, Mridula. Forced vibration of a non-homogeneous anisotropic sphere or cylinder having a rigid inclusion. *Indian Journal of Theoretical Physics* Volume 31 No. 2 (June, 1983) pp 55-64.
 17. Kong, A. Electromagnetic Fields Due to Dipole Antennas over Stratified Anisotropic Media. *Geophysics* Volume 37 Number 6 (December, 1972) pp 985-996.
 18. Kong, Jin Au. *Electromagnetic Wave Theory*. New York: John Wiley (1986)
 19. Leon, J. Ponce de. New Analytical Models for Anisotropic Spheres in General Relativity. *Journal of Mathematical Physics* Volume 28 No. 5 (May, 1987) pp 1114-1117.
 20. Markiewicz, R. S. Alfvén Wave Oscillations in a Sphere, with Applications to Electron Hole Drops in Ge. *Physical Review B* Volume 18, Number 8 (October 15, 1978)
 21. Meeten, G. H. The Birefringence of Colloidal Dispersions in the Rayleigh and Anomalous Diffraction Approximations. *Journal of Colloid and Interface Science* Volume 73 Number 1 (January, 1980) pp 38-44
 22. Mochida, Isao, Keiko Maeda, and Kenjiro Takeshita. Structure of Anisotropic Spheres Obtained in the Course of Needle Coke Formation. *Carbon*. Volume 15 (1977) pp 17-23.
 23. Lacheisserie, Etienne de. Magnetisme. Effet de forme non uniforme en magnetostriction. *C. R. Acad. Sc. Paris t. 268* (June 30, 1969) pp 1696-1699. Transmitted by M. Louis Neel.
 24. Ruck, George T., Donald E. Farrick, William D. Stuart, and Clarence K. Krichbaum. *Radar Cross Section Handbook*. Volume 1 New York: Plenum Press (1970)
 25. Sanchez, Richard. Integral Form of the Equation of Transfer for a Homogeneous Sphere with Linearly Anisotropic Scattering. *Transport Theory and Statistical Physics* 15 (3) (1986) pp 333-343.
 26. Sheehan, J. P. and L. Debnath. Forced Vibrations of an Anisotropic Elastic Sphere. *Archives of Mechanics* 24 (1972) pp 117-125.
 27. Stein, Richard S. and Marion B. Rhodes. Photographic Light Scattering by Polyethylene Films. *Journal of Applied Physics*. Volume 31, Number 11 (November, 1960) pp 1873-1884.
 28. Stein, Richard S. and Robert Prud'homme. Origin of Polyethylene Transparency. *Polymer Letters* Volume 9 (1971) pp 595-598.
 29. Stevens, G. L. Radiative Transfer on a Linear Lattice: Application to Anisotropic Crystal Clouds. *Journal of Atmospheric Science* 37 (1980) pp 2095-2104.
 30. Stewart, B. W. Conformally Flat Anisotropic Spheres in General Relativity. *J. Physics A. Math. Gen.* 15 (1982) pp 2419-2427.
 31. Treves, F. *Linear Partial Differential Equations with Constant Coefficients*. New York: Gordon and Breach (1966).
 32. Van de Hulst, H. C. *Light Scattering by Small Particles*. New York: Dover Publications (1981).
 33. Wang, R. T. and J. M. Greenberg. Scattering by Spheres with nonisotropic refractive indices. *Applied Optics* 15 (1976) p 1212.
 34. Wolff, Ingo. A Generalized Description of the Spherical Three Layer Resonator with an Anisotropic Dielectric Material. *IEEE MTT-S Digest* (1987) pp 307-310.

Blank

LIGHT SCATTERING BY ORIENTED AND RANDOMLY DISPERSED

CHIRAL PARTICLES

Shermila Brito Singham
Life Sciences Division, Los Alamos National Laboratory,
Los Alamos, New Mexico 87545.

RECENT PUBLICATIONS AND SUBMITTALS FOR PUBLICATION:

- A) S.B. Singham and G.C. Salzman, "Evaluation of the Scattering Matrix of an Arbitrary Particle using the Coupled Dipole Approximation", J. Chem. Phys. 84, 2658-2667 (1986).
- B) S.B. Singham, C.W. Patterson and G.C. Salzman, "Polarizabilities for Light Scattering from Chiral Particles", J. Chem. Phys. 85, 763-770 (1986).
- C) M.K. Singham, S.B. Singham and G.C. Salzman, "The Scattering Matrix for Randomly Oriented Particles", J. Chem. Phys. 85, 3807-3815 (1986).
- D) S.B. Singham, "Intrinsic Optical Activity in Light Scattering from an Arbitrary Particle", Chem. Phys. Lett. 130, 139-144 (1986).
- E) S.B. Singham and C.F. Bohren, "Light Scattering by an Arbitrary Particle: a Physical Reformulation of the Coupled Dipole Method", Opt. Lett. 12, 10-12 (1987).
- F) S.B. Singham, "Form and Intrinsic Optical Activity in Light Scattering by Chiral Particles", J. Chem. Phys. 87, 1873-1881 (1987).
- G) S.B. Singham, "Coupled Dipoles in Light Scattering by Randomly Oriented Chiral Particles", submitted to J. Chem. Phys.

Abstract

The use of coupled dipoles in modelling light scattering by oriented and randomly dispersed chiral particles is examined in this paper. The chirality considered here is form chirality which results from macroscopic structural mirror asymmetry in the particle. For a chiral particle described by spherical dipoles, it is shown that large magnitude terms that contribute the chiral matrix elements of an oriented particle do not contribute at all in the orientation average. This result will be used in future work to obtain a more efficient method of evaluating light scattering by randomly dispersed chiral particles.

The coupled dipole method¹ is known to be a good approximate technique for evaluating light scattering by arbitrarily shaped particles. In this method, an arbitrary particle is subdivided into units where each unit is small compared with the wavelength of light. Each unit is then assumed to behave like a spherical dipolar oscillator with its polarizability specified

by its dimension and the bulk dielectric constant of the particle. The fields at the dipoles are determined by the incident field and interactions among all the dipoles in the collection. These resultant fields are obtained by solving, self-consistently, a set of linear, coupled equations and retardation effects are taken fully into account. The scattered field at the detector is then evaluated by summing the fields scattered by the dipolar oscillators.

For a set of N optically inactive dipoles, the field \underline{E}_i at an oscillator i is determined by the incident field ($\underline{E}^0 e^{i\mathbf{k}\cdot\underline{r}_i}$) as well as by the scattered fields from the other dipolar oscillators, i.e.,

$$\underline{E}_i = \underline{E}^0 e^{i\mathbf{k}\cdot\underline{r}_i} + \sum_{j \neq i}^N [a_{ij} \hat{\alpha}_j \underline{E}_j + b_{ij} (\hat{\alpha}_j \underline{E}_j \cdot \underline{n}_{ji}) \underline{n}_{ji}] \quad (1)$$

$$\text{where } a_{ij} = \frac{e^{i\mathbf{k}\cdot\underline{r}_{ij}}}{r_{ij}} \left(k^2 \cdot \frac{1}{r_{ij}^2} + \frac{i\mathbf{k}}{r_{ij}} \right)$$

$$\text{and } b_{ij} = \frac{e^{i\mathbf{k}\cdot\underline{r}_{ij}}}{r_{ij}} \left(\frac{3}{r_{ij}^2} - k^2 - \frac{3i\mathbf{k}}{r_{ij}} \right)$$

k is the wavenumber of the radiation, r_{ij} is the distance and \underline{n}_{ji} the unit vector from j to i . The explicit time dependence of the fields is omitted and only elastic light scattering is considered. Retardation effects are completely accounted for in this model. The electric dipole moment is given by $\underline{p}_j = \hat{\alpha}_j \underline{E}_j$, where \underline{E}_j is the field at the scattering center and $\hat{\alpha}_j$ is, in general, a complex polarizability tensor. If the dipolar units are taken to be spherical, the polarizability of each unit (α) is a scalar.

The scattered field at the detector (\underline{E}_d) is the sum of the amplitudes of the far-field contributions from the N spherical dipoles, i.e.,

$$\underline{E}_d = \frac{k^2 e^{i\mathbf{k}\cdot\underline{r}_d}}{r_d} (1 - \underline{n}_d \underline{n}_d) \alpha \sum_j^N e^{-i\mathbf{k}\cdot\underline{n}_d \cdot \underline{r}_j} \underline{E}_j \quad (2)$$

where r_d is the distance and \underline{n}_d the unit direction of the detector from the origin. The amplitude scattering matrix elements² of the particle can be

obtained by determining E_d for two orthogonal polarizations of the incident light. The incident light propagates in the positive z direction and the xz plane is chosen to be the scattering plane; the amplitude scattering matrix elements can be obtained from

$$\begin{aligned} S_1 &= C E_y^y, & S_2 &= C [E_x^x \cos \theta - E_z^x \sin \theta], \\ S_3 &= -C [E_x^y \cos \theta - E_z^y \sin \theta], & S_4 &= -C E_y^x \end{aligned} \quad (3)$$

where, $C = \frac{-ikr}{e^{ik(r-z)}}$, and θ is the scattering angle. The scattered field components of E_d along the x, y and z axes are specified by $E_{x,y,z}$ and the superscript refers to the incident light which is linearly polarized in the x or y directions.

The elements of the 4 x 4 scattering matrix² are obtained by linear combinations of products of the amplitude scattering matrix elements. The products

$$\begin{aligned} \text{Re} [(S_2 - S_1)(S_3^* - S_4^*)] &= S_{13} - S_{31} \\ \text{Im} [(S_2 - S_1)(S_3^* - S_4^*)] &= S_{24} + S_{42} \\ \text{Re} [(S_2 + S_1)(S_3^* - S_4^*)] &= S_{23} - S_{32} \\ \text{Im} [(S_2 + S_1)(S_3^* - S_4^*)] &= S_{14} + S_{41} \end{aligned} \quad (4)$$

contain only the 2 x 2 off-block-diagonal matrix elements which are sensitive to chirality and will be referred to as chiral matrix elements. For a collection of randomly oriented particles, these products become $2S_{13}(-2S_{31})$, $2S_{24}(-2S_{42})$, $2S_{23}(-2S_{32})$ and $2S_{14}(-2S_{41})$.²

We write equation (1) in the form

$$E_i = E_i^0 + \sum_{j \neq i} E_j^i + \sum_{\substack{jk \\ i \neq j \neq k}} E_{jk}^i + \sum_{\substack{jkl \\ i \neq j \neq k \neq l \\ j < k < l}} E_{jkl}^i + \dots \quad (5)$$

where E_i^0 is the incident field at dipole i ($= E^0 e^{ik \cdot r_i}$), E_j^i is the field at i due to interactions (to all orders) with only the jth dipole, E_{jk}^i is the

field at i due to interactions involving both the j^{th} and k^{th} dipoles and the other fields in the series are similarly defined. The summations are over the total number of dipoles, i.e., N . In this series, the field at a given dipole is determined by the incident field and the fields due to many center interactions with the other dipoles which are used to describe the particle. Equation (5) is a finite series in which the last term is a summation over the field at i due to interactions with the remaining $(N-1)$ dipoles. As the interactions are retained to all orders, equation (5) is simply equation (1) with the interaction fields specified in terms of the dipolar centers involved.

The scattered field at the detector can also be written in terms of a series over many center terms and the product $(S_2 - S_1)(S_3^* - S_4^*)$ can then be written as

$$\begin{aligned}
 (S_2 - S_1)(S_3^* - S_4^*) = k^6 a a^* [& \sum_{\substack{ijk \\ j \neq k}} E_j^i E_k^{jb} + \sum_{\substack{ijkl \\ j \neq k \neq l \\ k < l}} E_j^i E_{kl}^{jb} + \dots \\
 & + \sum_{\substack{ijkl \\ i \neq j \neq k \neq l}} E_j^{ia} E_l^{kb} + \sum_{\substack{ijklm \\ k \neq l \neq m \\ i \neq j \neq l < m}} E_j^{ia} E_{lm}^{kb} + \dots \\
 & + \sum_{\substack{ijklm \\ i \neq j \neq k \\ l \neq m \neq j < k}} E_{jk}^{ia} E_m^{lb} + \sum_{\substack{ijklmn \\ i \neq j \neq k \\ l \neq m \neq n \\ j < k \neq m < n}} E_{jk}^{ia} E_{mn}^{lb} + \dots] \quad (6)
 \end{aligned}$$

with $E^i = e^{-ik \rho_d \cdot \underline{r}_i} e^{ikz_i} (\cos \theta - 1)$

$$E_j^{ia} = e^{-ik \rho_d \cdot \underline{r}_i} \{ E_{jx}^{ix} \cos \theta - E_{jz}^{ix} \sin \theta - E_{jy}^{iy} \}$$

$$E_j^{ib} = e^{ik \rho_d \cdot \underline{r}_i} \{ -E_{jx}^{iy*} \cos \theta + E_{jz}^{iy*} \sin \theta + E_{jy}^{ix*} \} \quad (7)$$

and E_{jk}^{ia} , E_{jk}^{ib} , ... defined similarly. The other product $(S_2 + S_1)(S_3^* - S_4^*)$ is given by a similar series with a different linear combination for the E^i and E^{ia} terms, i.e.,

$$E^i = e^{-ik\Omega_d \cdot \mathbf{r}_i} e^{ikz_i} (\cos\theta + 1)$$

$$E_j^{ia} = e^{-ik\Omega_d \cdot \mathbf{r}_i} [E_{jx}^{ix} \cos\theta - E_{jz}^{ix} \sin\theta + E_{jy}^{iy}] \quad (8)$$

and so on.

For a collection of randomly oriented particles, the orientation averages of the products $(S_2 - S_1)(S_3^* - S_4^*)$ and $(S_2 + S_1)(S_3^* - S_4^*)$ are required. These averages are zero unless the particle is chiral. The orientation averages are obtained by numerically summing the magnitudes of the products over a large number of orientations until convergence is reached or, equivalently, by using an analytic averaging method.

The orientation average of $(S_2 - S_1)(S_3^* - S_4^*)$ can also be obtained from the sum of the orientation averages of the field products in the series given in equation (6). That is, the average can be obtained by summing the integrals over all space of each of the field products $E^i E_k^{jb}$, $E^i E_{kl}^{jb}$, etc., in equation (6). Some of these field products become identically zero when integrated over all space. This is found to be the case for those products which derive from dipolar centers which do not form a chiral structure.

The first term in the series in equation (6), $E^i E_k^{jb}$, is derived from fields involving at most three dipolar centers. For a given orientation of the structure described by the three dipoles, its mirror image in the scattering plane exists if all possible orientations of the particle are allowed, i.e., the particle can be rotated to another orientation such that the three dipoles now form the mirror image of the original three dipole structure. This is always possible when the subunits are not optically active. The y coordinates of the three dipoles change sign while the x and z coordinates are unchanged in the mirror image in the scattering plane (xz). The term $e^{-ik\Omega_d \cdot \mathbf{r}_i}$ is unchanged on reflection in the scattering plane because Ω_d lies in this plane; E^i is then the same for the original and reflected

structures. The field E_j^{ia} is also unchanged on reflection in the scattering plane because E_{jx}^{ix} , E_{jz}^{ix} and E_{jy}^{iy} are unaffected on changing the sign of the y axis. However, E_j^{ib} changes sign on reflection because E_{jx}^{iy} , E_{jz}^{iy} and E_{jy}^{ix} change sign with reflection of i,j,k in the xz plane. The product $E_k^i E_k^{jb}$ then has opposite signs for a pair of mirror symmetric structures and goes to zero when it is averaged over all space because the mirror symmetric pair exists in the orientation average.

The products $E_k^i E_k^{jb}$ and $E_j^{ia} E_i^{kb}$ involve two, three or four dipolar centers. The terms involving two or three dipolar centers will again average to zero because the mirror images of the structures in the scattering plane exist in the orientation average. The products involving four dipolar centers will also average to zero if the four dipoles do not form a chiral structure. However, if the four dipoles do form a chiral arrangement, the mirror image of the structure is not present in the orientation average and the field products will be non-zero when averaged over all space. For the same reasons, all other field products in the series described in equation (6) will also average to zero unless the dipolar centers involved in the products form a chiral structure. The same result is true for $(S_2 + S_1)(S_3^* - S_4^*)$ because the same symmetry considerations hold and the only difference is that E^i and the E^{ia} terms are different linear combinations from those in $(S_2 - S_1)(S_3^* - S_4^*)$.

The large difference in the magnitudes of the 2 x 2 off-block-diagonal matrix elements for oriented and orientationally averaged chiral structures is now evident. Many of the field products which contribute to the matrix elements of the oriented structure, do not contribute at all in the orientation average. In particular, the leading term in the series given in equation (6) is of large magnitude and expected to be a major component of the 2 x 2 off-block-diagonal matrix elements of oriented particles and this term

$$\begin{aligned}
 E^i &= e^{-ik\mathbf{n}_d \cdot \mathbf{r}_i} e^{ikz_i} (\cos\theta + 1) \\
 E_j^{ia} &= e^{-ik\mathbf{n}_d \cdot \mathbf{r}_i} [E_{jx}^{ix} \cos\theta - E_{jz}^{ix} \sin\theta + E_{jy}^{iy}]
 \end{aligned} \tag{8}$$

and so on.

For a collection of randomly oriented particles, the orientation averages of the products $(S_2 - S_1)(S_3^* - S_4^*)$ and $(S_2 + S_1)(S_3^* - S_4^*)$ are required. These averages are zero unless the particle is chiral. The orientation averages are obtained by numerically summing the magnitudes of the products over a large number of orientations until convergence is reached or, equivalently, by using an analytic averaging method.

The orientation average of $(S_2 - S_1)(S_3^* - S_4^*)$ can also be obtained from the sum of the orientation averages of the field products in the series given in equation (6). That is, the average can be obtained by summing the integrals over all space of each of the field products $E_k^{i,jb}$, $E_{kl}^{i,jb}$, etc., in equation (6). Some of these field products become identically zero when integrated over all space. This is found to be the case for those products which derive from dipolar centers which do not form a chiral structure.

The first term in the series in equation (6), $E_k^{i,jb}$, is derived from fields involving at most three dipolar centers. For a given orientation of the structure described by the three dipoles, its mirror image in the scattering plane exists if all possible orientations of the particle are allowed, i.e., the particle can be rotated to another orientation such that the three dipoles now form the mirror image of the original three dipole structure. This is always possible when the subunits are not optically active. The y coordinates of the three dipoles change sign while the x and z coordinates are unchanged in the mirror image in the scattering plane (xz). The term $e^{-ik\mathbf{n}_d \cdot \mathbf{r}_i}$ is unchanged on reflection in the scattering plane because \mathbf{n}_d lies in this plane: E^i is then the same for the original and reflected

goes to zero in the orientation average.

In order to illustrate this difference in oriented and orientationally averaged scattering, we describe a model calculation for a simple chiral structure. Four spherical dipoles which form a chiral structure are chosen as a model and the dipoles form one third of a turn of a helix with a radius of 100 nm and a pitch of 200 nm. The (x,y,z) coordinates of the four dipoles in the oriented structure are (100, 0, 0), (86.6, 50, 16.67), (50, 86.6, 33.33) and (0, 100, 50) and the polarizability of each dipole is $3 \times 10^3 \text{ nm}^3$. The incident light has a wavelength of 600 nm and is propagating along the positive z direction.

The fields corresponding to interactions among specific dipolar centers were evaluated by obtaining the self-consistently coupled fields for each group of dipoles. Thus, the field at dipole i due to j was obtained by evaluating the final field at i in the 'particle' described by i and j and subtracting the incident field at i (i.e., E_i^0). In a similar manner, the field at i due to all interactions with j and k was obtained by finding the final field at i from the self-consistent solution for interactions with j and k and subtracting the incident field at i and the fields at i due to two center interactions with j and two center interactions with k. The fields due to four center interactions were obtained similarly.

Figures 1 and 2 show the angular distributions of the real and imaginary parts of $(S_2 \pm S_1)(S_3^* - S_4^*)$ for the oriented particle composed of four spherical dipolar units. The solid lines are the total calculated values of the chiral matrix elements while the dashed lines are two and three center field products and the chain-dashed lines are the four center field products. From the results, it is evident that the two and three center field products dominate and that the four center terms are an extremely small component at

most angles of the angular distributions for the oriented particle.

The cancellation of the field products that do not contribute to the orientation averages of the chiral matrix elements is a source of the slow convergence that has been observed for these elements when calculated by summing the magnitudes over a large number of orientations. The chiral matrix elements when calculated this way are contained as small differences between large magnitude field products. When the orientation averages of the chiral matrix elements for a simple model were calculated using only the field products that survive the averaging, convergence was rapidly achieved. If this feature, i.e., retention of only the field products that contribute to the average, can be efficiently incorporated into an orientation averaging method for arbitrarily shaped chiral particles, it is probable that the computational difficulties in calculating the chiral matrix elements will be significantly improved.

References

1. E.M. Purcell and C.R. Pennypacker, *Astrophys. J.* **186**, 705 (1973).
2. C.F. Bohren and D.R. Huffman, *Absorption and Scattering of Light by Small Particles* (Wiley, New York, 1983).

Acknowledgements

I am grateful to Dr. Gary Salzman for his encouragement and interest in this work. This work was performed under the auspices of the US Department of Energy and supported in part by the US Army CRDEC.

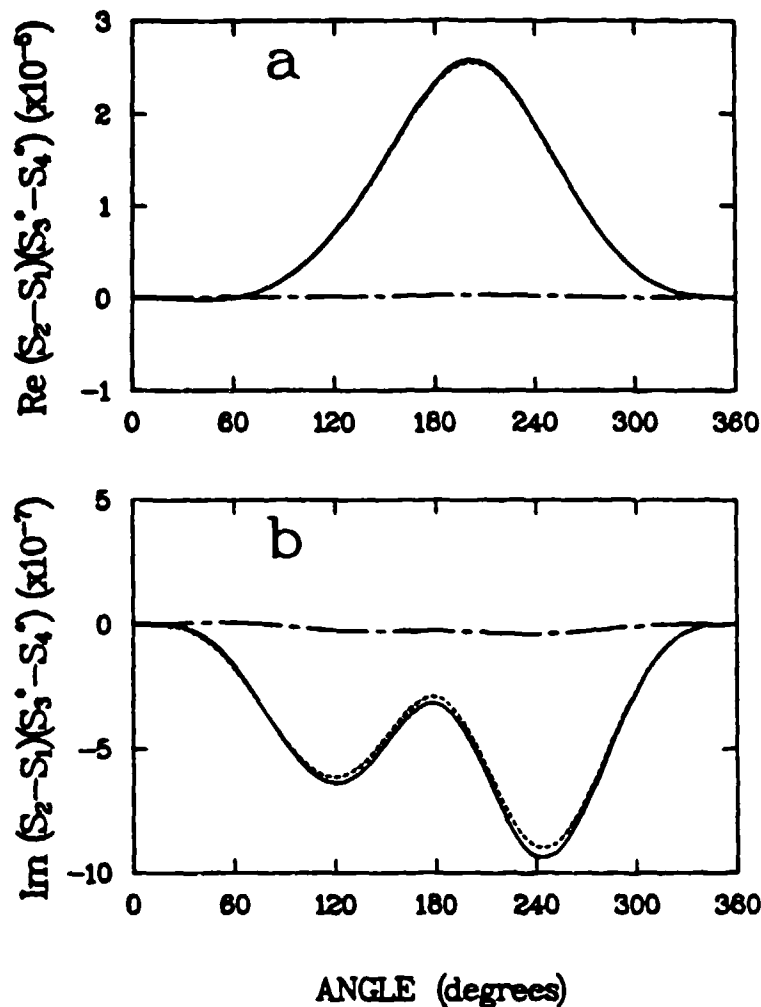


Figure 1.

Angular distributions of two chiral matrix elements of a helical structure. A third of a turn of a helix with a radius of 100 nm and a pitch of 200 nm is modelled by four spherical dipoles each with a polarizability of $3 \times 10^3 \text{ nm}^3$. The incident light is in the z direction and has a wavelength of 600 nm. The xz plane is the scattering plane. (a) Solid line - angular distribution of the real part of $(S_2 - S_1)(S_3^* - S_4^*)$ for the oriented particle. Dashed line - two and three center field products. Chain-dashed line - four center products. (b) Solid line - angular distribution of the imaginary part of $(S_2 - S_1)(S_3^* - S_4^*)$ for the oriented particle. Dashed line - two and three center field products. Chain-dashed line - four center field products.

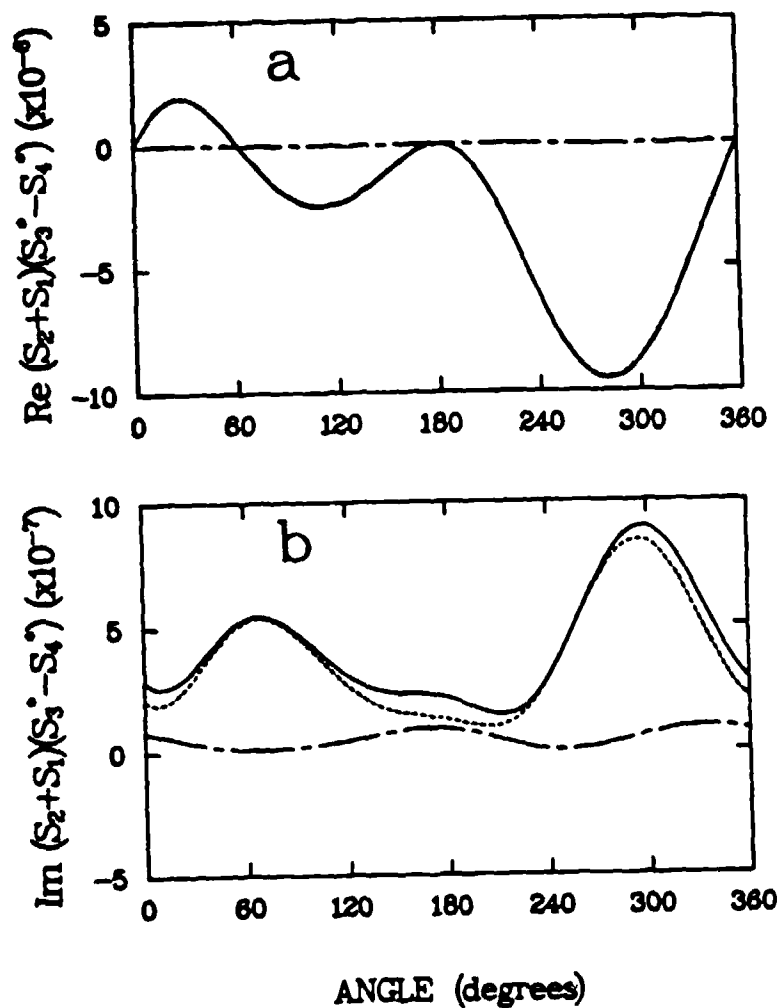


Figure 2.

Two chiral matrix elements for the helical particle described in the caption for Figure 1. (a) Solid line - angular distribution of the real part of $(S_2 + S_1)(S_3^* - S_4^*)$ for the oriented particle. Dashed line - two and three center field products. Chain-dashed line - four center field products. (b) Solid line - angular distribution of the imaginary part of $(S_2 + S_1)(S_3^* - S_4^*)$ for the oriented particle. Dashed line - two and three center field products. Chain-dashed line - four center field products.

EXPERIMENTAL TEST OF A TIME-DEPENDENT INVERSE SCATTERING ALGORITHM

R. A. ELLIOTT

DEPARTMENT OF APPLIED PHYSICS AND ELECTRICAL ENGINEERING
OREGON GRADUATE CENTER
19600 N.W. VON NEUMANN DRIVE
BEAVERTON, OREGON 97006-1999

AND

T. DURACZ AND N.J. MCCORMICK

DEPARTMENT OF NUCLEAR ENGINEERING
UNIVERSITY OF WASHINGTON
SEATTLE, WASHINGTON 98195

RECENT PUBLICATIONS AND SUBMITTALS:

A) R.A. Elliott, T. Duracz, N.J. McCormick and D.R. Emmons, "Experimental Test of a Time-Dependent Inverse Radiative Transfer Algorithm for Estimating Scattering Parameters," J. Opt. Soc. Am. A (to be published).

B) T. Duracz and N.J. McCormick, "Numerical Study of the Time-Dependent Radiative Transfer Inverse Problem," J. Opt. Soc. Am. A, 4 (October 1987).

ABSTRACT

Experimental and numerical simulation tests have been performed on an inverse radiative transfer algorithm designed to estimate the Legendre moments of the single scatter phase function. Measurements of the time-resolved backscattered radiance from a plane geometry "semi-infinite" medium consisting of suspensions of nonabsorbing or weakly absorbing spheres were used in the inversion algorithm. It has proven possible, even in the presence of experimental noise, to estimate the single scatter albedo with a relative error of < 1%. Estimates of the asymmetry factor have been found to be less accurate (< 12%), and estimating higher moments appears to be impractical. Similar experiments on more highly absorbing spheres are planned.

INTRODUCTION

The general objective of this research program is to infer the fraction of energy absorption and the angular scattering pattern for a multiple scattering (optically very thick) target illuminated by a pulsed laser. The algorithm used is based on the radiative transfer equation and requires only the backscattered radiance at asymptotically long times, i.e., many collision times after the pulse. Potential applications of this work include the ability to remotely determine the scattering properties of aerosols, clouds, and smokes so that the

effects of multiple scattering on the operation of optical systems in a low visibility atmosphere can be predicted. The specific objectives of the project are to estimate the albedo of single scattering f_0 and as many of the coefficients f_n , $n \geq 1$, as possible of a Legendre polynomial expansion of the angle-dependent single-interaction scattering function

$$p(\Omega' \cdot \Omega) = (4\pi)^{-1} \sum_{n=0}^{\infty} f_n P_n(\Omega' \cdot \Omega). \quad (1)$$

The albedo, f_0 , and the asymmetry factor, $g = f_1/f_0$, are of special interest.

THE INVERSION ALGORITHM

The time-dependent inverse radiative transfer algorithm¹⁻⁴ is based on the use of Fourier azimuthal moments $B^m(\mu, t)$ of the radiance backscattered from a plane geometry semi-infinite medium. These moments are calculated from the surface backscattered radiance $B(\mu, \phi, t)$ using

$$B^m(\mu, t) = [\pi(1 + \delta_{m0})]^{-1} \int_0^{2\pi} d\phi B(\mu, \phi, t) \cos m\phi, \quad (2)$$

where μ is the cosine of the polar angle measured from the outward surface normal and ϕ is the azimuthal angle in the plane of the surface, as measured from the direction opposite to the incident illumination. Long after the incident pulse centered about time $t = 0$, the Fourier backscatter moments asymptotically decay according to

$$B^m(\mu, t) \cong C^m(\mu) t^{-\frac{1}{2}} \exp[-v(1 - f_m)t], \quad (3)$$

where v is the inverse of the mean time between photon collisions with the scattering centers.

Although the f_m can be extracted from Eq. (3) by differentiation of the data in the asymptotic regime,^{2,3} a least squares curve fitting procedure is preferable for experimental data. In this procedure, the coefficients can be estimated using the equation⁴

$$v(1 - f_m) = \frac{\langle t \rangle \langle \ln[t^{\frac{1}{2}} B^m(\mu, t)] \rangle - \langle t \ln[t^{\frac{1}{2}} B^m(\mu, t)] \rangle}{\langle t^2 \rangle - \langle t \rangle^2}, \quad (4)$$

where $\langle f(t) \rangle$ is the average of N values of $f(t)$ for N time points t_i , $i = 1$ to N , if a linear logarithmic curve fitting is used. An exact exponential curve fitting is employed in this paper for which the value given by Eq. (4) has been shown to be a good approximation.⁴

THE EXPERIMENT

An experimental setup designed to validate the inversion algorithm is illustrated in Fig. 1. A frequency doubled, passively mode-locked, Nd:YAG laser is used to produce 532 nm light pulses of about 35 psec duration and 50 μ J energy. A $\lambda/4$ waveplate converts the linearly polarized laser beam to circular polarization and the beam is expanded to 3.1 cm

diameter (e^{-1} intensity) by lenses $L1$ and $L2$ before being directed into the scattering cell at an angle θ_0 to the normal to the entrance window. The scattering cell, a 15 cm diameter by 15 cm blackened glass cylinder with an AR coated window on one end and a black anodized aluminum plate on the other, is intended to simulate a semi-infinite medium. The mirrors $M1$ and $M2$, aperture, and lens $L3$ collect the light scattering in the direction (θ, ϕ) and direct it to the streak camera which records the temporal variation of the backscattered radiance with a time resolution of less than 20 psec. The azimuthal angle, ϕ , can be varied throughout the range 0° to 360° , 0° being in the forward direction of the incident beam. Beam splitters and a variable delay line are used to obtain a reference light pulse needed for precise time registry and amplitude normalization. Figure 2 is a typical example of an intensity vs time record constructed from the digitized data provided by the streak camera. The record shows the reference pulse on the left and the backscattered radiance on the right. The unit of time is a "channel," i.e., the streak camera sampling interval; each channel has a width of 4.31 psec at the sweep speed used throughout these experiments.

Scattering experiments have been performed on systems of both nonabsorbing latex spheres and weakly absorbing polymer dynospheres as detailed in Table I. The time resolved backscattered radiance was measured for azimuthal angles of $\phi = 0^\circ, \pm 45^\circ, \pm 90^\circ$, and $\pm 135^\circ$ at a polar angle of 21° in water corresponding to 28° in air. The polar angle of the incident beam was fixed at 36° in water, corresponding to 52° in air.

An average of 10 individual pulses in each measurement direction was used to reduce the effects of random fluctuations in the experimental data. Additional measurements were made for all cases with the scattering cell replaced by a white plane paper card at the same location as the surface of the scattering medium in order to locate in time the incident pulses with respect to the backscattered radiance.

RESULTS OF THE EXPERIMENT

Data obtained from the experiments were processed to produce moments for $m = 0$ and $m = 1$. Figures 3 and 4 are typical examples of the time evolution of these moments. The moments were subsequently used in the inversion algorithm to give the results in Tables II and III.

CONCLUSIONS

The method offers a viable technique of determining the single scatter albedo, at least for weak absorbers, since even in the presence of experimental noise it was possible to determine its value with a relative error of less than 1%. However the degree of anisotropy of the scattering kernel can in most cases only be roughly estimated. For very small spheres (Case A), where the scattering is almost isotropic, no estimate could be made. For larger spheres with more anisotropic scattering, relative errors of 5% (Case B), 0.4% (Case C), and 12% (Case C*) were obtained.

ACKNOWLEDGMENT

This work was supported by the U.S. Army Research Office and the San Diego Supercomputer Center.

REFERENCES

1. N.J. McCormick, "Remote characterization of a thick slab target with a pulsed laser," *J. Opt. Soc. Am.* **72**, 756-759 (1982).
2. K.K. Hunt and N.J. McCormick, "Numerical test of an inverse method for estimating single-scattering parameters from pulsed multiple-scattering experiments," *J. Opt. Soc. Am. A* **2**, 1965-1971 (1985).
3. T. Duracz and N.J. McCormick, "Analytical error estimates for the time-dependent radiative transfer inverse problem," *J. Opt. Soc. Am. A* **3**, 1871-1875 (1986).
4. T. Duracz and N.J. McCormick, "Numerical study of the time-dependent radiative transfer inverse problem," *J. Opt. Soc. Am. A* **4**, (to be published).

TABLE I

TEST SCATTERING SYSTEMS

Case	Particle Type	Diameter	Scattering Length
A	latex sphere	0.091 μm	1.21 mm
B	latex sphere	0.482 μm	1.00 mm
C	dynosphere*	1.900 μm	0.92 mm

* polymer doped with Rhodamine B

TABLE II

ALBEDO, f_0

Case	Mie Calculation	Num. Simulation	Experiment
A	1.0000	1.0020	1.0025
B	1.0000	1.0085	0.9991
C	0.9993	**	0.9976
C*	0.9993	**	0.9949

* measurements made at 24 azimuthal angles

** not calculated

TABLE III

ASYMMETRY FACTOR, f_1

Case	Mie Calculation	Num. Simulation	Experiment
A	0.0889	0.1424	***
B	0.8497	0.8638	0.8923
C	0.8964	**	0.9002
C*	0.8964	**	0.7957

* measurements made at 24 azimuthal angles

** not calculated

*** not determined because no asymptotic region was found

FIGURE 1

OPTICAL SYSTEM FOR TIME RESOLVED
BACKSCATTER MEASUREMENTS

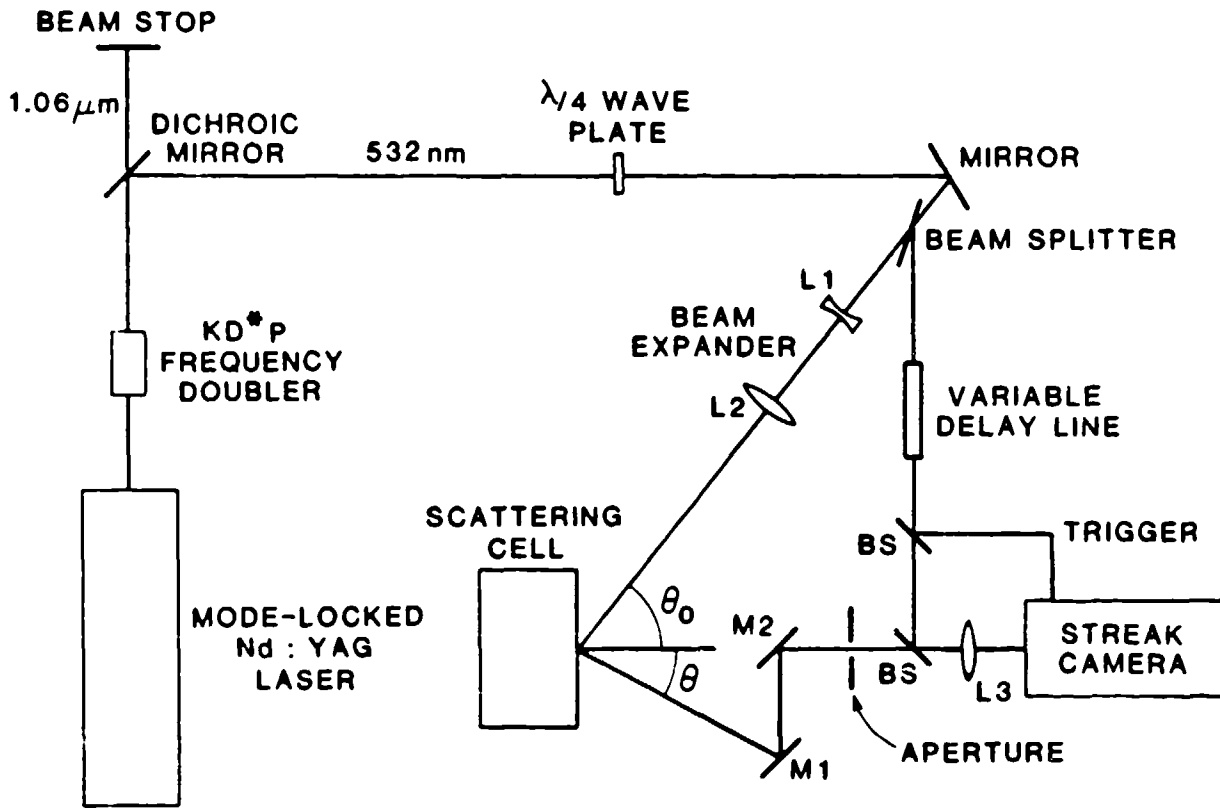


FIGURE 2

MEASURED BACKSCATTERED RADIANCE

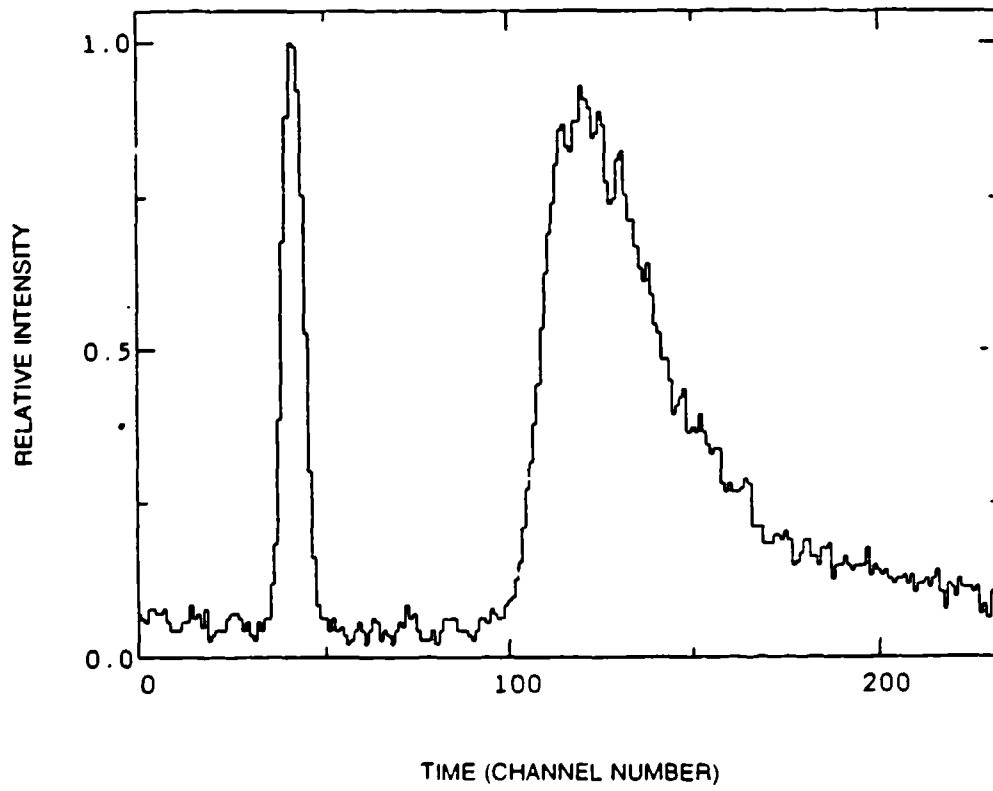


FIGURE 3

ZEROth FOURIER MOMENT (CASE B)

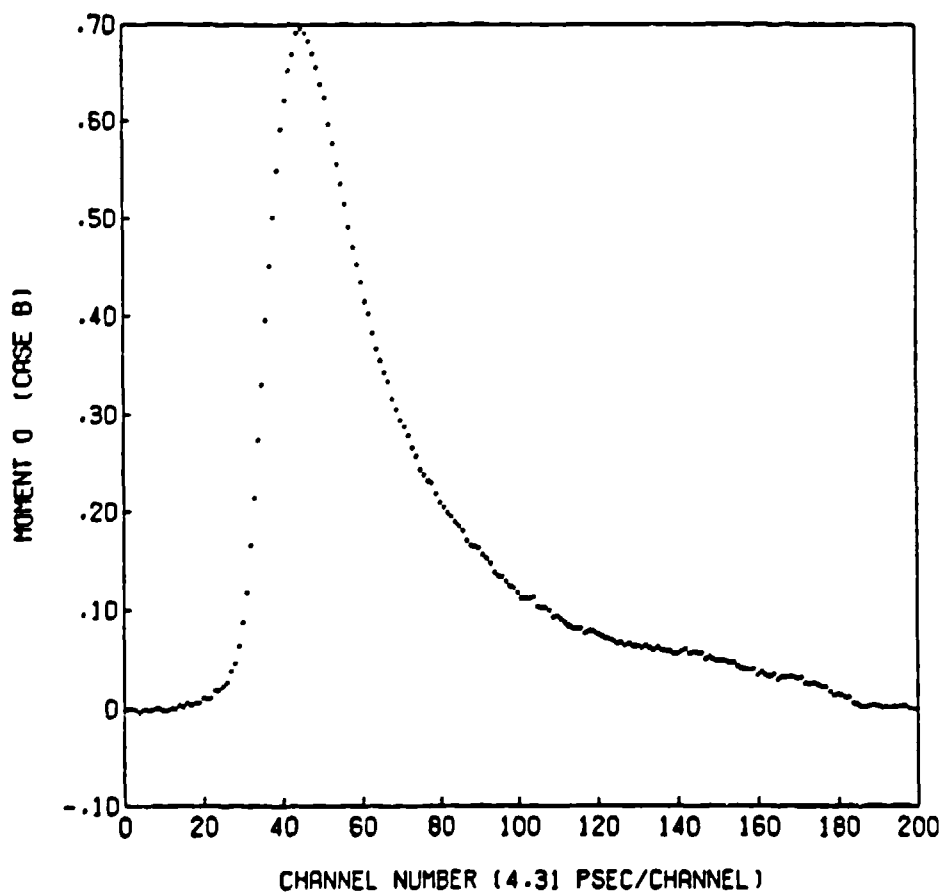
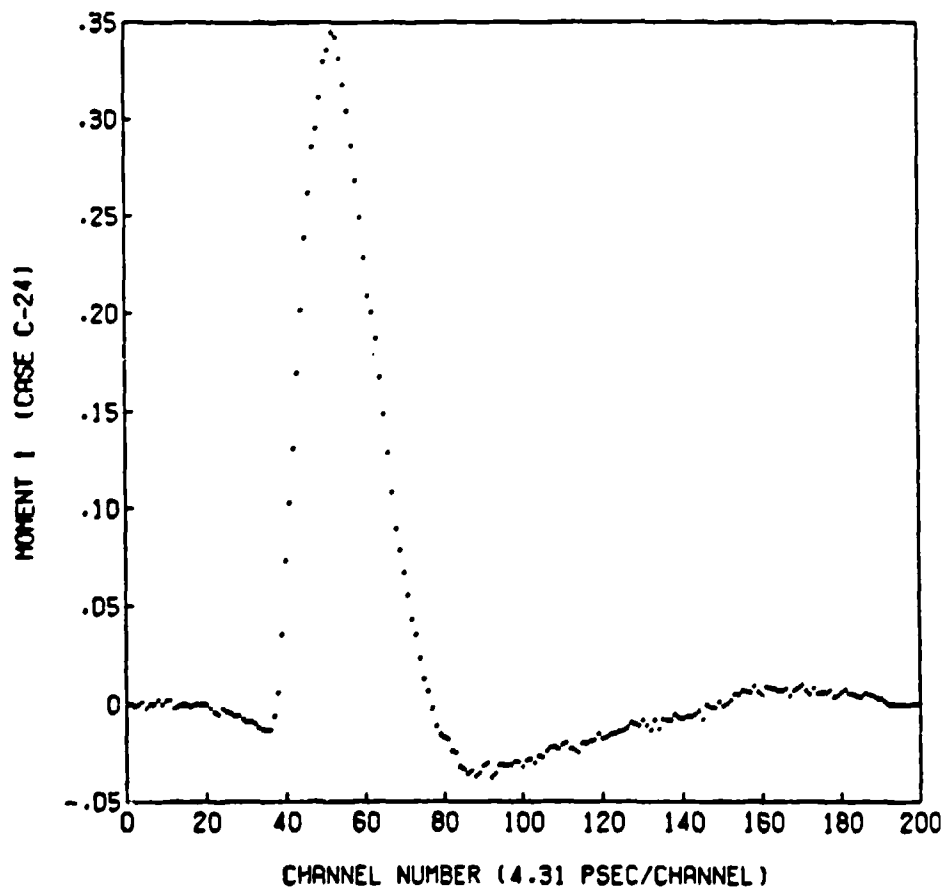


FIGURE 4
FIRST FOURIER MOMENT (CASE C')



Blank

BACKSCATTERING ENHANCEMENT OF WAVES IN RANDOM MEDIA

V.K. Varadan, V.V. Varadan and Y. Ma
Research Center for the Engineering of Electronic and Acoustic Materials
Department of Engineering Science and Mechanics
The Pennsylvania State University
University Park, PA 16802

RECENT SUBMITTALS FOR PUBLICATION AND PRESENTATIONS:

- A) V.V. Varadan, V.K. Varadan and Y. Ma, "Multiple scattering of waves in random media containing nonspherical scatterers," presented at the Electromagnetic Wave Propagation Panel Symposium sponsored by AGARD, NATO, Italy, April 1987.
- B) V.V. Varadan, Y. Ma and V.V. Varadan, "Scattered intensity of a wave propagating in a discrete random medium," submitted to *Applied Optics*, August 1987.
- C) V.K. Varadan, Y. Ma and V.V. Varadan, "Enhanced backscattering of optical waves due to densely distributed scatterers," submitted to SPIE's 1988 technical Symposium Southeast on Optics, Electro-Optics, and Sensors.

ABSTRACT

Recently, an interesting phenomenon has been reported as a result of a series of optical backscattering experiments conducted using collimated light sources (lasers). A locally high intensity maximum has been observed in the range of $\pi - \epsilon < \theta < \pi + \epsilon$ where ϵ is of the order of milliradians and $\theta = \pi$ is the backscattering direction. Albeit similar phenomena found in backscattering from various random media, e.g., scattering of electrons by impurities in metals and light scattering from random rough surfaces, this is the first observation of enhanced backscattering from suspensions.

In this paper, based on multiple scattering theory, we use the improved two scatterers T matrix program, which takes all back and forth scattering into account between two scatterers and considers the multiple scattering effect, in the intensity calculation. The widths and magnitudes of the backscattered intensity peak of our computations compare favorably with those of optical experiments.

INTRODUCTION

Backscattering enhancement or similar phenomena have been observed in various backscattering experiments, for example, the Anderson localization from scattering of electrons by impurities in metals [Abrahams et al., 1979 ; Bergmann, 1984], scintillation in turbulent media [Yeh et al., 1975; Rino et al., 1982] and speckling from light scattering by random rough surfaces [Dainty, 1984; Hecht, 1986]. And generally speaking, the enhanced backscattering can happen when (i) waves scattered by turbulent media - continuous random media (e.g., atmosphere); (ii) waves scattered by a collection of randomly distributed scatterers with high concentration; (iii) waves scattered by moving scatterers or by scatterers having Brownian motion; (iv) waves scattered by scatterers (moving or stationary) in a turbulent medium ; (v) waves scattered from random rough surfaces; (vi) waves scattered by scatterers in front of a rough

boundary.

The reason for this is partly that although waves are travelling in random media, the propagation of waves in such media (cases (i) - (vi)) is accompanied by multiple scattering as well as specific coherent effects and the enhancement is caused by positive interference of all the scattered waves. The recently observed enhanced backscattering phenomenon from dense suspensions appears to be the similar result which cannot be explained by radiative-transfer theory. Albeit the cyclic diagram in conjunction with point scatterer approximation introduced in multiple scattering theory to explain the enhanced backscattering [Tsang and Ishimaru, 1985], however, the experimental observations all deal with scatterer's size large compared with the incident wavelength [Kuga and Ishimaru, 1983; Albada and Lagendijk, 1985; Wolf and Maret, 1985], and therefore a detailed computation based on anisotropic scattering for finite size scatterers is essential. In addition, the back and forth scattering between a pair of scatterers, which has been neglected in the ladder approximation, may have major contribution toward backscattering rather than in the forward direction mentioned in one previous paper [Bringi et al., 1980] coauthored with us.

In this paper, based on multiple scattering theory, we use the improved two scatterers T matrix program, which takes all back and forth scattering into account between two scatterers and considers the multiple scattering effect, in the intensity calculation. The widths and magnitudes of the backscattered intensity peak of our computations compare favorably with those of optical experiments.

INCOHERENT INTENSITY FORMULATION

The detailed derivations and intermediate steps in obtaining the final expression for intensity can be referred to our paper [Varadan et al., 1987]. The average incoherent intensity $\langle I \rangle$ can be obtained as follows

$$\begin{aligned} \langle I \rangle &= n_0 \int \langle |u_j|^2 \rangle_j dr_j \\ &\quad + n_0^2 \iint \langle u_k u_j^* \rangle_{jk} g(r_{jk}) dr_k dr_j \\ &\quad - n_0^2 \iint \langle u_k \rangle_k \langle u_j^* \rangle_j dr_k dr_j \end{aligned} \quad (1)$$

where n_0 is the number density ($n_0 = N/V$), u_k is the scattered field from the k -th scatterer, $\langle \cdot \rangle_j$ and $\langle \cdot \rangle_{jk}$ are conditional configuration averages holding the positions of the j -th and both the j -th and k -th scatterers fixed, respectively, and $g(r_{jk})$ the radial distribution function for spherical scatterers. Equation (1) is an exact expression for the incoherent intensity $\langle I \rangle$.

In order to perform the computation, we need to make approximations for the expression of $\langle |u_j|^2 \rangle_j$ and $\langle u_k u_j^* \rangle_{jk}$, which are both unknown, in terms of the effective exciting field $\langle u_k \rangle_k$ which is known [Varadan et al., 1985]. By neglecting higher order statistics and considering only the two particle pair correlation function [Varadan et al., 1987], we can obtain

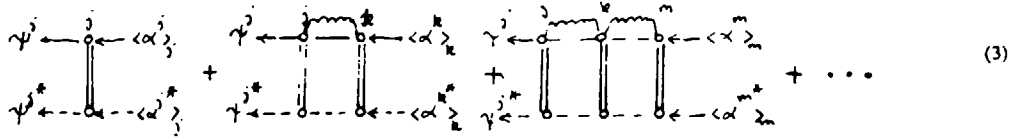
$$\begin{aligned} \langle I \rangle &= n_0 \int [\langle \psi^j T^j \rangle_{\alpha^j} \langle \alpha^j \rangle_j] [\langle \psi^j T^j \rangle_{\alpha^j} \langle \alpha^j \rangle_j]^* dr_j \\ &\quad + n_0^2 \iint [\langle \psi^j T^j \rangle_{\sigma_{jk} T^k} \langle \alpha^k \rangle_k] [\langle \psi^j T^j \rangle_{\sigma_{jk} T^k} \langle \alpha^k \rangle_k]^* g(r_{jk}) dr_j dr_k \\ &\quad + n_0^3 \iint [\langle \psi^j T^j \rangle_{\sigma_{jk} T^k} \langle \sigma_{km} T^m \rangle_{\alpha^m} \langle \alpha^m \rangle_m] \times \\ &\quad \times [\langle \psi^j T^j \rangle_{\sigma_{jk} T^k} \langle \sigma_{km} T^m \rangle_{\alpha^m} \langle \alpha^m \rangle_m]^* g(r_{jk}) g(r_{km}) dr_j dr_k dr_m \end{aligned}$$

+ ... (ladder diagrams)

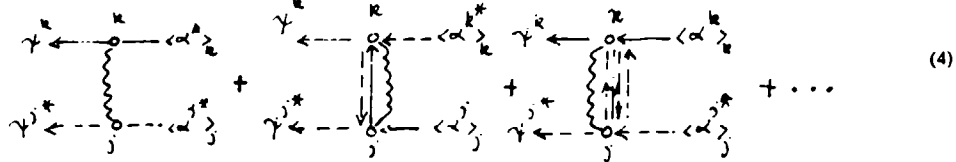
$$\begin{aligned}
 & + n_0^2 \int \int [\Psi^k T^k \langle \alpha^k \rangle_k] [\Psi^j T^j \langle \alpha^j \rangle_j]^\circ [g(r_{jk}) - 1] dr_j dr_k \\
 & + n_0^2 \int \int [\Psi^k T^k \sigma_{kj} T^j \langle \alpha^j \rangle_j] [\Psi^j T^j \sigma_{jk} T^k \langle \alpha^k \rangle_k]^\circ g(r_{jk}) dr_j dr_k \\
 & + n_0^2 \int \int [\Psi^k T^k \sigma_{kj} T^j \sigma_{jk} T^k \langle \alpha^k \rangle_k] \times \\
 & \times [\Psi^j T^j \sigma_{jk} T^k \sigma_{kj} T^j \langle \alpha^j \rangle_j]^\circ g(r_{jk}) dr_j dr_k \\
 & + \dots \text{ (cyclic diagrams)}
 \end{aligned} \tag{2}$$

In Eq. (2) T^j is the T - Matrix of the j-th scatterer [Varadan and Varadan, 1980], Ψ^k is the outgoing function (Hankel function) of the k-th scatterer and σ_{kj} the translation operator. Each term of the two series in (2) represents a certain order of scattering. For the same order of scattering, the cyclic terms are proportional to a higher power in the number density. Thus at low concentrations cyclic terms contribute less than the ladder terms to the the same order of scattering. Eq. (2) can be represented diagrammatically as follows,

(a) Ladder Diagram



(h) Cyclic Diagram



In fact the so called cyclic terms can all be summed if one replaces the infinite series in (4) with the T-matrix of a pair of scatterers which considers all the back and forth scattering between them. The back and forth scattering between a pair of scatterers, which has been neglected in the ladder approximation, may have major contribution toward backscattering rather than in the forward direction mentioned in one previous paper [Bringi et al., 1980] coauthored with us. Eq. (4) may hence be written diagrammatically as

where T^{jk} , the two scatterer T - matrix has the following form [Varadan and Varadan, 1981]

$$T^{jk} = R(r_0) T^j [1 - \sigma(r_{jk}) T^k \sigma(r_{kj}) T^j]^{-1} [1 + \sigma(r_{jk}) T^k R(r_{kj})] R(-r_0)$$

$$+ R(r_0) T^k [1 - \sigma(r_{jk}) T^j \sigma(r_{jk}) T^k]^{-1} [1 + \sigma(r_{jk}) T^j R(r_{jk})] R(-r_0) \quad (6)$$

In the above expression, $R(r_0)$ is the regular part of the translation matrix $\sigma(r_0)$, $r_{jk} = r_j - r_k$ and $r_0 = (r_j + r_k)/2$.

RESULTS AND DISCUSSION

In general, at low concentrations, both the magnitude of scattered intensity and multiple scattering contribution are not strong enough to reach the threshold of the enhanced backscattering. When the enhanced backscattering happens, the width of the intensity peak is proportional to the imaginary part of the effective wavenumber. In other words, the width is inversely proportional to the mean free path which is getting smaller when the concentration is getting larger (the average separation distance between two scatterers is getting smaller). The calculated mean free path length, which compares very well with that of the experiment, and the data used in the intensity calculation are shown in Table 1.

To perform the calculation, one needs to adopt the cylindrical coordinates instead of the spherical one to match the experimental set-up which brings the complexities in converting the spherical functions to their cylindrical counterparts. Furthermore, in order to compare with the experimental results, especially the magnitude and the width of the intensity peak, the proper integration limits must be taken care of very carefully. The widths and the magnitudes of the backscattered intensity peak of our computations compare favorably with those of Albada's experiments in which the receiver used has a very small field of view and, hence, gives a much better signal resolution (see Fig. 1). However, due to the truncation of the orders of scattering due to the tremendous amount of CPU time required, we did not obtain a full match.

REFERENCES

- E. Abrahams, P.W. Anderson, D.C. Licciardello and T.V. Ramakrishnan, *Phys. Rev. Lett.* **42**, 673 (1979).
- E. Akkermans, P.E. Wolf, and R. Maynard, *Phys. Rev. Lett.* **56**, 1471 (1986).
- M.P. Van Albada and A. Lagendijk, *Phys. Rev. Lett.* **55**, 2692 (1985).
- G. Bergmann, *Phys. Rev.* **107**, 1 (1984).
- V.N. Brinkl, T.A. Seliga, V.K. Varadan and V.V. Varadan, "Bulk propagation characteristics of discrete random media," in *Multiple Scattering and Waves in Random Media*, edited by P.L. Chow, W.E. Kohler and G.C. Papanicolaou, North-Holland, 1981.
- J.C. Dalnty (ed.), *Laser Speckle and Related Phenomena*, Springer-Verlag, 1984.
- Y. Kuga and A. Ishimaru, *J. Opt. Soc. Am.* **A1**, 831 (1984).
- C.L. Rino, *IEEE Trans. Antennas Propagat.* **AP-24**, 912 (1976).
- L. Tsang and A. Ishimaru, *J. Opt. Soc. Am.* **A2**, 1331 (1985).
- V.K. Varadan and V.V. Varadan, Eds., *Acoustic, Electromagnetic and Elastic Wave Scattering - Focus on the T - Matrix Approach*, Pergamon Press, New York, 1980.
- V.V. Varadan and V.K. Varadan, *J. Acoust. Soc. Am.* **70**, 213 (1981).

V.V. Varadan, Y. Ma and V.K. Varadan, *J. Opt. Soc. Am. A2*, No. 12, 2195 (1985).

V.V. Varadan, Y. Ma and V.V. Varadan, "Scattered intensity of a wave propagating in a discrete random medium," submitted to *Applied Optics*, August 1987.

P.E. Wolf and G. Maret, *Phys. Rev. Lett.* **55**, 2696 (1985).

K.C. Yeh, *Radio Sci.* **18**, 159 (1983).

Table 1. Data used in the calculation [Ref : Albada and Lagendijk, 1985]

Concentration n_0	(i)	$14.1 \times 10^{16} / \text{m}^3$	(corresponding volume fraction $c = 0.09587$)
	(ii)	$3.48 \times 10^{16} / \text{m}^3$	($c = 0.02366$)
	(iii)	$1.49 \times 10^{16} / \text{m}^3$	($c = 0.01013$)

Particle size $d = 1.091 \mu\text{m}$ (in diameter)

Refractive index n (latex 5100) = 1.6

Refractive index n (distilled water) = 1.33

He-Ne laser wavelength $\lambda = 633 \text{ nm}$

Nondimensional frequency kd ($2\pi d/\lambda$) = 10.8294 ($\gg 1$)

Calculated effective $K = K_1 + iK_2$

(i) $K_1/k_w = 1.01266$, $K_2/k_w = 0.1514 \times 10^{-1}$ ($c = 0.09587$)

(ii) $K_1/k_w = 1.00231$, $K_2/k_w = 0.3839 \times 10^{-2}$ ($c = 0.02366$)

(iii) $K_1/k_w = 1.00093$, $K_2/k_w = 0.1618 \times 10^{-2}$ ($c = 0.01013$)

Mean free path (Albada's experiment) = $2.6 \mu\text{m}$ (for $n_0 = 14.1 \times 10^{16} / \text{m}^3$)

Calculated mean free path (from K_2) = $2.5 \mu\text{m}$

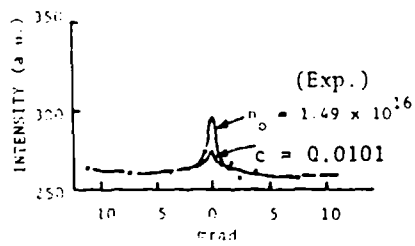
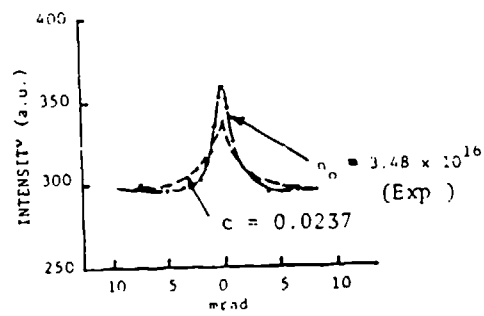
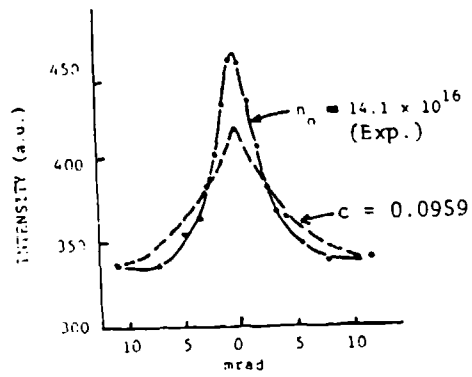


Fig. 1 Backscattered intensity : Comparison with optical experiments [Albada and Legendijk, 1985]

ELECTROMAGNETIC ABSORPTION IN A CHIRAL COMPOSITE LAYER

VIJAY K. VARADAN, VASUNDARA V. VARADAN and AKHLESH LAKHTAKIA
Research Center for the Engineering of Electronic and Acoustic Materials
Department of Engineering Science and Mechanics
The Pennsylvania State University
University Park, PA 16802

RECENT PUBLICATIONS, SUBMITTALS FOR PUBLICATION, AND PRESENTATIONS:

1. A. Lakhtakia, V.V. Varadan and V.K. Varadan, "A parametric study of microwave reflection characteristics of a planar achiral-chiral interfaces," *IEEE Trans EMC* **28**, 90 (1986).
2. V.K. Varadan, V.V. Varadan and A. Lakhtakia, "On the possibility of designing anti-reflection coatings using chiral composites," *J. Wave-Mater. Interact.* **2**, 71 (1987).
3. V.K. Varadan, A. Lakhtakia and V.V. Varadan, "A comment on the solutions of the equation $\nabla \times \mathbf{a} = \mathbf{ka}$," *J. Phys. A* **20**, 2649 (1987).
4. V.K. Varadan, A. Lakhtakia and V.V. Varadan, "Radiated potentials and fields in isotropic chiral media," *J. Phys. A* **20**, 000 (1987).
5. V.V. Varadan, A. Lakhtakia and V.K. Varadan, "On the equivalence of sources and duality of fields in isotropic chiral media," *J. Phys. A* **20**, 000 (1987).

ABSTRACT

The possible use of chiral composite media for designing coatings instrumental in reducing EM reflection from metallic surfaces has been investigated. Such coatings may be fabricated by suspending chiral microgeometries in a dielectric matrix material. It can be shown that these coatings can significantly cut down reflections, regardless of the incident polarization, over a wide frequency range (50-300 GHz) and incidence angles ($0^\circ - 30^\circ$). A sample result has been given.

INTRODUCTION

A chiral substance might exist in two distinct molecular forms, which are otherwise identical in their chemical and physical properties; but although one is a mirror image of the other it cannot be superposed on its mirror image. In other words, the two molecules are incongruent mirror images of each other [Lakhtakia *et al* 1986]. Chirality, however, is a phenomenon which can be found in the less exotic everyday life. Mobius strips, golf clubs, helices, sea-shells, and, of course, the hands of a human being are examples of chiral objects found everywhere. Substances with chiral microgeometries can, therefore, be tailored to possess desirable electromagnetic properties and their use exploited.

With the proliferation in the use of the electromagnetic spectrum at frequencies around 100 GHz witnessed by the past few years, it has become desirable to design efficient anti-reflection coatings for metallic surfaces. Low-weight, low-loss dielectric composites have been particularly attractive for this purpose, but such materials turn out

to be poor absorbers of electromagnetic energy. There has been a need, therefore, to find materials which are lightweight but, in addition, are effective absorbers as well. It will be shown in this report that chiral composites can be attractive as highly efficient absorbers. The electromagnetic boundary value problem of a plane chiral coating on a perfectly conducting surface will be investigated and several designs of such coatings discussed. From the numerical studies presented, it will be shown that endowing low loss dielectric composites with chiral properties can easily cut down the reflected power density by a factor of 4 or more.

THE ANTI-REFLECTION COATING ON A METALLIC SUBSTRATE

Let V be the region $0 \leq z \leq d$ occupied by a chiral medium whose properties are described above, and V' be the half-space $z \leq 0$ which does not exhibit chirality. The plane $z = d$ is assumed to be perfectly conducting so that the presented geometry describes a metallic surface coated with a chiral layer of thickness d . The primed quantities refer to the achiral half space V' , whereas the unprimed quantities hold in the layer V .

Consider a plane monochromatic wave

$$\mathbf{E}_i = (A_E \mathbf{j} - A_H \cos\theta_0 \mathbf{i} + A_H \sin\theta_0 \mathbf{k}) \exp[ik'(\cos\theta_0 z + \sin\theta_0 x)] \quad (1a)$$

$$\mathbf{H}_i = (1/i\omega\mu') \nabla \times \mathbf{E}_i \quad (1b)$$

be traveling in V' towards the interface $z = 0$, making an angle θ_0 with the z axis, \mathbf{i} , \mathbf{j} and \mathbf{k} are the usual Cartesian unit vectors. In Eqs. (1a,b), $k' = \omega\sqrt{\mu'\epsilon'}$ is the wavenumber in the achiral material occupying V' , and whereas the coefficients $A_E \neq 0$, $A_H = 0$ refer to a TE-polarized incident planewave, the coefficients $A_E = 0$, $A_H \neq 0$ denote an incident TM-polarized field.

Inside the chiral layer V , the existing field has to be expressed in terms of \mathcal{Q}_R , the right-circularly polarized (RCP) waves, and \mathcal{Q}_L , the left-circularly polarized (LCP) waves. One RCP and one LCP wave, in general, exist in V propagating towards $z = d$, and another pair of a LCP and a RCP wave propagating towards $z = 0$. Thus, the appropriate representation of the field in V is given by [Lakhtakia *et al* 1986, Varadan *et al* 1987]

$$\begin{aligned} \mathcal{Q}_L = & A_1 (-\cos\theta_L \mathbf{i} - \mathbf{ij} + \sin\theta_L \mathbf{k}) \exp[ik_L(\cos\theta_L z + \sin\theta_L x)] \\ & + A_2 (\cos\theta_L \mathbf{i} - \mathbf{ij} + \sin\theta_L \mathbf{k}) \exp[-ik_L(\cos\theta_L z - \sin\theta_L x)] \end{aligned} \quad (2a)$$

and

$$\begin{aligned} \mathcal{Q}_R = & C_1 (-\cos\theta_R \mathbf{i} + \mathbf{ij} + \sin\theta_R \mathbf{k}) \exp[ik_R(\cos\theta_R z + \sin\theta_R x)] \\ & + C_2 (\cos\theta_R \mathbf{i} - \mathbf{ij} + \sin\theta_R \mathbf{k}) \exp[-ik_R(\cos\theta_R z - \sin\theta_R x)] \end{aligned} \quad (2b)$$

In this representation, the coefficients A_1 , A_2 , C_1 , C_2 are as yet unknowns to be determined as solutions of the boundary value problem; the coefficients A_1 , C_1 refer to the waves going out to $z = d$, while the remaining two to those going towards $z = 0$. The field in the chiral region is given in terms of Eqs. (2a,b) by

$$\mathbf{E}_{ch} = \mathcal{Q}_L + a_R \mathcal{Q}_R, \quad \mathbf{H}_{ch} = a_L \mathcal{Q}_L + \mathcal{Q}_R \quad (3)$$

where

$$a_R = [k_R(1 - k^2\alpha\beta) + \alpha k^2] / j\omega\epsilon \quad , \quad (4a)$$

$$a_L = [k_L(1 - k^2\alpha\beta) - \beta k^2] / j\omega\mu \quad , \quad (4b)$$

$$k_R = k \left\{ [1 + (\alpha - \beta)^2 k^2 / 4]^{1/2} - (\alpha + \beta)k / 2 \right\} [1 - k^2\alpha\beta]^{-1} \quad , \quad (4c)$$

and

$$k_L = k \left\{ [1 + (\alpha - \beta)^2 k^2 / 4]^{1/2} + (\alpha + \beta)k / 2 \right\} [1 - k^2\alpha\beta]^{-1} \quad , \quad (4d)$$

with $k = \omega\sqrt{\mu\epsilon}$ being appropriate to the chiral medium. The parameters ϵ , μ , α and β relate to the constitutive equations of the chiral medium [Lakhtakia *et al* 1986].

The representation of the reflected field in V takes the form

$$\begin{aligned} \mathbf{E}_{ref} = & [A_3(\cos\theta'i - ij + \sin\theta'k) + C_3(\cos\theta'i + ij + \sin\theta'k)] \cdot \\ & \cdot \exp[-ik'(\cos\theta'z - \sin\theta'x)] \end{aligned} \quad (5a)$$

$$\mathbf{H}_{ref} = (1 / i\omega\mu') \nabla \times \mathbf{E}_{ref} \quad (5b)$$

so that the reflected field also consists of a LCP and a RCP wave; while Snell's law yields $k_L \sin\theta_L = k_R \sin\theta_R = k' \sin\theta_0 = k' \sin\theta'$. Following Lakhtakia *et al* [1986], the boundary value problem is solved, and the total reflected power density in V' is evaluated as

$$P_{ref} = (1/2) \sqrt{\epsilon' / \mu'} \cos\theta_0 \{2|A_3|^2 + 2|C_3|^2\} \quad (6)$$

whereas the incident power density is given by

$$P_i = \begin{cases} (1/2) \sqrt{\epsilon' / \mu'} \cos\theta_0 |A_E|^2 & , \text{ TE incidence} \\ (1/2) \sqrt{\epsilon' / \mu'} \cos\theta_0 |A_H|^2 & , \text{ TM incidence} \end{cases} \quad (7)$$

Computations of the reflection efficiencies

$$R = P_{ref} / P_i \quad (8)$$

can therefore be made. It must be noted that $(1 - R)$ is the absorption efficiency of the chiral layer since whatever energy is not reflected back into V' must have been absorbed in V . Furthermore, it should be noted that in order to guarantee the energy conservation principle in an otherwise lossless medium, the condition $\alpha = \beta^*$ in the constitutive equations for the chiral medium is sufficient [Fedorov 1959]. Since $\beta = \alpha$ guarantees the time-reversal symmetry of the solution [Satten 1958]; therefore, along with the condition $\beta = \alpha^*$ for energy conservation to hold [Fedorov 1959], in all subsequent numerical studies made $\beta = \alpha$ was assumed to be real.

NUMERICAL RESULTS AND DISCUSSION

The boundary value problem was implemented on a DEC VAX 11/730 minicomputer and the reflection efficiencies R_{TE} , R_{TM} of Eq. (8) were computed for both incident polarizations. The achiral half-space V' was taken

to be free-space so the $\epsilon' = \epsilon_0$ and $\mu' = \mu_0$. In addition, the chiral layer was taken to be devoid of magnetic properties and μ was set equal to μ_0 . On the other hand, V was filled up by a low loss chiral dielectric medium so that its relative permittivity ϵ/ϵ_0 was complex with $\text{Im}\{\epsilon/\epsilon_0\} \ll \text{Re}\{\epsilon/\epsilon_0\}$. The thickness d of the coating was assumed to be 2 mm for all of our numerical studies.

A design of a wideband anti-reflection chiral coating, however, cannot afford to have both ϵ/ϵ_0 and β independent of frequency. Once it became clear from numerical experimentation that (i) chirality is ineffective in the reduction of the reflection efficiency if ϵ/ϵ_0 is purely real, and (ii) that either β or ϵ/ϵ_0 or both must be frequency dependent in order to obtain a wideband anti-reflection coating, design of such a coating becomes more of an optimization problem. Shown in Figs. 1-3 is a sample design with ϵ/ϵ_0 assumed to be constant, whereas $\beta = \beta(f)$ assumed is shown in Fig. 1. In Figs. 2 and 3, the enhancement of the absorption efficiency of over a 50-300 GHz frequency range by incorporating this frequency dependent $\beta = \beta(f)$ is illustrated, for the TE- and TM- polarization incidence cases, respectively. The relative permittivity ϵ/ϵ_0 is set at $5.0 + i0.05$ for all frequencies considered. It should be noted from these two figures that whereas the design objective of achieving R_{TE} and R_{TM} less than 20% for $50 \leq f \leq 300$ GHz and $0^\circ \leq \theta_0 \leq 30^\circ$ can be achieved using the β of Fig. 1, the reflection efficiencies hover around 92% if β were to be set equal to zero.

From our numerical studies, several conclusions can be drawn. Firstly, in reducing reflection if a larger constant β is used, then the values of ϵ/ϵ_0 tend to decrease over the entire frequency band of interest, a goal which appears to be desirable for a material scientist. However, this also tends to reduce the bandwidth over which the desired absorption efficiencies can be achieved. Secondly, and as stated earlier, chirality in the absence of a lossy ϵ is of no use whatsoever in reducing reflected power density. A small loss must be present for ϵ to be effective. Therefore, chirality serves only as an enhancement factor for absorption, but of itself it is not an absorbing mechanism. Thirdly, and very importantly, both ϵ/ϵ_0 and β should be frequency dependent. This last conclusion, however, was not verified here because of the complexities of multivariate optimization problems.

In summary, this report describes the use of low loss dielectric chiral composites to fabricate low weight and highly effective anti-reflection coatings. Low loss dielectrics in the ~100 GHz frequency range of this kind are quite commonly available and are attractive because of their low mass densities. However, such materials are not very effective absorbers. Suspension of chiral microgeometries in these materials can, however, endow them with rotational activity, and simultaneously, turn them into efficient absorbers of electromagnetic radiation.

REFERENCES

- Fedorov, F.I. [1959]: On the Theory of Optical Activity in Crystals, I. The Law of Conservation of Energy and the Optical Activity Tensors, *Opt. Spectrosc. (USSR)* 6, 49-53.
- Lakhtakia, A., Varadan, V.V. and Varadan, V.K. [1986]: A parametric study of microwave reflection characteristics of a planar achiral-chiral interfaces, *IEEE Trans. EM* 28, 90-95.
- Satten, R.A. [1958]: Time-reversal Symmetry and Electromagnetic Polarization Fields, *J. Chem. Phys.* 28, 742-743.
- Varadan, V.K., Varadan, V.V. and Lakhtakia, A. [1987]: On the possibility of designing anti-reflection

Figure 1 The frequency profile $\beta = \beta(f)$ used for the results shown in Figs. 2 and 3. The parameter β carries the unit of meter.

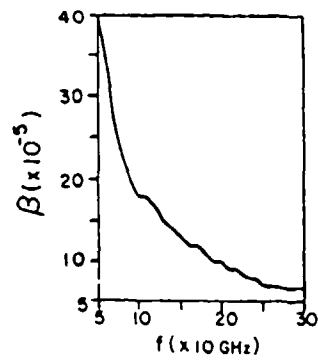


Figure 2 Reflection efficiency R_{TE} plotted as a function of θ_0 and frequency f for a 2 mm thick anti-reflection coating. The complex permittivity $\epsilon/\epsilon_0 = 5.0 + i0.05$. In the upper figure the $\beta = \beta(f)$ of Fig. 1 is used while in the lower figure β is set equal to 0.0 m.

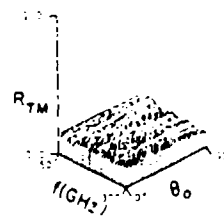
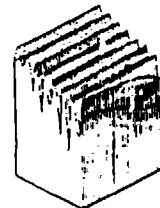
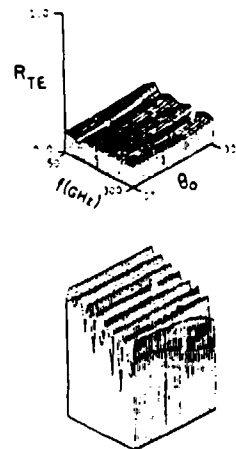


Figure 3 Same as Fig. 2, but R_{TM} is plotted

Blank

Summary of Recent Work at the University of Michigan
Relevant to Electromagnetic Wave Scattering and
Absorption by Small Particles

Herschel Weil and Thomas M. Willis III
Radiation Laboratory, EECS Department, University of Michigan
Ann Arbor, MI 48109-2122

RECENT PUBLICATIONS, SUBMITTALS FOR PUBLICATION AND
PRESENTATIONS*

A) T.B.A. Senior, "A Critique of Certain Half Plane Diffraction Analyses",
Electromagnetics Z pp. 81-90, 1987.

B) T.B.A. Senior and J.L. Volakis, "Sheet Simulation of Dielectric Layers",
presented at the URSI National Radio Science Meeting, Boulder, CO, January 1987.

C) T.B.A. Senior and J.L. Volakis, "Sheet Simulation of a Thin Dielectric Layer",
Radio Science 22, to appear December 1987.

D) J.L. Volakis and T.B.A. Senior, "Diffraction by a Thin Dielectric Halfplane",
IEEE Transactions A-P-35, to appear December 1987.

E) H. Weil, "Surface Roughness Clustering and Material Effects in Absorption
and Scattering by Electrically Small Particles", Proceedings of the 1985 CRDEC
Scientific Conference on Obscuration and Aerosol Research, R.H. Kohl, Ed., CRDEC-
SP- 86019, July 1986.

F) H. Weil and T.M. Willis, "Improved Computational Method and Results for
Scattering, Absorption and Internal Fields of Disk-like Particles with Diameters $\leq \lambda$ ",
Proceedings of the 1986 CRDEC Scientific Conference on Obscuration and Aerosol
Research, (submitted, September 1986).

G) T.M. Willis and H. Weil, "Internal Induced Fields, Scattering and Absorption of
Electromagnetic Radiation by Disc-Shaped Aerosols: An Improved Computational
Formulation and Computer Code", Report RL 023618-1-T, The University of Michigan,
EECS Department, Radiation Laboratory, December 1986.

*This list concerns only research supported in whole or in part by CRDEC.
Publications regarding work described in the paper but not supported by CRDEC are
referenced explicitly in the .ext.

H) T.M. Willis and H. Weil, "Improved Computational Method for Scattering, Absorption of Internal Fields of Disc-like Particles with Diameters $\lesssim 4\lambda$, presented at the 1987 URSI Radio Science Meeting, Virginia Polytechnic Institute and State University, Blacksburg, VA, June 1987.

I) T.M. Willis and H. Weil, "Disk Scattering and Absorption by an Improved Computation Method", Applied Optics 26 to appear September 1987.

J) T.M. Willis, H. Weil and D.M. Le Vine, "Applicability of Physical Optics Thin Plate Scattering Formulas for Remote Sensing", submitted for publication to IEEE Transactions on Geoscience and Remote Sensing, April 1986.

ABSTRACT

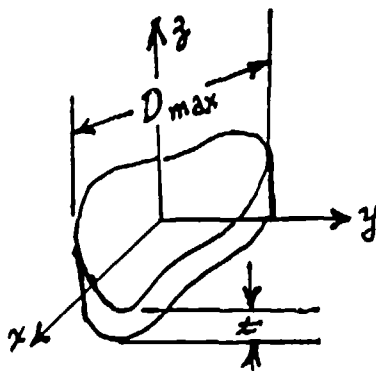
Brief descriptions are given of theoretical and computational scattering research in progress or recently completed at the Radiation Laboratory.

INTRODUCTION

The research is summarized under the following headings:

A) Individual particles

1. Thin plates as shown in the following figure, $kt \lesssim 0.5$, $kD_{\max} < l$ where l is a "moderate" integer and k is the free space wave number.



2. Rayleigh particles, $kD_{\max} < 0.1$.

- B) Distributions of scatterers
 - C) Combined Electric and magnetic current sheet approximations to thin slabs of infinite extent and application to semi-Infinite thin bodies.
- In the remainder of this paper we expand on the work listed in this outline.

INDIVIDUAL PARTICLES

Thin Plates

The thin plate efforts may be divided into two "exact" methods in which the induced current densities \bar{J} are numerically computed, and two "approximate" methods in which a priori assumptions for the form of the \bar{J} 's are used. Each of the "exact" procedures requires relatively heavy numerical computation in the solution of integral equations for the \bar{J} 's. With both approximate methods, the only computations needed are simple numerical evaluations of explicit formulas for the scattering cross-sections.

The exact methods are:

[Refs. F., G., I., J]

The first "exact" method is discussed in Refs. F., G., I. and J., for the homogeneous dielectric circular plate or disk. A method we have labelled CWW is used to solve an integral equation for the total (conduction plus polarization) induced current density \bar{J} . This equation involves both volume and surface integrations. It is solved using twice differentiable continuous basis functions tailored especially for this problem. With these functions one avoids the numerical instabilities evident in other methods to solve for \bar{J} (electric field \bar{E}) in bodies where one dimension is much smaller than the other dimensions. We mention explicitly that all three components of \bar{J} , (J_x , J_y , J_z) are obtained by CWW since this is not true in the remaining methods described. In these J_z is assumed constant or, in particular, zero. Ref. H summarizes the theory and also includes the details of an extensive verification of the method by comparison of backscatter results with experimental results and with computational results by other methods. The conclusions from these comparisons are that the CWW method works very well for disks where

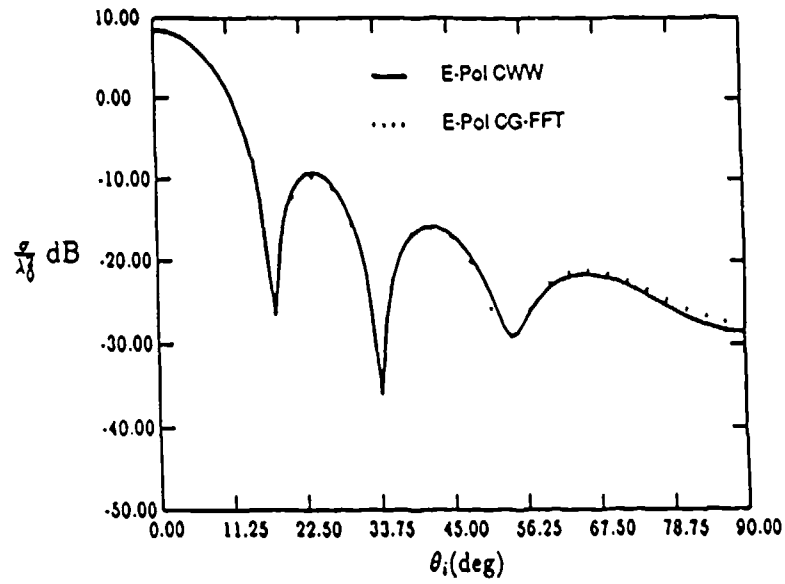
$$0 \leq ka \leq 12$$

$$0 \leq kt < 0.5$$

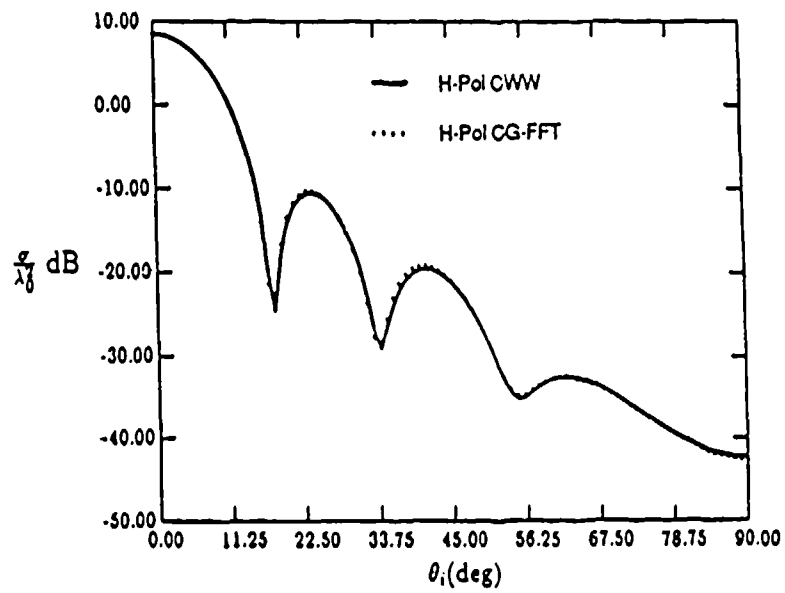
$$0 < a/t \leq 10^4$$

for arbitrary direction and polarization of the incident radiation and for arbitrary index of refraction, where a is the radius and t is the thickness of the disk. The limitation on ka is due to an arbitrary limitation placed on the maximum matrix size (30 x 30) in the code and can probably be successfully relaxed. We are particularly interested in using CWW to explore the internal field and current density structure of a disk during the next year. We will also use it in connection with our work on distributions of scatterers.

The second exact procedure [T.J. Peters and J.L. Volakis, "Application of a Conjugate Gradient FFT Method to Scattering from Thin Planes Plates", (submitted to IEEE Transactions A-P).] is applicable to thin flat plates of any shape and may be used for homogeneous dielectric or magnetic materials. It is designed to be efficient for very large plates. The method starts with a volume integral equation reduced to 2-dimensional integrals by assuming \bar{J} is z independent. It finds surface current components J_x^s and J_y^s . Results for circles, squares and triangles have been found, but the computations are very "heavy" even for 2λ on a side. Work is continuing to make the code much more efficient and to run on parallel processors. In the following figures we show a comparison of backscatter cross section vs. angle of incidence θ for a circular disk as computed by CWW and by this CG-FFT method.



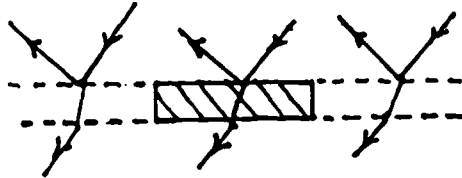
Circular plate: $r_0 = \lambda_0, \tau = .01\lambda_0, \epsilon_r = 2.0 - j10.0,$



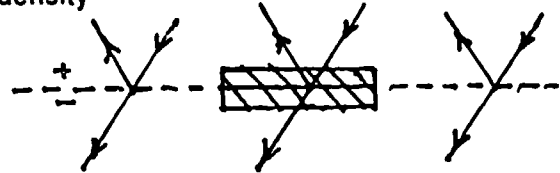
Circular plate: $r_0 = \lambda_0, \tau = .01\lambda_0, \epsilon_r = 2.0 - j10.0,$

The approximate methods are two so called "physical optics" methods. they differ according to whether the assumed current densities \bar{J} correspond to:

(A) Infinite slabs volume distribution of current density



(B) Infinite equivalent membranes carrying a 2d current density



The plates are shown by the cross-hatched regions.

All modifications of \bar{J} due the effects of the finite plate size and shape are neglected except for setting $\bar{J} = 0$ outside the plate.

[Ref. J.]

The infinite slab method derived and evaluated in Ref. J. was first introduced by D.M. Le Vine [The Radar Cross-section of Dielectric Disks", IEEE Transactions AP-32, pp. 6-12, 1984]. We have checked its range of validity for circular plates so thin that $e^{inkt} = 1$ (where the disk's complex index of refraction is n) as a function of n , t and a by comparing back scattering cross sections based on this method with the cross-sections computed by the exact CWW method. The results of these comparisons show that this physical optics method (with e^{inkt} replaced by 1 in the formulas) gives good results for all angles of incidence and polarizations for low refractive index materials provided $a/t \gg 1$. As nka increases for fixed a/t the results deteriorate for near grazing and grazing incidence for \bar{E} polarization parallel to the flat surfaces of the disk.

The equivalent membrane method was applied to finite plates [T.B.A. Senior, K. Sarabandi and F.T. Ulaby, "Measuring and Modeling the Backscattering Cross Section of a Leaf", Radio Science, (to appear December 1987).] The membrane was a resistive sheet of complex resistance R (ohms/square) carrying surface current density \bar{J}_s (c/m) where,

$$R = iZ / [kt(e - 1)]$$

$$\bar{J}_s = (\hat{n} \times \bar{H})|_+^* = -\hat{n} \times (\hat{n} \times \bar{E}^+) / R$$

Here \bar{E} and \bar{H} are the total electric and magnetic fields, + and - represent the upper and lower surface values and the normal \hat{n} is pointing upward. Z is the impedance of free space.

The back scattering cross-section formulas were found analytically for rectangular plates and verified against 35 GHz experiments on rectangular sections of moist and dry vegetation leaves. The formulas agree with measurements only for angles of incidence well away from edge-on (grazing incidence). This method has been generalized to hold for curved plates and checked vs. 35 GHz experimental results for the two cases illustrated here.



We are presently exploring analytically the sources for the disagreements between the two methods near grazing incidence.

Rayleigh Particles

[Ref. E and also L. Pierce and H. Weil, these proceedings.]

For particles or particle aggregates of dimensions much less than the free space wavelength we have studied the internal and near fields of aggregating spheres in a region when $\text{Re}(\epsilon) < 0$. Enhanced resonance absorption bands occur when $\text{Re}(\epsilon) < 0$. Absorption spectra were generated for pairs of gold spheres close together and/or aggregated. This work is continuing with emphasis on computing and plotting the detailed internal fields.

DISTRIBUTIONS OF SCATTERERS

We revised an old UM program, CLOUDS [H. Weil and T.M. Willis, Radio Science 17, 1018-1026 (1982).] for bistatic scattering by clouds made of homogeneous spheres and discs of arbitrary size distributions and, for the discs, arbitrary orientations. Specifically CWW was introduced to replace a much less accurate disc program originally used. This program allows for simple scattering only. It computes the Stokes parameters of the received signals.

We intend to explore some aspects of transmission through such clouds and also the use of Rayleigh and physical optics formulas, where applicable, in order to speed up the computations.

COMBINED ELECTRIC AND MAGNETIC CURRENT SHEET APPROXIMATIONS TO THIN SLABS OF INFINITE EXTENT AND APPLICATION TO SEMI-INFINITE THIN BODIES

[Refs. I., J.]

In order to be able to take into account the normal component of current while still using a membrane model of a dielectric slab the following research was carried out on Ref. I and applied to a half plane in Ref. J as a step toward treating finite particles.

The slab is theoretically replaced by a zero thickness electrically resistive sheet carrying tangential electric current density $\hat{n} \times (\vec{H}^+ - \vec{H}^-)$ superimposed on a "modified" magnetically conductive sheet carrying tangential magnetic current density $\hat{n} \times (\vec{E}^+ - \vec{E}^-)$ which simulates a normal component of electrical current density. The basis of this reduction are the boundary conditions.

Resistive sheet:

$$\hat{n} \times \{ \hat{n} \times (\vec{E}^+ + \vec{E}^-) \} = -2 R \hat{n} \times (\vec{H}^+ - \vec{H}^-)$$

Modified conductive sheet:

$$\hat{n} \times \{ \hat{n} \times (\vec{H}^+ + \vec{H}^-) \} - \frac{iY}{k} \hat{n} \times \frac{\partial}{\partial n} (\vec{E}^+ + \vec{E}^-) = 2 R \theta^x \hat{n} \times (\vec{E}^+ - \vec{E}^-)$$

where

$$R = \frac{iZ}{kt(\epsilon - 1)} \quad \text{and} \quad R^x = \frac{iY\epsilon}{kt(\epsilon - 1)}$$

A similar reduction has been carried out for magnetic materials. For general materials the procedure reduces the number of variables from 6 to 4, when solving for the current densities corresponding to a finite size thin scatters. It could of course improve the accuracy of the physical optics method for finite plates as well.

In addition to the application to half-planes in Ref. D, these boundary conditions have been used by M. Ricoy and J.L. Volakis to solve 2-dimensional scattering problems for structures of arbitrary cross-section, formulated as two coupled 2-dimensional integral equations. However in analytically eliminating the computational inaccuracy inherent in evaluating the integrals within the self cell and adjacent cells they did not employ the zero thickness approximation.

Typical Structures:



Homogeneous



Layered
Transversely



Layered
Longitudinally

The method can be used to generate simple asymptotic results for scattering and diffraction as was done by Herman and Volakis using the simpler single current sheet models of thin layers. [M.I. Herman and J.L. Volakis, "High frequency scattering by a resistive strip and extensions to conductive and impedance strips", *Radio Science*, **22**, 335-349 (1987).] The method involves a uniform asymptotic evaluation of the multiply diffracted fields from the edges.

Blank

AVERAGE INTENSITY SCATTERED BY DENSELY DISTRIBUTED NONSPHERICAL PARTICLES

Y. Ma, V.V. Varadan and V.K. Varadan
Research Center for the Engineering of Electronic and Acoustic Materials
Department of Engineering Science and Mechanics
The Pennsylvania State University
University Park, PA 16802

RECENT PUBLICATIONS, SUBMITTALS FOR PUBLICATION AND PRESENTATIONS:

- A) V.V. Varadan, V.K. Varadan and Y. Ma, "EM wave propagation in discrete random media: nonspherical statistics," in Proceedings of the 1986 CRDC Scientific Conference on Obscuration and Aerosol Research.
- B) V.V. Varadan, V.K. Varadan, Y. Ma, and W.A. Steele, "Effects of nonspherical statistics on EM wave propagation in discrete random media," *Radio Science* 22, No. 4, 491 (1987).
- C) Y. Ma, V.V. Varadan and V.K. Varadan, "Calculations of the incoherent intensity for random media containing nonspherical scatterers," Presented at the URSI Radio Science Meeting, Blacksburg, Virginia, June 1987.
- D) V.V. Varadan, Y. Ma and V.K. Varadan, "Scattered intensity of a wave propagating in a discrete random medium," submitted to *Applied Optics*, August 1987.

ABSTRACT

This paper investigates the second moment (average intensity) of an EM wave field propagating in a medium containing densely distributed nonspherical scatterers whose positions are random. The effective propagation constant K obtained from our previous work, using the nonspherical statistics in the investigation of multiple EM wave scattering by aligned prolate and oblate dielectric spheroids, and the appropriate pair correlation function for nonspherical scatterers obtained by the Monte Carlo method are required in implementing the moment equation to get the numerical results for intensity. The comparison between the results using correct nonspherical statistics and approximated spherical statistics indicates that even a small difference for the effective propagation constant K will produce a remarkable difference in intensity. Numerical results for average intensity scattered by spherical particles using our intensity formalism are also presented and compared with some microwave measurements. The extension of the present work is to study wave propagation in a medium containing a random distribution of randomly oriented nonspherical scatterers and investigate the isotropic properties of the medium.

INTRODUCTION

The statistical moments of a wave propagating in a random medium are of great interest for use in communication, probing and remote sensing. The present paper following the trace of our previous work, in which the first moment of a random wave field has been carefully investigated using appropriate statistics, starts to examine the effects of nonspherical statistics on the second moment (average intensity) of a wave field propagating in a medium consisting of randomly distributed nonspherical scatterers. In our intensity formalism, shape factor, size

distribution, orientation distribution and physical properties of scatterers can all be considered, however, the intensity equation for densely distributed scatterers requires the pair correlation function which is available at the present time only for simple shaped scatterers with special alignments.

To make the problem tractable, nonspherical scatterers with rotational symmetry properties randomly distributed in free space are first considered. Scatterers of this kind whose scattering responses are able to be represented by the T-matrix [Varadan and Varadan, 1980]. Further, we consider only the aligned case which means the symmetry axes of the scatterers are all parallel to the direction of the incident wave.

In the calculation of intensity, without losing generality, we used the distorted Born approximation in the intensity equation in which the required effective propagation constant K is obtained from our previous work [Varadan et al., 1986, 1987] using the nonspherical statistics in the investigation of multiple EM wave scattering by aligned prolate and oblate dielectric spheroids. The pair correlation function for nonspherical scatterers is obtained by the Monte Carlo method which has been introduced in our paper [Varadan, et al, 1987]. The comparison between the results using correct nonspherical statistics and approximated spherical statistics indicates that even a small difference for the effective propagation constant K will produce a remarkable difference in intensity. Numerical results for average intensity scattered by spherical particles using our intensity formalism are also presented and compared with some microwave measurements.

MULTIPLE SCATTERING FORMULATION FOR THE INTENSITY

We consider $N(N \rightarrow \infty)$ rotationally symmetric oriented scatterers randomly distributed in a volume $V(V \rightarrow \infty)$ so that the number of particles per unit volume $n_0 = N/V$ is finite. For the scattering of waves by those scatterers located at r_1, r_2, \dots, r_N , we represent the total field outside the scatterer by

$$U(r) = u_0(r) + \sum u_j(r - r_j) \quad (1)$$

where u_0 is the incident wave field and u_j the field scattered from the j -th scatterer. If the scatterers are randomly distributed in space, the total field can be divided into two parts and expressed as

$$U(r) = \langle U(r) \rangle + v \quad (1-a)$$

We call $\langle U(r) \rangle$ or $\langle U \rangle$ the average or coherent field and v the fluctuation or incoherent field. The angular brackets $\langle \rangle$ represent the configuration or ensemble average whose definition is quite common in statistics.

Similarly, we average the "intensity" (or the second moment of the field) $|U|^2$ over the ensemble, and write the "average total intensity" as

$$\begin{aligned} \langle |U|^2 \rangle &= |\langle U \rangle|^2 + \langle |v|^2 \rangle \\ &= |\langle U \rangle|^2 + V \end{aligned} \quad (2)$$

where $|\langle U \rangle|^2$ is the coherent intensity and can be determined if the average field $\langle U \rangle$ is known. However, the incoherent intensity V which is the ensemble average of the absolute square of the field fluctuation is not a directly obtainable quantity. By the use of (1) and some operation rules for the configuration average, the incoherent intensity V in (2) can be written as

$$V = \sum \langle |u_j|^2 \rangle + \sum \sum \langle u_k u_j^* \rangle - \sum \sum \langle u_k \rangle \langle u_j^* \rangle \quad (3)$$

where the superscript "*" represents the complex conjugate of the attached quantity. (3) is a finite sum though "N",

the number of scatterers, can be fairly large; its computation becomes impractical even for a moderate N and in most cases impossible. In terms of an appropriate probability distribution function and the conditional configuration average, (3) can be expressed in the following integral form

$$\begin{aligned}
 V &= n_0 \int \langle |u_j|^2 \rangle_j dr_j \\
 &+ n_0^2 \iint \langle u_k u_j^* \rangle_{jk} G(r_{jk}) dr_k dr_j \\
 &- n_0^2 \iint \langle u_k \rangle_k \langle u_j^* \rangle_j dr_k dr_j
 \end{aligned} \tag{4}$$

where $\langle \cdot \rangle_j$ and $\langle \cdot \rangle_{jk}$ are conditional configuration averages holding the positions of the j -th and both the j -th and k -th scatterers fixed, respectively. $G(r_{jk})$ the pair correlation function, for aligned spheroidal particles, can be expanded in the Legendre polynomials as [Varadan et al., 1987]

$$G(r) = \sum_n g_n(r) P_n(\cos\theta)$$

where the coefficients depend on the distance between particles and azimuthal angle and implicitly on the concentration of scatterers. For spherical scatterers, the pair correlation function becomes the radial distribution function $g(r_{jk})$ upon which spherical statistics bases. Eq. (4) is an exact expression for the incoherent intensity V .

If the scatterer locations are random and independent of one another, only the first term on the RHS of (4) remains. This is the single scattering approximation to the intensity. Otherwise, in addition to incoherent single scattering, a relatively coherent intensity appears as the contribution of the second term grows. As the concentration of scatterers increases a local order is introduced in the near field of the scatterers since the particles can only be packed in a limited number of ways. In order to proceed further with the computation of the incoherent intensity as stated in (4), we need expressions for $\langle u_j \rangle_j$; $\langle |u_j|^2 \rangle_j$; and $\langle u_k u_j^* \rangle_{jk}$.

Distorted Born Approximation

In order to calculate the incoherent intensity V from (4) an approximation needs to be made for $\langle |u_j|^2 \rangle_j$ as well as for $\langle u_k u_j^* \rangle_{jk}$, which are both unknown. If we consider only first order scattering, we can use the distorted Born approximation (DBA) as follows:

$$\langle u_k u_j^* \rangle_{jk} \approx \langle u_k \rangle_k \langle u_j^* \rangle_j. \tag{5}$$

This approximation was used by Twersky [Twersky, 1957] in solving the rough surface scattering problems and has subsequently been used by several other authors. Using (5), in the distorted Born approximation, (4) can thus be written as

$$\begin{aligned}
 V &= n_0 \int \langle u_j \rangle_j \langle u_j^* \rangle_j dr_j \\
 &+ n_0^2 \iint \langle u_k \rangle_k \langle u_j^* \rangle_j [G(r_{jk}) - 1] dr_k dr_j.
 \end{aligned} \tag{6}$$

Equation (6) represents the incoherent intensity in the DBA. Its source is the coherent field, $\langle u_j \rangle_j$. Later we show that the average scattered field $\langle u_j \rangle_j$ is related to the average exciting field when we neglect the field fluctuations in the field exciting a scatterer. Equation (6) tells us that the second term has a contribution to the intensity whenever the i -th and j -th scatterers are close to each other (position dependence), otherwise the contribution can be neglected. Eq. (6) is a deterministic equation since only the average exciting field is involved and the calculation is straight forward as long as the pair correlation function is known.

Implementation of the T-Matrix

To compute the intensity in the DBA, or to proceed further with the analysis of (4), we need an expression for the coherent field. For a single scatterer, the scattered field from the j -th scatterer can be expressed as

$$u_j = \sum f_n^j \Psi_n^j \quad (7)$$

where f_n^j are the scattered field coefficients and Ψ_n^j the outgoing functions (Hankel functions). The scattered field coefficients f_n^j and the exciting field coefficients α_n^j are related through the T matrix [Varadan and Varadan, 1980]:

$$f_n^j = \sum T_{nn}^j \alpha_n^j \quad (8)$$

Substituting (8) into (7) and taking the conditional configuration average, we have

$$\langle u \rangle_j = \sum \sum \langle T_{nn}^j \alpha_n^j \Psi_n^j \rangle_j \quad (9)$$

Further, to simplify the computation, we assume the shape, size, and physical properties of all the scatterers are independent of their positions. In such a case, (9) can be written as

$$\langle u \rangle_j = \sum \sum T_{nn}^j \langle \alpha_n^j \rangle_j \Psi_n^j \quad (10)$$

where the exciting field coefficients of the j -th scatterer can be shown to be [Varadan et al., 1985]

$$\alpha_n^j = a_n^j + \sum \sum \sigma_{nn'}(r_k - r_j) T_{n'n}^{k} \alpha_n^{k'} \quad (11)$$

In (11), a_n^j are the incident field coefficients of the j -th scatterer and $\sigma_{nn'}$ is the translation matrix for spherical wave functions. Although α_n^j are, in general, unknown for a random distribution of scatterers, their conditional average $\langle \alpha_n^j \rangle_j$ (average exciting field coefficients of the j -th scatterer whose position is fixed) are assumed to have the following form [Varadan et al., 1985]

$$\langle \alpha_n^j \rangle_j = X_n \exp(i K k_0 \cdot r_j) \quad (12)$$

which states that for an incident plane wave field, the average exciting field propagates with a new propagation constant K along the incident wave direction k_0 . The new propagation constant K is complex and frequency dependent and can be obtained by solving the dispersion equation [Varadan et al., 1986].

RESULTS AND DISCUSSION

In order to show the effect of nonspherical statistics on intensity, results based on the approximation for randomly distributed spheroids using single scattering theory and the spherical statistics (Circumscribing Sphere Approximation and Equivalent Volume Approximation [Varadan et al., 1986] are compared with those using nonspherical statistics. We have picked values of the effective wavenumber, which is obtained using the nonspherical statistics in the investigation of multiple EM wave scattering by aligned prolate and oblate dielectric spheroids [Varadan et al., 1987], and used them to compute the intensity and show the results in Figs 1 and 2. One sees from both figures that, off-forward scattering at the fixed frequency as well as forward scattering at different frequencies, without using the correct pair statistics for nonspherical scatterers, the computed intensities are quite different from case to case. This fact explains why it is necessary to introduce the nonspherical statistics into the intensity calculation.

To check the validity of our formalism, we compared our incoherent intensity calculations with the microwave experiments conducted by Beard et al. [1965]. The transmitted intensity was calculated using the DBA as given in

(6) where $\theta = 0^\circ$ represents the forward direction. This calculation is based on the experimental set-up which consists of a slab region styrofoam container, for various concentrations of scatterers at the fixed frequency. For the case $ka = 20.8$ for tenuous scatterers with relative index of refraction 1.016 the computed results match very well with the measurements for off-forward scattering as depicted in Fig. 3.

REFERENCES

- C.I. Beard, T.H. Kays and V. Twersky, "Scattered intensities for random distributions - microwave data and optical applications," *App. Opt.* 4, 1299 (1965).
- V. Twersky, "On scattering and reflection of sound by rough surfaces," *J. Acoust. Soc. Am.* 29, 209 (1957).
- V.K. Varadan and V.V. Varadan, eds., *Acoustic, Electromagnetic and Elastic Wave Scattering-Focus on the T-matrix Approach*, Pergamon Press, New York, 1980.
- V.V. Varadan, Y. Ma and V.K. Varadan, "Propagator model including multiple fields for discrete random media," *J. Optical Soc. Am.* 78(5), 1879 (1985).
- V.V. Varadan, V.K. Varadan and Y. Ma, "EM wave propagation in discrete random media: nonspherical statistics," in the Proceedings of the 1986 CRDC Scientific Conference on Obscuration and Aerosol Research.
- V.V. Varadan, V.K. Varadan, Y. Ma, and W.A. Steele, "Effects of nonspherical statistics on EM wave propagation in discrete random media," *Radio Science* 22, No. 4, 491 (1987).
- V.V. Varadan, V.K. Varadan and Y. Ma, "Multiple scattering of waves in random media containing non-spherical scatterers," in the Electromagnetic Wave Propagation Panel Symposium sponsored by AGARD, NATO, 1987.
- V.V. Varadan, Y. Ma and V.K. Varadan, "Scattered intensity of a wave propagating in a discrete random medium," submitted to *Applied Optics*, August 1987.

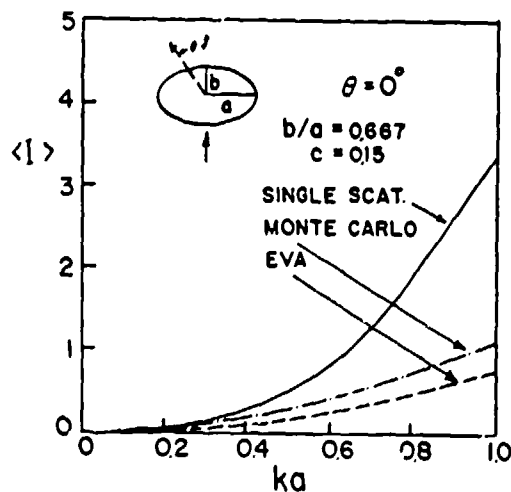


Fig. 1 Forward scattered incoherent intensity versus nondimensional frequency ka . (oblate spheroid $b/a = 0.667$, $c = 0.15$)

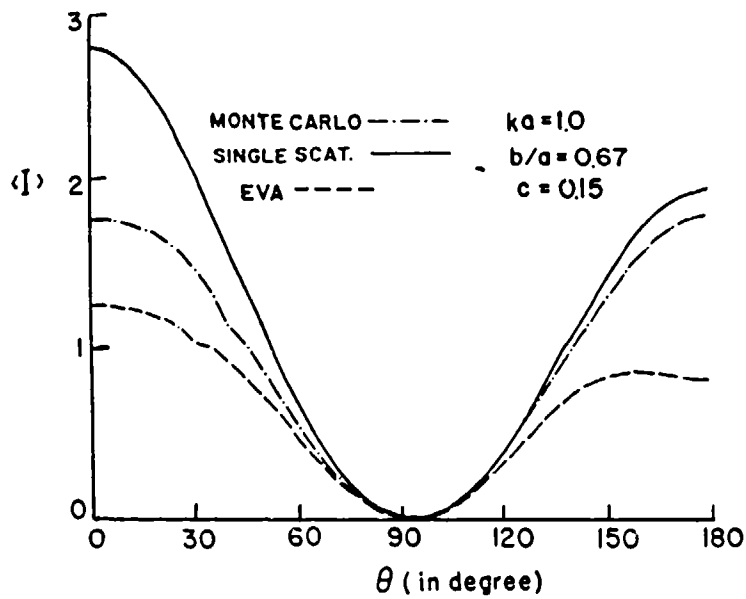


Fig. 2 Incoherent intensity versus scattering angle at $ka = 1.0$.
(oblate spheroid $b/a = 0.667$, $c = 0.15$)

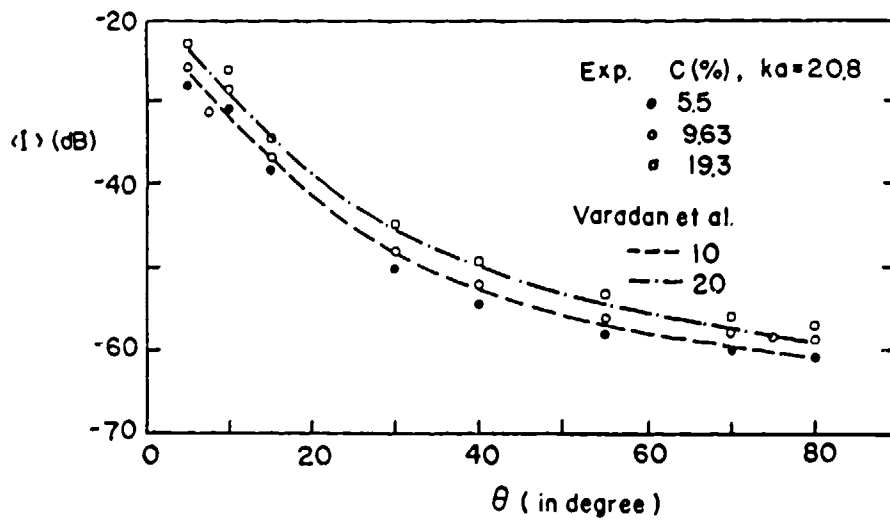


Fig. 3 Incoherent intensity : Comparison with microwave experiments [Beard et al., 1965]

BACKSCATTER ENHANCEMENT OF INFRARED AND OPTICAL RADIATION FROM FINITELY CONDUCTING PARTICLES WITH SMOOTH AND VERY ROUGH SURFACES--FIRST ORDER AND MULTIPLE SCATTER

Ezekiel Bahar and Mary Ann Fitzwater
Electrical Engineering Department
University of Nebraska-Lincoln
Lincoln, Nebraska 68588-0511

RECENT PUBLICATIONS, SUBMITTALS FOR PUBLICATION AND PRESENTATIONS:

- A) E. Bahar, "Co-Polarized and Cross-Polarized Incoherent Diffuse Specific Intensities for Linearly Polarized Excitations of Irregular Shaped Particles," 1986 CRDC Scientific Conference on Obscuration and Aerosol Research, Aberdeen, Maryland, June 23-27, 1986.
- B) E. Bahar, "Extinction Cross Sections and Albedos for Particles with Very Rough Surfaces," 1986 CRDC Scientific Conference on Obscuration and Aerosol Research, Aberdeen, Maryland, June 23-27, 1986.
- C) E. Bahar, "Scattering and Depolarization of Linearly Polarized Waves by Finitely Conducting Particles of Irregular Shape," 1986 International Union of Radio Science, Commission F Symposium on Wave Propagation: Remote Sensing and Communications, University of New Hampshire, Durham, New Hampshire, July 28-August 1, 1986.
- D) E. Bahar, "Application of Full Wave Theory to Computer Aided Geometric Design," 20th Midwest Symposium on Circuits and Systems, University of Nebraska-Lincoln, August 11-12, 1986.
- E) E. Bahar, "Incoherent Diffuse Scattering by Irregular Shaped Particles of Finite Conductivity," International Union of Radio Science (URSI) Symposium on Electromagnetic Theory, Budapest, Hungary, August 25-29, 1986.
- F) E. Bahar, "SEASAT Microwave Altimeter Measurement of the Ocean Gravity-Wave Equilibrium-Range Spectral Behavior Using Full Wave Theory," 1986 International Geoscience and Remote Sensing Symposium (IGARSS '86), University of Zurich-Itchel, Switzerland, September 8-11, 1986.
- G) E. Bahar, "Scattering and Depolarization by Rough Terrain and Vegetation Covered Terrain--Unified Full Wave Approach," Fall 1986 Electromagnetic Wave Propagation Panel Symposium on "Terrestrial Propagation Characteristics on Modern Systems of Communications Surveillance, Guidance and Control," Sponsored by Advisory Group for Aerospace Research and Development (NATO), Ottawa, Canada, October 20-24 1986.
- H) E. Bahar, "Scattering and Depolarization by Layers of Particles with Rough Surfaces Excited at Oblique Incidence," International Union of Radio Sciences (URSI) Meeting at the University of Colorado, Boulder, January 12-15, 1987.
- I) E. Bahar, "Scattering from Random Rough Surfaces and Random Media Consisting of Irregular Shaped Particles," U. S. Army Research Office Workshop on "Propagation in Random Media, Scattering from Rough Surfaces," Washington, D. C., March 23-25, 1987.
- J) E. Bahar, "Multiple Scattering Effects of Random Distributions of Irregularly Shaped Particles on Infrared and Optical Propagation," Spring 1987 Electromagnetic Wave Propagation Panel Specialists' Meeting on Scattering and Propagation in Random Media sponsored by Advisory Group for Aerospace Research and Development (NATO), Rome, Italy, May 18-22, 1987.
- K) E. Bahar, "Enhancement of Backscatter from Random Rough Surfaces--Full Wave Solution," 1987 IEEE AP-S International Symposium and URSI Radio Science Meeting, Virginia Tech., Blacksburg, Virginia, June 15-19, 1987.
- L) E. Bahar, "Backscatter Enhancement of Infrared and Optical Radiation from Finitely Conducting Particles with Smooth and Very Rough Surfaces--First Order and Multiple Scatter," 1987 CRDC Scientific Conference on Obscuration and Aerosol Research, Aberdeen, Maryland, June 22-26, 1987.
- M) E. Bahar, "Radar Cross Section of Rough Terrain and Vegetation Covered Terrain," XXII General Assembly of the International Union of Radio Science, Tel Aviv, Israel, August 24-September 2, 1987.
- N) E. Bahar, "Multiple Scattering in Media Consisting of Nonspherical Finitely Conducting Particles," with M. A. Fitzwater, .roceedings of the 1985 CRDC Scientific Conference on Obscuration and Aerosol Research, in press.
- O) E. Bahar, "Scattering and Depolarization by Conducting Cylinders with Rough Surfaces," with M. A. Fitzwater, Applied Optics, Vol.25, pp. 1826-1832, June 1986.
- P) E. Bahar, "Full Wave Solutions for Electromagnetic Scattering and Depolarization in Irregular Stratified Media," Special Issue of Radio Science on Waves in Inhomogeneous Media, Vol. 21, No. 4, pp. 543-550, July-August 1986.
- Q) E. Bahar, "Multiple Scattering by Conducting Particles with Random Rough Surfaces at Infrared and Optical Frequencies," with M. A. Fitzwater, Radio Science, Vol. 21, No. 4, pp. 689-706, July-August 1986.
- R) E. Bahar, "Co-Polarized and Cross-Polarized Incoherent Diffuse Intensities Scattered by Finitely Conducting Particles of Irregular Shape," with M. A. Fitzwater, Proceedings of the 1986 International Union of Radio Science Symposium on Wave Propagation and Remote Sensing, Durham, New Hampshire, pp. 4.2.1-4.2.4, August 1986.

- S) E. Bahar, "Extinction Cross Sections and Albedos for Particles with Very Rough Surfaces," with S. Chakrabarti and M. A. Fitzwater, Applied Optics, Vol. 25, No. 15, pp. 2530-2536, August 1986.
- T) E. Bahar, "Scattering and Depolarization of Linearly Polarized Waves by Finitely Conducting Particles of Irregular Shape," with M. A. Fitzwater, Journal of Applied Physics, Vol. 60, No. 6, pp. 2123-2132, September 1986.
- U) E. Bahar, "Incoherent Diffuse Scattering by Irregular Shaped Particles of Finite Conductivity," with M. A. Fitzwater, Proceedings of the International Radio Science Union Symposium on Electromagnetic Theory, Budapest, Hungary, pp. 63-65, August 1986.
- V) E. Bahar, "SEASAT Microwave Altimeter Measurement of the Ocean Gravity-Wave Equilibrium-Range Spectral Behavior Using Full Wave Theory," Proceedings of the 1986 International Geoscience and Remote Sensing Symposium, IGARSS 1986, Zurich, USA, SP-254, pp. 1345-1349, September 1986.
- W) E. Bahar, "Scattering and Depolarization by Random Rough Terrain and Vegetation Covered Terrain--Unified Full Wave Approach," Proceedings of the Advisory Group for Aerospace Research and Development (NATO) on Terrestrial Propagation Characteristics in Modern Systems of Communication, Surveillance, Guidance and Control, AGARD-CP-407, pp. 4.1-4.14, October 1986.
- X) E. Bahar, "Scattering and Depolarization by Random Rough Surfaces, Unified Full Wave Approach--An Overview," Proceedings of the International Symposium on Multiple Scattering of Waves in Random Media and Random Rough Surfaces, Editors, V. V. Varadan and V. K. Varadan, pp. 715-733, Pennsylvania State University, 1987.
- Y) E. Bahar, "Application of Full Wave Theory to Computer Aided Geometric Design," with S. Chakrabarti, Proceedings of the 29th Midwest Symposium on Circuits and Systems, Editor, M. Ismail, pp. 911-915, North Holland, NY 1987.
- Z) E. Bahar, "Co-Polarized and Cross-Polarized Incoherent Specific Intensities for Waves at Oblique Incidence Upon Layers of Finitely Conducting Particles of Irregular Shape," with M. A. Fitzwater, Journal of the Optical Society of America A, Vol. 4, pp. 41-56, January 1987.
- AA) E. Bahar, "Review of the Full Wave Solutions for Rough Surface Scattering and Depolarization--Comparisons with Geometric and Physical Optics, Perturbation and Two-Scale Solutions," Journal of Geophysical Research, Vol. 92, No. 65, pp. 5209-5224, May 15, 1987.
- BB) E. Bahar, "Full Wave Theory Applied to Computer Aided Graphics for Three Dimensional Objects," with S. Chakrabarti, IEEE Computer Graphics and Applications, Special Issue, Supercomputers for Graphics, Vol. 7, No. 7, pp. 46-60, July 1987.
- CC) E. Bahar, "Comparison of Unified Full-Wave Solutions for Normal-Incidence Microwave Backscatter from Sea with Physical Optics and Hybrid Solutions," with D. E. Barrick and M. A. Fitzwater, International Journal of Remote Sensing, in press.
- DD) E. Bahar, "Albedos and Extinction Cross Sections for Particles with Very Rough Surfaces," with S. Chakrabarti and M. A. Fitzwater, Proceedings of the 1986 CRDC Scientific Conference on Obscuration and Aerosol Research, in press.
- EE) E. Bahar, "Co-Polarized and Cross-Polarized Incoherent Diffuse Specific Intensities for Linearly Polarized Excitation of Irregular Shaped Particles," with M. A. Fitzwater, Proceedings of the 1986 CRDC Scientific Conference on Obscuration and Aerosol Research, in press.
- FF) E. Bahar, "Incoherent Diffuse Scattering by Irregular Shaped Particles of Finite Conductivity," Invited paper in special issue of Radio Science, in press.
- GG) E. Bahar, "Multiple Scattering Effects of Random Distributions of Irregularly Shaped Particles on Infrared and Optical Propagation," with M. A. Fitzwater, Proceedings of the Advisory Group for Aerospace Research and Development (NATO) Spring 1987 Electromagnetic Wave Propagation Panel Symposium "Scattering and Propagation in Random Media," in press.
- HH) E. Bahar, "Full Wave Theory and Controlled Optical Experiments for Enhanced Scattering and Depolarization by Random Rough Surfaces," with M. A. Fitzwater, Optics Communications, in press.
- II) E. Bahar, "Generalized Fourier Transforms for the Acoustic Pressure and Velocity in Compressible Viscous Stratified Media," submitted for review.
- JJ) E. Bahar, "Scattering of Acoustic Waves in Irregular Layered Media--Full Wave Solutions," submitted for review.
- KK) E. Bahar, "Full Wave Solutions for the Scattering of Acoustic Waves Excited by Arbitrary Source Distributions in Irregular Layered Media," submitted for review.
- LL) E. Bahar, "Enhancement of the Backscattered Diffuse Specific Intensities from Random Distributions of Finitely Conducting Particles with Rough Surfaces," with M. A. Fitzwater, submitted for review.
- MM) E. Bahar, "Use of the Full Wave Approach to Demonstrate the Respective Regions of Validity of the Perturbation, Physical Optics and Hybrid Solutions for Electromagnetic Scattering by Random Rough Surfaces," submitted for review.
- NN) E. Bahar, "Physical Interpretation of the Full Wave Solutions for the Electromagnetic Fields Scattered from Irregular Stratified Media," submitted for review.

ABSTRACT

The incoherent diffuse specific intensities (modified Stokes parameters) backscattered from a parallel layer consisting of random distributions of finitely conducting particles with smooth and rough surfaces are evaluated. The normally and obliquely incident excitations at infrared and optical

frequencies are vertically or horizontally polarized. The particle surface roughness, which is characterized by its joint probability density function, is assumed to be sufficiently rough in order to significantly effect the diffuse specific intensities. Thus the full wave approach is used to determine the phase matrix as well as the extinction coefficient that appears in the equation of radiative transfer. The enhanced backscattered intensities that depend upon the particle surface roughness are compared with the enhanced backscatter that is associated with Mie scattering from smooth spherical particles. The enhanced backscattered diffuse specific intensities are evaluated for different particle sizes, complex permittivities, roughness parameters and excitations. The effects of varying the optical thickness of the layer are also considered. Since the enhanced backscatter phenomenon reported here is primarily due to the particle surface roughness it appears in both the first order and the multiple scatter solutions of the radiative transfer equations.

1. INTRODUCTION

The incoherent diffuse specific intensities (modified Stokes parameters) backscattered from a parallel layer consisting of random distributions of finitely conducting particles are derived for vertically and horizontally polarized excitations at infrared and optical frequencies. Normal incidence and oblique incidence are considered, thus the incident electric field is parallel or perpendicular to the scattering plane.

Both smooth spherical particles as well as spherical particles with two dimensional random rough surfaces are considered. The particle rough surface height (measured normal to the unperturbed spherical surface) is characterized by its joint probability density function which is related to the surface height correlation function or its spectral density function. A unified full wave approach that accounts for specular point as well as diffuse (Bragg) scattering in a self-consistent manner is used to derive the expressions for the phase matrix and the extinction coefficient appearing in the equation of radiative transfer (Bahar et al. 1986, 1987a).

By comparing the results for the specific intensities backscattered from both smooth and rough particles with different sizes, roughness parameters and complex permittivities it is possible to distinguish between the phenomenon of enhanced backscatter due to Mie scatter from spherical particles and enhanced backscatter due to the diffuse scatter generated by the rough surface of the particle. The polarization dependence of the backscattered diffuse specific intensities at normal and oblique incidence as well as the effects of varying the optical thickness of the layer of particles are considered in the illustrative examples.

2. FORMULATION OF THE PROBLEM

In this section, the principal equations leading to the solution of the incoherent diffuse specific intensities (modified Stokes parameters) are formulated for a layered medium consisting of a random distribution of irregularly shaped particles characterized by their random surface height spectral density functions and finite conductivity (see Fig. 1). Of particular concern in this work is the phenomenon of enhanced backscatter. The average surface of the particles is assumed to be spherical with radius a , between 2.5 and 5 wavelengths λ . The random surface height h , measured normal to the unperturbed spherical particle, is assumed to have a Gaussian probability density with

mean square height $\langle h^2 \rangle$, such that the roughness parameters $\beta = 4k_0^2 \langle h^2 \rangle$ varies between ten and forty. Thus the perturbation technique (Rice 1951) cannot be used to account for diffuse scattering due to particle surface roughness. The full wave technique which accounts for specular point as well as Bragg scatter in a unified self-consistent manner (Bahar and Fitzwater 1984) is used here to determine the fields scattered by the particles with rough surfaces. The backscatter incoherent diffuse specific intensities are derived for both the smooth and rough particles in order to distinguish between enhanced backscatter inherent in the Mie solution for spherical particles and the enhanced backscatter that can be attributed to the effects of the surface roughness of the irregular finitely conducting particles.

Linearly polarized electromagnetic waves are assumed to be normally or obliquely incident upon a parallel layer of irregularly shaped particles (see Fig. 2). The radius vector from the center to the surface of the particle is

$$\vec{r}_s = (a+h)\vec{a}_r \quad (2.1)$$

in which the random rough surface height is characterized by the two dimensional spectral density function W or its Fourier transform, the autocorrelation function $\langle hh' \rangle$, a is its average radius, and \vec{a}_r is the unit radius vector.

The incoherent diffuse specific intensity matrix $[I]$ satisfies the equation of radiative transfer (Chandrasekhar 1950; Ishimaru 1978).

$$\mu \frac{d[I]}{d\tau} = -[I] + \int [S][I'] d\mu' d\phi' + [I_1] \quad (2.2)$$

in which the elements of the column matrix $[I]$ are the modified Stokes parameters (Ishimaru 1978).

A suppressed $\exp(i\omega t)$ time dependent excitation is assumed. The vertically and horizontally polarized components of the electric field are E_1 and E_2 respectively. The optical distance τ is measured in the z direction, normal to the plane of the parallel layer (see Fig. 2). The matrices $[I]$ and $[I']$ represent the incoherent diffuse intensities for waves scattered by the particles in the direction $\theta = \cos^{-1} \mu$ and ϕ and for waves incident on the particles in the direction $\theta' = \cos^{-1} \mu'$ and ϕ' respectively. The 4×4 scattering (phase) matrix $[S]$ in the reference coordinate system (x, y, z) (see Fig. 2) is expressed in terms of the scattering matrix $[S']$ associated with the scattering plane (that contains the incident and scatter wave normals \vec{n}^i and \vec{n}^f respectively) through the following transformation

$$[S] = [\mathcal{L}(-\pi+\alpha)][S'][\mathcal{L}(\alpha')] \quad (2.3)$$

In (2.3) $[S']$ is the weighted sum of two matrices

$$[S'] = |\chi(\vec{v} \cdot \vec{a}_r)|^2 [S_{MIE}] + [S_D] \quad (2.4)$$

where $[S_{MIE}]$ is obtained from the Mie solution for finitely conducting spherical particles of radius a (Ishimaru 1978) and $[S_D]$ is the diffuse scattering contribution to the matrix $[S']$ due to the particle

surface roughness (Bahar and Fitzwater 1987a). The full wave approach is used to determine the elements of $[S_D]$. The quantity χ in (2.4) is the scattering particle's random rough surface height characteristic function. The coefficient $|\chi|^2$ in (2.4) accounts for the degradation of the specular point contribution to the scattered fields by the rough surface ($|\chi|^2 \leq 1$ and as $\beta \rightarrow 0, |\chi|^2 \rightarrow 1$). For $k_0 a \gg 1$ the Mie solution $[S_{MIE}]$ accounts for the specularly reflected waves as well as the shadow forming wave scattered by the spherical particle. Thus in view of the coefficient $|\chi|^2$, as β increases the contribution to $[S']$ due to specular scatter decreases, while the diffuse scattering contribution $[S_D]$ increases. The transformation matrices $[L]$ in (2.3) are expressed in terms of the angle α' between the reference plane of incidence and the scattering plane and the angle α between the scattering plane and the reference plane of scatter (see Fig. 2) (Bahar and Fitzwater 1987a).

Since in this work it is assumed that linearly polarized waves (vertical, (V) or horizontal, (H)) are obliquely incident upon a parallel layer of optical thickness τ_0 containing a random distribution of irregularly shaped particles, the incident Stokes matrix at $z=0$ is

$$[I_{inc}^P] = [I_0^P] \delta(\mu' - \mu) \delta(\phi') \quad (2.5)$$

in which $\mu^i = \cos \theta^i$, the direction of the incident wave is $(\theta^i, 0)$, $\delta(\cdot)$ is the Dirac delta function and

$$[I_0^V] = \begin{bmatrix} 1 \\ 0 \\ 0 \\ 0 \end{bmatrix} \quad [I_0^H] = \begin{bmatrix} 0 \\ 1 \\ 0 \\ 0 \end{bmatrix} \quad (2.6)$$

Thus the reduced incident intensity is

$$[I_{r1}] = [I_{inc}^P] \exp(-\tau/\mu^i) \quad (2.7)$$

and the (4x1) excitation matrix in (2.2) is

$$[I_1] = \int [S][I_{r1}] d\mu' d\phi' \equiv [F] \exp(-\tau/\mu^i) \quad (2.8)$$

where the (4x1) matrix $[F]$ is

$$[F] = [S][I_0^P] \Big|_{\substack{\mu' = \mu^i \\ \phi' = 0}} \quad (2.9)$$

and the matrix $[I_0^P]$ (P=V,H) is defined by (2.6). Using a Fourier series expansion for the diffuse specific intensities and the matrices $[S]$ and $[F]$, (Ishimaru et al. 1982, Bahar and Fitzwater 1987a) the equation of radiative transfer for the m^{th} component of the Fourier series expansion can be written as follows

$$\mu \frac{d}{d\tau} [I]_m = -[I]_m + \int_{-1}^1 [S]_m [I']_m d\mu' + [I]_m \exp(-\tau/\mu^i) \quad (2.10)$$

For details of the analysis see Bahar and Fitzwater 1987b where only forward scatter is considered.

3. ILLUSTRATIVE EXAMPLES

The particle random two dimensional rough surface height h (measured normal to the unperturbed surface) is assumed in this work to be homogeneous and isotropic with a Gaussian probability density. The unperturbed surface is assumed to be spherical (2.1). Thus, the rough surface height autocorrelation function $\langle h(\vec{r})h(\vec{r}') \rangle = \langle hh' \rangle$ is only a function of the distance $\vec{r}_d = |\vec{r} - \vec{r}'| = (x_d^2 + z_d^2)^{1/2}$ measured along the surface of the spherical particle of radius a . It is also assumed that the rough surface correlation distance r_c (where $\langle hh' \rangle = \langle h^2 \rangle \exp(-1)$) is smaller than the circumference of the particle.

The two dimensional surface height spectral density function $W(v_x, v_z)$ is the two dimensional Fourier transform of the surface height autocorrelation function $\langle hh' \rangle$ (Bahar and Fitzwater 1987b). In these illustrative examples the following special form is assumed for the surface height spectral density function.

$$W(v_T) = \frac{2C}{\pi} \left[\frac{v_T}{v_T^2 + v_m^2} \right]^8 \quad (3.1)$$

in which the constant C has the dimension of (meters)⁻⁴. The above expression for $W(v_T)$ vanishes for $v_T \rightarrow 0$ and $v_T \rightarrow \infty$ and its peak value is $W(v_T = v_m) = C/128\pi v_m^8$. Thus the choice of the constant v_m determines the dominant scales of the surface roughness. The surface height normalized autocorrelation function R is given in closed form in terms of the modified Bessel functions of the second kind of order zero and one, K_0 and K_1 , respectively.

$$R(\xi) = \left[1 - \frac{3\xi^2}{8} + \frac{3\xi^4}{32} + \frac{\xi^6}{3072} \right] \xi K_1(\xi) + \left[\frac{1}{2} - \frac{\xi^2}{4} + \frac{\xi^4}{96} \right] 2K_0(\xi) = \langle hh' \rangle / \langle h^2 \rangle \quad (3.2)$$

in which the dimensionless argument is

$$\xi = v_m r_d \quad (3.3)$$

Three cases are considered at infrared and optical frequencies

Case (a) $\lambda = 0.555\mu\text{m}$, $D = 10\lambda$, $\epsilon_r = -40-112$ (aluminum)

Case (b) $\lambda = 10\mu\text{m}$, $D = 5\lambda$, $\epsilon_r = 1.5-18$ (dissipative dielectric)

Case (c) $\lambda = 10\mu\text{m}$, uniform distribution of $D/\lambda = 5, 5.5, 6, 6.5, 7, 7.5$ and 8

$\epsilon_r = 1.5-18$ (dissipative dielectric)

In all the following illustrations the diffuse scattering intensities are given for the particles with the smooth and the rough surfaces and both first order scatter (solid lines) and multiple scatter results are presented.

In Figures 3 and 4 the backscattered specific intensities I_1 and I_2 respectively, are plotted as functions of the scatter angle θ . The excitation at $\lambda = 0.555\mu\text{m}$ (case a) is normally incident and linearly polarized with the electric field in the \vec{a}_x direction. The optical thickness of the layer is

$\tau_0 = 0.1$. The particle surface roughness is given by (3.1) with $v_m D = 4$. Thus, the correlation length is $r_c = 0.1 \pi D$. The roughness parameter $\beta = 40$, corresponding to a mean square slope $\langle \sigma_s^2 \rangle = \beta/k_0^2 r_c^2 = 1/\pi^2$ and the mean square radius of curvature is given by $k_0^2 \langle \rho^2 \rangle = 417$. In Figure 3, I_1 is obtained in the $\phi = 0, 180^\circ$ plane (both the incident and scattered electric fields are in the scatter plane which is normal to $\vec{n}^i \vec{x}^i$) while in Figure 4, I_2 is plotted in the $\phi = 90^\circ, 270^\circ$ plane (both the incident and scattered electric fields are perpendicular to the scatter plane). Since the optical thickness is $\tau_0 = 0.1$ the first order and multiple scatter results are not very different, however the particle surface roughness does have a very significant effect of smoothing out the fluctuations in the diffuse specific intensities as a function of the scatter angle. These fluctuations in the diffuse specific intensities scattered by smooth particles are more pronounced for the vertically polarized case than for the horizontally polarized case. This results directly from the Mie solution for large conducting spheres. The enhanced backscatter manifested in these illustrative examples is due to the peak in the backscattered differentiated cross sections for spherical particles (Mie solution) as well as due to the particle surface roughness. In Figures 5 and 6, the backscattered diffuse scattering intensities I_1 and I_2 are plotted as functions of the scatter angle θ in the plane of incidence, $\phi = 0, 180^\circ$. The excitations which are vertically and horizontally polarized respectively, at $\lambda = 10\mu\text{m}$ (case (b)) are obliquely incident at angle $\theta^i = 15^\circ$. The particle surface roughness is given by (3.3) with $v_m D = 4$ ($r_c = 0.1 \pi D$). The roughness parameter is $\beta = 10$ corresponding to $\langle \sigma_s^2 \rangle = 1/\pi^2$ and $k_0^2 \langle \rho^2 \rangle = 102$. The optical thickness of the layer is $\tau_0 = 1$. The vertically polarized diffuse scattering intensity I_1 (Figure 5) is more oscillatory than the horizontally polarized intensity I_2 (Figure 6) and the backscatter enhancement is present only for the particles with rough surfaces.

In Figure 7 the backscattered specific intensity I_1 is plotted as a function of the scatter angle θ in the $\phi = 0, 180^\circ$ plane. The excitation at $\lambda = 10\mu\text{m}$ (case (c) mixture of particles of different sizes) is normally incident and linearly polarized with the electric field in the \vec{a}_x direction. The optical thickness of the layer is $\tau_0 = 2$. The particle surface roughness is given by (3.3) with $v_m D = 4$ ($r_c = 0.1 \pi D$). The roughness parameter is $\beta = 10$ corresponding to $\langle \sigma_s^2 \rangle = .0645$ and $k_0^2 \langle \rho^2 \rangle = 331$. There is no enhanced backscatter associated with the mixture of smooth particles. However, the results do exhibit enhanced backscatter for the particles with rough surfaces. In Figure 8 the backscattered specific intensity I_2 is plotted as a function of the scatter angle θ in the $\phi = 90^\circ, 270^\circ$ plane. The excitation is as in Figure 7 (case (c)). Thus, in the $\phi = 90^\circ, 270^\circ$ plane both the incident and scattered intensities are horizontally polarized. The optical thickness of the layer is $\tau_0 = 2$. The particle surface roughness is the same as in Figure 7. Here too, the phenomenon of the enhanced backscatter manifests itself only when the surface of the particles is rough. This enhanced backscatter

is more distinct when the scattering plane is perpendicular to the direction of the electric field, namely for the horizontally polarized case.

4. CONCLUDING REMARKS

The incoherent diffuse specific intensities (modified Stokes parameters) that are scattered, in the backward direction, from a parallel layer consisting of a random distribution of irregular shaped particles are computed for both vertically and horizontally polarized excitations at infrared and optical frequencies. The finitely conducting particles considered here are spherical in shape with average diameter D and a rough surface height h (measured normal to the unperturbed spherical surface) characterized by its correlation function $\langle hh' \rangle$ or its Fourier transform, the surface height spectral density function. Waves that are both normally and obliquely incident upon the layer of particles are considered. It is shown that there is a pronounced backscatter enhancement that is due to the surface roughness of the particle. On comparing the solutions for the backscattered specific intensities for particles with smooth and rough surfaces it is seen that the Mie differential scatter contribution $[S_{Mie}]$ to the total phase matrix $[S']$ (2.4) does not result in backscatter enhancement for all the cases considered. However, for particles with roughness parameters $\beta = 4k_0^2 \langle h^2 \rangle \geq 10$ the backscatter intensities were enhanced even when there is no corresponding enhancement due to Mie scatter from smooth spherical particles. The diffuse scatter contribution $[S]_D$ to the total phase matrix $[S']$ (2.4) is derived using a full wave approach.

Since the Mie solution for the vertically polarized scattered intensity is more oscillatory than for horizontally polarized intensity, the phenomenon of enhanced backscatter is usually more pronounced in the scatter plane perpendicular to the incident electric field (horizontally polarized incident wave). Both first order as well as multiple scatter results for particles with smooth and rough surfaces are presented. Thus, it is shown that the enhanced backscatter phenomenon described in this work is primarily due to the particle surface roughness and not multiple scatter. Particles with different complex permittivities are considered and the effects of changing the optical thickness of the layers are obtained.

5. REFERENCES

1. Bahar, E. and M. A. Fitzwater (1984), "Scattering Cross Sections for Composite Rough Surfaces Using Full Wave Approach," IEEE Trans. Antennas Propag. AP-32, pp. 730-734.
2. Bahar, E., S. Chakrabarti, and M. A. Fitzwater (1986), "Extinction Cross Sections and Albedos for Particles with Very Rough Surfaces," Applied Optics, 25, pp. 2530-2536.
3. Bahar, E., and M. A. Fitzwater (1987a), "Co-polarized and Cross-polarized Incoherent Specific Intensities for Waves at Oblique Incidence Upon Layers of Finitely Conducting Particles with Rough Surfaces," Journal of the Optical Society of America A, 4, pp. 41-56.
4. Bahar, E., and M. A. Fitzwater (1987b), "Enhancement of the Backscattered Diffuse Specific Intensities for Random Distributions of Finitely Conducting Particles with Rough Surfaces," Journal of the Optical Society of America A, in press.
5. Chandrasekhar, S. (1950), Radiative Transfer, Dover, New York.

7. Ishimaru, A., R. Woo, J. W. Armstrong, and D. C. Blackman (1982), "Multiple Scattering Calculations of Rain Effects," Radio Science, 17, pp. 1425-1433.
8. Rice, S. A. (1951), "Reflection of Electromagnetic Waves from a Slightly Rough Surface," Communication of Pure and Applied Math., 4, pp. 351-378.

ACKNOWLEDGMENTS

The work was partially sponsored by the U. S. Army Research Contract DAAG-29-82-K-0123. The authors also acknowledge the National Science Foundation Engineering Supercomputer Grant ECS 8515794/5. The manuscript was prepared by Mrs. E. Everett.

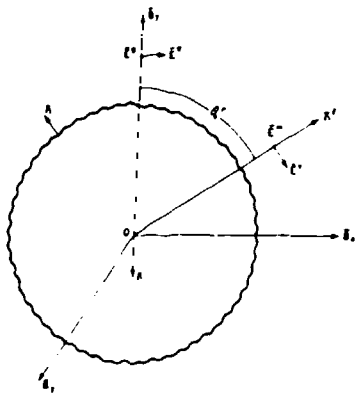


FIGURE 1. Scattering geometry for a rough conducting sphere.

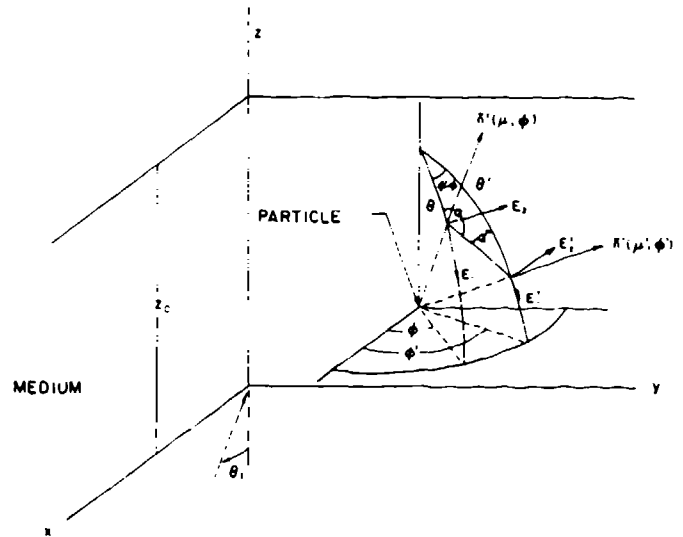


FIGURE 2. Scattering geometry indicating incident and scattered wave normals \bar{n}^i and \bar{n}^f and corresponding field components E_1 parallel (vertical) and E_2 perpendicular (horizontal) polarizations.

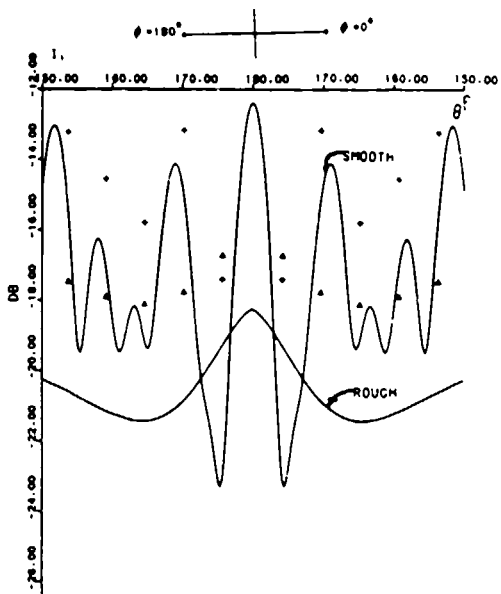


FIGURE 3. Backscattered incoherent specific intensity I_1 for a vertically polarized normally incident wave; $90^\circ \leq \theta \leq 180^\circ$, scatter plane $\phi = 0^\circ, 180^\circ$, case (a), optical thickness $\tau_0 = .1$ __, first order scatter for smooth and rough particles; multiple-scatter (Eqn. 2.2) for smooth (+) and rough (Δ) particles. Roughness parameter $\beta = 4k_0^2 \langle h^2 \rangle = 40$, correlation length $r_c = 0.1\pi D$, $D/\lambda = 10$.

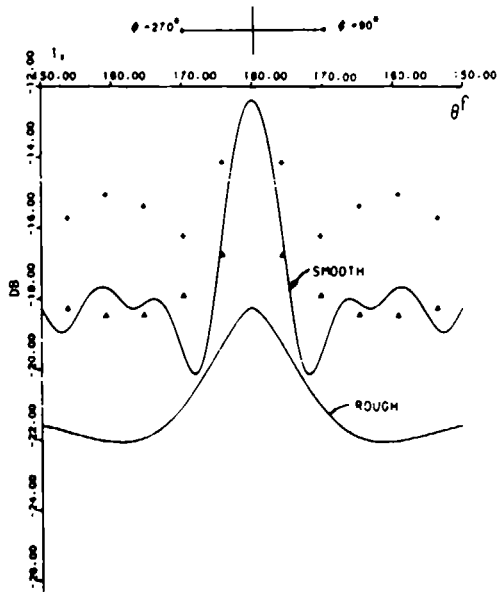


FIGURE 4. Backscattered incoherent specific intensity I_2 for a vertically polarized normally incident wave; $90^\circ \leq \theta \leq 180^\circ$, scatter plane $\phi = 90^\circ, 270^\circ$, case (a), optical thickness $\tau_0 = .1$ __, first order scatter for smooth and rough particles; multiple-scatter (Eqn. 2.2) for smooth (+) and rough (Δ) particles. $\beta = 40$, $r_c = 0.1\pi D$, $D/\lambda = 10$.

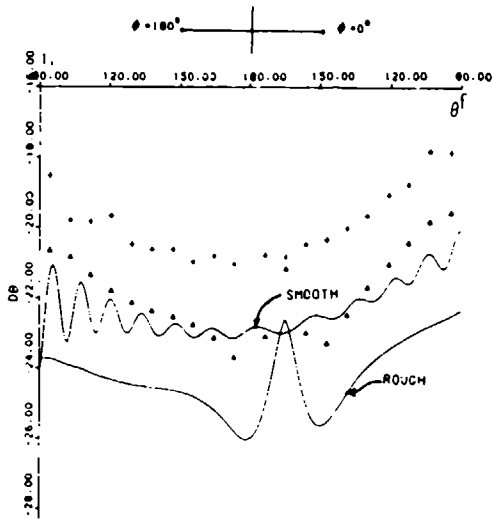


FIGURE 5. Backscattered incoherent specific intensity I_1 for a vertically polarized wave incident at $\theta^i = 15^\circ$, $\phi^i = 0^\circ$, $90^\circ \leq \theta \leq 180^\circ$, scatter plane $\phi = 0^\circ, 180^\circ$, case (c), optical thickness $\tau_0 = 1$. —, first order scatter for smooth and rough particles; multiple-scatter (Eqn. 2.2) for smooth (+) and rough (Δ) particles. $\beta = 10$, $r_c = 0.1\pi D$, $D/\lambda = 5$.

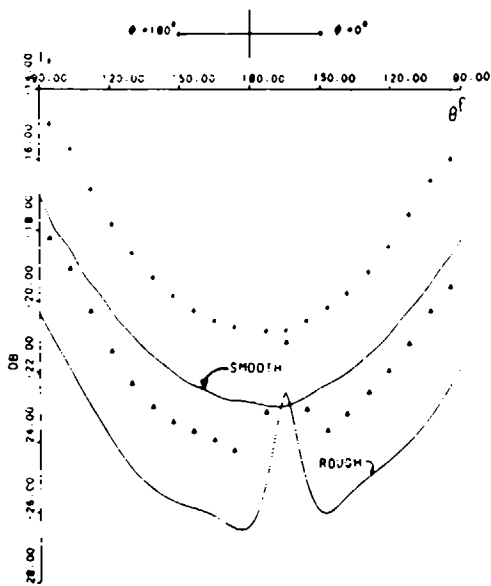


FIGURE 6. Backscattered incoherent specific intensity I_2 for a horizontally polarized wave incident at $\theta^i = 15^\circ$, $\phi^i = 0^\circ$, $90^\circ \leq \theta \leq 180^\circ$, scatter plane $\phi = 0^\circ, 180^\circ$, case (c), optical thickness $\tau_0 = 1$. —, first order scatter for smooth and rough particles; multiple-scatter (Eqn. 2.2) for smooth (+) and rough (Δ) particles. $\beta = 10$, $r_c = 0.1\pi D$, $D/\lambda = 5$.

FIGURE 7. Backscattered incoherent specific intensity I_1 for a vertically polarized normally incident wave, $90^\circ \leq \theta \leq 180^\circ$, scatter plane $\phi = 0^\circ, 180^\circ$, case (d), optical thickness $\tau_0 = 2$. — first order scatter (Eqn. 2.2) for smooth (+) and rough (Δ) particles. $\beta = 10$, $r_c = 0.1\pi D$, uniform distribution of $D/\lambda = 5, 5.5, 6, 6.5, 7, 7.5, 8$.

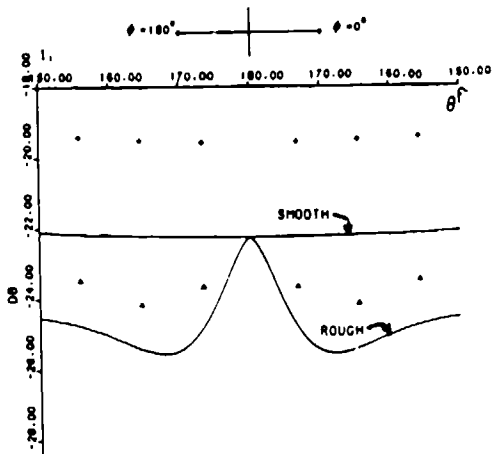
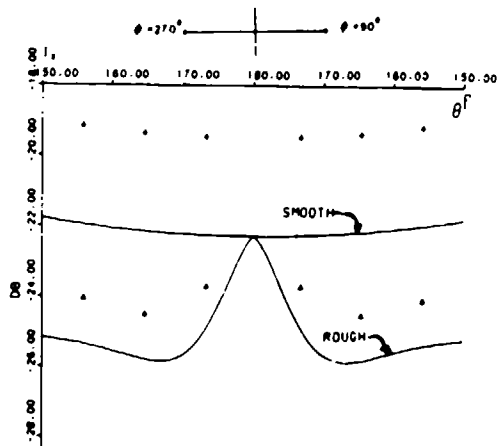


FIGURE 8. Backscattered incoherent specific intensity I_2 for a vertically polarized normally incident wave, $90^\circ \leq \theta \leq 180^\circ$, scatter plane $\phi = 90^\circ, 270^\circ$, case (d), optical thickness $\tau_0 = 2$. —, first order scatter for smooth and rough particles; multiple scatter (Eqn. 2.2) for smooth (+) and rough (Δ) particles. $\beta = 10$, $r_c = 0.1\pi D$, uniform distribution of $D/\pi = 5, 5.5, 6, 6.5, 7, 7.5, 8$.



LIGHT SCATTERING BY AN ARBITRARILY CONFIGURED
CLUSTER OF SPHERES

K. A. Fuller and G. W. Kattawar
Texas A&M University, Department of Physics
College Station, Texas, 77843

RECENT PUBLICATIONS, SUBMITTALS FOR PUBLICATION,
AND PRESENTATIONS:

- (A) K. A. Fuller, G. W. Kattawar, and R. T. Wang, "Electromagnetic Scattering from Two Dielectric Spheres: Further Comparisons Between Theory and Experiment," *Appl. Opt.* **25**, 2521(1986)
- (B) K. A. Fuller and G. W. Kattawar, "A New Approach to Electromagnetic Scattering by Interacting Spheres," in *Proceedings of the 1986 CRDC Scientific Conference on Obscuration and Aerosol Research*, R. H. Kohl, ed.
- (C) K. A. Fuller and G. W. Kattawar, "A New Method for the Study of Light Scattering by Ensembles of Interacting Spheres," Presented at the Joint Fall Meeting of the Texas Sections of the American Physical Society and of the American Association of Physics Teachers, Nacogdoches, Tx (Nov. 7, 1986)
- (D) K. A. Fuller and G. W. Kattawar, "Light Scattering by Ensembles of Interacting Spheres," presented to the Life Sciences Division of Los Alamos National Laboratory, Los Alamos NM, July 20, 1987.
- (E) K. A. Fuller, *Cooperative Electromagnetic Scattering by Ensembles of Interacting Spheres*, PhD Dissertation, Texas A&M University, 1987.
- (F) K. A. Fuller and G. W. Kattawar, "A Consummate Solution to the Problem of Classical EM Scattering by an Ensemble of Spheres Part I: Linear Chains," submitted to *Optics Letters*.
- (G) K. A. Fuller and G. W. Kattawar, "A Consummate Solution to the Problem of Classical EM Scattering by an Ensemble of Spheres Part II: Clusters," to be submitted to *Optics Letters*.
- (H) C.-R. Hu, G. W. Kattawar, M. E. Parkin, and P. Herb, "Symmetry Theorems on the Forward and Backward Scattering Mueller Matrices for Light Scattering from a Nonspherical Dielectric Scatterer," accepted for publication in *Appl. Opt.*
- (I) G. W. Kattawar, C.-R. Hu, M. E. Parkin, and P. Herb, "Mueller Matrix Calculations for Dielectric Cubes: Comparison with Experiments," accepted for publication in *Appl. Opt.*

ABSTRACT

This is the third in a series of reports appearing in these proceedings on our study of cooperative scattering by clusters of spheres. Our second report included outlines of the derivation of our newly developed order of scattering (OS) technique and of a more familiar method for the study of light scattering by two or more interacting spheres for the case where translation of coordinate origins was restricted to the z -axis of a fixed or primary coordinate system. For completeness, those outlines (with slight modifications that are needed when a general ensemble of spheres is considered) and the requisite schematics are reproduced in this report as well. Comparisons between selected calculations and experimental results are made for a triangular cluster of three spheres. Comparisons between the more established technique, which involves matrix inversion, and the new method are also made. The two methods are in complete agreement with one another, but for the cases considered, the OS technique is much more efficient and its description of the physics involved is much more complete. The agreement between experiment and theory is most gratifying.

INTRODUCTION

We report here on the extension of our solution of the problem of light scattering by ensembles of interacting spheres to include cases other than that of linear chains. This extension establishes our capability to model a cluster of arbitrary configuration with the only theoretical constraint being that the spheres do not intersect.

The scattering geometry used in this study is depicted in Fig. 1. Parameters of the form $kz = 2\pi z/\lambda$, where λ is the wavelength of the incident radiation, will be used henceforth to describe the dimensions of the system. The constituent spheres are assumed to be of identical size and composition, with size parameter ka (radius a) and complex refractive index N_1 . Such uniformity is not a requirement of the theory, but is employed both for simplicity and for comparison with existing experimental data. Linearly polarized plane wave radiation with wave vector \mathbf{k}_0 impinges on this particle, with the angle between \mathbf{k}_0 and the z -axis specified by α . Although \mathbf{k}_0 could be restricted to the z -axis without loss of generality, allowing for $\alpha \neq 0$ leads to very substantial simplifications when calculating the scattering properties of linear chains.¹⁻³ The polarization angle γ of the incident electric field \mathbf{E}_0 will be allowed to take on only the values 0° and 90° for \mathbf{E}_0 lying in or perpendicular to the xz -plane, respectively.

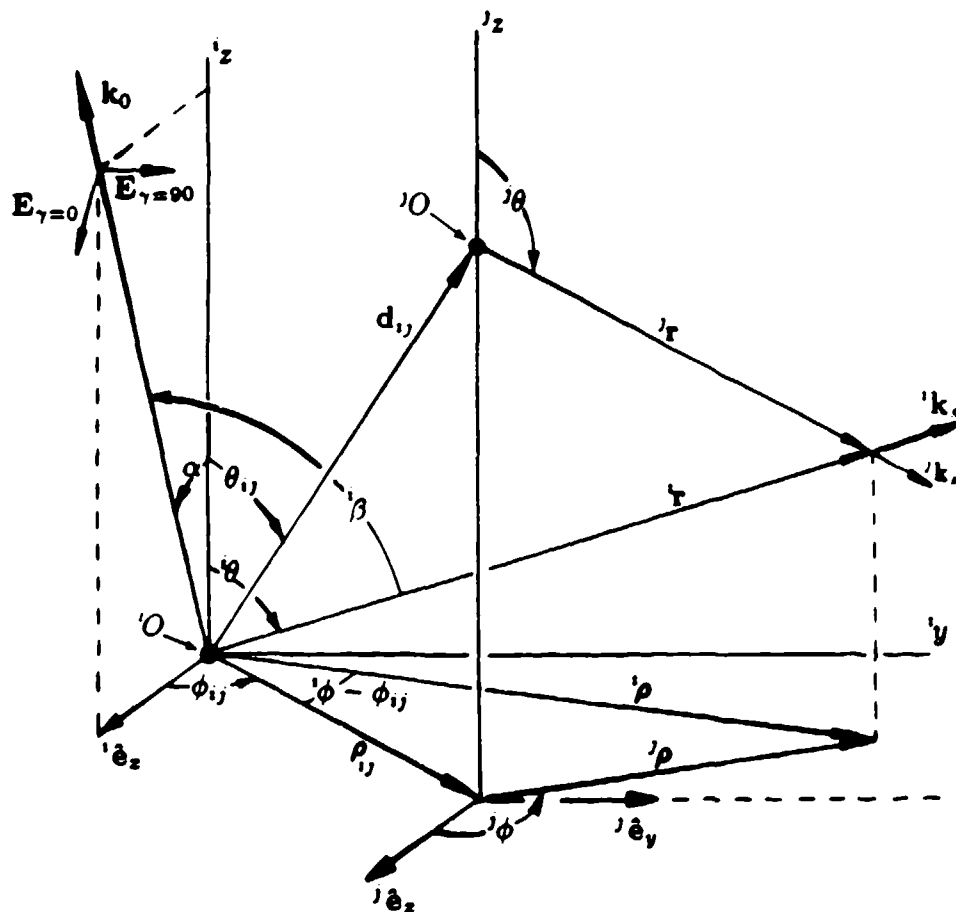


Fig. 1 The scattering geometry. Those quantities preceded by a superscript denote coordinates measured with respect to the corresponding origin iO , and the spheres in the cluster are centered about these origins. Quantities marked with a subscript ij denote the coordinates that locate the j^{th} origin in the i^{th} coordinate system. The quantities ${}^i \hat{e}_z$ are unit vectors in the i^{th} system. The cylindrical components ρ are employed here to help provide perspective but will not be involved in the text of this paper.

THE STANDARD METHOD

It is necessary to begin with a brief outline of the standard method for determining the fields scattered by such a system. The first comprehensive solution to the problem was obtained through the efforts of Liang and Lo¹ and Bruning and Lo.² In their theory (as well as ours), it is assumed that the scattered fields can be expanded as

$$\mathbf{E}_s = \sum_{\ell=1}^L \sum_{n=1}^{\infty} \sum_{m=-n}^n \left({}^{\ell}A_{mn} {}^{\ell}N_{mn}^{(3)} + {}^{\ell}H_{mn} {}^{\ell}M_{mn}^{(3)} \right). \quad (1)$$

where, once again, ℓ is an index used to identify specific constituents of a cluster of L spheres. The expansion coefficients ${}^{\ell}A_{mn}$ and ${}^{\ell}H_{mn}$ correspond, respectively, to the E- and H-type modes of the ℓ^{th} sphere, and ${}^{\ell}N_{mn}^{(3)}$ and ${}^{\ell}M_{mn}^{(3)}$ are the vector spherical harmonics in the ℓ^{th} coordinate system, the origin of which lies at the center of the ℓ^{th} sphere. Vector wave functions with superscripts (1) and (3) have a radial dependence based on the spherical Bessel functions, $j_n(kr)$ and spherical Hankel functions of the first kind, $h_n^{(1)}(kr)$, respectively. If $L = 1$ then the coefficients ${}^{\ell}A_{mn}$ and ${}^{\ell}H_{mn}$ take on the form $v_n p_{mn}(\cos \alpha)$ and $u_n q_{mn}(\cos \alpha)$, respectively, where v_n and u_n are the Mie coefficients, and $p_{mn}(\cos \alpha)$ and $q_{mn}(\cos \alpha)$ are the expansion coefficients of the incident plane wave.

In order to apply boundary conditions successfully, one must be able to expand the fields scattered by the ℓ^{th} sphere about the center of any i^{th} constituent of the chain. This can be accomplished through the use of the addition theorem for vector spherical harmonics¹⁻⁶ which allows us to write

$$\begin{aligned} {}^{\ell}M_{mn}^{(3)} &= \sum_{\nu=1}^{\infty} \sum_{\mu=-\nu}^{\nu} \left({}^{\ell}M_{\mu\nu}^{(1)} A_{\mu\nu}^{mn}(k\mathbf{d}_{i\ell}) + {}^{\ell}N_{\mu\nu}^{(1)} B_{\mu\nu}^{mn}(k\mathbf{d}_{i\ell}) \right) \\ {}^{\ell}N_{mn}^{(3)} &= \sum_{\nu=1}^{\infty} \sum_{\mu=-\nu}^{\nu} \left({}^{\ell}N_{\mu\nu}^{(1)} A_{\mu\nu}^{mn}(k\mathbf{d}_{i\ell}) + {}^{\ell}M_{\mu\nu}^{(1)} B_{\mu\nu}^{mn}(k\mathbf{d}_{i\ell}) \right). \end{aligned} \quad (2)$$

The procedure for finding the scattering coefficients now closely parallels that used in finding the Mie coefficients, and one is led to a set of $2L$ coupled linear equations of the form

$$\begin{aligned}
{}^{\ell}A E_{mn} &= {}^{\ell}v_n \left[{}^{\ell}p_{mn} + \sum_{i \neq \ell} \sum_{\nu} \sum_{\mu} \left({}^iA E_{\mu\nu} A_{mn}^{\mu\nu}(k\mathbf{d}_{i\ell}) + {}^iA H_{\mu\nu} B_{mn}^{\mu\nu}(k\mathbf{d}_{i\ell}) \right) \right] \\
{}^{\ell}A H_{mn} &= {}^{\ell}u_n \left[{}^{\ell}q_{mn} + \sum_{i \neq \ell} \sum_{\nu} \sum_{\mu} \left({}^iA H_{\mu\nu} A_{mn}^{\mu\nu}(k\mathbf{d}_{i\ell}) + {}^iA E_{\mu\nu} B_{mn}^{\mu\nu}(k\mathbf{d}_{i\ell}) \right) \right]
\end{aligned} \tag{3}$$

Furthermore, it can be shown³ that

$$A_{\mu\nu}^{mn}(k\mathbf{d}_{\ell i}) = (-1)^{n+\nu} A_{\mu\nu}^{mn}(k\mathbf{d}_{i\ell})$$

and

$$B_{\mu\nu}^{mn}(k\mathbf{d}_{\ell i}) = -(-1)^{n+\nu} B_{\mu\nu}^{mn}(k\mathbf{d}_{i\ell}).$$

Eq. 3 can be cast in the form of a matrix equation in which the translation coefficients give rise to the coefficient matrix, and the scattering coefficients can then be found by direct matrix inversion.

THE NEW METHOD

Rather than matrix inversion, we have found a straightforward way to obtain the scattering coefficients through an order of scattering (OS) technique. Fig. 2 depicts the scattering process in the context of this method where, for ease of visualization, we have set $L = 2$. The "scattering ladders" in Fig. 2a should be interpreted as follows: Plane wave radiation strikes the first sphere which then scatters a field (as prescribed by Lorentz-Mie theory) both to the field point and to the second sphere. The second sphere then responds to the field incident on it from the first sphere, scattering radiation to the field point and back to the first sphere. This process is continued indefinitely, and the total scattered field is then obtained by adding all of these contributions to a sum of similar terms which arise from plane wave radiation incident on the second sphere. In Fig. 2, a term of the form ${}^{\ell}\mathbf{k}^{(j)}$ is understood to be the wave vector of the j^{th} -order multiply scattered field, or the j^{th} -order partial field, emanating from the ℓ^{th} sphere, and ${}^{\ell}\theta$ is the angle between the wave vectors ${}^{\ell}\mathbf{k}^{(j)}$ and the z -axis. Our theory applies equally well to the calculation of far, near, and internal fields, and this is why ${}^1\theta \neq {}^2\theta$ in Fig. 2.

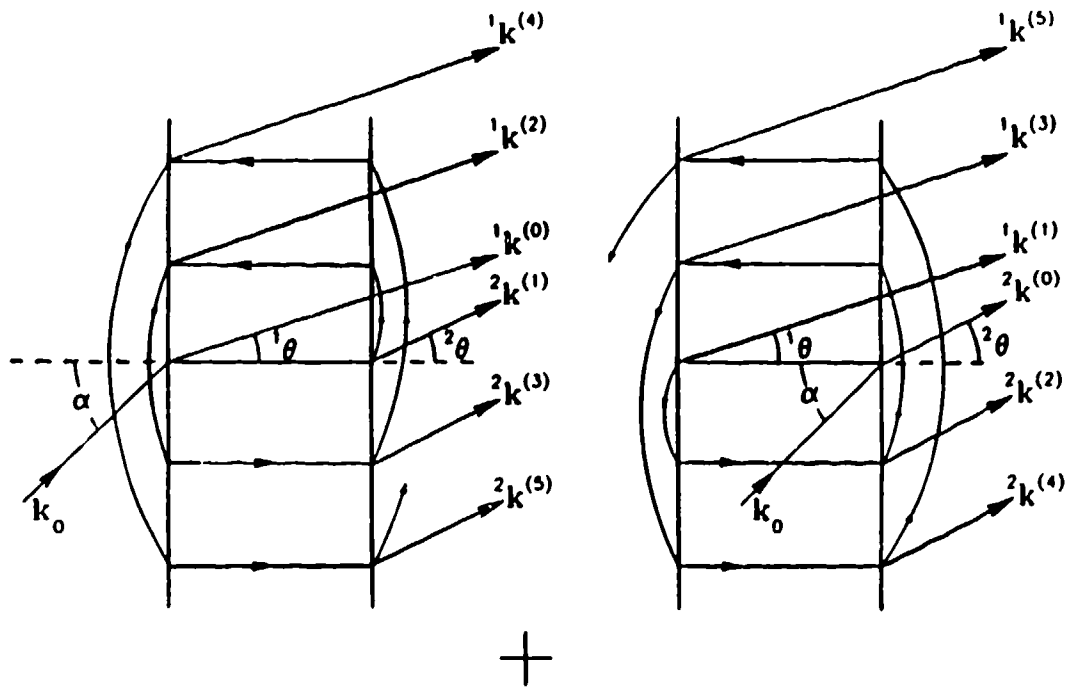


Fig. 2 An illustration of the order of scattering process through the use of scattering ladders. The contributions to the total scattered field by the partial fields generated from radiation incident on the first sphere are shown on the left and those arising from radiation incident on the second sphere are shown on the right.

To obtain explicit expressions for the partial fields, we first expand the j^{th} -order partial field of the ℓ^{th} sphere as

$${}^{\ell}\mathbf{E}^{(j)} = \sum_{n,m} \left({}^{\ell}a_{mn}^{(j)} {}^{\ell}\mathbf{N}_{mn}^{(3)} + {}^{\ell}b_{mn}^{(j)} {}^{\ell}\mathbf{M}_{mn}^{(3)} \right). \quad (4)$$

In the context of a more generalized form of the Lorentz-Mie theory, this scattered field is now regarded as the incident field seen by the other (i^{th}) sphere, and with the help of the addition theorem, it can then be expanded about the i^{th} origin. Upon solving the resulting boundary value problem one finds that the j^{th} -order scattering coefficients can be written as

$$\begin{aligned} {}^1a_{mn}^{(j)} &= {}^1v_n \sum_{\nu} \sum_{\mu} \left({}^2a_{\mu\nu}^{(j-1)} A_{\mu\nu}^{mn}(k\mathbf{d}_{12}) + {}^2b_{\mu\nu}^{(j-1)} B_{\mu\nu}^{mn}(k\mathbf{d}_{12}) \right) \\ {}^1b_{mn}^{(j)} &= {}^1u_n \sum_{\nu} \sum_{\mu} \left({}^2b_{\mu\nu}^{(j-1)} A_{\mu\nu}^{mn}(k\mathbf{d}_{12}) + {}^2a_{\mu\nu}^{(j-1)} B_{\mu\nu}^{mn}(k\mathbf{d}_{12}) \right) \\ {}^2a_{mn}^{(j)} &= {}^2v_n \sum_{\nu} (-1)^{n+\nu} \sum_{\mu} \left({}^1a_{\mu\nu}^{(j-1)} A_{\mu\nu}^{mn}(k\mathbf{d}_{12}) - {}^1b_{\mu\nu}^{(j-1)} B_{\mu\nu}^{mn}(k\mathbf{d}_{12}) \right) \\ {}^2b_{mn}^{(j)} &= {}^2u_n \sum_{\nu} (-1)^{n+\nu} \sum_{\mu} \left({}^1b_{\mu\nu}^{(j-1)} A_{\mu\nu}^{mn}(k\mathbf{d}_{12}) - {}^1a_{\mu\nu}^{(j-1)} B_{\mu\nu}^{mn}(k\mathbf{d}_{12}) \right). \end{aligned} \quad (5)$$

In addition to quantifying the partial fields which combine to produce the net scattered field, Eq. 5 allows one to see exactly what role each of the ν^{th} -degree, μ^{th} -order TH and TE modes arriving from one sphere play in stimulating any n^{th} -degree, m^{th} -order TH or TE mode in the other sphere for any order of scattering.

For brevity, the notation

$$\begin{aligned} {}^1a_{mn}^{(j)} &= {}^1v_n {}^2\Xi_{mn}(k\mathbf{d}_{12}) \\ {}^1b_{mn}^{(j)} &= {}^1u_n {}^2\tilde{\Xi}_{mn}(k\mathbf{d}_{12}) \\ {}^2a_{mn}^{(j)} &= {}^2v_n {}^1\Xi_{mn}(k\mathbf{d}_{21}) \\ {}^2b_{mn}^{(j)} &= {}^2u_n {}^1\tilde{\Xi}_{mn}(k\mathbf{d}_{21}) \end{aligned} \quad (6)$$

may be employed, where it is understood that if $j = 0$ then the ${}^{\ell}\Xi_{mn}(k\mathbf{d}_{\ell\ell})$ and ${}^{\ell}\tilde{\Xi}_{mn}(k\mathbf{d}_{\ell\ell})$ are to be replaced with ${}^{\ell}p_{mn}$ and ${}^{\ell}q_{mn}$, respectively. The expansion coefficients of the total

scattered field are then given by

$$\begin{aligned} {}^L A E_{mn} &= \sum_{j=0}^{\infty} {}^L \tilde{a}_{mn}^{(j)} \\ {}^L A H_{mn} &= \sum_{j=0}^{\infty} {}^L b_{mn}^{(j)}. \end{aligned} \tag{7}$$

DISCUSSIONS AND COMPARISONS WITH EXPERIMENTAL DATA

When one is dealing with two spheres, it is clear that a j^{th} -order scattering term is encountered exactly twice for any j : One from each sphere. For $L(> 2)$ spheres, any partial field ${}^L \mathbf{E}^{(j)}$ will have more than L histories (except for $j = 0$), and the number of these possible histories increases very dramatically with either L or j . If one is not careful, the problem of keeping track of the possible ways to generate a particular j^{th} -order partial field will become intractable, even for $L = 3$. A very natural way to proceed is to replace each particle in the scattering ladder with an appropriate set of scattering ladders, thereby reducing an L -sphere scattering problem to a continued sequence of 2-body problems. Fig. 3 diagrams such an extension for the case of three spheres. We have tested this method against that involving matrix inversion and have obtained excellent numerical agreement.

In addition to checking our OS calculations against those of the older method, we have also compared our results with experimental data which were kindly provided by Dr. R. T. Wang of The Space Astronomy Laboratory at the University of Florida. Some of the results of this latter study are shown in Figs. 4a and 5. Attention is called to the fact that the converged "sparkle" function in Fig. 4a is symmetric about $\alpha = 55^\circ$ whereas the particle possesses only threefold symmetry. This feature is due to the fact that reciprocity has combined with particle symmetry to yield a more periodic scattering pattern than might otherwise be anticipated. In the present case it is, more precisely, a reflection of reciprocal scattering across the yz -plane that accounts for the added symmetry.

It is the close agreement between experiment and theory which can be seen in the above figures that best validates our calculations. With that, we proceed to examine in Fig. 4b

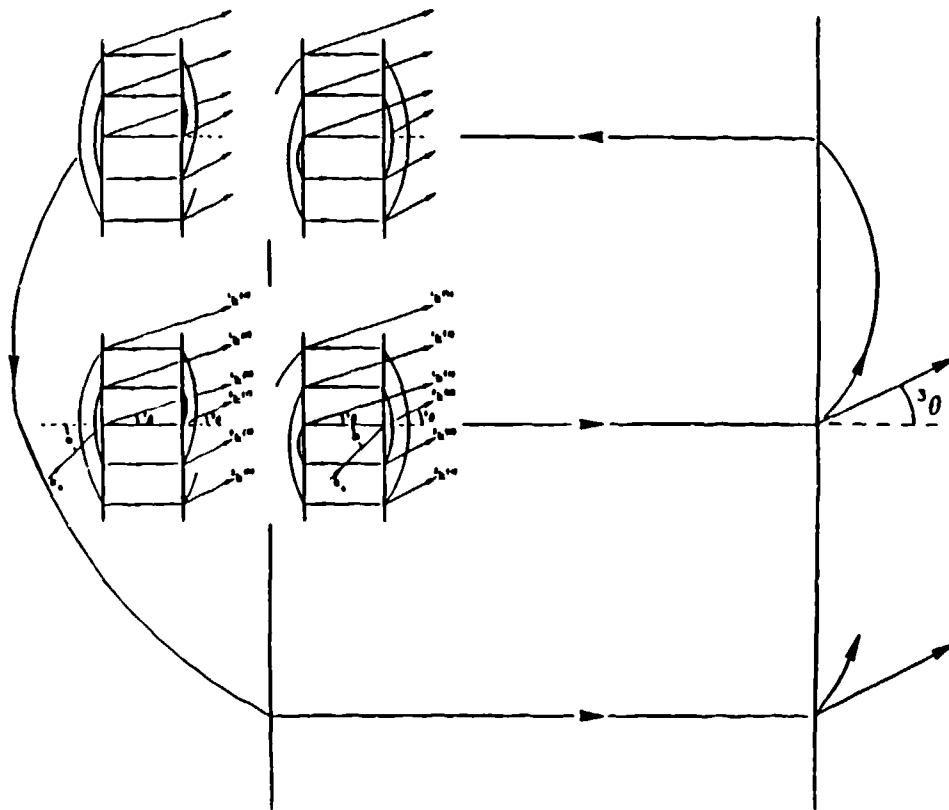


Fig. 3 A partial illustration of light scattering by three spheres in which the incident radiation impinges on a specific pair of spheres in the system. The total scattered field is obtained by adding the partial fields from this figure to those generated by radiation that is incident on the third sphere.

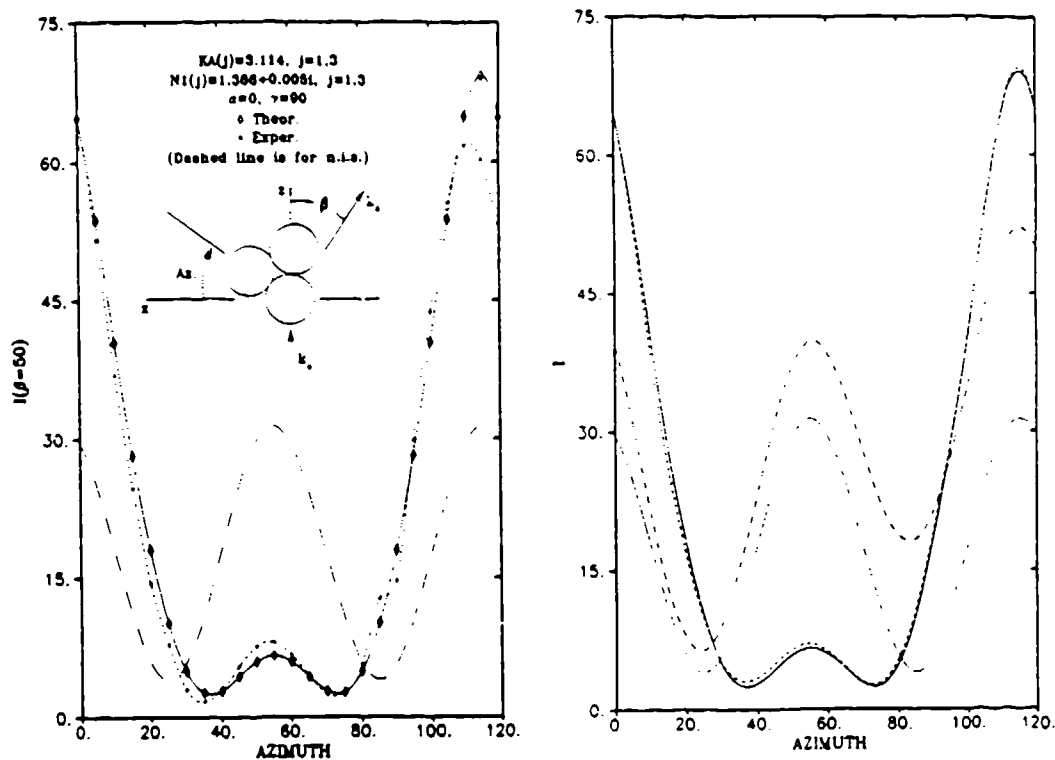


Fig. 4 (a) A comparison of experimental measurements with theoretical values for the intensity of light scattered into $\beta = 50^\circ$ by a triangular cluster of spheres as a function of cluster orientation. Results for the case in which all correlation effects have been neglected are labeled n.i.s. (noninteracting spheres). (b) A study of the convergence properties of the OS method. The solid line is for the converged solution and the dotted line is for n.i.s. The curve made up of long dashes corresponds to the case of scattering by a noninteracting sphere and bisphere and that made up of short dashes corresponds to the sum of the two first order interactions between these particles. At an azimuth angle of 0° the incident radiation impinges on the bisphere at broadside.

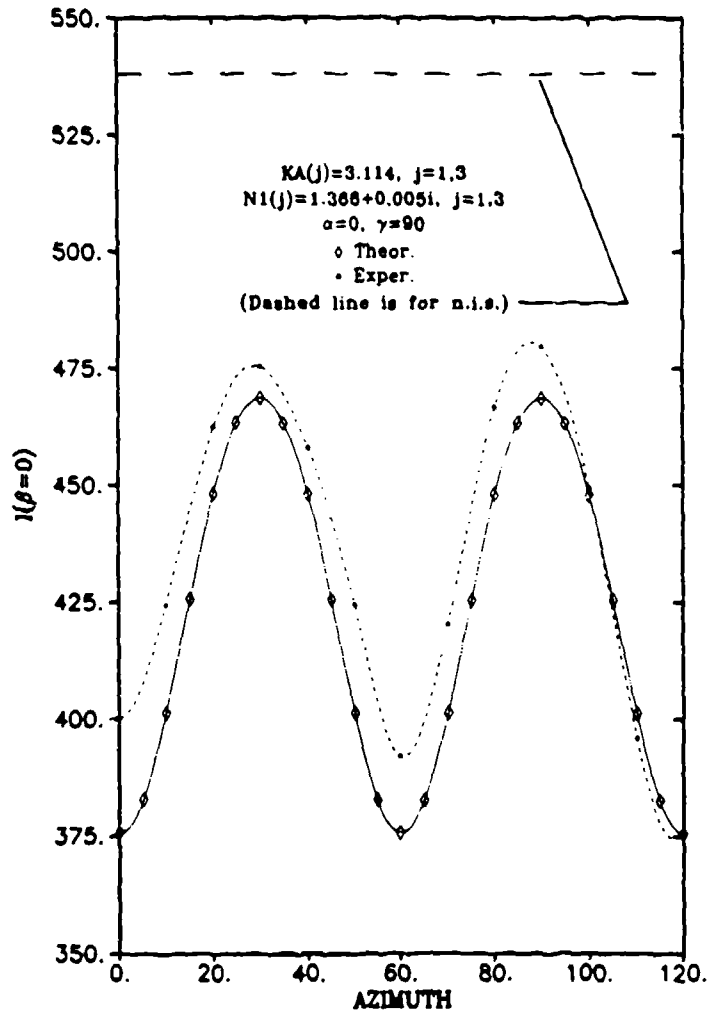


Fig. 5 A comparison of experimental measurements with theoretical values for the intensity of light scattered into $\beta = 0^\circ$ by a triangular cluster of spheres as a function of cluster orientation. Results for the case in which all correlation effects have been neglected are labeled n.i.s. (noninteracting spheres).

the convergence of OS for the situation illustrated in Fig. 4a. To do this the three-sphere is divided into a bisphere and a singlet, and the following notation is introduced: Let the intensity of radiation scattered by a noninteracting singlet and bisphere be expressed as

$$I_{sb}^{(j=0)} = |({}^1\mathbf{E}_s + {}^2\mathbf{E}_s)^{(0)} + {}^3\mathbf{E}_s^{(0)}|^2 \equiv |{}^b\mathbf{E}_s^{(0)} + {}^3\mathbf{E}_s^{(0)}|^2,$$

where *b* stands for bisphere and *sb* is to be read singlet-bisphere. Extension of this notation to higher orders of singlet-bisphere interactions should be obvious. In this context, the progression of the interaction for the cluster being studied in Fig. 4a is shown in Fig. 4b. Further calculations have been made to determine the phase functions of this triangular cluster at specific orientations with respect to the incident beam. These phase functions are displayed in Fig. 6.

In addition to the increased amount of physical insight that can be gained from this approach, OS also avoids the need to perform matrix inversions, and hence it actually requires less computing time in many cases. For linear chains of up to five spheres, the amount of computing time required by OS is typically 1/2 to 2/3 of that required by matrix inversion, provided that morphological resonances of the independent constituents are avoided. If a singlet resonance is encountered, it may be more advantageous (computationally) to use matrix inversion, though this point warrants further study. As mentioned earlier, restriction of the cluster geometry to linear chains results in simplification of the calculations. This simplification is particularly marked in the case of the matrix method since inversion of the relatively large array generated from Eq. (3) can then be broken up into a *sequence* of inversions of substantially smaller arrays due to the decoupling of azimuthal modes that is brought on by the introduction of cylindrical symmetry to the problem.¹⁻³ Consequently, calculation of the scattering coefficients of the triangular cluster via Eq. (3) with its attendant increase in array size takes 15 times longer than when OS is used. As seen in Fig. 4b, ignoring interactions between the bisphere and singlet beyond $j = 1$ provides a very good approximation to the exact sparkle function. Such an approximation runs in about 1/20 the time required by matrix inversion.

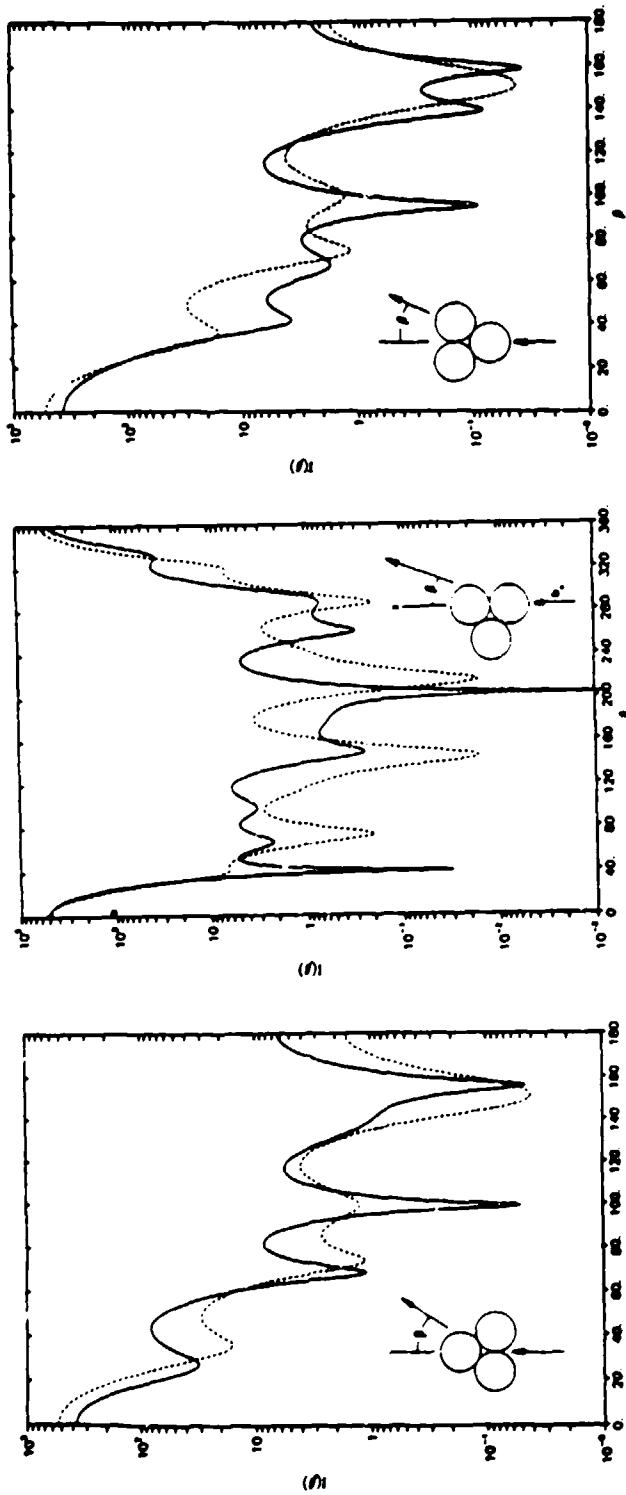


Fig. 6 The angular intensity distribution of light scattered from a triangular cluster of spheres for the orientations shown. Each constituent of the array has size parameter $ka = 3.114$ and refractive index $N_1 = 1.366 + 0.005i$. The polarization of the incident radiation is taken to be perpendicular to the scattering plane. The dashed line is for noninteracting spheres.

This work was supported by the U. S. Army Research Office under contract DAAL03-86-K-0168.

REFERENCES

1. C. Lang and Y. T. Lo, *Radio Science*, **2**, 1481(1967).
2. J. H. Bruning and Y. T. Lo, *IEEE Trans. Antennas Propag.*, **AP-19**, 378(1971).
3. K. A. Fuller, *Cooperative Electromagnetic Scattering by Ensembles of Interacting Spheres*, PhD Dissertation, Texas A&M University, 1987.
4. B. Friedman and J. Russek, *Quart. Appl. Math.*, **12**, 13(1954).
5. S. Stein, *Quart. Appl. Math.*, **19**, 15(1961).
6. O. R. Cruzan, *Quart. Appl. Math.*, **20**, 33(1962).

**THE POSSIBILITY OF USING SEVEN DIMENSIONAL
ELECTROMAGNETIC THEORY TO SOLVE THREE
DIMENSIONAL LIGHT SCATTERING PROBLEMS**

D. K. Coakon

Department of Mathematics 033-16

Temple University

Philadelphia, Pennsylvania 19122

ABSTRACT

The Cayley algebra is used to construct a curl operation. An electromagnetic theory is fully developed using this curl operation. Every differentiable vector field is a gradient plus a curl which means that the standard potential theory of electromagnetic theory in three dimensional space carries over. Unlike the usual higher dimensional electromagnetic theory using exterior differentials as the curl operation, the electric and magnetic vectors are vector fields of the same form. The uniqueness theory based on radiation conditions of Silver Mueller type carries over to the seven dimensional scattering problems. The impetus for this work is the structure theorem of Zorn ([29]) developed

3

in 1931. The curl is shown to be self adjoint which means that variational formulations of scattering problems also carry over to seven dimensional space.

By considering separable expansions of the vector fields in seven dimensional space, there may be a possibility of solving scattering problems in three dimensional space, because the first three components of the seven dimensional curl of the imbedding of a three dimensional vector field in seven dimensional space is exactly the three dimensional curl of the original vector field. So every solution of a three dimensional scattering problem is a solution of the seven dimensional Maxwell equations. Conversely, to every solution of the seven dimensional Maxwell equations in free space we can associate in a natural way a solution of the three dimensional Maxwell equations possibly with sources.

A uniqueness theorem is established for seven dimensional, magnetically lossy, penetrable, anisotropic scatterers covered by impedance sheets.

1. INTRODUCTION

We define the curl operation on the space $C^\infty(\Omega, C^7)$, where Ω is an open set in real seven dimensional space by the rule,

$$\begin{aligned} \text{curl}(\mathbf{E}) = & \left(\frac{\partial E_3}{\partial x_2} - \frac{\partial E_2}{\partial x_3} + \frac{\partial E_5}{\partial x_4} - \frac{\partial E_4}{\partial x_5} + \frac{\partial E_7}{\partial x_6} - \frac{\partial E_6}{\partial x_7} \right) \mathbf{e}_1 + \\ & \left(-\frac{\partial E_3}{\partial x_1} + \frac{\partial E_1}{\partial x_3} + \frac{\partial E_6}{\partial x_4} - \frac{\partial E_7}{\partial x_5} - \frac{\partial E_4}{\partial x_6} + \frac{\partial E_5}{\partial x_7} \right) \mathbf{e}_2 + \\ & \left(\frac{\partial E_2}{\partial x_1} - \frac{\partial E_1}{\partial x_2} - \frac{\partial E_7}{\partial x_4} - \frac{\partial E_6}{\partial x_5} + \frac{\partial E_5}{\partial x_6} + \frac{\partial E_4}{\partial x_7} \right) \mathbf{e}_3 + \\ & \left(-\frac{\partial E_5}{\partial x_1} - \frac{\partial E_6}{\partial x_2} + \frac{\partial E_7}{\partial x_3} + \frac{\partial E_1}{\partial x_5} + \frac{\partial E_2}{\partial x_6} - \frac{\partial E_3}{\partial x_7} \right) \mathbf{e}_4 + \\ & \left(\frac{\partial E_4}{\partial x_1} + \frac{\partial E_7}{\partial x_2} + \frac{\partial E_6}{\partial x_3} - \frac{\partial E_1}{\partial x_4} - \frac{\partial E_3}{\partial x_6} - \frac{\partial E_2}{\partial x_7} \right) \mathbf{e}_5 + \\ & \left(-\frac{\partial E_7}{\partial x_1} + \frac{\partial E_4}{\partial x_2} - \frac{\partial E_5}{\partial x_3} - \frac{\partial E_2}{\partial x_4} + \frac{\partial E_3}{\partial x_5} + \frac{\partial E_1}{\partial x_7} \right) \mathbf{e}_6 + \\ & \left(\frac{\partial E_6}{\partial x_1} - \frac{\partial E_5}{\partial x_2} - \frac{\partial E_4}{\partial x_3} + \frac{\partial E_3}{\partial x_4} + \frac{\partial E_2}{\partial x_5} - \frac{\partial E_1}{\partial x_6} \right) \mathbf{e}_7 \end{aligned} \quad (1.1)$$

where \mathbf{e}_j for $j = 1, 2, 3, 4, 5, 6,$ and 7 denotes the unit vector in the direction of the positive x_j axis, and each E_j is a complex valued infinitely differentiable function of the points $(x_1, x_2, x_3, x_4, x_5, x_6, x_7)$ in Ω . Thus, the function

$$\mathbf{E} = E_1 \mathbf{e}_1 + E_2 \mathbf{e}_2 + E_3 \mathbf{e}_3 + E_4 \mathbf{e}_4 + E_5 \mathbf{e}_5 + E_6 \mathbf{e}_6 + E_7 \mathbf{e}_7 \quad (1.2)$$

is valued in C^7 , complex 7 dimensional space, and its curl is also in the space $C^\infty(\Omega, C^7)$, which means that the curl defined by (1.1) is a topological endomorphism of this space of functions. The rule for the curl defined by equation (1.1) is based on the structure theorem of Caley space (e.g. Zorn [29], or Calabi [3]).

If we start with a solution of Maxwell's equations in three dimensional space and extend the \mathbf{E} and \mathbf{H} vector fields to seven

dimensional space by requiring that partial derivatives with respect to the variables x_4 through x_7 vanish, then with the above definition of curl and the natural definition of Maxwell's equations in seven dimensional space based on the curl operation, we see that our solution in three dimensional space satisfies the seven dimensional Maxwell equations.

We note that the curl operation defined by equation (1.1) is self adjoint in the sense that if \mathbf{A} and \mathbf{C} are infinitely differentiable functions from an open set Ω in real seven dimensional space valued in complex seven dimensional space and vanishing outside of a compact subset K of Ω , then

$$\int_{\Omega} \text{curl}(\mathbf{A}(\mathbf{x})) \cdot \mathbf{C}(\mathbf{x}) d\mathbf{x} = \int_{\Omega} \mathbf{A}(\mathbf{x}) \cdot \text{curl}(\mathbf{C}(\mathbf{x})) d\mathbf{x} \quad (1.3)$$

The above relationship follows by a simple integration by parts.

Zorn ([29], 1931) showed that a vector space satisfying the axioms of a Cayley space algebra, which is the type of algebra for which one can define a traditional type of curl operation, is necessarily seven dimensional.

To have a traditional type of electromagnetic theory one needs the concept of scalar and vector potentials. The following theorem shows that this is possible with the curl we have defined in equation (1.1).

Theorem 1.1. If the curl operation is defined on the function space $C^{\infty}(\Omega, C^7)$ of infinitely differentiable functions on open subsets Ω of real seven dimensional space and valued in complex seven dimensional space, C^7 , then

$$\text{curl}(\text{curl}(\mathbf{E})) = \text{grad}(\text{div}(\mathbf{E})) - \Delta \mathbf{E} \quad (1.4)$$

This follows from a computation. Observe that if $\text{curl}(\text{curl}(\mathbf{E}))_j$ denotes the j th component of the curl of the curl, then the first component of the curl is given by

$$\begin{aligned} \text{curl}(\text{curl}(\mathbf{E}))_1 = & \\ & \frac{\partial}{\partial x_2} \left(\frac{\partial E_2}{\partial x_1} - \frac{\partial E_1}{\partial x_2} - \frac{\partial E_7}{\partial x_4} - \frac{\partial E_6}{\partial x_5} + \frac{\partial E_5}{\partial x_6} + \frac{\partial E_4}{\partial x_7} \right) \\ & - \frac{\partial}{\partial x_3} \left(-\frac{\partial E_3}{\partial x_1} + \frac{\partial E_1}{\partial x_3} + \frac{\partial E_6}{\partial x_4} - \frac{\partial E_7}{\partial x_5} - \frac{\partial E_4}{\partial x_6} + \frac{\partial E_5}{\partial x_7} \right) \\ & + \frac{\partial}{\partial x_4} \left(\frac{\partial E_4}{\partial x_1} + \frac{\partial E_7}{\partial x_2} + \frac{\partial E_6}{\partial x_3} - \frac{\partial E_1}{\partial x_4} - \frac{\partial E_3}{\partial x_6} - \frac{\partial E_2}{\partial x_7} \right) \\ & - \frac{\partial}{\partial x_5} \left(-\frac{\partial E_5}{\partial x_1} - \frac{\partial E_6}{\partial x_2} + \frac{\partial E_7}{\partial x_3} + \frac{\partial E_1}{\partial x_5} + \frac{\partial E_2}{\partial x_6} - \frac{\partial E_3}{\partial x_7} \right) \\ & + \frac{\partial}{\partial x_6} \left(\frac{\partial E_6}{\partial x_1} - \frac{\partial E_5}{\partial x_2} - \frac{\partial E_4}{\partial x_3} + \frac{\partial E_3}{\partial x_4} + \frac{\partial E_2}{\partial x_5} - \frac{\partial E_1}{\partial x_6} \right) \\ & - \frac{\partial}{\partial x_7} \left(-\frac{\partial E_7}{\partial x_1} + \frac{\partial E_4}{\partial x_2} - \frac{\partial E_5}{\partial x_3} - \frac{\partial E_2}{\partial x_4} + \frac{\partial E_3}{\partial x_5} + \frac{\partial E_1}{\partial x_7} \right) \end{aligned} \quad (1.5)$$

We collect terms in the above expression and find that there is considerable cancellation of terms. Some manipulation will show that

$$\text{curl}(\text{curl}(\mathbf{E}))_j = \frac{\partial}{\partial x_j}(\text{div}(\mathbf{E})) - \Delta E_j \quad (1.6)$$

which completes the proof of Theorem 1.1.

The following theorem will give us a generalization of the notion that every vector field is a curl plus a gradient. In the following theorem you can let n be three or seven and let L denote respectively the three dimensional curl or the seven dimensional curl defined by equation (1.1).

Theorem 1.2. Let Ω be an arbitrary open subset of real n dimensional space. Let $C^\infty(\Omega, \mathbb{C}^n)$ denote the infinitely differentiable functions from the open set Ω to complex n dimensional space. We let L denote a linear partial differential operator from $C^\infty(\Omega, \mathbb{C}^n)$ into itself.

We suppose that there is an elliptic partial differential operator with constant coefficients

$$P(D) = P\left(-i\frac{\partial}{\partial x_1}, -i\frac{\partial}{\partial x_2}, \dots, -i\frac{\partial}{\partial x_n}\right) \quad (1.7)$$

such that if \mathbf{E} is a member of $C^\infty(\Omega, C^n)$, then

$$L(L(\mathbf{E})) = \text{grad}(\text{div}(\mathbf{E})) + P(D)\mathbf{E} \quad (1.8)$$

then there is a vector field \mathbf{A} , a kind of vector potential, in $C^\infty(\Omega, C^n)$ and a scalar valued function ϕ in $C^\infty(\Omega, C^1)$ such that

$$\mathbf{E} = L(\mathbf{A}) + \text{grad}(\phi) \quad (1.9)$$

Proof. The fact that $P(D)$ is elliptic (or in the special case where L is a curl that Δ , the Laplacian, is elliptic implies that for any scalar valued function such as a component E_j of the vector field \mathbf{E} we can always find a solution G_j of the equation,

$$P(D)G_j = E_j \quad (1.10)$$

If we now define for the special case of $n = 7$

$$\mathbf{G} = G_1\mathbf{e}_1 + G_2\mathbf{e}_2 + G_3\mathbf{e}_3 + G_4\mathbf{e}_4 + G_5\mathbf{e}_5 + G_6\mathbf{e}_6 + G_7\mathbf{e}_7 \quad (1.11)$$

and observe that with $L = \text{curl}$ as defined by (1.1) that

$$L(L(\mathbf{G})) = \text{grad}(\text{div}(\mathbf{G})) - P(D)\mathbf{G} \quad (1.12)$$

Since equations (1.10) and (1.11) imply that

$$\mathbf{E} = P(D)\mathbf{G} \quad (1.13)$$

the last two equations imply that

$$\mathbf{E} = L(\mathbf{A}) + \text{grad}(\phi) \quad (1.14)$$

where

$$\mathbf{A} = -L(\mathbf{G}) \quad (1.15)$$

and

$$\phi = \text{div}(\mathbf{G}) \quad (1.16)$$

We see from the above argument and its obvious

generalizations that solvability of elliptic equations in spaces of infinitely differentiable functions will give us many ways to develop a set of vector and scalar potentials and that the traditional curl and gradient decompositions of an arbitrary vector field are valid when this vector field is an infinitely differentiable function from open subsets of real three or seven dimensional space, respectively, into complex three or seven dimensional space.

2. INTEGRAL EQUATION FORMULATIONS

A key to integral equation formulations of electromagnetic scattering problems in anisotropic, penetrable, dispersive, heterogeneous material bodies in 3 or 7 dimensions is (a) the development of the fundamental solution of the free space Helmholtz equation, and (b) the possibility of introducing artificial electric and magnetic charges and currents.

We begin with a concept of functional averages (Treves [25]), Haar measures on the group of rotations in R^n and averages involving integrals over the surface of a sphere of radius one of the function under consideration acting on the distance of a point x in R^n to the origin multiplied by a vector point on the unit sphere and divided by the surface area of this unit sphere. These two natural ways of averaging physical quantities are the same for rotationally invariant functions. The rotation group average of the function f is

$$Gf(x) = \int_G f(T^{-1}x) dT \quad (2.1)$$

where the group G is $O(n)$, the group of real orthogonal transformations, and the sphere average of f is

$$Sf(x) = S_n^{-1} \int_{|\xi|=1} f(|x|\xi) dS_n(\xi) \quad (2.2)$$

then

$$S(Gf)(x) = (Sf)(x) \quad (2.3)$$

and

$$G(Sf)(x) = (Gf)(x) \quad (2.4)$$

where S and G are the sphere and rotation group average operators defined by (2.2) and (2.1) respectively. But by the Fubini theorem

$$SGf = GSf \quad (2.5)$$

Hence,

$$Sf = Gf \quad (2.6)$$

which means that the two means of getting a rotationally invariant function from an arbitrary one are identical. By relating functions on the nonnegative real numbers to rotationally invariant functions on R^n through the use of higher dimensional spherical coordinates, we can develop a natural means of transforming the Helmholtz operator into an ordinary differential operator and extract from this differential operator the most general rotationally invariant fundamental solution of the Helmholtz operator and by a judicious choice of the parameter appearing in this solution, we can obtain from this class a temperate fundamental solution of the free space Helmholtz operator. This process is, in fact the origin of the familiar fundamental solution,

$$E = \frac{-\exp(-ik_0 r)}{4\pi r}$$

that appears in three dimensional electromagnetic scattering problems.

In this short note we will simply write down the fundamental solution in general and specialize it to dimension 2 and also to odd dimensions where it can be expressed in terms of spherical Bessel and Neumann functions and write it down explicitly in three and seven dimensions.

We now discuss a general property of fundamental solutions of partial differential operators,

$$P(D) = P\left(-i\frac{\partial}{\partial x_1}, -i\frac{\partial}{\partial x_2}, \dots, -i\frac{\partial}{\partial x_n}\right) \quad (2.7)$$

if

$$P(D)E = \delta$$

where δ is the Dirac delta distribution, and if u is an infinitely differentiable function such that

$$P(D)u = 0 \quad (2.8)$$

then

$$P(D)(E + Cu) = \delta \quad (2.9)$$

implies that $E + Cu$ is also a fundamental solution for every constant C . Some lengthy manipulations show that the most general rotationally invariant fundamental solution of the Helmholtz operator, $\Delta + k_0^2$, is

$$E_{k_0} = \left[\frac{(-k_0)^{(n-2)}}{2^{n/2} \pi^{n/2-1} (-rk_0)^{(n-2)/2}} \right] Y_{(n-2)/2}(-rk_0) + \left[\frac{C(-k_0)^{(n-2)/2}}{(-rk_0)^{(n-2)/2}} \right] J_{(n-2)/2}(-rk_0) \quad (2.10)$$

The expression (2.10) will seem to be more familiar to the reader if we specialize to $n = 2$ or $n = 2m + 1$. If $n = 2$, then

$$E_{k_0} = (1/2)Y_0(-k_0 r) + CJ_0(-k_0 r) \quad (2.11)$$

If we set $C = i/2$, then we obtain the familiar relation,

$$E_{k_0} = \frac{iH_0^{(2)}(-k_0 r)}{2} \quad (2.12)$$

Letting $n = 2m + 1$ we see that if

$$C = \frac{(2k_0/\pi)^{1/2} (-k_0)^{m-1}}{2^{m+1} \pi^{m+1}} \quad (2.13)$$

then given the fact that $(n-2)/2 = m-1/2$, $n-2 = 2m-1$, $(n-1)/2 = m$, and $(n+1)/2 = m+1$ that

$$\begin{aligned}
E_{k_0} &= \left[\frac{(-i)(-k_0)^{2m-1}}{2^{m+1}\pi^m(-rk_0)^{m-1}} \right] (j_{m-1}(-rk_0) + iy_{m-1}(-rk_0)) \\
&= \left[\frac{(-i)(-k_0)^{2m-1}}{2^{m+1}\pi^m(-rk_0)^{m-1}} \right] h_{m-1}^{(1)}(-rk_0) \quad (2.14)
\end{aligned}$$

If $m = 1$, then $n = 3$ and we get the familiar result,

$$\begin{aligned}
E_{k_0} &= \left[\frac{(-i)(-k_0)}{4\pi} \left[\frac{\sin(-rk_0)}{-rk_0} - \frac{i\cos(-rk_0)}{-rk_0} \right] \right] \\
&= - \left[\frac{\cos(rk_0) - i\sin(rk_0)}{4\pi r} \right] = - \frac{\exp(-rk_0)}{4\pi r} \quad (2.15)
\end{aligned}$$

If $m = 3$, then $n = 7$ and

$$E_{k_0} = \left[\frac{(-i)(-k_0)^6}{2^4\pi^3(-rk_0)^2} \right] (j_2(-rk_0) + iy_2(-rk_0)) \quad (2.16)$$

where

$$j_2(z) = \left[\frac{3}{z^3} - \frac{1}{z} \right] \sin(z) - \left[\frac{3}{z^3} \right] \cos(z) \quad (2.17)$$

and

$$y_2(z) = \left[\frac{-3}{z^3} \right] \sin(z) + \left[\frac{1}{z} - \frac{3}{z^3} \right] \cos(z) \quad (2.18)$$

In $n = 3$ dimensional space charges have a $1/r$ potential and in 7 dimensional space charges have a

$$V = \frac{C}{r^5}$$

potential. If the permeability μ , the permittivity ϵ , and the conductivity σ are tensor functions of three or seven dimensional space and our radiation has a $\exp(i\omega t)$ time dependence, then in three or seven dimensional space Maxwell's equations can be recast in the form,

$$\text{curl}(\mathbf{E}) + i\omega\mu_0\mathbf{H} = -i\omega(\mu - \mu_0\mathbf{I})\mathbf{H} = \mathbf{J}_m \quad (2.19)$$

and

$$\text{curl}(\mathbf{H}) - i\omega\epsilon_0\mathbf{E} = (i\omega\epsilon + \sigma - i\omega\epsilon_0\mathbf{I})\mathbf{E} = \mathbf{J}_e \quad (2.20)$$

Thus, with the introduction of magnetic charge densities ρ_m and electrical charge densities ρ_e via the relations,

$$\left(\frac{\rho_m}{\mu_0} \right) = \text{div}(\mathbf{H}) \quad (2.21)$$

and

$$\left(\frac{\rho_e}{\epsilon_0} \right) = \text{div}(\mathbf{E}) \quad (2.22)$$

and developing scalar and vector potentials in the analogous manner, the entire theory of electromagnetism extends easily from 3 to 7 dimensions. In developing the coupled integral equation formulation of the interaction problem we simply solve the system of Maxwell equations (2.19) and (2.20) with sources.

Uniqueness is established in a natural function space by showing that in this space (cf [2]) that the Maxwell equation and integral equation formulation of the problem are equivalent. If σ is a strictly positive definite tensor, then uniqueness of the Maxwell equation formulation of the problem may be established if the scattered radiation is required to satisfy the appropriate Silver Mueller radiation condition.

3. UNIQUENESS FOR SEVEN DIMENSIONAL ANISOTROPIC SCATTERERS

Let \mathbf{E}' denote the difference between two solutions of the problem of describing scattering by anisotropic materials. Let Ω be an open set in real seven dimensional space whose material properties or constitutive relationships are tensorial. If α is a tensor, then $\text{Im}(\alpha)$ is a tensor whose entries are the imaginary parts of the entries of α and $\text{Re}(\alpha)$ is a tensor whose entries are the real parts of the entries of the tensor α . We will give here a proof of the uniqueness of the transmission problem in three or seven dimensional space when the scatterer is anisotropic and covered by an impedance sheet with a positive definite surface conductivity tensor in the sense that if the boundary condition at the outer surface $\partial\Omega$ of the scattering body Ω requires continuity of tangential components of \mathbf{E} and the relation

$$\mathbf{n} \times (\mathbf{H}_{p+1} - \mathbf{H}_p) = \sigma_s^{(p)} \cdot \mathbf{E}^p \quad (3.1)$$

where p denotes the region index just inside the outer portion of the scatterer and $p + 1$ denotes the region index in the free space surrounding the scatterer Ω and where the relation indicated by (3.1) is valid exactly on the boundary of the scattering body Ω , then the conductivity tensor σ_s , where for simplicity we have dropped the superscript p , satisfies the condition that if \mathbf{E} is a nonzero vector, then

$$((\sigma_s \cdot \mathbf{E}) \cdot \mathbf{E}' + (\sigma_s' \cdot \mathbf{E}') \cdot \mathbf{E}) > 0 \quad (3.2)$$

We will establish in this section uniqueness of the scattering problem of determining the radiation transmitted into the interior of and scattered by a penetrable anisotropic scatterer Ω when the conductivity tensor σ is positive definite in the sense that if \mathbf{E} is a

vector field defined in the interior of Ω with values in complex seven dimensional space, then a relationship of the form (3.2) is satisfied if \mathbf{E} is nonzero. We require special relationships for the tensors $i\omega\epsilon$ and the tensors $i\omega\mu$. Specifically, we insist that if \mathbf{E} is a nonzero vector then it is true everywhere in the interior of Ω that

$$((i\omega\epsilon \cdot \mathbf{E}) \cdot \mathbf{E}^* - (i\omega\epsilon^* \cdot \mathbf{E}^*) \cdot \mathbf{E}) > 0 \quad (3.3)$$

or else the left side of inequality (3.3) is zero. Furthermore, if \mathbf{H} is not identically zero, then

$$(\mathbf{H}^* \cdot (i\omega\mu \cdot \mathbf{H}) - \mathbf{H} \cdot (i\omega\mu^* \cdot \mathbf{H}^*)) > 0 \quad (3.4)$$

or else the left side of inequality (3.4) is identically zero. We require that the difference between two supposedly different solutions of the scattering problem satisfy the Silver Mueller radiation condition. The proof is then carried out by examining the Silver Mueller radiation condition in the form,

$$\frac{LIM}{R \rightarrow \infty} \int_{C_R} |(\mathbf{n} \times \text{curl}(\mathbf{E}^s) - ik_0 \mathbf{E}^s)|^2 d\mathbf{a} = 0 \quad (3.5)$$

where C_R is a surface defined by

$$C_R = \left\{ \mathbf{x} \in \mathbb{R}^3 : \sum_{i=1}^3 x_i^2 = R^2 \right\} \quad (3.6)$$

By using the impedance sheet boundary condition which becomes the standard boundary condition if σ_s , the surface conductivity, is zero and by realizing that the Silver Mueller radiation conditions imply that

$$\begin{aligned}
0 = & \left(\frac{\text{LIM}}{R \rightarrow \infty} \right) \int_{C_R} (|\mathbf{n} \times \text{curl}(\mathbf{E})|^2 + k_0^2 (|\mathbf{E}|^2)) d\mathbf{a} + \\
& \omega \mu_0 k_0 \int_{\partial \Omega} ((\boldsymbol{\sigma}_s \cdot \mathbf{E}) \cdot \mathbf{E}^* + (\boldsymbol{\sigma}_s^* \cdot \mathbf{E}^*) \cdot \mathbf{E}) d\mathbf{a} + \\
& \omega \mu_0 k_0 \int_{\Omega} \text{div} ((\mathbf{H} \times \mathbf{E}^*) + (\mathbf{H}^* \times \mathbf{E})) d\mathbf{v} \quad (3.7)
\end{aligned}$$

We immediately establish uniqueness by noting that if the difference \mathbf{E} between two solutions of the scattering problem were nonzero anywhere, then the right side of equation (3.7) would be positive giving a contradiction since the left side of this equation is zero.

Theorem. If the electrical properties of a scatterer Ω satisfies (3.2) on separating sheets if $\boldsymbol{\sigma}_s$ is nontrivial, satisfies (3.2) with $\boldsymbol{\sigma}_s$ replaced by $\boldsymbol{\sigma}_s^*$, satisfies (3.3), and satisfies (3.4) in the interior of the scatterer if $\boldsymbol{\sigma}_s$, ϵ , and μ , respectively, are nontrivial then there is at most one classical solution of the scattering problem.

By combining these concepts a myriad of different uniqueness theorems can be derived. Note that while the hypotheses in the above theorem may seem stringent, they do not require directly that the frequency domain Maxwell equations be an elliptic system.

By making use of the function G derived in section 2 of this paper and by introducing a magnetic charge conductivity $\boldsymbol{\sigma}_m$ we can show that a symmetric system of coupled electric and magnetic field integral equations describing the scattering of a general object in seven dimensional space is, following the three dimensional development in Graglia and Uslenghi [8], given by,

$$\begin{aligned}
\mathbf{E} - \mathbf{E}^1 &= -\text{grad} \int_{\Omega} \left(\frac{\text{idiv} (i\omega(\epsilon - \epsilon_0 \mathbf{I}) + \sigma_e) \mathbf{E}}{\omega \epsilon_0} \right) G(\mathbf{r}, \mathbf{s}) dv(\mathbf{s}) \\
&\quad - \text{grad} \int_{\partial \Omega} \left(\frac{(i\omega(\epsilon - \epsilon_0 \mathbf{I}) + \sigma_e)}{i\omega \epsilon_0} \right) \cdot \mathbf{E} \mathbf{n}(\mathbf{s}) G(\mathbf{r}, \mathbf{s}) da(\mathbf{s}) \\
&\quad - i\omega \mu_0 \int_{\Omega} (i\omega(\epsilon - \epsilon_0 \mathbf{I}) + \sigma_e) \cdot \mathbf{E}(\mathbf{s}) G(\mathbf{r}, \mathbf{s}) dv(\mathbf{s}) + \\
&\quad - \text{curl} \int_{\Omega} (i\omega(\mu - \mu_0 \mathbf{I}) + \sigma_m) \cdot \mathbf{H}(\mathbf{s}) G(\mathbf{r}, \mathbf{s}) dv(\mathbf{s}) \quad (3.8)
\end{aligned}$$

and

$$\begin{aligned}
\mathbf{H} - \mathbf{H}^1 &= -\text{grad} \int_{\Omega} \frac{\text{idiv} (i\omega(\mu - \mu_0 \mathbf{I}) + \sigma_m) \mathbf{H}}{\omega \mu_0}(\mathbf{s}) G(\mathbf{r}, \mathbf{s}) dv(\mathbf{s}) \\
&\quad - \text{grad} \int_{\partial \Omega} \left(\frac{(i\omega(\mu - \mu_0 \mathbf{I}) + \sigma_m)}{i\omega \mu_0} \right) \cdot \mathbf{H} \mathbf{n}(\mathbf{s}) G(\mathbf{r}, \mathbf{s}) da(\mathbf{s}) \\
&\quad - i\omega \epsilon_0 \int_{\Omega} (i\omega(\mu - \mu_0 \mathbf{I}) + \sigma_m) \mathbf{H}(\mathbf{s}) G(\mathbf{r}, \mathbf{s}) dv(\mathbf{s}) + \\
&\quad \text{curl} \int_{\Omega} (i\omega(\epsilon - \epsilon_0 \mathbf{I}) + \sigma_e) \cdot \mathbf{E}(\mathbf{s}) G(\mathbf{r}, \mathbf{s}) dv(\mathbf{s}) \quad (3.9)
\end{aligned}$$

where here the function $G(\mathbf{r}, \mathbf{s})$ is the function E_k , given by equation (2.16).

We remark that the use of dyadic identities can transform the surface volume integral equations given by (3.4) and (3.5) into volume integral equations by making use of the dyadic relationship,

$$\int_{\partial \Omega} (\mathbf{n} \cdot \mathbf{F}) G da = \int_{\Omega} (\text{div}(\mathbf{F}) G + (\mathbf{F} \cdot \nabla) G) dv \quad (3.10)$$

This identity is applied to each of the integrals over the boundary $\partial \Omega$ of

Ω and permits us to get a coupled system of volume integral equations. From equation (3.8) and (3.10) we get the volume electric field integral equation,

$$\begin{aligned} \mathbf{E} - \mathbf{E}^i = & \\ & \frac{i}{\omega\epsilon_0} \int_{\Omega} (((i\omega(\epsilon - \epsilon_0\mathbf{I}) + \sigma_e) \cdot \mathbf{E} \cdot \mathbf{n})(\mathbf{s})(\mathbf{grad})_s (\mathbf{grad})_r G(\mathbf{r}, \mathbf{s}) dv(\mathbf{s}) \\ & - i\omega\mu_0 \int_{\Omega} (i\omega(\epsilon - \epsilon_0\mathbf{I}) + \sigma_e) \cdot \mathbf{E}(\mathbf{s}) G(\mathbf{r}, \mathbf{s}) dv(\mathbf{s}) + \\ & - \text{curl} \int_{\Omega} (i\omega(\mu - \mu_0\mathbf{I}) + \sigma_m) \cdot \mathbf{H}(\mathbf{s}) G(\mathbf{r}, \mathbf{s}) dv(\mathbf{s}) \end{aligned} \quad (3.11)$$

From equation (3.9) and (3.10) we get the companion magnetic field integral equation,

$$\begin{aligned} \mathbf{H} - \mathbf{H}^i = & \\ & \frac{i}{\omega\mu_0} \int_{\Omega} (((i\omega(\mu - \mu_0\mathbf{I}) + \sigma_m) \cdot \mathbf{H} \cdot \mathbf{n})(\mathbf{s})(\mathbf{grad})_s (\mathbf{grad})_r G(\mathbf{r}, \mathbf{s}) dv(\mathbf{s}) \\ & - i\omega\epsilon_0 \int_{\Omega} (i\omega(\mu - \mu_0\mathbf{I}) + \sigma_m) \cdot \mathbf{H}(\mathbf{s}) G(\mathbf{r}, \mathbf{s}) dv(\mathbf{s}) + \\ & + \text{curl} \int_{\Omega} (i\omega(\epsilon - \epsilon_0\mathbf{I}) + \sigma_e) \cdot \mathbf{E}(\mathbf{s}) G(\mathbf{r}, \mathbf{s}) dv(\mathbf{s}) \end{aligned} \quad (3.12)$$

4. REFERENCES

1. Bergshoeff, E, I. G. Koh, and E. Sezgin. Yang-Mills-Einstein supergravity in seven dimensions. *Physics Review D*. 32 (6) (September 15, 1985) pp 1353-1357
2. Boyer, C. P. and G. N. Flemming. Quantum field theory on a seven dimensional homogeneous space of the Poincare group. *Journal of Math. Phys.* Volume 15, Number 7 (1974) pp 1007-1024
3. Calabi, Eugenio. Construction and Properties of some 6-Dimensional Almost Complex Manifolds. *Transactions of the American Mathematical Society* 87 (1958) pp 407-438
4. Cohoon, D. K. Electromagnetic scattering in three and seven dimensional space - - the equivalence of integral equation and Maxwell equation formulation of scattering problems with applications. AP-S International Symposium 1986, 1986 International Symposium Digest Antennas and Propagation (Cat. No 86CH2325-9) Volume 2 Philadelphia, Pennsylvania USA (8-13 June, 1986) pp 1023-1026
5. Dine, Michael and Nathan Seiberg. Couplings and scales in superstring models. *Physics Review Letters* B. 155 No. 3 (1985) pp 151-155
6. Dunderer, Resit, Feza Gursey, and Chia-Hsiung Tze. Generalized vector products, duality, and octonionic identities in $D = 8$ geometry. *APB. Math. Phys.* 25 (5) (May, 1984) pp 1496-1506.
7. Gonzalez-Diaz, P. F. Closed Theory of Electrodynamics and

- Gravitation. Inst. De Optica Daza de Valdes, CSIC, Serrano, Madrid, Spain Atti Fond. Giorgio Ronchi (Italy) Volume 34, No. 4-5 (July- October, 1979) pp 403-411
8. Graglia, R. D. and P. L. E. Uslenghi. Electromagnetic scattering from anisotropic materials, Part I: General Theory. IEEE Transactions on Antennas and Propagation. Volume 12, Number 8 (August, 1984) pp 867-869
 9. Green, M. and D. Gross. Workshop on Unified String Theories. Papers from the Workshop Held at the University of California, Santa Barbara, California, July 29 - August 16, 1985. Singapore: World Scientific Publishing Company (1986) 745 pages
 10. Horowitz, Gary T. What is a Calabi-Yau Space? IN Green, M. and D. Gross (Eds) Workshop on Unified String Theories. Papers from the Workshop Held at the University of California, Santa Barbara, California, July 29 - August 16, 1985. Singapore: World Scientific Publishing Company (1986) pp 635-653
 11. Kim, Jae Kwan, I. G. Koh, and Yongsung Yoon. Calabi-Yau Manifolds from arbitrary weighted homogeneous spaces. Physics Review D 33 (No 10) (May 15, 1986) pp 2893-2895
 12. Kim, Kee Yong, Yong Duk Kim, Y. S. Myung, and Young Jai Park. Stability analysis of $M_4S^2S^2$ in the Einstein Maxwell System. Physical Review D. Particles and Fields. Third Series. Volume 33 Number 2 (1986) pp 477-483
 13. Koh, I. G. and E. Sezgin. Yang-Mills-Einstein supergravity in seven dimensions. Physical Review D. Particles and Fields.

Third Series. Volume 32. Number 6 (1985) pp 1353-1357

14. Li, Shu Chen. Interaction of Electromagnetic Radiation with Simulated Biostructures. Ph.D. thesis. Philadelphia, Pennsylvania 19122: Temple University (March 31, 1986), 456 pages
15. Lindstrom, U. and J. Grundberg. A torsion potential. *Nuovo Cimento B* (11) 75, No. 2 (1983) pp 171-184
16. Mecklenburg, W. Aspects of seven-dimensional relativity. *Physics Review D*. 21 (8) (April 15, 1980) pp 2149-2166
17. Media, K. Cosmological solutions with Calabi-Yau Compactification. *Physics Letters B*. 166, No. 1 (1986) pp 59-64
18. Media, K. Attractor in a superstring model: The Einstein Theory, the Friedman Universe and inflation. *Physics Review D*. 35 (2) (January 15, 1987) pp 471-479
19. Pernici, M., K. Pilch., P. van Nieuwenhuizen, and N. P. Warner. Noncompact gaugings and critical points of maximal supergravity in seven dimensions. *Nuclear Phys. B*. 249, No. 3 (1985) pp 381-395
20. Pernici, M. and K. Pilch. Guaged maximally extended supergravity in seven dimensions. *Physics Lett. B*. 143 No 1-3 (1984) pp 103-107
21. Rayski, J. Multidimensional Unified Theory. *Inst. of Phys., Jagellonian Univ., Krakow, Poland. Acta Phys. Austriaca Suppl. 19 Facts and Prosepects of Guage Theories* 21 Feb. - 3 March 1978 Schladming, Austria (1978) pp 869-870
22. Redner, S. and Z. R. Yang. Size and shape of directed lattice

- animals. *J. Phys. A.* Vol. 15 No. 4 (1982) pp L177-L187
23. Romans, L. J. and N. P. Warner. Some supersymmetric counterparts of the Lorentz Chern Simons term. *Nuclear Physics B.* Vol. 273 No. 2 (1986) pp 320-332
 24. Salam, Abdus. $SO(4)$ Gauging of $N=2$ supergravity in seven dimensions. *Physics Lett. B.* Vol. 126, No. 5 (1983) pp 295-300
 25. Treves, F. *Linear Partial Differential Equations with Constant Coefficients.* New York: Gordon and Breach (1966)
 26. Van Nieuwenhuizen, P. and N. P. Warner. New compactifications of ten and eleven dimensional supergravity on manifolds which are not direct products. *Communications in Mathematical Physics* Vol. 99 No. 1 (1985) pp 141-151
 27. Witten, Edward. Dimensional Reduction of Superstring Models. *Physics Letters B* Volume 155, No. 3 (1985) pp 151-155
 28. Yasuda, Osamu. Higher derivative terms and zero modes in $D=10$ supergravity. *Physics Letters B.* Volume 169 No. 1 (1986) pp 64-68
 29. Zorn, M. *Theorie der alternativen Ringe.* *Abh. Math. Sem. Hamb. Univ.,* Volume 8 (1931) pp 123-147.
 30. Zorn, M. *Alternativkorper und quadratische Systeme.* *Abh. Math. Sem. Hamb. Univ.* vol. 9 (1933) pp 395-402

Blank

**OBLIQUE INCIDENCE RADIATIVE HEATING OF
ANISOTROPIC AEROSOL PARTICLES WHOSE REGIONS OF
CONTINUITY OF TENSORIAL ELECTROMAGNETIC
PROPERTIES ARE DELIMITED BY COAXIAL CYLINDERS
COVERED BY IMPEDANCE SHEETS**

D. K. Cohen

Department of Mathematics 058-18

Temple University

Philadelphia, Pennsylvania 19122

ABSTRACT

A computer program has been written which predicts first of all the internal and scattered radiation associated with the interaction of plane electromagnetic waves (possibly more than one) with an anisotropic cylindrical structure whose regions of continuity of tensorial electromagnetic properties are delimited by coaxial cylinders covered by impedance sheets, and then uses the calculated power density

distribution as a source term for an energy equation to calculate the radiation induced thermal excursions. The motivation for this work is to (i) be able to predict the precise radiation induced temperature distribution in a cylindrically symmetric simulated biostructure modeled by an N layered infinite cylinder (ii) be able to model the interaction of light with a fibrous aerosol particle, or (iii) to be able to develop a benchmark for elongated structures arising in radar design considerations, hardening structures against electromagnetic pulses, or in the design of structures with maximal extinction or absorption properties. This program will carry out the calculations in the difficult wavelength region and when the structure has an arbitrary orientation with respect to the incoming radiation. The oblique incidence problem requires the analysis of four by four matrices to relate expansion coefficients in one layer to those of another layer. The more widely studied normal incidence problem just requires the use of two by two matrices. While the electric and magnetic vectors of radiation interacting with a sphere have two components each which are tangential to the surface of the sphere, relations involving Legendre polynomials permit one to reduce the problem of plane waves interacting with an N layer sphere to an analysis of two sets of two by two matrices. So in some sense this solution is necessarily more complex and rich in structure than that provided by the Mie solution. The program could with effort be extended to treat the problem of scattering by structures possessing a surface charge distribution which makes the usual boundary conditions which state that the tangential components of E, the electric vector, and H, the total magnetic vector, are continuous across separating boundaries slightly different because of

surface conductivity. The fact that electrical properties of the material with which the radiation is interacting could depend on temperature would mean that even the electric fields themselves could depend in a nonlinear way on the electric and magnetic vectors of the incoming radiation. By estimating the temperature, we may be able to predict whether or a linear analysis would give useful results. This would be true if the temperature increases were small enough that the electrical properties did not change significantly.

We prove a theorem showing that a graph of percent power versus percent body weight is necessarily a concave function with a strictly negative second derivative. This shows the invalidity of any uniform heating assumptions while at the same time suggesting that the problem of using microwaves to treat cancer could be solved by determining the source location and phase relationships that will cause a hot spot to move to the location of a tumor.

Also, we show that multiple beams or sources which we will simulate mathematically by combinations of plane waves can be used to move hot spots and can in fact in our special case produce a z dependent power density distribution in a simulated biostructure modeled by an infinite cylinder.

A shooting method based eigenfunction expansion scheme was used to get an exact analytical expression for the microwave induced temperature excursions in the simulated biostructure modeled as an N layer infinite cylinder structure. The purpose of the research is to show that by moving a hot spot to the location of a tumor one could by raising the temperature of the tumor a few degrees centigrade destroy the cancer without harming nearby normal tissue. By use of a full

wave solution one can simulate from a variety of microwave sources such as helices and plates. We would of course have to know how a direct contact structure could be modeled by a complex combination of remote sources which would mean that we would have to solve this more difficult problem by other means.

In the past water filled bags have been used to attempt to couple power to a penetrable body such as human tissue in an attempt to achieve a therapeutic thermal increase that would be effective in treating cancer. This can be achieved, as our calculations show, by simply creating the proper phase relationship between the electric and magnetic vectors. This concept can also be applied to the nuclear fusion problem.

1. INTRODUCTION TO SCATTERING BY N LAYER CYLINDERS

The solution of the problem of describing the scattering of radiation by an anisotropic N layer cylinder is based on (i) a basis of singular vector fields for a space of vector valued functions which are invariant with respect to the curl operation which we use to generate a base of solutions of the Maxwell equations in each layer, (ii) the completeness of the Hilbert space generated by these separation of variables solutions, and (iii) a proof of uniqueness of the solution of the scattering problem which satisfies the Silver Mueller radiation conditions on a sequence of cylinders whose axis coincides with the scatterer axis and whose radii approach infinity and the continuity of tangential components of the electric and magnetic vectors across the separating boundaries. Condition (iii) enables us to say that a positive definite bilinear functional acting on the difference between two solutions of the problem is identically zero.

We begin with a review of the solution of the problem for isotropic multilayer cylindrical structures delimited by coaxial cylinders with a circular cross section. For the case of structures with isotropic layers, solutions of the vector Maxwell equations are obtained by starting with solutions of the scalar Helmholtz equation and computing the curl of this function times the unit vector along the cylinder axis. A second group of solutions is obtained by taking the curls of the first equation; these solutions are denoted by N with appropriate subscripts and superscripts. The original solutions, the curl of the product of a solution of the scalar Helmholtz equation and the unit vector along the axis of the cylinder, are denoted by the letter M . The M vectors only have components in the radial and theta

directions, and the N vectors have components in the radial, theta, and axial directions. We let ϕ denote the angle between the direction of incidence of the radiation and a plane perpendicular to the cylinder axis, and we let ζ denote the angle between the direction of incidence and the cylinder axis. We will let h denote the product of the propagation constant and $\cos(\zeta)$. The quantity κ in each layer will be a kind of modified propagation constant which is the square root of the difference between the square of the usual propagation constant and the square of h , and is always complex if our material is dissipative, and in the nondissipative case of free space κ is equal to the ordinary propagation constant of free space, which is the ratio of the angular frequency of the light and the vacuum speed of light multiplied by $\sin(\zeta)$. Since $\sin(\zeta)$ is exactly 1 for normally incident light which corresponds to ζ equal to 90 degrees, we see that κ is equal to k in this case. The basic solutions of the scalar Helmholtz equation are

$$\Psi_{(N+1,a)}^{(j)} = Z_a^{(j)}((k_0 \sin(\zeta))r) e^{-ik_0 z} e^{i\alpha \phi} \quad (1.1)$$

in free space which is the $(N+1)$ st layer and in the layer indexed by p , we have

$$\Psi_{(p,a)}^{(j)} = Z_a^{(j)}(\kappa_p r) e^{-ik_0 z} e^{i\alpha \phi} \quad (1.2)$$

where the Z function is an ordinary Bessel function if $j = 1$ and is a Hankel or a Neumann function if $j = 2$ and where

$$\kappa_p^2 = k_p^2 - h^2 \quad (1.3)$$

with

$$k_p^2 = \omega^2 \mu_p \epsilon_p - i\omega \mu_p \sigma_p \quad (1.4)$$

In the layer indexed by p we have

$$\mathbf{M}_{(p,a)}^{(j)} = \text{curl}(\Psi_{(p,a)}^{(j)} \mathbf{e}_z) \quad (1.5)$$

and the N vector in the layer indexed by p is given by

$$\mathbf{N}_{(p,a)}^{(j)} = (1/k_p) \text{curl}(\mathbf{M}_{(p,a)}^{(j)}) \quad (1.6)$$

We note that if somehow we know the electric vector in the layer indexed by p , that the magnetic vector is easily determined by the relation,

$$\mathbf{H}_p = \left[\frac{1}{-i\omega\mu_p} \right] \text{curl}(\mathbf{E}_p) \quad (1.7)$$

An important identity which enables us to express the magnetic vector in terms of the \mathbf{M} vectors and the \mathbf{N} vectors is the relation,

$$(1/k_p) \text{curl}(\mathbf{N}_{(p,a)}^{(j)}) = \mathbf{M}_{(p,a)}^{(j)} \quad (1.8)$$

In the layer indexed by p the electric vector is given by the relation,

$$\mathbf{E}_p = \sum_{s=-\infty}^{\infty} \left(A_{(s,p)} \mathbf{M}_{(p,s)}^{(1)} + B_{(s,p)} \mathbf{N}_{(p,s)}^{(1)} + a_{(s,p)} \mathbf{M}_{(p,s)}^{(2)} + b_{(s,p)} \mathbf{N}_{(p,s)}^{(2)} \right) \quad (1.9)$$

Thus, once the expansion coefficients are known in each layer, the electric and magnetic fields are completely known. We get the magnetic vector by computing the curl of the electric vector and making use of equation (1.7). The equation for the curl of the electric vector is

$$\left[\frac{1}{k_p} \right] \text{curl}(\mathbf{E}_p) =$$

$$\sum_{s=-\infty}^{\infty} \left(A_{(s,p)} \mathbf{N}_{(p,s)}^{(1)} + B_{(s,p)} \mathbf{M}_{(p,s)}^{(1)} + a_{(s,p)} \mathbf{N}_{(p,s)}^{(2)} + b_{(s,p)} \mathbf{M}_{(p,s)}^{(2)} \right) \quad (1.10)$$

By combining equations (1.7), (1.9), and (1.10) and using the equation for the curl in cylindrical coordinates we get the following relationship between the expansion coefficients in layer p and the expansion coefficients in layer $p+1$.

$$\frac{k_p^2 - h^2}{\mu_p} J_n(\kappa_p R_p) A_{(n,p)} + \frac{k_p^2 - h^2}{\mu_p} Z_n^{(2)}(\kappa_p R_p) a_{(n,p)} =$$

$$\frac{k_{p+1}^2 - h^2}{\mu_{p+1}} J_n(\kappa_{p+1} R_p) A_{(n,p+1)} + \frac{k_{p+1}^2 - h^2}{\mu_{p+1}} Z_n^{(2)}(\kappa_{p+1} R_p) a_{(n,p+1)} \quad (1.11)$$

$$- \kappa_p J_n'(\kappa_p R_p) A_{(n,p)} + - \kappa_p Z_n^{(2)'}(\kappa_p R_p) a_{(n,p)} +$$

$$\frac{h n}{k_p R_p} J_n(\kappa_p R_p) B_{(n,p)} + \frac{h n}{k_p R_p} Z_n^{(2)}(\kappa_p R_p) b_{(n,p)} =$$

$$- \kappa_{p+1} J_n'(\kappa_{p+1} R_p) A_{(n,p+1)} + - \kappa_{p+1} Z_n^{(2)'}(\kappa_{p+1} R_p) a_{(n,p+1)} +$$

$$\frac{h n}{k_{p+1} R_p} J_n(\kappa_{p+1} R_p) B_{(n,p+1)} + \frac{h n}{k_{p+1} R_p} Z_n^{(2)}(\kappa_{p+1} R_p) b_{(n,p+1)} \quad (1.12)$$

$$\frac{k_p^2 - h^2}{k_p} J_n(\kappa_p R_p) B_{(n,p)} + \frac{k_p^2 - h^2}{k_p} Z_n^{(2)}(\kappa_p R_p) b_{(n,p)} =$$

$$\frac{k_{p+1}^2 - h^2}{k_{p+1}} J_n(\kappa_{p+1} R_p) B_{(n,p+1)} + \frac{k_{p+1}^2 - h^2}{k_{p+1}} Z_n^{(2)}(\kappa_{p+1} R_p) b_{(n,p+1)} \quad (1.13)$$

$$\left(\frac{h n}{\mu_p R_p} \right) J_n(\kappa_p R_p) A_{(n,p)} + \left(\frac{h n}{\mu_p R_p} \right) Z_n^{(2)}(\kappa_p R_p) a_{(n,p)} +$$

$$\frac{-k_p \kappa_p}{\mu_p} J_n^{(2)'}(\kappa_p R_p) B_{(n,p)} + \frac{-k_p \kappa_p}{\mu_p} Z_n^{(2)'}(\kappa_p R_p) b_{(n,p)} =$$

$$\frac{h n}{\mu_{p+1} R_p} J_n(\kappa_{p+1} R_p) A_{(n,p+1)} + \frac{h n}{\mu_{p+1} R_p} Z_n^{(2)}(\kappa_{p+1} R_p) a_{(n,p+1)} +$$

$$- \frac{k_{p+1} \kappa_{p+1}}{\mu_{p+1}} J_n^{(2)'}(\kappa_{p+1} R_p) B_{(n,p+1)} + \frac{-k_{p+1} \kappa_{p+1}}{\mu_{p+1}} Z_n^{(2)'}(\kappa_{p+1} R_p) b_{(n,p+1)} \quad (1.14)$$

We can express the above relationships compactly in matrix language in the form

$$S^{(n,p)} \begin{pmatrix} A_{(n,p)} \\ a_{(n,p)} \\ B_{(n,p)} \\ b_{(n,p)} \end{pmatrix} = S^{(n,p+1)} \begin{pmatrix} A_{(n,p+1)} \\ a_{(n,p+1)} \\ B_{(n,p+1)} \\ b_{(n,p+1)} \end{pmatrix} \quad (1.15)$$

We note that in the case of normal incidence, the parameter h is proportional to the cosine of ninety degrees and is therefore zero which means that the matrix equation (1.15) reduces to two 2 by 2 matrix equations for the case of incoming radiation with a general polarization. For the case of an incoming electromagnetic wave with the electric vector or the magnetic vector parallel to the cylinder the axis, the solution of the problem becomes particularly simple as then H or, respectively, E is proportional to a vector having the same form as M . The form of the coefficient matrices appearing in equation (1.15) enable one to conveniently write the inverse of the coefficient matrices explicitly even though they are 4 by 4 matrices. A particularly useful fact is the Wronskian relationship,

$$J'_n(z)Y_n(z) - J_n(z)Y'_n(z) = \frac{-2}{\pi z} \quad (1.16)$$

This enables us to write out the inverse explicitly and accurately since some of the terms in the determinant of the 4 by 4 matrix appearing on the left side of equation (1.15) may be accurately evaluated using the relationship (1.16). In developing the equations we also make use of the fact that the cylindrical Bessel functions with either integer or complex index satisfy the equation,

$$\left(\frac{1}{s}\right) \frac{d}{ds} \left(s \frac{dw}{ds} \right) + \left(1 - \frac{v^2}{s^2} \right) w = 0 \quad (1.17)$$

By setting the layer index p equal to $N+1$ and making use of equation (1.9) we can get the scattered radiation as a function of position outside the cylindrical scatterer. By using Poynting's theorem we can derive simple formulas for the total scattered and total absorbed power per unit length along the cylinder. Since the electric field is represented in vector form we can predict what would be measured in a photomultiplier tube placed behind a polarizer simply by calculating the intensity using the component of the electric vector that is parallel to the gratings of the polarizer.

Previous work on cylinder scattering typically considered multilayer structures subject to normally incident radiation (Bussey, [5]), or single layer structures subject to obliquely incident radiation (Wait [20]) and typically considered materials with real indices of refraction and assumed that the electric vector \mathbf{E} was either perpendicular to the plane containing the direction of propagation or was parallel to this plane (Bohren and Huffman ([2], pp 195-200)). We systematically treat all cases by considering a completely general form for the electric vector of the incoming radiation. In the region labeled $N+1$ the electric vector of the incoming radiation is given by

$$\mathbf{E}_{N+1}^i = \sum_{s=-\infty}^{\infty} (F_s \mathbf{M}_{(N+1,s)}^{(i)} + G_s \mathbf{N}_{(N+1,s)}^{(i)}) \quad (1.18)$$

Although the field represented by equation (1.12) can be quite complex, we assume that the expansion coefficients F_s and G_s are completely known thereby leaving only two unknown coefficients of the type 2 vector wave functions associated with Hankel functions for the

representation of the field in the region of space outside the cylinder. Since the type 2 vector wave functions are unbounded on the cylinder axis, they must not make any contribution in the inner layer. Thus, there are two unknown expansion coefficients in the inner layer, and there are two unknown coefficients representing the scattered radiation in the space surrounding the scatterer. By inverting one of the four by four matrices in equation (1.11) we can relate coefficients in layer p to layer p+1. By matrix composition we can get a system of four equations in four unknowns relating for each n the representation of the field in the inner layer to the expansion coefficients for the scattered radiation.

Note that the power density distribution is given by

$$S = \frac{(\sigma_1 + \omega \epsilon_2) E_0^2}{10^9 \times 4.184} \quad (1.19)$$

We further note that if we had two radiation sources coming in at two different angles, then their individual electric fields would have the form,

$$E_1 = F_1 e^{-i h_1 z} \quad (1.20)$$

and

$$E_2 = F_2 e^{-i h_2 z} \quad (1.21)$$

where

$$h_j = k_0 \cos(\zeta_j) \quad (1.22)$$

for $j = 1$ or $j = 2$ where ζ_j denotes the beam angle of the j th beam.

This would mean that the power density distribution is proportional to

$$S = c(E_1 + E_2)(E_1 + E_2)^* \quad (1.23)$$

Substituting (1.20) and (1.21) into (1.23) we find that the power density induced in the infinite cylinder structure by the two plane wave

sources is given by

$$S = c(|E_1|^2 + |E_2|^2 + P_1 P_2 e^{-\lambda_1 - \lambda_2} + P_1 P_2 e^{-\lambda_1 - \lambda_2}) \quad (1.24)$$

This yields a z dependent power density distribution.

In the following theorem X denotes the cylinder cross section, μ denotes the cross sectional area measure, Lebesgue measure, and S is the power density function defined above. The integral of S over a region in the cross section will be the energy deposited per unit length per unit time in that region of the cross section. Also, $E(r)$ will denote the integral of S over that region of points (x,y) in the cross section for which $P(x,y)$ is greater than r . The theorem shows that the second derivative of $E(r)$ with respect to

$$r(r) = \mu(\{(x,y) \in X: P(x,y) > r\}) \quad (1.25)$$

is necessarily negative. The following abstract mathematical theorem explains why shape of the graph of percent power versus percent body weight is concave down.

Theorem 1. Let X be a Hausdorff space. Let μ be a monotone measure on the σ algebra of Borel sets of X such that $\mu(X) = 1$. Let $P: X \rightarrow [a,b]$ be a continuous function from the nonempty set X into the closed interval $[a,b]$. Assume that a is smaller than b and that there is a point x_1 in X and a point x_2 in X such that $P(x_1) = a$ and $P(x_2) = b$. Let r be a member of $[a,b]$ and let

$$r(r) = \mu(\{x \in X: P(x) > r\}) \quad (1.26)$$

and let $E(r)$ be defined by

$$E(r) = \int_{x \in X: P(x) > r} P d\mu \quad (1.27)$$

then

$$\frac{dE}{d\zeta} = r \quad (1.28)$$

and the function $E(r)$ defined by equation (1.27) has a negative second derivative and is consequently a concave function of ζ .

Proof. It is clear that $\zeta(r)$ is a decreasing function of r . The theorem then follows from the fact that the second derivative of $E(r)$ with respect to r is the derivative of the left side of (1.22) with respect to r divided by the derivative of $\zeta(r)$ with respect to r . Thus, the second derivative of $E(r)$ with respect to ζ is therefore 1 divided by a negative number.

2. SUMMARY OF RADIATIVE HEAT TRANSFER CONCEPTS

The source term for the heat equation is given by the relation

$$S = (1/T) \int_{T_1}^{T_2} \left(\frac{\text{div}(\mathbf{E} \times \mathbf{H}^*)}{10^9 \times 4.184} \right) dt \quad (2.1)$$

where we let the time t for the source term driving the heat equation be the midpoint of the interval from T_1 to T_2 , since the heat equation is on a much lower time scale than the oscillations of the incoming electromagnetic wave and since it is itself the result of averaging microscopic energy equations and where

$$T = T_2 - T_1 \quad (2.2)$$

Another simpler form for the source term of the radiatively driven heat equation is given by

$$S = \frac{(\sigma_1 + i\omega\epsilon_2) \overline{E_s^2}}{10^9 \times 4.184} \quad (2.3)$$

where σ_1 denotes the real part of the electrical conductivity and ϵ_2 denotes the imaginary part of the complex permittivity of the aerosol particle, and where the subscript s indicates a local time average of the length of the electric vector was taken. Once the source term is determined in the more natural centimeter-gram-second units using equation (2.1) or (2.3), we can then calculate using eigenfunction expansions the solution of a slightly generalized heat equation which includes a heat sink term $-bu$ where u denotes the increase in temperature within the aerosol particle above the ambient temperature and satisfies the equation,

$$\rho c \left(\frac{\partial u}{\partial t} \right) = \text{div}(K(\text{grad}(u))) - bu + S \quad (2.4)$$

where ρ is the density in grams per cubic centimeter, c denotes the

specific heat in calories per gram degree centigrade, and K symbolizes the thermal conductivity in calories per centimeter per degree centigrade per second, and b denotes a heat sink term in calories per cubic centimeter per second per degree. We seek a solution of the radiatively driven heat equation which satisfies zero initial conditions so that $u = 0$ when the time parameter t is zero and Newton cooling law conditions on the boundary of the aerosol particle of the form

$$K_N \left[\frac{\partial u}{\partial r} \right]_{r=R_N} + Hu(R_N, \theta, \lambda, t) = 0. \quad (2.5)$$

where

$$r = R_p \quad (2.6)$$

is the equation of the cylinder separating layer p from layer $p+1$ and when $p = N$ equation (2.6) defines the surface separating the multilayer cylindrical scatterer from the surrounding space. It is at this surface that the Newton cooling law given by equation (2.5) is valid.

We begin our discussion of the solution of the heat equation by writing some general relationships that are valid for heat transfer problems in any dimension. If we are solving the heat transfer problem defined by the energy equation (2.4) in an arbitrary bounded open set Ω with a smooth normal vector N in a space of any dimension, all considerations are the same except that the surface boundary condition (2.5) is replaced by

$$(K \text{grad}(u) \cdot N + Hu)(r) = 0 \quad (2.7)$$

for all points r in the boundary, $\partial\Omega$ of the scattering object Ω .

We will solve this more general boundary value problem by the method of representation of the solution in a Hilbert space generated by eigenfunctions of the elliptic portion of the heat operator. This

gives an exact solution and permits one to accurately compute temperatures at thousands of points within the aerosol particle once the expansion coefficients are known. We will seek functions ψ_k which are solutions of the elliptic partial differential equation,

$$\operatorname{div}(K(\operatorname{grad}(\psi_k))) - b\psi_k = -\lambda_k \rho c \psi_k \quad (2.8)$$

We find solutions ψ_k of equation (2.8) which satisfy the generalized Newton cooling law given by equation (2.7). The theory of semicontinuous functions on a compact subset of the unit ball in the Hilbert space of square integrable functions shows that a Rayleigh Ritz procedure could yield and show the existence of a sequence of eigenfunctions. Suppose we simply make use of the Gauss divergence theorem and note that

$$\int_{\Omega} \operatorname{div}(\psi_k K(\operatorname{grad}(\psi_k))) d v = \int_{\partial \Omega} \psi_k K(\operatorname{grad}(\psi_k)) \cdot N d s \quad (2.9)$$

An important and obvious relationship is that if ψ_k and ψ_j are eigenfunctions corresponding to distinct eigenvalues, then

$$-\left(\int_{\partial \Omega} H \psi_j \psi_k d s\right) = \int_{\Omega} \operatorname{div}(\psi_j (K(\operatorname{grad}(\psi_k)))) d v \quad (2.10)$$

This implies in view of other relationships and the subtraction of the forms of the right side of (2.10) with j and k interchanged that

$$(\lambda_k - \lambda_j) \int_{\Omega} \psi_k \psi_j \rho c d v = 0 \quad (2.11)$$

The eigenvalues λ_k and the eigenfunctions ψ_k satisfy the Rayleigh form

$$\lambda_k = \left\{ \frac{\int_{\partial \Omega} H \psi_k^2 d s + \int_{\Omega} (K(\operatorname{grad}(\psi_k)) \cdot \operatorname{grad}(\psi_k)) + \psi_k^2 b d v}{\int_{\Omega} \psi_k^2 \rho c d v} \right\} \quad (2.12)$$

Carrying out this analysis is precisely the Rayleigh Ritz procedure for the estimation of eigenfunctions and eigenvalues. This procedure could

be used with particles of a general shape. To get the eigenvalues and eigenfunctions we begin by minimizing the functional suggested by the right side of equation (2.12); this gives us the eigenfunction corresponding to the smallest eigenvalue. If we assume that k such eigenfunctions and eigenvalues have been determined we get the next one by minimizing the functional in the subspace of functions on the unit ball of the Hilbert space which are regular and which are orthogonal to each of the first k eigenfunctions.

We next discuss uniqueness of the solution of the heat equation (2.4) which satisfies the Newton cooling law relationship (2.7). We let w denote the difference between two such solutions and first of all note that w satisfies the equation

$$\rho c \left(\frac{\partial w}{\partial t} \right) = \text{div} (K (\text{grad} (w))) - bw \quad (2.13)$$

After multiplying both sides of the above equation by w and using the Gauss divergence theorem, we see that

$$\left(\frac{\partial}{\partial t} \right) \int_0 (\rho c w^2 / 2) d v = - \left(\int_0 (K \text{grad} (w) \cdot \text{grad} (w) + w^2 b) d v + \int_{\partial 0} H w^2 d s \right) \quad (2.14)$$

Since it is clear that if the conducting body is physical in the sense that it dissipates heat or b is positive, heat flows from hot to cool or K is positive and given that the dot product of the temperature gradient and the outward directed normal is positive which means that the body is hotter than the outside medium that the body should lose heat to its environment which is to say that H should be positive, then

$$\left(\frac{\partial}{\partial t} \right) \int_0 (\rho c w^2 / 2) d v \leq 0 \quad (2.15)$$

Furthermore, at $t = 0$ the fact that each solution is zero certainly implies this for the difference of two solutions and if we let

$$F(t) = \int_{\Omega} (w^2 \rho c) d\tau \quad (2.16)$$

we see from (2.15) that the derivative of $F(t)$ is nonpositive so that $F(t)$ is nonincreasing, that by its very definition $F(t)$ is nonnegative, and $F(0) = 0$, which taken together means that $F(t)$ is zero for all positive values of t . This implies that since ρc is positive everywhere in Ω that the difference between the two solutions is identically zero for all positive values of t .

The existence proof is completely constructive and in fact shows us how to get a very robust method of calculating the temperature for all times at thousands of points even when the radiative heating scheme is temporally or even spatially quite complex. We simply take a series expansion

$$u = \sum_{k=1}^{\infty} a_k(t) \psi_k \quad (2.17)$$

realizing that if we knew the expansion coefficients $a_k(t)$ the radiation induced thermal excursion u would be completely known, and substitute this function, which is guaranteed to satisfy the Newton cooling law boundary condition given by equation (2.5), into equation (2.4). When we do this we obtain the relation,

$$\sum_{k=1}^{\infty} (\rho c \frac{da_k(t)}{dt} \psi_k - (ba_k(t) - \lambda_k \rho c a_k(t)) \psi_k + ba_k(t) \psi_k) = \frac{S}{\rho c} \quad (2.18)$$

We now use the fact that the eigenfunctions ψ_k form a complete orthogonal set of functions in the sense that the only function in our Hilbert space which is orthogonal to all of them with respect to the weight function ρc is the function which is identically zero. Indeed, the

Rayleigh procedure guarantees this. Thus, we let

$$b_k(t) = \left\{ \frac{\int_{\Omega} \frac{S}{\rho c} \psi_k \rho c d v}{\int_{\Omega} \psi_k^2 \rho c d v} \right\} \quad (2.19)$$

If we multiply both sides of equation (2.18) by ψ_j and integrate over Ω , make use of the orthogonality relation given by equation (2.11), and substitute in the relation suggested by equation (2.19), we see that

$$\frac{d a_k(t)}{dt} + \lambda_k a_k(t) = b_k(t) \quad (2.20)$$

We see that since $b_k(t)$ is completely known for each k since the source term S is known and since equation (2.20) is a simple first order linear equation, it follows that the expansion coefficients are given by

$$a_k(t) = \int_0^t \exp(-\lambda_k(t-r)) b_k(r) dr \quad (2.21)$$

This is in fact the exact procedure which is used in our computer program.

We remark that the computation of temperature excursions when plane waves impinge on the simulated biostructure from different directions is carried out simply by breaking up the source term into a sum of source terms with different s dependencies and solving the heat equation for each source term separately and adding up the results. The source term is written in the form

$$S = S_0 + S_1 e^{-i h_1 s} + S_2 e^{-i h_2 s} + \dots + S_n e^{-i h_n s} \quad (2.22)$$

We then solve $n + 1$ heat equations of the form (2.4). If S_j is a function of r and θ , then the heat equation is solved by seeking a solution of the form

$$v_j e^{-i h_j s} = u_j \quad (2.23)$$

where v_j depends only on r and θ and

$$\rho c \left(\frac{\partial u_j}{\partial t} \right) = \text{div} (K (\text{grad} (u_j))) - b u_j + S_j e^{-a_j r} \quad (2.24)$$

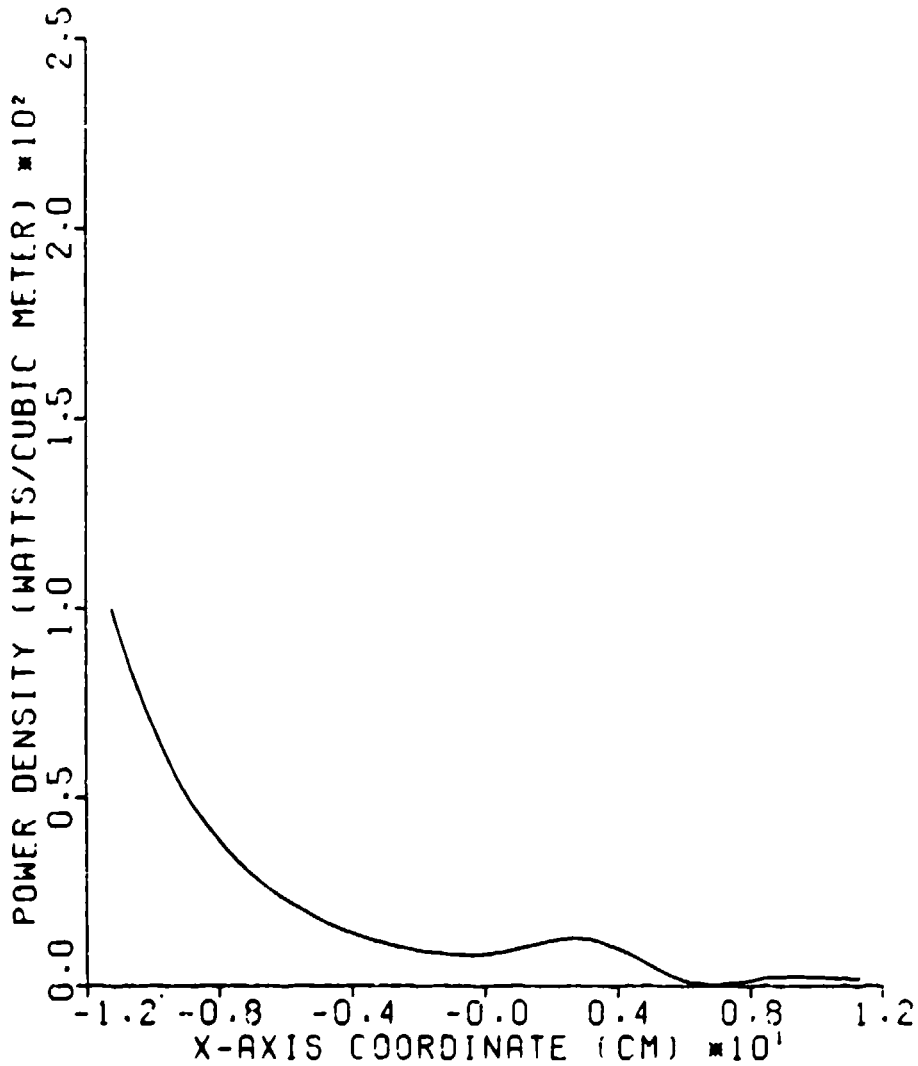
Then the solution u of (2.4) is given by

$$u = u_0 + u_1 + u_2 + \dots + u_n \quad (2.25)$$

The functions v_j are obtained in the usual way except that the blood flow cooling or bioheat transfer term b is modified by a radiative cooling term b_j^2 .

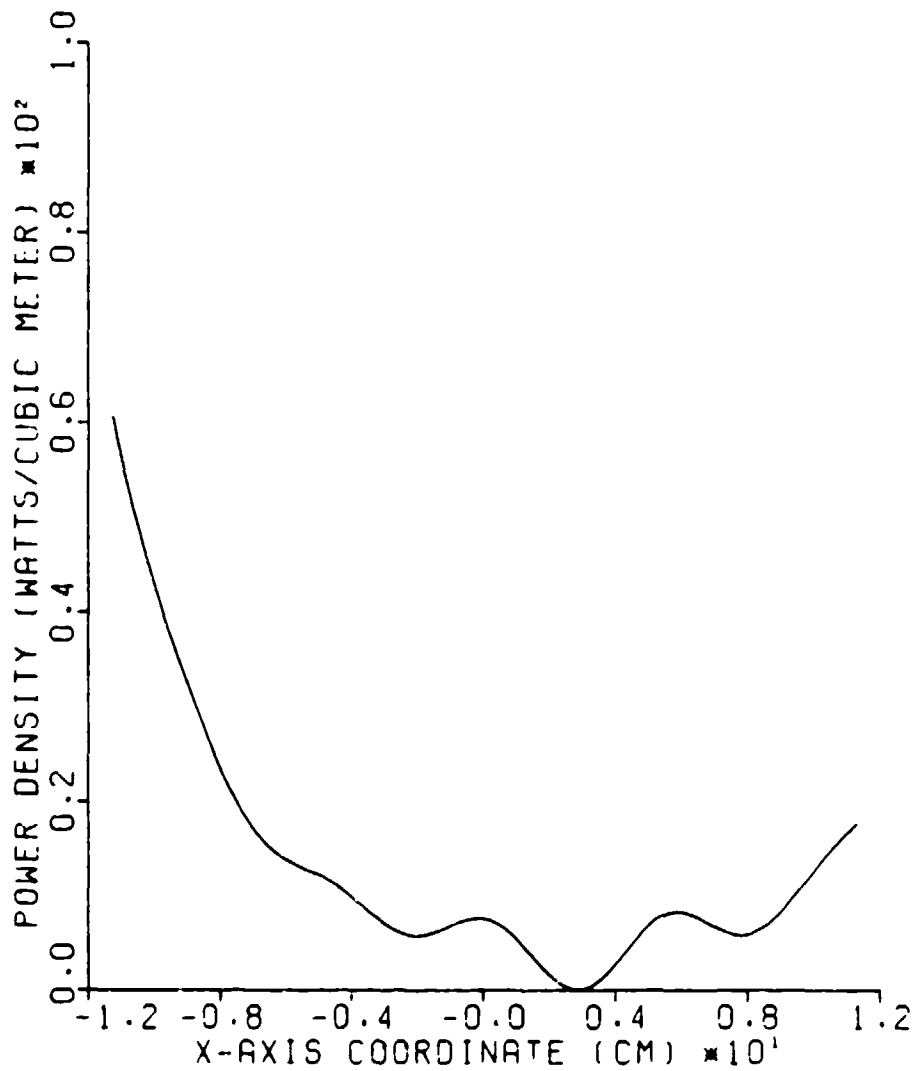
TRANSVERSE MAGNETIC EXPOSURE
 FREQUENCY = 500.00 MHZ
 PEAK ELECTRIC FIELD = 61.30 VOLTS/METER

LAYER BOUNDARY (CM)	RELATIVE DIELECTRIC CONSTANT	ELECTRICAL CONDUCTIVITY (MHOS/M)	DENSITY (GRAMS/CC)
11.29	39.600	0.6500	1.0000



TRANSVERSE ELECTRIC EXPOSURE
 FREQUENCY = 500.00 MHZ
 PEAK ELECTRIC FIELD = 61.38 VOLTS/METER

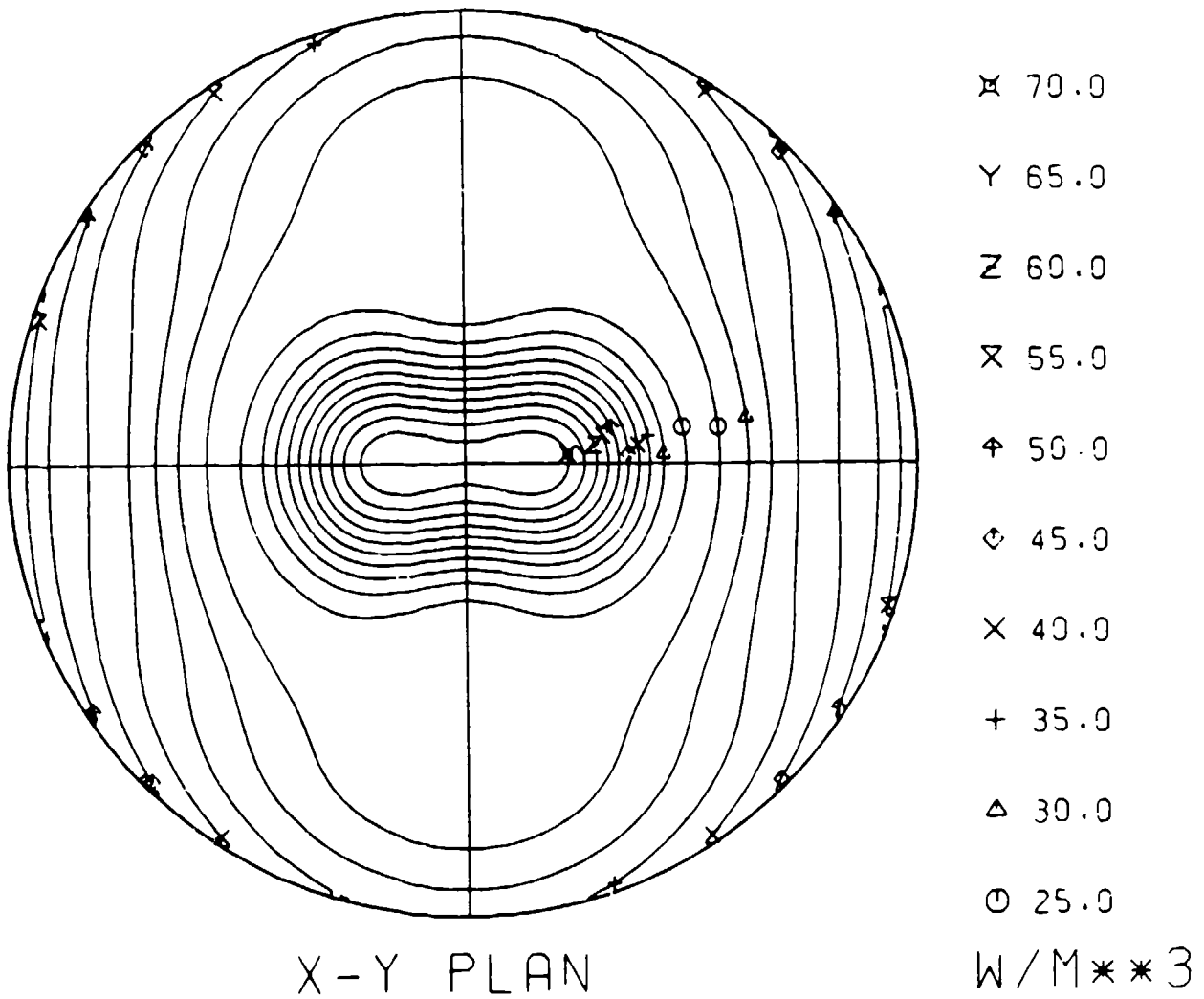
LAYER BOUNDARY (CM)	RELATIVE DIELECTRIC CONSTANT	ELECTRICAL CONDUCTIVITY (MHOS/M)	DENSITY (GRAMS/CC)
11.28	39.600	0.6500	1.0000



POWER DISTRIBUTION IN A MULTILAYER ED SPHERE
EXPOSED TO MICROWAVE RADIATION

FREQUENCY = 500.00 MHZ
PEAK ELECTRIC FIELD = 61.38 VOLTS/METER

LAYER BOUNDARY (CM)	RELATIVE DIELECTRIC CONSTANT	ELECTRICAL CONDUCTIVITY (MHOS/M)	DENSITY (GRAMS/CC)
11.28	39.600	0.6500	1.0000

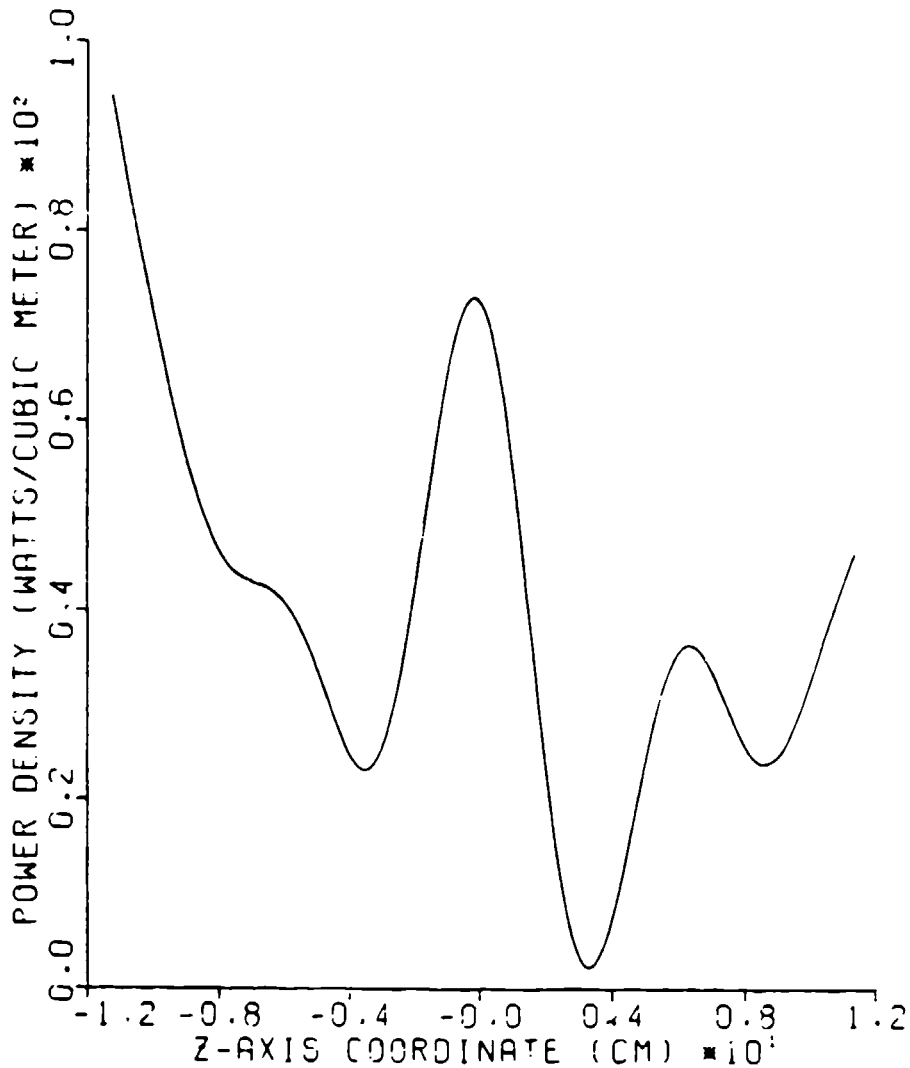


POWER DISTRIBUTION IN A MULTILAYERED SPHERE
EXPOSED TO MICROWAVE RADIATION

FREQUENCY = 500.00 MHZ

PEAK ELECTRIC FIELD = 51.30 VOLTS/METER

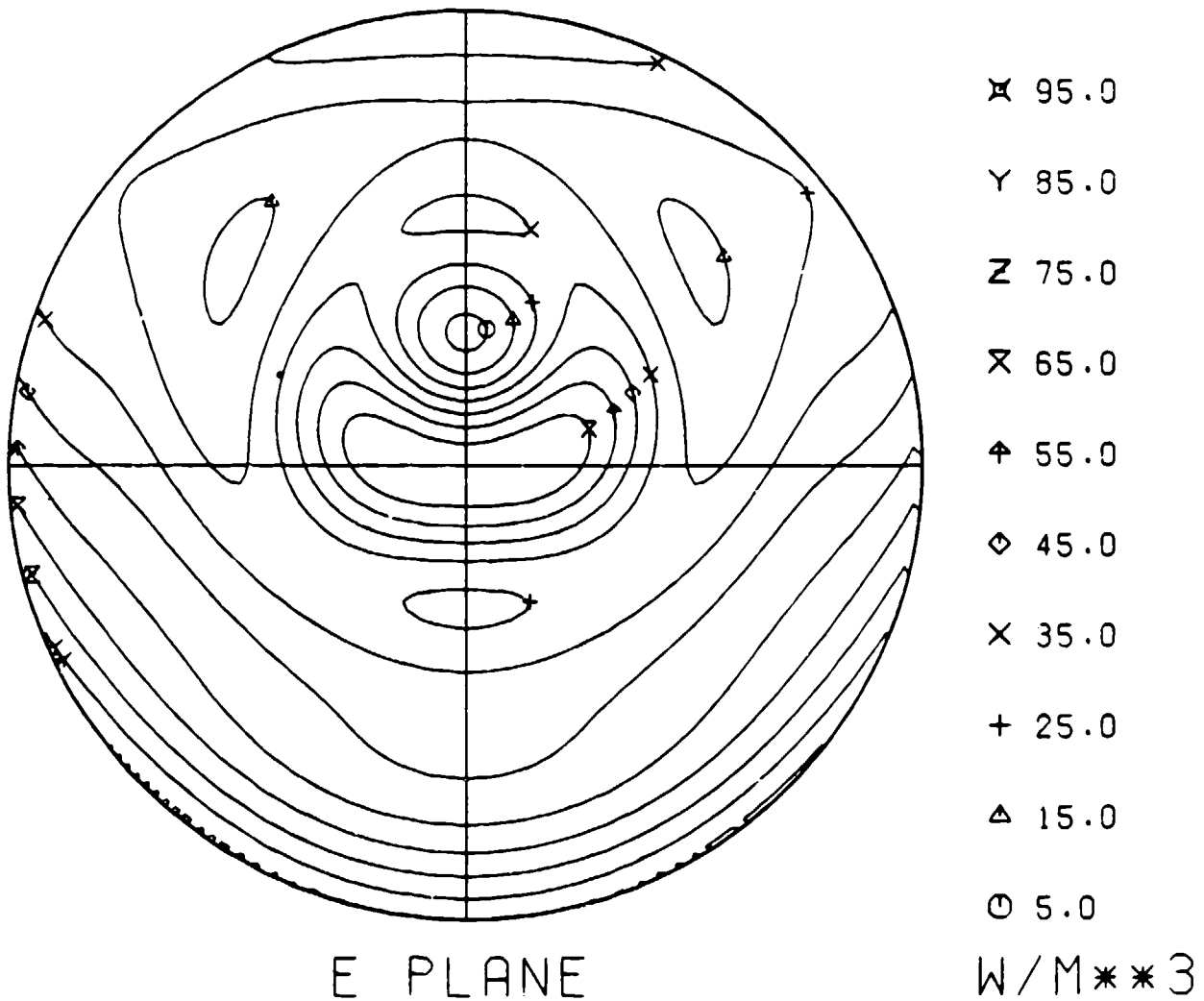
LAYER BOUNDARY (CM)	RELATIVE DIELECTRIC CONSTANT	ELECTRICAL CONDUCTIVITY (MHOS/M)	DENSITY (GRAMS/CC)
11.28	39.600	0.6500	1.0000



POWER DISTRIBUTION IN A MULTILAYERED SPHERE
EXPOSED TO MICROWAVE RADIATION

FREQUENCY = 500.00 MHZ
PEAK ELECTRIC FIELD = 61.38 VOLTS/METER

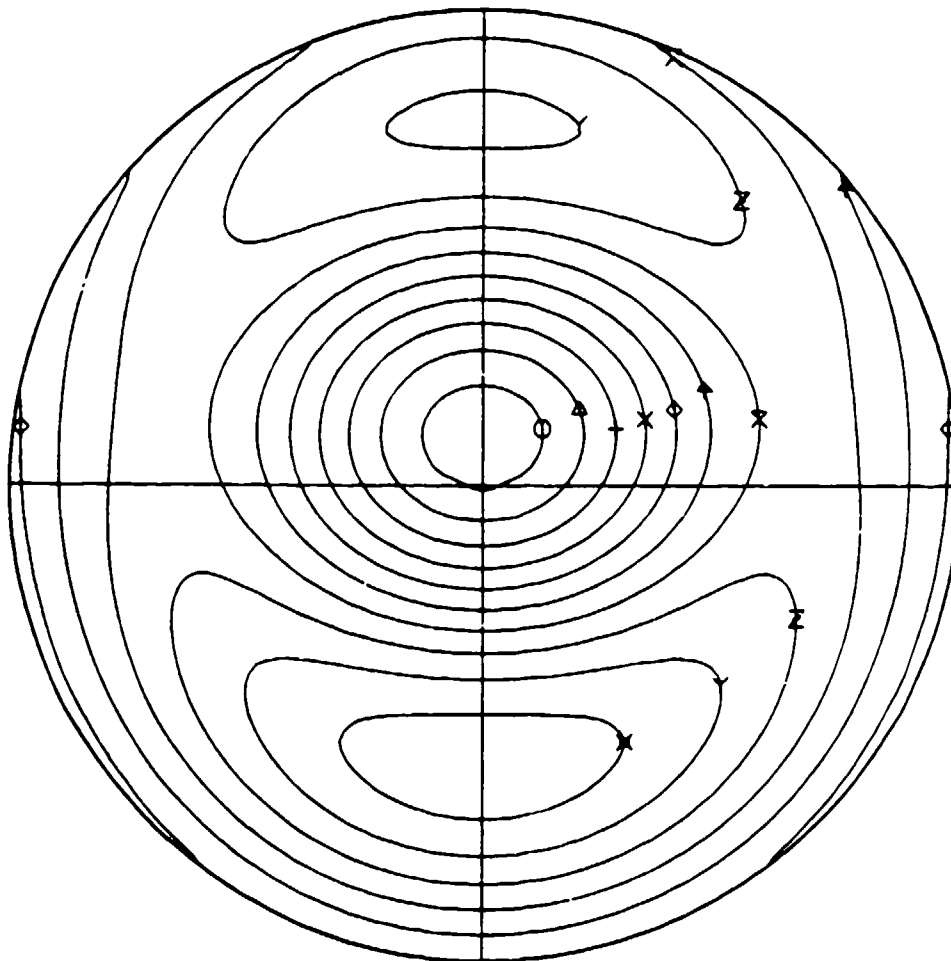
LAYER BOUNDARY (CM)	RELATIVE DIELECTRIC CONSTANT	ELECTRICAL CONDUCTIVITY (MHOS/M)	DENSITY (GRAMS/CC)
11.28	39.600	0.6500	1.0000



LAYER BOUNDARY (CM)	RELATIVE DIELECTRIC CONSTANT	ELECTRICAL CONDUCTIVITY (MMOS/M)	DENSITY (GRAMS/CC)
3.30	79.200	0.6430	1.0000
LAYER BOUNDARY (CM)	SPECIFIC HEAT (CAL/G/S)	THERMAL CONDUCTIVITY (CAL/CM-SEC-C)	BLOSS FLOW RATE (CC/SEC)
3.30	0.993	0.00250	0.00196

THERMAL RESPONSE OF A MULTILAYERED SPHERE
EXPOSED TO MICROWAVE RADIATION

FREQUENCY = 500.00 MHZ
PEAK ELECTRIC FIELD = 61.39 VOLTS/METER
EXPOSURE TIME = 1.00 SECONDS

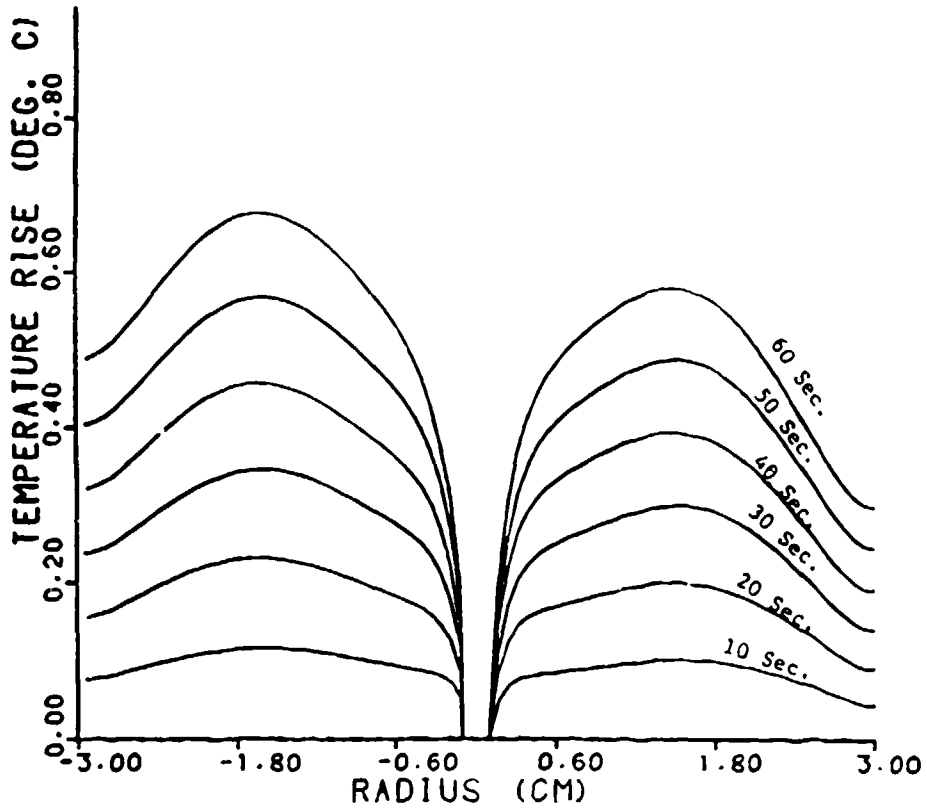


E PLANE

- X 1.535×10^{-4}
 - Y 1.375×10^{-4}
 - Z 1.215×10^{-4}
 - X 1.055×10^{-4}
 - ◇ 8.95×10^{-5}
 - ◇ 7.35×10^{-5}
 - X 5.75×10^{-5}
 - + 4.15×10^{-5}
 - △ 2.55×10^{-5}
 - 9.5×10^{-5}
- DEG. C :

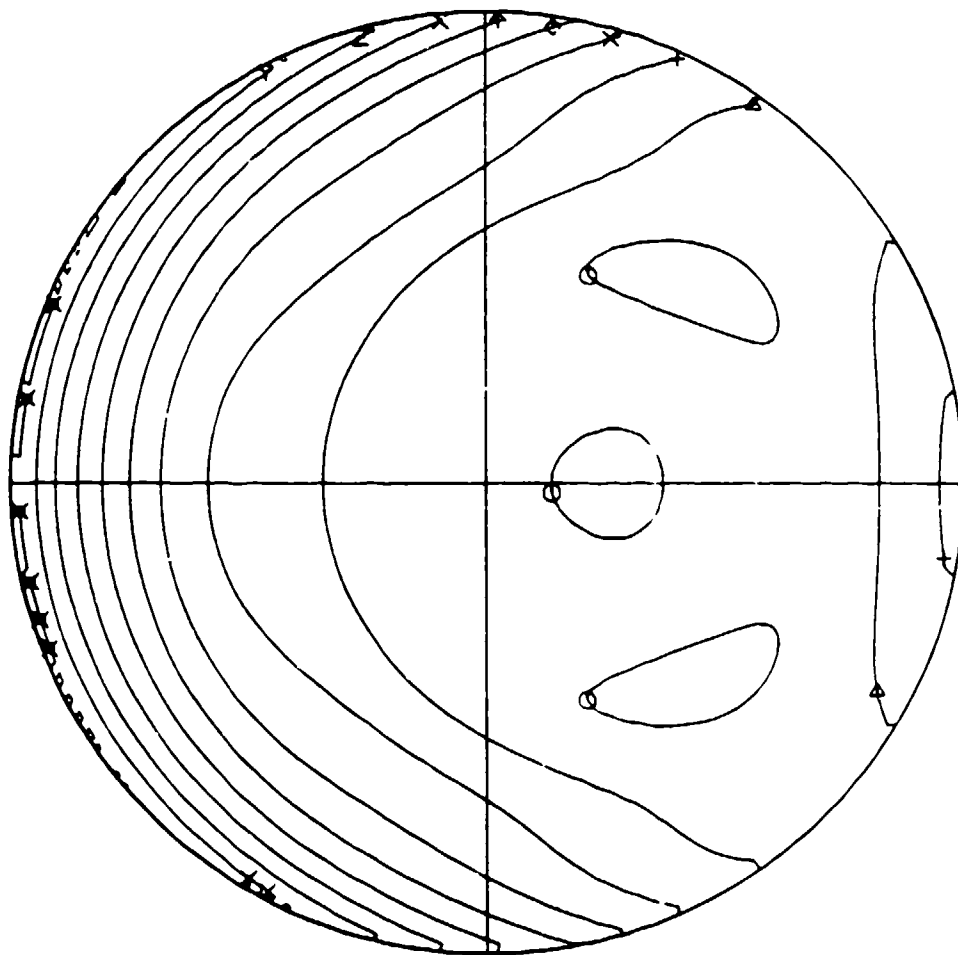
CYLINDRICAL MODEL
 TRANSVERSE MAGNETIC EXPOSURE
 FREQUENCY = 500.00 MHZ
 PEAK ELECTRIC FIELD = 194.09 VOLTS/METER

LAYER BOUNDARY (CM)	RELATIVE DIELECTRIC CONSTANT	ELECTRICAL CONDUCTIVITY (MHOS/M)	DENSITY (GRAMS/CC)
0.10	60.000	1.0000	1.0000
3.00	79.200	0.6490	1.0500



TRANSVERSE ELECTRIC EXPOSURE
 FREQUENCY = 500.00 MHZ
 PEAK ELECTRIC FIELD = 61.38 VOLTS/METER

LAYER BOUNDARY (CM)	RELATIVE DIELECTRIC CONSTANT	ELECTRICAL CONDUCTIVITY (MHOS/M)	DENSITY (GRAMS/CC)
11.28	39.600	0.6500	1.0000



⊠ 57.5

Y 51.5

Z 45.5

⊠ 39.5

⊠ 33.5

◇ 27.5

× 21.5

+ 15.5

△ 9.5

○ 3.5

CROSS SECTION

W/M**3

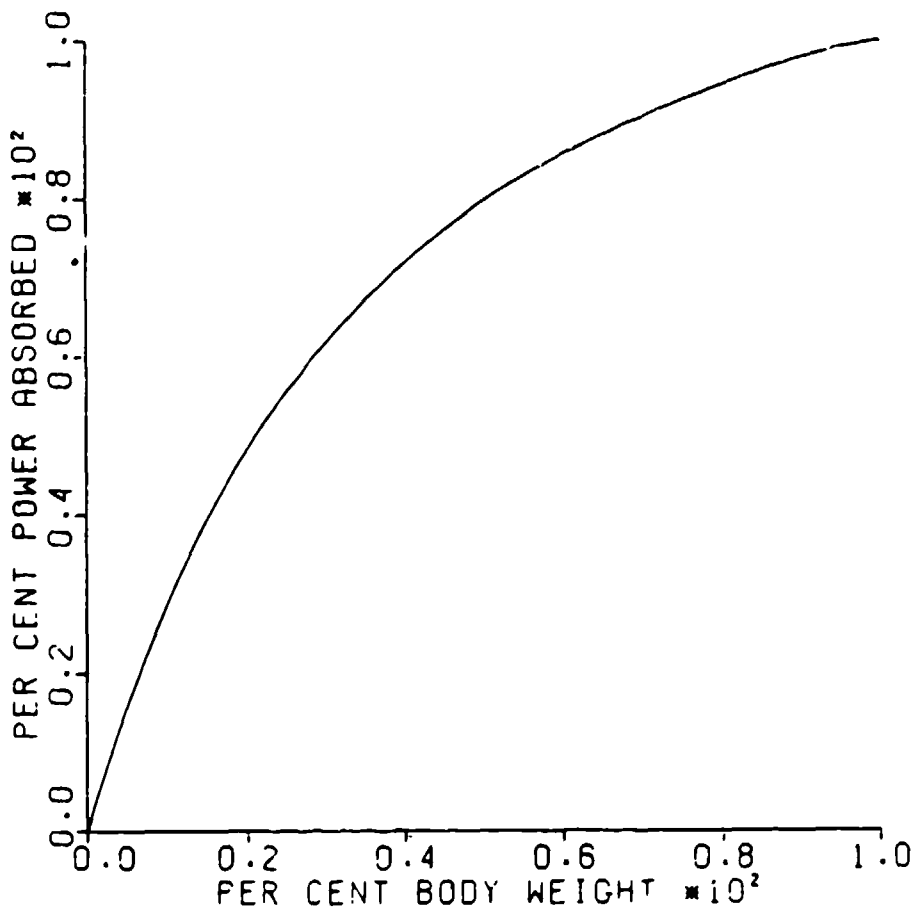
SUM OF POWER ABSORPTIONS OVER THAT
 PER CENT OF EQUAL BODY WEIGHT SUBUNITS
 WITH THE HIGHEST POWER DENSITIES

TRANSVERSE ELECTRIC EX OSURE

FREQUENCY = 500.00 MHZ

PEAK ELECTRIC FIELD = 61.38 VOLTS/METER

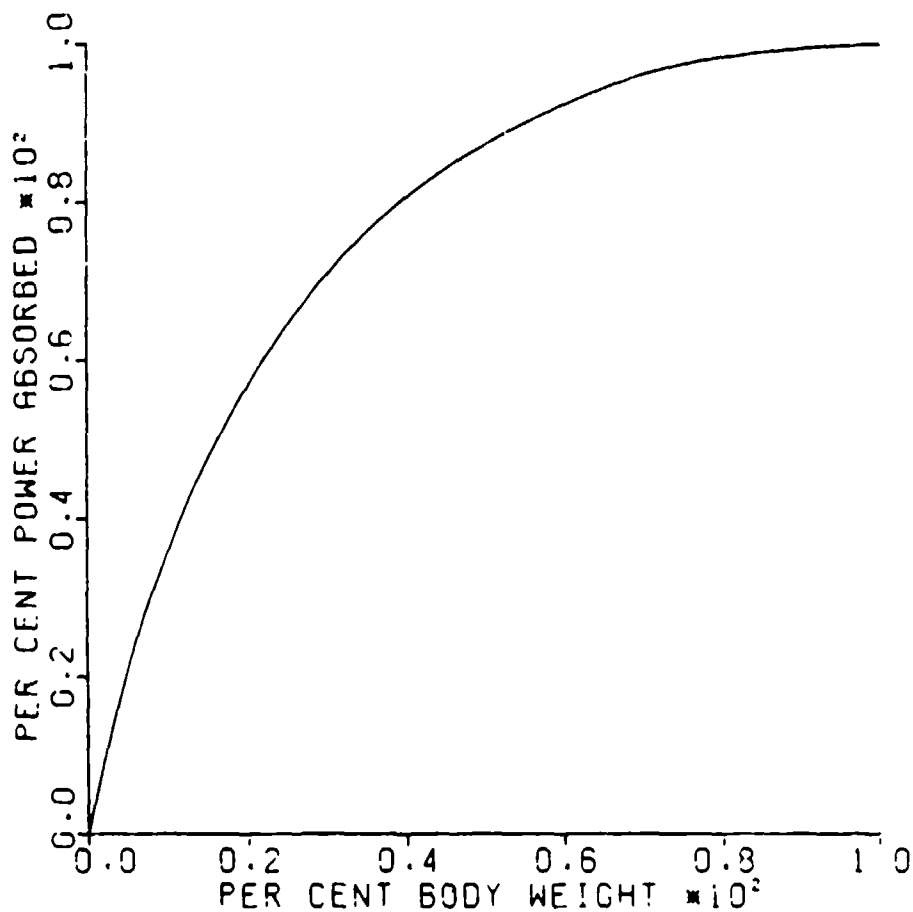
LAYER BOUNDARY (CM)	RELATIVE DIELECTRIC CONSTANT	ELECTRICAL CONDUCTIVITY (MHOS/M)	DENSITY (GRAMS/CC)
11.28	39.600	0.650	1.000



SUM OF POWER ABSORPTIONS OVER THAT
 PER CENT OF EQUAL BODY WEIGHT SUBUNITS
 WITH THE HIGHEST POWER DENSITIES

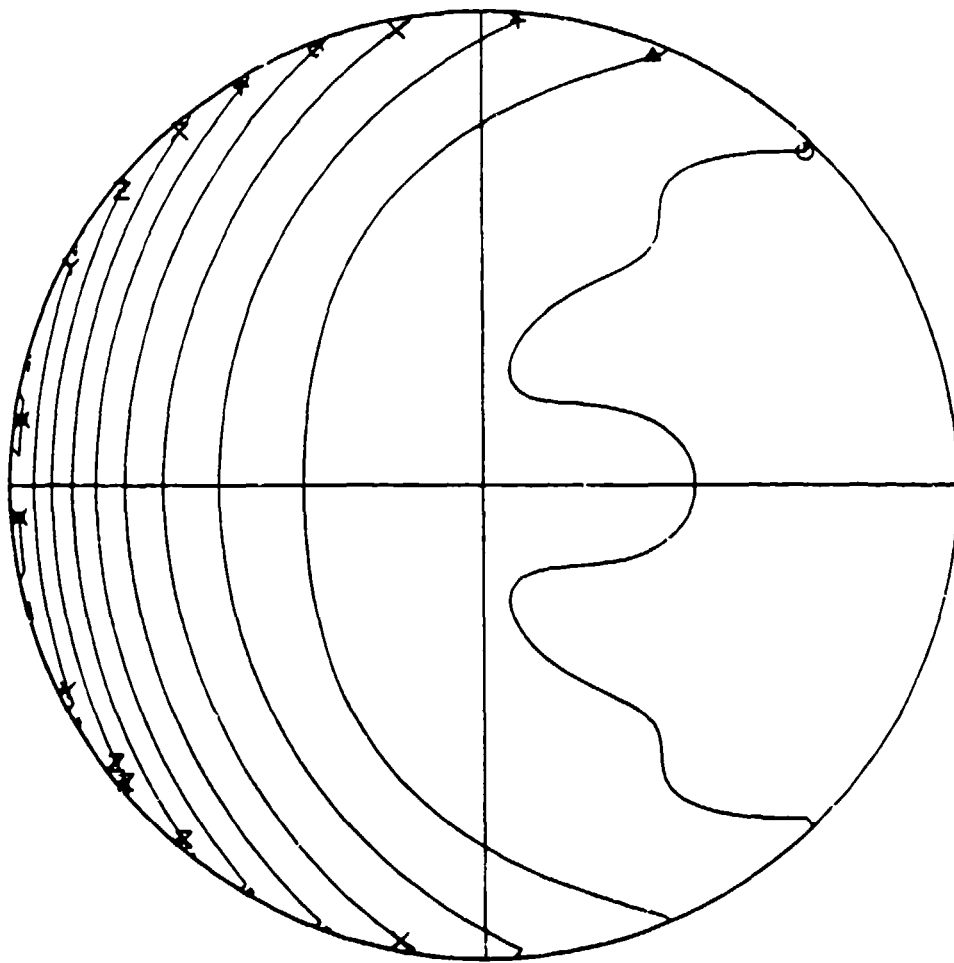
TRANSVERSE MAGNETIC EXPOSURE
 FREQUENCY = 500.00 MHZ
 PEAK ELECTRIC FIELD = 61.30 VOLTS/METER

LAYER BOUNDARY (CM)	RELATIVE DIELECTRIC CONSTANT	ELECTRICAL CONDUCTIVITY (MHOS/M)	DENSITY (GRAMS/CC)
11.28	39.600	0.5500	1.0000



TRANSVERSE MAGNETIC EXPOSURE
 FREQUENCY = 500.00 MHZ
 PEAK ELECTRIC FIELD = 61.38 VOLTS/METER

LAYER BOUNDARY (CM)	RELATIVE PERMITTIVITY CONSTANT	ELECTRICAL CONDUCTIVITY (MHOS/M)	DENSITY (GRAMS/CC)
11.28	39.500	0.6500	1.0000



⊗ 95.0

Y 85.0

Z 75.0

⊗ 65.0

⊕ 55.0

◇ 45.0

× 35.0

+ 25.0

△ 15.0

○ 5.0

CROSS SECTION

W/M***3

2. NUMERICAL STABILITY OF THE TEMPERATURE COMPUTATION

The numerical stability of the temperature excursion calculation was verified in several ways. We compared the calculation of the source term by the primary electromagnetic calculation and the representation of s by linear combinations of eigenfunctions of the elliptic part of the heat operator. We showed that using different sufficiently large numbers of eigenfunctions did not change the predicted temperature before the third decimal place. Similar calculations carried out for spherical structures ([4], [8]) were verified by experimental measurement.

4. ANISOTROPIC SCATTERING

We begin by considering the gradient and the curl operations in cylindrical coordinates. The curl operation is

$$\begin{aligned} \text{curl}(\mathbf{F}) = & \left(\frac{1}{r} \frac{\partial F_z}{\partial \theta} - \frac{\partial F_\theta}{\partial z} \right) \mathbf{e}_r + \\ & \left(\frac{\partial F_r}{\partial z} - \frac{\partial F_z}{\partial r} \right) \mathbf{e}_\theta + \\ & \left(\frac{1}{r} \frac{\partial}{\partial r}(rF_\theta) - \frac{1}{r} \frac{\partial F_r}{\partial \theta} \right) \mathbf{e}_z \end{aligned}$$

The gradient operator in cylindrical coordinates is given by

$$\text{grad} = \mathbf{e}_r \frac{\partial}{\partial r} + \mathbf{e}_\theta \frac{1}{r} \frac{\partial}{\partial \theta} + \mathbf{e}_z \frac{\partial}{\partial z} \quad (4.2)$$

The basic method we use to develop a representation of solutions of the Maxwell equations that we can use in solving the electromagnetic interaction problem in an anisotropic material is the development of classes of vector fields which may mathematically be regarded as members of a module, in the abstract algebra sense, over a ring of functions of the radial variable such that the curl of a vector field in this class is a linear combination of the other vector fields in the class. In the case of scattering by cylinders, the class of vector fields that we consider are radial functions, that is to say functions of the distance r from the common axis of the delimiting cylinders, multiplied by either $A_{(m,h)}$, $B_{(m,h)}$, or $C_{(m,h)}$, where

$$A_{(m,h)} = e^{im\theta} e^{-ihz} \mathbf{e}_r, \quad (4.3)$$

$$B_{(m,h)} = e^{im\theta} e^{-ihz} \mathbf{e}_\theta, \quad (4.4)$$

and

$$C_{(m,h)} = e^{im\theta} e^{-ihz} e_r \quad (4.5)$$

We note that after multiplication of vector fields of the form (4.3)–(4.5) by a function of r , then no new vector fields are formed by computing the curl of one of these vector fields that could not have been obtained by an addition of vector fields of the other two types. Specifically we find that

$$\text{curl}(F(r)A_{(m,h)}) = (-ih)F(r)B_{(m,h)} + \frac{F(r)}{r}imC_{(m,h)} \quad (4.6)$$

$$\begin{aligned} \text{curl}(F(r)B_{(m,h)}) = \\ ihF(r)A_{(m,h)} + (F'(r) + \frac{F(r)}{r})C_{(m,h)} \end{aligned} \quad (4.7)$$

$$\text{curl}(F(r)C_{(m,h)}) = im\frac{F(r)}{r}A_{(m,h)} + ihF(r)B_{(m,h)} \quad (4.8)$$

With this formulation it is possible to solve the Maxwell equations within the layer when there is a fairly general relationship between B and H and between $\frac{\partial D}{\partial t}$ plus J and E . To solve the Maxwell equations we assume that the magnetic permeability tensor μ has a bounded inverse and express the electric vector E of the induced wave in the form,

$$\begin{aligned} E = \sum_{m=-\infty}^{\infty} (a_m U_m^{(a)}(r)A_{(m,h)} + \\ b_m U_m^{(b)}(r)B_{(m,h)} + c_m U_m^{(c)}(r)C_{(m,h)}) \end{aligned} \quad (4.9)$$

While the situation is particularly simple when the tensor μ is diagonal in the cylindrical coordinate system we see that if we use the Maxwell equation

$$\text{curl}(\mathbf{E}) = -i\omega\mu\mathbf{H} \quad (4.10)$$

to solve for \mathbf{H} , that in fact \mathbf{H} has the representation,

$$\begin{aligned} \mathbf{H} = \frac{i}{\omega\mu}^{-1} \sum_{m=-\infty}^{\infty} & \left((ib_m U_m^{(b)}(r) + imc_m \frac{U_m^{(c)}(r)}{r}) \mathbf{A}_{(m,\lambda)} + \right. \\ & \left. (-iba_m U_m^{(a)}(r) + ibc_m U_m^{(c)}(r)) \mathbf{B}_{(m,\lambda)} \right. \\ & \left. \left(-a_m \frac{U_m^{(a)}(r)im}{r} + b_m \left[U_m^{(b)'}(r) + \frac{U_m^{(b)}(r)}{r} \right] \right) \mathbf{C}_{(m,\lambda)} \right) \end{aligned} \quad (4.11)$$

By applying the curl operation to the left side of (4.11) and making use of the Maxwell equation

$$\text{curl}(\mathbf{H}) = i\omega\epsilon\mathbf{E} + \sigma\mathbf{E} \quad (4.12)$$

we get a system of coupled differential equations involving the coefficients used to represent the electric vector \mathbf{E} . These are solved in each layer and by making use of singular and regular radial functions we have a relationship between the expansion coefficients in layer p and the expansion coefficients in layer $p+1$ by simply for the expression for \mathbf{E} and the expression for \mathbf{H} on opposite sides of a cylinder delimiting regions of continuity of tensorial electromagnetic properties equating the coefficients of $\mathbf{B}_{(m,\lambda)}$ and the coefficients of $\mathbf{C}_{(m,\lambda)}$. From the coupled system of differential equations in the radial functions $U_m^{(a)}$, $U_m^{(b)}$ and $U_m^{(c)}$ we obtain a knowledge of the values of these functions and their derivatives at the cylindrical interfaces between the layers

which will then enable us to relate expansion coefficients in one layer to those in the adjacent layers. From a knowledge of the regularity of the solutions at the origin and a knowledge of the expansion coefficients used to represent the incoming electromagnetic wave, the representation of the \mathbf{E} and \mathbf{H} in each layer is completely determined.

3. REFERENCES

- 1. Bell, Earl L., David K. Cohoon, and John W. Penn. Electromagnetic Energy Deposition in a Concentric Spherical Model of the Human Head SAM-TR-79-6. Interim Report for the Period January 1977 - September 1977 96 pages Brooks AFB, Texas 78235: USAF School of Aerospace Medicine (December, 1979)**
- 2. Bohren, Craig F. and Donald R. Huffman. Absorbtion and Scattering of Light by Small Particles. New York: John Wiley (1983)**
- 3. Bohren, C. F. and V. Trimble. Computer Programs for Calculating Scattering and Absorption by Normally Illuminated Infinite Cylinders Project No. 38 Institue of Occupational and Environmental Health, Montreal (1979)**
- 4. Burr, John G., David K. Cohoon, Earl L. Bell, and John W. Penn. Thermal Response of a Model of a Simulated Cranial Structure Exposed to Radiofrequency Radiation, IEEE Transactions on Biomedical Engineering. Volume BME-27, Number 8(August, 1980) pp 452-460.**
- 5. Bussey, Howard E. and Jack H. Richmond. Scattering by a Lossy Dielectric Circular Cylindrical Multilayer, Numerical Values. IEEE Transactions on Antennas and Propagation. Volume 23 (1975) pp 723-725**
- 6. Cohen, Ariel, Leonard D. Cohen, and Richard D. Haracs. Double scattering by randomly oriented long cylinders. Journal of Applied**

Physics. Volume 57. Number 3 (February 1, 1985) pp 698-703

7. Cohen, Ariel, Richard D. Haracz, and Leonard Cohen. Asymmetry Factors for Randomly Oriented Infinite Cylinders. Journal of Applied Physics. Volume 58, Number 3 (August, 1985) pp 1135-1140

8. Coboon, David K., John W. Penn, Earl L. Bell, David R. Lyons, and Arthur G. Cryer. A Computer Model Predicting the Thermal Response to Microwave Radiation. Final Report for the Period January 1980-November 1980. 152 pages Brooks AFB, Texas 78235: USAF School of Aerospace Medicine (December, 1982)

9. Davis, J. Electromagnetic Resonance Absorption by a Uniform Plasma Cylinder. Journal of Applied Physics. Volume 41 Number 4 (March 15, 1985) pp 1867-1868

10. Hammond, W. S. and Mak Hamid. Diffraction by an Infinite Dielectric Cylinder due to a Normally Incident Cylindrical Wave. Electron Letters. Volume 6 (December 27, 1969) pp 675-676

11. Harrington, Roger F. and Joseph R. Mautz. Impedance Sheet Approximation for Thin Dielectric Shells. IEEE Transactions on Antennas and Propagation. Volume AP-23 Number 4 (July, 1975) pp 531-534

12. Ho, Henry S. Dose Rate Distribution in Triple Layered Dielectric Cylinder with Irregular Cross Section Irradiated by Plane Wave Sources Journal of Microwave Power. Volume 10, Number 4 (December, 1975) pp 421-423

13. Massoudi, Habib, Carl H. Durney, Peter W. Barber, and Magdy F.

Iskander. Electromagnetic Absorption in Multilayer Cylindrical Models of Man. IEEE Transactions on Microwave Theory and Techniques Volume MTT-27, Number 10 (October, 1979) pp 825-830

14. Maystre, D. and P. Vincent. Diffraction D'une Onde Electromagnetic Plane par un Object Cylindrique Non Infiniment Conducteur de Section Arbitraire. Optics Communications. Volume 5, Number 5 (August, 1972) pp 327-330

15. Morita, Nagayoshi. Surface integral representations for electromagnetic scattering from dielectric cylinders. IEEE Transactions on Antennas and Propagation. Volume AP-26 Number 2 (March, 1978) pp 261-266

16. Richmond, J. H. Efficient Recursive Solutions for Plane and Cylindrical Multilayers. Report 1968-1 Columbus Ohio Electroscience Laboratory (August 10, 1965)

17. Samaddar, S. N. Scattering of Plane Electromagnetic Waves by Radially Inhomogeneous Infinite Cylinders. Nuovo Cimento B (Italy) Volume 66B Number 1 (March 11, 1970) pp 33-50

18. Van Bladel, J. Scattering of Low Frequency Electromagnetic Waves by Dielectric Cylinders. IEEE Transactions on Antennas and Propagation.

19. Wait, James R. Electromagnetic Radiation from Cylindrical Structures. New York: Pergamon Press (1959)

20. Wait, James R. and David A. Hill. Electromagnetic Surface Fields Produced by a Pulse Excited Loop Buried in the Earth. Journal of

Applied Physics. Volume 43 Number 10 (October, 1972) pp 3988-3989

21. Wu, Le-Kao and Leonard L. Tsai. Electromagnetic Fields Induced inside Arbitrary Cylinders of Biological Tissue. IEEE Transactions on Antennas and Propagation

22. Wu, Le-Kao and Leonard L. Tsai. Scattering by Arbitrarily Cross Sectioned Layered Lossy Dielectric Cylinders. IEEE Transactions on Antennas and Propagation. Volume AP-25 Number 4 (July, 1977) pp 518-524

INDEX A
INDEX OF AUTHORS
OF PAPERS IN THESE PROCEEDINGS

ACQUISTA, C., 357
ALCORN, M. W., 29
ALEXANDER, D. R., 251
ALEXANDER, JR., R. W., 201, 217
ALFOS, D. J., 29
ARMSTRONG, R. L., 239, 273, 521
ARNOLD, S., 443, 453

BARTON, J. P., 251
BAHAR, E., 619
BELL, R. J., 201, 217
BENNETT, G. T., 387
BISWAS, A., 239, 521
BOTTIGER, J. R., 139
BREEN, J. J., 187
BROCK, J. R., 107, 279, 315, 467
BRONK, Burt V., 191, 513

CAMPILLO, A. J., 341
CARLS, J. C., 279, 467
CARSTENS, J. C., 29
CASTLEMAN, JR., A. W., 187
CERMAK, J. E., 103
CHANG, Yu-Jain, 129
CHEN, Y. L., 315
CHITANVIS, Shirish M., 289
COHEN, A., 357, 365
COHEN, L. D., 357, 365
COHOON, D. K., 401, 413, 533, 645, 667

DAO, P. D., 187
DRUGER, S. D., 453
DURACZ, T., 395, 581

ELLIOT, R. A., 581
EMANUEL, M. A., 251
EVANS, Kenneth L., 163
EVERSOLE, J. D., 341, 513

FARRELL, R. A., 347
FITZWATER, M., 619
FOLAN, L., 443, 453
FRICKEL, Robert H., 191
FRIEND, J., 39
FRY, E. S., 387
FRY, S., 217
FULLER, K. A., 631

GALLILY, I., 95

HAGEN, D. E., 29
HARACZ, R. D., 357, 365
HERB, P., 387
HICKS, David L., 129
HOPKINS, A. R., 29
HSIEH, M. T., 225

JACKSON, Christian, 129

KASSNER, J. L., 29
KATTAWAR, G. W., 387, 631
KEESE, R. G., 187
KOSUGE, H., 107

LAKHTAKIA, A., 597
LATIFI, H., 239
LAWLESS, P. A., 225
LETTIERI, Thomas R., 305
LIN, H. B., 341, 513
LITTMAN, H., 23, 157
LONG, L. L., 201, 217

MA, Y., 591, 613
MANUCCIA, T. J., 17
MARKLAND, Richard A., 179
MCCORMICK, N. J., 395, 581
MONCIVAIS, G., 467
MORGAN III, M. H., 23, 157
MORGAN, S., 187

NEWQUIST, L. A., 201, 217
NOLAN, P., 39

ORDAL, M. A., 201, 217

PEKAREVICH, M., 95
PIERCE, Leland, 495
POREH, M., 103

QUERRY, Marvin R., 117, 201

RACZIEMSKI, L. J., 239, 521
REIST, P. C., 225
RUBEL, G. O., 13

SCHAUB, S. A., 251
SCHMITT, J. L., 29
SCOTT, Peter D., 151
SEEVER, M., 17
SHAH, P., 521
SHAW, David T., 151
SINGHAM, S. B., 571
STOYANOV, B. J., 347

THOMSON, George M., 179
THOMSON, Sandra M., 179
TRACHTENBERG, I., 315
TRUEBLOOD, M. B., 29
TSANG, Tate T. H., 163
TZENG, W. B., 187

VAN DIVER, R., 201, 217
VARADAN, V. K., 591, 597, 613
VARADAN, V. V., 591, 597, 613

WANG, R. T., 323, 357, 473
WANG, W-X., 473, 489
WEIL, Herschel, 495, 603
WHITE, D. R., 29
WHITE, W. E., 387
WIELICZKA, David M., 117
WILLIS III, Thomas, 603
WYATT, Philip J., 129

XU, W., 387

ZARDECKI, A., 273
ZHANG, J., 251

INDEX B

INDEX OF AUTHORS' ORGANIZATIONS
AND COUNTRIES (IF NOT U.S.A.)
FOR PAPERS IN THESE PROCEEDINGS

- Aberdeen Proving Ground (U.S. Army)
Chemical Research, Development and
Engineering Center, 13, 139, 163, 179, 191, 513
Army Munitions and Chemical Command, 179
Ballistic Research Laboratory, 179
- Colorado State University, 103
- Drexel University
Department of Chemistry, 39, 357, 365
- GEO-CENTERS, 39
- Hebrew University of Jerusalem (Israel)
Department of Atmospheric Sciences, 95
- The Johns Hopkins University
Milton S. Eisenhower Research Center, 347
Applied Physics Laboratory, 347
- Los Alamos National Laboratory
Life Sciences Division, 571
Theoretical Division, 273, 289
- National Bureau of Standards, 305
- Naval Research Laboratory
Optical Sciences Division, 17, 341, 513
- New Mexico State University
Physics Department, 239, 273, 521
Applied Laser Optics Group, 239, 273, 521
- Northwestern University
Materials Research Center and
Department of Chemistry, 453
- Oregon Graduate Center, 581
- Pennsylvania State University
Department of Chemistry, 187
Department of Engineering Science
and Mechanics, 591, 597, 613

Polytechnic University
Microparticle Photophysics Laboratory, 443
Department of Physics and Institute
for Imaging Science, 453

Potomac Photonics, Inc., 341, 513

Rensselaer Polytechnic Institute
Department of Chemical Engineering, 23, 157

Research Triangle Institute, 225

State University of New York at Buffalo
Laboratory for Power and Environmental
Studies, 151

Temple University
Department of Mathematics, 401, 413, 533, 645, 667

Texas A&M University
Department of Physics, 387, 631

University of Florida
Space Astronomy Laboratory, 323, 473, 489

University of Kentucky, 163

University of Michigan
EECS Department, 495, 603

University of Missouri-Kansas City
Physics Department, 117, 201

University of Missouri-Rolla
Physics Department, 29, 201, 217

University of Nebraska-Lincoln
Laboratory of Electro-Optical
Measurements, 251
Department of Mechanical Engineering, 251
Electrical Engineering Department, 619

University of North Carolina, 225

University of Texas
Chemical Engineering Division, 107, 279, 315, 467

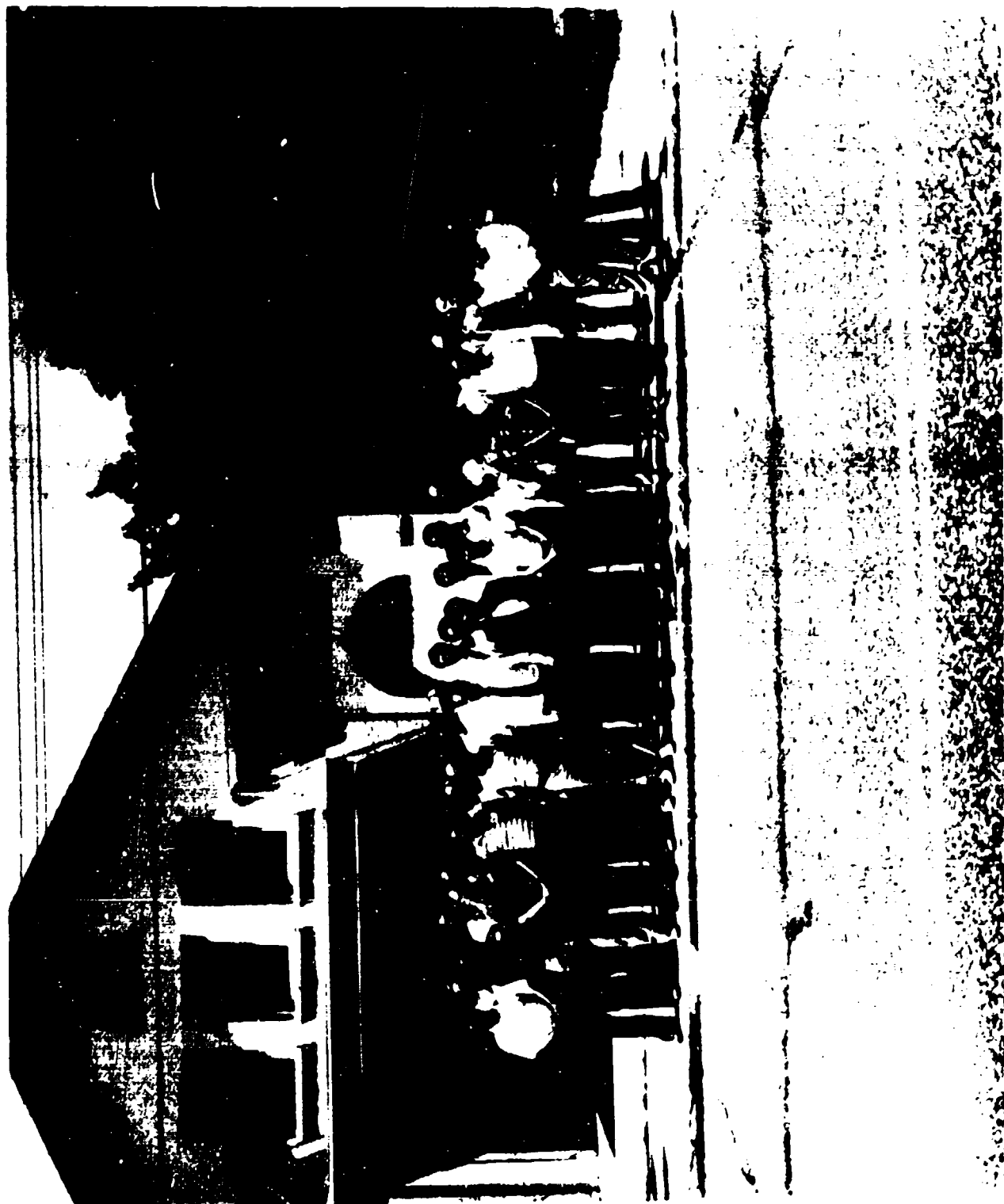
University of Washington
Department of Nuclear Engineering, 395, 581

Wyatt Technology Corporation, 129

APPENDIX A
PHOTOGRAPHS OF CONFERENCE ATTENDEES
(TAKEN MIDWEEK)

Blank

PHOTOGRAPH 1
1987 CRDEC SCIENTIFIC CONFERENCE ON OBSCURATION AND AEROSOL RESEARCH



PHOTOGRAPH 1 (Right Half)

(Left to Right)

First Row: George Kattawar, Chia-Ren Hu, Gary Salzman, Roger Johnston, Dave Pendleton,
John Barton, Kenneth Evans, Ming Leung, Ignatius Tang, H. B. Lin, Chui Lin Mang
Jerald Bottiger

Second Row: Ru Wang, Thomas Lettieri, Steve Druger, Glenn Bennett, W. Flood, G. Rubel,
Norman McCormick, W. P. Van de Merwe, L. Folan, Duane Smith, Wan-Xian Wang

Third Row: D. Capps, Dennis Alexander, , Bob Johnson, R. McCally, Dave Ensor,
Tom Avidesian, Jay Eversole, John Carstens

PHOTOGRAPH 2
1987 CRDEC SCIENTIFIC CONFERENCE ON OBSERVATION AND AEROSOL RESEARCH



APPENDIX A

PHOTOGRAPH 2 (Left Half)

(Left to Right)

First Row: N. Presser, R. Remaly, C. Wood, E. Engquist, C. Richardson, Sherwin Amimoto,
John White, R. A. Elliott, R. K. Chang, Tony Pluchino, Mel Lax, Orazio Sindoni,
Kirk Fuller, John Yen

Second Row: Bill Acker, David Leach, Ed Stuebing, E. Bahar, Curt Wagner, Mark Seaver,
Jim Davis, D. Cohoon, Joe Carls, Marek Sitarski

Third Row: A. Snelson, S. M. Chitanvis, L. J. Radziemski, E. S. Fry, Kris Chatrathi,
Robert Frickel, Arthur Carrieri

APPENDIX B
LIST OF CONFERENCE ATTENDEES

Blank

APPENDIX B

1987 CRDEC Scientific Conference
on
Obscuration and Aerosol

Attendees List

ACKER, William
Yale University
Applied Physics Laboratory
P.O. Box 2157
New Haven, CT 06520

ALEXANDER, Dr. Dennis R.
Mechanical Engineering Dept.
255 WSEC
University of Nebraska-Lincoln
Lincoln, NE 68588

AMIMOTO, Sherwin
The Aerospace Co.
P.O. Box 92957-M5-753
Los Angeles, CA 90009

ARNOLD, Professor Stephen
Dept. of Physics
Polytechnic Institute of New York
333 Jay St.
Brooklyn, NY 11201

AVIDESIAN, Dr. Thomas
Dept. of Mechanical & Aerospace Engineering
Cornell University
Upson hall
Ithaca, NY 14853-7501

BACH, Walter
U.S. Army Research Office
P.O. Box 12211
Research Triangle Park, NC 27709

BAHAR, Dr. Ezekiel
Dept. of Electrical Engineering
University of Nebraska-Lincoln WSEC 209N
Lincoln, NE 68588-0511

BARBER, Dr. Peter W.
Dept. of Electrical Engineering
Clarkson University
Potsdam, NY 13676

BARTON, Dr. John P.
University of Nebraska-Lincoln
255 WSEC
Dept. of Mechanical Engineering
Lincoln, NE 68588-0525

BELL, Dr. Robert J.
Physics Dept.
University of Missouri-Rolla
Rolla, MO 65401

BENNETT, Glenn T.
Dept. of Physics
Texas A & M University
College Station, TX 77843

BIRD, Joe
Applied Physics Laboratory
Johns Hopkins University
Laurel, MD 20707

BLEIWEISS, Max
Commander
USA DGP
STEDP-MT-TM-0
Dugway, UT 84022

BOTTIGER, Jerald
Commander
U.S. Army Chemical Research, Development
and Engineering Center
ATTN: SMCCR-RSP-B
Aberdeen Proving Ground, MD 21010-5423

BREEN, Jack
Penn State University
128 Davey Lab.
Dept. of Chemistry
University Park, PA 16802

BROCK, Professor James R.
Dept. of Chemistry Engineering
University of Texas
Austin, TX 78712

BRONK, Burt
Commander
U.S. Army Chemical Research, Development
and Engineering Center
SMCCR-RSP-B
Aberdeen Proving Ground, MD 21010-5423

BRUNO, John
SAIC
1710 Goodridge Dr.
McLean, VA 22180

CAPPS, Dr. C. David
Boeing Aerospace Co.
P.O. Box 3999, MS 87-50
Seattle, WA 98124

CARLON, Hugh
Commander
U.S. Army Chemical Research, Development
and Engineering Center
ATTN: SMCCR-RSP-8
Aberdeen Proving Ground, MD 21010-5423

CARLS, J.C.
University of Texas
Dept. of Chemical Engineering
Austin, TX 78712

CARPIN, John
Commander
U.S. Army Chemical Research, Development
and Engineering Center
ATTN: SMCCR-RST-E
Aberdeen Proving Ground, MD 21010-5423

CARSTENS, Professor John C.
Graduate Center for Cloud Physics Res.
109 Norwood Hall
University of Missouri-Rolla
Rolla, MO 65401

CHANG, Professor Richard
Applied Physics Lab
Yale University
P.O. Box 2157
Yale Station
New Haven, CT 06520

CHATRATHI, Kris
IIT Research Institute
Chemistry Division
10 West 35th St.
Chicago, IL 60616

CHITANVIS, Dr. Shirish
Los Alamos National Lab
T-DOT-MS-P371
Los Alamos, NM 87545

CHYLEK, Dr. Peter
Dept. of Physics
New Mexico State University
Las Cruces, NM 88003

COHEN, Professor Ariel
Dept. of Atmospheric Sciences
Hebrew University
Jerusalem
ISREAL

COHEN, Leonard
Dept. of Physics and Atmospheric Sciences
Drexel University
Philadelphia, PA 19104

COHOON, Dr. David
Temple University
43 Skyline Dr.
Glen Mills, PA 19342

COMEFORD, Jack
USA Dugway Proving Ground
ATTN: STEOP-MT-C
Dugway, UT 84022

CURRY, Bill
Argonne National Laboratory
9700 S. Cass Ave
Eng Bldg 207
Argonne, IL 60439-4841

DAUBER, Edwin
W.L. Gore & Associates
P.O. Box 1100
Elkton, MD 21921

DAVIS, James E.
Dept. of Chemical Engineering
BF-10
University of Washington
Seattle, WA 98195

DIMMETE, James
Commander
U.S. Army Chemical Research, Development
and Engineering Center
ATTN: SMCCR-MUS-S
Aberdeen Proving Ground, MD 21010-5423

DOHERTY, Bob
Commander
U.S. Army Chemical Research, Development
and Engineering Center
ATTN: SMCCR-RSP-B
Aberdeen Proving Ground, MD 21010-5423

DRUGER, Stephen
Dept. of Chemistry
Northwestern University
Evanston, IL 60201

ELLIOTT, Dr. R.A.
Oregon Graduate Center
19600 N.W. Von Neumann Dr.
Beaverton, OR 97006-1999

ELLINGSON, Bob
University of MD
Dept. of Meteorology
College Park, MD 20742

ENSOR, Dave S.
Research Triangle Institute
P.O. Box 12194
Research Triangle Park, NC 27709

EVANS, Kenneth
Commander
U.S. Army Chemical Research, Development
and Engineering Center
ATTN: SMCCR-MUS-S
Aberdeen Proving Ground, MD 21010-5423

EVERSOLE, Jay
Commander
Naval Research Lab.
ATTN: Code 6546
Washington, DC 20375

FARRELL, Richard
Applied Physics Lab.
Johns Hopkins University
Laurel, MD 20707

FLANIGAN, Dennis
Commander
U.S. Army Chemical Research, Development
and Engineering Center
ATTN: SMCCR-RSP-B
Aberdeen Proving Ground, MD 21010-5423

FOLAN, Lorcan
Physics Dept.
Polytechnic Institute of New York
333 Jay St.
Brooklyn NY 11201

FLOOD, Dr. W.A.
Army Research Office
P.O. Box 12211
Research Triangle Park, NC 27709

FRICKEL, R. H.
Commander
U.S. Army Chemical Research, Development
and Engineering Center
ATTN: SMCCR-RSP-B
Aberdeen Proving Ground, MD 21010-5423

FRICK, Glendon
Naval Research Lab
ATTN: Code 4116
Washington, DC 20375-5000

FREUND, David
Applied Physics Lab
Johns Hopkins University
Laurel, MD 20707

FRY, Professor Edward
Dept. of Physics
Texas A & M University
College Station, TX 77843

FULLER, Kirk
Texas A & M University
Dept. of Physics
College Station, TX 77843

GALLILY, Professor Isaiah
Dept. of Atmospheric Sciences
Hebrew University
Jerusalem 91904
ISRAEL

GIERYIC, Michael S.
Commander
U.S. Army Chemical Research, Development
and Engineering Center
ATTN: SMCCR-RSC-A
Aberdeen Proving Ground, MD 21010-5423

GUSTAFSON, Dr. Bo
Space Astronomy Lab
University of Florida
1810 N.W. 6th St.
Gainesville, FL 32601

HALLIDAY, John
Commander
U.S. Army Natick R&D Engineering Center
Materials Science Branch
Physical Science Division/SATD
Attn: STRNC-YSA
Natick, MA 01760

HARACZ, Dick
Dept. of Physics & Atmospheric Sciences
Drexel University
Philadelphia, PA 19104

HEBERLEIN, Jockel
Westinghouse R & D Center
1310 Beulah Rd.
Pittsburg, PA 15235

HENDERSON, Patrice
Commander
U.S. Army Chemical Research, Development
and Engineering Center
ATTN: SMCCR-RSC-A
Aberdeen Proving Ground, MD 21010-5423

HOLLAND, Dr. Paul
General Research Corp
5383 Hollister Ave.
Santa Barbara, CA 93111

HU, Professor Chia-Ren
Dept. of Physics
Texas A & M University
College Station, TX 77843

JAFOLLA, Dr. James
Photon Research Association
3377 N. Torrey Pines Ct.
Suite 300
La Jolla, CA 92037

Johnson, R.B.
Aerospace Corp.
Bldg, A6-1647
P.O. Box 92957
Los Angeles, CA 90009

JOHNSTON, Roger
MS M888
Los Alamos National Lab
Los Alamos, NM 87545

JORDAN, Hans
Battelle Columbus Division
505 King Ave.
Columbus, OH 43201

KAGAN, Jeff
Commander
U.S. Army Chemical Research, Development
and Engineering
ATTN: SMCCR-RSP-B
Aberdeen Proving Ground, MD 21010-5423

KATTAWAR, Dr. George
Dept. of Physics
Texas A & M University
College, Station, TX 77843

KENNEDY, Dr. John
Naval Weapons Support Center
Code 5063
Crane, IN 47401

KLEINMAN, Dr. Ralph
University of Delaware
Dept of Math Sciences
Newark, DE 19716

KLETT, James
PAR Associates
1741 Pomona Drive
Las Cruces, NM 88001

LATHAM, John
Dept. of Pure & Applied Physics
U.M.I.S.T.
P.O. Box 88
Manchester M60 1QD
ENGLAND

LAWLESS, Phil
Research Triangle Institute
Box 12194
Durham, NC 27709

LAX, Melvin
City College of New York
Physics Dept.
New York, NY 10031

LEACH, David
Yale University
Applied Physics
P.O. Box 2157
Yale Station
New Haven, CT 06520

LEONG, Dr. Keng
Argonne National Lab
Bldg 207
5700 South Cass Ave.
Argonne, IL 60439

LETTIERI, Thomas R.
National Bureau of Standards
MET-A117
Gaithersburg, MD 20899

LIN, H.B.
Code 6501
Naval Research Lab
Washington, DC 20375-5000

LITTMAN, Howard
123 Ricketts Bldg
Rensselaer Polytechnical Institute
Dept. of Chemical Engineering
Troy, NY 12180-3590

LEUNG, Ming K.
Dept. of Physics
Polytechnic Institute of New York
333 Jay Street
Brooklyn, N.Y. 11201

MA, Yushieh
Dept. of Eng. Science & Mechanics
227 Hammond Bldg
Pennsylvania State University
University Park, PA 16802

MAJESKI, John
PM/Smoke
USA TECOM
ATTN: AMSTE-TC-M
Aberdeen Proving Ground, MD 21005-5005

MARTIN, Dan
Commander
Dugway Proving Ground
ATTN: STEDP-MT-L
Dugway, UT 84022

McCALLY, Russell
Dept of Physics
Johns Hopkins University
Laurel, MD 20707

McCORMICK, Norman
Dept. of Nuclear Engineering
University of Washington
Bldg BF 10
Seattle, WA 98195

MORGAN, Morris
Dept. of Chemical Engineering
Rensselaer Polytechnic Institute
Troy, NY 12180-3590

NOLAN, Pat
Dept. of Chemistry
Drexel University
32nd & Market St.
Philadelphia, PA 19104

PATERNI, Dorothea
Commander
U.S. Army Chemical Research, Development
and Engineering Center
ATTN: SMCCR-RSL
Aberdeen Proving Ground, MD 21010-5423

PENDLETON, Dr. David
Atmospheric Sciences Lab
P.O. Box 236
White Sands Missile Range, NM 88002

PIERCE, Joe
W.L. Gore & Associates
P.O. Box 1100
Elkton, MD 21921

PIERCE, Leland
University of Michigan
EECS Dept.
Ann Arbor, MI 48105-2122

PINNICK, Dr. Ronald
Atmospheric Sciences Lab
ATTN: DELAS-E0-ME
White Sands Missile Range, NM 88002

PLUCHINO, Antonio (Tony)
Aerospace Corp
Bldg A 6-1647
P.O. Box 92957
Los Angeles, CA 90009

POZIOMEK, Ed
Commander
U.S. Army Chemical Research, Development
and Engineering Center
SMCCR-RS
Aberdeen Proving Ground, MD 21010-5423

PRESSER, Nathan
Aerospace Corporation
P.O. Box 92957
Los Angeles, CA 90009

QUERRY, Marvin
Dept. of Physics
University of Missouri
Kansas City, MO 64110

RADZIEMSKI, Dr. Leon J.
Dept. of Physics
New Mexico State University
P.O. Box 30001/ Dept 3D
Las Cruces, NM 88003-0001

REMALY, Bob
IIT Research Institute
Chemistry Division
10 West 35th St.
Chicago, IL 60616

RILEY, Erica
Commander
U.S. Army Chemical Research, Development
and Engineering Center
ATTN: SMCCR-RSP-B
Aberdeen Proving Ground, MD 21010-5423

RIN, Chun Hsun
Commander
U.S. Army Chemical Research, Development
and Engineering Center
ATTN: SMCCR-DDE
Aberdeen Proving Ground, MD 21010-5423

RUBEL, Glenn
Commander
U.S. Army Chemical Research, Development
and Engineering Center
ATTN: SMCCR-RSP-B
Aberdeen Proving Ground, MD 21010-5423

SALZMAN, Dr. Gary
Los Alamos National Lab
P.O. Box 1663
M5 M888
Los Alamos, NM 87545

SAUTER, David
Atmospheric Sciences Lab
ATTN: DELAS-E0
White Sands Missile Range, NM 88002

SCARBOROUGH, Sharon
W.L. Gore & Associates
P.O. Box 1100
Eikton, MD 21921

SCOTT, Peter
Dept. of Elec. Eng./LAPES Lab
State University of N.Y./Buffalo
Room 330 Banner Hall
Amherst, N.Y. 14260

SEAVER, Mark
Naval Research Lab
Code 6540
Washington, DC 20375

SHAW, Dr. David
Dept. of Electrical Engineering
State University of New York
330 Bonner Hall
Buffalo, NY 14260

SINDONI, Orazio
Commander
U.S. Army Research, Development
and Engineering Center
ATTN: SMCCR-RSP-B
Aberdeen Proving Ground, MD 21010-5423

SITARSKI, Marek
U.S. Dept of Energy
P.O. Box 880
Morgantowne Energy
Technology Center
Morgantowne, WV 26505

SMITH, Dr. Duane
Aerospace Corp.
M2-253
P.O. Box 92957
Los Angeles, CA 90009

SNELSON, Dr. Alan
Illinois Institute of Technology
Research Institute
10 W. 35th St.
Chicago, IL 60616

STEPHENS, John R.
CHM-2
M/S C-348
Los Alamos National Lab
Los Alamos, NM 87545

STOYANOV, Basil
Johns Hopkins Applied Physics Lab
Johns Hopkins University
Laurel, MD 20707

STUEBING, Edward
Commander
U.S. Army Chemical Research, Development
and Engineering Center
ATTN: SMCCR-RSP-B
Aberdeen Proving Ground, MD 21010-5423

TANG, Ignatius
Bldg 815
Brookhaven National Lab
Upton, NY 11973

THOMSON, George
USA BRL
ATTN: SLCBR-SE-E
Aberdeen Proving Ground, MD 21005

THOMSON, Sandra
Commander
U.S. Army Chemical Research, Development
and Engineering Center
ATTN: SMCCR-RST-C
Aberdeen Proving Ground, MD 21010-5423

TSANG, Tate
Dept. of Chemical Engineering
University of Kentucky
Lexington, KY 40506

TURETSKY, Abraham
Commander
U.S. Army Chemical Research, Development
and Engineering Center
ATTN: SMCCR-RSP-B
Aberdeen Proving Ground, MD 21010-5423

TZENG, Wen-Bih
Penn State University
128 Davey Lab
Dept. of Chemistry
University Park, PA 16802

VAN DE MERWE, Wim
Laser Bio Physics
Uniform Services of the Health Sciences
4301 Jones Bridge Rd.
Bethesda, MD 20814-4799

VAN DE WAL, Dr. Anthony
Project Manager, Smoke/Obscurant
ATTN: AMCPM-SMK-T
Bldg 324
Aberdeen Proving Ground, MD 21005

VARADAN, V.V.
Dept. of Engineering Science & Mechanics
Penn State University
227 Hammond Bldg
University Park, PA 16802

VOGT, Dr. Gerald
Los Alamos National Lab
NST-e
MAIL STOP-C348
Los Alamos, NM 87545

VU, Bien
Systems Planning
1500 Wilson Blvd.
Arlington, VA 22209

WAGNER, Dr. Curt
Physics Dept
Southwest State University
Marshall, Minnesota
56258

WANG, Chui Lin
The Dept. of Physics
The City College
University of New York
New York, NY 10031

WANG, Chuen Chung
Dept. of Chemical Engineering
University of Maryland
College Park, MD 20742

WANG, Ru T.
Space Astronomy Lab
University of Florida
1810 N.W. 6th St.
Gainesville, FL 23601

WANG, Dr. Wan-Xian
Space Astronomy Lab
University of Florida
1810 N.W. 6th St.
Gainesville, FL 23601

WEIL, Herschel
Dept. of Electrical and Computer Science
University of Michigan
Ann Arbor, MI 48109

WEINBERG, Dr. Jerry
Space Astronomy Lab
University of Florida
1810 N.W. 6th St.
Gainesville, FL 32601

WHITE, John R.
Commander
U.S. Army Chemical Research, Development
and Engineering Center
ATTN: SMCCR-RSP-B
Aberdeen Proving Ground, MD 21010-5423

WHITE, William
Texas A&M University
Dept. of Physics
College Station, TX 77843-4242

WILLIS, Thomas M.
University of Michigan
Dept. of EECS
Ann Arbor, MI 48109-2122

WOOD, Carol
Yale University
Applied Physics Lab
P.O. Box 2157
New Haven, CT 06520

WYATT, Dr. Philip
Wyatt Technical Co.
P.O. Box 3003
Santa Barbara, CA 93130-3003

YEN, John
Naval Ocean Systems Center
ATTN: Code 843
San Diego, CA 92152

YUDANIN, Boris
Physics Dept.
City College of NY
New York, NY 10031

ZARDECKI, Andrew
Los Alamos National Lab
MS-P371
Los Alamos, NM 87545

APPENDIX C
CONFERENCE AGENDA

Blank

AGENDA

1987 CRDEC SCIENTIFIC CONFERENCE

ON

OBSCURATION AND AEROSOL RESEARCH

22-26 JUNE 1987

Bldg. E4810 (Conference Center/Post Theater) Edgewood Area

Each presentation is listed with the appropriate session topic, and if it is scheduled for presentation at a different time, it is listed again at the appropriate place in the schedule. POSTERS are identified by the proper session topic symbol (I, II, III, IV, V) and in the sequence of preview presentations.

MONDAY, 22 JUNE

- 09:15 Registration Opens
 10:00 Opening of Conference
 10:05 Welcome - Dr. E. J. Pezloemek, Director of Research, CRDEC
 10:15 Overview of Aerosol Research Program -
 E. W. Stuebing, (Aerosol Science Coordinator)
 G. O. Rubel, (Aerosol Dynamics)
 J. R. Bowler, (Aerosol Characterization by Light Scattering)
 O. I. Sindoni, (HEL Nonlinear Effects)
 B. V. Bronk and R. H. Frickei (Aerosol Optics)

11:45 LUNCH

I. AEROSOL DYNAMICS

Moderator: Glenn Rubel

A. Single Particle Dynamics

- 1:00 Glenn Rubel (CRDEC), Determination of Liquid Vapor Pressures from Single Particle Geometrical Resonances [16]
 1:20 James Brock (U.Texas), On the Interaction of Particles with Surfaces [20]
 1:45 Ignatius Tang (Brookhaven Nat.Lab.), Measurement of Thermal Accommodation Coefficients for Helium Gas on Single Water Droplets [20]
 2:10 M. Seaver (NRL), Gas/Droplet Transport Measurements by Acoustic Levitation in a Horizontal Wind Tunnel [16]
 NOTE: James Davis (U.Wash.), Fluorescence Measurements in Single Reacting Droplets [20] (Presented 1:00 pm Thursday)

2:30 BREAK

B. Many Particle Dynamics

- 3:00 M. Morgan (RPI), Prediction of Pressure Profiles in Systems Involving Pneumatic Transport of Particles [16]
 3:20 Tain Tsang (U.Kentucky), Condensation Growth and Evaporation of Aerosols [16]
 3:40 John Carstens (U.Mo.,Rolla), Measurement of the Condensation Coefficient of Water in the UMR Simulation Chamber [16]
 4:00 Pat Nolan (Drexel U.), Photo-Induced Nucleation of Sulfuric Acid Droplets [16]
 4:20 James Brock (U.Texas), Studies of Fine Particle Formation and Dispersion [20]
 4:45 I. Gattily M. Bskerevitz (U. Jerusalem), On the Coagulation & Dispersion of Nonspherical Aerosol Particles with Inertial Memory, in a Turbulent Field [16]

TUESDAY, 23 JUNE

OBSERVATIONS ON SCIENCE WITH ANNUAL MEETING OPEN HOUSE

from 8:15 to 10:00 at Bldg. ES651

See information in the Conference Folder given out at the Registration Table.

I. AEROSOL DYNAMICS (continued)

Moderator: Glenn Rubel

B. Many Particle Dynamics (continued)

- 10:15 John Latham (UMIST-England), Mixing Processes in Clouds [16]
 10:35 Michael Poreh (Colorado St.U.), Wind Tunnel Studies of Large Particle Settlement [15]

II. AEROSOL CHARACTERIZATION METHODS

Moderator: Jerold Bottiger

- 11:00 Marvin Querry (University of Missouri - Kansas City), Optical Constants of Selected Liquids, Solids, and Powders [15]
 11:20 Phillip J. Wyatt, Christian Jackson, David Hicks, Yu-Juin Chang, Randall G. Parker, William Procter (Wyatt Technology Company), Aerosol Particle Analyzer Measurements and Second Generation Instrument [15]
 11:40 Jerold Bottiger (CRDEC), Particle Discrimination Using the Aerosol Particle Analyzer [15]

12:00 LUNCH

01:15 David Shaw, M. Yeng (SUNY), Determination of Size Distribution of Fibers and Plates by Light Scattering [16]

01:35 David Shaw, T. Fu, M. Yeng (SUNY), Effects of Particle Orientation on Filtration [16]

01:55 P. Scott, D. P. Shaw (SUNY), Superresolution Techniques for Aerosol Holography [16]

02:15 D. P. Shaw, H. S. Kweh, P. Rossi, W. S. Lee, P. Mukherjee (SUNY), Generation of Acoustic Shock Waves and Plasmas by Pulsed CO₂ Laser-Aerosol Interaction [15]

TUESDAY POSTER SESSION

PREVIEWS 2:40 to 3:10

POSTERS OPEN, 3:15 - 5:15 (with refreshments)

The presenters have only 2 (two) minutes to give an overview of their poster; please do not exceed your time. To the audience, please refrain from asking questions during presentation.

Related
Session

- I. Howard Litzman (RPI), Investigation of Boundary Conditions for Pneumatic Transport
 I. Kenneth Evans (CRDEC), Simulation of Aerosol Plumes of Diesel Fuel and Fog Oil
 I. George Thomson (BRL), An X-Ray Fluorescence Device for Concentration Measurement in Aerosols of Medium to High Atomic Number
 I. W-S Tseng and J.Breen (Penn St.), Clusters: Studies of Aerosol Precursors

TUESDAY POSTER SESSION (continued)

Related
Session

- I. J. C. Carle, G. Manciușa, J. R. Brock (Univ. of TEXAS), Semiconductor Etching
- I. William Curry (Argonne Labs.), The Effect of Evaporation on Cloud Extinction Characteristics
- I. A. Turetsky and D. Paterno (CRDEC), Thermally Induced Morphological Alteration of Intumescent Fiber Forming Precursors
- I. B. Bronk, R. Frickel (CRDEC) General Remarks on Structures Likely to be Observed on Spherical Surfaces Inferred from Equilibrium Calculations Under Coulomb Forces
- II. R. J. Bell, L. Newquist, R. W. Alexander, L. L. Long, M. Ordal, M. Query (University of Missouri-Rolla) Experimental Optical Properties of Liquids
- II. R. J. Bell, S. Fry, R. Vanderver, M. Ordal, L. L. Long, L. Newquist, R. W. Alexander (University of Missouri-Rolla), A New Class of Interferometer for Graphite Studies
- II. Phil Lawless P. C. Reist, M. T. Heick (Research Triangle Institute) Sensitivity of Fractal Analysis for Describing Particulate Shapes

WEDNESDAY, 24 JUNE

III. NONLINEAR EFFECTS AT HIGH ENERGY

Moderator: Oratio I. Sindora

- 08:15 P. Chylek, M. Jazdzemski, V. Srivastava, R. G. Pinnick (NMSU), Pressure Dependence of Laser Induced Breakdown of Aerosols and Gases [15]
- 08:35 R.G. Pinnick, P. Chylek, M. Jazdzemski, E. Cregeen, V. Srivastava, J. Crudeleon (Atmospheric Sciences Lab), Aerosol-Induced Laser

Breakdown: Wavelength Dependence [16]

- 08:55 R. K. Chang, W. F. Heick, J. B. Zhang, and J. H. Eichmann (Yale University), High Intensity Visible Laser Induced Plasma with Transparent Liquid Droplets [15]
- 09:15 L. J. Radzilewski, R. Armstrong, H. Biess and H. Lefjif (NMSU), Time Resolved Spectra of Plasmas Initiated by Single Aerosols: an Update (High Irradiance Plasma Formation) [15]
- 09:30 BREAK
- 10:00 D. R. Alexander, J. P. Barton, S. A. Scheub, M. A. Emsend (University of Nebraska-Lincoln), Experimental and Theoretical Analysis of the Interaction of CO₂ Laser Beam with Fluid Cylinders and Adjacent Spheres. [15]
- 10:20 A. Zardochi, R. L. Armstrong (Los Alamos National Laboratory), Energy balance in Laser Irradiated Vaporizing Droplets [16]
- 10:40 J. C. Carle, S. C. Davies, and J. R. Brock (University of Texas), Response of Single Particles and Aerosol to High Energy Laser Radiation [25]
- 11:10 S. M. Chitanvis (Los Alamos National Laboratory), Laser Induced Turbulence in Aerosol-loaded Atmospheres [15]
- 11:30 K. M. Leung (Polytechnic Univ. NY), Intrinsically Nonlinear Interaction of Intense Electromagnetic Waves with Microparticles [16]
- 11:50 LUNCH
- 1:00 C. F. Wood, D. H. Lesch, J. Z. Zhang, and R. K. Chang (Yale University), Explosive Vaporization of Liquid Droplets by High Intensity CO₂ and Visible Lasers [15]
- 1:20 M. Lax, J. M. Chitanvis, C. L. Wang, B. Yedemin, A. Zardochi (CCNY), Computer Simulation of Finite Pulse Propagation in a Droplet [25]

1:50 M. Starski (Clarkson University, c/o DOE/METC), Dynamics of Response of Small Nonhomogeneous Droplet to Intense Optical Fields (High Temperature Thermal Radiation Laser Beam) [15]

2:10 BREAK

IV. WORKSHOP: HANDLING INDIVIDUAL PARTICLES

Moderator: Edward W. Stuebing

2:30 Stephen Arnold (Polytechnic Institute of New York), Spectroscopy of Single Levitated Particles [25]

3:00 Ignatius Tang (Boothaven National Laboratories), Physical and Chemical Measurements of Single Suspended Particles [25]

3:30 E. James Davis (University of Washington), Single Microparticle Measurements [26]

4:00 Thomas Lettner (National Bureau of Standards), Optical Levitation of Single Particles [25]

4:30 GENERAL DISCUSSION

5:00 Continuing Discussions over Cocktails and Dinner at the Officer's Club (Beef and Burgundy, 6:00 - 8:00 pm)

THURSDAY, 26 JUNE

V. OPTICAL PROPERTIES OF AEROSOLS

Moderators: Burt V. Dronk and Robert H. Fricke

A. Scattering by Single Particles and Small Aggregates

08:15 Ru T. Wang (University of Florida), Findings Through Microwave Scattering Facility Upgrade [15]

08:35 J. D. Pendleton, R. G. Finnick, and Peter Gligel (Atmospheric Sciences Laboratory), Mie Theory Poynting Flux Lines at Resonance [15]

08:55 Peter W. Barber, S. C. Hill (Clarkson University), Resonance Effects Associated with Nonspherical Particles [15]

09:15 Jay Eversole, H. B. Lin, A. J. Campillo (Polomac Photonics, Inc.), Angular Scattering from Single, Suspended Cylinders [15]

09:35 BREAK

10:00 Basil J. Szymsnov, Richard A. Farrell (Johns Hopkins University), Effects of Simple Shadowing on Variational Calculations [15]

10:20 Leonard Cohen, Richard Harsarz, Ariel Cohen (Drexel University), Scattering From a Dielectric Knot [15]

10:40 Ariel Cohen, Richard Harsarz, Leonard Cohen (Drexel University), Calculation of Scattering From a Helix Using Exact Cylinder Scattering Functions [15]

11:00 C. T. Bennett, E. S. Fry, W. E. White, P. Herb, G. W. Kattawar (Texas A. & M.), The Scattering of Femtosecond Optical Pulses by Small Dielectric Spheres [15]

11:20 R. B. Johnson (Aerospace Corp.), Novel Methods for Nonspherical Scattering Calculations [15]

11:40 T. Duraz, N. J. McCormick (U. of Washington-Seattle), Radiative Transfer Calculations for Detecting an Object behind Obscuring Atmospheres [15]

12:00 LUNCH

B. Single Particle Spectroscopy

1:15 E. James Davis (University of Washington), Fluorescence Measurements of Single Reacting Microparticles [15]

1:50 M. SitarSKI (Clarkson University, c/o DOE/METC), Dynamics of Response of Small Nonhomogeneous Droplet to Intense Optical Fields (High Temperature Thermal Radiation Laser Beam) [15]

2:10 BREAK

IV. WORKSHOP: HANDLING INDIVIDUAL PARTICLES

Moderator: Edward W. Szebing

2:30 Stephen Arnold (Polytechnic Institute of New York), Spectroscopy of Single Levitated Particles [25]

3:00 Ignatius Tang (Bookhaven National Laboratories), Physical and Chemical Measurements of Single Suspended Particles [25]

3:30 E. James Davis (University of Washington), Single Microparticle Measurements [25]

4:00 Thomas Letzler (National Bureau of Standards), Optical Levitation of Single Particles [25]

4:30 GENERAL DISCUSSION

5:00 Continuing Discussions over Cocktails and Dinner at the Officer's Club (Beef and Burgundy, 6:00 - 8:00 pm)

THURSDAY, 25 JUNE

V. OPTICAL PROPERTIES OF AEROSOLS

Moderators: Burt V. Bronk and Robert H. Frickel

A. Scattering by Single Particles and Small Aggregates

08:15 Ru T. Wang, (University of Florida), Findings Through Microwave Scattering Facility Upgrade [15]

08:35 J. D. Pendleton, R. G. Finnick, and Peter Chylek (Atmospheric Sciences Laboratory), Mie Theory Poynting Flux Lines at Resonance [15]

08:55 Peter W. Barber, S. C. Hill (Clarkson University), Resonance Effects Associated with Nonspherical Particles [15]

09:15 Jay Eversole, H. B. Lin, A. J. Campillo (Potomac Photonics, Inc.), Angular Scattering from Single, Suspended Cylinders [15]

09:35 BREAK

10:00 Basil J. Stoyanov, Richard A. Ferrell (Johns Hopkins University), Effects of Simple Shadowing on Variational Calculations [15]

10:20 Leonard Cohen, Richard Harsocz, Ariel Cohen (Drexel University), Scattering From a Dielectric Knot [15]

10:40 Ariel Cohen, Richard Harsocz, Leonard Cohen (Drexel University), Calculation of Scattering From a Helix Using Exact Cylinder Scattering Functions [15]

11:00 C. T. Bennett, E. S. Fry, W. E. White, P. Herb, G. W. Kattauer (Texas A. & M.), The Scattering of Femtosecond Optical Pulses by Small Dielectric Spheres [15]

11:20 R. B. Johnson (Aerospace Corp.), Novel Methods for Nonspherical Scattering Calculations [15]

11:40 T. Duracz, N. J. McCormick (U. of Washington-Seattle), Radiative Transfer Calculations for Detecting an Object behind Obscuring Atmospheres [15]

12:00 LUNCH

B. Single Particle Spectroscopy

1:15 E. James Davis (University of Washington), Fluorescence Measurements of Single Reacting Microparticles [15]

1:35 L. Folan, S. Arnold (Polytechnic University of New York),
Electromagnetic Sounding of Molecular Structure at Surface and
Interior of Aerosol Particles: Theory [15]

1:55 S. Arnold, L. Folan (Polytechnic University of New York),
Electromagnetic Sounding of Particles: Experiment [15]

2:15 BREAK

2:35 S. Druger (Northwestern University), Theory of Inter-molecular
Energy-Transfer Enhancement by Mie Resonances [15]

THURSDAY POSTER SESSION

PREVIEWS 3:00 to 3:30

POSTERS OPEN: 3:30 - 5:30 (with refreshments)

The presenters have only 2 (two) minutes to give an overview of their poster; please do not exceed your time. To the audience, please refrain from asking questions during presentation.

Related Session

V. George W. Kottawar, Pascal Herb (Texas A. & M. University),
Mueller Matrix Calculations for Two Interacting Dielectric Cubes

V. W. X. Wang (University of Florida), Theoretical Calculations on
Scattering by Spherical Particles and Comparison with Microwave
Extension Measurements

V. W. E. White, E. S. Fry (Texas A. & M. University), Femtosecond
Laser Scattering from Spheres

V. T. Willis, H. Weil (University of Michigan), Verification of Disc
Scattering by the CWW (Full Wave) Method and Range of Validity

V. L. Pierce, H. Weil (University of Michigan), Absorption by
Spheres and Aggregates of Spheres

THURSDAY POSTER SESSION (continued)

Related Session

V. H. B. Lin, J. D. Everette, and B. Bronk (Naval Research
Laboratory and CRDEC), Various Geometrical Designs for
Electromagnetic Particle Traps and Their Characteristics

III. L. Radziemski, H. Bierwa (New Mexico State University),
Experimental Investigation of Effects following immediately after
the Formation of Laser Induced Breakdown Plasma

III. P. Chylek, M. Jarembski, V. Srivastava, R. Pinnick (NMSU),
Pressure Dependence of Laser Induced Breakdown of Aerosols
and Gases

III. K. M. Leung (Poly. Univ. NY), Effective Nonlinear Dielectric
Function of a Random Collection of Rayleigh Sized Particles

V. D. Cochoen (Temple University), Interrogation of Clouds of
Fibers— Mueller Matrix Entry Computation for Finite Length
Cylinders with Fixed or Random Orientation

V. D. Cochoen (Temple University), Theorems on Scattering by
Penetrable Dispersive Anisotropic Aerosol Particles

V. C. Richardson, R. L. Hightower (University of Arkansas),
Scattering Studies of Evaporation of Levitated Ammonium Nitrate
Droplets

V. G. Salzman and S. Singham (Los Alamos National Laboratory),
Scattering from Chiral Particles

V. R. A. Ellioth, T. Duracz, N. J. McCormick (Oregon Graduate
Center) Experimental Tests of a Time-Dependent Inverse
Scattering Algorithm

FRIDAY, 20 JUNE

V. OPTICAL PROPERTIES OF AEROSOLS (continued)

Moderators: *Robert H. Fricke* and *Burt V. Dront*

C. Multiple Scattering and Radiative Transfer

08:15 V. V. Varadan, V. K. Varadan, Y. Ma (Pennsylvania State University), Backscattering Enhancement of Waves in Random Media [15]

08:30 V. K. Varadan, V. V. Varadan (Pennsylvania State University), Electromagnetic Absorption by Chiral Materials [15]

08:55 Herschel Well (University of Michigan), Summary of Recent Progress on Aerosol Scattering and Absorption Analysis at the University of Michigan [25]

09:25 Yushih Ma (The Pennsylvania State University), Average Intensity Scattered by Densely Distributed Nonspherical Particles [15]

09:45 BREAK

10:05 Ezekiel Bahar, M. A. Fitzwater (University of Nebraska - Lincoln), Backscatter Enhancement of Infrared and Optical Radiation from Finitely Conducting Particles with Smooth and Very Rough Surfaces - First Order and Multiple Scatter [15]

10:25 K. A. Fuller, G. W. Kattawar (Texas A. & M. University), Light Scattering by an Arbitrary Cluster of Spheres [15]

VI. DISCUSSION

Moderator: *Edward W. Stubbins*

10:45 Directions for Future Research in the CRDEC Aerosol Science Program